NAS CR-66136

VOLUME V

BOOK 2

SUBSYSTEM AND TECHNICAL ANALYSES

AEROMECHANICS and THERMAL CONTROL

MARS PROBE

FINAL REPORT

CONTRACT NO. NAS 1-5224

AVCO CORPORATION

BOOK INDEX

COMPARATIVE STUDIES OF CONCEPTUAL DESIGN AND QUALIFICATION PROCEDURES FOR A MARS PROBE/LANDER

FINAL REPORT

VOLUME V SUBSYSTEM AND TECHNICAL ANALYSES

Book 2 AEROMECHANICS AND THERMAL CONTROL

Prepared by

SPACE SYSTEMS DIVISION
AVCO CORPORATION
Lowell, Massachusetts

AVSSD-0006-66-RR
Contract NAS 1-5224

11 May 1966

Prepared for

NATIONAL AERONAUTICS AND SPACE ADMINISTRATION
LANGLEY RESEARCH CENTER
LANGLEY STATION
Hampton, Virginia 23365

PREFACE

The results of Mars Probe/Lander studies, conducted over a 10-month period for Langley Research Center, NASA, are presented in detail in this report. Under the original contract work statement, studies were directed toward a direct entry mission concept, consistent with the use of the Saturn IB-Centaur Launch Vehicle, wherein the landing capsule is separated from the spacecraft on the interplanetary approach trajectory, some 10 to 12 days before planet encounter. The primary objectives of this mission were atmospheric sampling by the probe/lander during entry and terrain and atmosphere physical composition measurement for a period of about 1 day after landing.

Studies for this mission were predicated on the assumption that the atmosphere of Mars could be described as being within the range specified by, NASA Mars Model Atmospheres 1, 2, 3 and a Terminal Descent Atmosphere of the document NASA TM-D2525. These models describe the surface pressure as being between 10 and 40 mb. For this surface pressure range a payload of moderate size can be landed on the planet's surface if the entry angle is restricted to be less than about 45 degrees.

Midway during the course of the study, it was discovered by Mariner IV that the pressure at the surface of the planet is in the 4 to 10 mb range, a range much lower than previously thought to be the case. The results of the study were re-examined at this point. It was found that retention of the direct entry mission mode would require much shallower entry angles to achieve the same payloads previously attained at the higher entry angles of the higher surface pressure model atmospheres. The achievement of shallow entry angles (on the order of 20 degrees), in turn, required sophisticated capsule terminal guidance, and a sizeable capsule propulsion system to apply a velocity correction close to the planet, after the final terminal navigation measurements.

Faced with these facts, NASA/LRC decided that the direct entry from the approach trajectory mission mode should be compared with the entry from orbit mode under the assumption that the Saturn 5 Launch Vehicle would be available. Entry of the flight capsule from orbit allows the shallow angle entry (together with low entry velocity) necessary to permit higher values of M/C_DA, and hence entry weight in the attenuated atmosphere.

It was also decided by LRC to eliminate the landing portion of the mission in favor of a descent payload having greater data-gathering capacity, including television and penetrometers. In both the direct entry and the entry from orbit cases, ballistic atmospheric retardation was the only retardation means considered as apecifically required by the contract work statement.

Four months had elapsed at the time the study ground rules were changed. After this point the study continued for an additional five months, during which

period a new design for the substantially changed conditions was evolved. For this design, qualification test programs for selected subsystems were studied. Sterilization studies were included in the program from the start and, based on the development of a fundamental approach to the sterilization problem, these efforts were expanded in the second half of the study.

The organization of this report reflects the circumstance that two essentially different mission modes were studied -- the first being the entry from the approach trajectory mission mode and the other being the entry from orbit mission mode -- from which two designs were evolved. The report organization is as follows:

Volume I, Summary, summarizes the entire study for both mission modes.

Volume II reports on the results of the first part of the study. This volume is titled Probe/Lander, Entry from the Approach Trajectory. It is divided into two books, Book 1 and Book 2. Book 1 is titled System Design and presents a discursive summary of the entry from the approach trajectory system as it had evolved up to the point where the mission mode was changed. Book 2, titled Mission and System Specifications, presents, in formal fashion, specifications for the system. It should be understood, however, that the study for this mission mode was not carried through to completion and many of the design selections are subject to further tradeoff analysis.

Volume III is composed of three books which summarize the results of the entry from orbit studies. Books 1 and 2 are organized in the same fashion as the books of Volume II, except that Book 2 of Volume III presents component specifications as well. Book 3 is titled Development Test Programs and presents, for selected subsystems, a discussion of technology status, test requirements and plans. This Book is intended to satisfy the study and reporting requirements concerning qualification studies, but the selected title is believed to describe more accurately the study emphasis desired by LRC.

Volume IV presents Sterilization results. This information is presented separately because of its potential utilization as a more fundamental reference document.

Volume V presents, in six separate books, Subsystem and Technical Analyses. In order (from Book 1 to Book 6) they are:

Trajectory Analysis
Aeromechanics and Thermal Control
Telecommunications, Radar Systems and Power
Instrumentation
Attitude Control and Propulsion
Mechanical Subsystems

Most of the books of Volume V are divided into separate discussions of the two mission modes. Table of Contents for each book clearly shows its organization.

CONTENTS

CONTENTS (Cont'd)

CONTENTS (Cont'd)

CONTENTS (Cont'd)

CONTENTS (Cont'd)

CONTENTS (Cont'd)

CONTENTS (Concl'd)

ILLUSTRATIONS

ILLUSTRATIONS (Cont'd)

ILLUSTRATIONS (Cont'd)

ILLUSTRATIONS (Cont'd)

ILLUSTRATIONS (Cont'd)

ILLUSTRATIONS (Cont'd)

ILLUSTRATIONS (Cont'd)

ILLUSTRATIONS (Cont'd)

ILLUSTRATIONS (Cont'd)

ILLUSTRATIONS (Cont'd)

ILLUSTRATIONS (Con t'd)

ILLUSTRATIONS (Cont'd)

ILLUSTRATIONS (Cont'd)

ILLUSTRATIONS (Cont'd)

ILLUSTRATIONS (Cont'd)

ILLUSTRATIONS (Cont'd)

ILLUSTRATIONS (Cont'd)

ILLUSTRATIONS (Cont'd)

ILLUSTRATIONS (Cont'd)

ILLUSTRATIONS (Cont'd)

ILLUSTRATIONS (Cont'd)

ILLUSTRATIONS (Concl'd)

TABLES

TABLES (Cont'd)

TABLES (Cont'd)

TABLES (Cont'd)

TABLES (Cont'd)

TABLES (Concl'd)

ACKNOWLEDGEMENT

Responsible Managers

R. M. Davis
O. L. Zappa

Major Contributors

Name	Sections
P. T. Andrews	2, 3, 4
Boehringer, J. C.	8, 10
H. P. DeMoss	9
H. Hurwicz	11 12
R. W. Johnson	5, 6, 7
H. R. Meck	5, 6, 7
B. M. Morgan	2, 3, 4
T. R. Munson	10
P. J. Norton	5, 6, 7
T. J. O'Neill	8
J. J. Pierro	5, 6, 7
A. F. Robb	2, 3, 4
H. F. Steinle	11, 12
Wagner, R. W.	2, 3, 4

Approved by

Signature	Title
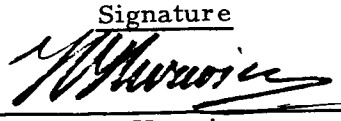 H. Hurwicz	Sr. Project Manager, Aeromechanics

PRECEDING PAGE BLANK NOT FILMED.

1.0 INTRODUCTION AND SUMMARY

1.1 SCOPE OF THE STUDY

This book describes the aerodynamics, thermodynamics, structural mechanics, and thermal control studies which led to the definition of the entry-shell environments, conceptual designs, and performance characteristics. Various vehicle configurations, mission concepts and selected modes of system operation were investigated.

The mission specifications (described in detail elsewhere in this report) established the basic vehicle requirements, design constraints and guidelines. They formed the basis for the parametric studies of interactions between the often contradictory requirements of the elements of the shell and the overall system, and were used as feedback in the system optimization and tradeoff studies. As a rule, both nominal and failure modes for critical design conditions were analyzed prior to the selection of reference designs for performance evaluation.

The study, as originally planned, was to have been divided into two parts. Part I was to consist of parametric studies involving mainly evaluation of three or four aerodynamic shapes, selection of critical design conditions (including atmospheres) and failure modes. Concurrently, structural and heat shield weight fractions for the critical conditions were to be evaluated as a function of the mission concepts, aerodynamic shape, size (diameter) and geometry, structural concepts and materials, and heat shield concepts and materials. The scope of the parametric variation of vehicle flight envelope and characteristic parameters (V_e, γ_e, α_e, M/C_DA etc.) of necessity was to be somewhat limited for the structural and thermal studies until a more definitive design was established. The same approach was to be taken in the thermal control analysis where the purpose was to establish the parametric relationships between power requirements, thermal control coating characteristics and the resulting temperature histories throughout the mission sequence, to be then used in the selection of a control system for a chosen reference design. The outcome of these studies was to be used in the overall systems tradeoffs, and selection of a conceptual design limited to one generic shape and a mission concept.

In Part II, the conceptual design was to have been evaluated in detail. While, for instance, the shape, diameter, materials, and some of the mission constraints were to be fixed, variations in the operating map (V_e, γ_e, α_e, spin, M/C_DA etc.) resulting from systems considerations were to be evaluated in both nominal and failure modes. More detailed thermostructural studies were to have been conducted, and more rigorous analytical methods were to have been used especially for the final performance analysis.

This plan was essentially executed as far as the contents of the analysis was concerned; however, a major extension in the scope of the study was required

as a result of Mariner IV Mars atmospheric data. (See the Preface to this book.) Consequently, in Part I a probe/lander mission, with direct entry from the approach trajectory was evaluated; in Part II the mission was changed to a probe mission, with entry from orbit, with the attendant changes in the system. The extent of some of the parametric studies in Part I was reduced, but some of the probe/lander preliminary performance data (previously to be supplied under Part II) was provided. On the other hand, it was necessary to extend the scope of the parametric analysis in Part II and repeat some of the previously performed tradeoff studies for the selected aerodynamic shape.

In summary, the study was performed in two parts: the first was the conceptual design and analysis of the probe/lander, direct entry from the approach trajectory. This part was of a broad nature as covering several aerodynamic shapes, configurations and mission concepts coupled with the evaluation of a number of structural and heat shield concepts and materials for several system perturbations. The second part was of a more limited scope in that only one blunted-cone forebody aerodynamic shape (with three afterbodies) was considered. Several nominal and failure entry modes were evaluated as dictated by other system constraints. One mission concept (entry from orbit) was treated, but extensive evaluation of the entry operational map was performed. A minimum of practical structural and heat shield materials and concepts were studied, but the methods of analysis were more advanced and rigorous in nature. A rather detailed analysis of the thermal control system was conducted, leading to establishment of the basic coatings and power requirements and the evaluation of their performance for the reference design and mission sequence.

The arrangement of this book reflects the phasing of the work. Within each of the technical areas - Aerodynamics, Structures, Heat Shield and Thermal Control - a chapter on the analysis of the conceptual designs is first presented for entry from the approach trajectory, and then a chapter for entry from orbit. For each area, a chapter is provided describing the theoretical analysis and methods used in the conceptual design. The conceptual design studies are basically divided into three parts: the parametric studies, a description of the reference design and concepts, and finally, the performance analysis for various modes of entry and other flight phases.

A summary follows for both the Entry from the Approach Trajectory and Entry from Orbit modes and a comparison is made.

1.2 PROBE/LANDER, ENTRY FROM APPROACH TRAJECTORY

A broad parametric study of aerodynamic, structural and thermal protection configurations, for several mission concepts, atmospheres and aerodynamic shapes, and for various system requirements, was conducted to determine critical design conditions and to select conceptual design(s) of probe/lander direct entry from approach trajectory.

1.2.1 Requirements, Constraints, and Criteria

The objectives of the study were to:

(1) Analyze and define the critical environments and design conditions for the flight capsule and entry shell throughout its operational sequence from assembly to landing;

(2) Provide conceptual design of the entry-shell structure and heat shield to survive this environment;

(3) Analyze thermal control requirements to provide the required thermal environment for payload, components, entry-shell and sterilization canister;

(4) Optimize the entry-shell performance (minimize the weight fraction of heat shield and structure) and minimize the power required from the spacecraft.

Detailed requirements, constraints and criteria used in the conceptual analysis are given in Sections 2.0, 5.0, 8.0, and 11.0 of this book, respectively for aerodynamics, structures, heat shield, and thermal control. A summary of the study constraints and guidelines is shown in Table I. They were bounded by the conditions shown later in Figure 4. The blunt cone, modified Apollo and tension shell configurations used in this study are schematically represented in Figures 1, 2, and 3 in Section 2.0.

Four mission concepts were originally investigated:

(1) Multi-mission shell (heat shield and structure) design

(2) Multi-mission structure design (heat shield designed for each mission)

(3) 1971 mission structure and heat shield design

(4) Future mission shell designs.

As a result of the parametric studies and other considerations, the first of these concepts as well as the use of the Model 1 atmosphere were eliminated. The final concepts for which the bulk of the data is provided were:

(1) Multi-mission structure, 1971 heat shield (reference design)

(2) 1971 structure and 1971 heat shield

(3) Future mission (atmosphere model 3) shell

TABLE I

REQUIREMENTS AND CONSTRAINTS ENTRY FROM APPROACH TRAJECTORY

Entry Condition Parameters	Range of Parametric Values	Entry Parameter for Critical Design Conditions					
		Blunt Cone		Blunt Tension		Modified Apollo	
		Loads	Heating	Loads	Heating	Loads	Heating
A. Entry Conditions							
Nominal Entry							
Velocity (ft/sec)	18 to 25,000	23,000	23,800	23,800	23,800	23,800	23,800
Entry Angle (degrees)	-20 to -90	-90	-20	-90	-20	-90	-20
Altitude (feet)	800,000 to 2,500,000	800,000	800,000	800,000	800,000	800,000	800,000
Angle of Attack for: (degree)							
1971 Mission	11 to 60	19.5	α at $(\dot{q})$ max	----	α at $(\dot{q})$ max	21.8	α at $\dot{q})_{max}$
Multi-Mission	11 to 60	15.8	α at	----	α at	10.6	α at $\dot{q})_{max}$
Future Mission	11 to 60	----	α at	----	α at	----	α at $\dot{q})_{max}$
Spin Rate	1 to 8	----	Lunar Motion	----	Lunar Motion	----	Lunar Motion
Failure Mode							
Angle of Attack (degree)	0 to 360	240	240	----	----	179	179
Spin Rate (Rad/sec)	0 to 2	0.2	0.2	0.2	0.2	0.2	0.2
Atmospheres							
1971 Mission	1, 2, 3	3	2	3	2	3	2
Multi-Mission	1, 2, 3	3 and 2	2	2	2	3 and 2	2
Future Mission	1, 2, 3	3	3	3	3	3	3
B. Vehicle Parameters							
M/C_DA (slugs/ft^2)							
1971 Mission	0.15 to 1.69	0.15	0.15	0.15	0.15	0.15	0.15
Multi-Mission		0.487 or 0.15	0.15	0.492	0.15	0.465 or 0.15	0.15
Future Mission		0.15	0.487	0.15	0.492	0.15	0.465
Maximum Weight (pounds)	4500	4500	4500	4500	4500	4500	4500
Allowable Weight (pounds)							
1971 Mission		1390	1390	1435	1435	1450	1450
Multi-Mission		4500 or 1390	1390	4500	1435	4500 or 1450	1450
Future Mission		1390	4500	1435	4500	1450	4500
Diameter (inches)	150, 170, 180, 200	180	180	180	180	180	180
R_N/R_B	Depending on the Shape	0.25	0.25	0.1	0.1	2.4	2.4
Half Angle (degrees)		60	60	----	----	----	----
C. Terminal Descent Constraints							
Reefed Chute Mach No.	1.3	1.3	1.3	1.3	1.3	1.3	1.3
Full Deployment Mach No.	0.8	0.8	----	0.8	----	0.8	----
Full Deployment Altitude (feet)	15,000	15,000	15,000	15,000	15,000	15,000	15,000
D. Thermal Control							
As dictated by selected component, heat shield, structure and flight phase temperature and power limitations (see Table LXXXVII).							

1.2.2 Performance Characteristics and Comparison of Conceptual Designs

The results of the aerodynamic, structural, thermodynamic and thermal control analyses are given in paragraphs 2.1, 5.1, 8.1 and 11.1, of this book. They are summarized and compared in Table III in paragraph 1.3 with the results of the study of the probe, entry from orbit mission, for the blunted cone reference design. The critical environments and design conditions, and the resulting structure and heat shield requirements for various materials investigated are indicated. They form the basis for the conclusions to be drawn relative to the merits of configurations to be optimized, and the existing thermal control problems. The theoretical analysis and methods used for design are described in Sections 4.0, 7.0 and 10.0. Review of the results, problem areas, and conclusions reached leads to the following general conclusions and comments.

The structure of the multimission tension shell is about 20 percent lighter than that of the blunt cone. However, the combined heat shield structure weight is lower for the blunt cone for the light payload vehicle and considerably lighter for the heavy payload vehicle. A comparison of the blunted cone and modified Apollo shapes showed that although the latter has a lighter heat shield, it has a heavier structure. This is true for all the concepts examined except perhaps for the future mission concept where the difference in structural weight may not compensate for the low weight of the Apollo heat shield. Considering the uncertainties in the absolute weight calculations and the fact that only the basic structure and heat shield are compared, the two shapes appear comparable. Aerodynamic considerations, indicate a higher drag potential, as well as a less severe thermal environment (as evidenced by heat shield weights) in spite of the higher radiative heating contribution for the modified Apollo configuration. The availability of meaningful test data also favor the blunt cone and to a lesser degree the modified Apollo shapes.

Of the four heat shield materials examined in the course of the study, the cork silicone appeared to result in lowest thermal protection weights. The acquisition of additional material property and characteristics could reverse some of the trends observed and change the ranking of the materials. All the candidate materials appear to be compatible with the structure for the temperature histories estimated. Honeycomb sandwich construction utilizing beryllium face sheets and stainless steel core results in lower weights than other structural materials and construction methods considered.

The effect of the rearward entry may result in significant weight penalties (because of relatively high heating levels and large exposed areas in that mode) on the backface of the structure and the afterbody. It should be noted that the heat shield weights required for thermal protection for this failure mode were not calculated. These possible penalties point to the

need for further heating analysis (and experimental data) and selection of proper material for this portion of the vehicle.

The analysis of thermal control requirements indicated that the post-separation and post-landing phases were critical since the batteries tended to cool off rapidly without an additional source of power. The problem (which appeared to be easier to manage for the tension shell) may be resolved by preseparation warmup and insulation of the batteries. The postlanding situation will be less critical for the oblate spheroid landed capsule. A more detailed performance analysis was made in the entry from orbit study. The validity of the results will depend on the final definition of the flight spacecraft-flight capsule thermal interface.

The combination of the initial design and environmental factors in conjunction with the lack of complete system definition and the lack of a complete body of aerodynamic experimental data and proper heat shield material characterization, may well have resulted in conservative weight estimates for nominal entry. The next iteration of the results and incorporation of the system and design data of similar nature to that described in the entry from orbit study might have resulted in weight savings.

1.2.3 Technology Status and Problem Areas

In the course of the study several problem areas were indicated. These relate broadly to either a lack of basic experimental information or to difficulties due to a problem complexity heretofore not encountered which resulted in a lack of directly applicable analytical methods.

A great deal of experimentation will be required to assure increased confidence in the design to be evaluated. The experiments will be required to determine the real-gas effects to establish drag coefficients and to provide the coefficients required to confirm static and dynamic stability. The predictions of the afterbody performance will have to be corroborated by testing. The heat shield design will require a comprehensive test program to characterize the heat shield material performance particularly under the Martian entry conditions including the effect of radiative heating.

Use of more rigorous structural and thermodynamic analytical methods will be necessary (as was done in the entry from orbit study to cope with the complexity of the problems presented by this study for all the shapes considered, while a particular effort will be required to aerodynamically and structurally analyze and test the tension shell.

The main problem in the thermal control system design and performance analysis lies in the definition of the spacecraft-capsule thermal interface. The final selection of coatings and capsule power requirements hinge on this definition.

By the nature of the conceptual design and analysis, the results obtained in this phase may deviate somewhat from those shown in vehicle layouts and inboard profiles. The conceptual design is carried out on fixed reference concepts and values which are expected to change in the actual design process due to practical overall system and manufacturing considerations. This in turn would necessitate another analytical iteration.

1.3 PROBE, ENTRY FROM ORBIT

A study of a 60-degree blunted cone entry shell utilizing practical (state-of-the-art) structural and thermal protection configurations for several orbital trajectories and flight envelope parameters (V_e, γ_e ; α and M/C_DA), was conducted to determine the critical design conditions in terms of the atmospheres and failure modes. The entry shell and thermal control preliminary designs were established and their performance was evaluated for the probe entry from orbit.

1.3.1 Requirements, Constraints, and Criteria

Although the scope of this phase of the program was limited to one aerodynamic shape and thus was less general than the previous one, a much more detailed performance analysis was conducted for a specific preliminary design. The objectives of the study were essentially the same as for entry from direct approach; however, more emphasis was put on rigorous analytical methods applied to the state-of-the-art materials and concepts. A comprehensive analysis was made of power requirements from the spacecraft for thermal control. The effect of the spacecraft-capsule thermal interface on control system and temperature distribution was studied in more detail.

Detailed requirements, constraints and criteria used in the conceptual analysis and preliminary design are given in Sections 3.0, 6.0, 9.0, and 12.0 of this book, for aerodynamics, structures, heat shield and thermal control, respectively. The common study constraints and guidelines imposed by the system (including communication requirements) and selected missions are reflected in the summary Table II. The blunt cone entry shell configuration, used in the study is shown in Figures 79 to 81 of Section 3.0. As may be seen from Table II, preliminary concepts considered for nominal and failure modes depended on spin and despin for control of ACS system failure; for the reference design, which utilized an active attitude control system, tumble was the critical failure mode design condition. Since ΔV considerations allowed a finite (invariant) spent shell weight, increase in M/C_DA was no consideration in the failure mode. Furthermore planet rotation was taken into account for performance evaluation for the Syrtis Major impact area.

TABLE II

REQUIREMENTS AND CONSTRAINTS
ENTRY FROM ORBIT

A. Entry Condition - Nominal Entry

1.

Entry Condition Parameters	Range of Parametric Values	Critical Design Conditions ACS			
		Preliminary Concept*		Reference Design**	
Nominal Entry		Loads	Heating	Loads	Heating
Velocity (ft/sec)	10,000 to 16,000	15,350	15,250	15,200	15,200
Entry Angle (degrees)	-30 to skip limit	18	13.5	16	14
Angle of Attack (degrees)	0 to 180	0	0	0	0
Spin Rate (rad/sec)	0 to 5	0	0	0	0

*Same afterbody configuration as in entry from Orbit Trajectory.

**Modified afterbody configuration.

TABLE II (Cont'd)

B. Entry Conditions - Failure Mode

2.

Entry Condition Parameters	Critical Design Conditions (ACS)							
	Preliminary Concept*				Reference Design**			
	Spin		Spin Despin		Design (tumble)		Syrtis Major Impact (tumble)	
	Loads	Heating	Loads	Heating	Loads	Heating	Loads	Heating
Velocity (ft/sec)	12, 700	12, 900	12, 700	12, 900	15, 200	15, 200	15, 200	15, 200
Entry angle (degrees)	17.9	12.8	17.9	12.8	16	14	16	14
Angle of attack (degrees)	90	86	90	86	180	90***	180	90***
Spin rate (rad/sec)	4.18	4.18	4.18 → 0	4.18 → 0	0.1	0.1	0.1	0.0
Azimuth (degrees)	-	-	-	-	0	-	40	60
Atmospheres (range of parametric study VM-3, 4, 7 & 8)	VM-8	VM-7	VM-8	VM-7	VM-8	VM-7	VM-8	VM-7

* Same afterbody configuration as in Entry from Approach Trajectory
** Modified afterbody configuration
*** Critical for maximum diameter region.
(for the afterbody-180 degree used; remainder of forebody-0 degree used)

TABLE II (Concl'd)

C. Vehicle Parameters

3.

Entry Condition Parameters	Range of Parametric Values	Critical Design Conditions (ACS)							
		Preliminary Concepts*				Reference Design**			
		Spin		Spin Despin		Design (tumble)		Syrtis Major Impact (tumble)	
		Loads	Heating	Loads	Heating	Loads	Heating	Loads	Heating
M/C_DA (slug/ft^2)	.15 → .33	.24	.24	.24	.24	.22	.22	.22	.22
W (pounds)	1500° → 3000	2279	2279	2279	2279	2040	2040	2040	2040
D (inches)	60 → 180	180	180	180	180	180	180	180	180

D. Terminal Descent Constraints

Entry Condition Parameters		
Reefed Chute Mach No.	1.2	→ 1.2
Full Deployment Mach No.	Subsonic	→ Subsonic
Full Deployment Altitude (feet)	15,000	→ 15,000
Minimum Descent Time (secs)	160	→ 160
Maximum Descent Time (secs)	360	→ 360

E. Thermal Control

As dictated by the component, heat shield and structure temperature and compatibility limitations, and defined by power availability and flight phase requirements. (See Table XCVIII)

Constraints imposed on the entry capsule during all phases of flight were taken into account in the structural design as the entry shell, the internal structure and the adapter were analyzed. Constraints possibly imposed on the heat shield material during low-temperature soak were also considered.

Finally, as a result of refinement of the orbit and dispersion analysis, the V-γ operational map was further restricted and limited to somewhat lower entry angles than the earlier concepts. This resulted in a decrease in critical loads for the upper entry angle limit, as well as a decrease in heating due to the concurrent change in the angle of attack histories for the reference design failure mode (tumble). The latter change shifted the heat shield design point to a higher entry angle and velocity.

1.3.2 Performance Characteristics

The results of the analyses and the resulting performance characteristics of the reference design are summarized in paragraphs 3.1, 6.1, 9.1 and 12.1 of this book. The preliminary and reference design are compared for nominal and failure modes. They are also discussed and compared with the results of the study of probe/lander entry from approach trajectory for the blunted cone design in Table III of paragraph 1.4. The critical environments and design conditions and the resulting structure, heat shield, and thermal control reference designs are indicated. The theoretical analysis and methods used are described in Sections 4.0, 7.0 and 10.0.

The conceptual design considered in this phase of the study was the blunted-cone configuration which evolved from previous studies. However, as noted previously, the drastic change in the character of the mission necessitated additional parametric studies to define the operational map, afterbody configuration and a new design philosophy or concept. All concepts considered employed an attitude control system (ACS). However, to design for the critical entry mode it was necessary to evaluate the effect of a backup stabilization system and/or the failure mode resulting from ACS malfunction. The first of the early concepts utilized spin to minimize dispersion due to thrusting errors, while the second (spin-despin) introduced despin to alleviate or minimize the heavy penalty associated with the first. In both cases the penalty was due to the effect of large angles of attack, coning angles and rates which converged slowly for the spin stabilized vehicles. This effect was most pronounced for low velocities. A further weight penalty was due to consideration of the increased M/C_DA for ΔV rocket malfunction resulting in unspent fuel and thus increased entry weight.

As a result of these studies the spin backup system was dropped from consideration, and instead angular rate control ("sentry") was adopted and "tumble" became the reference design failure mode. The reference design angle of attack envelope converged faster than for the earlier concepts, and the weight penalty was considerably smaller. The ΔV malfunction was eliminated from consideration.

In all concepts, the angle of attack resulted in exposure of the maximum diameter area to prolonged stagnation heating and an ensuing increase in weight. For the spin case, it was due to the separation geometry and vehicle orientation at entry, while for the reference design it represented the extreme of random entry. In addition, the high angles of attack effectively increased the M/C_DA and thus further increased the loads and heating.

The spin and tumbling concepts were reflected in the structural and heat shield design. The structure net weight savings for the reference design case would amount to about 10 percent, if the nosecap material and base-ring dimensions were not changed. In the primary heat shield the savings were of the same order for the same bondtime temperature, however, the weight of the secondary and afterbody heat shield was reduced by more than 50 percent (including the effect of the smaller afterbody). Since higer M/C_DA (for the tumble failure mode) allowed higher entry weights, the effect on the total weight fraction was even more pronounced. The entry shell was designed by critical entry loads with consideration of cold-soak induced stresses. The internal structure and adapter were designed by parachute deployment and launch loads respectively. Safety factors selected for the reference design ranged from 1.0 to 1.5 for the structure and 1.2 for the heat shield.

Evaluation of the entry-shell performance for the rotating planet Syrtis Major impact area, indicated conservatism for both the structural and heat shield design in excess of these provided by safety factors used; this was due to the conservatism in both dynamics and rotating planet effect.

The performance of the thermal control system was evaluated for the nominal case of a 1000 by 10, 000-km orbit, and typical flight spacecraft-flight capsule interface. All phases of the flight were considered and a nominal power requirement of 200-300 watts (including maximum peak demand) was established for state-of-the-art coatings and heating elements supplying heat to the heat shield and critical components. A possibility of weight saving in the shell was indicated by lowering the initial entry temperatures depending on the actual power supplied.

As a result of this study it was concluded that the updating of the atmospheric data and change to entry from orbit, although resulting in lower entry velocities did not significantly reduce the severity of the heating environment; the aerodynamic loading decreased by an order-of-magnitude. The angle of attack and spin effects combined with shallow entry angles produced the relatively high heat shield weights, and resort to ACS with limited failure mode consideration was desirable to minimize the weight penalty.

Practical structural materials were shown to be sufficient for the application. An acceptable weight fraction resulted and large safety margins often occurred due to minimum gage requirements. For the low range of pressures encountered, the shell weight was found to be a weak function of pressure. The investigation of thermo-structural compatibility showed large safety margins for the ablator; however, the stresses in the aluminum honeycomb sandwich shell approach critical buckling stress for hydrostatic pressure loading.

The thermal protection study showed that Purple Blend, Mod 5, was a typically desirable material for the heat shield, and that for this application it was more efficient than cork silicone. The studies revealed the necessity of use of rigorous ablation-conduction analysis for proper comparison of material performance. Possible weight savings are anticipated for lower entry temperatures; but such a conclusion must be held in abeyance until more detailed material characterization studies are conducted and the assumption of the effect of Mars atmospheric composition on surface reactions is verified and its effect on safety margins is determined.

1.3.3 Technology Status and Problem Areas

The technology status and the problems anticipated in the entry-shell design for entry from orbit are not at variance with the previous phase of the study.

The rearward entry mode indicates significant weight penalties and points again to the need for further heating analysis and experimental data, and perhaps selection of a more efficient material for this segment of the vehicle.

A preliminary study indicates feasibility of the use of smaller afterbodies with flaps for assurance of rearward instability. Further test data are required to confirm that as well as the elimination of transonic stability problems. Experimentation is also required to establish real-gas effects on pressure and heating distributions and aerodynamic performance derivatives for the whole body.

The low-density effects were augmented in this case due to high-density ratios present. Vorticity interaction accounts for a 15-percent heating increase on the whole body while an additional 40-percent increase over the conical portion was due to varying entropy.

The more advanced structural and thermodynamic analysis methods used in this phase of the study appear to be satisfactory, but require experimental verification. Thus an extensive heat shield material characterization program will be required to assure confidence in the design, to determine

mechanical characteristics for low-temperature soak and to determine the effect of decontamination, sterilization, and vacuum exposure on thermal and mechanical characteristics. This is of importance since the heat shield weight fraction is of the order of 15-20 percent.

The method of analysis developed for determination of the stiffness requirement of the aft ring appears to give satisfactory criteria but also requires experimental verification. The determination of design criteria for sandwhich shell structures for failures associated with core strength and stiffness presents problems (present analyses are extensions of results for plates and columns). Design criteria for ground handling of very light shell structures should be established to evaluate their effect on the design.

The application of the heat shield to the structure and the thermal control coating to the heat shield will require investigation. In the first case, unbonded areas may create problems during cold soak in addition to the usual problems during entry. In the second case, degradation of optical performance may be expected and must be established for correlation with power requirements.

Finally, the thermal interface between the spacecraft and capsule may seriously affect the thermal control design and operation as well as heat shield weight and must be defined before finalizing the design.

1.4 COMPARISON OF ENTRY FROM APPROACH TRAJECTORY AND ENTRY FROM ORBIT

The direct entry from approach trajectory and the entry from orbit studied during this program present a rather diverse approach to Mars exploration. To satisfy the two different mission objectives and ensuing payloads different design philosophy was evolved. While the entry from approach trajectory design was critically weight limited, the weight was not the major consideration in entry from orbit studies. This significantly affected the choice of structural and heat shield materials and concepts.

Although widely differing in mission objectives and payloads, the two approaches may be easily compared in terms of the entry shell environments and aerodynamic performance. After this, direct comparison becomes more involved. On the one hand, many of the design criteria, constraints, and assumptions had to be changed with a change in the mission objectives and concepts and, on the other hand, the differences in the environments and aerodynamic performance make direct comparison of structural, thermal and thermal control performance difficult. Finally, the entry from approach trajectory design was more general and conceptual in nature, while the entry from orbit design was more specific. Detailed comparison of environments and aerodynamic performance is given in paragraph 2.3.1. It is noted that heating resulting from use

of Model 2 and VM-7 atmospheres should be similar, while loads should be somewhat higher for VM-8 compared with Model 3 atmosphere (everything else being equal). However, selection of the $V_e - \gamma_e$ operational map for the reference design for entry from orbit resulted in a significant reduction of entry velocities and shallow (near skip) entry angles. As a result, the loads decreased by an order-of-magnitude and the radiative heating became negligible. The integrated stagnation heating did not change significantly because of the long duration of the heat pulse (low γ_e) and the low-density effects (vorticity interaction and entropy variation increased the heating). Furthermore, consideration of high angles of attack for the entry from orbit design resulted in an order-of-magnitude heating increase at the maximum diameter point which is the most sensitive to weight changes. Thus, even though the decrease in loads permitted the use of conventional structural materials and concepts, the heat shield design requirements could not be relaxed. In this respect, it should be noted that the heat shield design for entry from approach trajectory did not account for the rearwards (tumble) failure mode while it did for the entry from orbit. The dynamic behavior was satisfactory and similar. Primary differences were associated with spin cases and were due to the separation geometry which produced higher angles of attack and rates because of the large magnitude of the thrust vector for entry from orbit.

The basic comparison of the structural and thermal protection aspects of the two reference designs is shown in Table III. The aerodynamic environment, and some design conditions and criteria are also shown as a background for the comparison. It may be noted that in spite of the seeming relaxation of entry conditions for the entry from orbit case, no major structural (not including the internal or adapter structures) or heat shield weight savings were realized. In addition, although the loads decreased sizeably, the weights did not decrease proportionally because of the use of more conventional materials made feasible by lower surface pressures. This was due to: (a) minimum gauge limitations introducing insensitivity to load variation relative to the entry from approach trajectory case, and consequently higher safety margins, and (b) the use of aluminum for entry from orbit instead of beryllium (had aluminum been used in entry from approach trajectory case, the entry-shell structure weight would have been doubled). On the other hand, the use of the multi-mission structure for the 1971 entry from approach trajectory mission imposed a 16-percent weight penalty.

The primary heat shield weight fraction, on the other hand, decreased although contraindicated to some extent by the a priori heating environment analysis described above. This was due to a combination of several factors: (a) the higher allowable entry from orbit weight, due to increased M/C_DA, more than compensated for the attendant additional heat shield weight; (b) the higher heat capacity of the structure was accounted for and a larger temperature increase at the bond line was allowed for the entry from orbit design; (c) the response of the heat shield was calculated at parachute deployment rather than using the conservative calculations until impact for the entry from approach trajectory

TABLE III

COMPARISON OF THE STRUCTURAL AND HEAT SHIELD DESIGNS FOR ENTRY FROM APPROACH TRAJECTORY AND ENTRY FROM ORBIT

Design Concept / Flight Envelope and Vehicle Parameter	Structure (Entry Shell)				Heat Shield			
	Entry From Approach Trajectory		Entry from Orbit		Entry From Approach Trajectory		Entry from Orbit	
	Multimission Structure							
	Light Vehicle (Ref. Mission)	Heavy Vehicle (Ref. Structure)	Reference Design	Spin (40 RPM)	Heavy Vehicle (Future Mission)	Light Vehicle (1971 Mission & Multimission (Ref. Design & Mission)	Reference Design	Spin (40 RPM)
D - vehicle diameter (feet)	15	15	15	15	15	15	15	15
W - vehicle weight (pounds)	1390	4500	2040	1855	4500	1390	2040	1885
V_e - entry velocity (ft/sec)	23,800		15,200	12,700	23,800		15,200	12,900
γ_e - entry angle (degrees)	-90		016.0	-17.8	-20		-14	-12.8
M/C_DA - ballistic coefficient (slugs/ft^2)	0.15	0.49	0.22	0.20	.49	.15	.22	.20
Atmosphere Model	3	2	VM-8		3	2	VM-7	
α_e - entry angle of attack (degrees)	179		179	90	11		90	86
α peak heating - angle of attack (degrees)	37	-	-	-	1	1	11	59
α peak loads - angle of attack (degrees)	20	16	10	27	-	-	-	-
P_{stag} - pressure (lb/ft^2)	2020	2870	229	358	835	152	-	-
A_x axial acceleration (g)	209	91	15.5	29	28.1	16.5	-	-
A_n normal acceleration (g)	18.9	5.6	0.6	2.1	-	-	-	-
Q_{stag} - integ. heating (Btu/ft^2)	1226	2845	1300	1010	4405	2798	2227	2052
$q_{stag\ max}$ - heating rate (Btu/ft^2/sec)	311	323	33	44	188	70	18.6	23.6
$Q_{max\ diam}$ - integ. heating (Btu/ft^2)	-	-	745	-	1890	803	1705	6240
$q_{max\ diam}$ - heating rate (Btu/ft^2/sec)	-	-	32.2	-	93	20	24	79
Pulse duration (seconds)	18	60	80	46	85	130	240	220
$T_{bondline}$ - temperature (°F)	-	-	-	-	300-500		500	
$T_{at\ entry}$ - temperature (°F)	-	-	-	-	100-300		100	60
Thermal safety factor	-	-	-	-	1.0		1.2	
End of pulse	-	-	-	-	Impact		Parachute deployment	
Structural material	Beryllium		Aluminum		Beryllium (0.020")		Aluminum	
Structural concept	Steel Core Honeycomb Sandwich		Al. Core Honeycomb Sandwich				Al. Core Honeycomb Sandwich	
Heat shield material	cork silicone		Purple Blend, Mod 5		cork silicone		Purple Blend Mod 5	
Approximate weight fraction (forebody only) (percent)*	31	10	17	19	7	20	14	15
Approximate total weight fraction (percent)*	-	-	24	27	-	-	19	28

*(Includes 20-percent contingency)

case; and (d) more rigorous evaluation methods of the ablator performance together with a change in the material possibly tended to decrease the weight estimates. On the other hand, the use of a safety factor of 1.2 together with the rearwards entry or tumble failure mode for the entry from orbit design as opposed to no safety factor and no failure mode for the entry from approach trajectory would tend to increase the weight of the entry from orbit reference design.

The comparison of the thermal control designs for the two cases is even more difficult to execute, since only preliminary evaluation (rather than design) was performed for the entry from approach trajectory case. It is clear, however, that elimination of the post-impact requirement facilitated the thermal control design, and that the much shorter postseparation period alleviated the power requirement present in the entry from approach trajectory case for this phase of the mission. On the other hand, a more detailed treatment of the entry from orbit thermal control design and use of a more conservative spacecraft-flight capsule interface indicated higher power demand on the spacecraft for joint operation during cruise and Mars orbit. This demand, however, does not seem to be exorbitant even for the peak period. In either case, thermal control coatings of relatively low emissivity ($\epsilon = 0.05$) and heating elements were required. The heating element distribution for entry from orbit included heaters in the heat shield substructure, while only the components were directly heated in the other case.

2.0 AERODYNAMICS - CONCEPTUAL DESIGN PROBE/LANDER, ENTRY FROM THE APPROACH TRAJECTORY

2.1 INTRODUCTION AND SUMMARY

Aerodynamic analyses fulfill two basic functions within a parametric study: 1) the definition of the environments which lead to the selection of the design criteria, and 2) the evaluation of the performance and stability of the candidate shapes to provide a means for selecting a reference configuration.

The specifying of the environments requires knowledge of the flow-phenomena extant which are dependent upon the trajectories to be flown and the atmospheric model (composition).

The flow-field analyses were conducted for entry from the approach trajectory for three generic shapes: a blunted cone ($R_N/R_B = 25$, $\theta_c = 60$ degrees), a modified Apollo and a blunt tension shell. The methods and techniques used are described in detail in paragraph 2.4. The stability and performance analyses considered mass characteristics (I_x, I_y, I_{zy}, X_{cg}, Y_{cg}, etc.), spin rates, entry angle of attack, entry angle and velocity, and atmosphere. To evaluate the sensitivity of the lander performance to the dynamics, zero damping was also considered. The trajectory studies were performed with a 4 degree-of-freedom digital program which also provided heating data. Critical trajectories and conditions were further investigated by means of a full 6 degree-of-freedom program.

The residual weight (defined as the total injected weight minus the weight of the shell structure and thermal protection system) was found to be very dependent upon the configuration considered. There is a strong interplay between the heat shield and structural requirements, stability, and performance. Although maximum drag and maximum vehicle diameter were found early in the studies to be desirable, the maximum drag configuration considered (the tension shell) with its high heating and subsequently large heat shield weights resulted in the minimum residual weight.

The parametric studies consisted of three phases. Initial studies were related to the selection of the three configurations within the three generic shapes (i.e., blunt cone, Apollo, and tension shell). The second phase which comprised the major portion of the Part I studies consisted of a broad parametric study, wherein vehicle geometry (size and shape), mass characteristics, entry conditions (velocity and angle as well as angle of attack and spin), and atmosphere (Reference 1) were considered for tradeoffs. Studies were made to determine the conditions critical to establishing the design loads (pressure and heating). The final phase consisted of restricting the atmospheres considered to Models 2 and 3, in addition to confining the analyses to a vehicle maximum diameter of 180 inches.

2.1.1 Configuration Descriptions

The blunt cones consisted of cone angles of 55 and 60 degrees half-cone angle (an initial cone angle of 50 degrees was discarded early as not having sufficiently large drag with a bluntness ratio (R_N/R_B) of 0.25, (see Figure 1). The Apollo shapes consisted of the standard Apollo forebody (double circle arc) in addition to a single arc (comparable to the Apollo nose radius, i.e., $R_N = 2.4\ R_B$) configuration designated as the Modified Apollo (see Figure 2). The tension shell shapes included a sharp nosed and a blunt ($R_N/R_B = 0.1$) configuration (see Figure 3). The afterbodies for these shapes consisted of a reference double conic (see Figure 1); however, analyses indicated the possibility of a single conic consistent with the payload volume and turnaround requirements (see Figure 2). The turn around requirements are dictated by the performance and subsequent weight penalties. Considerable improvement for all shapes is indicated when employing a flap, which is most efficient at an angle of attack of 180 degrees, where the afterbody has an unstable trim point (zero restoring moment). The flap however is ineffective at angles of attack near 90 degrees.

All shapes considered rely upon a sharp break in the body contour at the maximum diameter to provide a stable boundary-layer separation point thereby minimizing any boundary-layer hysteresis phenomena associated with unstable damping characteristics. Experimental values were available for most aerodynamic coefficients (although some interpolation was necessary); however, damping coefficient data, C_{mq}, was lacking. Based on information supplied by Langley Research Center (LRC), Newtonian values were used throughout the Mach number range (the dynamic considerations for the shapes were assumed to terminate with chute deployment, $M = 1.3$).

2.1.2 Mission Concepts

Systems considerations were factored into the parametric analysis with the objective of considering mission concepts as nominal with parameter variations resulting in associated tradeoffs. The mission concepts manifest themselves through design philosophy. Briefly, these concepts were:

2.1.2.1 Multi-Mission Shell Design

An entry vehicle concept capable of surviving entry over all possible weights (up to the 4500-pound limit), entry angles and velocities (-90 to -20 degrees and 18,000 to 25,000 ft/sec respectively), and all atmospheres (Models 1, 2, and 3).

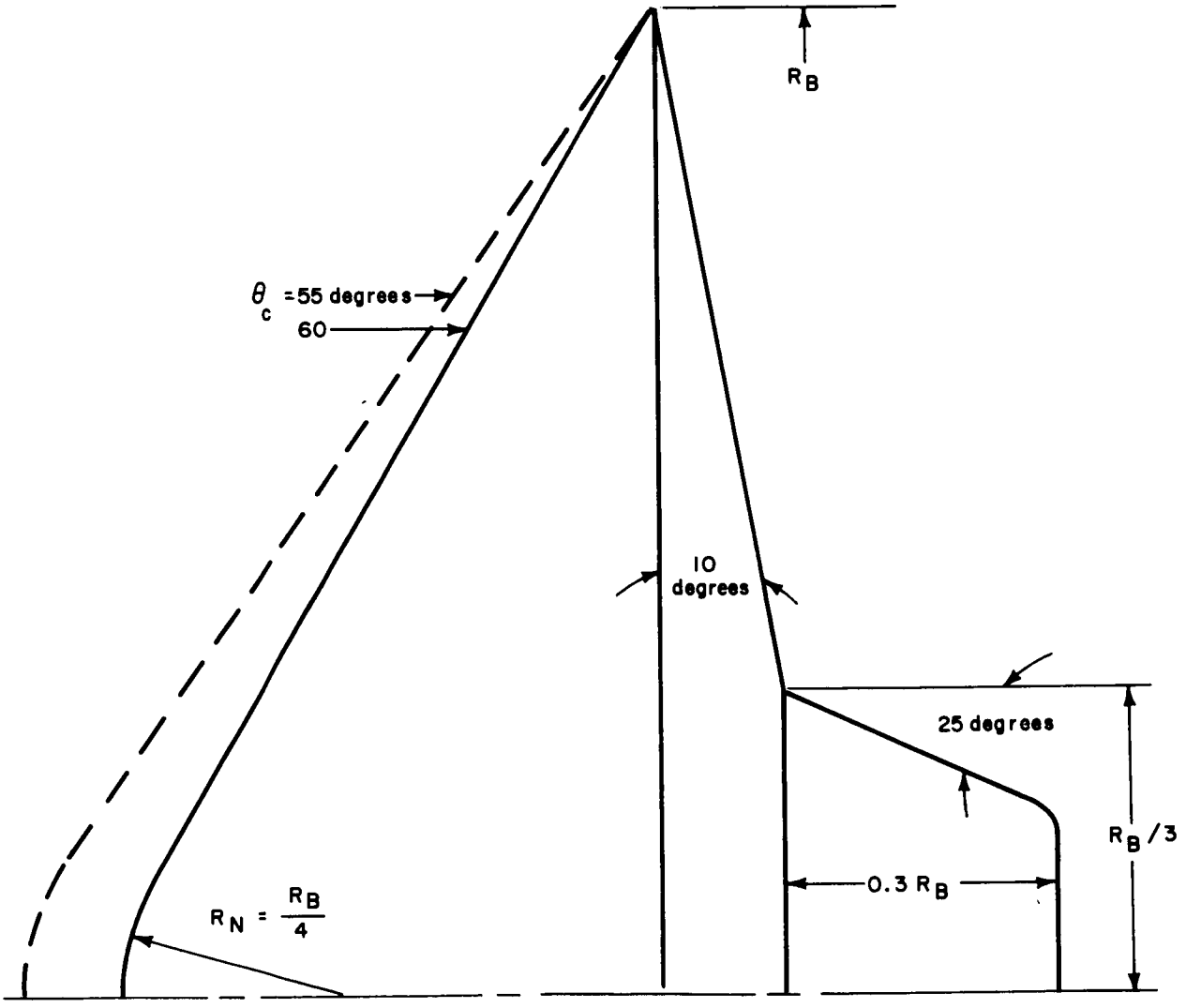

Figure 1 BLUNT CONE GEOMETRIES

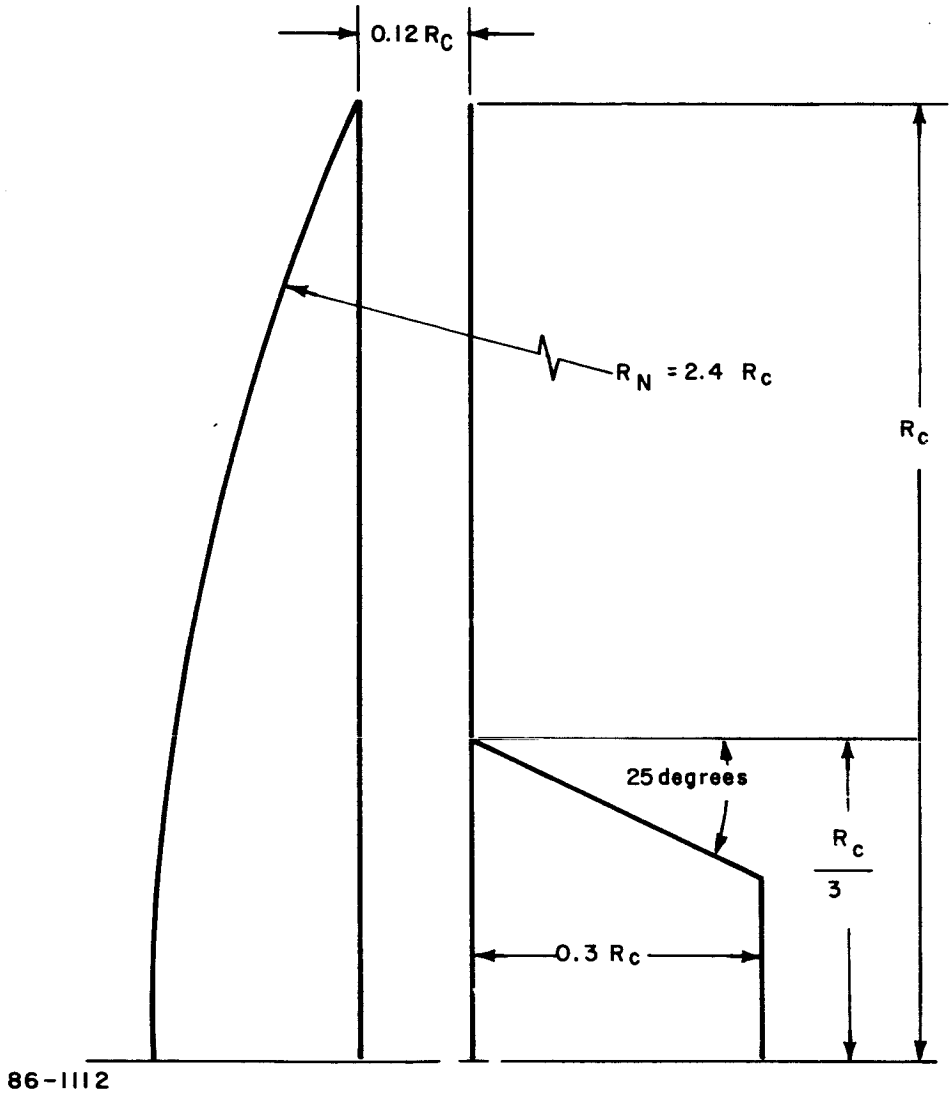

Figure 2 MODIFIED APOLLO GEOMETRY

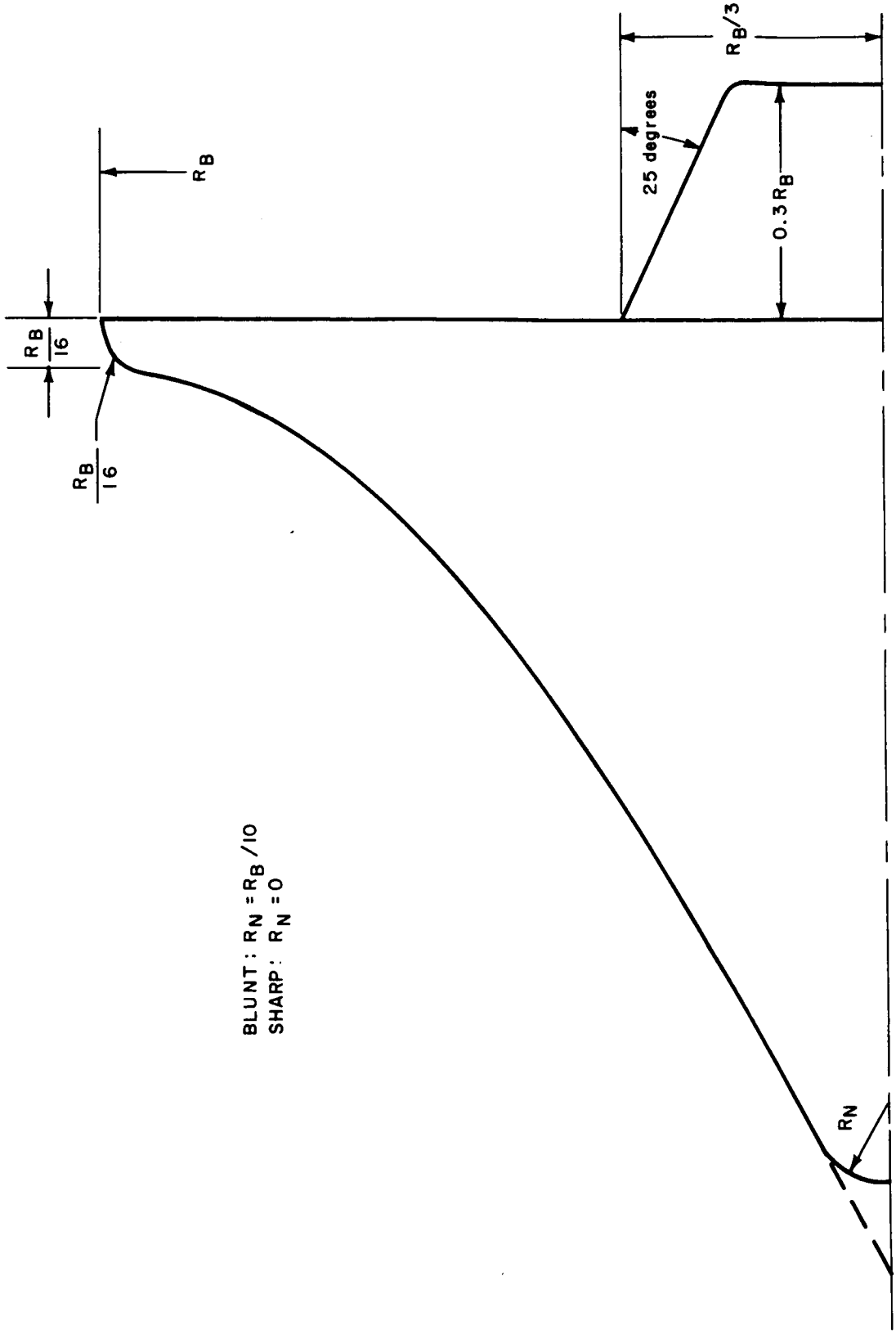

Figure 3 TENSION SHELL GEOMETRY

2.1.2.2 Multi-Mission Structure Design

This concept differs from the multimission shell design in that only the structure is designed for entry survival for the above conditions.

2.1.2.3 1971 Structure and Heat Shield Design

This concept would consider only an m/C_DA equal to 0.15 slug/ft^2 (descent system limitation) necessary for the early mission, considering all specified atmospheres.

2.1.2.4 Future Mission Shell Designs

These concepts considered survival capability into only one atmosphere (Models 1, 2 or 3); however, the descent system requirements were considered to limit the ballistic coefficient for the specified entry angle.

The combination of diameter and atmosphere models required preliminary investigation to ascertain which combination results in the design environments (loads and heating) for a specified diameter. The problem is introduced since the m/C_DA limitation imposed by the descent system varies with entry angle and atmosphere. The heat shield, however, being designed for the maximum convective heating is evaluated for the Model 1 atmosphere (the scale height is largest for this model) which is compatible with the smallest diameter and maximum weight considered. All diameters and vehicle mass combinations were thus designed for the Model 1 atmosphere in terms of the thermal protection system for the multimission shell parametrics.

The maximum loads are associated with the smallest scale height (Model 3); however, since the terminal descent requirements permit an increase in m/CDA as the scale height increases, it is not immediately obvious which atmosphere and mass will result in the maximum load for a given diameter. Analyses indicated that the higher scale height with the larger mass resulted in the maximum loads for a given diameter. In addition, for a given atmosphere and diameter, increasing the entry angle (which results in lower allowable vehicle total mass) does not reduce the loads (the maximum loads are expected at an entry angle of -90 degrees).

The multimission structure concept considers the penalties associated only with a vehicle structure design which is compatible with all missions in contrast to the multimission shell which has both the heat shield and structure designed for all possible entry conditions (within the parametric matrix). The design environment considerations are as indicated above.

The 1971 shell design considers all atmospheres, however since entry angles as steep as -90 degrees are possible the ballistic coefficient is limited to 0.15 slug/ft^2. The heating is therefore evaluated for the Model 1 atmosphere at γ_e = -20 degrees with the structure analyzed in the Model 3 atmosphere at -90-degrees entry angle.

The future mission concepts reflect designs which are designed specifically for a particular atmosphere model, giving a comparison of the shell-weight variation with atmosphere. The loads were evaluated at the steepest entry angle with the minimum ballistic coefficient whereas the heat shield has been evaluated for the maximum weight at an entry angle of -20 degrees.

All diameters and mass combinations resulted in predominantly laminar heating for the blunt cone and modified Apollo, since transition occurs very late in the heat pulse and at steep entry angles for the Model 1 atmosphere. Although transition (the transition was assumed at a local Reynolds number of 300,000) occurs in Models 2 and 3, the integrated convective heating was significantly higher in the Model 1 atmosphere. In contrast, the blunt tension shell experiences early transition over a major portion of the vehicle surface especially in the critical areas near the maximum diameter. This early transition manifested itself not only in the Model 1 atmosphere but also for the lightweight vehicles. The local Reynolds number for this shape was an order-of-magnitude larger than either the blunt cone or the modified Apollo, which were comparable.

The parametric studies indicated that severe weight penalties were associated with the multimission shell concept (A), and as such further consideration was eliminated. In addition, redirection resulted in elimination of the Model 1 atmosphere (the maximum surface pressure atmosphere). As a result the following concepts were studied for specific designs: (B) Multimission structure -- The structure was designed for all m/C_DA consistent with the terminal descent system and atmospheres 3 and 2. The heat shield was designed for the shallow entry into the Model 2 atmosphere for an m/C_DA = 0.15 slug/ft^2. (C) 1971 shell -- Both the structure and the heat shield were designed for the terminal descent criterion of m/C_DA equal to 0.15 slug/ft^2 considering both Models 3 and 2. (D) Future mission shell -- The future mission shell was designed expressly for the Model 3 atmosphere considering vehicle weight growth (shallow entry angles).

The results for the tension shell indicated predominantly turbulent convective heating in the Model 2 atmosphere (having a greater scale height than the Model 3). Transition considerations for the other two shapes were important only with respect to the heavy future mission concept.

The multimission structure was designed for the large total mass vehicle and the Model 2 atmosphere for the steep entry condition, this combination resulting in maximum peak pressures.

2.1.3 Requirements, Constraints, and Design Criteria

The initial parametric studies considered a broad range of vehicle diameters, mass characteristics and entry conditions, and atmospheres. Since analyzing all possible combinations results, in many cases, in violations of system requirements and constraints, preliminary emphasis was placed on defining the vehicle parameters and entry conditions which were compatible with the system considerations. The requirements and constraints were summarized in Table I.

2.1.3.1 Entry Conditions

The entry conditions were based on the analysis of spacecraft/capsule separation conditions. Entry velocities ranged from 18,000 to 25,000 ft/sec and flight path angles from -90 to -20 degrees. The angle of attack varied with entry angle, being a maximum of 35 degrees for a -90-degree entry and 11 degrees for a -20-degree entry for the spin stabilization mode. Additional angles of attack up to 60 degrees were considered for dynamic studies.

Failure modes (e.g., spin rocket failure) could result in random angles of attack (up to 180 degrees) with negligible rates of spin, yaw, and pitch. Spin rates were varied from 1 to 8 rad/sec. A study was made to determine the precession angle caused by the misalignment of the separation thrust axis, spin rocket asymmetries, etc., as a function of the ratio of the longitudinal to transverse moments of inertia, vehicle mass and size. Internal damping for the moments of inertia ratios extant was not factored into the study. Since the longitudinal moment of inertia is greater than the transverse this is a conservative approach. Precession angles were also obtained for spin and despin. The precession angle variation is shown in Table IV.

TABLE IV

PRECESSION CONE ANGLES

Spin Rate (rad/sec)	Precession Cone Half Angle (degrees)
1	10.0
2	2.3
3	1.1
4	0.5

Diameter = 180 inches

2.1.3.2 Atmosphere

The atmospheres considered were Models 1, 2, and 3 of Reference 1. Considering the scale height variation among these atmospheres, it is expected that Model 1 will result in maximum integrated convected heating whereas Model 3 will be critical with respect to loads and performance. The compositions of these atmospheres (mixtures of CO_2 and N_2) result in the highest radiative heating in the Model 2 atmosphere. The performance of the thermal protection system, however, indicates that the convective heating is the predominant factor in the heat shield design.

2.1.3.3 Vehicle Parameters

The most important vehicle parameter is the ballistic coefficient, m/C_DA, since the performance and environments associated with this parameter for a given diameter will ultimately determine the payload weight. The minimum weight associated with a given diameter is that determined by the terminal descent requirements, which impose a limit of 0.15 slug/ft^2 on m/C_DA for a 90-degree entry into the Model 3 atmosphere. The maximum total weight of 4500 pounds (from spacecraft/systems considerations) is only possible for specific combinations of vehicle diameter, entry angle, and atmospheric model. These specific combinations were obtained parametrically by means of particle trajectories, the results of which are presented in Figure 4. This figure provides a means for eliminating those combinations which violate booster limitations or the presently considered terminal descent system (a reefed parachute at a Mach number of 1.3 with full deployment at a Mach number of 0.8 and 15,000-feet altitude). The vehicle diameters investigated considered packaging and volume requirements, attainable centers of gravity and interface limitations (both bus and ascent shroud) and were initially varied from 100 to 250 inches to encompass the range of interest.

Three shapes were considered in detail during this study: Blunt Cones (θ_c = 60 degrees R_N/R_B = 0.25); Modified Apollo (R_N/R_B = 2.4); Blunt Tension Shell (R_N/R_B = 0.1). These shapes are comparable in their respective drag coefficients but differ greatly in other respects. The blunt-cone and modified Apollo are characterized by extensive subsonic flow with a maximum local Mach number of 1 at the maximum diameter. In contrast, the tension shell, although blunt, has supersonic flow over a major portion of the vehicle surface. This occurs since the boundary layer as it grows, "swallows" the high entropy normal shock flow. At several nose radii downstream of the stagnation point, the flow is identical to that associated with a sharpnosed vehicle. The resulting flow has two dominant effects; the compression process gives pressures greater than the stagnation point pressure and in addition the local Reynolds numbers

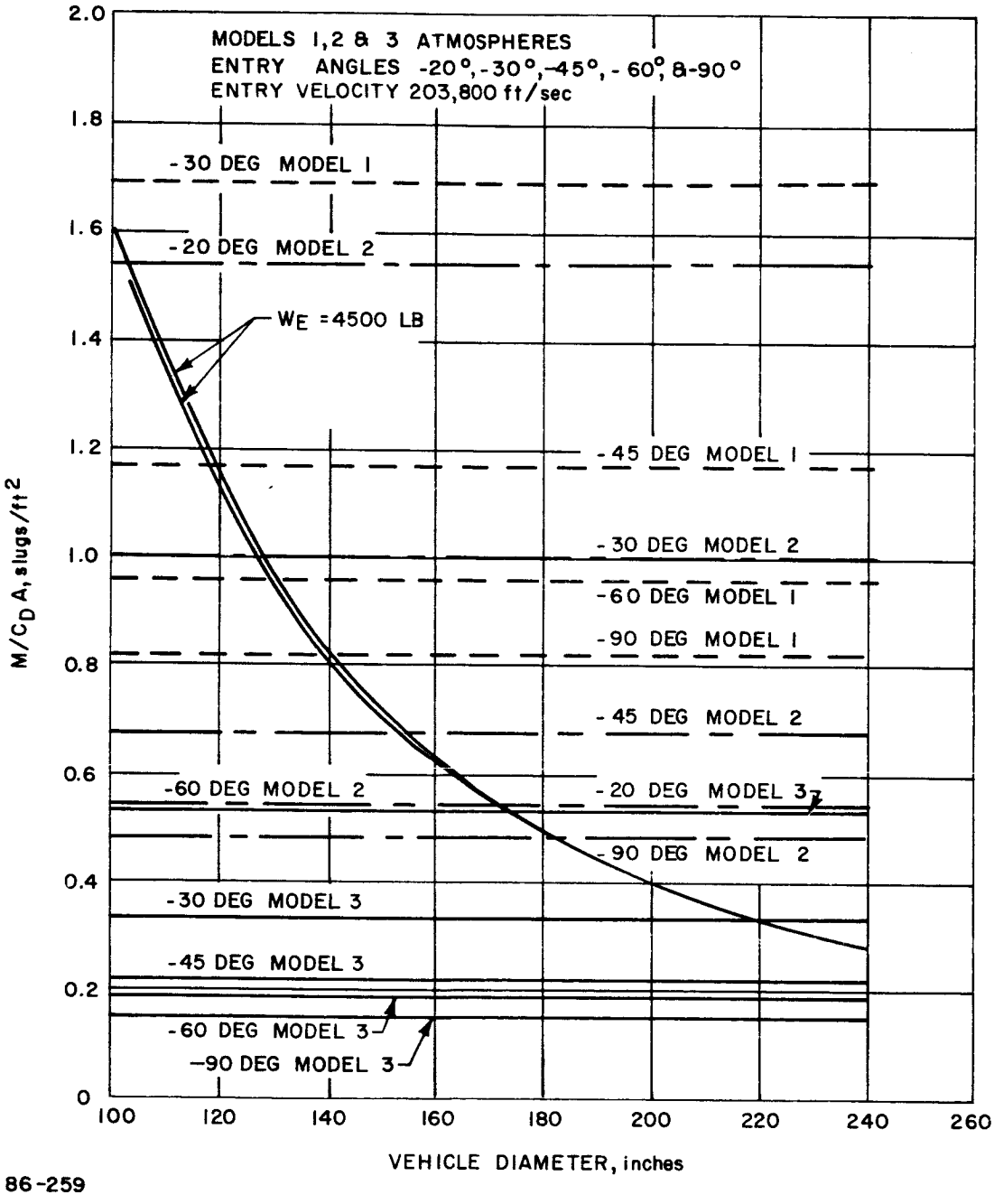

Figure 4 MAXIMUM M/C_DA ALLOWABLE VERSUS VEHICLE DIAMETER

are high. The heating will thus be laminar for the blunt-cone and modified Apollo whereas turbulent flow will dominate the tension shell heating. The tension shell provides the maximum available volume and the modified Apollo the minimum. The afterbody requirements for the tension shell are dictated by the turnaround requirement whereas for the modified Apollo the requirement for volume and thermal protection is predominant. Considerable improvement in the turnaround capability (especially at 180 degrees angle of attack) can be achieved by means of the flaps which have been considered.

2.1.4 Performance Summary (Loads, Heating, Dynamics)

Only the revised design concepts are summarized here. For brevity, the concepts are referred to in the following manner:

Concept B - Multimission Structure

Concept C - 1971 Mission Shell

Concept D - Future Mission Shell

2.1.4.1 Loads

Tables V and VI present the summary of pertinent loading parameters for the cases of forward and rearward entry, respectively. For the forward entry case, the blunt cone experiences the highest peak dynamic pressure in the B concept. For concepts C and D, all shapes experience virtually identical peak dynamic pressures. Identical peak decelerations are experienced by all shapes for each concept.

For rearward entry conditions, with the vehicle righting itself without the aid of a flap, the blunt cone again experiences the maximum loads for concept B. Maximum peak decelerations are obtained with the same configurations for the same concepts, although peak "g" is nearly insensitive to shape in other B concepts. The blunt tension shell experiences the maximum normal forces, primarily because of its large projected area. A 25-percent increase in load is generally obtained in rearward entry.

As noted previously, higher local loads will be produced on the tension shell than on the other shapes.

The aerodynamic coefficients and the mass characteristics used in the analysis are indicated in Table VII and are indexed to the appropriate figure numbers.

TABLE V

LOAD SUMMARY (PARTICLE TRAJECTORY)

α_e = 0 degrees, D = 15 feet V_e = 23,800 fps, Z_e = 800,000 feet

	Weight Pounds	Atmos-phere	Entry Angle (γ_e - degrees)	Peak Dynamic Pressure (q_∞ psf)	Peak Deceleration (g)	Design Concept
Modified Apollo	4500	2	-90	1098	73	B
Modified Apollo	1450	3	-90	775	161	C and D
Blunt Cone	4500	2	-90	1152	73.3	B
Blunt Cone	1390	3	-90	777	161	C and D
Blunt Tension Shell	4500	2	-90	1114	73.3	B
Blunt Tension Shell	1435	3	-90	778	161	C and D

2.1.4.2 Heating

Pertinent heating data are presented in Table VIII. The tension shell produces an order of magnitude increase in heating over the other shapes in the D concept, but only about double the heating for concepts B and C. The modified Apollo shape encounters the lowest total heating in all configurations. The addition of radiation heating to these values does not change the comparison, even though the radiation heating represents as much as 33 percent of the convective heating on the Apollo shape.

The effect of angle of attack on total integrated heating is to cause increased heating on the blunt shapes and decreased heating on the tension shell for large angles (on the basis of available data).

In general, high spin rates decrease heating, although some increase is produced on the modified Apollo shape.

TABLE VI

LOAD SUMMARY (DYNAMIC TRAJECTORY)

α_e = 179 degrees, D = 15 feet, V_e = 23,800 fps, Z_e = 800,000 feet

Shape	Weight (pounds)	Atmos-phere	Design Concept	Peak Dynamic Pressure	α at Peak "g"	Max-mum D/W	Max-mum N/W
Mod-ified Apollo	4500	2	B	1333	11	89	3
Mod-ified Apollo	1450	3	C and D	1020	22	211	11
Blunt Cone	4500	2	B	1426	16	91	7
Blunt Cone	1390	3	C and D	1009	20	209	19
Blunt Tension Shell	4500	2	B	1375	9	87	10
Blunt Tension Shell	1435	3	C and D	1110	31	224	42

TABLE VII

SUMMARY OF AERODYNAMIC DATA

	Configuration		
Aerodynamic Function	Blunt Cone	Apollo	Blunt Tension
Axial Force -- C_x versus α	Figure 5	Figure 10	Figure 15
Normal Force -- C_N versus α	Figure 6	Figure 11	Figure 16
Pitching Moment -- C_M versus α	Figure 7	Figure 12	Figure 17
Pitch Damping -- C_{m_q} versus Mach No.	Figure 8	Figure 13	Figure 18
Drag --C_x α = 0 versus Mach No.	Figure 9	Figure 14	Figure 19
Mass Characteristics	Table IX	Table X	Table XI

2.1.4.3 Dynamics and Stability

All shapes performed adequately with respect to stability except for the tension shell shape which diverged supersonically. All configurations should be dynamically stable at transonic speeds. However, trajectory analysis shows that no vehicle will go completely unstable or diverge totally with no aerodynamic damping.

2.1.5 Conclusions and Problem Areas

On the basis of the aerodynamic parametric shape comparison the modified Apollo shape appears to show the maximum potential. It combines the highest drag with the lowest convective heating. Its high radiative heating will be significant only for a heat-sink thermal protective system. (Available data indicate ablative heat shields are more efficient for a radiative pulse). The tension shell which had a comparable drag has a heating

TABLE VIII

HEATING SUMMARY
(PARTICLE TRAJECTORIES)

D = 15 feet, γ_e = -20 degrees, V_e = 23,800 fps, Z_e = 800,000 feet

	Concept	Wt. (lbs.)	Atm.	q_{max} x (Btu/ft^2/sec)	Q_s (Btu/ft^2)	Q_I (Btu/ft^2)	$q_{max\,I}$ (Btu/ft^2/sec)	Q_r (Btu/ft^2)
Modified Apollo	D	4500	3	49	989	1345	106	963
Modified Apollo	B and C	1450	2	19	753	750[x]	19	304
Blunt Cone	D	4500	3	188	4405	1889	7.0	62
Blunt Cone	B and C	1390	2	70	2798	803[x]	1.0	19
Blunt Tension Shell	D	4500	3	291	6824	15090[y]	225	2278
Blunt Tension Shell	B and C	1435	2	111	4416	4303[z]	38	683

I) refers to sonic point

x) entire heat pulse laminar

y) heat pulse at S/Rn = 14.7 (not sonic point)

z) heat pulse at S/Rn = 11.6 (not sonic point)

environment an order-of-magnitude more severe due to the existing flow phenomena. Its more efficient compression (multiple shocks), although beneficial to drag, also results in high Reynolds numbers with concommitant turbulent flow. Further, the shock structure at low Mach numbers can result in unstable aerodynamics as evidenced by wind-tunnel test data.

Further test data reflecting real-gas effects are necessary to establish the drag coefficient and to provide the coefficients necessary to confirm static and dynamic stability. Although all shapes performed adequately with respect to stability (except for the tension shell shape which evidenced supersonic static instability), these results were obtained with Newtonian damping values. Precaution was taken to minimize any dynamic instability by providing a fixed boundary-layer separation point at the base. The data indicate that this definitely improves the dynamic stability subsonically; however data are lacking at transonic speeds (especially the critical range $0.9 < M < 2.0$).

The spin effects were found to be most important for the critical entry condition for the descent system (γ_e = -90 degrees), low spin rates being desired. The effect on heating at the design entry conditions was found to be very small but resulted in increased heating with increasing spin for the modified Apollo shape. Based on wind-tunnel test data, heating on the tension shell may be considerably reduced by high spin rates for high angles of attack with a concommitant loss in the drag advantage. Lunar motion represents the most critical conditions.

The effects of angle of attack on trajectory and loads are generally small, except as noted below for rearward entry. The effect of angle of attack on heating environments is to increase the overall integrated heating input to the blunt cone and modified Apollo. Heating on the tension shell is decreased considerably for large angles of attack based on wind-tunnel test data.

Difficulties exist in determining the real-gas effects on the aerodynamic data because of a lack of data on specific configurations and because the available data exists only for ideal gases. The correlation between ideal and real gases, which used the stagnation point to free-stream density ratio, appeared adequate for pressure distributions, heating and drag coefficients. Although this technique is not as exact for predicting normal force and pitching moment coefficients, some correlation was achieved and was used in this study.

A second difficulty exists in predicting the dynamic coefficients in the transonic speed range which digress from the Newtonian values. This has been minimized by terminating the configuration abruptly at the maximum diameter and by minimizing the size of the afterbody.

There is a lack of sufficient test data and theoretical methods of analysis for predicting heating for the afterbody shapes considered. These afterbodies contain a high percent of the vehicles total area and with the uncertainty of the data, could produce a weight penalty of some significance.

The tension shell presents a major problem in the definition of the flow field about the body. Such definition must be made with sufficient accuracy for design purposes to warrant further consideration of this configuration. Although the methods developed to deal with the flow field are of sufficient accuracy to define the tension shell performance relative to that of the blunt cone and the modified Apollo shapes, a highly refined analysis will be required for final design.

2.2 DESIGN CRITERIA

The evaluation of the environments comprises a process wherein the trajectory dependent parameters (i.e., flight velocity, Mach number, density ratio, angle of attack, etc.) are utilized to define the flow field. The complete evaluation of the variation of the flow field along the trajectory presents a formidable task within a parametric study. Previous studies have indicated that it is the periods of flight peak loads, pressure and heating which are critical, and that qualitatively correct results are obtainable without resort to detailed and tedious analyses.

The evaluation of the flow field consists of determining the pressure distribution and the shock shape. These in turn permit the determination of the thermodynamic properties and species necessary to evaluate the radiative* and convective heating. The blunt cone and modified Apollo configurations were assumed to result in negligible variation in pressure distribution due to composition. The primary contribution due to the composition was that associated with the stagnation point density ratio (velocity gradient and shock standoff distance).

In contrast, the blunt tension shell required, in addition to the shock shape, a complete flow-field analysis to define the pressure distributions and the heating because of the complex shock-wave interaction occurring. The flow field in this case, however, could also be correlated to a certain extent with the stagnation point density ratio.

To facilitate the parametric analyses, the flow field was also defined parametrically; specifically, pressure and convective heating distributions normalized with respect to the stagnation point pressure and heating respectively were generated for various angles of attack. These distributions were in

* Nonequilibrium radiative heating would ordinarily require a complete flow field analysis. This difficult problem may be circumvented (in an approximate manner) as described below.

turn used to define the heating aggravations associated with angle of attack by evaluating the surface integral of heating assuming lunar motion for various angles of attack. All shapes except the tension shell resulted in higher heating both through the effects of angle of attack on the trajectory and with the increased surface area integral of the normalized heating.

2.2.1 Critical Design Environments Determination

To determine the critical design environments, preliminary investigations were initiated to ascertain the governing phenomena. This process required interfaces with both the thermal protection system and the structure. The initial studies indicated that maximum integrated heating occurred for the shallow entry angles in the high scale height atmospheres (Model 1 and after a redirection, the Model 2). The radiative heating, however, was a maximum for the Model 2 atmosphere (89.2-percent N_2 and 10.8-percent CO_2 by volume) with the maximum integral occurring at steep entry angles. The thermal protection system analyses indicated that the critical environment was that associated with the maximum convective heating pulse.

Considering the broad range of parameters involved in the studies, particular attention must be focused on ensuring that the critical design environments have been obtained for a particular concept and vehicle diameter. To obtain an insight into the variation of the environments with entry conditions, simple approximations can be made by means of a straight-line assumption for the steep entry trajectories. Caution must be exercised for shallow entries which can deviate for two reasons: 1) the planet is spherical rather than flat and 2) gravity effects give rise to a curved trajectory. The first effect is predominant during early entry, whereas the latter effect occurs as the dynamic pressure increases. These effects compensate to an extent, relative to the straight-line assumption; however, the effective entry angle is not initially available.

The straight line approximations result in the following relations for velocity:

$$V_\infty = V_E \exp\left\{-\frac{\rho_o}{2\beta}\,\frac{e^{-\beta Z}}{\frac{m}{C_D A}\sin\gamma_E}\right\}$$

where

V_∞ is the velocity at any altitude, Z,

V_E is the entry velocity

β is the inverse scale height (stratosphere)

γ_E is the entry angle

ρ_o is the constant in the relation

$\rho_\infty = \rho_o e^{-\beta Z}$ (the exponential variation for the density, ρ_∞ , at an altitude Z)

The above relations, as well as those to follow, apply strictly only in the stratosphere; however, the results of similar studies indicate that this assumption gives qualitatively correct results in general.

The peak loads are given by

$$\frac{D}{W} \sim \beta \sin \gamma_E$$

with maximum pressures obtained from

$$P_{max} \sim (m/C_D A)\, \beta \sin \gamma_E \quad .$$

For peak loads and pressures occurring at steep entry angles, the maximum loads are seen to depend only on the inverse scale height, β. The maximum pressures, however, depend upon the ballistic coefficient also. For the multimission concept, the problem of which condition or combination of $m/C_D A$ and β results in maximum pressures is of concern. (Structural considerations indicate that maximum pressures rather than inertial loads are the dominant factor on structural design). The descent system requirement imposes the conditions of

$$e^{-\beta Z_o} / \beta\,(m/C_D A) = K, \text{ a constant (from the velocity relation)} \quad .$$

Thus $P_{max} \sim e^{-\beta Z_o}$. It is seen that the maximum pressures for a given diameter will be obtained for the large scale height atmosphere with the $m/C_D A$ obtained from descent systems studies relevant to that particular atmosphere.

Additional expressions are available for the maximum heating rates and integrated heating, both laminar and turbulent.

The maximum heating rates are given as

$$\dot{q}_{sm} = K_{\dot{q}s} \frac{V_E^{3.15}}{D^{0.5}} \sqrt{\beta \frac{m}{C_D A} \sin \gamma_E} \quad \text{, for laminar heating}$$

and

$$\dot{q}_{Tm} = K_{\dot{q}T} \frac{V_E^{3.18}}{D^{0.2}} \left(\beta \frac{m}{C_D A} \sin \gamma_E\right)^{0.8} \quad \text{, for turbulent heating .}$$

The integrals for the heating are expressed as

$$Q_s = K_{Qs} \frac{V_E^{2.15}}{D^{0.5}} \sqrt{\frac{m/C_D A}{\beta \sin \gamma_E}} \quad \text{for laminar}$$

and

$$Q_T = K_{QT} \frac{V_E^{2.18}}{D^{0.2}} \frac{(m/C_D A)^{0.8}}{(\beta \sin \gamma_E)^{0.2}} \quad \text{for turbulent heating .}$$

These expressions, in addition to the insight provided, facilitate the evaluation of the environments for Earth entry simulation. These can only be used as first order approximations; further refinements are necessary for the reasons indicated. The above relations also facilitate the procedure by providing the necessary entry condition perturbations. The relations used for determination of radiative heating are given in paragraph 4. 3. 2. The critical environments are summarized for the initial ground rules (prior to eliminating the Model 1 atmosphere).

2.2.2 Multi-mission shell

The shell is designed for the maximum mass at a given diameter (consistent with the terminal descent system). The heating is evaluated at the shallow entry limit (-20 degrees), highest velocity (25, 000 ft/sec), and largest scale height (Model 1). The structural load (in this case the maximum pressures) is designed for the steepest entry angle and highest velocity. Figure 4 presented the limiting ballistic parameter for the three atmospheres for various entry angles. In addition, the performance variation with diameter for the maximum total vehicle weight of 4500 pounds is indicated. Considering the factors presented in the previous discussions, for the steep entry angle (-90 degrees), the modified Apollo maximum pressures are realized in Models 2 and 1 at 183- and 141-inch diameters respectively. The Model 3 atmosphere at this entry angle would require a 344-inch diameter vehicle (m/C_DA = 0. 15 slug/ft^2). The maximum pressures for the intermediate diameters were obtained by interpolation.

2.2.3 Multi-mission Structure

This concept utilizes the structure as evolved for the multi-mission shell, however the heat shield is designed for a 1971 mission (m/C_DA = 0. 15 slug/ft^2), and γ_E = -20 degrees with the Model 1 atmosphere.

The remaining concepts and their respective design environments have been discussed in the introduction.

2.3 RESULTS AND DISCUSSION

2.3.1 Mass and Aerodynamic Characteristics

2.3.1.1 Blunt Cone (for various mission concepts)

The reference blunt cone shape is the 60-degree cone blunted with a spherical nose of one-quarter the base radius, and having a small truncated 25-degree cone afterbody. Initially, a 55-degree blunted cone had also been considered, but was eliminated early in the study because it had no outstanding advantages to offset its lower drag coefficient.

Force and moment coefficient data for the 60-degree cone are shown as a function of angle of attack for three representative Mach numbers in Figures 5 through 7. In the computer program, coefficients are programmed for five Mach numbers, covering the full required range. The static coefficients are based on data in Reference 2. The dynamic coefficient, C_{ma} (Figure 8) is assumed (for the purpose of comparison with the other shapes) to be the Newtonian variation at all Mach numbers. The axial force (drag coefficient) data

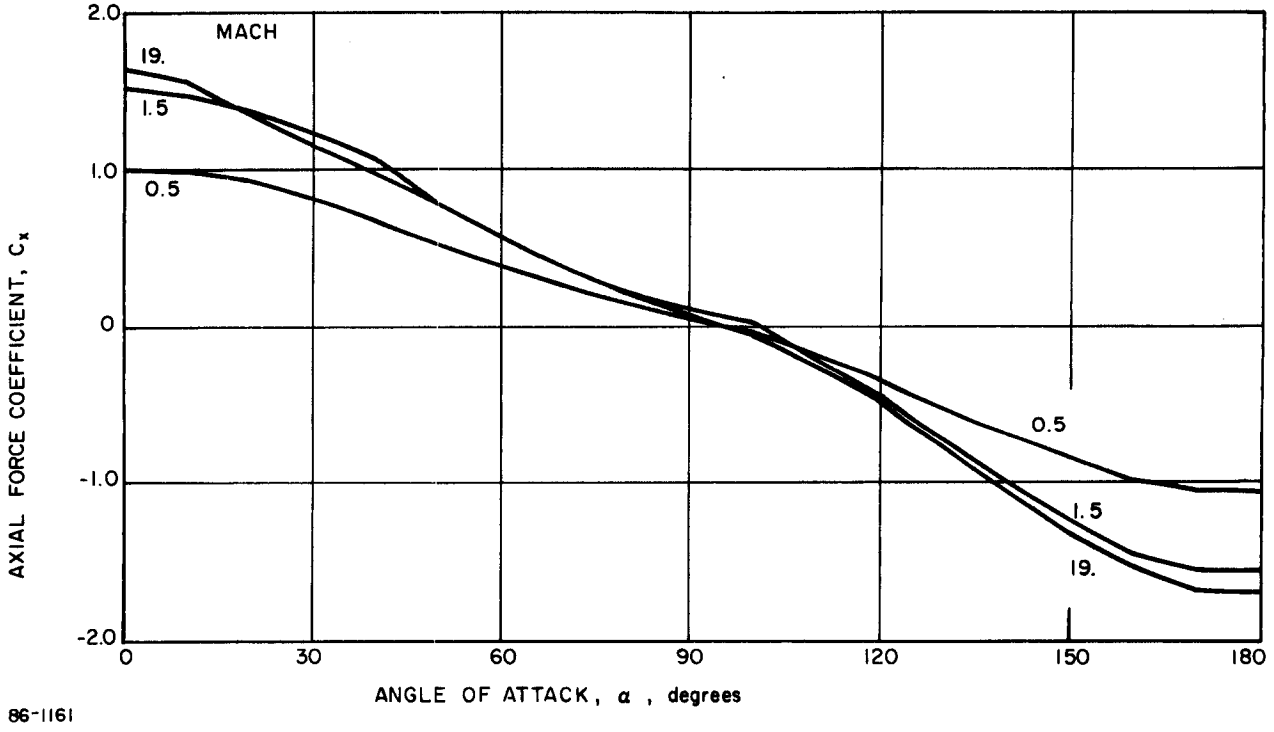

Figure 5 AXIAL FORCE COEFFICIENTS VERSUS ANGLE OF ATTACK -- 60-DEGREE BLUNTED CONE

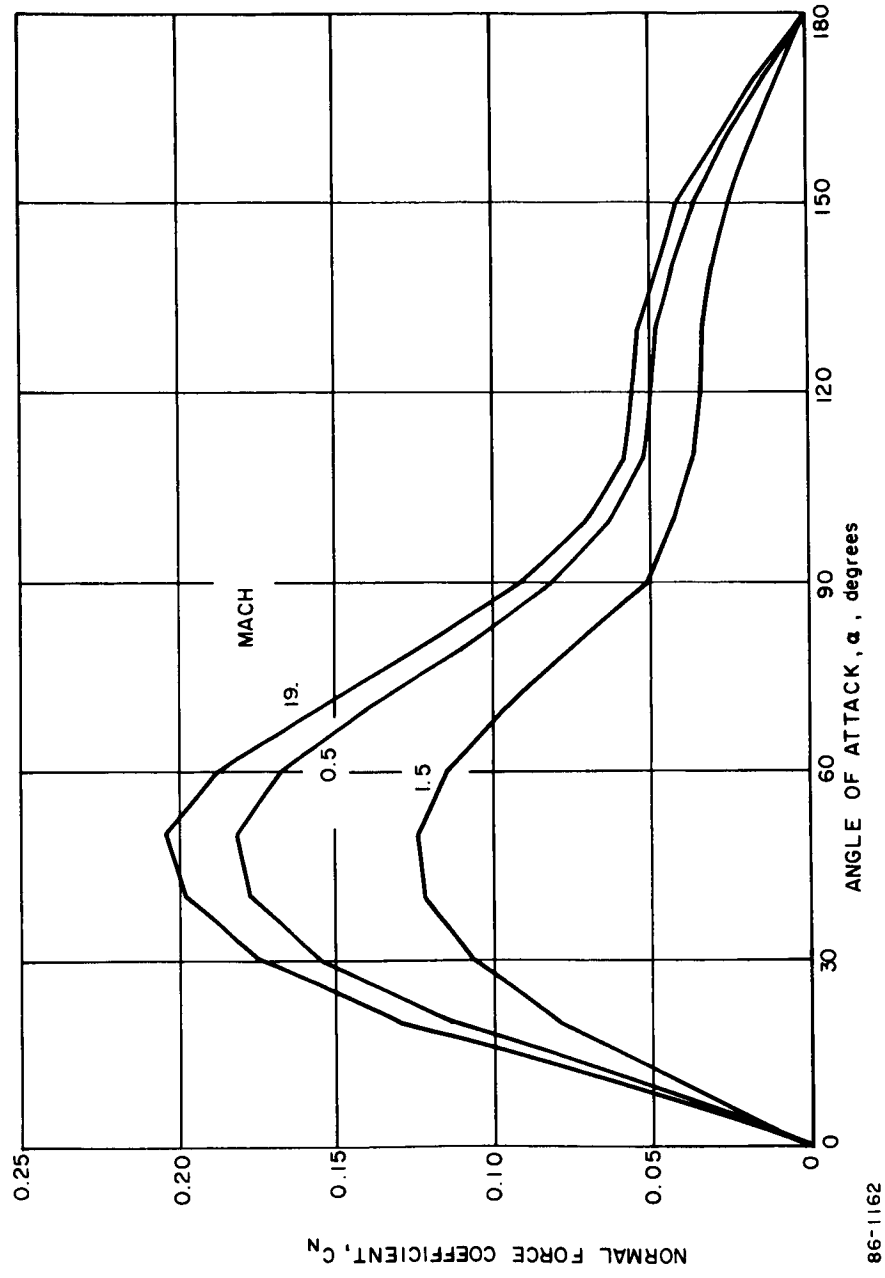

Figure 6 NORMAL FORCE COEFFICIENT VERSUS ANGLE OF ATTACK -- 60-DEGREE BLUNT CONE

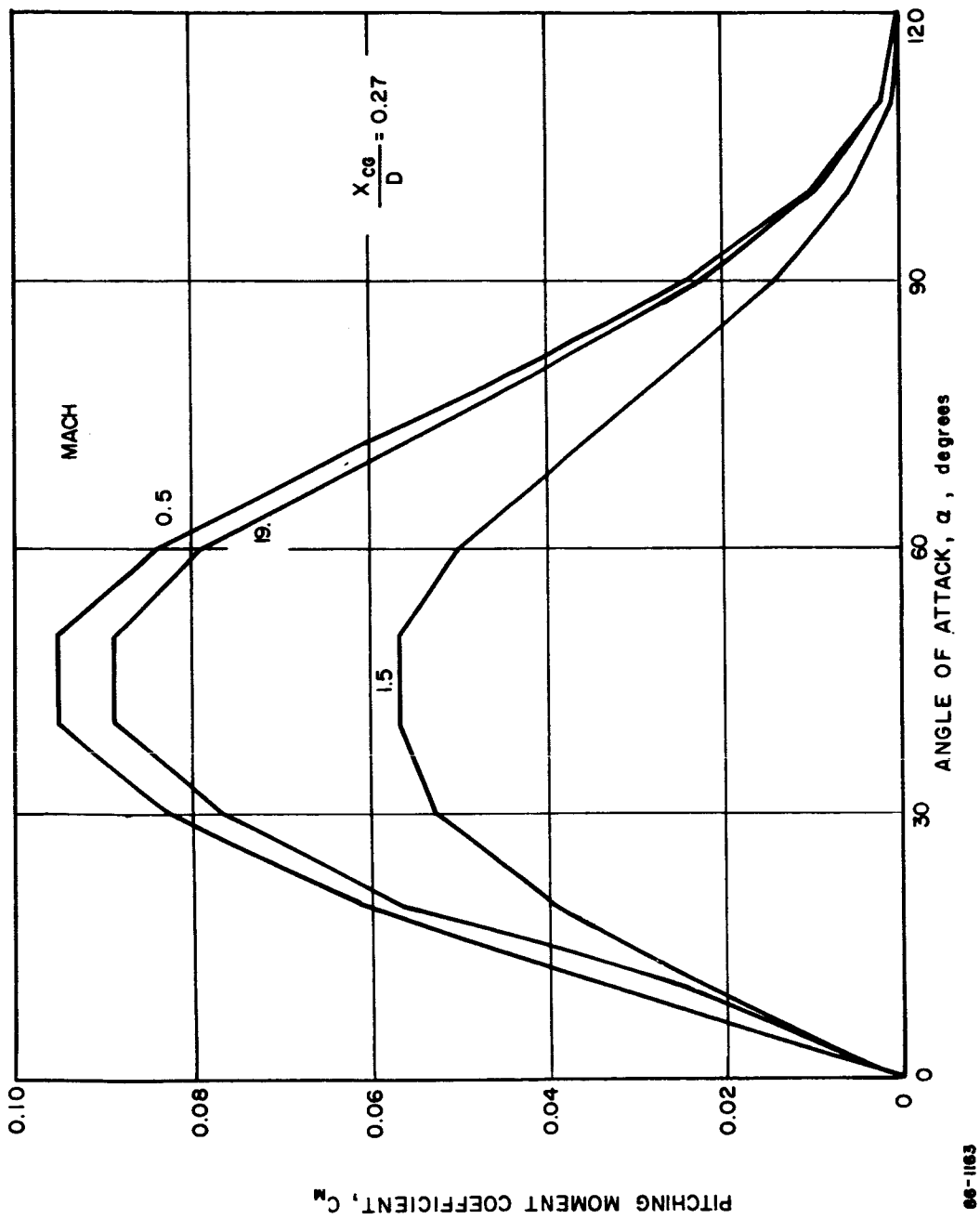

Figure 7 PITCHING MOMENT COEFFICIENT VERSUS ANGLE OF ATTACK--60 DEGREE BLUNTED CONE

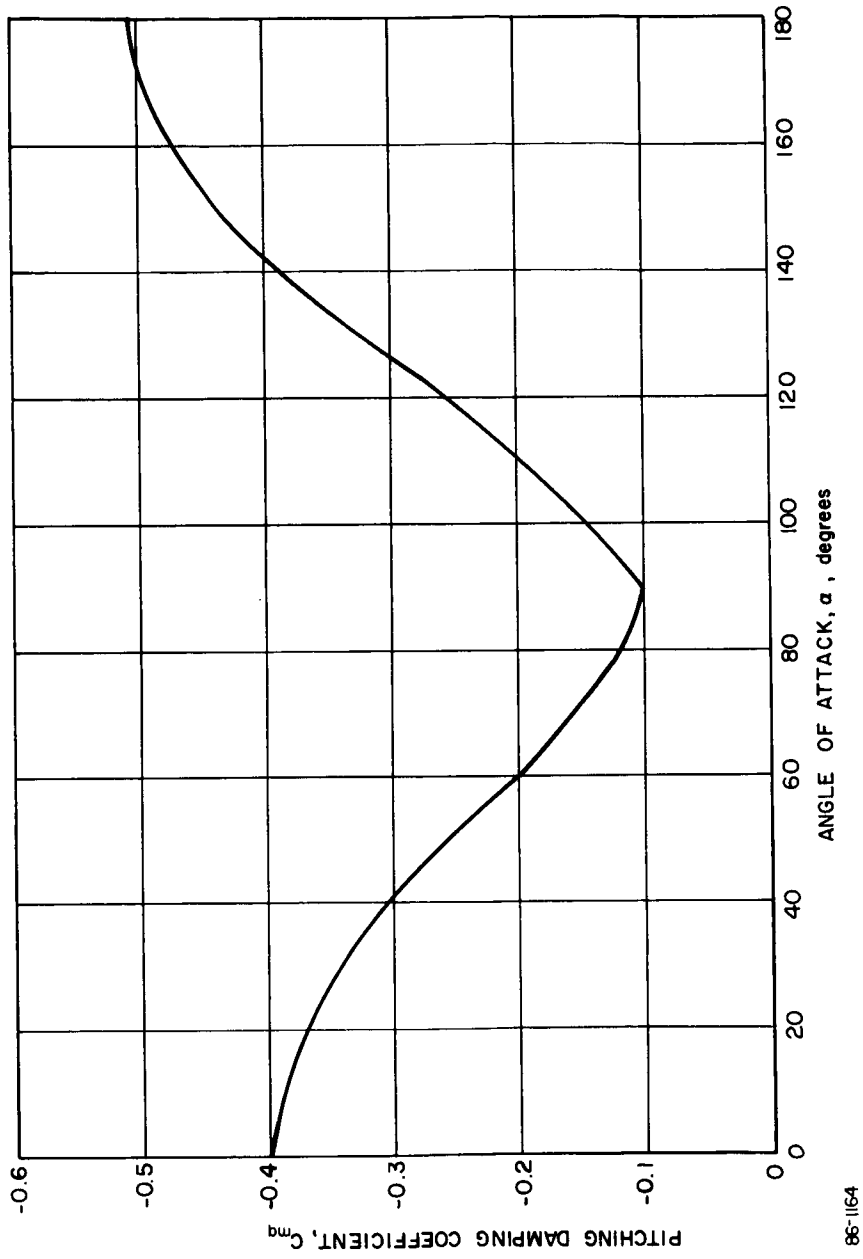

Figure 8 PITCH DAMPING COEFFICIENT NEWTONIAN -- BLUNT CONE SHAPE

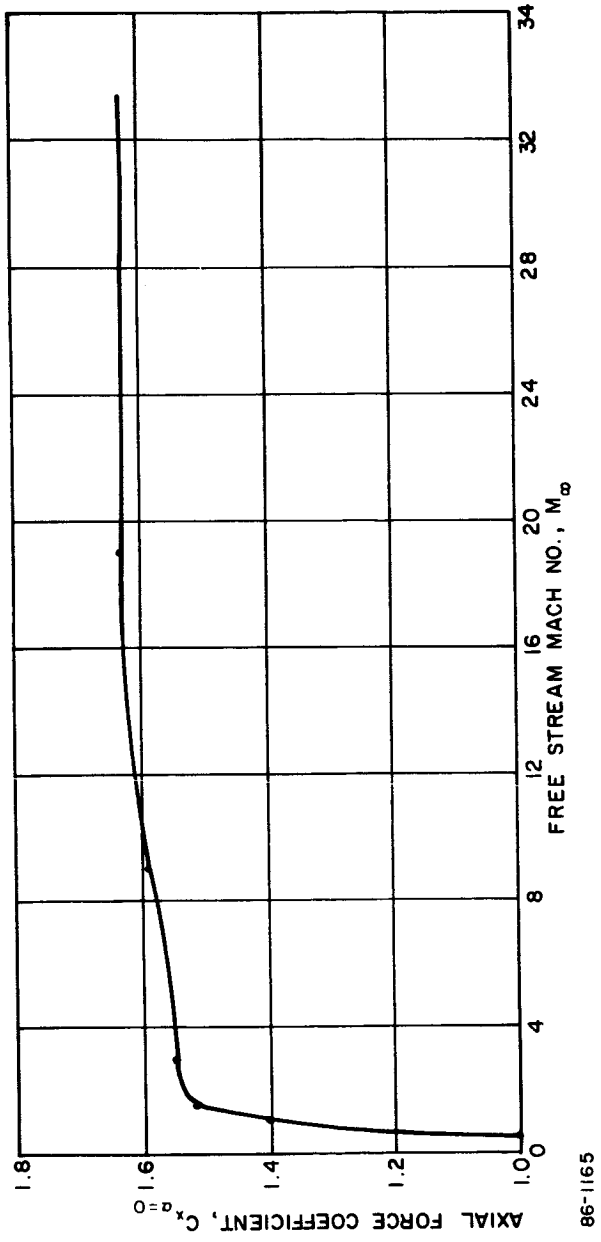

Figure 9 AXIAL FORCE COEFFICIENT -- 60-DEGREE BLUNTED CONE

have been corrected for real-gas effects, and the resulting drag variation with Mach number is shown in Figure 9.

Mass characteristics were estimated for both the multimission vehicle (4500 pounds), and the 1971 mission vehicle (m/C_DA = 0.15). The center of gravity locations, moments of inertia, and radii of gyration as used in the computer programs for the parametric studies are given in Table IX.

TABLE IX

BLUNT CONE MASS CHARACTERISTICS

Mass (Slugs)	D (feet)	m/C_DA (Slug/ft^2)	X_{GG}/D	σ_X/D	σ_Y/D	I_x (slug/ft^2)	I_y (slug/ft^2)
139.9	15.	0.50	0.150	0.232	0.184	1680	1060
	16.67	0.40	0.139	0.229	0.184	2043	1340
	12.9	0.673	0.166	0.239	0.185	1326	794
31.3	12.9	0.15	0.200	0.229	0.205	278	221
42.3	15.	↓	0.186	0.228	0.204	500	400
52.4	16.67		0.183	0.225	0.202	749	598

2.3.1.2 Modified Apollo

The basic Apollo shape was dropped from serious consideration early in the study because of its low drag and impractical afterbody as compared to the other shapes.

A higher drag configuration was substituted. It consists of a spherical segment of the same ratio of nose to base radius, but having sharp corners and an afterbody consistent with the other configurations under consideration.

The resulting shape is called "Modified Apollo". The aerodynamic coefficients plotted in Figures 9 through 12 were estimated based on data in Reference 2 for a 60-degree spherical segment, and data in Reference 3 for a 66.4-degree spherical segment. The axial-force (drag coefficient) data have been corrected for real-gas effects, and the resulting drag variation with Mach Number was presented in Figure 14. The damping coefficient, C_{m_q} is assumed to be the Newtonian variation with angle of attack at all Mach numbers (see Figure 13).

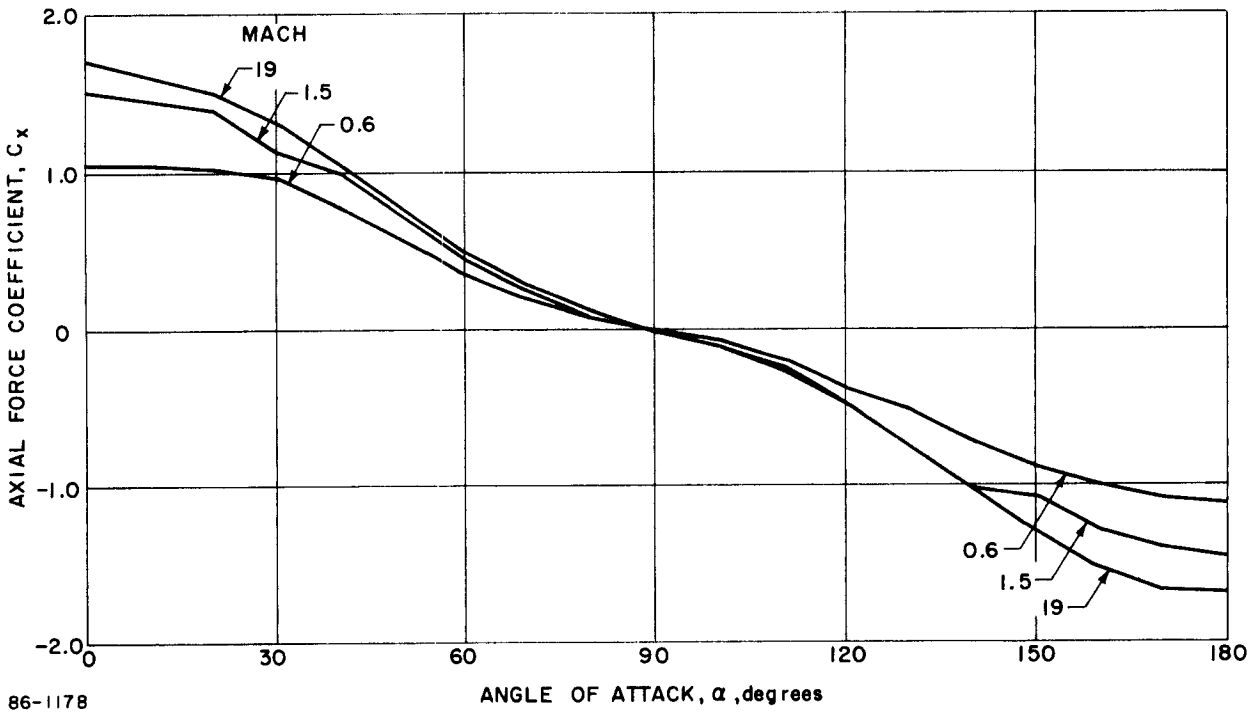

Figure 10 AXIAL FORCE COEFFICIENT VERSUS ANGLE OF ATTACK -- MODIFIED APOLLO

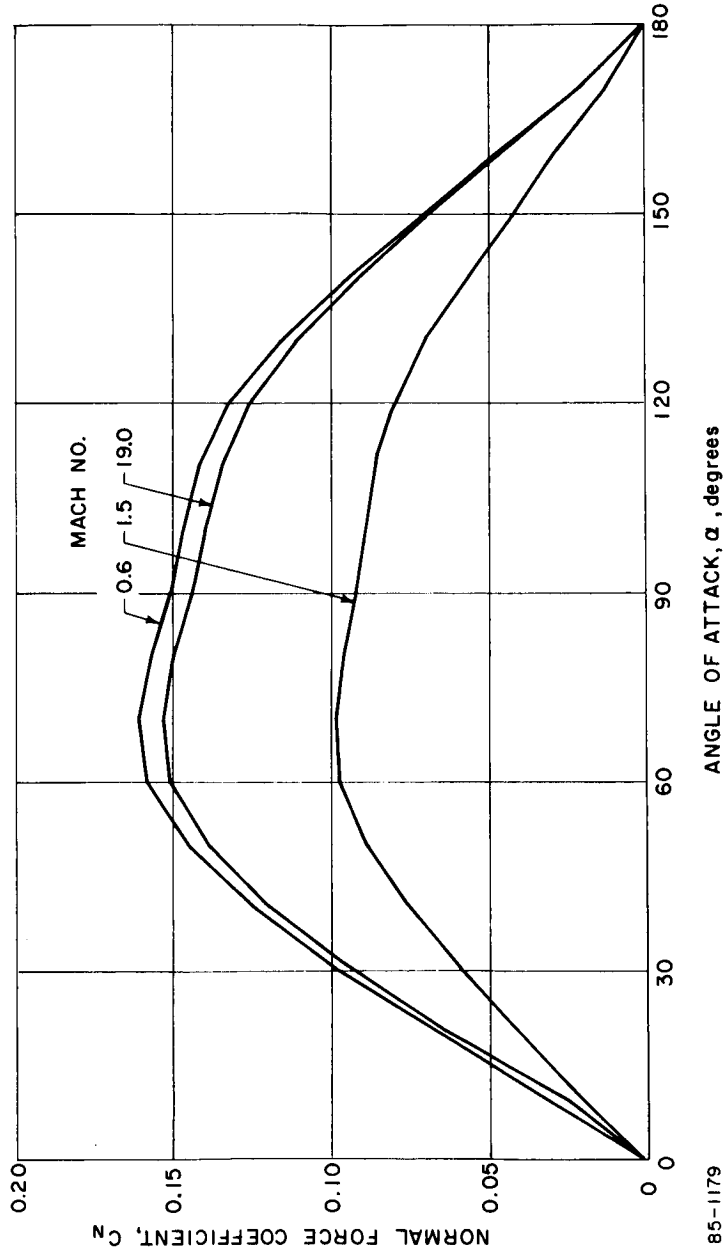

Figure 11 NORMAL FORCE COEFFICIENT VERSUS ANGLE OF ATTACK -- MODIFIED APOLLO

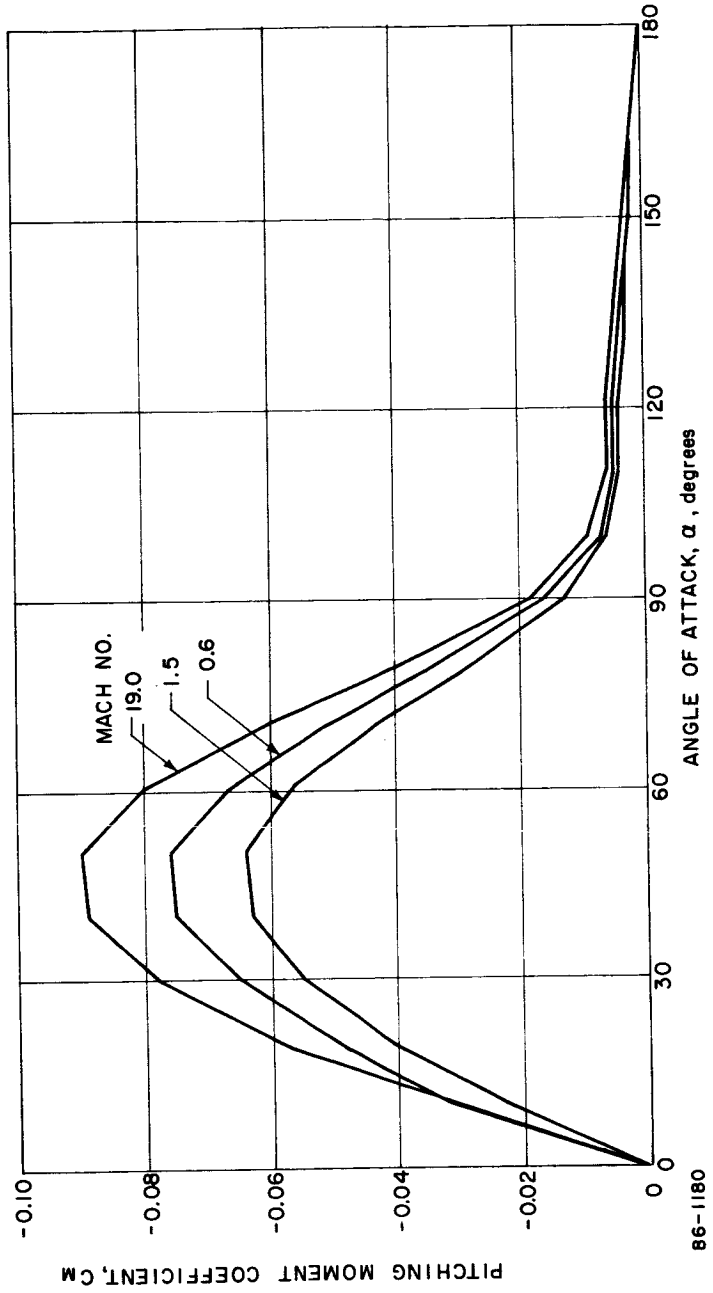

Figure 12 PITCHING MOMENT COEFFICIENT VERSUS ANGLE OF ATTACK -- MODIFIED APOLLO

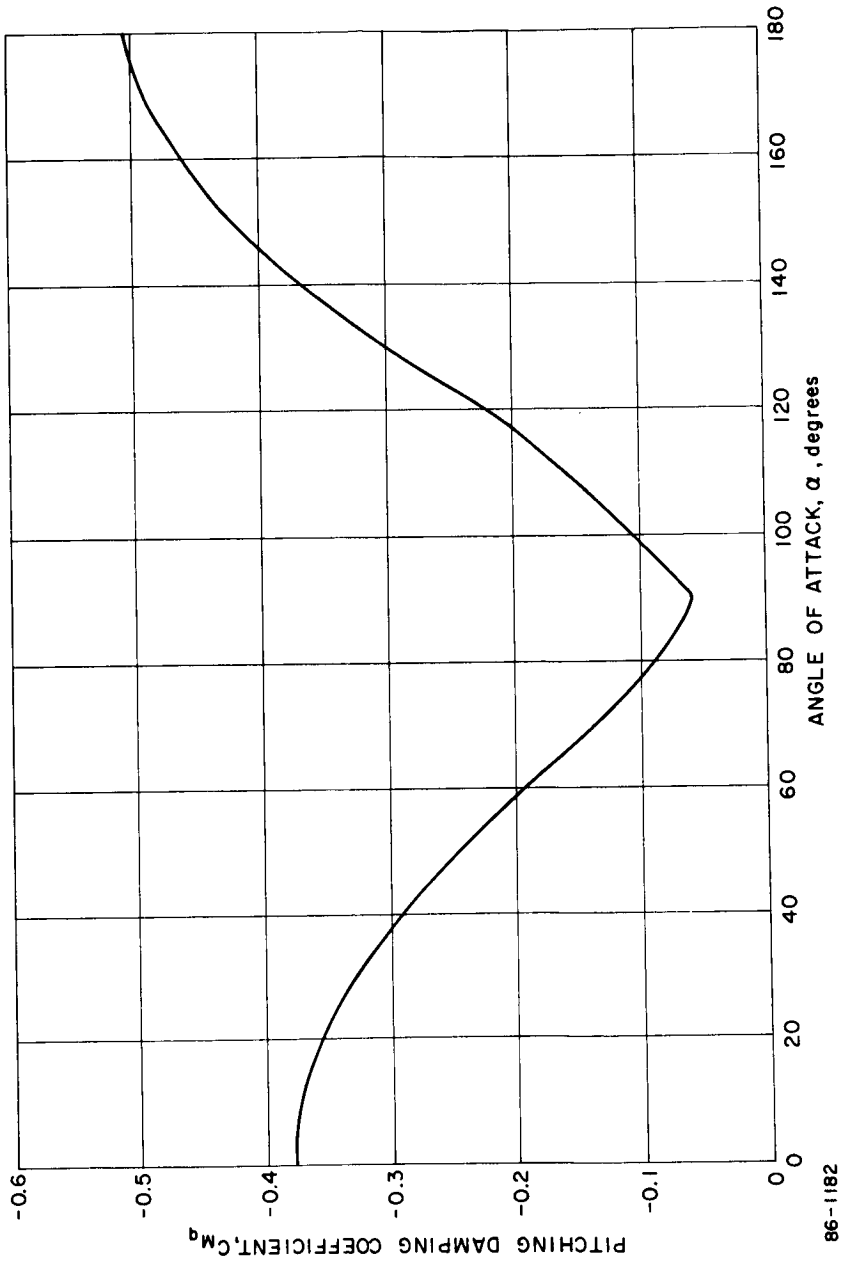

Figure 13 PITCH DAMPING COEFFICIENT -- MODIFIED APOLLO

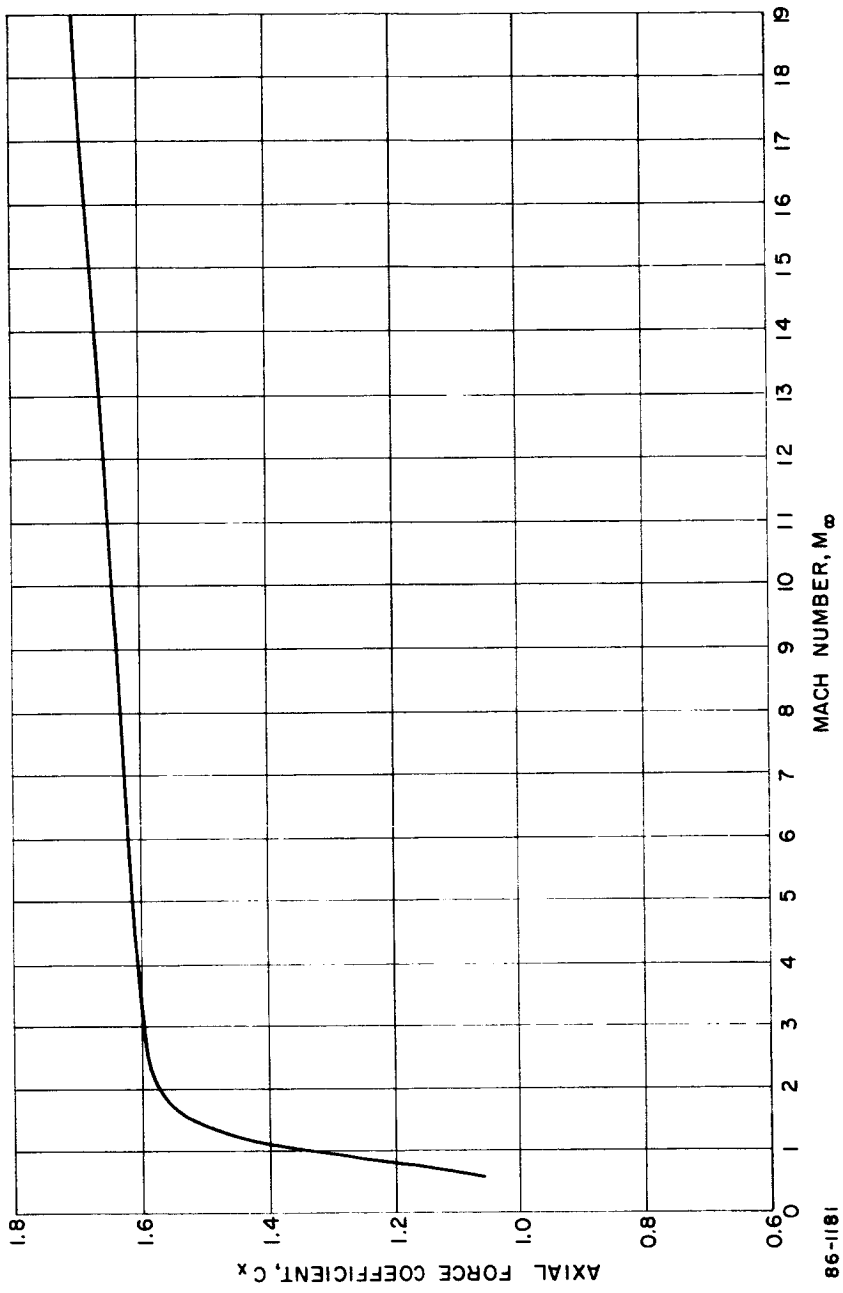

Figure 14 AXIAL FORCE COEFFICIENT -- MODIFIED APOLLO SHAPE

Mass Characteristics were estimated for both the multi-mission vehicle (4500 pounds) and the 1971 mission vehicle ($m/C_DA = 0.15$). The center of gravity locations, moments of inertia, and radii of gyration as used in the computer programs for the parametric studies are given in Table X.

TABLE X

MODIFIED APOLLO MASS CHARACTERISTICS

Mass (slugs)	D (feet)	m/C_DA (slug/ft^2)	X_{CG}/D	σ_X/D	σ_Y/D	I_x (slug ft^2)	I_y (slug ft^2)
139.9	15.	0.50	0.125	0.173	0.14	941	616
↓	16.67	0.40	0.113	0.173	0.135	1181	717
.	12.9	0.677	0.147	0.174	0.15	712	511
31.2	12.9	0.15	0.154	0.194	0.150	196	117
42.2	15.	↓	0.142	0.192	0.145	350	199
52.1	16.67		0.139	0.189	0.139	521	281

2.3.1.3 Tension Shell

The two tension shell configurations proposed by NASA/LRC for the present study have been described previously. The only difference is a slight blunting of the nose. The coefficients for the sharp and blunt tension shells (experimental data provided by LRC) are presented Figures 15 through 17 and Figures 20 through 22. At angles of attack where experimental data were not available, the coefficients were estimated based on the Newtonian variation. The damping coefficient, C_{m_q}, for which no experimental data were available, is assumed to have Newtonian values at all Mach numbers (see Figure 18).

The chief difference in the coefficients between the two shapes appears in the Mach 3 data. The drag of the blunt tension shell drops sharply at 0-degree angle of attack, but when the drag is compared with that of the sharp tension shell at the trim point and dynamic trajectories are considered, there is very little difference.

After comparing trajectories of the two shapes, the blunt tension shell became the reference shape. Real-gas effects were subsequently determined and incorporated in the axial force coefficients in Figure 15, and in the drag curve of Figure 19.

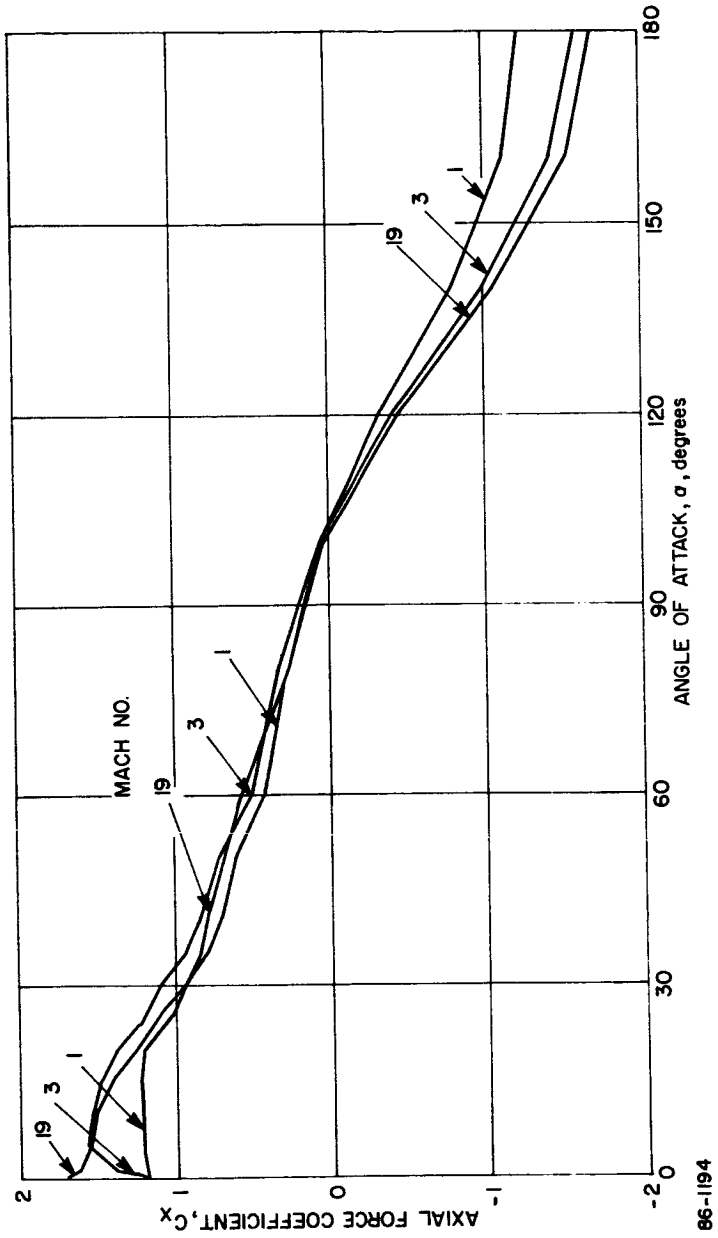

Figure 15 BLUNT TENSION SHELL -- AXIAL FORCE COEFFICIENT

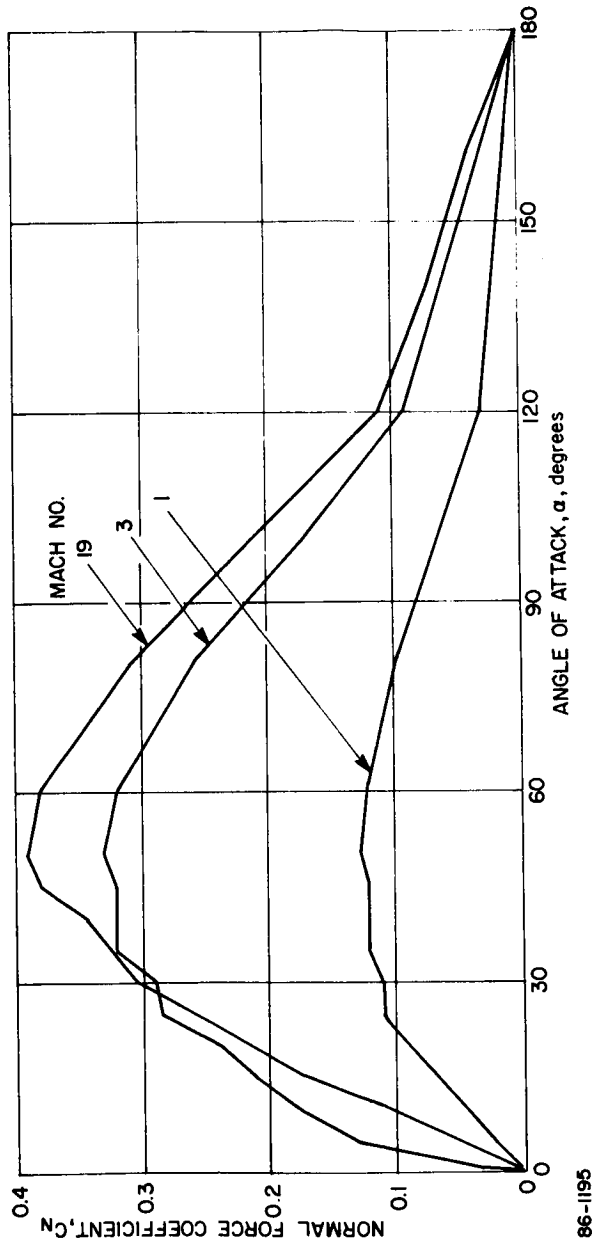

Figure 16 BLUNT TENSION SHELL -- NORMAL FORCE COEFFICIENT

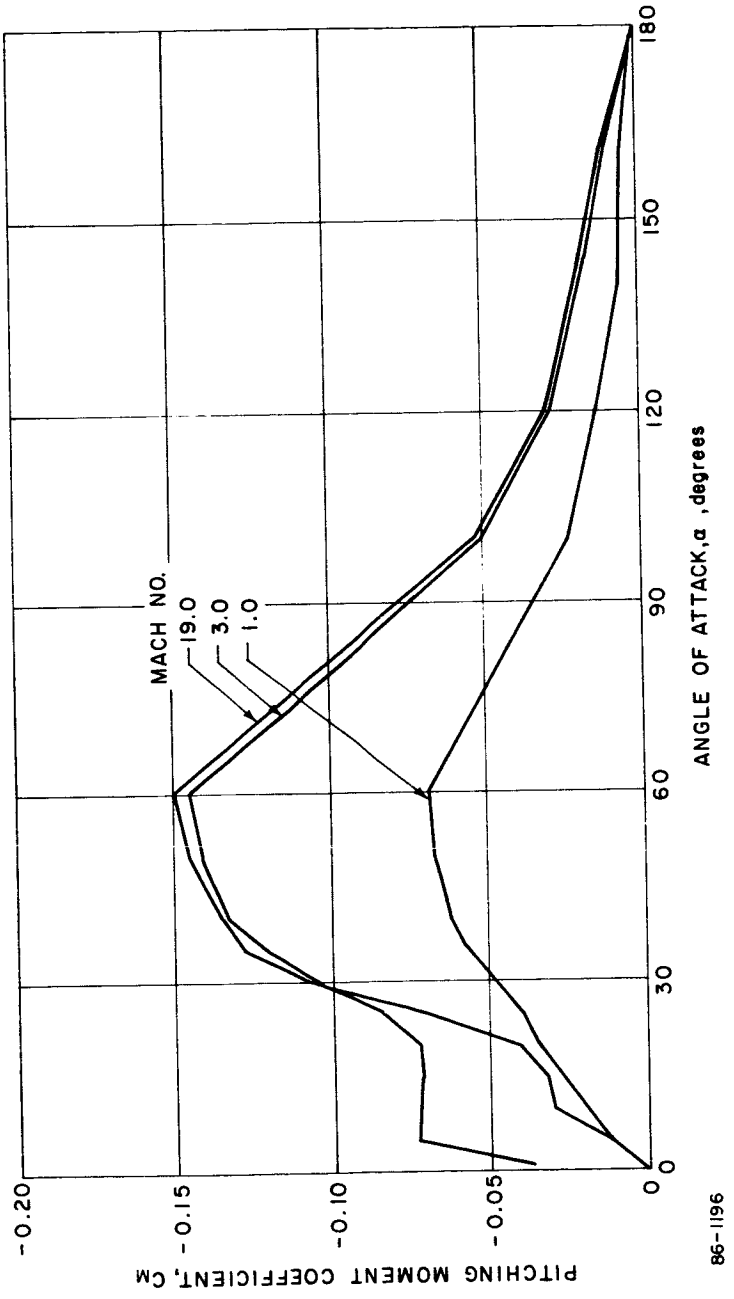

Figure 17 BLUNT TENSION SHELL -- PITCHING MOMENT COEFFICIENT

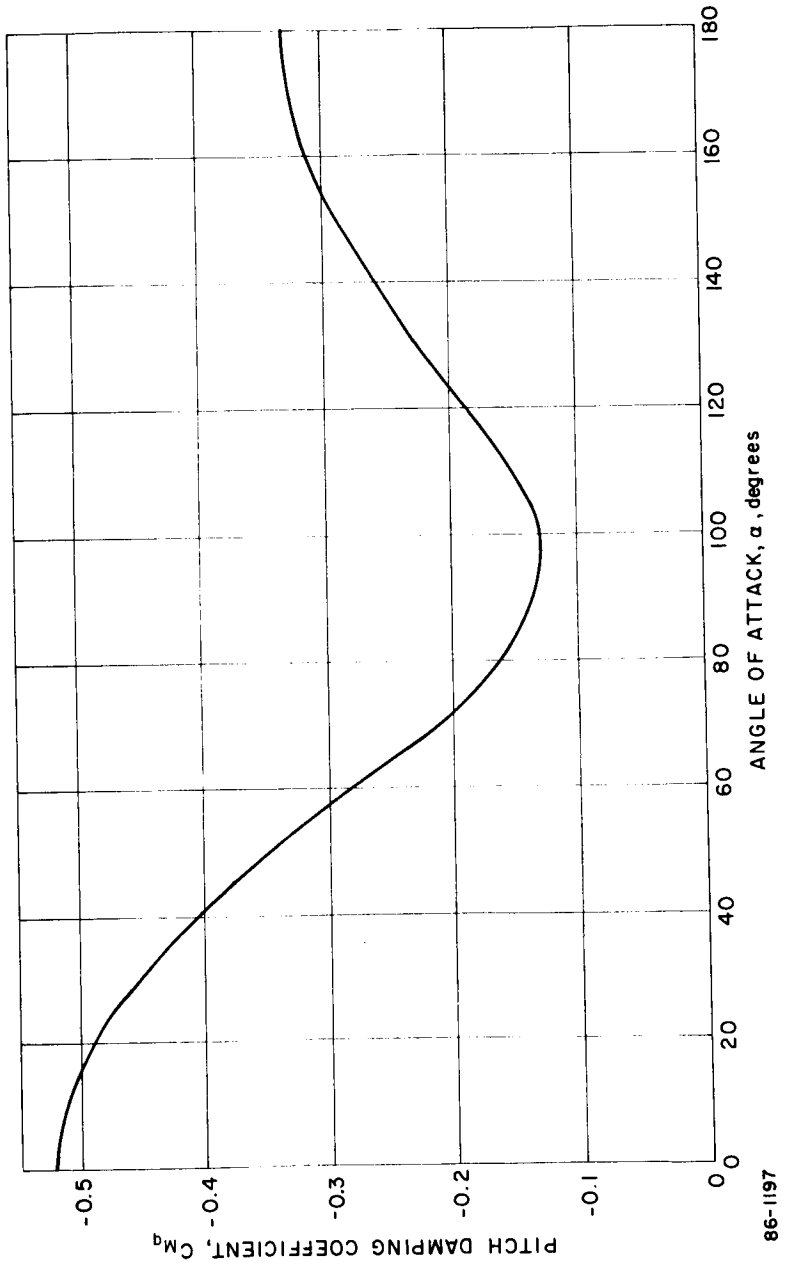

Figure 18 BLUNT TENSION SHELL PITCH DAMPING COEFFICIENT -- NEWTONIAN

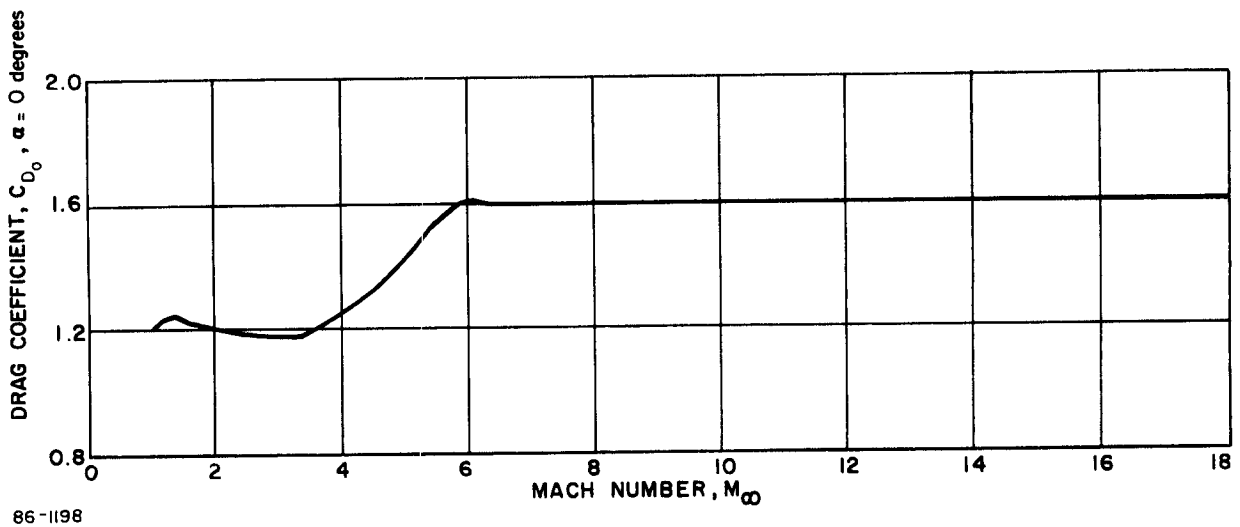

Figure 19 BLUNT TENSION SHELL AXIAL FORCE COEFFICIENT

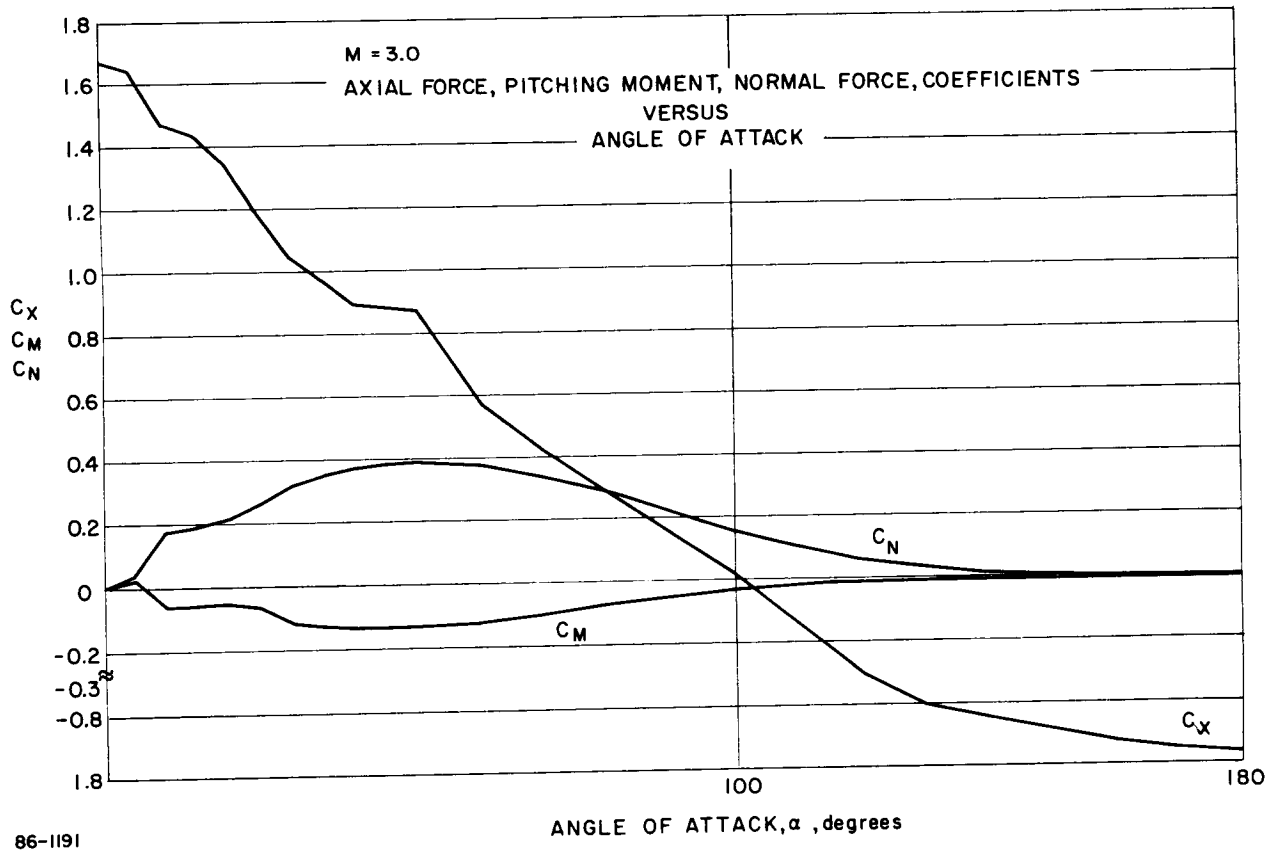

Figure 20 SHARP TENSION SHELL (NO AFTERBODY) COEFFICIENTS (M=3)

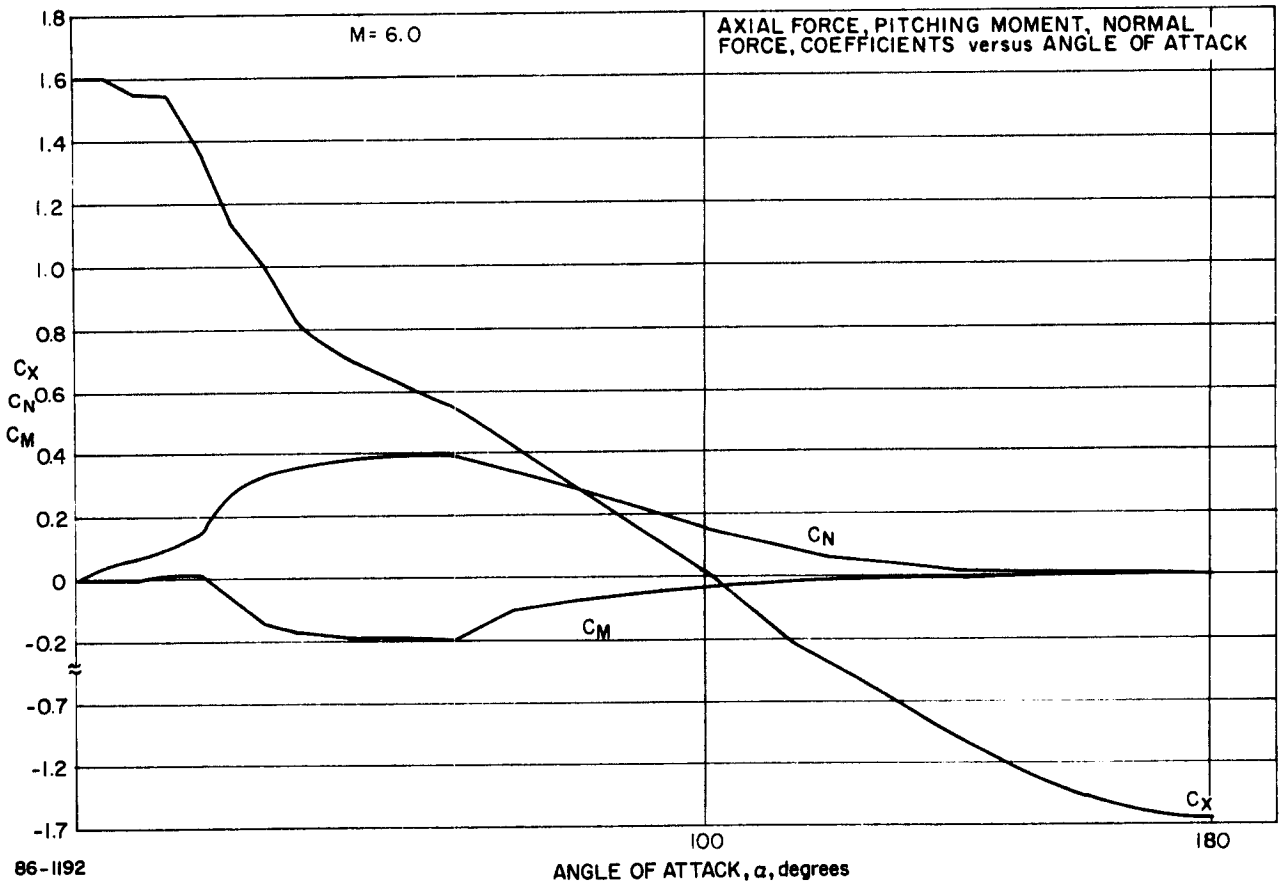

Figure 21 SHARP TENSION SHELL (NO AFTERBODY) COEFFIEICNTS (M=6)

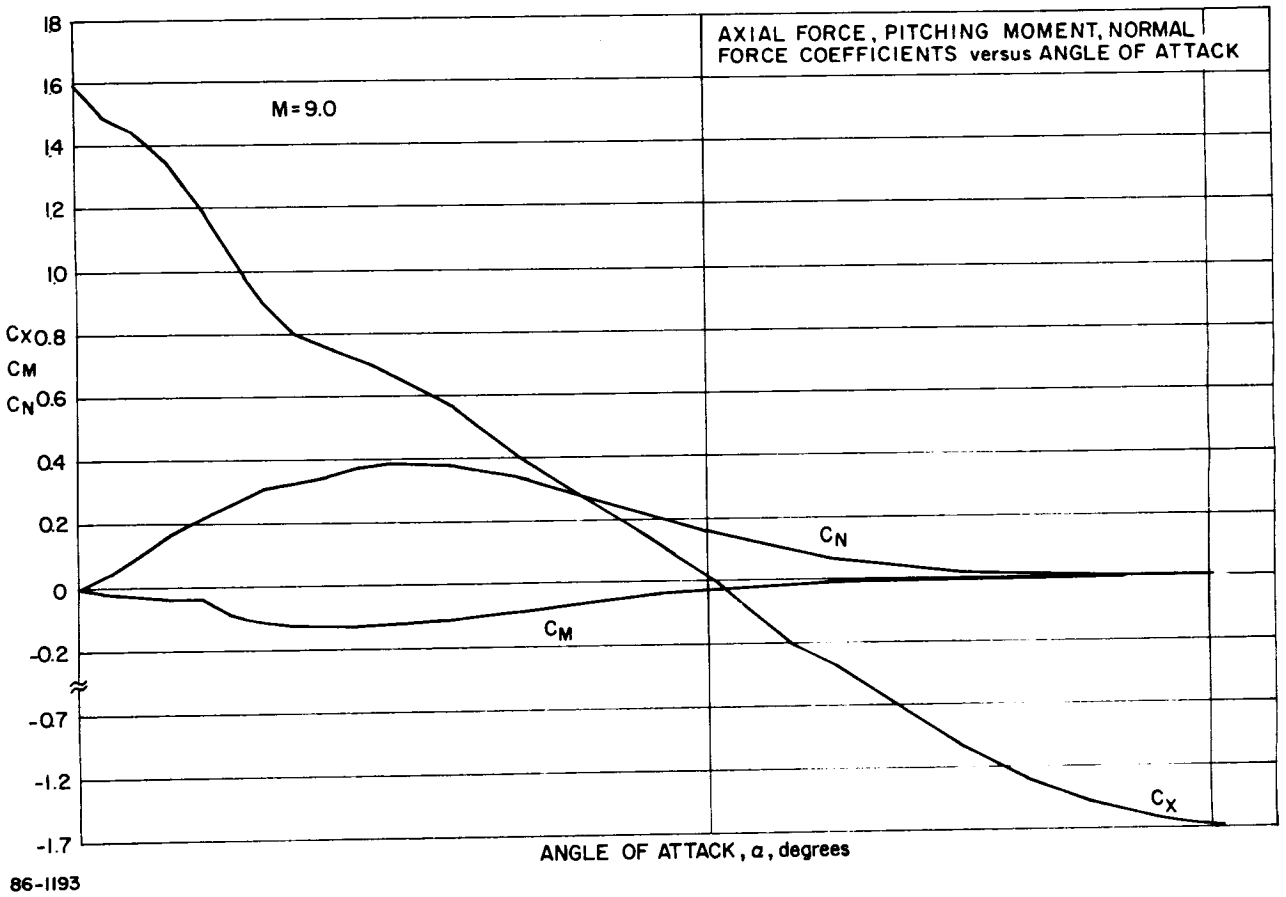

Figure 22 SHARP TENSION SHELL (NO AFTERBODY) COEFFICIENTS (M=9)

A typical trajectory illustrating the comparison of the blunt and sharp tension shells for the case of γ_E = -90 degrees with the Model 3 atmosphere is depicted in Figure 23. There is no significant difference in performance. The heating and loads are almost identical. The altitude at Mach 1.3 is about 1000 feet higher for the sharp shell, but the angle of attack diverges to about 22 degrees at Mach 5 (not shown in the figures). However, it converges again to less than 6 degrees at M = 1.3.

Mass characteristics were estimated for both the multi-mission vehicle (4500 pounds) and the 1971 mission vehicle (m/C_DA = 0.15). The center of gravity locations, moments of inertia, and radii of gyration as used in the computer programs for the parametric studies are given in Table XI.

TABLE XI

BLUNT TENSION SHELL MASS CHARACTERISTICS

Mass (slugs)	D (feet)	m/C_DA (slugs/ft^2)>	X_{GG}/D	σ_X/D	σ_y/D	I_x (slug/ft^2)	I_y (slug/ft^2)
139.9	15.	0.49	0.305	0.196	0.176	1260	965
139.9	16.67	0.39	0.281	0.200	0.176	1559	1221
139.9	12.9	0.67	0.348	0.177	0.176	921	723
31.4	12.9	0.15	0.401	0.253	0.195	337	201
42.4	15.	0.15	0.376	0.252	0.200	609	379
52.8	16.67	0.15	0.366	0.250	0.200	915	591

2.3.2 Loads and Heating

A parametric study was performed with the aid of a trajectory computer program to determine the effects on heating and loads of varying the vehicle diameter, atmosphere model, and entry conditions. Atmosphere Models 1, 2, and 3 were used, and the range of diameters considered was from 10 to 20 feet. The following facts were found to be common to all three configurations.

The critical loading trajectories were found to occur at the steepest entry angles (γ_E = -90 degrees) in each atmosphere. Both particle and dynamics (α_E = 35 degrees) trajectories were investigated.

The particle trajectories (α_E = 0 degrees) result in the minimum loads. The loads for the rearward entry condition (α_E = 179 degrees) represent the loads which might be obtained in a failure mode if no flaps are used to improve the righting moment in this range of angle of attack.

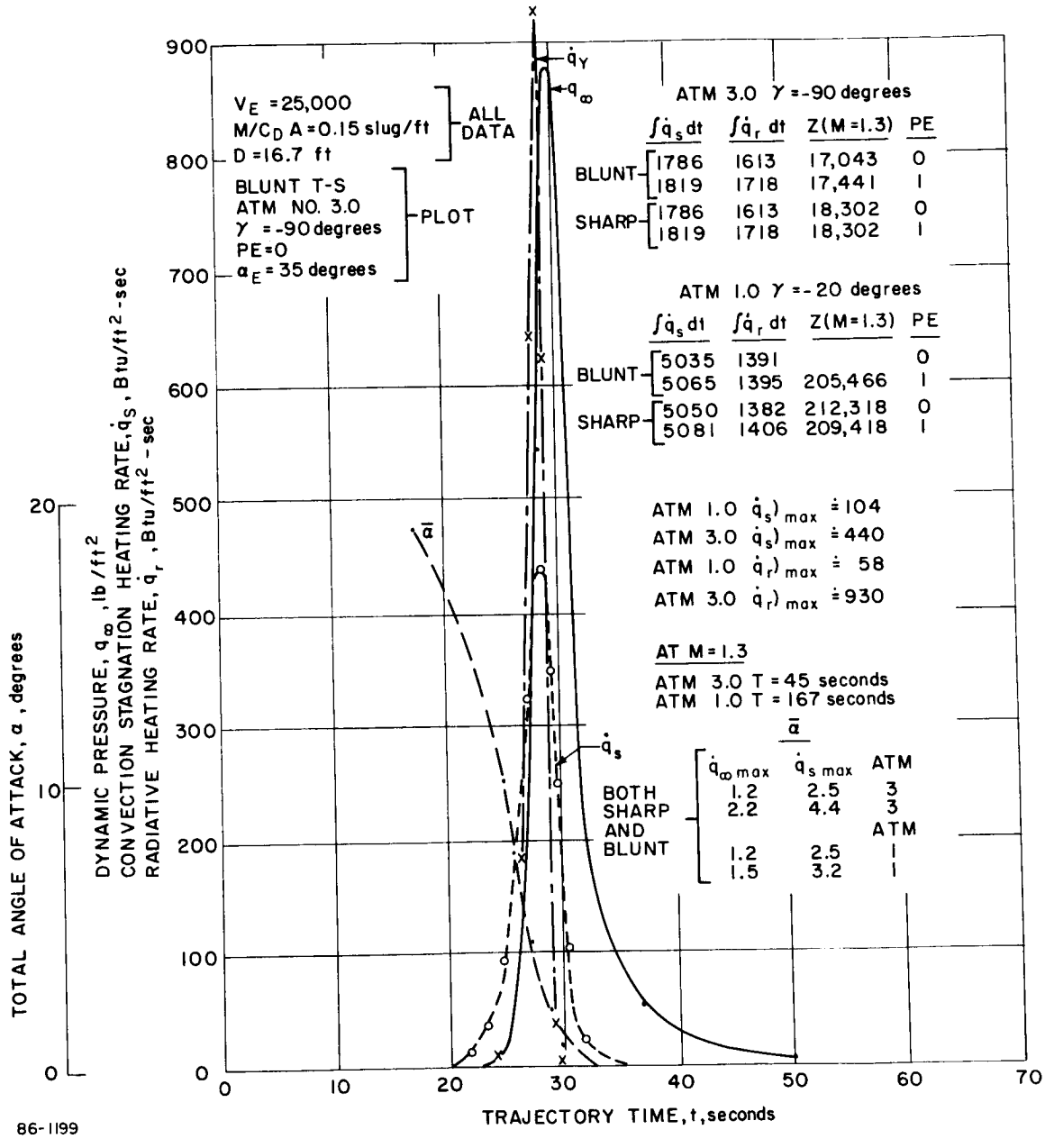

Figure 23 COMPARISON OF BLUNT AND SHARP TENSION SHELLS

The greatest integrated convective heating is obtained at the smallest entry angle, -20 degrees.

2.3.2.1 Blunt Cone

1. Loads -- Maximum loads for the multimission shell (W_E = 4500 pounds) are plotted versus diameter in Figure 24. It can be seen that the greatest loads are obtained at the small diameters (due to the high m/C_DA) in the atmosphere 2. The corresponding data for the 1971 mission are plotted in Figure 25.

For the revised design concepts, (B, C, D)* additional trajectories were computed. The resulting load data are summarized in Table XII.

TABLE XII

DYNAMICS SUMMARY
(Blunt cone)

Design Concept	(B)*		(C* and D)*	
Entry weight, pounds	4500		1390	
Entry angle of attack, degrees	0	179	0	179
Peak dynamic pressure, psf	1152	1426	777	1009
α at peak dynamic pressure	-	16	-	20
Maximum axial "g"	73.3	91	161	209
Maximum normal "g"	-	7	-	19

2. Heating

a. Convective -- The effect on the heat pulse of varying vehicle diameter is summarized in Figure 26 for the 4500-pound entry vehicle. The greatest convective heating for the blunt cone is obtained at the stagnation point in the Model 1 atmosphere, and the maximum radiative heating is obtained at the sonic point in the Model 2 atmosphere.

A similar study was performed for the 1971 mission (m/C_DA = 0.15). At this value of m/C_DA, radiative heating is much less, and only atmosphere 1 need be considered for heat shield design. Figure 27 summarizes the heating as a function of diameter.

*B. C. D concepts as defined in section 2.1.2.4 and Load and Heating tables.

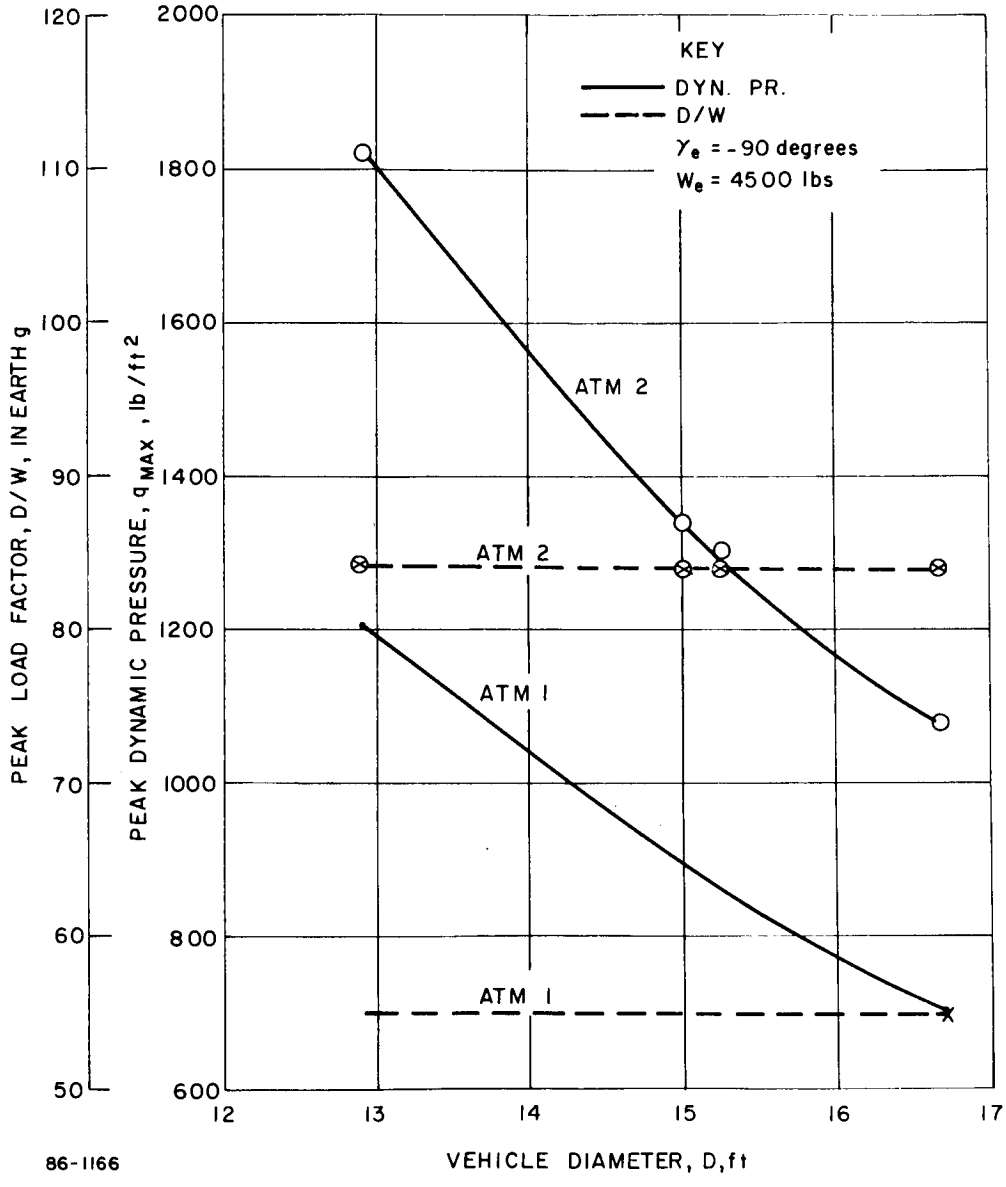

Figure 24 LOADING PARAMETERS -- 60 DEGREE BLUNTED CONE

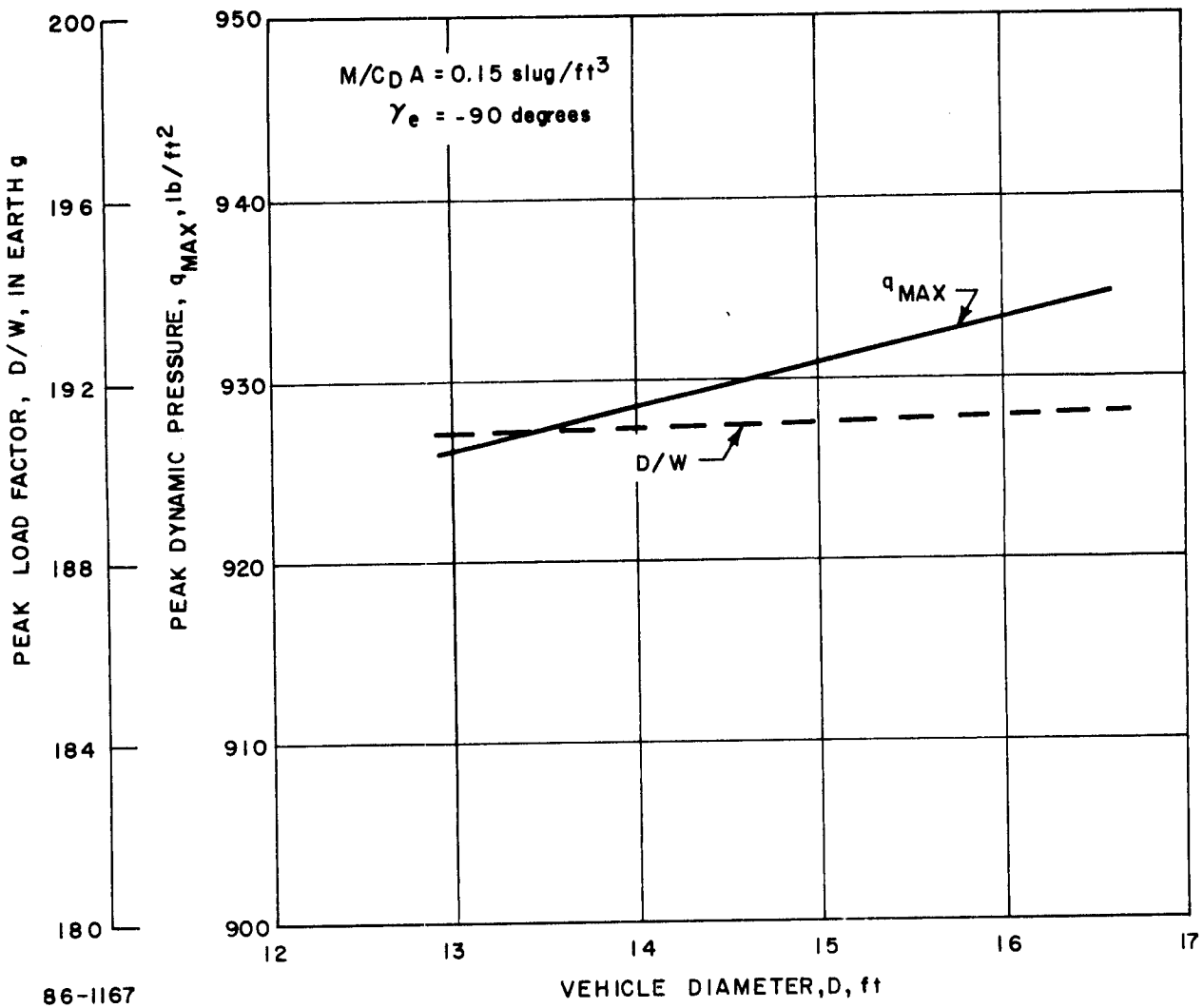

Figure 25 LOADING PARAMETERS--60-DEGREE BLUNTED CONE

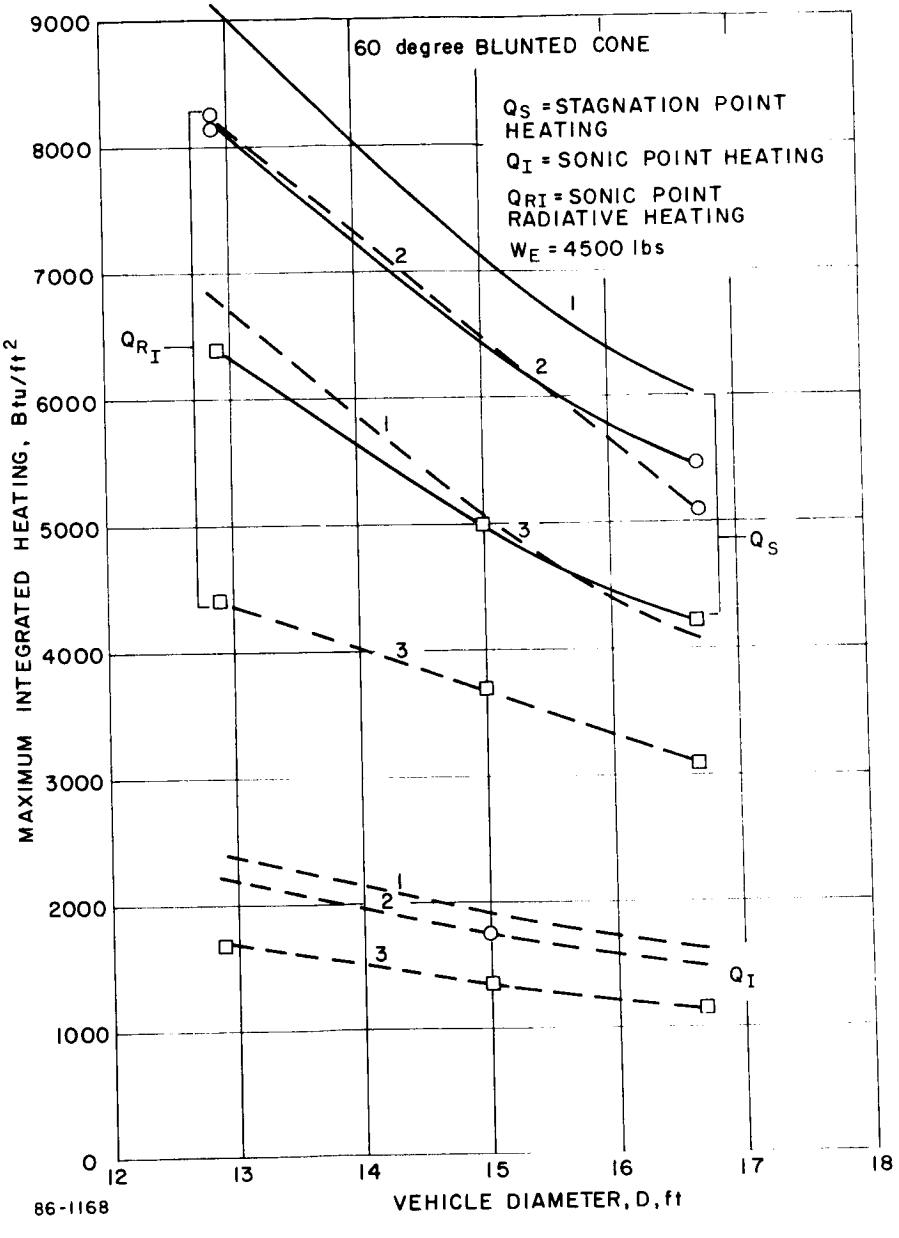

Figure 26 INTEGRATED HEATING -- 60-DEGREE BLUNTED CONE

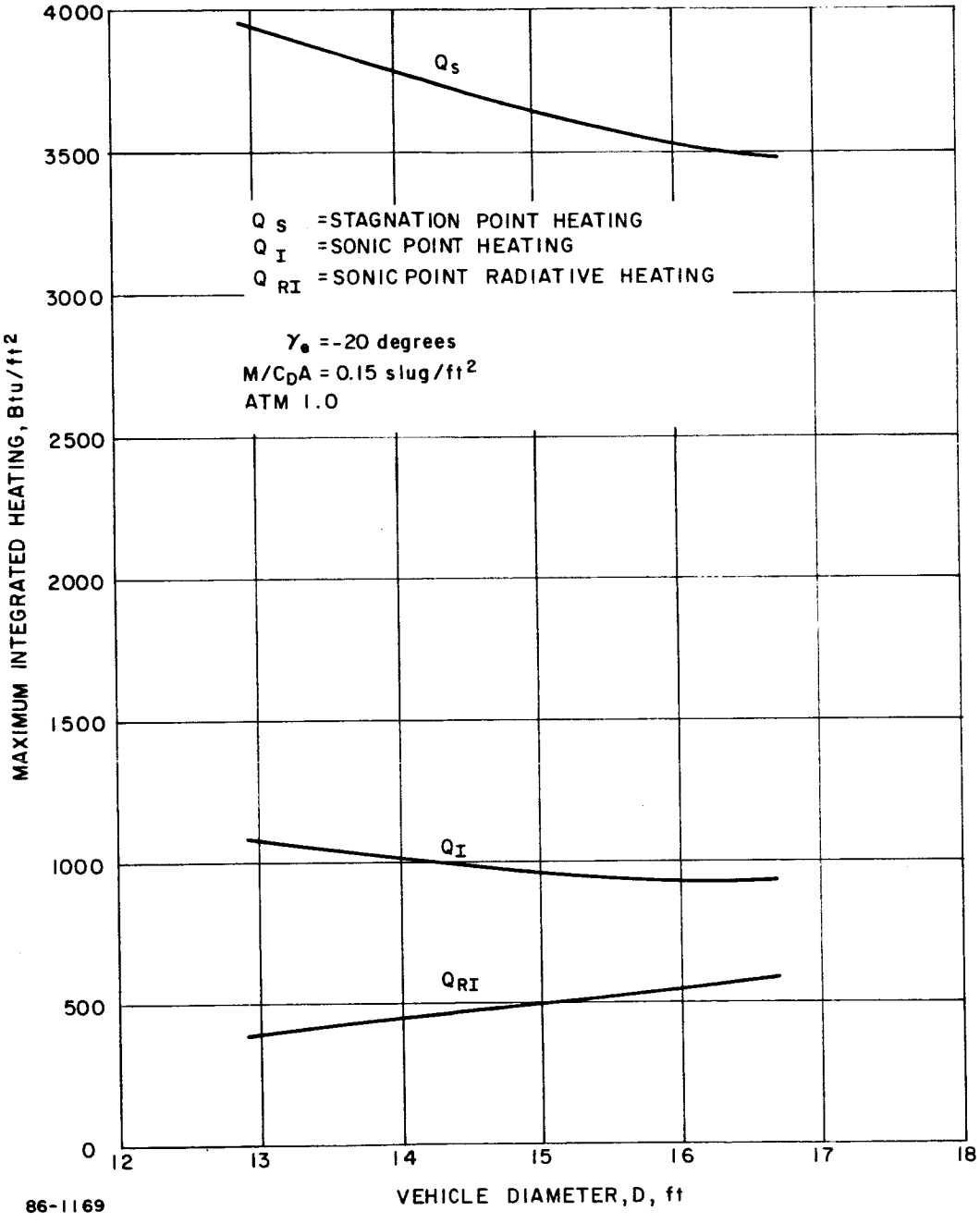

Figure 27 INTEGRATED HEATING -- 60 DEGREE BLUNTED CONE

Typical heating environments are presented for the revised concepts in Figure 28 through 33 along with the corresponding enthalpy variations. The occurrence of transition does not affect the design environments with the exception of the future mission concept. Although transition occurs in the steep entry trajectories ($\gamma_E \leq -45$ degrees) for the light weight configurations ($m/C_DA = 0.15$ slug/ft^2), the integrated heating is much less than for the all-laminar heating at the shallow entry. The future mission results in earlier transition as the entry angle is steepened ($\gamma_E < -20$ degrees); however, the total integrated heating again decreases.

b. Radiative -- Stagnation point time histories at zero-angle of attack are shown in Figure 34. The variation of the radiative distributions were obtained for the Model 1 atmosphere (Figure 35). The angle of attack levels at peak radiative heating indicated that the angle of attack effect was small when considering the contribution of the radiative heating to the total heating.

2.3.2.2 Modified Apollo

1. Loads -- Maximum loads for the multi-mission shell (W_E = 4500 pounds) are plotted versus diameter in Figure 36. It can be seen that highest loads occur in the Model 2 atmosphere, and increase with decreasing diameter. The data for the 1971 mission are plotted in Figure 37. In this case, since the m/C_DA is constant, there is little change in loads with diameter. Highest loads occur in Model 3 atmosphere.

For the revised design concepts, additional trajectories were computed. The resulting load data are summarized in Table XIII.

TABLE XIII

LOAD SUMMARY MODIFIED APOLLO

Design Concept	(B)		(C) and (D)	
Entry Weight, pounds	4500		1450	
Entry angle of attack, degrees	0	179	0	179
Peak dynamic pressure, psf	1098	1333	775	1020
α at peak dynamic pressure, degrees	---	11	---	22
Maximum axial g	73	89	161	211
Maximun normal g	---	3	---	11

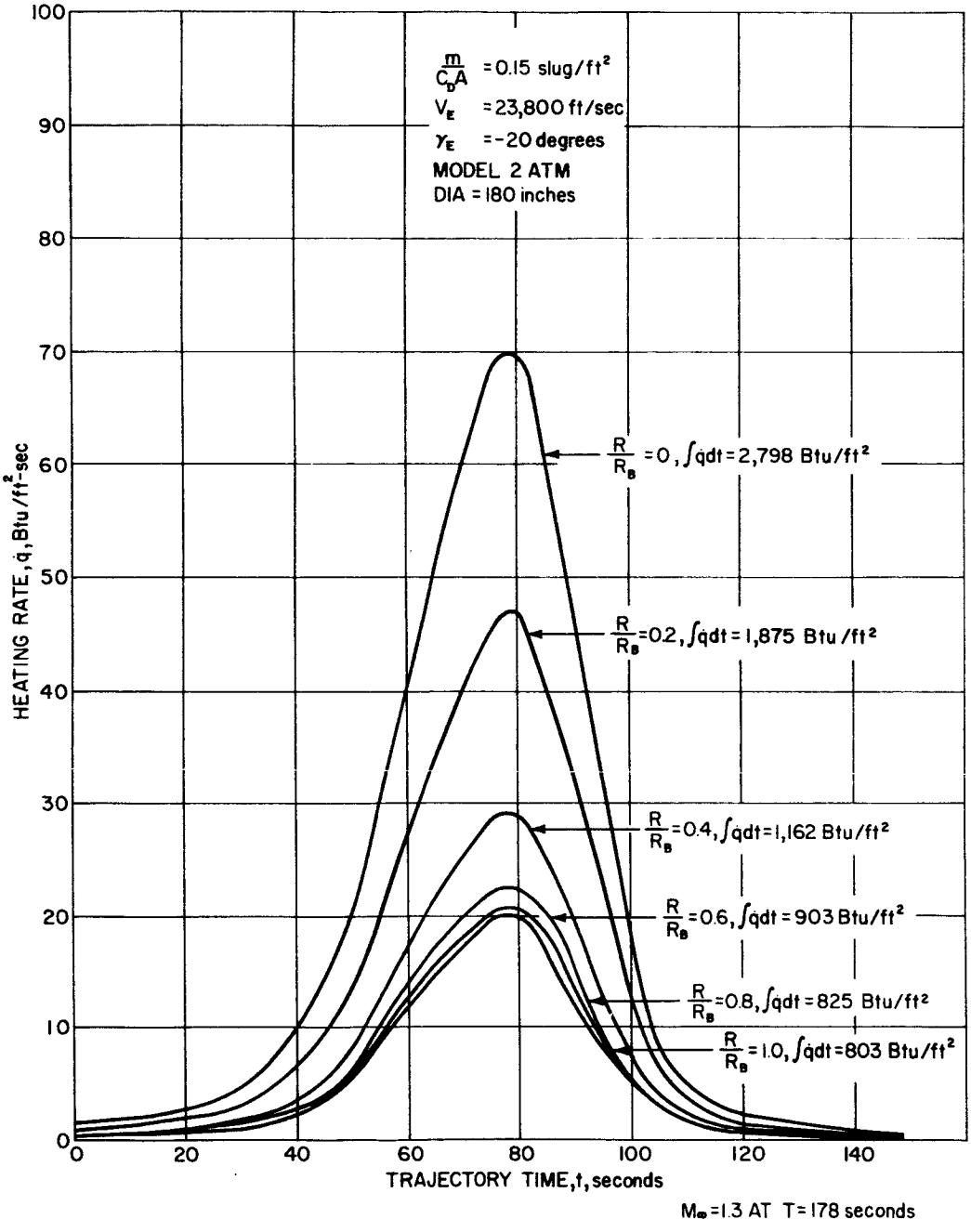

Figure 28 BLUNT CONE AERODYNAMIC HEATING PULSES $\left(\frac{M}{C_D A} = 0.15 \frac{slug}{ft^2}\right)$

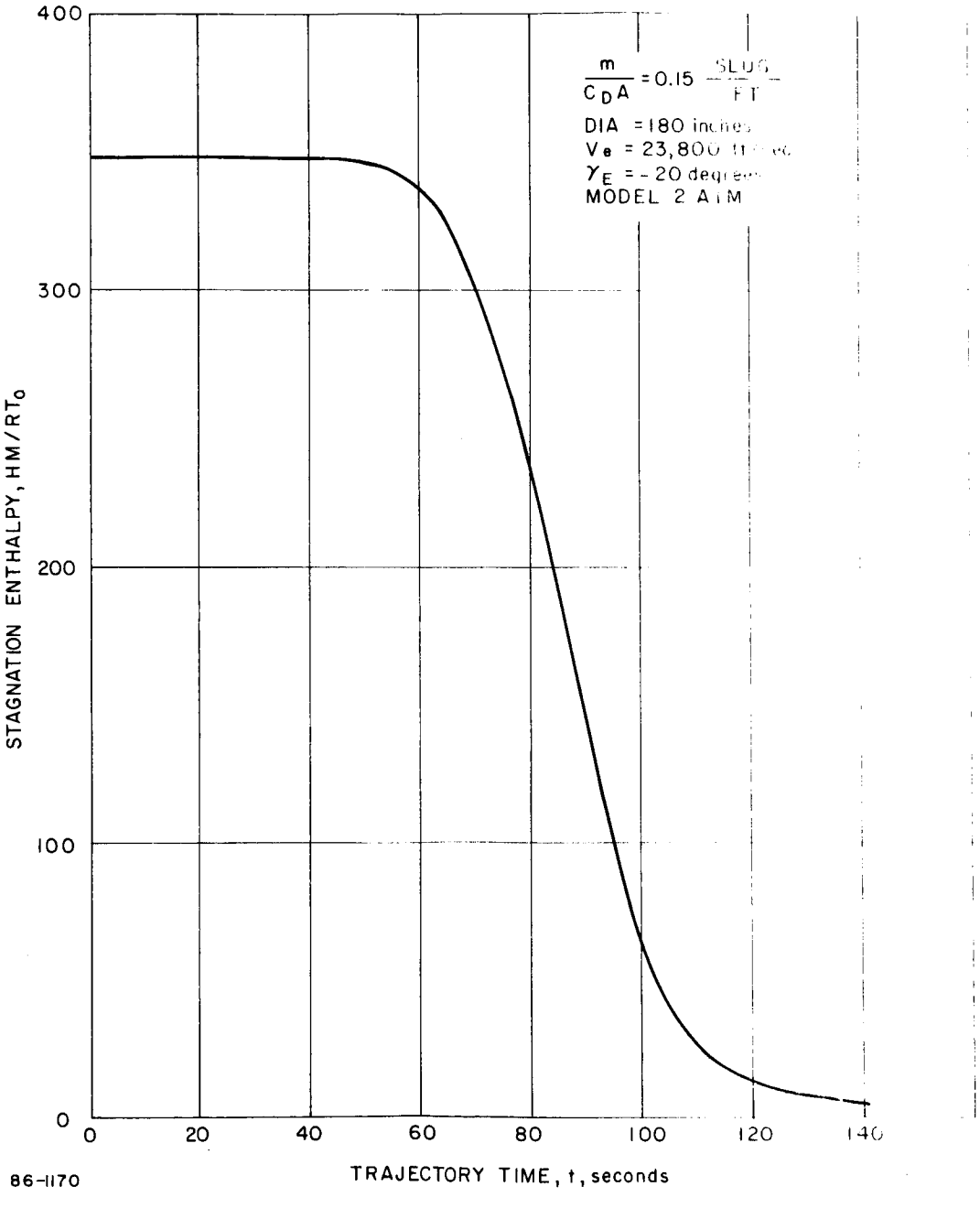

Figure 29 BLUNT CONE STAGNATION ENTHALPY

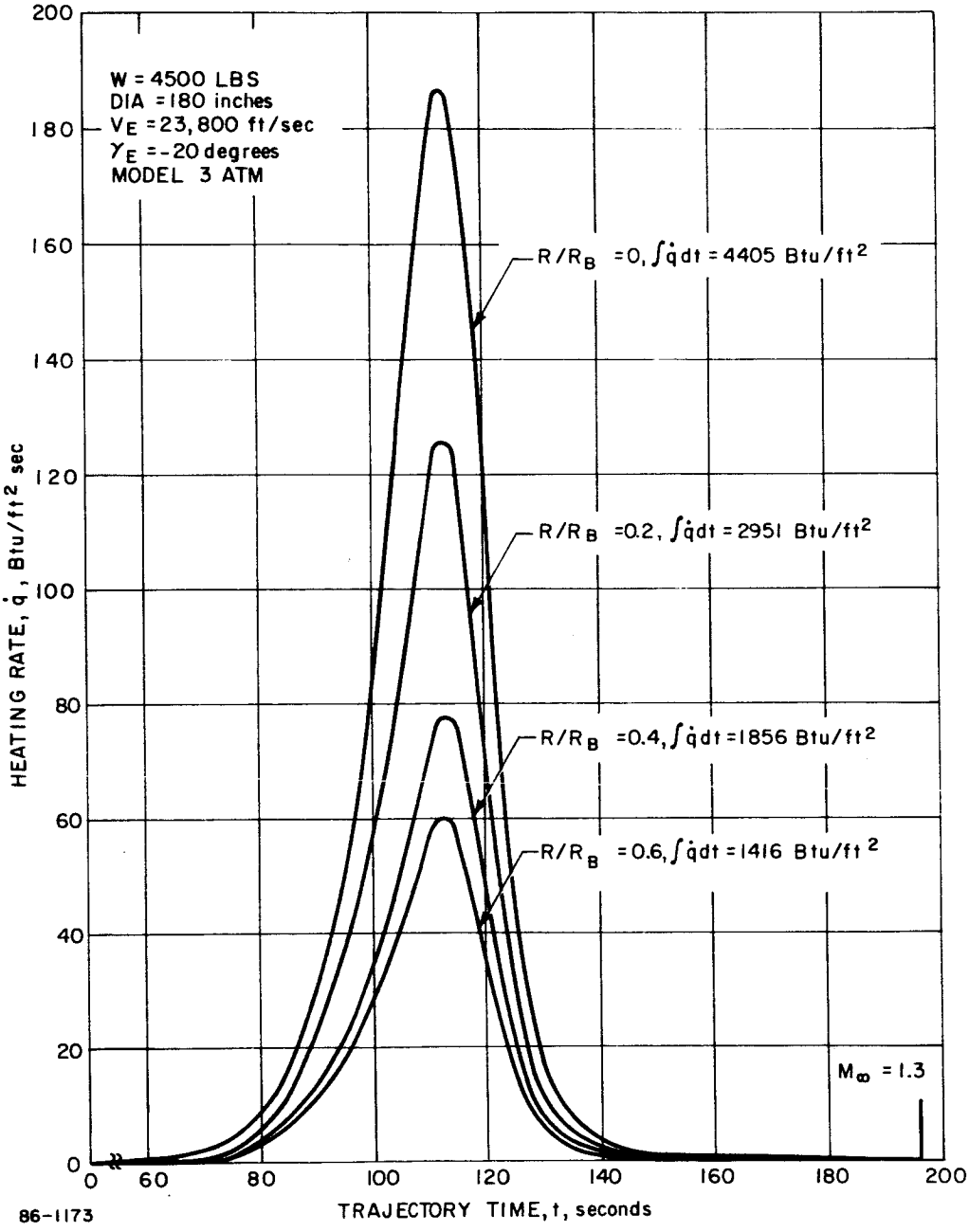

Figure 30 BLUNT CONE AERODYNAMICS HEATING PULSES (W = 1500 POUNDS)

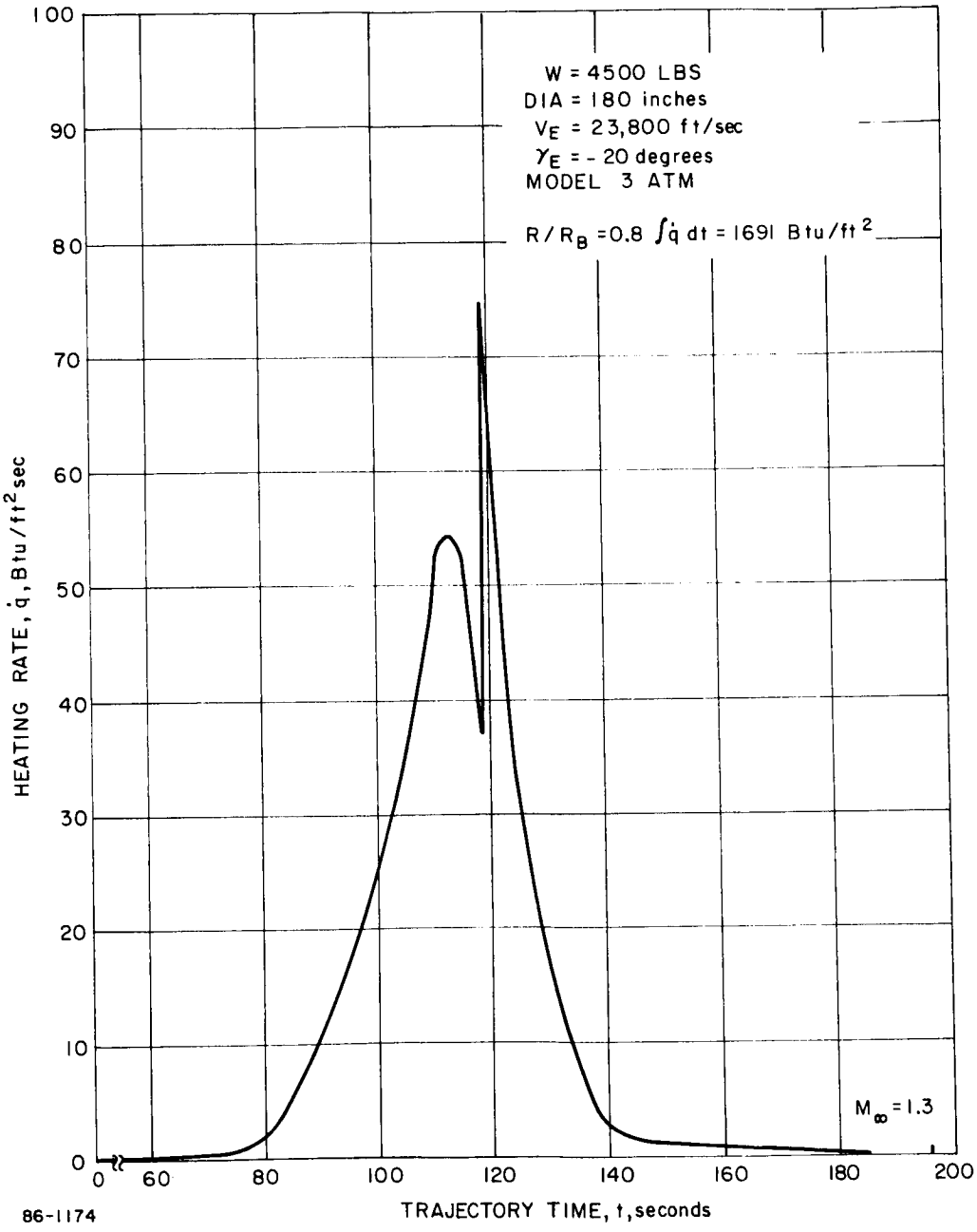

Figure 31 BLUNT CONE AERODYNAMICS HEATING PULSES (W = 9500 POUNDS)

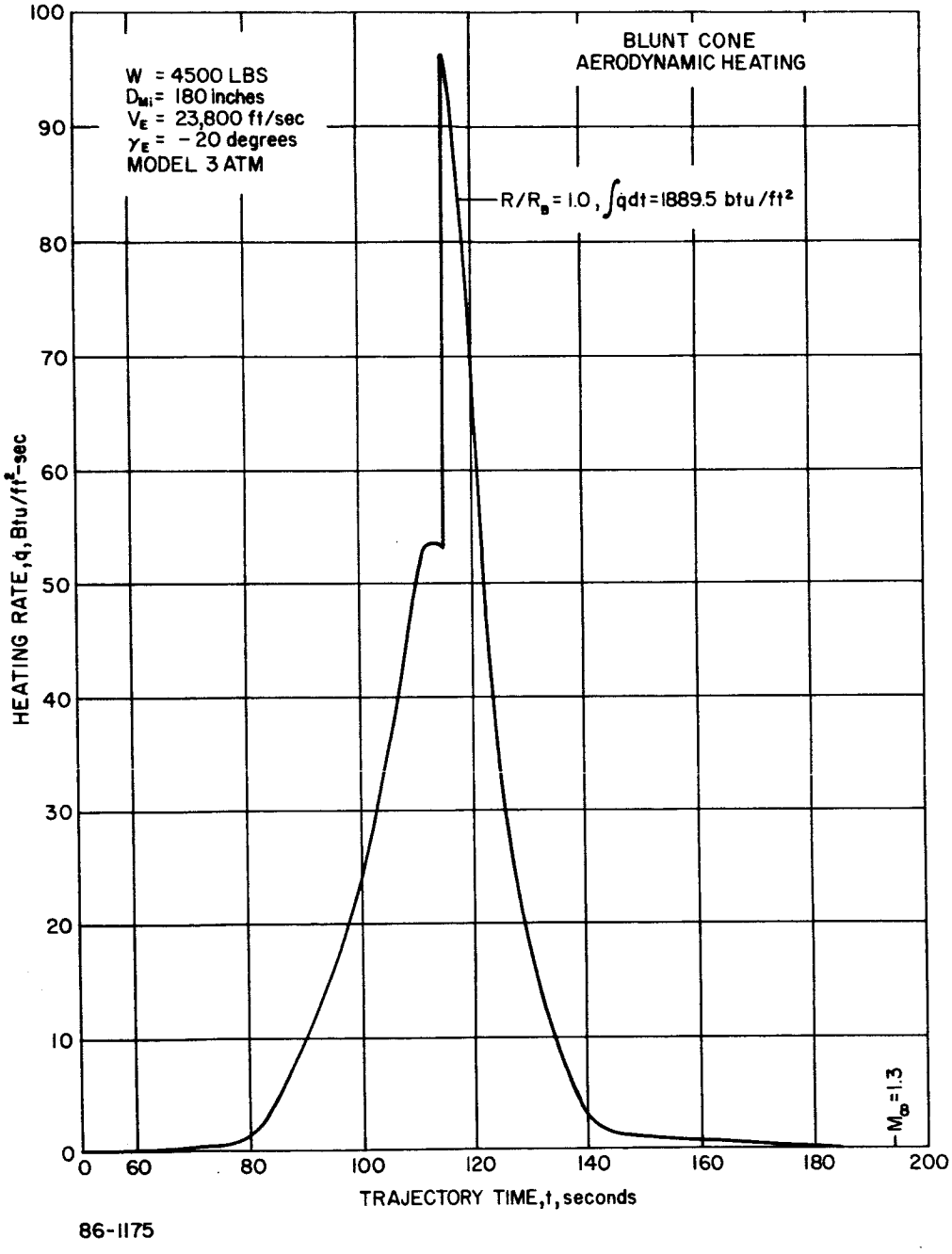

Figure 32 BLUNT CONE AERODYNAMIC HEATING PULSES (W = 4500 POUNDS)

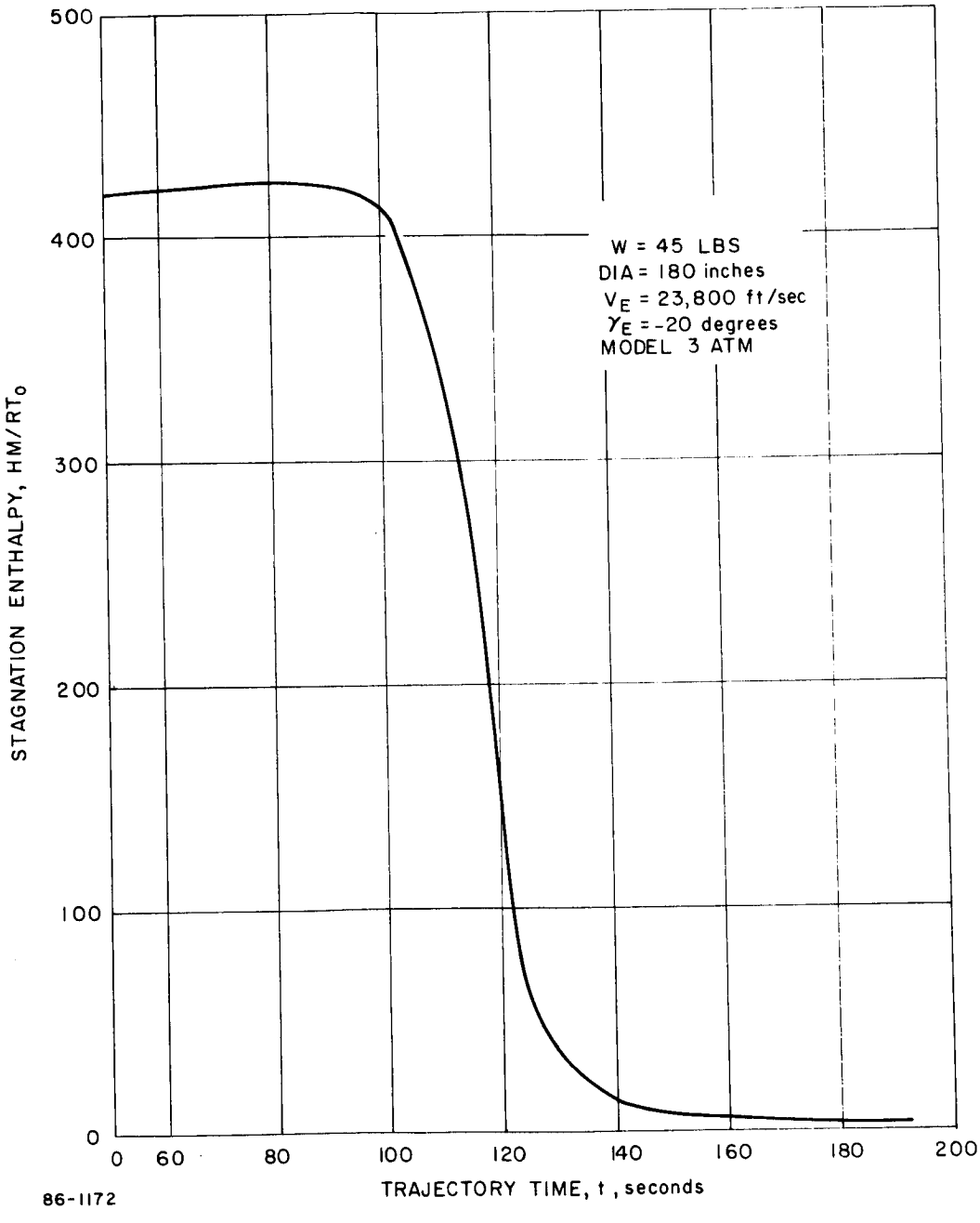

Figure 33 BLUNT CONE STAGNATION ENTHALPY

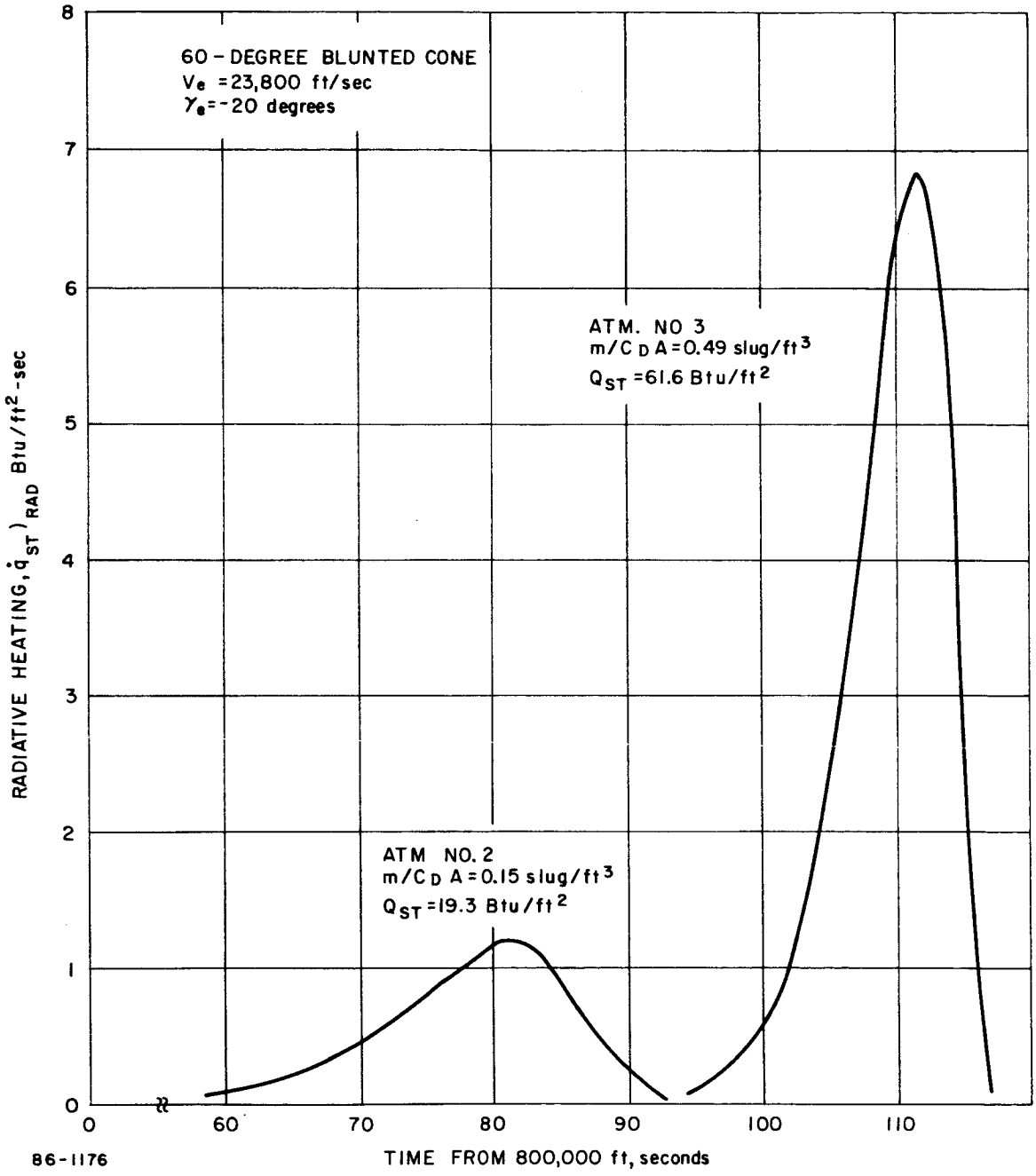

Figure 34 RADIATIVE HEATING (BLUNT CONE)

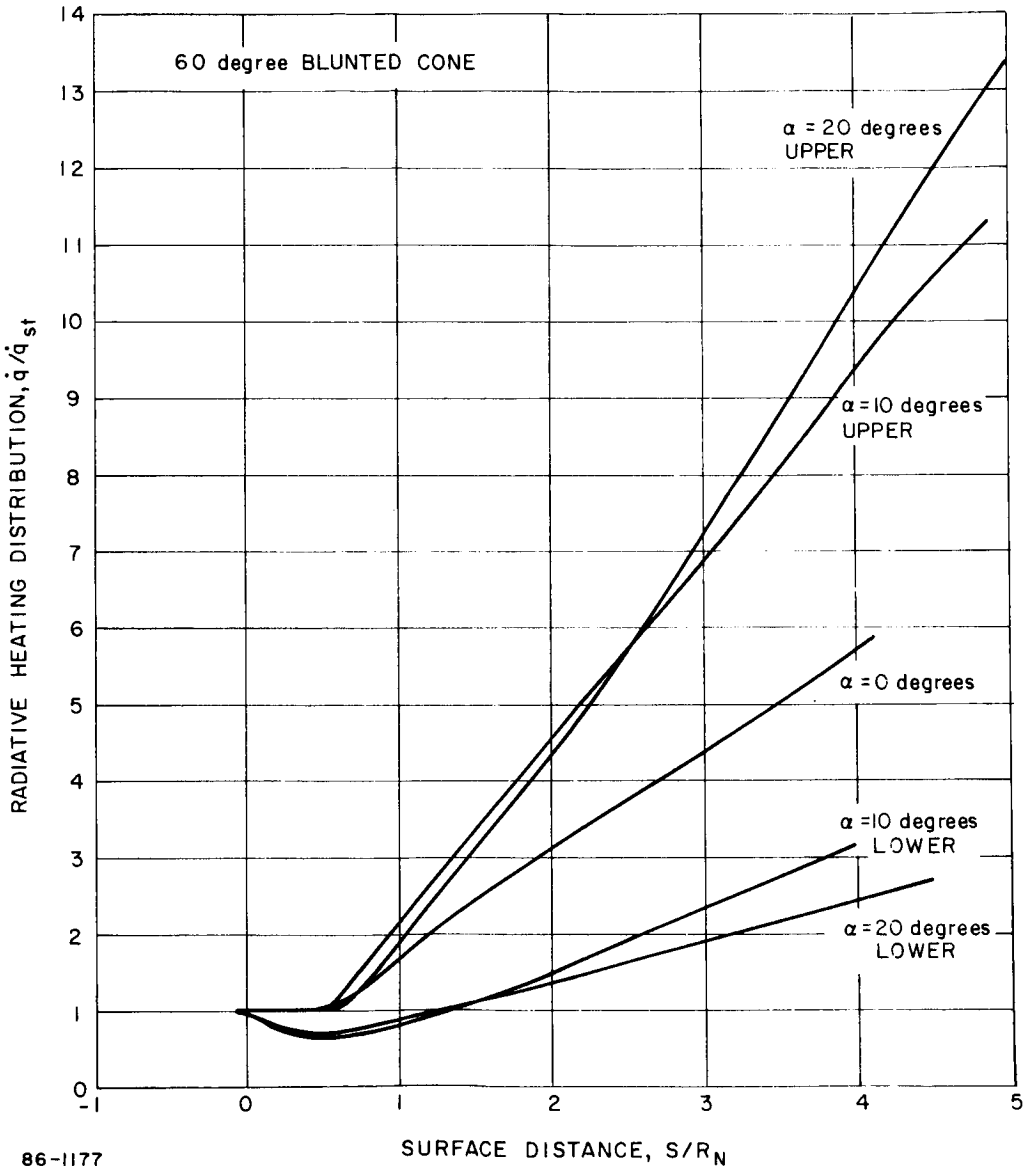

Figure 35 RADIATIVE HEATING DISTRIBUTIONS (BLUNT CONE)

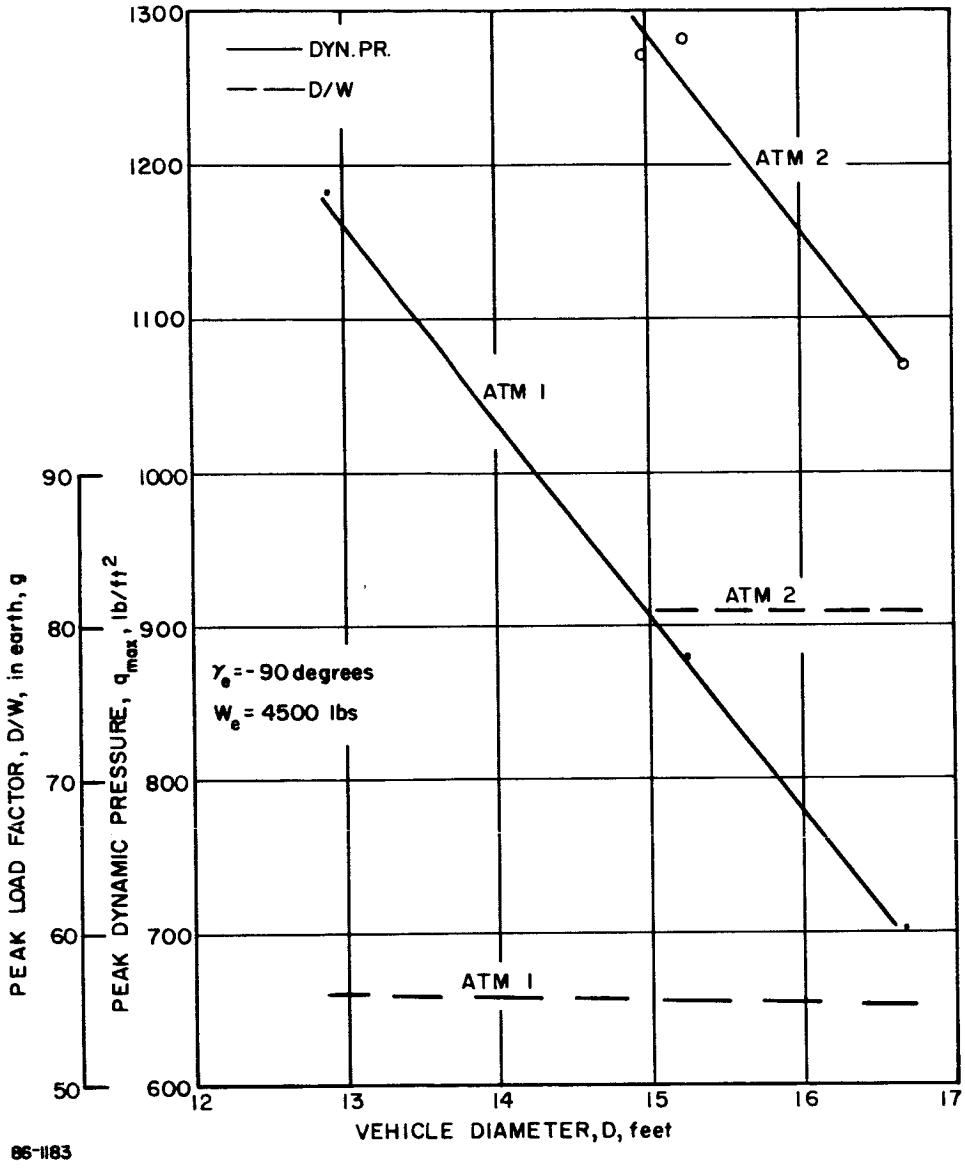

Figure 36 LOADING PARAMETERS--MODIFIED APOLLO

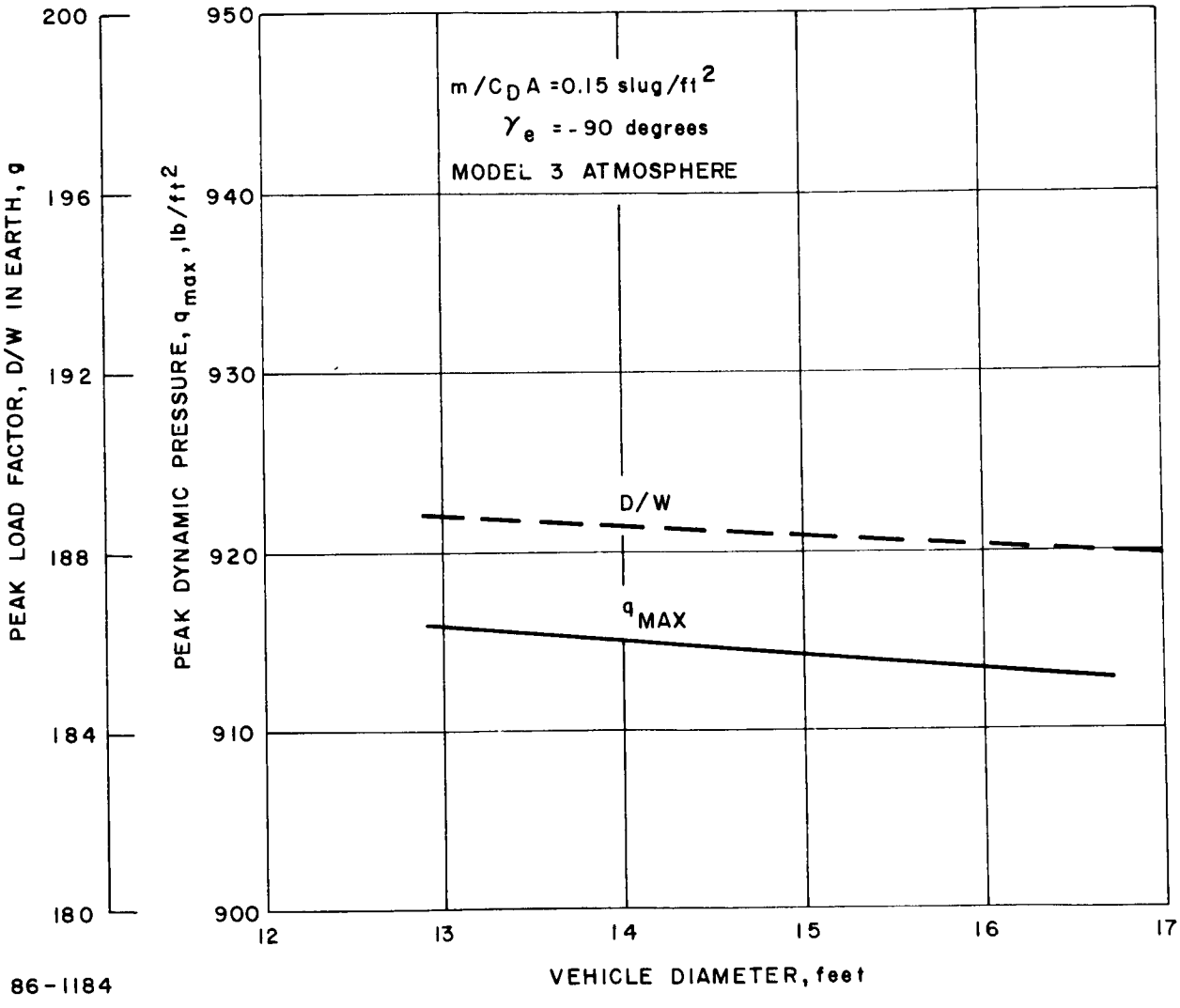

Figure 37 LOADING PARAMETERS--MODIFIED APOLLO

2. Heating

a. Convective-- The effect on the heat pulse of varying vehicle diameter is summarized in Figure 38, for the 4500-pound (multi-mission) entry vehicle. The greatest convective heating for the modified Apollo is obtained at the sonic point (rim) for turbulent flow in the Model 1 atmosphere, and the maximum radiative heating is obtained in the Model 2 atmosphere.

A similar study was performed for the 1971 mission (m/C_DA =0.15). At this value of m/C_DA, radiative heating is much less and only atmosphere 1 need be considered for heat shield design. The greatest heating now occurs at the stagnation point for most diameters. Figure 39 summarizes the heating as a function of diameter.

Typical heating environments for the revised design concepts together with the corresponding enthalpy histories are presented in Figures 40 and 41. The occurrence of transition does not effect the design environments except in the future mission concept.

b. Radiative -- Stagnation point time histories at zero-angle of attack are shown in Figures 42 and 43. This shape appears to carry the heaviest radiant flux penalty relative to the convective (at least for the 4500-pound vehicle - m/C_DA = 0.47) due to the relatively flat distribution over the large blunt face. The variation with angle of attack resulted in a decrease in the radiative heating (reduced standoff distance at the stagnation point in conjunction with the standoff slope variation, or shock shape). The zero angle of attack distribution was therefore used.

2.3.2.3. Tension Shell

1. Loads -- Maximum loads for the multi-mission shell (W_E = 4500 pounds) are plotted versus diameter in Figure 44. It can be seen that the highest loads occur in the Model 2 atmosphere, and increase with the decreasing diameter. The data for the 1971 mission are plotted in Figure 45. In this case, since the m/C_DA is constant, there is little change in loads with diameter. Highest loads occur in the Model 3 atmosphere.

For the revised design concepts, additional trajectories were computed. The resulting load data are summarized in Table XIV.

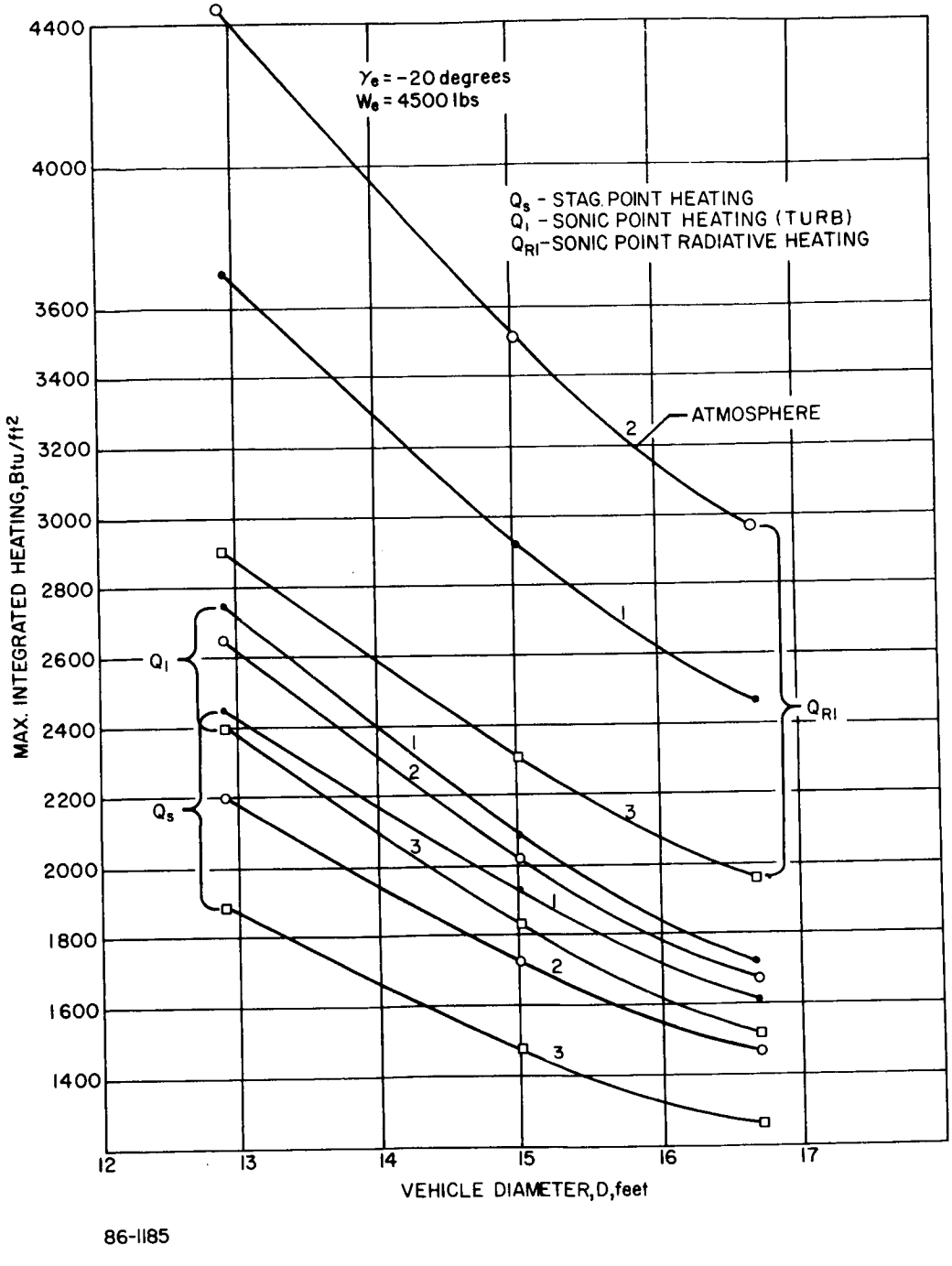

Figure 38 INTEGRATED HEATING--MODIFIED APOLLO

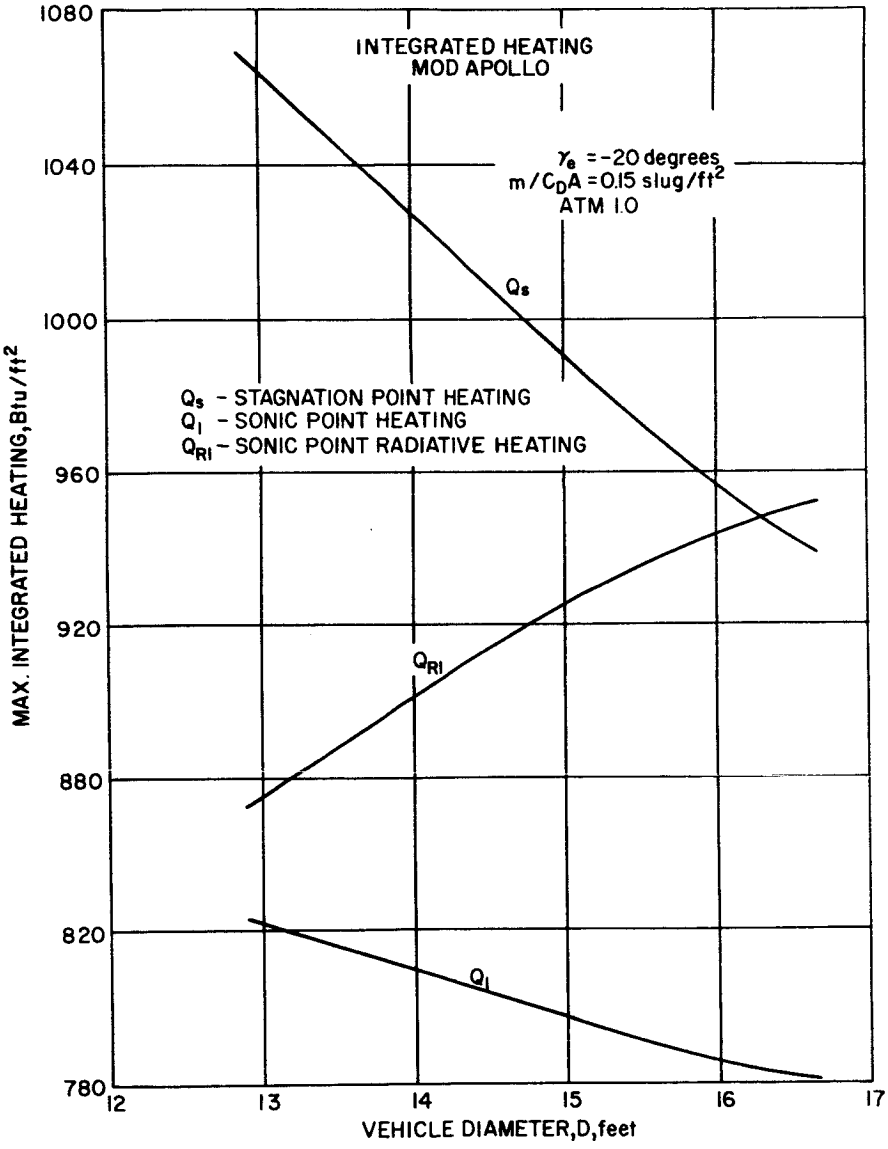

86-1186

Figure 39 INTEGRATED HEATING--MODIFIED APOLLO

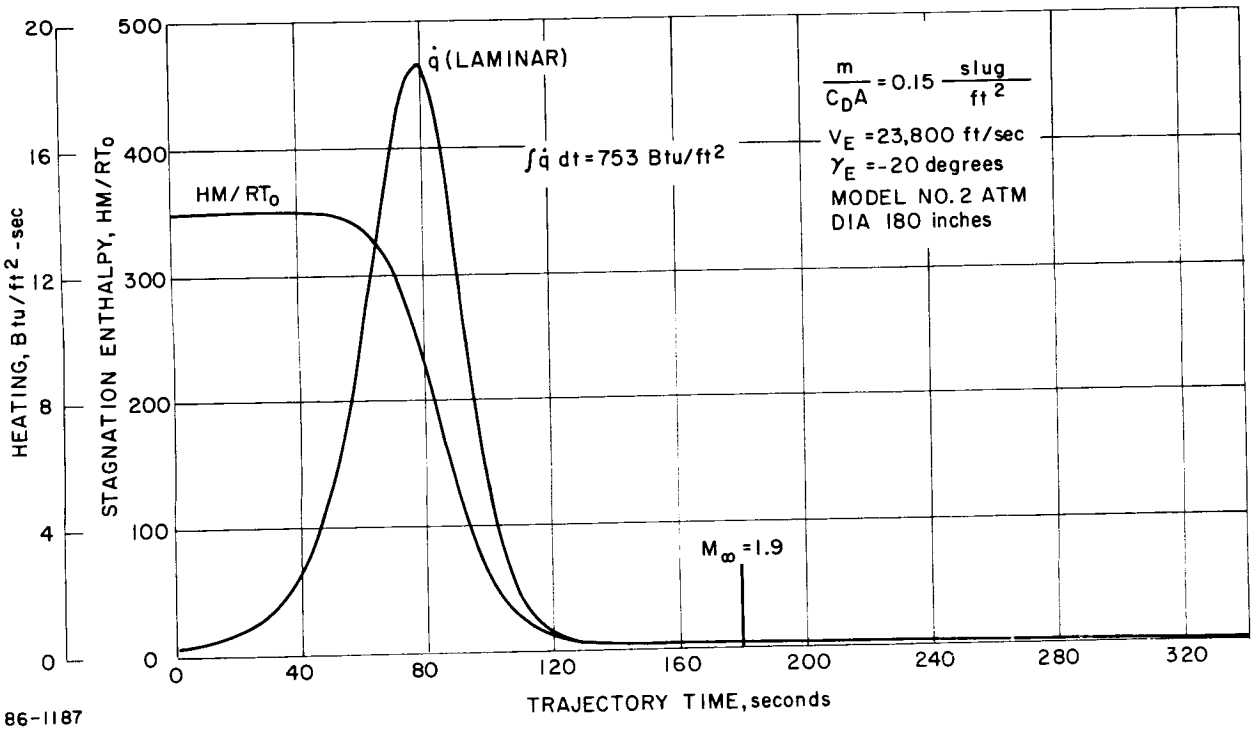

Figure 40 MODIFIED APOLLO HEATING

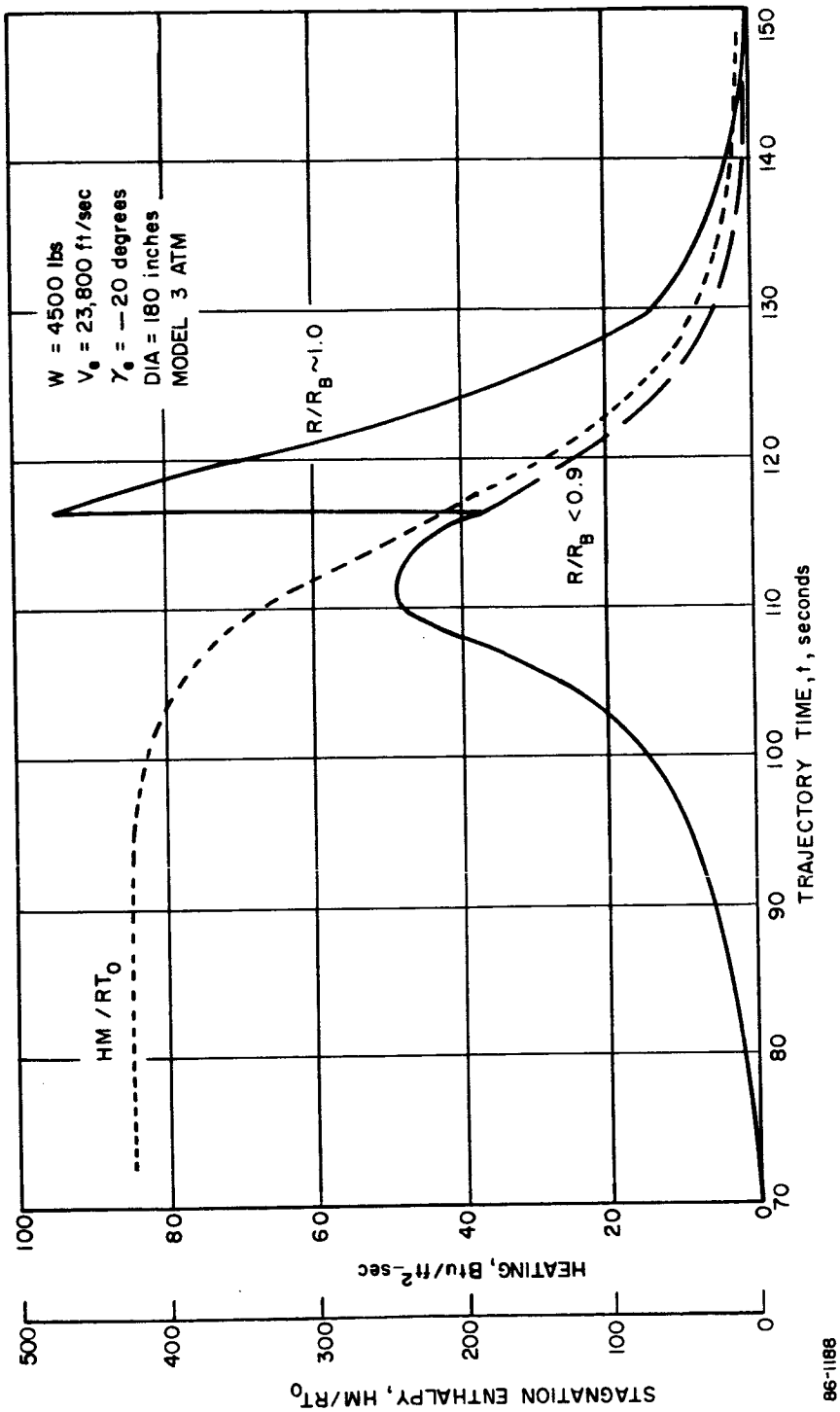

Figure 41 HEATING (MODIFIED APOLLO)

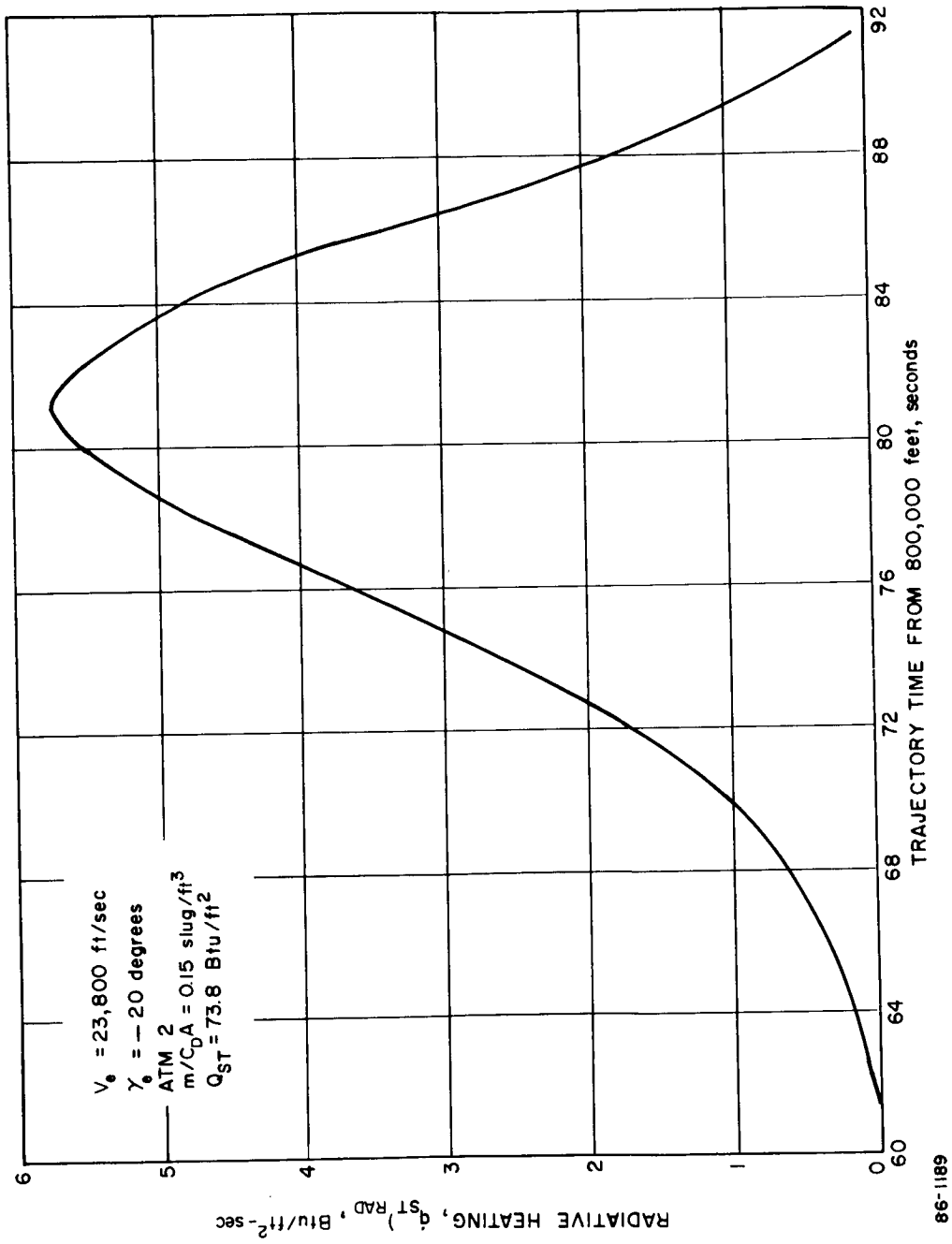

Figure 42 RADIATIVE HEATING (MODIFIED APOLLO)

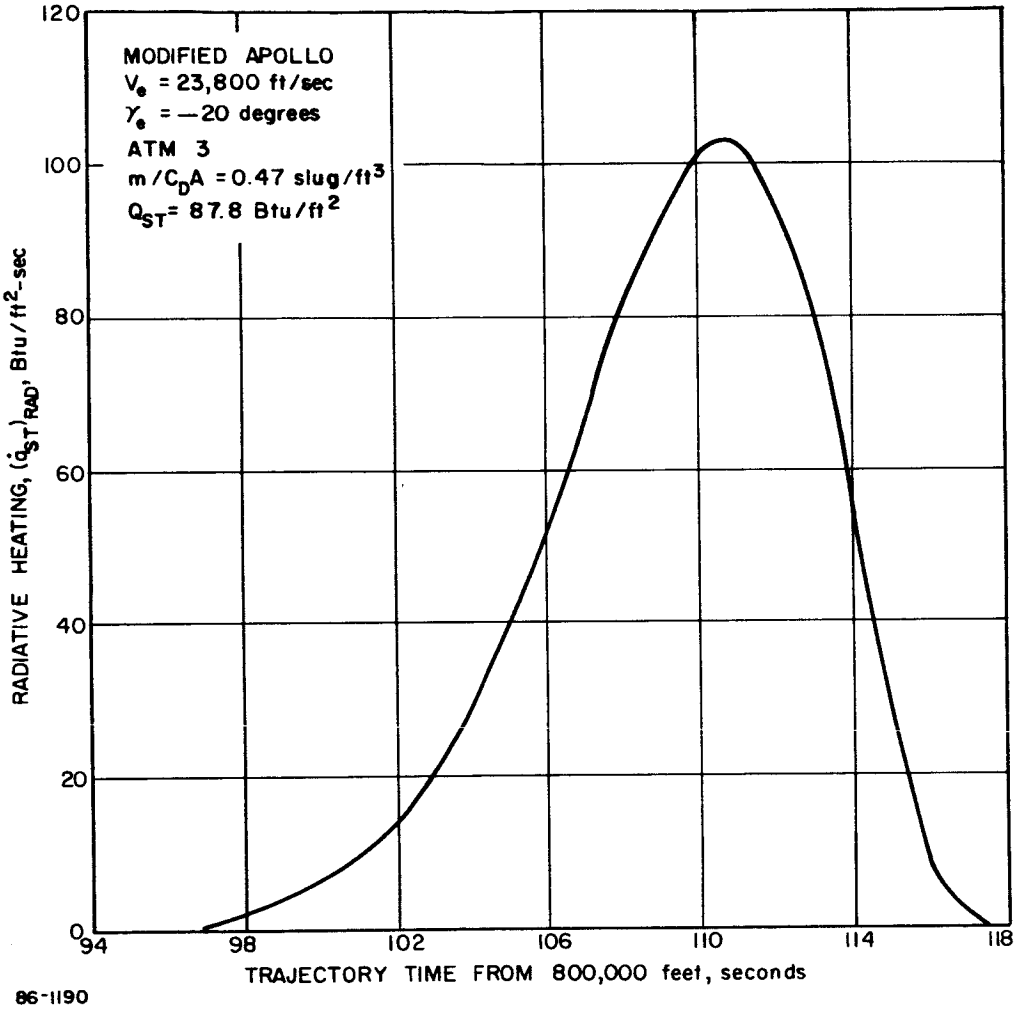

Figure 43 RADIATIVE HEATING (MODIFIED APOLLO)

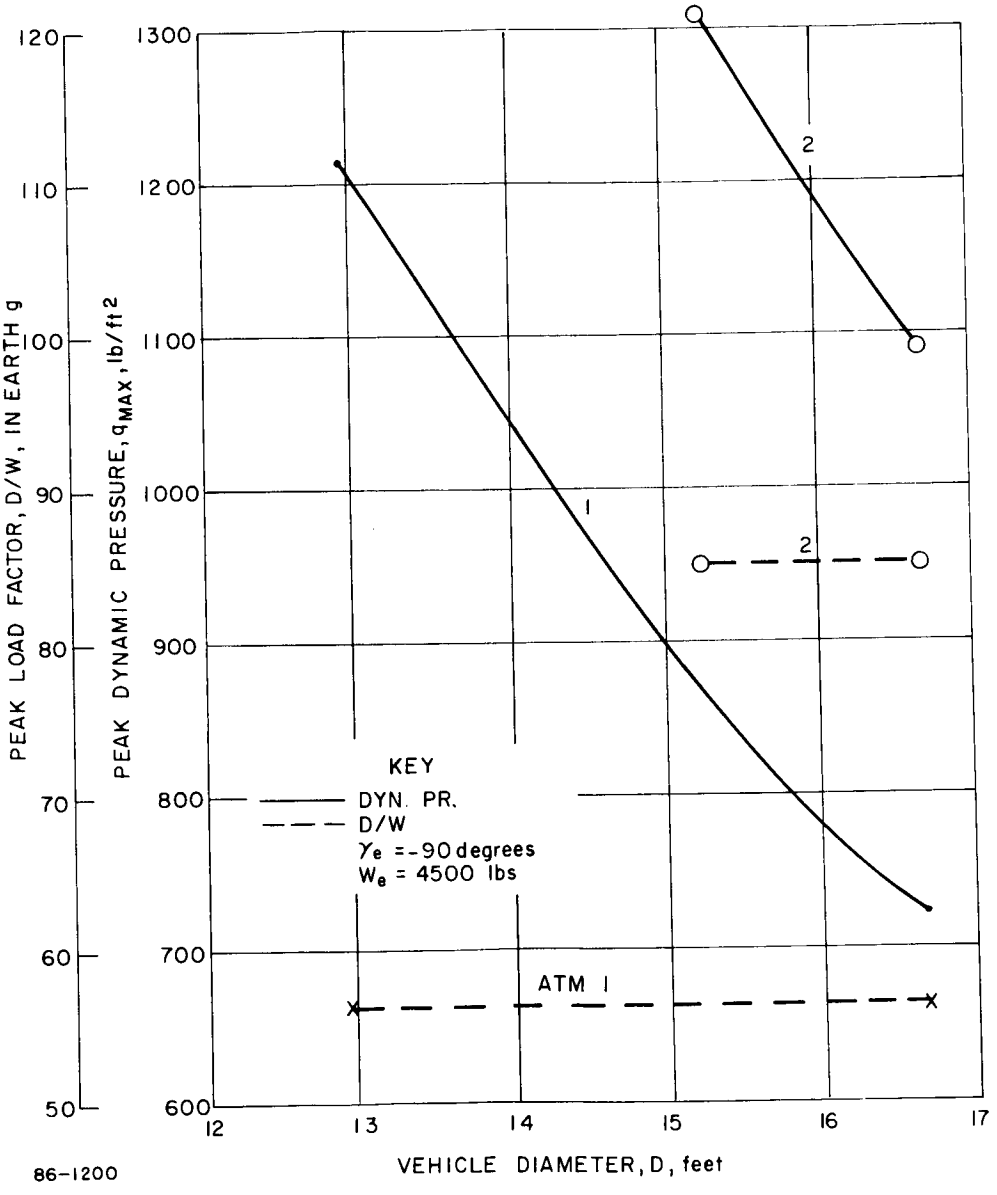

Figure 44 LOADING PARAMETERS--TENSION SHELL

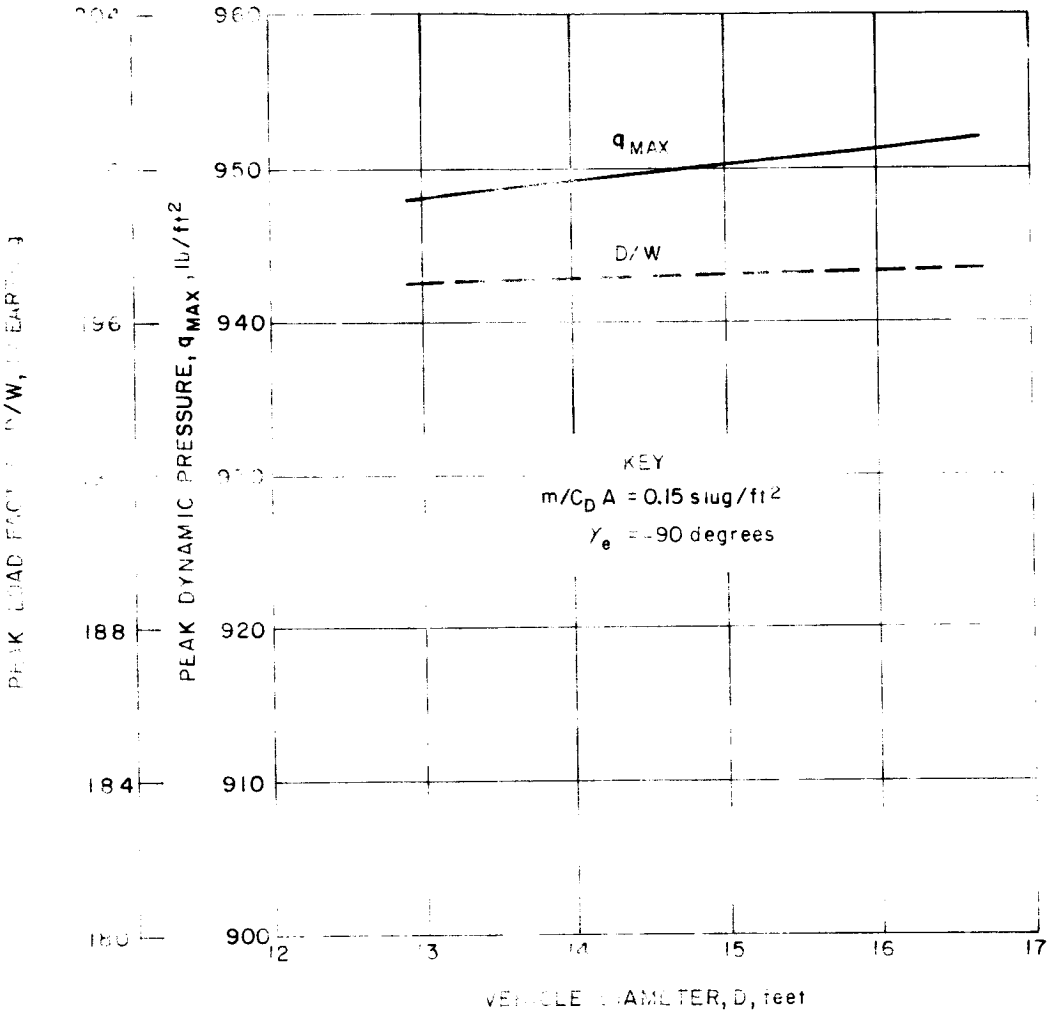

Figure 45 LOADING PARAMETERS--TENSION SHELL

TABLE XIV

LOAD SUMMARY BLUNT TENSION SHELL

Design concept	(B)		(C) and (D)	
Entry Weight (pounds)	4500		1435	
Entry angle of attack, degrees	0	179	0	179
Peak dynamic pressure, psf	1114	1375	778	1110
α at peak dynamic pressure, degrees	-	9	--	31
Maximum axial g	73.3	87	161	224
Maximum normal g	-	10	-	42

Aerodynamic loading is represented by the distribution of pressure over the vehicle. The pressures of interest are those which produce the maximum stresses in the vehicle structure and are generally the highest pressures to be encountered within the range flight conditions anticipated for the vehicle. The maximum absolute pressures may be presented for the desired flight condition; however, the pressures so specified refer specifically to a single flight speed at a single altitude. A high degree of generality is obtained and more meaningful graph offered if the ratios of the local static pressures to the stagnation pressure (at that flight condition) are presented as a distribution over the body. The resultant is a pressure distribution which is accurate over a fairly wide range about the design condition of flight speeds ($\Delta V \cong \pm$ 2000 ft/sec) and altitudes ($\Delta V \cong \pm$ 10, 000 feet). Only the proper absolute stagnation pressure need be used to obtain the proper absolute local static pressure. Further, for any atmosphere, the ratio of stagnation pressure to dynamic pressure is generally very nearly constant above M_∞ = 10. (For Model 2 and 3 atmospheres, the ratio is about 1.93.) Thus by computing dynamic pressure over a trajectory, the maximum loading condition is specified by the maximum dynamic pressure.

The ground rules and maximum loading condition considered, after the deletion of atmosphere 1, are:

Concept: Multi-mission (B) W_{max}= 4500 pounds		1971 Mission and Future Mission (m/C_DA) max = 0.15 (C & D)
Atmosphere: 2		3
Entry Condition:	V_E = 23, 800 ft per sec.	
	γ_E = -90 degrees	
	Z_E = 800, 000 r335	
Maximum Loads Point:		
V = 14, 641		V = 15, 073 ft/sec
Z = 108, 329 ft		Z = 73, 466 ft
q_∞ = 1114 psfa		q_∞ = 778 psfa

The applicable pressure distribution for these conditions is shown in Figure 46. This distribution is exact for the multi-mission concept. For the 1971 mission and future mission concepts, the same distribution is to be used as a conservative estimate for the low ballistic coefficient atmosphere 3 flight. For these latter design conditions, the maximum stagnation pressure ratio is 1.85 based on approximate thermochemical data. The degree of conservatism, is, in any case, less than 10 percent.

The attitude which presents the highest loads is zero-angle of atack. Newtonian flow is assumed over the blunt portion of the body to the point where a Prandtl-Meyer expression gives an equal pressure gradient pressure; this is sufficiently accurate for this phase of the study since only 1 percent of the vehicle is affected. Further, the over-expansion region generally encountered in blunt-body flow is neglected for the same reasons.

The maximum pressure ratio is assumed to hold constant for $0.675 < R/R_B \leq 0.945$. The analysis presented in paragraph 4.2.1.2 shows that properties may be considered constant in this region. The maximum pressure ratio is used here as a conservative assumption in order to account for (1) boundary-layer attenuation or spreading of the peaks and (2) the possibility of traveling or cscillating peaks to unsteady flow.

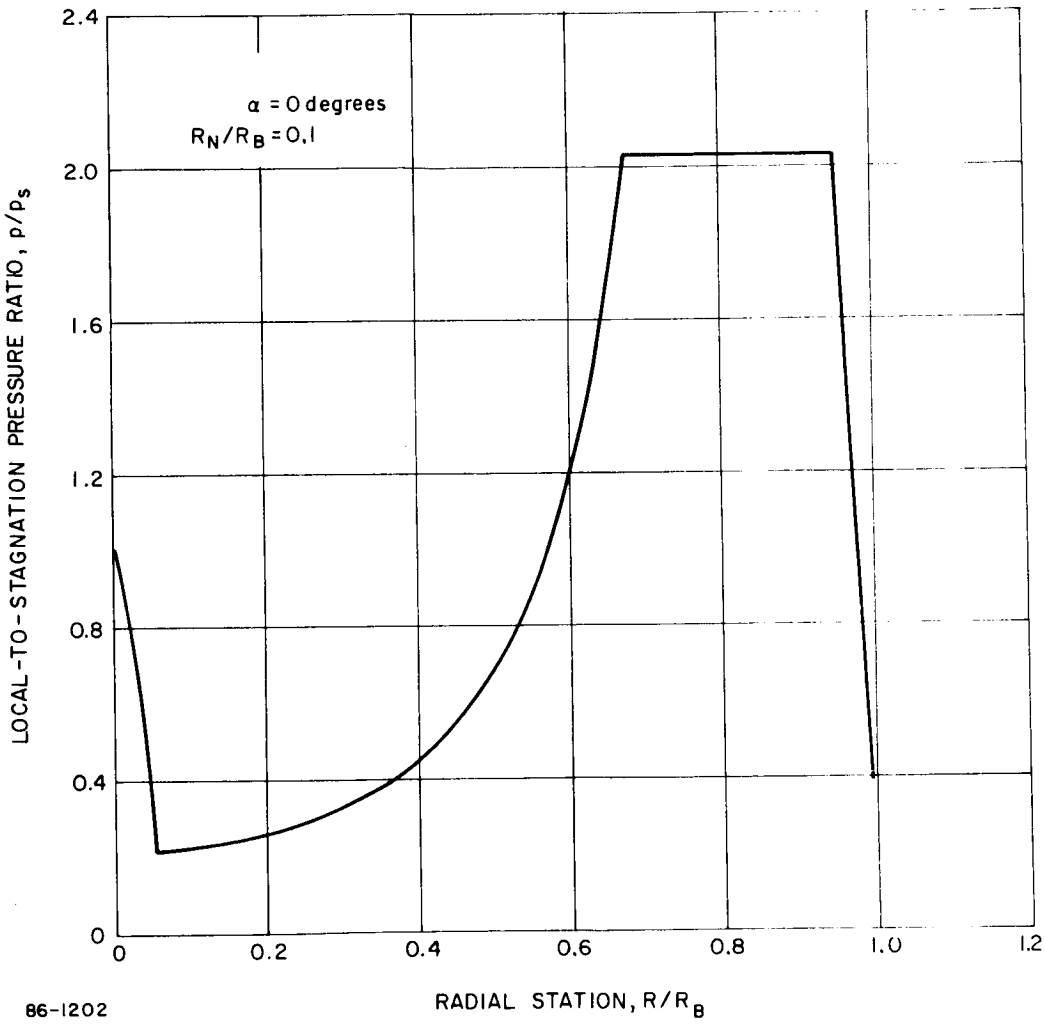

Figure 46 TENSION SHELL PRESSURE DISTRIBUTION--MAXIMUM LOADINGS CONDITIONS

2. Heating

a. Convective -- The effect on the heat pulse of varying vehicle diameter is summarized in Figure 47 for the 4500-pound (multi-mission) vehicle. The greatest convective heating for the tension shell is obtained at the sonic point (rim) in the Model 1 atmosphere. As has been noted, the heating for this shape is an order of magnitude greater than that of the other shapes. The maximum radiative heating occurs in the Model 2 atmosphere, and is also in the vicinity of the rim.

A similar study was performed for the 1971 mission ($m/C_DA = 0.15$). At this m/C_DA, radiative heating is much less and only the Model 1 atmosphere need be considered for heat shield design. The greatest heating for this mssion also occurs at the sonic point. Figure 48 summarizes the heating as a function of diameter.

Aerodynamic heating rates were also calculated for two revised design concepts, representing two different missions. Entry conditions are the same for both: $V_e = 23{,}800$ ft/sec, $\gamma_e = -20$ degrees, $Z_e = 800{,}000$ feet, since the shallow trajectory produces the maximum integrated heating at any point on the body, despite lower peak heating rates. The cases considered were the early mission, for which $m/C_DA = 0.15$ and the critical atmosphere was Model 2; and the future mission for which the vehicle weight requirement was 4500 pounds and the atmosphere was Model 3.

Conical-flow heating theory, as outlined in paragraph 4.2.1.2 was utilized for the calculations, except over the blunt nose ($R_N/R_B = 0.1$) of the vehicle. Conical heating is conservative if blunt-body flow actually exists at the point of calculation. The extent of blunt-body can be calculated, but this high degree of definition is not warranted for two reasons. First, for this nose configuration the heating rates can be shown to be nearly identical (Reference 4) and second, the heat shield affected represents less than four percent of the total heat shield weight.

Heating distributions for the two flight conditions are presented in Figures 49 and 50. Fully laminar and fully turbulent distribution are shown. The basic heat pulses--stagnation point and turbulent sonic point rate histories--are shown in Figures 51 and 52.

Figures 53 and 54 show, for each flight condition, the most severe severe heat pulse experienced at any point on the tension shell surface. The local transition Reynolds Number is 3×10^5. Delaying transition to $Re_S = 10^6$ (a radical assumption) has been found to produce only about a 10-percent reduction in integrated heating.

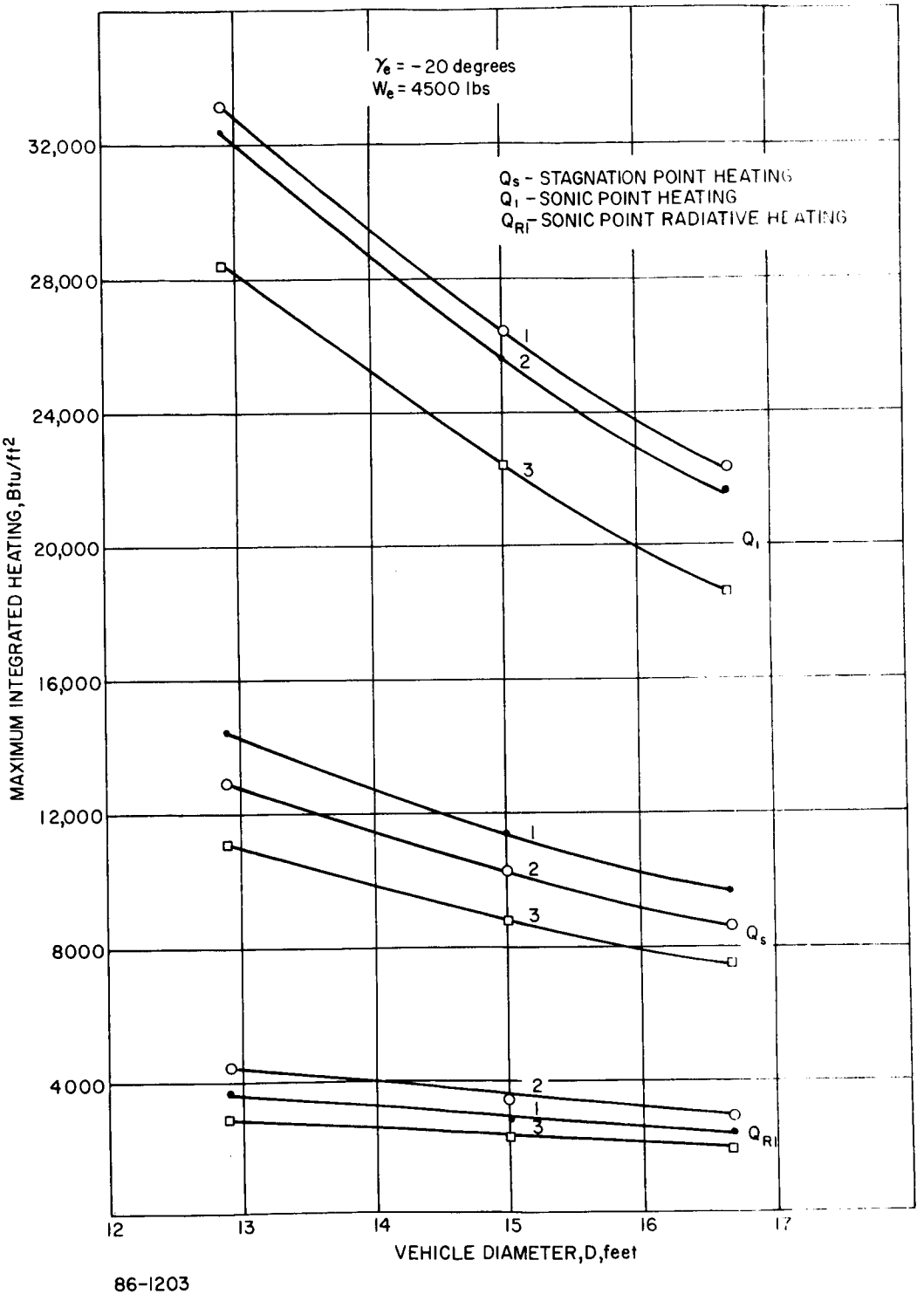

Figure 47 INTEGRATED HEATING--TENSION SHELL

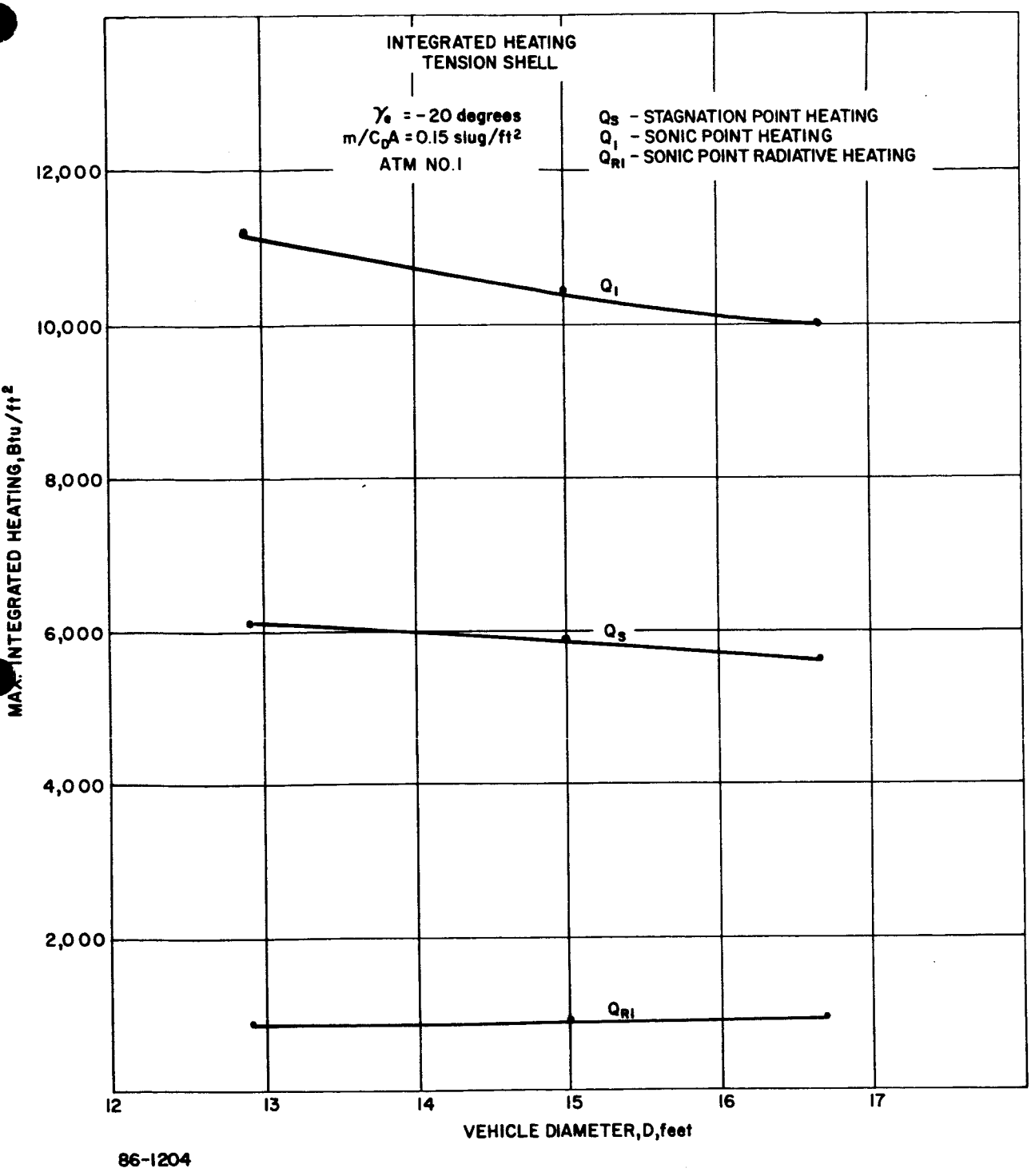

Figure 48 INTEGRATED HEATING--TENSION SHELL

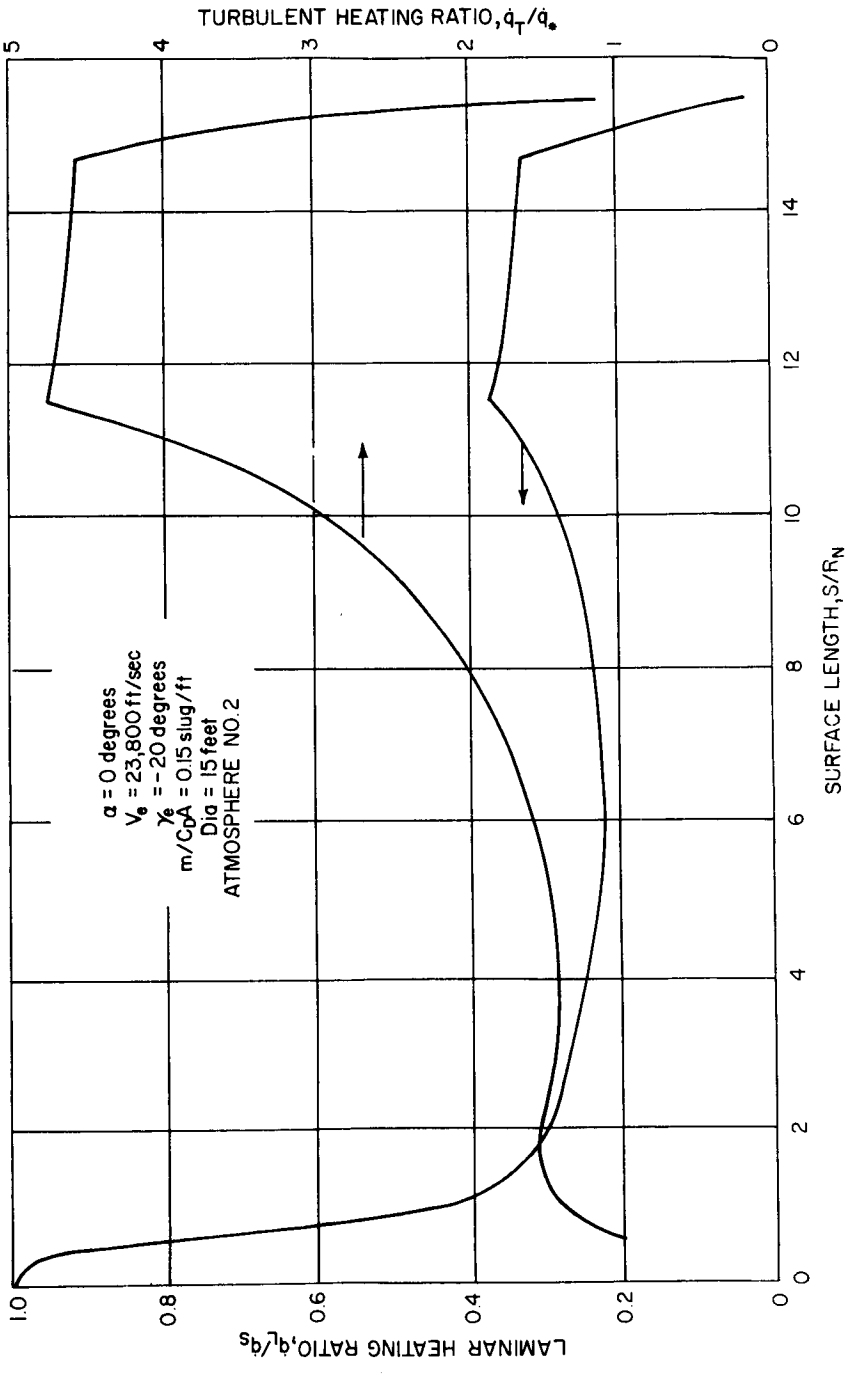

Figure 49 TENSION SHELL AERODYNAMIC HEATING DISTRIBUTION

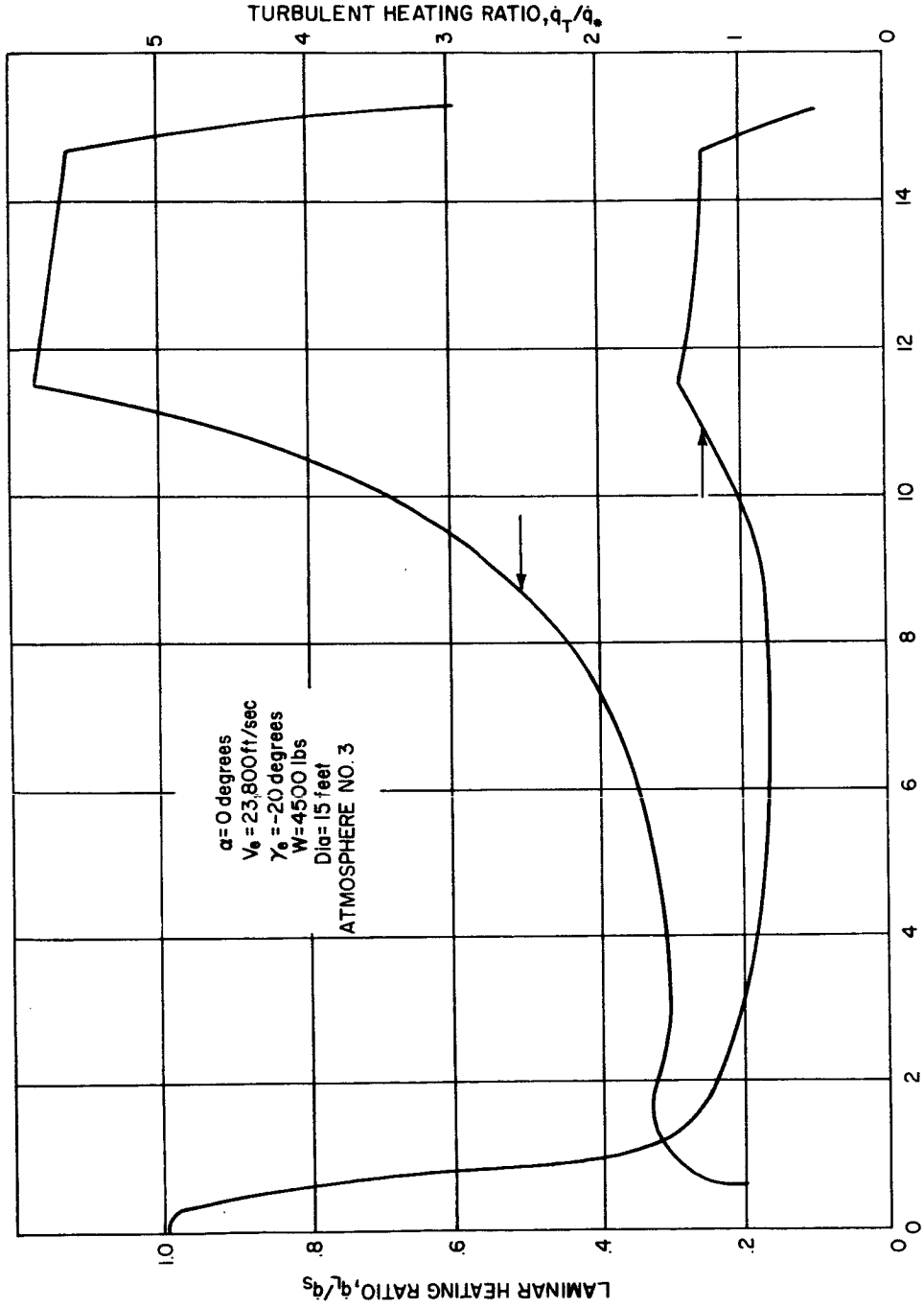

86-1206

Figure 50 TENSION SHELL AERODYNAMIC HEATING

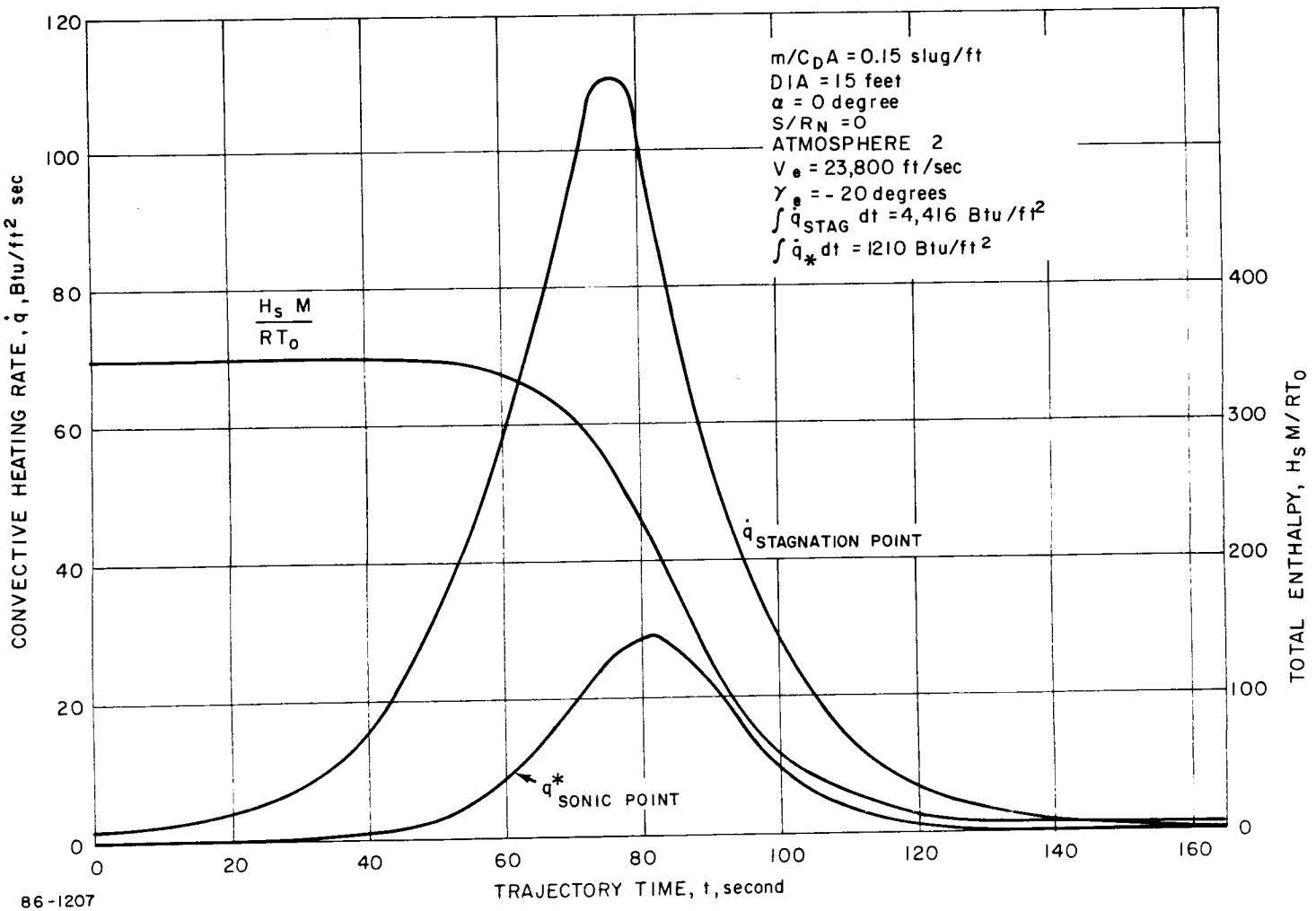

Figure 51 TENSION SHELL AERODYNAMIC HEATING

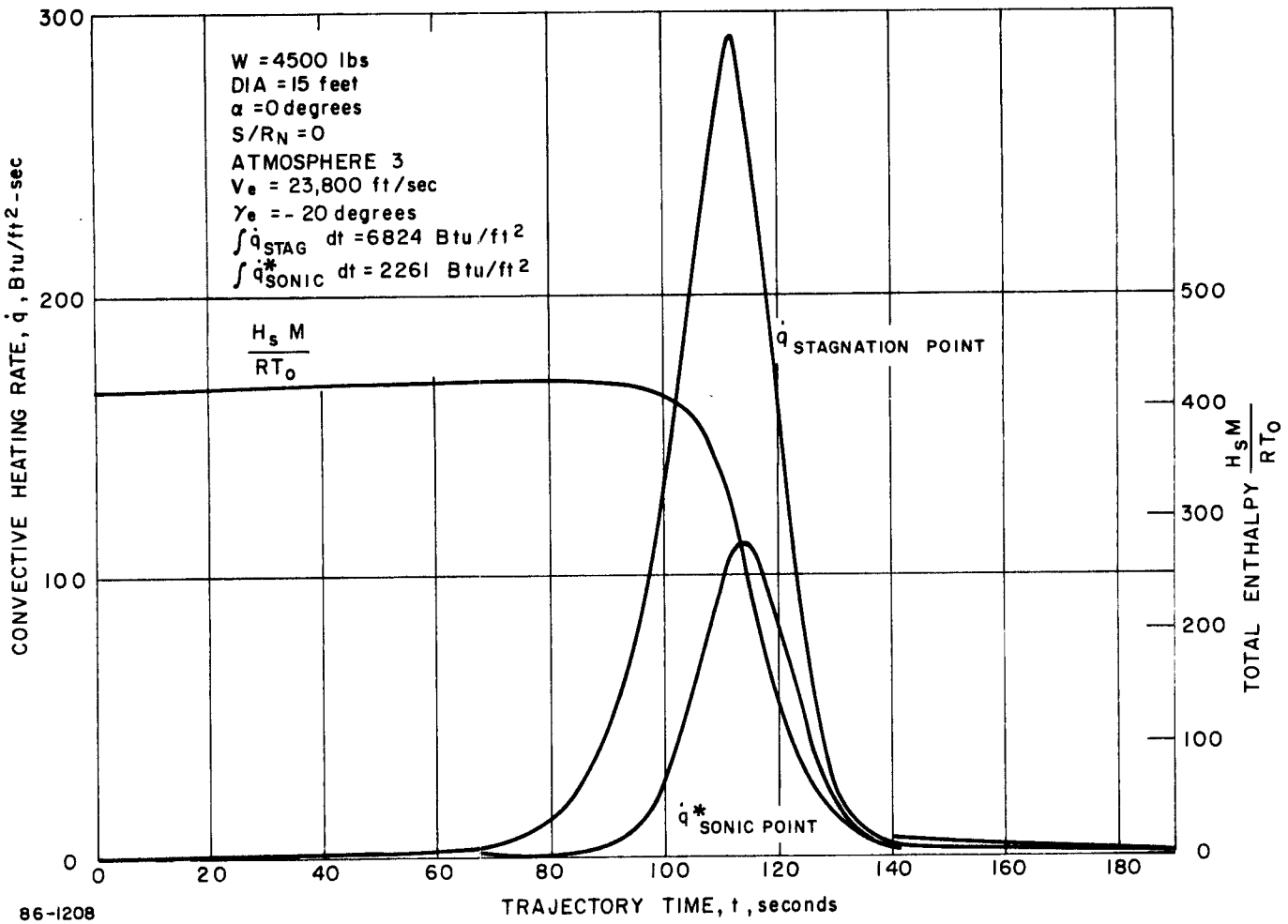

Figure 52 TENSION SHELL AERODYNAMIC HEATING

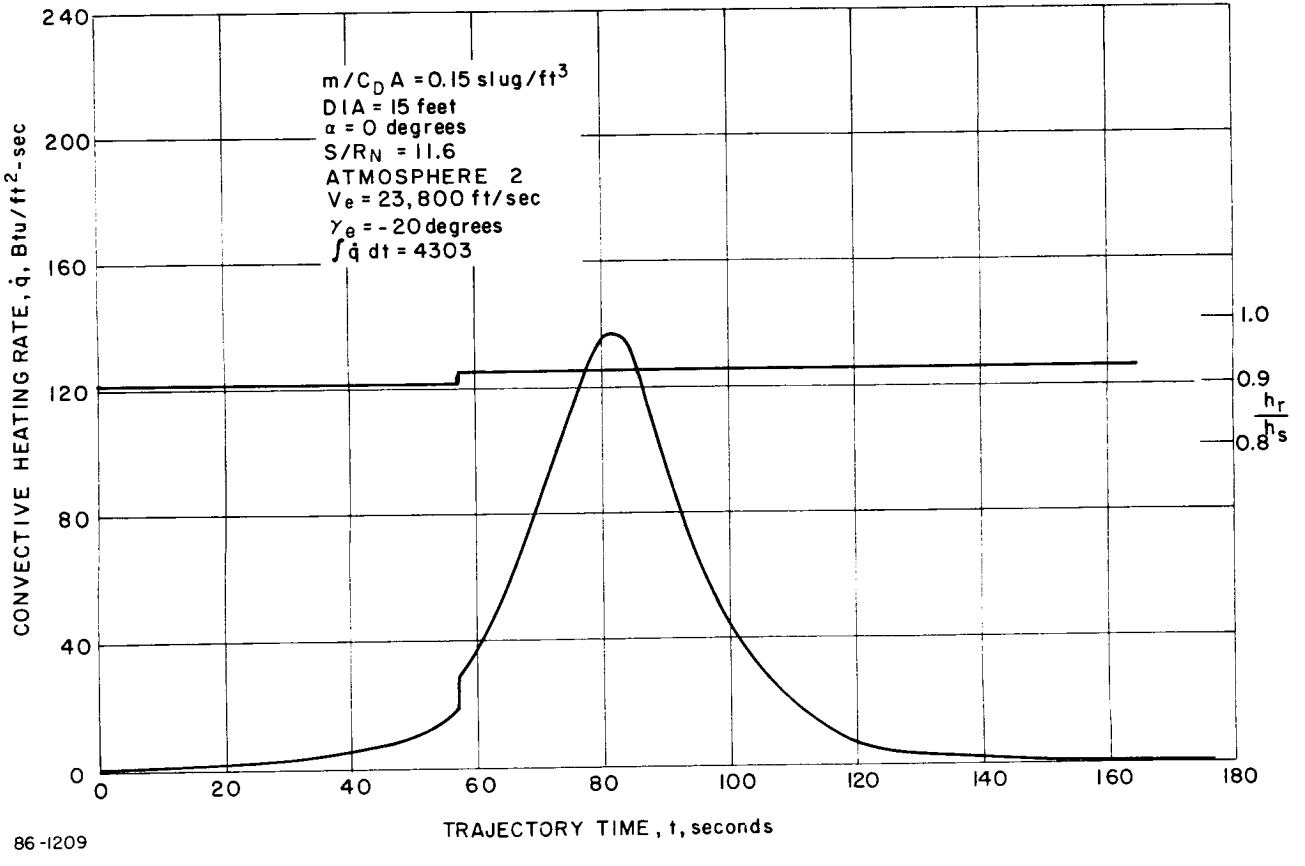

Figure 53 TENSION SHELL AERODYNAMIC HEATING

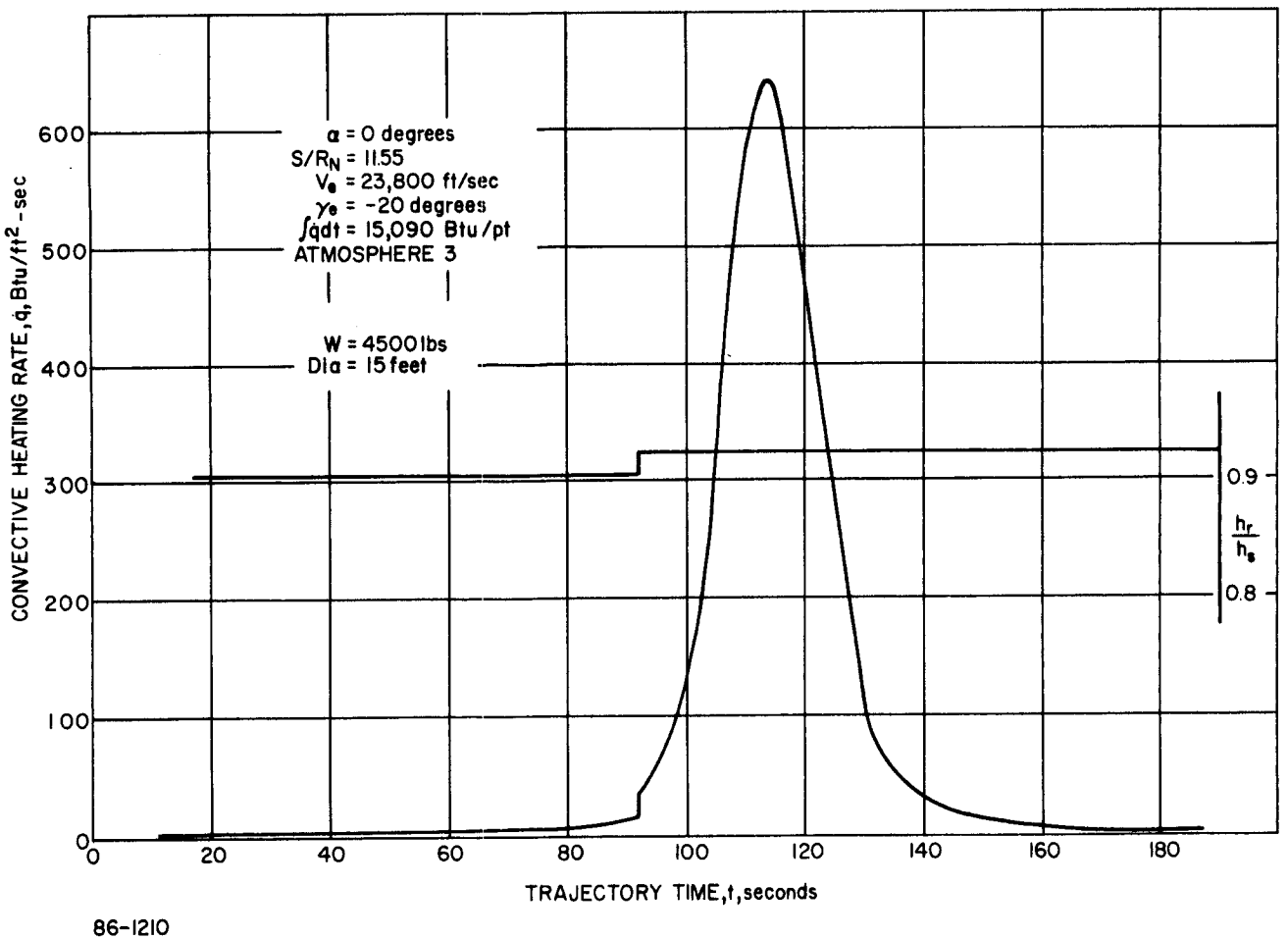

Figure 54 TENSION SHELL AERODYNAMIC HI ING

The effects of changing atmospheric models cannot be adequately demonstrated in graphical form by any one parameter. However, the general tendency has been to decrease total convective heating in the thinner atmosphere despite higher heating rates. This trend is caused, as with other vehicles, by the shorter traverse times in the thinner atmospheres. At the maximum heating point (which position varies on the body) on the 4500-pound vehicle, integrated heating decreases by approximately 25 percent from the Model 1 to Model atmosphere 3. Smaller decreases will occur on the 1971 mission vehicle design.

b. Radiative -- Time histories are shown in Figure 55. It is noted that the area receiving significant radiation is that downstream of the secondary shock wave. A complete explanation of radiative heating is presented in paragraph 4.3.2 as are the reference heating distribution for this figure.

Because of the complexity of the tension shell analysis and relative scarcity of previous information concerning this shape, a more extensive analysis of this shape was performed in the course of this study phase. It appears desirable to sum up at this point some of the conclusions pertaining specifically to this shape.

Further refinement is necessary to define the shape which will result in the tension shell concept. The resulting flow field, comprising a complex shock interaction system, depends upon the atmospheric composition, as well as the free-stream velocity. To consider the complete range of parameters necessary to ensure an adequate shell design as well as to provide the complete aerodynamic analysis (pressure and heating distributions, coefficients, etc.) requires extensive theoretical as well as experimental studies. In light of the extreme heating environments associated with this shape, these studies appear to be of academic interest. A blunter configuration would result in reduced heating.

2.3.3 Dynamic Analysis

Various vehicle parameters play a significant roll in the dynamic behavior of an entry vehicle; in addition, various system constraints and requirements interact with these parameters thereby effecting tradeoffs. The dynamic response of the vehicle can impose severe local aggravations, especially when considering failure modes. Since preliminary evaluation of the dynamic characteristics is required prior to a definitized set of mass characteristics, a parametrization is necessitated. Since there is a broad range of entry condition possible (entry velocity, angle, angle of attack, etc.) in addition to several configurations and postulated atmospheres, the parametrics seem formidable.

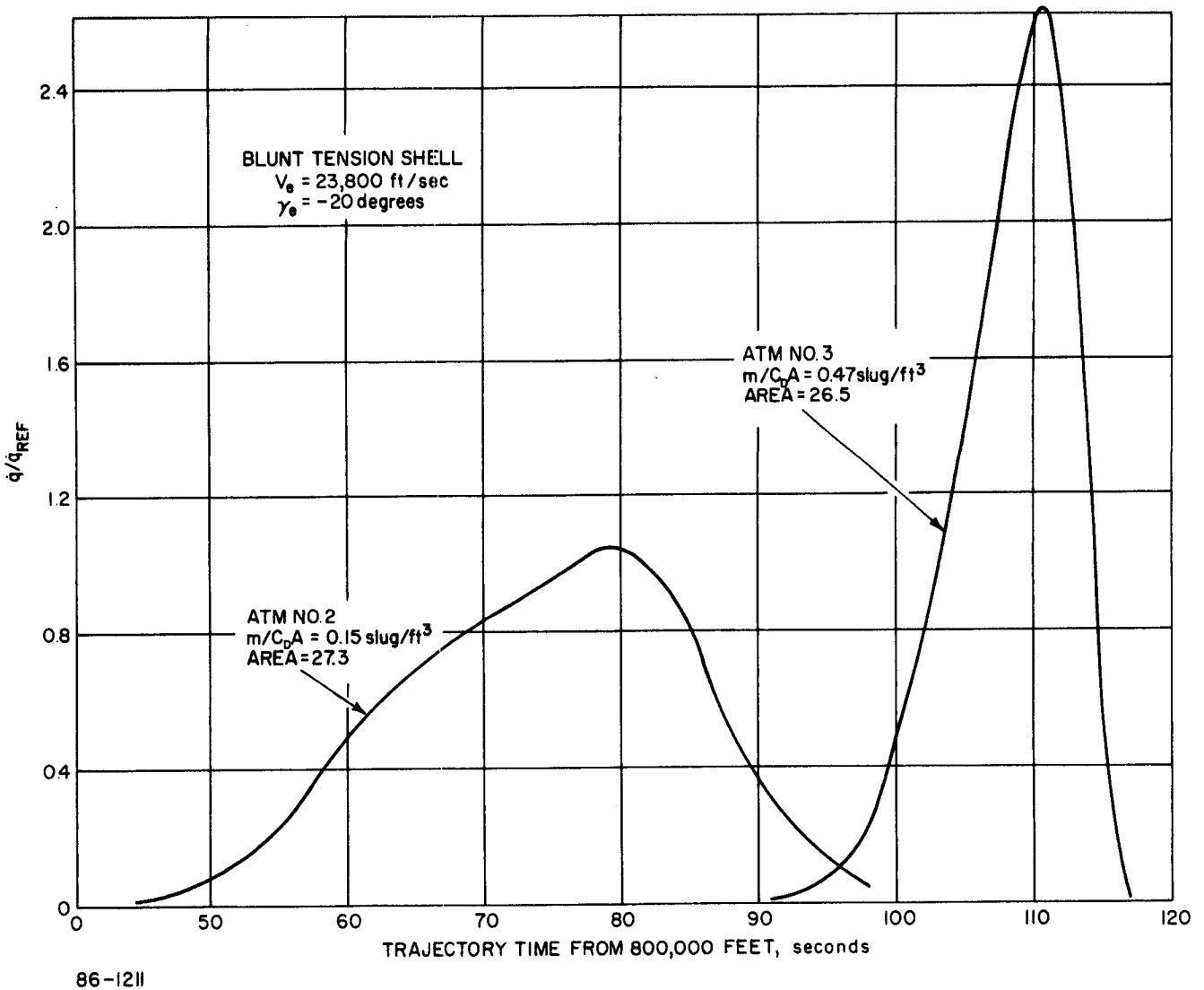

Figure 55 TENSION SHELL RADIATIVE HEATING (DIMENSIONLESS)

Limitations were imposed in the analysis to reduce variations and permutations while still resulting in bases for generalization and providing information relevant to system considerations and selection.

The blunt cone was selected as the principal configuration for investigation, with the modified Apollo and blunt tension shell receiving a cursory examination for comparison and corroboration of the generalized trends.

The various limitations imposed on the parametrics follow; typical results are illustratively presented. Further details have been presented in Reference 5.

2.3.3.1 Blunt Cone

1. Reference Trajectory Analysis -- The entry conditions associated with entry form the approach trajectory were investigated for a particular set of reference conditions to provide a basis for comparison. A spin rate of 2.0 rads/sec with an initial angle of attack of 35 degrees into the Model 3 atmosphere were considered for a vehicle diameter of 200 inches. The lower limit on the ballistic coefficient was 0.15 slug/ft^2 with the upper limit defined by the maximum weight considered, 4500 pounds.

The results obtained were consistent with the results to be predicted from the straight-line trajectory analysis which are summarized in Table XV.

TABLE XV

ENVIRONMENTAL DEPENDENCE

Criteria	Parameter Dependence			
	Entry Angle	Entry Velocity	m/C_DA	Atmospheric Scale Height
1. Loads	$\sin \gamma_E$	V_E^2	m/C_DA	β
2. Integrated Heating	$(\sin \gamma_E)^{-1/2}$	V_E^2	$(m/C_DA)^{1/2}$	$\beta^{-\frac{1}{2}}$
3. Heating Rates	$(\sin \gamma_E)^{1/2}$	V_E^3	$(m/C_DA)^{1/2}$	$\beta^{\frac{1}{2}}$

Of particular interest is the altitude of chute deployment and its variation with entry angle and ballistic coefficient (m/C_DA). The heavy vehicle was compatible with a chute system for terminal descent over a restricted range (γ less than -40 degrees, Figure 56) whereas the

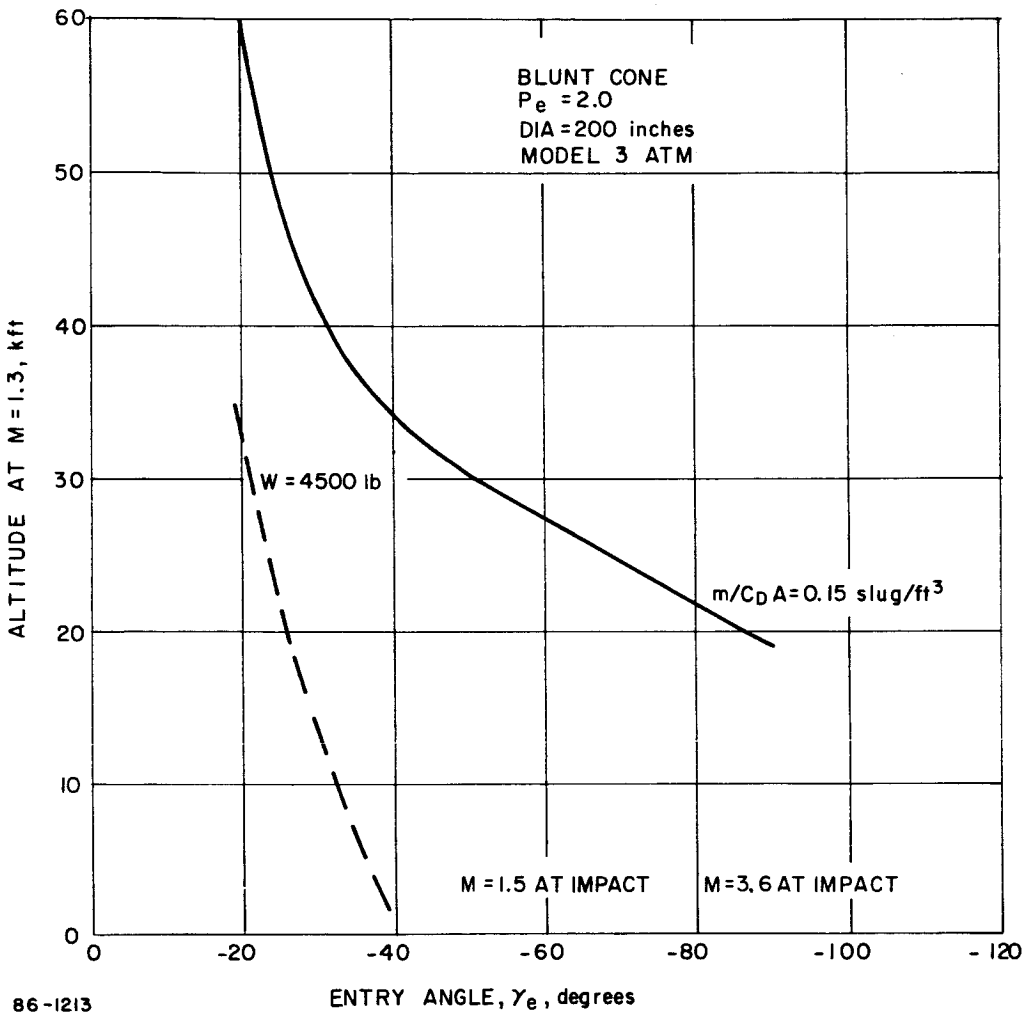

Figure 56 EFFECT OF ENTRY ANGLE ON M = 1.3 ALTITUDE -- BLUNT CONE

low-performance configuration resulted in an altitude of approximately 19, 000 feet, which satisfies the chute deployment criteria (Mach 1.3 at 16, 500 feet, for an entry velocity of 25, 000 ft/sec.). As is to be expected this altitude decreases with increasing velocity (Figure 57).

2. Spin and Despin -- Increased spin resulted in consistently higher angle of attack histories. As a consequence the effective m/C_DA is increased (due to the drag variation with angle of attack) with the concomittant results indicated in Table XV. The variation in parachute deployment altitude was nominal (decreasing with spin) for the steepest descent trajectories whereas the variation was negligible at shallow entry. The sensitivity to spin is more pronounced when negligible aerodynamic damping is present. The resulting angle of attack divergence near chute deployment not only introduces problems with actual deployment, but in addition decreases the altitude of deployment (Figure 58). A typical variation in the angle of attack envelopes for the limiting cases of Newtonian and zero damping derivative, cm_q, is shown in Figure 59. The increased angle of attack results in the same trends associated with an increase in ballistic coefficient.

Despin can be utilized to negate the deleterious effects of spin commensurate with the extent of despin. Although the initial angle of attack increases with despin prior to entry, (due to the increased coning angle) the convergence is more rapid. Figure 60 presents typical variations and also indicates later onset of convergence for high spin rates. Again the trends associated with angle of attack variation can be reflected in the relative effect on the ballistic coefficient.

3. Mass Characteristic - Offset Center of Gravity -- The angle of attack convergence for an offset center of gravity is of course limited in that the trim angle is other than zero and is directly related to the offset. In addition, a roll resonance can occur with a divergence in the angle of attack envelope (Figure 61).

a. Products of Inertia -- The products of inertia resulted in greater coning motion and as a consequence, the angle of attack envelopes reflect an irregular early entry variation as well as convergence. The products resulted in an increased angle of attack, however, no trend with products variation was indicated (Figure 62).

b. Moment of Inertia -- As would be expected with spin an increase in the roll axis moment of inertia results in a reduced convergence as indicated in Figure 63.

4. Failure Modes -- In order to fully substantiate the vehicle stability an analysis of two types of failure modes was undertaken.

Condition 1 -- The assumption the vehicle would fail to spin. In this event the entry could occur at any angle of attack from zero to

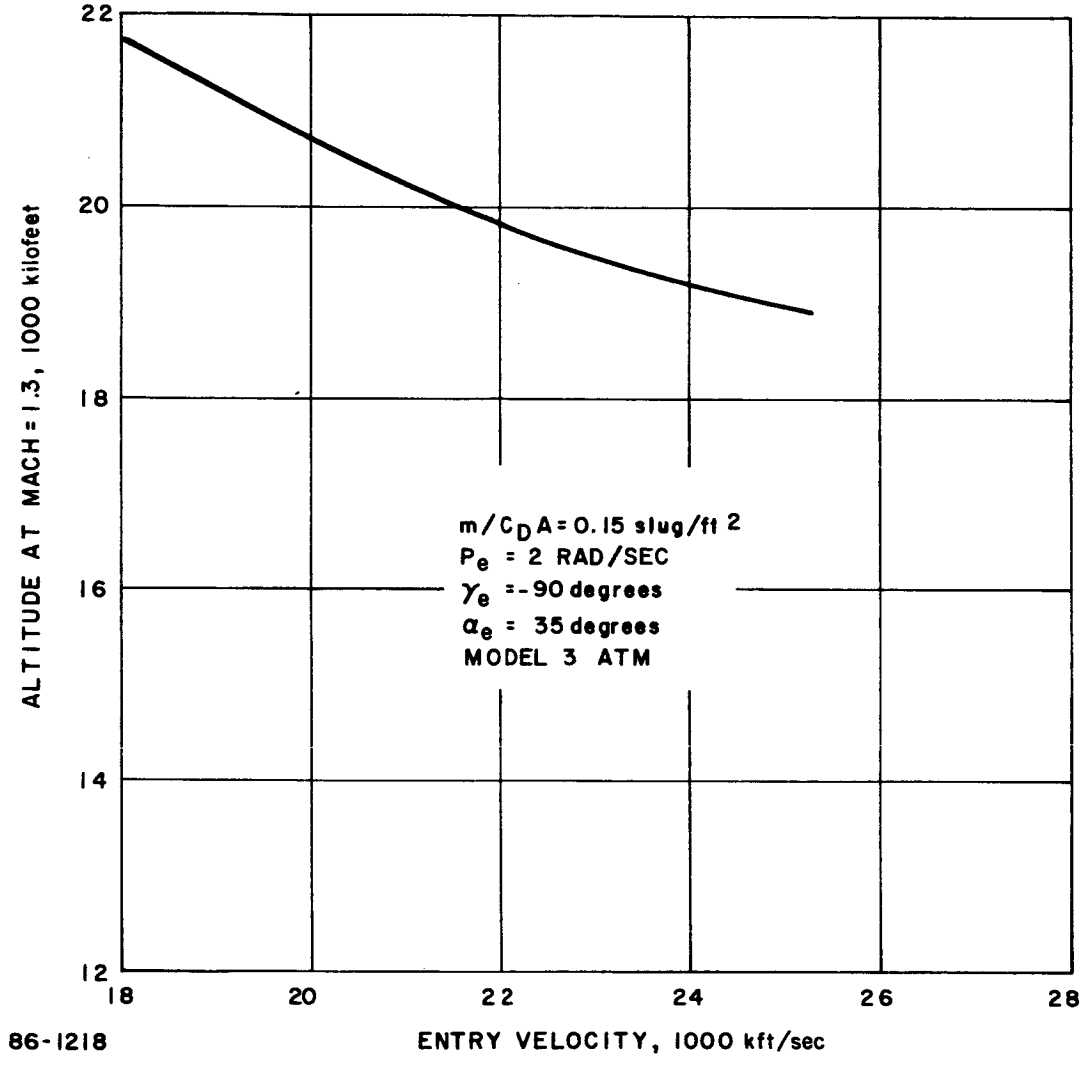

Figure 57 EFFECT OF ENTRY VELOCITY ON ALTITUDE AT MACH 1.3--BLUNT CONE

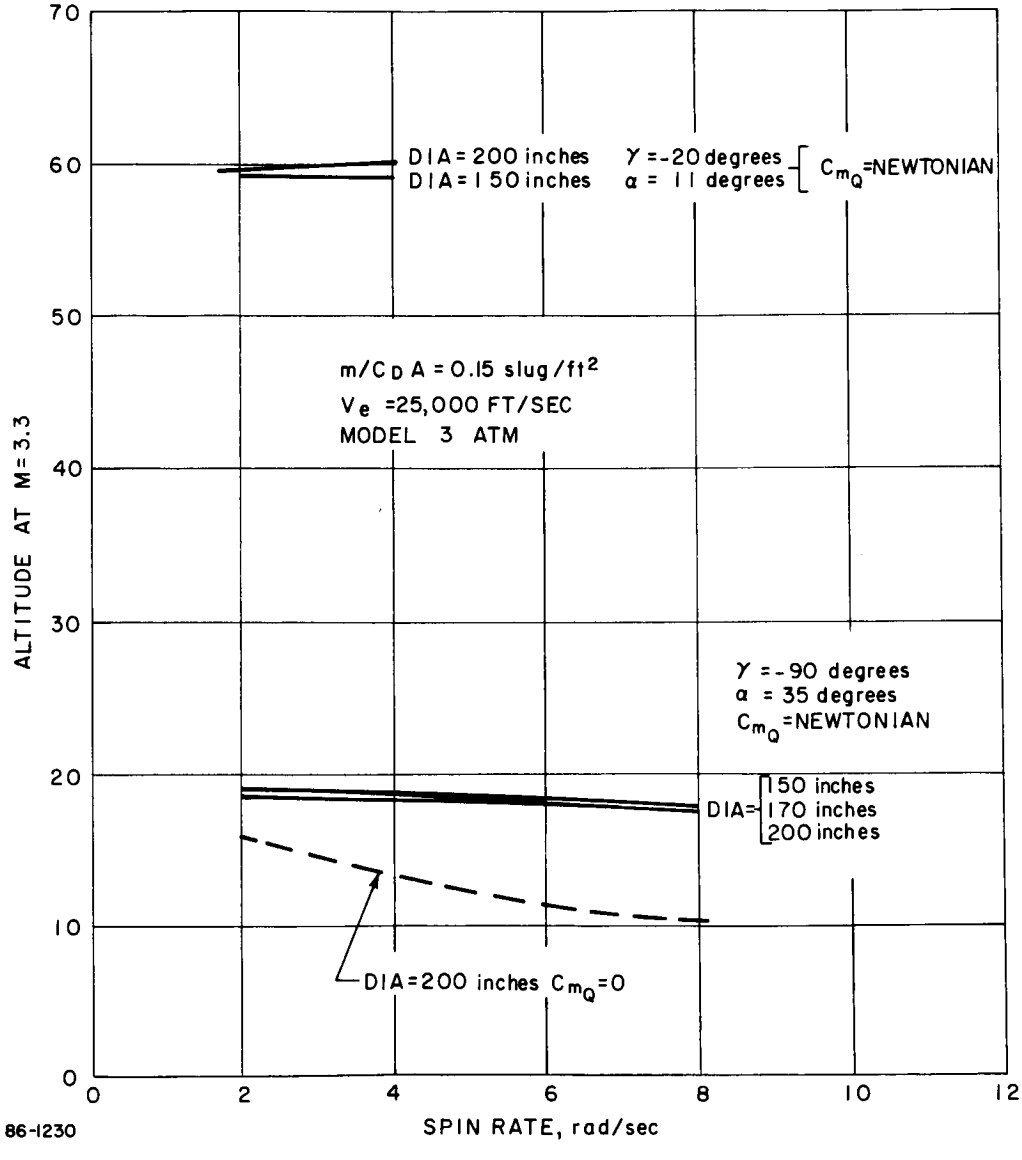

Figure 58 EFFECT OF SPIN RATE ON ALTITUDE AT M = 1.3--BLUNT CONE

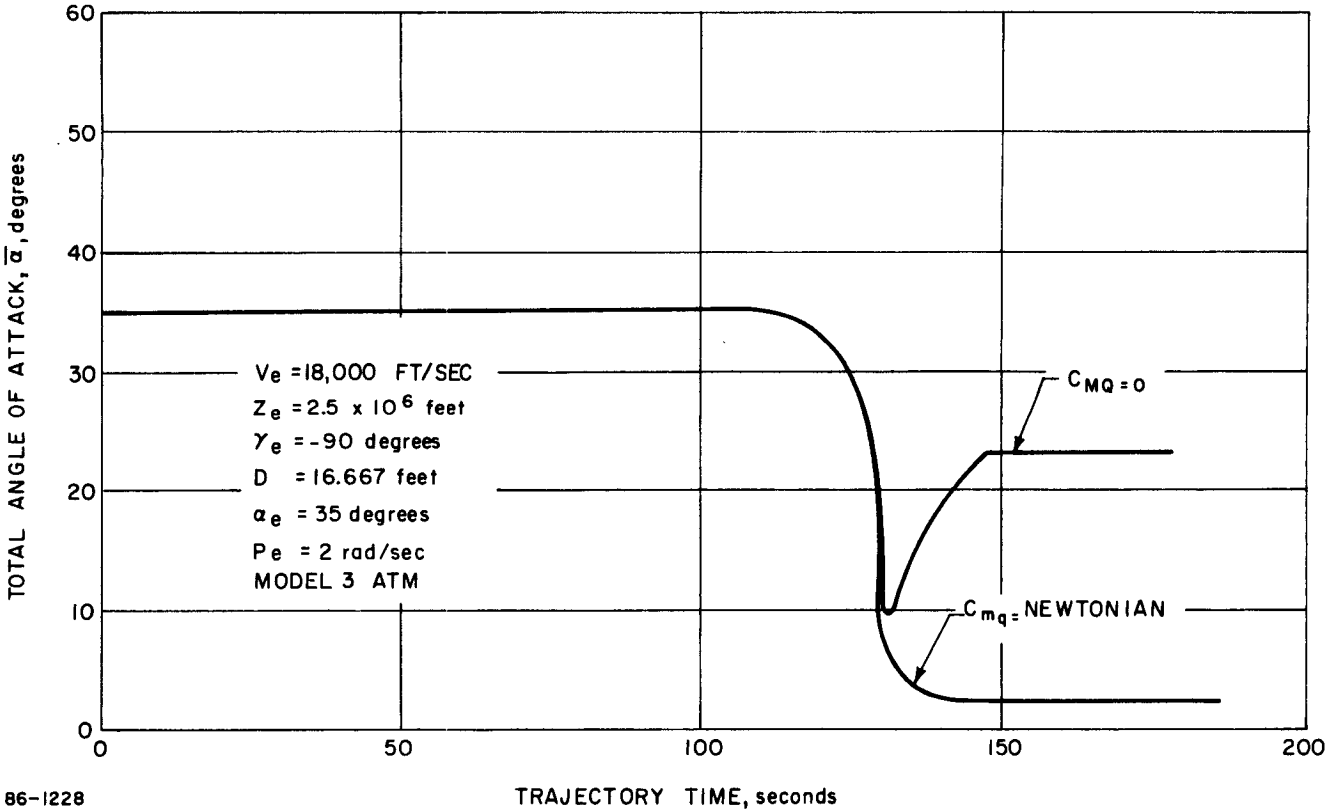

Figure 59 EFFECT OF AERODYNAMIC DAMPING--BLUNT CONE

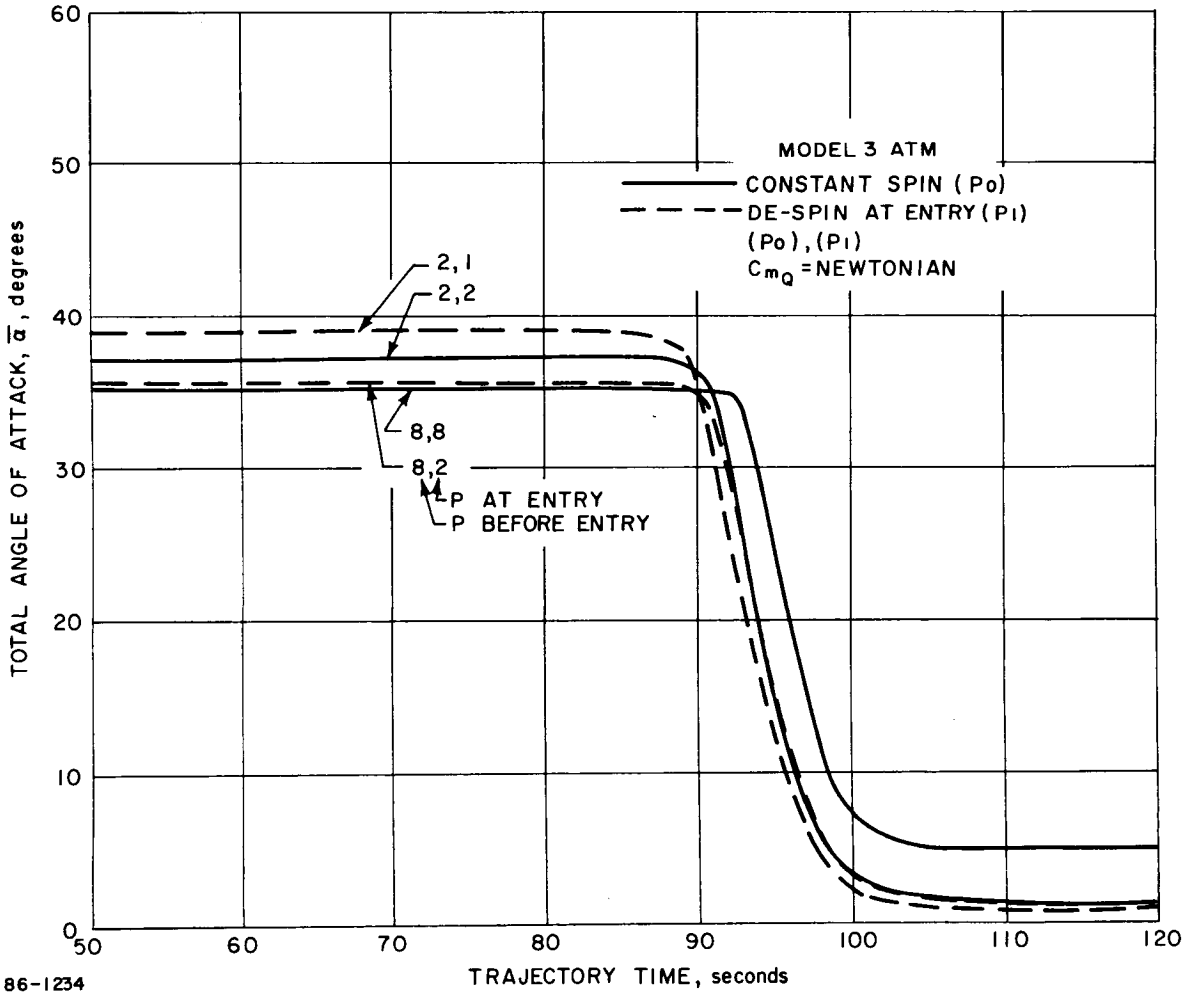

Figure 60 EFFECTS OF DESPIN (MODEL 3 ATM) -- BLUNT CONE

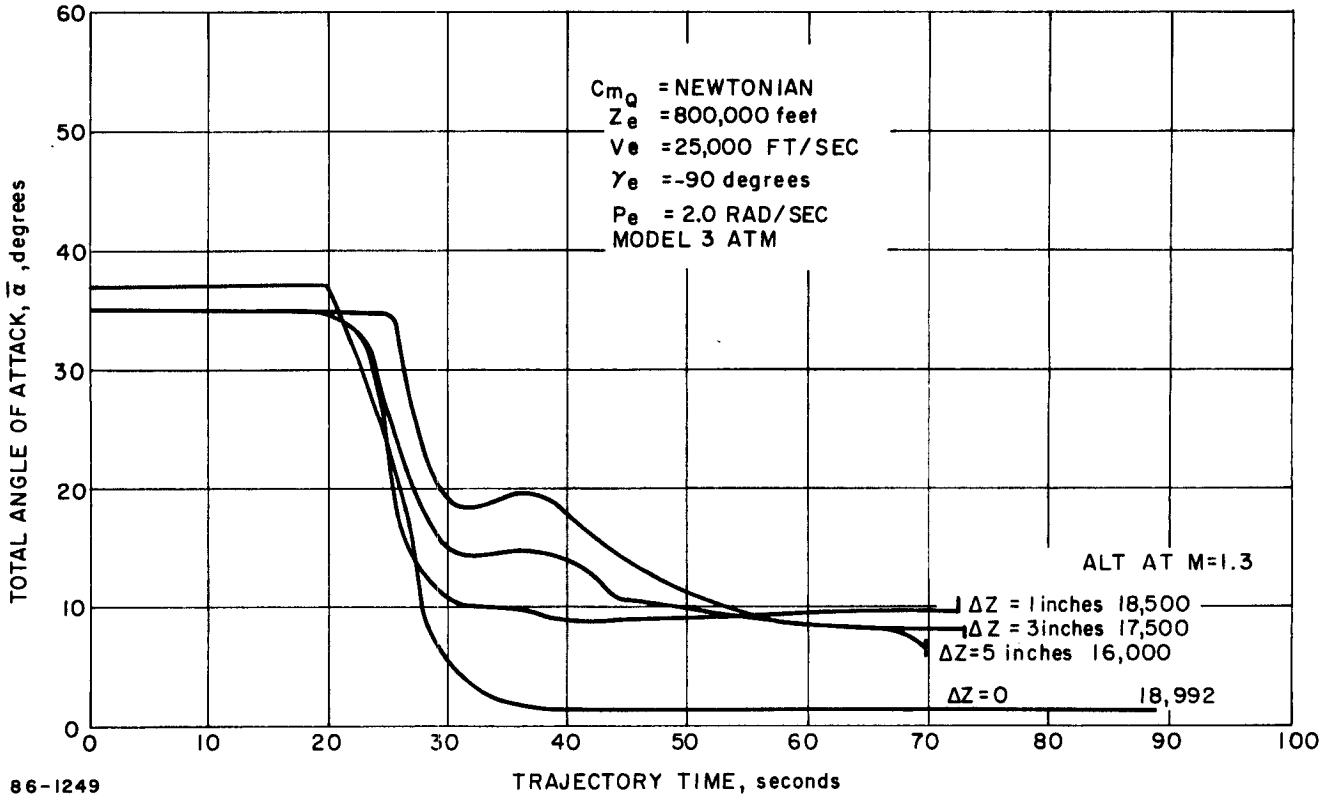

Figure 61 EFFECT OF OFFSET CENTER OF GRAVITY--BLUNT CONE

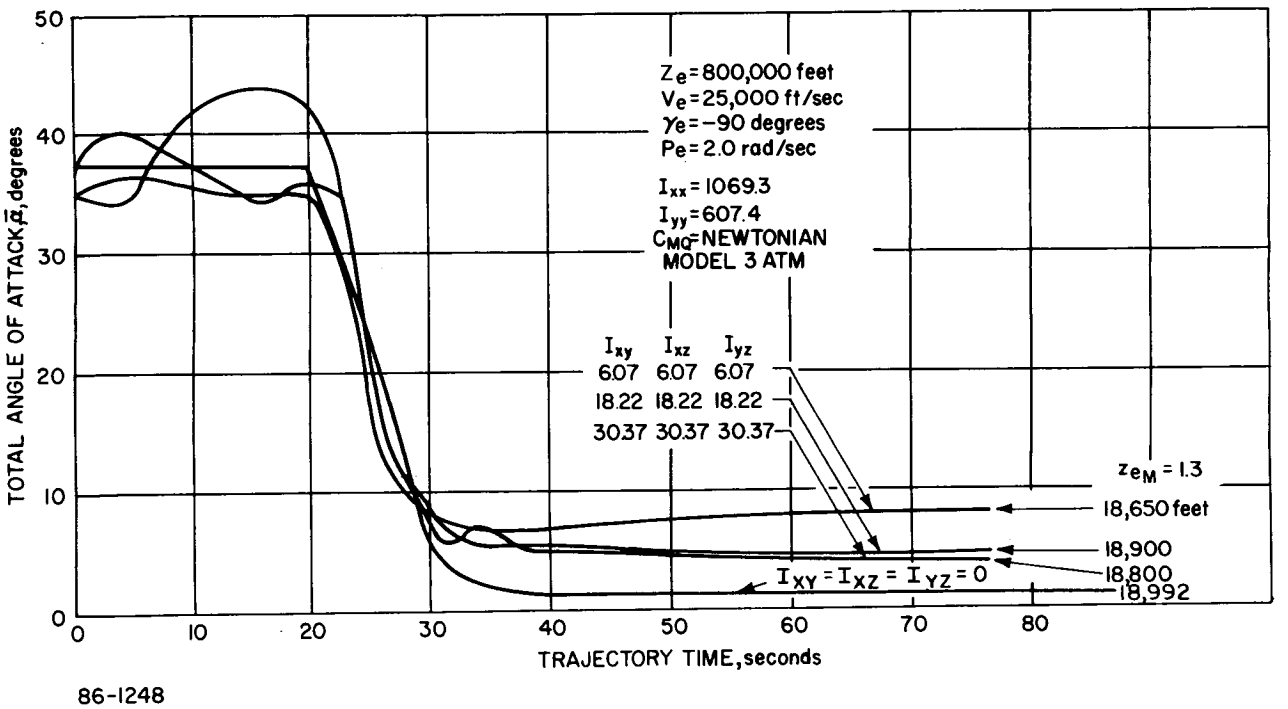

Figure 62 EFFECT OF PRODUCTS OF INERTIA--BLUNT CONE

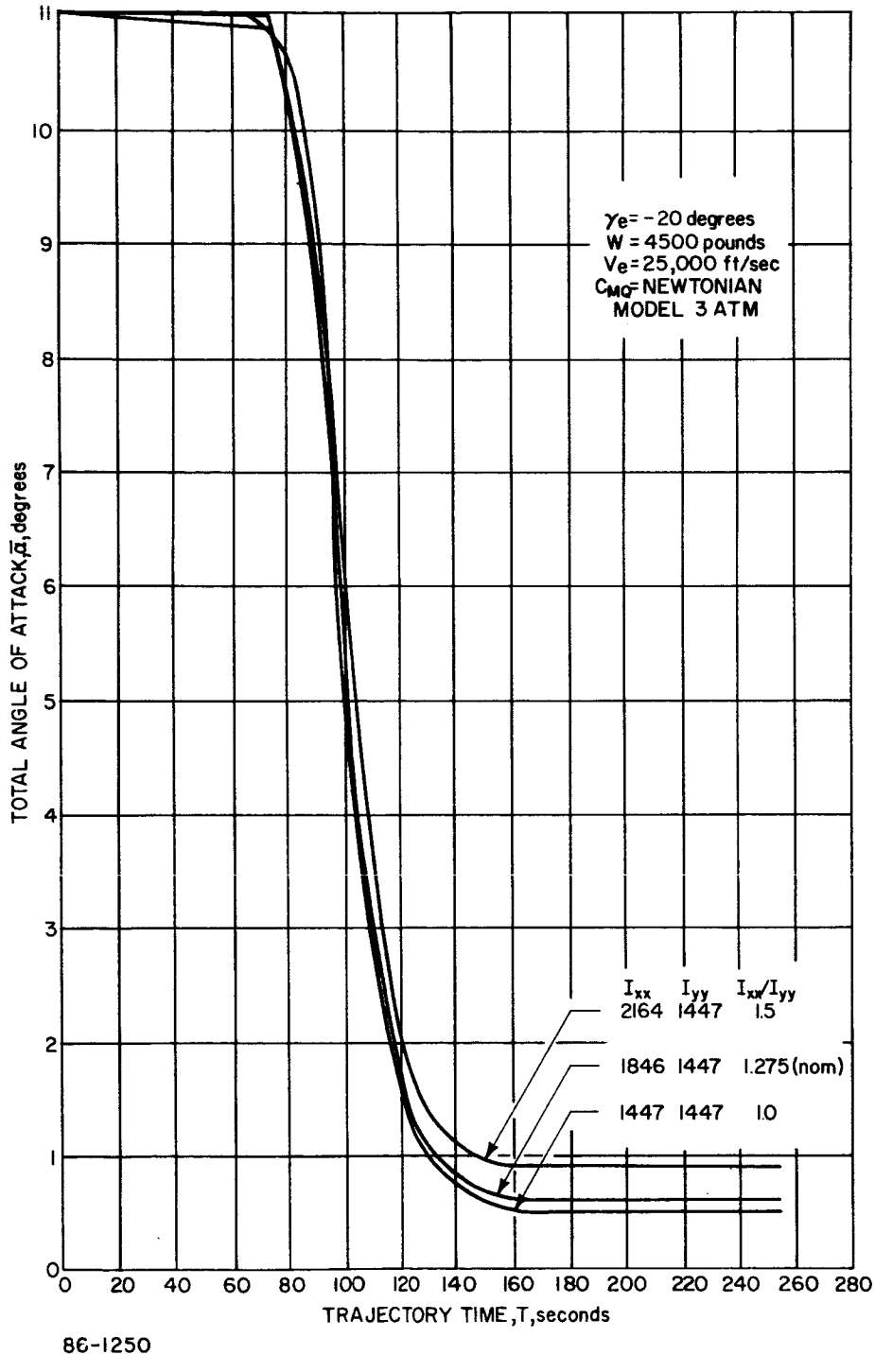

Figure 63 EFFECT OF MOMENT OF INERTIA ON TOTAL ANGLE OF ATTACK--BLUNT CONE

180 degrees. In order to assure a single trim point both, an afterbody and various size flaps were used to pitch the vehicle to $\alpha = 0$. The condition which was analyzed was an angle of attack of 179 degrees with zero spin rate and flaps extended.

Condition 2 -- The assumption that the vehicle was spinning, but that the flaps failed to retract. The condition analyzed was that the entry angle of attack was nominal for a spining vehicle; that is 35 degrees, spin rates were set at 1 and 2 rad/sec. and the flaps remained extended to impact although it is quite probable that they would have burned off by that time.

Condition 1 Analysis - Rearward Entry -- The effect of afterbody design on rearward entry dynamics has been investigated. The results indicate that the use of a 1 -or 2 ft^2 at the rim of a 15-foot diameter blunt cone will considerably reduce the envelope of oscillations at peak heating as well as eliminating any possible rearward static stability.

Figure 64 shows the effect on the time to the start of the first oscillation, and Figure 65 shows the resulting envelopes at peak heating and peak loads. The reference afterbody is the standard 25 degrees truncated cone (Figure 1).

The effect of c. g. location on rearward entry dynamics was investigated. The comparison of configurations shows that in all cases, the angles of attack for the flap configuration converge more rapidly than with the afterbody and are also lower at the maximum dynamic pressure. There appears to be relatively little change with center of gravity location with the exception of the afterbody configuration at the most aft c. g. of 0. 27D (refer to Figure 66). This case is slower converging and also has a higher angle of attack at the maximum dynamic pressure point (approximately 52 degrees).

Condition 2 Flap Retraction Failure -- The analysis of the flap retraction failure mode resulted in higher angle of attack motion, down to impact. The angles of attack for all cases converge and indicated relatively small changes between the various conditions of spin rate, atmosphere, and centers of gravity.

With the addition of the flap, the pitching moment coefficient at 180 degrees is no longer zero but has some finite value. One additional consideration was therefore made to determine the righting characteristics of the vehicle when entering at an angle of attack near the $C_m=0$ which occurs at approximately 240 degrees angle of attack. The angel of attack histories with the vehicle pitching from the 240 degree position was compared with the afterbody configuration at 179 degrees. The flap configuration pitches sooner than the afterbody shape which provides lower angle of attack during the heating periods.

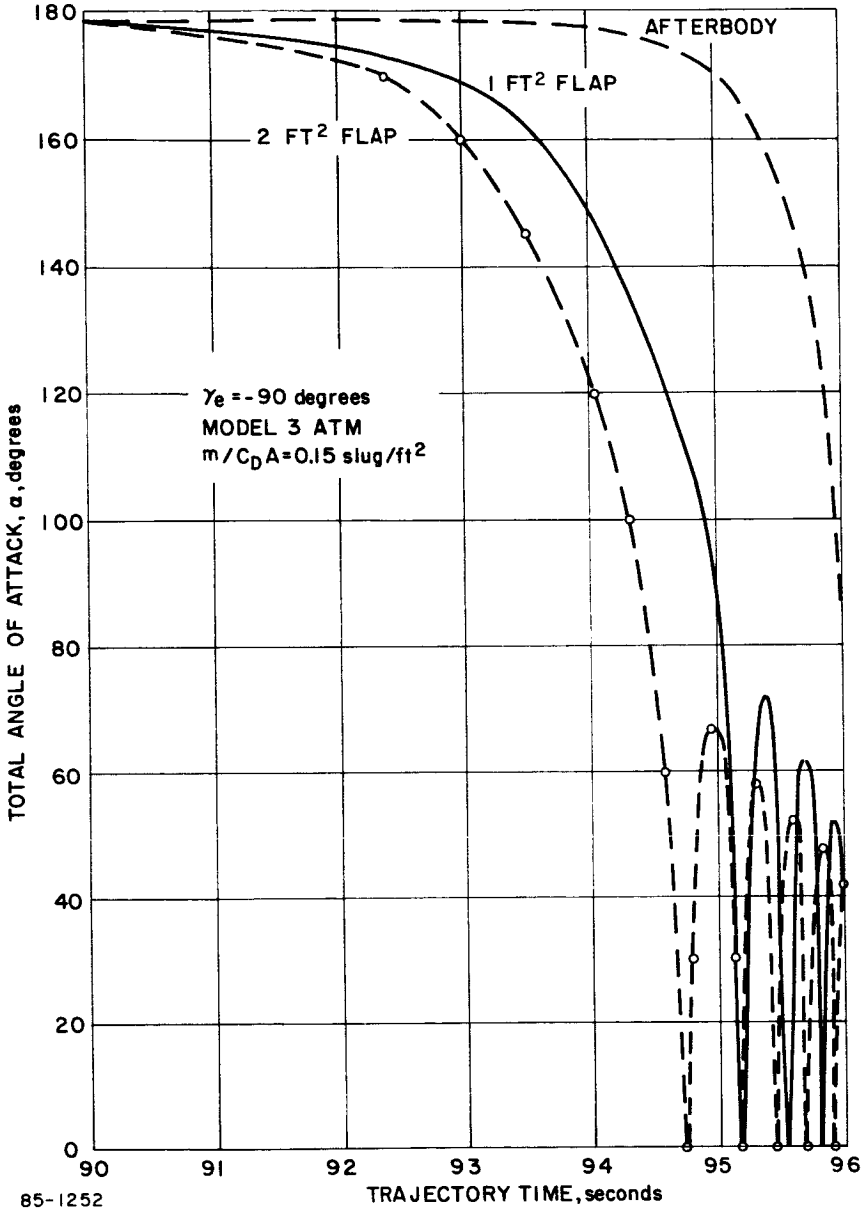

Figure 64 REARWARD ENTRY -- 60° BLUNT CONE

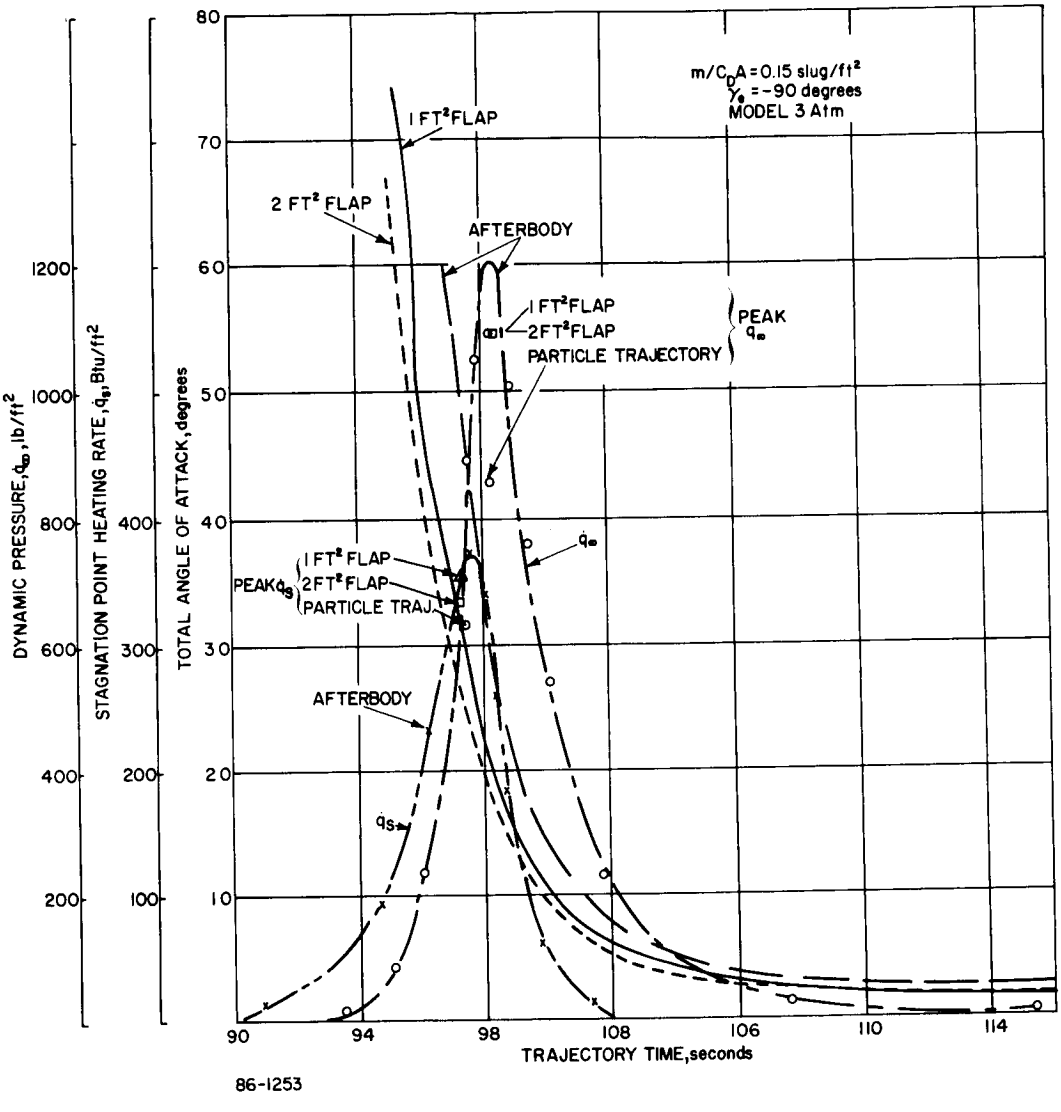

Figure 65 REARWARD ENTRY -- 60° BLUNT CONE

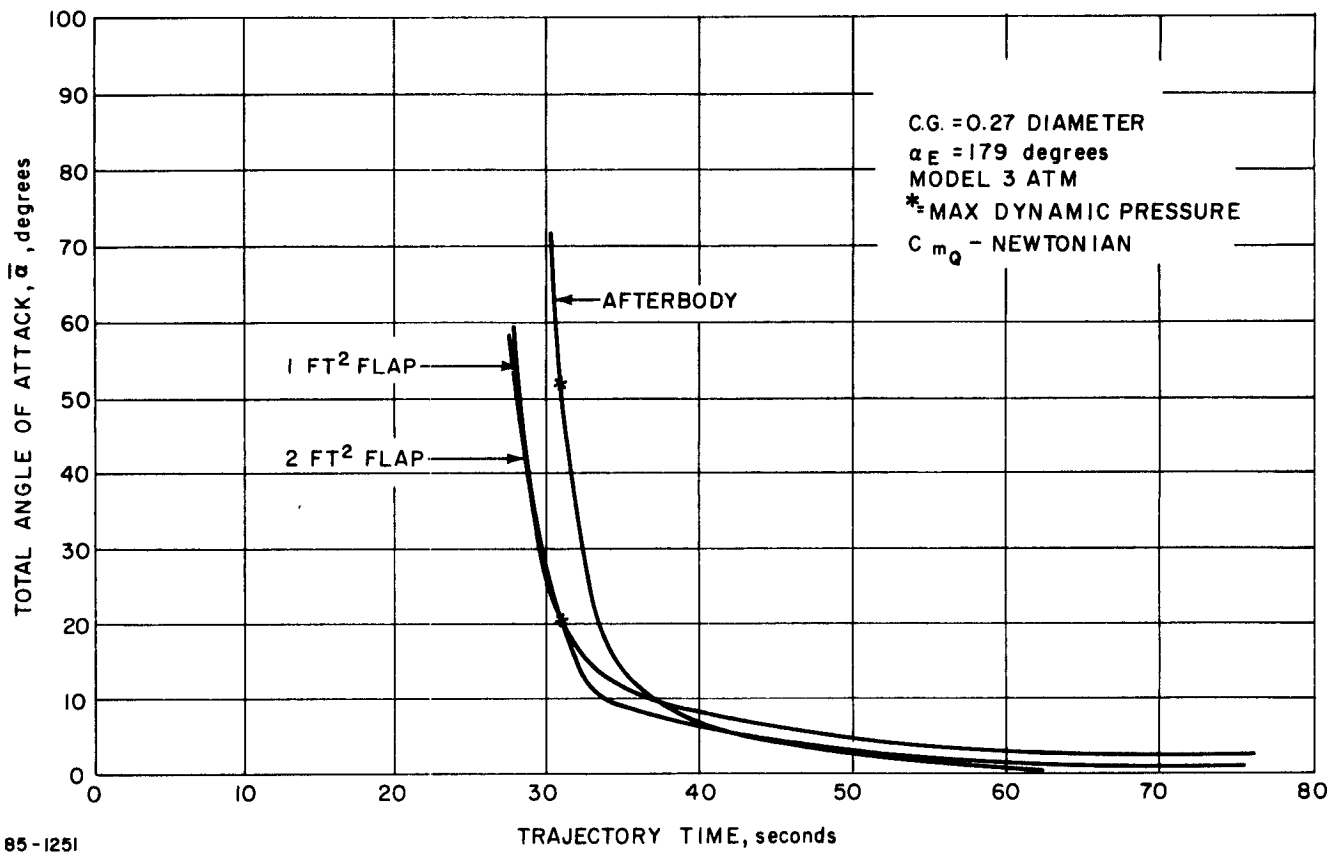

Figure 66 FAILURE MODE STUDY--BLUNT CONE CONFIGURATION STUDY

2.3.3.2 Modified Apollo Shape

The performance parameters for the modified Apollo shape were investigated as a function of spin rate and pitch damping parameters. Of the three performance parameters only the altitude at M = 1.3 is effected by the value of pitch damping to any sizable degree. This is also true for variations in spin rate for $C_{m_q} = 0$. The condition corresponding to $C_{m_q} = 0$ and a spin rate of 3.0 rad/sec will satisfy required altitude of 16,500 feet at Mach 1.3. Altitudes in excess of this design point are obtained for all spin rates when Newtonian values of C_{m_q} are used.

The effect of these parameters and moments of inertia on the angle of attack properties were similar to those of the blunt cone. For all cases divergence is indicated with $C_{m_q} = 0$ while convergence is indicated for the Newtonian value. The maximum divergent angle of attack increases as the spin rate increases and, at a spin rate of 8 rad/sec, diverges to a 33-degree angle for an entry angle of attack of 35 degrees. Spin rates must be kept as small as possible in order to prevent the high divergent angles of attack associated with negligible damping.

The moment of inertia effects also show the divergence which is typical of the zero damping condition. The variations indicate an increase in the divergent angle of attack as the ratio of I_{xx} to I_{yy} increases.

Apollo shape - failure mode -- contrary to the blunt cone shape the vehicle showed a strong divergence following the maximum dynamic pressure condition. This is most likely due to the very strong influence of the flap compared to the stability of the vehicle itself. This ratio is larger than that of the blunt cone shape which does not diverge.

2.3.3.3 Blunt Tension Shape

The blunt tension shape was analyzed for the effects of spin rate and pitch damping coefficients. The loads and heating increase as the spin rates increase because the high spin rates produce higher effective angles of attack and therefore higher effective M/C_DA. In like manner, the $C_{m_q} = 0$ conditions also produce higher loads and heating. Generally the effects of C_{m_q} are small except for the angle of attack at peak heating which showed a significant change at $\gamma_e = -90$ degrees. The altitude at Mach = 1.0 did not vary with spin rate except for the $C_{m_q} = 0$ condition at $\gamma_e = -90$ degrees; here the Mach 1 altitude decreases with spin rate.

The angles converge for the Newtonian values of C_{m_q} and diverge at low altitudes for $C_{m_q} = 0$. The divergence becomes more severe as the spin rate is increased. An additional divergence is associated with the static instability at zero angle of attack at supersonic speeds. The condition is not severe as the vehicle rapidly passes through this condition and the convergence process continues. For $C_{m_q} = 0$ divergence continues and a maximum angle of attack of 34.4 degrees is reached with a spin rate of 8 rad/sec.

2.3.4 Comparison of Configurations and Characteristics

The previous sections contained the results of the analytical investigations. A detailed comparison of these results is now in order and the overall effects of vehicle shape on the three concepts which have evolved, in terms of aerodynamic loads, convective and radiative heating, and performance and dynamics will be considered in this section.

A typical set of entry history parameters which relate to the above categorical considerations is shown in Figure 67 for the 60-degree blunt cone. Shown are the dynamic pressure history (q), the convective (q_c) and radiative (q_r) heating pulse, and the angle of attack envelope ($\bar{\alpha}$). These parameters are indicative of the effects of vehicle diameter, atmosphere and entry conditions on the performance for each of the configurations.

2.3.4.1 Loads

Maximum pressure loads for the multi-mission shell (w_e = 4500 pounds) are plotted versus diameter for each of the configurations in Figure 68. The points for 200-inch diameter vehicles are based on a 90-degree entry angle into an interpolated atmosphere which results in an altitude of approximately 15,000 feet at M = 1.3. The corresponding data are plotted for the 1971 mission (M/C_DA 0.15) in Figure 69, and indicate no significant dependence on the diameter when the performance (M/C_DA) is specified.

Figures 70 and 71 compare the maximum loads in atmosphere Models 1 and 2 for the three configurations as a function of diameter for an entry weight of 4500 pounds. (The high weight precludes steep entries into atmosphere Model 3.)

Particle trajectories have been computed simulating the revised design entry conditions for each of the entry shapes as explained below.

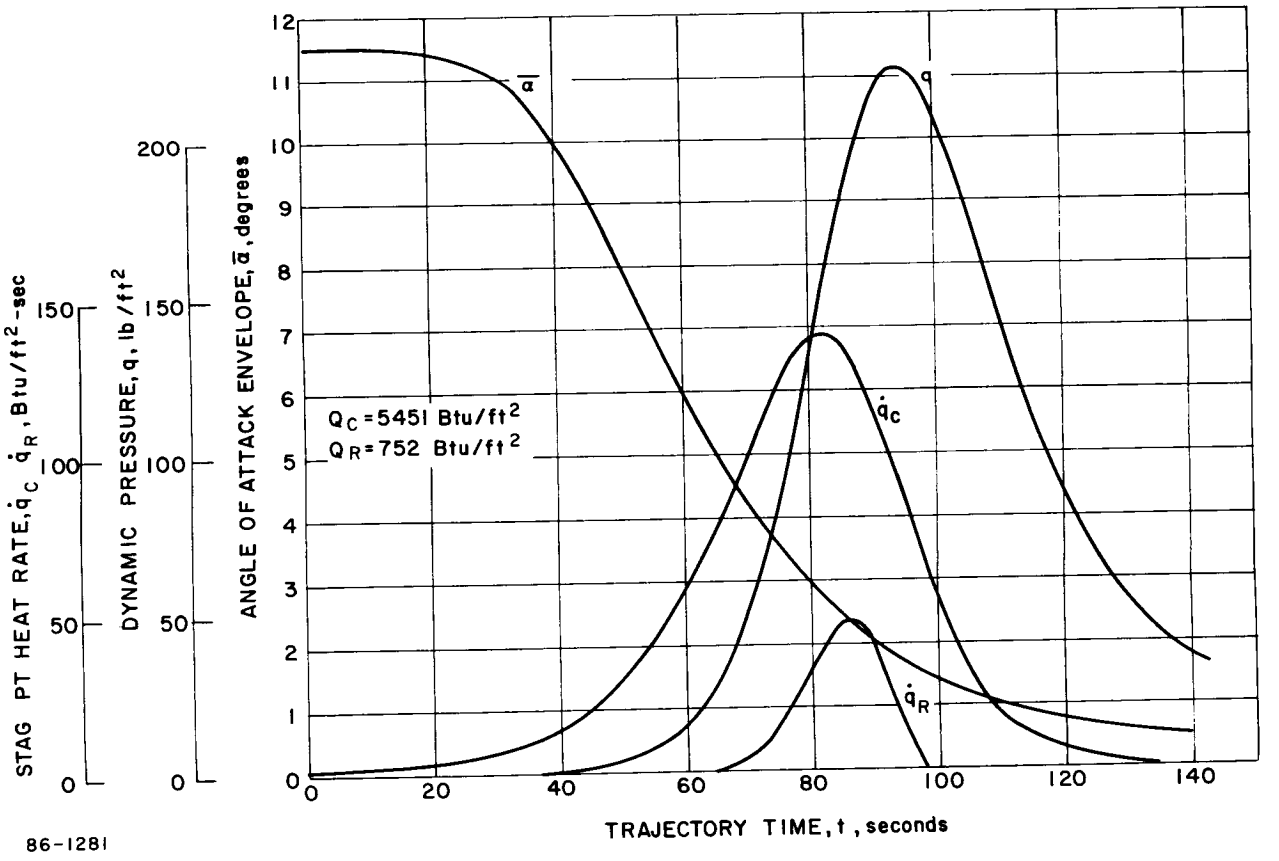

Figure 67 ENTRY TRAJECTORY (MODEL 2 ATM) -- BLUNT CONE

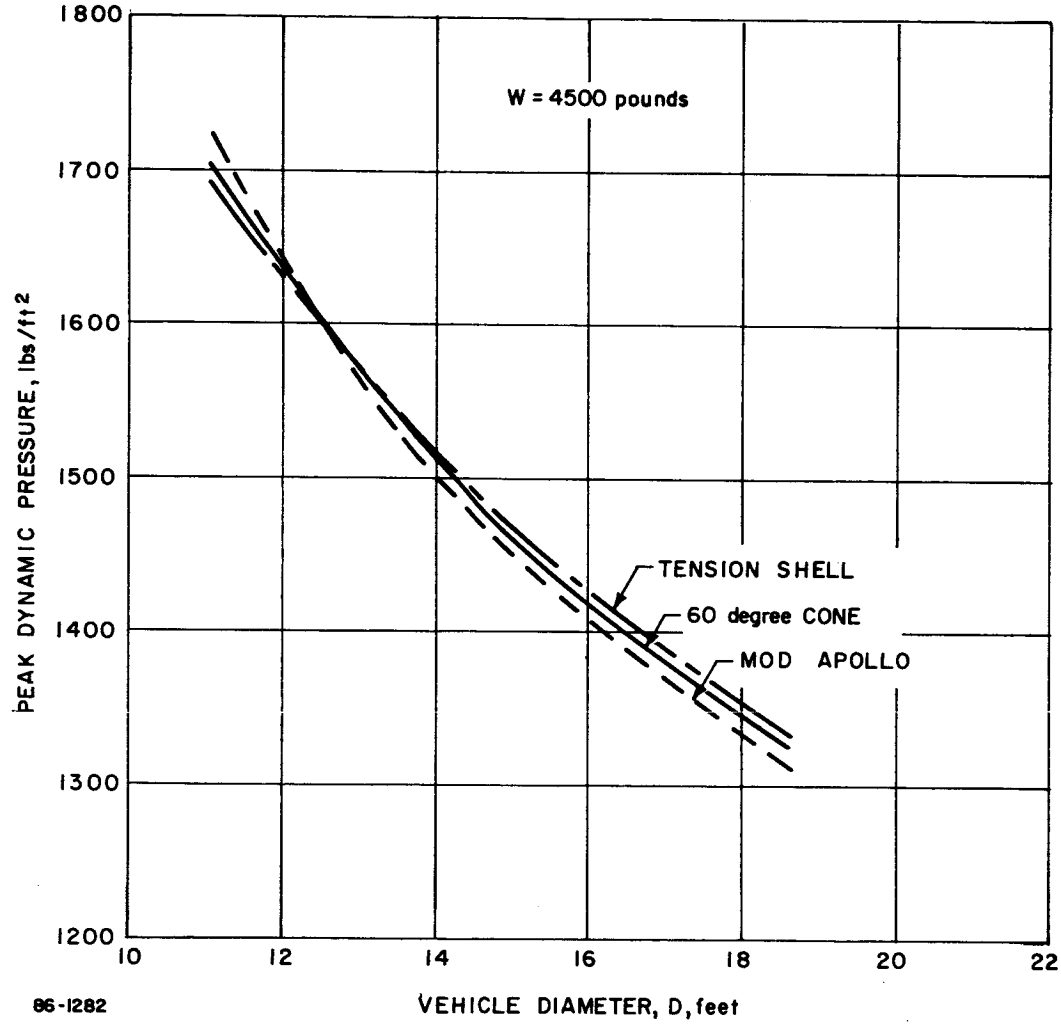

Figure 68 EFFECT OF DIAMETER ON LOADS

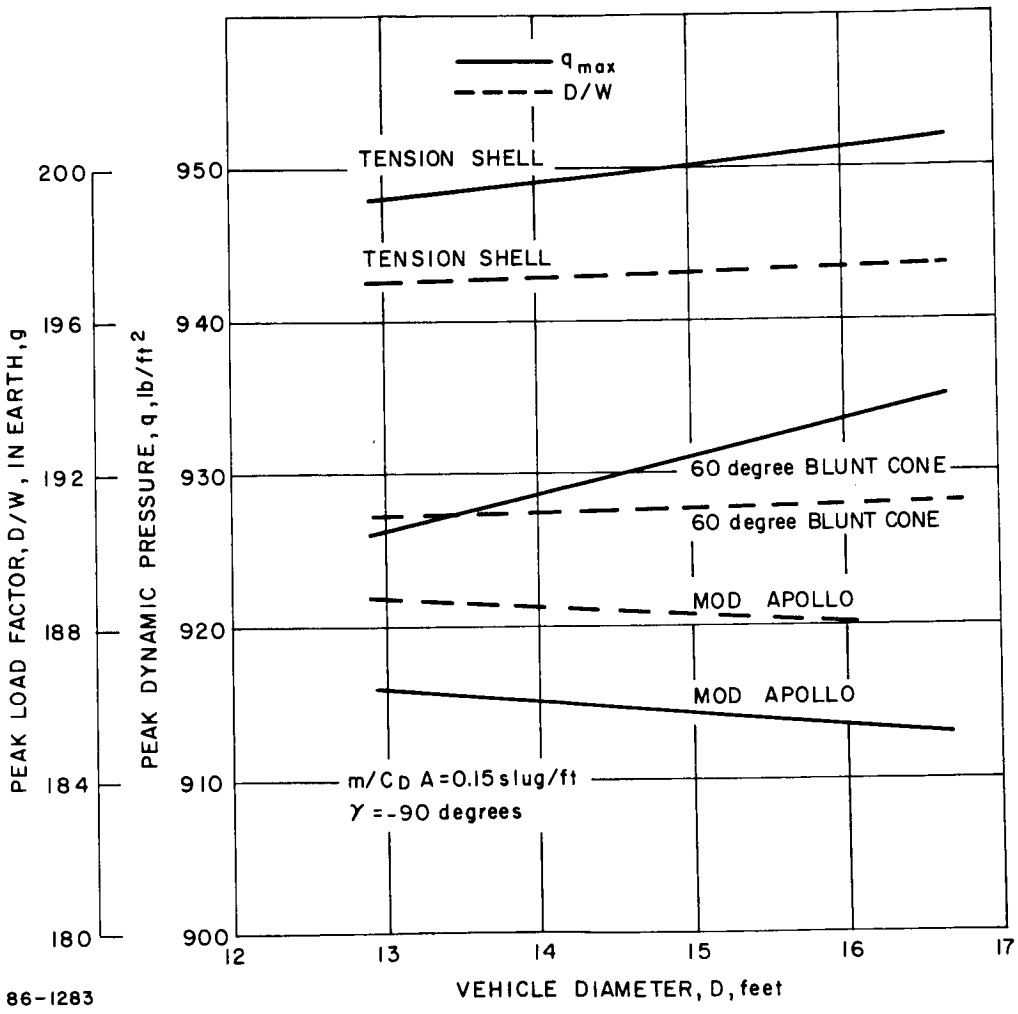

Figure 69 LOADING PARAMETERS ($M/C_DA = 0.15$ SLUG/ FT^2)

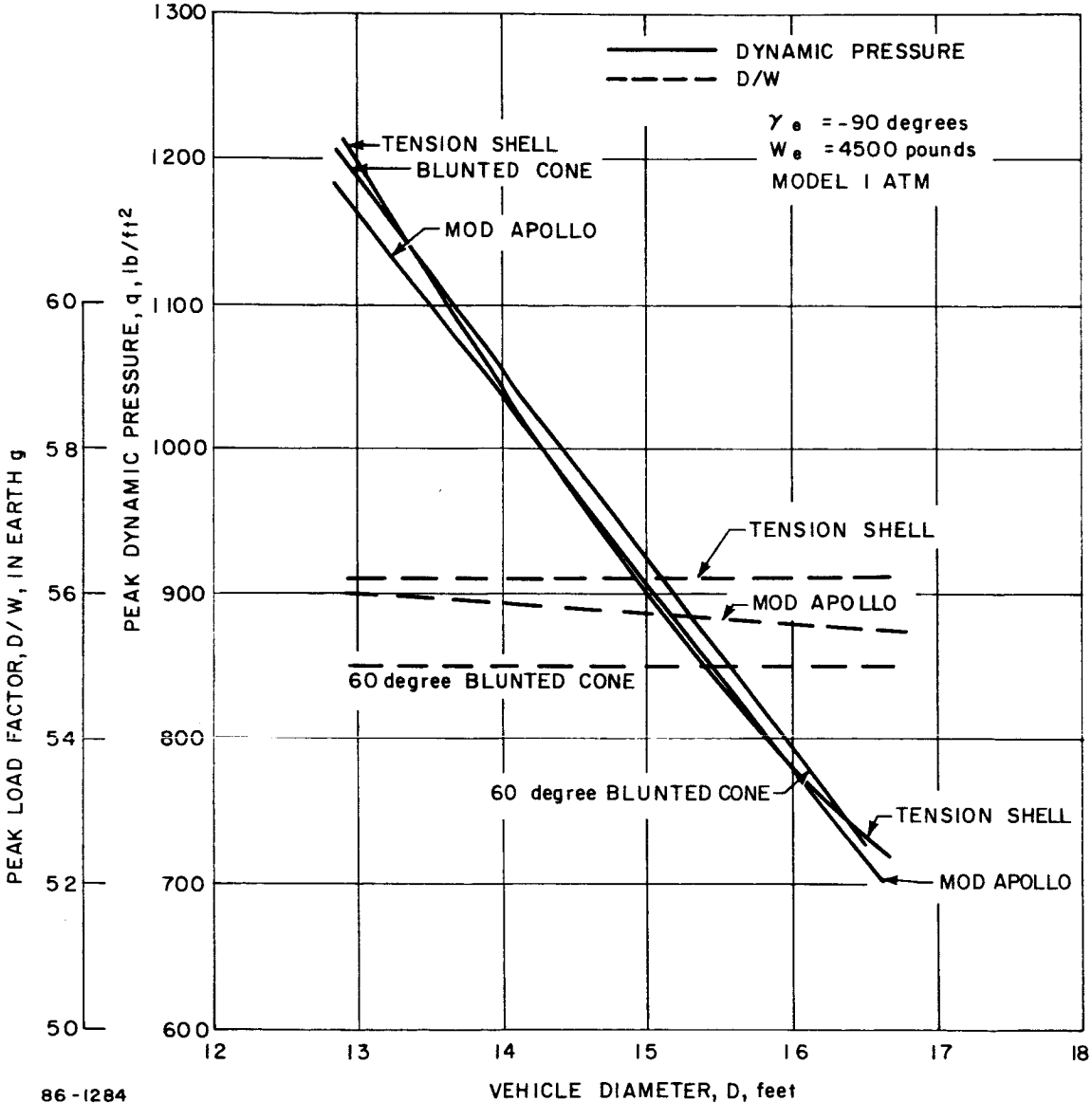

Figure 70 EFFECT OF DIAMETER ON LOAD PARAMETERS (ATM 1)

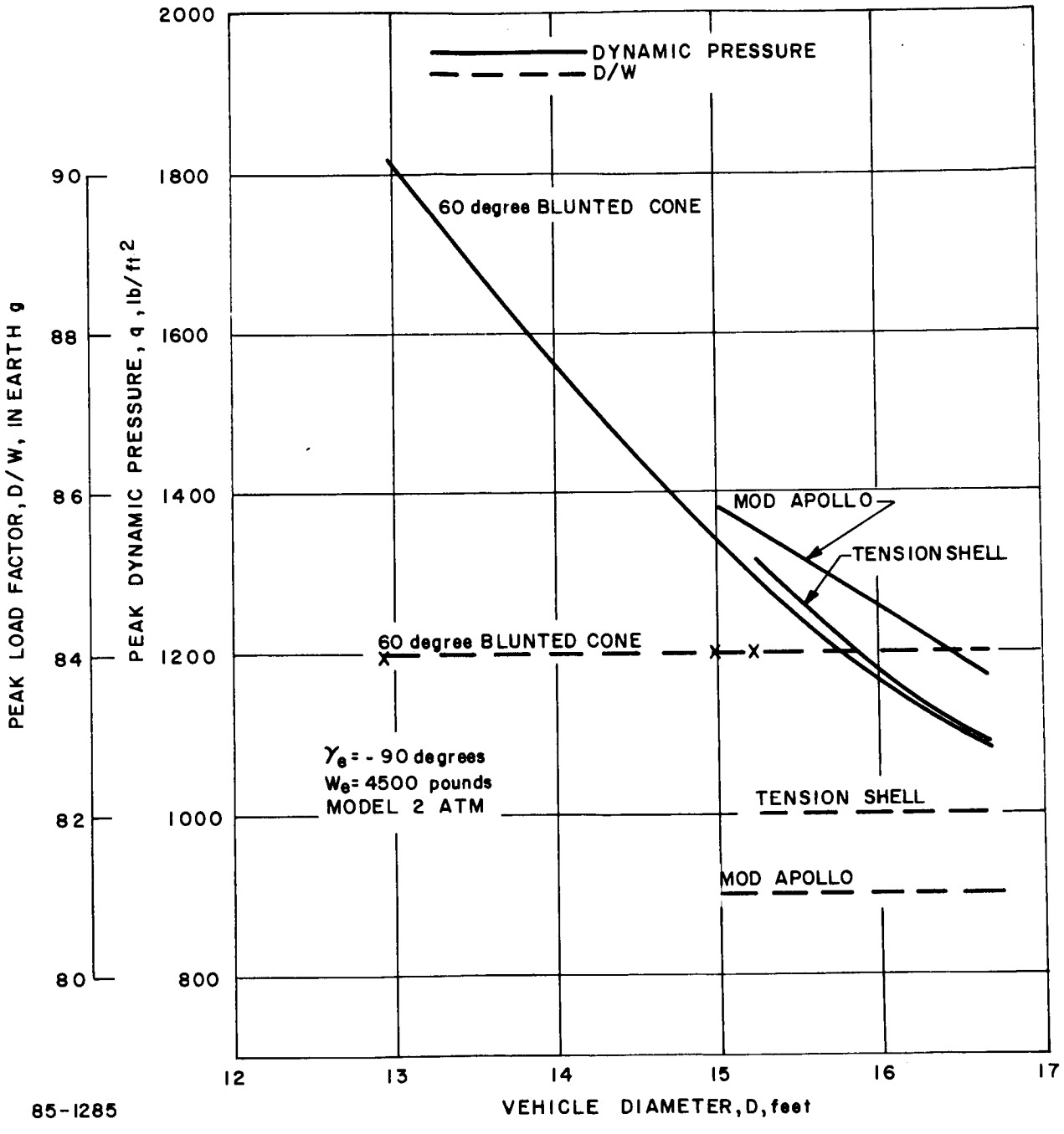

Figure 71 EFFECT OF DIAMETER ON LOAD PARAMETERS (Atm.2)

1. Concept (B) - Multi-Mission Structure -- Maximum load is obtained for the maximum weight (4500 pounds) entering the Model 2 atmosphere at -90 degrees (V_e = 23,800 ft/sec).

2. Concepts (C) and (D) - 1971 Structure and Future Mission Shell -- Specified by LRC to be designed for M/C_DA = 0.15 at an entry angle of -90 degrees in the Model 3 atmosphere.

A summary of the loads obtained in particle trajectories for these design conditions is provided in Table XVI. It should be pointed out that a particle trajectory results in the minimum load for a given set of entry conditions. The effect of angle of attack at entry is to increase the peak values of dynamic pressure and axial g as will be shown later. A rearward entry can cause loads 25 percent greater than indicated in the table. Table XVII shows the loads resulting when the entry angle of attack is 179 degrees, and no flap is used to improve the righting moment.

2.3.4.2 Integrated Heating

Greatest integrated heating is obtained at the shallowest entry angle, -20 degrees. Integrated heating variation with vehicle diameter is summarized for the three configurations in Figures 72 through 74 for the entry weight of 4500 pounds in each of the atmospheres. It is seen that convective heating (Q_S and Q_1) is greatest in the Model 1 atmosphere, while the radiation heating (Q_R) is greatest in the Model 2 atmosphere. Subscripts s and 1 refer to the stagnation and sonic points respectively. Sonic point heating is based on computed convective heating distributions. (For the tension shell, maximum heating point data are given instead of sonic point data.)

It can be seen that the heating at the rim of the tension shell configuration (about 40 percent of the surface area) is an order-of-magnitude higher than that for the other shapes. This resulted in heat shield weights which were far greater than originally estimated. A similar study was performed for the 1971 mission (M/C_DA = 0.15). At this M/C_DA, radiation heating is much less. Only atmosphere 1 need be considered for heat shield design. Figures 75 through 77 summarize the heating as a function of diameter for the three configurations.

A further analysis of the revised design concepts was undertaken on the following definition of ground rules:

1. Concepts (B) and (C) - 1971 Heat Shield -- Heat shield to be designed for M/C_DA = 0.15 evaluated at an entry angle of -20 degrees in the Model 2 atmosphere.

TABLE XVI

LOAD SUMMARY

D = 15 feet V_E = 23,800 ft/sec Z_E = 800,000 feet

(From Particle Trajectories)

Shape	Weight (pounds)	Atmosphere	γ_e (degrees)	Reference Trajectory	Peak Dynamic Pressure (psf)	Peak g	Design Concept
Modified Apollo	4500	2	-90	986-17.1	1098	73	(B)
Modified Apollo	1450	3	-90	986-12	775	161	(C) & (D)
Blunt Cone	4500	2	-90	987-11.1	1152	73.3	(B)
Blunt Cone	1390	3	-90	987-6	777	161	(C) & (D)
Blunt tension shell	4500	2	-90	988-9.1	1114	73.3	(B)
Blunt tension shell	1435	3	-90	988-6	778	161	(C) & (D)

TABLE XVII

LOAD SUMMARY

Dynamic Trajectories (α_e = 179°) - 25-degree Afterbody

D = 15 feet γ_E = -90 degrees V_E = 23,800 ft/sec Z_E = 800,000 feet

Weight (lbs)	Atmospheres	Design Concept	Peak Dynamic Pressure	α Peak g (degrees)	Max D/W	Max N/W	Reference Trajectory
Modified Apollo:							
4500	2	(B)	1333	11	89	3	5-2
1450	3	(C) & (D)	1020	22	211	11	5-1
Blunt Cone:							
4500	2	(B)	1426	16	91	7	6-2
1390	3	(C) & (D)	1009	20	209	19	6-1
Blunt tension shell:							
4500	2	(B)	1375	9	87	10	7-3.1
1435	3	(C) & (D)	1110	31	224	42	7-2.1

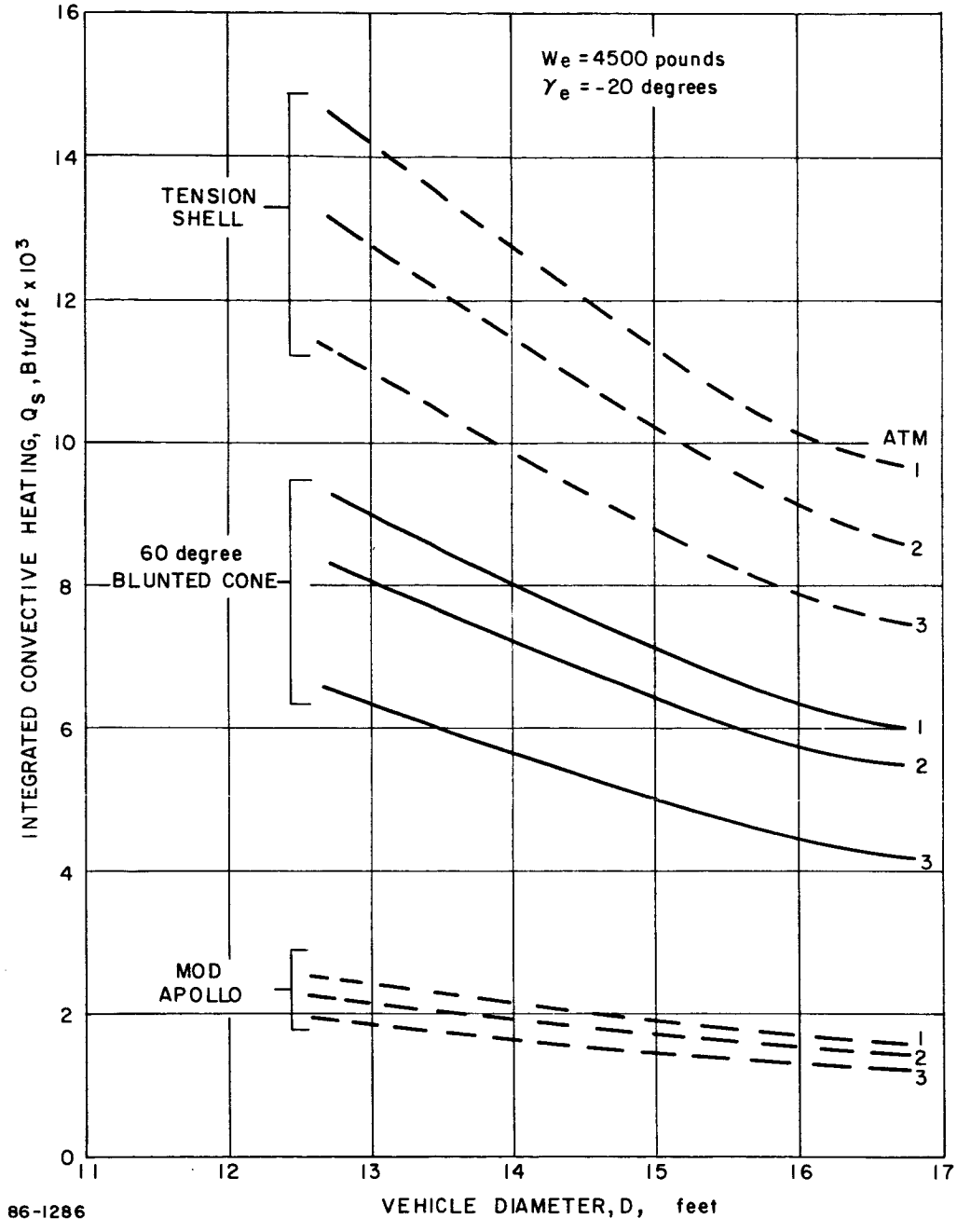

Figure 72 INTEGRATED CONVECTIVE HEATING--STAGNATION POINT ($M/C_DA = 0.15$ slug/ft^2)

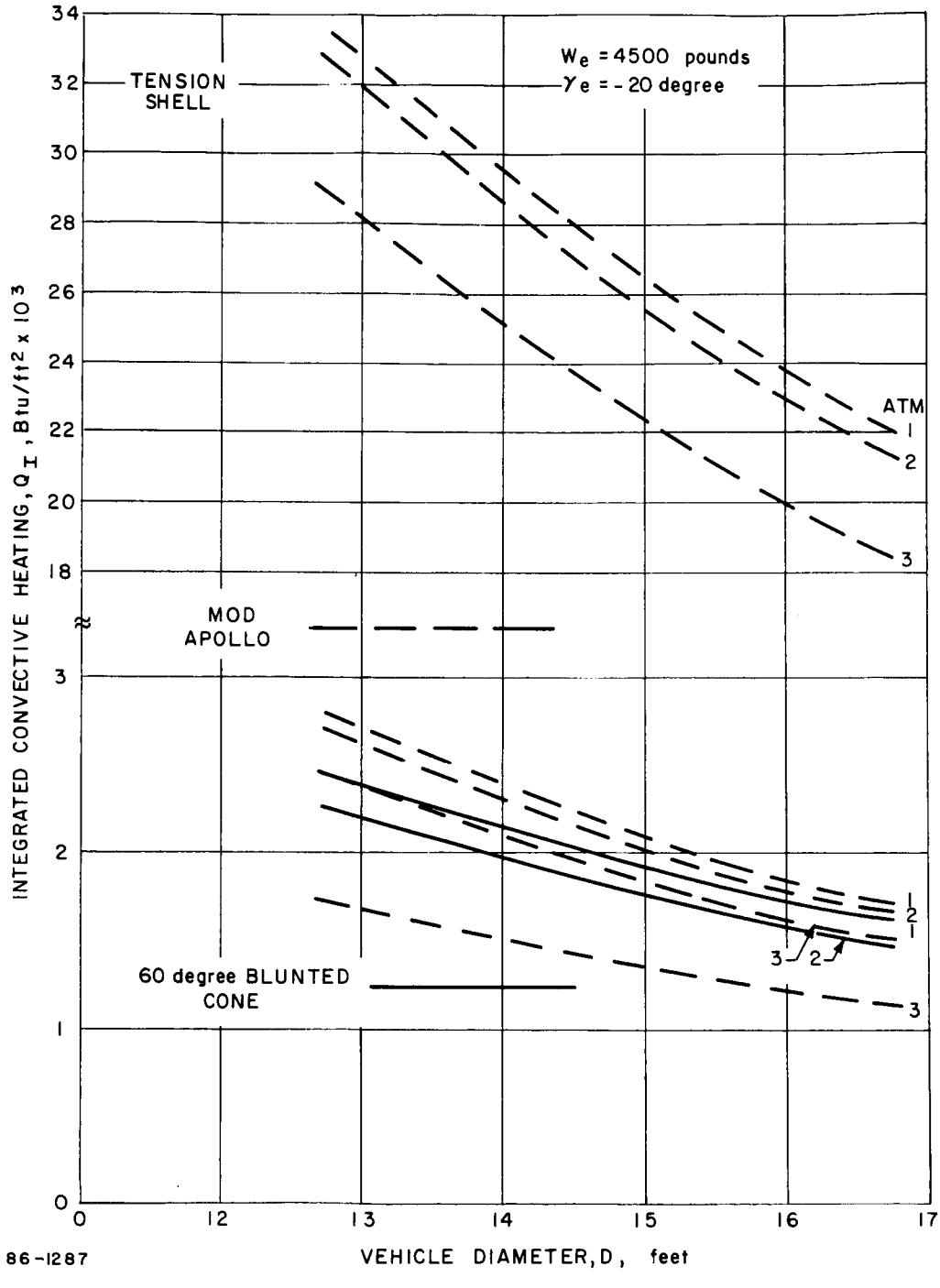

Figure 73 INTEGRATED CONVECTIVE HEATING (AT OR NEAR SONIC POINT) ($M/C_DA = 0.15$ slug/ft^2)

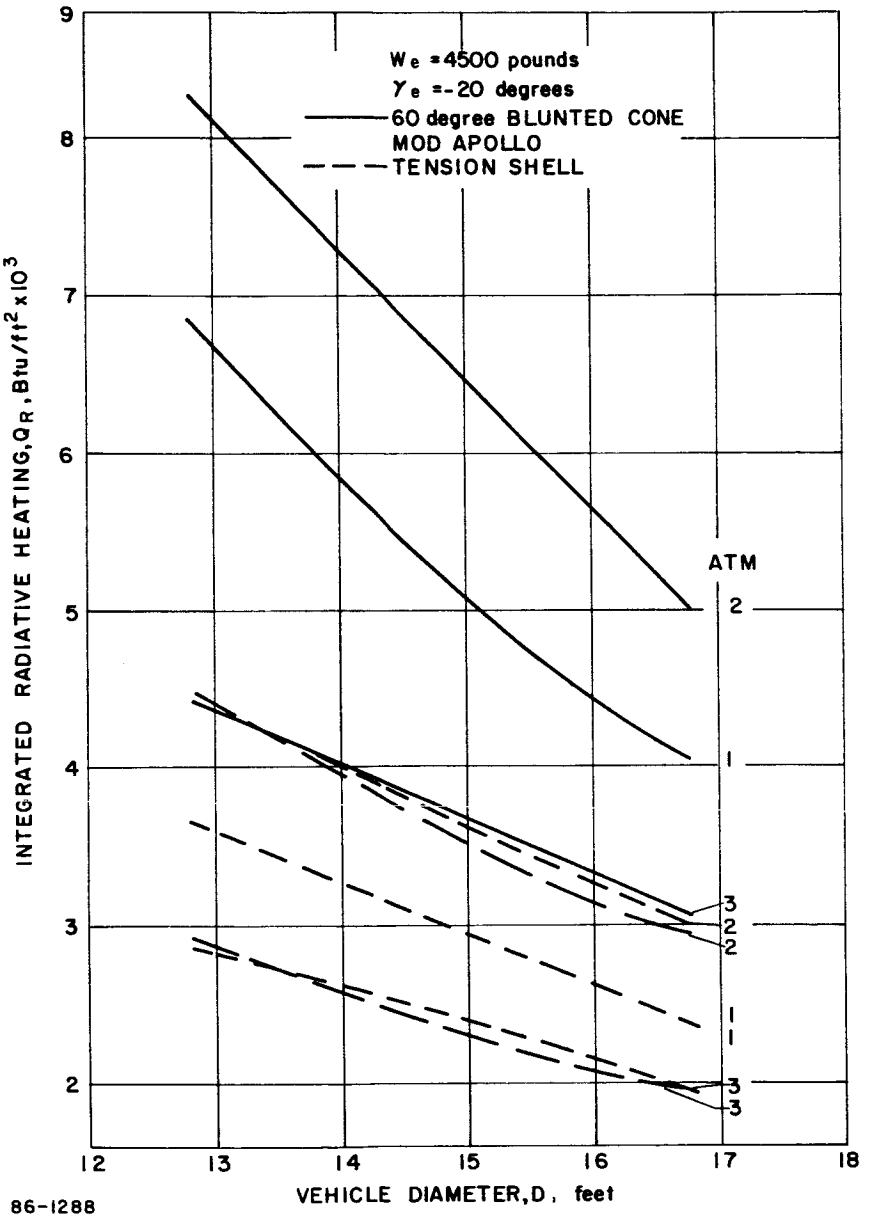

Figure 74 INTEGRATED RADIATIVE HEATING (M/C_DA = 0.15 slug/ft^2)

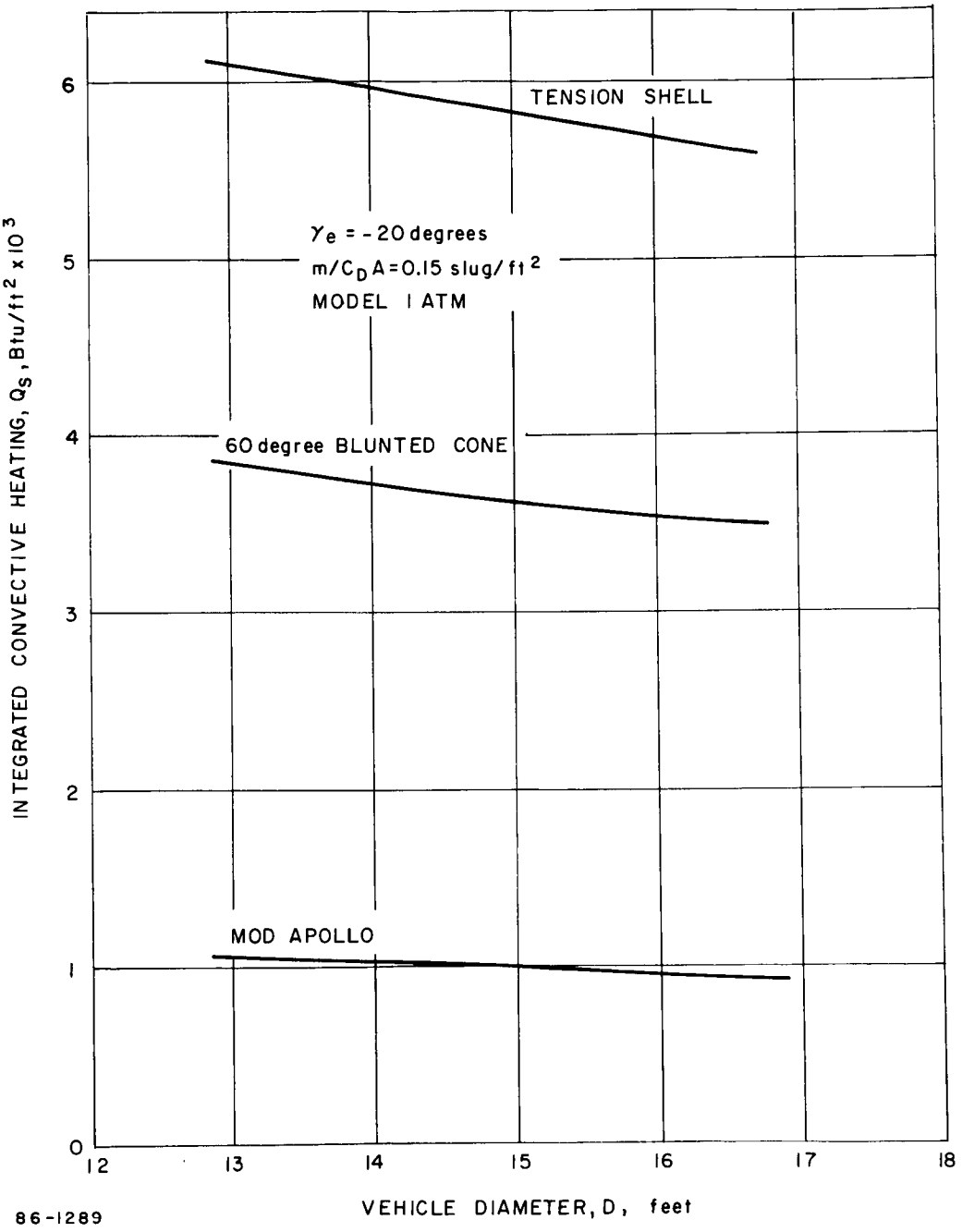

Figure 75 INTEGRATED CONVECTIVE HEATING--STAGNATION POINT (W = 4500 pounds)

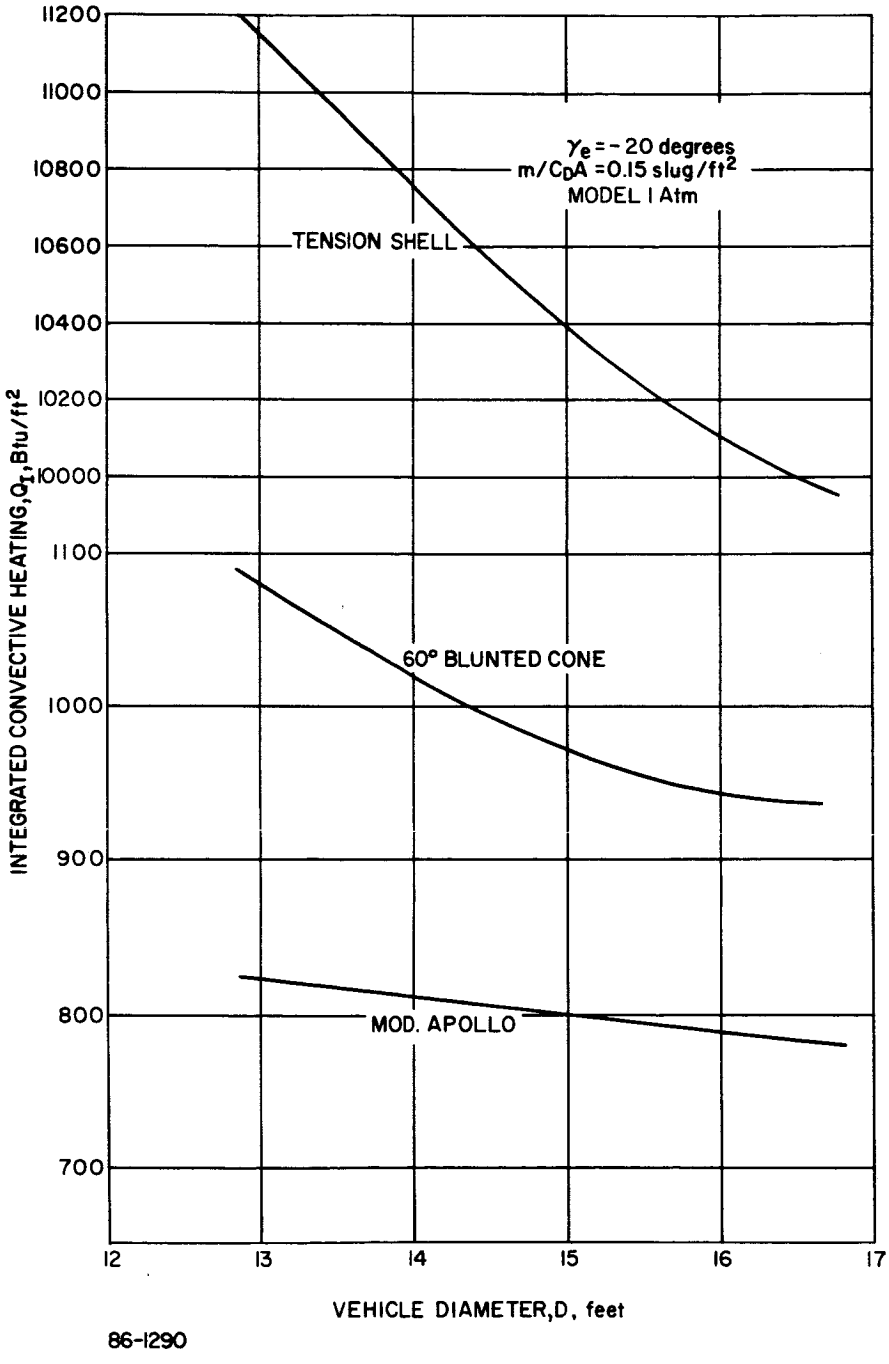

Figure 76 INTEGRATED CONVECTIVE HEATING -- AT OR NEAR SONIC POINT (W = 4500 POUNDS)

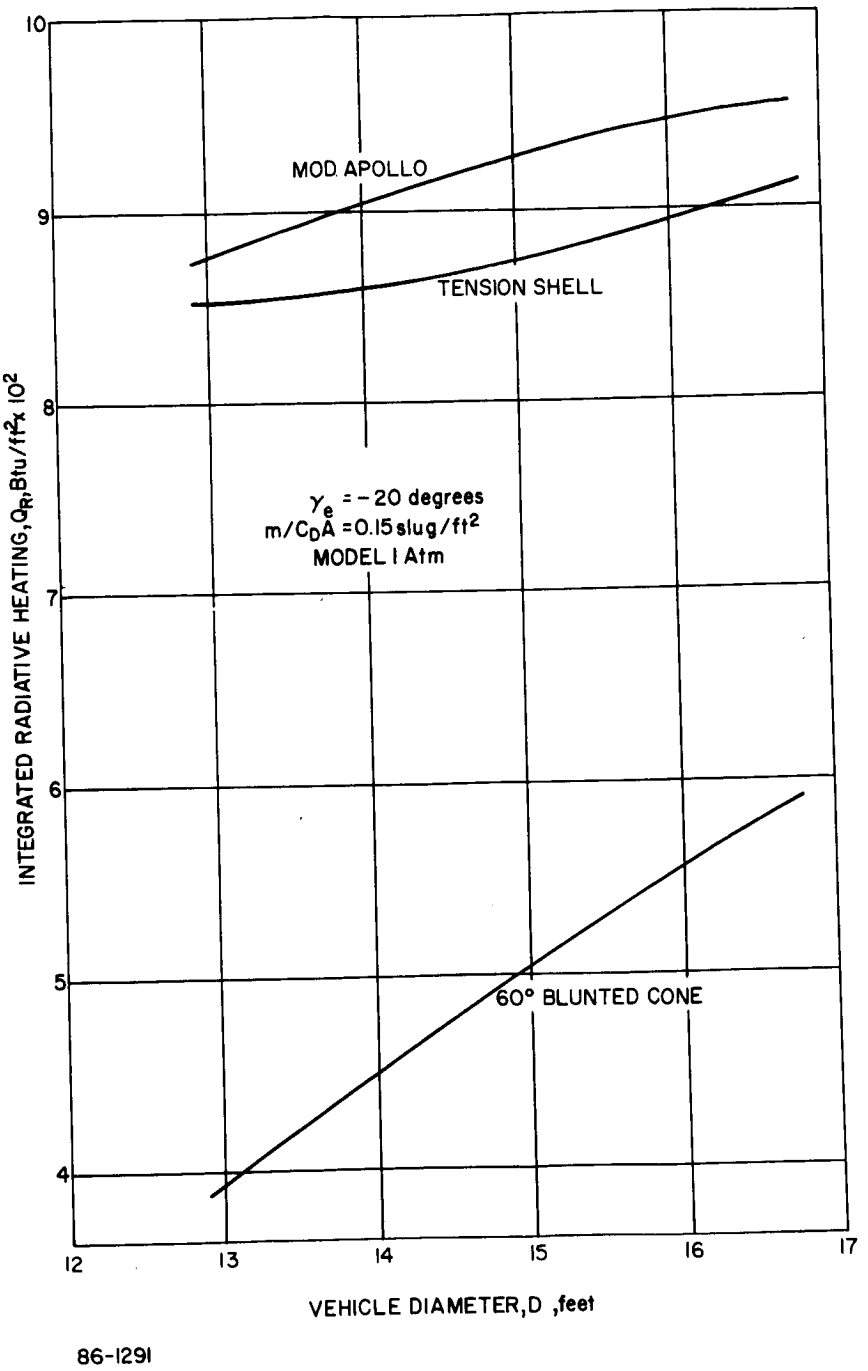

Figure 77 INTEGRATED RADIATIVE HEATING (W = 4500 pounds)

2. Concept (D) - Future Mission Shell -- Heat shield design for maximum weight (4500 pounds), evaluated at an entry angle of -20 degrees in the Model 3 atmosphere.

A comparison of the heating obtained in particle trajectories ($\alpha_e = 0$ degree) for these design conditions is provided in Table XVIII. The results indicate that the tension shell still has the greatest heating and will require the heaviest heat shield. Of the remaining two shapes, the blunt cone has the higher convective heating, but the least radiative heating.

Some explanation is required for the integrated turbulent sonic point heating (Q_I*) data. For the modified Apollo and blunt cone, sonic point integrated heating is given, but for the tension shell, the maximum heating rate extant is indicated.

The maximum equilibrium radiative heating given in the table occurs at the stagnation point on the modified Apollo, but occurs toward the rim on the other configurations. A typical comparison of radiation and convective heat pulses is shown in Figure 78. (Again the basic convective pulse is at the stagnation point for the blunt vehicle and at the maximum heating point for the tension shell.) Atmosphere 2 - the atmosphere producing maximum radiation is used here as an indication of the upper level of radiation for concepts B and C.

2. 3. 4. 3 Dynamics

The blunt tension shape attains a Mach No. of 1. 3 at the lowest altitude followed by the blunt cone and modified Apollo in increasing altitude order. All of the shapes meet the requirement of a 16, 500 foot altitude for C_{m_q} = Newtonian. For $C_{m_q} = 0$ each of the shapes can achieve the 16, 500-foot altitude, provided that spin rates are minimal.

The comparison of maximum dynamic pressure indicates relatively small changes between the three shapes with the highest pressure occuring at the high spin rates with the blunt tension shape. This occurred for both $C_{m_q} = 0$ and the Newtonian value.

The pressures on the modified Apollo were lowest and those on the blunt cone were intermediate. The crossing of the curves at the low spin rates show only small changes between the three configurations.

TABLE XVIII

HEATING SUMMARY

D = 15 ft. γ_E = -20 degrees V_E = 23,800 fps Z_E = 800,000 feet

(Particle Trajectories)

Weight (pounds)	Atmospheres Model Number	$\dot{q}_s$ Maximum Btu/ft^2/sec	Q_s (Btu/ft^2)	Q_I (Btu/ft^2)	$\dot{q}_r$ Maximum (Btu/ft^2/sec)	Q_r (Btu/ft^2)	Design Concept
Blunt Cone:							
4500	3	188	4405	2182	7.0	62	(D)
1390	2	70	2798	803[x]	1..0	19	(B) & (C)
Modified Apollo:							
4500	3	49	989	1345	106	963	(D)
1450	2	19	753	750[x]	19	304	(B) & (C)
Blunt Tension Shell:							
4500	3	291	6824	15090[y]	225	2278	(D)
1435	2	111	4416	4303[z]	38	683	(B) & (C)

x) Entire heat pulse is laminar

y) Heat pulse at S/R_N = 14.7 (not sonic point)

z) Heat pulse at S/R_N = 11.6 (not sonic point)

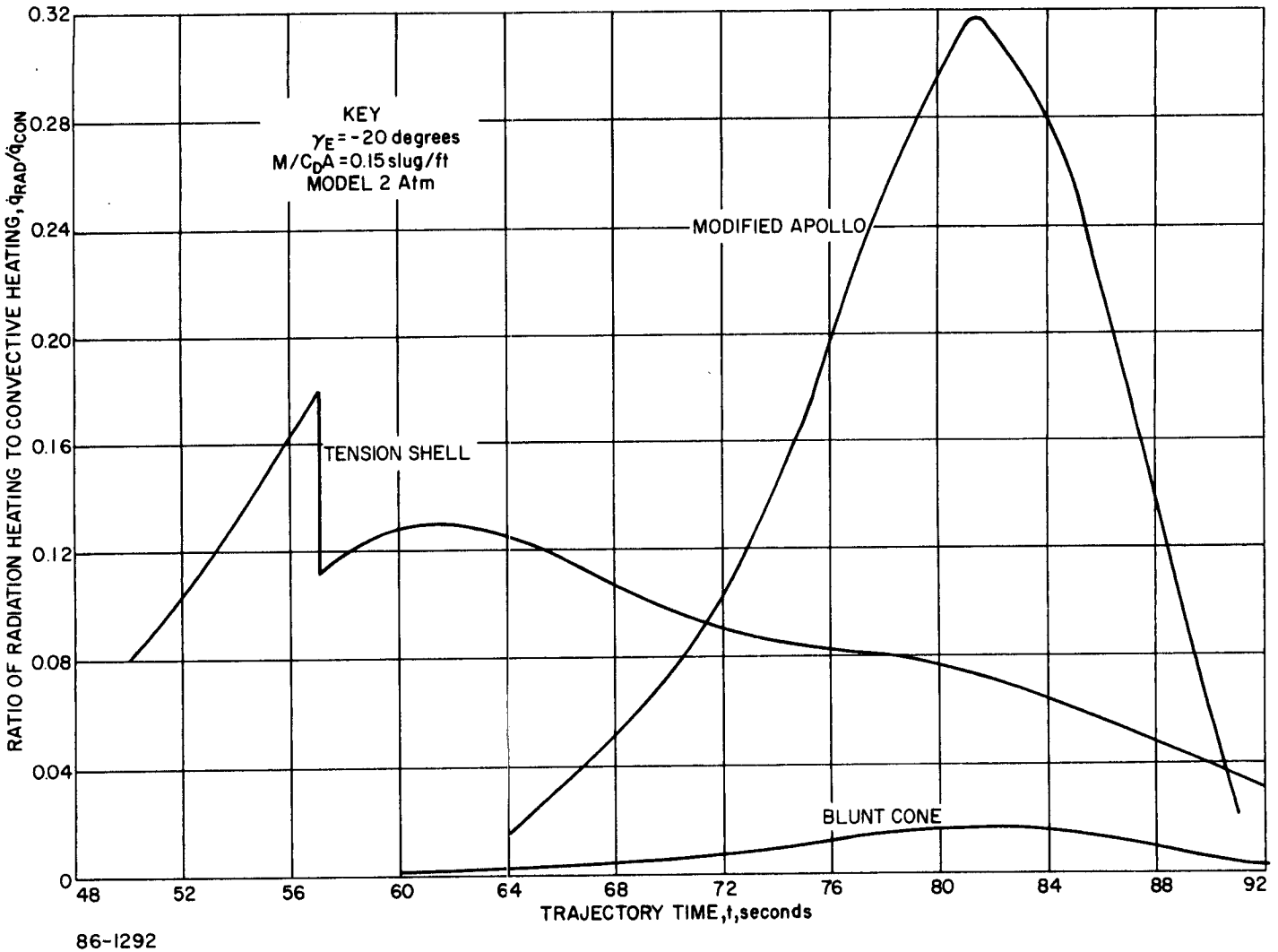

Figure 78 COMPARISON OF RADIATION HEATING TO CONVECTIVE HEATING

2.3.5 Problem Areas

The primary problem area was the consideration of the real-gas effects. The stability and performance analyses are confronted with a dearth of aerodynamic coefficient data for a specific configuration and that data available is limited to ideal gas conditions. Considerable effort was expended to include real gas effects on the coefficients as well as on the heating and pressure distributions. Correlation between the ideal and real gas effects were effected by means of the stagnation point to free-stream density ratio, ρ_s/ρ_∞ , which facilitated the ancillary analyses associated with the parametric study. By this means computer programs which handle air calculations could be used by determining the equivalent flight conditions resulting in identical density ratios for air and the Martian atmospheric model composition. These procedures, while adequate for evolving the pressure and heating distributions and the drag coefficient, are suspect with regard to the normal force and moment coefficients since these parameters are the result of differentials rather than absolute quantities. The data, however, do indicate some correlation. On the other hand, shapes with multiple shock flow fields require further analyses. The blunt tension shell configuration, which falls into this category, was examined by a detailed flow-field analysis, which for expediency and within the time-scale extant was conducted manually rather than attempting to automate the process. The correlation of the density ratio was accepted as applicable to the tension shell configuration with detailed distributions obtained initially for the specific flight conditions and atmospheres during the critical phases of entry (peak loads, heating, etc.).

In addition to the static coefficient the dynamic coefficients, specifically the damping moment, presented a problem. Although ground-test data indicate Newtonian theory is adequate in the hypersonic regime, the data digresses within the transonic regime, the exact Mach Number for which this digression occurs depending primarily on the vehicle shape. This often results in positive damping moments (dynamically unstable); however, evidence exists that these phenomena are associated with smooth contour shapes, especially in the maximum diameter and afterbody region. The hysteresis between the separated wake and shock interactions in this region gives rise to the dynamic instability. To circumvent or to minimize these phenomena the configurations considered terminated abruptly at the maximum diameter, with the afterbody size minimized within the packaging and turnaround capability requirements. Subsonic tests indicate that this is also beneficial in this flight region, the data indicating better than Newtonian damping.

The afterbody poses an additional complication since, in addition to the turnaround ability requirement, packaging considerations and spacecraft interfaces must be factored into the design. The afterbody configurations are important in that a considerable portion of the vehicle surface is associated with this region (greater than 50 percent for the blunt cone and modified Apollo shapes). The rearward entry possibility (a failure mode) poses a design problem in establishing the environments not only for the rearward attitude but also for the low angle of attack condition. Since all shapes are characterized by sonic conditions at the maximum diameter, little variation in the base pressures is to be expected. Instead this pressure is primarily dependent upon the Reynolds Number at the separation point. Difficulty is experienced when applying theory in that the sonic condition results in singularities in the analyses. The data that exist indicate pressures higher than free-stream valves, with the possibility of comparatively high heating. Very little data exist with which to analyze this region of the configuration.

The tension shell presents a major problem in the definition of the flow field about the body. Such definition must be made with sufficient accuracy for design purposes. Although the methods developed to deal with the flow field are of sufficient accuracy to define the tension shell performance relative to that of the blunt cone and the modified Apollo shapes, a highly refined analysis will be required for final design.

In that phase, flow-field definition will require determination of the boundary-layer and blowing effects as well as of the inviscid flow field. To do so within the accuracy required by the stringent trajectory constraints while allowing for atmosphere-based unknowns will be difficult. The tension shell (either sharp or blunt) form is characteristic of a sharp-nosed body. The frontal shock system and the flow behind it are not, therefore, simply functions of the stagnation density ratio -- low-speed, high-density flow affects a maximum of 1 percent of the surface - but are, rather, dependent upon the composition of the atmosphere and the free-stream velocity as well as the local density ratio.

The effect of this complex dependency is that a long and costly development program will be required. Flight testing can not adequately define the effects of atmospheric composition. Flight testing can however substantiate the effects of other variables and analyses. A great deal of emphasis would, therefore, be placed on wind-tunnel and shock-tube testing despite the inherent scaling and nonequilibrium problems. The expense would be greater than that associated with the blunt shapes, to provide an equally confident configuration.

3.0 AERODYNAMICS - CONCEPTUAL DESIGN
PROBE, ENTRY FROM ORBIT

3.1 INTRODUCTION AND SUMMARY

The initial aerodynamic analysis for the entry from orbit consisted of a parametric study. It was conducted to provide an indication of the tradeoffs associated with various orbital parameters and to definitize various system concepts. These tradeoffs were based on the values of environmental loads and heating and the related structural and heat shield weights. Subsequent to the parametric analyses, an initial operating γ_e - V_e map was determined; a spin system was considered as the backup mode for the attitude control system. Analyses were conducted for this concept to provide both the environments and the performance prior to the final selection of the range of entry conditions (γ_e - V_e map) and selection of the entry mode (both reference and backup failure mode designs).

The aerodynamic analyses were conducted for the blunt-cone configuration that evolved from the entry from the approach trajectory phase of the study. Further system requirements and constraints (associated with the spacecraft interfaces and minimum weight requirements) resulted in the selection of a minimum weight afterbody configuration for the reference design and final performance analyses.

The aerodynamic analyses provided the information necessary to 1) define the environments which led to the selection of the design criteria, and 2) evaluate the performance and stability for the candidate configuration.

The specifying of the environments required additional flow-field analyses to account for the flight parameters and atmospheres associated with the entry from orbit. The methods and techniques used were similar and in some cases in common with the entry from the approach trajectory. Details of the analyses are presented in paragraph 2.4.

The atmospheres considered (VM-3, 4, 7, and 8) were somewhat redundant in that, although the surface pressure varied, the characteristic scale heights (which is of primary importance for the loads and heating environment) were the same for VM-3 and VM-7. The atmospheres VM-7 and VM-8 (the low-pressure atmospheres) were selected for design purposes. The same environments would be expected (except for gravitational effects on the trajectory) but at a different altitudes for the VM-3 and VM-7 atmospheres. An apparent anomaly occurs as the skip limit is approached - lower velocities resulted in higher loads than for the high velocities. This is due to the fact that the high velocity entries remained at high altitudes giving low dynamic pressures.

It is of interest to note that for the spin mode, using the appropriate initial angle of attack for a particular entry condition (determined from separation geometry), the highest angle of attack case evolved the critical load. The reference design critical loads were associated with the maximum entry velocity.

3.1.1 Configuration Description

The aerothermodynamic analyses were conducted on the spherically blunt cone ($R_N/R_B = .25$) with one-half angle of 60 degrees. Three afterbody configurations were considered. These configurations were established primarily on the basis of system requirements and interfaces, and in particular on the basis of antenna requirements and the bus attachment and separation considerations. The configurations are shown in Figures 79, 80, and 81. The reference design configuration (Figure 81) was selected on the basis of the above considerations as well as minimum weight. The performance (i.e. turnaround capability) of the three was comparable on the basis of Newtonian predictions. The dearth of data relevant to the configurations considered precludes a definitive statement about the rearward stability. Data that are available indicate a neutrally stable trim point. Therefore, flaps have been included to ensure the existence of only one stable trim point. The configuration considered relies upon a sharp break in the body contour to provide a stable separation point to enhance the transonic stability. Although the optimum shoulder radius is zero (maximum drag also results in a maximum payload), a 2-inch radius ($R_S/D = 1/90$) has been considered due to mechanical reasons.

The configuration has discontinuities in the body contour in addition to the flaps in the form of both protuberances and cavities associated with the thrust vector control and attitude control system nozzles. Although these were not considered in the vehicle performance evaluation, their interaction with the environment and concomitant local heating aggravations have been considered in the design analyses.

3.1.2 Requirements, Constraints, and Design Criteria

Initially, vehicle diameter and mass were considered parametrically along with the entry conditions consistent with the range of orbital parameters selected. The effects of spin were also determined parametrically and later analyzed for a specific system (the initial angle of attack is a function of the separation geometry, which in turn depends upon the orbit and desired entry velocity and angle).

The final analyses concentrated on a conceptual design consistent with the range of entry conditions that are compatible with system requirements and constraints. In the sections to follow, the aerodynamic analyses for the entry from orbit have been divided into three parts:

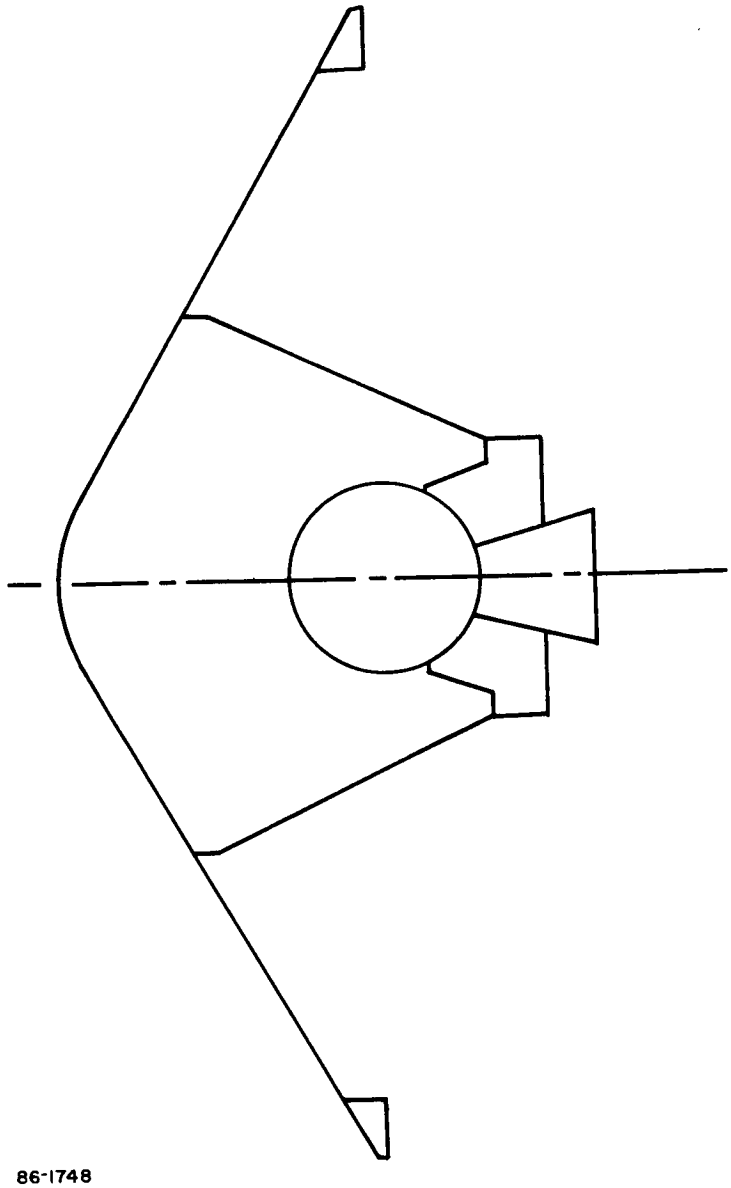

Figure 79 BLUNT CONE AFTERBODY GEOMETRY - ORIGINAL (EFAT) CONCEPT

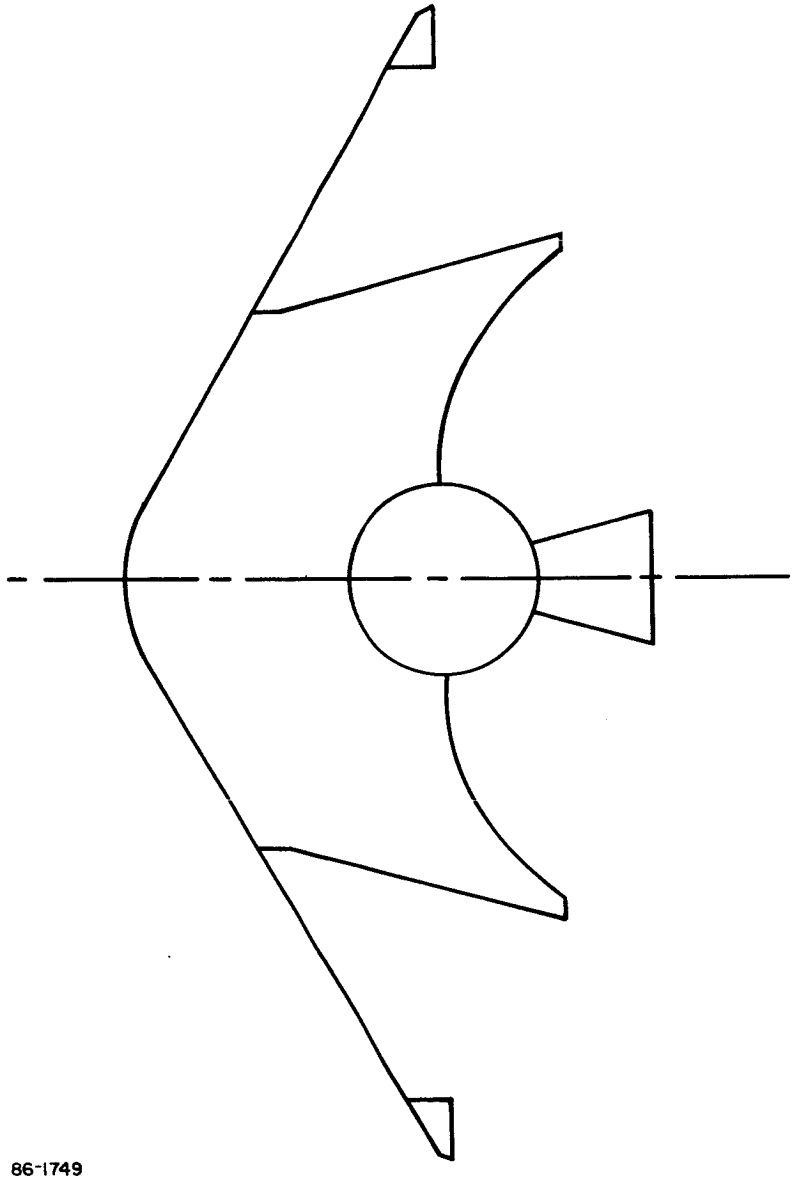

Figure 80 BLUNT CONE IMPROVED SEPARATION CONCEPT

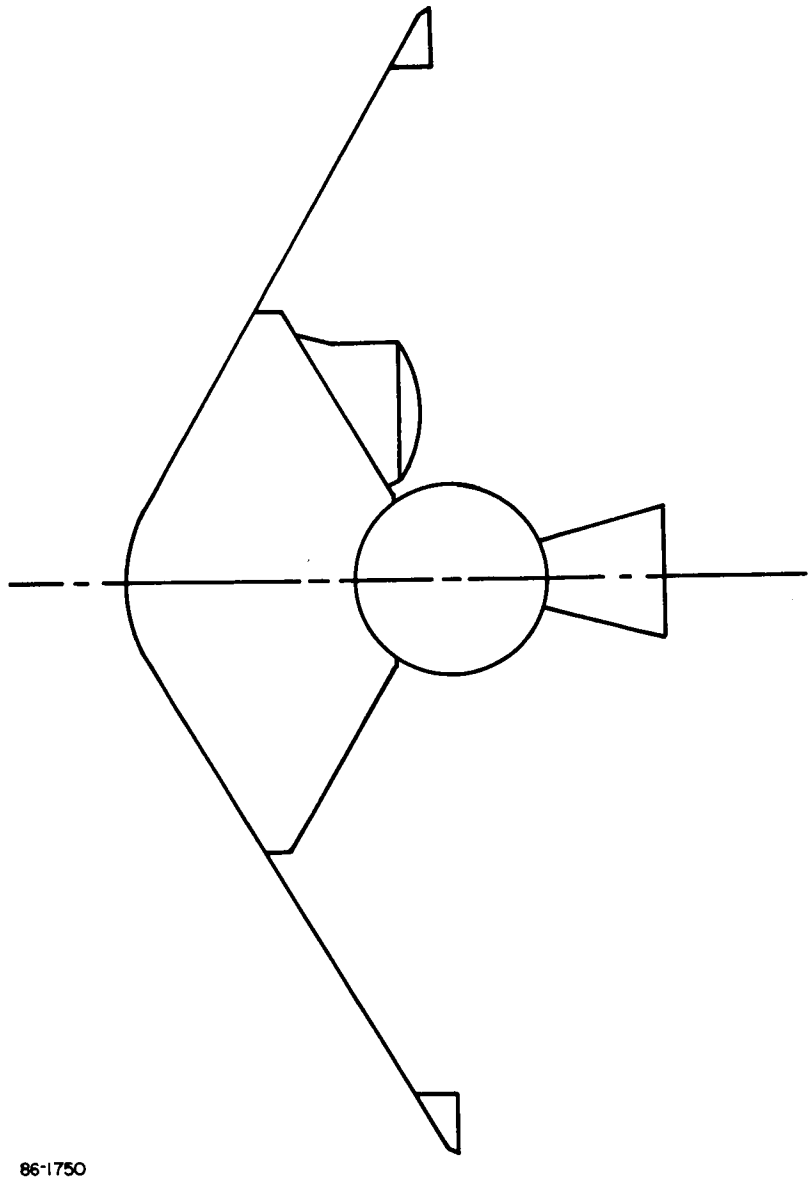

Figure 81 BLUNT CONE MINIMUM WEIGHT CONCEPT

a) Parametric Studies

b) Spin-System Design

c) Reference Design

3.1.2.1 Entry Conditions

1. Parametric Studies -- The entry conditions were based on the anticipated variations to be obtained from the de-orbit analyses. Entry velocities ranged from 10,000 to 16,000 ft/sec, with flight path angles of -30 to -8 degrees. The entry angle of attack range considered was 30 to 120 degrees with spin rates varying from 1 to 5 rads/sec.

2. Spin-System Design -- The spin-system design analyses were conducted for a specific γ_e - V_e map which resulted from a de-orbit error analysis. The upper bound (maximum entry angle for a given velocity) was dictated by the descent system requirement. The resulting range of velocities and angles is significantly reduced (see Figure 82) from those considered in the parametric study. Also indicated, and most important are the angles of attack at entry (excluding the precession cone angles associated with ΔV rocket thrust misalignments). It is seen that the angles of attack for entry at high velocities (entry from very elliptical orbits) are nominal whereas the angles of attack are as large as 90 degrees at lower velocities, this has a significant effect on the critical environments as will be indicated later.

In addition to the angle of attack at entry, the precession angles associated with de-orbit thrusting must be included to define the necessary conditions for the dynamic analysis. Figure 83 illustrates the results of an error analysis showing the reduced coning angles and rates associated with high spin rates. Despin requirements varied from full despin to none at all. The selected design spin rate was 40 RPM consistent with de-orbit dispersion errors.

3. Reference Design -- Various system considerations, in addition to limiting the range of orbital parameters, resulted in a further modification of the entry conditions (see Figure 84). In addition to the changes in entry velocity and angle, the spin-despin mode was eliminated. Maximum angular rates were limited to 0.1 rad/sec. Various combinations of this limiting rate were considered for the failure mode - e.g., rearward entry with spin, tumble, etc.

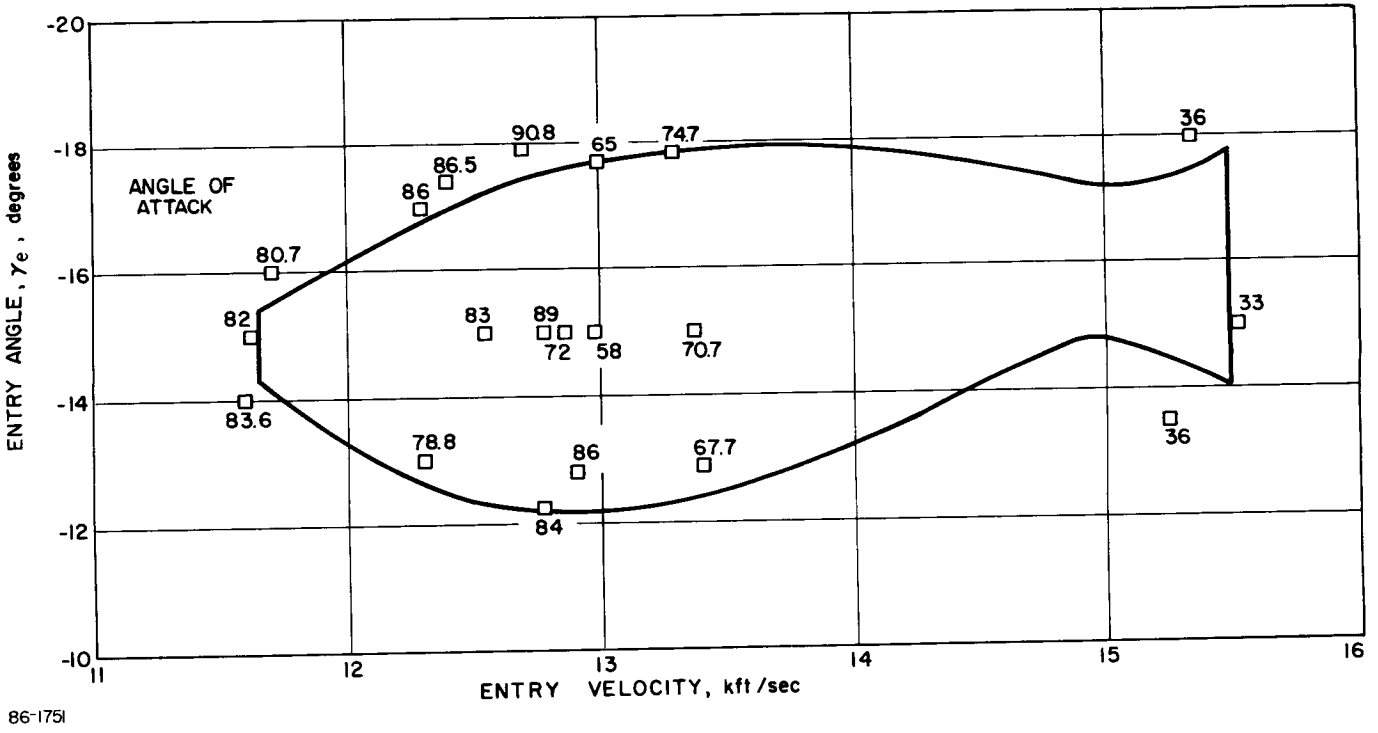

Figure 82 ENTRY CONDITIONS -- SPIN AND SPIN-DESPIN MODE

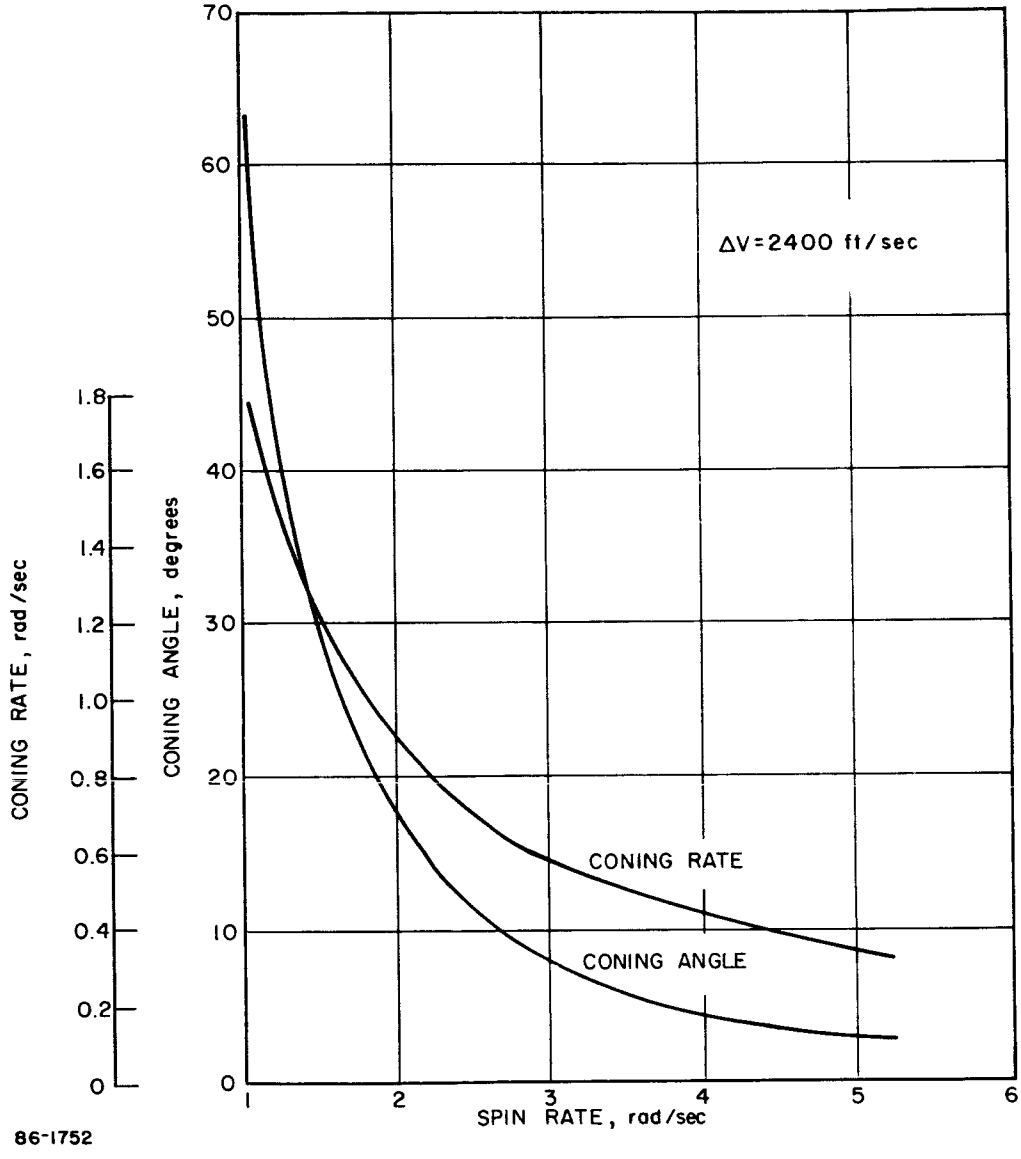

Figure 83 SEPARATION CONING

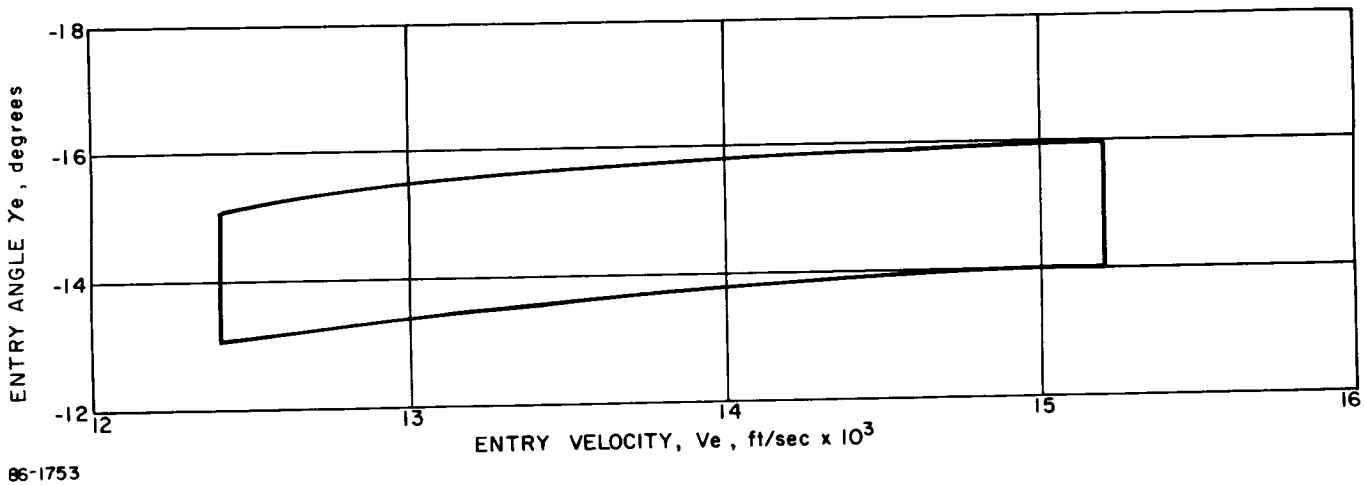

Figure 84 ENVELOPE OF ENTRY CONDITIONS

3.1.2.2 Atmospheres

The atmospheres considered were the VM-3, 4, 7 and 8 (see Table XIX). Considering the scale height variation among these atmospheres it was expected that the VM-3 and VM-7 atmospheres would result in the maximum integrated convective heating whereas VM-8 would be critical in so far as loads and performance are concerned. None of the atmospheres at the entry velocities considered resulted in any substantial radiative heating. The two low-surface pressure atmospheres considered were analyzed in depth while a cursory investigation of the others was made.

3.1.2.3 Vehicle Parameters

The critical parameter which will ultimately determine the payload for a given diameter is the ballistic coefficient (M/C_DA). The minimum weight associated with a given diameter is that determined by the terminal descent requirements which imposes a limit on M/C_DA.

The parametric studies considered a large variation in diameter (60, 120, and 180 inches) for the blunt-cone shape with the ballistic coefficient varying from .15 to .33 slug/ft^2.

The three design concepts considered spin, spin-despin and reference design, restricted the analyses to a diameter of 180 inches and a ballistic coefficient of approximately .2 slug/ft^2.

TABLE XIX

ATMOSPHERE PARAMETERS

Atmosphere	VM-3	VM-4	VM-7	VM-8
Surface Pressure (millibars)	10	10	5	5
Composition by Volume N_2	80	0	80	0
Composition by Volume CO_2	20	70	20	100
Composition by Volume A	0	30	0	0
Inverse Scale Height ($FT^{-1} \times 10^{-5}$)	2.15	5.89	2.15	6.07

3.1.3 Concepts and Performance Summary

3.1.3.1 Concepts

The parametric analyses were conducted with the objective of determining various system tradeoffs. As a result, three design philosophies or concepts evolved for which conceptual design studies were performed. All these concepts considered attitude control as the reference mode, the differences were related to the backup or failure mode. These concepts were as follows:

1. Spin Concept -- To provide for ACS malfunction a spin system was utilized to minimize dispersion which results from thrusting errors.

2. Spin-Despin Concept -- To eliminate the deleterious aspects of spin on the entry performance despin was considered.

3. Reference Design -- The weight penalties associated with the spin system were such that spin as a backup mode was eliminated. The reference design considered an ACS malfunction in terms of maximum angular rates. A "sentry" sensing any angular rate greater than 0.1 rad/sec immediately terminates the ACS. Entry at any attitude is possible with this mode.

All designs considered a shell diameter of 180 inches. This diameter was selected from the parametric study as consistent with the system requirements and growth/potential, (the optimum diameter however, was found to be smaller). The diameter, in addition to the ballistic coefficient considered, resulted in mass characteristics similar to the 1971 mission considered for the entry from the approach trajectory.

Two atmospheres VM-7 and VM-8 were considered for the heating and loads, respectively. The concepts considered had no influence on the atmospheric model selection, in contrast to the concepts considered for the entry from the approach trajectory.

In the case of the spin system, a failure mode consisting of a ΔV rocket separation malfunction was considered which increased the entry weight. The reference design, utilizing a constant ΔV, results in a small-weight increment (motor casing) in contrast to the spin case where unspent fuel is also retained. In addition to the weight consideration, there is also an effect of the failure mode upon the center of gravity.

Both the spin system and the reference design considered entry conditions which resulted in prolonged exposure of the maximum diameter region to stagnation point heating. In the spin system case this was the result of orientation of the vehicle at entry associated with the separation geometry; for the reference design this was the result of an extreme for random entry. The sensitivity of the total weight to the heating in this region is obvious, however, the only means for reducing the heating in this region is by increasing the shoulder radius. The effect of this on the vehicle drag is such that the allowable payload weight decreases faster than the heat shield weight requirement (the ballistic coefficient is held constant).

Difficulty was experienced in the determination of the design environments for the spin systems. Since each point on the $\gamma_e - V_e$ map can be associated with an orbit (also true anomaly) in addition to a given separation geometry (ΔV and thrust application angle), there is also associated with each point a given angle of attack and coning angle and rate. The trend observed showed increased angles of attack with decreasing entry velocities. The design point for the spin systems occur for the entry conditions which result in the maximum angle of attack.

3.1.3.2 Design and Performance Summary

1. Concepts -- Direct comparisons of the concepts analyzed are difficult since the entry variations tend to mask the effect of the system concept on the environments. The tabulation given in Table XX reflects the design conditions for the maximum diameter region which is most indicative of the relative environments and penalties in the design (i.e., weight). Although the stagnation point heating does not vary systematically, the heating at the zero-angle-of-attack sonic point ($S/R_N = 4.5$) definitely reflects the angle of attack effects associated with the concept. This is also evident from the results given in the loads summary (Table XXI), where the maximum loads for the spin system are evolved from the maximum angle of attack at a nominal velocity. The following general comparison applies to the concepts considered:

Concept	Loads	Heating
1. Attitude Control System	Lowest	Lowest
2. Spin System	Highest	Highest
3. Spin-Despin System	Less than with spin	Less than with spin
4. Reference Design (Tumble)	Higher than ACS	Higher than ACS

TABLE XX

SUMMARY OF DESIGN HEATING - ENTRY OUT OF ORBIT

Design Concept	Attitude Control System	Spin Backup (40 rpm)	Spin-Despin Backup (40 rpm Initial Spin)	Reference Design
D (feet)	15	15	15	15
W (pounds)	2040	1855	1855	2040
V_E (ft/sec)	15200	12900	12900	15200
γ_E (degrees)	-14	-12.8	-12.8	-14
ATM	VM-7	VM-7	VM-7	VM-7
m/C_DA (slug/ft2)	.22	.20	.20	.22
α_E (degrees)	0	86	86	90
Qs (BTU/ft2)	1900	2052	1790	2227
MAX $\dot{q}_s$ (BTU/ft2sec)	16.6	23.6	18.8	18.6
$Q(S/R_N = 4.5)$, (BTU/ft2)	627	6240	2184	1705
MAX $\dot{q}(S/R_N = 4.5)$, (BTU/ft2sec)	5.5	79	39.5	24
$\bar{\alpha}_{PK_{\dot{q}}}$ (degrees)	0	59	30	11

TABLE XXI

SUMMARY OF DESIGN LOADS - ENTRY OUT OF ORBIT

Design Concept	Attitude Control System	Spin Backup (40 rpm)	Spin-Despin Backup (40 rpm Initial Spin)	Reference Design
D (feet)	15	15	15	15
W (pounds)	2040	1855	1855	2040
V_E (ft/sec)	15200	12700	12700	15200
γ_E (degrees)	-16	-17.8	-17.8	-16
Atmosphere	VM-8	VM-8	VM-8	VM-8
m/C_DA (slugs/ft^2)	.22	.20	.20	.22
α_E (degrees)	0	90.3	90.3	179
q_∞ Maximum (lb/ft^2)	90	188	130	128
$\bar{\alpha}$ at Maximum q_∞ (degrees)	0	27	18	10
$\frac{X}{W}$ (Maximum Axial Force)	14	29	20	17.8

The spin system weight penalties are associated with the initial angle of attack (approximately 90 degrees for the design trajectory) coupled with the spin, which exposes the maximum diameter to stagnation point heating. In addition the drag of the vehicle is minimized at this angle of attack thereby increasing the effective m/C_DA which aggravates the heating (and the loads) further.

The above penalties associated with the spin and spin-despin modes of entry in addition to systems considerations resulted in a tumble mode being selected as the failure mode for the attitude control system.

2. Reference Design Summary -- The failure mode selected for the reference designs was that associated with an attitude control system malfunction, wherein any rate exceeding 0.1 rad/sec resulted in an immediate ACS termination. Various combinations of this rate, either in spin or pitch, with angle of attack were considered. The maximum loads were associated with rearward entry with a spin rate of 0.1 rad/sec. The loads are summarized in Table XXII. The design loads were obtained for the maximum effect due to planet rotation (entry with rotation along the equator). The actual loads associated with entry were obtained considering Syrtis Major as the desired impact area. The variation in the orbital inclination angle with the equator is between 40 and 60 degrees. The actual maximum loads that would be experienced with these limitations is designated in the table as "Loads". Also summarized are the loads associated with a nominal entry (zero-angle of attack) as well as those experienced for the critical heating (heat shield design point) entry. The design environments are seen to be slightly conservative thus providing a safety margin over the expected operational map.

The maximum heating was predicted to occur for a non-rotating planet condition. The design heating environment associated with Syrtis Major entry were obtained and compared in Table XXIII. The heating was obtained for the critical loads trajectory to provide the structural temperature for the structure design point. The margins on integrated heating are evident at both the sonic point and the stagnation point. The variations in the sonic-point heating is not only the result of the entry conditions but also of the dynamics since the major part of the sonic point critical environment (in terms of integrated heating) occurs at angles of attack greater than 30 degrees.

3.1.4 Comparison with Entry from Approach Trajectory Studies

A comparison between the entry from orbit and the entry from the approach trajectory is possible since the vehicle size and performance are comparable. The significant parameter change is that of the entry velocity

TABLE XXII

LOADS SUMMARY (Performance)

($\alpha_E = 179°$ $p = .1$ RAD/SEC)

	Reference	Syrtis Major Impact		
	Design	Nominal (particle)	Heating (Critical Design Point)	Loads (Critical Design Point)
V_E Inertial	15,200	15,200	15,200	15,200
γ_E Coordinates	-16°	-15°	-14°	-16°
Atmosphere	VM-8	VM-8	VM-7	VM-8
Azimuth	No Rotation	50°	60°	40°
At Maximum X/W:				
X/W	15.9	10.1	4.1	13.6
N/W	.61	.01	.22	.54
q_∞ (lb/ft^2)	114.6	72.0	31	98.3
α (degrees)	10.3	.28	13.5	10.1
$\dot{\alpha}$ (rad/sec)	1.63	.03	.9	1.6
$\ddot{\alpha}$ (rad/sec^2)	15.0	.25	4.3	15
At Maximum N/W:				
X/W	15.7	8.5	3.2	11.5
N/W	.71	.01	.25	.61
q_∞ (lb/ft^2)	113.2	60	27.5	83
α (degrees)	13.8	.39	16.7	13.5
$\dot{\alpha}$ (rad/sec)	1.53	.03	1.2	1.84
$\ddot{\alpha}$ (rad/sec^2)	9.8	.31	5.6	15.1

TABLE XXIII

HEATING SUMMARY (Performance)

	Reference	Syrtis Major Impact		
	Design (Nonrotating planet)	Nominal (particle)	Heating (Critical Design Point)	Loads (Critical Design Point for Structure)
V_E (ft/sec) } Inertial	15, 200	15, 200	15, 200	15, 200
γ_E (degrees) } Coordinates	-14	-15	-14	-16
Atmosphere	VM 7	VM 7	VM 7	VM 8
Azimuth (degrees)	-	50	60	40
Q_s (Btu/ft^2)	2227	1666	2030	1300
Max $\dot{q}_S$(Btu/ft^2 sec)	18.6	17.8	20.0	34.0
Q (S/Rn = 4.5), (Btu/ft^2)	1705	550	1333	745
Max $\dot{q}$ (S/Rn = 4.5), (Btu/ft^{2}sec)	24	5.9	15.3	32.2

which is reduced approximately 35 percent for the entry from orbit case. The entry angle was also reduced; this also had a major influence on the environments.

A comparison of the atmospheres considered can be summarized in the following table for the critical design conditions:

Atmosphere	Model 2	Model 3	VM-7	VM-8
Surface Pressure (mb)	25	10	5	5
Composition N_2	89.2	51.2	80	0
by Volume CO_2	10.8	48.8	20	100
A	0	0	0	0
Inverse Scale Height ($FT^{-1} \times 10^{-5}$)	2.18	4.695	2.15	6.07

The convective heating resulting from entry into the Model 2 and VM-7 atmospheres should be comparable on the basis of the inverse scale height comparison. The VM-8 atmosphere should be more critical than the Model 3 atmosphere in terms of loads. The reduction in entry velocity eliminated the effect of radiative heating; however the contribution of the radiative heating to the thermal protection system design for the entry from the approach trajectory cases was small. The comparison of the convective heating for entry from orbit and entry from the approach trajectory is given in Table XXIV.

The most significant variant from the entry from the approach trajectory is the reduction in the entry velocities. The environment becomes devoid of radiative heating, greatly simplifying the analyses. However, the consideration of near skip entry angles results in significant low-density effects such as vorticity interaction and variation in entropy along the boundary layer, both of which increase the heating. Although the heating levels are significantly lower for entry from orbit, the shallow entry angles give comparable integrated heating.

The loads were an order-of-magnitude less than those experienced during entry from the approach trajectory as a consequence of the lower velocities and shallow entry angles.

TABLE XXIV

HEATING COMPARISON

Design Concept		EFAT		EFO		
		Light Vehicle	Heavy Vehicle	Spin 40 RPM	Despin	Tumble m
D	(feet)	15	15	15	15	15
W	(pounds)	1390	4500	1855	1855	2040
V_E	(ft/sec)	23800	23800	12900	12900	15200
γ_E	(degrees)	-20	-20	-12.8	-12.8	-14
ATM		Model 2	Model 3	VM 7	VM 7	VM 7
$m/C_D A$	(slugs/ft^2)	.15	.49	.20	.20	.22
α_E	(degrees)	11.5	11.5	86	86	90
Q_s	(BTU/ft^2)	2798	4405	2052	1790	2227
$\dot{q}_{s_m}$	(BTU/ft^{2}sec)	70	85	23.6	18.8	18.6
Q at $S/R_N = 4.5$	(BTU/ft^{2}sec)	--	--	59	30	11
$\dot{q}_m$ at $S/R_N = 4.5$	(BTU/ft^2)	803	1889	6240	2184	1705
$\bar{\alpha}$ at $\dot{q}_m$	(degrees)	20	96	79	39.5	24

An additional interface was introduced in the performance evaluation. The characteristic coning motion associated with a spinning vehicle entering an atmosphere results in a possible loss in communication due to antenna pattern directionality. The time during which this loss occurs is a function of the initial angle of attack, entry velocity, entry angle and atmosphere. Additional difficulty in communication or blackout occurs because of the plasma sheath and contaminants in the heat shield material.

Heating for the entry from orbit results in significantly higher heating in the region of the maximum diameter. When comparing the spin systems the variations in initial angle of attack result in an order of magnitude higher heating at the maximum diameter location for the entry orbit. The entry from orbit has however resulted in a significant decrease in the loads as shown in Table XXV.

The dynamic behavior was similar for both cases and it was found to be satisfactory. No divergence was obtained or anticipated with the coefficients used. Transonic stability and the rearward stability derivatives were based upon Newtonian results. The primary differences in the dynamic behavior were those associated with spin. The difference in the separation geometry between entry from orbit and approach trajectory resulted in larger angles of attack and higher rates for the former due to the larger magnitude of the thrust vector. These resulted in much larger angle of attack envelopes.

3.1.5 Conclusions and Problem Areas

Entry from orbit, although resulting in lower velocities, does not decrease the severity of the environments to the degree expected. The shallow entry angle effects, although contributing in part to the increased heating, were subordinate to the angle of attack and spin effects.

Spin effects were found to be most important and critical, resulting in substantial increases in heating which could be reduced by despin. The despin, being initiated at the onset of aerodynamic loads to avoid tumbling, still results in excessive heating in the maximum diameter region. This local heating effect (due to the location of the stagnation point at angles of attack greater than 30 degrees) can be alleviated somewhat by increasing the local radius; however this will result in a decrease in the drag coefficient which, for the same ballistic coefficient, reduces the total weight allowable by an amount which is greater than would be realized in heat shield weight reduction.

To avoid the attendant environmental problems associated with a spin system (including despin), only an attitude control system with limited failure mode considerations can be considered. Although the failure mode considered for the reference design resulted in rearward entry, the effects on the environment were tolerable.

TABLE XXV

LOADS COMPARISON

Design Concept	EFAT	EFO		
	Light Vehicle	Spin	Despin	Tumble
D	15	15	15	15
W	1390	1855	1855	2040
V_E	23800	12700	12700	15200
γ_E	-90°	-17.8	-17.8	-16
ATM	Model 3	VM 8	VM 8	VM 8
$m/_{CD^A}$	.15	.2	.2	.22
α_E	179	90.3	90.3	179
$q_{\infty max}$	1009	188	130	128
$\bar{\alpha}_{max\ q_\infty}$	20	27	18	10
$(x/w)_{max}$	209	22	20	17.8

On the basis of preliminary investigations an afterbody significantly smaller than considered during the entry from the approach trajectory study is possible with flaps provided to ensure rearward instability. The data available (after correcting for forebody geometry and center of gravity) indicate no worse than neutral stability for a cavity-like backside contour (the afterbody is recessed within the blunt-cone shell) which can be easily modified by flaps. In addition the turnaround capability at angles other than 180 degrees is enhanced by this cavity or dish.

Further test data are necessary not only to establish the rearward instability but to confirm that a discontinuity at the maximum diameter eliminates the transonic stability problems. This discontinuity, it is believed, will provide a stable separation point for the wake eliminating the possibility of an hysteresis process between the local boundary-layer shock-structure-interaction at transonic speeds.

Test data are also required to establish the real-gas effects on the pressure and heating distributions and the aerodynamic performance derivatives.

The low-density effects were found to be very significant for entry from orbit due to the prolonged exposure to the environment at high altitude. Vorticity interaction accounted for an increase of 15 percent of the heating over the entire body with an additional increase of 40 percent over the conical portion of the body due to varying entropy (conical heating effects).

3.2 DESIGN CRITERIA

The general discussion of critical design environments and problems associated with definition of design criteria, in paragraph 2.2 of this book, apply here as well.

Considerably more detailed study was required in the entry from orbit analysis to account for the prolonged exposure to the heating environment at high angles of attack. In addition the various initial conditions at entry resulted in considerable complexity in evolving the critical design environments.

Preliminary thermal protection system analysis indicated the critical heating environment was that which resulted in the maximum integrated heating. This resulted from the relative insensitivity of the heating pulse to the entry condition variation for the conceptual designs under consideration. The pulse time was relatively invariant with the entry condition variation for the conceptual designs. Thus detailed analysis could be restricted to the entry conditions which resulted in the maximum integrated heating. The most sensitive body station was the maximum diameter location where environment was closely coupled to the trajectory and dynamic behavior. This in turn was critically dependent on the entry conditions.

The flow-field analyses had to be extended to encompass the wide range of angles of attack associated with the entry condition variations. The evolved pressure and heating distributions were considered invariant with the atmospheric composition and as such the previously generated low angle of attack distributions could be utilized. The normalizing parameters (stagnation point heating and pressure) were evaluated for the appropriate atmosphere.

The evolution of the critical environments for the three concepts considered in the analysis (spin, spin-despin and reference design) was tedious, requiring the analysis of many dynamic trajectories to determine the maximum thermal and aerodynamic loads.

3.2.1 Spin and Spin-Despin Criteria

Results from the de-orbit dispersion analysis were used to define the entry conditions in terms of entry velocity and angle, angle of attack, coning angle and rates. The lower envelope of entry angle was utilized for the heating analysis whereas the upper envelope was used for the loads analysis. The critical environments were obtained by completely covering the operational V_E - γ_E bounds, as given above, to determine the maximum loads and integrated heating.

3.2.2 Reference Design

The spin and spin-despin modes required analyses to determine the appropriate γ_E and V_E which resulted in the critical environments. The reference design, in constrast, required analyses with respect to the appropriate rates and angle of attack. The critical entry velocity was the maximum within the operational γ_E - V_E map (resulting from a modified de-orbit dispersion analysis). The variation in angle of attack and rate indicated that a particular body station would require analyses at different entry conditions; for instance, the stagnation point critical environment is obtained for a ninety degree angle of attack, which is also critical for the maximum diameter regions. An angle of attack of 180 degrees is critical for the afterbody region. Further analyses were performed to evaluate the aggravations due to protuberances and cavities, primarily those associated with the attitude control system and thrust vector control. An additional environment of importance for the afterbody is that generated by the exhaust plume from the de-orbit rocket.

3.3 RESULTS AND DISCUSSION

The entry from orbit analyses were conducted in three phases which comprised (a) a broad parameter study, (b) an initial conceptual design utilizing spin-despin as a backup mode, and (c) the final reference designs. The parametric studies utilized the blunt-cone configuration which evolved from the entry from the approach trajectory studies. This shape was retained in the spin-despin analyses, but was modified on the basis of system considerations to a minimum weight configuration for the reference design.

3.3.1 Parametric Studies

The reference blunt-cone shape (60-degree cone blunted with a spherical nose whose radius is one-quarter of the base radius) with an afterbody (see Figure 79) was used in the parametric studies. The range of diameter and mass was such that the mass characteristics (nondimensionalized) were assumed comparable to those that evolved from the entry from the approach trajectory.

The primary purpose of the parametric studies was to define the variation of the environments, both aerodynamic and thermal, and their dependence on vehicle diameter, mass and entry conditions. These in turn permitted the determination of the shell weight tradeoffs. In addition, various system tradeoffs could be effected by means of parametric studies associated with spin and angle of attack.

3.3.1.1 Mass and Aerodynamic Characteristics

The variation in mass was consistent with the variation in vehicle diameter and ballistic coefficient. The bounds of these parameters were

$$0.15 \leq m/C_D A \leq 0.25 \text{ slugs/ft}^2$$

and

$$5 \leq D \leq 15 \text{ feet}$$

The inertial characteristics were given by the radii of gyration and the center of gravity, which were $\sigma_{xx}/D = 0.224$, $\sigma_{yy}/D = 0.182$, and $X_{c.g.}/D = 0.21$, respectively.

The aerodynamic coefficients used are those previously shown in Figures 83 to 85.

3.3.1.2 Heating and Loads

1. Particle Trajectories -- The broad range in entry velocity resulted in a large variation in the characteristics of the heat pulse. High rates of short duration are associated with steep entry angles, whereas the shallow entry angles near skip result in low rates, but in a pulse duration which gives a maximum integrated heating. Similar results were obtained for the variation in ballistic coefficient, velocity and atmosphere. These results are most efficiently presented in the form of carpet plots for the atmospheres considered (Figures 85 to 87). The variation with diameter are obtained by means of the geometric correction $\sqrt{R_N/R_{NO}}$, permitting a simple scale adjustment. The increase in heating as the skip limit is approached is indicated as well as the increase with the increase in the ballistic coefficient. Velocity has been used as the carpet parameter, the lower limit of which is given by the entry from a 2000-km circular orbit.

Typical load (the maximum stagnation pressure) variations are given in Figures 88 to 90 as a function of entry angle for various velocities and vehicle performance. As expected the loads increase with entry angle, however, an anomaly is observed at shallow angles near skip where the lower velocities result in higher loads. This is a reflection of the gravitational effects on the trajectory - the lower velocities being more sensitive to these effects with the result that at the instant of maximum loads the descent is steeper.

For the two critical atmospheres (VM-7 and VM-8) additional carpet plots are given in Figures 91 and 92 summarizing the results for the integrated heating variation and the maximum loads. These atmospheres were critical provided that the skip limit was avoided.

It was found that, as skip limit entry conditions were approached, the gravitational effects coupled with the atmospheric effects resulted in higher heating in atmospheres other than the VM-7. This becomes apparent upon closer scrutiny of Figures 85 to 87). Figure 93 indicates the lines of constant integrated heating and constant maximum loads for the VM-7 and VM-8 atmospheres, respectively.

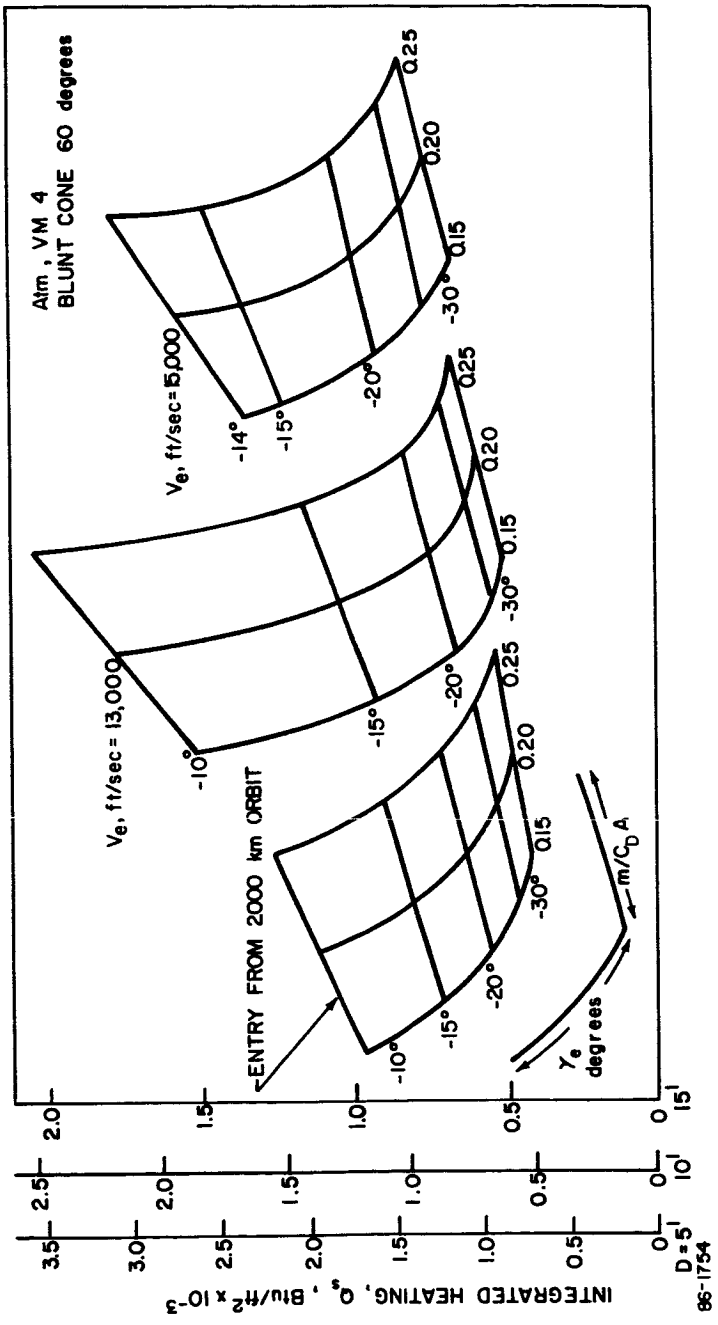

Figure 85 HEATING SUMMARY -- ATM. VM-4

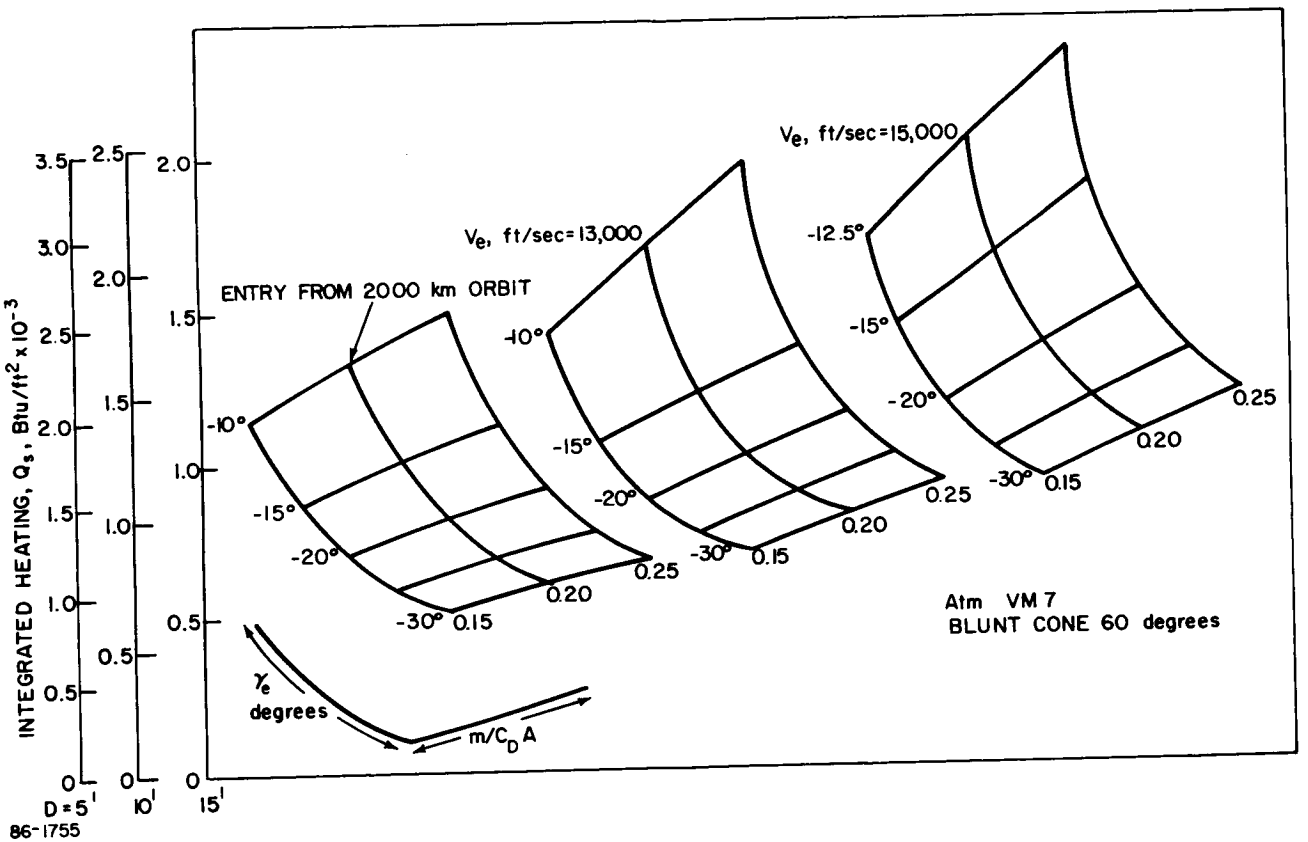

Figure 86 HEATING SUMMARY -- ATM.VM-7

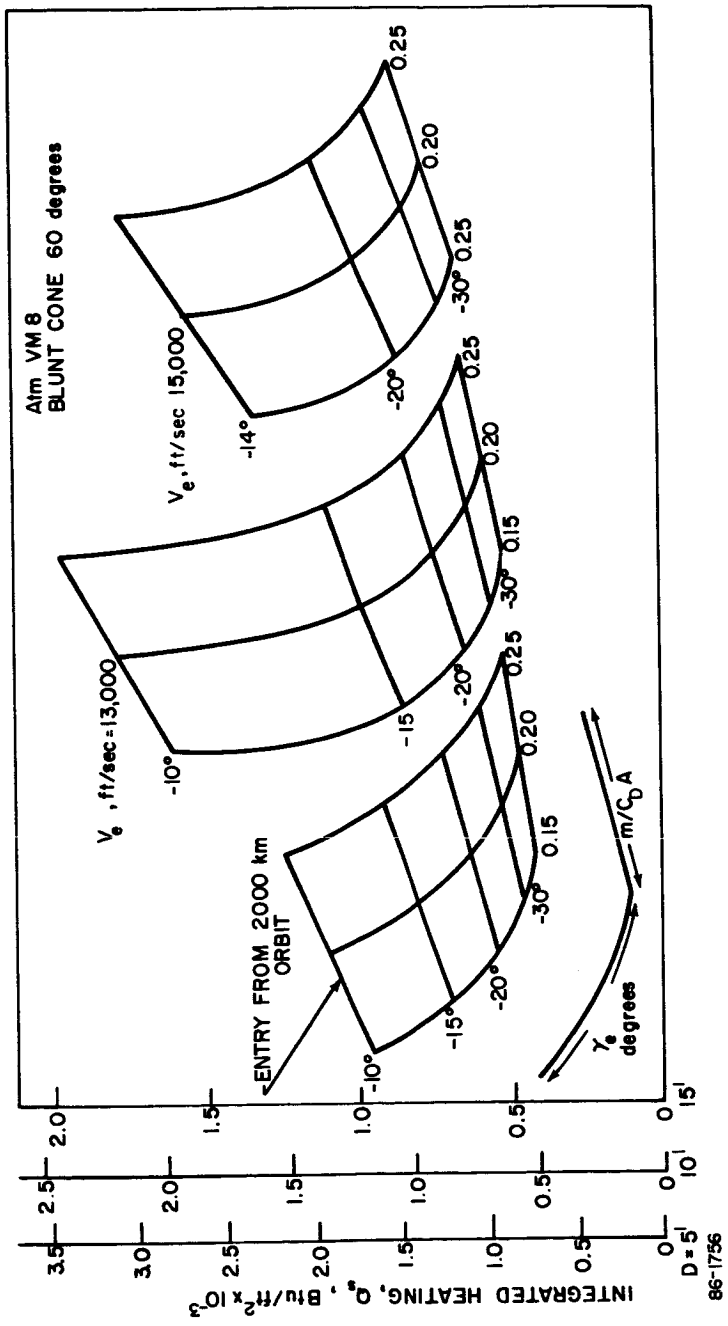

Figure 87 HEATING SUMMARY -- ATM. VM-8

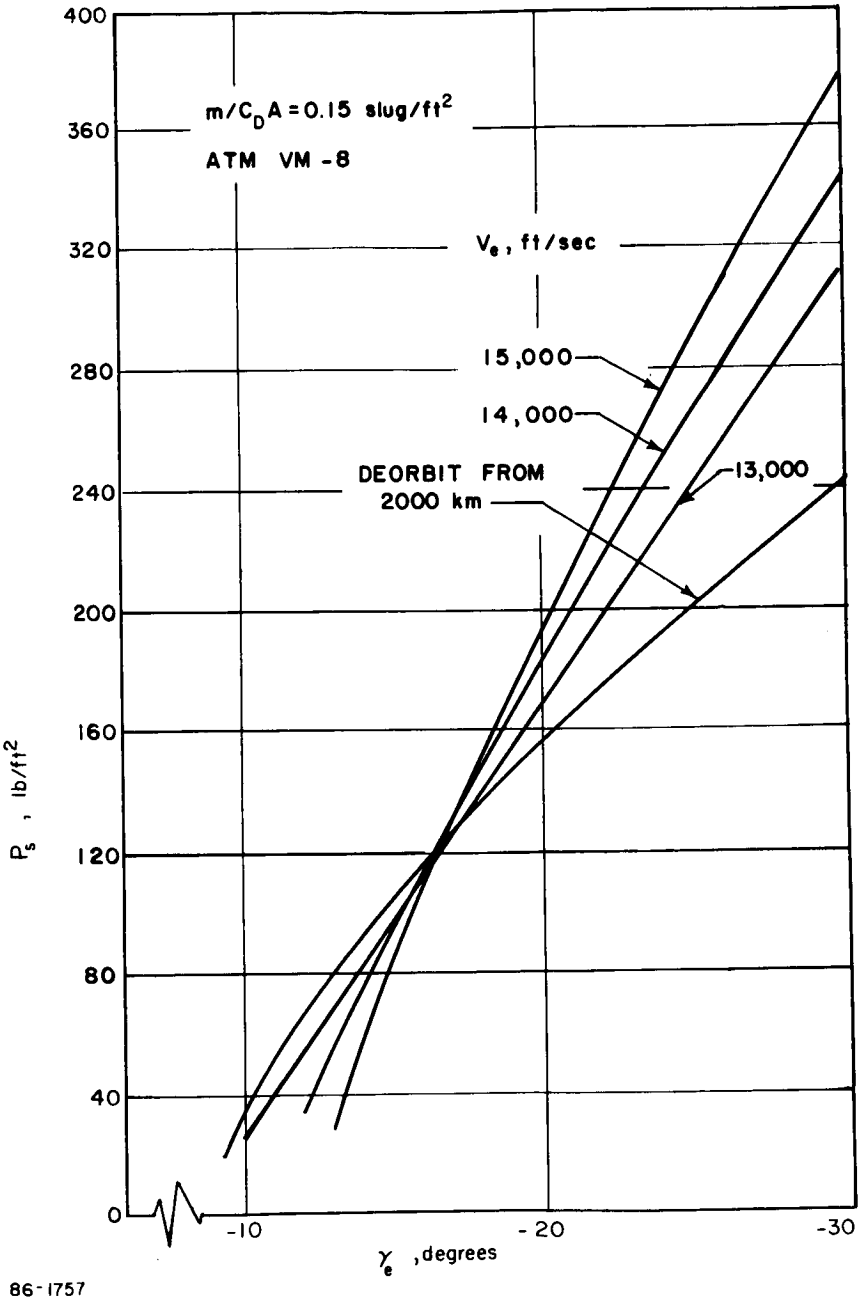

Figure 88 PERFORMANCE SUMMARY

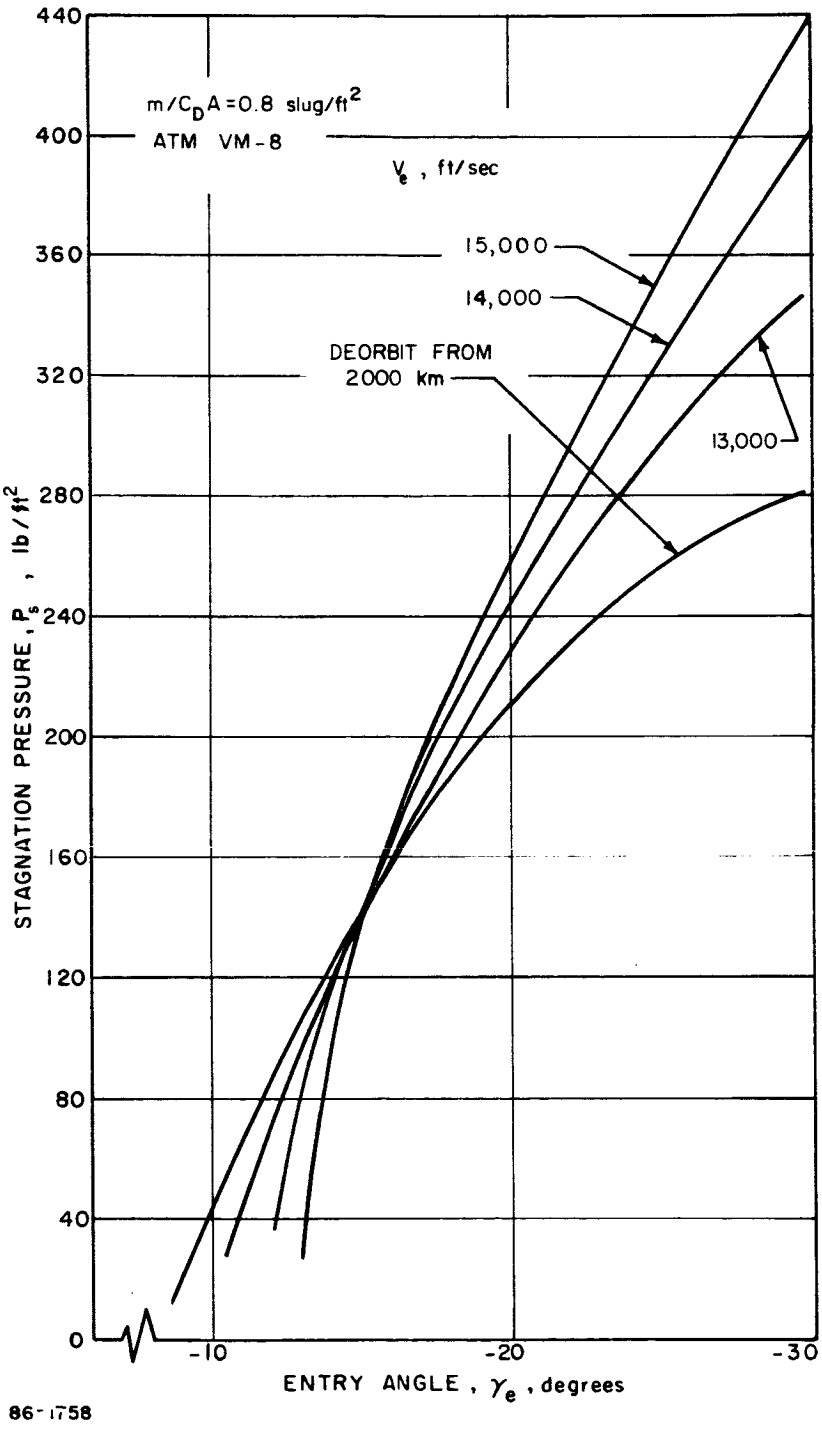

Figure 89 PERFORMANCE SUMMARY

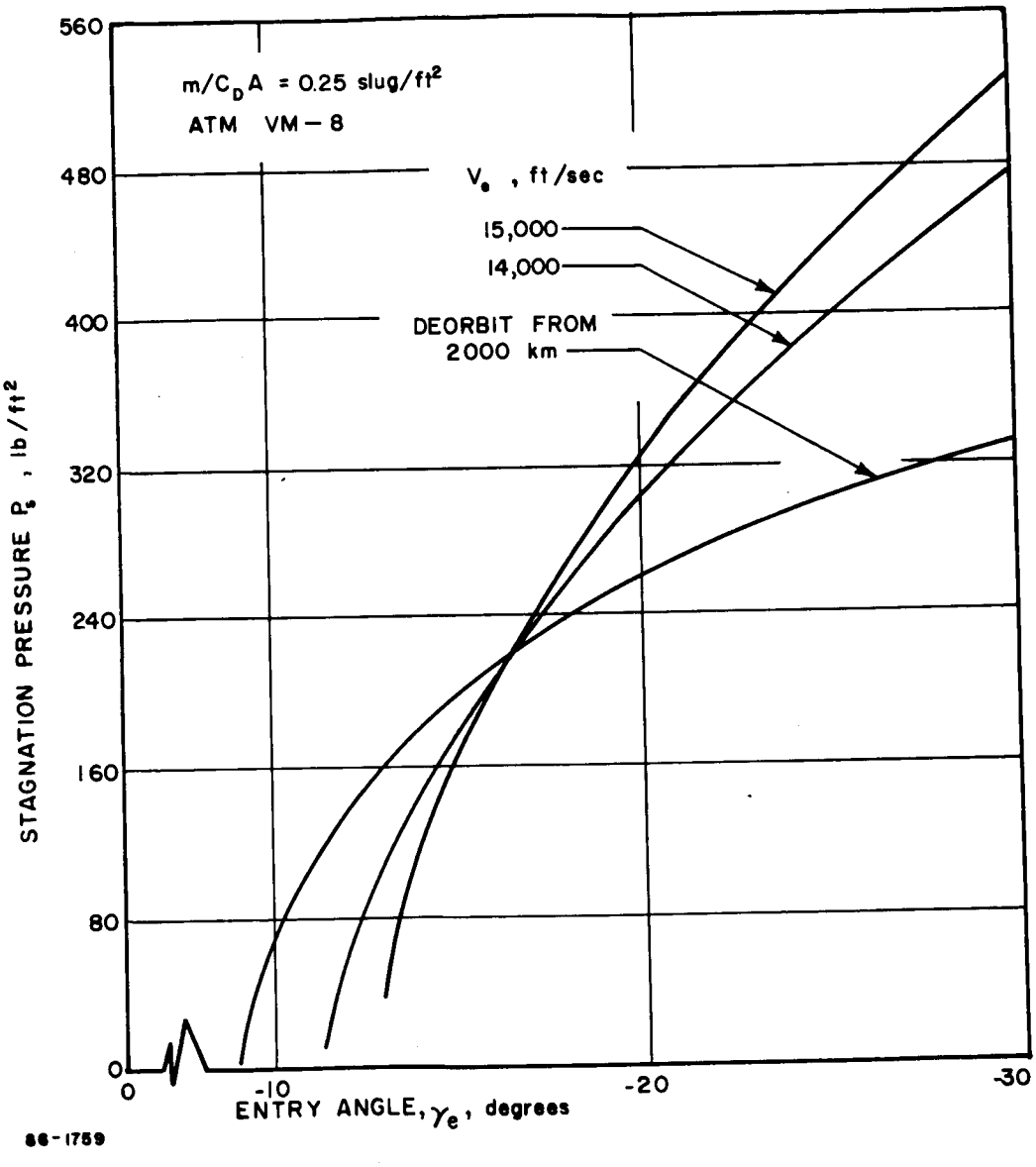

Figure 90 PERFORMANCE SUMMARY

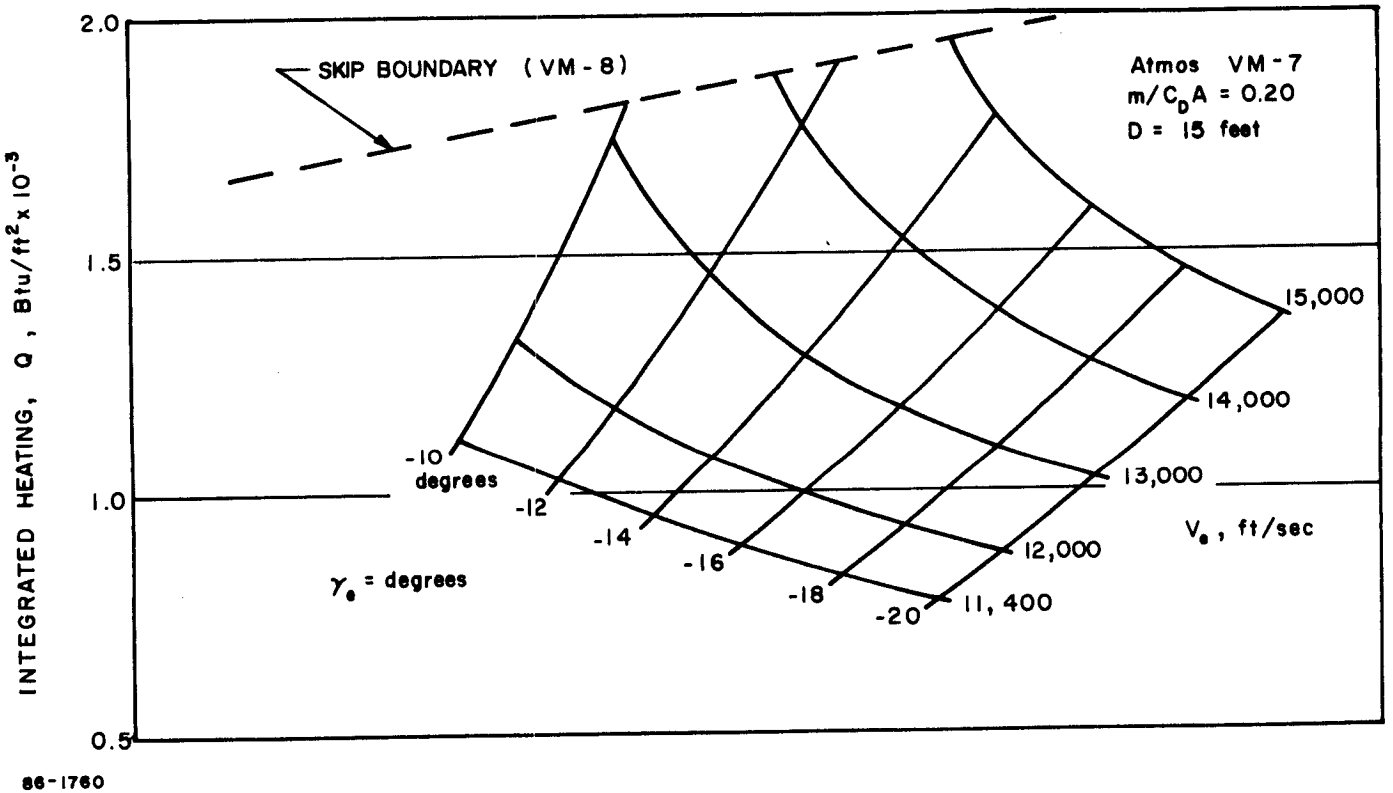

Figure 91 HEATING SUMMARY--ATM. VM 7

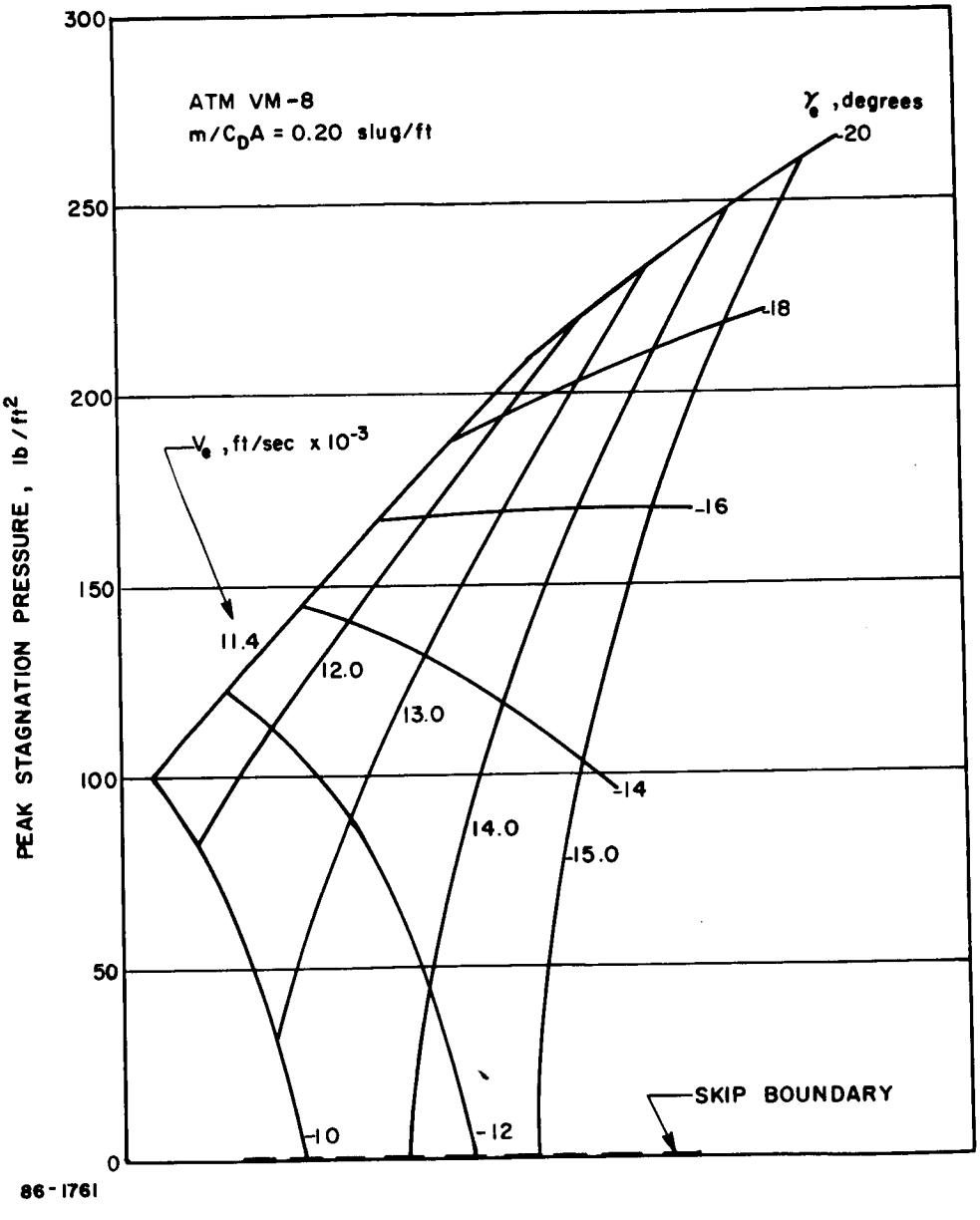

Figure 92 LOADS SUMMARY — ATM VM-8

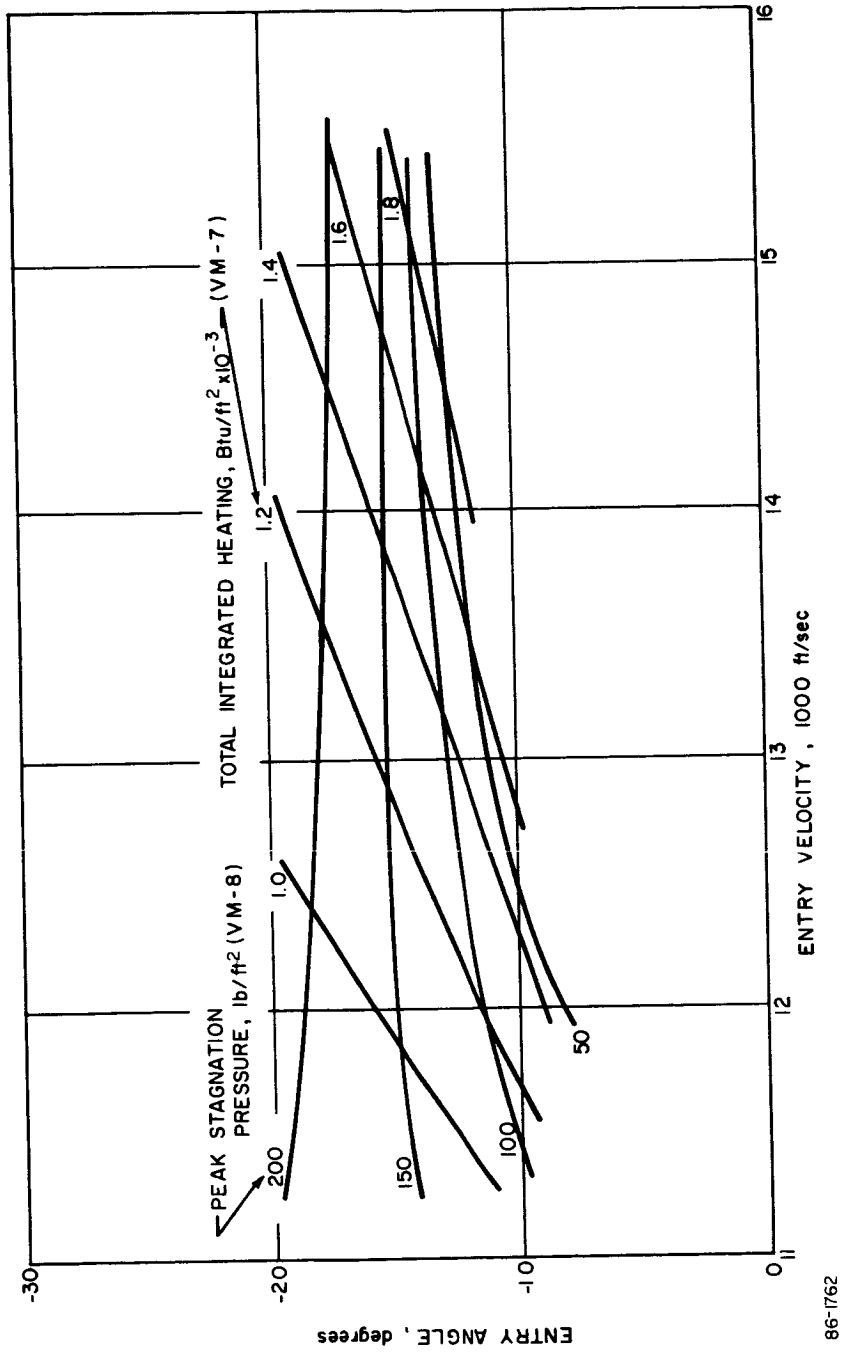

Figure 93 PERFORMANCE SUMMARY -- LOADS AND HEATING

2. Dynamic Analysis -- The parametric studies included an investigation of the shell dynamics and its interaction with the environments and pertinent trajectory parameters. The range of entry conditions considered were consistant with the particle trajectory analyses and included variations in the spin rate and pitch rate. These bracketed the anticipated rates associated with the de-orbit rocket misalignment errors. The entry angle of attack considered the de-orbit thrust application geometry. The range of entry conditions (other than indicated for the particle trajectory analyses) were:

Angle of attack	$0 \leq \alpha_E \leq 120$ degrees,
Spin rates	$1 \leq P_E \leq 3$ rad/sec,
Pitching rate	$0 \leq Q_E \leq 2$ rad/sec.

The large pitch rates were associated with the large thrust levels considered for de-orbit.

The following are typical of the results and trends evolved during these analyses.

a. Effects of Spin Rate -- The spin rate was found to have a negligible effect upon the altitude of chute deployment; however, this performance characteristic was found to be relatively insensitive to all parameter variations. The post-entry trajectories associated with entry from orbit were found to be independent of the high altitude history. The high ballistic coefficient vehicles (it is to be understood that the higher performance can also be associated with angle of attack as with spin and pitch rates) resulted in a flatter trajectory. For a spherical planet this results in a higher altitude for a given velocity.

The maximum loads, the maximum heating rates, and the integrated heating were found to increase with the spin rate. The results for an angle of attack at entry of 120 degrees are presented in Figures 94 through 97. The results for other angles of attack are similar. The trends are indicated (increasing with the angle of attack at entry), in Figures 98 through 100.

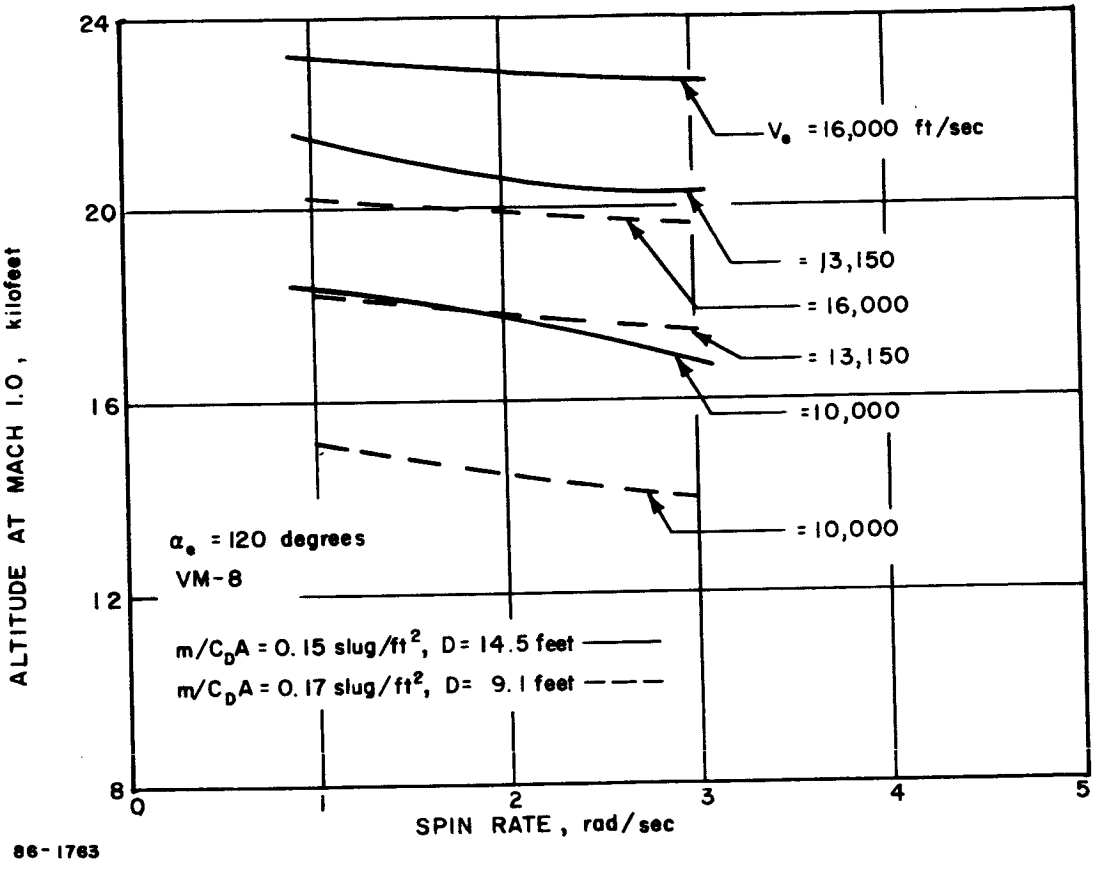

Figure 94 ALTITUDE AT MACH 1.0

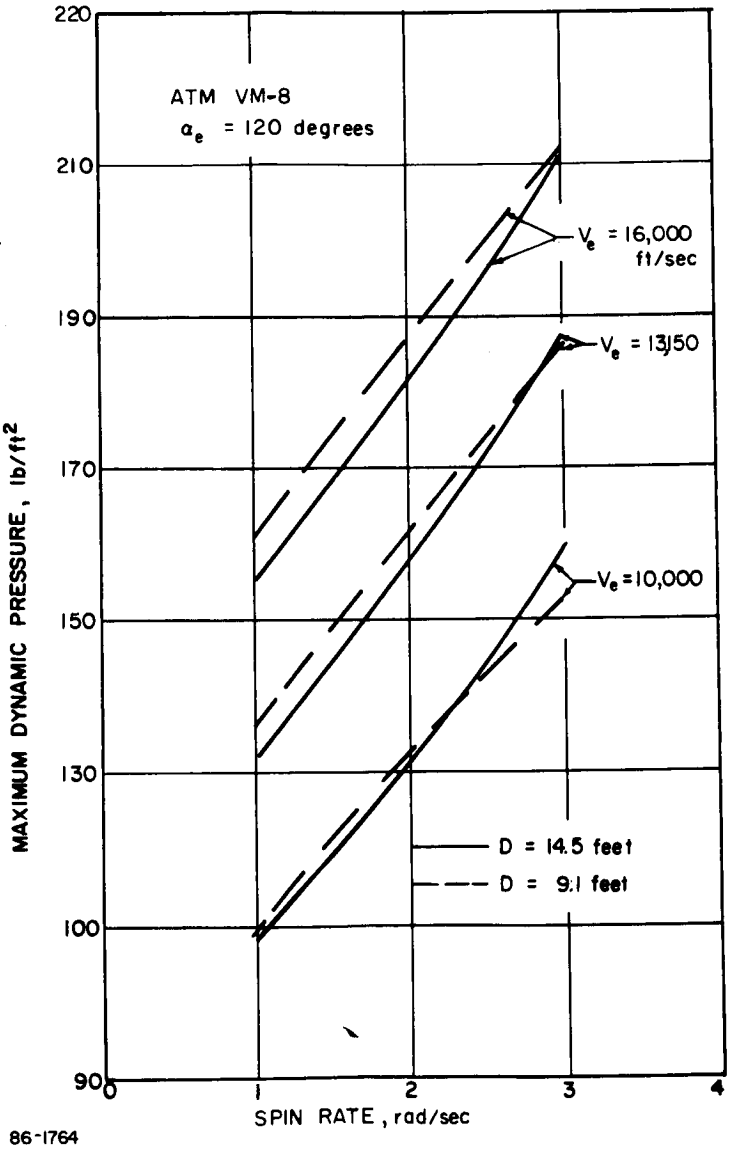

Figure 95 MAXIMUM DYNAMIC PRESSURE -- ATM VM-8

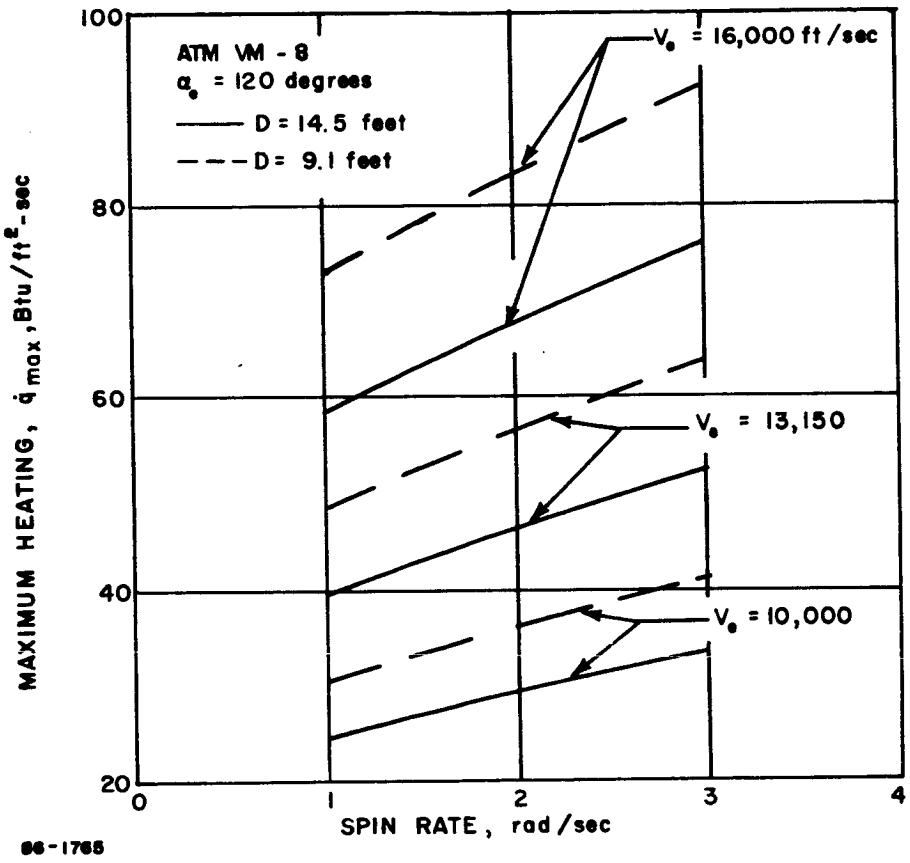

Figure 96 MAXIMUM HEATING RATE

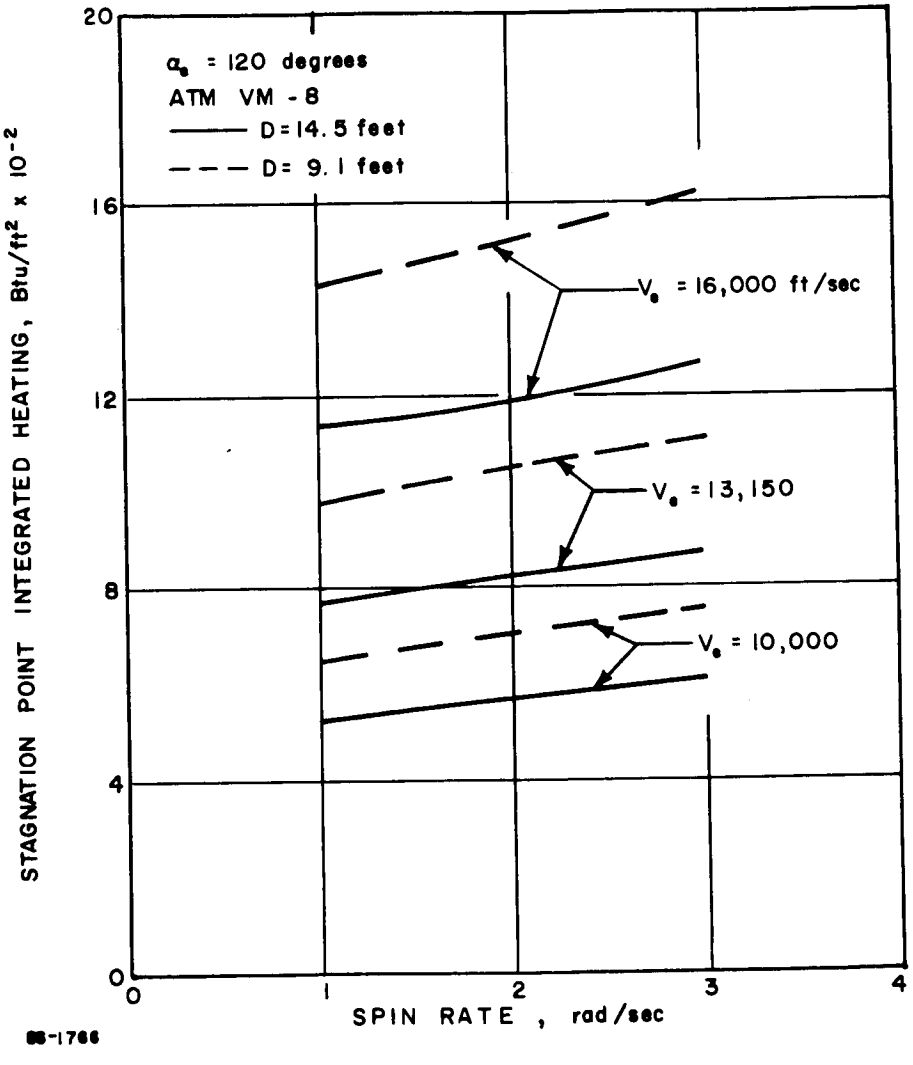

Figure 97 TOTAL INTEGRATED HEATING

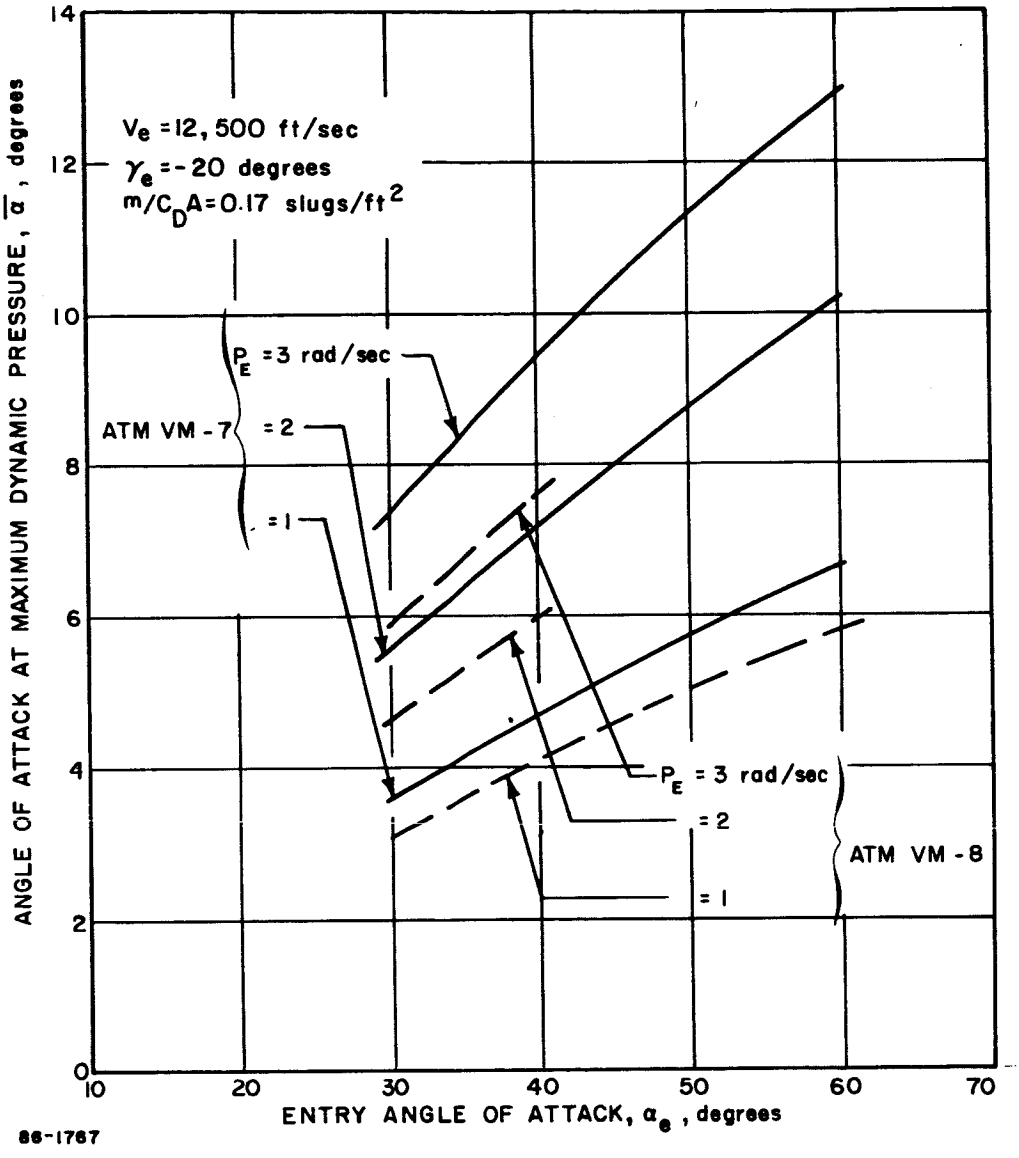

Figure 98 ANGLE OF ATTACK AT MAXIMUM DYNAMIC PRESSURE

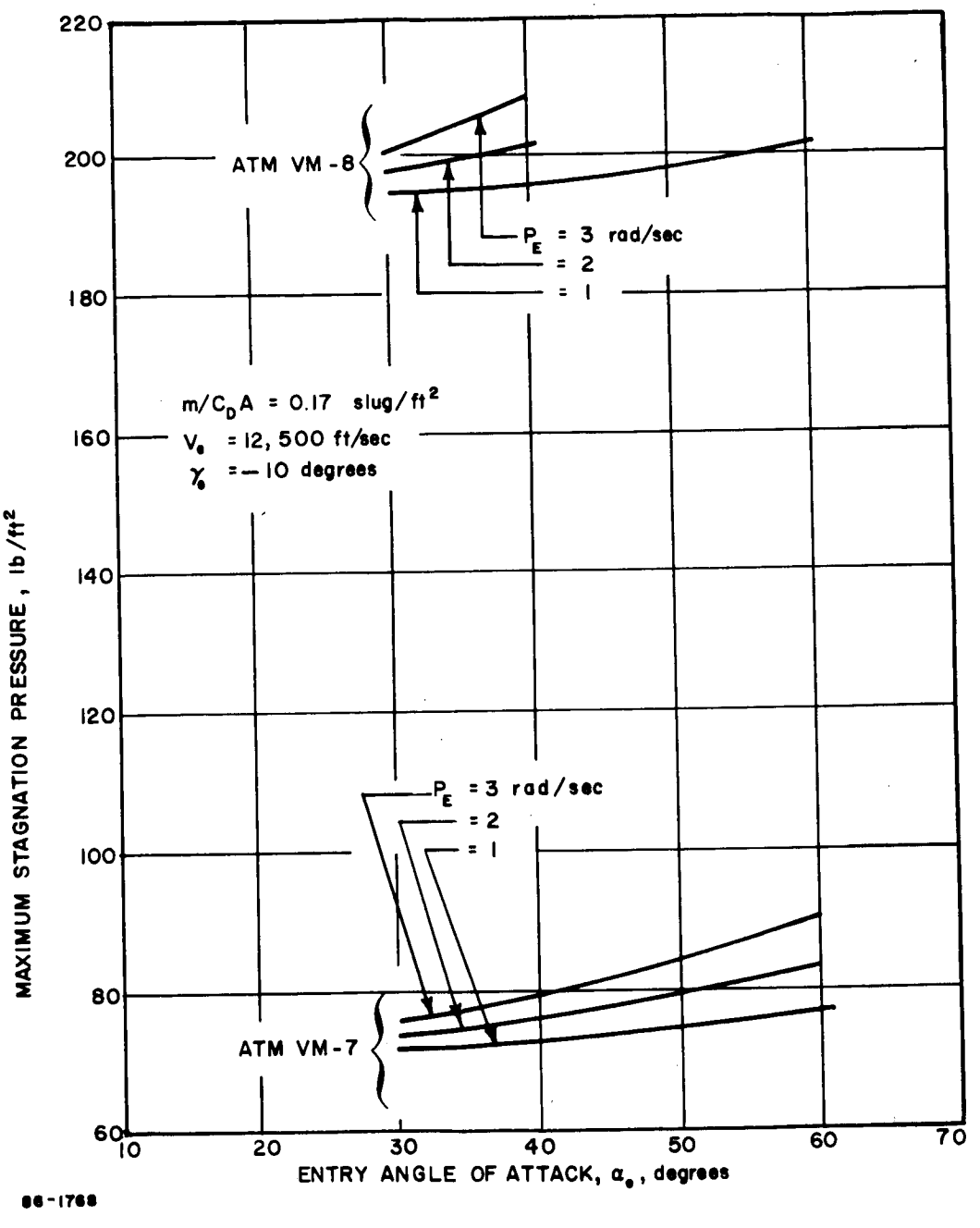

Figure 99 MAXIMUM STAGNATION PRESSURE

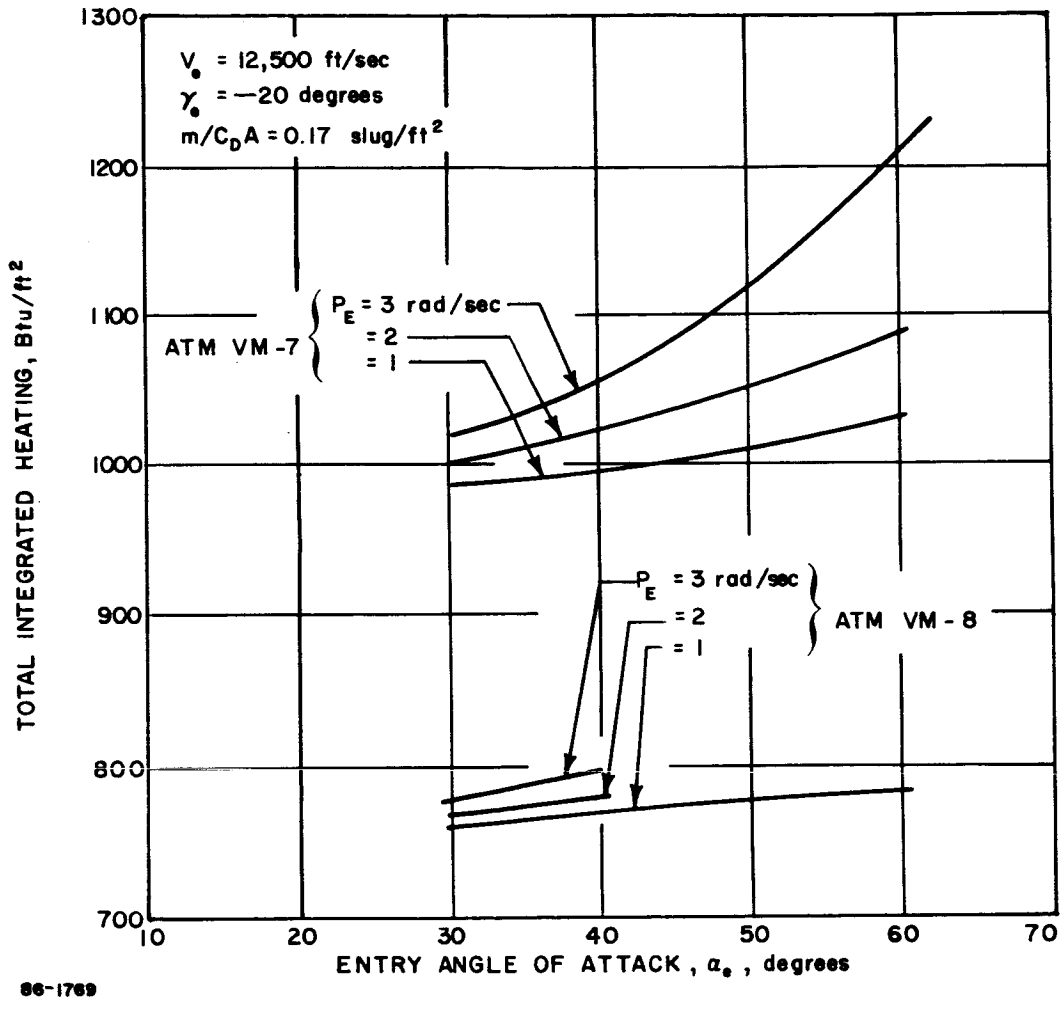

Figure 100 TOTAL INTEGRATED HEATING

b. Pitch Rate -- The maximum heating rates, pressures and total integrated heating at the stagnation point were found to increase with the pitch rate; however the dependence upon the angle of attack (with pitch rates) was small. (See Figures 101 to 103).

3.3.2 Spin and Spin-Despin Analyses

A conceptual design which considered either spin or spin-despin as the backup modes for the attitude control system was initially selected as a reference design. The separation geometry was examined to define the appropriate entry conditions including the angle of attack, coning angle and rate. The variation in these "dynamic" parameters for the entry velocities and angles were such that a "trajectory by trajectory" analysis was required to ensure that the critical environments were indeed specified. On the basis of structural and thermal protection system analyses the critical environments were peak stagnation pressure and maximum integrated heating. With respect to the heating this could, and in most cases did, mean a number of trajectories for complete specification of the environments over the entire vehicle. Further performance analyses were required to indicate the effects of the dynamics on communications. Since the antenna radiated predominantly rearward along the axis, the inherent coning motion could result in a loss in communication. Tradeoffs were possible with respect to the spin rates. The coning angle and rates increase inversely with the spin. From the parametric studies, the critical loads and heating environments were found to increase with both the spin and the rates indicating a possible optimum spin rate. Initial studies verified this conclusion; however, other considerations (for instance - entry dispersion associated with thrust misalignment) resulted in the selection of 40 rpm as the design spin rate.

The combination of the spin rate and angles of attack associated with the deorbit geometry resulted in severe heating and load environments. As a consequence despin was considered in combination with spin to minimize these effects. The reduction was substantial, however the environments were still severe in terms of the thermal protection requirements.

3.3.2.1 Entry Conditions

The de-orbit geometry and the nomenclature associated with the definition of the entry conditions are shown in Figure 104. In addition to the angle of attack, α_e , the entry angle, γ_e , and the coning angle, $\Delta\alpha_c$, the angle between the line of sight to the orbitor and the vehicle axis, θ , (the view angle) and the angle between the line-of-sight and the vehicle velocity vector, β_e are shown. The coning angle is the result of tipoff and thrust misalignment; associated with this coning angle

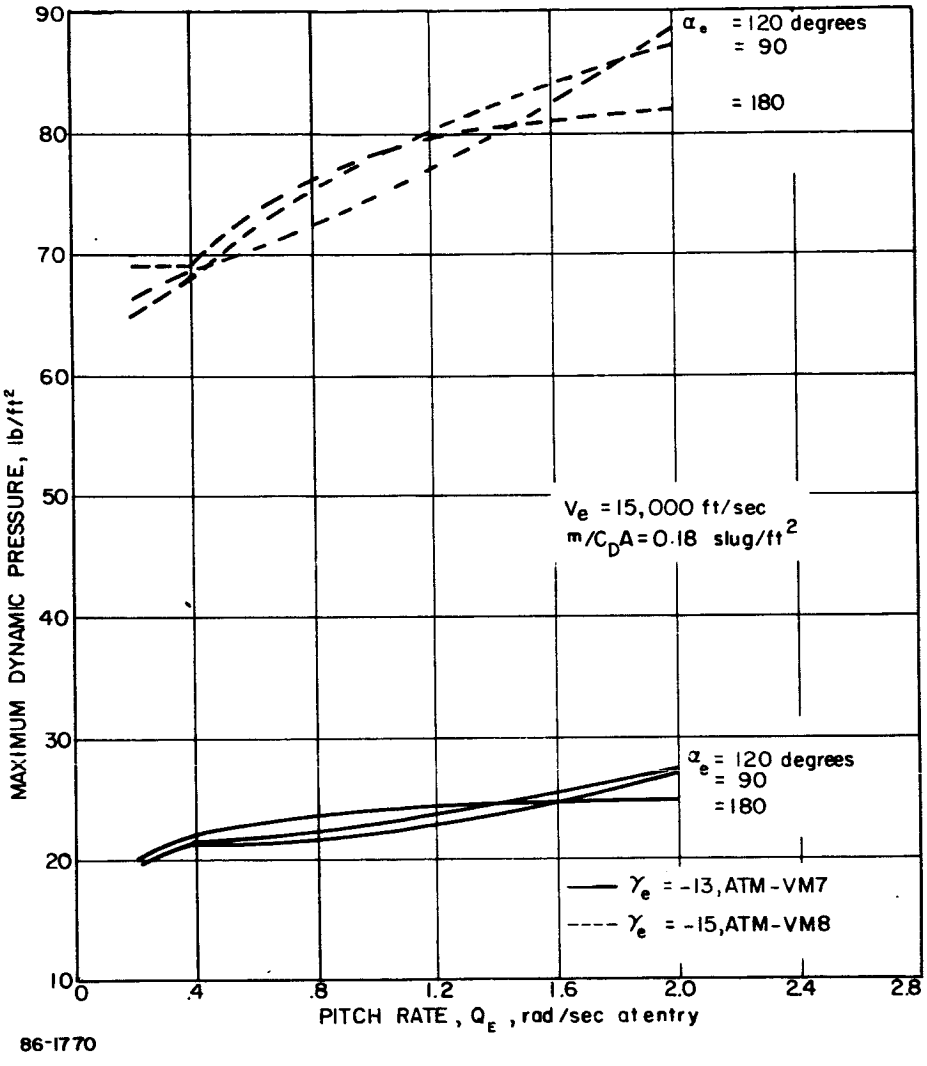

Figure 101 MAXIMUM DYNAMIC PRESSURE VERSUS PITCH RATE

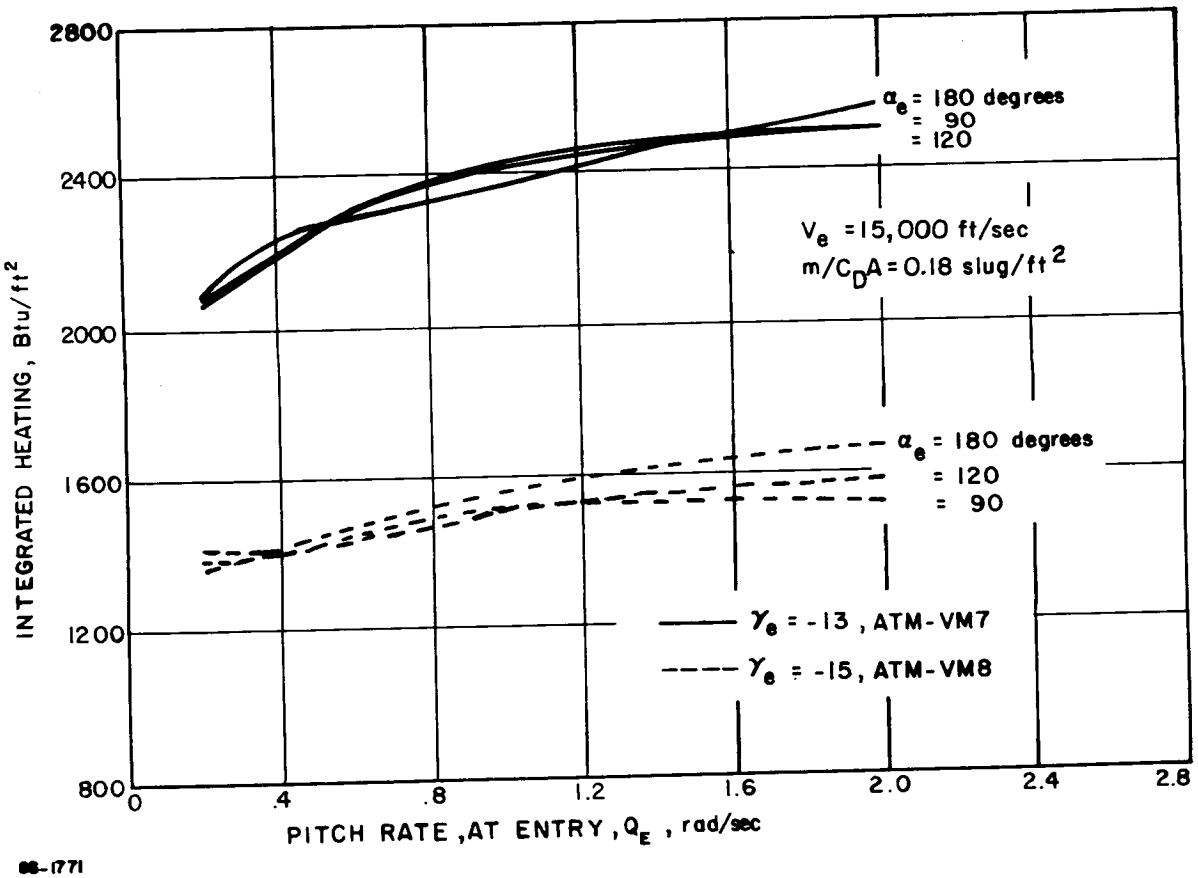

Figure 102 INTEGRATED HEATING VERSUS PITCH RATE

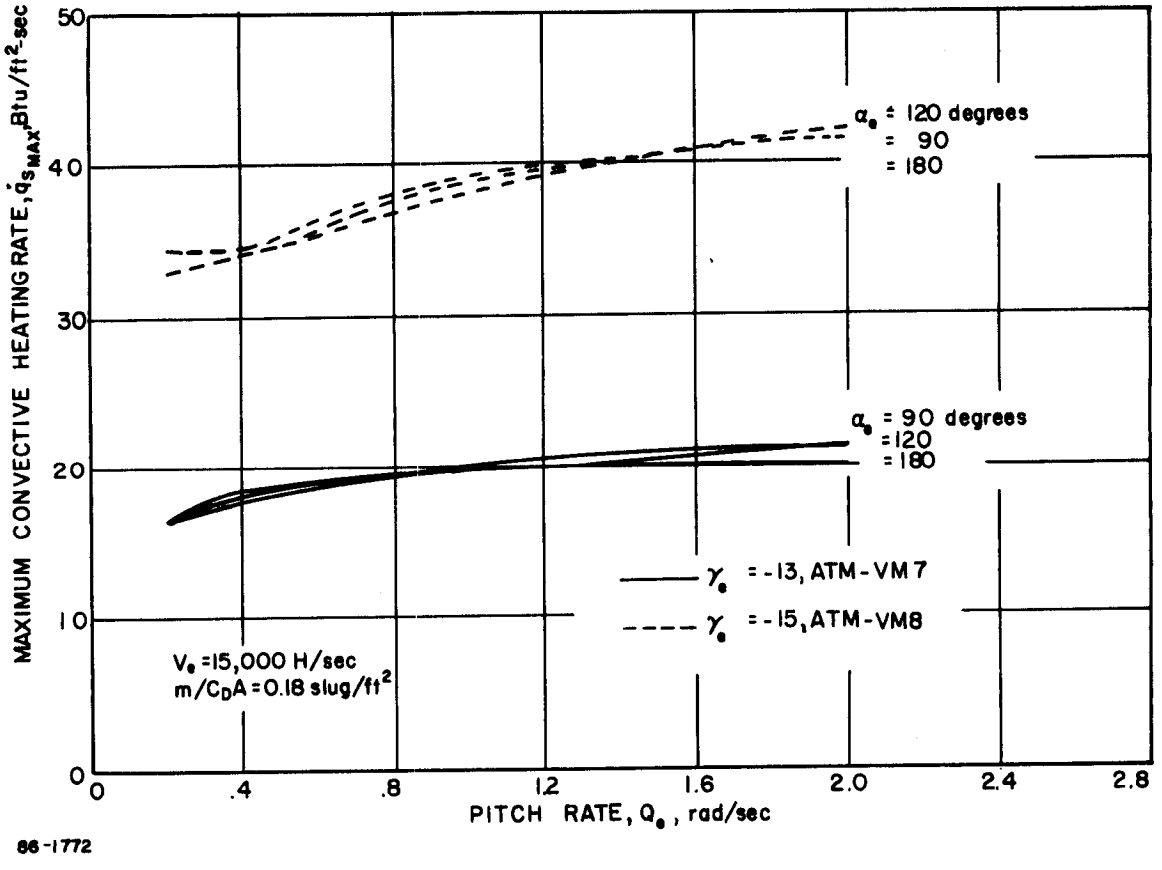

Figure 103 MAXIMUM CONVECTIVE HEATING RATE VERSUS PITCH RATE

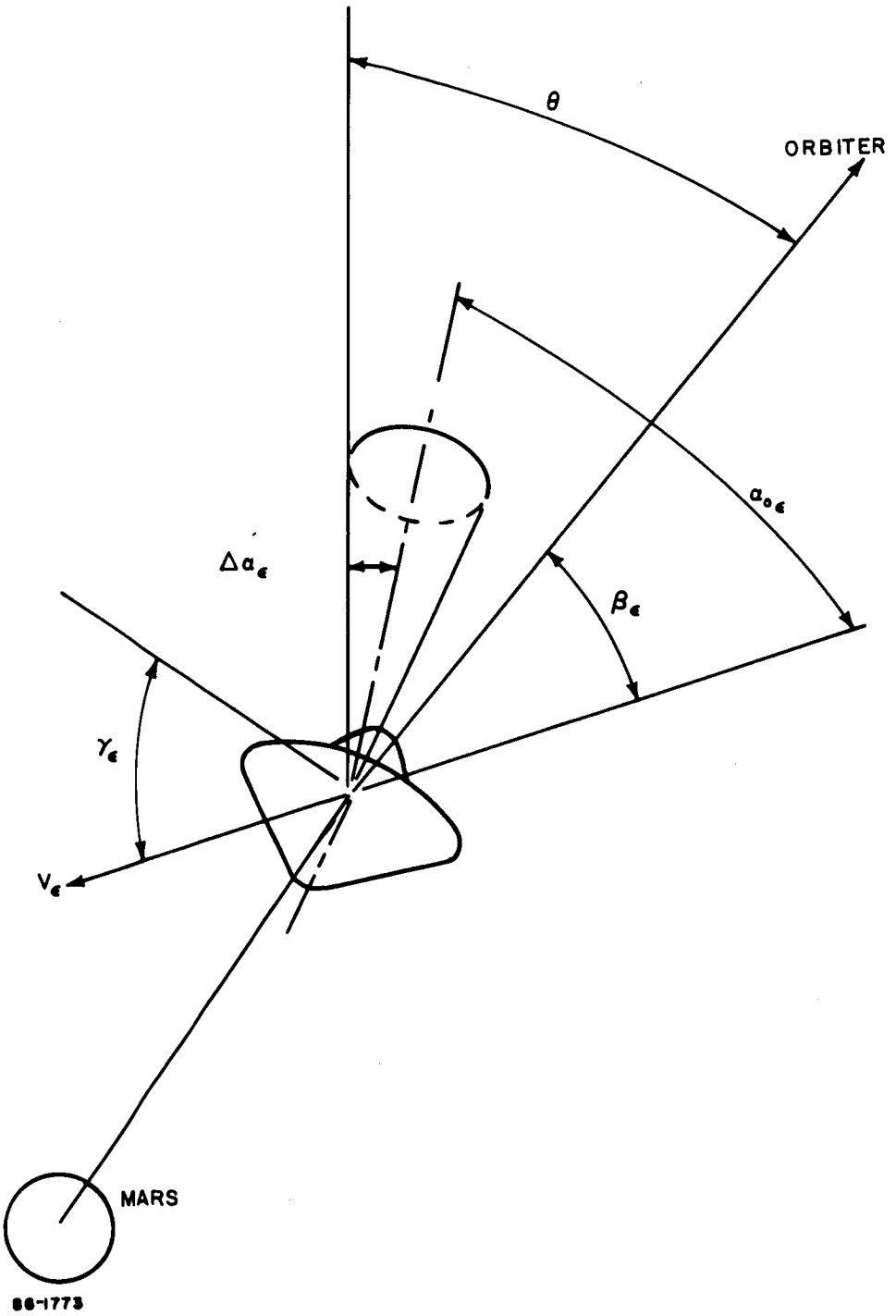

Figure 104 ENTRY GEOMETRY

(taken as 3-sigma error) and spin is a rate. The orientation of the thrust vector and the de-orbit trajectory result in the angle of attack. De-orbit analyses defined the entry angle and velocity as well as the angle of attack (see Figure 105 as well as Figure 82) where, for an entry angle of -15 degrees, the variations of angle of attack with velocity are shown for various orbits. The result of tipoff and misalignment analyses is given in terms of the 3-sigma coning angle and the associated rates in Figure 83 as a function of the spin rate. The de-orbit analyses are summarized in Figure 82 where an operational $\gamma_e - V_E$ map was shown with the angles of attack indicated.

3.3.2.2 Spin Tradeoff

The mass and aerodynamic characteristics used in the parametric analysis were retained throughout the spin and spin-despin analyses. To ascertain the existence of an optimum spin rate (optimum in terms of aerodynamic performance) an investigation was made of spin rate variation with the appropriate coning angle and rates. The high spin rates while introducing large gyroscopic forces, have nominal coning and rates. Improvement in the aerodynamic performance should be expected until the large coning angle and rates become dominant.

From the point of view of maximum loads, the optimum spin rate is approximately 2 rads/sec (see Figure 106). The angle of attack convergence was superior as evidenced by the values at peak loads also indicated in the figure. The performance associated with these lower spin rates, however, still resulted in excessive heating, particularly at the maximum diameter region. Because of this, the possibility of despin was considered.

Two parameters were considered in the despin analyses - first, the extent of despin and second, the initiation time for despin.

It was found that the optimum time for despin was during early entry upon the onset of aerodynamic loads. In this case, the coning and angular rates can be made compatible with the aerodynamic loads inhibiting tumbling motion which would result in communication loss. As evidenced by the results presented in Figure 107, the earlier the despin is initiated the better the performance while a delayed despin results in negligible improvement.

The analyses also indicate the advantage of complete elimination of spin. In that case 50-percent reduction in the integrated heating over the vehicle can be realized (Figure 108) while the performance (Figure 109) is significantly improved.

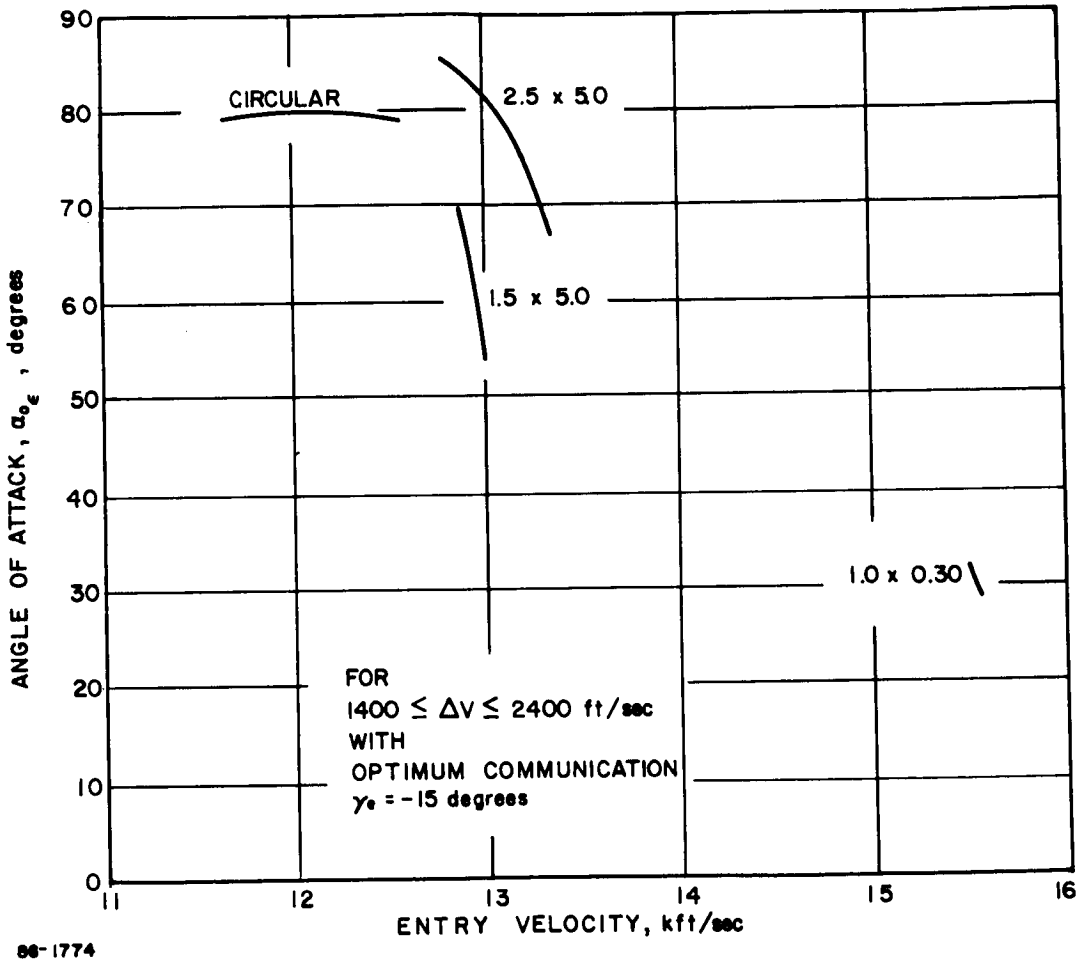

Figure 105 ENTRY ANGLE OF ATTACK

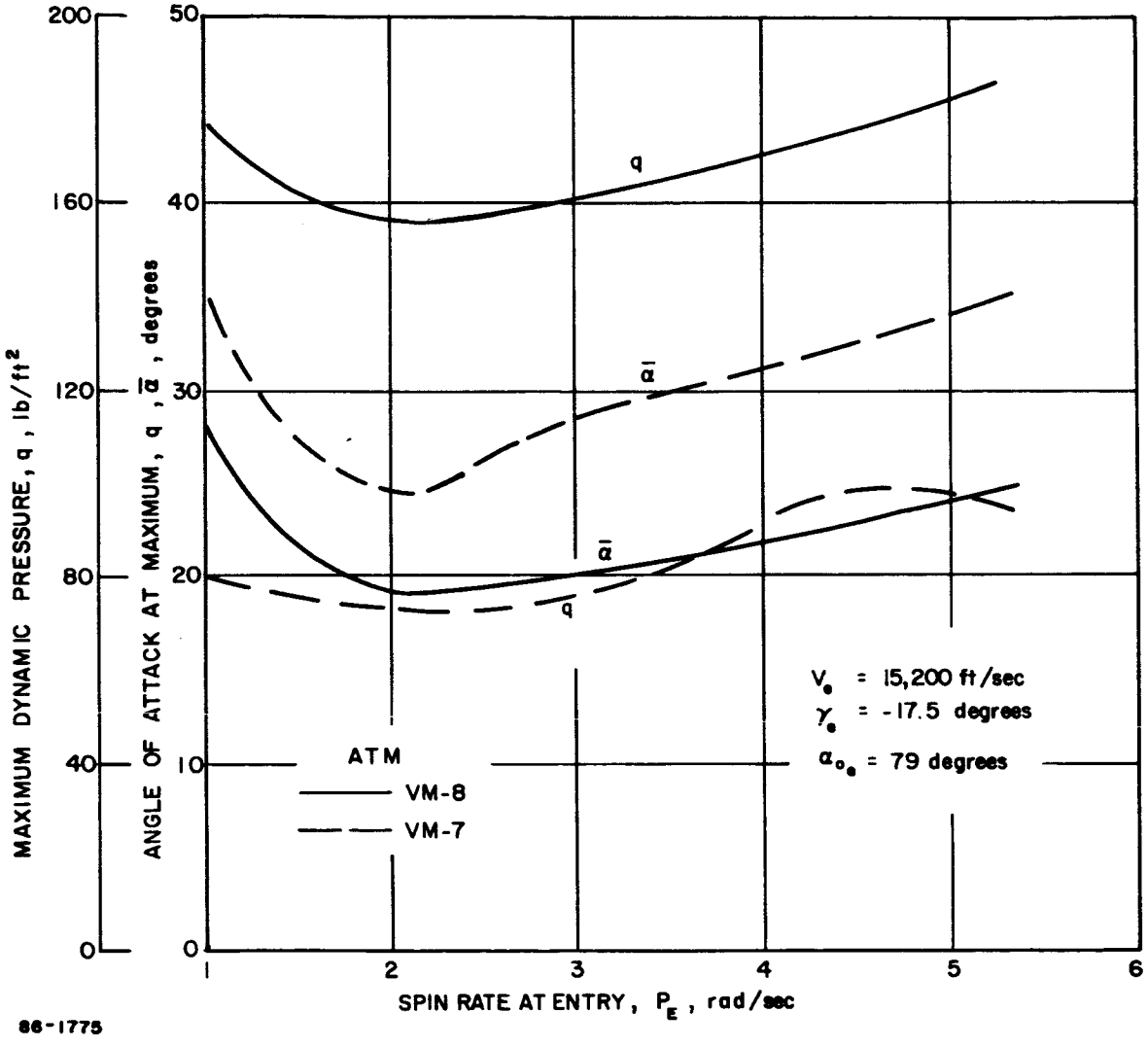

Figure 106 MAXIMUM DYNAMIC PRESSURE AND ANGLE OF ATTACK AT MAXIMUM DYNAMIC PRESSURE VERSUS SPIN RATE

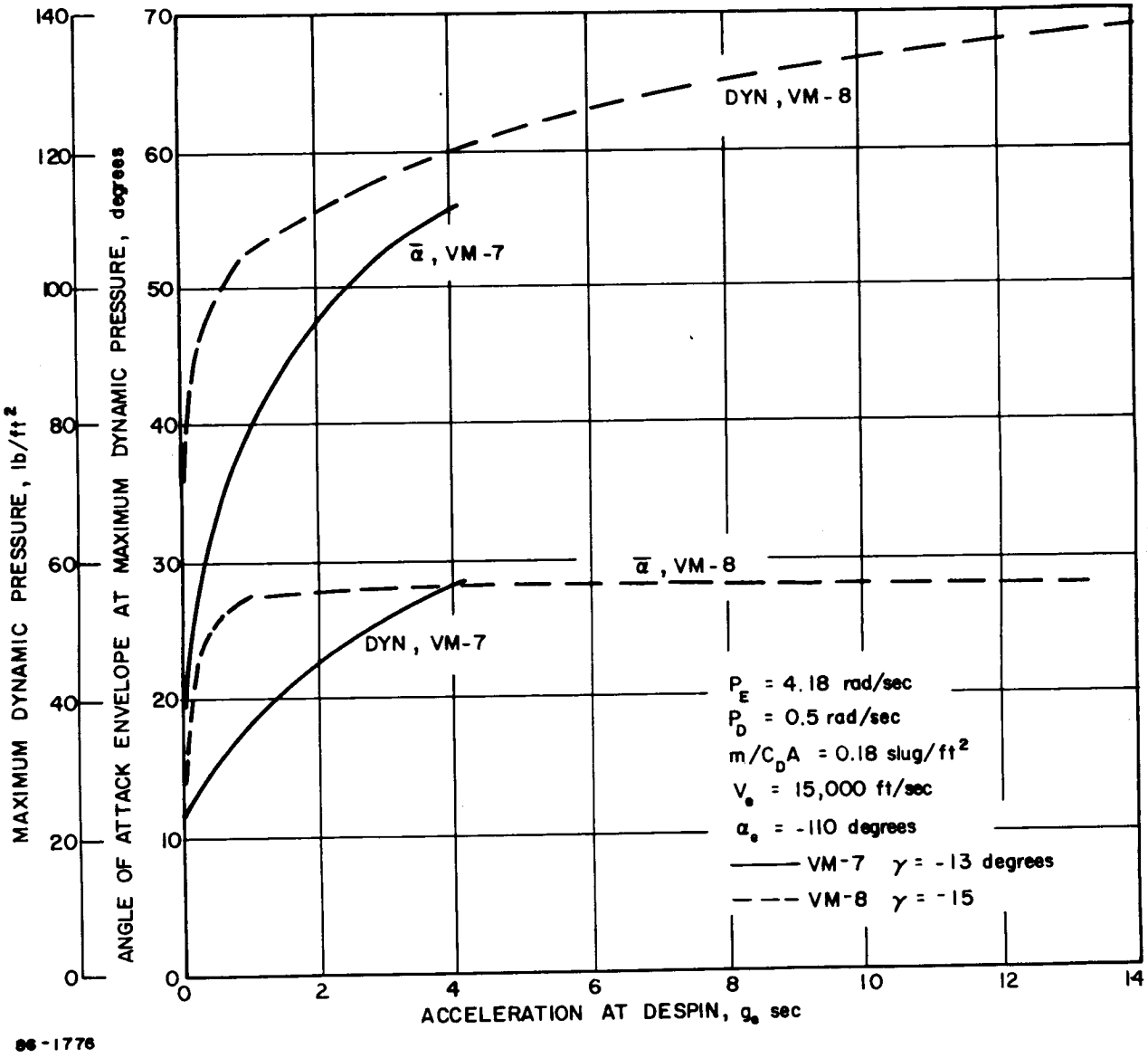

Figure 107 MAXIMUM DYNAMIC PRESSURE AND ANGLE OF ATTACK AT MAXIMUM DYNAMIC PRESSURE VERSUS ACCELERATION AT DESPIN

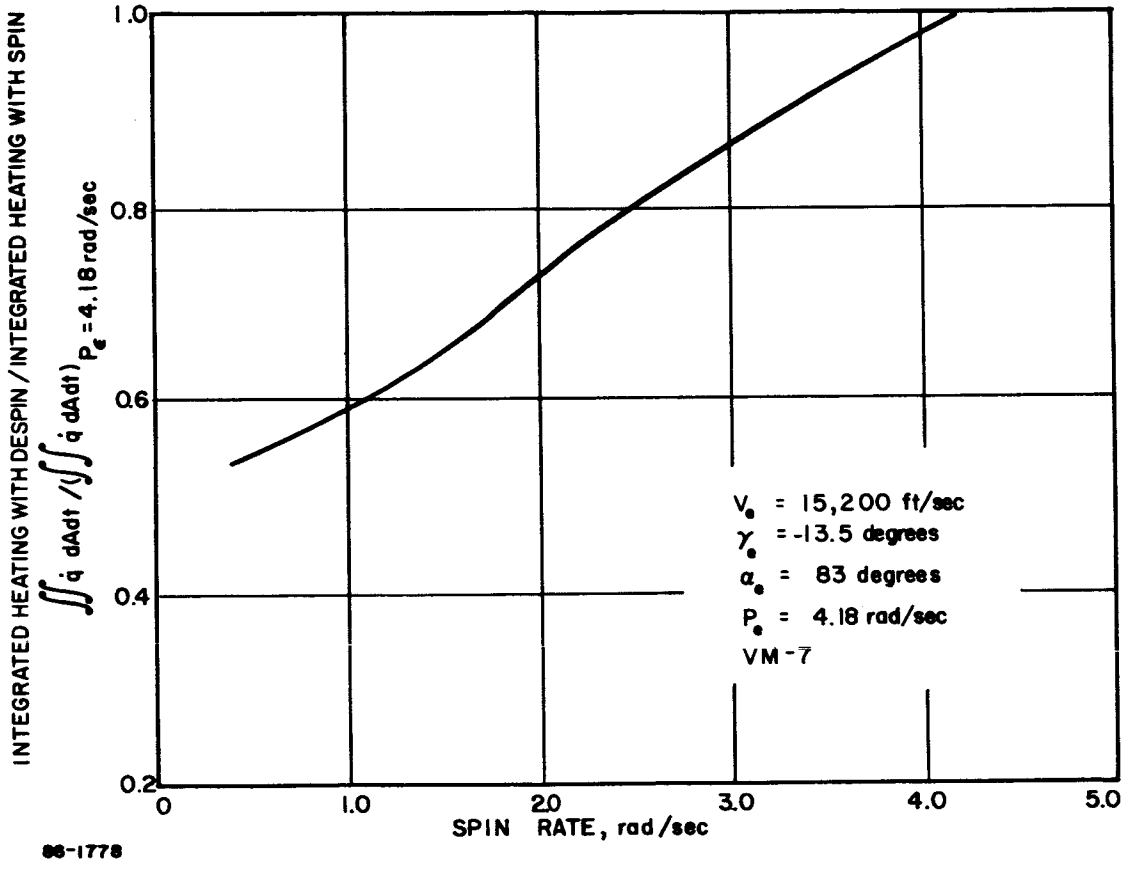

Figure 108 HEATING VARIATION WITH RESIDUAL SPIN

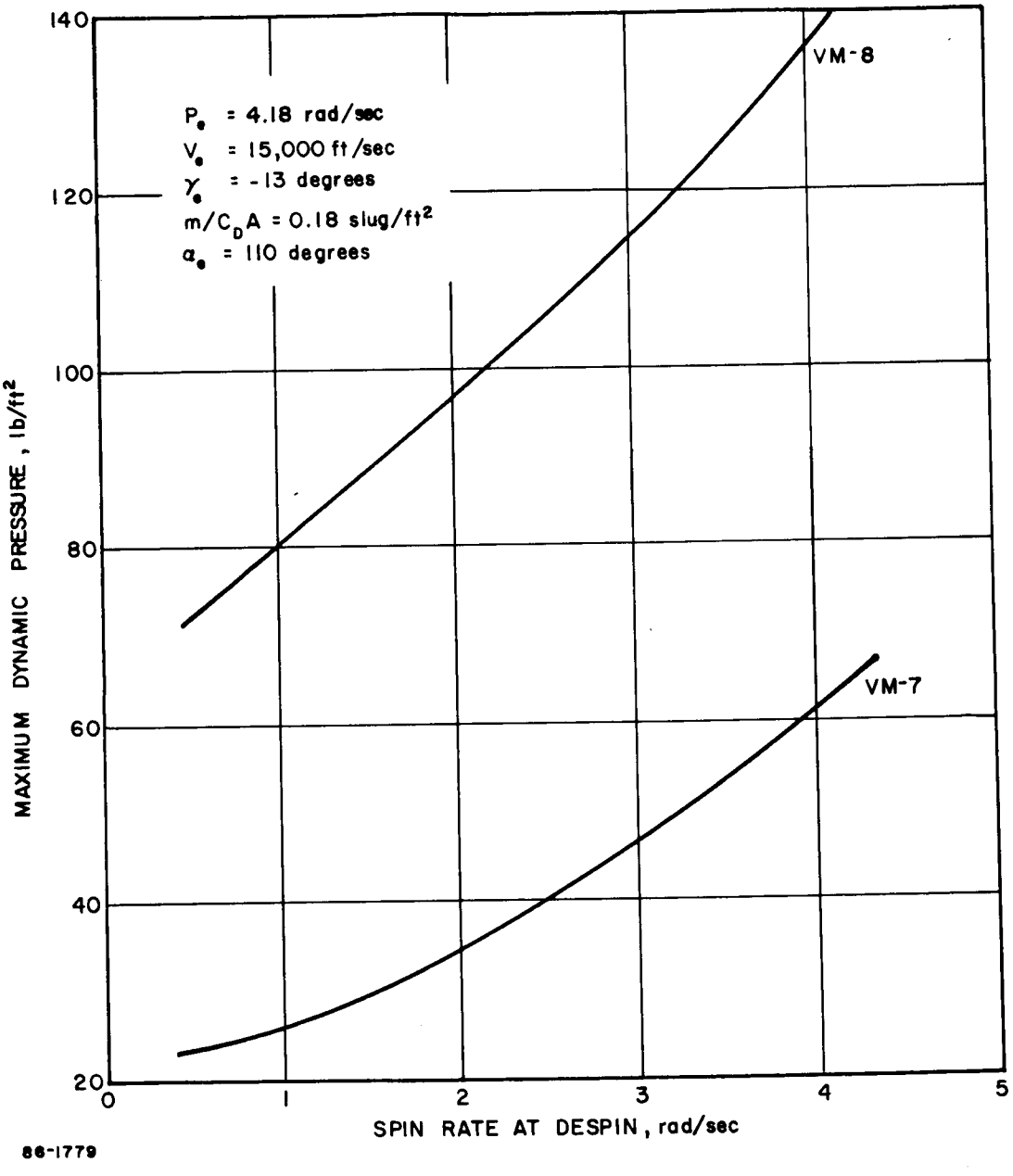

Figure 109 DESPIN ANALYSIS

The selected spin rate of 40 rpm is predicated on the desire to limit the entry dispersion which permits an operational $\gamma_e - V_E$ map "hugging" the limiting entry-angle envelope for chute deployment requirements; It also results in steeper entry angles which reduce the heating environment.

3.3.2.3 Heating and Loads

As indicated by the $\gamma_e - V_E$ map of entry conditions the angle of attack variation is such that large angles are associated with low entry velocities (Figures 82 and 105). It was not immediately obvious which were the critical entry conditions for loads and heating. Therefore, results from the de-orbit analyses were investigated in toto. Both spin and spin-despin (zero residual spin) cases were considered.

The critical entry conditions are shown below:

ENTRY CONDITIONS

Design Criterion	Velocity ft/sec	Angle (degrees)	Angle of Attack (degrees)
Loads	12700	-17.9	90
Heating	12900	-12.8	86

The coning angle and rate were 4 degrees and .42 rad/sec, respectively.

Typical heating pulses for the critical heating environment for the case of spin and spin-despin are shown in Figures 110 and 111 for the stagnation point (zero angle of attack) and the sonic point ($S/R_N \approx 4.5$). The high heating rates at the sonic point are associated with the stagnation point location at angles of attack greater than 30 degrees. The effect of spin on heating is obvious both through its effect on the trajectory as well as the local aggravation at the sonic point. The poorer convergence is evident as the stagnation point movement occurs much later in time for the spin case.

The peak dynamic pressure of 130 lb/ft^2 was obtained for entry velocity = 12,700 ft/sec, entry angle = -17.9 degrees and an entry angle of attack of 90 degrees. Typical flight parameter histories are shown in Figures 112 and 113 for spin and spin-despin entry.

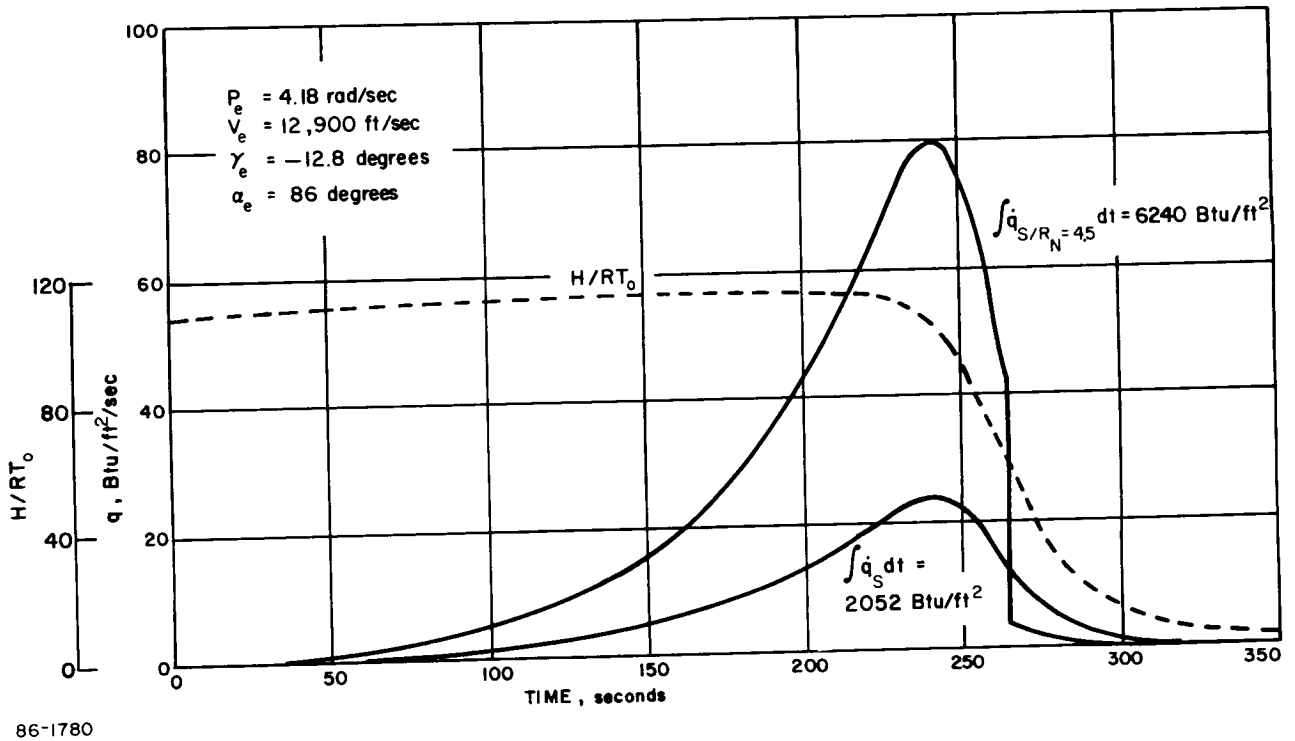

Figure 110 BLUNT CONE HEATING -- SPIN BACKUP

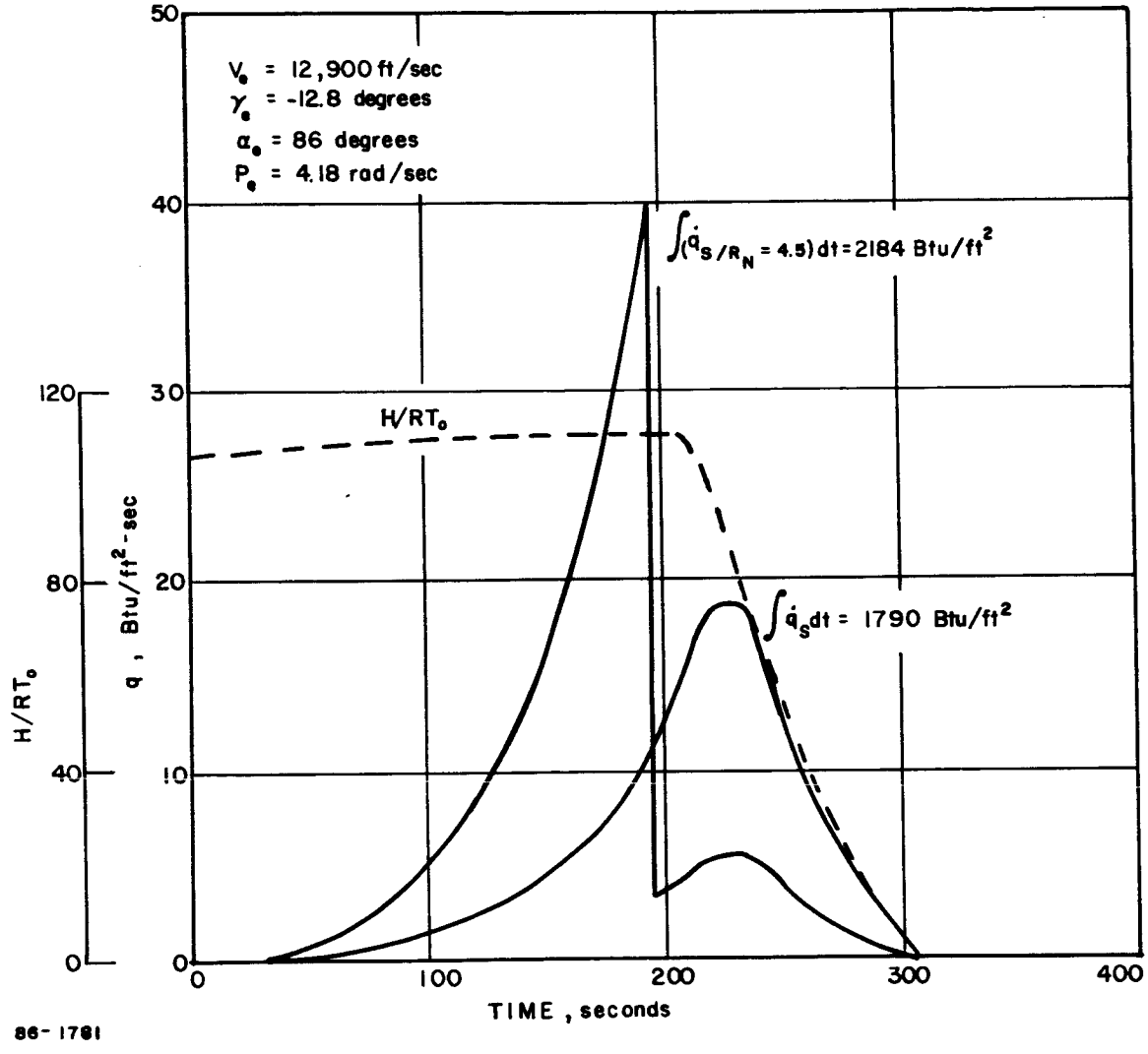

Figure 111 BLUNT CONE HEATING--SPIN-DESPIN BACKUP

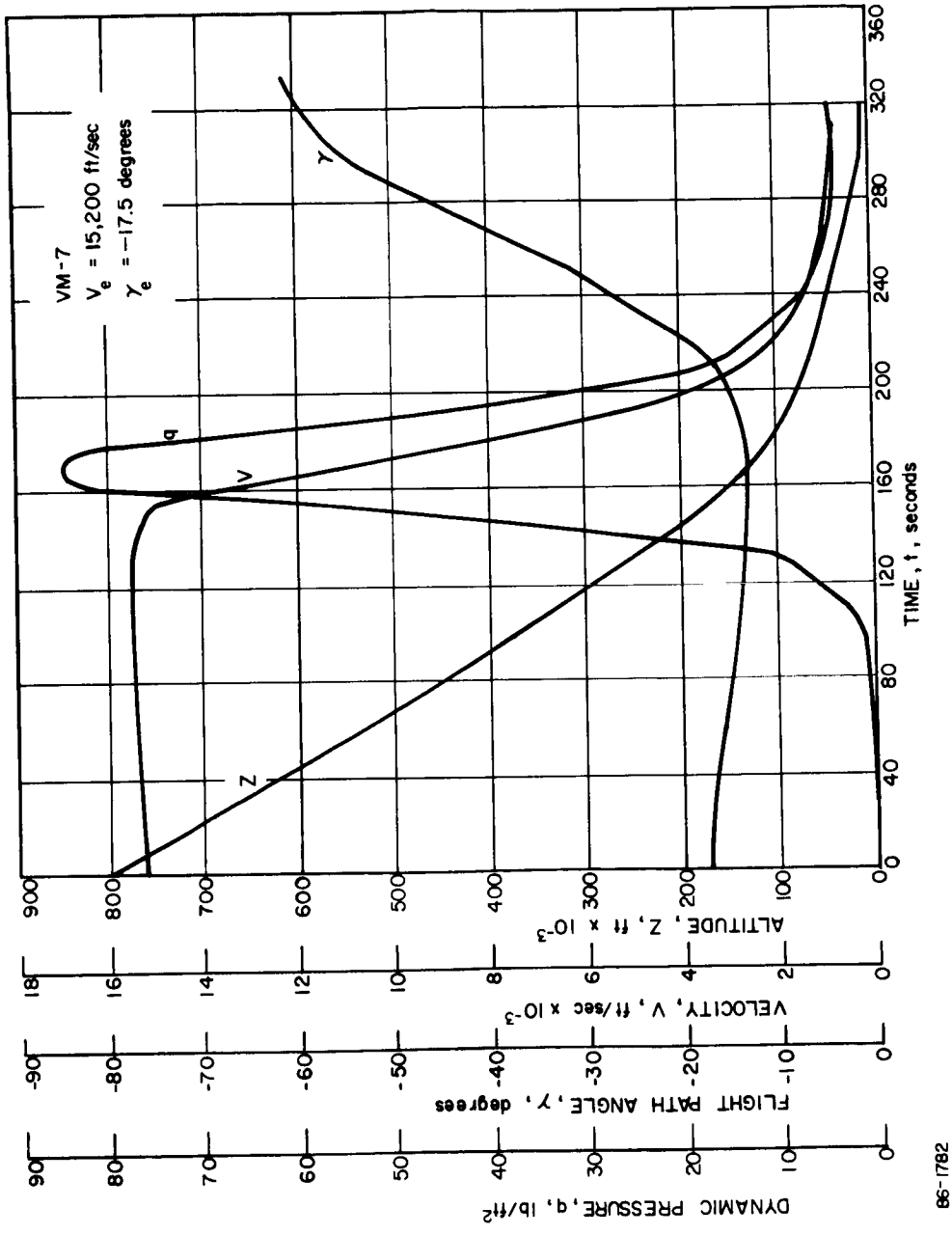

Figure 112 ENTRY TRAJECTORY PARAMETERS -- NO DESPIN

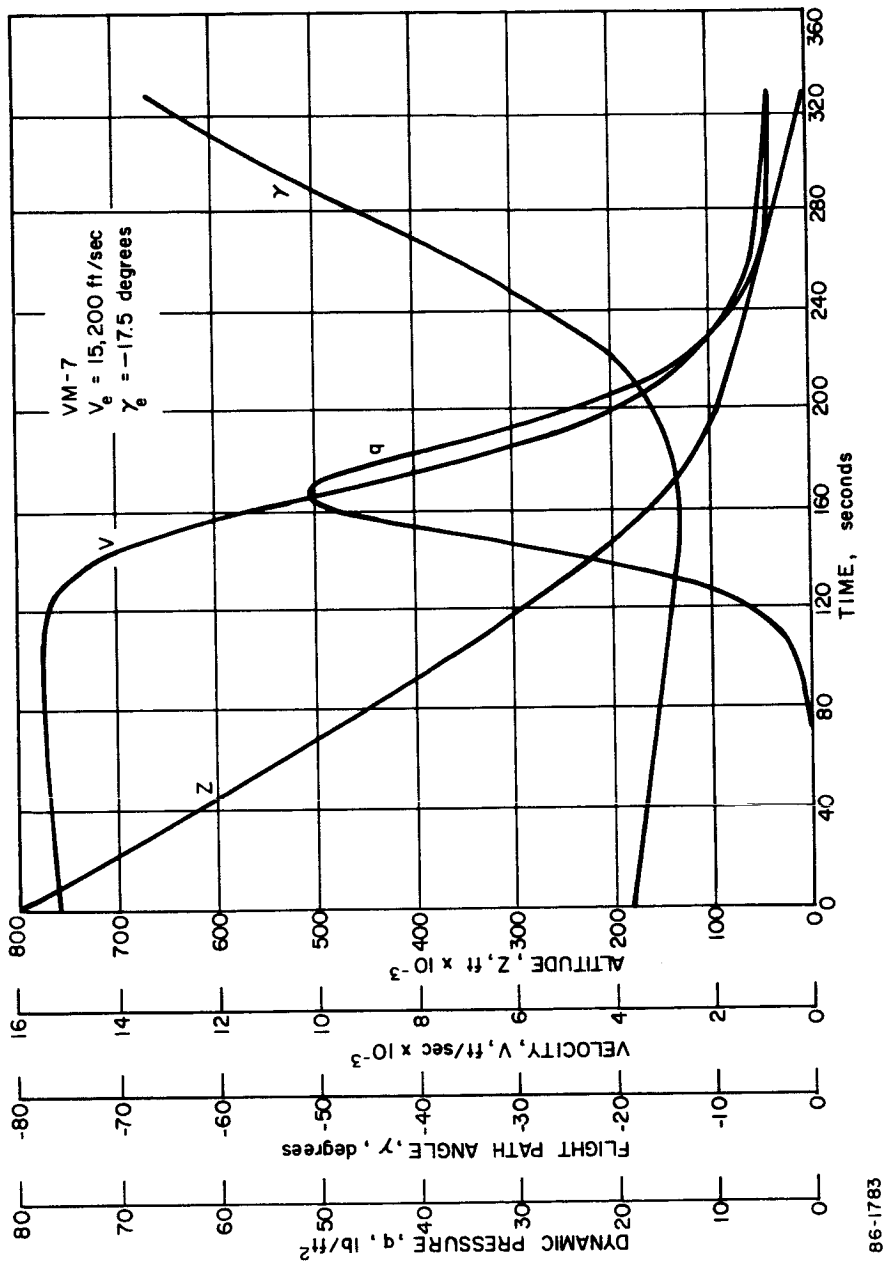

Figure 113 ENTRY TRAJECTORY PARAMETERS -- DESPIN

3.3.2.4 Aerodynamic Performance

The variation in performance over the operational entry conditions was found to correlate best with the angle of attack at entry. Considered were the altitude for chute deployment, loss in communication (view angle exceeding 90 degrees), and also the load variation. These results are summarized in Figures 114 through 117 for both spin and spin-despin. The improvement in performance for the above is apparent for the despin concept. Velocities have been indicated to show the insensitivity to this entry condition, the important parameters being entry angle and angle of attack. Typical angle of attack histories are shown in Figures 118 and 119. The initial "spike" in the envelope values is associated with the despin initiation prior to any sensible aerodynamic load. The required axial load should be 0.1 g; the mechanics of the digital program are such that time of initiation is necessary, implying an iteration to obtain the exact loading condition. The results for these cases however is substantially that which would result for proper despin initiation.

3.3.3 Reference Design

The results of the analysis of the spin and spin-despin concepts forced a reevaluation of the conceptual design and elimination of the spin backup system. The failure mode which was then adopted consisted of the termination of attitude control when rates of 0.1 rad/sec about any axis were attained. Further de-orbit dispersion analyses resulted (in combination with other systems considerations, discussed elsewhere) in a modified $V_E - \gamma_e$ entry map.

The definition of the new critical environments required an investigation of the combination of the above rate and initial angle of attack. In this case, however, the anticipated and previously evaluated $V_E - \gamma_e$ combinations were adequate.

Further analyses were performed for the conceptual design to determine the aggravations in heating associated with protuberances and cavities. These are manifested in the form of nozzles for the attitude control system and thrust vector control system. Additional heating was associated with the de-orbit thrust rocket which was mounted in the base. The heating over the afterbody and the back side (secondary heat shield)of the shell was also evaluated.

The effects of the plasma sheath on communications was also investigated and found to result in blackout over almost the entire range of entry conditions considered. These results were based on "clean" gas in the absence of ablation products. In actuality, however the primary heat shield ablation will aggravate the situation further.

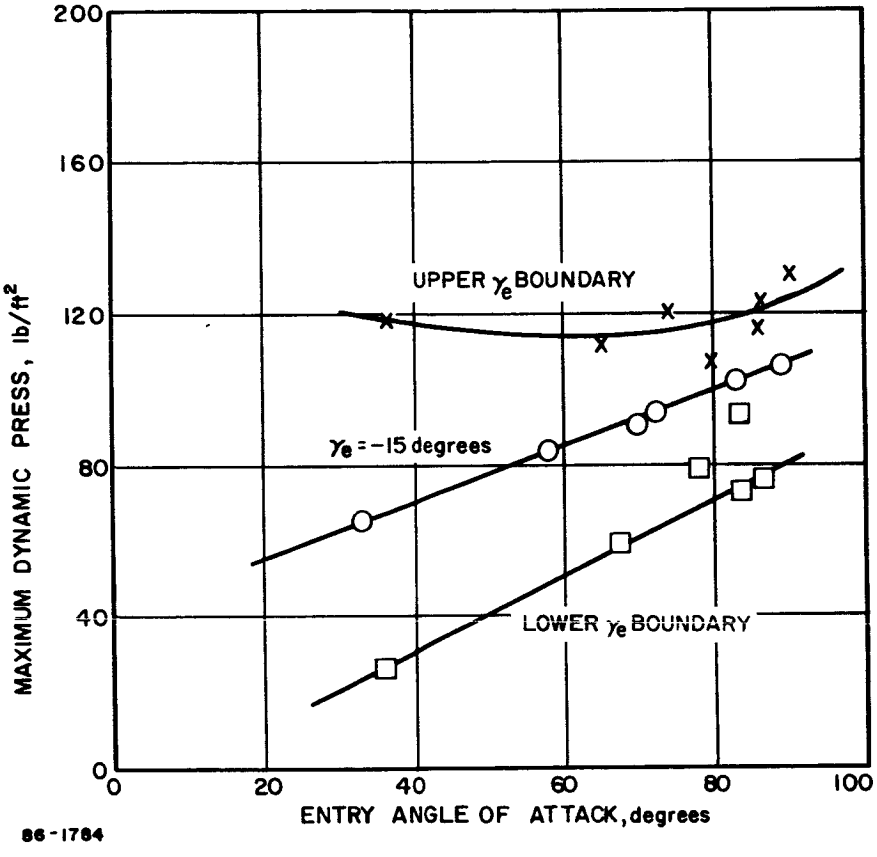

Figure 114 PEAK DYNAMIC PRESSURE--ATM. VM-8 SPIN

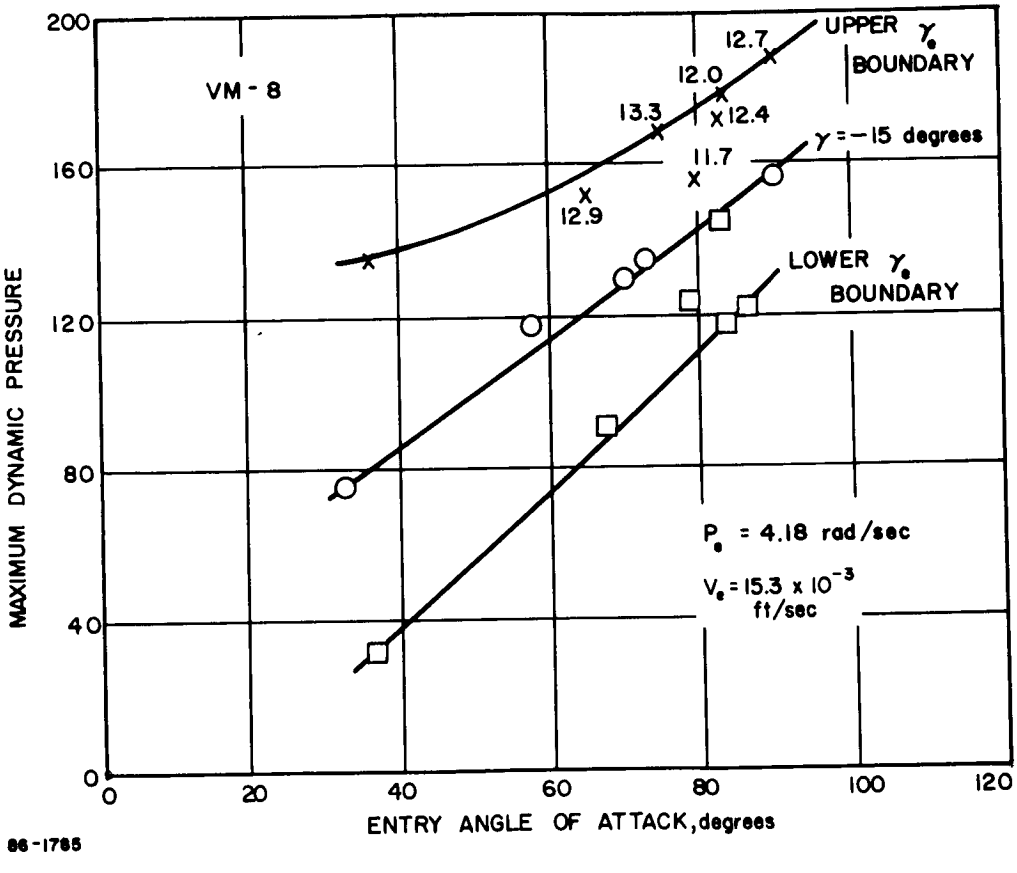

Figure 115 PEAK DYNAMIC PRESSURE--ATM.VM-8 DESPIN

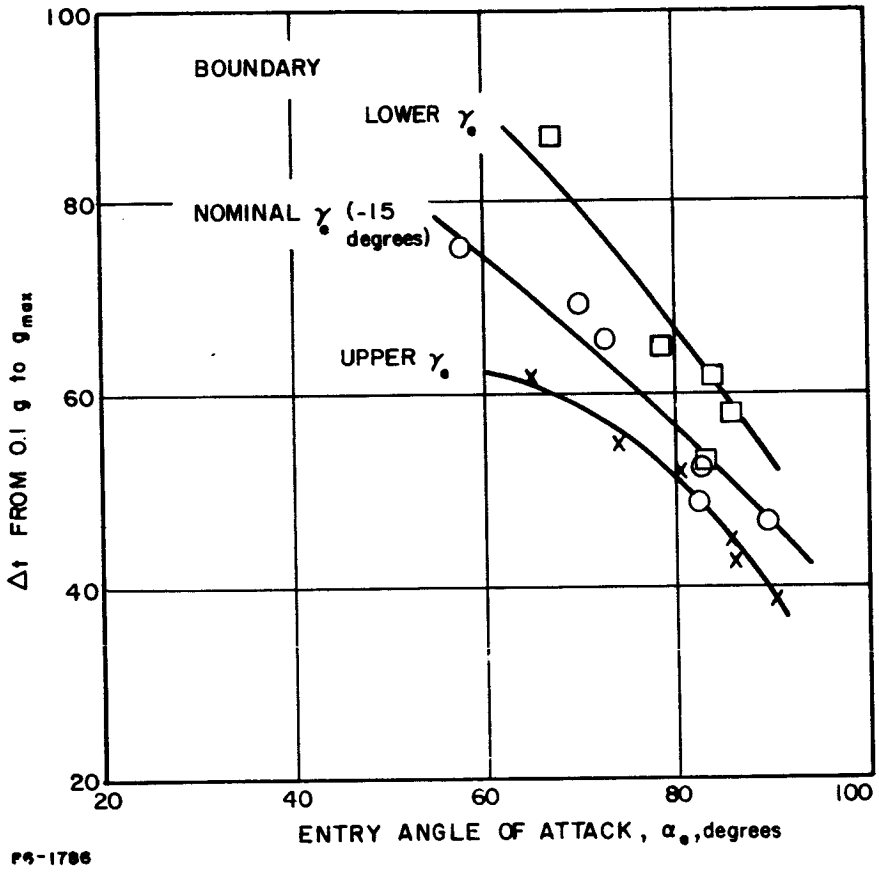

Figure 116 LOSS IN COMMUNICATION DUE TO CONING

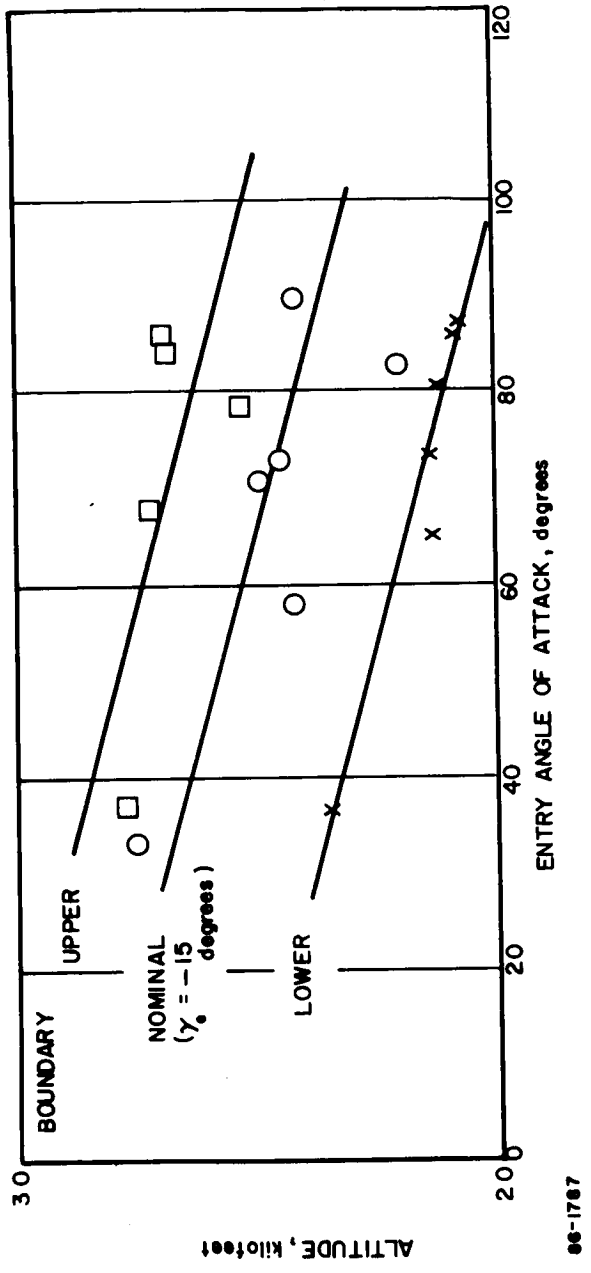

Figure 117 VARIATION IN ALTITUDE AT MACH 1.2

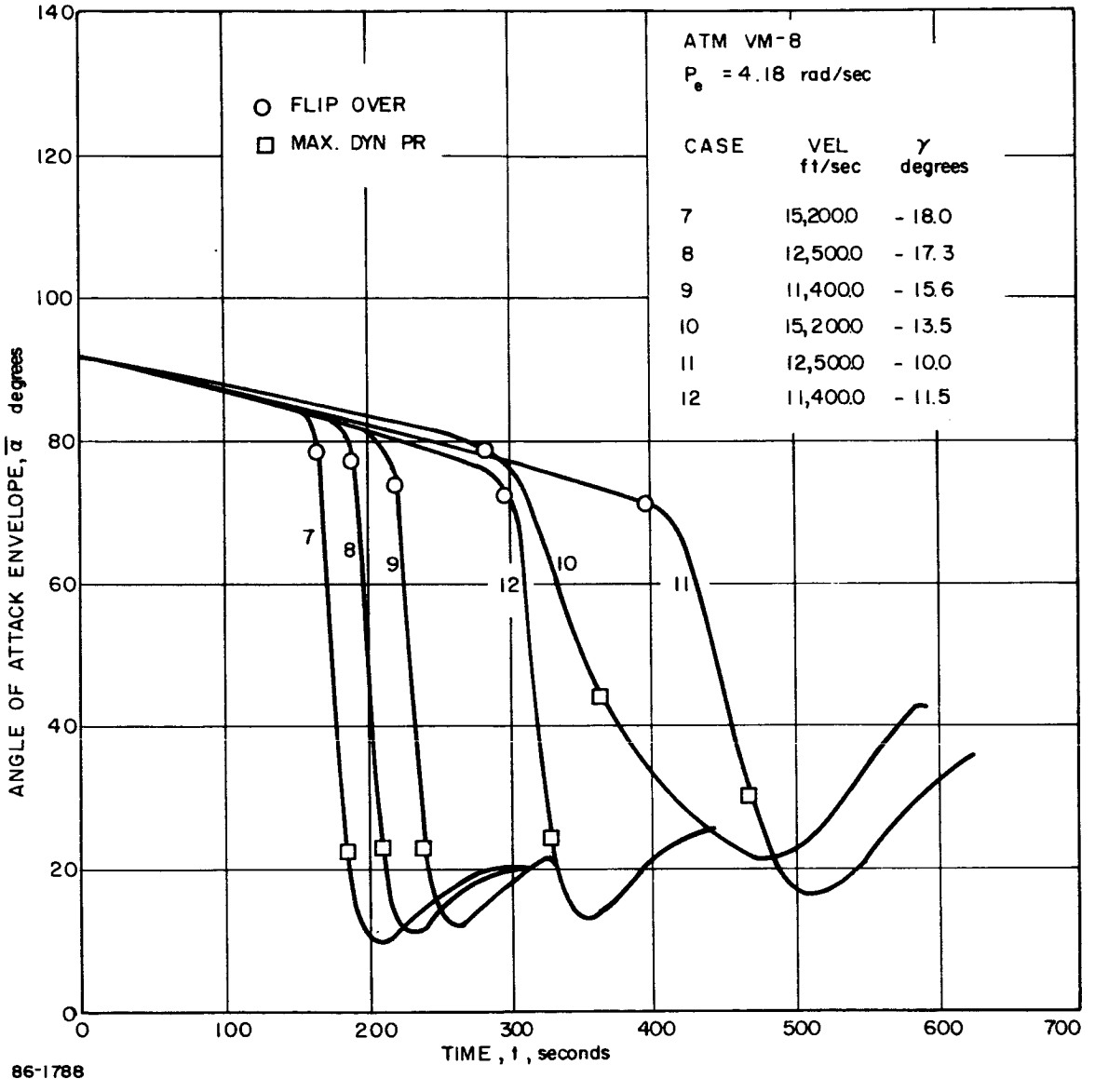

Figure 118 ANGLE-OF-ATTACK ENVELOPE--SPIN

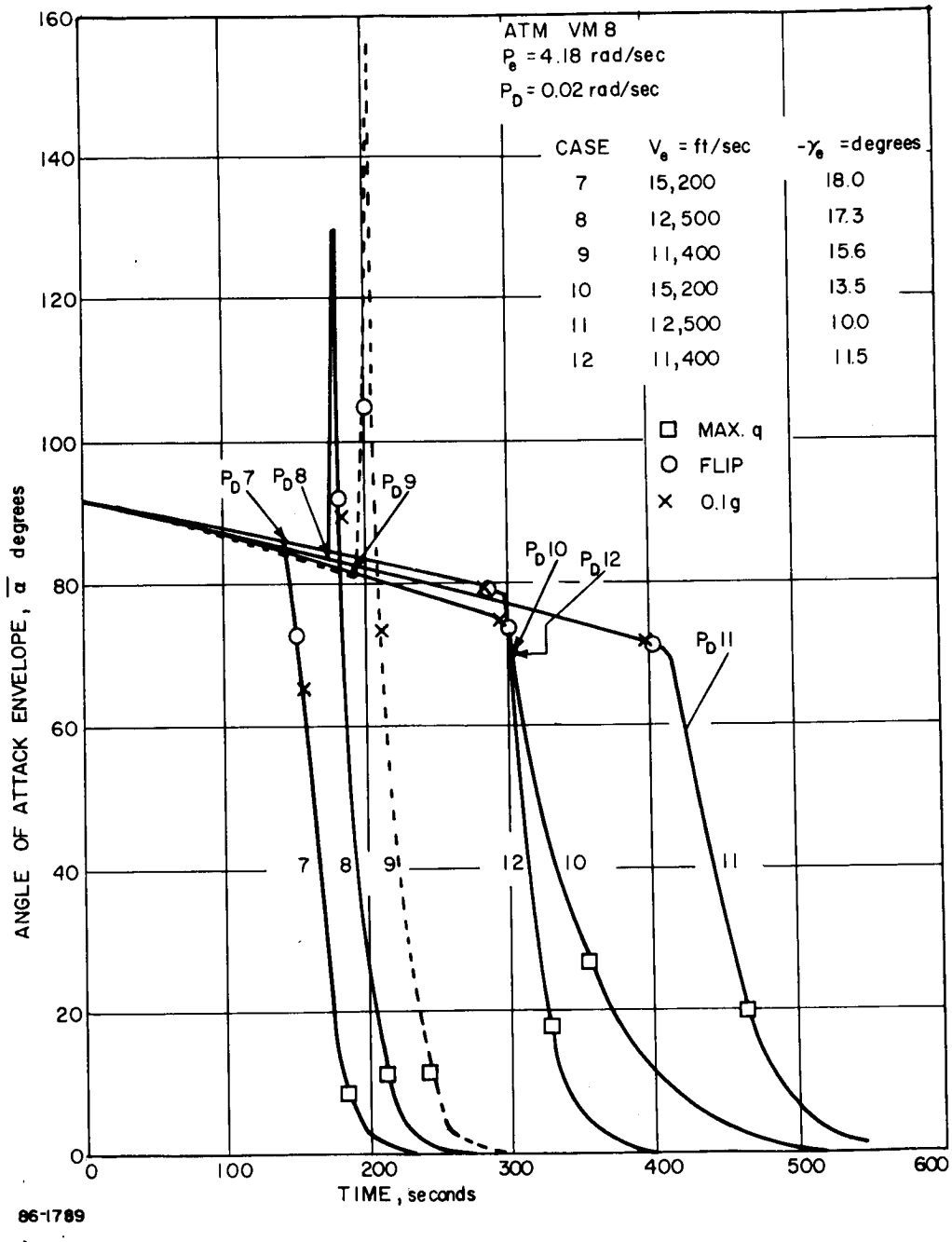

Figure 119 ANGLE-OF-ATTACK ENVELOPE--DESPIN

3.3.3.1 Reference Configuration

1. Afterbody Selection -- The afterbody performs two critical functions; 1) it provides a turnaround capability for rearward entry and 2) it protects the payload from the thermal environment associated with this mode of entry. Thermal protection is of course also necessary for the normal mode of entry near zero angle of attack however, the thermal environment is less severe. The dearth of data with respect to an optimum afterbody configuration restricts the designer to the utilization of forebody technology. This results in a weight penalty since, in order to provide only one stable trim point, shallow afterbody angles are required (see Figure 120), with the attendant excessively large surface areas. In eliminating the rearward entry difficulty, however, a serious problem is introduced during the transonic phase of flight. Similarly shaped afterbodies exhibit dynamic instability, which is associated with the hysteresis movement of the shock-boundary-layer separation phenomena at these Mach Numbers (approximately $0.8 < M_\infty < 2.0$). To circumvent this problem a stable separation point can be provided by utilizing a pronounced step from the maximum diameter to the afterbody; the step must be sufficiently large to avoid reattachment of the boundary layer to the afterbody. The problem now is that of predicting the rearward stability. On the basis of Newtonian theory, adequate turnaround capability is available for the afterbody configuration shown in Figure 79. Additional requirements on the afterbody result in additional configurations which satisfy the following: improved separation and adapter (Figure 80) and minimum packaging and weight (Figure 81). These configurations provide satisfactory turnaround capability when utilizing Newtonian theory, particularly when accounting for the "dish" effect on the moment. Available data indicate a pronounced effect associated with the "dish" shape at angles of attack other than 180 degrees. At 180 degrees, however, the data indicate a region of stability. These data provided a means for factoring out the forebody and sting contribution since data were generated about several moment centers. The reduced data (see paragraph 4.1) resulted in a neutrally stable condition for the dish shaped afterbody which was easily circumvented by means of flaps.

To evaluate this type of afterbody (i.e., Figures 79, 80 and 81) a performance analysis was conducted utilizing Newtonian theory, accounting for the dish contribution and shadowing. The resulting moment coefficients are shown in Figure 121. These coefficients have considered the weight associated with the respective configurations which is reflected in the center of gravity location. The effect of the afterbody on the forward stability is due to the center of gravity location. The minimum afterbody compares very faborably, on this basis, with the other configurations considered during the study.

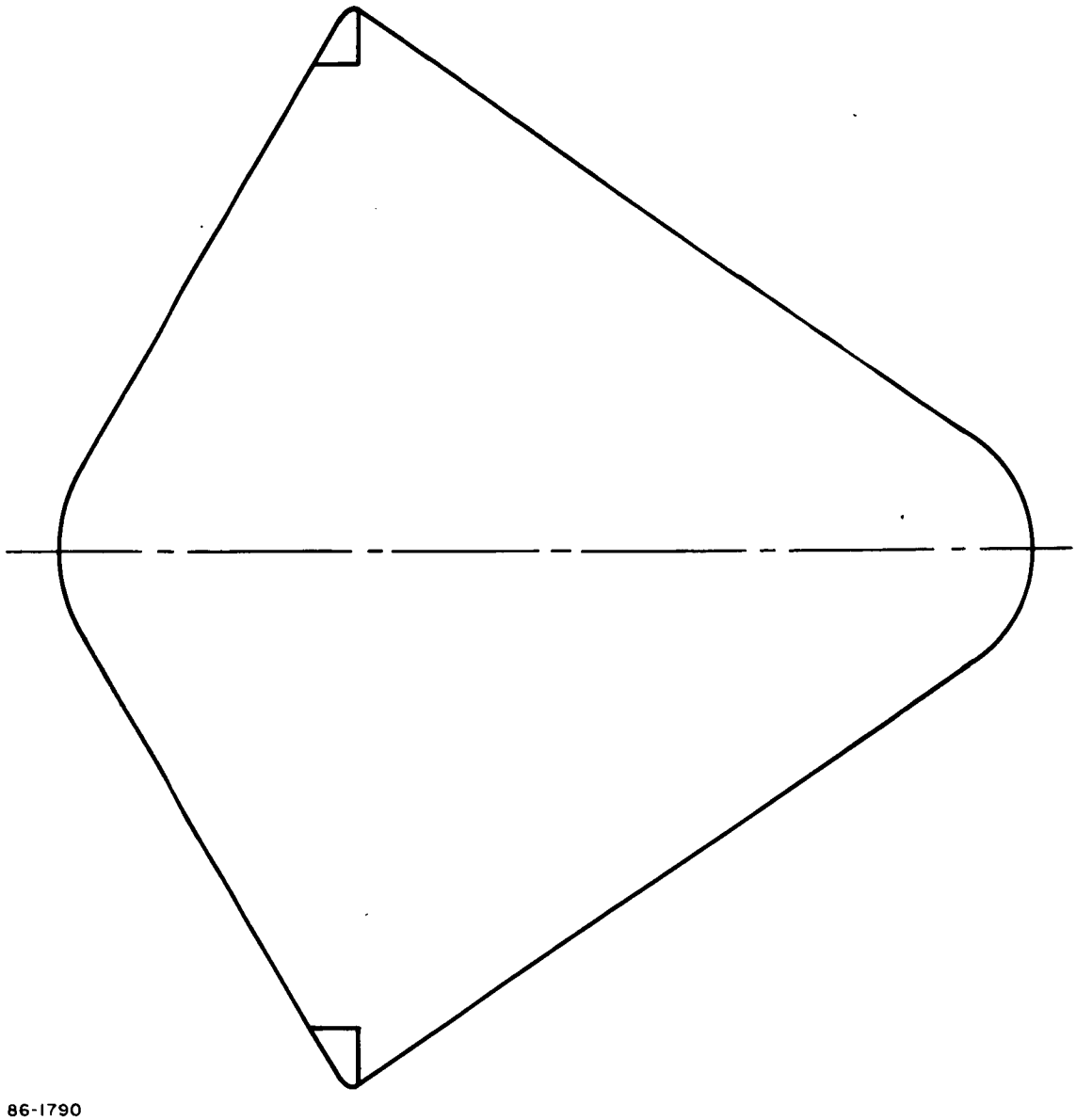

86-1790

Figure 120 BLUNT CONE MAXIMUM CONFIDENCE AFTERBODY

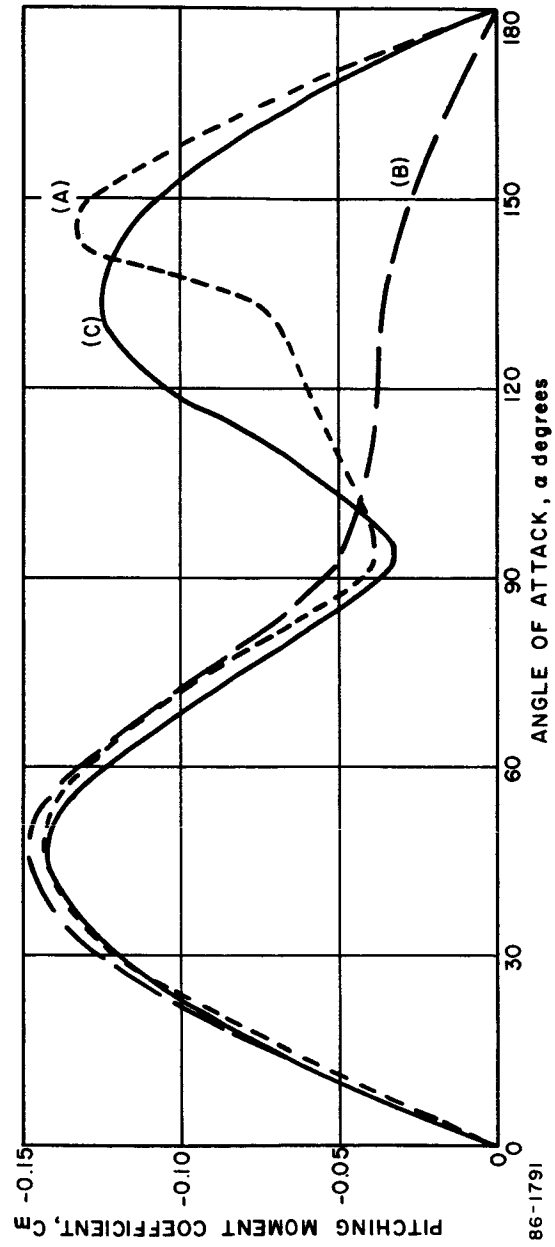

Figure 121 NEWTONIAN PITCHING MOMENT COEFFICIENTS

The performance was evaluated with coefficients and the mass characteristics given in Table XXVI, for a rearward entry with nominal spin. The parenthetic weights are the increments in weight associated with the afterbody. The resulting angle of attack envelopes are presented in Figure 122 and indicate adequate convergence for the minimum weight configuration. The configuration of Figure 79 exhibits only slightly better performance.

The minimum weight configuration shows an additional advantage as it experiences the lowest heating environment for rearward entry because the afterbody is recessed within the "dish".

TABLE XXVI

MASS CHARACTERISTICS (AFTERBODY COMPARISON)

Configuration	Entry From the Approach Trajectory Configuration	Improved Separation	Minimum Weight
W (pounds)	2040, (0)	2040, (+93)	2040, (-66)
$X_{C.G.}$ (inches)	35.2	35.9	34.0
I_{xx} (slug-ft.^{2})	1055	1061	1051
I_{yy} (slug-ft.^{2})	579	586	572

2. Mass and Aerodynamic Characteristics --On the basis of the previously generated results and considering system requirements inposed on weight distributions, the following mass characteristics were used:

Mass	$\frac{X_{C.G.}}{D}$	I_{xx}	I_{yy}	I_{zz}
63.3 slugs	0.19	1050 slug-ft^2	570	570

The improved center of gravity location is the result of utilizing the minimum weight afterbody which also permitted the rocket engine to be located farther forward.

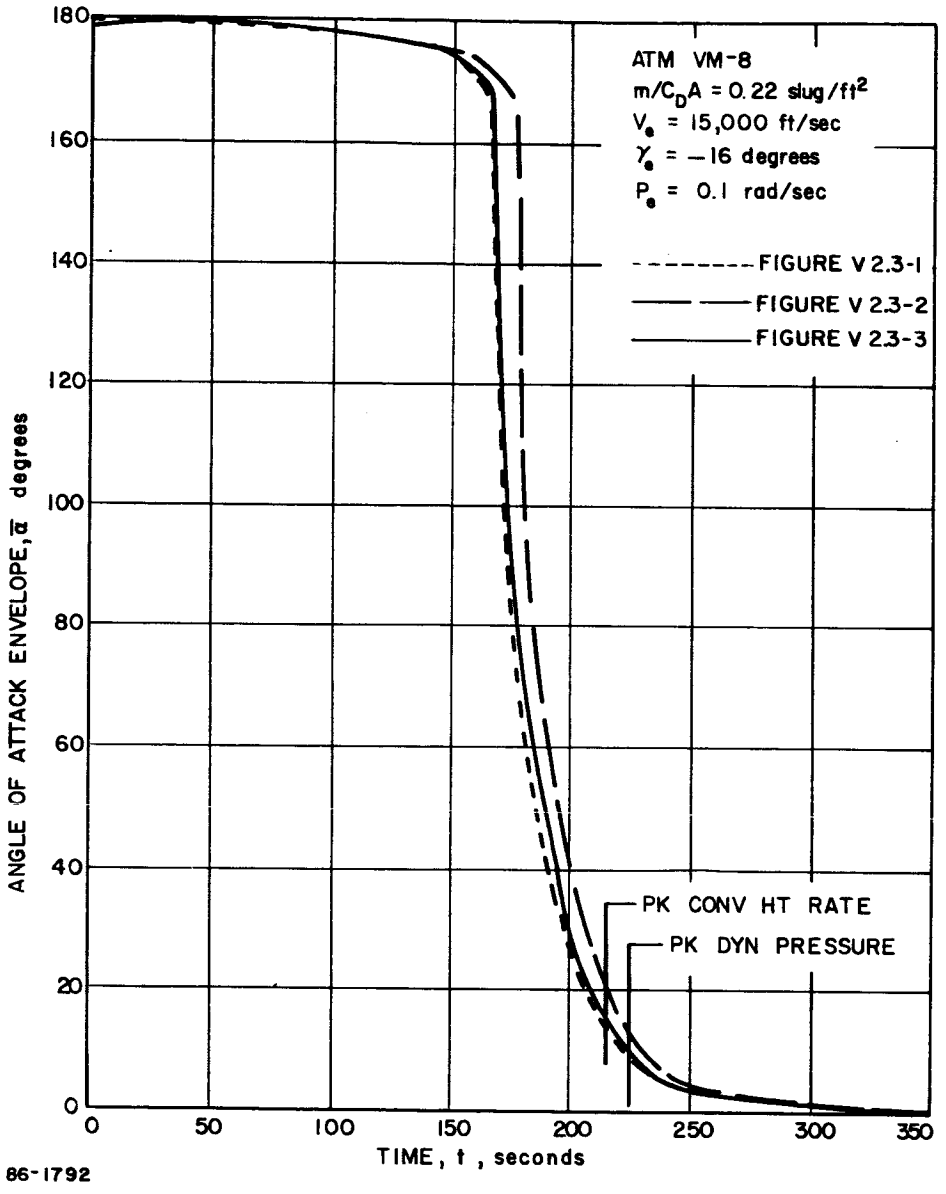

Figure 122 ANGLE-OF-ATTACK ENVELOPE $\tilde{\bar{\alpha}}$ DEGREES

The aerodynamic coefficients utilized are given in Figures 123 through 125.

3.3.3.2 Entry Conditions

The range of entry conditions considered for the reference design is given in Figure 84 in terms of entry velocity and angle. The limiting rate of 0.1 rad/sec was considered about any axis, possible random angle of attack was also considered. These conditions are given in an inertial space system. To account for rotating planet effects, the conditions must be transformed into a relative coordinate system. The combination of entry angle, angle of attack, and spin or roll (or both) is not known a priori, requiring a preliminary investigation to establish the critical conditions. Definition of the rotating planet effects requires a knowledge of the impact and entry points (range information). Investigations were thus made of the effects of planet rotation as well as of the various combinations of entry angle of attack and rates.

1. Roll and Varying Angle of Attack -- The maximum rate of 0.1 rad/sec was assumed about the roll axis with the angle of attack varying at entry. The result was an increase in the loads as the angle of attack was increased. A maximum was reached for the rearward entry (see Figure 126). The critical entry for heating was dependent upon body station; (a) maximum heating at the stagnation point (zero-angle of attack location) occurred for ninety degree angle of attack entry; (b) maximum sonic point heating occurred at 90-degree angle of attack and (c) maximum afterbody heating occurred for rearward entry.

2. Tumble -- There is a particular angle of attack for a specified pitch rate which will result in the vehicle attaining a rearward attitude at cessation of tumble. Tedious iterations are required for the determination of this angle of attack. For the rate considered the maximum load was obtained for an angle of attack of -8.2 degrees. The resulting envelope of angle of attack is shown in Figure 127.

3. Rotating Planet -- The effect of rotating planet upon the loads and heating were found to be in opposite directions; rotation resulted in higher loads whereas higher heating was obtained with non-rotation (see Figure 128).

The variation of the loads were as follows

Rotation	P (rad/sec)	Q (rad/sec)	α_e (degrees)	Maximum Dynamic Pressure (lb/ft^2)
None	0.1	0	180	98.5
None	0.1	0	90	94.2
None	0	0.1	- 8.2	106.0
With	0.1	0	180	114.6

The selected entry conditions for the design are given below:

Criteria	Rotation	Angle of Attack	Spin
Loads	With	180 degrees	0.1 Rad/sec
Heating	None	Function of Body Station	0.1 Rad/sec

The design environments were established for these conditions with performance analyses conducted to determine the off-design environments. Syrtis Major was selected as the impact area. Orbital inclinations were varied between 40 and 60 degrees with the equator, while entry with rotation was considered. On the basis of the preliminary analysis the orbital inclination for the loads was taken as 40 degrees, with 60 degrees resulting in maximum heating for a rotating planet case.

3.3.3.3 Heating

The heating distributions obtained as a function of angle of attack (see paragraph 4.3.1) were used in the analysis with the angle of attack variation obtained from the dynamics and analysis. The maximum convective heating was obtained at the maximum entry velocity and shallowest entry angle, 15,200 ft/sec and -14 degrees, respectively.

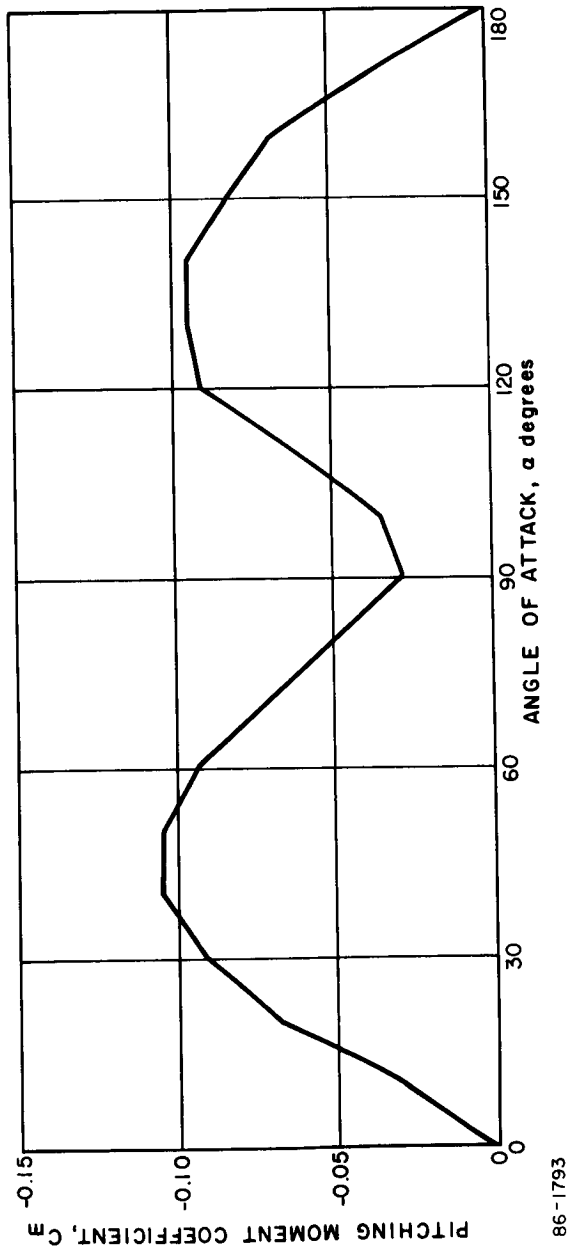

Figure 123 HYPERSONIC MOMENT COEFFICIENT REFERENCE DESIGN

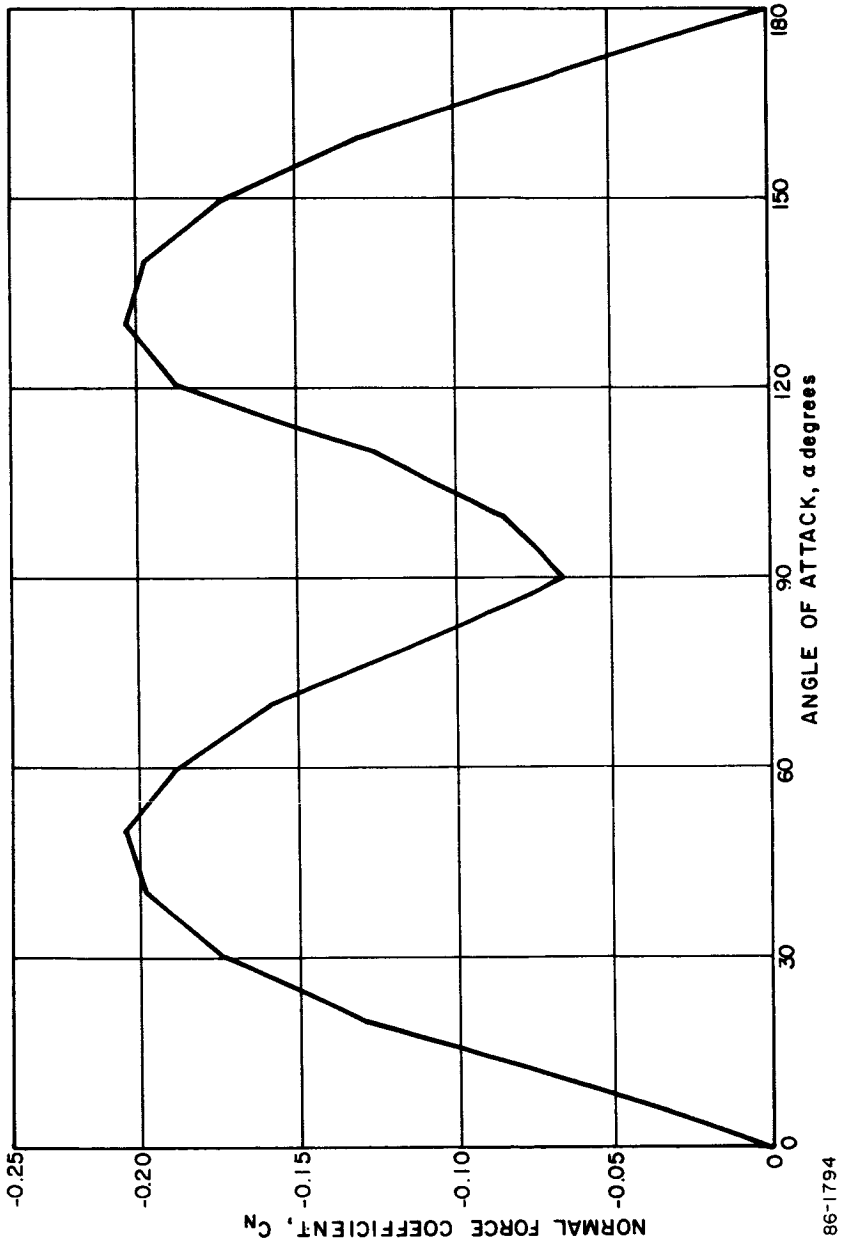

Figure 124 HYPERSONIC NORMAL FORCE COEFFICIENT REFERENCE DESIGN

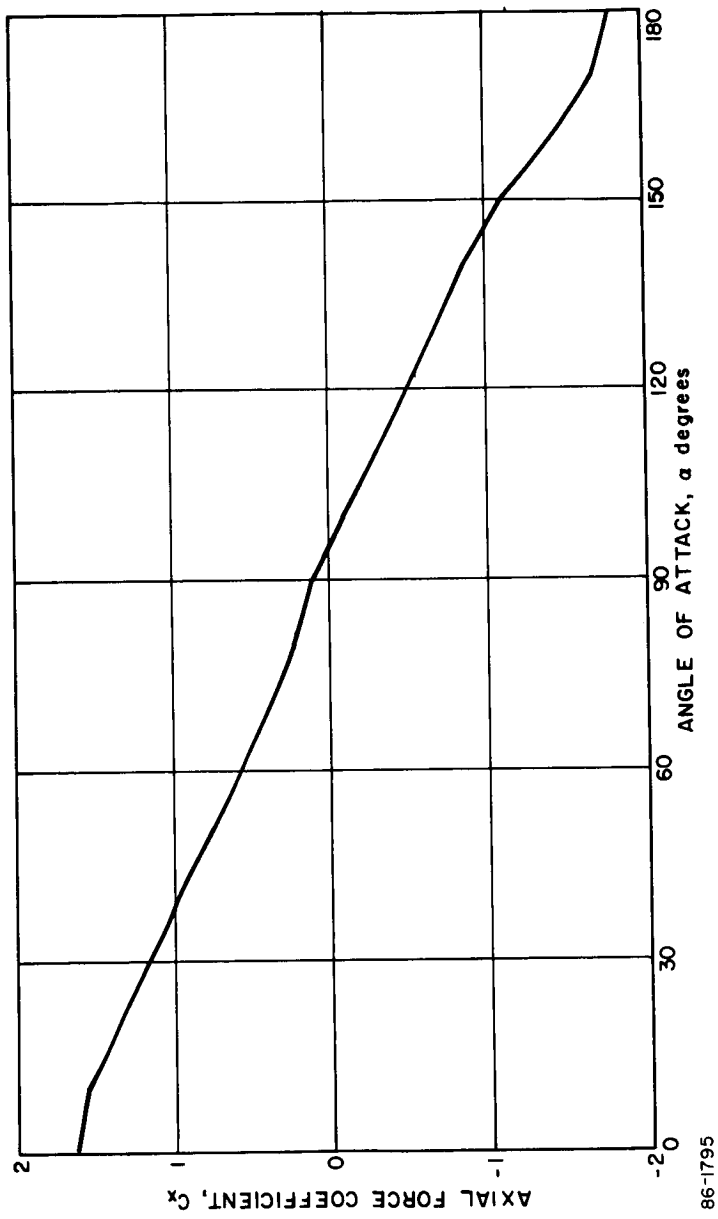

Figure 125 HYPERSONIC AXIAL FORCE COEFFICIENT REFERENCE DESIGN

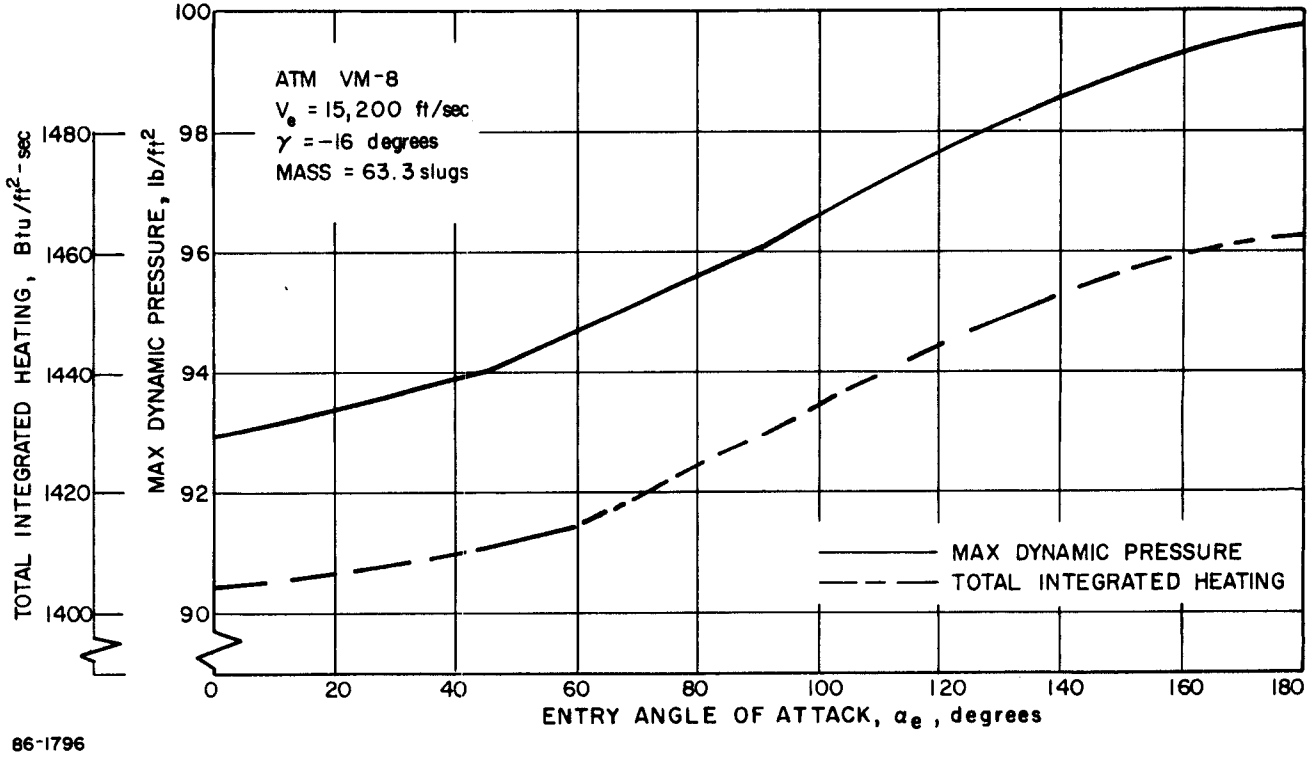

Figure 126 MAXIMUM DYNAMIC PRESSURE AND TOTAL INTEGRATED HEATING

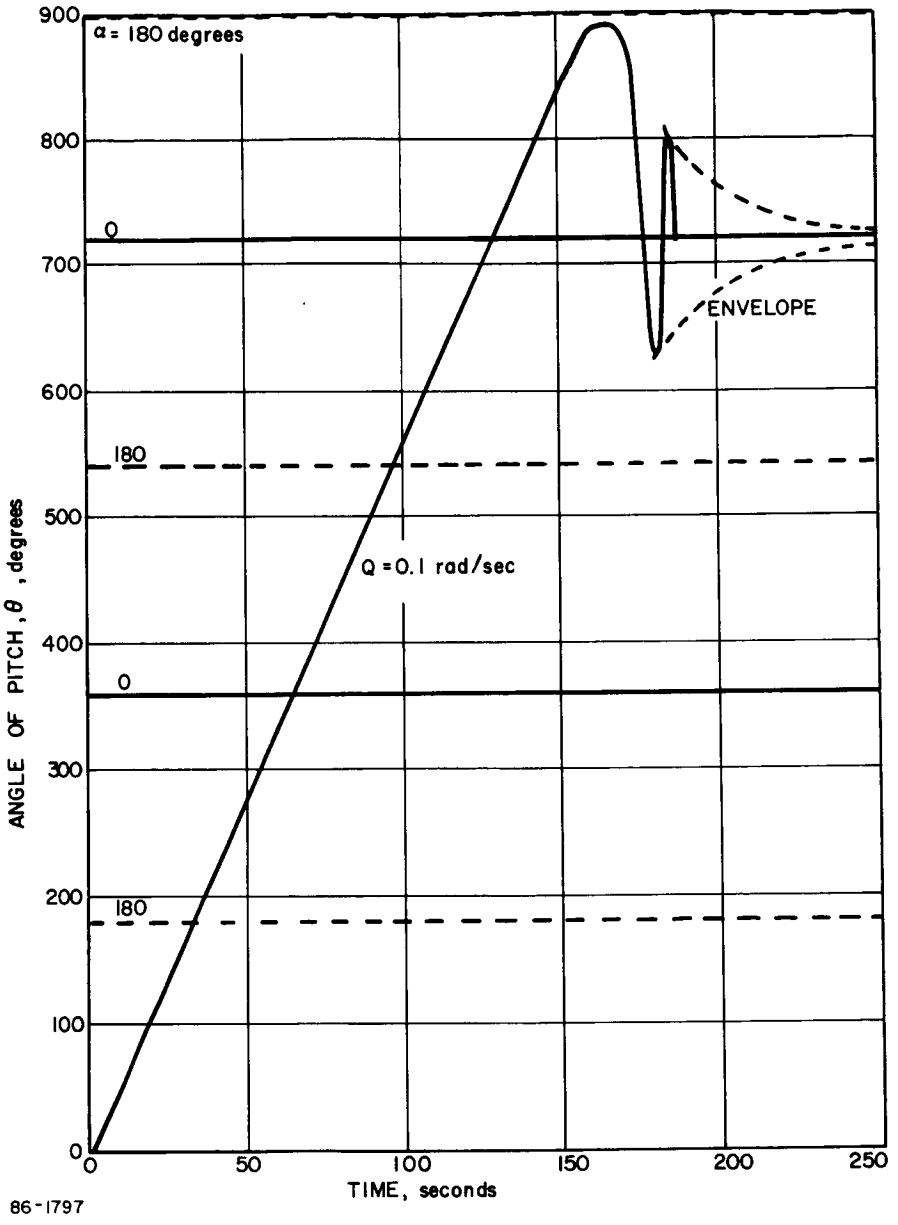

Figure 127 TUMBLING ENTRY -- ANGLE OF ATTACK VARIATION

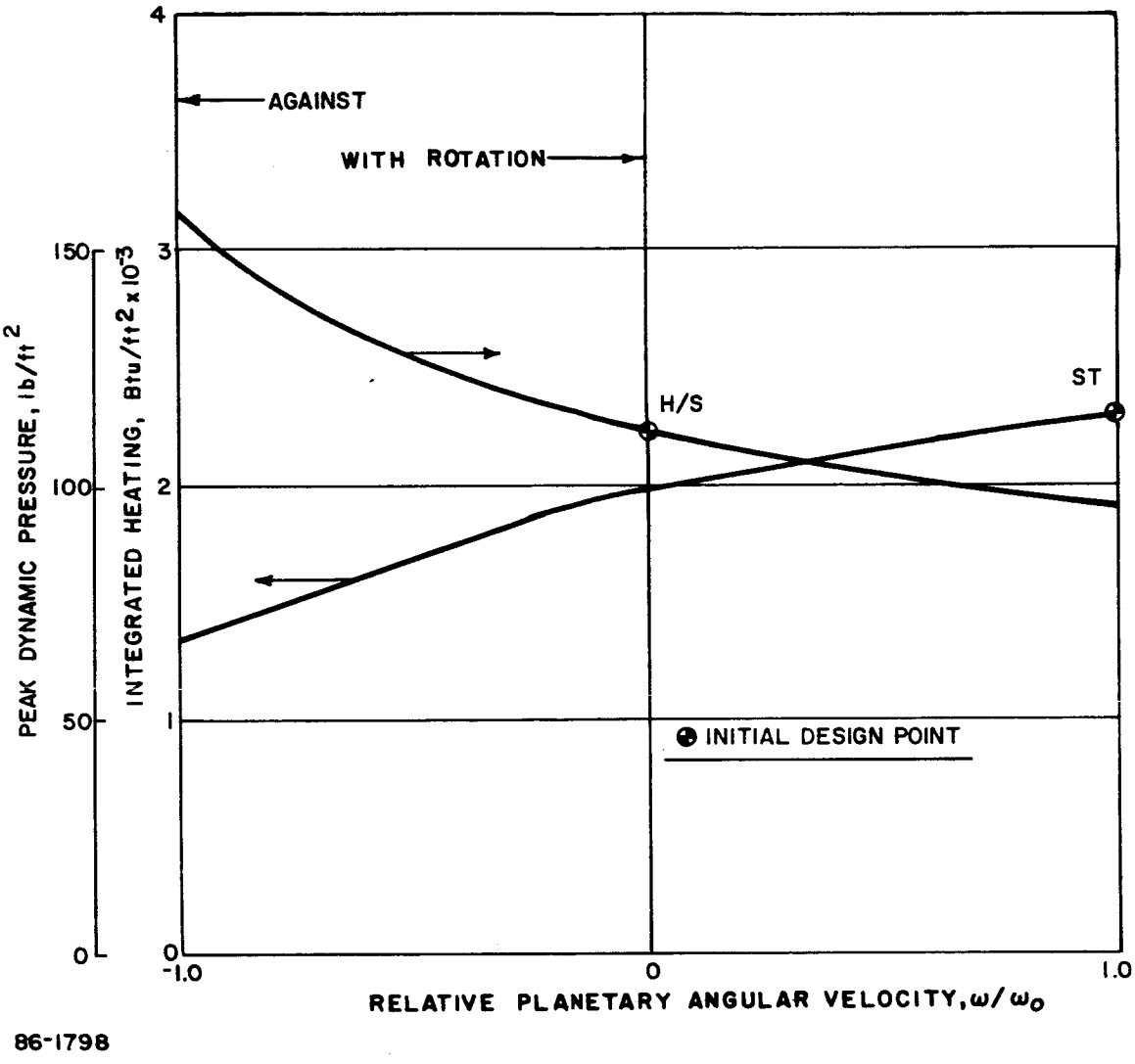

Figure 128 ROTATING PLANET EFFECTS

Typical heat pulse variations at various body stations are given in Figures 129 to 131, for entry at an angle of attack of 90 degrees. In addition, values for other angles of attack are given below.

The design heating has considered the conservatisms associated with imposing the worst combination of entry conditions with each body station, including non-rotating planet. The margins associated with the rotating planet were determined in addition to obtaining the heating for the structural design point. In the latter case (entry into the VM-8) a portion of the heat pulse was associated with turbulent flow. This occurred post maximum heat rate and was not of any significance. (see Figure 132). The heating and margins are compared in the following table:

INTEGRATED HEATING SUMMARY

Body Station (S/R_N)	0	1.5	2.5	4.5	Shell Backface	After Body
Angle Of Attack (Degrees At Entry)	Integrating Heating (Btu/ft^2)					
0	1900	1216	933	627	38	95
90	2227	1426	1197	1705	90	115
180	2060	1300	1083	1493	117	95

The variation of the heating with entry conditions (velocity and angle) was examined to indicate possible limits in heat shield performance (external to the operational $\gamma_E - V_E$ map. As expected, two limits (possibly more) were found - one associated with the stagnation point and the other, with the sonic point (see Figure 133). The effects of the dynamics resulted in a more restricted envelope for the sonic point.

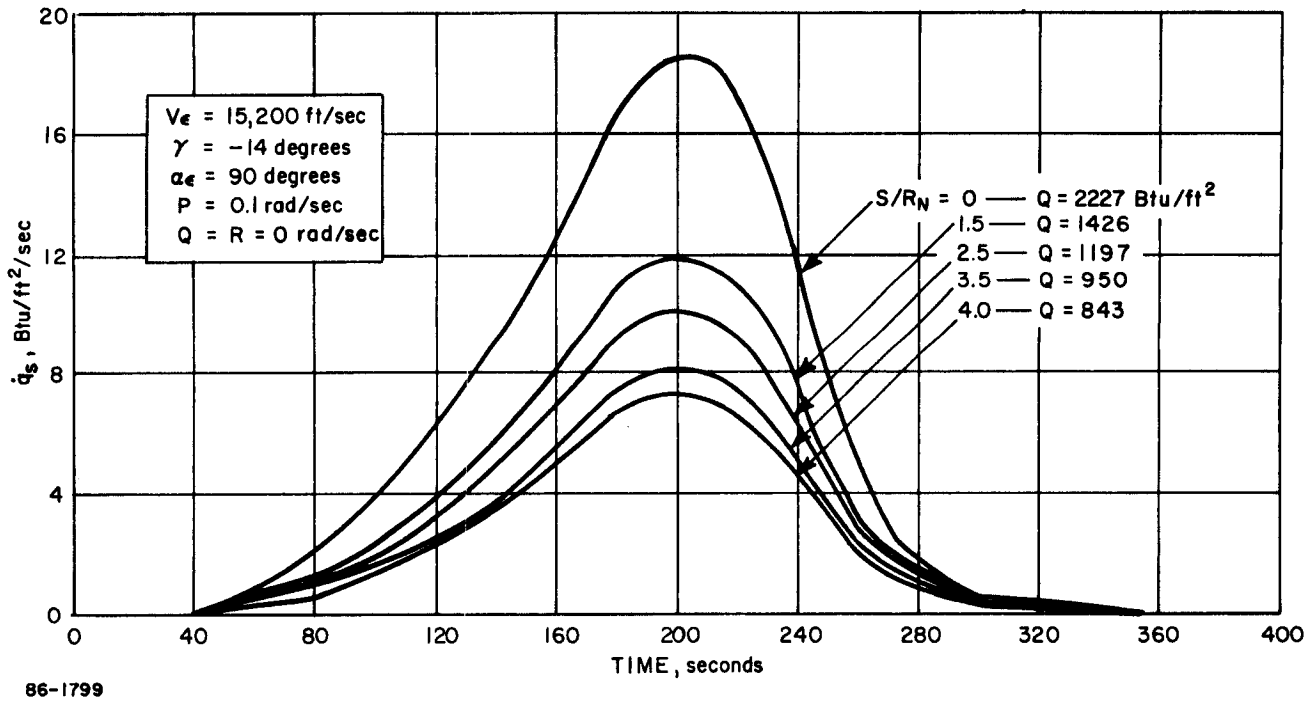

Figure 129 BLUNT CONE HEATING

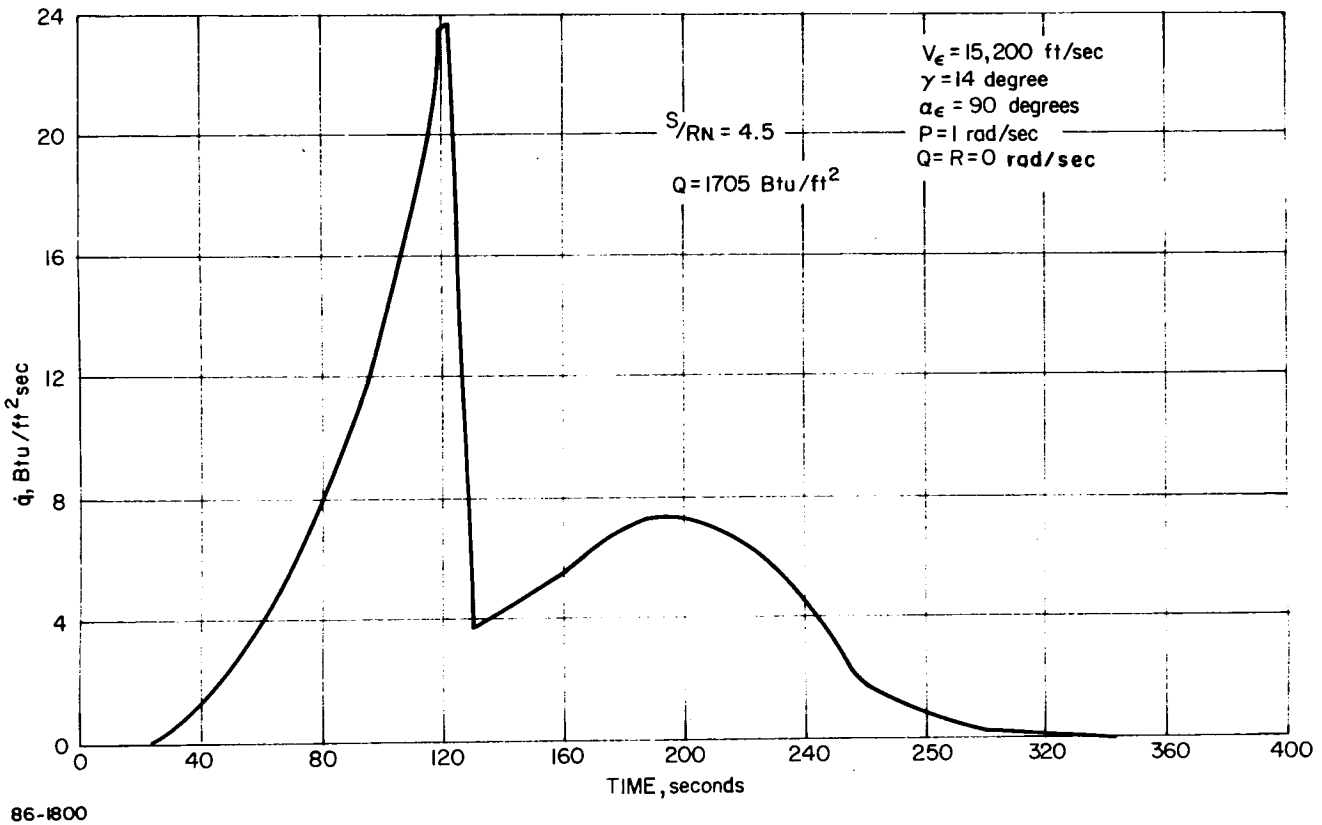

Figure 130 BLUNT CONE HEATING

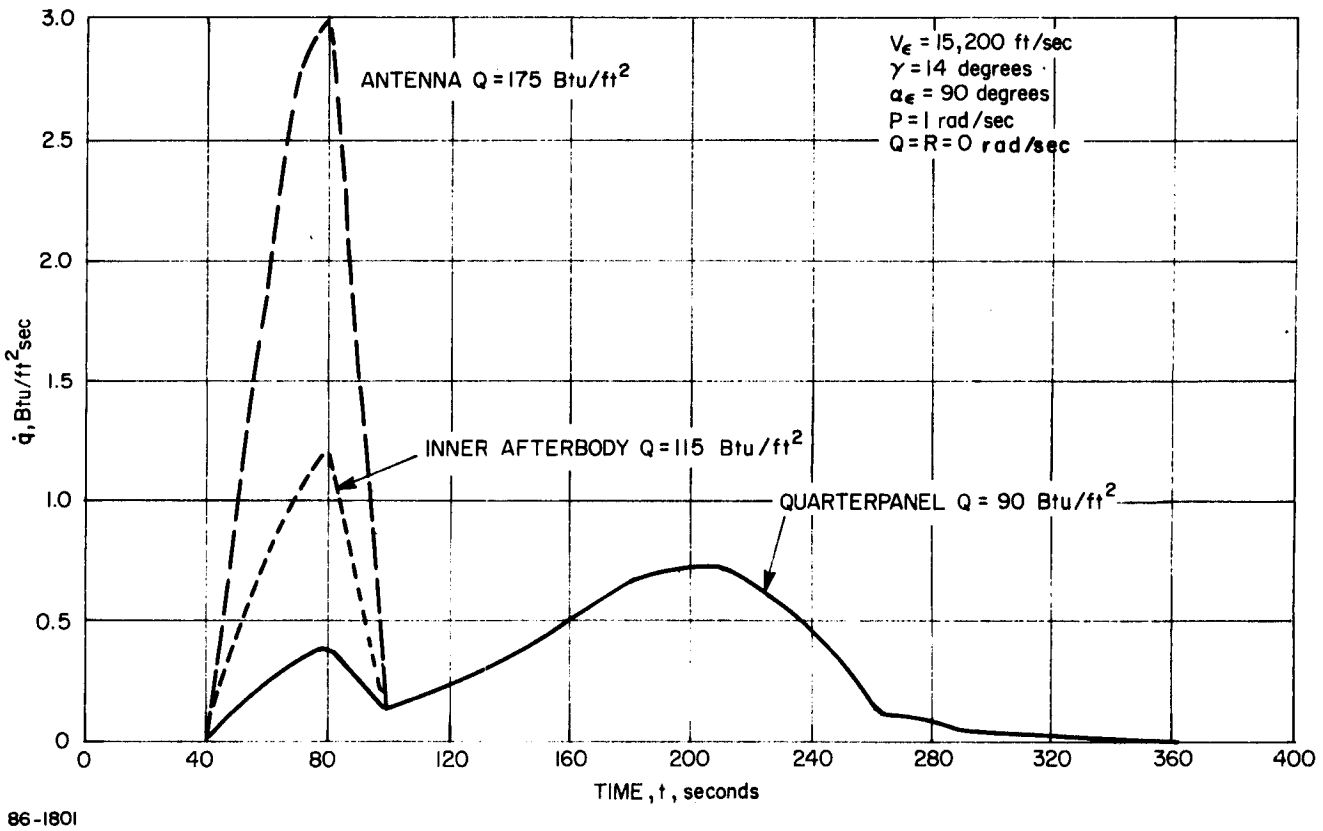

Figure 131 BLUNT CONE HEATING

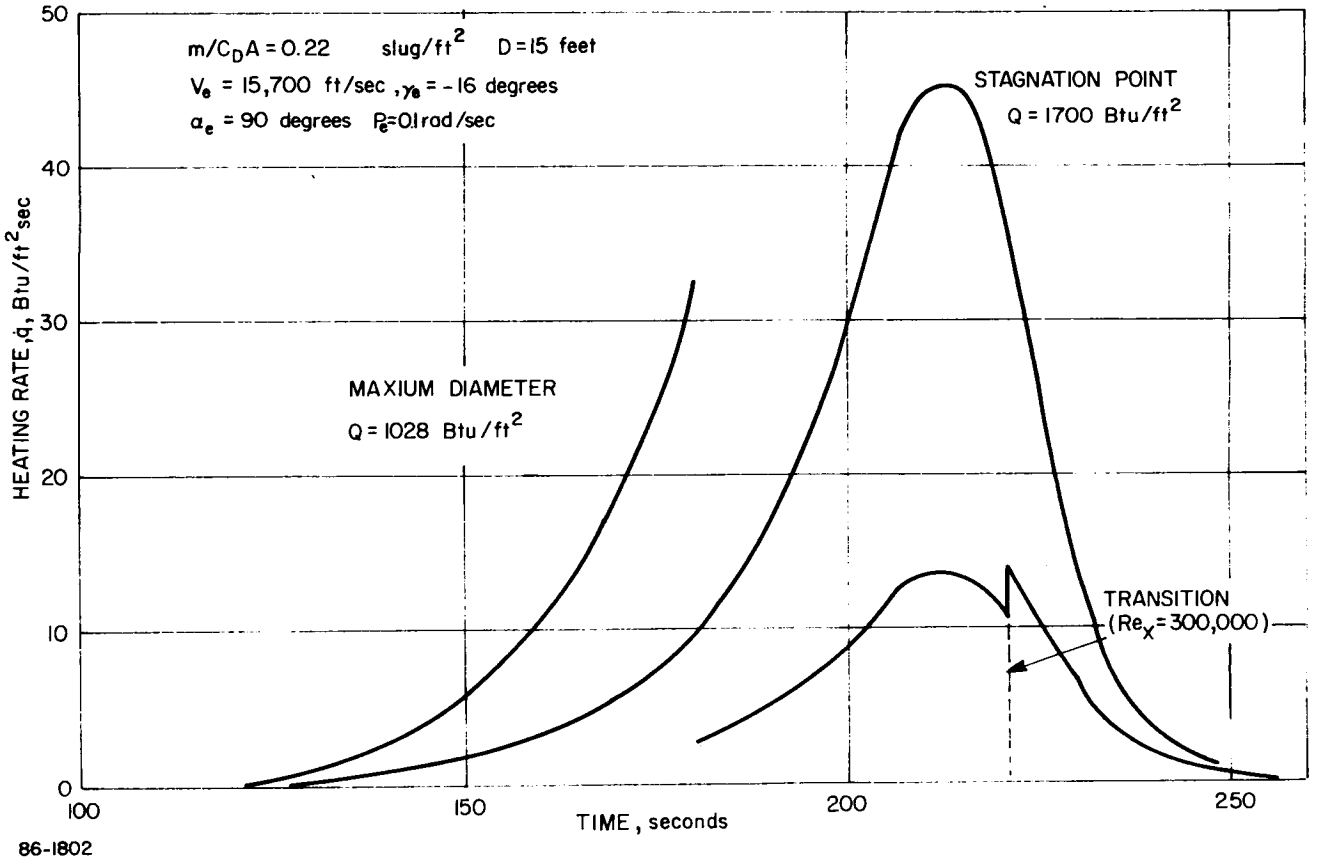

Figure 132 BLUNT CONE HEATING -- ATM VM-8

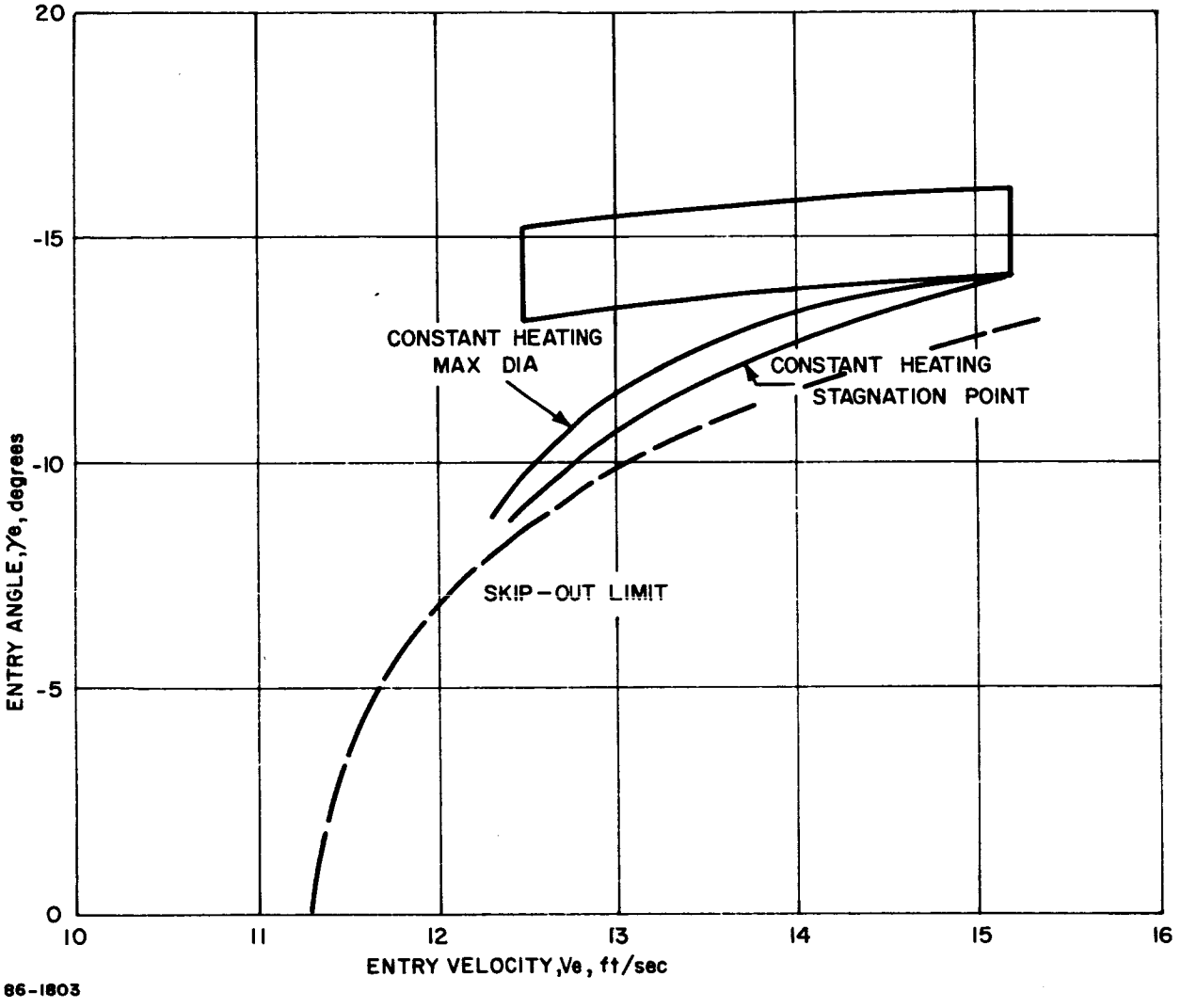

Figure 133 PERFORMANCE--HEATING

The variation of the heating over the vehicle for the design case is illustrated in Figure 134 which includes the critical heating for the various possible entry conditions.

1. Protuberances and Cavities-- Additional heating information was obtained to account for local effects such as the aggravations associated with protuberances and cavities. The methods and data used to obtain the aggravated heating rates around the TVC hardware yield rates ratio to rates encountered if there were no protuberances and cavities (see Paragraph 4.3.1.5). These "aggravation factors" were obtained for the design vehicle on the assumptions that (a) the cold-gas TVC nozzle was embedded in the heat shield, and (b) the hot-gas TVC hardware was completely exposed. Factors based on local undisturbed values are presented for this configuration in Table XXVII.

TABLE XXVII

TVC LOCAL HEATING AGGRAVATION FACTORS DESIGN CONFIGURATION

$(\dot{q} / \dot{q}_{local})$

Radial Station (R/R_B)	Angle Of Attack				
	0 degrees	30 degrees	45 degrees	60 degrees	90 degrees
0.90	1.0	1.0	1.0	1.0	1.0
0.95	1.0	1.0	1.2	1.5	1.5
0.97 (Cold-gas rocket)	3.0	2.0	3.0	3.0	3.0
0.98 (Shoulder tangent point)	1.0	1.0	1.6	1.3	1.0
1.0 (Maximum diameter)	2.8	1.6	1.6	1.6	1.6

Heating rates on the TVC hot-gas nozzles are shown in Figure 135 as a function of vehicle angle of attack. These factors are essentially unchanged from the predesign values since the hot-gas nozzles protrude from the additional OTWR heat shield.

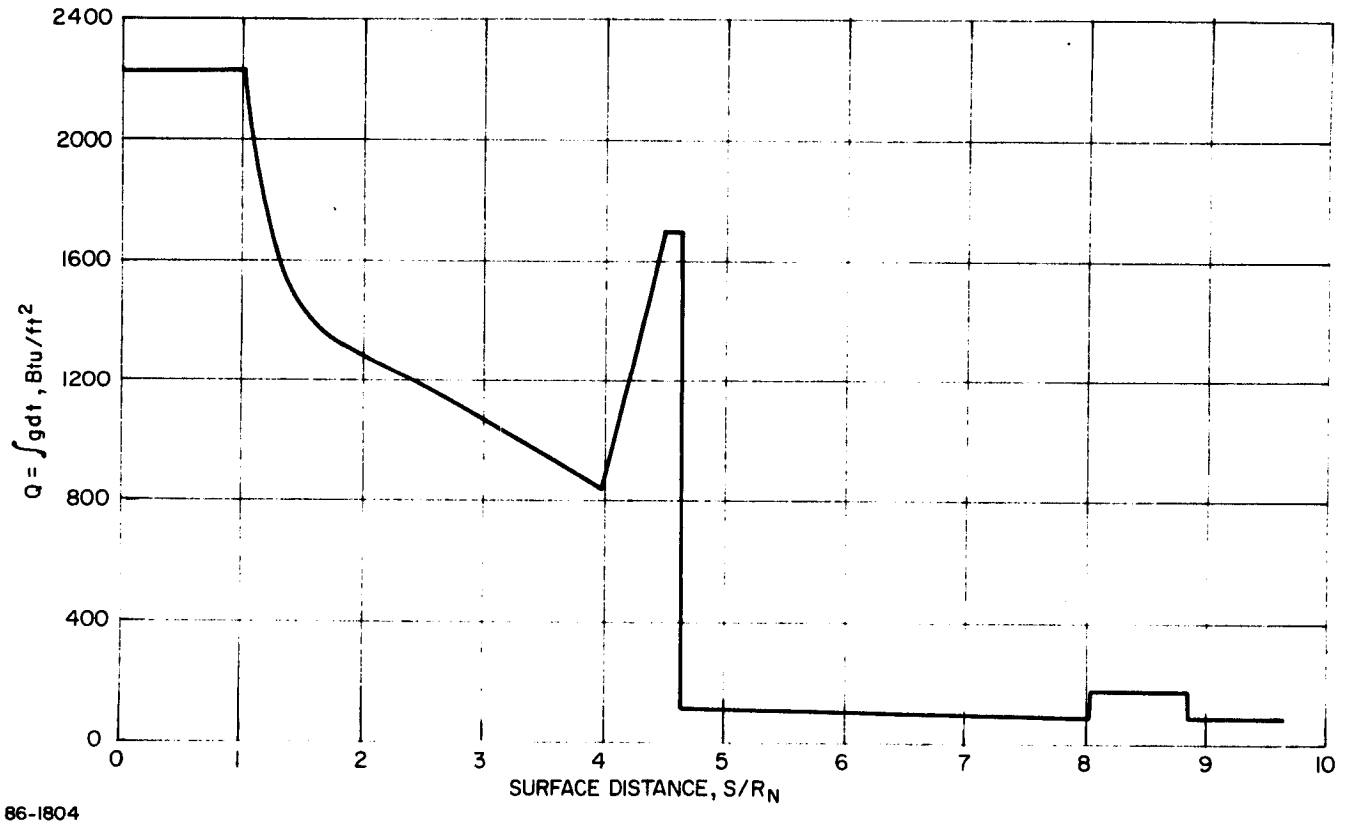

Figure 134 DESIGN HEATING DISTRIBUTION

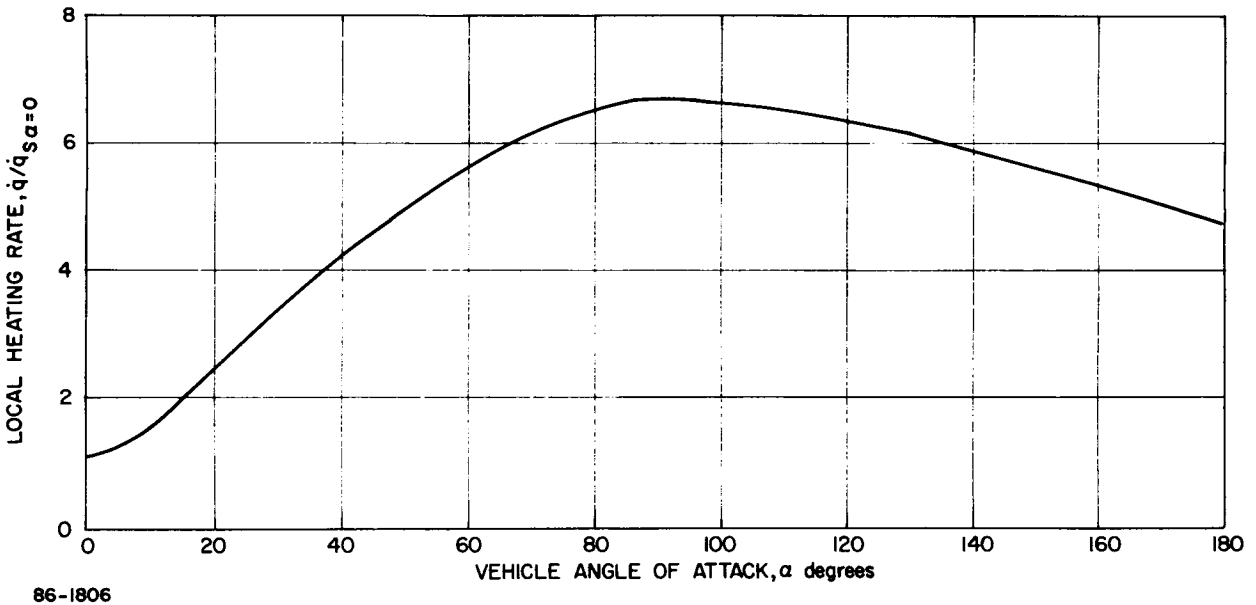

Figure 135 AERODYNAMIC HEATING TVC EXTERNAL NOZZLES AGGRAVATION HEATING FACTORS

It should be noted that the greatest aggravations occur around the lip of the cold-gas nozzle. The high heating rates experienced here are the result of coupling the aggravation factor due to lip heating with the factor due to heating in the wake of the hot-gas nozzle.

Figure 136 again shows the local heating aggravation factor, with a change in the reference value. The reference value here is the familiar which is nose stagnation point heating rate at zero-angle of attack. The abscissa in this figure is S/R_N - surface length/nose radius ratio, to facilitate the thermodynamic comparisons. This graph reflects the effects of angle of attack on local heating as coupled with the local aggravations. It also shows the extent of the region of influence of the aggravations.

The factors that have been affixed to evolve the heating aggravations are evaluated in the absence of blowing. Since ablation may exist these factors are conservative. (Blowing results in reduced aggravation). However, very little weight penalty is associated with the current configuration,

2. De-orbit Rocket Heating -- The entry heating over the back face of the forebody (secondary heat shield)shell and afterbody is augmented by the heating due to the expulsion of hot gases (rocket plume) by the de-orbit rocket. To improve the flow characteristics of the plume and to minimize the heating, an extension of the nozzle for the "shelf" motor was included. The heating for this extension and the subsequent afterbody heating were determined.

a. Nozzle Extension Heating Rates -- The design of the rocket motor and nozzle changed several times but the final design included a rocket engine with the characteristics listed in Table XXVIII.

TABLE XXVIII

BASIC ROCKET MOTOR CHARACTERISTICS

Chamber Pressure, P_c (psia)	450
Combustion Temperature T_c (°K)	3140
Mass Flow Rates $\dot{w}$ (lb/sec)	12.0
Throat Area, A*, (in^2)	4.00
Initial Expansion Ratio, ϵ_o	18.7
Expansion Angle, θ_N , (degrees)	18
Specific Impulse, I_{sp} , (seconds)	254
Exit Mach Number, M_e	3.88

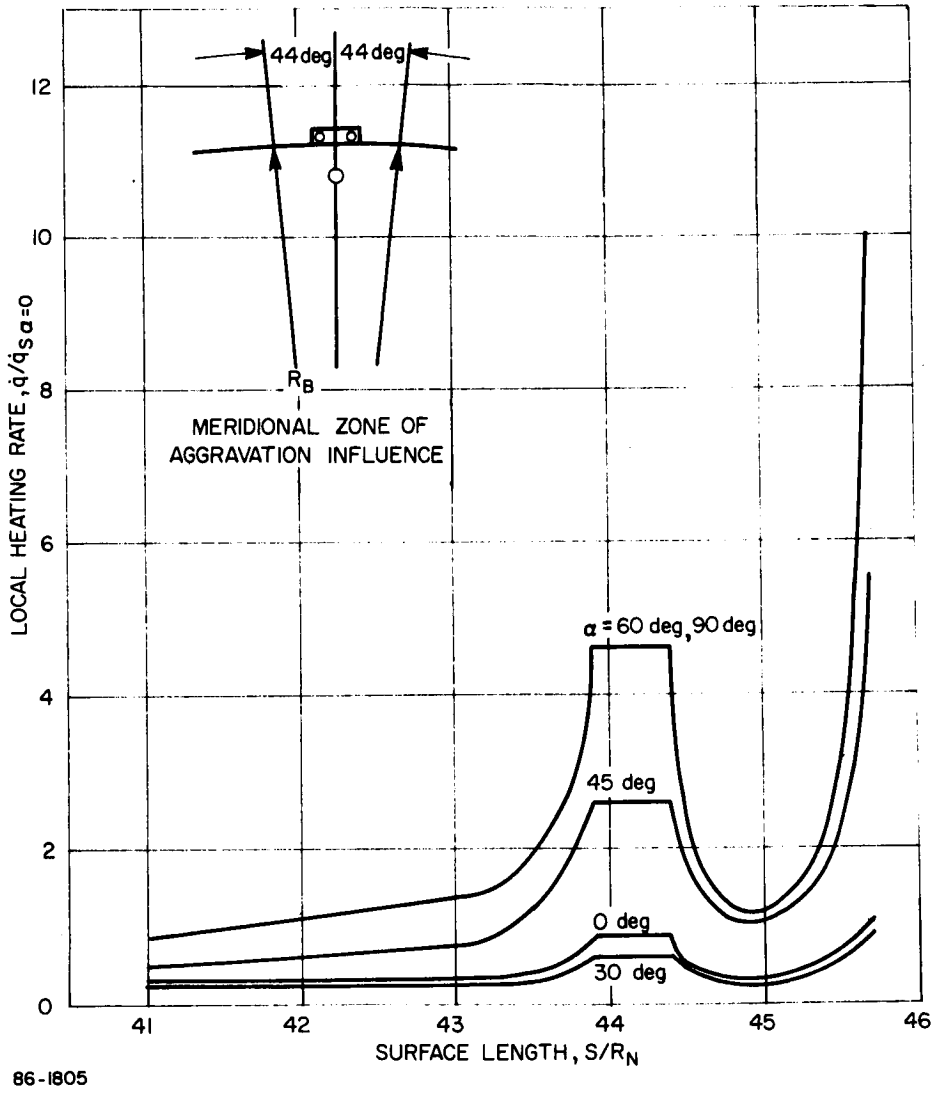

Figure 136 AERODYNAMIC HEATING TVC AGGRAVATION FACTORS

These characteristics were used in the computation of the nozzle extension heating rates. A 10-inch nozzle extension was added to this basic motor changing the overall expansion ratio to $\epsilon_f = 51.8$, and the exit Mach number to 4.685. Expanding from this Mach number to $M \to \infty$, the nozzle plume maximum flow angle was calculated to be $\theta_f = 107.1°$. Thus the exhaust flows (in part) back toward the lander afterbody. Based on these assumptions, heating rates to the inner and outer walls of the exhaust nozzle extension are presented in Figure 137. Heating on the outer wall is due to the nozzle boundary-layer "blowback" as detailed in Paragraph 4.3.17. Also presented in Figure 137 are the local recovery enthalpy ratios and the total enthalpy levels (h_s). The total enthalpy in the external flow is lower than that associated with the internal flow due to the energy dissipated by friction along the internal walls.

The local heat-transfer rate falls rapidly from 90.5 BTU/ft^2-sec at the extension lip. The external heat inputs decrease in the opposite direction from 26 BTU/ft^2-sec to a low of 1.5 BTU/ft^2-sec. Although these rates are relatively low, the total integrated heating will be approximately 3000 BTU/ft^2 at the minimum diameter, since the motor burn-time is about 33.3 seconds.

b. Rocket Plume Heating -- With the same rocket motor assumptions as detailed in the immediately preceding section, heating rates on the aft lander surfaces (reference design) are specified in Table XXIX.

TABLE XXIX

ROCKET PLUME HEATING - AFT LANDER SURFACES

Surface	Heating Rate (BTU/ft^2-Sec)
Rocket Body	1.0
Afterbody Inner Shoulder	8.8
Afterbody Outer Face	0
Antenna Dome	5.9
Antenna Cylinder	0
Aft Face of Cone Shell	0
Aft Ring	0
TVC Rocket Hardware	.8
Aerodynamic Flap	.3

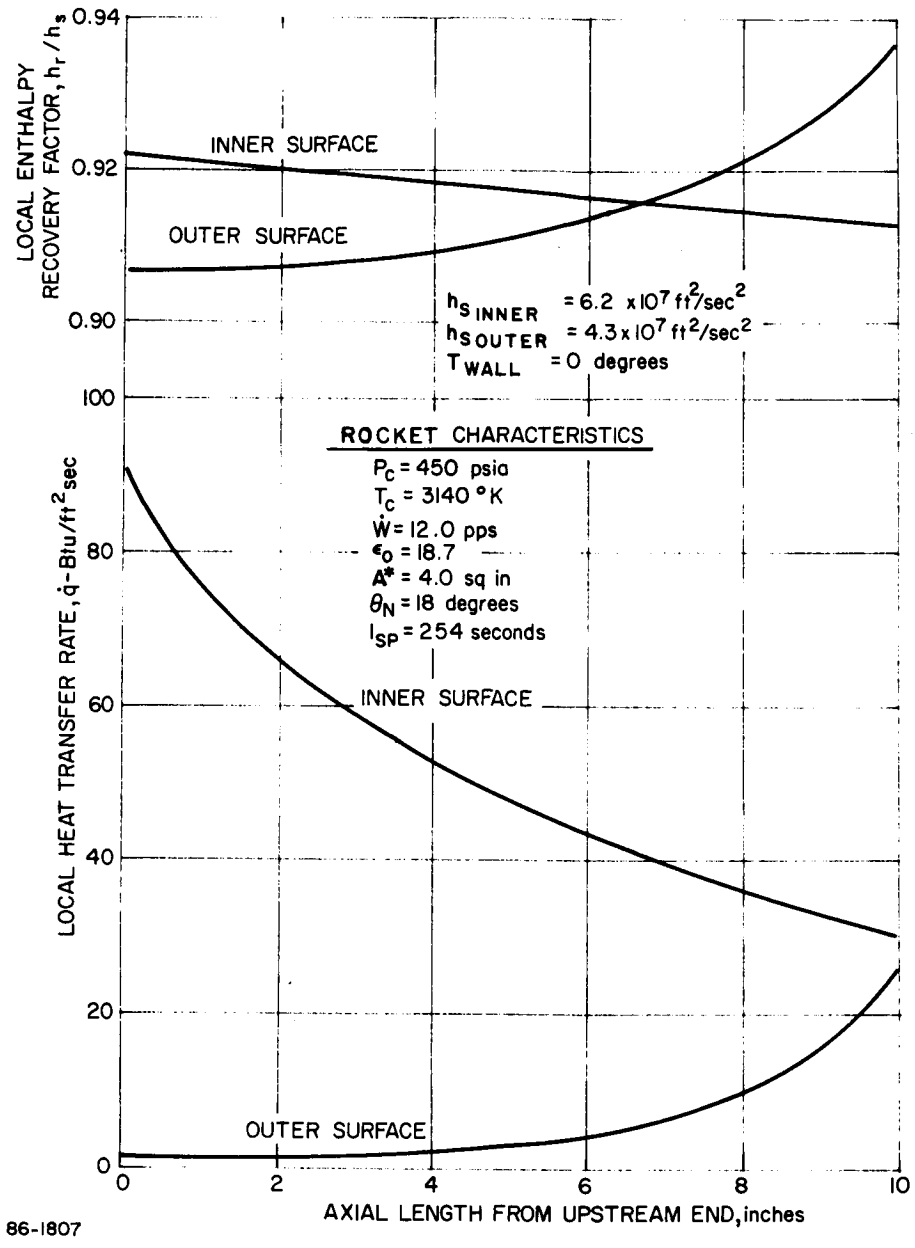

Figure 137 ΔV -ROCKET NOZZLE EXTENSION CONVECTIVE HEAT TRANSFER

Heating effects contributing to these values are the direct impingement of the plume and boundary layer blowback. Radiation heating was shown to be negligible in the section on analytical methods (paragraph 4.3.1.7). The highest heating rates occur on the afterbody inner shoulder and on the antenna dome.

On the first of these, stagnation of the blowback flow produces the high rate. On the antenna dome, a combination of the blowback flow, which is still near the stagnation condition, and plume impingement, which is very slight, produce the heating. Impingement alone is the cause of heating on the TVC rocket hardware (note that only the aft-facing hardware is affected) and on the aerodynamic flap. The zero values recorded in the table actually represent numbers which are considered negligible with respect to those used to design the heat shield required for rearward entry. It should be noted that the heating inputs due to de-orbit rocket firing are in addition to the aerodynamic heating at entry.

c. TVC Hot-Gas Rocket Heating Effects -- Heating from the hot-gas TVC rocket firing to the heat shield was investigated. Maximum possible integrated heating was found to be less than 17 BTU/ft^2, which is negligible compared to aerodynamic heating.

3.3.3.4 Loads

The critical loads are associated with the steepest entry at the maximum velocity. The rotation of the planet in effect steepens the entry angle but reduces the velocity (inertial to relative reference frame). The loads are more sensitive to the modified entry angle. As a conservative approach the design loads were specified for entry with rotation along the equator. The maximum loads are experienced in the VM-8 atmosphere.

Evaluation of entry for a Syrtis Major impact appeared to take under consideration loads most likely to be experienced. The possible range in azimuth being from 40 to 60 degrees (i.e. from southwest to northwest), the maximum loads would result for the maximum rotational entry(an azimuth of 40 degrees). Additional comparisons were made for entry with the critical heating conditions, which were at an azimuth of 60 degrees into the VM-7 atmosphere.

These results are tabulated in Table XXII together with a nominal case which represents the loads to be experienced for proper systems functioning (no failure mode) zero-angle of attack with no de-orbit dispersion.

The variation in these loads is nominal for entry into VM-8; however, a large variation is evident between the VM-7 and VM-8 atmospheres as expected.

3.3.3.5 Dynamics

The aerodynamic characteristics of the blunt cone utilized in the study resulted in adequate dynamic behavior for the reference design. No roll resonance was indicated in any of the results obtained with center of gravity offset. The maximum theoretical induced spin due to center of gravity offset for the VM-8 atmosphere is approximately seven revolutions per minute; however, no variation in spin was noted for the cases investigated.

Typical trajectory parameters are shown in Figures 138 through 141 for the extreme flight environs (low entry velocity and shallow angle into the VM-3 and high velocity, steep descent into the VM-8 respectively). Convergence was adequate for all cases including tumbling and various combinations of angular rates and angles of attack. No adverse damping is anticipated with the reference design, which would result in divergence in the angle of attack envelopes at transonic speeds. The effects of gusts, however, result in significant digressions. This is of interest for a chute failure, where the nosecap would be ejected and the terminal descent of the probe utilized for television picture taking.

Various wind profile gust combinations were investigated. The wind profile had a surface wind of 220 ft/sec with gusts of 335 ft/sec. The wind profile displayed a decay of 2 ft/sec per foot of altitude. The vehicle was subjected to gusts of approximately 10 seconds duration at various altitudes. In addition pulse duration was varied. The angle of attack variation was greater with the lower altitude of application since the wind component becomes more significant as the vehicle velocity decreases. Figure 142 illustrates two typical angle of attack and frequency variations. The initial spike in frequency is that due to the normal dynamic pressure rise associated with entry. Gust application near peak dynamic pressure results in negligible effect as shown for case 8 in this figure. A low-altitude gust resulted in an angle of attack of 40 degrees (case 7). The same gust applied in combination with high-altitude gusts results in significantly higher angles of attack (almost 80 degrees). No attempt was made to determine the application time for maximum divergence nor to apply the gusts at the natural frequency of the vehicle.

The angular motion of the vehicle axis is of prime consideration with respect to the use of television. Figures 143 and 144 present the

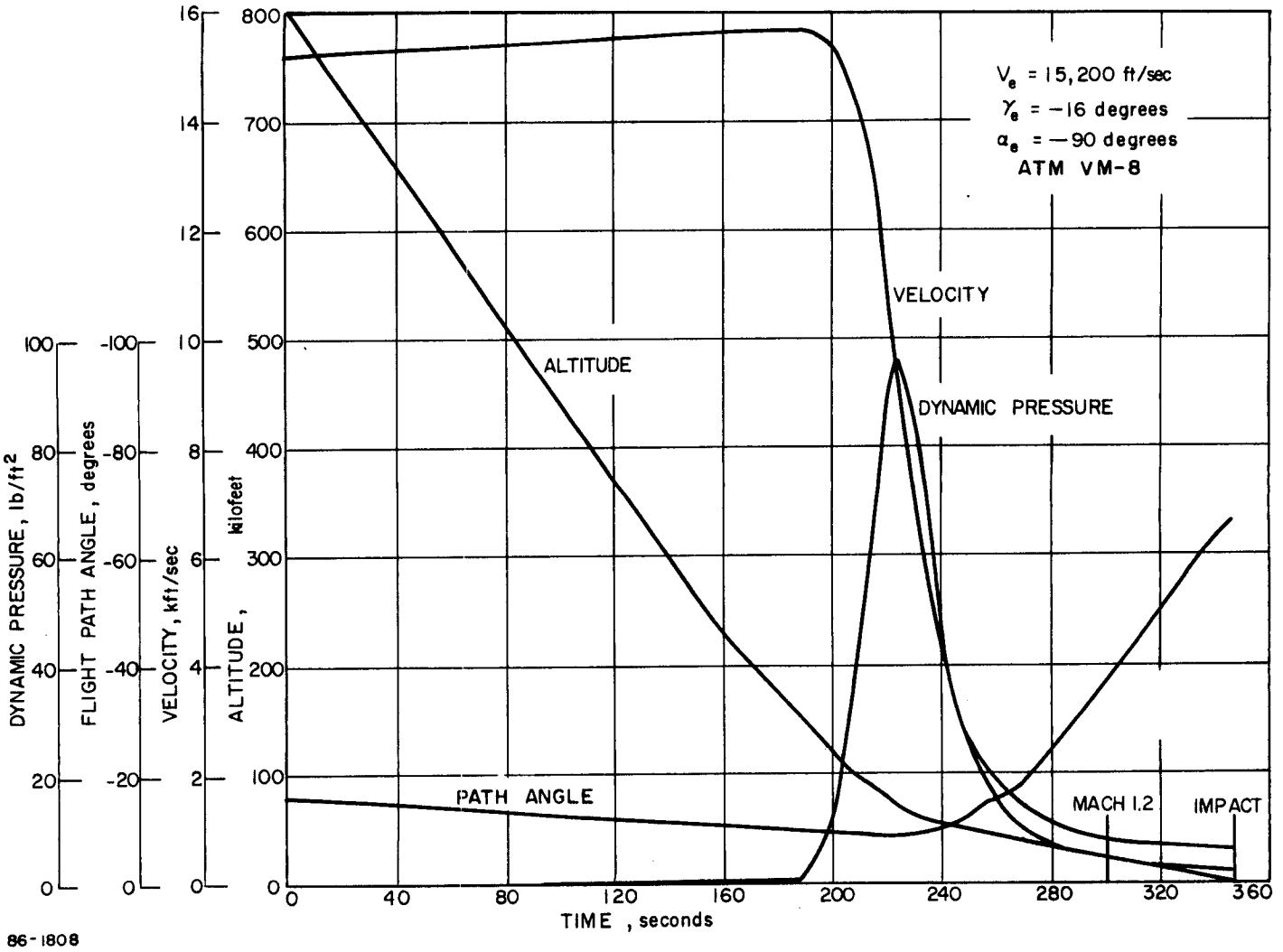

Figure 138 TRAJECTORY HISTORY -- ATM VM-8

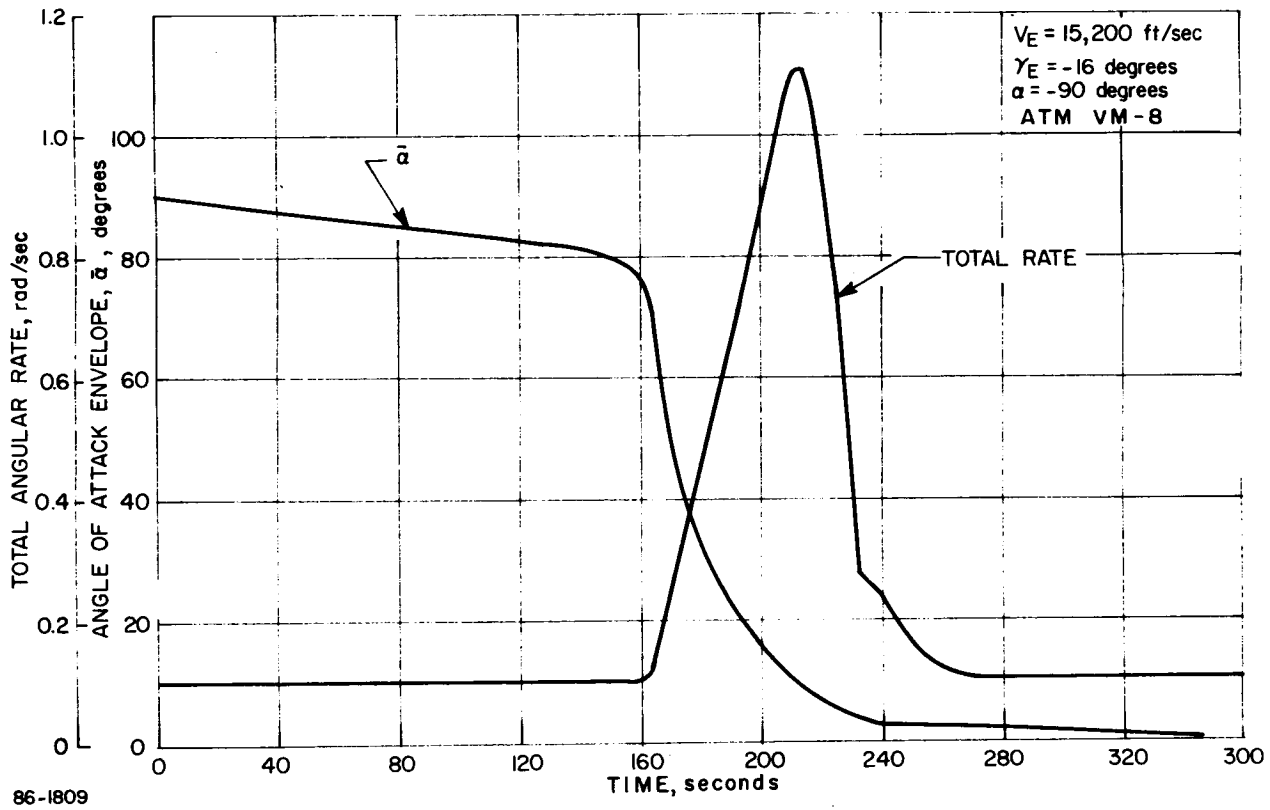

Figure 139 TRAJECTORY HISTORY -- ATM VM-8

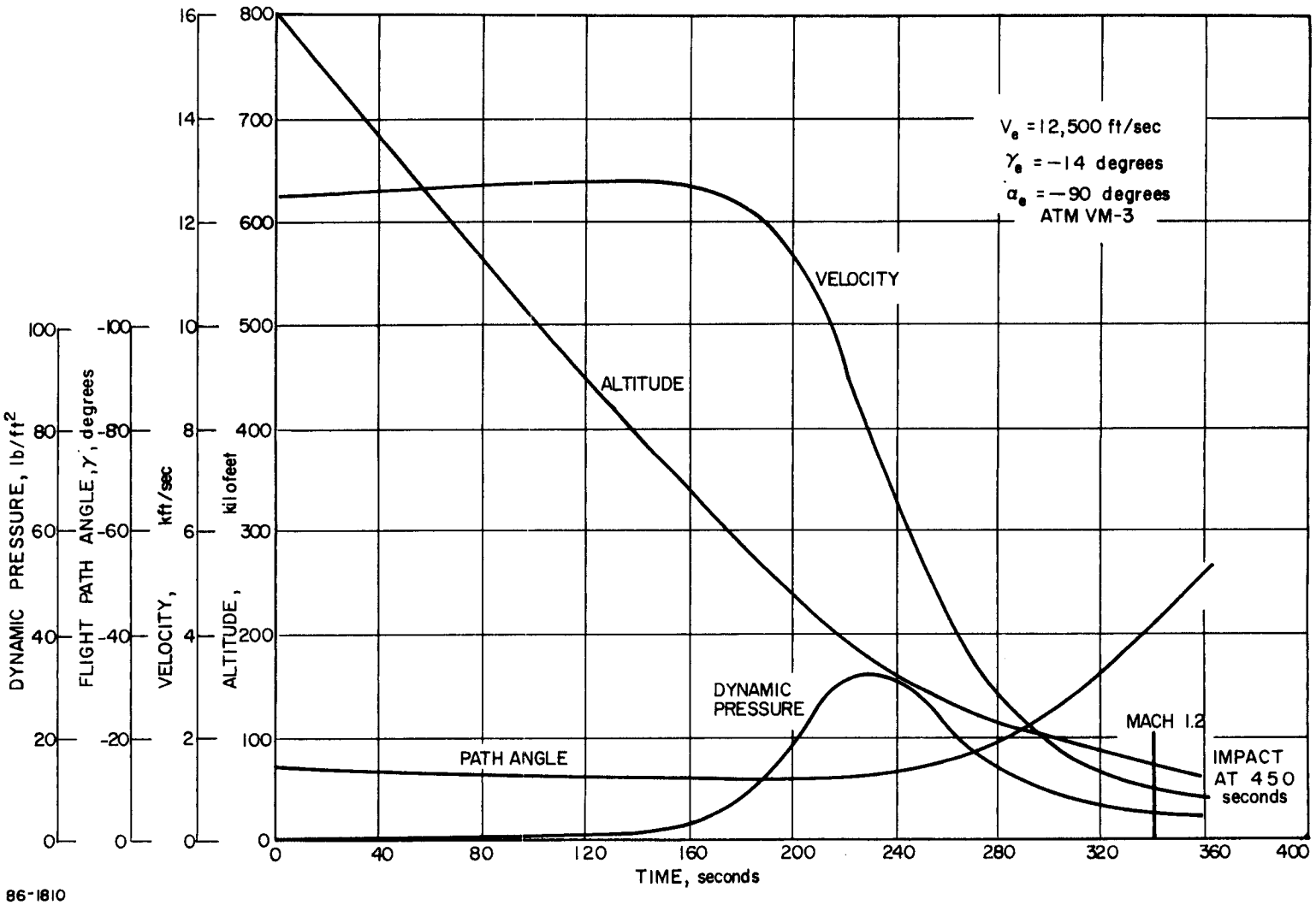

Figure 140 TRAJECTORY HISTORY — ATM VM-3

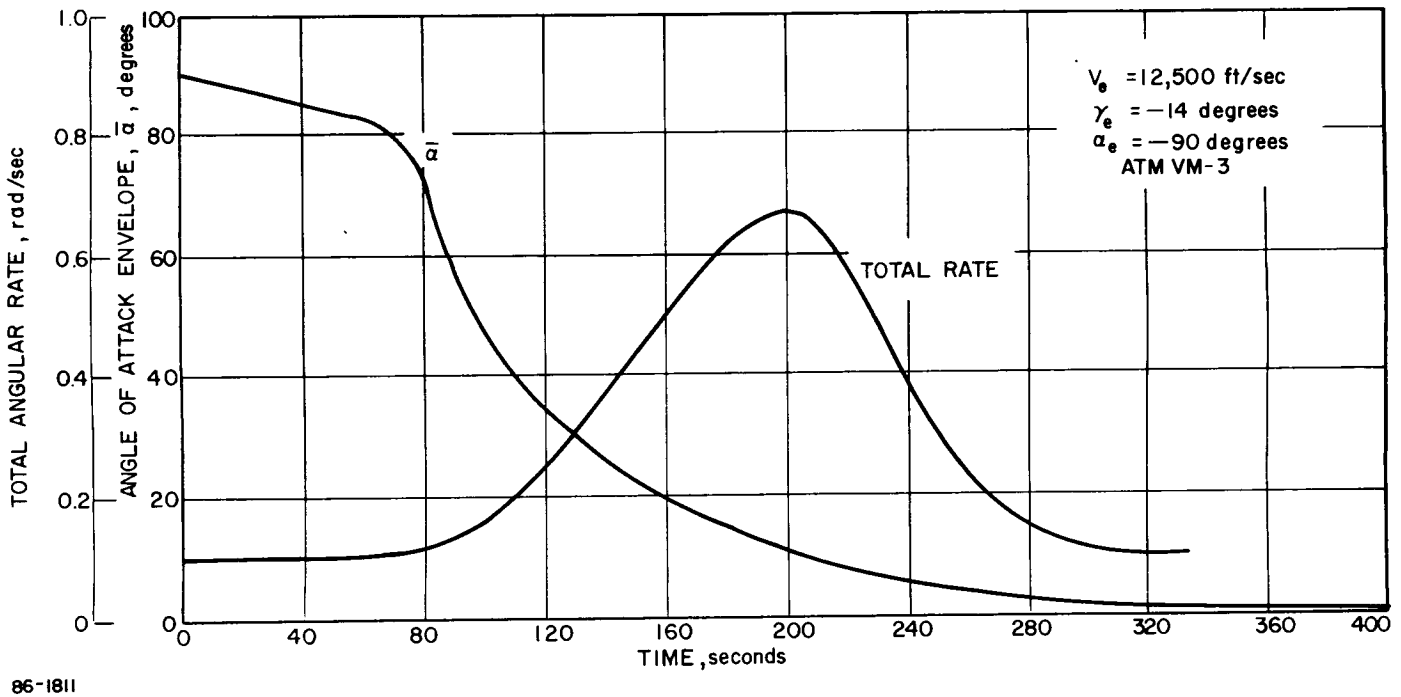

Figure 141 TRAJECTORY HISTORY -- ATM VM-3

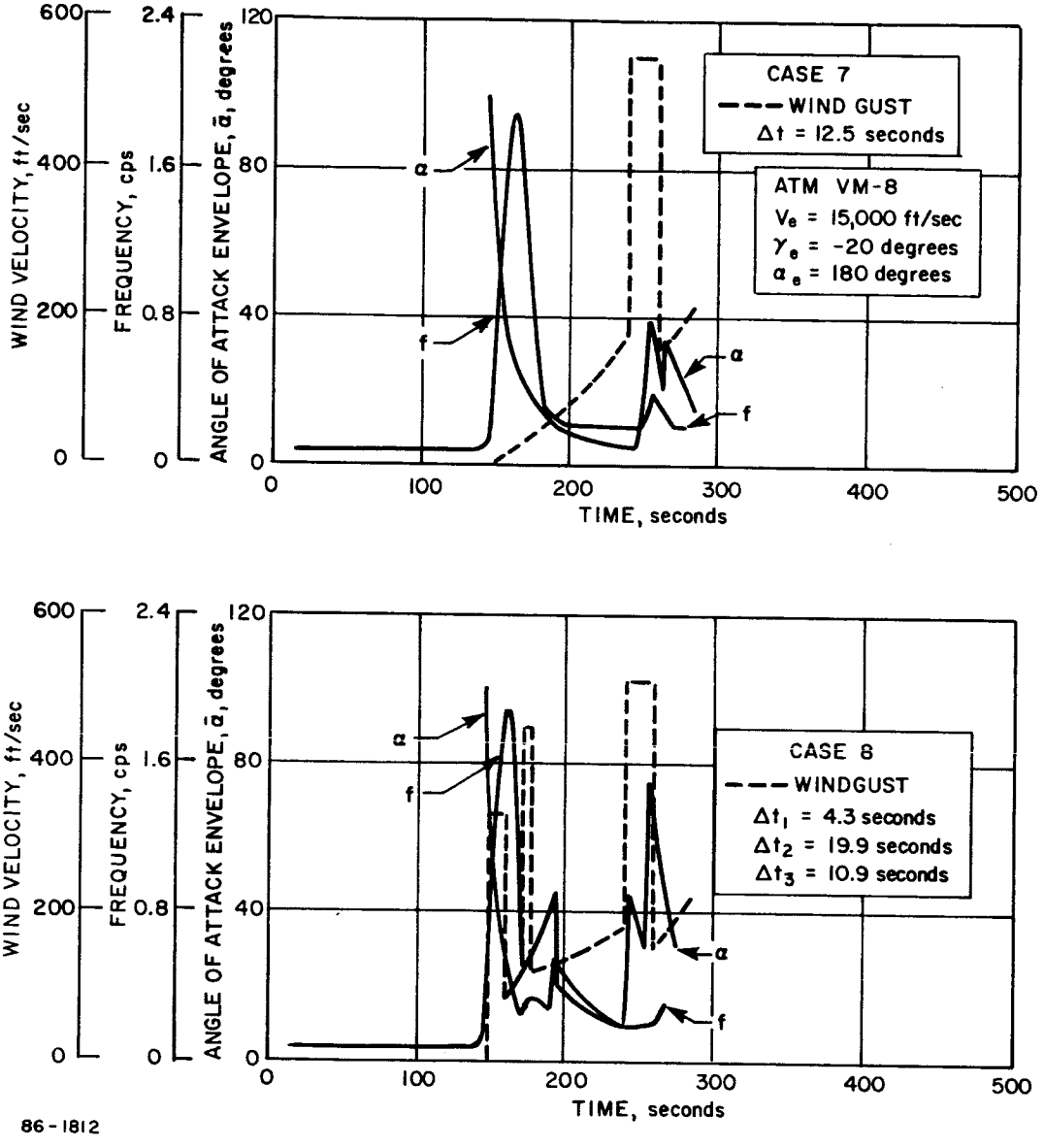

Figure 142 WIND GUST ANALYSIS

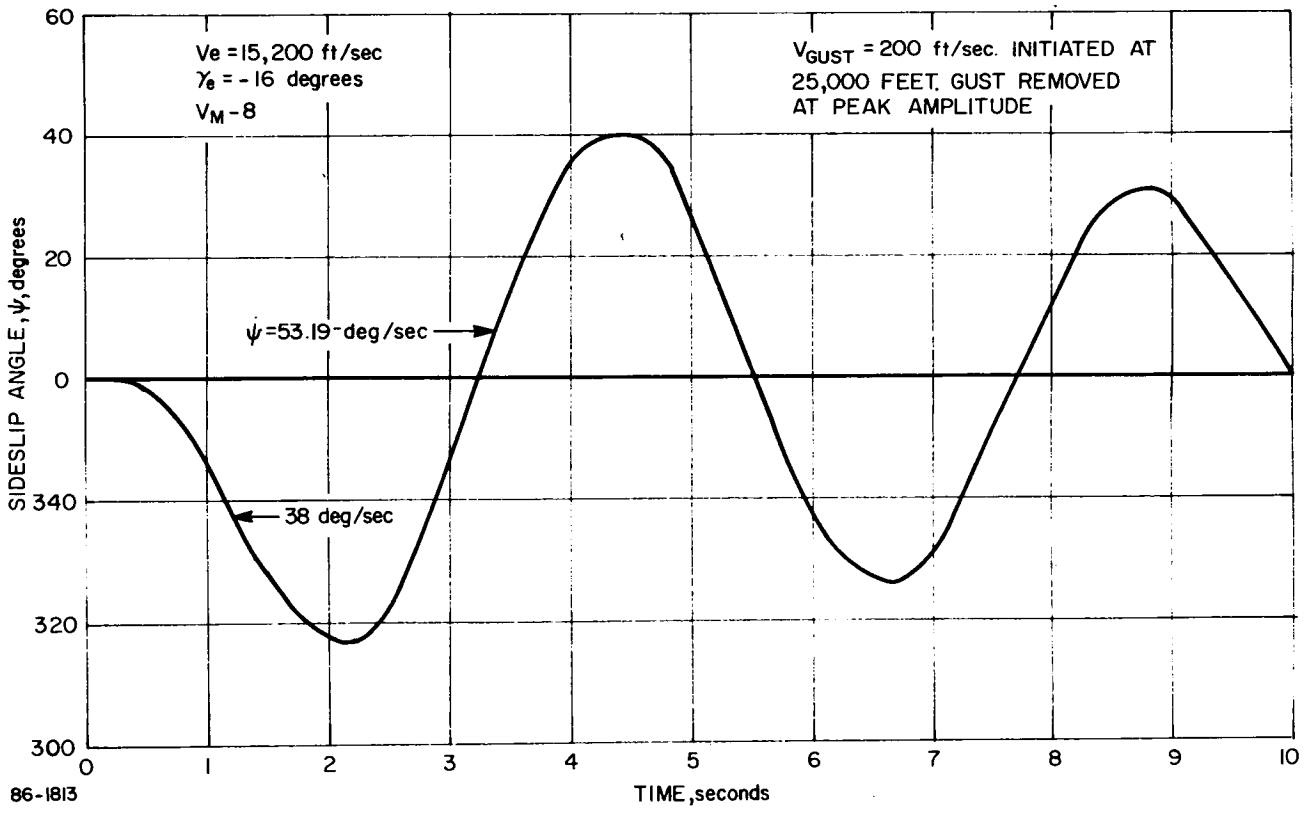

Figure 143 WIND GUST EFFECT

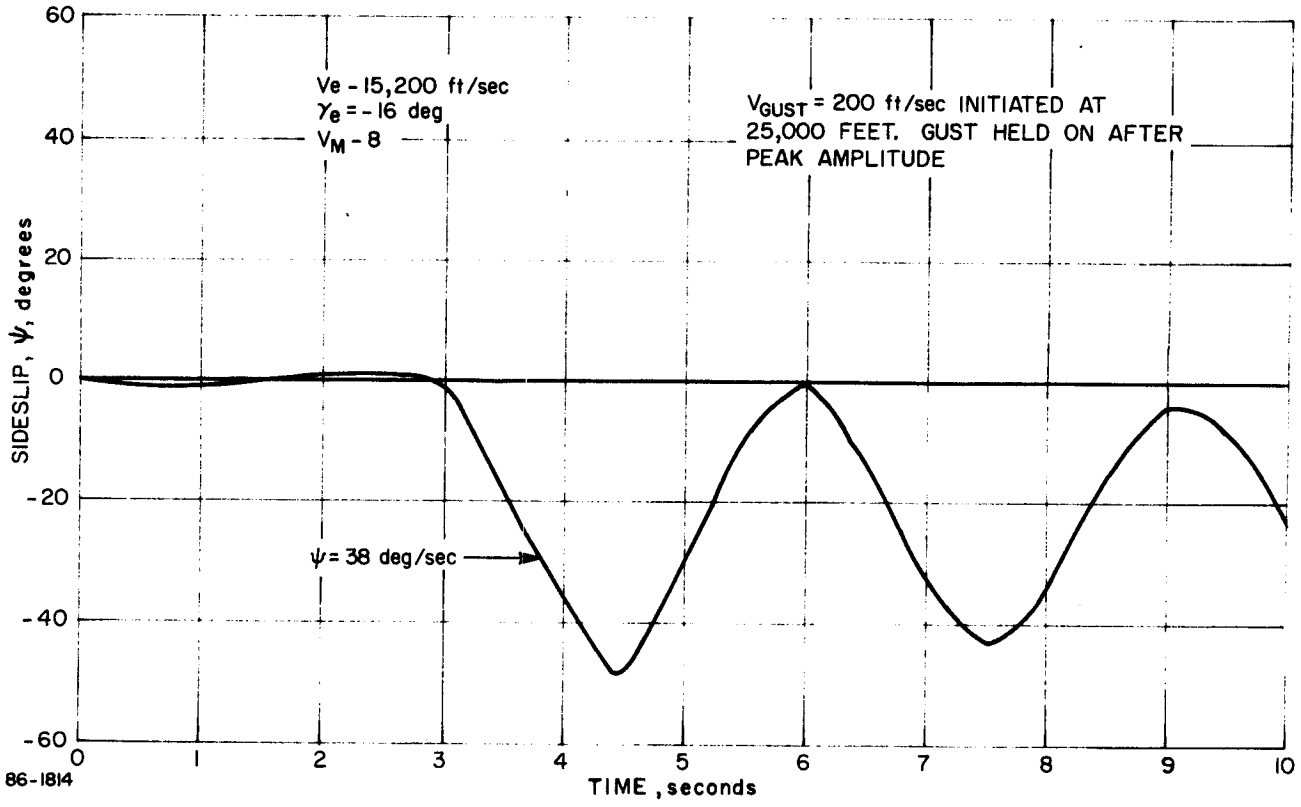

Figure 144 WIND GUST EFFECT

variation in the angle formed by the axis with the plane of the trajectory. The two cases are for a sustained gust (Figure 144) and a gust terminated at peak amplitude. There is a higher frequency associated with a sustained gust and only one-half the peak-to-peak amplitude (as is to be expected). The angular rate was as high as 60 deg/sec for the uninterrupted gust.

3.3.3.6 Blackout

The limits of blackout were investigated over the entire $V-\gamma$ entry map for the critical VM-7 atmosphere. Particle trajectories, using the reference ballistic coefficient of 0.22 slug/ft^2 and diameter of 15 feet, defined the velocity-altitude histories required. Figure 145 presents a typical history with the blackout limit superposed. For each entry angle, the altitudes of entry into, and exit from blackout are shown. The minimum entry velocity to avoid blackout is approximately defined by these curves.

By properly cross-plotting the data, the limiting $V_E - \gamma_e$'s may be defined. These are shown in Figure 146. To be noted is the fact that blackout virtually cannot be avoided within the operational entry map. Furthermore, contamination from ablation products has not been accounted for in this study. The ablation contaminants may be expected to produce at least an order of magnitude increase in electron density levels in the wake.

3.4 PROBLEM AREAS

The discussion of critical problem areas associated with the entry from the approach trajectory, in paragraph 2.3.5 of this book, apply to the entry from orbit as well.

The analysis for the entry from orbit studies indicated a significant increase in the heating when accounting for low-density effects. The two low-density effects considered were vorticity interaction and the variation of flow-properties along the boundary layer which approach conical values. Both of these phenomena are sensitive to the shock shape and/or detachment distance which in turn is dependent upon the density ratio, ρ_s/ρ_∞ . For normal test conditions this ratio seldom surpasses a value of 6 and, as such, the above effects are within the noise level of the test instrumentation.

Although theories are available (see paragraph 4.3.1.3 and 4.3.1.4) with which to determine these effects, further verification and corroboration is desirable. Conservatism has been introduced in the analysis to account for uncertainties. This is especially true for the boundary-layer growth which was obtained from similarity theory. Uncertainty exists with respect to the "effective" flow

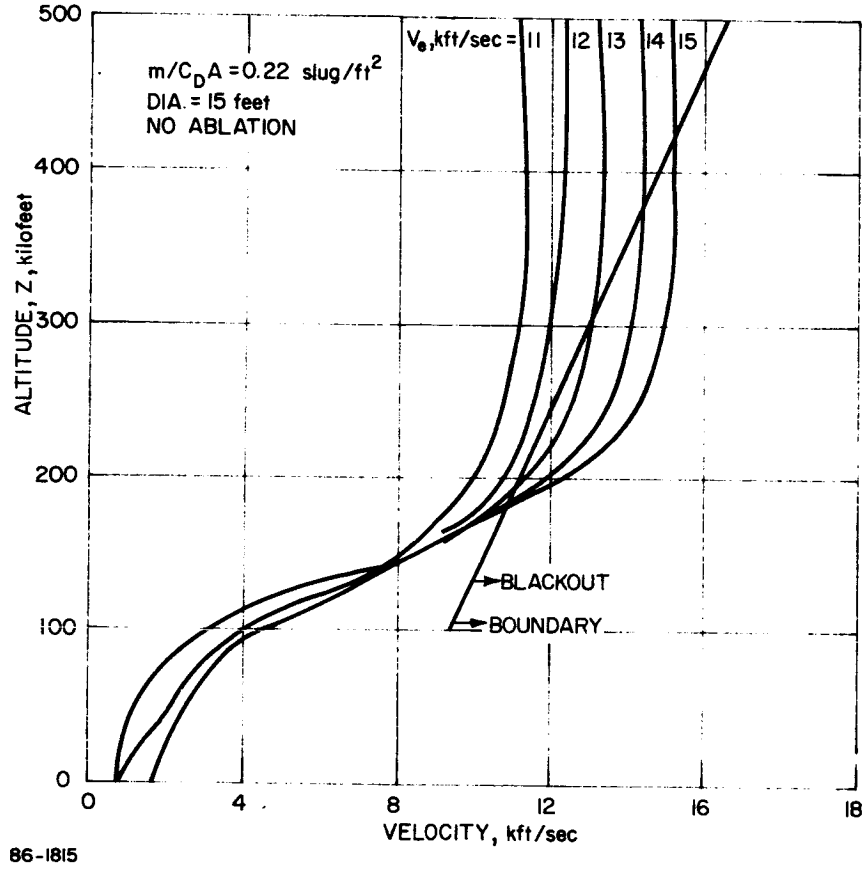

Figure 145 VELOCITY ALTITUDE HISTORIES

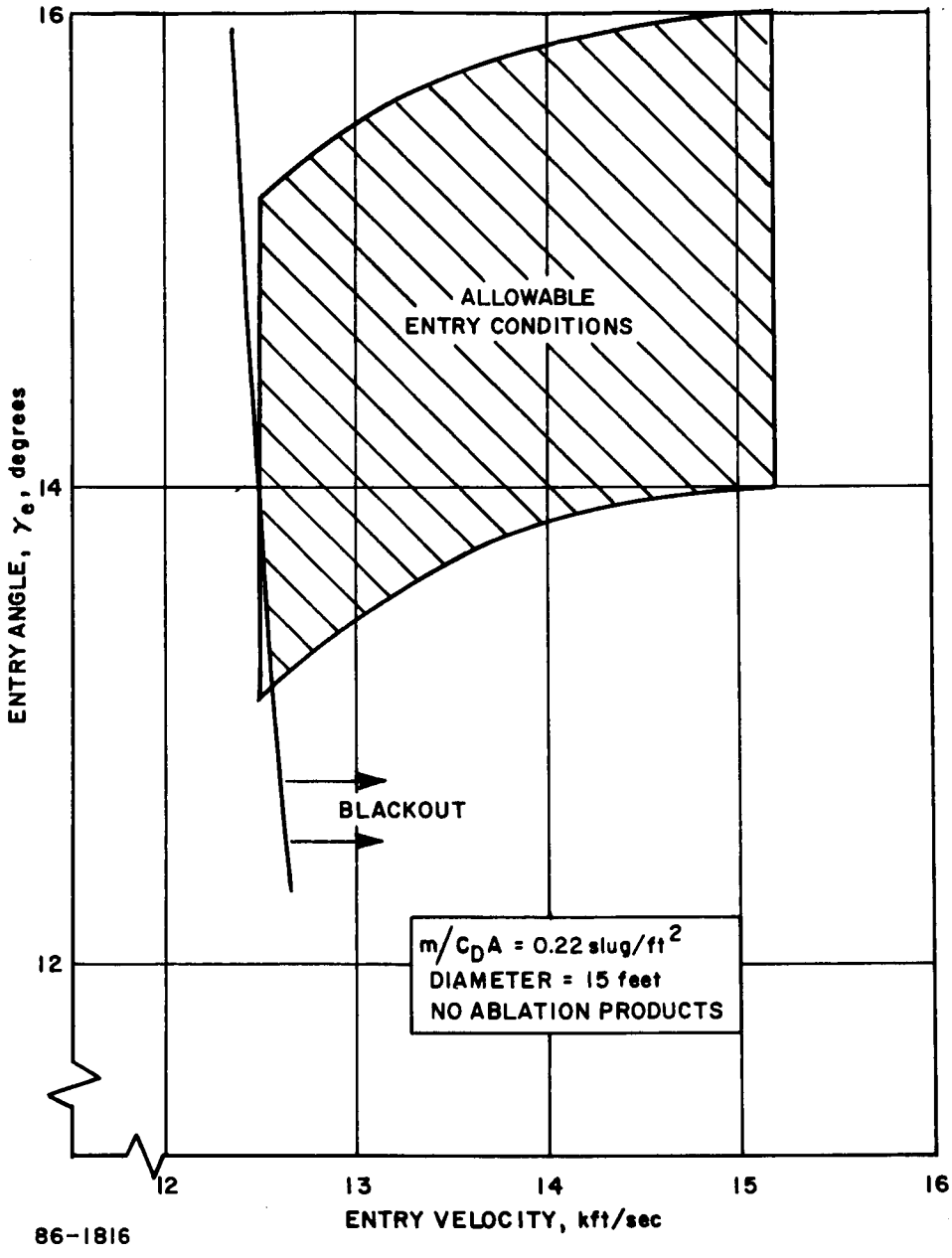

Figure 146 BLACKOUT BOUNDARY LIMITS

conditions external to the boundary layer. In the calculations the external conditions were obtained by means of a "mass balance."

In order to evaluate the theories adequately, density ratios higher than those normally available in test facilities are necessary; in addition, the energy variation behind the bow shock must be consistent with those associated with flight. Although various gases (such as Freon) can result in large density ratios, the energy level and variation present problems, since gas kinetics and chemistry are introduced if the energy levels are too high.

4.0 AERODYNAMICS - THEORETICAL ANALYSIS AND METHODS

The vehicle environments are evolved through a sequential process starting with the establishment of the vehicle characteristics in terms of aerodynamic coefficients which are necessary to determine the vehicle flight histories. These trajectories are necessary to define the flight environments (velocity, free-stream density, angle of attack, etc.) during the critical phases of entry (loads, pressures, heating, etc.). A parametric analysis provides bounds or ranges of interest relative to parameters such as the angle of attack. The flow field analyses may then proceed in order to establish the pressure distributions, shock shapes, thermodynamic properties, species concentrations, radiative intensities and convective and radiative heating distributions. The methods used for the Blunt Cone and Apollo were similar; the tension shell will be described separately. In addition, the same methods and results were found to be applicable to both entry from orbit and approach trajectory.

4.1 AERODYNAMIC COEFFICIENTS

The aerodynamic coefficients provide the means for evaluating the performance and environmental flight conditions. The aerodynamic data were obtained from numerous sources, while the tension shell data were provided by NASA/LRC. The blunt cone data were obtained from References 6-8. Since the angle of attack range for the data was limited, the variation was obtained by modifying the Newtonian predictions by the data. The modified Apollo required extensive investigation since no data exist for the precise nose geometry. However, a number of spherical arc-segment configurations were available to interpolate for the required geometry ($R_N/R_B = 2.4$). Where the data were deficient with respect to angle of attack effects, the modified Newtonian approach was taken.

4.1.1 Real-Gas Effects

The real-gas effects have been investigated with the conclusion that the effect on the drag may be accounted for if the drag coefficient is based upon the stagnation pressure, rather than the dynamic pressure. The variation of the approximate stagnation to dynamic pressure ratio ($2 - \rho_\infty/\rho_s$) was investigated for the atmosphere considered. A range of trajectories (M/C_DA, γ_e and atmospheres) was used to determine the variation of this parameter with Mach number. It was found that for the Models 1, 2, and 3 atmospheres, the ideal air data for the drag coefficients could be modified by the parameter K, where

$$K = \frac{(2 - \rho_\infty/\rho_s)\ \text{Gas}}{(2 - \rho_\infty/\rho_s)\ \text{Air Data}}$$

Figure 147 shows the variation of this parameter with Mach number, two straight-line segments being sufficiently accurate to describe the complete Mach number range.

With respect to the VM-4, 7, and 8 atmospheres, it was found that the same procedure was adequate for modifying the drag coefficient, although the VM-7 atmosphere does not correlate as well. Using the same variation for the entry from orbit as obtained for the entry from the approach trajectory results in a conservative variation (approximately 1 percent, see Figure 148).

This correction was applied to the axial force coefficient only. Whereas the axial force is representative of the absolute pressures acting, the coefficients such as normal force and pitching moment depend critically on the distribution. Real-gas solutions were used on the tension shell shape and indicated an improvement in the stability, with a possible correlation with the density ratio; however, insufficient calculations are available at present to verify this. The blunt cone and modified Apollo blunt-body solutions (single-strip integral method) have not resulted in any indicated trend for the normal force and pitching moment coefficients.

To evaluate or substantiate the above approximation, ($P_s/q_\infty = 2 - \rho_\infty/\rho_s$) an inviscid blunt-body flow-field program was utilized. This program (single-strip integral method) was used to obtain both an ideal-gas solution and a real-gas solution for air. The flight conditions were selected to correspond to conditions representative of those during the critical phases of Mars entry. The flight conditions were a velocity of 18, 900 ft/sec at an altitude of 200, 000 feet (equilibrium conditions were used) corresponding to a density ratio, ρ_s/ρ_∞ of 14. 5. The evolved pressure distributions were used to determine the drag coefficients. The ideal-gas computations were done for the test conditions for which data were available (γ = 1. 4, M = 9. 0, and M= 3. 98, for the blunt cone and the modified Apollo shapes, respectively).

It is to be expected that the pressure distributions would conform closely to the Newtonian prediction (the shock is coincident with the body for γ = 1. 0) since the real-gas shock standoff distance is reduced approximately by the ratio of the density ratios and the specific heat ratio at the stagnation point is approximately 1. 15. The evolved pressures are illustrated in Figures 149 and 150, indicating that this hypothesis is correct. The deviation from the Newtonian is associated with the singularity at the maximum radius (the sonic point) in addition to the shock being detached.

The evolved drag coefficients, compared with those of the tension shell, are given in Table XXX.

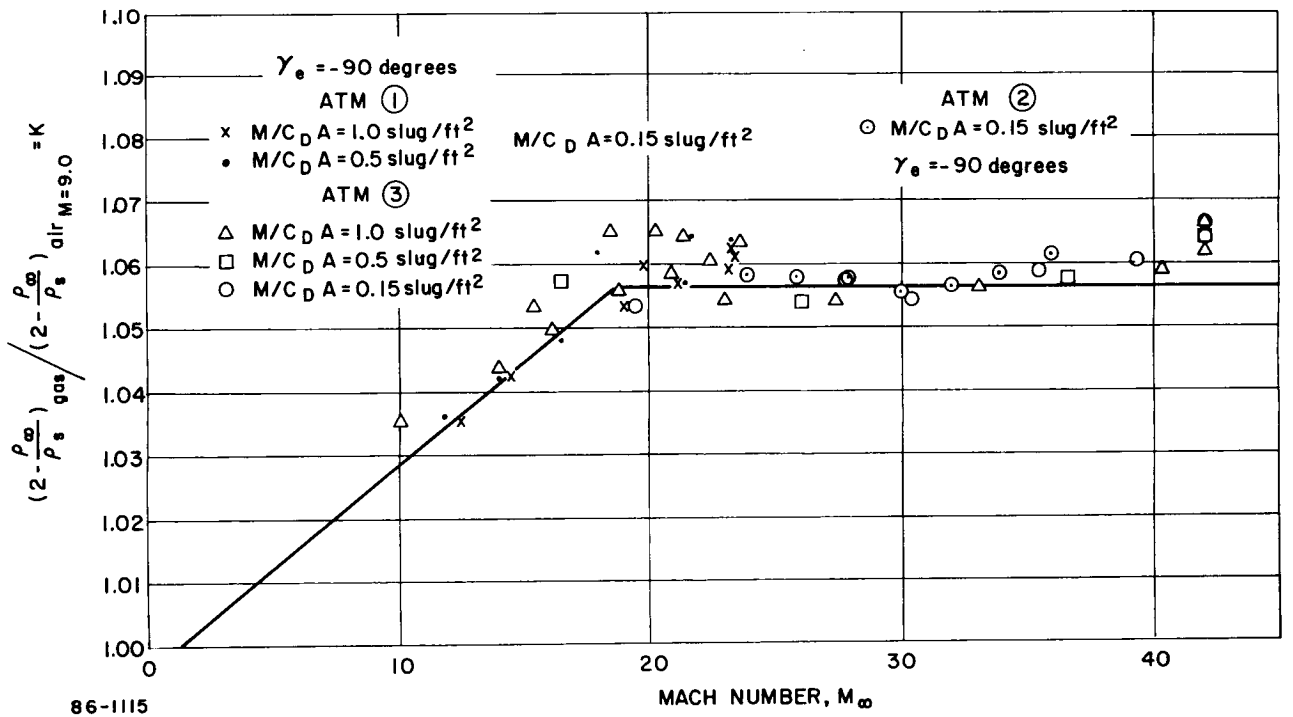

Figure 147 COEFFICIENT CONVERSION PARAMETER (K) VERSUS MACH NO. (M)

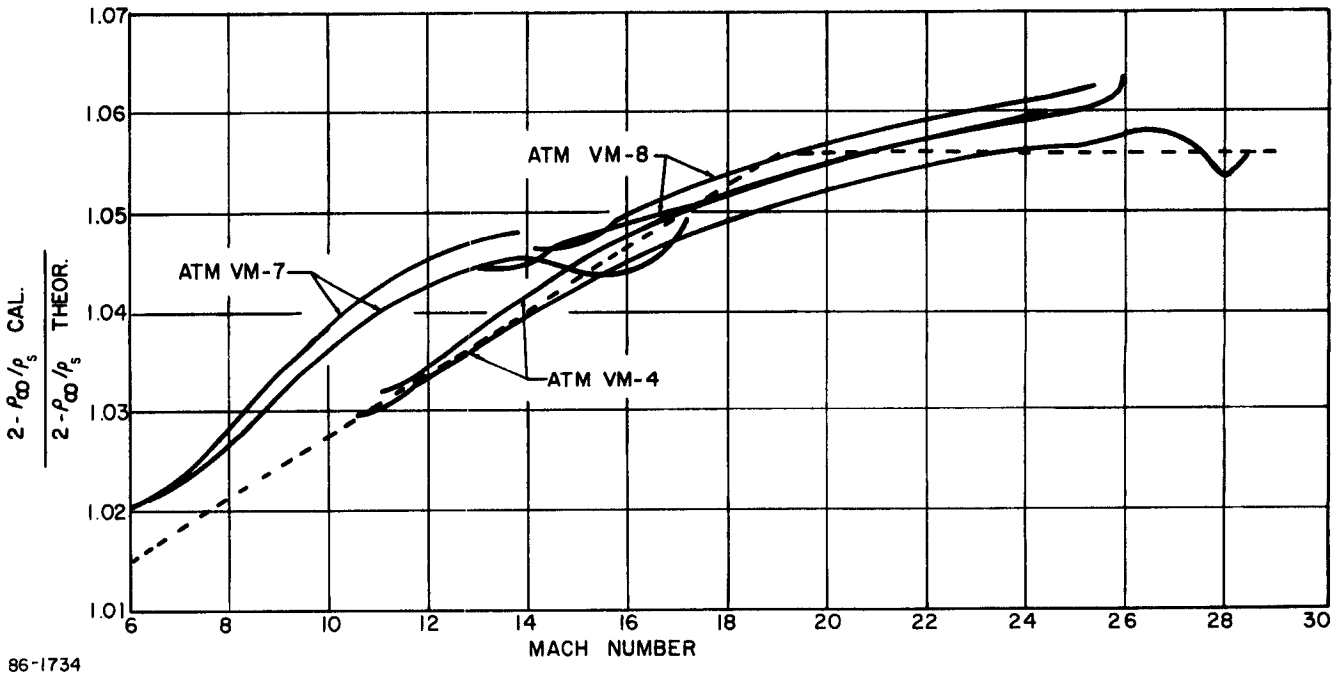

Figure 148 COEFFICIENT CONVERSION PARAMETER -- MODIFIED ATMOSPHERIC

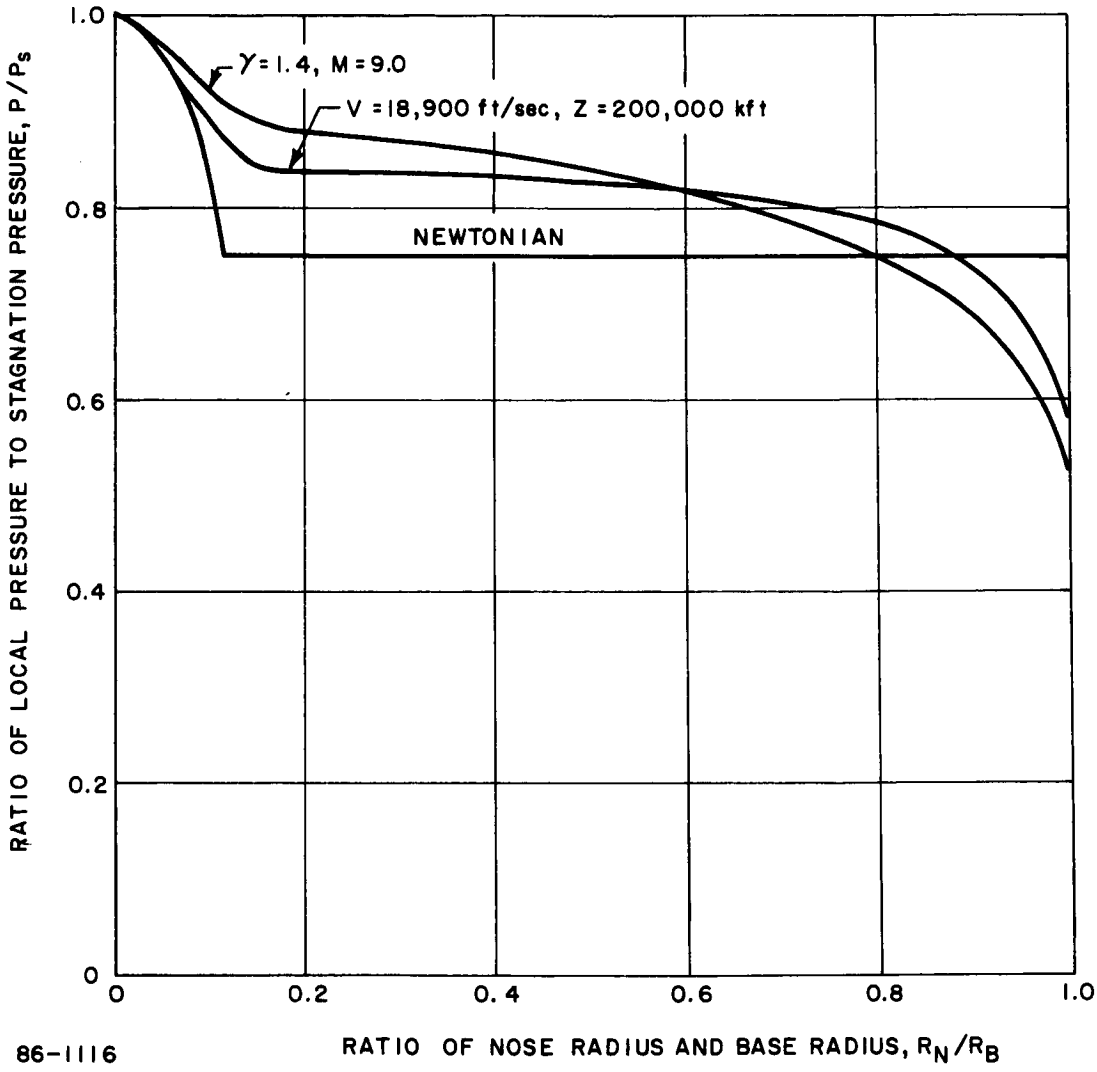

Figure 149 PRESSURE DISTRIBUTION--BLUNT CONE

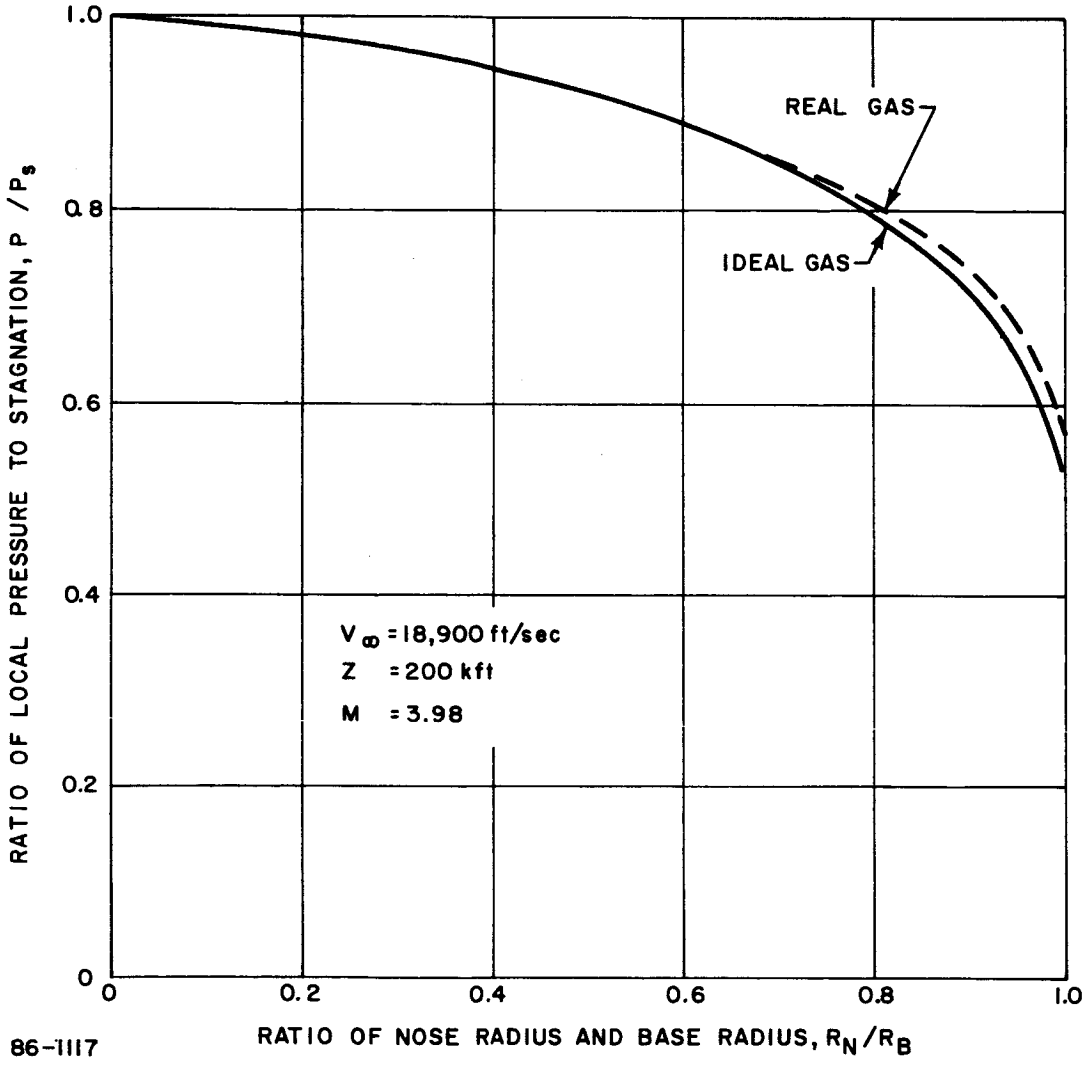

Figure 150 PRESSURE DISTRIBUTION--MODIFIED APOLLO

TABLE XXX

HYPERSONIC DRAG COEFFICIENTS

Shape	Blunt Cone	Modified Apollo	Blunt Tension Shell
Newtonian	1.50	1.82	1.20
Test	1.53 (M = 9.0)	1.58 (M = 3.98)	1.6 (M = 20)
Ideal-gas calculation	1.42 (M = 9.0)	1.52 (M = 3.98	---
Real-gas calculation	1.51 (M = 18.9)	1.62 (M = 18.9)	1.71 (M = 21.6)
Stagnation pressure correction on ideal-gas test data	1.62 (M = 9.0)	1.70 (M_{test} = 9.0	1.7 (M_{test} = 8.0

The ideal-gas calculation yields lower drag coefficients where the data exist; however, the trends appear to agree with the correction made with the stagnation pressure.

4.1.2 Afterbody Performance

An afterbody is required to protect the payload during the heat pulse, and to provide a center of pressure location which is aft of the c.g. at all angles of attack at hypersonic Mach Numbers.

A parametric study was undertaken to determine the optimum geometry of a blunted-cone afterbody. The parameters varied were bluntness ratio, cone angle, and ratio of afterbody base diameter to vehicle diameter, as illustrated in Figure 151.

The basis of comparison is the center of pressure location. Figure 152 shows the results of the study of an afterbody which starts at the maximum vehicle diameter. Maximum stability (most aft c.p. location) is obtained with the smaller cone angles and smallest bluntness ratio, cone angle having the greater effect.

The same trend is seen with the modified afterbody in Figure 153. The final choice of an afterbody design will depend on the c.g. location of the entry vehicle and the minimum area which will both enclose the payload and provide the minimum acceptable stability at large angles of attack.

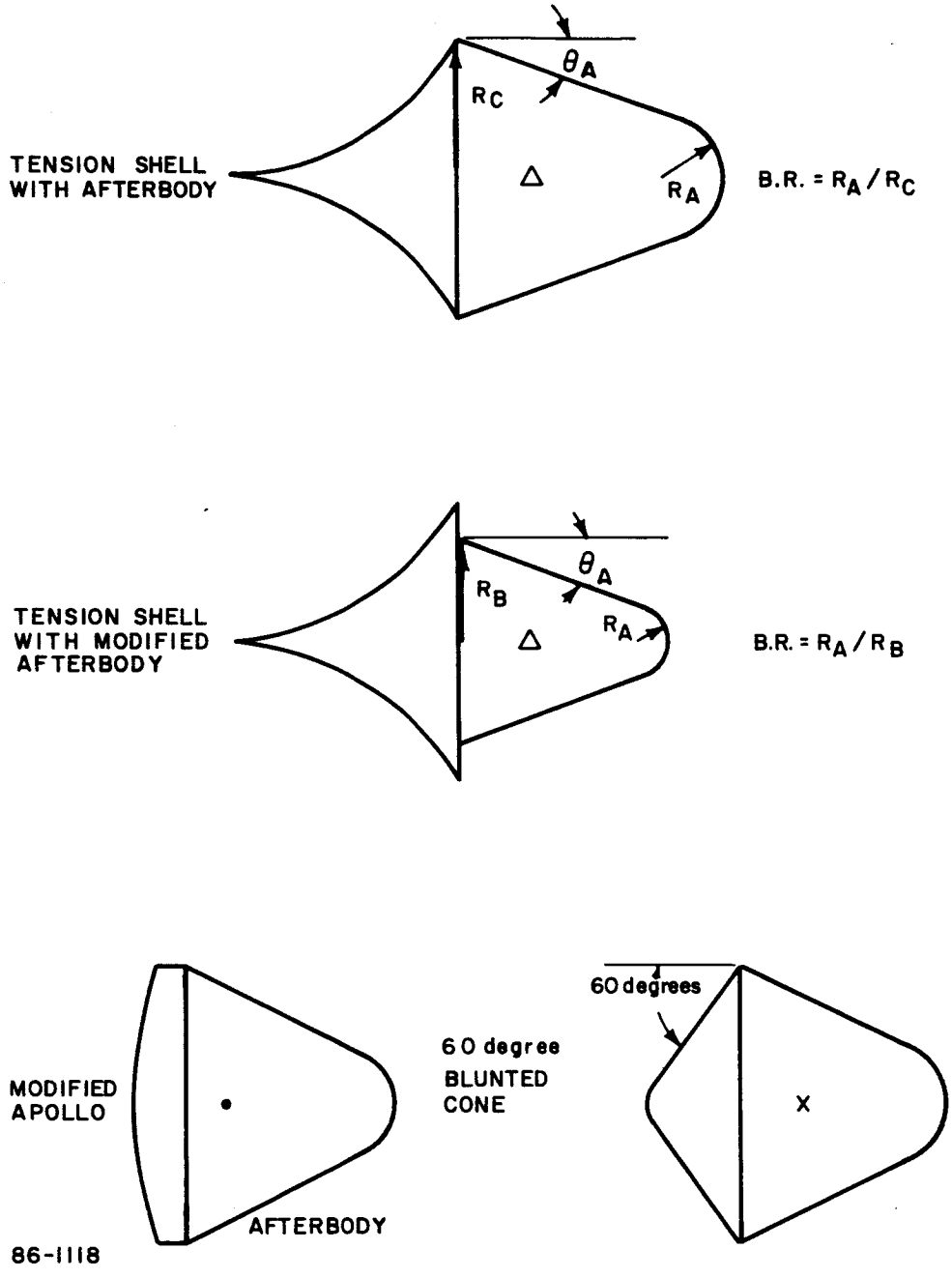

Figure 151 BASIC CONFIGURATIONS FOR AFTERBODIES

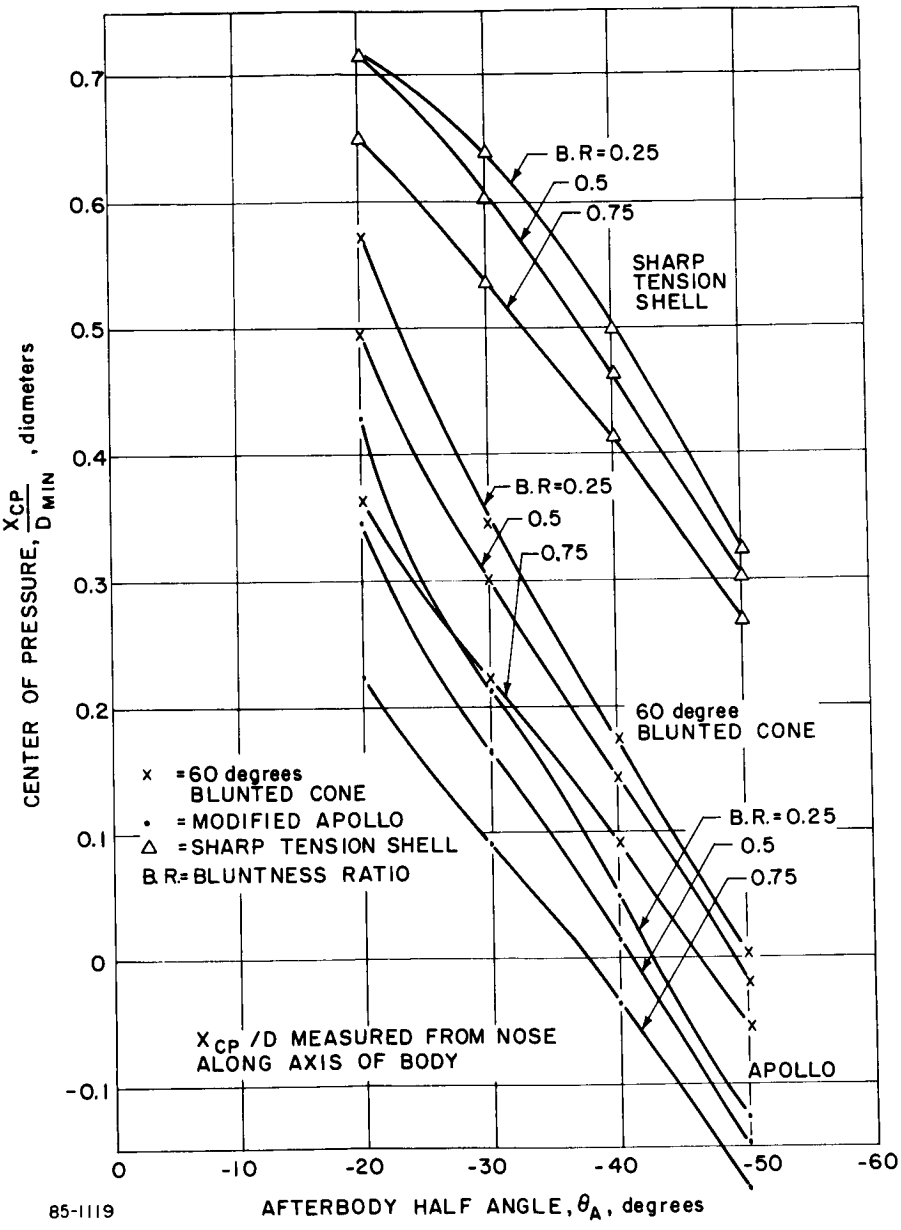

Figure 152 MINIMUM Xc.p./D VERSUS AFTERBODY ANGLE (θ_A) AT VARIOUS BLUNTNESS RATIOS

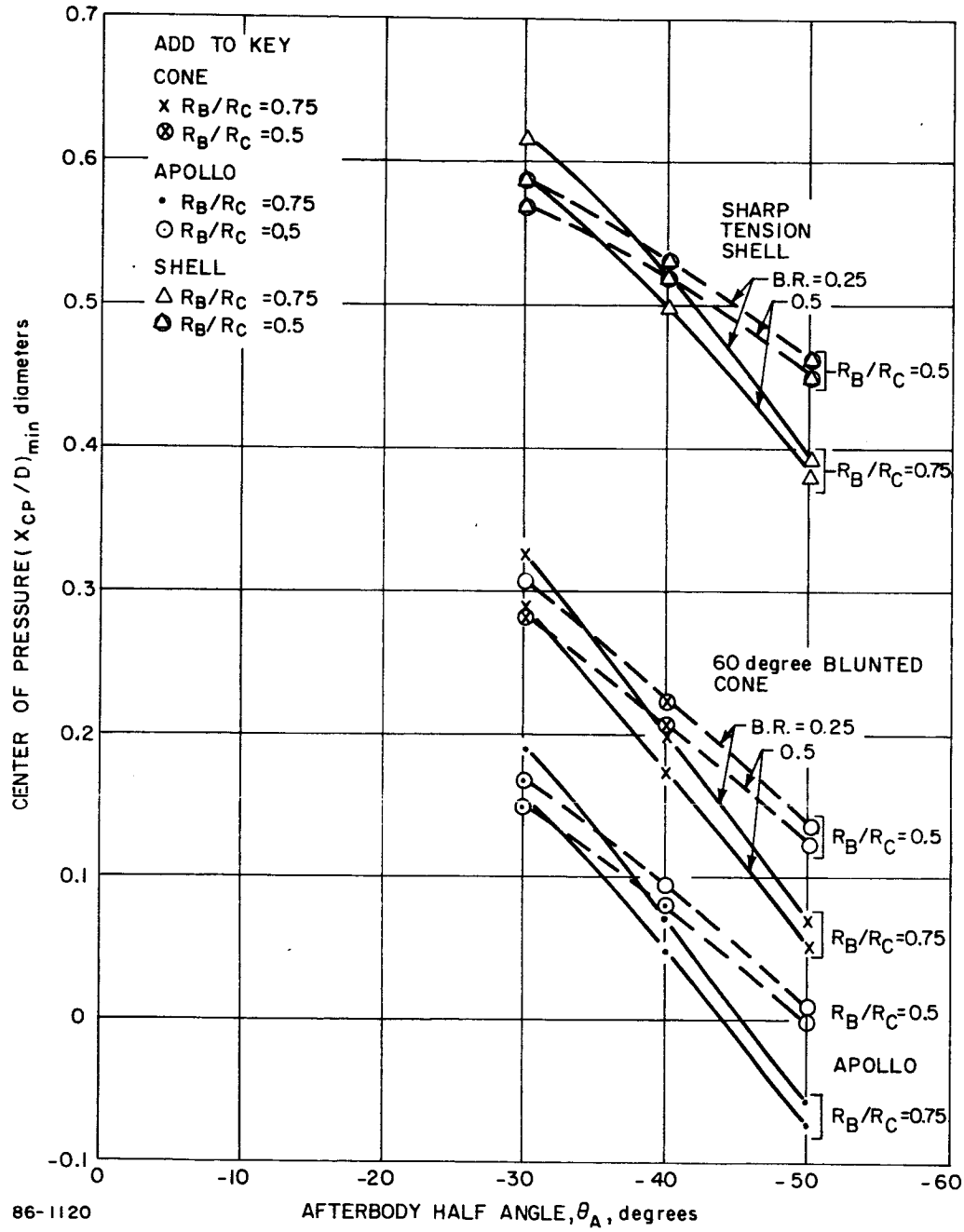

Figure 153 MINIMUM Xc.p./D VERSUS AFTERBODY ANGLE (θ_A) AT VARIOUS BLUNTNESS RATIOS FOR MODIFIED AFTERBODIES

It has been suggested that the afterbody could be eliminated, thereby simplifying the design, reducing weights, and improving the c. g. location. This would result in a concave base, for which there is some question as to the actual characteristics in the vicinity of 180-degree angle of attack. Newtonian predictions indicate no problem, but experimental data have shown a stable trim point at 180 degrees for some vehicles with this type of base. Figure 154 presents the results of tests on three different models corrected to the c. g. location of the 60-degree cone. It is seen that the two low Reynolds number tests ($R_e = 10^5$) indicate instability. It may be inferred from these data that, at the low Reynolds numbers which are associated with the possible rearward altitude during entry, the vehicle will tend to right itself automatically. However such limited data cannot be regarded as conclusive. The use of flaps is recommended to eliminate the possibility of a stable trim point for rearward entry. The flaps should be located at the maximum diameter region to provide the maximum moment.

For one of the models (Reference 9), additional data are available which permit a more definite indication of the pitching moment contribution of the concave afterbody. Reference 10 provides aerodynamic coefficients for several forebodies with both the concave base and a flat base, including a variation in c. g. location. It was therefore possible to separate the effects of base and forebody by comparing coefficients for identical forebodies with both bases, taking advantage of the fact that the flat base can contribute no normal force.

Figure 155 shows the variation of the pitching moment contribution due to a concave base versus angle of attack at three Mach numbers. The trend with Mach number indicates a reduction in the magnitude of the destabilizing moment with increase in Mach number. The following equations apply:

$$C_m = C_{m_b} + C_{m_f} + C_{N_L}\left(\frac{X_{c_g}}{d}\right)$$

$$C_m = C_{m_b} + C_{N_f}\left(\frac{\Delta X_{cpf}}{d}\right) + C_{N_b}\left(\frac{X_{cg}}{d}\right)$$

$$C_N = C_{N_f} + C_{N_b}$$

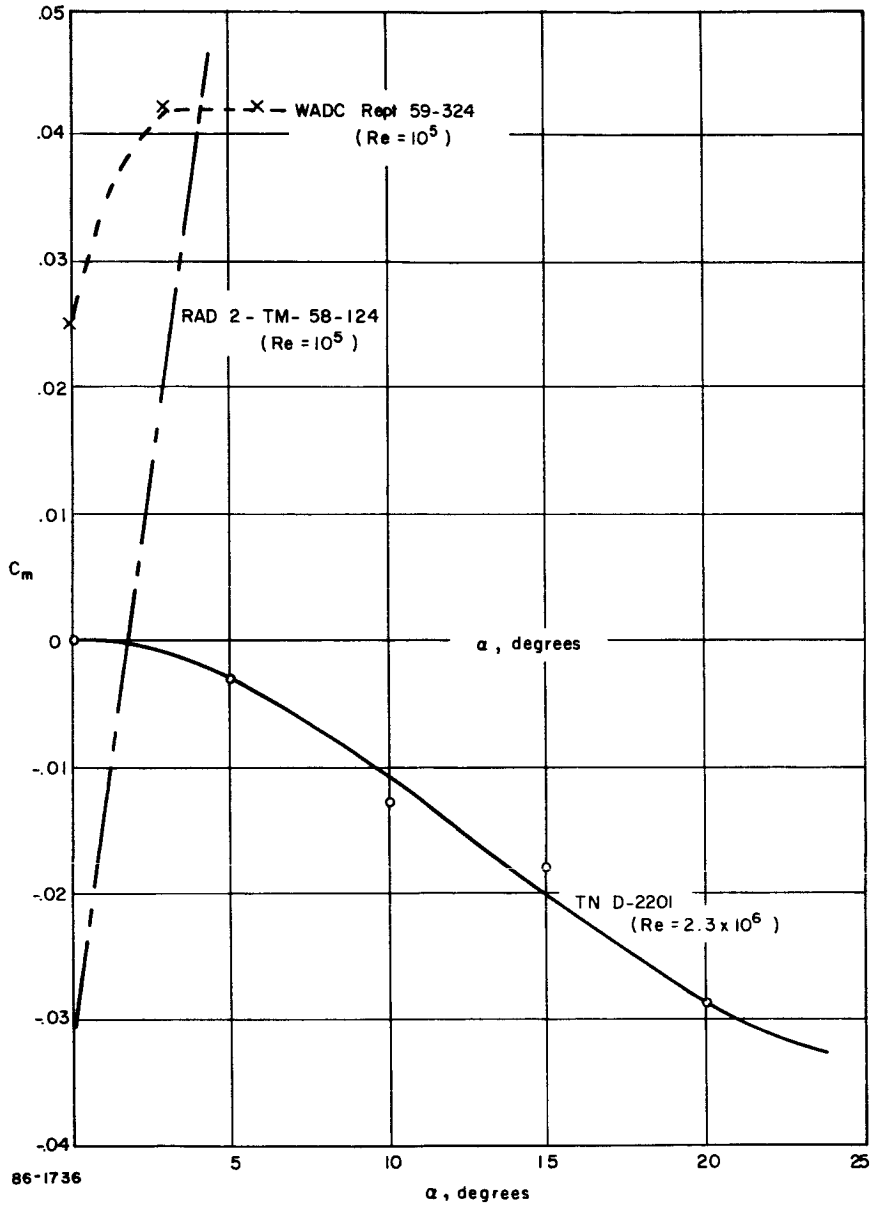

Figure 154 REARWARD STABILITY

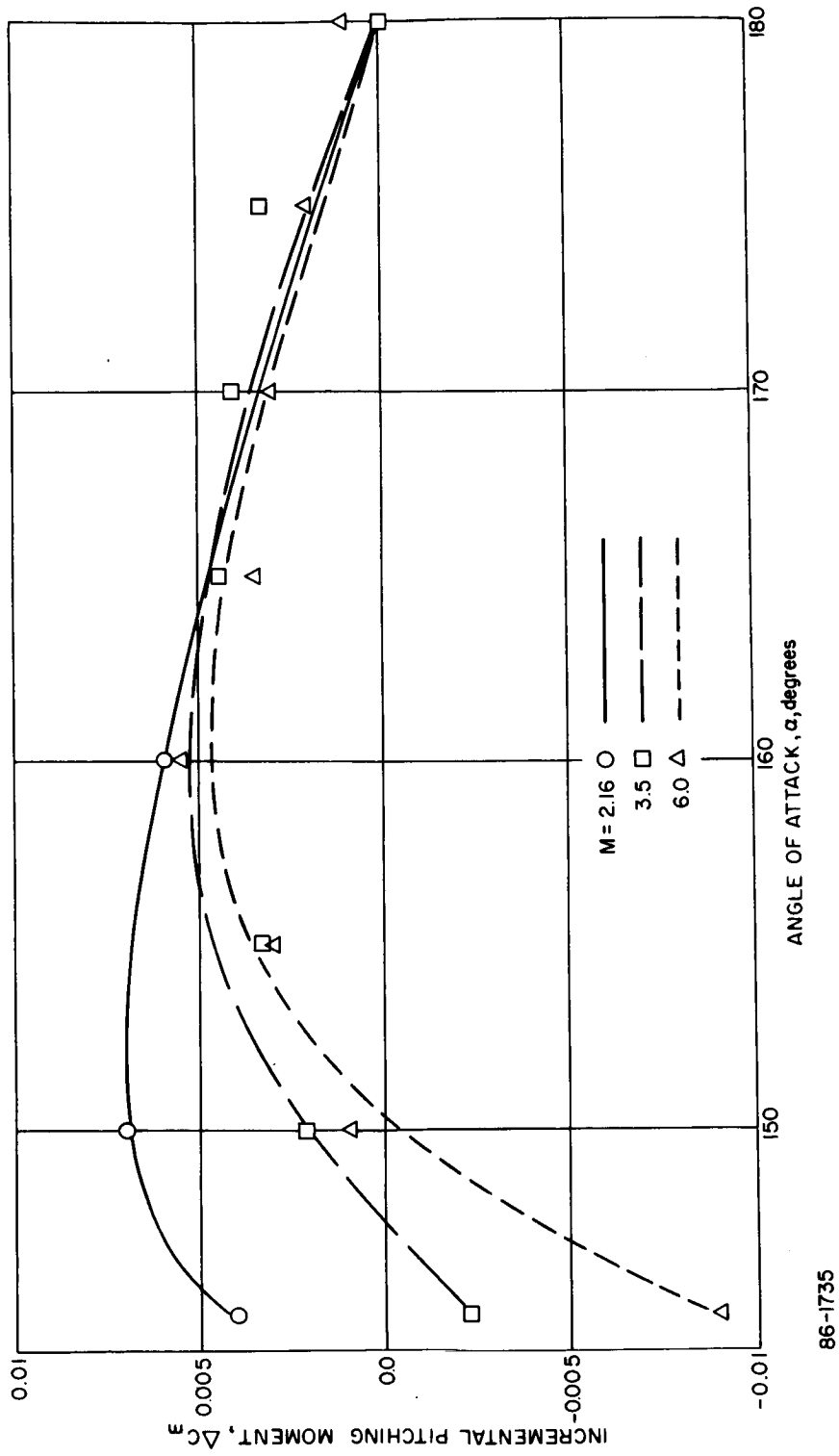

Figure 155 INCREMENTAL PITCHING MOMENT DUE TO CONCAVE BASE

At α = 160 degrees:

$$\Delta C_N = C_{N_b} = C_{N_3} - C_{N_1} = 0$$

$$\Delta C'_{m_b} = C_{m_3} - C_{m_1} = 0.006$$

$$\therefore \frac{\Delta Xc_{P_f}}{d} = \frac{C_{m_f}}{C_{N_f}} = \frac{C_{m_3} - \Delta C_{m_b}}{C_{N_3}} = \frac{0.038 - 0.006}{0.13} = 0.246$$

$$X_{c_{P_f}} = 0.246d + 0.333d = 0.579d$$

(Subscripts): f - forebody

b - base

1 - configuration with flat base

3 - configuration with concave base

Varying X_{cg} indicated that the $X_{c.p.}$ does not change, thus the couple ($C'_{m_b} = 0.006$) determined from the difference between flat and concave bases is the only couple present in the data. Within the accuracy of the above data, there is no moment due to the flat base.

4.1.3 Tension Shell Coefficients

Langley wind tunnel coefficient data were used for all trajectory performance predictions. However, the effects of compressibility were investigated through integration of the tension shell pressure distribution and by scaling for angle of attack effects. Pressure distributions were integrated for drag, lift, and pitching-moment coefficients. The equations for pressure integration are standard and need not be repeated here.

The scaling laws developed for this investigation are based on the wind-tunnel data. Starting with the zero angle of attack pressure distributions, the real-gas maximum pressure point (corresponding to the strong shock intersection point) was varied in position and magnitude in ratio with the ideal-gas values along each meridian. Unfortunately, this scaling was completed only for atmosphere 1 which is now obsolete.

4.2 FLOW-FIELD AND PRESSURE DISTRIBUTIONS

Although the velocities were considerably lower for the entry out of orbit compared to the entry from the approach trajectory, it is significant that the density ratio (ρ_s / ρ_∞), variation during the critical phases of flight were comparable. This greatly simplified the flow-field analysis. Rather than modify the analyses as obtained from the entry from the approach trajectory which would have yielded insignificant variations in the results, attention was focused on analyzing the flow field in greater depth. The significant areas of investigations were the low-density effects on the convective heating which included vorticity interaction and varying entropy. The latter results in increased heating downstream from the stagnation point due to the state of the gas external to the boundary layer as the boundary-layer mass flow increases. This gas state is that associated with the flow emanating from a region of lower entropy rise across the bow shock.

Additional analyses were necessary to account for the rocket plume effects especially with respect to the afterbody convective heating environment. This was particularly necessary for the entry out of orbit since the duration of the pulse was significantly longer.

In the following section, the methods and technology utilized to evolve the flow-field environs necessary for a conceptual design are described. The results are described in the relevant sections for both entry out of orbit and from the approach trajectory.

4.2.1 Pressure Distributions

4.2.1.1 Blunt Cone and Modified Apollo

The pressure distributions for the blunt cone were obtained by means of a single-strip integral method (Figure 149). In addition, test data were utilized where applicable to define the angle of attack variations (considering an equivalent body whose conical elements form an angle of $\theta_c + \alpha$ with the velocity vector).

The pressures for the modified Apollo were obtained from data on a similar shape (sharp shoulder and similar nose radius) in addition to the blunt-body solutions (Figure 156). The correlation of the data, obtained for air was on the basis of density ratio, correcting the pressures for real-gas effects by means of the parameter

$$\frac{(2 - \rho_\infty / \rho_s)_{gas}}{(2 - \rho_\infty / \rho_s)_{air}}$$

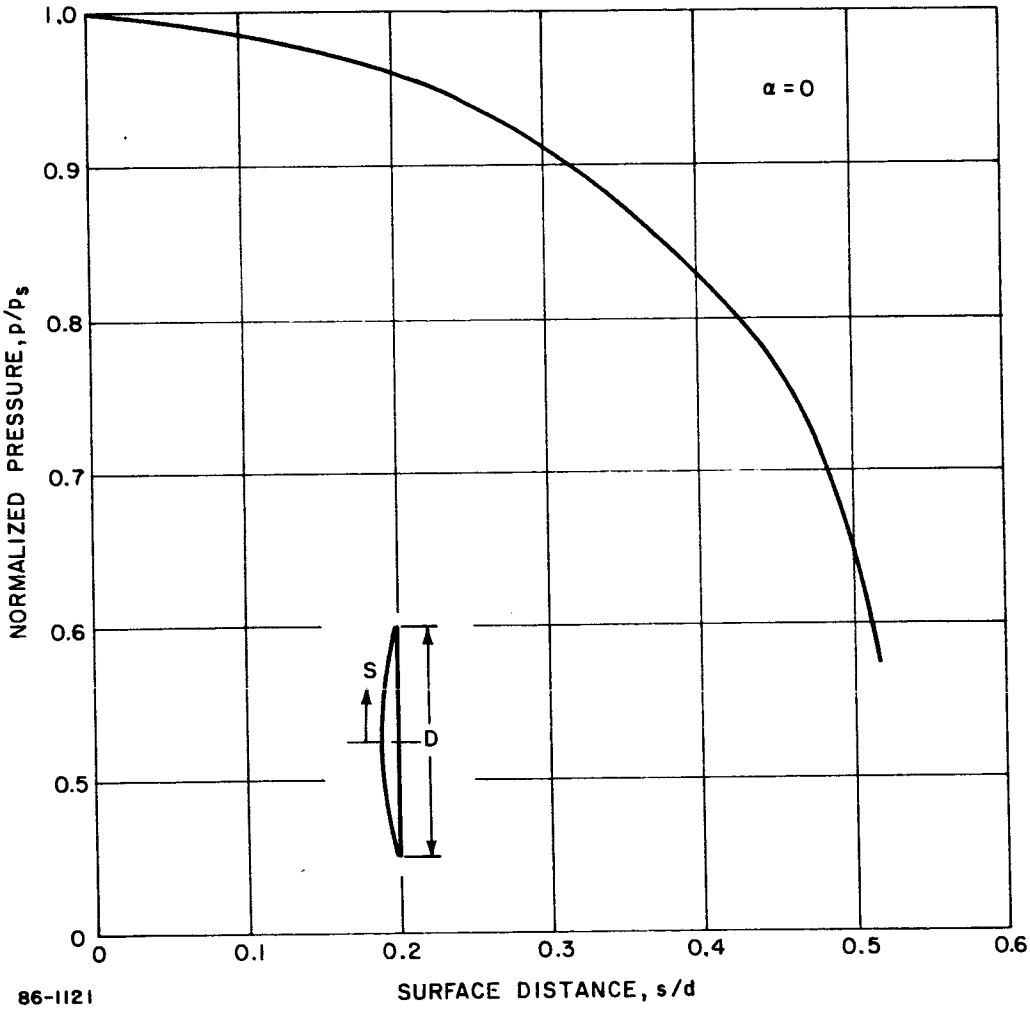

Figure 156 PRESSURE DISTRIBUTION--MODIFIED APOLLO

The flow over the blunt surfaces is relatively insensitive to the free-stream Mach number. This is especially true of the modified Apollo and blunt cone where the maximum Mach number is slightly supersonic, occurring at the maximum diameter. As a consequence, the base pressure is expected to be dependent only on the stagnation pressure and the Reynolds number. Directly applicable data are unavailable; however, the data on related very blunt configurations indicate that the base pressure can be higher than the free-stream pressure. The base pressure for a cylinder normal to the free stream (sting effects are replaced by end wall interactions; however, for high fineness ratios these effects are minimized) resulted in base pressures, measured at midspan, which were constant percentages of the stagnation pressure for a large range in Mach number (Reference 11). The variation of the pressure ratio, P_{base}/P_{stag}, was correlated with the Reynolds number $\rho_s V_\infty D/\mu_s$ (Figure 157). The base pressure data obtained with a truncated sphere (Reference 12) agree well with the above data giving a base pressure of 0.03 Ps, which was used in the parametric studies to evaluate the base heating.

4.2.1.2 Tension Shell

The analyses associated with the tension shell warrant separate consideration as well as more detail. A detailed description of the analytical methods used in tension shell evaluation is given below.

The general shape of the tension shell entry vehicle has evolved from structural considerations assuming Newtonian pressure distributions. The shape thus obtained, however, does not produce the presumed loading or the implied simple flow field. The actual flow field is extremely complex; a shock pattern typical of those encountered is shown in Figure 158.

The definition of the vehicle environs is dependent upon knowledge of the flow field about the body. With the flow field defined, convective and radiation heating, loads and shears become definable; thus the required structure, heat shield and mass distribution may be determined.

The tension shell shapes for which these analytical methods were derived are somewhat unique in terms of the flow field produced. Characteristic of the general flow field is the double shock and interaction system produced by the continuous body. Because of this unique feature, standard analyses do not apply. Simplifying assumptions were made which, if is felt, do not degrade or compromise the results obtained.

Flow-Field Analysis -- One sharp, and one blunt tension shell were considered in the entry from the approach trajectory phase of this study. The two body shapes were generated by identical error

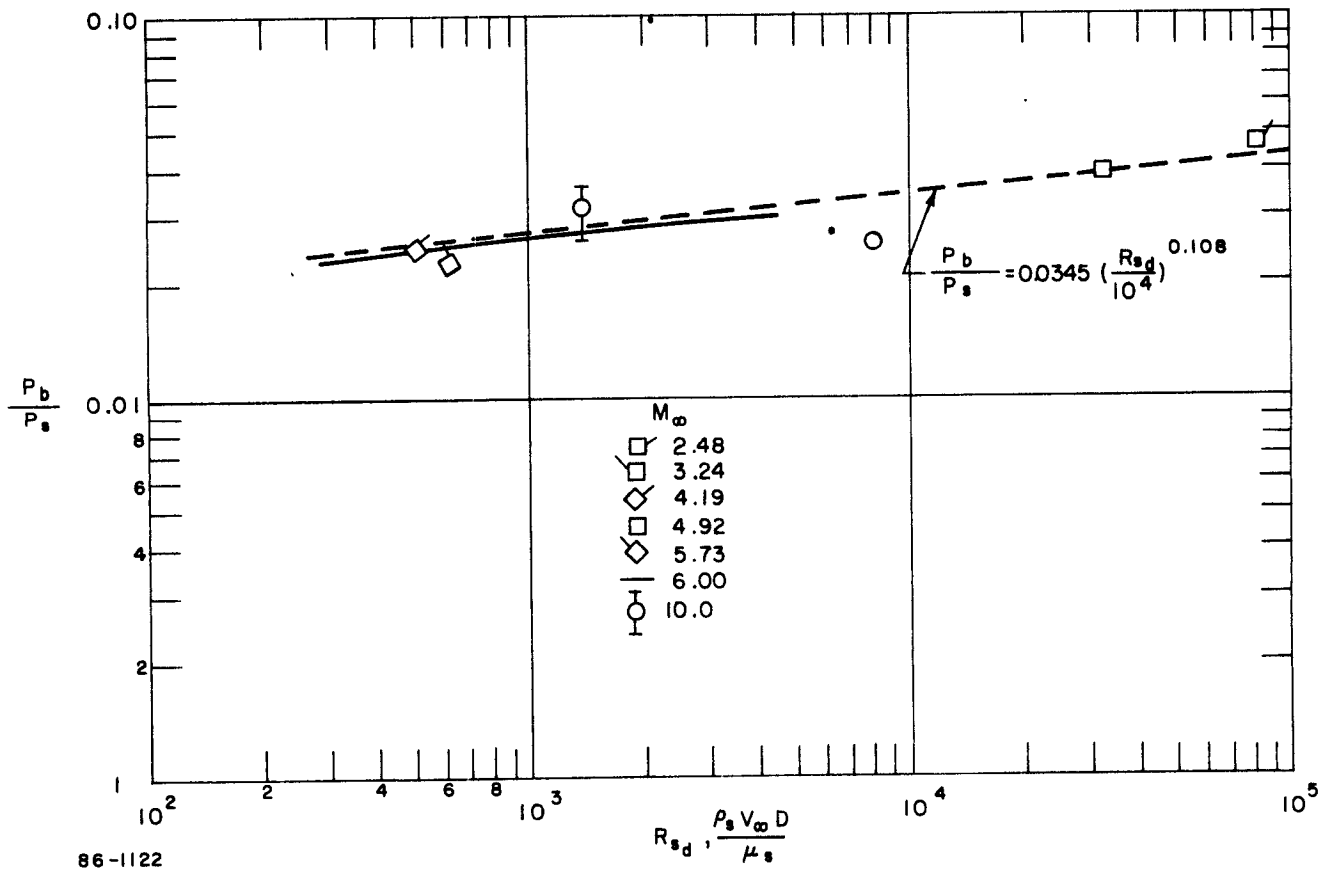

Figure 157 CYLINDER BASE PRESSURES

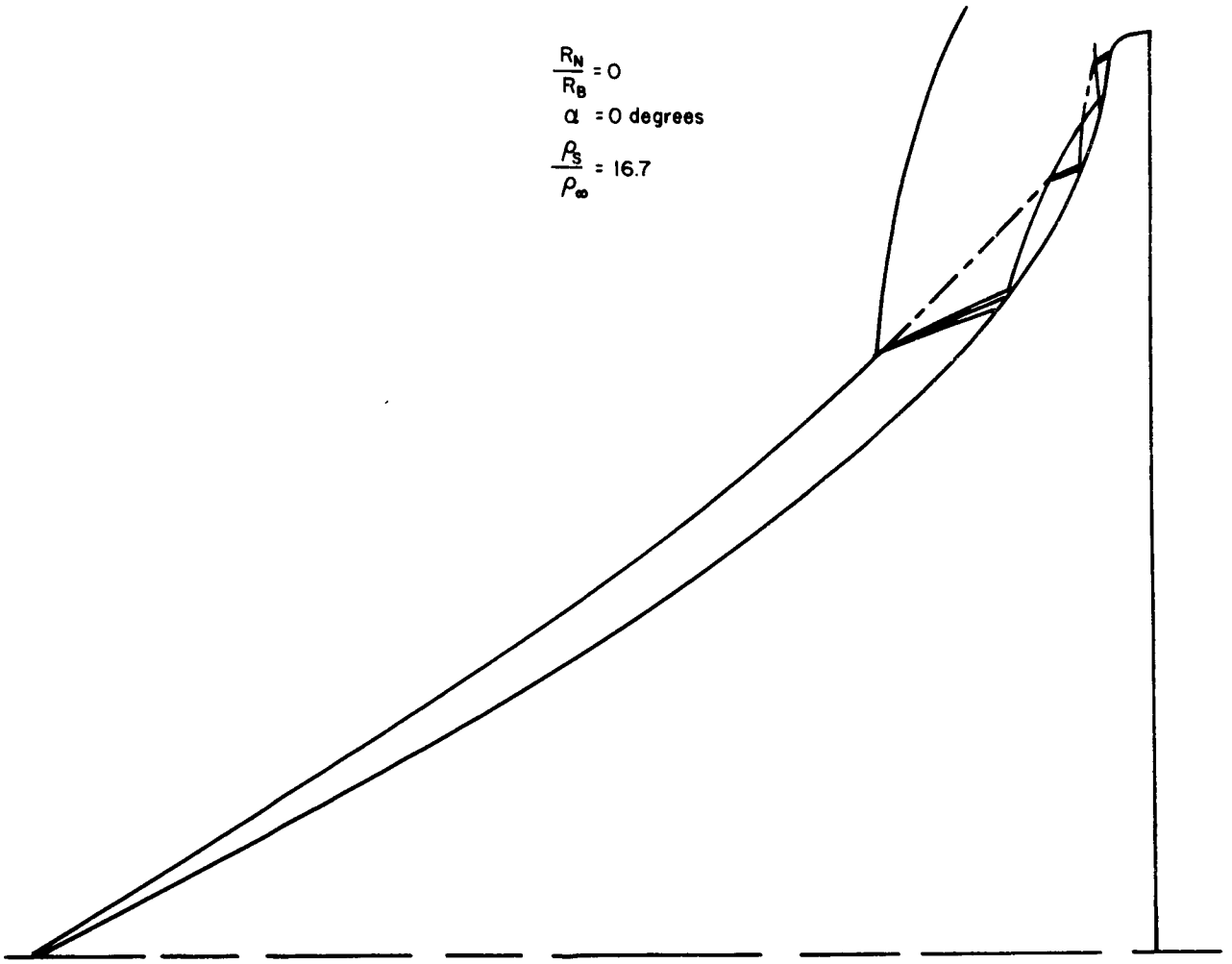

86-1146

Figure 158 TENSION SHELL FLOW FIELD GEOMETRY

function equations except for the difference in nose radii. Since the sharp tension shell represents the more difficult design problem, this shape has been selected as the basis for calculation of the flow field. The blunt body flow field can be derived rather simply from that of the sharp shape, as will be shown later.

In devising a mathematical model for the flow over the sharp tension shell, the effects of separation and the boundary layer have been neglected. The assumption that separation does not occur over the critical portion of any Mars entry trajectory appears reasonable from a comparison of free-stream Reynolds number (based on body radius) with those obtained in LRC wind tunnel tests (Reference 13). In addition, calculated values of absolute pressure gradient for pertinent flight cases were lower than those obtained at the Mach 8 test condition. The pressure gradient is, however, adverse to boundary-layer growth (except over certain discreet segments), thus supporting the assumption of negligible boundary layer effects. The only places where the boundary layer may play a significant role are where shock waves and expansion fans impinge on the body. In this case, some attenuation of these waves may occur through the boundary layer, but the boundary layer thickness should still remain small with respect to the flow between the shock and the body.

In general, the shock system associated with the sharp tension shell is initiated by an attached, conical compression wave. As the flow proceeds aft, the surface steepens, producing a steeper shock wave and causing the flow along the surface to compress in a manner which is essentially isentropic. This compression process is far more efficient than the compression through a normal shock. Thus pressures greater than Ps are obtained with relatively high local velocities. This process continues along the surface to the point where the turning angle behind the shock wave required to compress the flow becomes too great to support an attached shock system. At this point, a strong, detached shock wave forms. The intersection of the strong shock and the conical shock produces a slip discontinuity which acts as a "free" boundary between a subsonic outer region and a reflected wave system, the latter impinging alternately on the body and slip line.

To obtain a real-gas solution for the entire flow field, use was made of Avco computer programs which calculate the real-gas conditions behind a two-dimensional oblique shock of arbitrary angle for any Martian atmospheric composition. Using the two-dimensional solution, an equivalent conical flow solution is then obtained assuming constant density behind the wave. This method has been shown (Reference 14) to be accurate to within 1 percent for density ratios on the order of those encountered in Martian entry (Figure 159).

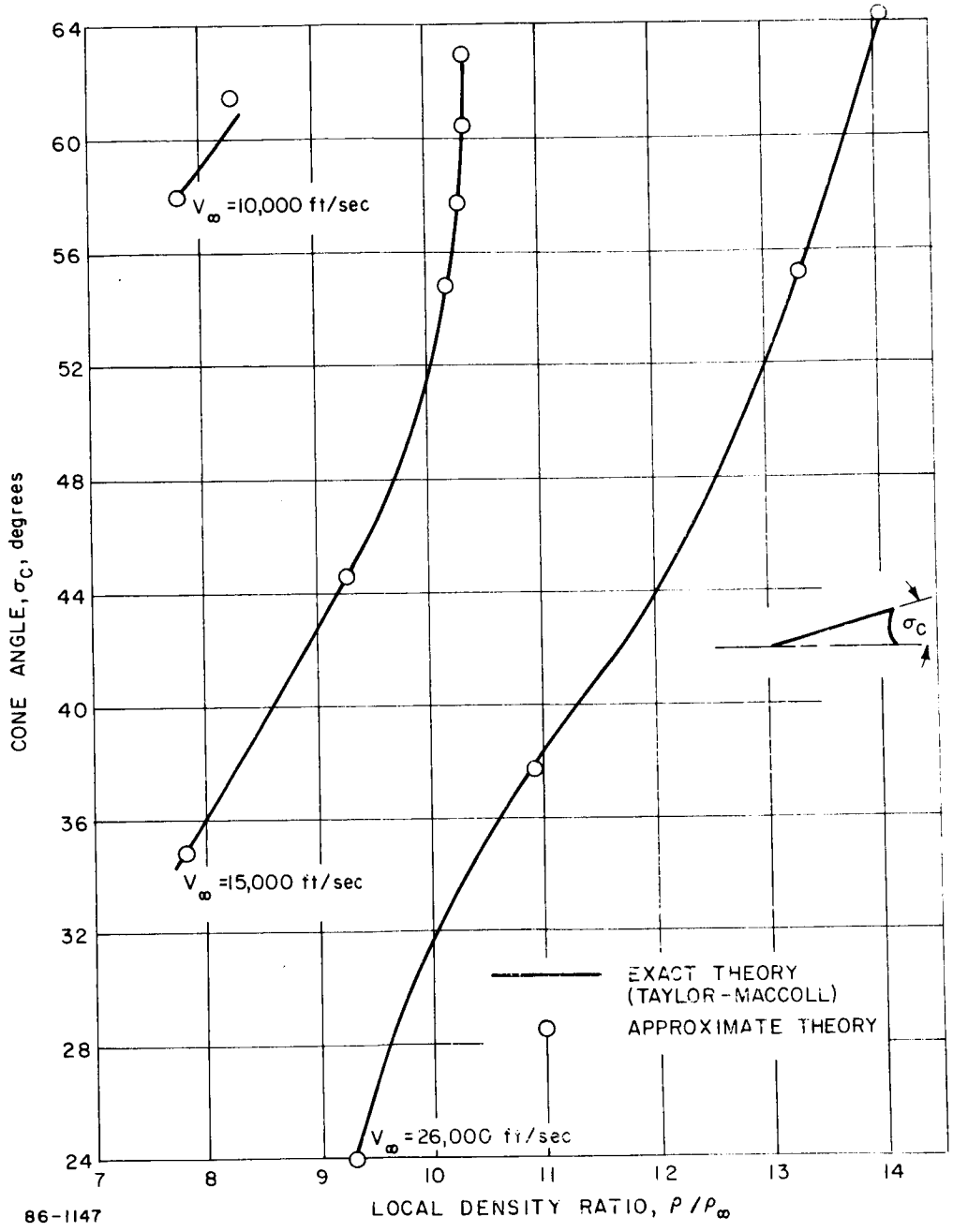

Figure 159 CONICAL SHOCK SOLUTION

By eliminating the spatial derivatives of density in the fluid flow equations, a single differential equation is obtained which can be solved in terms of Legendre functions. The resulting expression (following Feldman (Reference 14) is implicit in σ_c :

$$\frac{\cos\sigma_c}{\sin^2\sigma_c} - ln\left(\tan\frac{\sigma_c}{2}\right) = -ln\left(\tan\frac{\theta}{2}\right) - \frac{1}{\cos\theta} + \frac{1}{\cos\theta\left[\sin^2\theta - \left(\frac{U_w}{V_\infty}\right)\sin\theta\sin(\theta-\delta)\right]}$$

where θ is the common wave angle; δ is the two-dimensional deflection angle; (U_w/V_∞), the two-dimensional velocity ratio across the shock; and σ_c is the semivertex angle of the equivalent cone required to produce the same shock angle. This expression holds only for attached shocks (irrotational flow). The flow behind the shock is incompressible and adiabatic, therefore the Bernoulli equation holds and:

$$P_c + \frac{1}{2}\rho U_c^2 = P_w + \frac{1}{2}\rho U_w^2$$

or, in terms of stagnation pressure ratios:

$$\frac{P_c}{P_s} = \frac{P_w}{P_s} + \left(\frac{\rho}{\rho_\infty}\right)\left(\frac{q_\infty}{P_s}\right)\left[\left(\frac{U_w}{V_\infty}\right)^2 - \left(\frac{U_c}{V_\infty}\right)^2\right]$$

where the conical velocity ratio is evaluated from

$$\frac{U_c}{V_\infty} = \cos\sigma_c + \left[\cos\theta\sin^2\theta - \left(\frac{U_w}{V_\infty}\right)\cos\theta\sin\theta\sin(\theta-\delta)\right]\left[(\cos\sigma_c)\,ln\left(\frac{\tan\sigma_c}{\tan\theta}\right) - \frac{\cos\sigma_c}{\cos\theta} + 1\right].$$

In the above development, all two-dimensional parameters are obtained for the desired Martian atmosphere assuming thermochemical equilibrium. With the pressure, density and velocity as obtained above, the entire thermodynamic state of the gas at the cone is specified. Typical plots of θ, σ_c , P_c/P_s and U_c/V_∞ versus p/p_∞ are presented in Figures 160 through 163, respectively.

To obtain flow properties on the surface of the equivalent blunt-nosed tension shell, sufficient accuracy is obtained by the use of a Newtonian pressure distribution and normal shock entropy.

The flow along the steepening surface behind the conical flow region is assumed to compress isentropically to the point where the first reflection from the main shock intersection impinges on the shell surface.

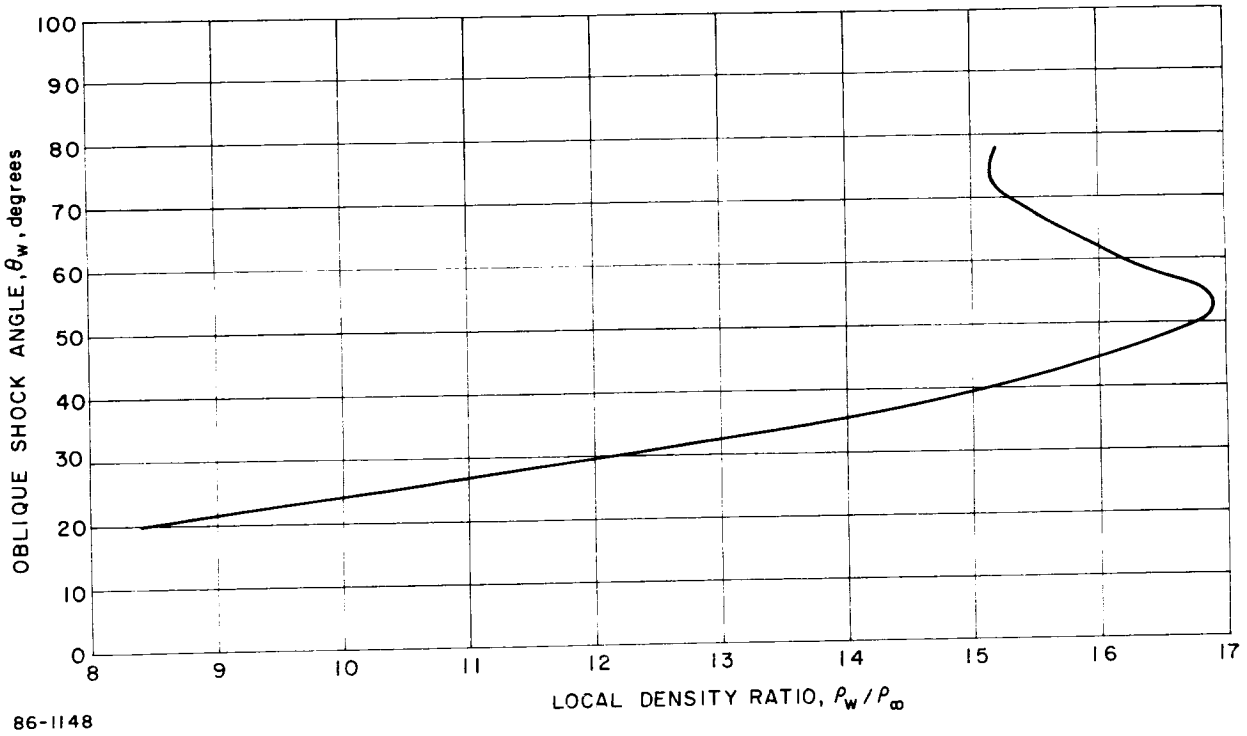

Figure 160 CONICAL SHOCK SOLUTION -- TWO DIMENSIONAL OBLIQUE SHOCK ANGLE

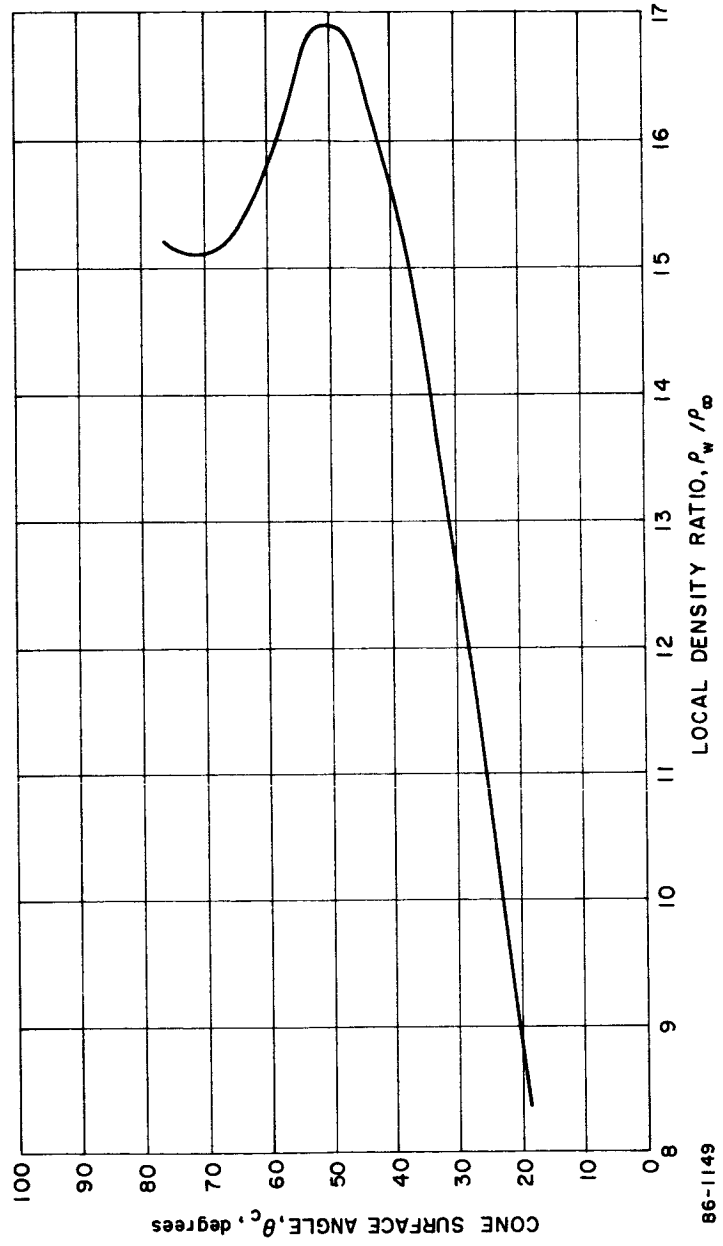

Figure 161 CONICAL SHOCK SOLUTION -- EQUIVALENT CONE SURFACE ANGLE

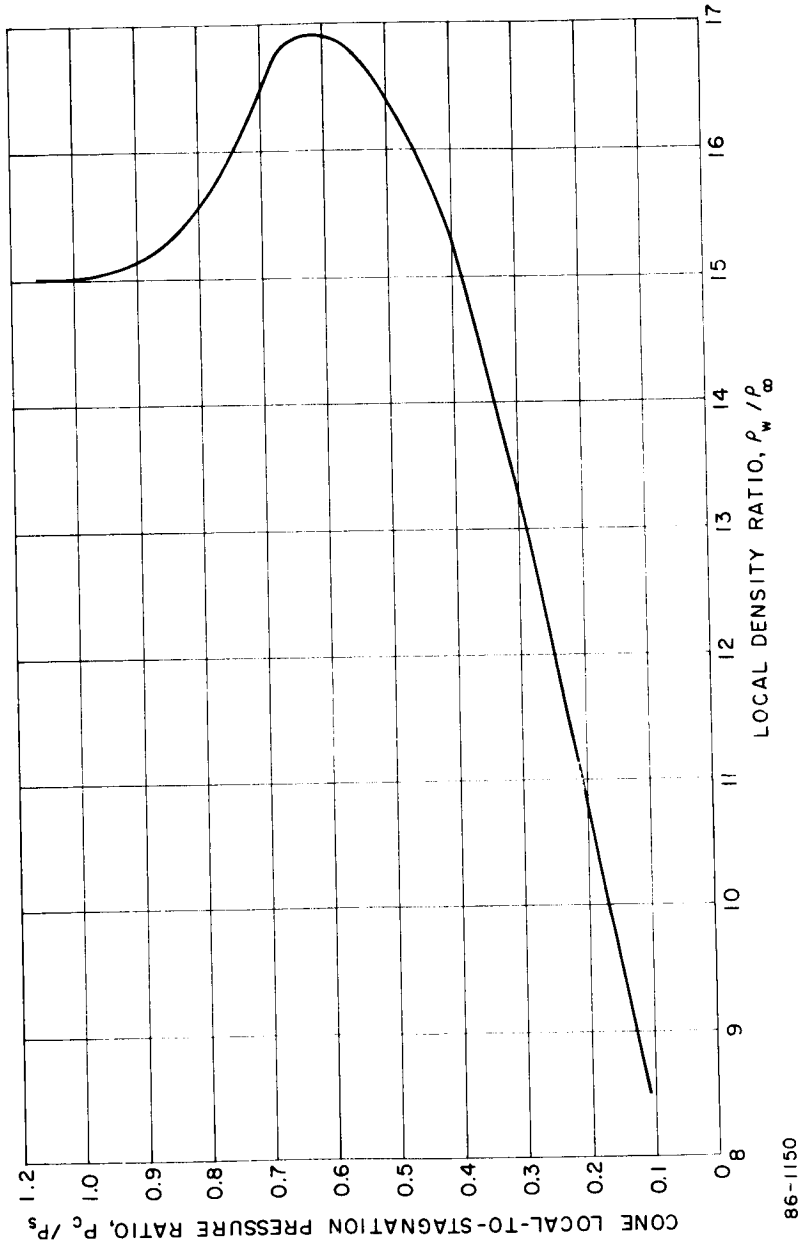

Figure 162 CONICAL SHOCK SOLUTION CONE PRESSURE RATIO

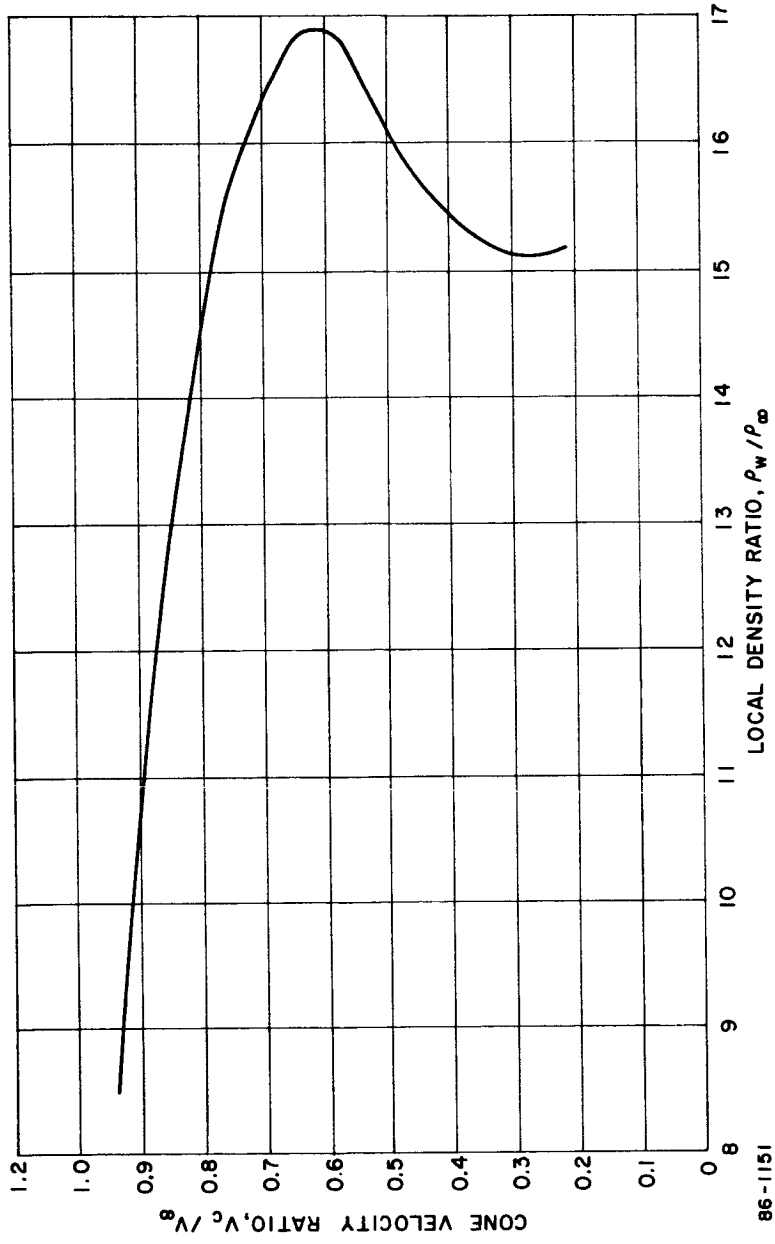

Figure 163 CONICAL SHOCK SOLUTION CONE VELOCITY RATIO

This point is not, however, known a priori. Therefore, the shock geometry is constructed from the initial conical shock to the point of (conical) shock detachment, assuming that the local cone angle defines the shock angle at the point normal to the conical surface. This concavely curving bow shock is approximated by short, straight-line segments as

$$\eta_2 = \eta_1 + (\xi_2 - \xi_1)(\tan \left[\left(\frac{\theta_2 + \theta_1}{2}\right) - \left(\frac{\sigma_2 + \sigma_1}{2}\right)\right]$$

where η is the coordinate of the shock relative and normal to the surface, and ξ is the coordinate along the shock.

The conical shock detachment point represents the limiting aft position possible for the intersection between the bow wave and the strong detached shock wave. However, since additional compression is required behind the bow shock to bring the flow parallel to the ever-steepening surface, the shock intersection will invariably lie forward of this point.

To define the intersection point requires a double iteration (actually trial and error) solution, which proceeds in the following manner, after assuming -- somewhat arbitrarily -- a point of intersection. The intersection of two shock waves requires, in general, that some manner of reflected wave pattern be produced, and that the pressures and flow angle behind the intersection be equal, which in turn implies a slip discontinuity (due to differing velocities and entropies) emanating from the intersection point. In addition, the fact that one shock is strong requires the flow to be subsonic behind it. The subsonic condition eliminates the standard four-shock pattern from consideration. However, three possibilities remain. These possible reflection patterns are (1) a compression shock plus a negligible expansion wave, (2) a strong, or normal compression shock followed by fully subsonic flow, and (3) a simple expansion fan. Which assumption satisfies the equal pressure and parallel flow requirements depends upon free-stream conditions and where the intersection point lies. (The strong compression shock has not been encountered in practice, but must still be considered possible.) With the above conditions satisfied, the wave angle of the strong shock is uniquely specified.

This angle and the coordinates of the intersection point are sufficient to define the shape of the strong shock wave. The shock shape has been obtained as an empirical curve fit of glow picture test data which holds to a point on the shock slightly beyond the maximum radius of the tension shell. The full primary shock system is now tentatively defined. Also determined is the shock standoff distance which, for this shape, is taken as the axial length between the virtual sonic point* on

*This is the point at which sonic flow would exist if the prior flow field were subsonic. The flow is actually supersonic over the entire surface in most cases.

the outer shoulder of the vehicle, and the strong shock. (The symbol used for the standoff distance as defined in this geometric manner is ΔG.)

A second means of determining the shock standoff distance can be obtained by invoking the continuity law. The standoff distance taken around the vehicle at the radius of the "sonic" point, R^*, represents a cylindrical control surface across which the average radial mass flow must equal the free-stream mass flow entering the bow shock system in a stream tube of equal radius. Thus:

$$(2\pi R^* \Delta_m) \overline{\rho V \sin \delta} = \pi R^{*2} \rho_\infty V_\infty$$

where $\overline{\rho V \sin \delta}$ is the average radial mass flux, δ is the local flow angle relative to the tension shell axis, and subscript m denotes that Δ is determined from mass flow considerations. The quantity $\overline{\rho V \sin \delta}$ must account for the mass flow through the entire frontal shock system as constructed on the assumption of the shock intersection point. Both Δ_m and Δ_G are, therefore, affected by the intersection assumption, but are otherwise independent. Thus if $\Delta_m = \Delta_G$, the intersection assumption satisfies all geometric and continuity considerations and is therefore correct. The double iteration process, previously mentioned, culminates in satisfying this criterion.

With the external shock structure, the first reflected wave and the initial slope of the slip line all defined, the remainder of the flow field is reasonably easily defined. The flow between the strong shock and the slip line is all subsonic until it is allowed to expand. A sonic point exists, therefore, at the slip line. The position of this point, which is not critical to the definition of properties along the body, is taken to be at the same radial station as the body virtual sonic point.

Between the slip line and the body, the flow is treated as two-dimensional. The problem here is, essentially, to define the shock-expansion pattern in a channel, one boundary of which is variable. The general problem of flow with shocks and expansion systems is given ample treatment in the literature (References 15 through 18). Application to the tension shell problem was straightforward, with gas properties defined on a pseudo-ideal gas basis for each local change, and with expansion fan systems replaced by single Mach lines based on the average Mach number of the expansion. This latter simplification is justifiable since all expansion systems have been found to be very small, of the order $\Delta_\nu < 5$ degrees.

The compressive shocks encountered were also generally weak, such that the entropy rise through this "channel" was very small. Because the compressions and expansions are relatively small, the flow properties immediately forward and aft of the first expansion wave represent, to a very good approximation, the upper and lower bounds of the flow properties throughout this channel. Mach number also changes very little through the channel up to the expansion around the shoulder of the tension shell. For this reason, the flow conditions at the vehicle virtual sonic point can be determined directly from the conditions immediately forward of the first expansion. Further, the channel area can be considered constant (on a three-dimensional basis) up to the shoulder.

The explanation for the fact that these fluctuations are small lies in the flow-boundary geometry. The rate of change of surface curvature with respect to axial length is generally sufficiently high to cause small impinging expansion systems to reflect as compression waves. The slip line acts as a free boundary, changing its inclinition to equalize pressures between the subsonic and supersonic flows.

In light of the above discussion it is evident that, for preliminary design purposes, properties in the channel region can be considered effectively constant, and the upper or lower bound -- whichever is critical -- can be used for each design parameter.

Thus, a method has been developed which may be used to predict the tension shell flow field, including the complete shock shape and internal flow field as well as the pressure distribution and all necessary properties along the body surface at zero-angle of attack (incidence effects are considered later).

This method was developed with due consideration given to matching the only available test data (Reference 19.) However this data was obtained at an ambient temperature sufficiently low to yield ideal-gas conditions ($\gamma = 1.4$). Thus, certain departures from the above method were taken, and perfect agreement was not expected. Flow-field simulation was attempted at the highest free-stream Reynolds number ($\sim 2 \times 10^6$ based on diameter) to minimize the effects of possible local flow separation. Figure 164 shows the first theoretical shock shape attempted and selected test point scaled (with certain attendant inaccuracies) from Schlieren photographs. Correlation was good up to the shock intersection. To simulate the shape of the strong shock, a spherical wave based on Kaattari's work (Reference 20) was assumed. This assumption led to incorrect placement of the shock intersection while satisfying continuity and pressure requirements. The resultant pressure distribution is shown in Figure 165. Agreement with test data is rather good except for the apparently misplaced peak. This situation was corrected with the improved strong shock shape outlined earlier.

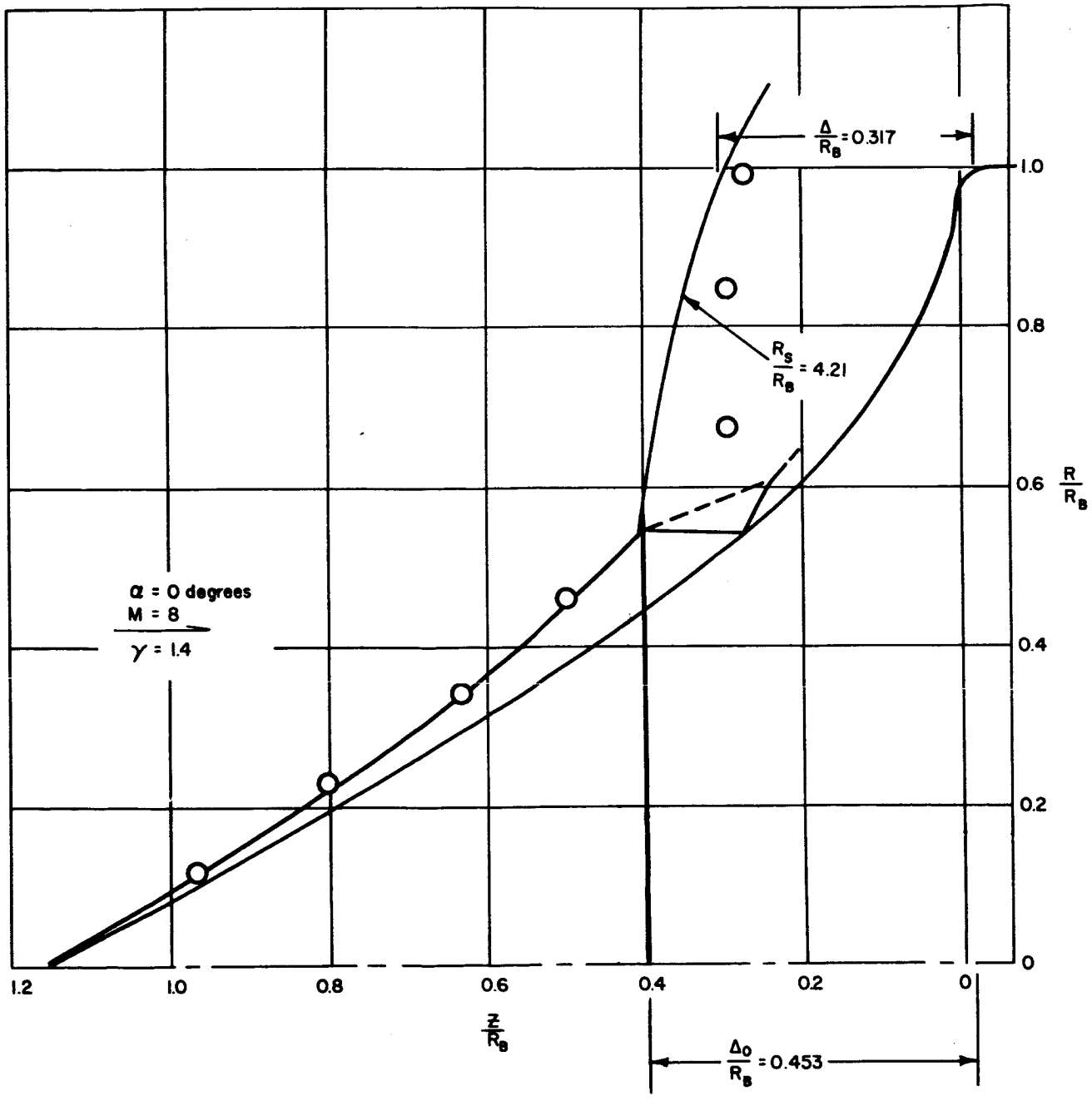

Figure 164 LRC TEST FLOW FIELD

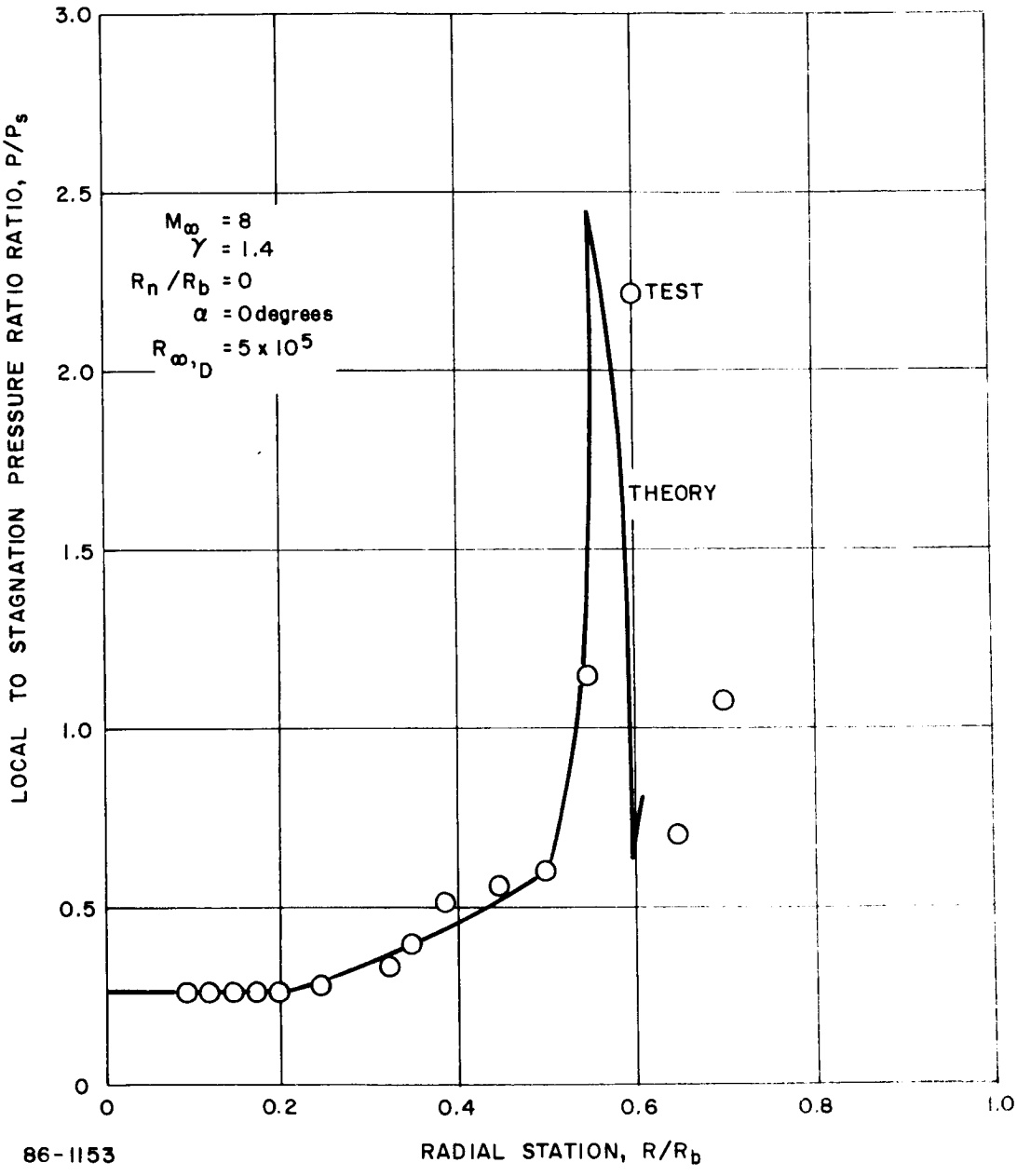

Figure 165 LRC WIND TUNNEL PRESSURE DISTRIBUTION

A typical example of the shock system had been presented as Figure 158. The complete shock structure is shown in this figure including the expansions and shocks in the "channel region." It is to be noted that each expansion emanating from the slip line is reflected from the steeper surface as a compression wave. The opposite reflection holds at the slip line or free boundary. The pressure distribution associated with this flow picture is shown in Figure 166. The strongest shock occuring in the channel produces a static pressure ratio of about 2:1, which is relatively small in terms of entropy rise. At the rear of the channel, the Mach number is within 10 percent of the entry Mach number.

It is to be noted here that Figures 158 and 166 represent only a typical result of the analysis and do not apply to specific trajectory conditions in the design study. Design conditions are calculated separately and the results shown in paragraph 2.3.2.3.

4.2.1.3 Blackout

The ever-present problem of plasma attenuation of telemetry signals - "blackout" - was evaluated with respect to the newly changed variables of the EFO phase. The effects of atmospheric chemistry and density, and vehicle entry velocity and entry angle, were evaluated using a relatively sophisticated flow model.

It was first necessary to define the most critical atmosphere with respect to aerodynamics telemetry interference, i.e., the atmosphere which presents the greatest blackout problem.

At the general energy level of interest in the entry out of orbit phase $\left(\frac{V_\infty^2}{2}\right) \approx 10^7 \text{ft}^2/\text{sec}^2$, the principle electron emission mechanism in any of the atmospheres under consideration can be most simply stated as

$$NO \rightarrow NO^+ + e^-$$

Atmospheres devoid of nitrogen (in this study, VM-2, -4, and -8) need not be considered further. In this respect atmospheres VM-1, -3 and -7 may be considered critical since their chemistry is identical.

A further criticality criterion is required to determine which of three atmospheric models provides the greatest blackout problem. The criterion sought is found in the minimum telemetry replay-time. Since the data gathered during blackout must be transmitted from lander to bus in the incremental time between exit from blackout and impact, the atmosphere which produces the minimum time increment will be critical.

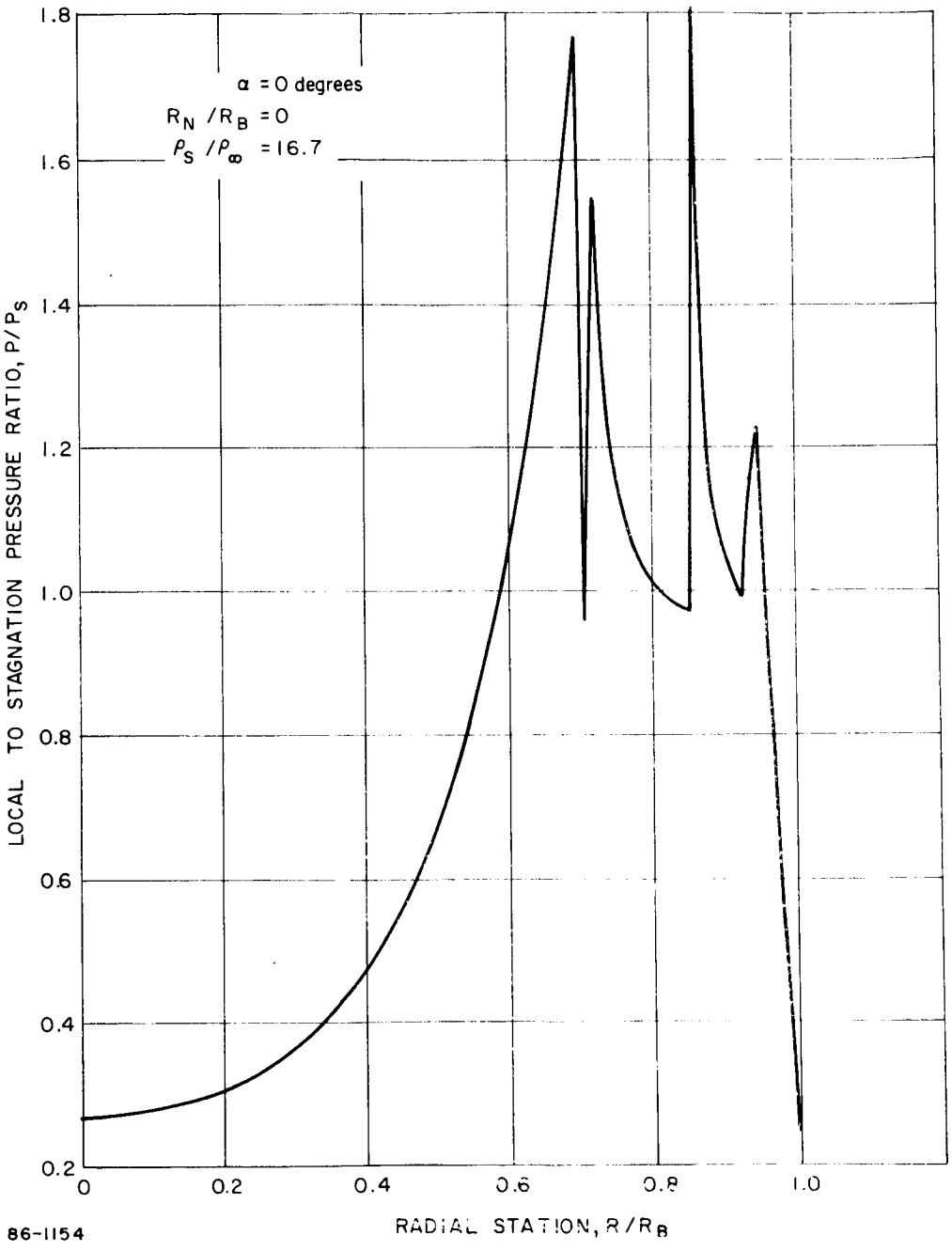

Figure 166 TENSION SHELL PRESSURE DISTRIBUTION

The three atmospheres differ essentially only in surface pressure and density. This means that the density-altitude profiles will be identical but displaced in altitude by the ratio of surface densities. Therefore, the vehicle deceleration histories will also be identical but displaced. Further, the electron density-time histories in the three atmospheres ("all other things being equal") will be identical but shifted only with respect to altitude. The peak electron density and exit from blackout will occur at the lowest altitude in the least-dense atmosphere. The least-dense atmosphere - VM-7 -- allows the least time before exit from blackout and impact, and is, therefore, the critical atmospheric model.

To devise a proper flow model, the position of the antenna and the path through the plasma must be specified. The antenna position was taken to be on the reference configuration afterbody. The antenna wave path taken was along a line lying 30 degrees above and aft of the vehicle longitudinal axis. The flow field was then determined from the shock back to this line as will be described. The computation of pertinent parameters was then carried out.

A shock shape compatible with the general conditions at exit from blackout was assumed, i.e. Mach 9-10 at approximately 200, 000 feet altitude with a stagnation density ratio of 9.5. The Avco thermochemical equilibrium programs (1313, 1561) were used to define the flow properties and electron density immediately behind the entire shock front to the point where the shock was intersected by the antenna path.

In the subsonic shock layer in front of the body, an approximate stream tube analysis was performed assuming frozen flow chemistry to the sonic line. Boundary-layer effects were neglected since the boundary layer has little influence on the electron density for highly blunted shapes. It should be noted here, however, that this analysis does presume a nonablating heat shield. Flow conditions and electron density values were thereby defined along the sonic line.

Using the standard base pressure value, $P_b/P_s \approx 0.03$ the isetropic expansion of this stagnation streamline was then computed. The trajectory of this streamline was found to converge toward the axis linearly, at least to its intersection with the antenna path. Electron density was assumed to vary as pressure (Reference 21.

$$N_e \sim p^{1/\gamma}$$

This streamline, which can be traced from the normal shock at the vehicle axis, to the vehicle stagnation point, along the body, and around the shoulder; becomes, behind the body, the dividing streamline (D.S.L) between the high velocity wake and the so-called dead

water region. The electron density inside the DSL is negligible. Once the DSL is established, a stream-tube analysis can be performed through the expansion region and downstream to the antenna path intersection, iterating on flow angle and mass flow rate to determine the proper flow area. This process is carried out in increments (stream-tubes) along the antenna path to the intersection of the path and the shock. At this point, the mass flow rate and flow direction are equal to those behind an oblique two-dimensional shock of the shock angle. Typical variations of local density, temperature and electron density, along the antenna wave path are shown in Figures 167 through 169, respectively.

The electron density level which will cause blackout, i.e., extreme attenuation of the telemetry signals, is a function of signal frequency only

$$N_{e_{crit}} = \frac{(2\pi f)^2}{3.18(10)^9}$$

Since the telemetry frequency is fixed at 272 mc, the critical electron density is 9.2×10^8 electron/cc. The occurance of this level at any point along the wave path is therefore an indication of incipient blackout. By using this criterion and the flow-field model previously derived, the critical electron density can be worked backward through the flow field and through the shock to determine a critical set of free-stream conditions. A five-point correlation of critical wake electron density (9×10^8 is used) in terms of free-stream velocity and altitude (p_∞) is shown in Figure 170. The V_∞ - Z correlation is perfectly linear over the range shown - which is also the range of interest. By plotting velocity-altitude histories for the range of V-γ entry conditions, the limits of blackout can be defined.

4.2.1.4 De-orbit Rocket Flow Field

The use of rocket thrust to provide the velocity decrement necessary to establish an entry trajectory for the lander vehicle produces certain problem areas which are considered in this section. If nozzle extensions are utilized for the purpose of governing the maximum exhaust expansion angle, the internal heating rates must be considered. If the rocket is fired in proximity to the bus, contamination or combusion of the bus surfaces (and instrumentation) may occur. Finally, the presence of the rocket plume may produce heating on the aft surfaces of the lander in three modes, as will be discussed later. This section details the analytical approaches used in the determination of the de-orbit rocket effects.

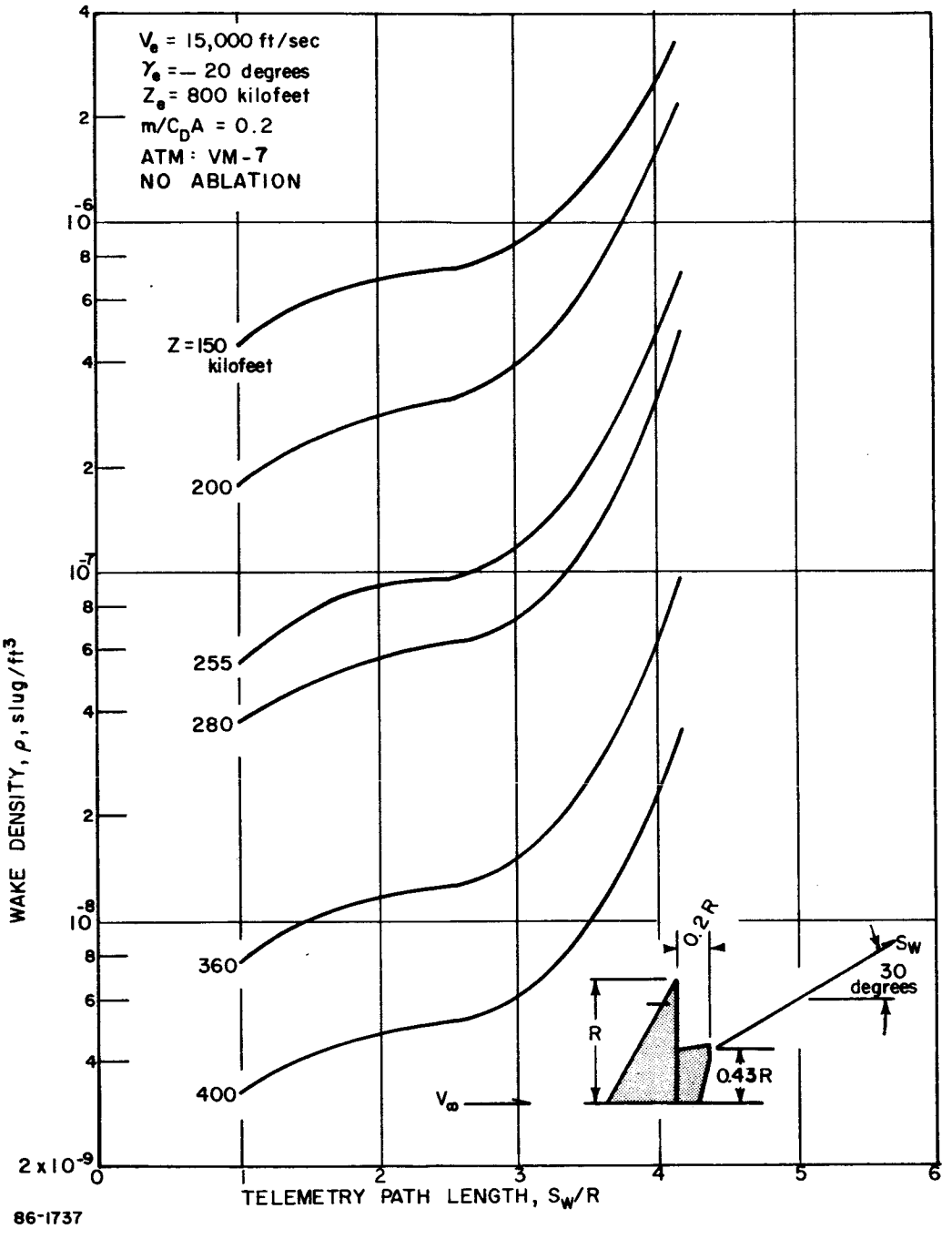

Figure 167 WAKE DENSITY PROFILES

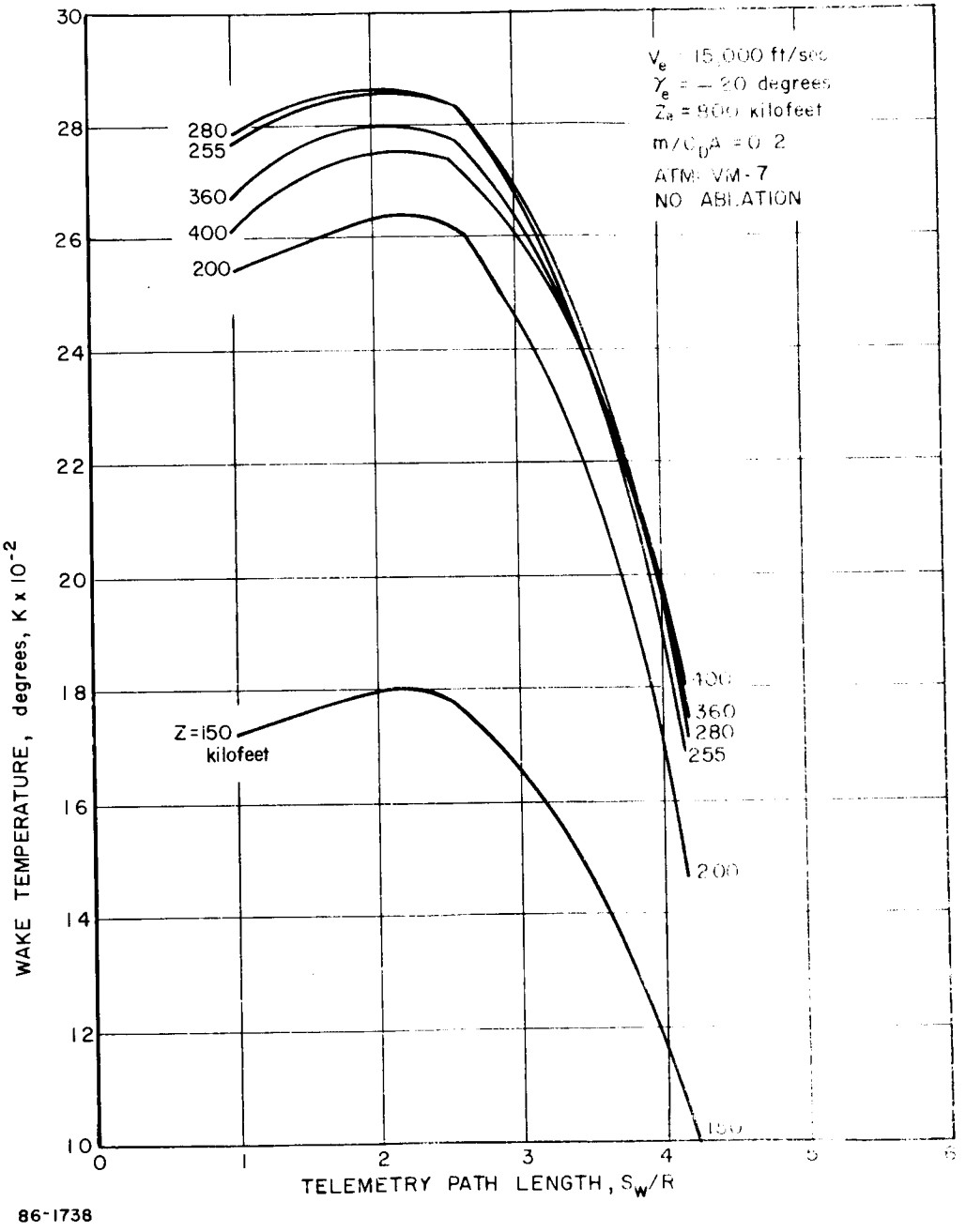

86-1738

Figure 168 WAKE TEMPERATURE PROFILES

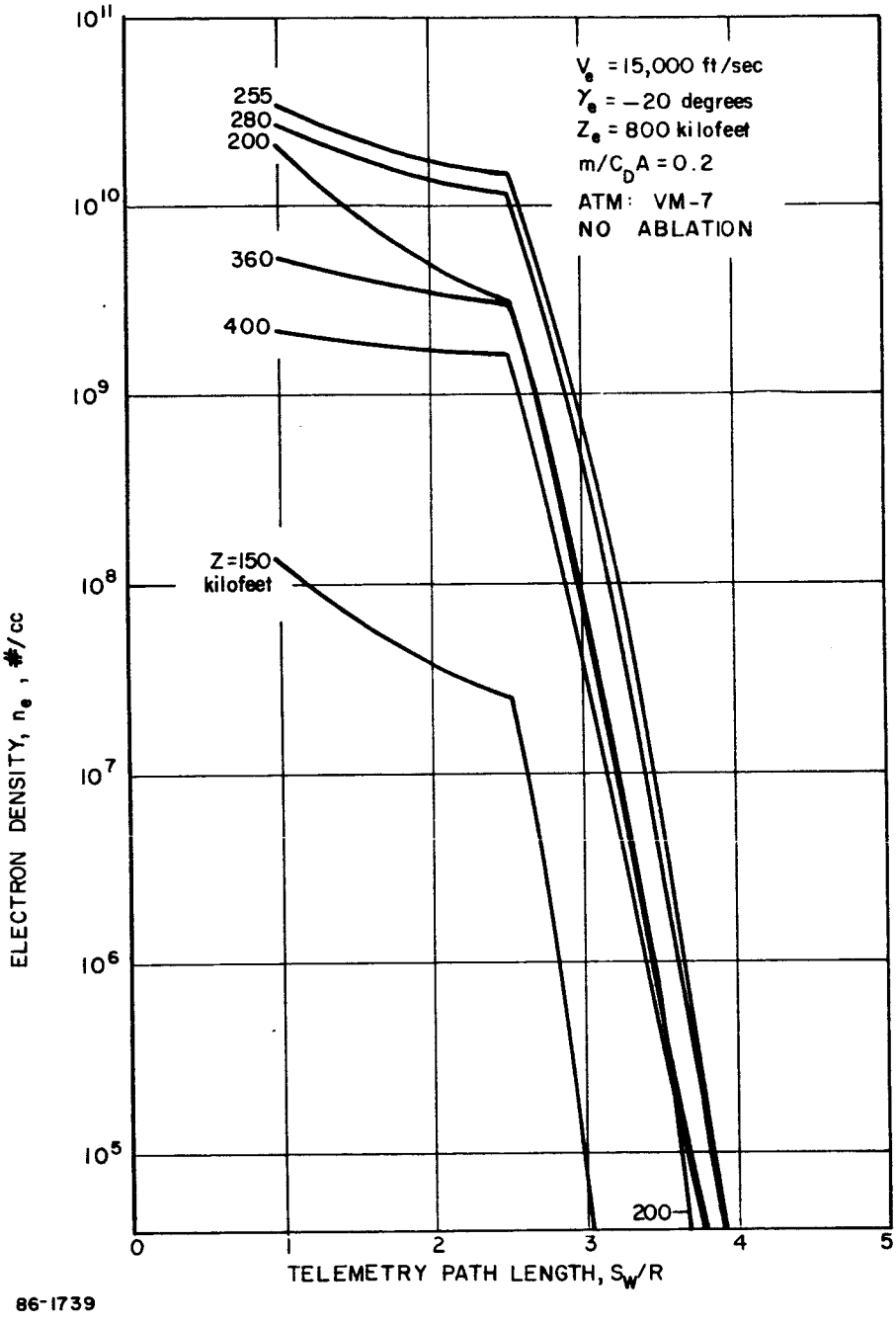

Figure 169 ELECTRON DENSITY PROFILES

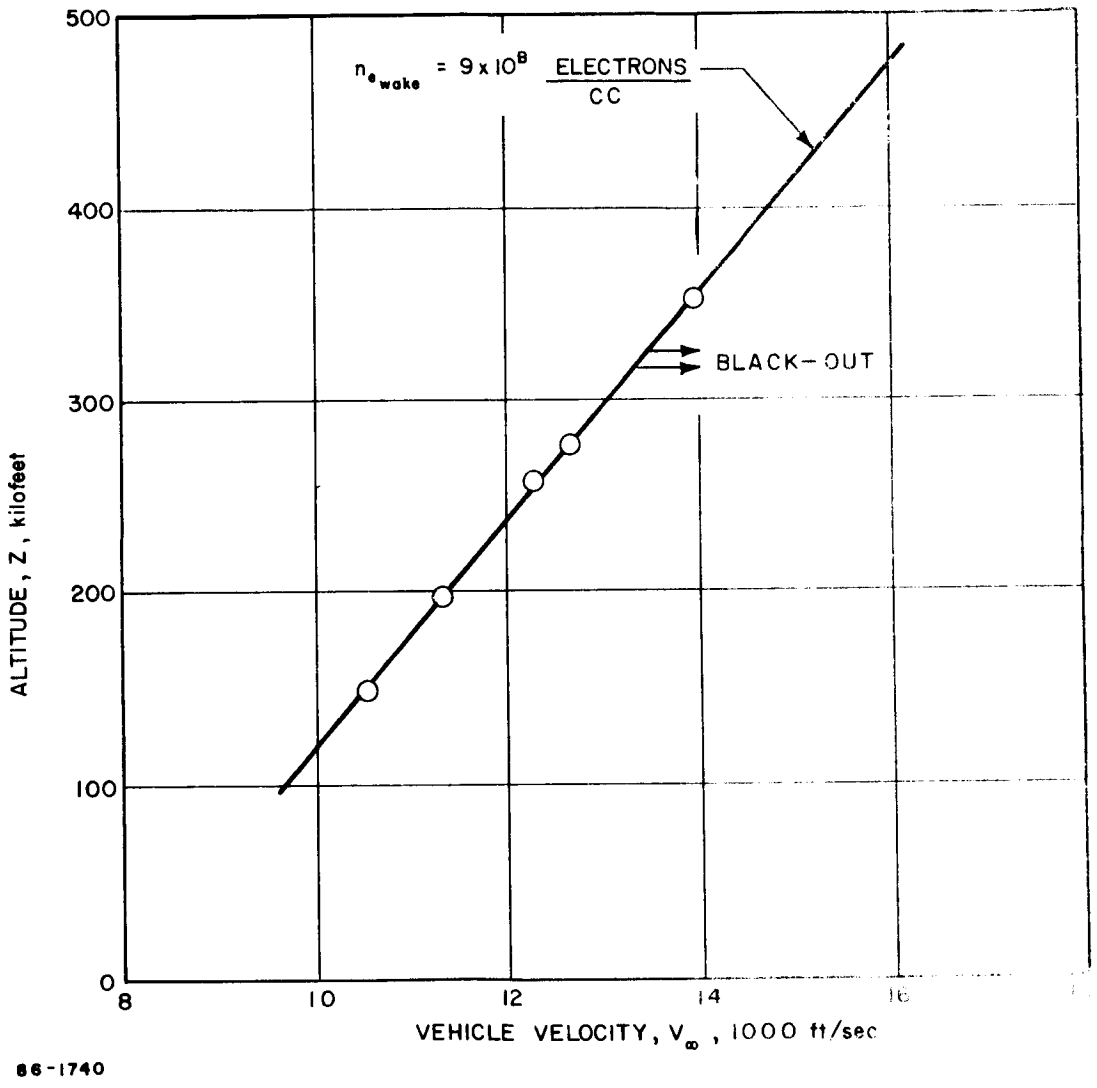

Figure 170 AERODYNAMIC TELEMETRY INTERFERENCE INCIDENT BLACKOUT CORRELATION

In all the above problems, consideration must be given to the working fluid, i.e. the rocket exhaust products. Overall systems considerations dictate the use of a solid propellant rocket motor for the de-orbit ΔV application. The best available information on exhaust products was used. The percentage of solids and liquids in the rocket exhaust was assumed small enough to have negligible effect on the gas dynamics of the exhaust. Table XXXI presents the concentrations of exhaust products used in these studies. Because the local gas temperature never exceeded 1200°K in any of the nozzles considered, frozen equilibrium chemistry was assumed for the working fluid.

TABLE XXXI

ROCKET EXHAUST PRODUCT CONCENTRATIONS

Constituent	Concentration (moles/100 gm)
CO	0.638
CO_2	0.593
HC	0.698
H_2	0.962
H_2O	1.000
H_2S	0.006
N_2	0.372

In order to determine the effects of plume impingement on bus and lander surfaces, flow-field calculations were necessary. The most efficient means is to obtain contours of pertinent parameters within the plume by the method of characteristics. A computerized solution (Avco Program 1268) was used to obtain the approximate flow field of the plume downstream of the nozzle exit. The solution is approximate since a finite value of ambient pressure must be used. The space environment, however, dictates an ambient pressure of the order of zero. Therefore, the plume was further expanded by hand-iterated solution of the method of characteristics finite difference equations (see reference 22.)

For the general interior point in R-X space, these equations are:

$$X_3^{(n+1)} = \frac{X_1 + \frac{1}{2}(K_1 + K_3^{(n)})\left[R_2 - R_1 - \frac{1}{2}X_2(\lambda_2 + \lambda_3^{(n)})\right]}{1 - \frac{1}{4}(\lambda_2 + \lambda_3^{(n)})(K_1 + K_3^{(n)})}$$

$$R_3^{(n+1)} = R_2 + \frac{1}{2}(X_3^{(n+1)} - X_2)(\lambda_2 + \lambda_3^{(n)})$$

$$M_3^{(n+1)} = (A_1 + A_2 + 2A_3^{(n)})^{-1}\left[2(\theta_2 - \theta_1) + M_2(A_2 + A_3^{(n)}) + M_1(A_1 + A_3^{(n)}) + (X_3^{(n+1)} - X_1)(B_3^{(n)} + B_1) + (X_3^{(n-1)} - X_2)(b_2 + b_3^{(n)})\right]$$

where

$$A = \left(\sqrt{M^2 - 1}\right) M^{-1} \left(1 + \frac{r-1}{2} M^2\right)^{-1}$$

$$B = \left(\sqrt{M^2 - 1} \cot\theta - 1\right)^{-1} R^{-1}$$

$$b = \left(\sqrt{M^2 - 1} \cot\theta + 1\right)^{-1} R^{-1}$$

$\lambda = \tan(\theta - \mu)$

$K = \cot(\theta + \mu)$

$\mu = \arcsin(1/M)$

M= Mach number

θ = flow angle from X-axis

n= iteration number

The theoretical boundary of the jet plume is found from the Prandtl-Meyer relation as modified for infinite Mach number ($P_a \to 0$):

$$\theta_b = \theta_N + \sqrt{\frac{\gamma+1}{\gamma-1}}\left[\frac{\pi}{2} - \arctan\sqrt{\frac{\gamma-1}{\gamma+1}(M_N^2-1)}\right] + \arctan\sqrt{M_N^2-1} - \frac{\pi}{2}$$

where subscript N denotes nozzle exit conditions. The practical significance of this boundary is somewhat nebulous since the gas density approaches zero. It should, however, be considered as the limit of the zone of influence of the rocket plume.

4.3 HEATING

4.3.1 Convective Heating

4.3.1.1 Blunt Cone and Modified Apollo

The heating distributions were obtained by means of laminar similarity methods (Reference 23 in conjunction with the pressure distributions described previously. The angle of attack distributions comprised a combination of data and theory. The distributions at angle of attack were considered equivalent to that for a body with a meridian rotated about the pitch axis an amount equal to the angle of attack and then rotated about the spin axis. This equivalent body was then evaluated by means of the similarity method or, where available, data were used.

The turbulent distributions were obtained by means of the methods discussed in Reference 24. The form factor was retained to ensure conservative estimates of the heating on both the blunt cone and modified Apollo shapes.

The equations for the laminar and turbulent distributions are as follows:

Laminar:

$$\dot{q}/\dot{q}_{stag} = \frac{r_b^j \rho_b \mu_b V_\infty}{1.068\sqrt{2\xi}} \sqrt{\frac{1 + 0.096\sqrt{\beta}}{2\rho_b \mu_b \left(\frac{du_e}{d_x}\right)_{stag}}} \sqrt{\frac{2}{j+1}}$$

where

$$\xi = \int_0^s \rho_o \mu_o U_e r_b^{2j} dS$$

$$\beta = 2 \frac{d \ln U_e}{d \ln \xi}$$

b, e and ∞ refer to wall, local inviscid, and free-stream conditions respectively.

Turbulent:

$$\dot{q} = \frac{C_f}{2} \rho_e U_e h F$$

where

$$C_f = \frac{0.0296 (2)^{0.2j}}{(\sigma)^{2/3} (R_e)^{0.2}} \left(\frac{\rho^*}{\rho_e}\right)^{0.8} \left(\frac{\rho^*}{\mu_e}\right)^{0.2}$$

$$h^* = h_e \left\{ 1 + \frac{1}{2} \left(\frac{h_b}{h_e} - 1\right) + 0.22 \sigma^{1/3} \left(\frac{h_{stag}}{h_e} - 1\right) \right.$$

$$F = 1.037 \left\{ \frac{1}{U_e^{5/2} r^{5/4} \rho_e^{5/4}} \left(\frac{U_e}{\nu_e}\right)^{1/4} \frac{1}{x} \int_0^x \left(\frac{\nu_e}{U_e}\right)^{1/4} U_e^{5/2} r^{5/4} \rho_e^{5/4} dx \right\}^{-1/5}$$

The reference enthalpy, h^* , in conjunction with the local pressure P_e, define the temperature, T^* , density, ρ^* , etc.

The resulting distributions are shown in Figures 171 and 172 for zero-angle of attack. The laminar rates have been normalized with respect to the stagnation point heating whereas the turbulent distribution has been normalized by a turbulent sonic point heating. Although the stagnation point heating has been correlated for N_2-CO_2 mixtures

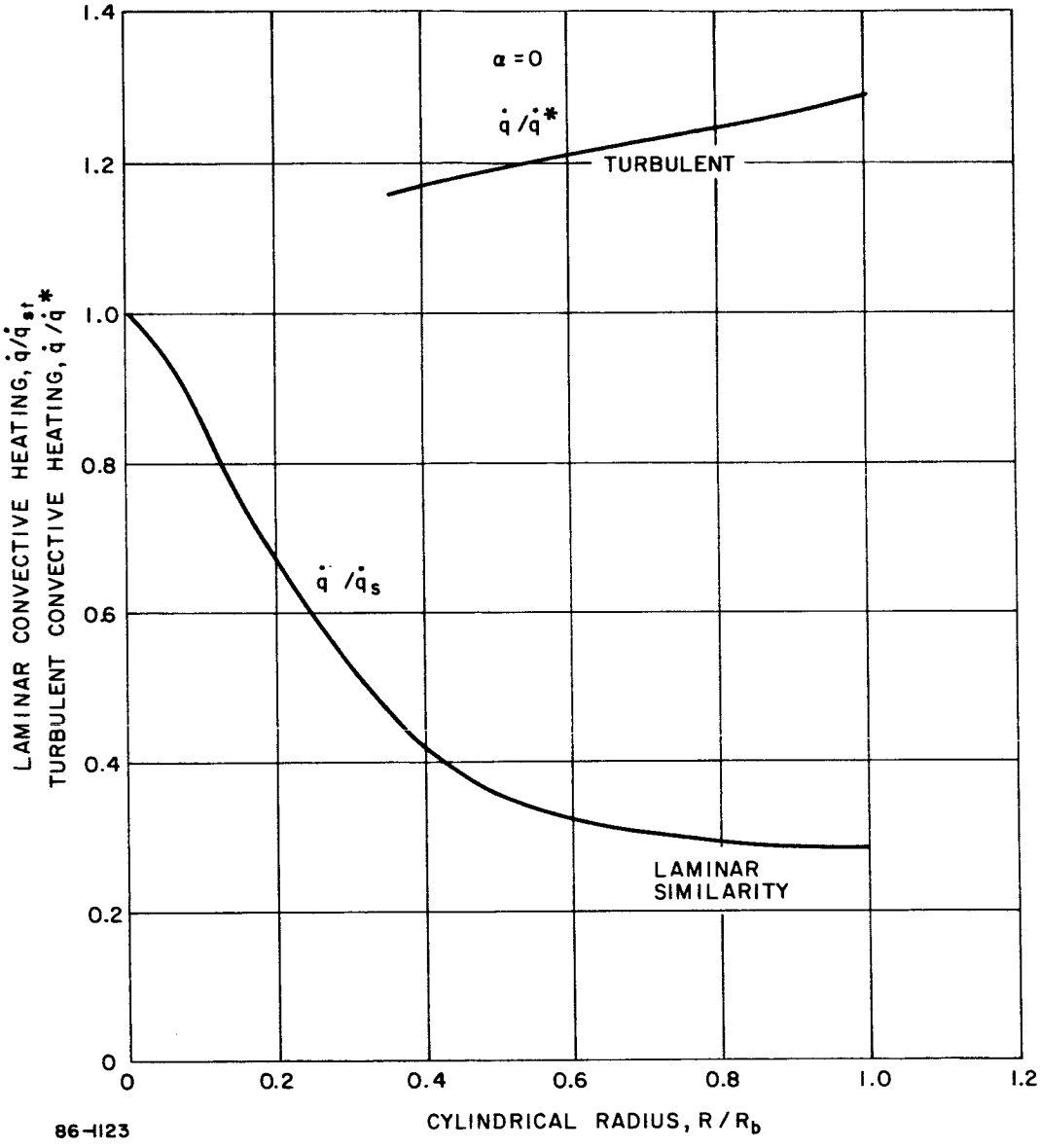

Figure 171 HEATING DISTRIBUTION--BLUNT CONE

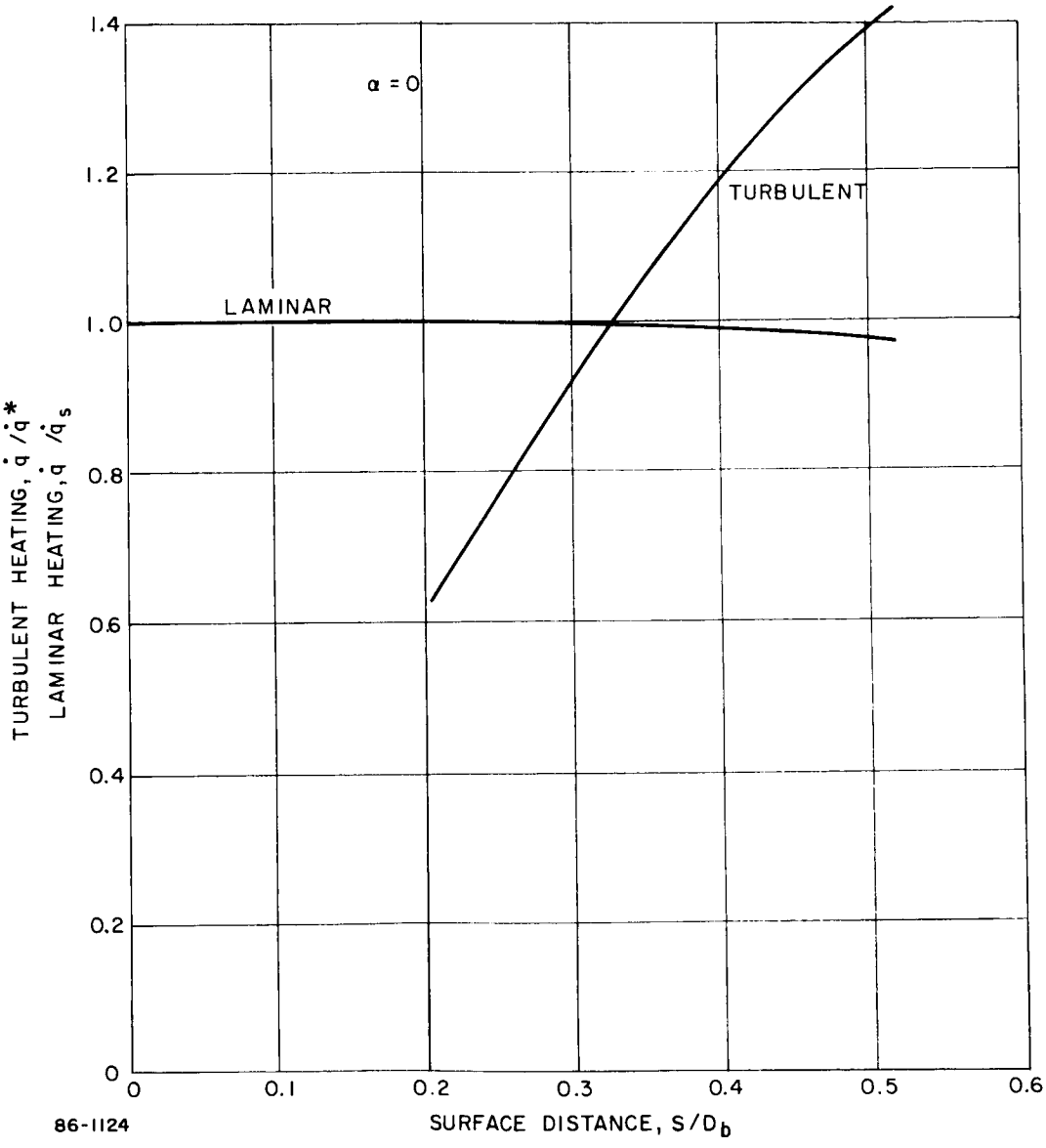

Figure 172 HEATING DISTRIBUTION--MODIFIED APOLLO

(Reference 25) the turbulent heating has shown no definite trend with composition. Test data (Reference 26) indicate that presently available theories predict the heating for Martian atmospheres satisfactorily.

These distributions were used in conjunction with the computed reference pulse for each trajectory considered.

The following expressions are those that are used in the Avco trajectory program to obtain reference heat pulses.

The stagnation point heating has been correlated for CO_2-N_2 mixture as

$$\dot{q}_s = \frac{K_L}{(D/2)^{1/2}} \rho_\infty^{1/2} \left(\frac{V_\infty}{10^4}\right)^{b_L}$$

where

$$K_L = (1.1 + 0.075\ \bar{M})(10^4)\left[\frac{D}{2V_\infty}\left(\frac{dU}{dS}\right)_S\right]^{1/2}$$

$$b_L = 3.909 - 0.0229\ \bar{M}$$

$\bar{M}$ = Molecular weight

$[D/2\ V_\infty (dU/dS)_S]$ = velocity gradient at the stagnation point.

This form depends only upon the density ratio ρ_∞/ρ_s which is computed as a function of time for the appropriate atmospheric composition. The effect of atmospheric composition is reflected through K_L, b_L and the velocity gradient.

No mixture correlation is available as yet for the turbulent sonic point heating which is expressed as

$$q_T^* = K_T \rho_\infty^{0.8} \left(\frac{V_\infty}{10^4}\right)^{3.18}$$

where

$$K_T = \frac{540{,}000}{(S^*)^{0.2}}$$

and S^* is the distance from the stagnation point to the sonic point at zero-angle of attack.

The angle of attack heating requires careful analysis. The heating environment is influenced first by the effects of the angle of attack histories on the trajectory and second by the local aggravations associated with angle of attack. The local effects are manifested on the modified Apollo through a nonaxisymmetric stagnation point in addition to the increased pressure gradients at the sonic point (windward meridian, see Figure 173). The asymmetric stagnation point heating was obtained by means of the methods of Reference 25, with the distribution obtained as indicated above.

The angle of attack motion with respect to a given point on the body is complex and involves an iterative technique to determine the meridian which experiences the most severe environment for a particular body station. An alternate approach, which is conservative, involves using the maximum heating within the angle of attack (envelope values). This approach (employed herein) is that associated with lunar motion. Two additional alternate approaches would consider infinite spin (which would average the heating circumferentially) and planar motion where the heating average places emphasis on the two heating extremities. The surface integration was normalized with respect to the zero-angle of attack stagnation point heating to facilitate the comparisons and tradeoffs associated with reentry conditions (spin rate, angle of attack, etc.).

4.3.1.2 Tension Shell

Laminar and turbulent convective heat transfer rates were computed using Eckert's reference enthalpy method as modified by Zappa (Reference 27) for conical flow. Basic heating rates were computed at specific points on the body for laminar and turbulent flow and heating rate distributions were obtained in ratio to these points. From Reference 27, the conical heating relations may be shown to be

$$\dot{q}_L \sqrt{S} = 0.72 (\rho_\infty V_\infty H_s) \left(\frac{R_\infty}{L}\right)^{-\frac{1}{2}} \left(\frac{U}{V_\infty}\right)^{\frac{1}{2}} \left(\frac{P_e}{P_\infty}\right)^{\frac{1}{2}} \left(\frac{h^*}{h_e}\right)^{-\frac{1}{8}} \left(\frac{h_r - h_w}{H_s}\right)_{\text{laminar}}$$

$$\dot{q}_T S^{0.2} = 0.0438 (\rho_\infty V_\infty H_s) \left(\frac{R_\infty}{L}\right)^{-0.2} \left(\frac{U}{V_\infty}\right)^{0.8} \left(\frac{P_e}{P_\infty}\right)^{0.8} \left(\frac{h^*}{h_e}\right)^{-0.67} \left(\frac{h_r - h_w}{H_s}\right)_{\text{turbulent}}$$

The recovery enthalpy is given by

$$h_r = rH_s + (1 - r) h_e$$

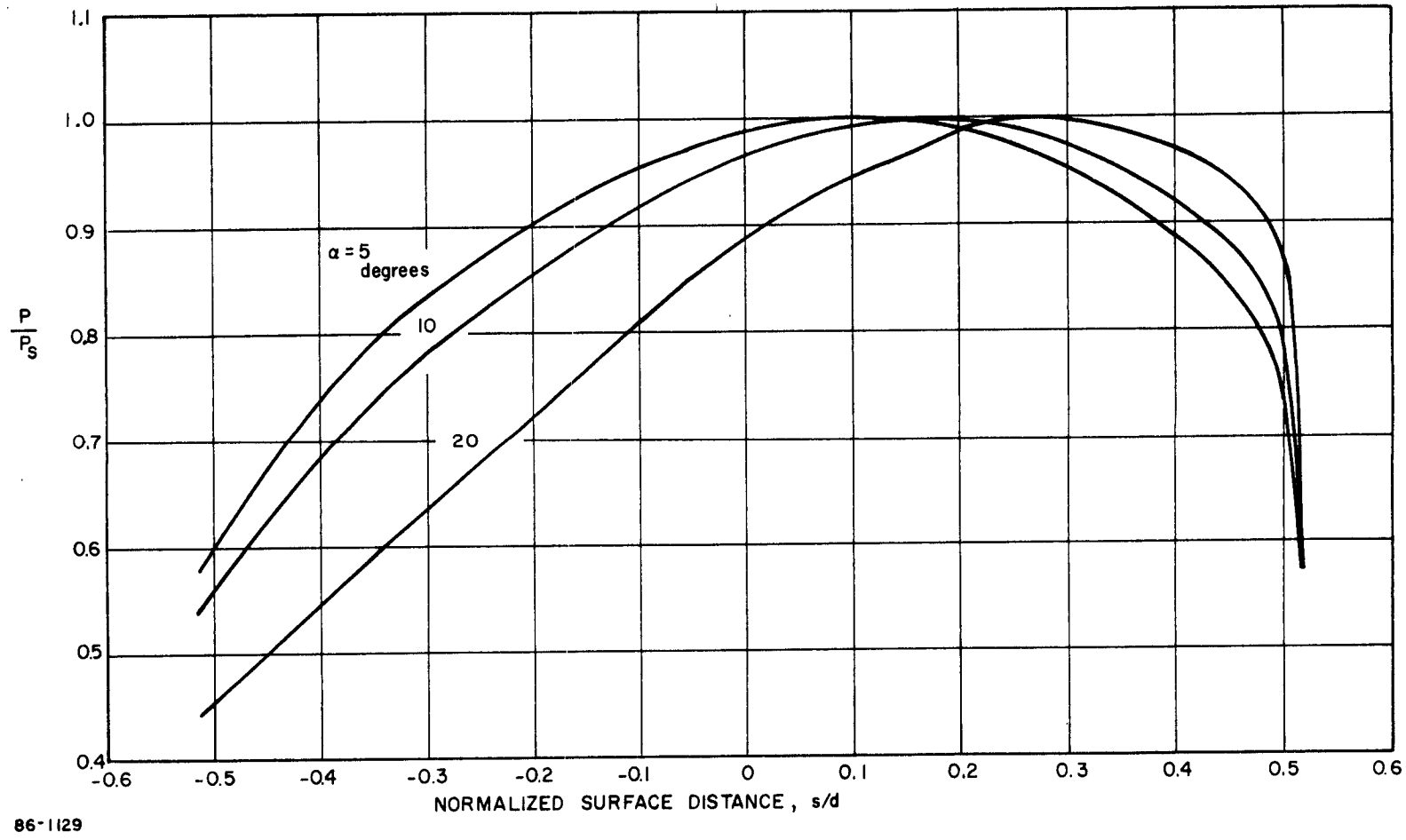

Figure 173 PRESSURE DISTRIBUTION -- MODIFIED APOLLO

where h_e is the local enthalpy of the inviscid stream and the recovery factor r, is 0.85 for laminar flow and 0.88 for turbulent flow. The reference enthalpy is evaluated from

$$h^* = 0.5\,(h_e + h_w) + 0.22\,(h_r - h_e)$$

With a little manipulation the point-to-point heating rate ratios are obtained (assuming zero wall enthalpy) as:

$$\frac{\dot{q}_L}{\dot{q}_{L_o}} = \left[\frac{(p/p_s)\,(U/V_\infty)\,S_o}{(p/p_s)_o\,(U/V_\infty)_o\,S}\right]^{\frac{1}{2}} \left[\frac{(h^*/H_s)_o}{(h^*/H_s)}\right]^{\frac{1}{8}}_{\text{laminar}}$$

$$\frac{\dot{q}_T}{\dot{q}_{T_o}} = \left[\frac{(p/p_s)\,(U/V_\infty)}{(p/p_s)_o\,(U/V_\infty)_o}\right]^{0.8} \left[\frac{S_o}{S}\right]^{0.2} \left[\frac{(h^*/H_s)_o}{(h^*/H_s)}\right]^{0.67}_{\text{turbulent}}$$

The general reference points for design are not, however, in the conical flow region of the tension shell. The nose stagnation point and sonic point are used as laminar and turbulent bases, respectively. For design purposes, heating at these two points is generally obtained by the method in Avco computer program 1880 which was outlined in a previous section. To incorporate program 1880 results into heat transfer distributions it is necessary only to form the expressions

$$\frac{\dot{q}_L}{\dot{q}_s} = \left(\frac{\dot{q}_{L_0}}{\dot{q}_s}\right)\left(\frac{\dot{q}_L}{\dot{q}_{L_o}}\right)_{\text{laminar}}$$

$$\frac{\dot{q}_T}{\dot{q}^*_T} = \left(\frac{\dot{q}_{T_o}}{\dot{q}^*_T}\right)\left(\frac{\dot{q}_T}{\dot{q}_{T_o}}\right)_{\text{turbulent}}$$

Here, the first ratios on the right hand side of the equations represent the obsolute values of laminar and turbulent heating at point "O" evaluated by the first equations of this section divided by the program 1880 output number. The second ratios represent the distribution functions.

Whether laminar or turbulent flow exists at any given point on the surface is a function of the transition Reynolds Number. A conservative value of 3×10^5 has been used for this parameter.

Application of this theory to the wind-tunnel test data is shown in Figure 174. The test data provide a good comparison for both laminar and turbulent heat transfer theory since both modes exist on the test vehicle. The comparison is not exact because the test data were

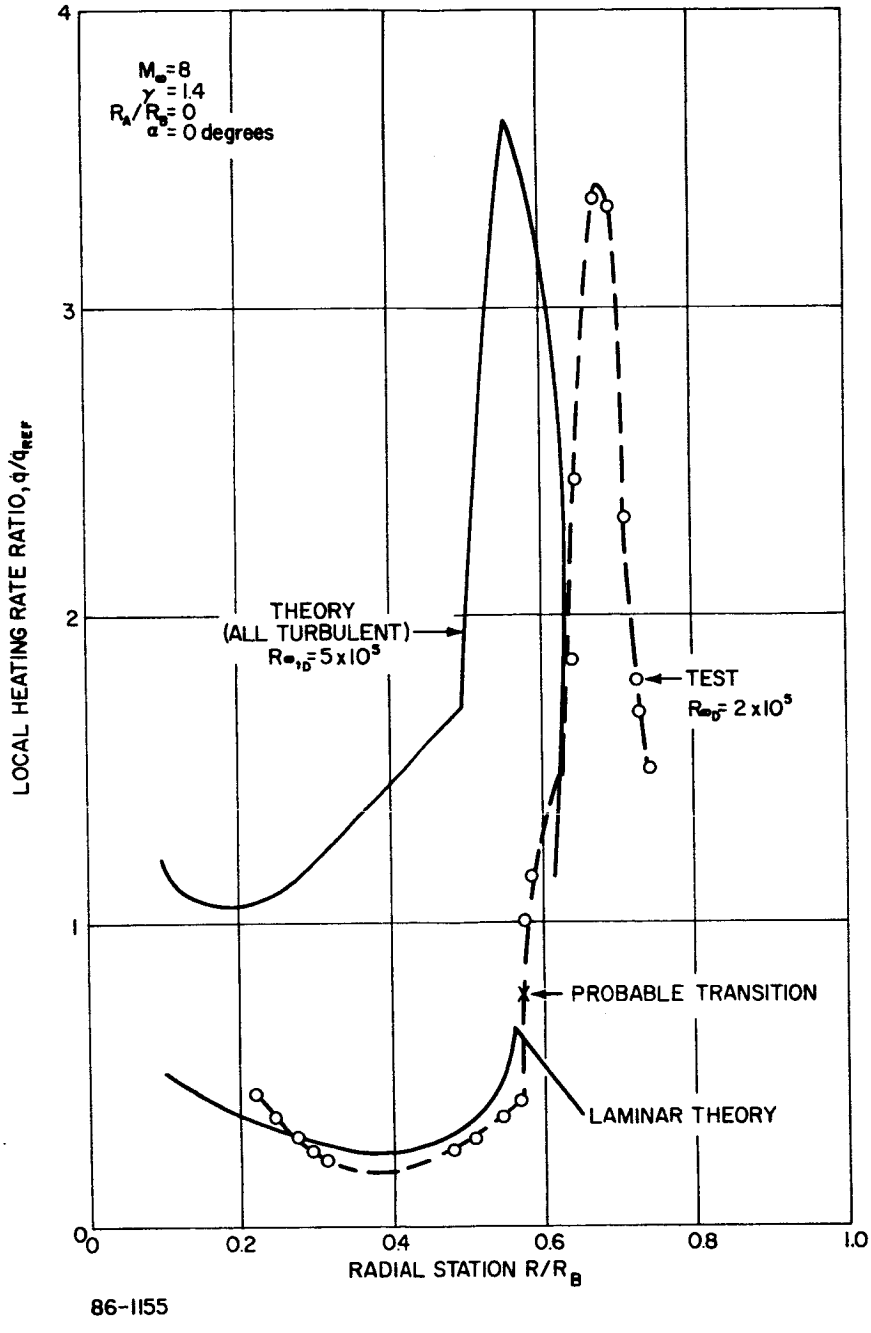

Figure 174 LRC WIND TUNNEL AERODYNAMIC HEATING DISTRIBUTION

obtained at a lower Reynolds number. The Reynolds number effect is however, small and the agreement between theory and test is good. A discrepancy in the body station (R/R_B) at which the maximum heating point occurs is caused by the misplacement of the theoretical pressure distribution as explained previously.

Again referring to the typical flow field (Figure 158), laminar and turbulent convective heating were calculated for the same conditions. The distributions of heating over the body are shown in Figure 175. The reference heating values $\dot{q}_s$ and $\dot{q}^*$ are stagnation point heating and turbulent sonic point heating. The ratio of surface distance to nose radius is used as a distribution parameter since S/R_N is most convenient for heat shield calculations. Blunt-body heating with a Newtonian pressure distribution was used over the front portion of the body.

The first peak heating rate ($S/R_N = 11.6$) was used to evaluate heat shield design over the entire jagged region. The distributions presented here do not, however, represent the design distributions since atmosphere and entry conditions produce major perturbations in heating.

4.3.1.3 Vorticity Interaction

In the EFAT phase of study, entry velocities were sufficiently high and atmospheres sufficiently dense, that the aerodynamic heating encountered during early entry could be considered negligible with respect to the heating encountered at lower altitudes. EFO studies considered less dense atmospheres and lower velocities, thus decreasing the Reynolds numbers of entry and causing the vorticity interaction flow regime to produce a significant portion of the heating. In this flow regime, the boundary layer is thin compared to the shock layer and can be considered as a continuum, but the vorticity in the inviscid layer between the shock and boundary layer dictates the conditions at the edge of the boundary layer and thus the boundary-layer behavior. Although a complete solution to the partial differential equations is not warranted here, an outline is given for reference purposes. The system of equations governing the flow in the vorticity interaction regime is, after simplification and neglecting small terms (after Ferri, Reference 28).

$$f''' + f'' f = 0$$

$$g'' + P_r f g = 0$$

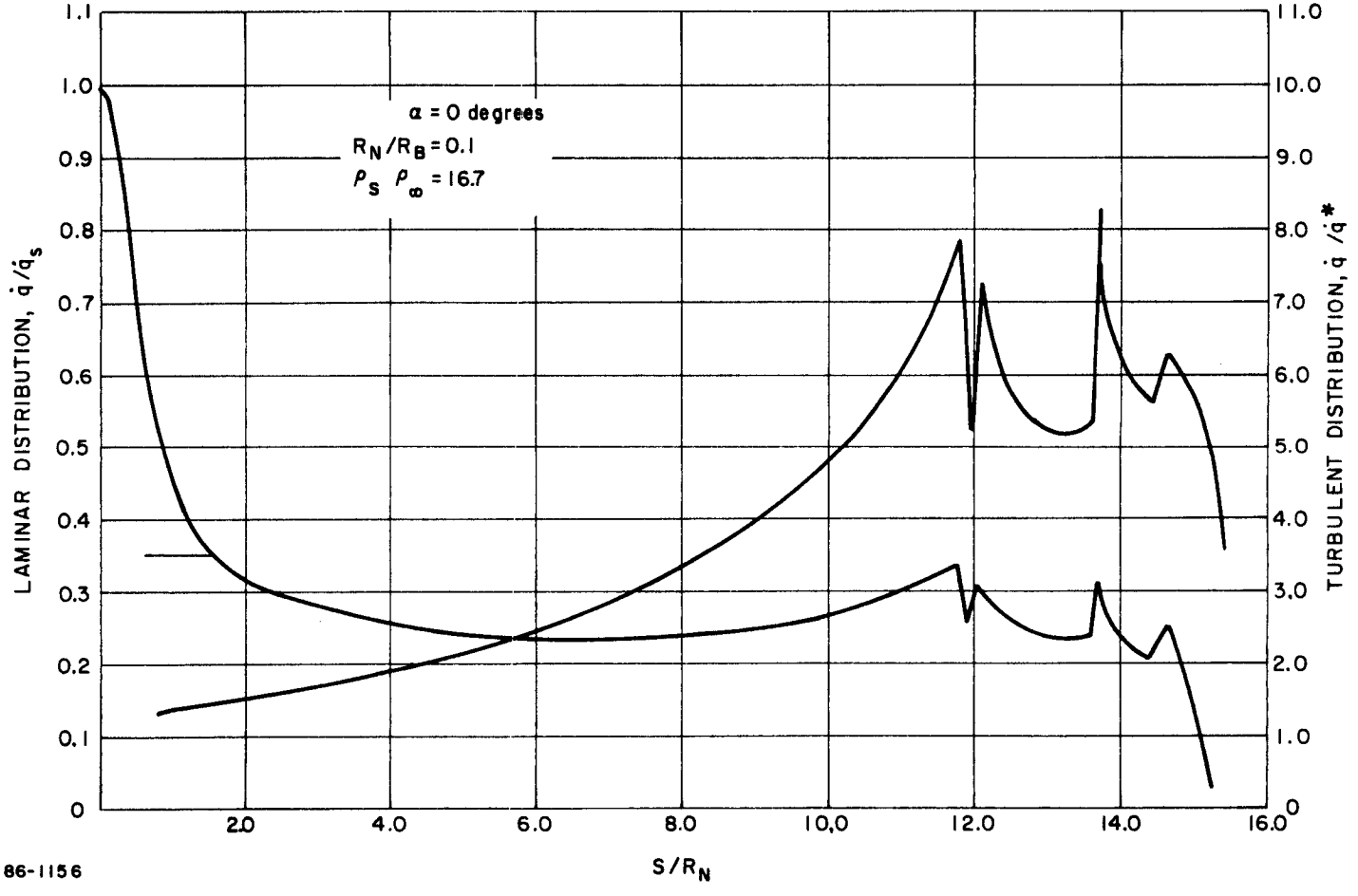

Figure 175 BLUNT TENSION SHELL HEATING DISTRIBUTIONS

$$f(0) = f'(0) = g(0) = 0$$

$$g(\infty) = 1$$

where the function g is defined by

$$g = (h - h_w) / (h_s - h_w)$$

and f is related to the stream function ψ by

$$\psi(s, \eta) = f(\eta)\sqrt{2S}$$

and s and η are transformed coordinates.

By assuming a linear velocity profile for the inviscid flow:

$$U = Uo\,[1 + \omega\,(y/R_N)]$$

where ω is the vorticity strength defined by

$$\omega = \left[\sqrt{\frac{\bar{\rho}+1}{2}} - 1\right]\left[1 + \frac{1}{(\Lambda/R_N)}\right]\left(\frac{1}{\bar{\rho}}\right)\left[\bar{\rho} - \frac{2h_s}{V_\infty^2}\right]$$

$$\left(\bar{\rho} = \frac{\rho_s}{\rho_\infty}\right),$$

by matching the velocity of the inviscid flow with the boundary-layer profile for equal mass flow rates, the foregoing system of equations can be solved. This solution is represented in terms of the parameter Γ:

$$\Gamma = \frac{\omega}{\sqrt{Re\left(\frac{\partial u}{\partial x}\right)\left(\frac{R_N}{V_\infty}\right)}}$$

where R_e is the Reynolds number based on the nose radius (R_N), free-stream velocity, and stagnation density and viscosity. At the stagnation point, the ratio of heating rate with vorticity interaction to the heating rate based on pure continuum theory is shown in Figure 176. Ferri, et al, investigated this function with respect to wall-temperature effects and found them negligible in the region indicated. (This encompasses the region of interest to heat shield designs.) Application of this theory to certain data is shown in Figure 177 taken from Reference 29. The extremely good agreement in the range of Reynolds numbers from 500 to 50,000 is noteworthy. Stagnation point Reynolds

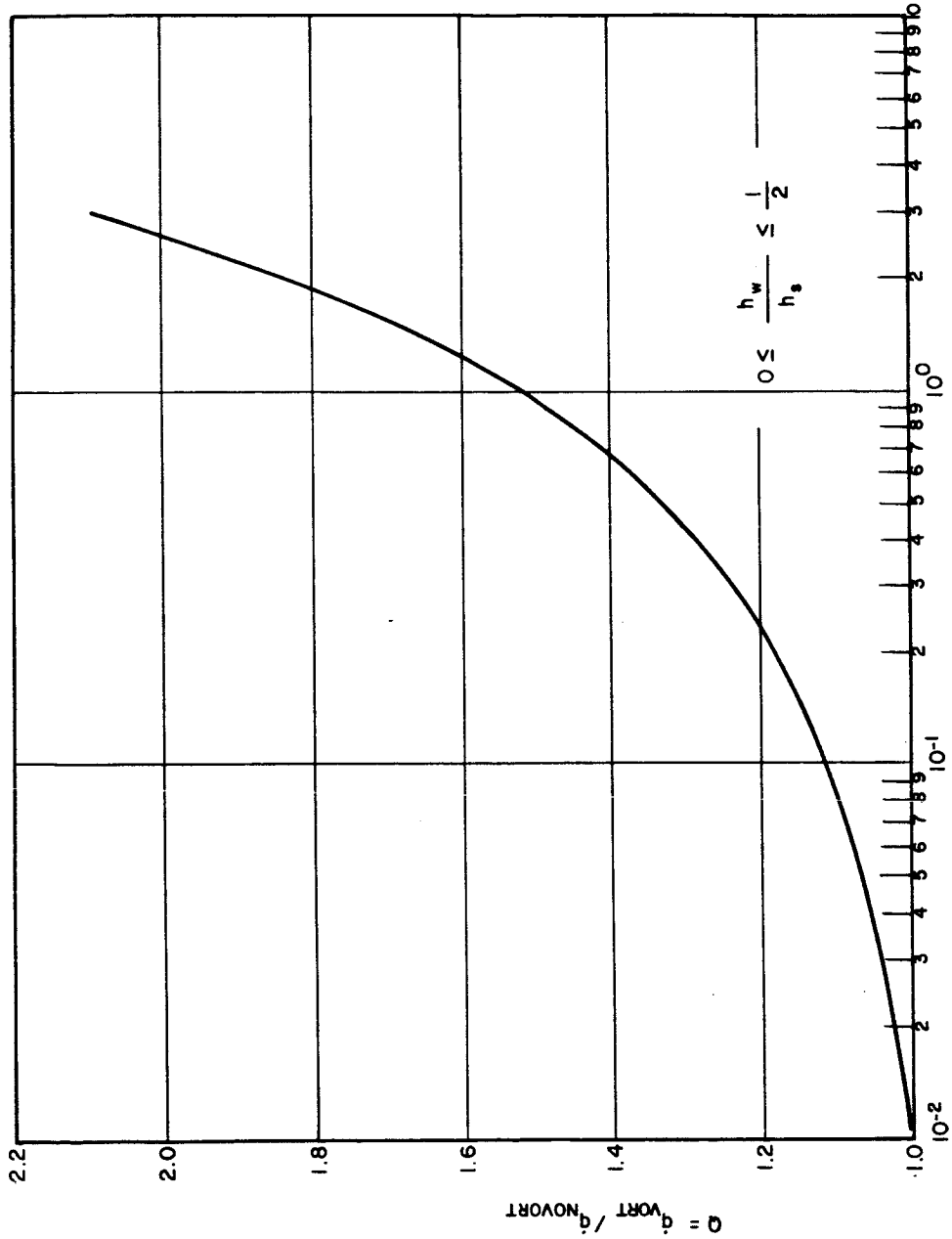

Figure 176 VORTICITY INTERACTION STUDY--INTERACTION EFFECT ON STAGNATION POINT HEAT TRANSFER

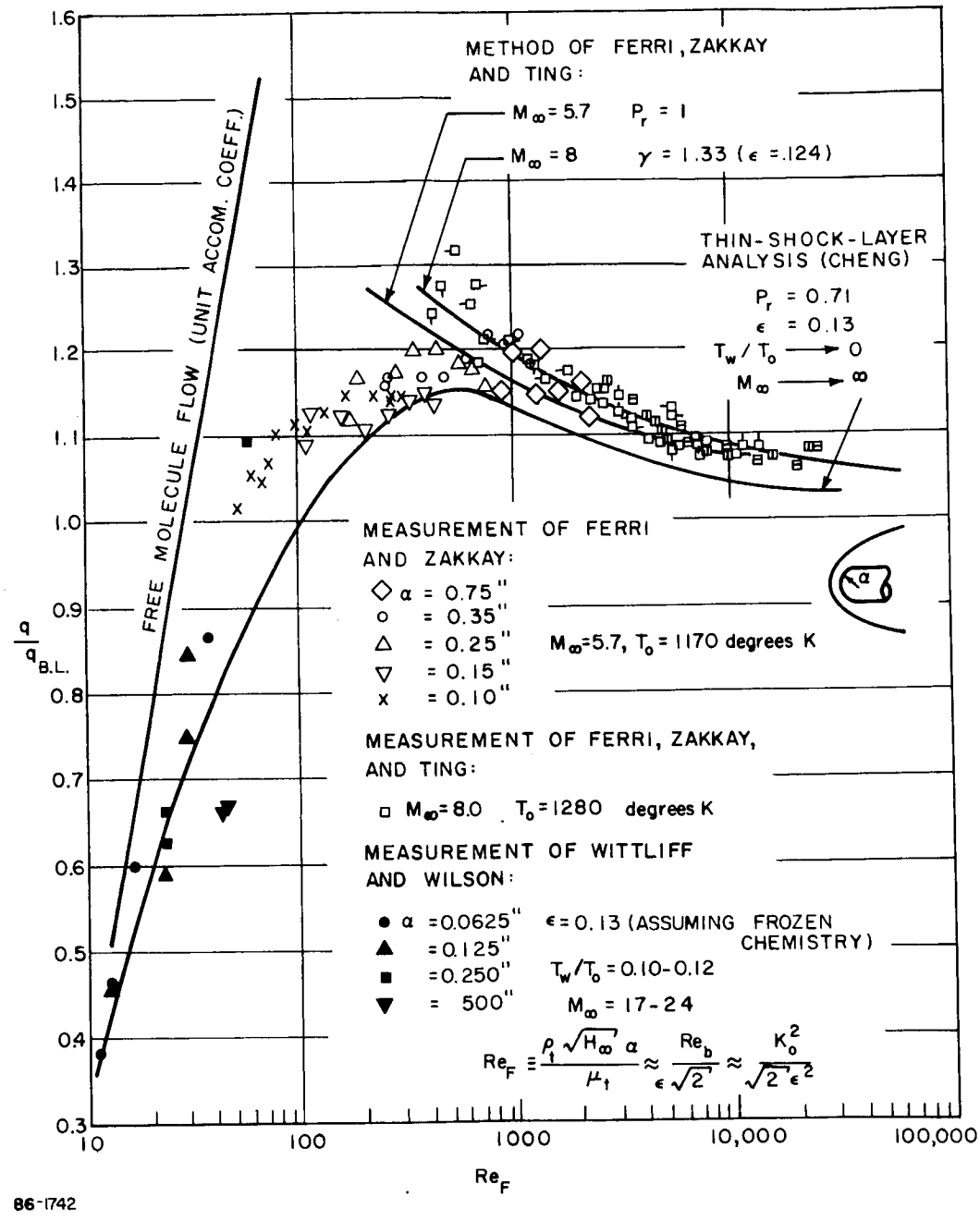

Figure 177 COMPARISON OF STAGNATION POINT HEAT-TRANSFER MEASUREMENTS ON SPHERICAL BODIES WITH THEORIES

number and density ratios can be factored out of Γ to provide the set of working curves needed for EFO investigations. These are shown in Figure 178. Further investigation of Ferri's work disclosed that the heating increase due to vorticity interaction is approximately unchanged up to 30 degrees away from the stagnation point. A very approximate solution (for several Mach numbers) bears this out, as shown in Figure 179. Therefore EFO studies assumed that the stagnation point factor applied over the whole body.

4.3.1.4 Entropy Variation

The impact of thinner atmospheres, lower velocities, and new atmospheric compositions on the distribution of aerodynamic heating over the face of the blunt cone, has been to increase the sensitivity of the local heating rate to variations in entropy and increase the local heating rate with respect to stagnation point heating. Avco standard computer programs 873C and 1115B (Aerodynamic heating programs) were utilized to study these effects. Laminar similarity theory heating rates were generated for several body radial stations. Figure 180 shows the comparison of effects of various entropy assumptions. The lowest curve represents normal shock entropy over the entire body. The middle curve represents an entropy variation based upon the local pressure and the true shock shape. The highest heating rates are generated assuming conical shock entropy. Basically, the high and low curves represent the upper and lower bounds of possible entropy variations. The middle curve is the most realistic. It should be noted that the entropy difference between the upper and lower bounds is nowhere greater than 3 percent of the normal shock value, yet the heating rate differs by as much as 65 percent. Of further note is the fact that the most realistic assumption corresponds very closely to the most pessimistic assumption.

The most realistic heating distributions for atmosphere VM-7 and (approximately) for VM-8 are shown in Figure 181 compared with the distribution used in the entry from the approach trajectory phase. The effects of lower velocities and greater density ratios are clearly evident. The new distributions were used for design of the entry from orbit vehicle.

4.3.1.5 Heating Due to Protuberances and Cavities

Wherever complex physical shapes are involved, the general equations of fluid flow, on which the aerodynamicist depends, become too complex for solution. As this point empiricism is necessary, as is the case with the heating aggravation effects of protuberances and cavities. Several authors (References 30 and 31) have made attempts to provide

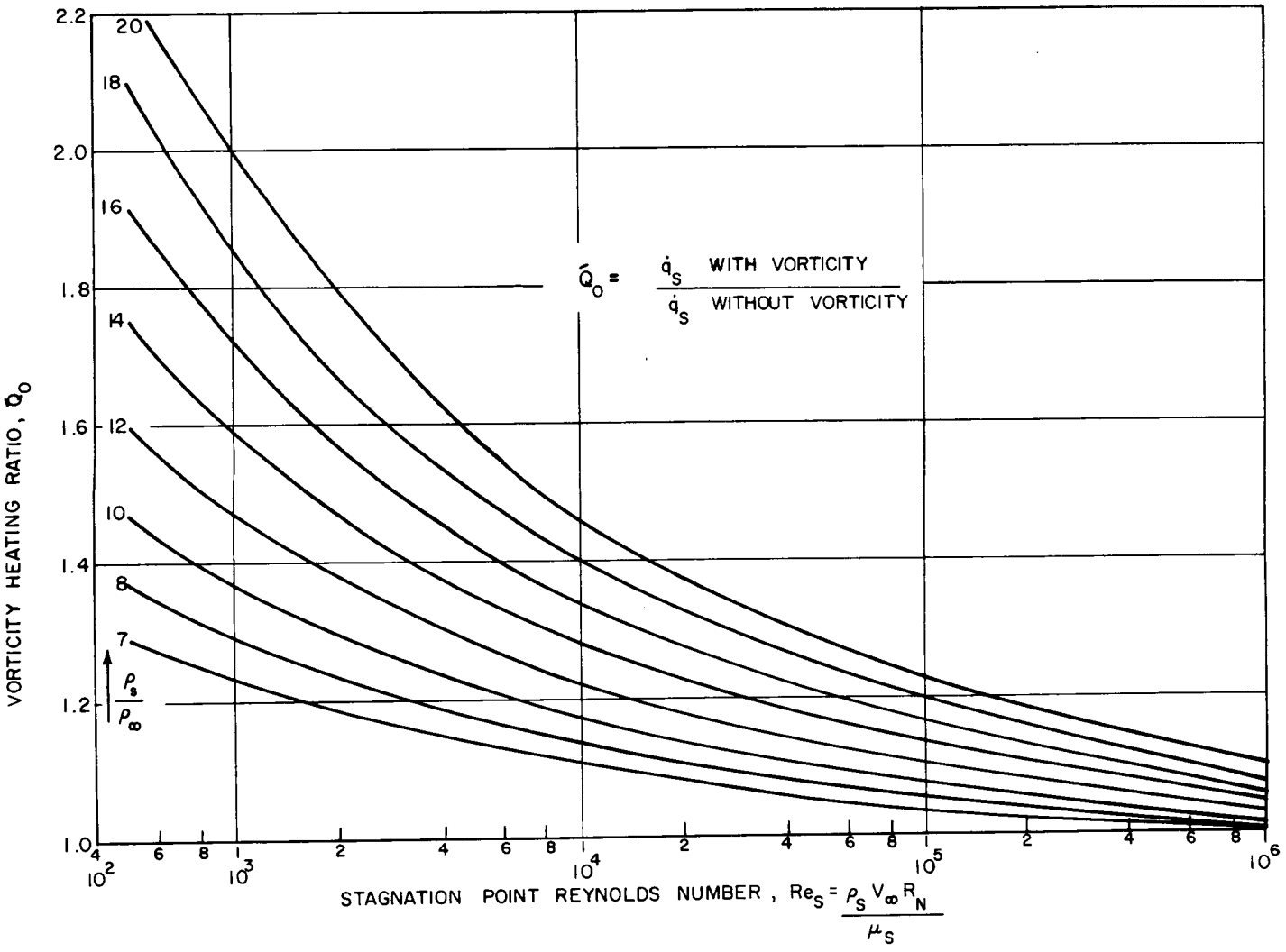

86-1743

Figure 178 VORTICITY INTERACTION HEATING RATIO STAGNATION POINT

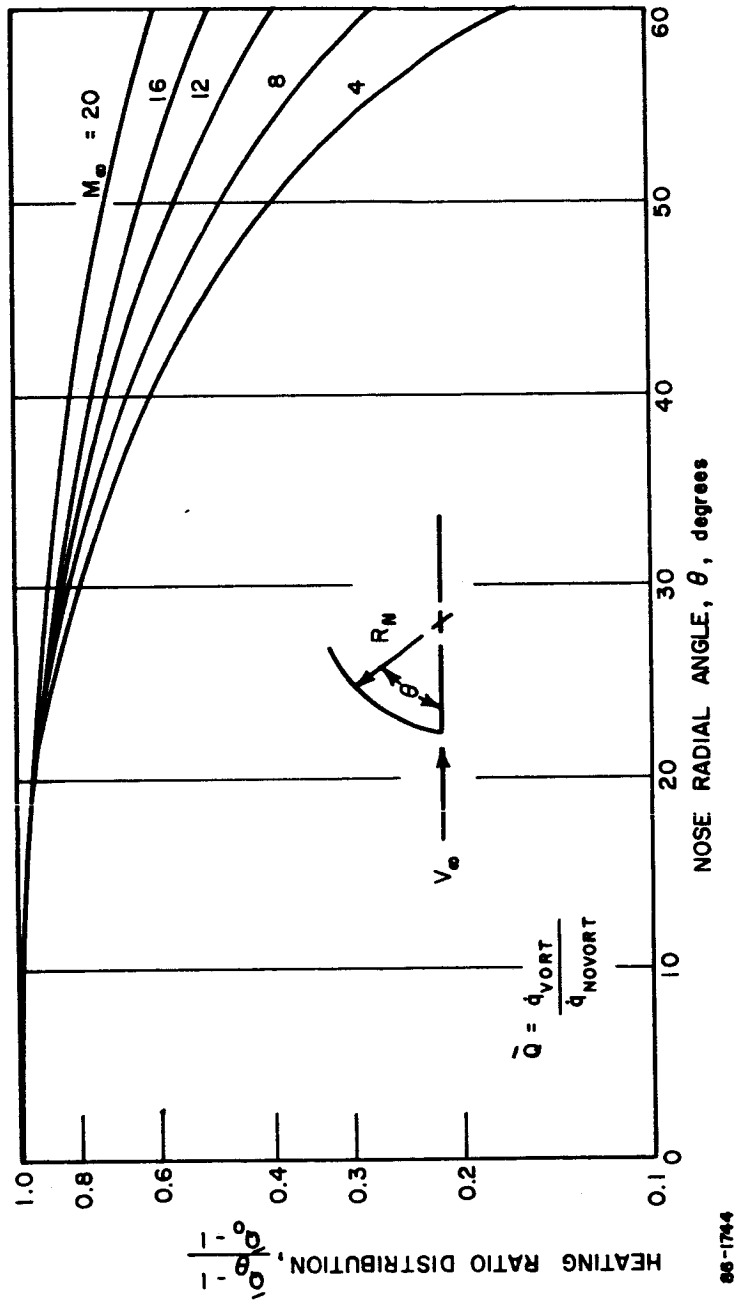

Figure 179 VORTICITY INTERACTION HEATING RATIO DISTRIBUTION

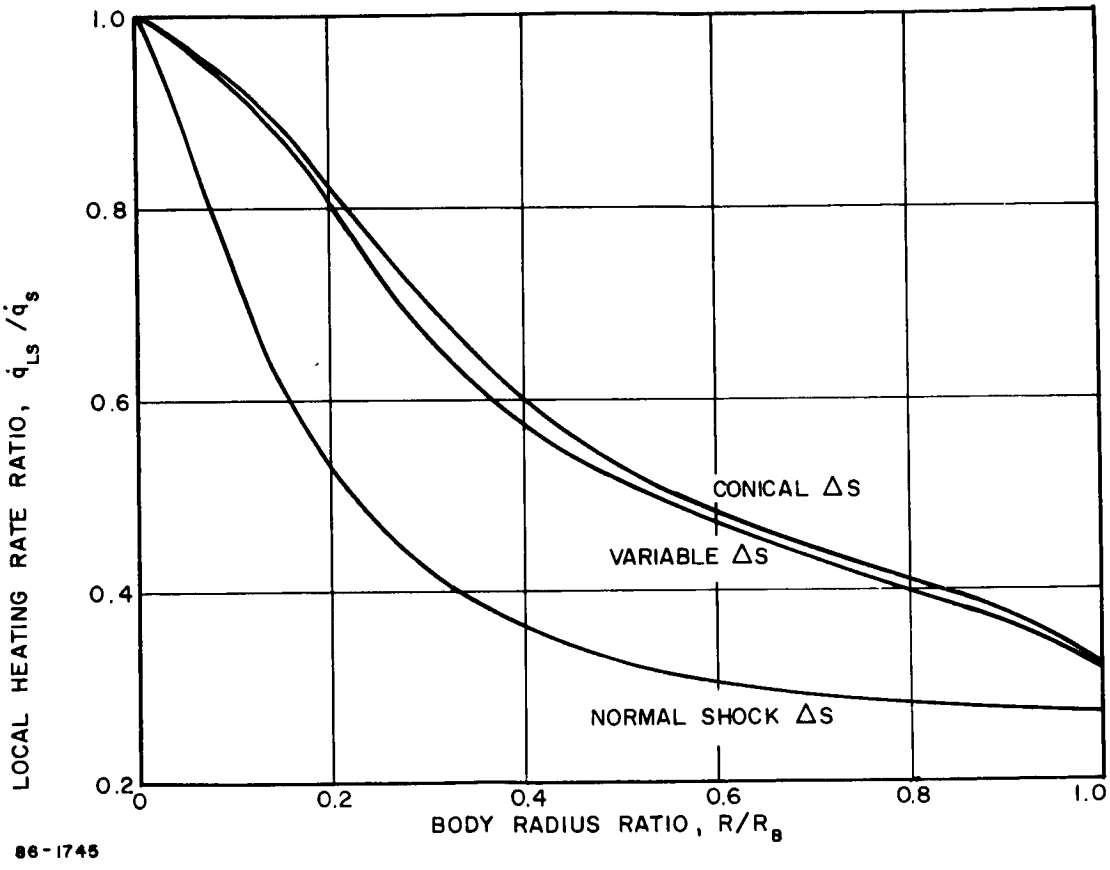

Figure 180 ENTROPY VARIATION COMPARISON HEATING RATE DISTRIBUTIONS

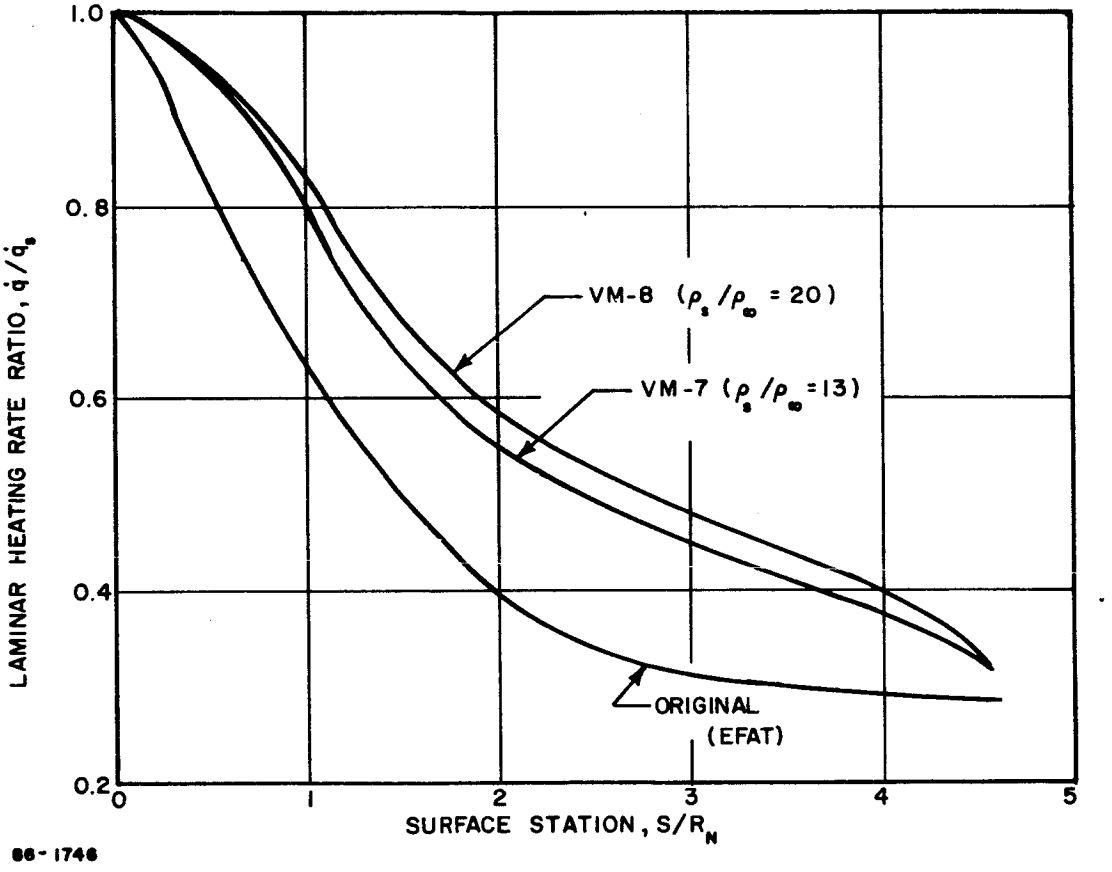

Figure 181 COMPARISON OF AERODYNAMIC HEATING RATE DISTRIBUTIONS

semitheoretical explanations to select data, but their results are rarely applicable to other data.

Cavities and protuberances are to be encountered, in the design of the entry vehicle, in the form of a thrust vector control (TVC) cold-gas rocket nozzle embedded in the heat shield and the TVC gas rocket nozzle and body protruding from the outer edge of the vehicle. The method of treatment used in this study was entirely empirical and is based on similar conditions of Mach and Reynolds numbers for similar shapes.

Cavity heating at and near α = 30 degrees is treated as stagnation heating in a hole in a flat plate normal to the flow (Reference 32), since at this angle of attack the flow over most of the cone surface approximates stagnation conditions. At angles of attack other than in the vicinity of 30 degrees, cavity heating is affected by the geometry of the boundary layer relative to that of the cavity. Both References 33 and 34 agree that increased heating within the cavity will only occur if the hole is sufficiently large for the free-shear layer to be perturbed. Since, in general, both d/h and d/δ (hole diameter-to-height and diameter-to-boundary-layer thickness ratios, respectively) are not greater than 1.0, no aggravation will occur within the nozzle opening for the TVC cold-gas system. However, at the rear lip of the hole, heating factors will increase over the unperturbed value. This value has never been exactly defined, but a limiting aggravation factor of about 3.0 is reasonable. This value, however, holds for the entire lip of the cavity, since any side may be the back side relative to the flow direction. The TVC hot-gas nozzles are treated as protuberances. At all angles of attack below α = 30 degrees, the flow direction is from vehicle nose toward the hot-gas nozzle. The sonic point occurs in the vicinity of this nozzle; thus the nozzle is assumed to generate a standing lambda type shock system upstream. The heating aggravation in the vicinity of the hot-gas nozzle is thus a function of the character of the boundary-layer and nozzle geometry.

Reference 35, as modified according to Truitt's suggested method (Reference 30) for laminar flow, was used for this configuration. Above approximately 30-degrees angle of attack, the flow encounters the TVC nozzles first, generating a perturbation in the vehicle shock structure and causing aggravated heating rates on the vehicle surfaces behind the nozzle. Good data for this configuration were obtained from References 36 through 38. The "wake" behind the TVC nozzle is assumed to be turbulent.

Note that for angles of attack greater than 30 degrees, with the flow initially disturbed by the hot-gas TVC nozzle hardware, the cold-gas

TVC cavity lies in the wake of the distrubance. Thus two aggravation factors couple to form very high heating rates at the cold-gas nozzle lip.

Because of the lack of any unifying theory, estimates are conservative where data is sparse.

4.3.1.6 Deorbit Nozzle Heating

In order to minimize the effects of exhaust plume impingement on the rear surfaces of the lander, extensions to a "basic" (manufacturers) rocket nozzle were considered. The heating rates on the inner surfaces of these extensions were obtained by assuming flat plate, turbulent heating to a cold wall:

$$\dot{q}_{cw} = \frac{2.37\,(10)^{-4}\,\rho_c\,U_c\,h_c}{(P_R)^{2/3}\,(\log_{10} Re_x)^{2.58}} \left(\frac{\rho^*}{\rho_e}\right)^{0.8} \left(\frac{\mu^*}{\mu_c}\right)^{0.2} \left(\frac{h_r - h_w}{hs}\right)$$

where ρ = density

u = velocity

h_c = combustion chamber enthalpy level for complete combustion

μ = viscosity

P_R = Prandtl number

R_{e_X} = Reynolds number based on surface length from throat.

Subscript r denotes recovery value

Subscript e denotes boundary layer edge conditions

Subscript w denotes wall conditions

Superscript (*) denotes reference enthalpy conditions

Although flat-plate values of heating are not generally applicable to nozzle flow conditions, experimental evidence (References 39 and 40) has shown that this method is accurate for downstream of the throat, where axial gradients are small.

4.3.1.7 Afterbody Heating

The evaluation of the heating in the base region of all shapes presents an analysis problem. Although correlations are available for a flat base on a relatively sharp nosed shape the local Mach number prior to separation at the base was relatively high (Ms = 2.5) as compared to the blunt cone and modified Apollo which have a Mach number near 1 at the maximum diameter. At this location the Mach number is invariant with the free stream Mach number when the flow is supersonic. The base pressure thus is only a function of the Reynolds number. The available data for base pressures of high drag shapes (in the absence of sting supports) is that for cylinders where, for sufficiently large fineness ratios, the base pressure measured at the midspan is independent of the wall interactions. Figure 157 indicated that very high base pressures are possible for a cylinder with pressures approximately 3 percent of the stagnation pressure at Reynolds numbers comparable to those at the time of peak laminar convective heating.

The correlations of heating indicate that the heating at the base axisymmetric stagnation point is equal to the heating evaluated at the separation local conditions. For the blunt cone and the modified Apollo with expansion from the sonic point, the heating was taken to be:

$$\dot{q}_{b_{s_L}} = \dot{q}_L^* \left(\frac{\rho_b\, u_b\, \mu_b}{\rho^*\, u^*\, \mu^*}\right)^{1/2} \quad \text{, for laminar flow, and}$$

$$\dot{q}_{b_{s_T}} = \dot{q}_T^* \left(\frac{\rho_b\, u_b}{\rho^*\, u^*}\right)^{0.8} \left(\frac{\mu_b}{\mu^*}\right)^{0.2} \quad \text{, for turbulent flow .}$$

The distribution was taken as correlated for the turbulent data available, and is illustrated in Figure 182.

The most severe environment associated with the afterbody, however, is that for the failure mode wherein random attitude at entry is possible. In this situation, since the heating pulse precedes the dynamic pressure pulse, considerable heating is experienced prior to turnaround. An investigation of the dynamics for this mode indicated that the heat pulse could be considered to comprise two parts: 1) the base faced forward into the velocity until the angle of attack was less than 90 degrees; and 2) the remainder of the pulse then considered the zero-angle of attack attitude. Both sections of the pulse were considered independent of the angle of attack; the trajectory calculations, however, did consider the effects of angle of attack on the flight history and also where the angle of attack was 90 degrees.

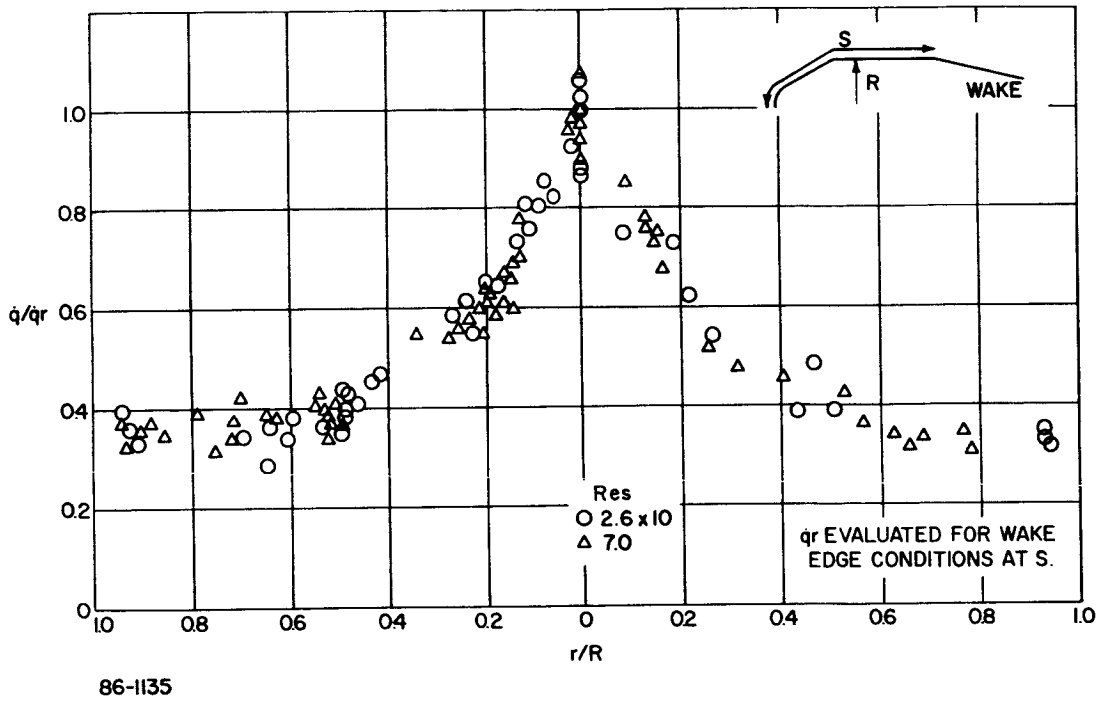

Figure 182 BASE HEATING -- TURBULENT

The base flow in the forward region was obtained in an approximate manner by considering the conical section independent from the remainder. That is, the shock standoff and velocity gradient were assumed to depend on the radius R_e (see Figure 183). The heating was then that for the particular shape in this region. The heating in the region of the maximum radius relied upon data giving heating in this region for concave nose shapes. Figure 184 gives the effect of the ratio R_b/R_N upon both the stagnation point and maximum diameter station. Utilizing these curves the ratio of the heating on the base, for an angle of attack of 180 degrees, to the zero-angle of attack stagnation point can be obtained. The resulting distributions are indicated in Figures 185 and 186 for the blunt cone and modified Apollo afterbodies considered early in the studies.

In addition to the convective heating during atmospheric entry, the afterbody experiences a heating environment associated with the de-orbit rocket. This heating can occur in three distinct modes. These modes are: (a) radiative heating from the hot-plume gases, (b) convective heating due to impingement of the plume on the aft surfaces, and (c) convective heating from the fluid in the nozzle boundary layer.

Radiation heating is calculated simply from the radiation equation assuming a surface temperature of zero degrees:

$$\dot{q}_{rad} \approx \sigma \epsilon T_{gas}^4$$

Knowing that the aft lander surfaces "see" gas temperatures no greater than 800°K and assuming blackbody radiation, the order-of-magnitude of radiation heating is seen to be

$$\dot{q}_{rad} < \sigma T_{gas}^4 = 4.5(10)^{-13} (800)^4 = 0.0184 \quad \frac{BTU}{ft^2 - sec}$$

The $\dot{q}_{rad}$ is negligible and need not be treated further.

Direct impingement of the plume on the aft surfaces is treated as convective heat transfer at a stagnation point. Plume impingement heating rates, in BTU/ft^2-sec are taken from Van Tassell and Levine (Reference 41) as

$$\dot{q}_p = \frac{2.22(10)^{-8} \sqrt{\rho_p} \; V_p^3}{\sqrt{2^a R}} \left(1 - \frac{hw}{hc}\right)$$

Here the local density and velocity (ρ_p , V_p) are obtained from the plume contours discussed previously. "R" represents the effective radius or

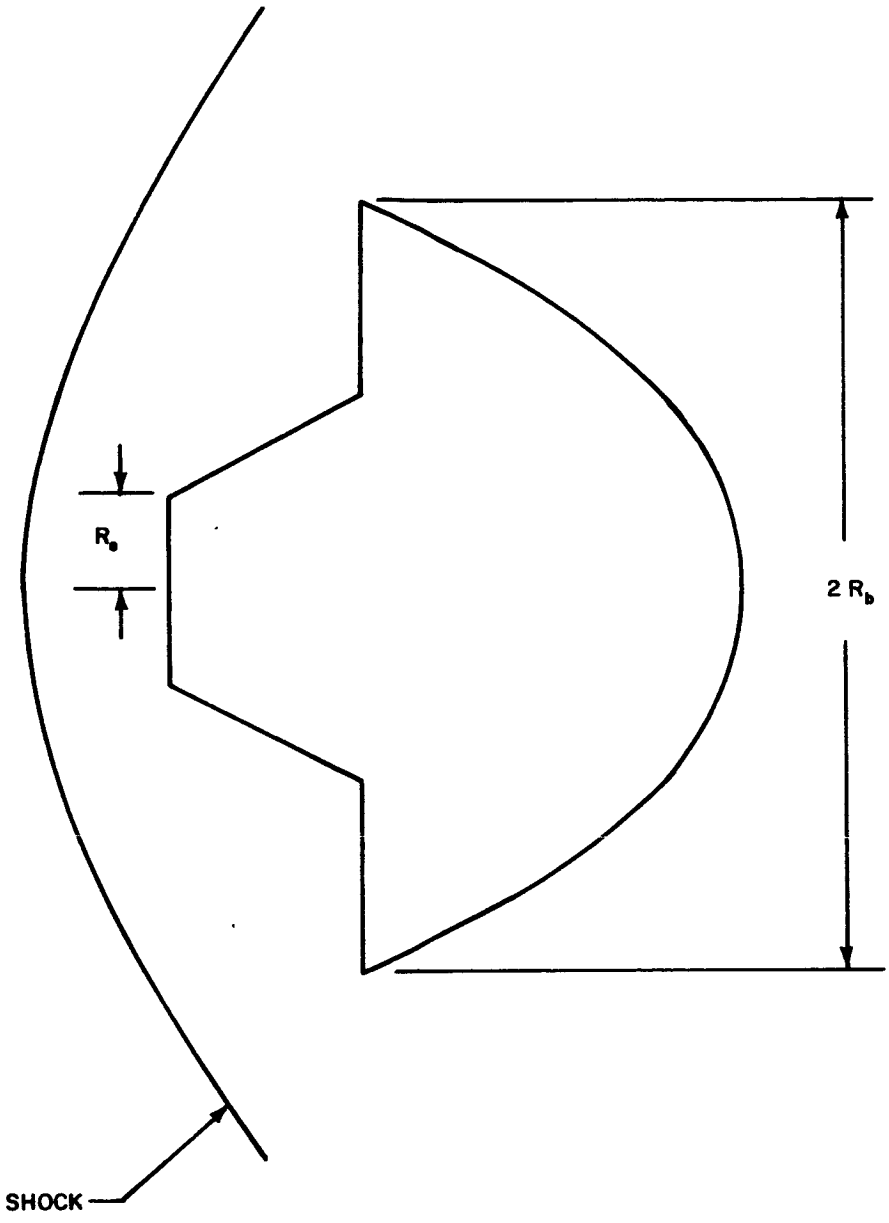

Figure 183 GENERAL FLOW MODEL AFTERBODY HEATING ANALYSIS

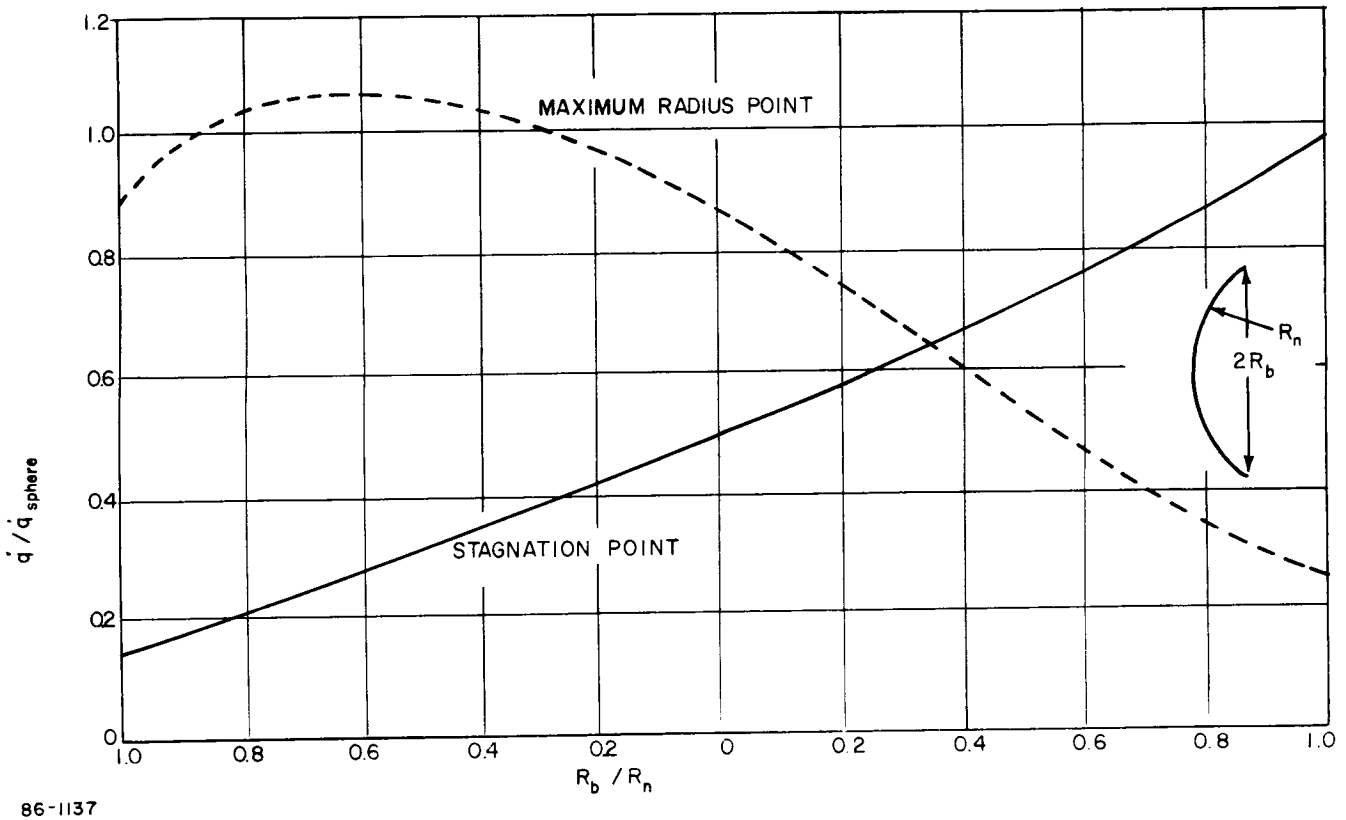

Figure 184 BLUNT BODY HEATING

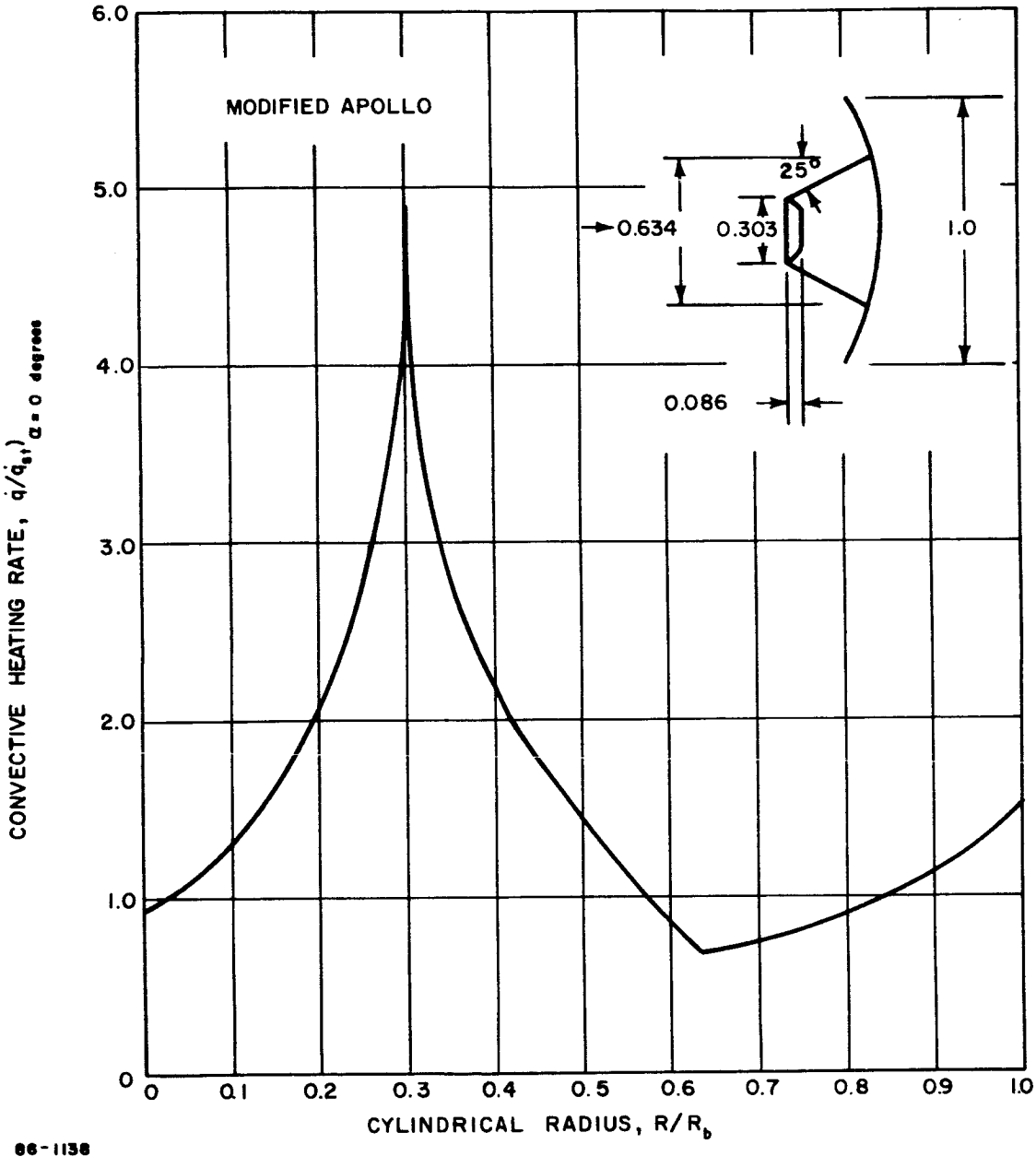

Figure 185 AFTERBODY HEATING DISTRIBUTION--MODIFIED APOLLO

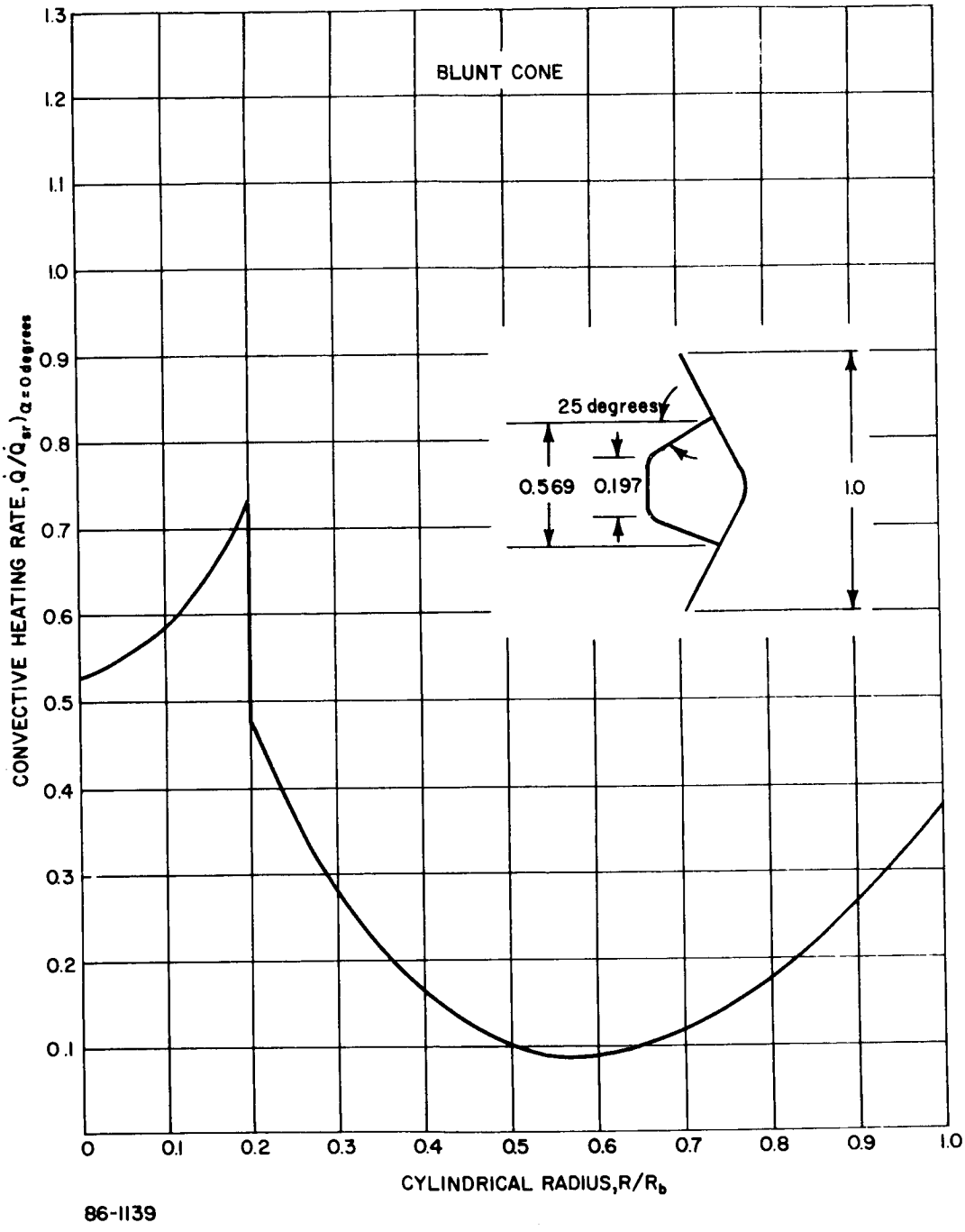

Figure 186 AFTERBODY HEATING DISTRIBUTION--BLUNT CONE

flat-plate width depending on whether the surface under consideration is axisymmetric or two-dimensional. The exponent (a) is 0 to 1 depending also on whether axial symmetry or two-dimensional flow is assumed.

Convective heating from the nozzle internal boundary layer occurs because the boundary layer contains sufficient energy to heat the aft lander surfaces as it flows and expands between the surfaces and the inviscid plume boundary. The mass flow in the boundary layer is determined at the nozzle exit (subscript E) as

$$\dot{m}_{bl} = 2\pi R_E \cdot \int_0^{\delta} \rho u dy = 2\pi R_E \rho_E U_E X_E \left(\frac{\delta - \delta^*}{X}\right)_E$$

The rationalized boundary layer and displacement thicknesses have been investigated by Grabow (Reference 42) using Avco computer programs 1356C and 1115B. His results are documented as function of local Mach number and Reynolds number at the edge of the boundary layer. Since M_E and Rex_E are predictable, the boundary-layer geometry and mass flow can be obtained. The area swept by the viscous flow is

$$A_{bl} = 2\pi R_E \delta$$

and assuming that the velocity, U^*, at $y = \delta^*$ is representative of the mass-averaged velocity within the boundary layer:

$$U_{bl_{av}} = U_E \left(\frac{\delta^*}{\delta}\right)^{0.2}$$

then,

$$\rho_{bl_{av}} = \dot{m}_{bl}/A_{bl} U_{bl}$$

and,

$$T_{bl_{av}} = T_E (\rho_E/\rho_{bl})$$

Thus average boundary-layer conditions are known, and

$$h_{s_{bl}} = C_p T_{bl_{av}} + \frac{1}{2} U^2_{bl_{av}}$$

The effect here has been to represent the boundary layer as a separate uniform flow field, the conditions of which are represented by the more averaged properties. The total or stagnation enthalpy represented by $h_{s_{bl}}$ will be lower than h_c, the stagnation enthalpy in the combustion chamber, thus reflecting the loss of energy in the boundary layer due to viscous shear.

This average flow is now assumed to turn around the lip of the nozzle, thence to expand between the aft surface of the lander and the boundary of the plume. The assumption that this flow does not disturb or displace the plume boundary is not strictly correct. It is, however, somewhat conservative. The flow is considered to be isentropic; the flow Mach number (and thus all other properties) is a function of the local channel area ratio normal to the local flow direction. However, where a sudden contraction occurs, the flow is assumed to go through a normal shock, thereafter to re-expand. Viscous turbulent and stagnation point heat rates for this flow system are calculated in the same manner as indicated above.

4.3.1.8 Transition

An examination of boundary-layer transition is necessary to define the design convective heat transfer. Parameters considered were M/C_DA, vehicle geometry, and atmosphere. The reentry angle was held constant at γ_E = -20 degrees (maximum heating) at 800,000 feet. Trajectories were examined using the three model atmospheres. It is important to determine if transition occurs since the turbulent heat transfer rates can be significantly larger than the laminar rates for a blunt body.

The sonic point was chosen as the characteristic body location for the transition study since the quantity $\rho_e u_e/\mu_e$ is a maximum at Mach 1.0, and sonic point locations for the modified Apollo and the blunt cone yield the maximum surface distance. Previously computed parametric trajectory studies were used to obtain the required data. The known quantities from the trajectories were free-stream Reynolds number referenced to vehicle diameter ($R_{\infty D}$), the stagnation to free-stream density ratio (ρ_s/ρ_∞) and stagnation temperature (T_s).

The sonic point Reynolds number (Re_s^*) may be computed as:

$$Re_s^* = \frac{\rho^*}{\rho_\infty} \quad \frac{u^*}{V_\infty} \quad \frac{\mu_\infty}{\mu^*} \quad \frac{S^*}{D} \quad R_{\infty D} \tag{1}$$

Equation (1) becomes the following when made compatible with the known data

$$Re_s^* = \frac{\rho^*}{\rho_s} \quad \frac{\rho_s}{\rho_\infty} \quad \frac{u^*}{V_\infty} \quad \frac{\mu_\infty}{\mu^*} \quad \frac{S^*}{D} \quad R_{\infty D} \tag{2}$$

The term ρ^*/ρ_s may be computed from the isentropic relationship

$$\rho^*/\rho_s = \left(\frac{2}{\gamma+1}\right)^{1/\gamma - 1} \tag{3}$$

The term u^*/V_∞ is likewise determined from the isentropic relationship

$$u^*/V_\infty = \frac{u^*}{V_m} = \sqrt{\frac{\gamma - 1}{\gamma + 1}} \tag{4}$$

The shock waves of the modified Apollo and the blunt cone are very close to normal shocks, hence, the sonic point temperature was taken to be the stagnation temperature. The specific heat ratio (γ) required in the above equations was computed from

$$\gamma = \frac{\rho_s/\rho_\infty + 1}{\rho_s/\rho_\infty - 1} \tag{5}$$

based on the assumption of a normal shock for the blunt cone and modified Apollo. The sonic point viscosity (μ^*) was determined from the sonic point temperature ($T^* \cong T_s$) using analytical data (Reference 43).

Previous experience with reentry vehicle design at Avco has shown that a transition Reynolds number of 300, 000 is sufficiently conservative with respect to convective heat transfer. Calculation of the local to free-stream Reynolds number distributions were computed for the candidate vehicles in the vicinity of peak heating. Presented in Figure 187 is the ratio of local Reynolds number (Re_s) to free-stream Reynolds number as a function of vehicle location (R/R_B) for the modified Apollo for atmosphere Model 1. The distribution for the Models 2 and 3 are similar, differing only through the free-stream viscosity, since the stagnation conditions are relatively insensitive to the free-stream temperature. Figures 188 and 189 present similar data for the blunt cone and tension shell values, respectively. Using the above data and a local transition Reynolds number of 300, 000, the characteristic maximum heating trajectories indicate that turbulent heating must be considered for the tension shell for all entry conditions whereas the blunt cone and modified Apollo experience turbulent flow for only specific entry conditions (with the maximum weight).

4.3.1.9 Angle of Attack Effects

The angle of attack histories result in effective M/C_DA's which are higher than the zero-angle of attack values. At angle of attack, the stagnation point moves and the problem now becomes three dimensional (see Figure 190). In addition, since the sonic point remains relatively fixed, the windward gradients are expected to increase. Refer to Figure 173, where the pressure distributions at angle of attack were presented for the modified Apollo, as an illustration. The angle of attack heating distributions are shown in Figure 191 and reflect the effect of pressure gradients in the vicinity of the sonic point. Figure 192 presents the resulting heating distributions for the blunt cone.

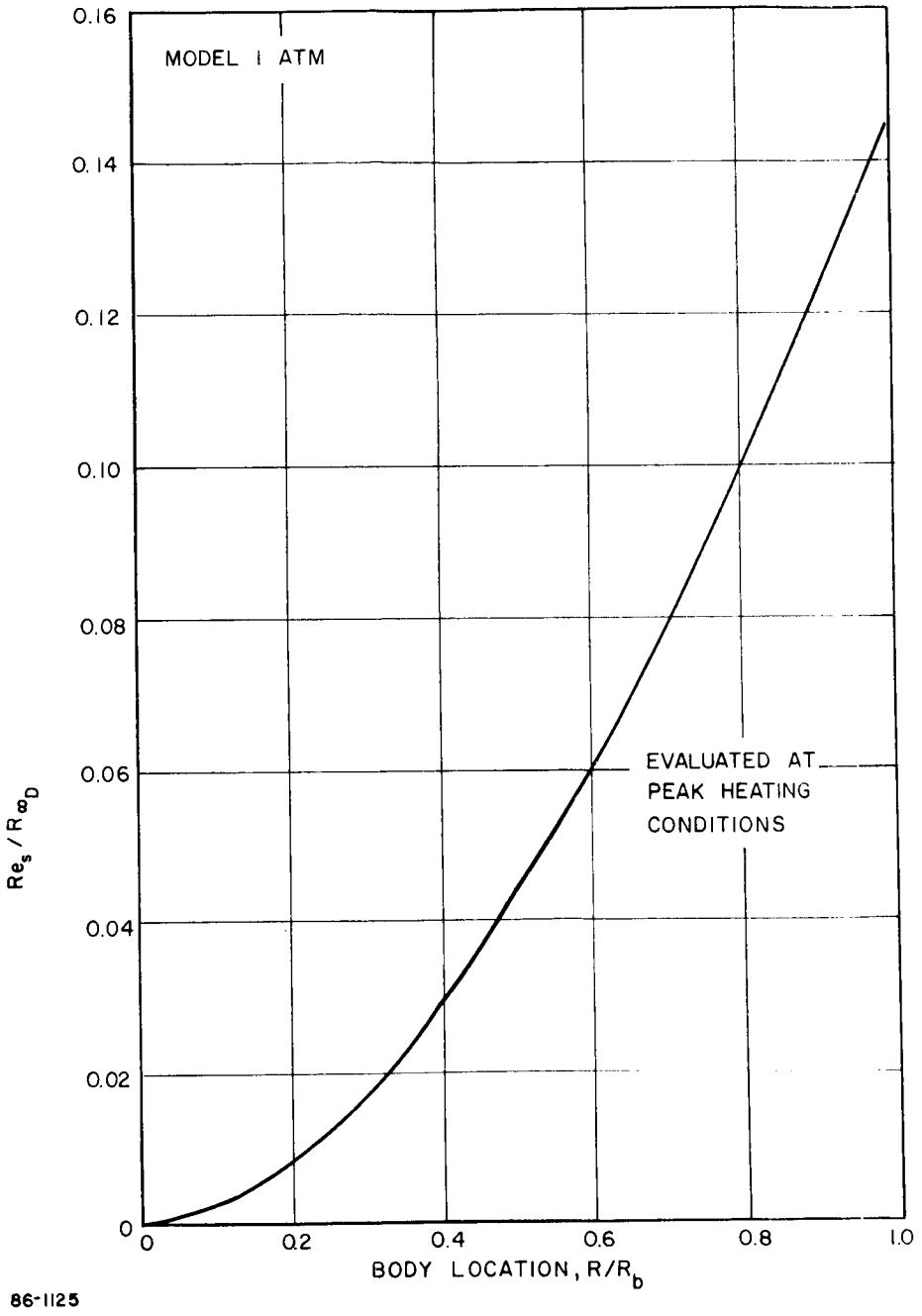

Figure 187 RATIO OF LOCAL TO FREE STREAM REYNOLDS NUMBERS VERSUS LOCATION MODIFIED APOLLO

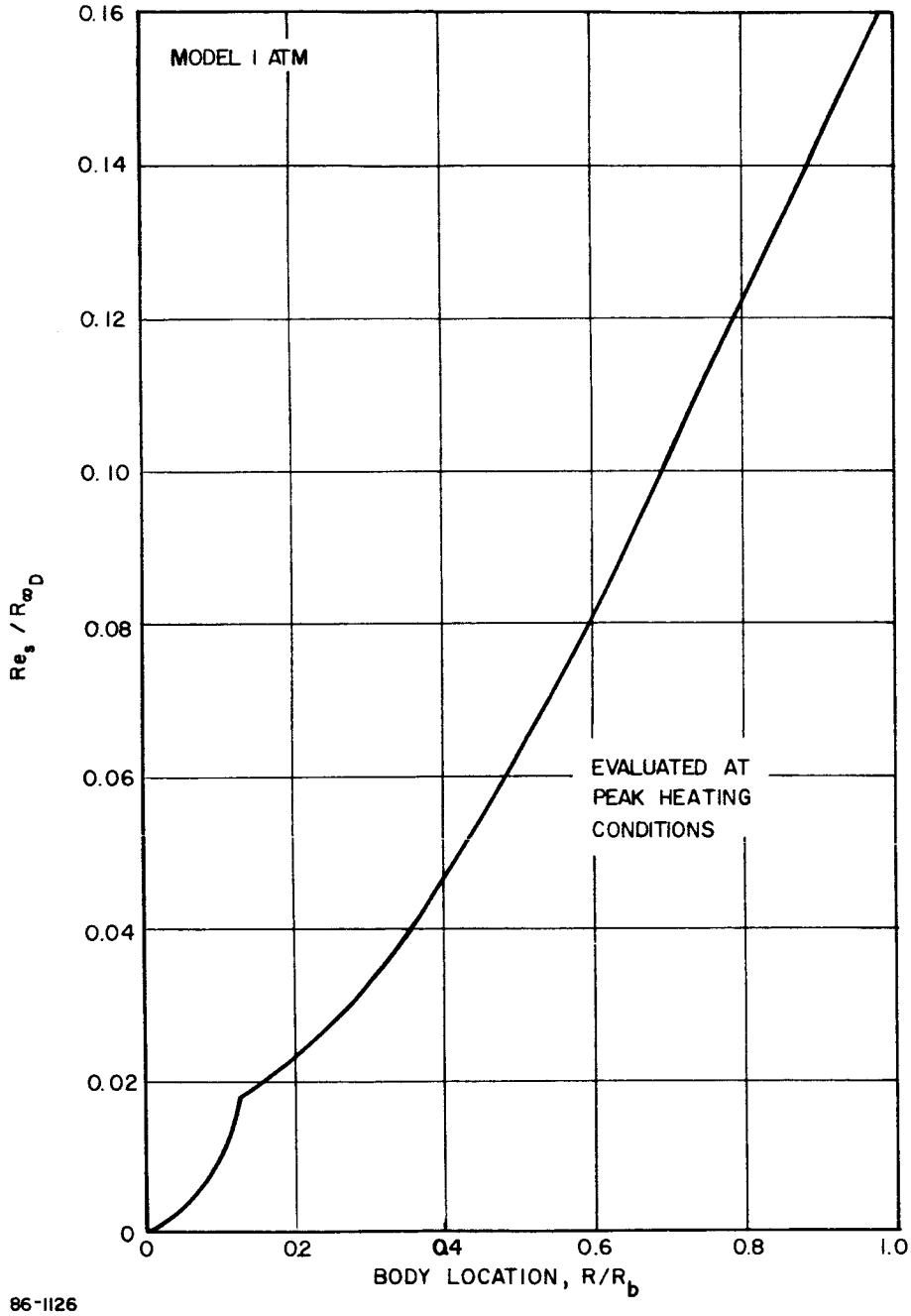

Figure 188 RATIO OF LOCAL TO FREE STREAM REYNOLDS NUMBERS VERSUS LOCATION BLUNT CONE

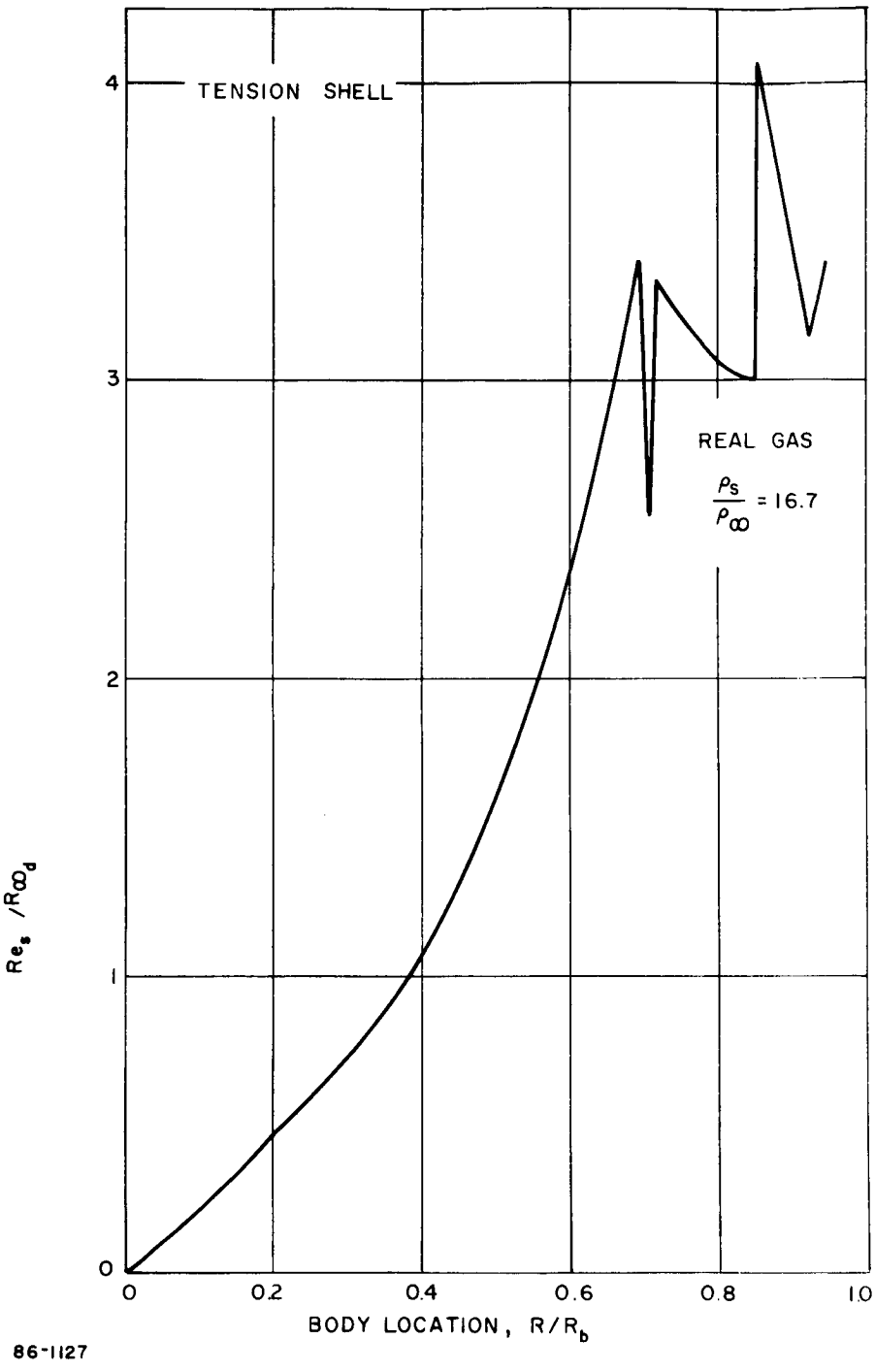

Figure 189 RATIO OF LOCAL TO FREE STREAM REYNOLDS NUMBER VERUS LOCATION TENSION SHELL

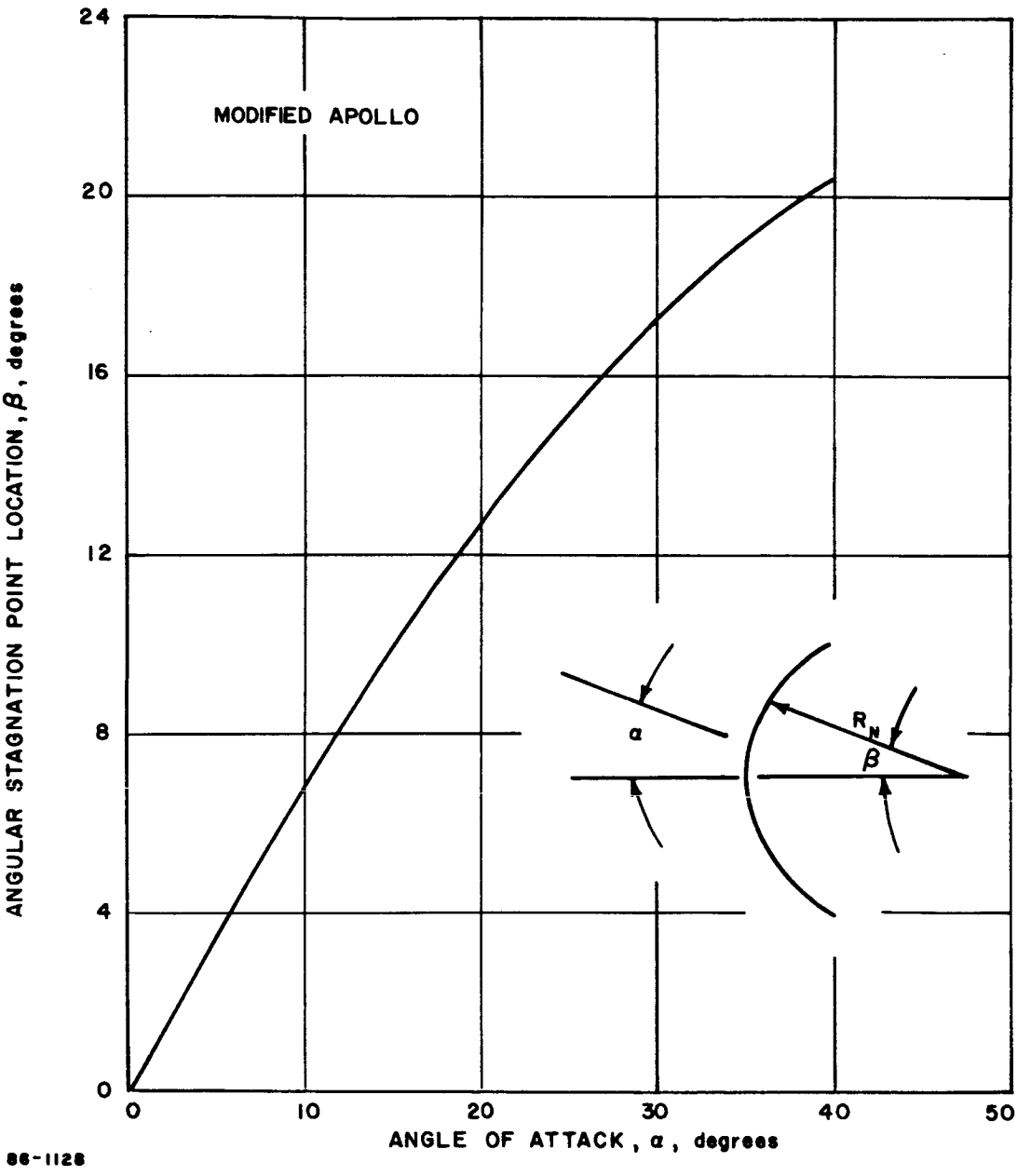

Figure 190 STAGNATION POINT LOCATION--MODIFIED APOLLO

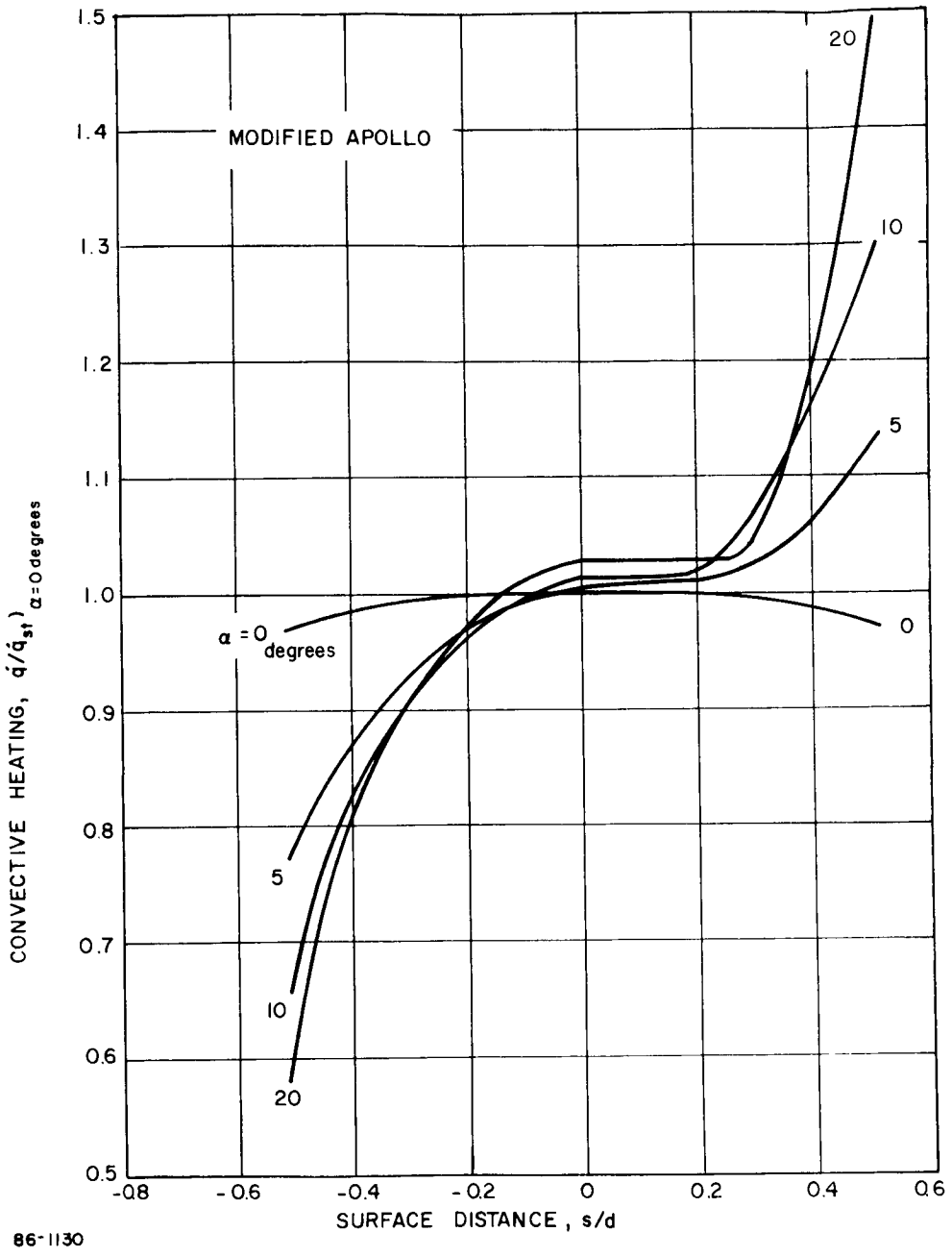

Figure 191 HEATING DISTRIBUTIONS--ANGLE OF ATTACK

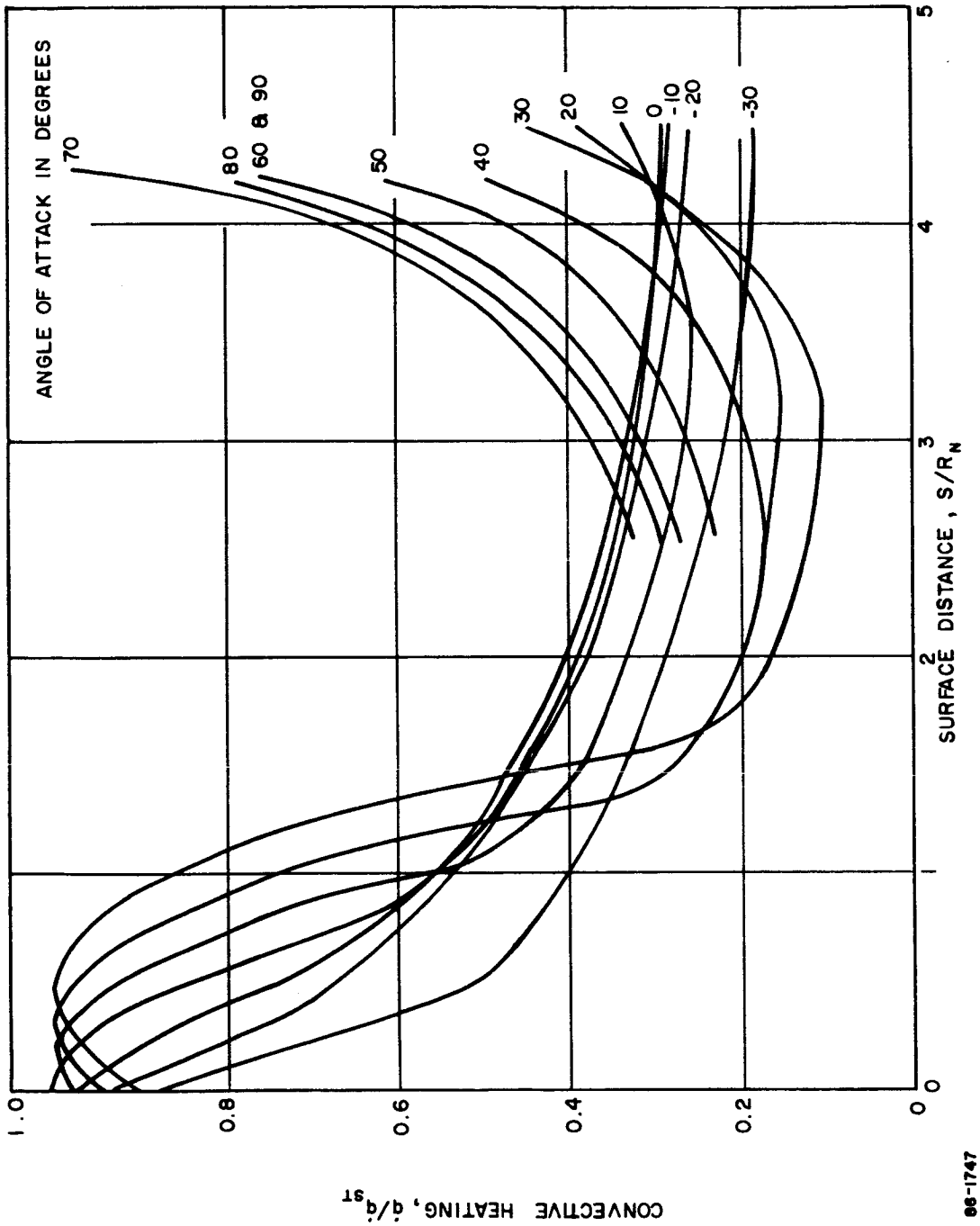

Figure 192 ANGLE OF ATTACK HEATING DISTRIBUTIONS--BLUNT CONE

To factor these local aggravations, four different body motion analyses can be made. They are:

a) A complete time history can be made for a particular body station of the heating history for the exact spin rate and precessions,

b) A planar oscillation can be assumed,

c) An infinite spin rate can be considered, and

d) A lunar type motion can be analyzed resulting in a conservative evaluation.

The first method is tedious and requires an iterative process since it is not known a priori which body meridian will result in the maximum heating environment for a given body station. The second motion results only for the case of random motion with small spin rates; its effect can be expressed as

$$\bar{q} = \frac{1}{\tau} \int_0^R q(\alpha)\, dt$$

where

$$\alpha = \bar{\alpha} \cos \omega t ,$$

($\bar{\alpha}$ is the envelope value of the angle of attack ω is the oscillation frequency and t is time). In this case time is a dummy variable in the sense that both $\bar{\alpha}$ and $\bar{q}$ are considered constant at a given instant of time in the trajectory. This is tantamount to assuming an infinite pitch frequency.

The infinite spin rate is the limiting case where the heating at a station is averaged circumferentially thereby compensating the high heating with the low heating (windward versus leeward meridian). The expression for this motion is given by

$$\bar{q} = \frac{1}{2\pi} \int_0^{2\pi} q(\phi)\, d\phi$$

The method selected to indicate the tradeoff or effect of angle of attack is that of lunar motion where the same body meridian faces the velocity vector. Since it is not known which meridian this will be, all body stations are considered to experience the worst environment within the angle of attack at any particular point in the trajectory. It should be noted that the body will experience lunar motion during two instances of time since the natural frequency varies with the dynamic pressure. In addition lunar motion is possible with an offset center of gravity. Figures 193 through 195 compare the heating aggravation over the three generic shapes. The heating distributions have been integrated over the entire surface area and referenced to the surface integral at zero-angle of attack. With the exception of the modified Apollo, infinite spin results in a net reduction in the heating whereas lunar motion results in relatively large increases.

The results for the tension shell differ for several reasons. Except for lunar motion at angles of attack between 0 and 11 degrees, any finite spin rate will produce a decrease in the total integrated heating over the vehicle. This phenomenon is caused by the lessening of shock strength on the full leeward side of the vehicle and on the windward side beginning at the shock intersection point. Although considerable improvement in the heating picture is produced by high spin rates, it should be stressed that these curves are based entirely on integration of LRC Mach 8 test data. Although the trends depicted are valid, the magnitude is probably optimistic. These values must, therefore, be considered tentative. However, the design is not affected by this trend, since the heat shield will be designed for the worst, or α = 0 degrees, case. The trend to decreased heating in lunar motion at angles of attack greater than 11 degrees is contrary to the trend shown for the blunt cone and modified Apollo. This difference is caused, as pointed out above, by the fact that test data are used here. The test data gave heating distributions at angle of attack for five different meridians and should therefore result in an adequate average.

4.3.2 Radiative Heating

The prediction of radiative heat transfer requires first the knowledge of the geometry and thermodynamic state of the radiation source and second the knowledge of particle responses upon the absorption of large amounts of kinetic energy. The former requirement is basically a problem in fluid mechanics and chemical kinetics (hence an input) while the second is concerned with atomic physics. In the design studies conducted to date, no attempts have been made to develop new techniques or extend existing ones. Rather, existing techniques and data have been employed where available, supplemented by what is believed to be reasonable estimates to fill in the gaps.

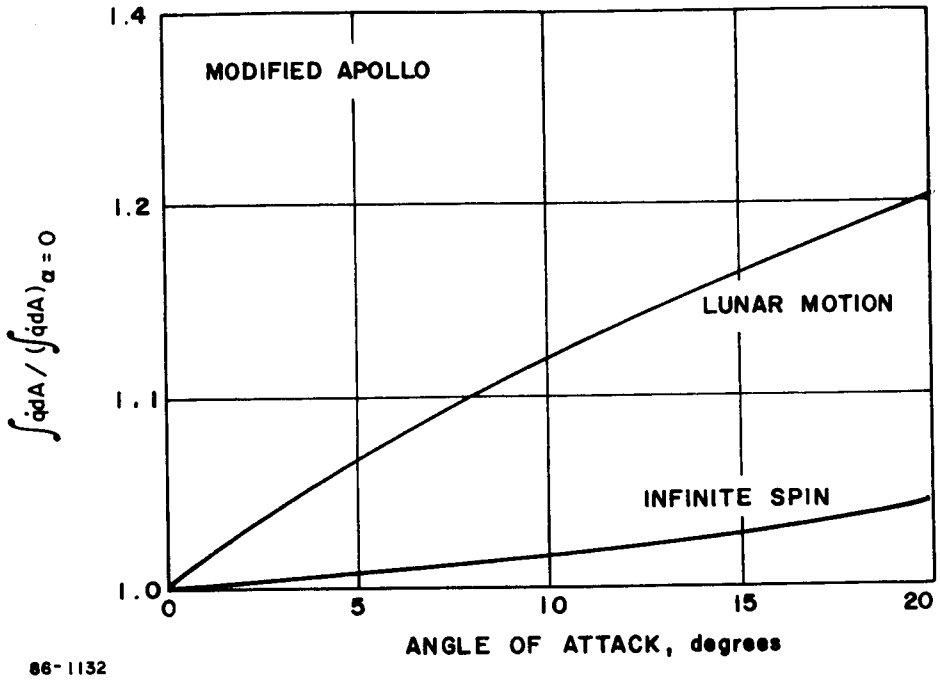

Figure 193 ANGLE-OF-ATTACK HEATING--MODIFIED APOLLO

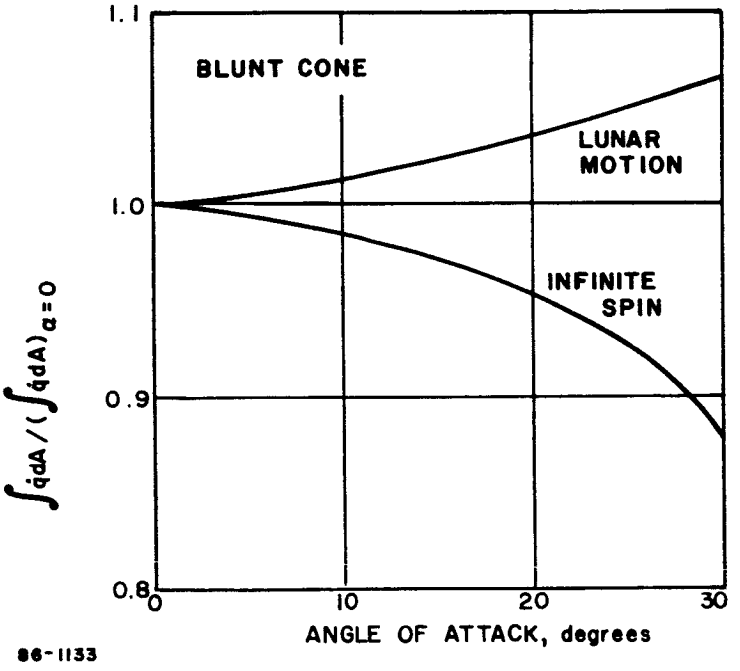

Figure 194 ANGLE-OF-ATTACK HEATING--BLUNT CONE

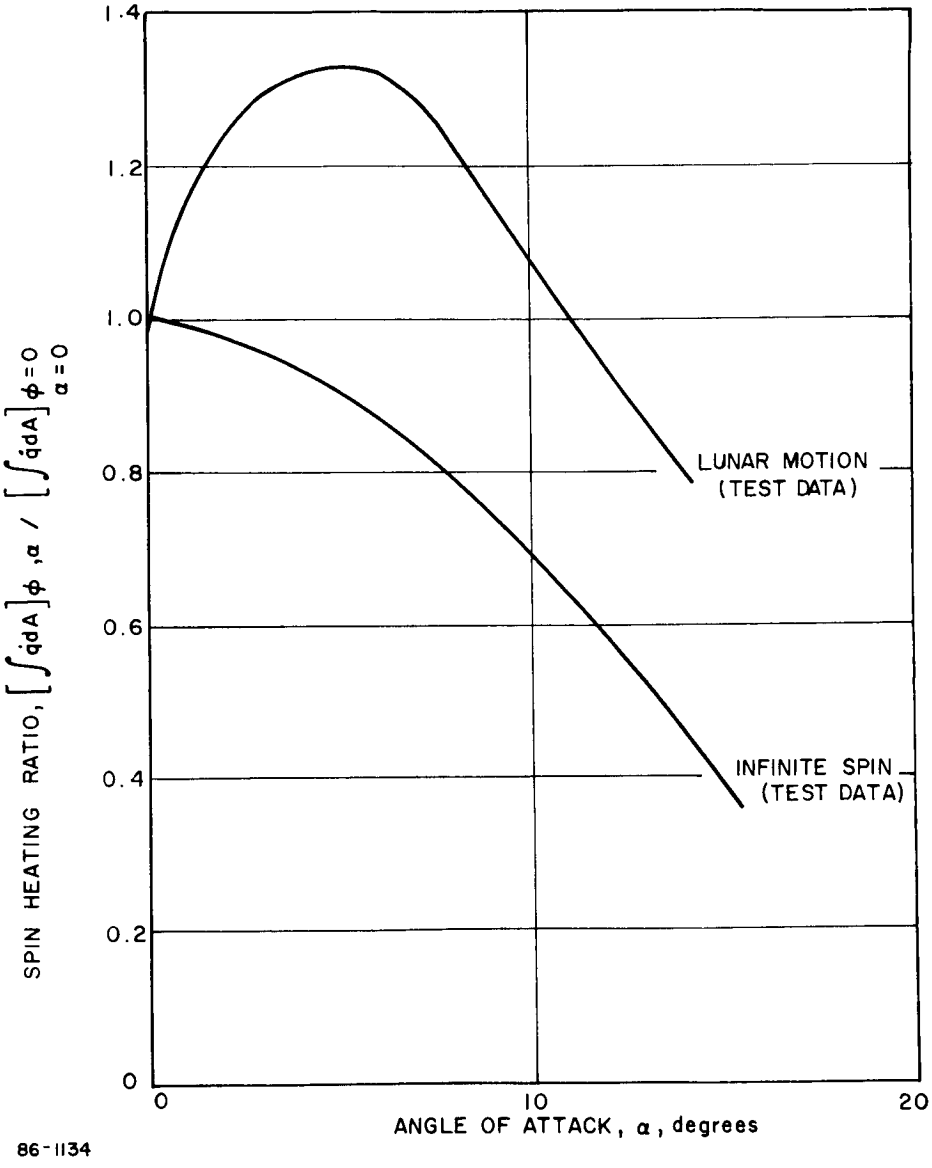

Figure 195 TENSION SHELL--EFFECTS OF SPIN AND ANGLE OF ATTACK ON AERODYNAMIC HEATING

In briefly discussing the methods of analysis, the following specific areas are considered:

a) Shock shape and location

b) The thermodynamic state of the flow field

c) The methods of radiant flux computation

Shock shape and location data for the modified Apollo shape were generated analytically (References 19 and 43).

Shown on the following pages are the equations pertinent to the determination of the shock location and shape. Reference should be made to the attached nomenclature. The following is an excerpt from reference 20.

Shock Trace in Vertical Plane of Symmetry -- The shock-wave trace is composed of circular arc elements whose radii depend on the inclination and location of the sonic points on the body. The sonic-point inclination angles are functions of angle of attack, α, and the angle

$$\epsilon = \sin^{-1}(r_b/R_b) \tag{1}$$

The upper sonic point is usually located on the corner of the body and its inclination is

$$\theta_b^{*}{}_u = 90^\circ - (\epsilon - \alpha) \tag{2}$$

The lower sonic-point inclination θ_b^{*l} is given by a limiting angle $\theta_{b_{min}}^{*}$ corresponding to that for a sphere if the lower corner inclination

$$\theta_b^l = 90^\circ - (\epsilon + \alpha) \tag{3}$$

is less than $\theta_{b_{min}}^{*}$. If θ_b^l is greater than $\theta_{b_{min}}^{*}$, the lower sonic point is at the lower corner and thus $\theta_b^{*l} = \theta_b^l$ and is given by Equation (3). The values of θ_b^{*u} and θ_b^{*l} together with the appropriate normal shock-density ratio for the flight conditions involved prescribe the values of $(\Delta^*/R_s)^u$, θ_s^{*u}, and $(\Delta^*/R_s)^l$, θ_s^{*l}. These values, obtained from the charts of ϵ, Figure 196, and the value of θ_b^{*u} from Equation (2) are used to calculate the vehicle sonic-point coordinates and shock radii, thus locating the vehicle with respect to the shock trace. The necessary equations are

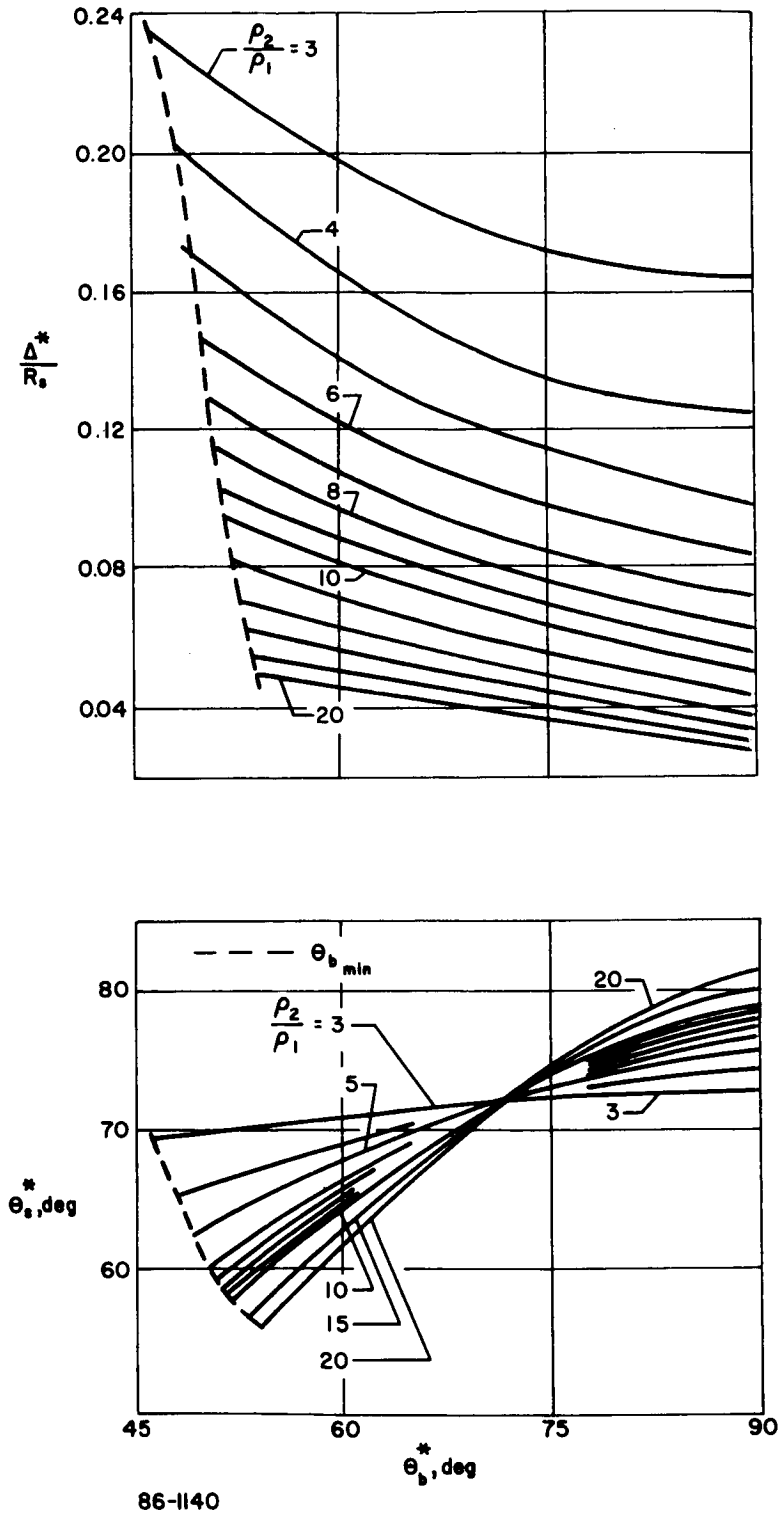

Figure 196 CHARTS OF SHOCK STAND-OFF DISTANCE AND SHOCK SLOPE AT THE SONIC POINT

$$\frac{X^{*u}}{R_b} = \frac{(\cos\theta_b^{*u} + \cos\theta_b^{*l}) - (\sin\theta_b^{*u} - \sin\theta_b^{*l})\dfrac{\cos\theta_s^{*l}}{(\Delta^*/R_s)^l + (1-\sin\theta_s^*)^l}}{\dfrac{\cos\theta_s^{*u}}{(\Delta^*/R_s)^u + (1-\sin\theta_s^*)^u} + \dfrac{\cos\theta_s^{*l}}{(\Delta^*/R_s) + 1 - \sin\theta_s^*)^l}} \quad (4)$$

$$\frac{Y^{*u}}{R_b} = \frac{X^{*u}}{R_b}\left[\frac{\cos\theta_s^{*u}}{(\Delta^*/R_s)^u + (1-\sin\theta_s^*)^u}\right] \quad (5)$$

$$\frac{R_s^u}{r_b} = \frac{Y^{*u}/R_b}{\sin\epsilon\cos\theta_s^{*u}} \quad (6)$$

and

$$\frac{R_s^l}{r_b} = \frac{\cos\theta_b^{*u} + \cos\theta_b^{*l} - (Y^{*u}/R_b)}{\sin\epsilon\cos\theta_s^{*l}} \quad (7)$$

Two additional geometric properties associated with the shock trace in the vertical plane of symmetry are the shock standoff distance Δ_o and the location of the stagnation point. Calculation of these quantities is based on the simple assumptions that the stagnation streamline is perpendicular both to the normal portion of the shock (Y-axis at the origin) and to the body surface and that the curvature of the stream between the shock and the stagnation point is constant. For the standoff distance these considerations give:

$$\frac{\Delta_o}{R_b} = \frac{X^{*u}}{R_b} + \cos(\epsilon - a) - \cos\epsilon_o \quad (8)$$

where

$$\epsilon_o = \sin^{-1}\left[\frac{Y^{*u}}{R_b} - \sin(\epsilon - a)\right] \quad (9)$$

R radius, feet

r radial coordinate with respect to vehicle axis of symmetry, feet

X, Y, Z	Cartesian coordinates
α	angle of attack, degrees
Δ	streamwise shock standoff distance from point on body, feet
Δ_o	shock standoff distance on X-axis, feet
ϵ	half-angle subtended by capsule forebody arc, degrees
ϵ_o	angle between the X-axis and the line drawn from the center of the forebody arc to the intersection of the forebody arc with the X-axis, degrees
θ	slope with respect to free-stream direction, degrees
ρ	density, slug/ft^3

Subscripts

1	conditions just upstream of shock
2	conditions just downstream of shock
b	body surface
s	shock wave

Superscripts

l	lower (ϕ = 180 degrees)
u	upper (ϕ = 0 degrees)
*	sonic point on body

It has been demonstrated, by comparing with test data, that the mass flow-continuity approach employed is quite satisfactory for capsule-type bodies even at moderate angles of attack.

Similar data for the blunted cone were generated using a combination of test data (Schlieren photographs), a real-gas (equilibrium air) blunt-body solution for a slightly different cone (65 degrees)* and a mass

* The choice of other than a 60-degree cone was made necessary due to numerical difficulties with the machine program (a one-strip Belotserkovskii-type solution). The difficulty appeared to be associated with the basic change in the character of the flow over the cone from all subsonic for 65 degrees to mixed subsonic-supersonic for smaller angles. This is also indicated in Figure 197.

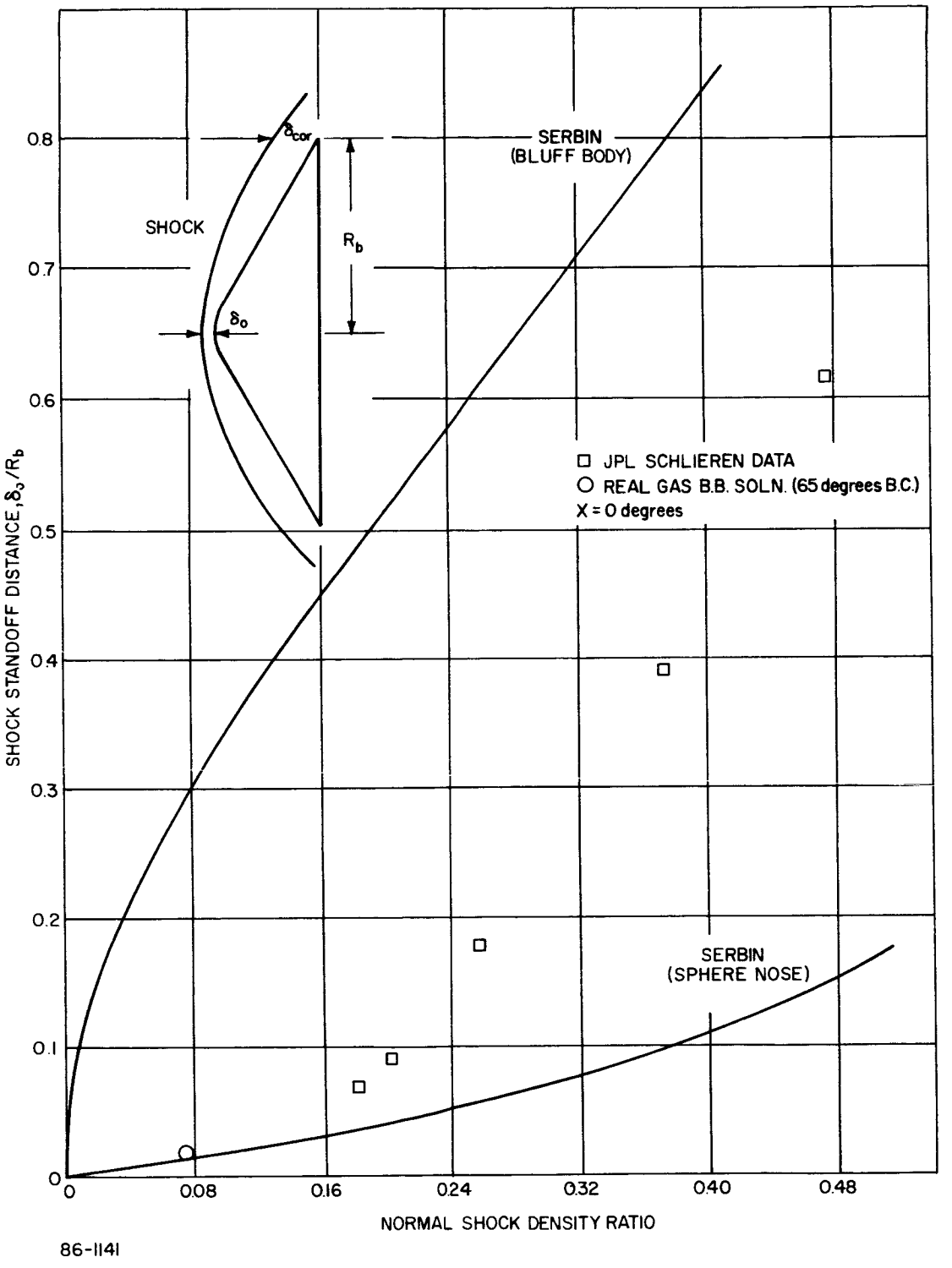

Figure 197 SHOCK STANDOFF DISTANCE--60-DEGREE BLUNTED CONE

flow-continuity calculation similar to that of references 19 and 43 where R is a radial coordinate, u is the radial velocity distribution at R and the integration is taken at constant R. Estimates of the integral were made using available data. Results of this study are shown in Figures 197 and 198 for zero-angle of attack. Good correlation with density ratio is indicated. It should be noted that the normal shock standoff distance at density ratios characteristic of entry conditions is essentially that of a sphere of the same nose radius; thus the sonic point is near the sphere-cone intersection point. At higher ratios the dependence on density ratio is similar to that for a bluff body, hence the sonic point must be at or near the outboard corner. Shock shape at angle of attack was estimated using the mass flow-continuity method noted.

It should be noted that the density ratio correlations presented were for a gas in thermodynamic equilibrium (or ideal). In Reference 43 the normal shock standoff distance correlation is extended to nonequilibrium flows by defining an integrated average nonequilibrium density:

$$\frac{\bar{\rho}_{ne}}{\rho_\infty} = \frac{1}{2}\,\frac{\rho_f}{\rho_\infty}\left\{\sqrt{\left(\frac{\Delta_f K}{V_\infty}\,\frac{\rho_f}{\rho_\infty} - 1\right)^2 + \frac{4\rho_e}{\rho_\infty}\,\frac{\Delta_f K}{V_\infty}} - \left(\frac{\Delta_f K}{V_\infty}\,\frac{\rho_f}{\rho_\infty} - 1\right)\right\}$$

where ne, f, e refer to nonequilibrium, frozen and equilibrium, respectively, Δ is shock detachment distance and K is a rate constant given for air to be

$$K = 1.29 \times 10^{-14}\ (\rho_\infty/\rho_o)\,(V_\infty \text{ meters/sec})^6 \quad .$$

Calculations showed that $\bar{\rho}_{Ne}$ was not particularly sensitive to the value of K over the pressure and velocity range of interest, hence it was used for both Model 2 and 3 atmospheres. In performing the integration, the density and velocity profiles across the shock layer were assumed to be exponential and linear respectively. This approach has been used in this preliminary study where necessary.

The flow field about the blunt tension shell is quite complex (Reference 44). Basically the shock pattern consists of a bow shock with a secondary shock arising due to the forced outward turning of the local flow. This secondary shock is really a system of shocks, slip lines and expansion waves. Necessarily such complex detail was omitted and only the two basic shock waves were considered. The bow wave was constructed using the mass flow-continuity method. The secondary wave was predicted as follows. Studies of Schlieren photographs indicated that this secondary wave's position very nearly coincided with a section of the bow wave of a bluff body of the same base radius (for near zero-angles of attack). Hence this secondary wave was determined essentially from the shock shape and location about a bluff body for the proper density ratio.

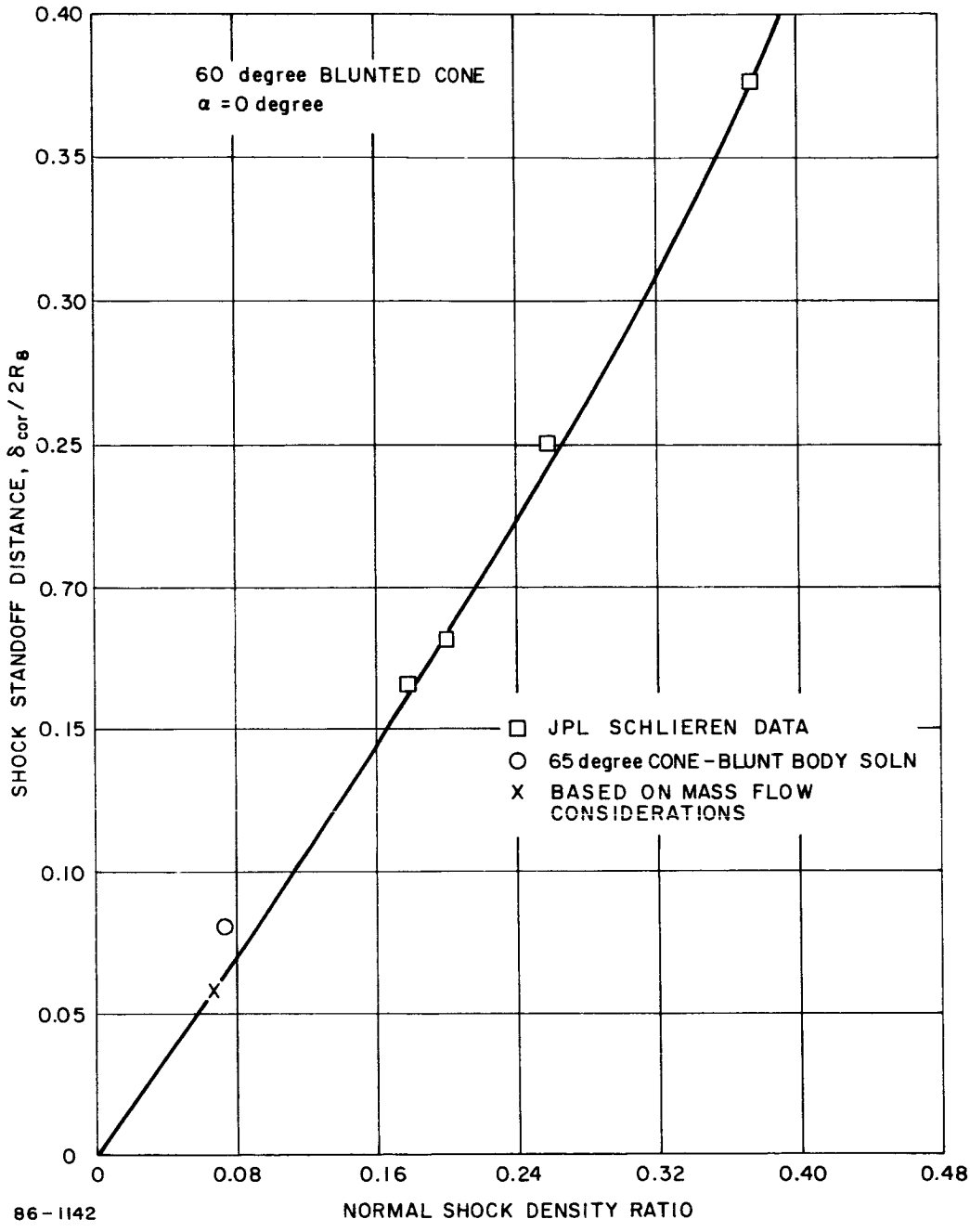

Figure 198 SHOCK LOCATION

Due to the low density of the Martian atmosphere and certain of the entry vehicles, it was felt quite likely that the bow-shock layer experienced chemical nonequilibrium conditions during a significant part of the period. To calculate these conditions properly would require a nonequilibrium flow analysis (blunt-body solution plus perhaps the method of characteristics, stream-tube method are typical). Such programs exist for air and for symmetric bodies at zero-angle of attack; however, the work to adapt them for the chemistry of carbon dioxide, nitrogen and argon mixtures has not been completed. In addition such analyses would not be applicable to the flow field about the tension shell. Hence recourse had to be made to experimental studies of the nonequilibrium radiation profile (e.g., time to reach within 10 percent of the equilibrium intensity level) to define the nonequilibrium region. Such data are only available from normal shock studies (no model). For typical Martian atmospheres, the data are quite limited, taken at one pressure level over a narrow velocity range and exhibiting considerable scatter (Reference 45). Nevertheless these data were used to estimate the extent of the nonequilibrium regions about each shape. Oblique shock effects were roughly accounted for by assuming that the shock strength (hence the normal velocity component) controlled the downstream relaxation processes.

The methods of radiative heating analysis are taken mainly from Reference 46. Equilibrium calculations were made assuming semi-infinite plane slab geometry subsequently modified to account for temperature and density variations through the slab as follows:

$$\dot{q} = \frac{\delta}{2} \frac{I_w - I_s}{ln\, I_w/I_s}$$

where I_w and I_s are the equilibrium intensities at the shock and wall (inviscid) respectively. This technique was used for distribution calculations.*

Three different approaches to the nonequilibrium prediction were considered. The first approach takes note of the fact that collision processes at high altitude are mainly binary, hence the integrated nonequilibrium intensity should be dependent on velocity only. (See Reference 47). Combining this method with equilibrium calculations essentially defines a conservative upper bound. The second alternative makes an approximation to the nonequilibrium radiation profile by assuming the pulse to be triangular with the time to peak intensity, time to within 10 percent of equilibrium intensity and the ratio of peak nonequilibrium to equilibrium intensity given by test data (Reference 45). Thus density independence is not assumed and effects of truncation can be considered.

* With the exception of the tension shell configuration - see below.

The final method is a modification of the second in that the ratio of the peak nonequilibrium to the equilibrium intensity is defined such that, where truncation is not occurring, the integrated nonequilibrium pulse is density independent. Thus this approach is a combination of the first two.

Stagnation point calculations were made using this third method. The equations are as follows:

$$q_{total} = q_{EQ}\, f\left(\frac{\Delta_p}{\Delta}\ ,\ \frac{\Delta_{neg}}{\Delta_e}\ ,\ \frac{I_{neg}}{I_e}\right)$$

where

Δ is the shock detachment distance

Δ_p is the distance to peak nonequilibrium intensity

(from data correlation $\Delta_p\,(\text{feet}) = \dfrac{0.23 \times 10^{-6}}{\rho_\infty\,(V_\infty \times 10^{-4})^{3.3}}$

Δ_{NEQ} is the distance to 1.1 equilibrium intensity

(from data correlation, $\Delta_{NEQ}\,(\text{feet}) = \dfrac{f(\text{atmos.}) \times 10^{-6}}{\rho_\infty\,(V_\infty \times 10^{-4})^{4.3}}$

I_{NEQ}, I_E are peak nonequilibrium and equilibrium radiative intensities respectively.

for

$\Delta < \Delta_{NEQ}$,

$$\dot{q}_{total} = \dot{q}_E \left\{1 - \frac{1}{2}\,\frac{\Delta_p}{\Delta} - \frac{1}{2}\,\frac{\Delta_{neQ}}{\Delta} + \frac{I_{neQ}}{I_e}\,\frac{\Delta_{neQ}}{2\Delta}\right\}$$

for

$\Delta_p < \Delta < \Delta_{NEQ}$,

$$\dot{q}_{total} = \dot{q}_E \left\{1 - \frac{1}{2}\,\frac{\Delta_p}{\Delta} - \frac{1}{2}\,\frac{\Delta_{neQ}}{\Delta} + \frac{I_{neQ}}{I_e}\,\frac{\Delta_{neQ}}{2\Delta} - \frac{1}{2\Delta}\,\frac{(\Delta_{neQ}-\Delta)^2}{(\Delta_{neQ}-\Delta_p)}\left(\frac{I_{neQ}}{I_e} - 1\right)\right\}$$

for

$$\Delta < \Delta_p \quad ,$$

$$\dot{q}_{total} = \dot{q}_E \left\{ \frac{1}{2} \frac{I_{neQ}}{I_e} \frac{\Delta}{\Delta_t} \right\}$$

where

$$\dot{q}_E = 1/2\, I_e\, \Delta$$

$$\frac{I_{neQ}}{I_e} = \frac{\Delta}{\Delta_{neQ}} \frac{\bar{I}(V)}{\dot{q}_E}$$

$\bar{I}(V)$ is the integrated nonequilibrium intensity, a function of velocity only. Zero angle of attack distributions about the modified Apollo and blunt cone shapes were made assuming equilibrium flow.* For the tension shell shape the surface was approximated as a series of two-dimensional sharp wedges and distributions obtained by an analysis similar to the well-known semi-infinite plane-parallel slab approach.

The following equations were employed. For equilibrium flow

$$\dot{q}_{EQ} = \frac{a\, I_e}{2\pi} \left\{ 1 - \cos\theta + \frac{2}{3} (x\, ln\, x)(\cos^3\theta - 1) + \pi x \left[\frac{2}{3} \sin\theta (2 + \cos^2\theta) + \sin\theta \right] + \frac{1}{2} \times \theta^2 \left[2\, ln\, (1 - x) - 1/(1 - x) \right] \right\}$$

and for nonequilibrium flow

$$\dot{q}_{NEQ} = \frac{\bar{I}(V)}{2\pi} \left\{ \frac{1}{2} \sin\theta\, ln \left(\frac{\sec^2\theta - 2x + x^2}{x^2} \right) + \cos\theta \left(\pi - \tan^{-1} \frac{\tan\theta}{1 - x} \right) \right\}$$

where

θ is the angular divergence of the shock layer

x is a chordwise coordinate (dimensionless)

* Calculations made for peak heating rate conditions indicated the radiation to be mainly equilibrium.

a is the wedge chord

I_e and $\bar{I}(V)$ are defined as before.

Both equilibrium and nonequilibrium distributions were obtained. The respective radiating zones were estimated using the radiation profile correlating parameters of Reference 45.

The distributions evolved for the Model 2 and 3 atmospheres are shown in Figures 199 through 201 for the blunt cone, modified Apollo and tension shell, respectively.

Referring to Figure 199, it is seen that the stagnation point heating is quite negligible in contrast to that seen by the cone surface where the large radiating volume and near-stagnation temperatures combine to yield much greater radiative thermal loads. The modified Apollo (Figure 200) exhibits a relatively flat distribution which, in conjunction with the relatively large standoff distances, results in extensive radiation over the entire forebody. The tension shell (Figure 201) radiation is significant in the area of the shock interaction region (the distribution in this case has been evaluated at specific flight conditions as noted). In comparing the blunt cone with the modified Apollo distributions, attention is called to the fact that the normalizing parameters on the respective configurations, the stagnation point radiative heating, differ significantly in their magnitudes. The difference is primarily due to the standoff and shock shape characteristics of the two shapes.

4.4 STABILITY AND PERFORMANCE

The complexity involved in the analysis of the dynamical behavior of a vehicle entering a planetary atmosphere was such that simple analytical methods were not applicable. The range of angle of attack variation eliminated the possibility of linearized theories, whereas a "spherical" atmosphere eliminated any straight line trajectory analyses; this is especially true in the case of entry from orbit. Emphasis was placed on the utilization of computer programs available, descriptions of which follow:

4.4.1 Program 1636

This program computes the vehicle motions in 6 degrees-of-freedom for a lifting entry vehicle. The program computes and prints as functions of time the following quantities: Planet reference trajectory parameters, the total angle of attack and its components (pitch and yaw), the body axis and angular velocities, linear and angular accelerations measured along and about the body axes, respectively, and the resultant normal acceleration of the body. The program also prints the computed extreme of total angle of attack, normal and axial accelerations, and angular velocity (Reference 48).

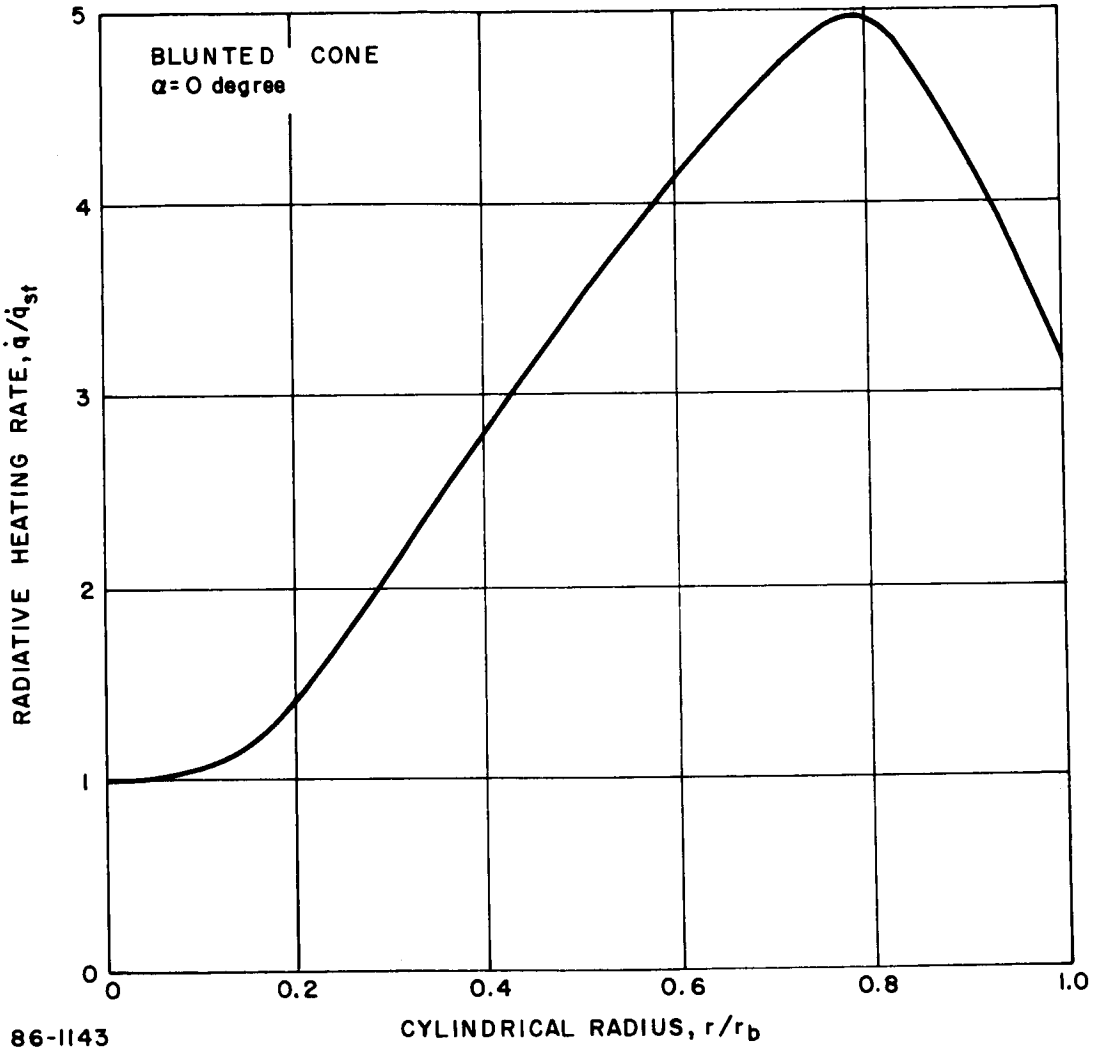

Figure 199 RADIATIVE HEATING DISTRIBUTION ($\alpha = 0$)--BLUNT CONE

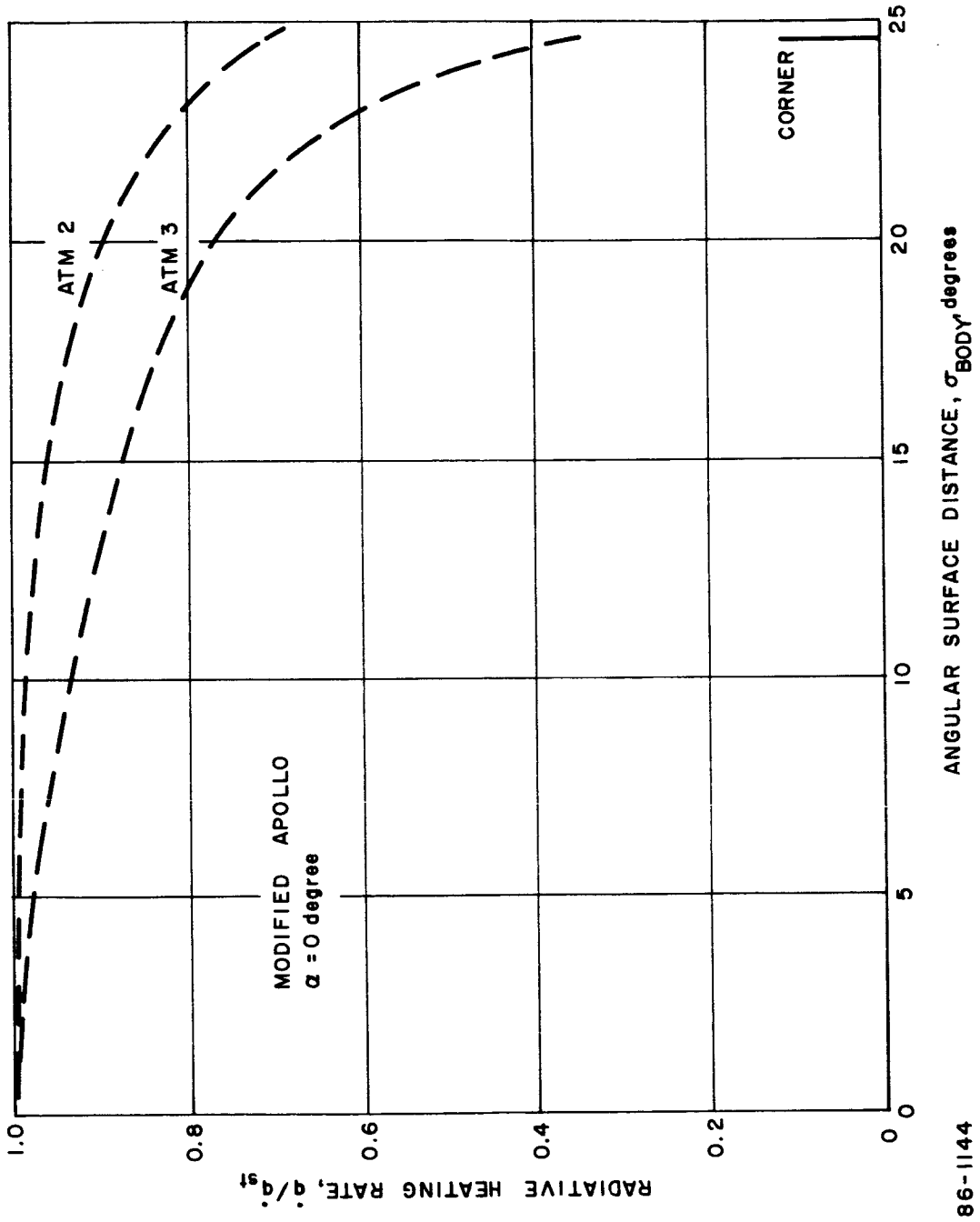

Figure 200 RADIATIVE HEATING DISTRIBUTION ($\alpha = 0$)--MODIFIED APOLLO

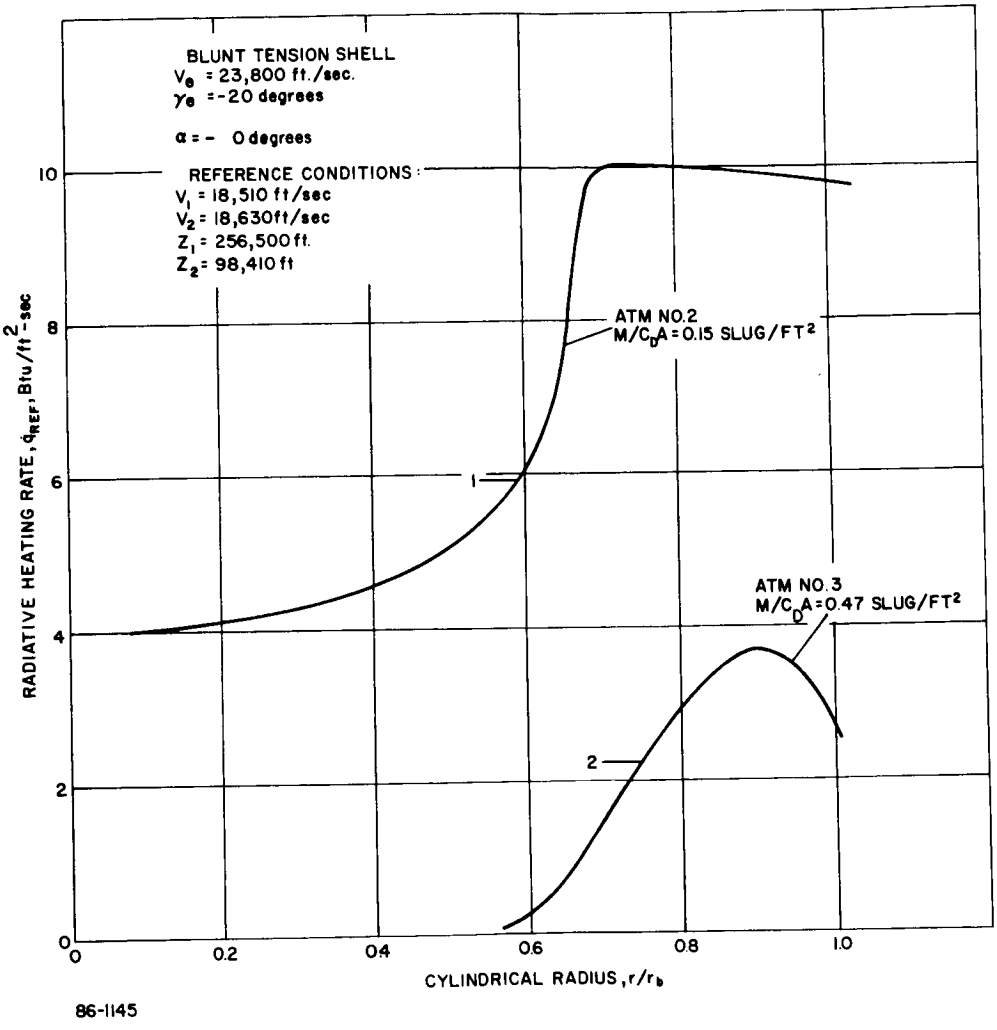

Figure 201 RADIATIVE HEATING DISTRIBUTIONS ($\alpha = 0$)--BLUNT TENSION SHELL

4.4.2 Program 1880

The purpose of this program is to determine the flight path, angle of attack envelope, heating, and loads as a function of time for an axisymmetric vehicle during its entry trajectory into planetary atmospheres. The general inputs required include:

1. Vehicle mass and moment of inertia
2. Aerodynamic coefficients
3. Entry conditions
4. Planet and atmospheric data
5. Heating factors based on vehicle shape.

Convective heat pulses are computed at the stagnation point (laminar) and at the sonic point (laminar and turbulent) as described in preceding sections. In addition, both equilibrium and nonequilibrium radiative heat pulses are computed.

The program (Reference 49) is in four degrees of freedom with no calculation for the side force equation or the lateral trajectory equation.

4.4.3 Digital Program 2026

This program computes the vehicle motion in 6 degrees-of-freedom for a ballistic reentry vehicle. It computes and prints as functions of time the following quantities: Planet referenced and inertial trajectory parameters, the total angle of attack and its component angles of attack and sideslip, the body axis angular velocities and angular accelerations, the resultant normal acceleration and the body axis forces. The program also prints the computed oscillatory envelope values of total angle of attack, normal and axial accelerations, and angular velocity.

Options are available for including the effects of horizontal winds, variations of mass with time and altitude, thrust along the body axis of symmetry, lateral thrust versus time and altitude, the effects of offset center of gravity and products of inertia and moments about the three-body axis. The aerodynamic coefficients may be entered as functions of angle of attack and either Mach Number or altitude.

The planet characteristics used assume a rotating oblate spheroid and the planet's gravitational field is described by a potential function which includes the third spherical harmonic. An option is available for entering other planetary conditions as desired.

4.5 FLIGHT TEST SIMULATION

The problem of simulation of heating and loads in Earth flight tests was investigated, and very good simulation has been achieved for both convective heating and dynamic pressure histories in representative high heating (Figure 202) and high loading (Figure 203) trajectories using a full-scale 4500-pound entry vehicle. The Earth entry conditions were determined by the method of Reference 50. Although the illustrated simulation is for a full-scale vehicle, equally good simulation for loads can be expected for smaller test entry vehicles of the same M/C_DA. For dynamic simulation it is necessary that the radii of gyration be the same fractions of the diameter.

A different technique is required to determine the flight test conditions which simulate the laminar convective heating with a scale model. Given the mass and diameter of the test vehicle, it is necessary to substitute these values into the following equations and solve for the velocity, density and flightpath angle at peak heating in the Earth trajectory.

$$\frac{Q_{s_\oplus}}{Q_{s_{\sigma}}} = 1 = \left(\frac{V_\oplus}{V_{\sigma}}\right)^{1.5} \left(\frac{m_\oplus}{m_{\sigma}}\right)^{0.5} \left(\frac{D_{\sigma}}{D_\oplus}\right)^{1.5} \left(\frac{\beta_{\sigma} \sin \gamma_{\sigma}}{\beta_\oplus \sin \gamma_\oplus}\right)^{0.5} \tag{1}$$

$$\frac{\sin \gamma_\oplus}{\sin \gamma_{\sigma}} = \left(\frac{\beta_{\sigma}}{\beta_\oplus}\right)\left(\frac{V_{\sigma}}{V_\oplus}\right) \tag{2}$$

$$\frac{q_{s_\oplus}}{q_{s_{\sigma}}} = 1 = \left(\frac{K_{L_\oplus}}{K_{L_{\sigma}}}\right)\left(\frac{D_{\sigma}}{D_\oplus}\right)^{0.5} \left(\frac{\rho_\oplus}{\rho_{\sigma}}\right)^{0.5} \left(\frac{(V_\oplus/10^4)^{b_\oplus}}{(V_{\sigma}/10^4)^{b_{\sigma}})}\right) \tag{3}$$

Equation (1) from relations given in Reference 51 matches the integrated laminar heating. Equation (2) from Reference 50 determines the flightpath angle. Equation (3), based on the equation for stagnation heating rate employed in the computer program, matches the peak heating rates. Using the conditions at peak heating thus obtained as initial conditions in the trajectory computer program, the entry conditions can be computed by running the trajectory "backward". The resulting simulation is illustrated in Figure 204.

Where it is desired to simulate the turbulent heating, a slightly more complicated approach is used. In this case, the trajectory point to be matched is determined by the Reynolds number at transition. The four equations which must be solved are:

$$\frac{R_\oplus}{R_{\sigma}} = 1 = \left(\frac{\rho_\oplus}{\rho_{\sigma}}\right)\left(\frac{V_\oplus}{V_{\sigma}}\right)\left(\frac{D_\oplus}{D_{\sigma}}\right)\left(\frac{\mu_{\sigma}}{\mu_\oplus}\right) \tag{4}$$

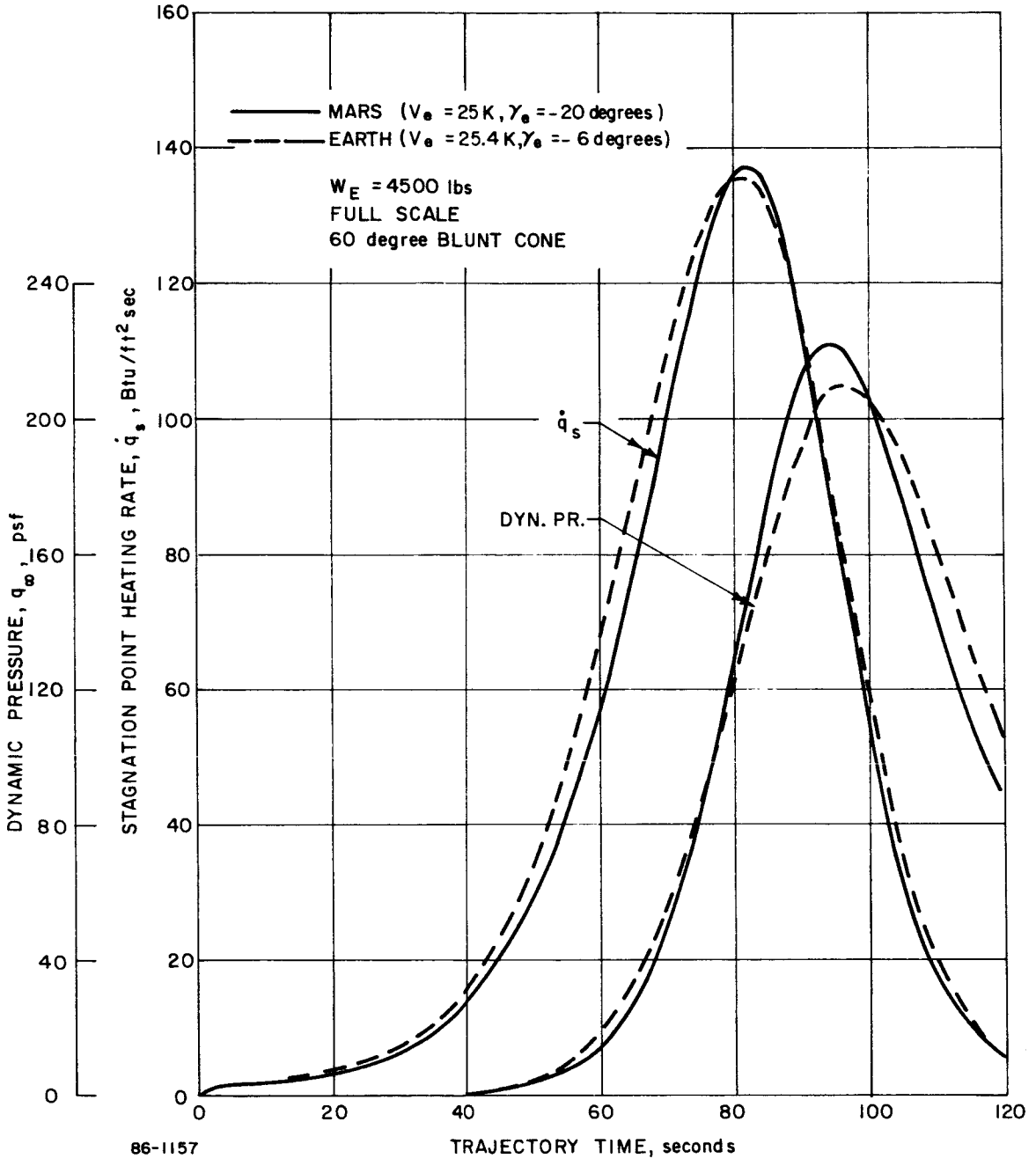

Figure 202 EARTH SIMULATION FOR MARS MODEL 2 ATMOSPHERE

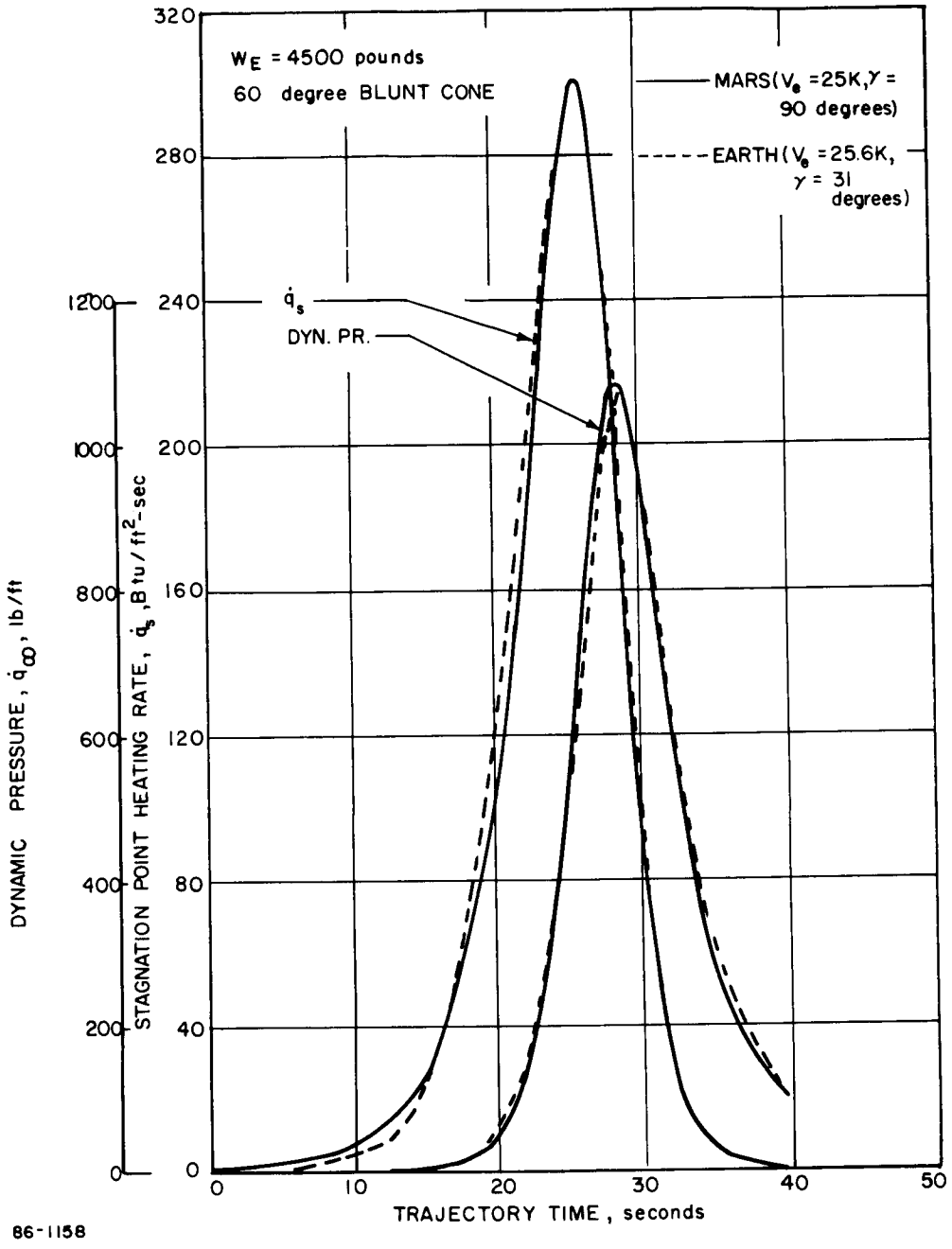

Figure 203 EARTH SIMULATION FOR MARS MODEL 2 ATMOSPHERE

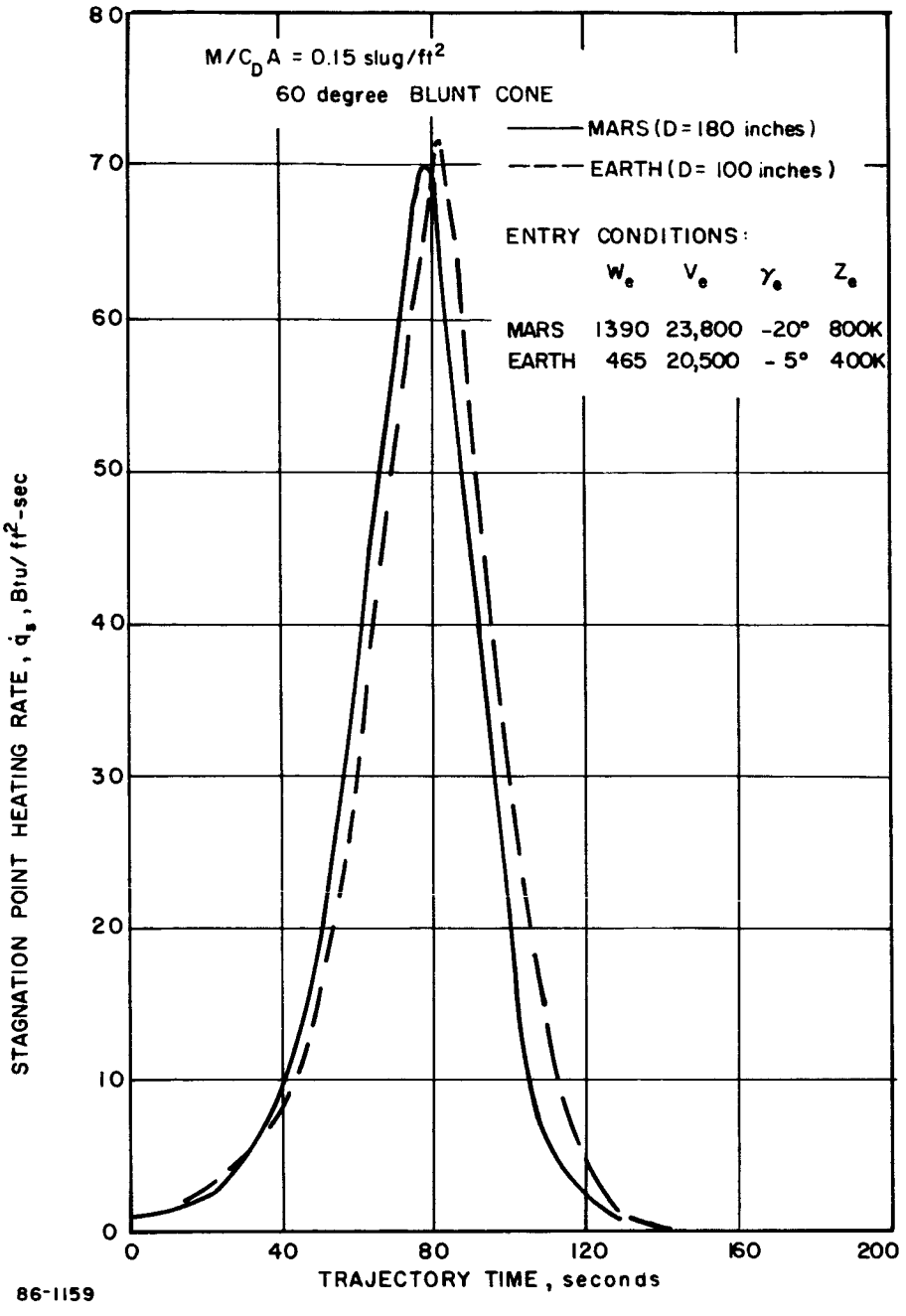

Figure 204 EARTH SIMULATION FOR MARS MODEL 2 ATMOSPHERE
$M/C_DA = 0.15$ slug/ft^2

$$\frac{\dot{q}_{T_\oplus}}{\dot{q}_{T_{\sigma'}}} = 1 = \left(\frac{\rho_\oplus}{\rho_{\sigma'}}\right)^{0.8} \left(\frac{V_\oplus}{V_{\sigma'}}\right)^{3.18} \tag{5}$$

$$\frac{\sin \gamma_\oplus}{\sin \gamma_{\sigma'}} = \left(\frac{\beta_{\sigma'}}{\beta_\oplus}\right)\left(\frac{V_{\sigma'}}{V_\oplus}\right) \tag{6}$$

$$\frac{Q_{T_\oplus}}{Q_{T_{\sigma'}}} = 1 \left(\frac{V_\oplus}{V_{\sigma'}}\right)^{2.18} \left(\frac{m_\oplus}{m_{\sigma'}}\right)^{0.8} \left(\frac{\beta_{\sigma'} \sin \gamma_{\sigma'}}{\beta_\oplus \sin \gamma_\oplus}\right)^{0.2} \left(\frac{D_{\sigma'}}{D_\oplus}\right)^{1.8} \tag{7}$$

Equation (4) matches the Reynolds number at transition. Equation (5) matches the turbulent heating rate at the same point. Equation (6) determines the flight-path angle. Equation (7) matches the integrated turbulent heating. Equations (6) and (7) are based on relations given in Reference 51. Using the trajectory program as in the laminar case, the desired entry conditions are obtained. The simulation achieved in this manner is illustrated in Figure 205.

It is not possible to simulate radiative heating in the Earth's atmosphere due to the very low concentration of CO_2.

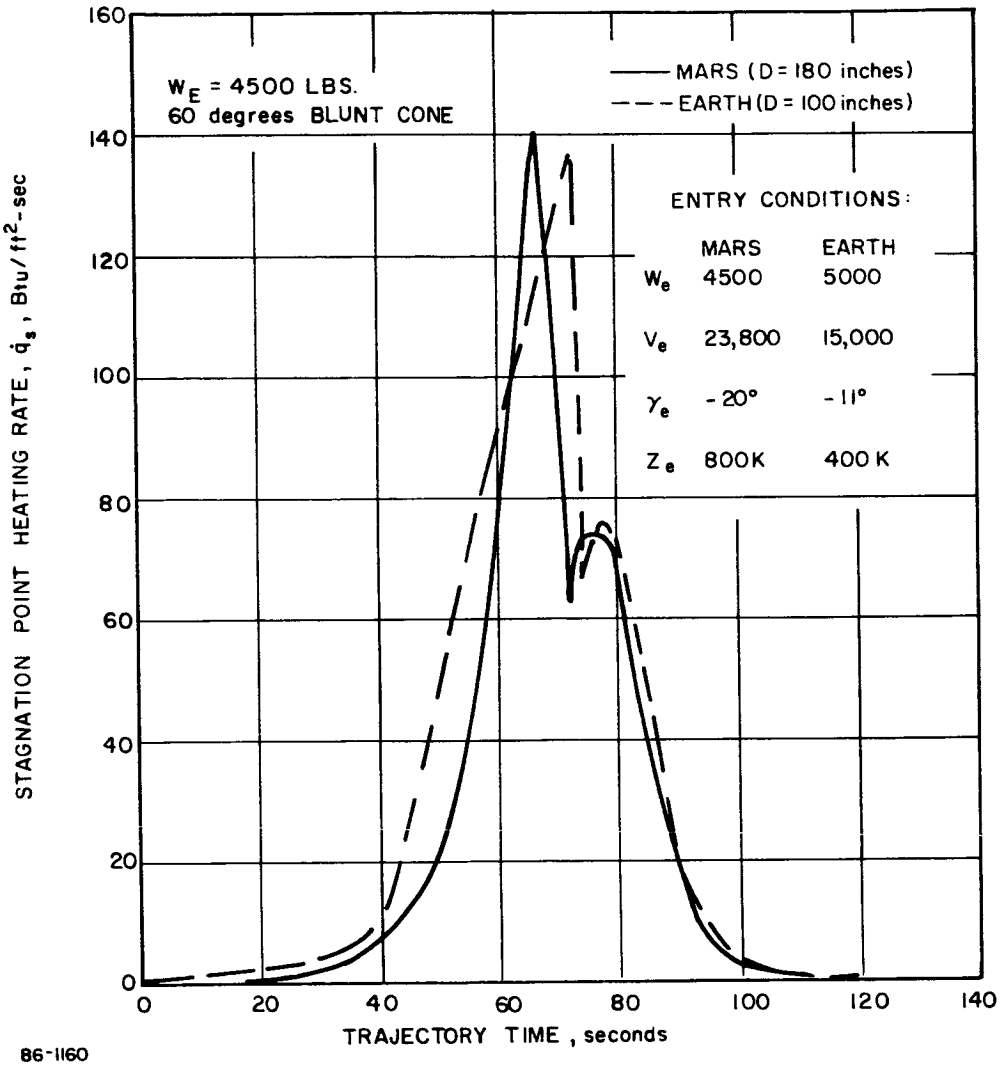

Figure 205 EARTH SIMULATION FOR MARS MODEL 3 ATMOSPHERE

5.0 STRUCTURES - CONCEPTUAL DESIGN

ENTRY FROM THE APPROACH TRAJECTORY

5.1 INTRODUCTION AND SUMMARY

The structural analysis effort was initially concentrated on supporting the parametric studies. These endeavors supplied approximate structural shell weights as a function of configuration, diameter and structural material. The computation of these parametric structural weights was based on simplified design formulas. The additional weight required for rings and fittings was estimated by using factors derived from analysis of earlier designs of typical entry vehicle.

The structural designs were then refined by using more rigorous analyses and incorporating improved loads data as it became available.

Since many changes in the design criteria could be expected due to the many conflicting requirements of the system, the major emphasis was placed on the components which were strong functions of vehicle size as well as having significant weight fractions.

5.1.1 Configuration Descriptions

The structural concept selected for the primary shell of the modified Apollo and blunt-cone shapes was honeycomb sandwich. For the lightly loaded large shell structures considered, this type of construction is the most efficient of the various state-of-the-art types of construction. Because of the requirements for very low weight, beryllium was used for the face sheet material. The honeycomb core selected was stainless steel due to its thermal expansion compatibility with beryllium and its lower cost and greater availability. In order to achieve an optimized structure, the face-sheet thicknesses and core depths were selected so that the stresses in the face sheet approached the yield strength of the material while, at the same time, the structure was at the point of incipient buckling. In order to accomplish this, it was necessary to increase face-sheet thicknesses and core depths locally at points of concentrated force application and at cutouts.

The structural concept analyzed for the tension shell consisted of a tapered fiberglass shell supported by a beryllium compression ring. Forward of the payload reaction circle, the structure was a conventional beryllium shell under a compressive load. A beryllium ring and a fiberglass shell were selected because the results of early membrane analyses (using a Newtonian pressure distribution) showed that a high ring-to-shell stiffness ratio was advantageous in suppressing compressive stresses in the shell.

When the predicted non-Newtonian pressure distributions were considered, this structural material selection showed little advantage from a structural weight efficiency point of view.

5.1.2 Mission Concepts

The primary structural shells of three different entry capsule concepts for the blunt cone and modified Apollo shapes were analyzed. These concepts were (1) the multi-mission structural shell, (2) the 1971 structural shell, and (3) the future mission shell for the model 3 atmosphere. Only the multi-mission concept was analyzed for the tension shell.

For the multi-mission primary shell, the inertia of the payload was assumed to be distributed over the rear face of the shell in the nosecap region for the early mission and concentrated on a circular line for the future missions. The inertial force of the future mission payload was larger than the inertial force of the 1971 payload although the deceleration of the capsule was greater for the 1971 mission. This was because the mass of the 1971 payload was considerably less than the future mission payload. Generally speaking, however, the structural requirement of the nose portion of the multi-mission shell was governed by the 1971 requirements while the outer portion of the shell was designed for the future mission loads. The inertial reaction of the payload of the 1971 mission shell was also distributed. However, only the maximum external pressure of the 1971 mission would be experienced by the shell with a resulting lower structural requirement.

The shell for the future mission concept has the same total forces acting upon it, since the entry angle, γ_e , would be decreased as the payload is increased with the net result that the external pressure remains constant. Although the loads will be unchanged over the range of entry angles, the structure temperature will increase as the entry angle becomes smaller. The degradation of material properties with the temperature rise will require an increase in structure weight. This concept must also consider both a concentrated and distributed payload inertia force on the shell structure, which will also require an increased weight. Therefore, the future mission concept will, in general, require a slightly heavier structure than the 1971 mission concept.

5.1.3 Requirements, Constraints, and Design Criteria

The primary shell and internal structure are required to maintain their integrity throughout the operating sequence. This sequence begins at the factory and includes (1) sterilization cycle temperatures and loads, (2) handling and transportation loads, (3) ascent loads, (4) spaceflight temperatures (5) ΔV maneuvering and separation forces, (6) entry temperatures and loads, and (7) parachute opening shock loads.

The most important constraint on the structural design is the need for minimum entry weight.

A summary of the design conditions for a typical Mars lander capsule is given in Table XXXII.

The tension shell structure has requirements and constraints in addition to those given above. These requirements and constraints are as follows:

a) The loading of the compression ring is to be determined by integrating the stress resultant in the ring as determined from the rotationally symmetric shell analysis.

b) Flat beryllium sections are to be used for the compression ring where possible.

c) The tension shell is to be designed for symmetrical loading only. An analysis is to be conducted for asymmetrical loading and the effect on shell weight noted.

d) No analysis is to be conducted to determine the effect of dynamic loading.

5.1.4 Performance Summary

When the weight of the primary shell structure is used as the criterion for relative merit, the ranking of the three generic shapes is the tension shell, blunt cone and the modified Apollo. This conclusion is based on comparing the blunt cone and modified Apollo having a beryllium honeycomb sandwich primary shell and the tension shell with a fiberglass shell and a beryllium compression ring.

Relative shell weights of the three concepts are given in Table XXXIII, and include weights for a multi-mission structure, a 1971 mission structure and a multi-mission shell of stainless steel honeycomb structure for the blunt cone. The data given should only be used to compare the generic shapes, since the results include only the weight of the face sheets, core and the end ring. The structural weights for the future mission shell (Model 3 atmosphere) were assumed to be identical to the 1971 mission shells.

The tension entry shell structure is more efficient than the blunt cone and Apollo entry shell structure when designed according to the requirements and constraints given in paragraph 5.1.3 providing the effects of circumferential stresses can be neglected.

TABLE XXXII

SUMMARY OF DESIGN CONDITIONS FOR THE BLUNT-CONE MARS LANDER CAPSULE

Mission Sequence	Design Condition		
Ground Handling	Vibration		
	± 3.5 g_e (rms)	2 to 50 cps	
	± 1.5 g_e	50 to 300 cps	
	Packaged		
	± 1.3 g_e	2 to 26 cps	
	0.036 in D.A.	26 to 52 cps	
	± 5.0 g_e	52 to 300 cps	
Launch	Sustained Acceleration		
	4.5 g_e axial		
	± 1.0 g_e lateral		
Capsule Trajectory Maneuver	ΔV Force = 800 pounds		
Capsule Cruise	Spaceflight temperature distribution -54°F to 230°F		
Capsule Entry		Multimission	1971 Mission
	a_x axial g	91.0	209
	a_n normal g at max a_x	5.6	16.2
	α angle of attack, at max a_x	15.8°	19.5°
	p_s stagnation pressure	19.9 lb/in^2	14.0 lb/in^2
Parachute Deployment	8500 pounds times 1.5 load factor		

TABLE XXXIII

RELATIVE SHELL WEIGHTS

Shape	Concept	Material	Relative Weight (pounds)
Blunt Cone	Multi-Mission Structure	Be	1.00
	Multi-Mission Structure	SS	1.52
	1971 Mission	Be	0.84
Apollo	Multi-Mission Structure	Be	1.06
	1971 Mission	Be	0.89
Tension	Multi-Mission Structure	Fiberglass Shell Be ring	0.80

5.1.5 Conclusions and Problem Areas

5.1.5.1 Conclusions

1. Unsymmetrical Loads -- The results of the analysis for unsymmetrical loading of the blunt-cone shape indicate that only minor increases in stiffness are required over that required for symmetrical loading with the same stagnation pressure. The conclusion is, therefore, that during the concept selection and preliminary design phase, only symmetrical loading need be considered for the modified Apollo and blunt cone when estimating structural weight for angles of attack less than 15 degrees.

Unsymmetrical loading on the tension shell, when evaluated at the maximum normal force condition on the reference trajectory, is not more critical than symmetrical loading at the maximum axial loading conditions.

2. Aeroelasticity -- It is still to early to make firm conclusions about the problem of flutter developing during the entry phase. The problem could exist, however, in all three generic shapes because the modified Apollo and blunt cone will be close to the buckling loads based on a static criterion at peak dynamic pressure.

3. Compatibility of the Ablative Material and the Primary Shell Substructure -- Because the relative stiffness of the ablator will be much less than that of the substructure and the temperatures are not expected to be less than -54°F during spaceflight, the problem of compatibility of the heat shield and substructure does not appear severe.

5.1.5.2 Problem Areas*

The problem areas summarized here pertain to the difficulties that arise in the analysis of the primary structural shell of the three generic shapes. The problems fall into three general classes. These are the static stability analysis of honeycomb sandwich shells static analysis of tension shells, and the structural dynamic response of shells.

There are several types of instability that can occur in sandwich shells which include: (1) general instability of the composite structures, (2) wrinkling instability of the face sheets, and (3) dimpling of the face sheets. In addition to these failure modes, shear failure of the core material can also occur. At present, data with which to conduct satisfactory design analyses and optimization of sandwich shell structures do not appear to be available.

Another important problem in this area, which applies also to homogeneous shells, is that the criteria for selecting the reinforcing rings at the outer edges of the shells are not accurate enough. These rings constitute a significant portion of the total weight of the primary structural shell.

The principal problem area for the tension shell is in determining the effect of the circumferential compressive stresses developed in the entry shell due to the non-Newtonian pressure distribution. These stresses are the result of the pressure distribution rather than the non-ideal boundary conditions at the outer edge of the entry shell structure.

5.2 DESIGN CRITERIA

The structural analysis effort was concentrated on the entry-to-parachute deployment phase of the mission, where weight considerations are most critical from the structural viewpoint.

* The following discussion reflects the status of the structural analysis at the time of the interim Mars Probe/Lander report (Reference 5). Improved methods developed subsequent to this date are given in Section 7 of the present report.

The primary shell structure is required to withstand a non-uniformly distributed aerodynamic pressure on its outer surface. The resultant force, obtained by integrating the pressure over the surface, induces accelerations which are directly related to the mass and mass moments of inertia of the capsule.

The rigid body acceleration determines the internal force and moment distribution in the capsule and is the design criterion during the entry phase for all of the structure not experiencing the pressure loading directly. The inertial forces due to the mass of the primary structural shell tend to reduce the net external pressure acting on the shell, hence are beneficial. The multi-mission shell is designed for both a future payload and the 1971 mission payload.

The manner in which the internal payload inertial force is brought into the primary shell has a major effect on the stress distribution and critical loads of the shell. If the payload force is distributed in the nose section, as the 1971 payload will be, a tensile stress is induced in the nose section since there is a net internal pressure. The structural requirements in the nose will therefore be based on a yield criterion for the blunt cone and Apollo shape. A concentrated payload reaction, as is expected for the future mission payload, induces high bending and shear stress in the vicinity of the circle of application. The stresses in the nose will be compressive, however; hence a combined yielding and buckling criterion would be used to determine structural requirements in the nose region.

The safety factors used in the blunt cone and Apollo design were different for the yielding and buckling failure modes. For a yielding failure, the limit (applied) loads were multiplied by 1.0 and compared to the yield strength of the material. Limit loads were increased by 25 percent for a buckling failure mode.

The symmetrical pressure distribution in the region of the multiple shocks on the tension shell was assumed to be uniform and adjusted so that the effective drag coefficient of the flight capsule was 1.10 times the value used in the aerodynamic analyses.

Since fiberglass does not have a well defined yield point, the limit loads were multiplied by 1.25 and the resulting stresses compared to the ultimate strength of fiberglass. Limit loads were also increased by 25 percent for buckling failure mode.

It should be noted that although the decelerations for the 4500 pound multi-mission capsule are much less than for the 1971 capsule, the critical loads for the primary shell structure correspond to the former entering into a Model 2 atmosphere at a -90 degree reentry angle. If the decelerations and mass of the capsule are considered, it can be seen that the forces acting on

the structure are greater for the 4500-pound capsule. In a preliminary design study such as this, all loading should be expressed as surface pressures or forces to avoid overlooking a critical design condition. Details of the loading are given in Tables XXXIV, XXXVI and XXXVII.

The aerodynamic forces are periodic and related to the rigid body motions of the capsule, which is both spinning and pitching. The upper limit on the frequency of the aerodynamic loads is of the order of 5 cps. The capsule structure has to be examined to determine if there are frequencies low enough to couple with the rigid-body frequency.

The temperatures and temperature gradients will induce thermal stresses and displacements during entry. However, the temperature rise of the structure is sufficiently slow that, when the capsule is experiencing maximum loading, the temperature increase is quite small; hence there will be only a minor degradation of material properties. This is particularly true for the γ_e = -90 degree trajectories.

If a given capsule designed for γ_e = -90 degrees enters on a shallower trajectory, the structural temperatures will rise, but generally the induced loads will decrease at a greater rate than the allowable loads as affected by the temperature rise.

Temperature gradients through the heat shield and substructure are not expected to produce significant thermal stresses in the substructure since the stiffness and thickness of the candidate ablative materials are significantly less than the corresponding properties of the substructure. As a consequence, thermal stresses were not computed in the preliminary design of the primary structure.

5.3 RESULTS AND DISCUSSION

5.3.1 Blunt Cone

5.3.1.1 Parametric Analysis

1. Design Conditions -- The design dynamic pressure as a function of base radius is given in Figure 206. These values are early estimates and are not used on the reference design. Since Newtonian pressure distribution was assumed, the pressure on the conical portion was 75 percent of the stagnation pressure. The structural temperature at the time of peak dynamic pressure was assumed to be 300° F. This estimate was made for a γ_e = -90 degree entry angle and an assumed 275° F initial entry temperature.

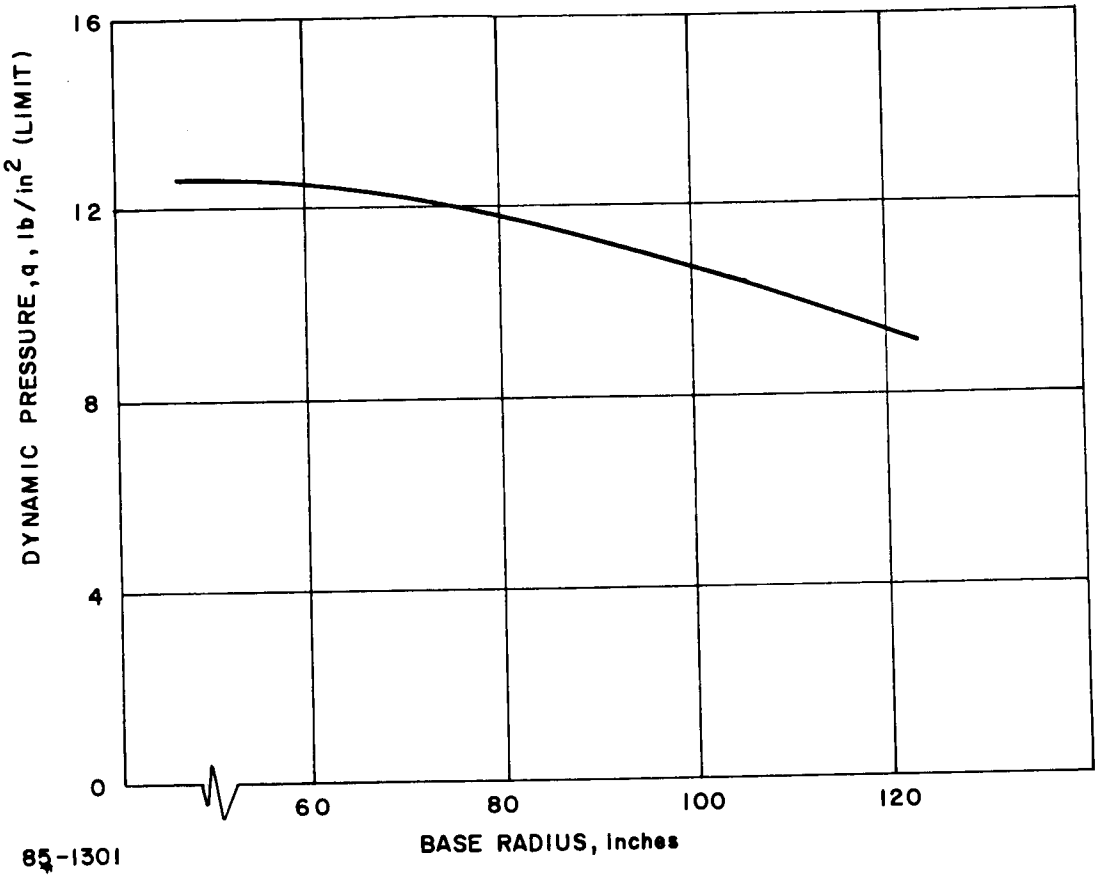

Figure 206 BLUNT CONE DYNAMIC PRESSURE VERSUS BASE RADIUS

2. Structural Weights and Thicknesses -- The structural weights and thicknesses are given in Figures 207 and 208 as functions of base diameter. Beryllium, stainless steel, fiberglass, aluminum, and magnesium were considered. The results demonstrate that beryllium is the most efficient material in the range of diameters being considered.

A more conservative buckling criterion was used for the reference design analysis than for the parametric analsis. The effect on overall shell weights of the later criterion (discussed in paragraph 7.1.2.1) is also indicated in Figure 207. The structural weights include a factor of 1.7 to account for rings, fittings, and the effects of bending stresses.

5.3.1.2 Static Analysis

1. Design Conditions -- The entry loading for the multimission shell concept corresponds to the failure mode case, i.e., entry angle of attack equal to 179 degrees. The pressure distribution corresponding to the critical loading occurs at an angle of attack of 15.8 degrees and is presented in Figure 209. The load factors are summarized in Table XXXIV.

The pressure distribution of the 1971 mission was assumed to be similar to the multimission distribution. The substructure temperature was assumed to be 300°F throughout.

TABLE XXXIV

BLUNT CONE LOADING CONDITIONS

	Multi-Mission Shell	1971 Mission	Future Mission Shell
Entry weight, lb	4500	1390	1390
Axial g's, a_x	91.0	209.	209.
Normal g's, a_n	5.6	16.2	16.2
Angle of attack, α	15.8	19.5	19.5
Stagnation pressure, P_s, psi	19.9	14.0	14.0

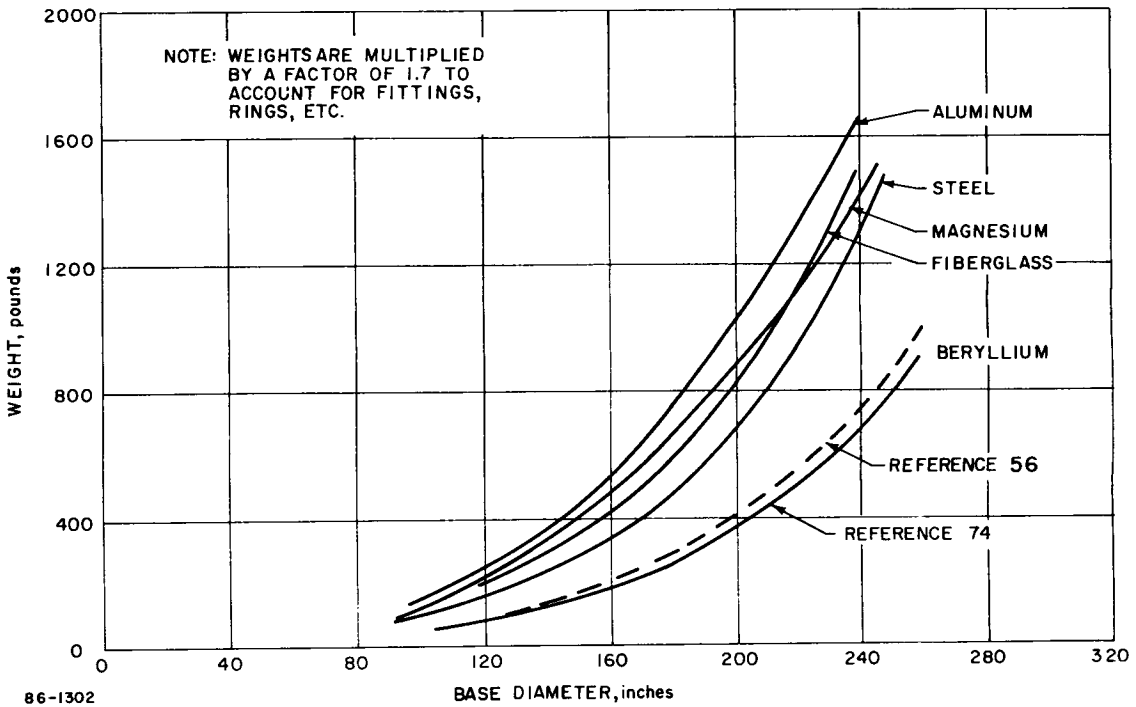

Figure 207 BLUNT CONE -- PARAMETRIC SHELL WEIGHTS

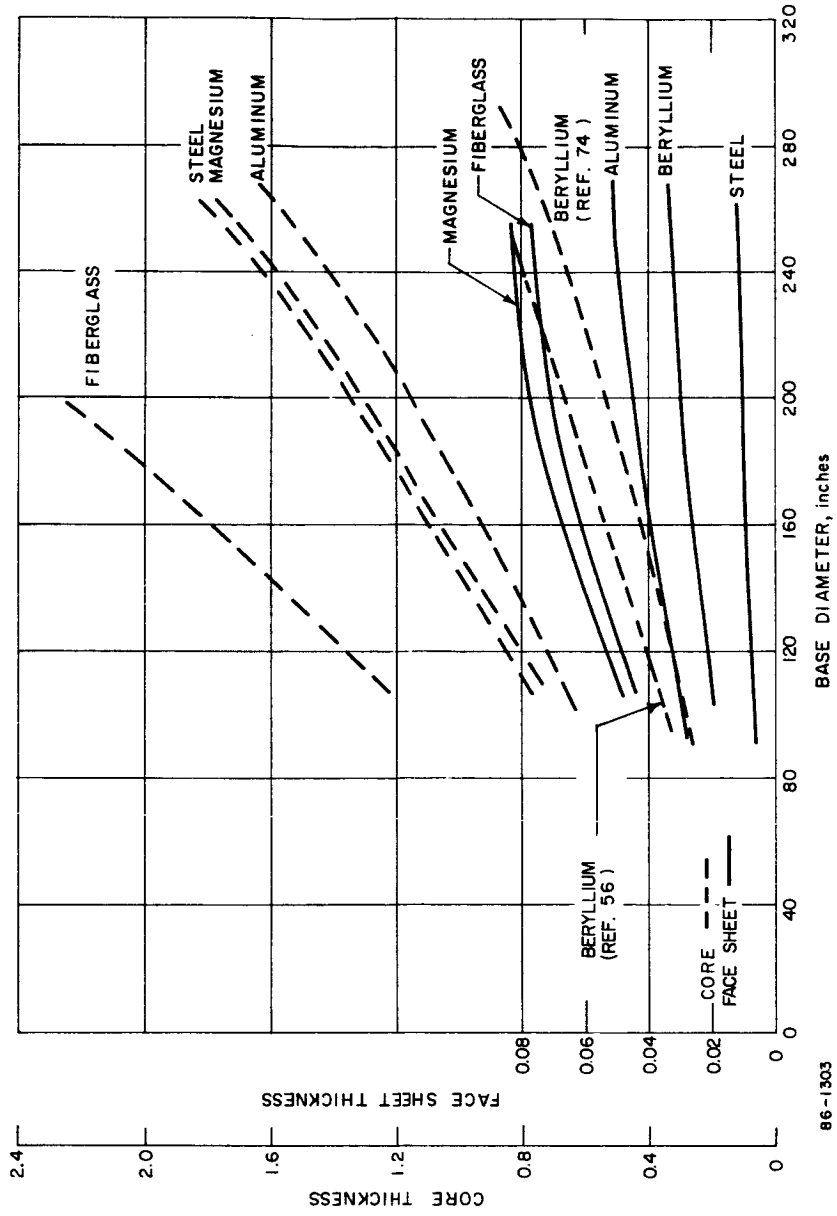

Figure 208 BLUNT CONE -- PARAMETRIC SHELL THICKNESS

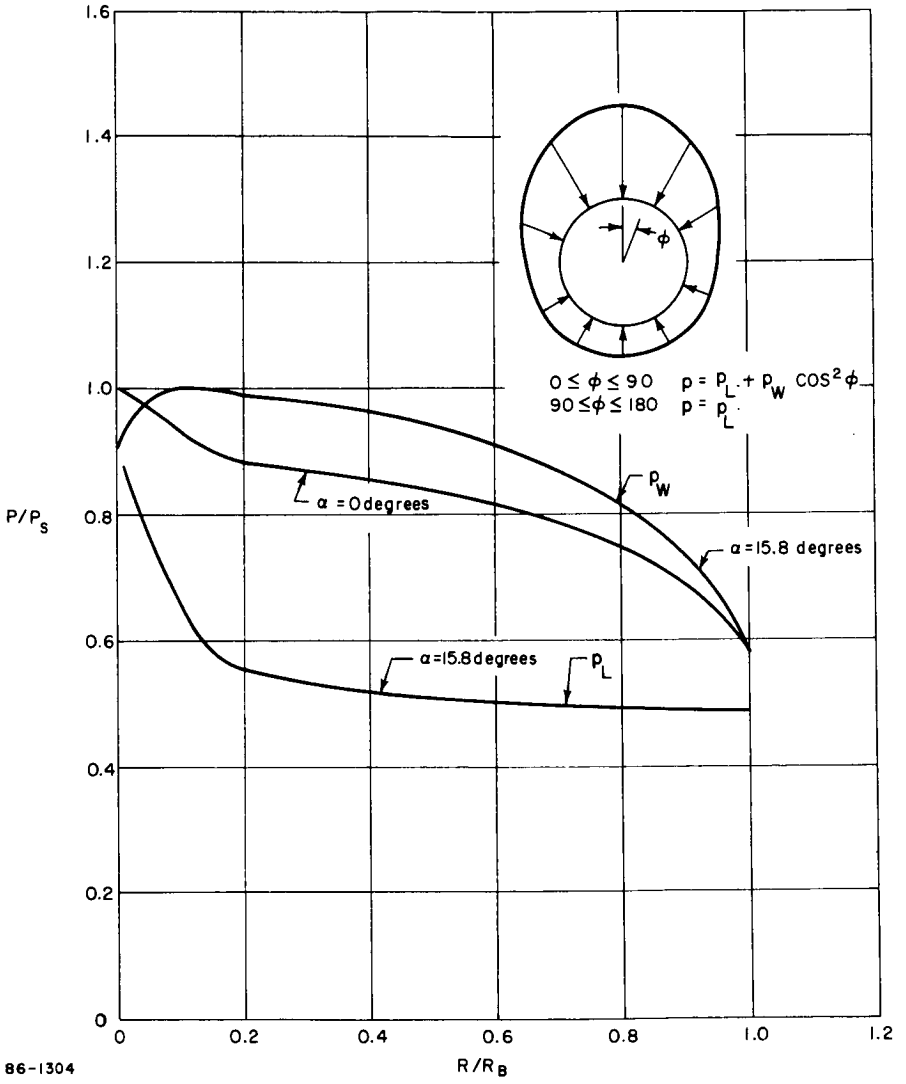

Figure 209 BLUNT CONE -- PRESSURE DISTRIBUTION

2. Structural Analysis Results -- The primary structure of the blunt cone is a complex shell which has been optimized to satisfy varying conditions in different regions of the shell. A schematic of the structure is shown in Figure 210. This is the shell configuration on which the following results are based unless otherwise stated.

The thickness of the solid beryllium nose was determined by the external heating, and the remaining shell thicknesses by the various load combinations.

The face sheet thickness and core depth in regions 2, 3, 4, and 6 were selected to withstand the large bending moments and stress resultants due to the introduction of the concentrated payload inertial force. The design in region 7 satisfies both the buckling and yielding requirements. The forward portion of the shell also had to be adequate for the 1971 mission with the payload inertial force distributed over the rear surface of the shell.

The buckling computations assumed that a uniform pressure equal to 1.25 times the stagnation pressure was applied to the spherical cap and $0.75 \times 1.25 \times p_s$ was acting on the cone.

The ring dimensions were determined by the procedure described in paragraph 7.1.2.1. The equivalent force on the ring equals 1080 lb/per unit length of circumference, requiring moments of inertia of 10.2 $in.^4$ and torsional rigidity of 11.7 $in.^4$.

The symmetrical stress distribution is given in Figure 211, and the axial and radial displacements in Figure 212 for the multimission loads. Figures 213 and 214 show the stresses and displacements developed by the 1971 mission load and the distributed payload inertia. The design is also adequate for this condition.

The effect of the asymmetrical pressure distribution (Figure 209); is shown in Figures 215 and 216. The resultants and couples are compared for the symmetrical and unsymmetrical cases. The stresses in the outer portion of the shell are relatively unaffected by the unsymmetrical loading. The stresses in the region of the payload reaction circle are increased in the windward meridian of the capsule. These stresses are evidently due to the unsymmetrical moment and shear force applied to the shell by the payload normal and angular accelerations. The reference design will therefore require an increased stiffness to accomodate these increased stresses.

The core density required to prevent face-sheet wrinkling and face-sheet dimpling is less than 2 lb/ft^3 from the formulas of paragraph

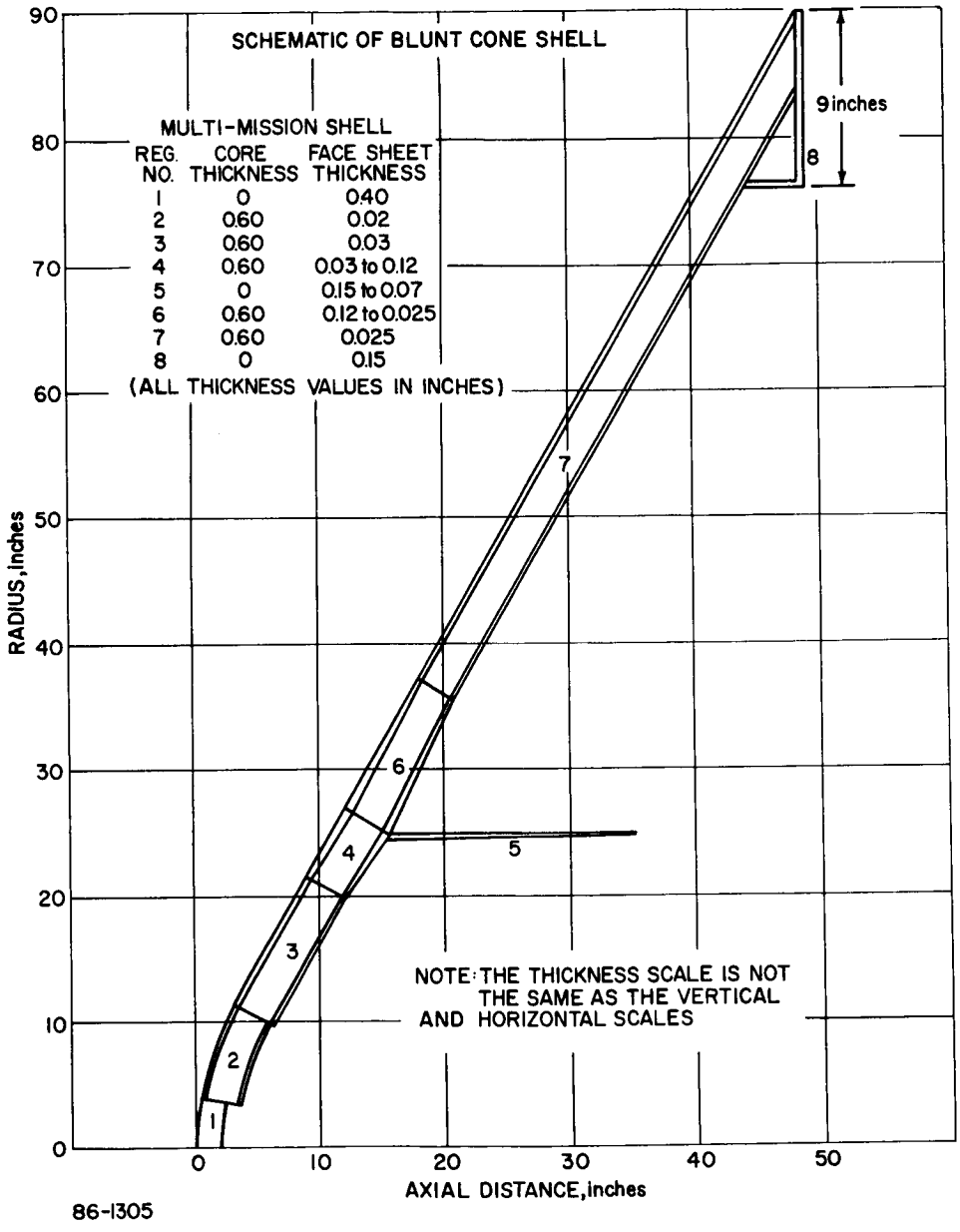

Figure 210 SCHEMATIC OF BLUNT CONE SHELL

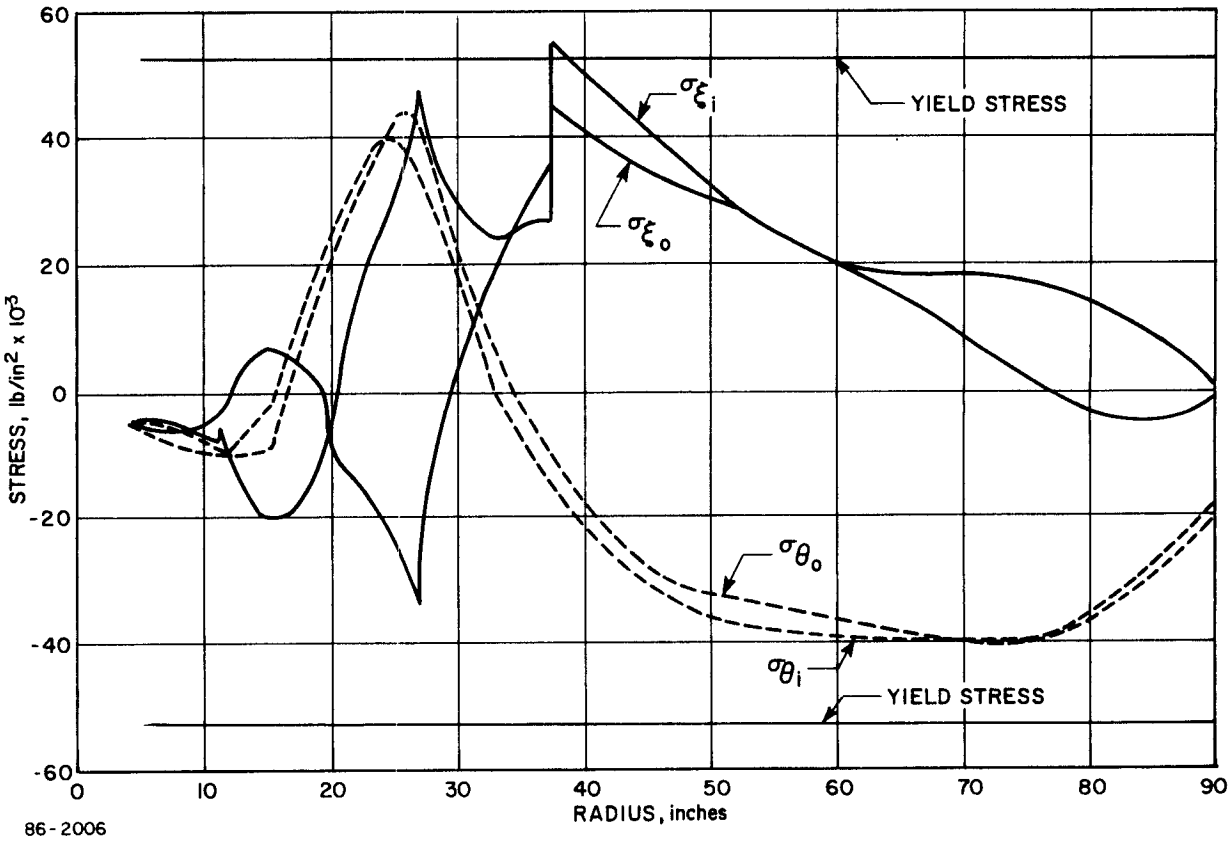

Figure 211 BLUNT CONE -- MULTI-MISSION SHELL STRESS VERSUS RADIUS WITH MULTI-MISSION LOADS

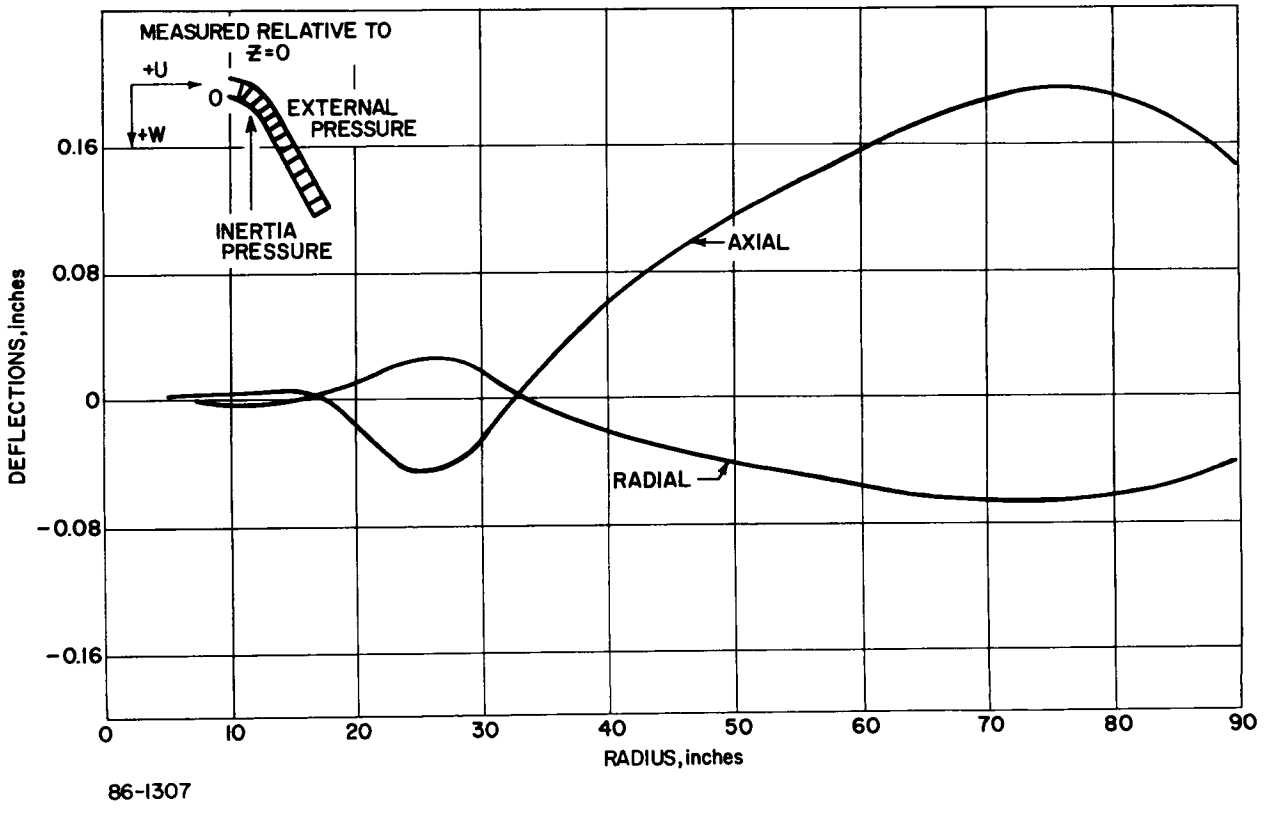

Figure 212 BLUNT CONE -- MULTI-MISSION SHELL DEFLECTIONS VERSUS RADIUS WITH MULTI-MISSION LOADS

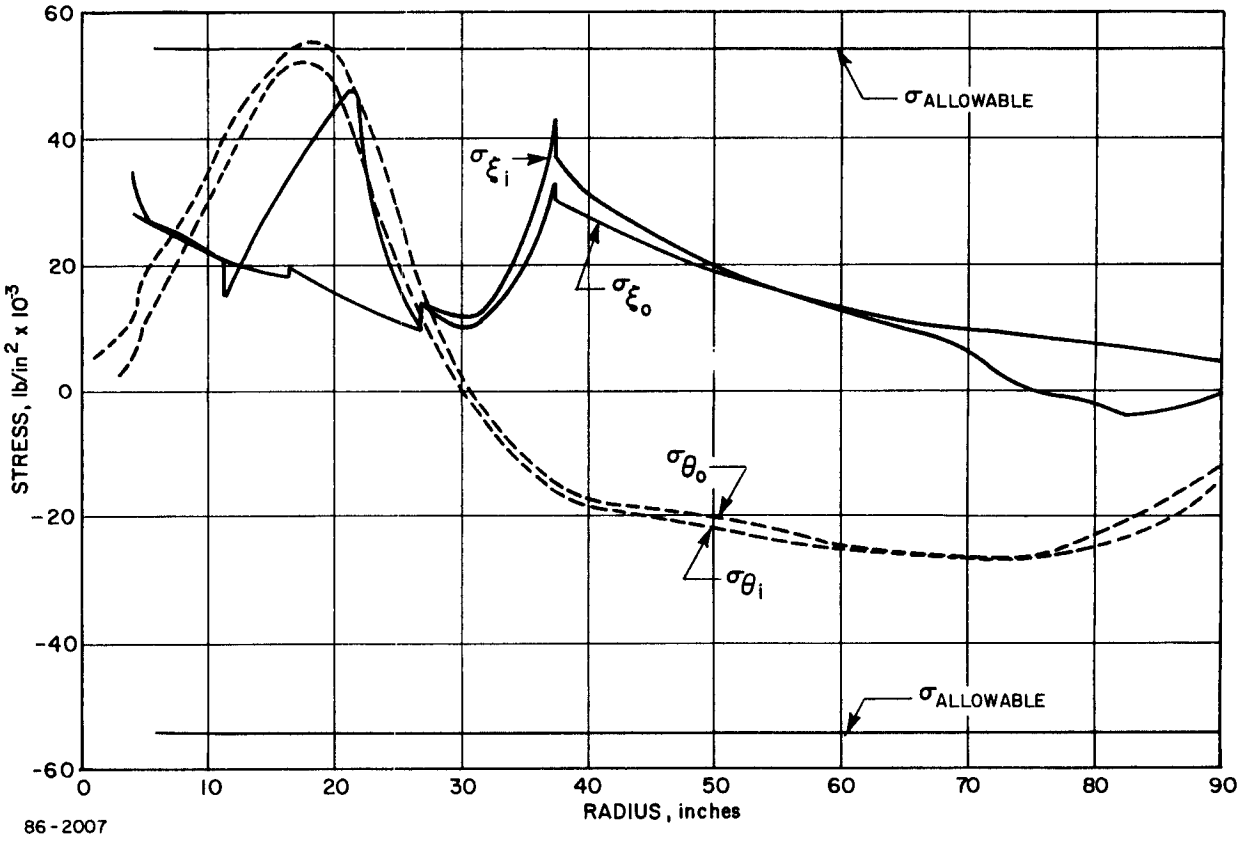

Figure 213 BLUNT CONE -- MULTI-MISSION SHELL 1971 LOADS STRESS VERSUS RADIUS

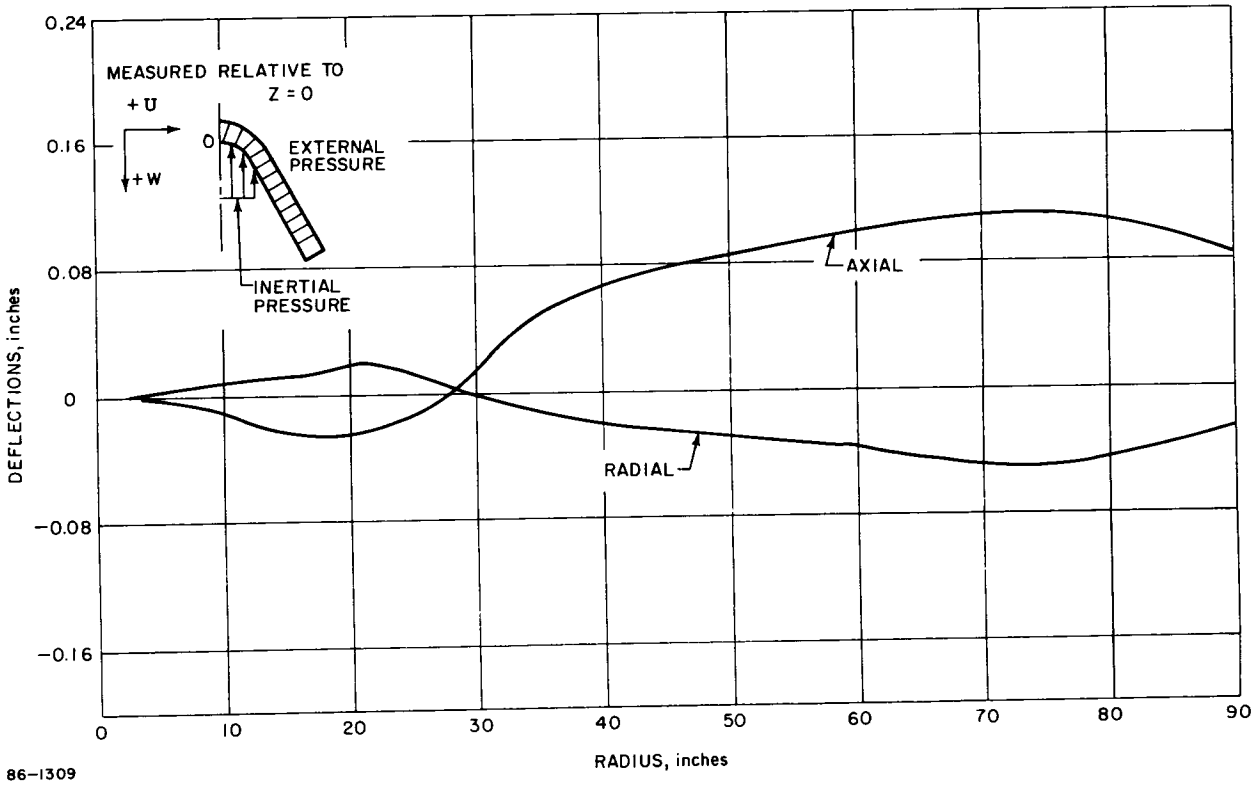

Figure 214 BLUNT CONE -- MULTI-MISSION SHELL 1971 LOADS DEFLECTION VERSUS RADIUS

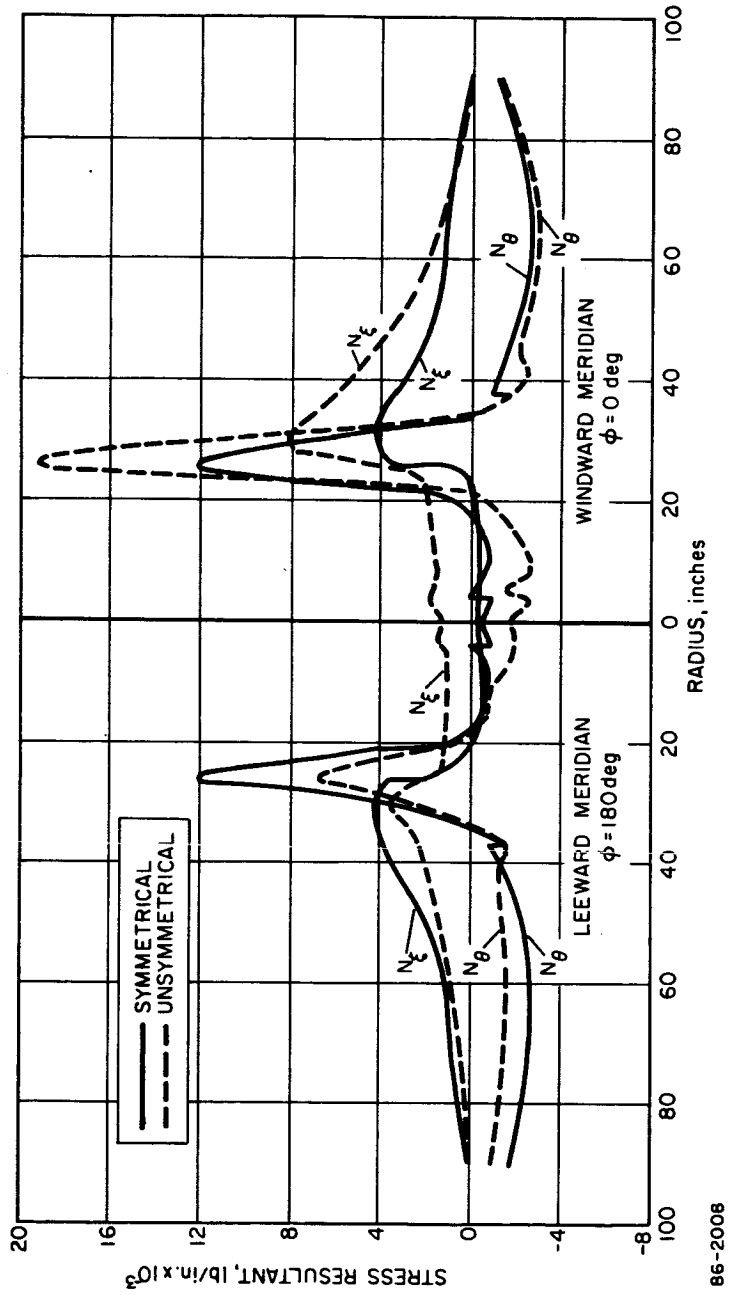

Figure 215 BLUNT CONE--SYMMETRICAL AND UNSYMMETRICAL STRESS VERSUS RADIUS

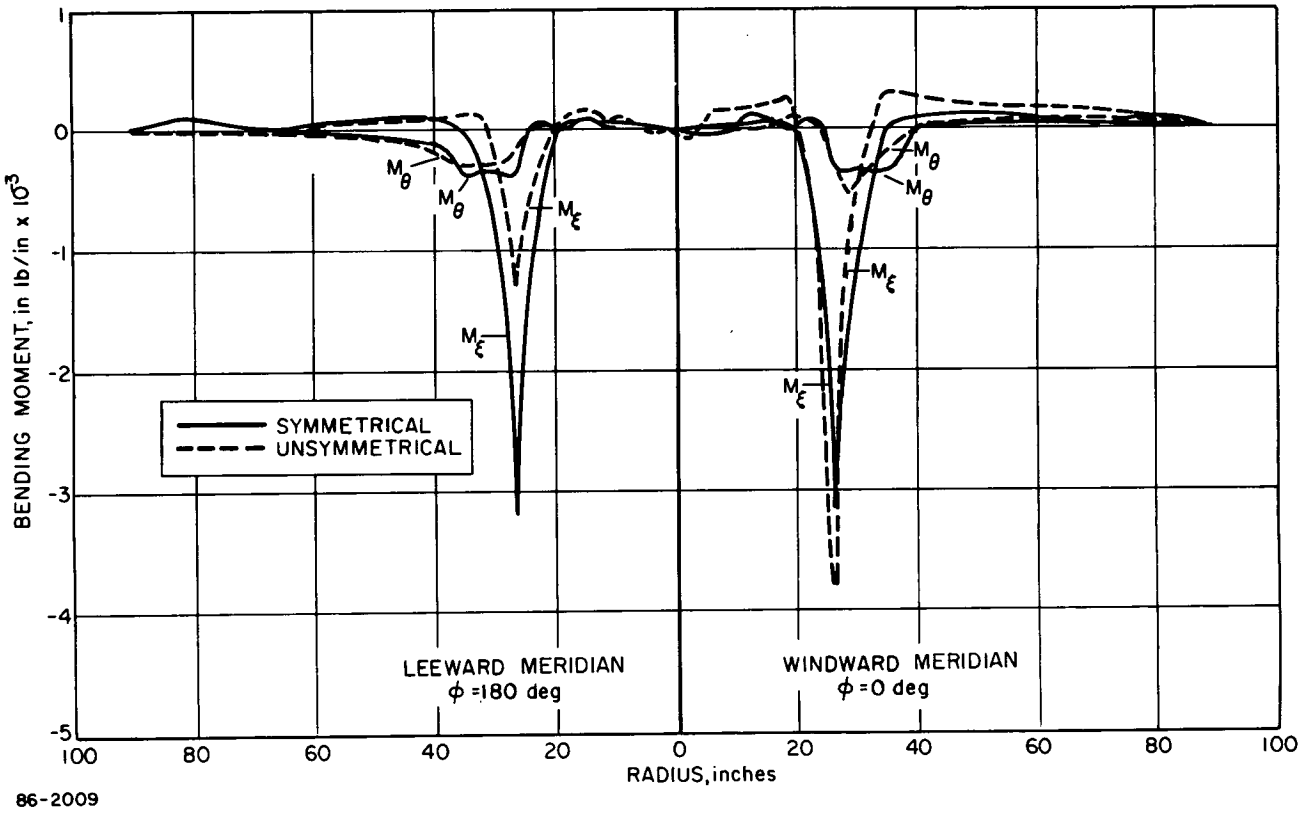

Figure 216 BLUNT CONE--COMPARISON OF SYMMETRICAL AND UNSYMMETRICAL BENDING MOMENT DISTRIBUTIONS

7.1.2.1, when using beryllium face sheets loaded to the yield stress of 53,000 lb/in.^{2} and stainless steel honeycomb core. Since the densities determined in this manner are less than the 6 lb/ft^3 suggest by NASA/LRC, the resulting structure using a 6-lb/ft^3 core appears to be conservative.

The structural shell requirements for a 1971 structural shell and a multimission stainless steel shell are given in Table XXXV. The shell thicknesses were scaled from the reference configuration, Figure 210, hence the relative weights for the different concepts can be compared on the same basis.

TABLE XXXV

BLUNT CONE REQUIRED SHELL THICKNESSES

1971 Mission Shell			Multimission-Stainless Steel	
Region No.	Core Thickness (inches)	Face Sheet Thickness (inches)	Core Thickness (inches)	Face Sheet Thickness (inches)
1	0	0.40	0	0.04 Be
2	0	0.020 0.040	1.64	.008
3	0	0.040→.075	1.64	.008
4	0	0.075→.10	1.64 → 1.80	.008 →.015
5	0	0.070	0	0.098
6	0.56	0.020	1.75 → 1.64	.019→.008
7	0.56	0.020	1.64	0.0103 → .008
8	0	0.15	0	.15 Be

The lower external pressure for the 1971 mission is not completely reflected in the structural shell thickness and associated weight because of minimum gage restriction in the outer portion of the shell. The stainless steel concept is significantly heavier than the beryllium shell as was expected.

The relative weights of the structural shell were compared in Table XXXIII. These weights include only the face sheet, core, and a beryllium reinforcing ring, bond, and bearing pad, with no allowance for fittings, etc.

5.3.1.3 Dynamic Analysis

The method of vibration analysis is described in paragraph 7.2. Vibration analyses were made for the blunt cone configuration using the analytical model shown in Figure 217.

The structure is defined by 24 nodal points. Since four coordinates exist at each node, the mass and stiffness matrices are 96 x 96 in size. This model was chosen to obtain reasonable estimates on the shell frequencies and is not identical to the configuration given in Figure 210.

The payload was considered attached directly to the payload mounting structure. This structure was assumed to be a cylindrical shell with no additional stiffening in the region of the shell and payload attachment point.

For the axisymmetric case, modal deflection data describes motion at any point along the circumference, i.e., $0° \geq \theta \geq 360$ degrees, where θ is the circumferential angle. To describe motion which varies with circumferential position, deflections are defined in a Fourier series, and variation with θ is given as a sin $n\theta$ or cos $n\theta$ function, n being a positive integer corresponding to the harmonic number.

Results are plotted in Figure 218 for the asymmetric case $n = 1$ (first harmonic). This case is somewhat analogous to beam bending vibrations.

Note that at a frequency of 301 cps, motion is due mainly to bending of the payload structure.

No structural response computations have been conducted at present. However, the predicted high frequency shell vibrations indicate that the shell will not be excessively excited by the external loading conditions. Reentry forces, for example, are expected to have an exciting frequency of less than 5 cps, Figure 219, which is far removed from the shell natural frequencies.

Several factors will definitely affect the range of natural frequencies. The presence of a ring structure at the maximum diameter of the shell will tend to increase the frequencies. Changes in the shell thickness, resulting in both mass and stiffness variations, will influence results.

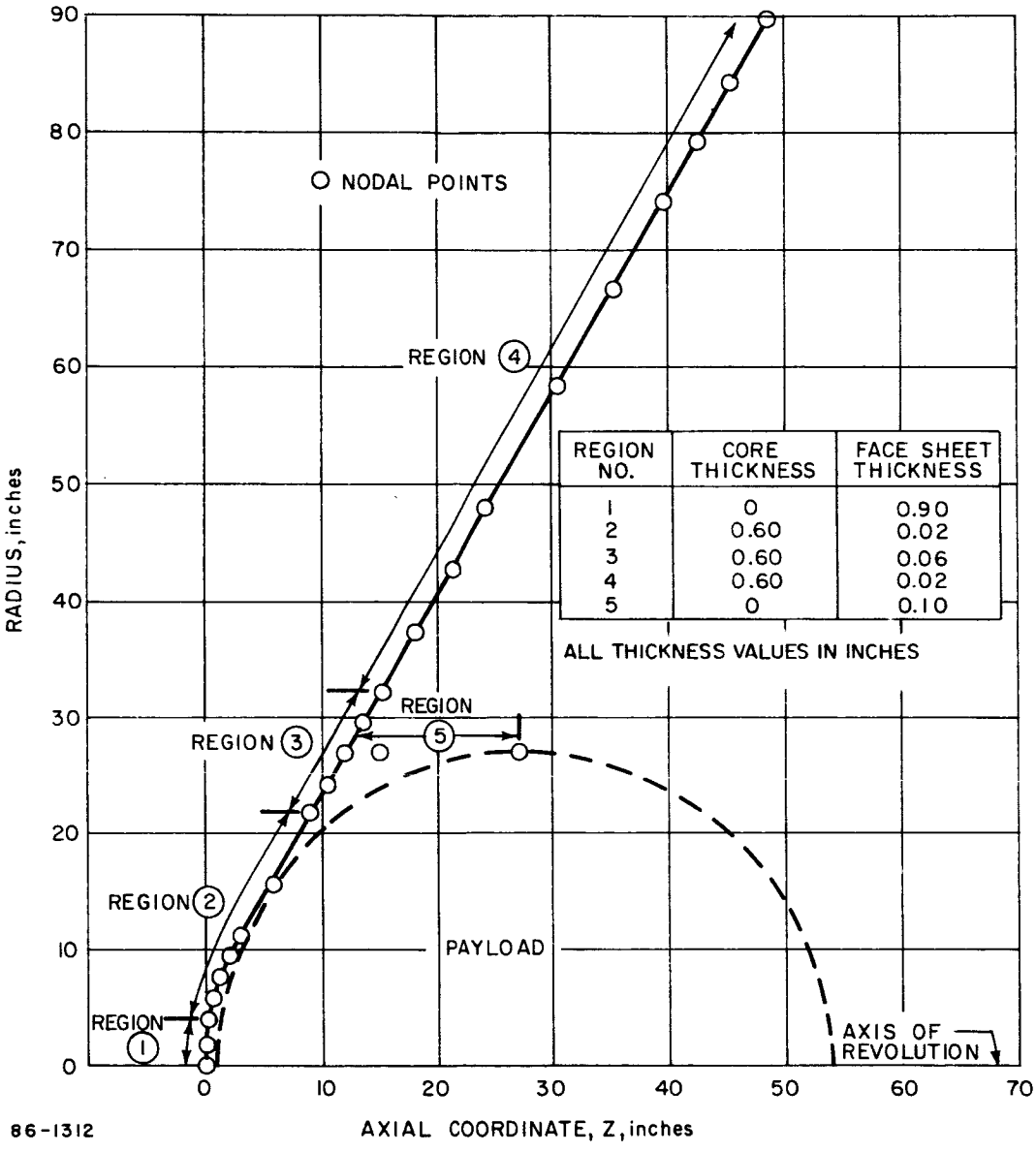

Figure 217 MULTI-MISSION-DYNAMIC ANALYTICAL MODEL BLUNT CONE WITH 1971 PAYLOAD

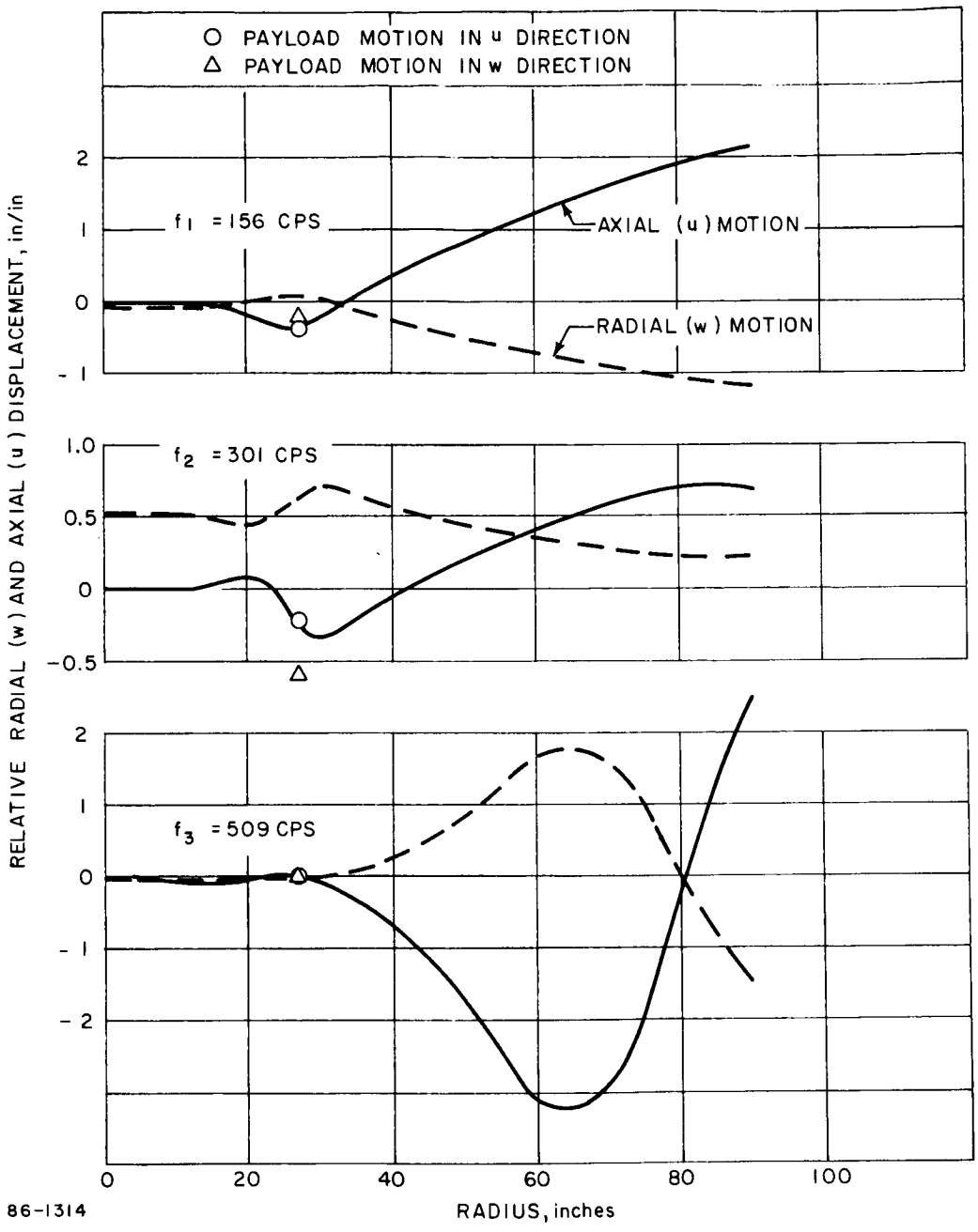

Figure 218 BLUNT CONE--MULTI-MISSION SHELL MODAL DISPLACEMENT -- ASYMMETRIC CASE (N = 1) 1971 PAYLOAD

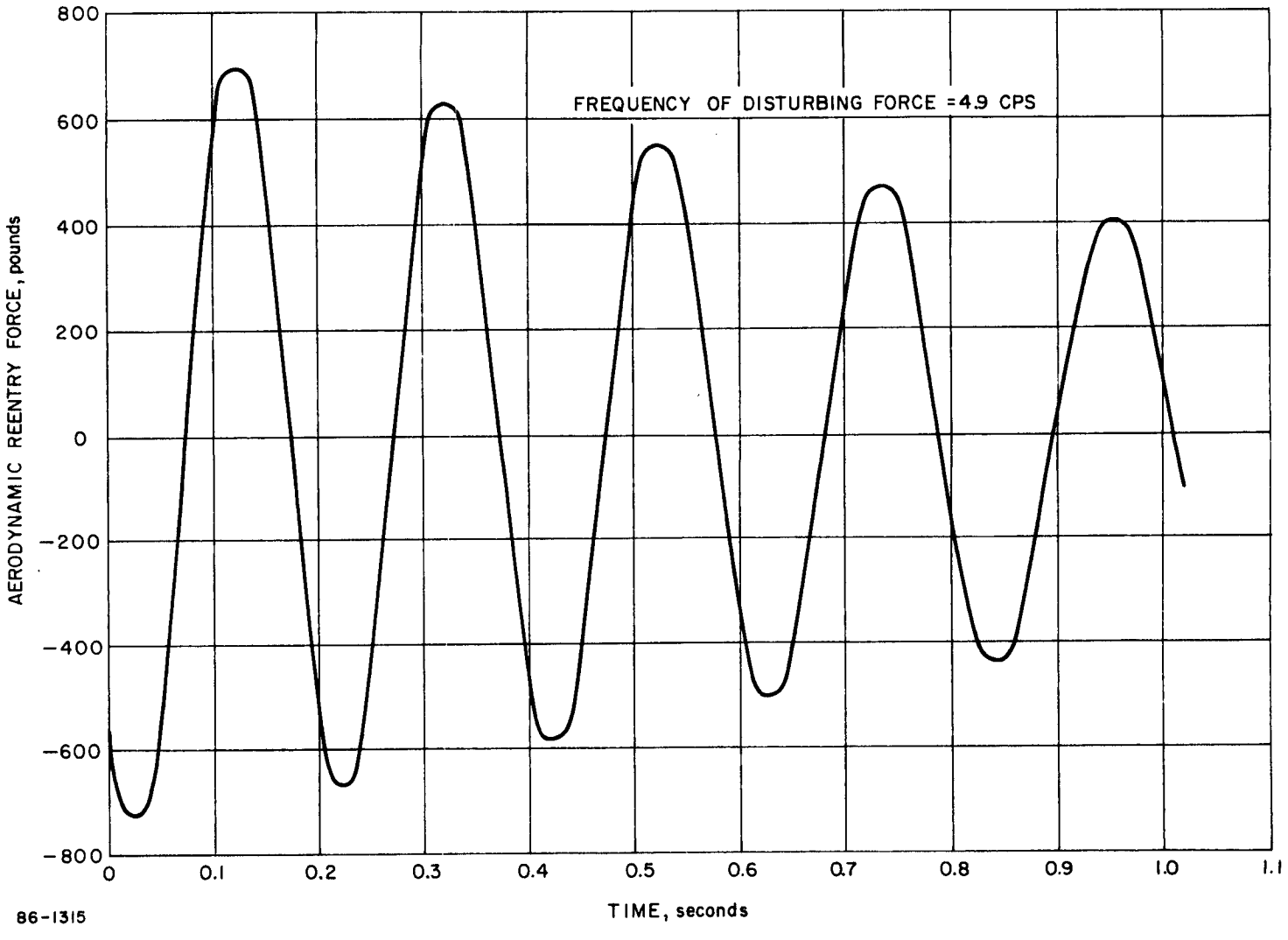

Figure 219 NORMAL AERODYNAMIC FORCE VARIATIONS WITH TIME FAILURE MODE -- ZERO SPIN FAILURE MODE, ZERO SPIN CASE

An important influence is the payload and its mounting structure. A detailed model of the payload, with explicit mass and stiffness distributions, must be formulated. Also, a good definition of the stiffness properties for the payload support structure must be obtained, especially where the structure attaches to the shell and to the payload. The 1971 payload mass of the multimission concept was used in the analysis; hence the larger future payload mass of the multimission concept can be expected to reduce the frequencies associated with payload motion by a factor as much as 2.5.

5.3.1.4 Support Structure

A continuing effort was made to monitor the design of the support structure and aid in selection of structural material, load paths, and concepts. The analysis was made only for the 1971 mission and the results of numerous design analyses are reflected in the design layouts.

The support structure was considered to consist of the ΔV rocket-thrust structure, afterbody, payload bearing structure, launch structure, and parachute load structure. A parametric analysis was made of the 65-degree conical afterbody considering magnesium, fiberglass, and beryllium. The fiberglass and magnesium structures were assumed to have a temperature of 300°F and the beryllium to be at 1000°F. The loading corresponded to 225-g axial and was independent of diameter. Figure 220 gives the structural weight and thickness. The beryllium structure is lightest, even though it is restricted to minimum gage.

Magnesium is lighter and more efficient than fiberglass. For this application, stainless steel and aluminum would be even heavier because of the monocoque construction.

The conical afterbody thickness determined in the parametric analysis at a capsule diameter of 180 inches was scaled to the design loads of 209 g. The resulting thickness was 0.056 inch for fiberglass and 0.02 inch for beryllium. The use of beryllium results in a lighter structure because of its much higher stiffness/density ratio.

The payload is supported within the crushup structure and was analyzed for the maximum axial condition (209.1 g limit) for entry. The total payload package which consists of the payload and the crushup structure is supported on the pad that rests on the heat shield substructure. This also was checked for the maximum axial load condition of entry. The straps over the aft end of the total payload package were analyzed for the effects of launch loads and the possible effects of the side component of the maximum normal entry loads. (18.9 g limit).

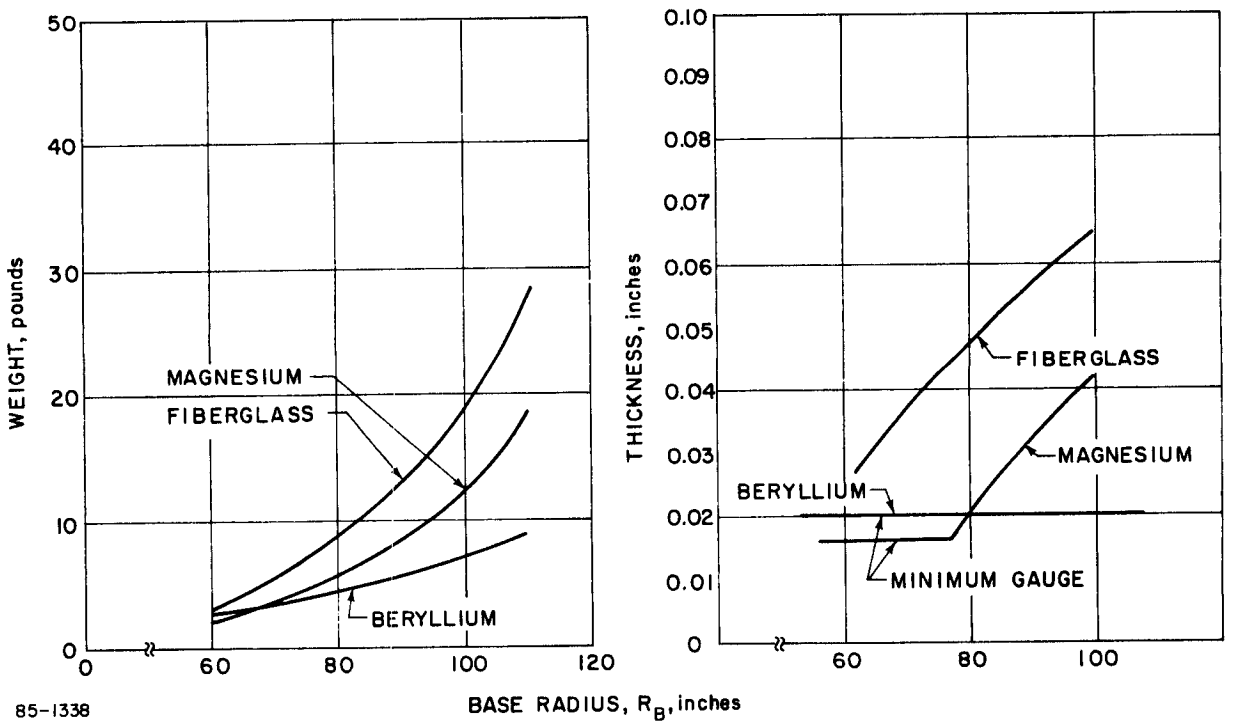

Figure 220 PARAMETRIC ANALYSIS -- AFTERBODY 65-DEGREE CONE

The parachute loads for the main chute reefed condition are applied at the bridle and go into the parachute fittings and support structure. The payload is supported by the heat shield substructure.

The parachute loads for the main parachute full-open condition enter the same paths as described above except that the parachute fittings support a series of straps which cradle the forward side of the total payload package after the heat shield and substructure have been jettisoned.

5.3.2 Modified Apollo

5.3.2.1 Parametric Analysis

1. Design Conditions -- The dynamic pressure as a function of base diameter was assumed to be the same as the blunt cone and is given in Figure 206; pressure was assumed to be distributed uniformly over the spherical surface. The structural temperature was assumed to be the same as the blunt cone shape-300°F.

2. Structural Weights and Thicknesses -- The structural weights and thicknesses are given in Figures 221 and 222. Beryllium, stainless steel, and aluminum were considered for the modified Apollo shape and beryllium is again the lightest structural material.

5.3.2.2 Static Analysis

1. Design Conditions -- The same general comments on design conditions, stated for the blunt cone in paragraph 5.3.1.2 apply to the modified Apollo. The details of the loadings are given in Table XXXVI.

TABLE XXXVI

APOLLO LOADING CONDITIONS

	Multi-Mission	1971 Mission	Future Mission
Entry weight, lb	4500	1450	1450
Axial g's, a_x	88.7	211.	211.
Normal g's, a_n (at max a_x)	1.5	8.5	8.5
Angle of attack, α	10.6°	21.8°	21.8
Stagnation pressure, Ps, lb/in^2	18.5	14.2	14.2

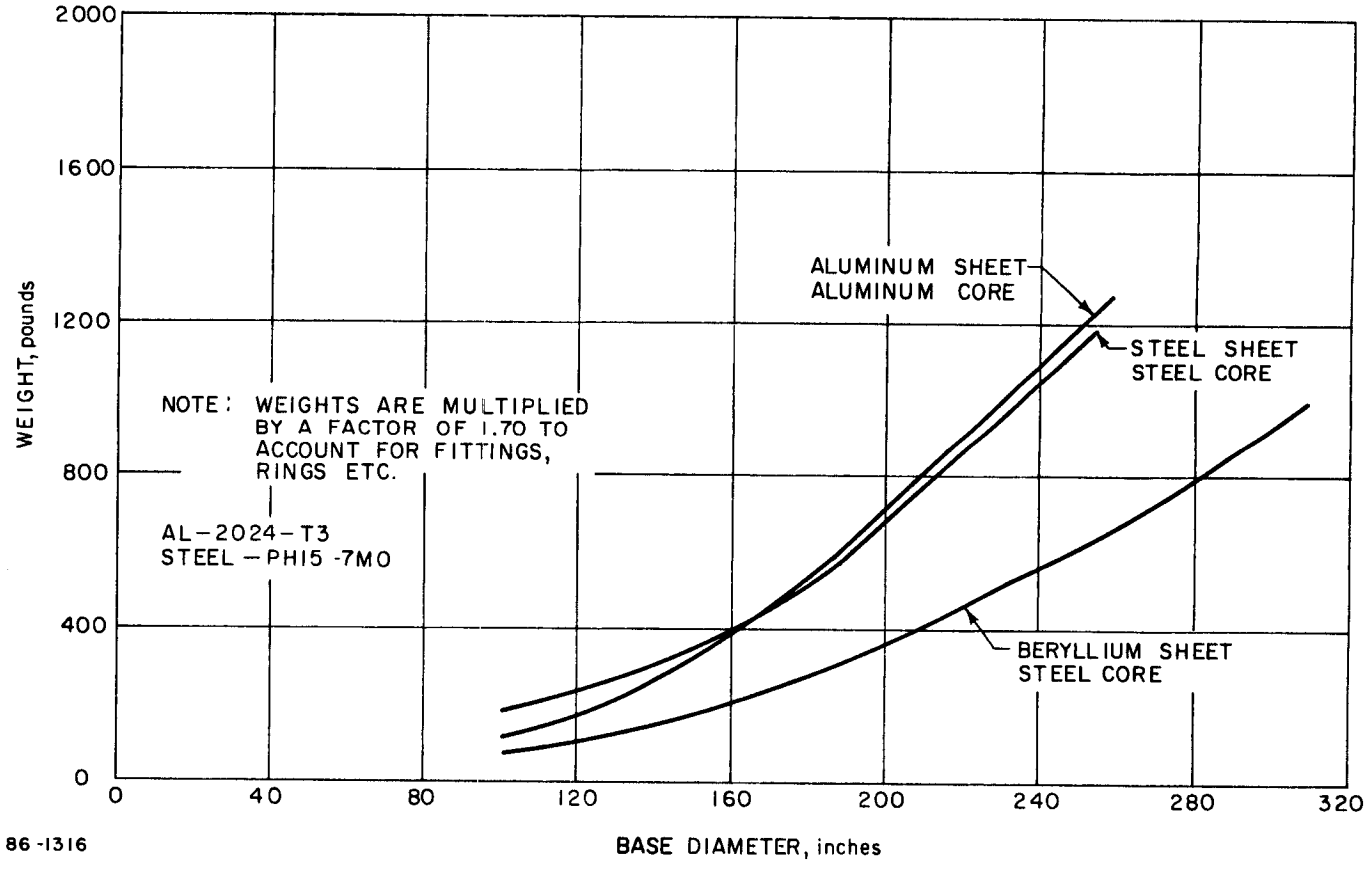

Figure 221 PARAMETERIC WEIGHTS--MODIFIED APOLLO SHELL

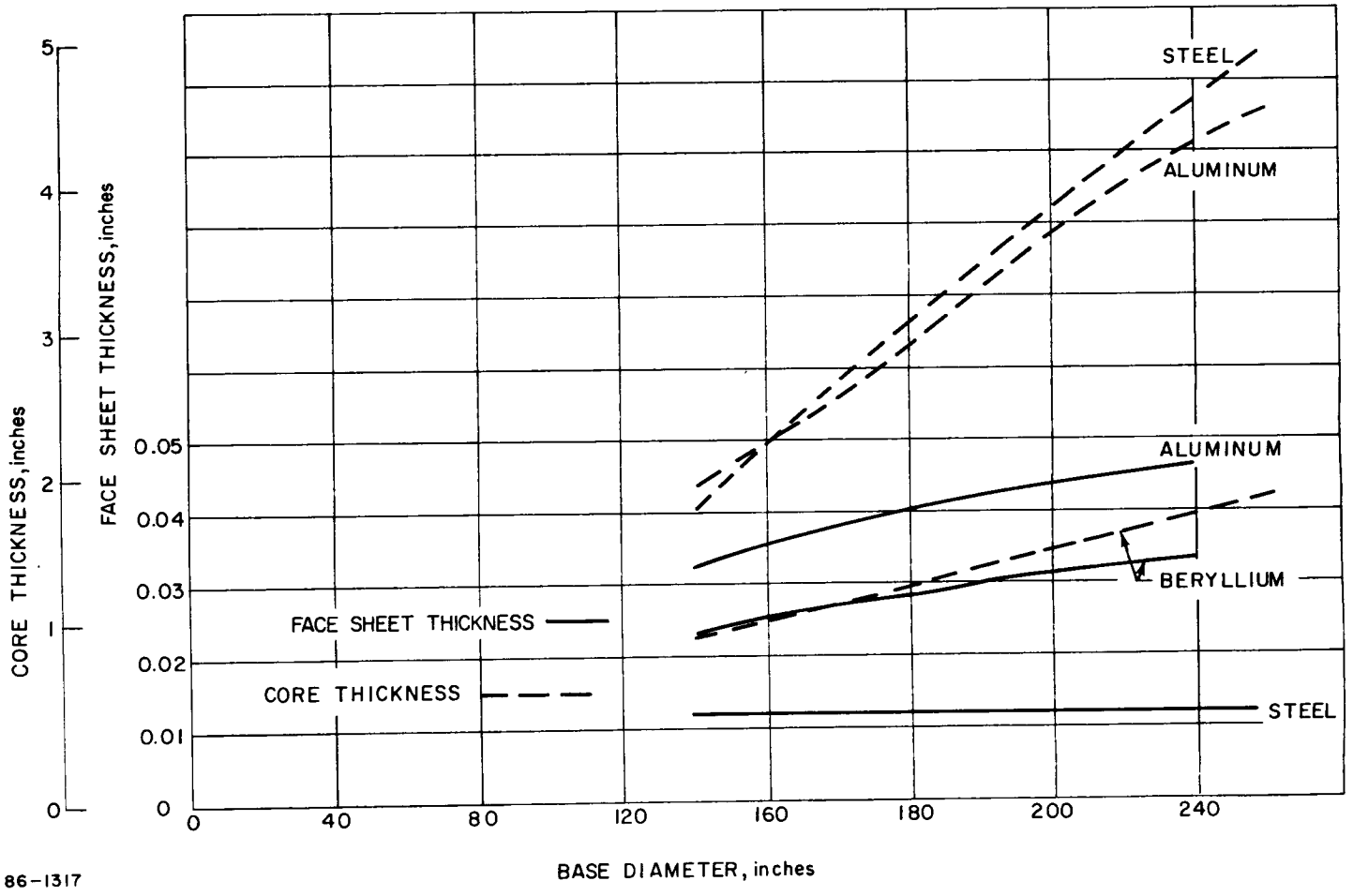

Figure 222 PARAMETRIC STRUCTURAL THICKNESS MODIFIED APOLLO SHELL

A schematic of the primary shell of the modified Apollo is given in Figure 223. The regions adjacent to the payload inertial force were designed to resist the bending moments and shear forces developed there while the outer region of the shell was optimized for face sheet yielding and buckling. It was believed that tapering the core depth was more feasible than the face sheet; hence, the stresses in the face sheet decrease towards the outer edge since the external aerodynamic pressure decreases. The buckling analysis conservatively assumed that the stagnation pressure was applied uniformly over the surface of the shell. The shell bending analysis considered the actual pressure distribution, Figure 224, as well as the equivalent inertial pressure of the shell wall.

2. Structural Analysis Results -- The symmetrical stress distribution and displacements are given in Figures 225 and 226 for the multimission critical loads and figures 227 and 228 for the 1971 mission critical loads with the distributed payload inertia. The design is adequate for both conditions.

The results of the asymmetrical loading case for the blunt cone indicate that similar loading on the modified Apollo will produce similar and probably increased effects due to the reduced bending stiffness of the shallower shell.

The core density requirement for face-sheet wrinkling and dimpling was calculated to be less than 2 lb/ft^3, again indicating that 6 lb/ft^3 is conservative.

5.3.2.3 Dynamic Analysis

The same philosophy for model formulation was used for this configuration as in the blunt-cone vibration analysis. Figure 229 shows the analytical representation of the modified Apollo shape.

Results are given for the axisymmetric (n = 0) case in Figure 230. It is seen that the shell has motion at all radii. This is due mainly to the location of the payload structure attachment point, which is located almost halfway out on the shell surface.

Asymmetric results for n = 1 (first harmonic) are presented in Figure 231. As in the blunt cone configuration, the mode representing bending of the payload support is evident.

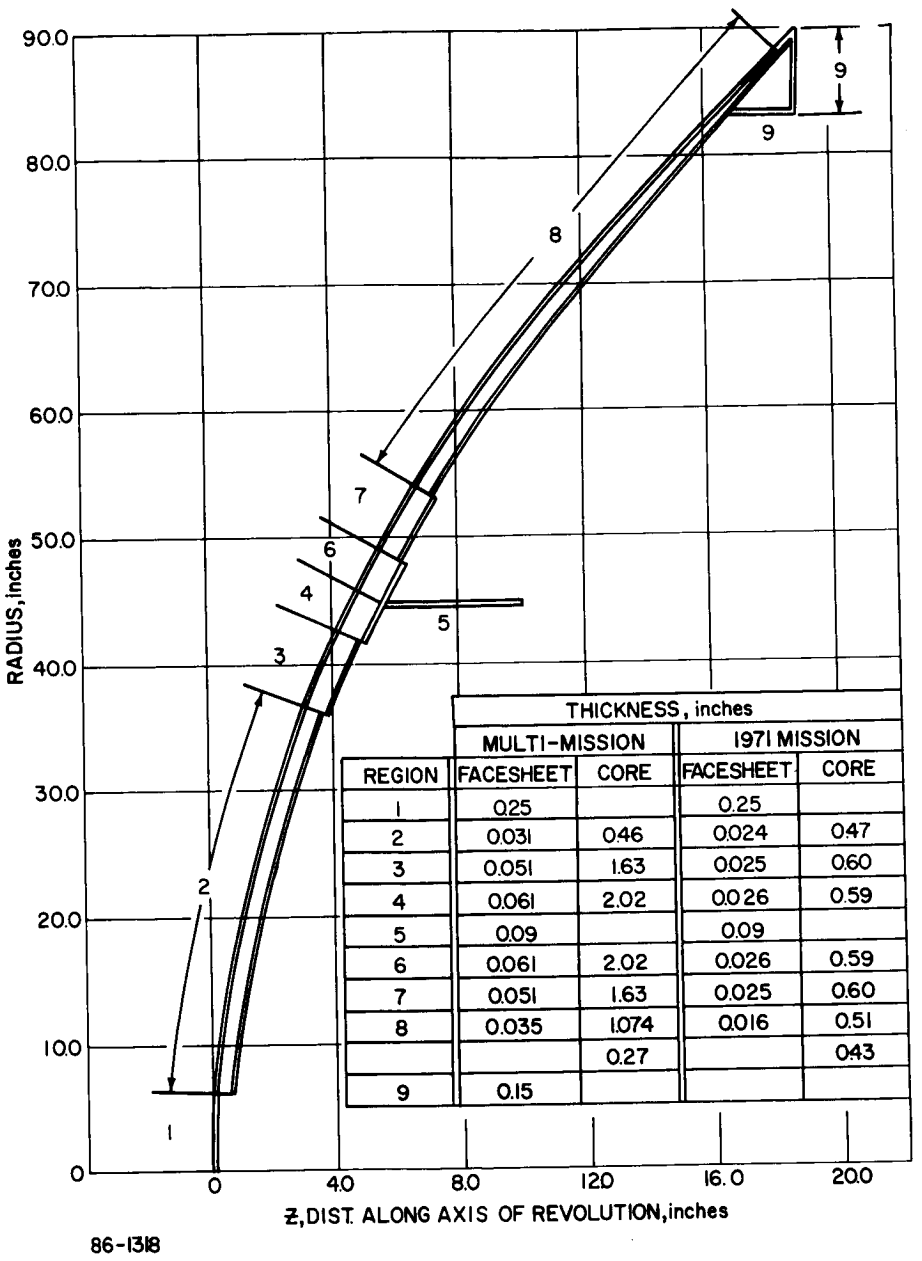

REGION	THICKNESS, inches			
	MULTI-MISSION		1971 MISSION	
	FACESHEET	CORE	FACESHEET	CORE
1	0.25		0.25	
2	0.031	0.46	0.024	0.47
3	0.051	1.63	0.025	0.60
4	0.061	2.02	0.026	0.59
5	0.09		0.09	
6	0.061	2.02	0.026	0.59
7	0.051	1.63	0.025	0.60
8	0.035	1.074	0.016	0.51
		0.27		0.43
9	0.15			

Figure 223 MODIFIED APOLLO ANALYTICAL MODEL

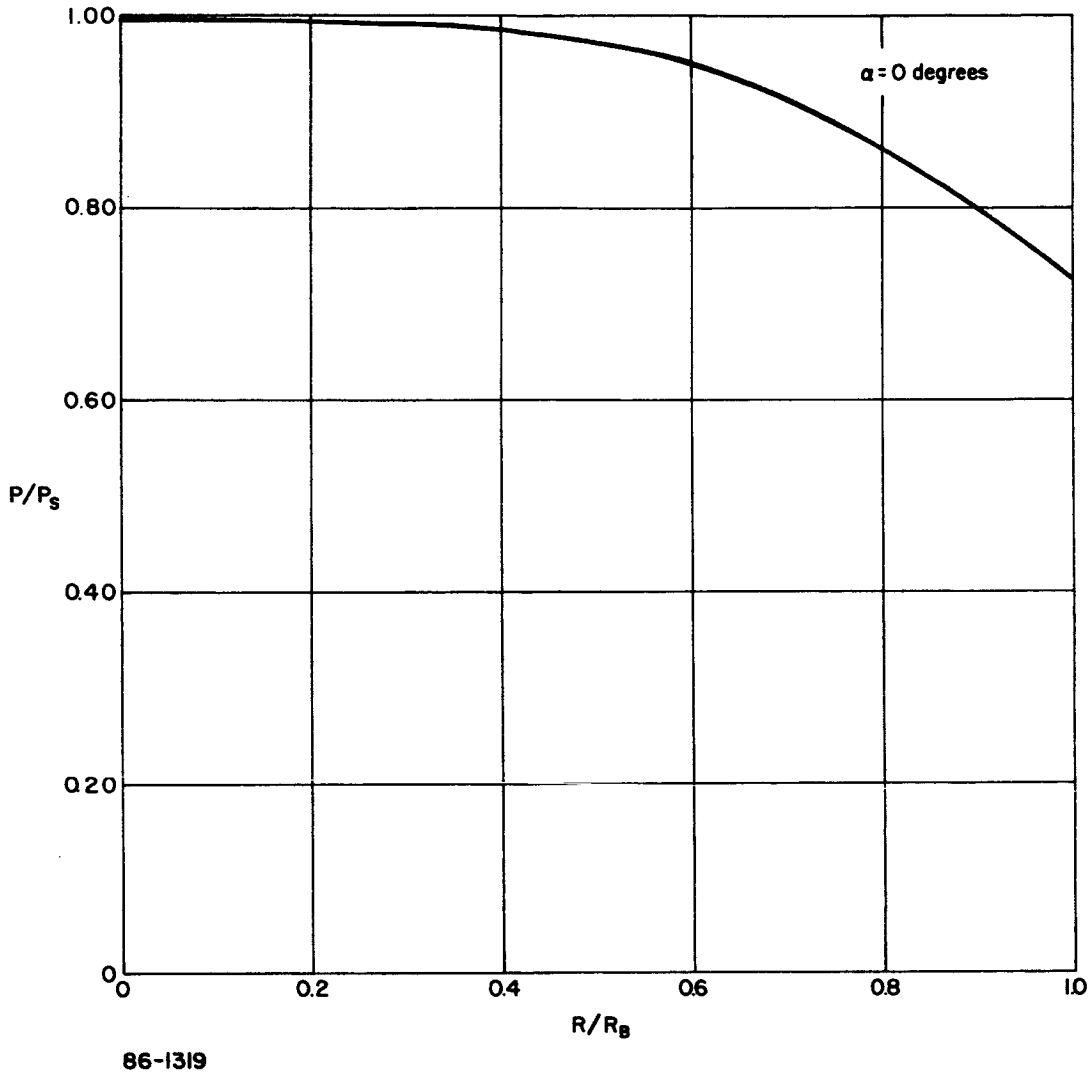

Figure 224 PRESSURE DISTRIBUTION FOR MODIFIED APOLLO

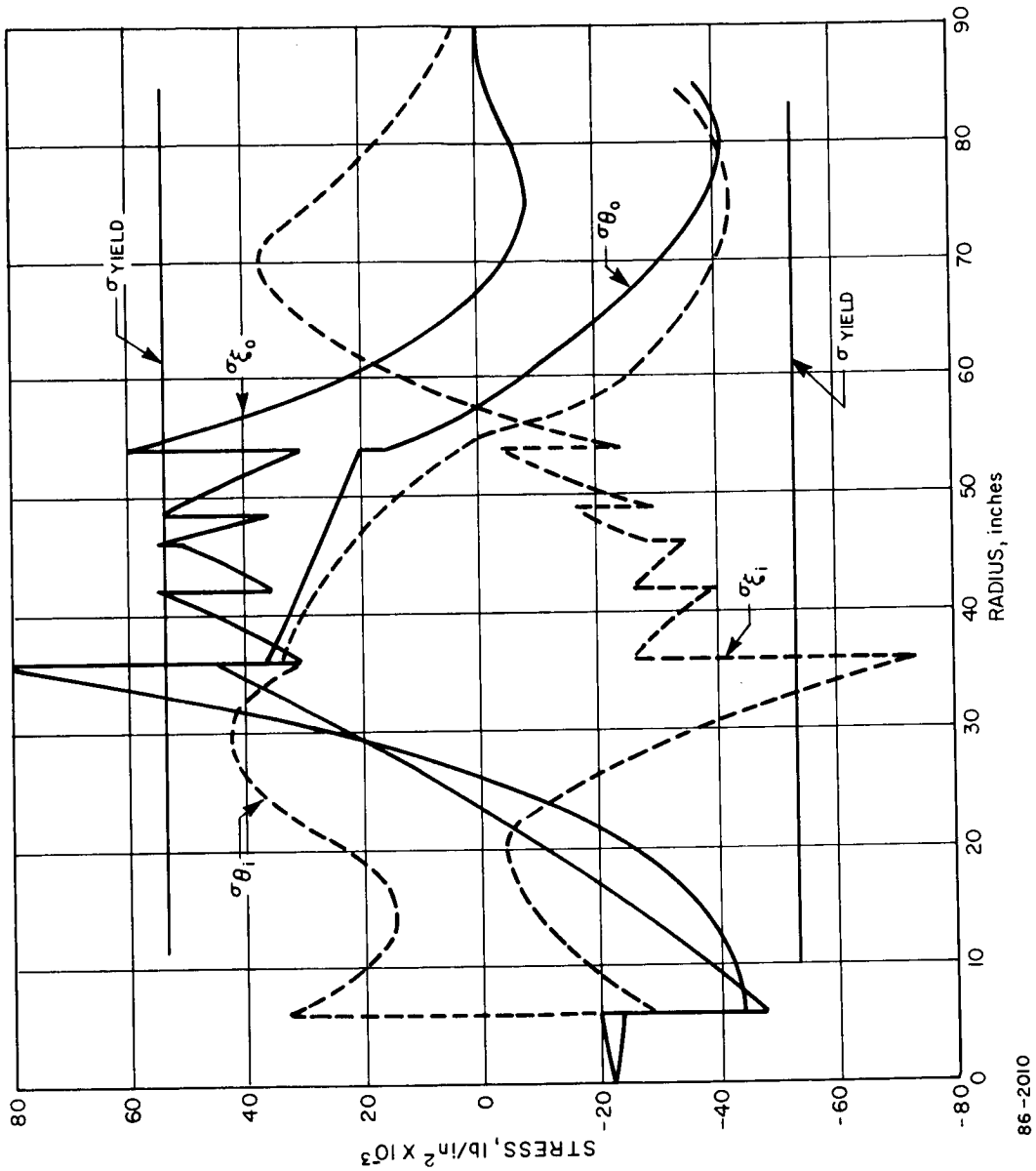

Figure 225 MERIDIONAL (ξ) AND CIRCUMFERENTIAL (θ) STRESSES FOR MULTI-MISSION STRUCTURE MODIFIED APOLLO WITH MULTI-MISSION LOADS

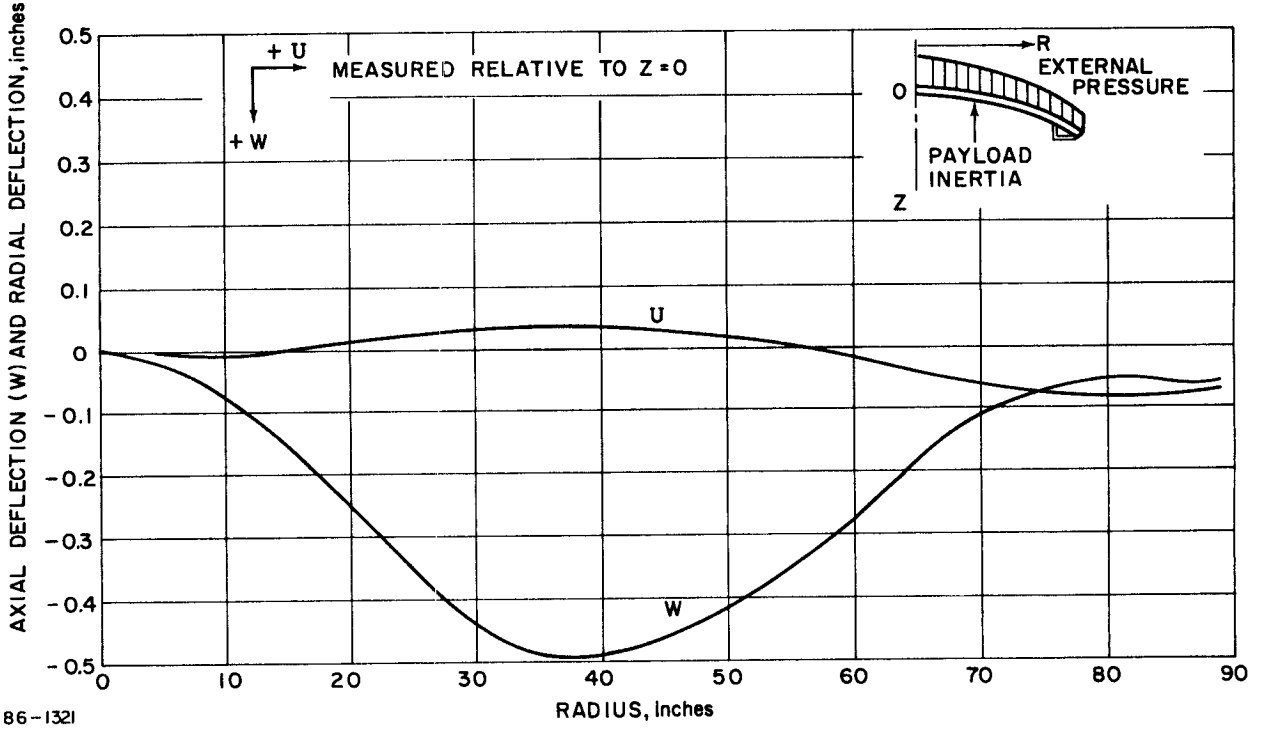

Figure 226 AXIAL AND RADIAL DEFLECTION VERSUS RADIUS FOR MULTI-MISSION STRUCTURE MODIFIED APOLLO WITH MULTI-MISSION LOADS

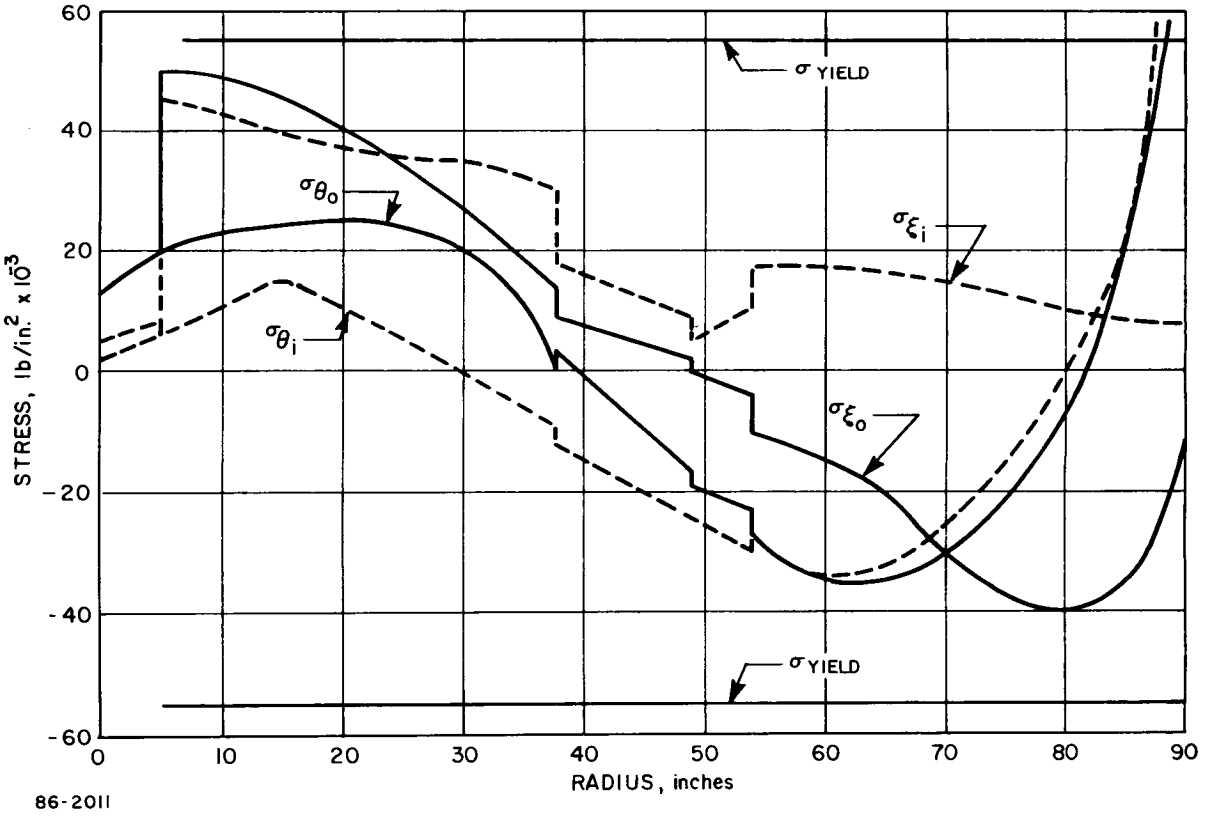

Figure 227 MERIDIONAL AND CIRCUMFERENTIAL STRESSES FOR MULTI-MISSION STRUCTURE MODIFIED APOLLO WITH 1971 LOADS

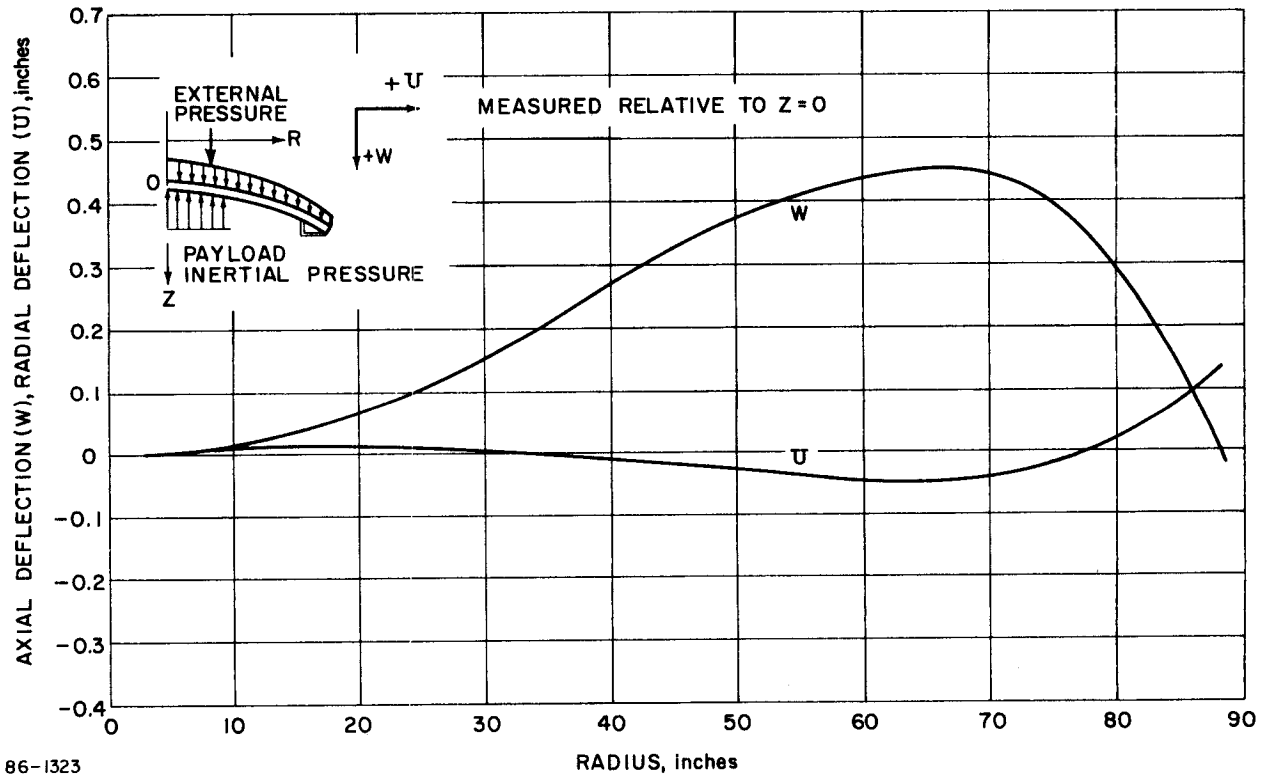

Figure 228 AXIAL AND RADIAL DEFLECTION VERSUS RADIUS FOR MULTI-MISSION STRUCTURE MODIFIED APOLLO WITH 1971 LOADS

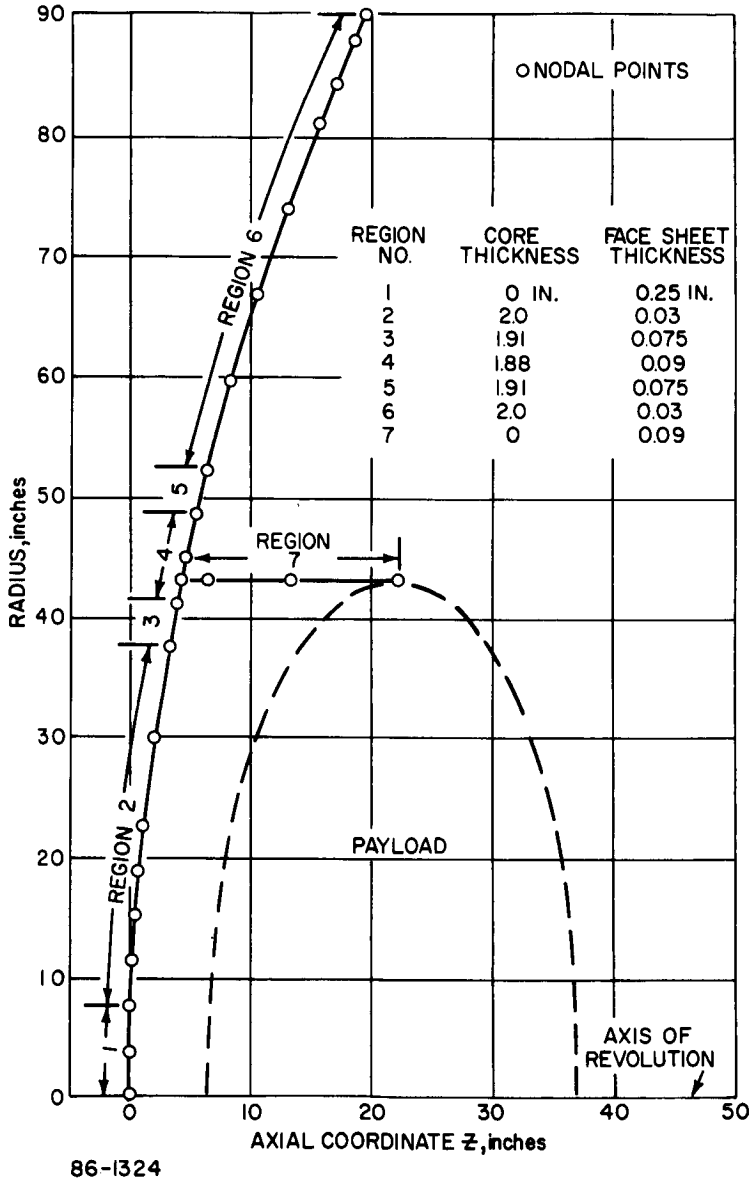

Figure 229 DYNAMIC ANALYTICAL MODEL -- MODIFIED APOLLO

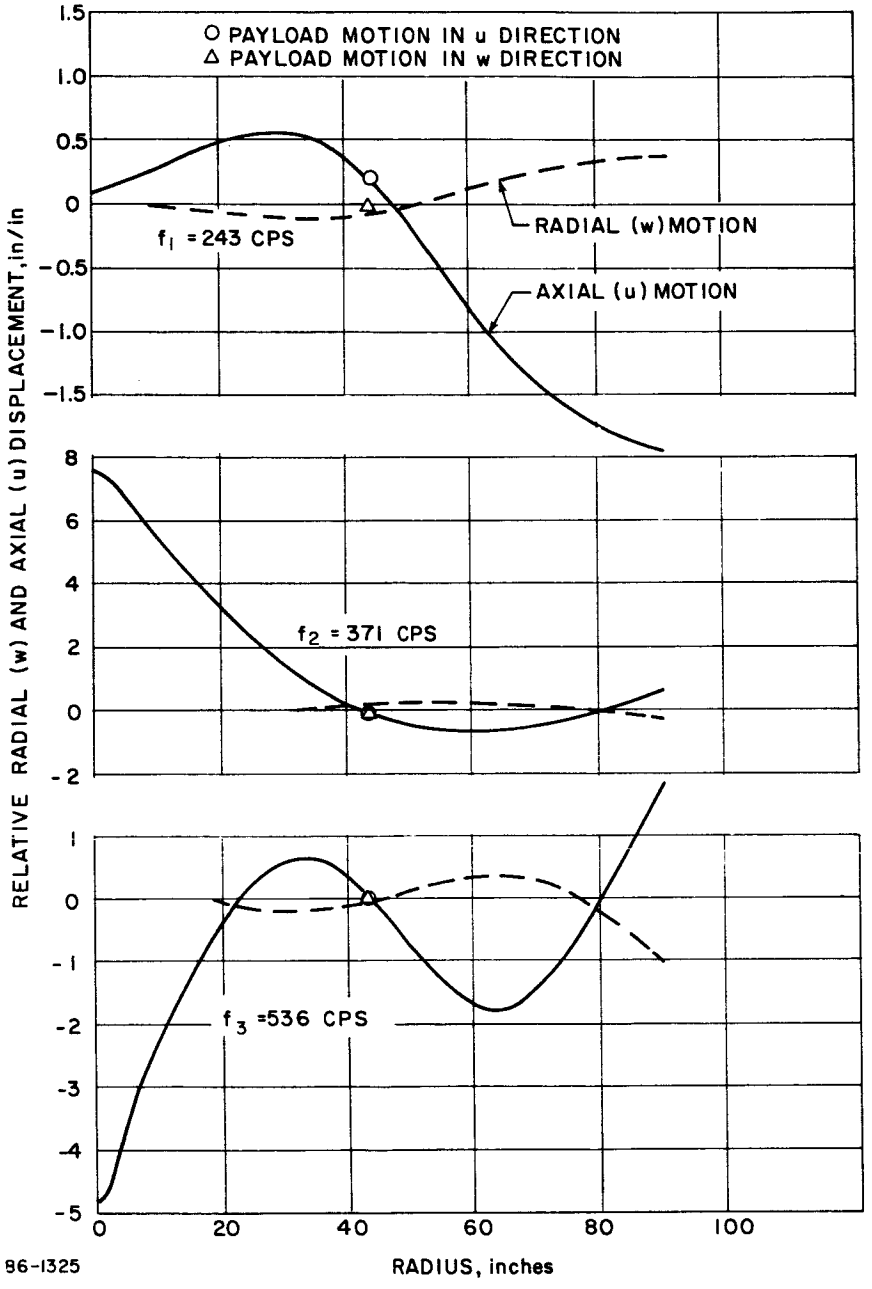

Figure 230 MODAL DISPLACEMENT -- AXISYMMETRIC CASE (N = 0)
MODIFIED APOLLO

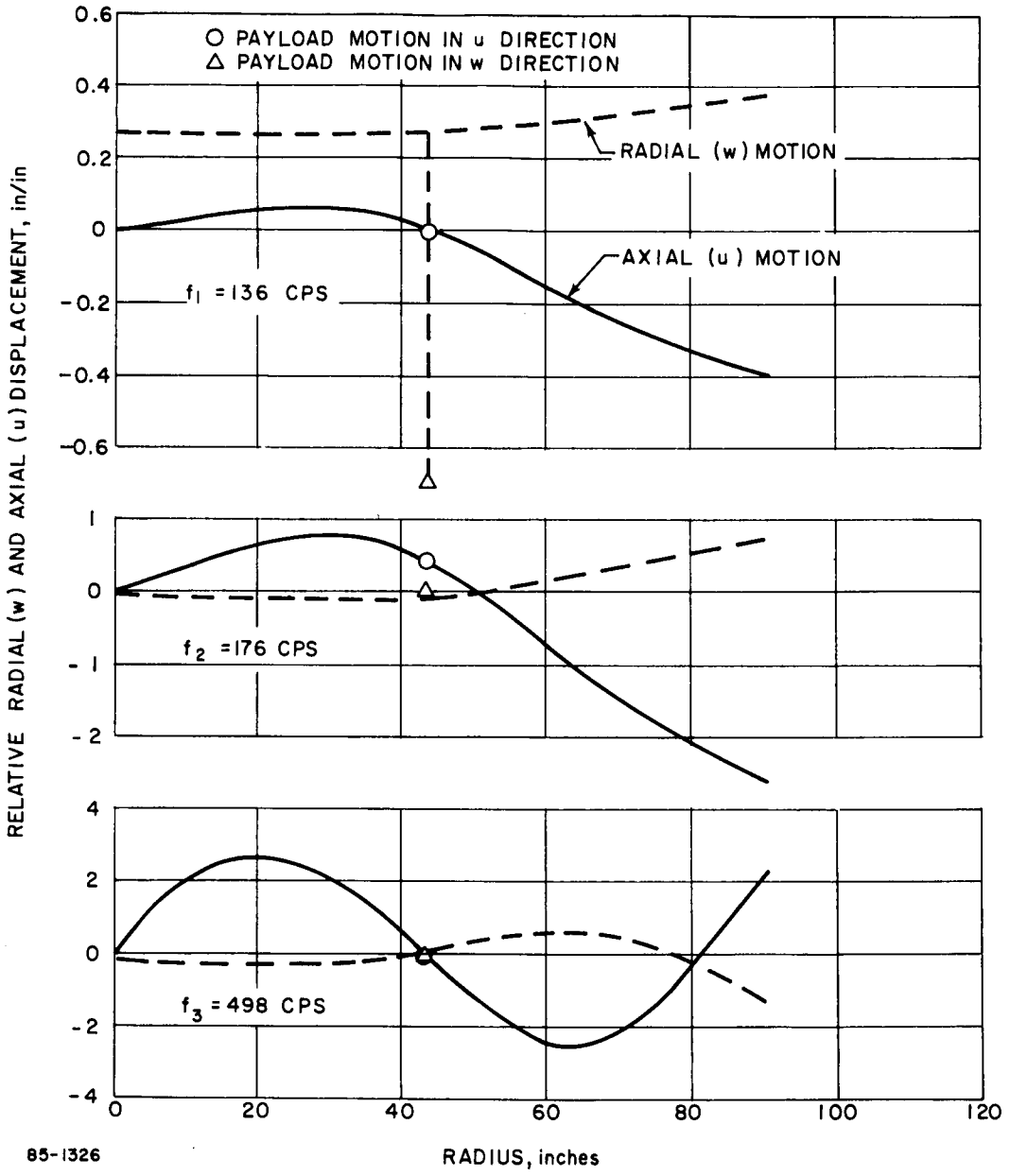

Figure 231 MODAL DISPLACEMENT--ASYMMETRICAL CASE (N= 1) MODIFIED APOLLO

5.3.2.4 Support Structure

The support structure for the modified Apollo is the same as presented in paragraph 5.3.1.4.

5.3.3 Tension Shell

5.3.3.1 Parametric Analysis

1. Design Conditions -- The stagnation pressure and structural temperature was assumed to be the same as for the blunt cone and modified Apollo. A Newtonian pressure distribution was considered to be applied to the tension shell surface.

2. Structural Weights and Thicknesses -- The structural weights and thicknesses are given in Figures 232 and 233. Fiberglass was used for the shell material and beryllium for the compression ring. The shell weights were multiplied by a factor of 1.2 to account for rings and fittings. This factor was lower than for the blunt cone and modified Apollo because bending stresses were not expected to predominate.

5.3.3.2 Static Analysis

1. Design Conditions -- The pressure distributions used for the symmetrical and unsymmetrical analyses are given in Figures 234, 235, and 236. The distributions were developed using analyses described in paragraph 4.2.1.2.

The loading conditions for the multimission and 1971 concepts are given in Table XXXVII. The distribution corresponding to the maximum normal acceleration for the future mission payload was used since it resulted in higher corresponding axial forces than for the 1971 payload maximum normal load distribution.

TABLE XXXVII

TENSION SHELL LOADING CONDITIONS

	Multimission	1971 Mission
Entry weight, pounds	4500	1435
Max axial g, a_x	87	224
Max normal g, a_n	10.3	41.6
Stagnation pressure at $a_x$max, psf	2650	2140
Stagnation pressure at $a_n$max, psf	2050	2140
Angle of attack at $a_n$max	23.9°	31.2°

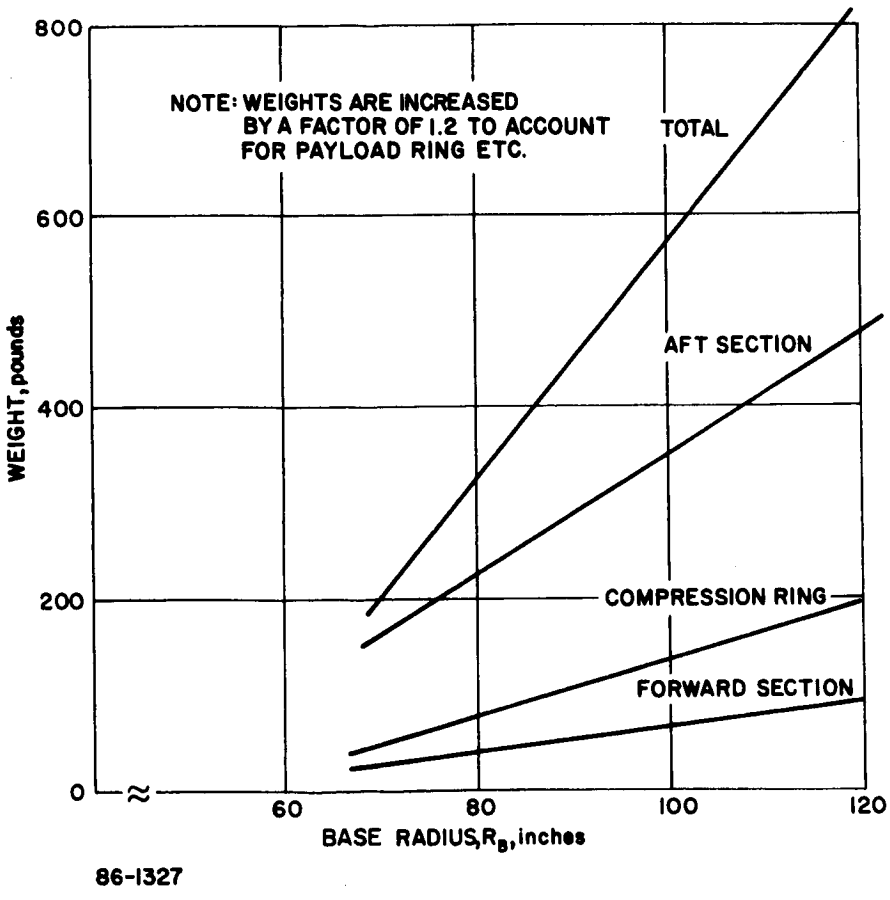

Figure 232 PARAMETRIC TENSION SHAPE--WEIGHT VERSUS RADIUS

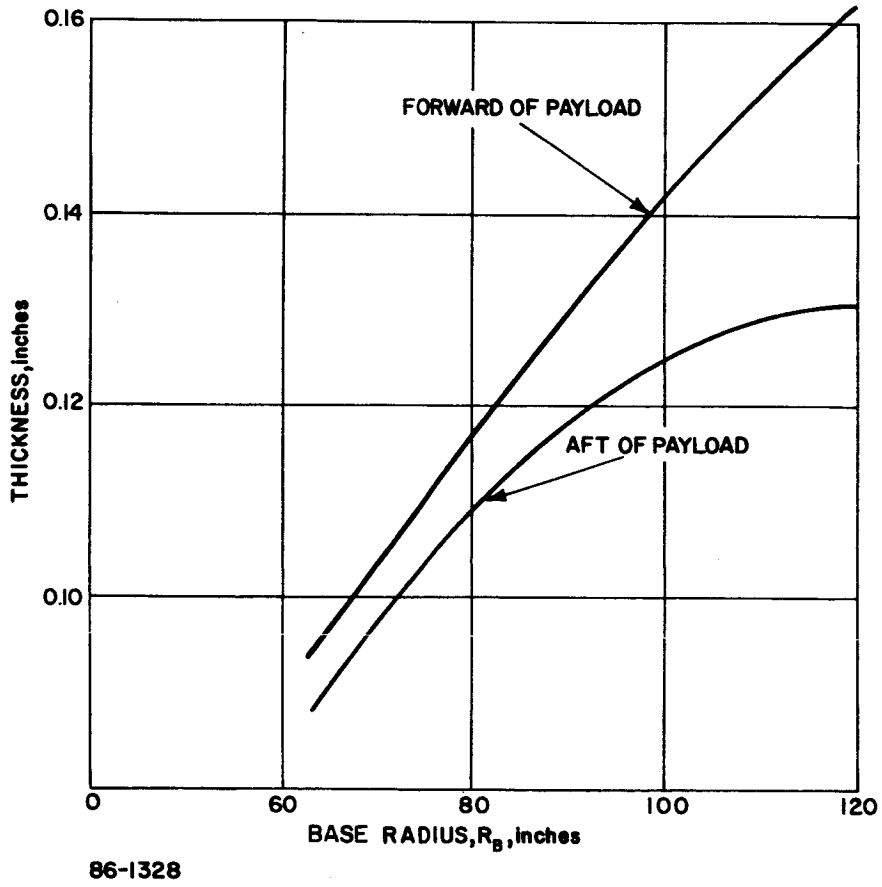

Figure 233 PARAMETRIC TENSION SHAPE--STRUCTURAL SHELL THICKNESS

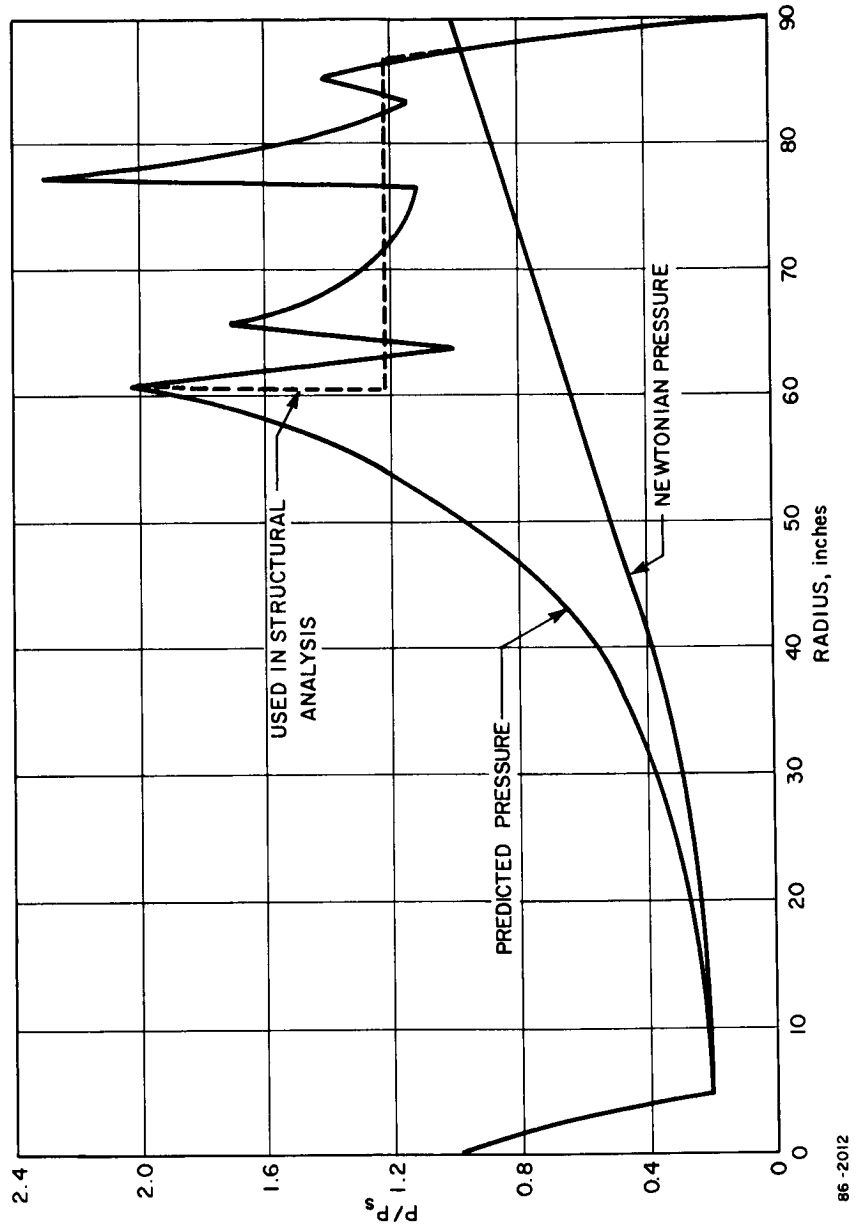

Figure 234 TENSION SHELL PRESSURE DISTRIBUTION

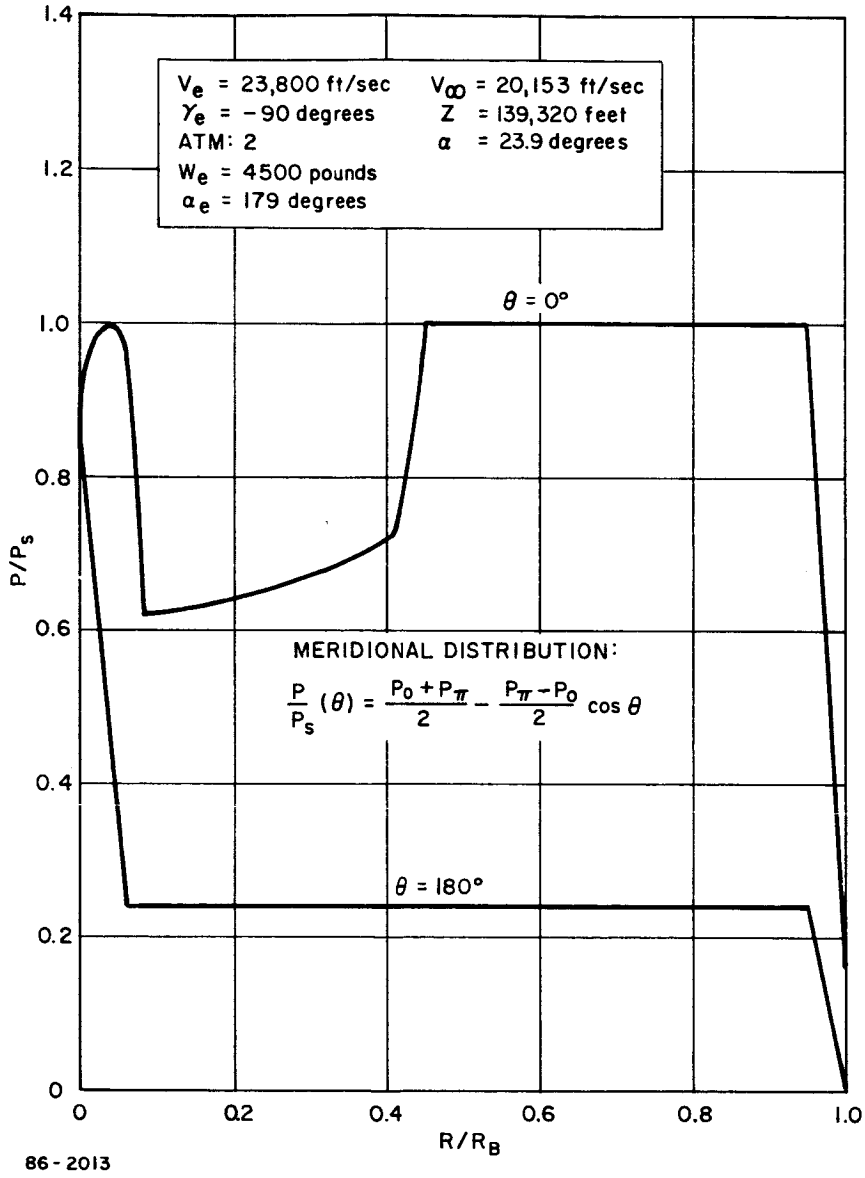

Figure 235 TENSION SHELL PRESSURE DISTRIBUTION

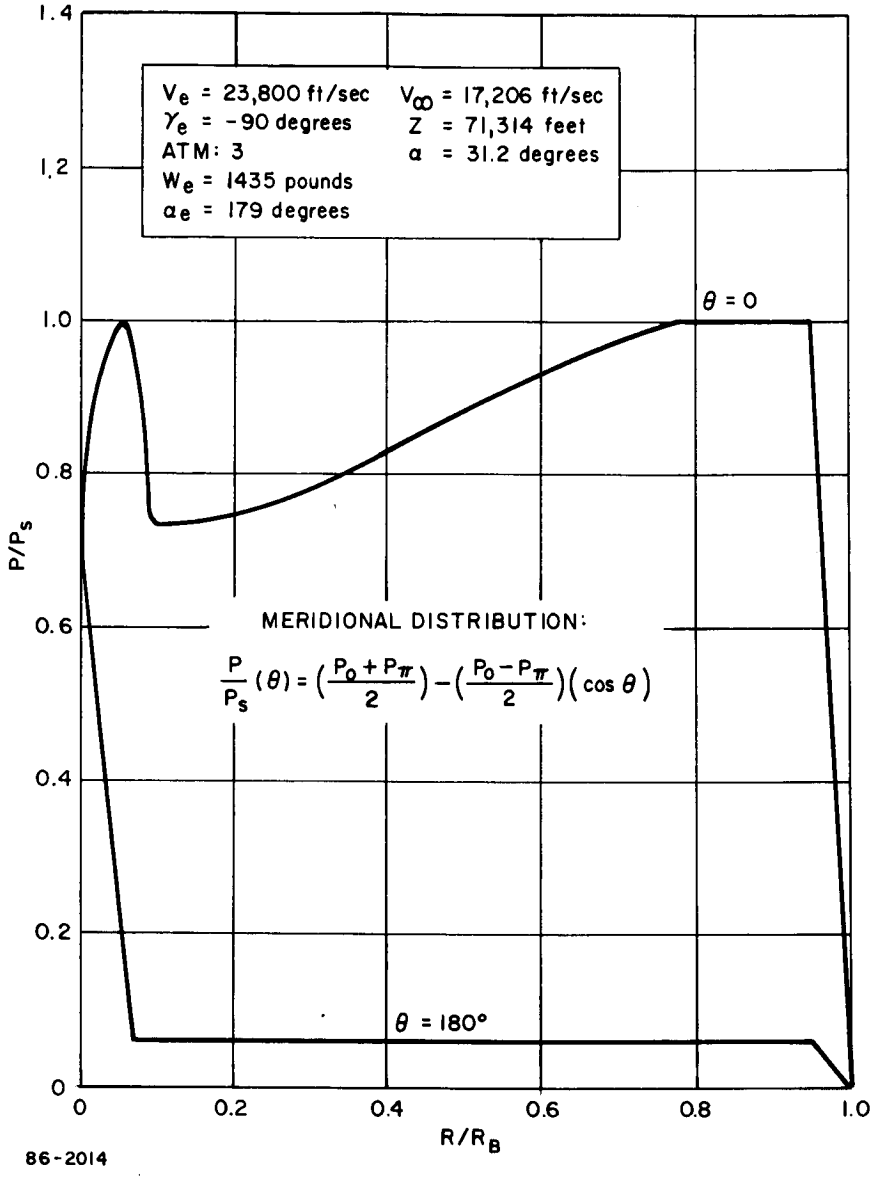

Figure 236 TENSION SHELL PRESSURE DISTRIBUTION

2. Structural Analysis Results -- The analysis and design presented here include two design concepts for the compression ring. These concepts are identified as the shallow-ring concept and the deep-ring concept and are described in Figure 237. Since early concepts of the tension shell used a compression ring of circular cross section, an attempt was made to obtain an efficient design using this configuration. When used with the reference aerodynamic contour, the circular cross section compressive ring proved to be impractical.

The basic difference between the rings is the depths of the rings measured normal to the aerodynamic surface. The deep ring has a greater depth than the shallow ring, hence greater moments of inertia, and therefore greater efficiency with respect to general instability of the ring. The deep ring requires more honeycomb to stabilize the fiberglass sheets which transmit the shell interaction forces to the ring. Accordingly, the shallow ring required more beryllium but less honeycomb.

The circular ring was studied to determine whether it could be incorporated into the design, since potentially it could be more efficient than either the shallow or deep ring concepts.

The result of the feasibility study is shown in Figure 238. Manufacturing techniques appear to limit the the maximum diameter of the cross section of the ring to 7.0 inches. Since the radius of the aerodynamic contour is greater than 3.5 inches, either a fairing is required to maintain the contour or the radius of the aerodynamic contour at the outer edge has to be changed to 3.5 inches. Figure 238 illustrates the concept of changed contour. Note that a flat section can replace the inner portion of the ring since it is at least as efficient as the curved section.

Since a change in aerodynamic contour is not likely to be acceptable, a fairing is required as shown in Figure 238. The most efficient material to use for this fairing is beryllium. It becomes immediately apparent that the outer portion of the circular tube can be removed and replaced by the fairing which has no less than the moments of inertia of the tube section. The inner portion of the tube also can be removed and replaced by an efficient flat section. The resulting concept is then very similar to the other two concepts, particularly the deep ring.

The stress distribution for the symmetrical loading is given in Figure 239. The stress level is not shown in the compression ring since the detail stresses will not be accurate in the ring even though the stress couples, stress resultants, and displacements are accurate. The shallow ring was used in this symmetrical shell analysis with an integrated stress resultant of 60,000 pounds developed in the ring. The difference in stress distribution developed in the shell between using either the shallow ring or the deep ring was negligible. Note the large

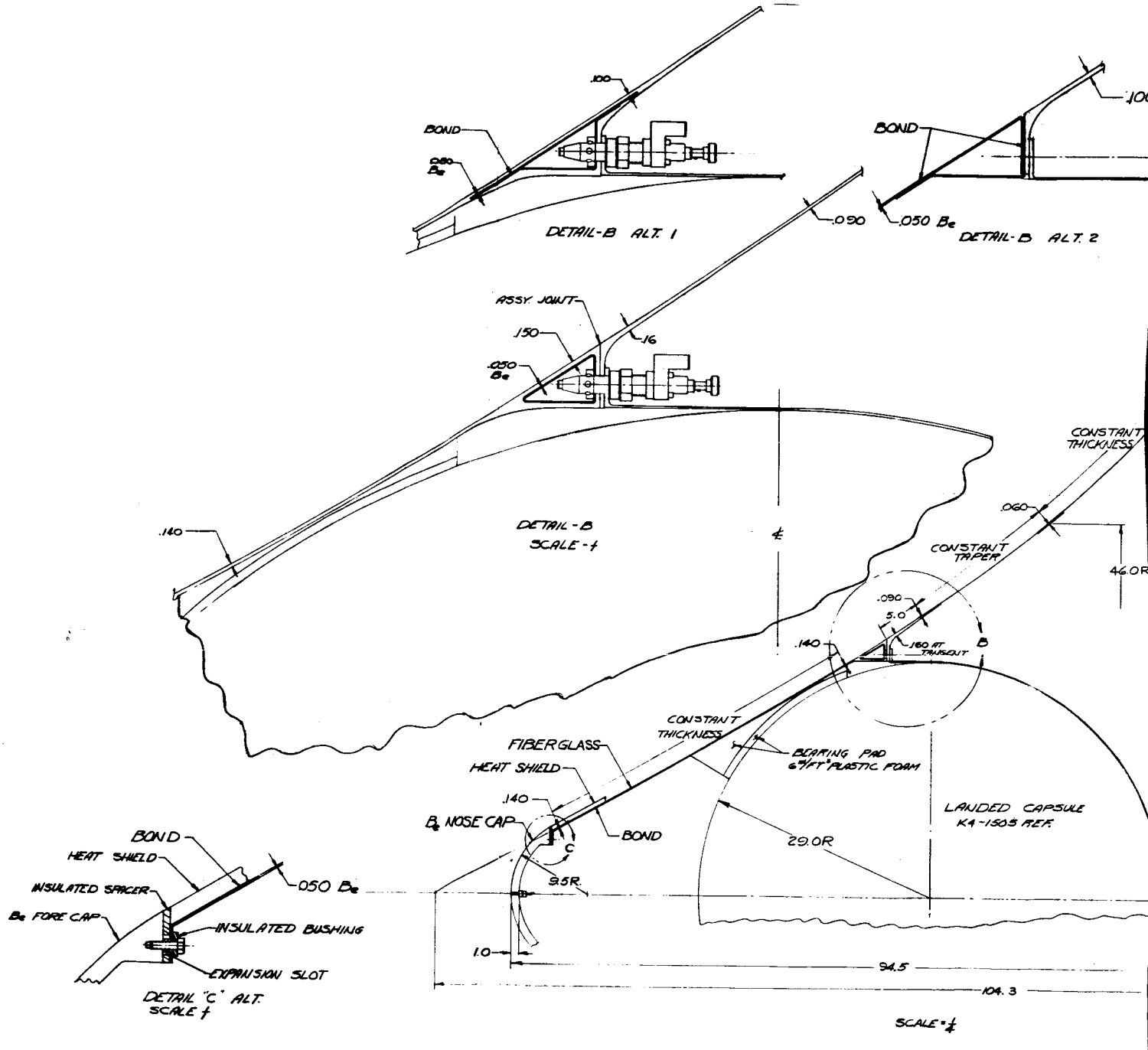

Figure 237 TENSION SHEL

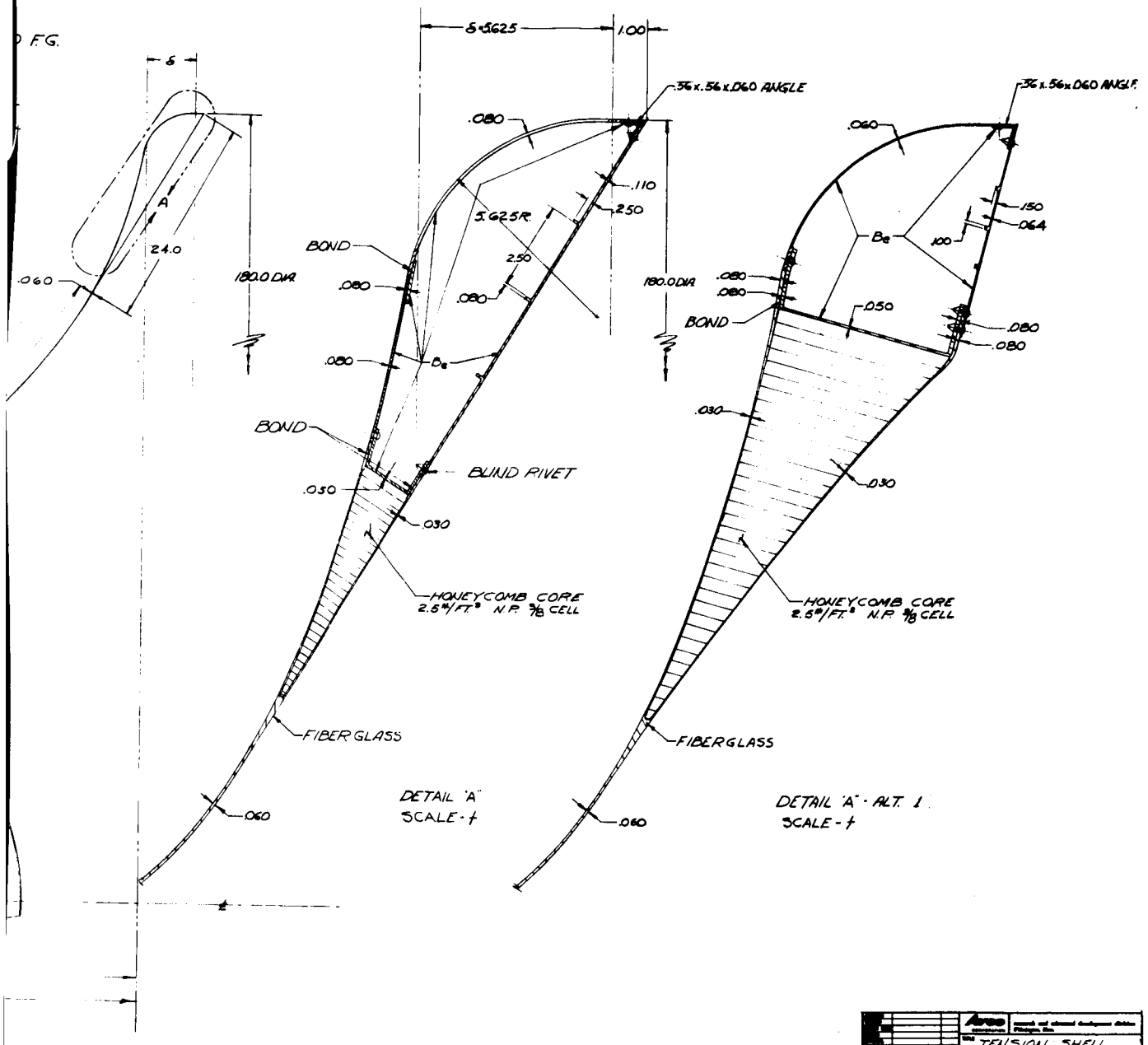

TENSION SHELL STRUCTURAL DETAILS

04614 | J | K4-1521

L STRUCTURE

390-2

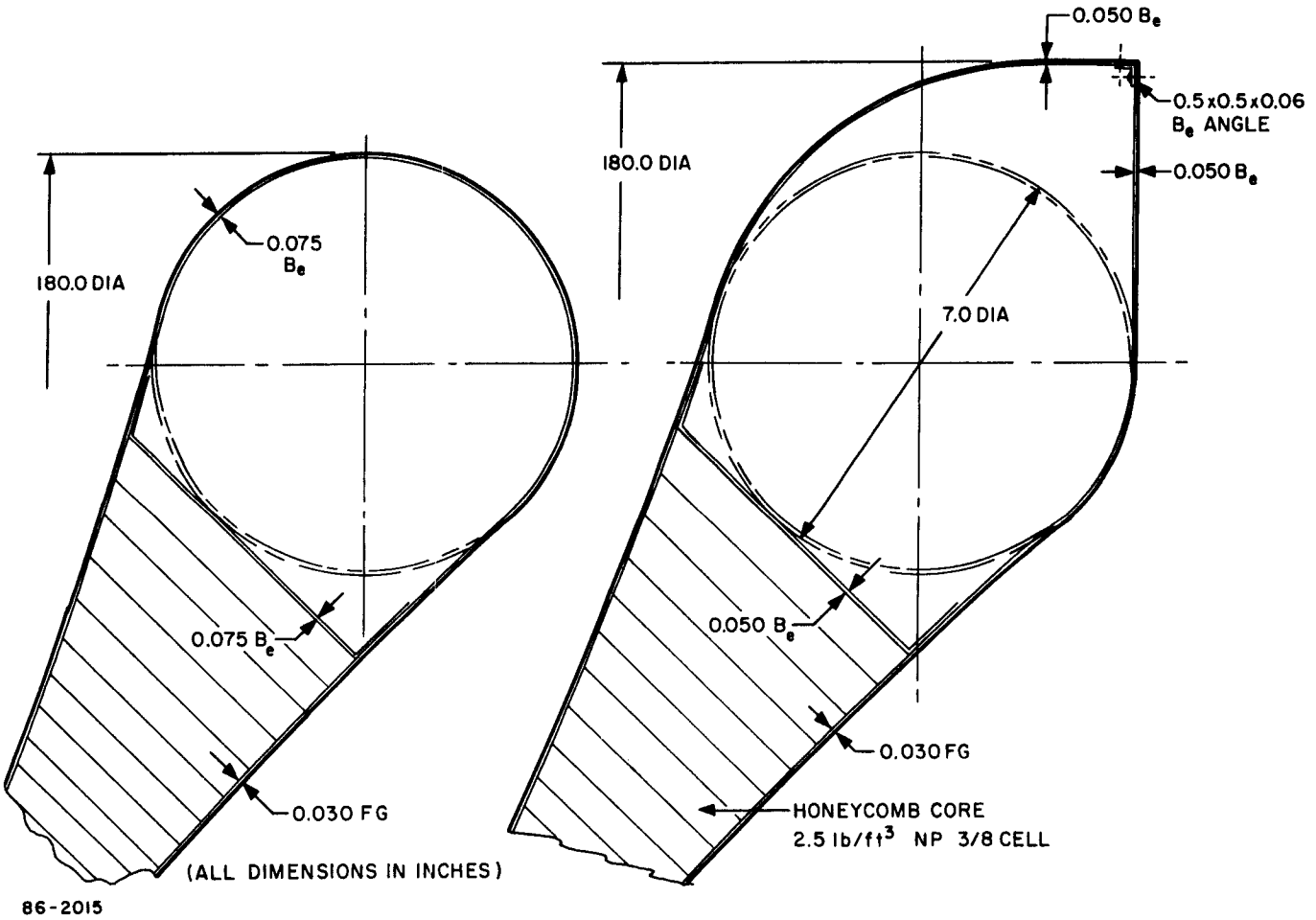

Figure 238 FEASIBILITY STUDY OF CIRCULAR RINGS

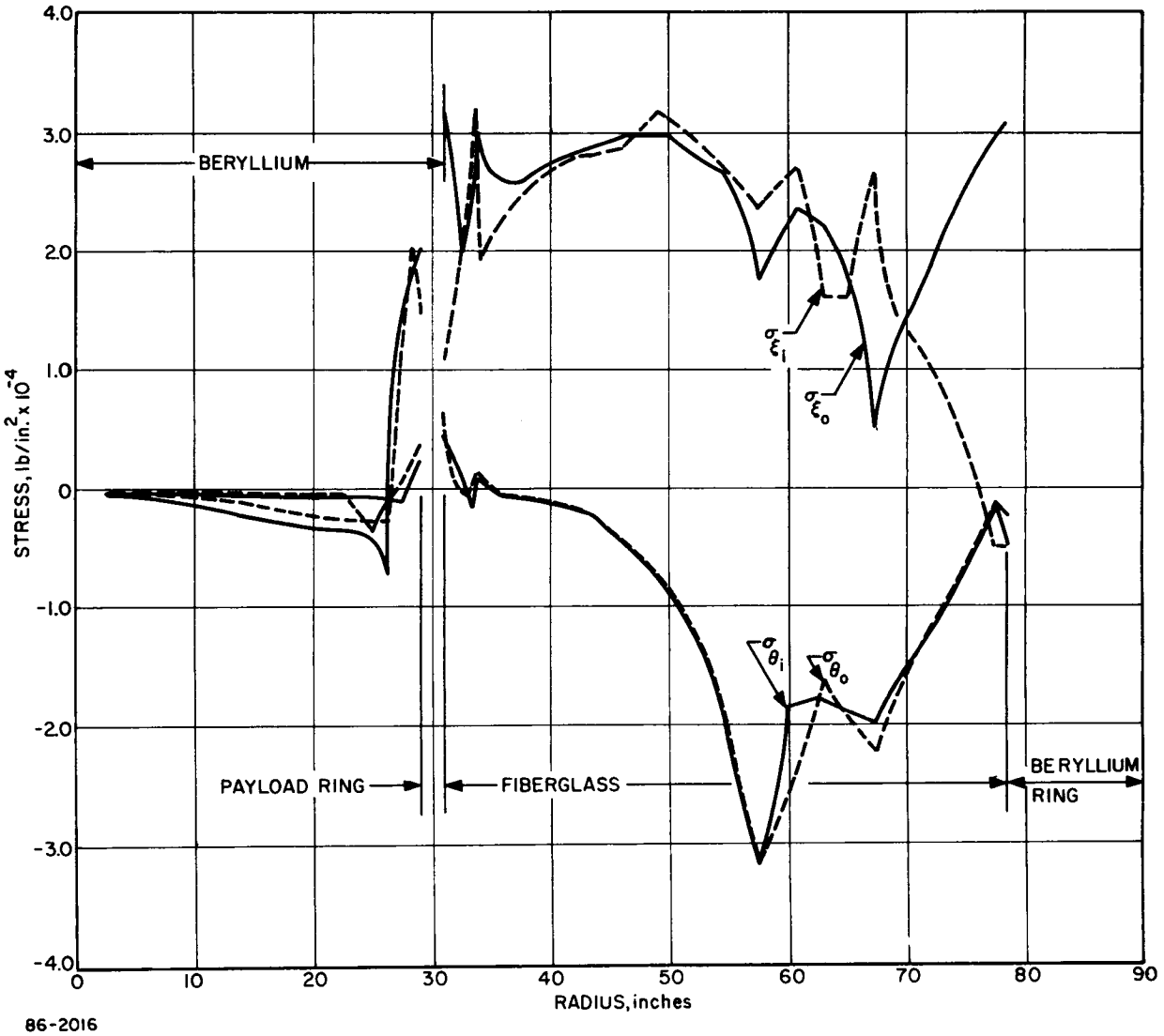

Figure 239 TENSION SHELL -- STRESS VERSUS RADIUS -- SYMMETRICAL PRESSURE DISTRIBUTION

compression stresses developed at a radius of approximately 57 inches. Wrinkling or some other form of non-rotationally symmetric deformation is quite likely to occur in this region. If such a deformation pattern occurs, large average radial displacements and increased compression ring loads could occur. The rotationally symmetric radial displacements are given in Figure 240. The shape of the displacements follows almost precisely the shape of the circumferential stresses. Positive radial displacements are outward.

The stress distribution for asymmetrical loading is given in Figures 241 and 242 at θ = 0 degrees and 180 degrees along the length of the shell, where θ = 0 degrees is the windward meridian. The circumferential variations at radii of 45 and 75 inches are given in Figure 243. As can be seen, the peak stresses are less than those for symmetrical loading.

The tangential displacement at θ = 90 degrees is given in Figure 244. This displacement represents the deflection of the entry shell structure in the beam-bending mode (n = 1) relative to the payload support. The variation of displacement around the circumference will be both greater and less than the value shown here. Positive displacement is shown in the direction of positive θ.

The structural material properties used in this analysis are given in Table XXXVIII.

TABLE XXXVIII

STRUCTURAL MATERIAL PROPERTIES

	F_{tu} (psi)	F_{cu} (psi)	F_{ty} (psi)	F_{cy} (lb/in^2)
Fiberglass	32, 000	29, 000	--	--
Beryllium	72, 000	--	55, 000	--

5.3.3.3 Dynamic Analysis

As specified in paragraph 5.1.3, no dynamic analysis was performed on the tension shell structure. The frequencies, however, are expected to be lower than for the blunt cone and modified Apollo.

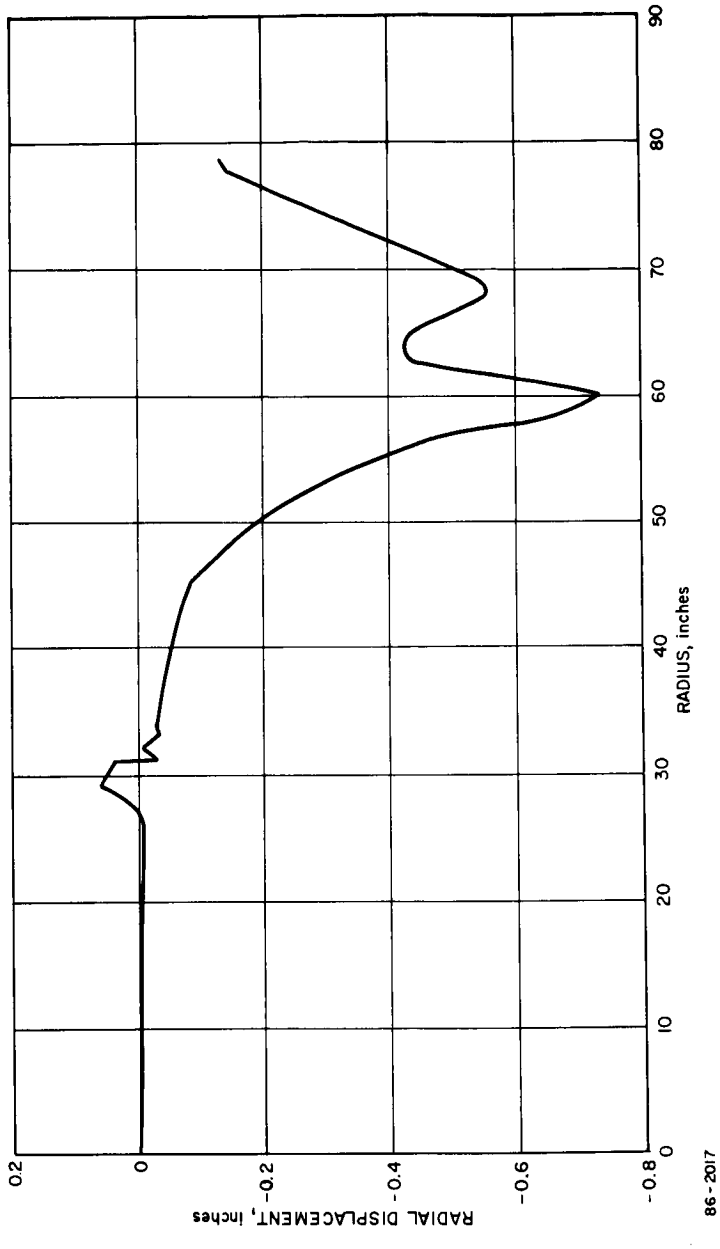

Figure 240 TENSION SHELL -- RADIAL DISPLACEMENT VERSUS RADIUS -- SYMMETRICAL PRESSURE DISTRIBUTION

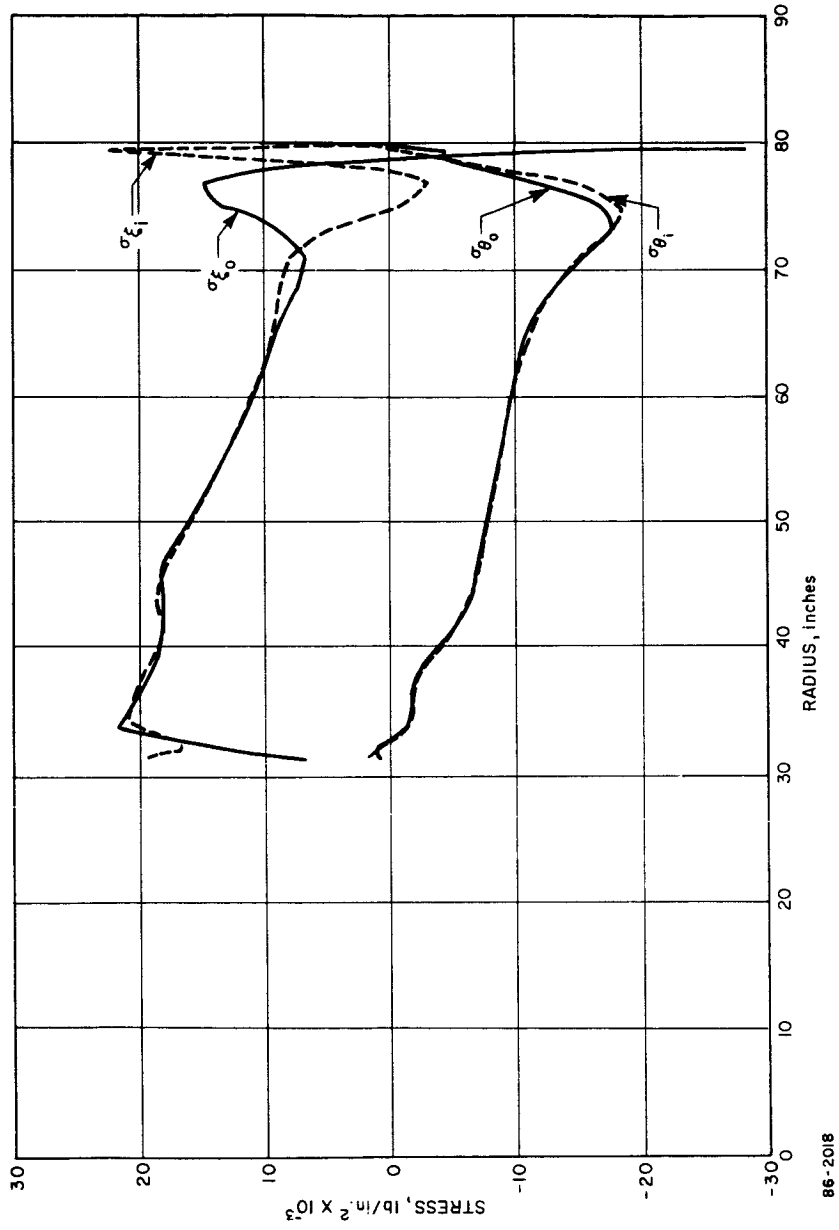

Figure 241 TENSION SHELL -- STRESS VERSUS RADIUS -- UNSYMMETRICAL PRESSURE DISTRIBUTION, θ = 0 DEGREES

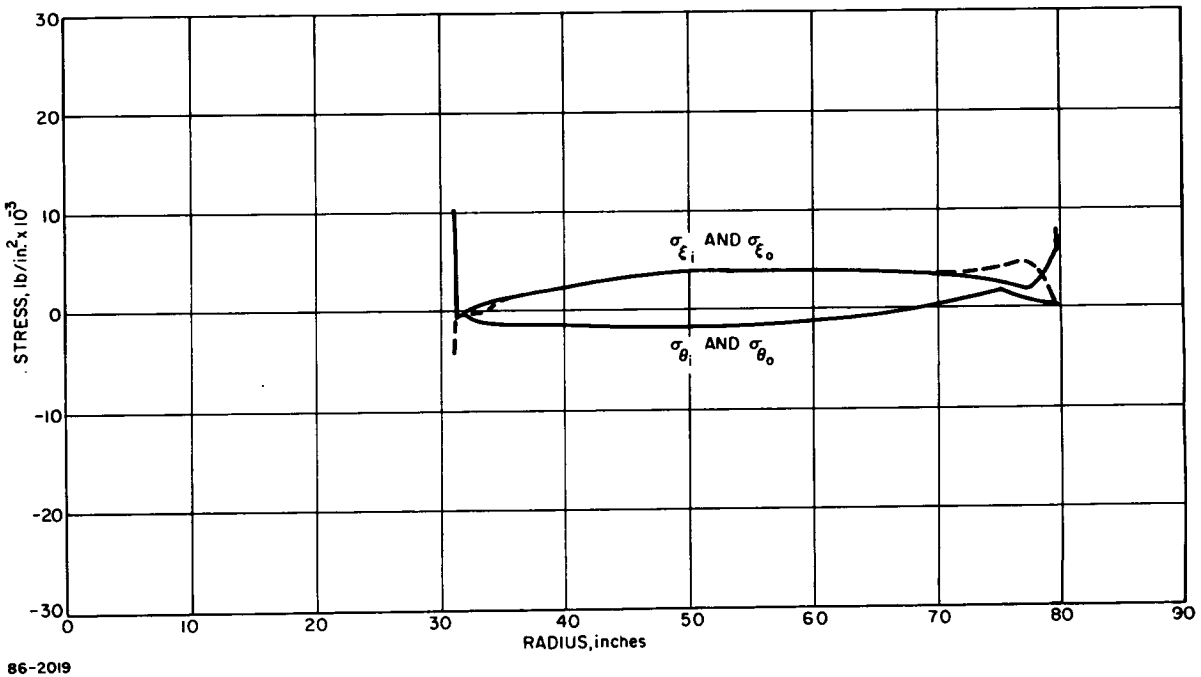

Figure 242 TENSION SHELL -- STRESS VERSUS RADIUS -- UNSYMMETRICAL PRESSURE DISTRIBUTION, θ = 180 DEGREES

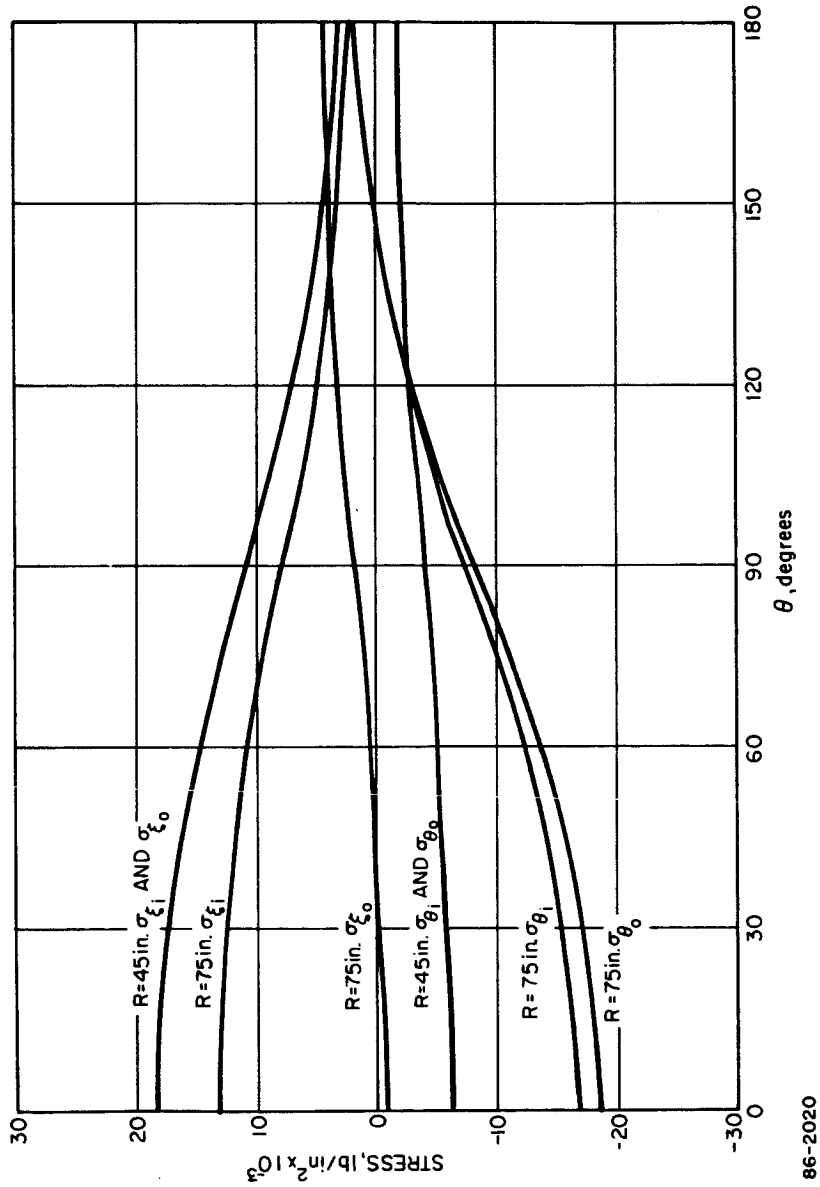

Figure 243 TENSION SHELL--STRESS VERSUS θ UNSYMMETRICAL PRESSURE DISTRIBUTION

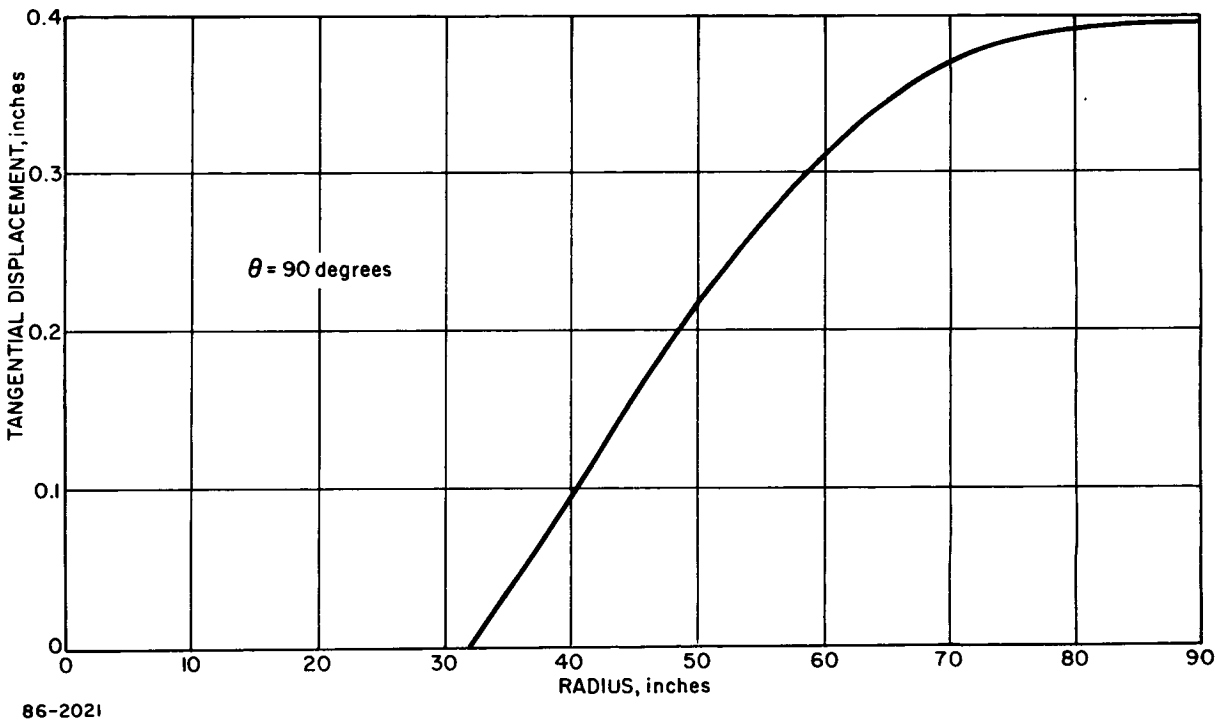

Figure 244 TENSION SHELL -- TANGENTIAL DISPLACEMENT VERSUS RADIUS -- UNSYMMETRICAL PRESSURE DISTRIBUTION

It is not certain that the SABOR III program, with its consistent mass and stiffness matrices, will be accurate enough for the dynamic analysis because of the extreme sensitivity of the tension shape static solution to errors in geometrical coordinates.

5.3.3.4 Support Structure

The support structure for the tension shell is the same as presented in paragraph 5.3.1.4.

5.3.4 Comparison of Shell Configurations and Discussion of Problem Areas

5.3.4.1 Structural Design Description

The reference shell designs analyzed for the blunt cone and modified Apollo, Figures 210 and 223, were optimized for the symmetrical loading and payload configuration described. Additional changes have been made to the payload configuration since completion of the analysis to decrease the bearing stresses on the impact attenuation material. These changes will tend to decrease the stresses in the reference design as indicated in Figure 245, where it is shown that the peak bending moment at the concentrated payload inertial reaction decreases as the diameter of the circle increases. The calculations were made for a 197-inch diameter blunt cone shape but the results are applicable to other diameters. The lower net pressure on the shell for the 1971 mission payload due to the larger bearing area will also reduce the stresses in the shell for that mission. Hence, the primary shell structural weight will decrease when these design changes are incorporated.

On the other hand, it was indicated in paragraph 5.3.1.2 that an increased stiffness will be required in the region of the payload reaction circle, to account for the effects of unsymmetrical loading. The extent to which these effects will cancel each other has not been determined. Providing that there are no major changes in external loading or design concept and that aeroelastic effects do not become important, the present structural weights for the primary shells of the modified Apollo and blunt cone shape can be considered close to their final values. Tradeoffs between structural and heat shield weight are also not expected to produce significant weight changes because beryllium is relatively insensitive to temperature in this reange of temperatures. The upper limit of the temperature allowable will be approximately 500° F due to the bond-material limitations.

The tension shell structure has been designed and analyzed for the multimission concept. The aerodynamic loading and inertial forces associated with the future mission payload governed the selection of the shell and compression ring structure. Analysis of the effect of

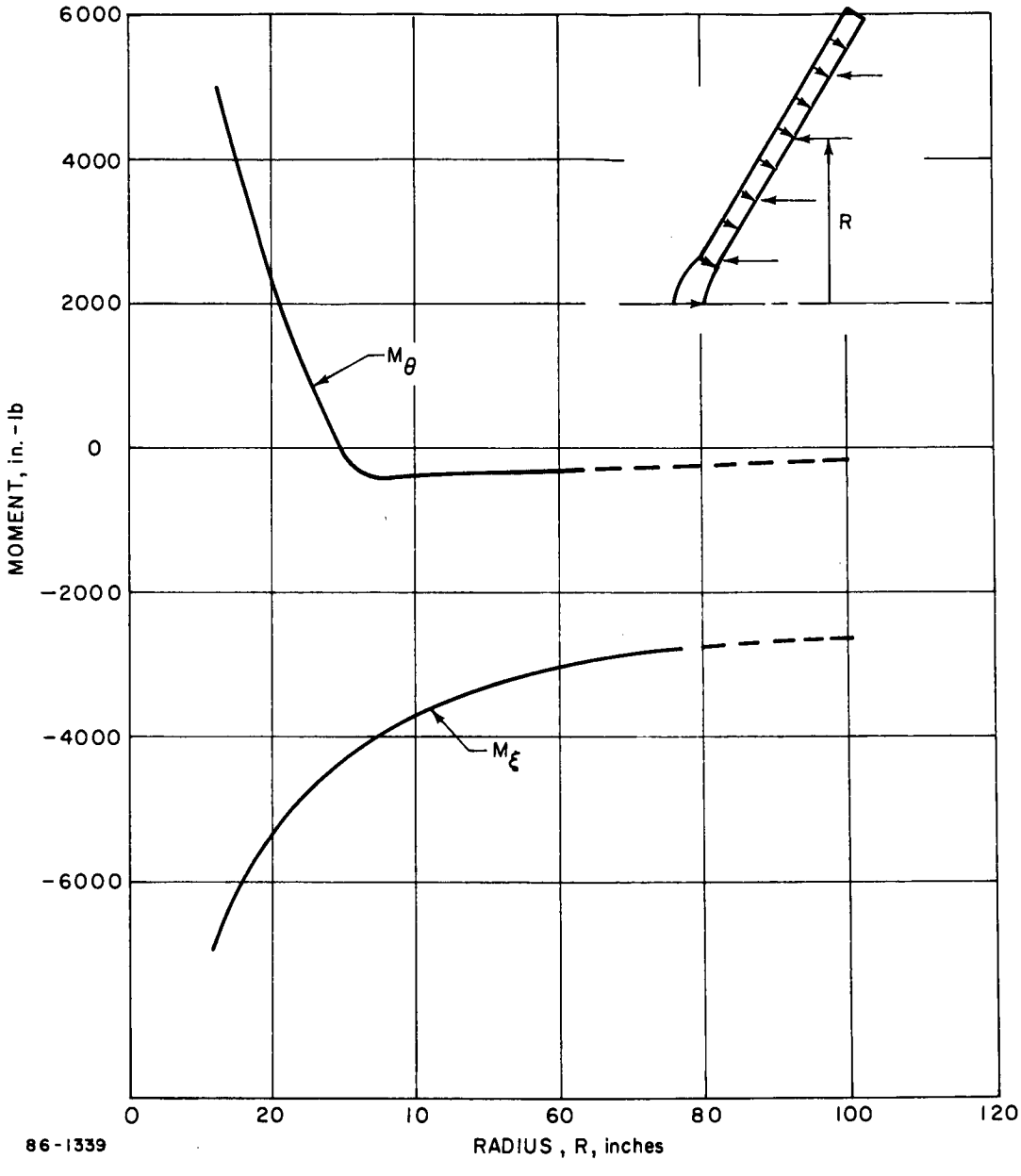

Figure 245 PEAK BENDING MOMENT VERSUS RADIUS OF REACTION CIRCLE--BLUNT CONE

asymmetrical loading indicated that the stress level did not become more critical. The choice of structural material has not been fully explored for the tension shell, nor has the effect of structural temperature rise which will induce thermal stresses in the ring and shell because of the dissimilar materials.

5.3.4.2 Comparison of the Primary Shell Structure of the Generic Shapes and Future Concepts

The tension shell concept demonstrated a relative structural weight advantage over the modified Apollo and blunted cone. The relative weight for the three generic shapes are given in Table XXXIII. These weights represent only the contribution to the total weight of face sheets, core, and end-rings, and should only be used for comparative purposes.

5.3.4.3 Problem Areas

The problem areas considered here pertain to the difficulties that arise in the analysis of the primary shell of the three generic shapes.

1. Honeycomb Sandwich Shells -- The general instability of the spherical and conical sandwich shells considered in this study was determined by utilizing the theoretical and experimental data for homogeneous shells. Since the effective thickness of sandwich shells is greater than the equivalent homogeneous shells, the effect of initial imperfections should be diminished; hence the stability criterion will be conservative. On the other hand, however the manufacturing techniques required to assemble a large honeycomb sandwich shell will probably introduce imperfections whose magnitude cannot presently be determined. As a result, it is difficult to estimate the degree of conservatism in the analysis.

The general instability of sandwich shells as well as homogeneous shells is influenced by the actual boundary conditions and the pressure distributions, both symmetrical and unsymmetrical. The effect of the boundary-conditions and arbitrary pressure distribution could be estimated by solving the nonlinear asymmetrical shell equation. However, experimental data generally falls well below the best theoretical estimate, particularly for spherical shells. Therefore, the theoretical results would at best indicate trends to be verified by experiment.

Consideration must be given to other modes of failure such as wrinkling of the face sheets, face-sheets dimpling and shear failure of the core material. The criteria generally available are based on data obtained from flat plates and cylinders. The accuracy for these modes of failure is therefore subject to question.

2. Tension Shell Stability -- The analysis of the tension shell showed that for the non-Newtonian pressure distribution, large circumferential compressive stresses can be developed. These compressive stresses are more a function of the deviation for the ideal Newtonian distribution than of the boundary conditions imposed at the boundary of the shell. Since the compressive stresses cannot be eliminated in the reference design, a method of determining the critical stresses is required.

The weight comparison of Table XXXIII shows an advantage in favor of the blunt cone over the modified Apollo. This is apparently due to the greater resistance to shell bending stresses of the blunt cone. This result, which is based upon the detailed static analysis of paragraph 5.3.1.2 and 5.3.2.2., reverses the preliminary comparison in the parametric analysis (paragraph 5.3.1 and 5.3.2 and Figures 207 and 221) which seem to favor the modified Apollo.

The weight advantage of the blunt cone over the Apollo shape can be expected to remain for increases in base diameter; however, as the diameter decreases the relative difference between the blunt cone and modified Apollo can be expected to decrease. This is because portions of the blunt cone shell are already down to the minimum gage for beryllium of 0.02 inch. The relative weight of the tension shape can be expected to decrease further as the pressure and diameters diminish since minimum gage limitations are applied to one sheet of material rather than two as in a sandwich shell.

A possible structural configuration which should be given consideration for future concepts is to distribute the payload inertial force over a major portion of the rear surface of the primary shell. By this method, the payload would support the primary shell and less structure would be required to bridge the payload inertia to a given reaction circle. This suggested approach applies to future payloads. The distributed inertia of the 1971 payload produces high stresses in the nose region of the primary structure. In actuality, the 1971 payload inertia force distribution is close to being a concentrated load because the

area over which it is distributed is less than 35 percent of the total area of the shell.

Possible improvements in the structural performance of the tension shell could be obtained by using a material having a higher strength to weight ratio than fiberglass. At a temperature of 300°F, the uniaxial strength/weight ratios of B120-VCA titanium and PH15-7 stainless steel are 2.4 and 1.77 times as great as fiberglass. Fiberglass was proposed initially because early analysis indicated an advantage in obtaining a large relative difference between the ring and shell stiffness: hence, a fiberglass shell and beryllium ring. The results of the present analysis indicate no particular structural advantage in this combination of materials, since the stresses on the shell were shown to be compressive even with an infinitely stiff ring.

3. Structural dynamic response of shell structures -- The problems associated with determining the dynamic response of shell structures occur principally in the general area of aeroelasticity. The response problems associated with the launch environment and parachute loads are generally within the state of the art.

For the structural aspect of the aeroelastic problem it is possible, with present day techniques, to formulate a reasonably accurate dynamic model of shell structures from which frequencies and mode shapes can be obtained. This is possible if the shell is not prestressed. The equations of motion would include a forcing function which would be a function of the structural displacement. Flutter would occur when the system becomes unstable. There are two major problems that arise, the first being that the relationship between the forcing function and displacement is very difficult to obtain. The second is that a structural shell optimized for static loads will be near incipient buckling when peak dynamic pressure is experienced. The stiffness coefficients will tend to become nonlinear with a resulting lowering of the natural frequencies, or in other words, the frequency of a structure will become zero at the buckling load. The importance of this effect at present is difficult to assess, but it does appear that an accurate estimate of aeroelastic effects will require that stiffness coefficients be obtained for a shell in a prestressed condition.

6.0 STRUCTURES - CONCEPTUAL DESIGN ENTRY FROM ORBIT

6.1 INTRODUCTION AND SUMMARY

6.1.1 Configuration Description

6.1.1.1 Entry Shell Structure

Aluminum honeycomb sandwich construction was selected for the entry-shell structure. A typical cross section of the entry shell consists of two 2024 aluminum alloy face sheets, 0.016 inch thick, bonded to a nominal 0.40-inch deep aluminum honeycomb core. The honeycomb core has a 3/16-inch cell and 0.002-inch foil thickness, with a resulting density of 5.7 lb/ft^3. The outer edge of the shell is stiffened by an aluminum end ring which also supports the ACS rockets. An integral ring is provided for attachment of the suspended capsule to the shell.

The forward edge of the conical portion of the shell is supported by a ring which is also the attachment point for the deployable aluminum spherical nose cap. The spherical cap is joined to the conical shell at four points by explosive bolts and thrusters. Detailed dimensions are given in Figure 246.

6.1.1.2 Suspended Capsule Structure

The suspended capsule structure consists of a space framework, after-body conical shell, a forward bulkhead, and fore and aft rings which join the frames together. Schematic and detailed dimensions are shown in Figures 247 and 248. The forward bulkhead is composed of component mounting boxes and covers which also act as structural members. The suspended capsule assembly includes the rocket motor casing and mounting structure as a structural member for all mission phases after assembly.

The forward ring is attached to a mating ring on the entry shell and adapter structure by vee-band clamps. Radial beams connect the forward mounting ring to the forward ring. These beams are loaded by the inertial forces of the component boxes as well as forces resulting from reactions with the other truss members.

The structural material used throughout the suspended capsule assembly was 2024-T_3 aluminum.

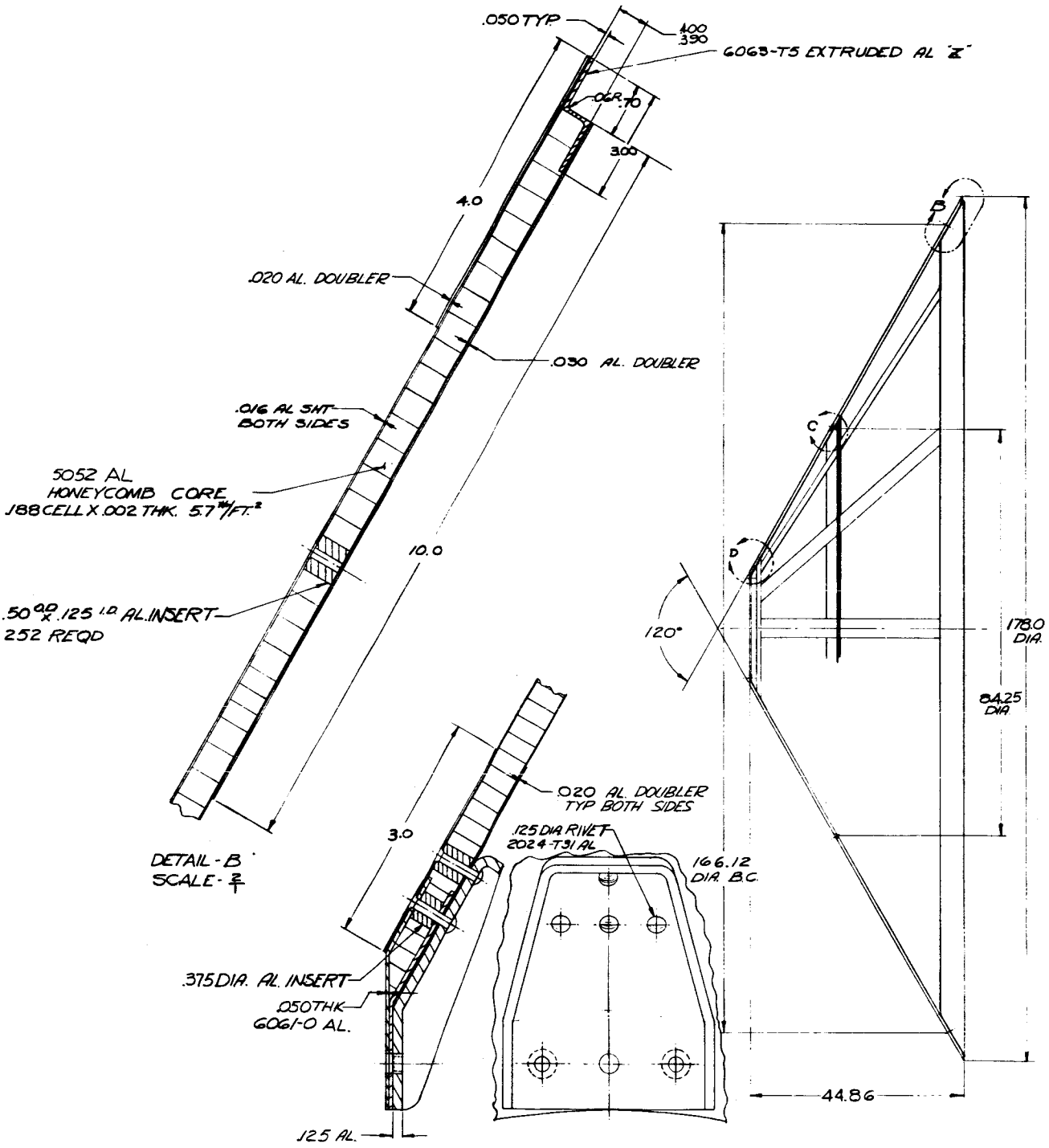

Figure 246 ENTRY SHELL

405-1

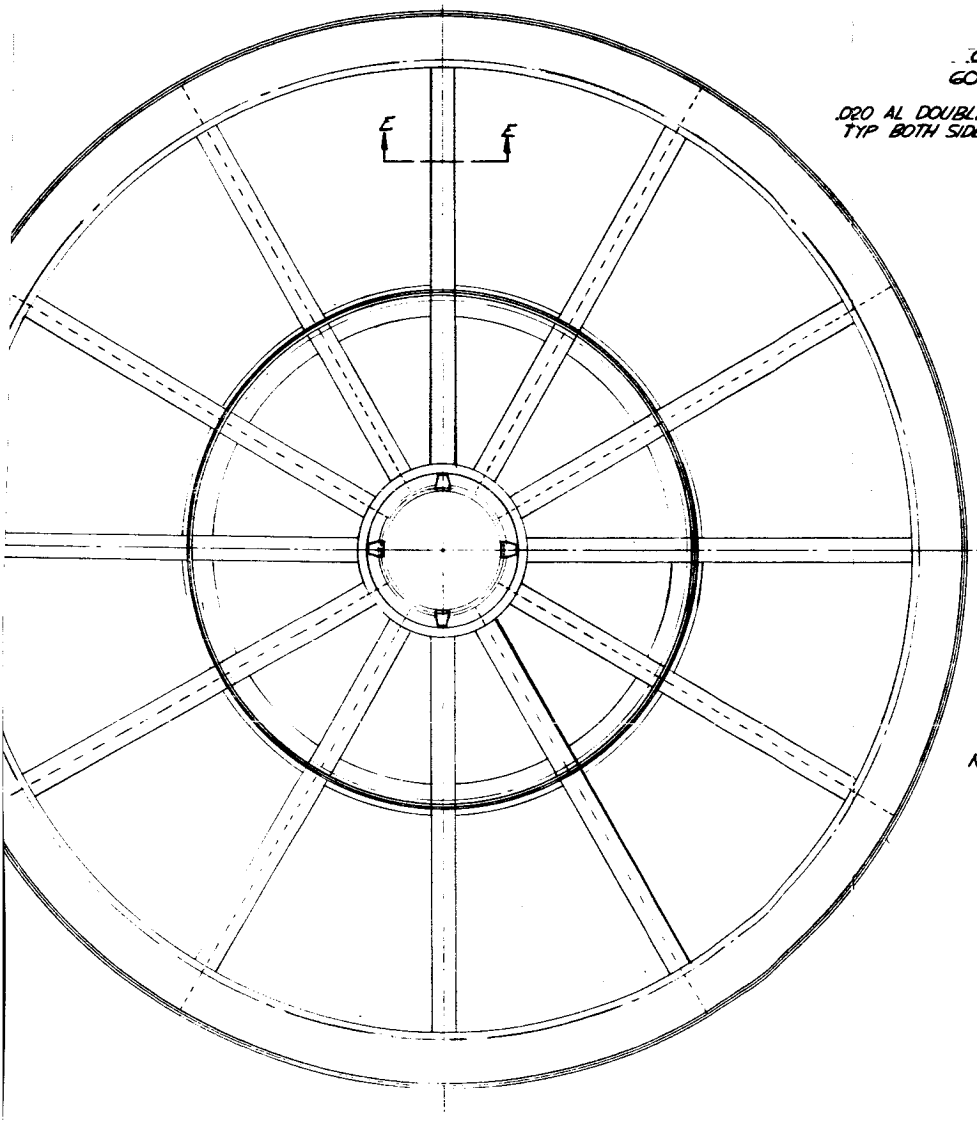

SECTION - E-E
SCALE 1
TYP. 12 PLCS

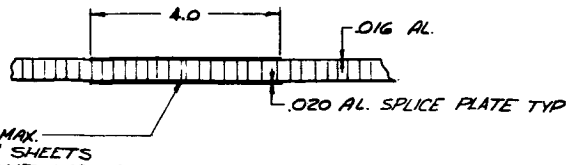

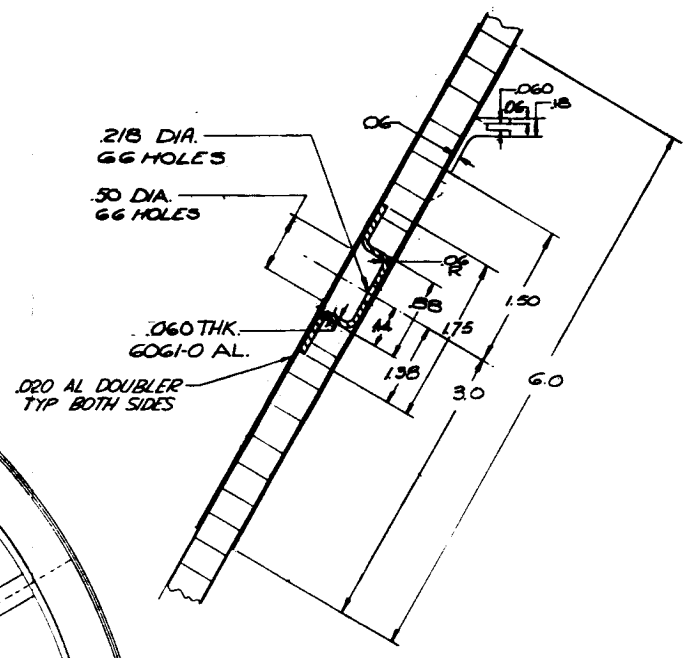

DETAIL - C
SCALE - 2

NOTE:
1. ALL JOINTS TO BE BONDED WITH HEXCELITE 840 NODE ADHESIVE EXCEPT AS NOTED
2. ALL MATL. 2024-T3 AL EXCEPT AS NOTED

LX-923210

MARS PROBE FLIGHT CAPSULE-PRIMARY STRUCTURE

04614 | J | K4 1547

STRUCTURE DESIGN LAYOUT

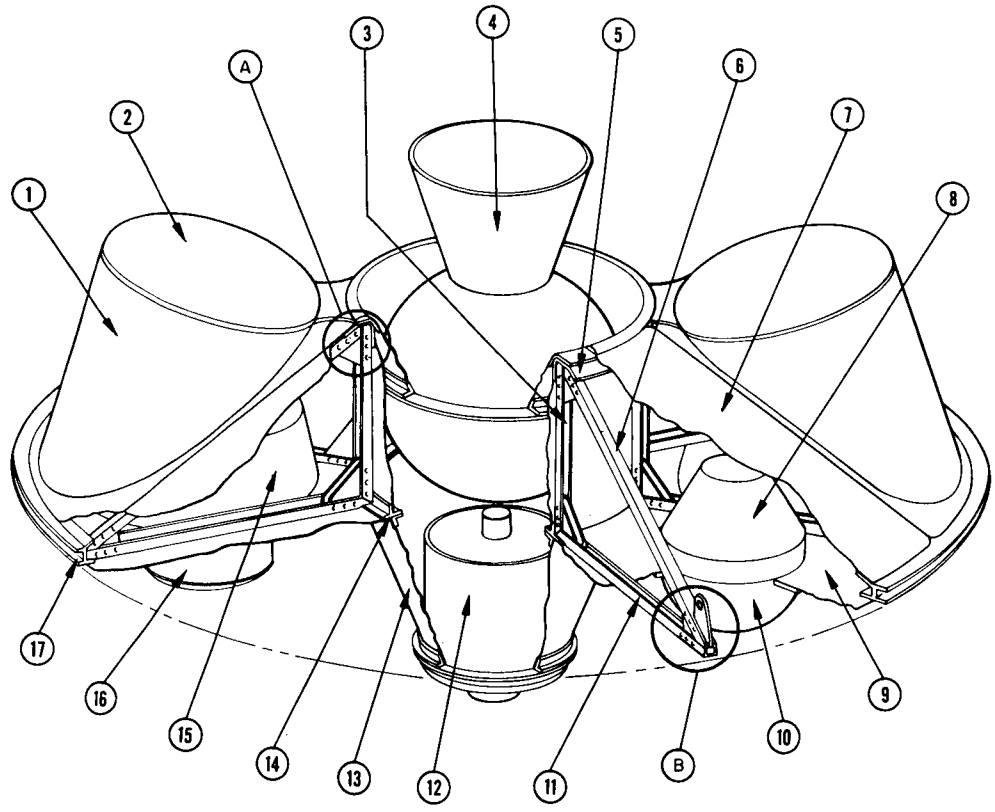

1. VHF RELAY ANTENNA NACELLE
2. VHF RELAY ANTENNA RADOME
3. LONGERON
4. ΔV PROPULSION
5. AFT RING
6. LONGERON
7. AFTERBODY COVER
8. PENETROMETER SEPARATION HOUSING
9. INSTRUMENTATION BAY
10. PENETROMETER
11. RADIAL BEAM
12. TV SUBSYSTEM
13. TV SUPPORT STRUCTURE
14. FORWARD RING
15. TELECOMMUNICATION POWER SUPPLY AND DATA HANDLING MODULE
16. DOPPLER RADAR ANTENNA
17. FORWARD MOUNTING RING

A. JOINT A

B. JOINT B (ALSO SHOWS PARACHUTE HARNESS LUG, TYPICAL 4 PLACES)

76-0283D

Figure 247 SCHEMATIC OF SUSPENDED CAPSULE STRUCTURE

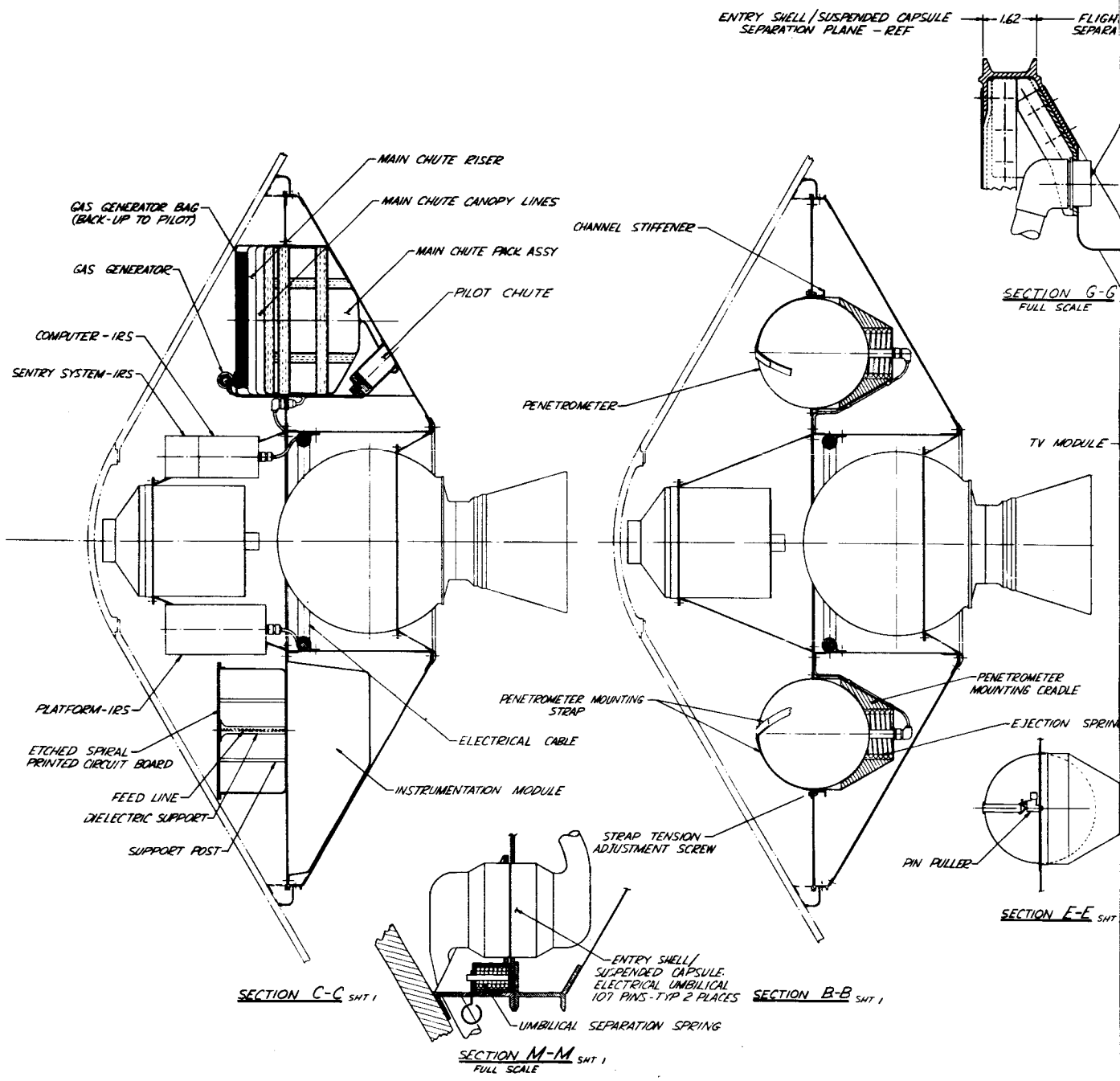

Figure 248 SUSPENDED CAPSU

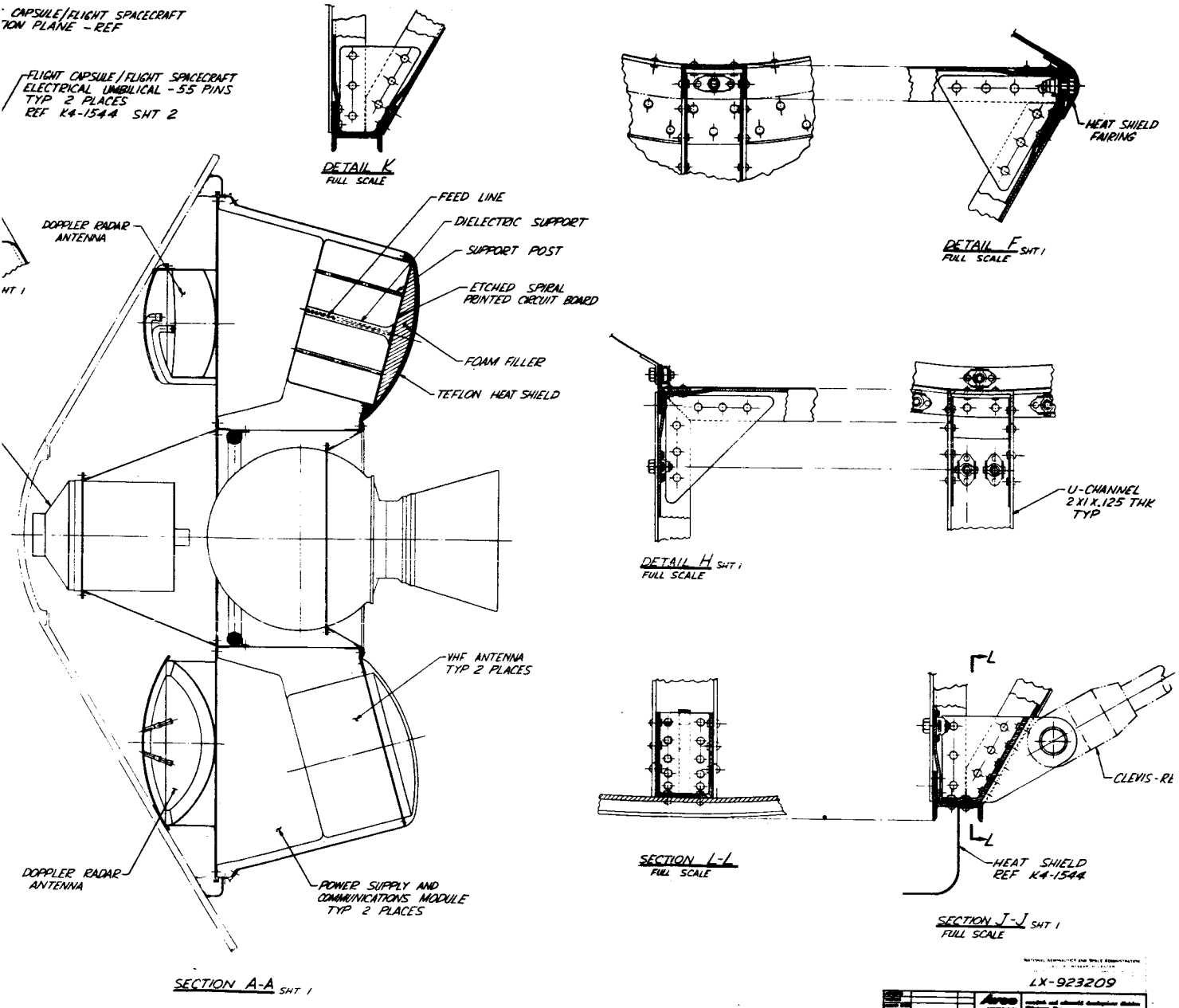

LX-923209

Aerojet	
MARS PROBE FLIGHT CAPSULE - SUSPENDED CAPSULE	
04614	K4-1546

E STRUCTURE DESIGN LAYOUT

6.1.1.3 Adapter Structure

Sheet and stringer construction was utilized for the adapter structure. Channel sections extend from the ring at the spacecraft interface to the mating ring of the vee-band clamp at the suspended capsule assembly. The channels were interrupted at the junction of the adapter structure and the sterilization canister shell where the sterilization canister shell was assumed to act as a bulkhead rigid in a plane normal to the adapter axis.

Dimensions of the adapter structure are given in Figure 249. The structural material was also 2024-T3 aluminum.

6.1.2 Requirements and Constraints

6.1.2.1 Entry Shell Structure

The entry shell structure is required to support the ablative thermal protection system, maintain the specified aerodynamic contour during entry, and transmit the aerodynamic drag forces to the remainder of the flight capsule structure. The structure is also required to withstand environments during all of the mission phases prior to entry without degrading its entry performance. During the launch, the entry shell is required to support the sterilization canister lid and during spaceflight the structure has to be thermally compatible with the ablator to avoid developing excessive tensile strains in the ablator or compressive stresses in the substructure.

Table XXXIX summarizes the loading conditions for the design trajectory as well as nominal maximum heating and maximum loading trajectories, as determined from the final trajectory analysis. The entry shell was analyzed also for loading conditions existing during other mission phases. These conditions, given in Table XL, also were considered in the design of the suspended capsule structure and adapter.

An efficient, but not necessarily minimum, weight type of construction was required for the entry shell structure. This requirement was subject to practical design constraints such as minimum face sheet thickness and core density. Practical structural materials whose mechanical properties were well established and manufacturing technology well developed were also specified.

The thermal protection system was specified as an ablating system; hence only a "cold" structural design was considered rather than a "hot" radiating structure.

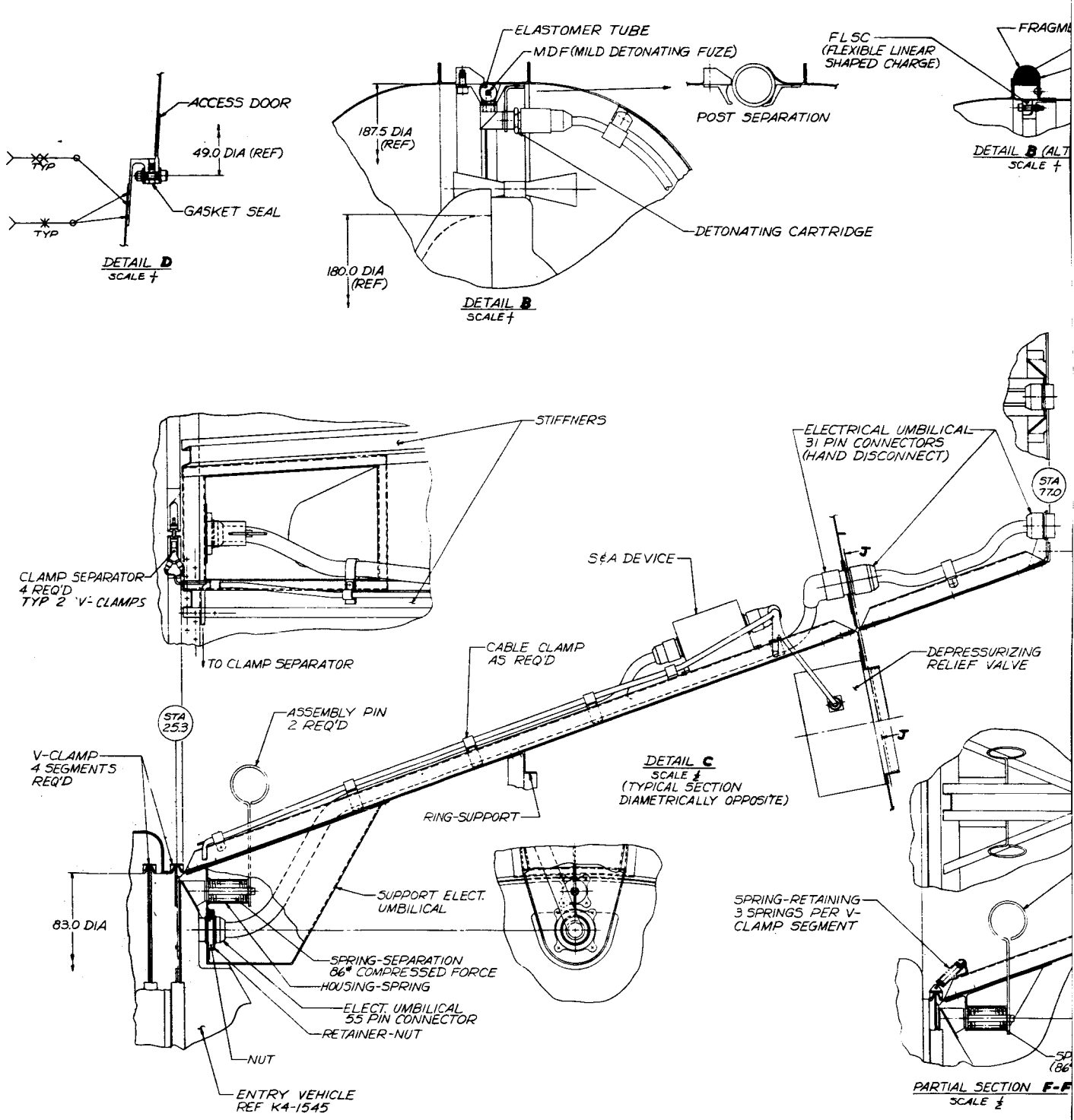

Figure 249 ADAPTER ST

ENTATION ABSORBER
PLASTIC FOAM
ALUM SHELL

ERNATE)

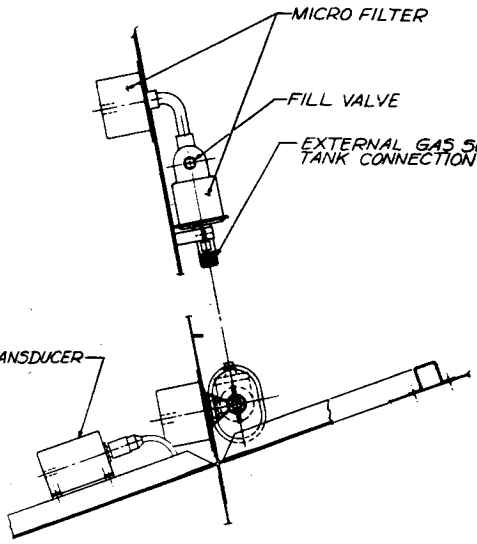

PARTIAL SECTION **G-G**
SCALE 1/2

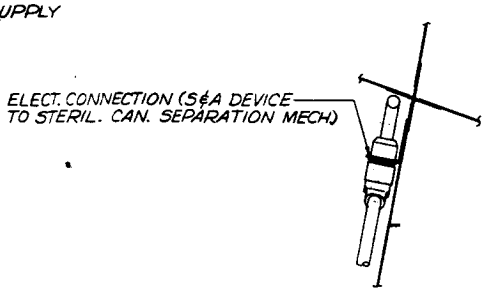

PARTIAL SECTION **H-H**
SCALE 1/2

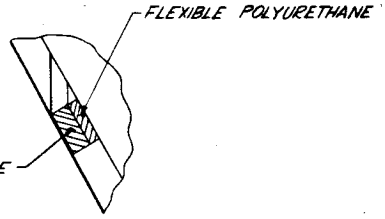

DETAIL **K**
SCALE +
BEARING PAD

120.0 DIA B.C.

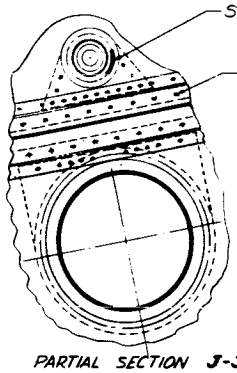

PARTIAL SECTION **J-J**

ASSEMBLY PIN 8 REQ'D

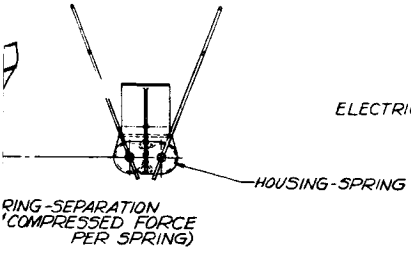

RING-SEPARATION
COMPRESSED FORCE PER SPRING)

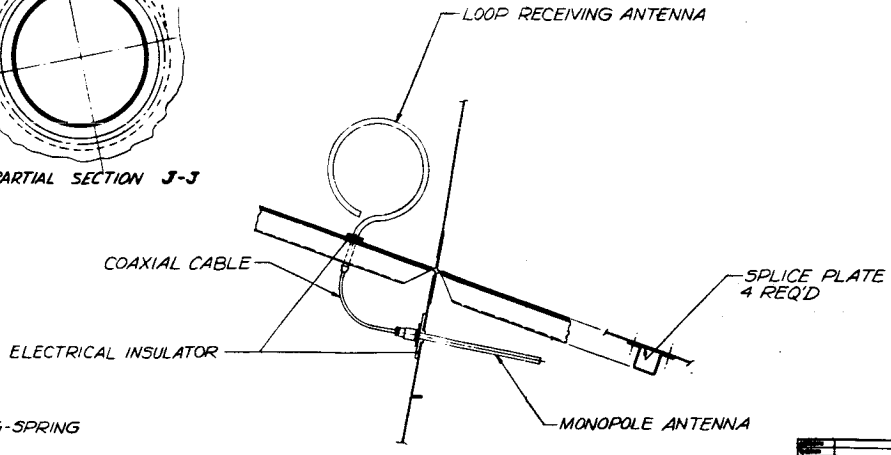

DETAIL **E**
SCALE 1/2
VHF. COMMUNICATIONS CHECK-OUT ANTENNA

LX923207

	Aerojet	
	TITLE: MARS PROBE FLIGHT CAPSULE LAUNCH CONFIGURATION	
	04614	K4-1544

RUCTURE DESIGN LAYOUT

TABLE XXXIX

LOADING CONDITIONS
(α_ϵ = 179° Roll Rate = 0.1 rad/sec)

	Reference Trajectory			
	Design	Nominal	Heating	Loads
V_ϵ } Inertial	15,200	15,200	15,200	15,200
γ_ϵ } Coordinates	-16°	-15°	-14°	-16°
Atmosphere	VM 8	VM 8	VM 7	VM 8
Azimuth	90° (north)	50°	60°	40°
At Maximum X/W:				
X/W	15.9	10.1	4.1	13.6
N/W	.61	.61	.22	.54
q_∞ (PSF)	114.6	72.0	31	98.3
α (degrees)	10.3	.28	13.5	10.1
$\dot{\alpha}$ (rad/sec)	1.63	.03	.9	1.6
$\ddot{\alpha}$ (rad/sec^2)	15.0	.25	4.3	15
At Maximum N/W:				
X/W	15.7	8.5	3.2	11.5
N/W	.71	.01	.25	.61
q_∞ (lb/ft^2)	113.2	60	27.5	83
α (degrees)	13.8	.39	16.7	13.5
$\dot{\alpha}$ (rad/sec)	1.53	.03	1.2	1.84
$\ddot{\alpha}$ (rad/sec^2)	9.8	.31	5.6	15.1

TABLE XL

SUMMARY OF DESIGN CONDITIONS FOR THE BLUNT-CONE MARS LANDER CAPSULE

Mission Sequence	Design Condition		
Ground Handling	Vibration		
	± 3.5 g_e (rms)	2 to 50 cps	
	± 1.5 g_e	50 to 300 cps	
	Packaged		
	± 1.3 g_e	2 to 26 cps	
	0.036 in D.A.	26 to 52 cps	
	± 5.0 g_e	52 to 300 cps	
Launch	Sustained Acceleration		
	4.5 g_e axial ± 1.0 g_e lateral		
Capsule Trajectory Maneuver	ΔV Force = 800 pounds		
Capsule Cruise	Spaceflight temperature distribution -54° F to 230° F		
Capsule Entry		Multimission	1971 Mission
	a_x axial g	91.0	209
	a_n normal g at max a_x	5.6	16.2
	α angle of attack, at max a_x	15.8°	19.5°
	p_s stagnation pressure	19.9 lb/in^2	14.0 lb/in^2
Parachute Deployment	8500 pounds times 1.5 load factor		

6.1.2.2 Suspended Capsule Structure

The suspended capsule structure was required to support all of the internal components and transmit the external forces developed during the mission phases from ground handling and transportation until impact with the Martian surface. The afterbody shell structure, which is a component of the suspended capsule, was required to support the afterbody thermal protection system, maintain the specified aerodynamic contour, and transmit aerodynamic forces and moments to the remainder of the capsule.

Component packaging requirements rather than structural efficiency dominated the selection of the structural configuration. The structure was required to have no permanent unsymmetrical deformations due to the mission environment from ground handling through the entry phase to minimize unsymmetrical movement of the center of gravity.

Standard aircraft construction materials and methods were specified which called for normally available cross sections of extruded parts, minimum edge distance and spacing for bolts and riveted joints and standard sizes of rivets, bolts and other attachments.

6.1.2.3 Adapter Structure

The purpose of the adapter structure was to transmit the ground handling, launch and spaceflight maneuver loads to the flight capsule and sterilization canister. Standard aircraft construction methods were required for the adapter structure. Although an efficient structural design was required, minimum weight was relatively less important here than in the design of the entry shell and suspended capsule structure. In the final design of the adapter structure, the dynamic environment during the launch phase will have to be considered. This information was not available for this conceptual design and hence placed no requirement or constraint on the design.

6.1.3 Concepts and Performance Summary

6.1.3.1 Concepts

Two concepts are considered here as they effect the structural design: an early concept with a failure mode where the capsule enters with a spin rate of 40 rpm, and a later concept with a failure mode where the capsule enters tumbling with a maximum rate of 0.1 rad/sec. A more detailed discussion of these concepts and their effect on loads and heating was given in Section 3.0 of this book.

The capsule entering with a 40-rpm spin rate experienced the peak loading, as a direct result of the large angle of attack (at least 30 degrees) and also because the slow convergence of the angle of attack raised the effective M/C_DA of the capsule. The tumbling-entry failure mode induced lower maximum loading, since the tumbling ceased and the angle of attack converged well before peak loading. The capsule ceased tumbling before the pressures on the afterbody and the rear of the entry shell became critical design conditions.

6.1.3.2 Performance Summary

The performance of the flight capsule shell is summarized using weights and margins of safety as the criteria. Table XLI gives the loading conditions and weights for comparison of the two concepts. Note that the weight for the tumbling entry was only slightly less than the weight for the spinning entry. This can be explained by the fact that the nose cap is designed with aluminum for the tumble case instead of with beryllium, and also, because the change in the structure was principally in the core thickness, which represents a smaller portion of the shell weight than the face sheets.

The tumbling entry concept was selected for the conceptual design of the capsule system. The structure was designed for a set of loading conditions which were subsequently reduced in severity after a more detailed analysis of the entry conditions was completed.

The margins of safety are given in Table XLII for the entry shell for these loading conditions and for the possible structural failure mode. All of the critical loadings for the entry shell occurs during entry except for a possible problem during spaceflight cold soak. A discussion of problems arising during cold soak is given in paragraph 6.3.3.4.

Margins of safety for the suspended capsule structure and adapter structure are given in Table XLIII. Critical loadings occur for these structures during parachute deployment and launch, respectively.

The performance of an aluminum honeycomb sandwich blunted cone entry shell as a function of diameter and stagnation pressure is given in Figure 250. The structural weight was computed using a symmetrical pressure distribution. The results are good approximations for angle of attack cases up to at least 30 degree angle of attack.

6.1.4 Comparison with Entry from Approach Trajectory Studies

The primary difference between the environments seen by the capsule structures for the EFAT and EFO studies is that the entry aerodynamic pressure

TABLE XLI

COMPARISON OF LOADING CONDITIONS

Design Concept		Entry from Orbit	
		40-rpm Spin	Rearward Entry
Diameter	feet	15	15
Weight	pounds	358	343
Entry Velocity	ft/sec	15, 200	15, 200
Entry Angle	degree	-18.0	-16.0
Atmosphere	Model	VM-8	VM-8
M/C_DA	slugs/ft^2	0.20	0.22
Entry Angle of Attack	degree	90.3	179
Stagnation Pressure	lb/ft^2	358	229
A_x	g	23	15.5
A_n	g	2.1	0.6
Structural Material		Aluminum	Aluminum
Structural Concept		H/C Sand.	H/C Sand.
Weight Fraction		0.193	0.168

TABLE XLII

ENTRY SHELL STRUCTURE PERFORMANCE SUMMARY

Condition	Safety Factor	Margin of Safety			
		Design Traj.	Nominal Traj.	Heating Traj.	Loads Traj.
Symmetrical					
Face-Sheet Yielding (Entry)	1.0	1.54	Large	Large	1.96
Core-Shear Stress (Entry)	1.25	1.46	2.92	Large	1.87
Face-Sheet Wrinkling (Entry)	1.25	Large	Large	Large	Large
Face-Sheet Dimpling (Entry)	1.25	Large	Large	Large	Large
Shell Buckling (Entry)	1.25	0.055	0.68	2.90	0.23
Aft-Ring Buckling (Entry)	1.50	0.24	1.02	Large	0.48
Face-Sheet Yielding (Launch)	1.0	Large	Large	Large	Large
Shell Buckling (Launch)	1.25	1.11	1.11	1.11	1.11
Face-Sheet Yielding (Spaceflight)	1.0	Large	Large	Large	Large
Shell Buckling (Spaceflight)	1.25	0.0	0.0	0.0	0.0
Ablator Cracking (Spaceflight)	1.25	2.62	2.62	2.62	2.62
Unsymmetrical					
Face-Sheet Yielding (Entry)	1.0	2.18	Large	Large	2.45
Shell Buckling (Entry)	1.25	-0.09	0.68	2.1	0.06

TABLE XLIII

PRELIMINARY MARGINS OF SAFETY -- SUSPENDED CAPSULE STRUCTURE

Location	Description of Structure	Load Condition	Type of Failure	Safety Margin
Joint A	Aft ring to Frame Longeron	Parachute Deployment	Bolt Shear Bearing	+0.01 +0.34
Joint B	Outer Forward Ring to Frame Longeron	Parachute Deployment	Bolt Shear Bearing	+0.01 Large
Element 1	Frame Longeron	Parachute Deployment	Crippling	0.0
Element 6	Outer Forward Ring	Parachute Deployment	Bending and Axial Loads	0.0
Element 4	Aft Ring	Parachute Deployment	Bending and Axial Loads	0.0
Adapter	Longeron	Launch Condition "C" Axial and Lateral Combined	Column Failure	+0.25

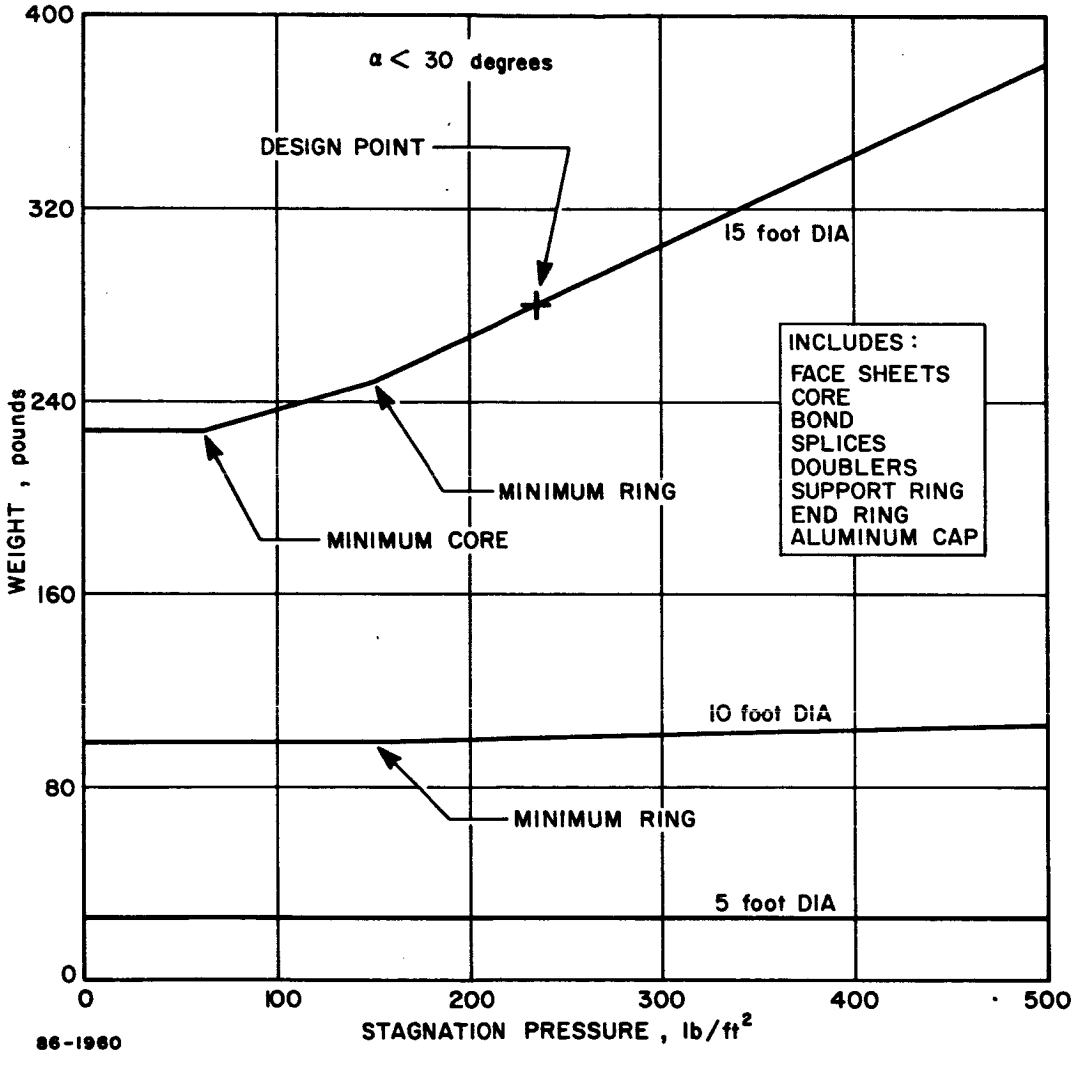

Figure 250 BLUNT CONE SHELL STRUCTURE--WEIGHT VERSUS STAGNATION PRESSURE

loadings are an order-of-magnitude smaller for the EFO studies as compared to EFAT. The payload inertia for the EFO studies was also introduced into the entry shell as a concentrated line force. This can have a significant effect on the stress distribution in the shell as demonstrated in paragraph 5.3.1.2.

With the lower surface pressures associated with the EFO concept, the structural weight fraction became less critical; hence the use of more conventional structural materials became feasible. The structural shell weight became relatively insensitive to load variations as compared to the EFAT concepts. This insensitivity was due to the minimum gage restriction that existed over the range of aerodynamic pressures expected for EFO.

As a consequence of the minimum gage restriction, the face sheets of sandwich shells were understressed by factors of two or more. The parametric structural weight studies, based on buckling criteria therefore, were better estimates of final design weights than in the EFAT studies because additional skin thickness and core depth was not required for shell bending stresses.

The resulting structural shell weights did not decrease in the same proportions as the relative loading between the EFAT and EFO concepts because of these minimum gage limitations. The EFAT concept used beryllium facesheets while aluminum was used for EFO. It should be noted that if aluminum were used for the EFAT concept, the structural weight would be at least twice the weight of the beryllium structure. A comparison of the weights and entry design condition is given in Table XLIV.

6.1.5 Conclusions and Problem Areas

The principal conclusion that can be drawn about the study of performance of honeycomb sandwich blunted cone entry shells is that for the low range of surface pressures experienced during entry, the shell weight is a weak function of aerodynamic loading. In fact, for a base diameter less than ten feet the weight is constant with pressure. This result is due to the minimum gage restrictions on the sandwich face sheets and core depth. Other environments and responses of the entry shell rather than static entry loading will likely impose restrictions on the minimum stiffness of the shell wall for lower pressures. For example, the minimum frequency of the entry shell occurs in the second harmonic and is approximately 7 cps. This minimum frequency does not present a problem for the present design since for the range of expected angles of attack, the second harmonic of the unsymmetrical pressure is very small and has a frequency of approximately 2 cps. The first harmonic dominates the unsymmetrical pressure distribution and the corresponding structural frequency of the shell is 53 cps, hence negligible coupling exists. A further reduction in stiffness of the shell, however, could increase the possibility of coupling between the structural and aerodynamic frequencies due to reduction of structural frequencies.

TABLE XLIV

LOADING CONDITIONS

Design Concept	Entry from Approach Trajectory		Entry from Orbit	
Diameter (feet)	15	15	15	15
Weight (pounds)	451	451	358	343
Entry Velocity (ft/sec)	23,800	23,800	15,200	15,200
Entry Angle (degrees)	-90	-90	-18.0	-16.0
Atm. Model	3	2	VM-8	VM-8
M/C_DA ($slug/ft^2$)	0.15	0.49	0.20	0.22
Entry Angle of Attack (degrees)	179	179	90.3	179
Stagnation Pressure (lb/ft^2)	2020	2870	358	229
A_x (g's)	209	91	23.0	15.5
A_n (g's)	16.2	5.6	2.1	0.6
Structural Material	Beryl.	Beryl.	Alum.	Alum.
Structural Concept	H/C Sand.	H/C Sand.	H/C Sand.	H/C Sand.
Weight Fraction	0.308	0.10	0.193	0.168

A preliminary investigation of the compatibility of the heat shield ablator and substructure, with Purple Blend Mod 5 as the reference ablator, revealed that the margin of safety for tensile fracture of the ablator is greater than 2 for a -100°F spaceflight cold soak assuming that the zero stress temperature of the composite was 300°F. The stresses in the aluminum honeycomb substructure, however, were equal to the critical buckling stresses for the design entry loading. Although comparing the thermal stresses to the critical buckling stresses for mechanical loading is quite likely to be a conservative method of analysis, the results do indicate that the stiffness of the entry shell structure should not be decreased or the stiffness of the ablator increased without first considering the stability of the entry shell structure. It should be noted that buckling of the substructure cannot occur due to thermal stresses alone unless there exists an unbonded area between the ablator and substructure. A weak or unbonded area is within the realm of possibility. The importance of the problem is also dependent on the actual value of the zero stress temperature of the composite and whether the stresses in the ablator material will relax when stored for a period of time at room temperature.

A problem existed in both the entry-from-orbit and entry-from-approach trajectory studies in determining the required stiffness of the reinforced ring at the aft end of the conical entry shell. A method of analysis was developed which appears to give a satisfactory criterion but requires experimental verification. Problems also exist in determining the design criteria of sandwich shell structures for failures associated with core strength and stiffness. Most available analyses were extensions of the results obtained for plates and columns. With very light shell structures, the problems of ground handling became more important. Realistic criteria have to be specified so that its influence on the design can be determined.

6.2 DESIGN CRITERIA

The structure of the blunted-cone entry shell, suspended capsule, and adapter were designed so that neither allowable yield stresses nor critical buckling loads were exceeded when compared to limit loads raised by a suitable safety factor. The safety factors used throughout the study, with one exception, were 1.0 times limit load for a yielding failure and 1.25 times limit load for a buckling or instability failure. Because of lack of applicable verification tests of the analysis of the end ring, a safety factor of 1.5 times limit loads was used.

6.3 RESULTS AND DISCUSSION

6.3.1 Parametric Studies

6.3.1.1 Structural Concepts and Material Selection

The structural concept and material selection for the entry shell structure is influenced by the failure criteria of the shell, the operating

temperatures, manufacturing methods and criticality of the structural weight fraction of the flight capsule.

Monocoque, ring-stiffened and sandwich structures are logical types of construction for a conical shell (that could fail by instability) when subjected to external pressure. These structural concepts were investigated as a function of stagnation pressure and base diameter using the methods described in paragraph 7.3. The relative weights of monocoque, ring-stiffened and honeycomb sandwich conical shell structures are compared in Figure 251. The weight comparison is made relative to the honeycomb sandwich construction. At the design point of 229 lb/ft^2, a ring-stiffened structure is 2.05 times and a monocoque structure is 3.9 times heavier than a sandwich structure. The comparison was made using aluminum as the structural material, with a base diameter of 15 feet.

The relative weights of structural materials are compared in Figure 252 using aluminum as the reference material. At the design pressure, magnesium and beryllium are more efficient than aluminum. Magnesium loses its weight advantage over aluminum at higher pressures because its lower Young's modulus requires a greater core depth than aluminum and at higher pressures the core weight becomes a major fraction of the total weight as seen by examining the relationships in paragraph 7.3. The assumption was made in this comparison that the minimum practical core depth was 10 times the face-sheet thickness for a given material. Below the pressure at which the depth criterion is reached, the materials such as fiberglass, titanium and beryllium increase in weight relative to aluminum. Actually aluminum decreases in weight and the other materials remain constant in weight.

The relative efficiency of structural concepts as a function of base diameter is shown in Figure 253 with pressure as a parameter and using aluminum as the structural material. The results demonstrate that the honeycomb sandwich structure becomes more efficient with increasing pressure and diameter. The relative weight of a ring-stiffened structure approaches that of a honeycomb sandwich structure at a diameter of approximately 5 feet. At this diameter the weight of sandwich construction is constant since both the face sheet and core are at minimum thickness. The weight of a ring-stiffened structural shell can continue to decrease since it utilizes only one sheet thickness which is not yet at the minimum gage. The total thickness of the sheet is less than two minimum gage face sheets of a honeycomb shell.

In order to obtain the realistic comparisons of ring-stiffened and sandwich shells, size and spacing of the rings had to be optimized with respect to minimum weight. The results presented in Figure 253 for the ring-stiffened shells included the optimization of stiffener spacing and stiffener size as a function of pressure.

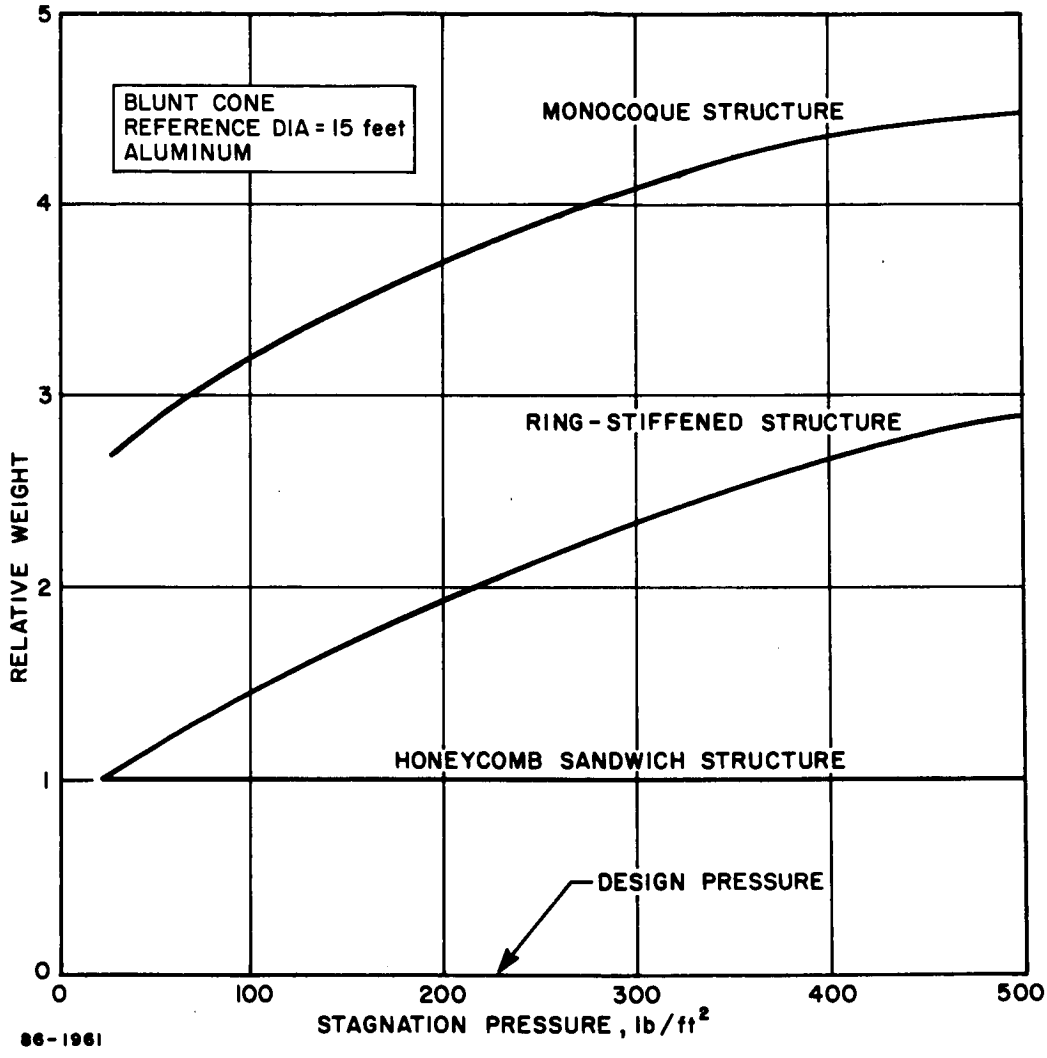

Figure 251 RELATIVE EFFICIENCY OF STRUCTURAL CONCEPTS

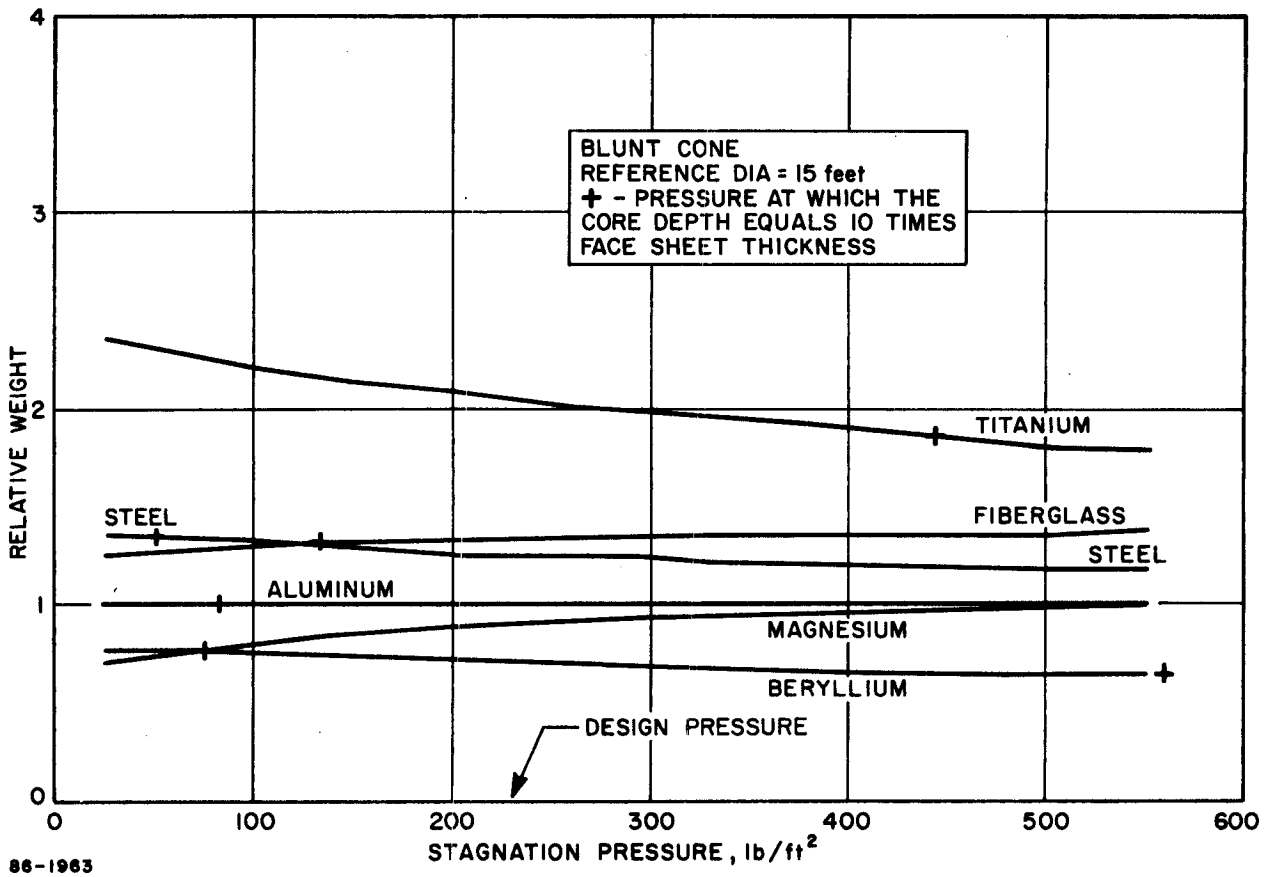

Figure 252 RELATIVE EFFICIENCY OF STRUCTURAL MATERIALS FOR HONEYCOMB SANDWICH CONSTRUCTION

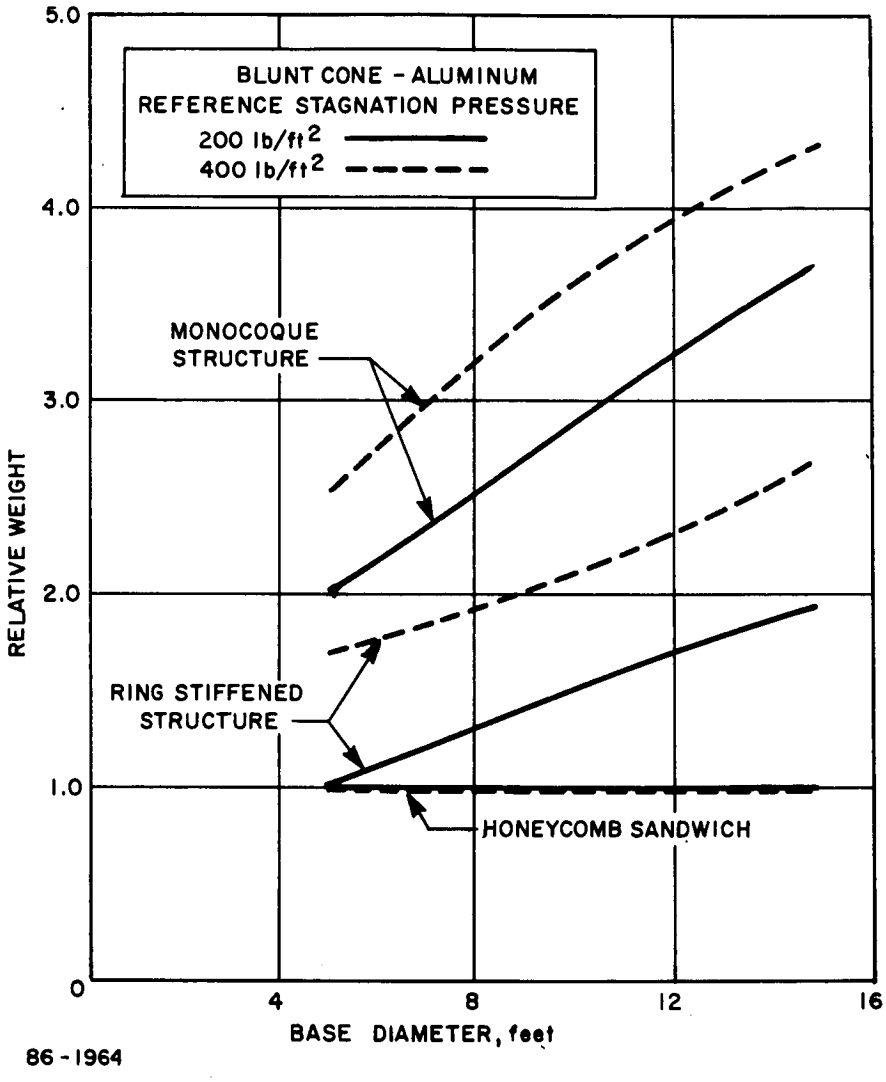

Figure 253 RELATIVE EFFICIENCY OF STRUCTURAL CONCEPTS BLUNT CONE--ALUMINUM

As was stated earlier, the honeycomb sandwich structure was subject to the constraints of minimum face-sheet thickness and core density. In order to determine what possible weight-saving could be achieved if these constraints were relaxed, the weights of aluminum honeycomb sandwich conical shells were obtained relative to the sandwich shells having the above constraints. In Figure 254 the lower curve represents the relative weight for an entry shell with no constraints in face-sheet thickness and core density other than face sheet dimpling and wrinkling and core shearing with the corresponding core depth required for stability. It can be seen that the weight is approximately one-half of the design weight. There will, however, be additional weight required to account for shell bending stresses in optimum design which will not be required for the reference design.

The middle curve in Figure 254 shows the effect of using a minimum core density as discussed in paragraph 7.1.2.1. In this case, the shell weight becomes 80 percent of the reference design. It is evident from these results that if the structural weight fraction becomes critical, significant weight savings are possible if the constraints on face-sheet thickness and core density can be relaxed.

The theoretical face sheet and core depths for the sandwich shell with no constraints, as noted above, are given in Figures 255 and 256.

6.3.1.2 Characteristics of Selected Configuration

Although as indicated in Figure 252, magnesium and beryllium have lower relative weights than aluminum, aluminum was chosen as the structural material because of its well developed manufacturing technology. A magnesium structure at the design pressure was only about 10 percent lighter than aluminum and, in view of the lesser criticality of the structural weight fraction for the EFO as compared with EFAT concepts, the weight difference did not warrant an imposition of increased manufacturing difficulty.

As can be seen in Figure 253, honeycomb sandwich construction had considerable weight advantage over ring-stiffened and monocoque constructions. The manufacturing problems for sandwich construction are also less severe than for a ring-stiffened construction with many small rings, particularly at large diameters and small skin gages.

For the selected configuration, the minimum face-sheet thickness was specified as 0.016 inch. The corresponding core depth required to satisfy stability as a function of base diameter and stagnation pressure is given in Figure 257.

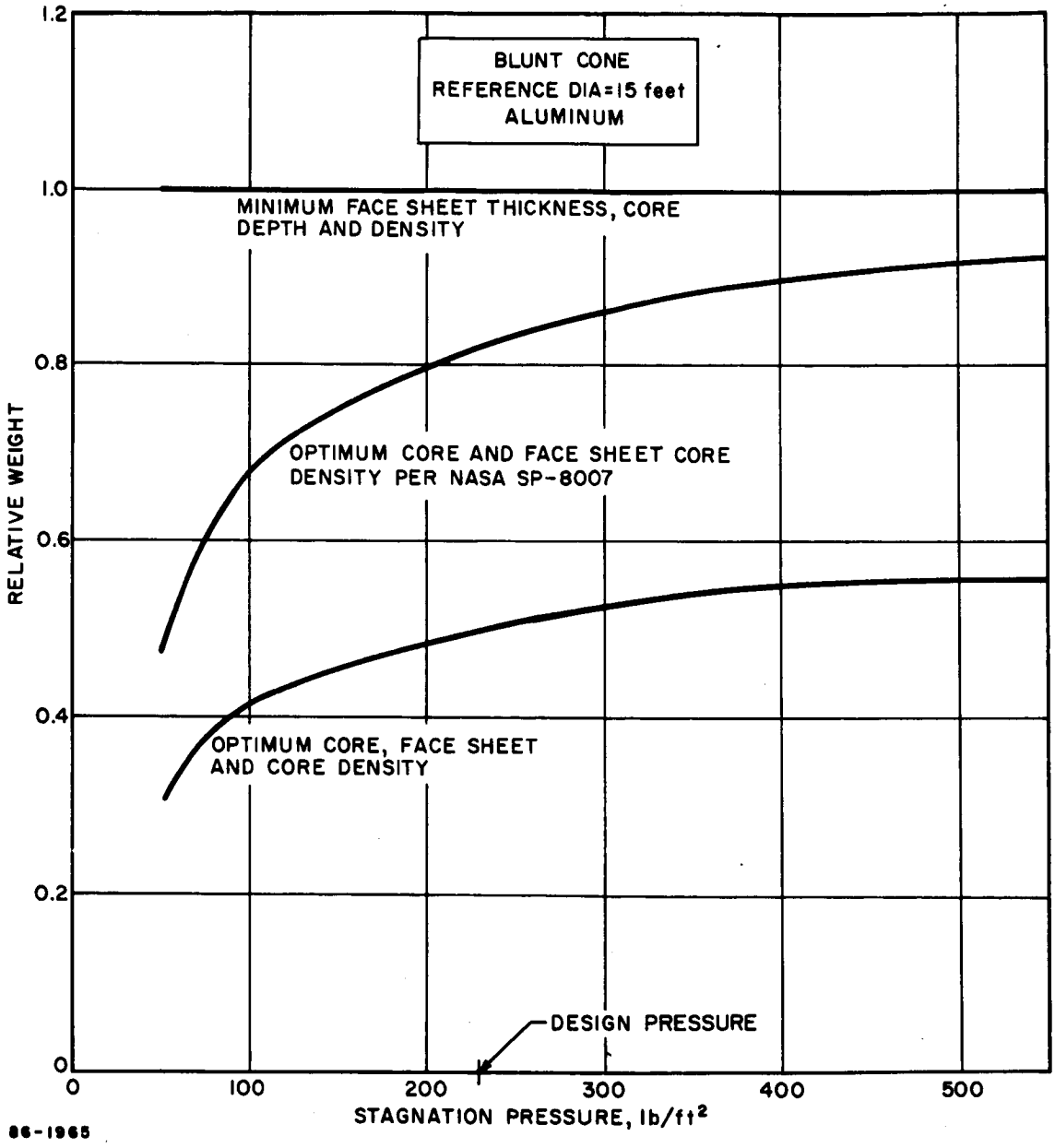

Figure 254 INFLUENCE OF DESIGN CONSTRAINTS ON FACE SHEET THICKNESS, CORE DEPTH, AND CORE DENSITY

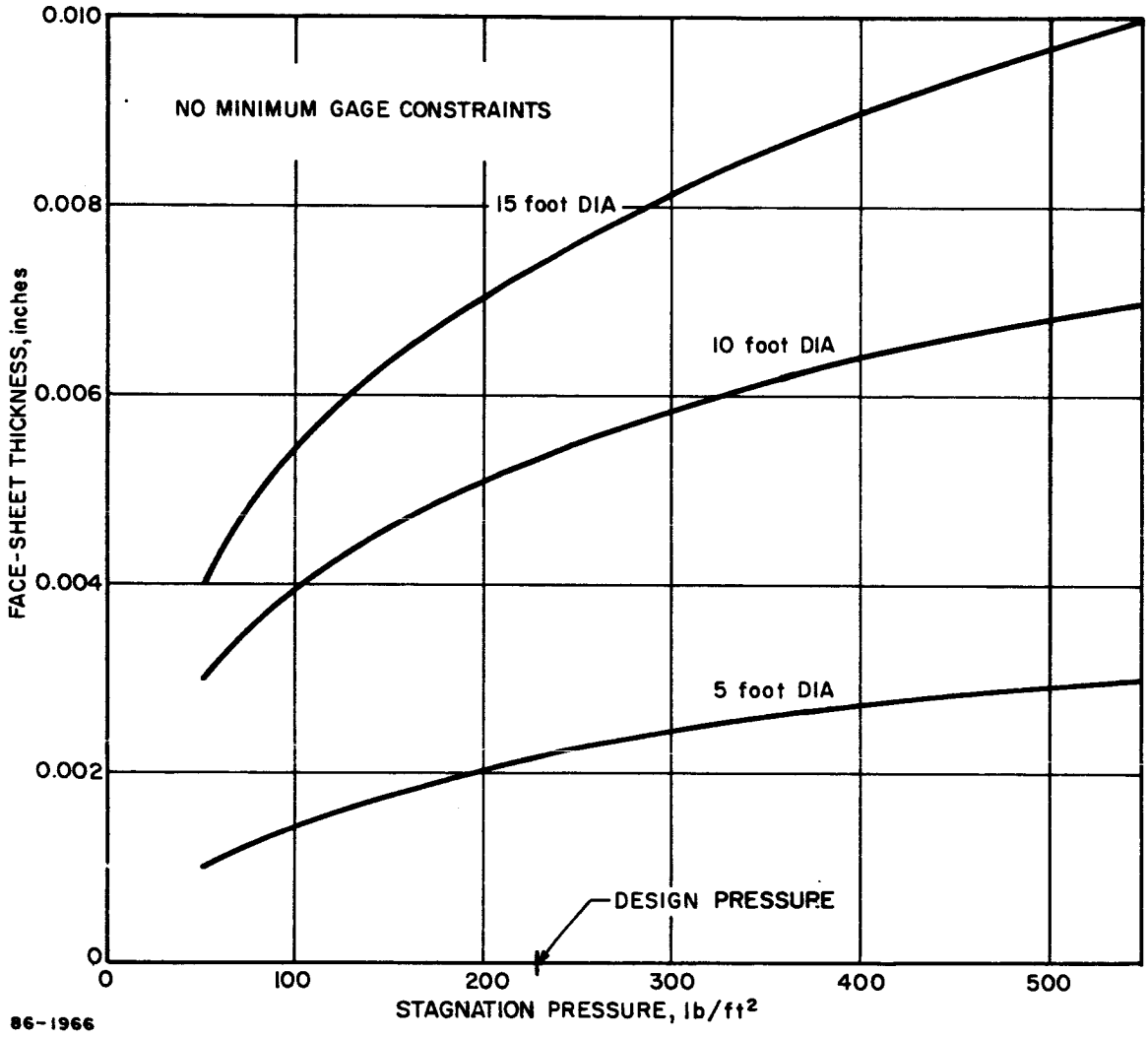

Figure 255 FACE SHEET THICKNESS VERSUS STAGNATION PRESSURE FOR BLUNT CONE--ALUMINUM

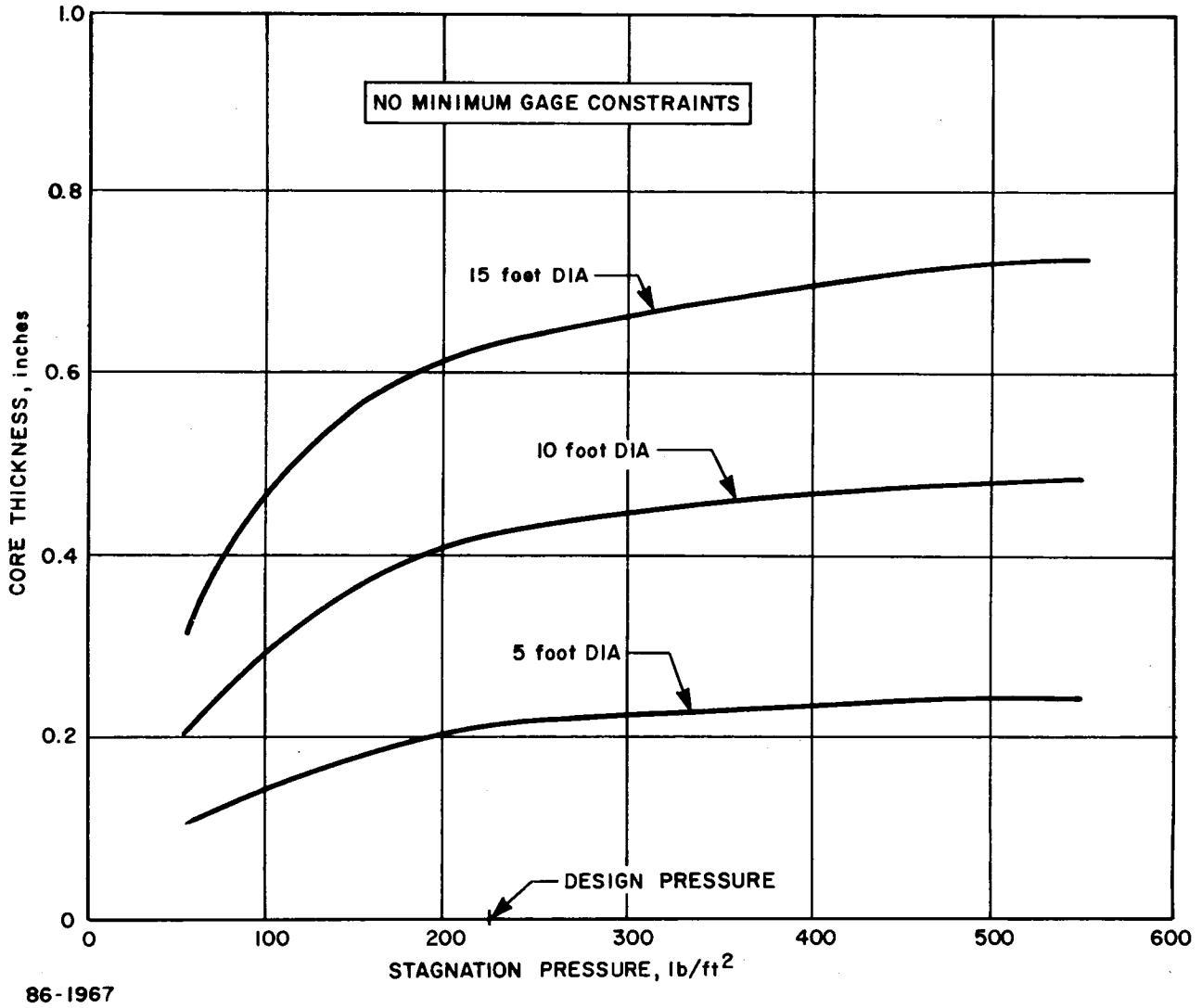

Figure 256 CORE THICKNESS VERSUS STAGNATION PRESSURE FOR BLUNT CONE--ALUMINUM

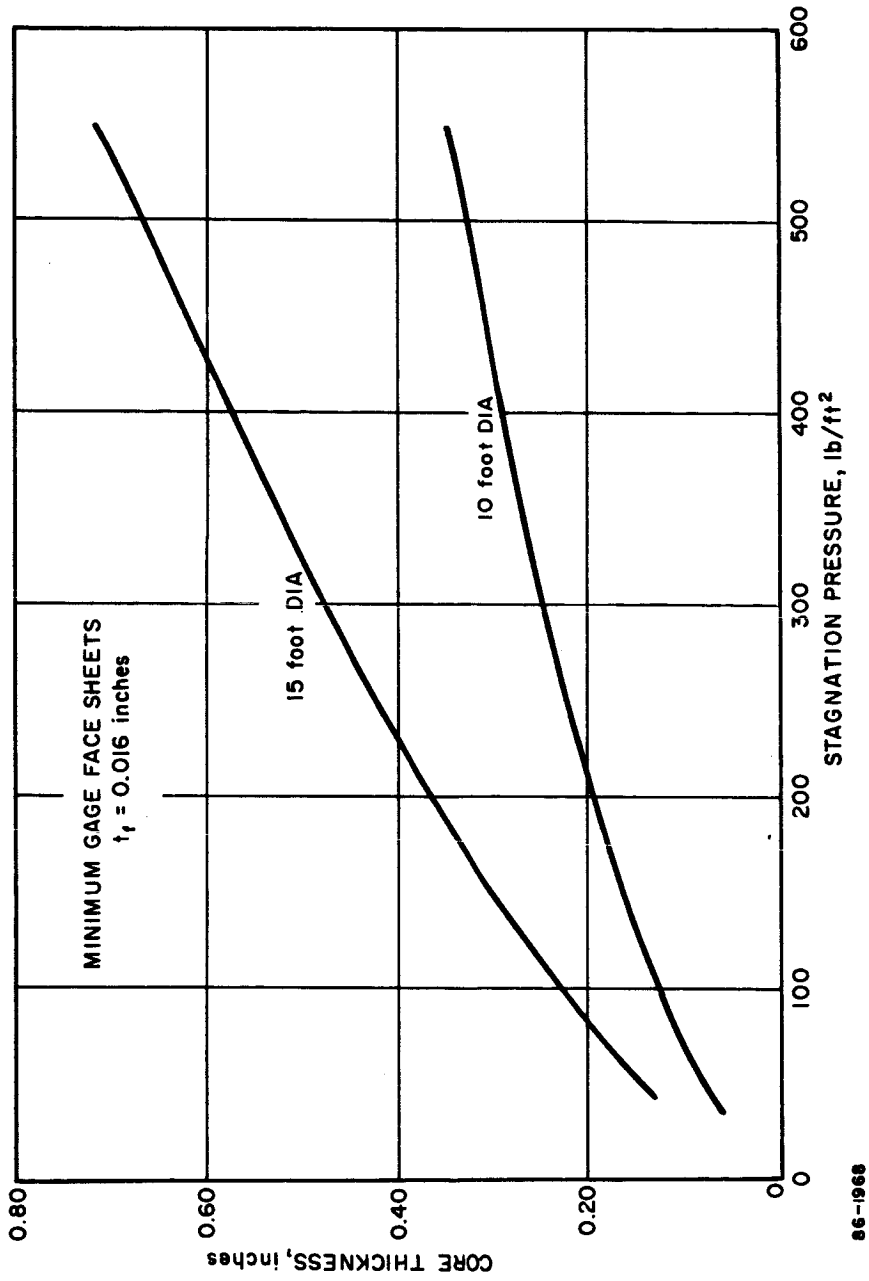

Figure 257 BLUNT CONE CORE THICKNESS VERSUS STAGNATION PRESSURE--
ALUMINUM F.S.

6.3.2 Design Concept Analysis and Tradeoff

6.3.2.1 Entry Shell Structure

System requirements dictated the selection of a base diameter of 15 feet for the conceptual design. Early tradeoff studies of de-orbit and entry conditions were conducted over a wide range of entry velocities, trajectory angles, angles of attack and body angular rates. Variation of these parameters produced variations in entry capsule loading conditions which can be characterized in terms of the stagnation pressure and angle of attack at the peak axial and normal loading points on a given trajectory.

The parametric results of paragraph 6.3.1 aided the selection of the structural concept and material and determined preliminary structural requirements. The design concept was then analyzed parametrically, but with the additional considerations of shell bending stresses and the effect of unsymmetrical pressure distribution due to angles of attack.

To design the entry shell parametrically for a range of angles of attack and stagnation pressures would require an excessive amount of computational effort, since both stress and buckling criteria would have to be satisfied at a large number of discrete angles attack and stagnation pressures.

In order to reduce this effort, a study was made which demonstrated that a satisfactory design would evolve if the structure was designed for a symmetrical pressure distribution with a stagnation pressure corresponding to the angle of attack case. This result appears to be true for angles of attack less than 30 degrees. The results are shown later in this section.

1. Symmetrical Loading -- The 15-foot base diameter design concept was analyzed for symmetrical pressure distribution with a stagnation pressure ranging from 100 to 400 lb/ft^2. A schematic of the shell is shown in Figure 258. The core depth was varied to satisfy the buckling criteria for the applied pressure. The von Mises yield criterion for a biaxial stress condition was used to compare the shell stresses to the allowable stress of the material.

The von Mises effective stress as a function of stagnation pressure is given in Figures 259, 260, and 261 for 100, 200, and 358 lb/ft^2 respectively. The 358 lb/ft^2 stagnation pressure corresponded to the design pressure for the 40 rpm no despin failure mode entry condition. The results show that the stress distribution in the entry shell due to symmetrical entry aerodynamic pressure is well below the allowable stress. The symmetrical pressure distribution used in the analysis is given in Figure 262. The core depth used in Figure 261 was obtained from the data in Figure 257. The core depths used for 100 and 200 lb/ft^2 are based on an earlier less conservative analysis and therefore are less than those given in Figure 257. Using the increased core depths indicated by Figure 257 would result in even lower effective stresses.

The actual stresses, given in Figure 263 will be compared to the results of an analysis of unsymmetrical loading in the following subsection.

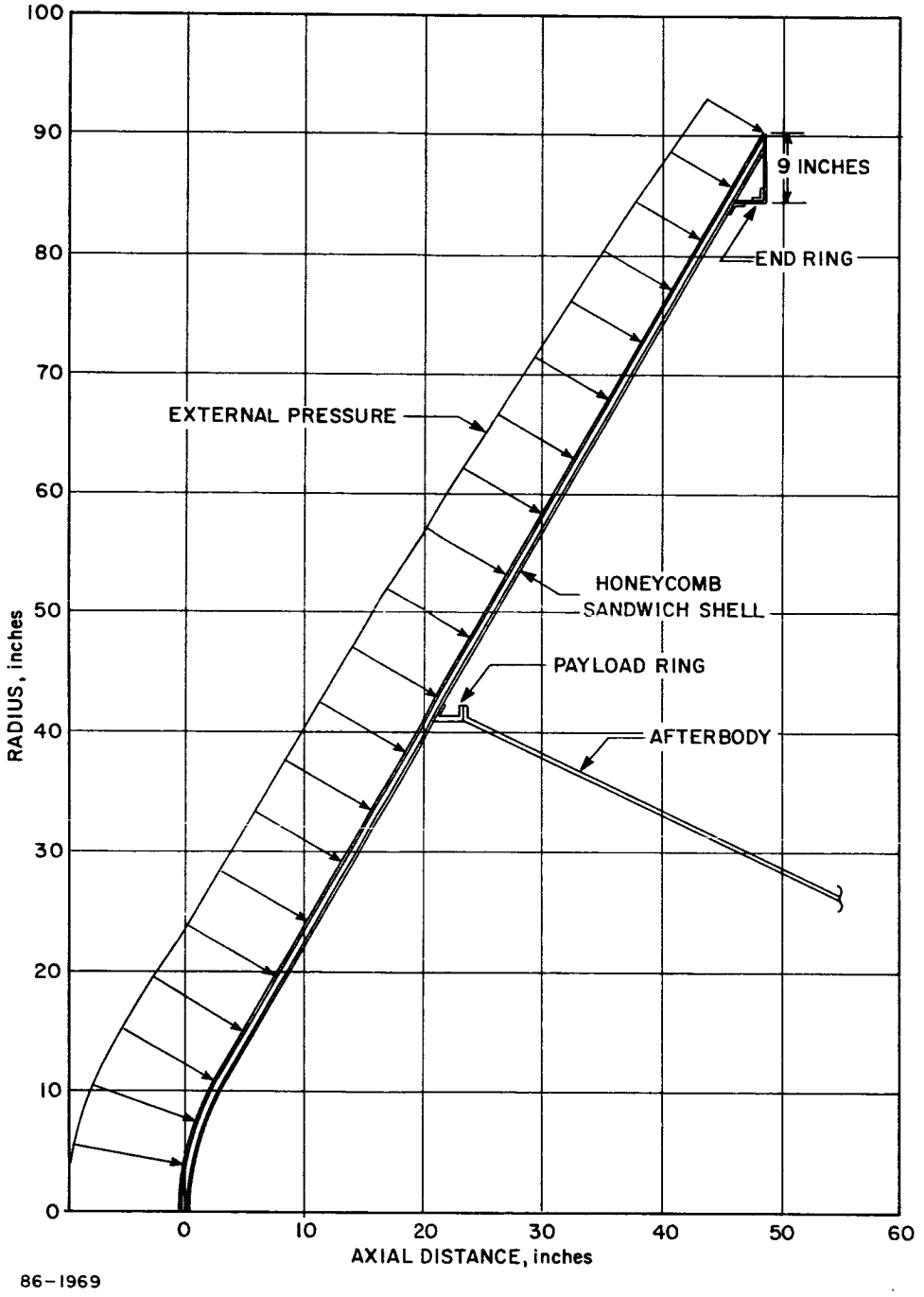

Figure 258 SCHEMATIC OF BLUNT CONE SHELL

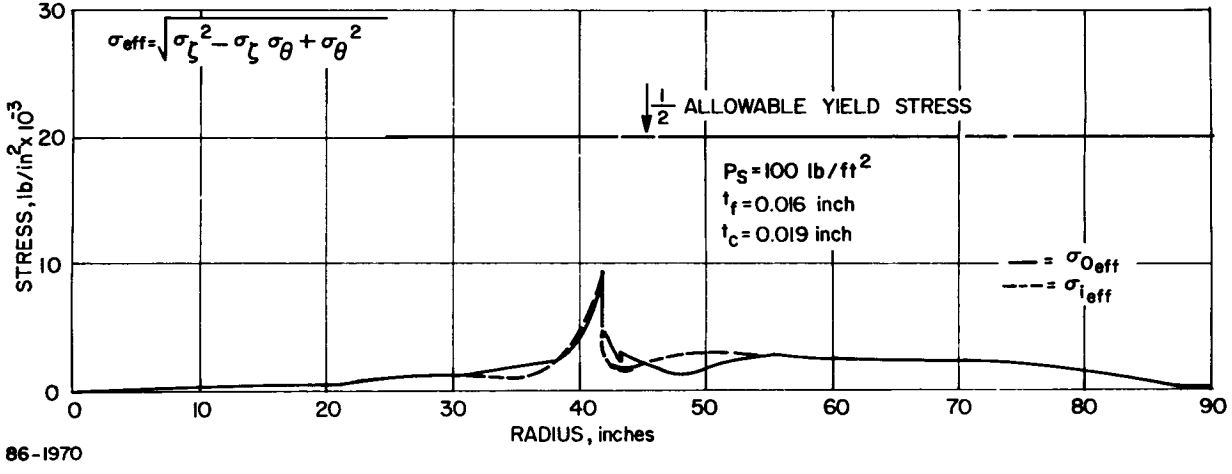

Figure 259 COMPARISON WITH THE VON-MISES YIELD CRITERIA FOR BIAXIAL STRESSES

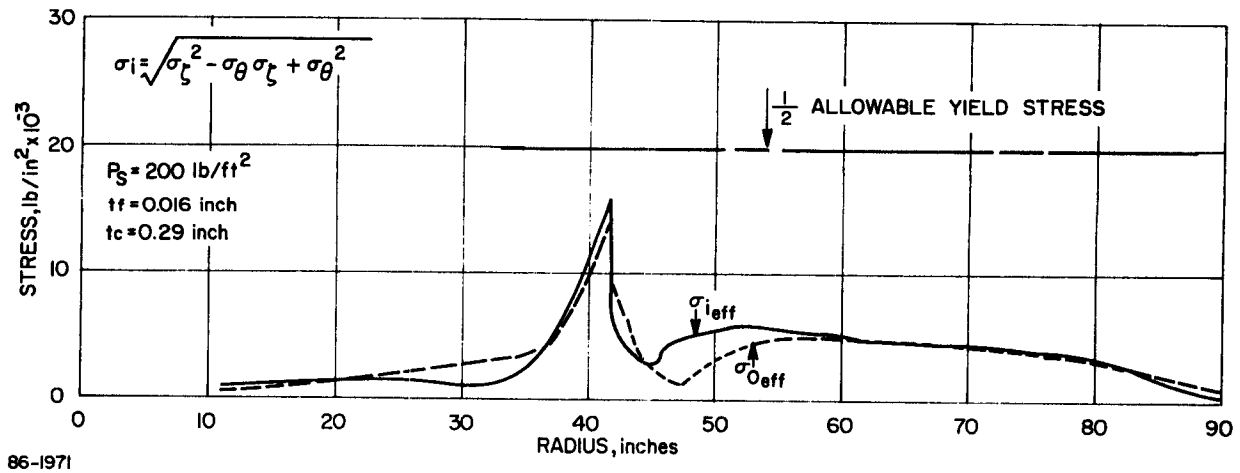

Figure 260 COMPARISON WITH THE VON-MISES YIELD CRITERIA FOR BIAXIAL STRESSES

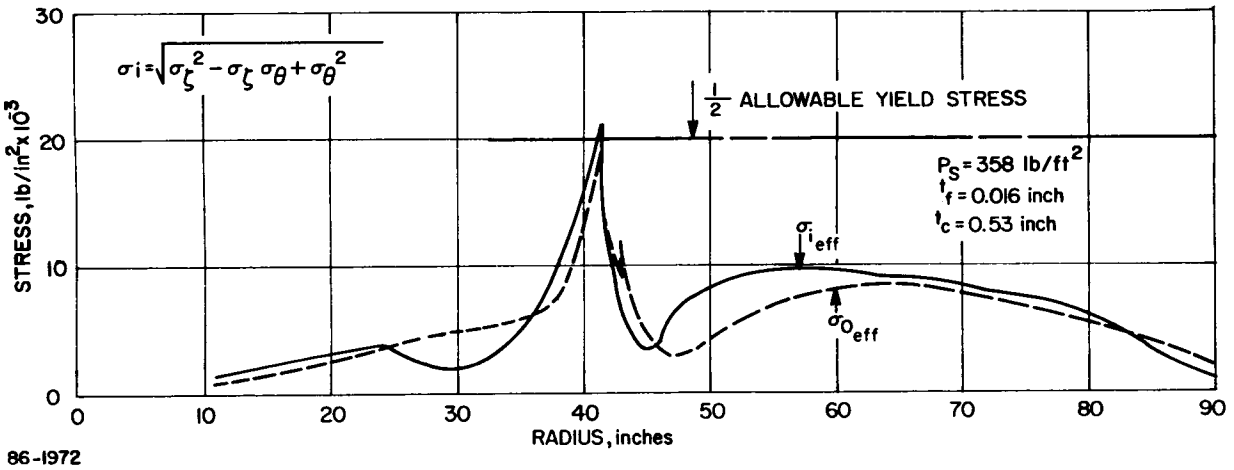

Figure 261 COMPARISON WITH THE VON-MISES YIELD CRITERIA FOR BIAXIAL STRESSES

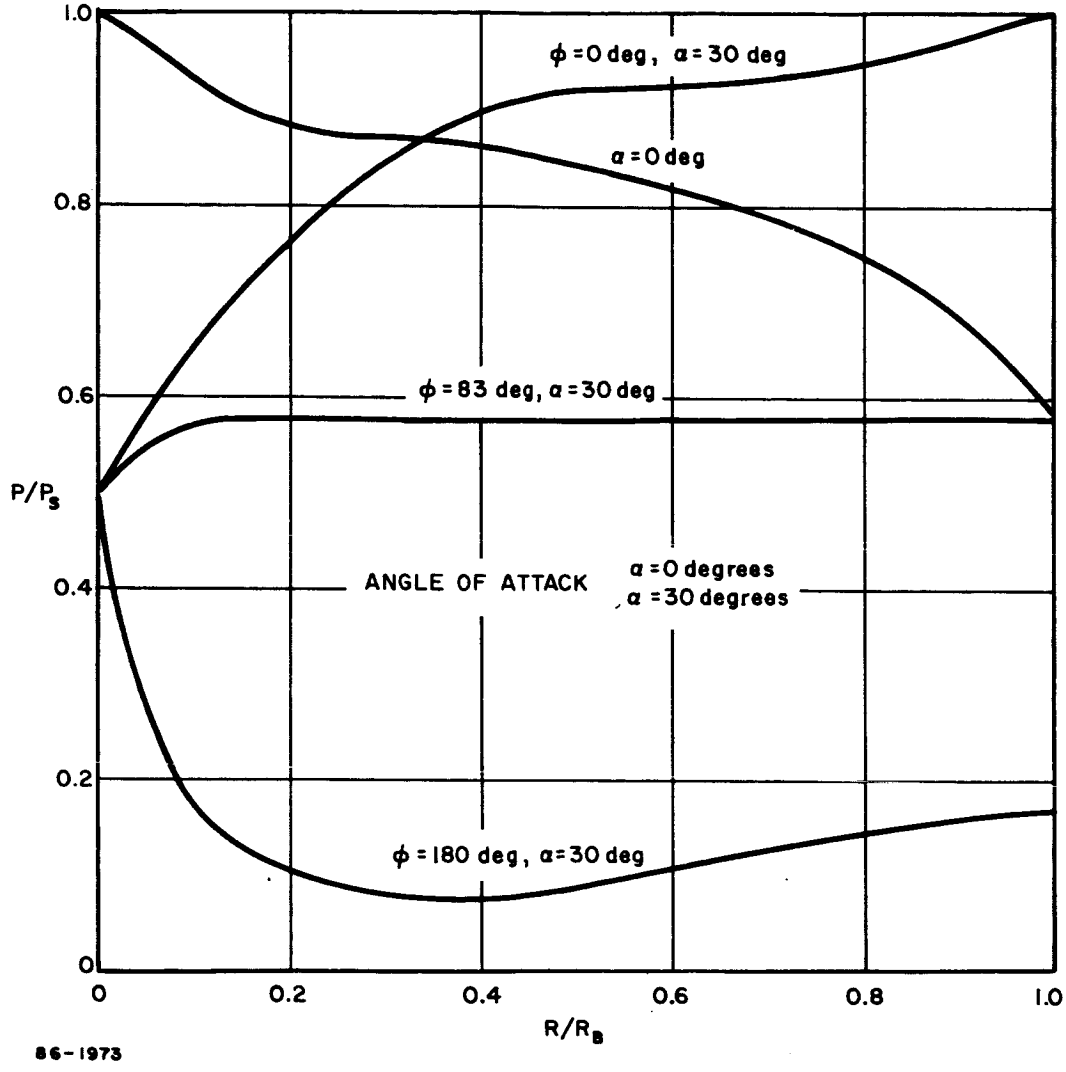

Figure 262 PRESSURE DISTRIBUTION--ANGLE OF ATTACK--$\alpha = 0^\circ$ AND $\alpha = 30^\circ$

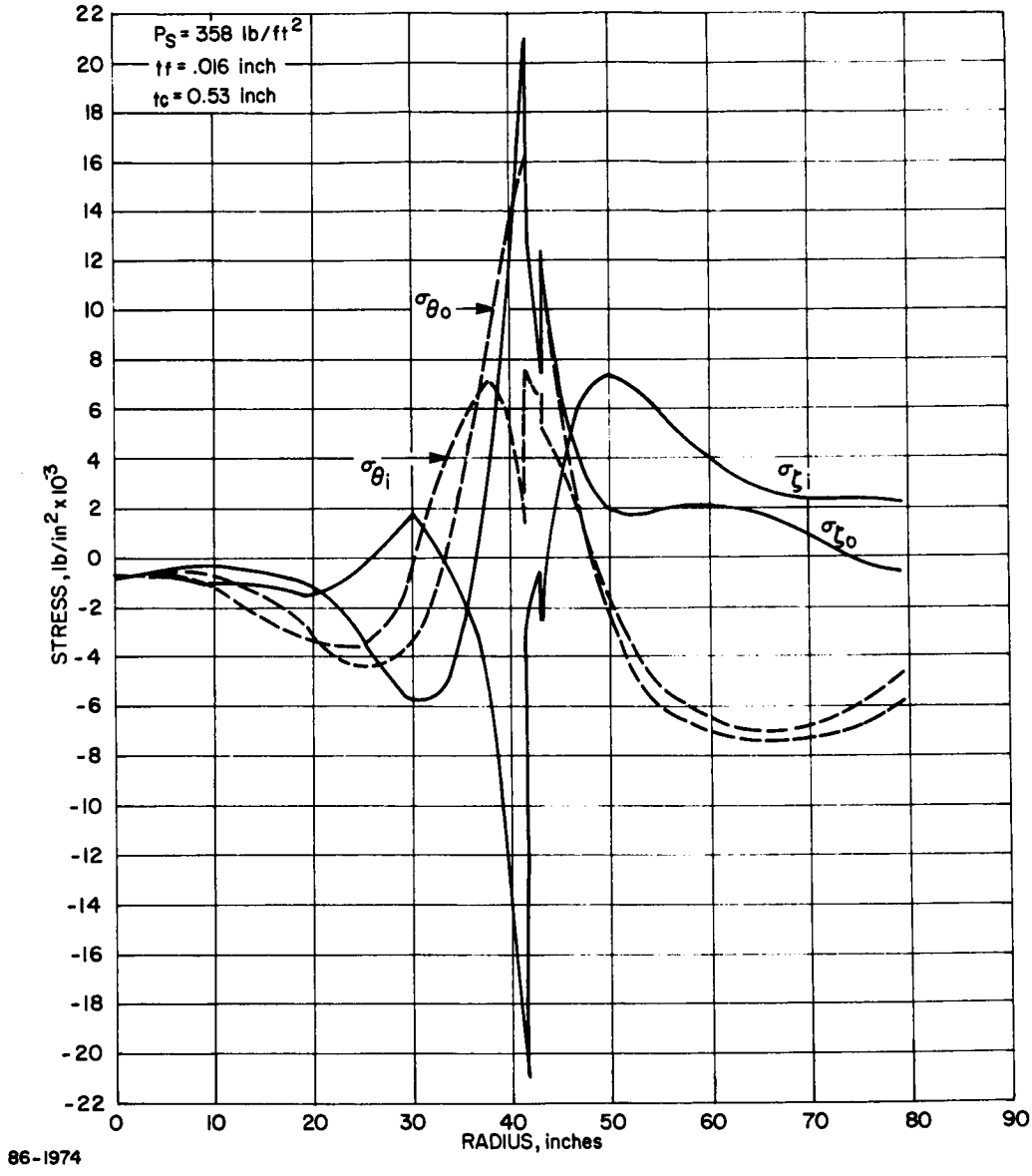

Figure 263 BLUNT CONE STRESS DISTRIBUTION

It should be noted that using the von Mises biaxial yield criterion is important for this type of design, when the stress level is near the allowable stress, because the stresses have opposite signs. When the biaxial stresses are equal and of opposite sign the effective stress is $\sqrt{3}$ times the uniaxial value.

2. Unsymmetrical Loading -- As discussed earlier, the parametric analysis and design of the entry shell for a range of angles of attack and stagnation pressures are formidable tasks. An analysis of the conceptual design for the 40-rpm no-despin entry condition showed that the effort could be simplified by merely designing the shell for a symmetrical distribution with a stagnation pressure corresponding to the angle of angle condition. In other words, the trajectory was examined to determine what appeared to be the worst combination of angle of attack and dynamic pressure. The point is usually where the instantaneous maximum angle of attack occurs close to the peak dynamic pressure. These conditions for the 40 rpm, no-despin case are a stagnation pressure of 358 lb/ft^2 and an angle of attack of 30 degrees.

The circumferential pressure distribution was approximated by a three-term truncated Fourier series, i.e., $p/p_s = 0.620 + 0.353 \cos \theta + 0.027 \cos 2\theta$. For this solution, the Fourier coefficients were assumed to be constant with respect to axial distance. This approximation was reasonably accurate for a radius ratio, R/R_b, greater than 0.4, where the principle effect of the unsymmetrical loading would be felt. The SABOR computer program described in paragraph 7.1.1.2 was used to obtain solutions for the unsymmetrical loading. The locations of the nodal circles are given in Figure 264.

The meridional and circumferential stress distributions are given in Figures 265 and 266.

The unsymmetrical loading increases the tensile meridional stress on the windward side and reduces it on the leeward side. The axial stress resultant is approximately zero on the leeward side, hence no instability will occur in this region. The circumferential stresses exhibit their highest compressive value on the windward side. However, if these stresses are compared to the stresses due to a symmetrical distribution with the same stagnation pressure, (see Figure 263), there is no increase in compressive stresses observed due to unsymmetrical loading, therefore the unsymmetrical loading at an angle of attack of 30 degrees is not more critical than symmetrical loading for the same stagnation pressure. This is the result of the fact that the total stress is obtained from the superposition of the stresses induced by the three Fourier components. The symmetrical component has been reduced to 62 percent of the value for pure symmetrical loading. When the

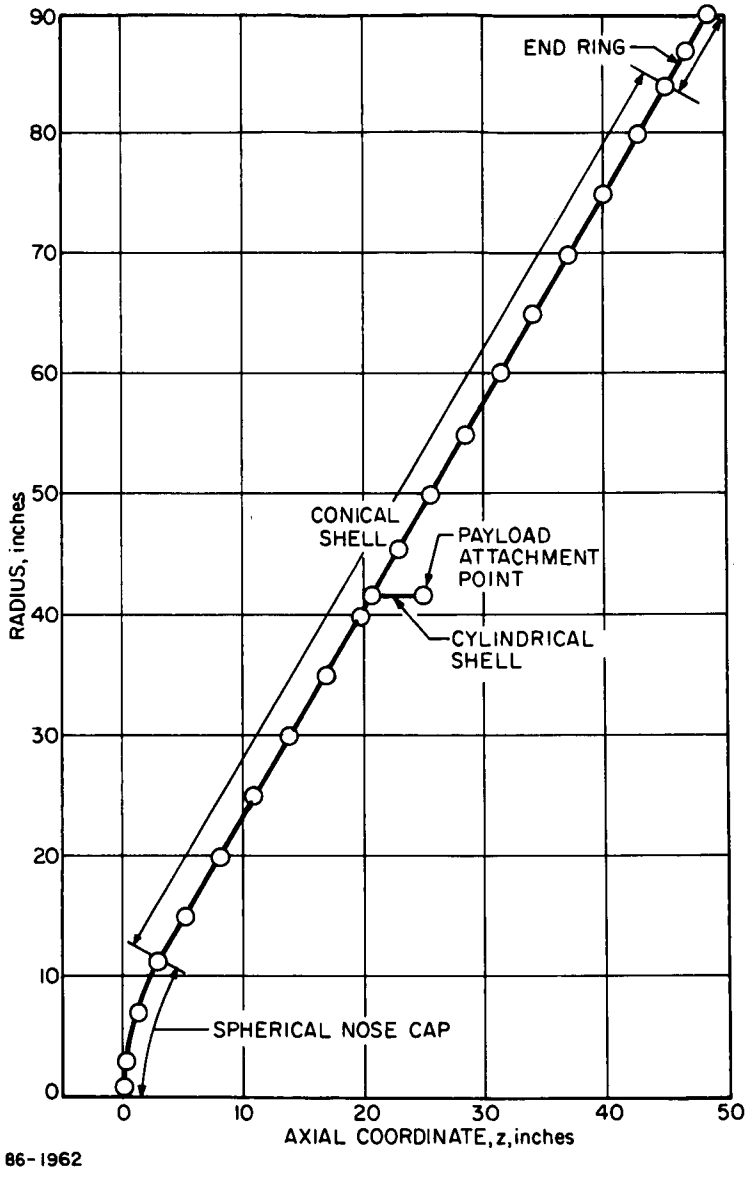

Figure 264 BLUNT CONE ANALYTICAL MODEL FOR UNSYMMETRIC LOADS ANALYSIS

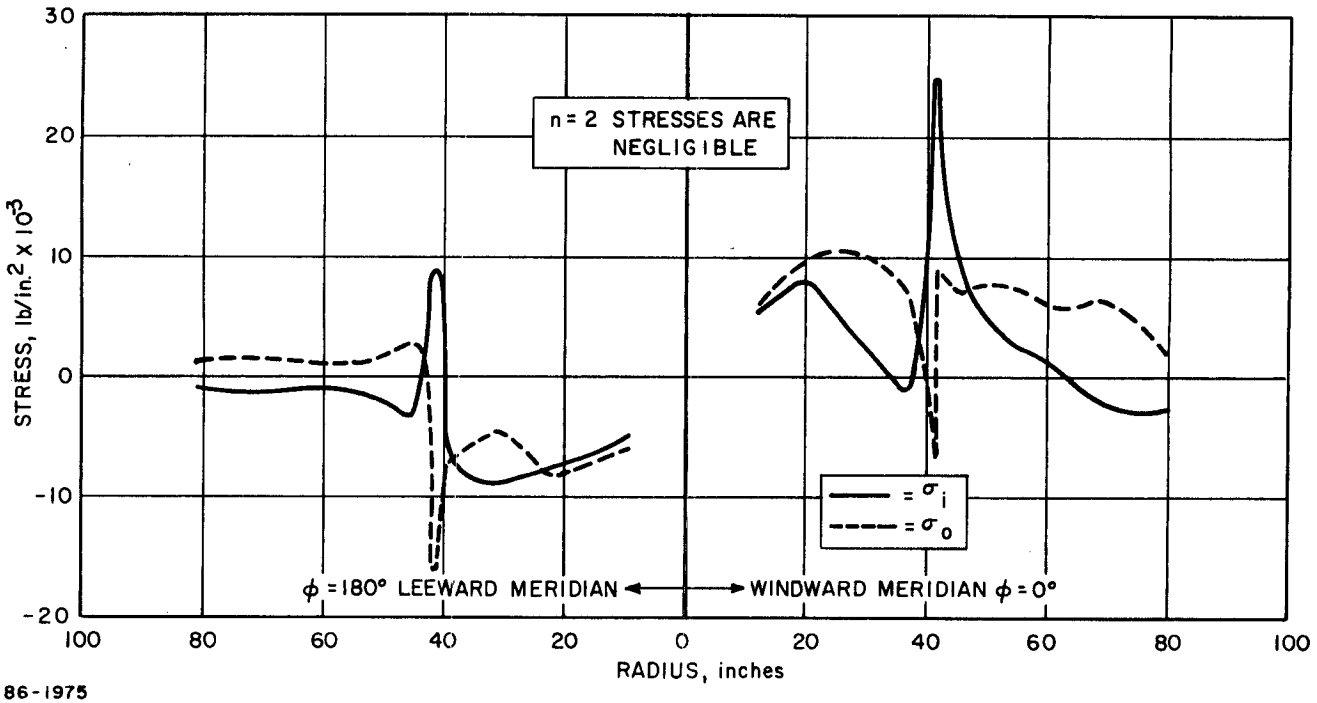

Figure 265 MERIDIONAL STRESS DISTRIBUTION UNSYMMETRICAL LOADING

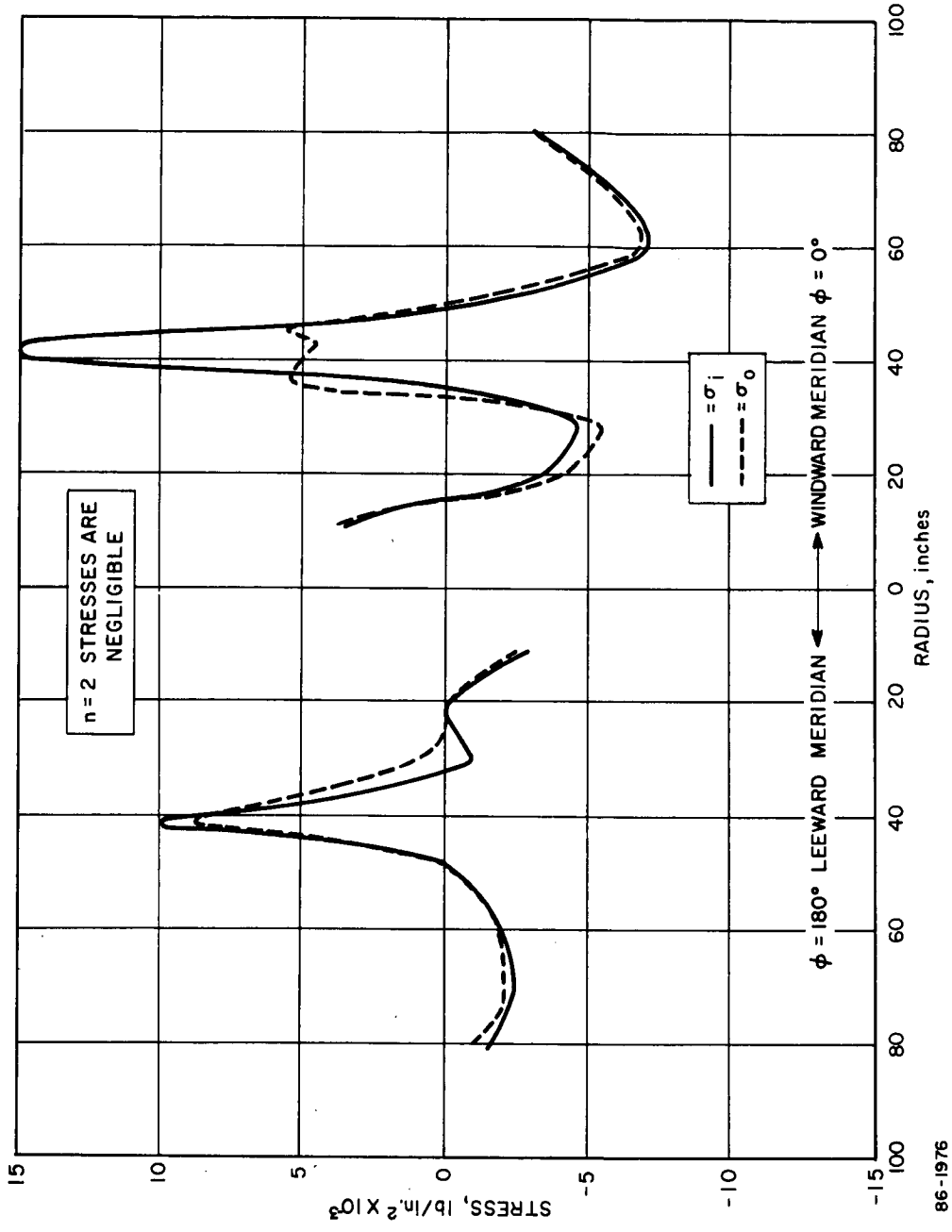

Figure 266 CIRCUMFERENTIAL STRESS DISTRIBUTION UNSYMMETRICAL LOADING

unsymmetrical components are superimposed on the symmetrical component the critical circumferential stress is not exceeded. This result was applied specifically to 30 degree angle of attack and generally is a good approximation down to 10 degree angle of attack.

A later analysis conducted at 10 degrees showed that the symmetrical component had decreased only about 2 percent; hence, superposition of the unsymmetrical component produced a small negative margin of safety for the design being investigated. The second harmonic of the loading, i.e., cos 2θ, produced negligible stresses in the shell and could be ignored in a preliminary analysis for angles of attack less than at least 30 degrees.

In summary, the analysis of angle of attack effects demonstrated that up to at least 30 degree angle of attack, a symmetrical analysis of the entry shell using the stagnation pressure corresponding to the angle of attack would yield a satisfactory design capable of withstanding the unsymmetrical loading. The curve of shell weight versus stagnation pressure given in Figure 250 is reasonably accurate for preliminary design purposes up to at least an angle of attack of 30 degrees.

6.3.2.2 Conical Shell End Ring

The end-ring shown in Figure 258 had a 9 inch depth and its wall thickness varied nearly linearly with stagnation pressure. Its wall thickness was .025 inch for a 358 lb/ft^2 stagnation pressure. The stiffness requirements were determined using an earlier version of the analysis described in paragraph 7.1.2.1. The inextensional shell-ring stability was also analyzed for the effect of unsymmetrical loading by adding to the energy expression the additional work done by the cos 2θ component of the pressure. No appreciable effect was noted because of the small magnitude of the cos 2θ component of the pressure and because the magnitude of the symmetrical component was reduced to 62 percent at an angle of attack of 30 degrees as noted before. The end ring was also designed for symmetrical loading with a stagnation pressure of 358 lb/ft^2. If the symmetrical component had remained at 358 lb/ft^2 then a small unsymmetrical cos 2θ loading would trigger large displacements.

6.3.3 Detailed Reference Structural Design and Performance Evaluation

6.3.3.1 Overall Structural Design Description

Detailed performance calculations were performed on the reference design concept. The entry mode is a tumbling entry with a 15,200 ft/sec velocity, -16.0 degree entry angle and 179 degree entry angle

of attack. The loading conditions were given in Table XXXIX. A detailed description of the entry shell, suspended capsule structure, and adapter structure is given in Volume V, Book 6. The details of the structural configurations were shown in Figures 246, 248, and 249.

Detailed weight breakdowns of the structure are given in Tables XLV, XLVI, and XLVII.

6.3.3.2 Entry Shell Structure

1. Static Analysis -- The symmetrical and unsymmetrical stress distributions are given in Figure 267, 268, and 269. The stress distributions correspond to the pressure distributions in Figure 270.

TABLE XLV

ENTRY SHELL STRUCTURE - DETAIL WEIGHT BREAKDOWN

	Weight (pounds)
Face sheets	94.5
Core	39.5
Splice Plates	7.5
Doublers	14.5
Bond	35.0
Base Ring	51.6
Mounting Ring	12.0
Nose cap Ring	2.4
Aluminum Nose cap	25.6
Inserts and attachments	3.0
Total - Entry Shell Structure (no contingency)	285.6
Contingency	57.4

TABLE XLVI

SUSPENDED CAPSULE STRUCTURE - DETAIL WEIGHT BREAKDOWN

	Weight (pounds)
Rings	25.0
Beams and Longerons	30.0
Shells and Covers	25.0
Instrumentation Module structure	14.4
Telecommunication module structure	14.4
Power supply module structure	14.4
Total - suspended capsule structure (no contingency)	123.2
Contingency	57.4

TABLE XLVII

FC - F/S ADAPTER STRUCTURE - DETAIL WEIGHT BREAKDOWN

	Weight (pounds)
Skin	33
Two flanges	21
Hat section	19
Splice plate	5
Hardware	10
Total - adapter structure	88
Contingency	33

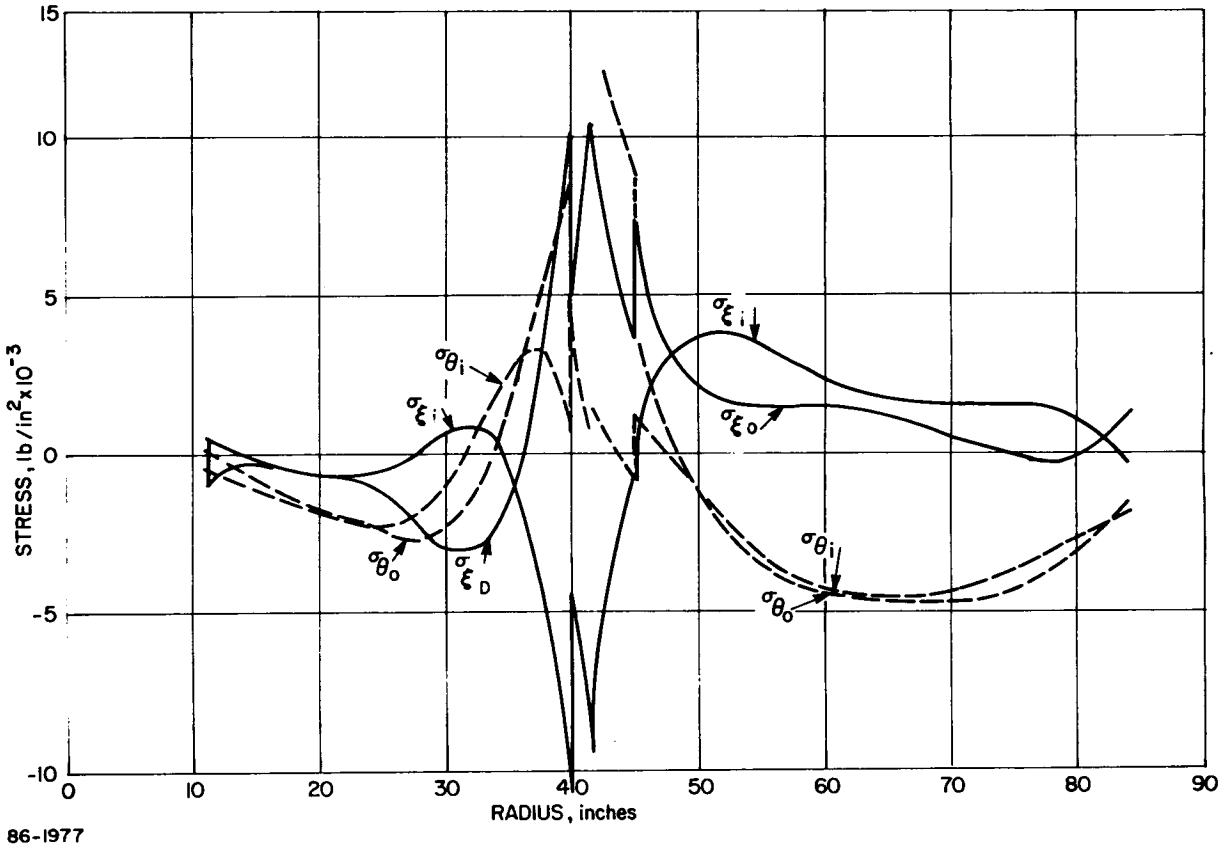

Figure 267 BLUNT CONE -- STRESS VERSUS RADIUS SYMMETRIC ANALYSIS

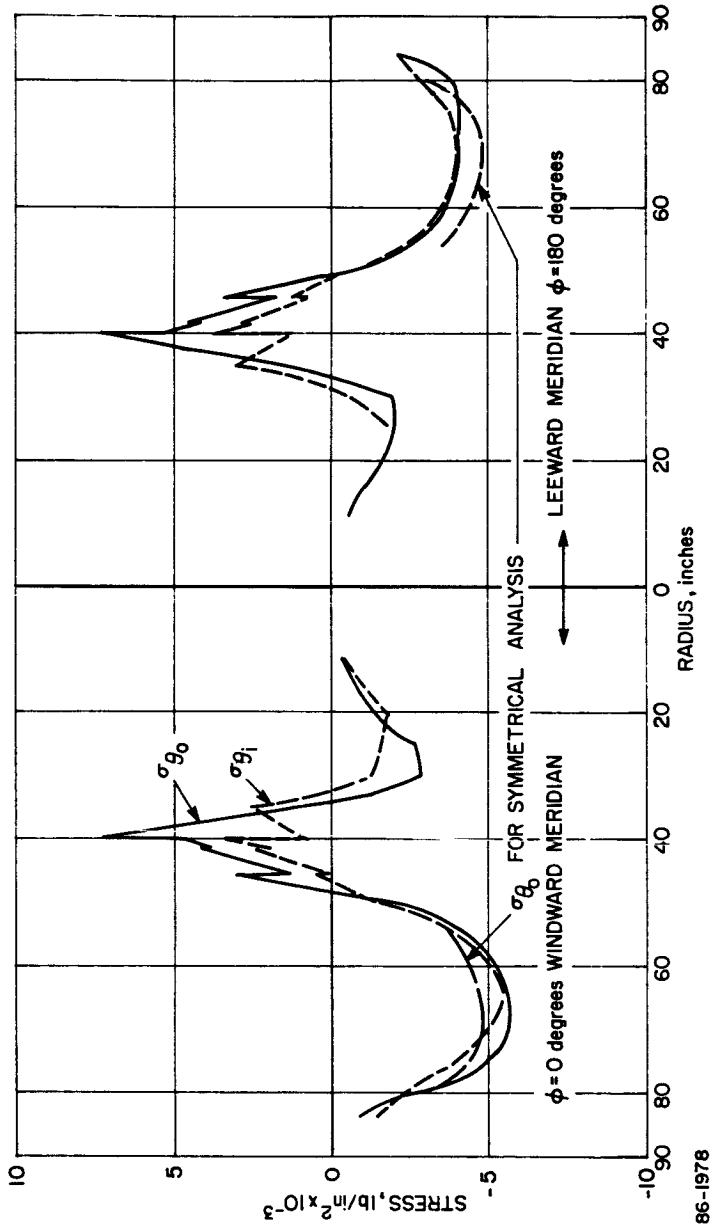

Figure 268 BLUNT CONE -- UNSYMMETRICAL LOADS STRESS VERSUS RADIUS

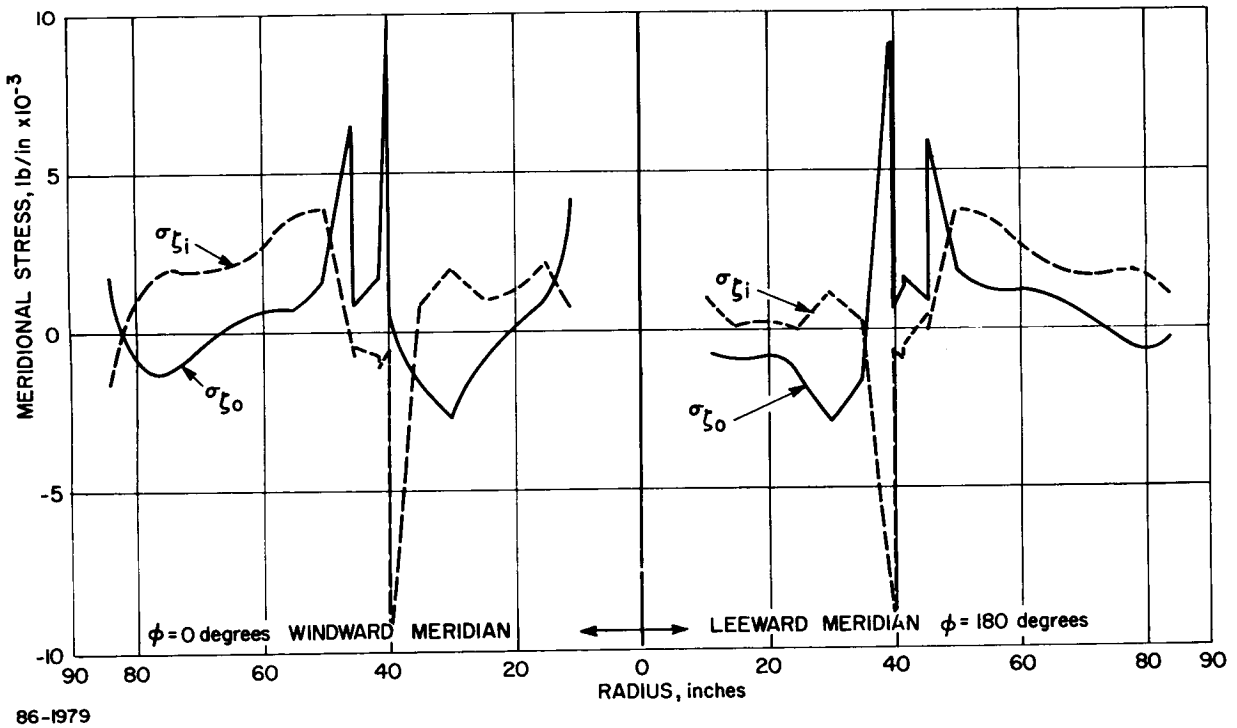

Figure 269 BLUNT CONE -- UNSYMMETRICAL LOADS MERIDIONAL STRESS VERSUS RADIUS

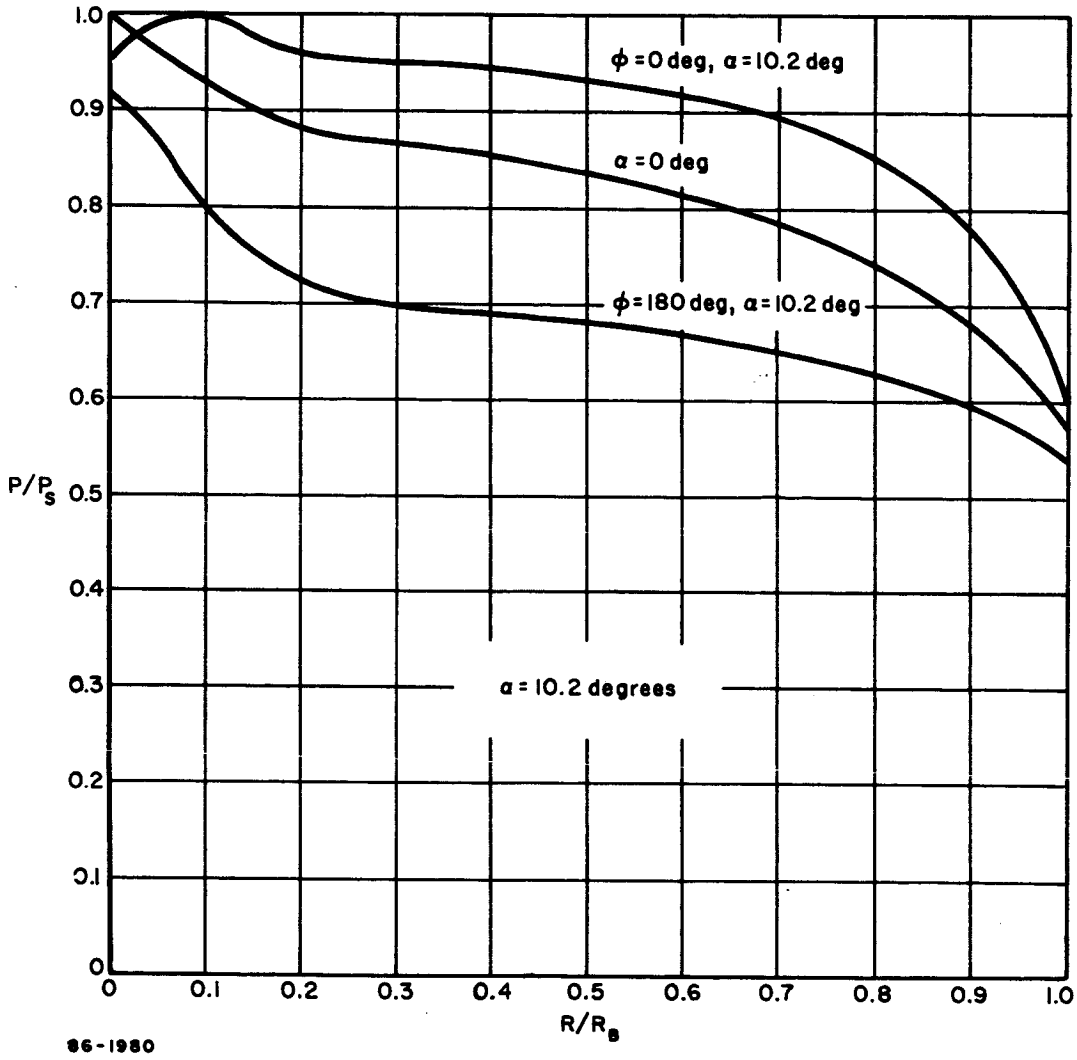

Figure 270 BLUNT CONE--SYMMETRICAL AND UNSYMMETRICAL PRESSURE DISTRIBUTION

Note that the unsymmetrical circumferential distributions on the windward side in Figure 268 exceeds the corresponding symmetrical circumferential stress distribution. This results from the very small reduction of the symmetrical component plus a much larger increase of the cos θ component in the pressure distribution at an angle of attack of 10.2 degrees as illustrated in Figure 271. Since the nominal core depth of 0.4 inch for the conceptual design was based on a symmetrical stress distribution, the increased circumferential stress results in a -0.09 margin of safety for buckling for the design loads. The selection of the core depth is based on a buckling criterion discussed in paragraph 7.1.2.1 which also includes the effect of axial tension resulting from payload inertia entering the shell at a radius of 40 inches. The axial tension increases the critical buckling pressure by 9.0 percent.

The von Mises effective stress was computed from the symmetrical stress distribution and compared to the allowable stress in Figure 272. As can be seen, the stress level is well below even one-half the allowable stress. The shell stress analysis included the end ring, payload ring and nose cap ring in the analysis. Since the ring elements have complex cross sections, it was possible only to simulate their stiffness in the shell solution in the manner described in paragraph 7.1.1.1. As a result the influence of the ring elements on the stress distribution in the shell and the moments and forces acting on the ring was accurately computed; however, the stresses in the ring could not be computed directly in the computer program, hence were not shown for the end-ring.

The stresses are not shown in the nose cap because the thickness was selected by ballast rather than structural requirements. The resulting stress level was too low to be seen on the scale of the graph.

The structural temperature at the time the computations were made was assumed to be 300°F. Subsequent heat transfer calculations predicted the temperature on the maximum heating trajectory to be 300°F or greater but only 150 degrees at the time of peak loading for the design trajectory. The lower structural temperature had negligible effect on the structural analysis results because the important mechanical properties of aluminum are relatively constant in this range of temperatures.

The end ring stiffness properties were determined by the analysis given in paragraph 7.1.2. The end ring base dimension was reduced to 6 inches to satisfy mechanical design requirements. This change required an increase in wall thickness to satisfy stiffness requirements with an accompanying increase in weight over that required for a 9-inch ring.

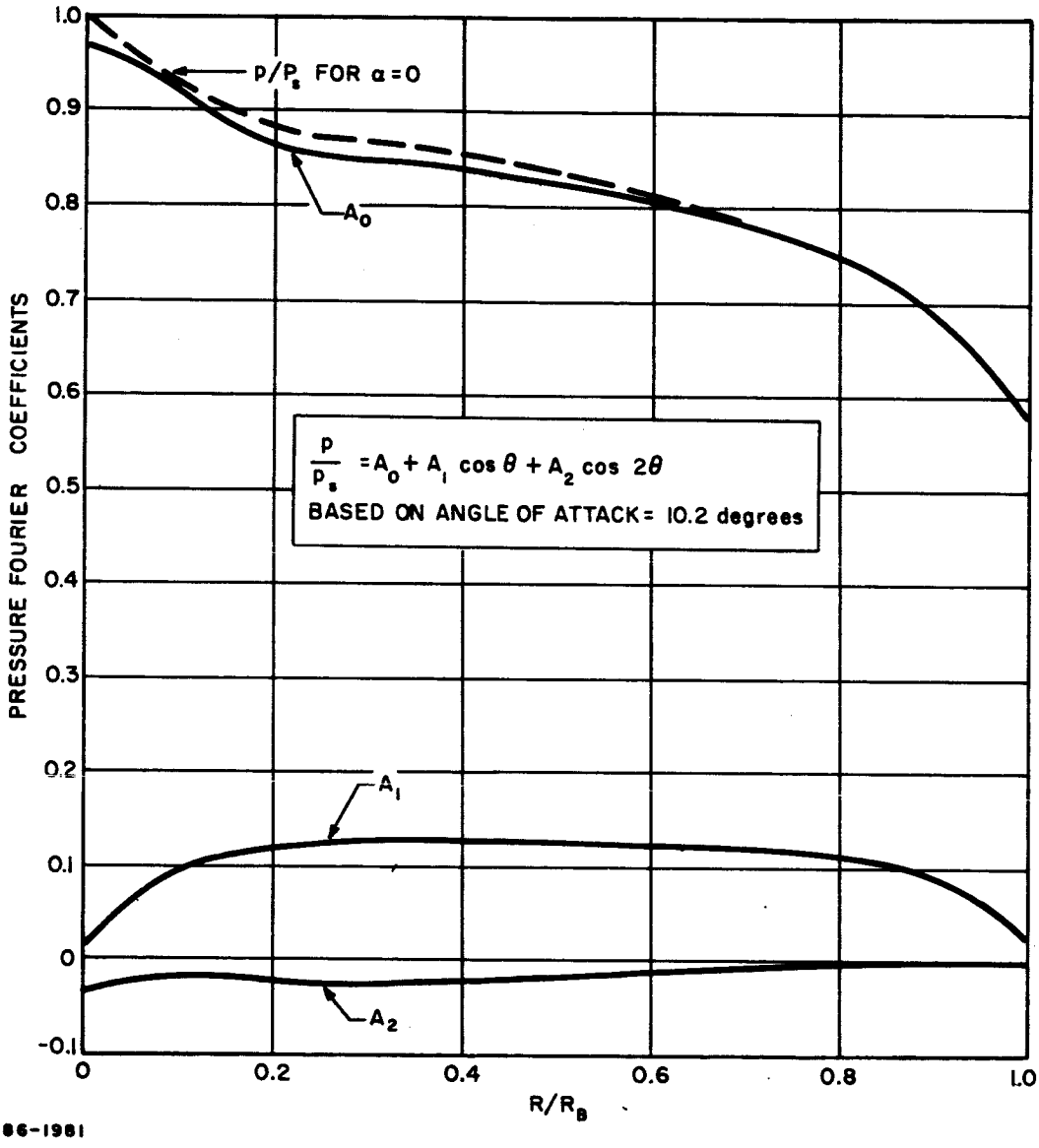

Figure 271 BLUNT CONE PRESSURE COEFFICIENTS UNSYMMETRICAL LOADS ANALYSIS

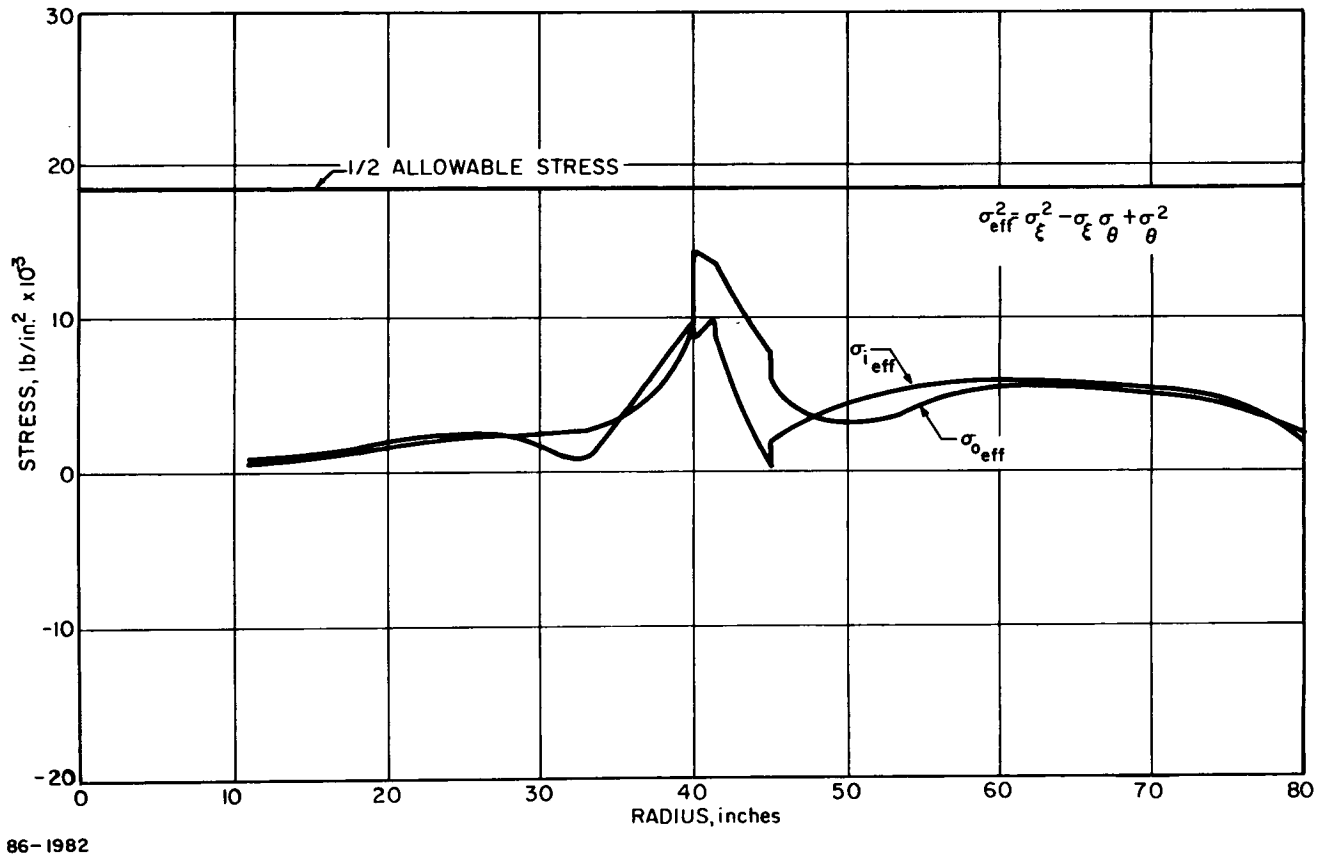

Figure 272 BLUNT CONE EFFECTIVE STRESS VERSUS RADIUS

The calculated stiffnesses as defined in paragraph 7.1.2.3, were $B_1 = 94.5 \times 10^6$, $B_2 = 56.3 \times 10^6$, $B_{12} = 32 \times 10^6$ and $C = 22.1 \times 10^6$ lb-in^2 for a wall thickness of 0.08 inch. The margin of safety for inextensional buckling of the shell-ring was computed to be 0.27 using a safety factor of 1.50.

A subsequent mechanical design change increased the base dimension to 7.0 inches. The margin of safety given in Table XLII was estimated to be 0.24 by scaling the stiffness properties of the 6-inch ring. The scaled stiffness properties for the 7-inch design were $B_1 = 110 \times 10^6$, $B_2 = 51 \times 10^6$, $B_{12} = 36 \times 10^6$ and $C = 20 \times 10^6$ lb-in^2 for a wall thickness of 0.05 inch.

The symmetrical shell stress analysis utilized a shell program which included the effect of shear deformations due to a weak sandwich core material. For the core depths and stiffness properties (0.4-inch depth, 3/16-inch cell, 0.002-inch ribbon) no significant difference was observed between the results of assuming a rigid core and those using the actual core properties.

The computed core shear stress distribution is shown in Figure 273. The shear stress is well below the allowable shear stress of the core material both parallel and perpendicular to the ribbon direction.

Symmetrical radial and axial displacements shown in Figures 274 and 275 and are small enough in magnitude to have no effect on the aerodynamic performance. The unsymmetrical tangential displacement at the meridian 90 degrees from the windward represents the beam bending displacement mode of the blunted cone. Figure 276 shows that the displacement is essentially linear with respect to the radius with a maximum amplitude of 0.285 inch. Again this displacement does not appear to have any significant effect on flight capsule performance.

2. Dynamic Analysis

a. Description -- Vibration analyses have been performed for the conceptual design blunted-cone configuration using the method of analysis described in paragraph 7.2. The analytical model used is shown in Figure 277. This model also incorporates the end ring structure, the local stiffening in the area of the payload mounting ring, and the payload-support structure. Stiffness data on the interior structure of the capsule were not available in time to incorporate it in the dynamic model; hence the payload was assumed to be a rigid mass attached directly to the cylindrical attachment ring. Although this model does not give any information on the interior behavior of the capsule, resulting data on the shell vibrational characteristics should be satisfactory.

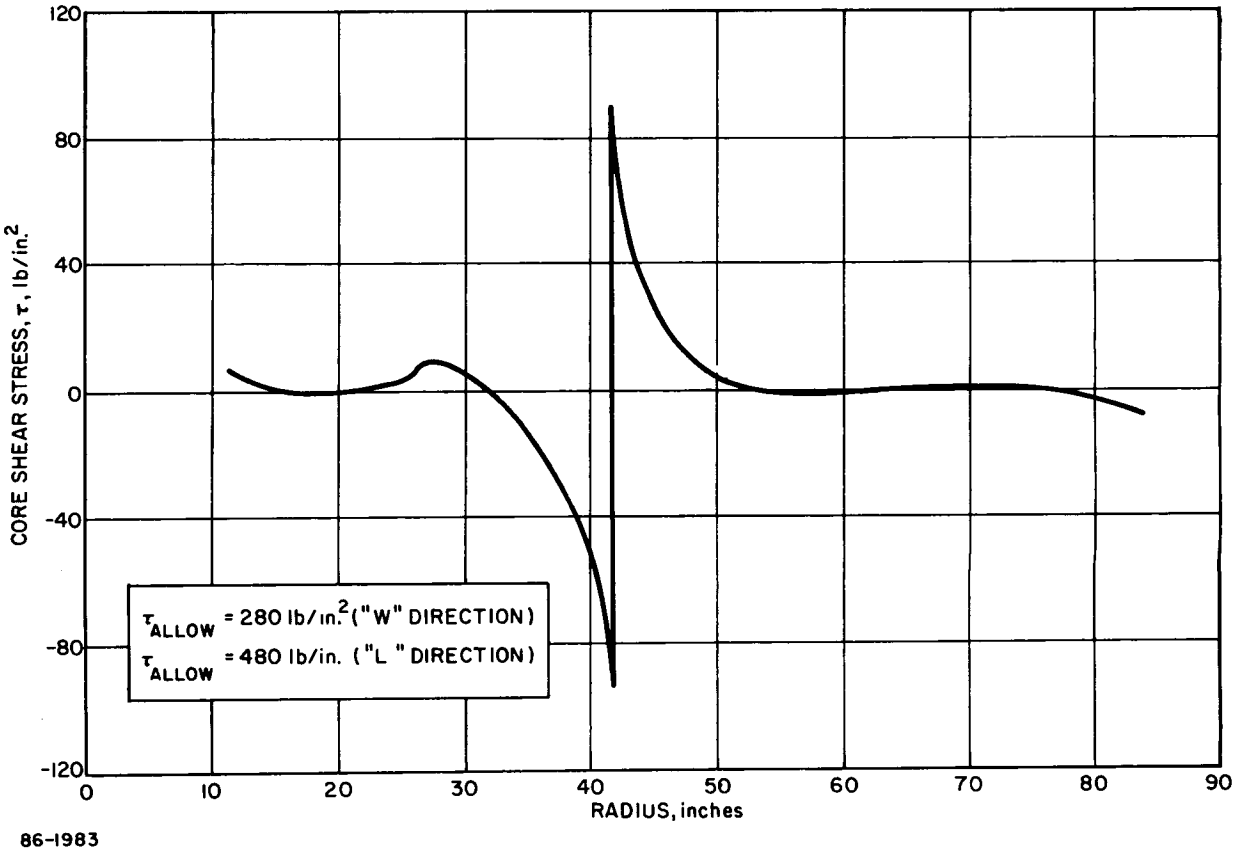

Figure 273 BLUNT CONE CORE SHEAR STRESS VERSUS RADIUS

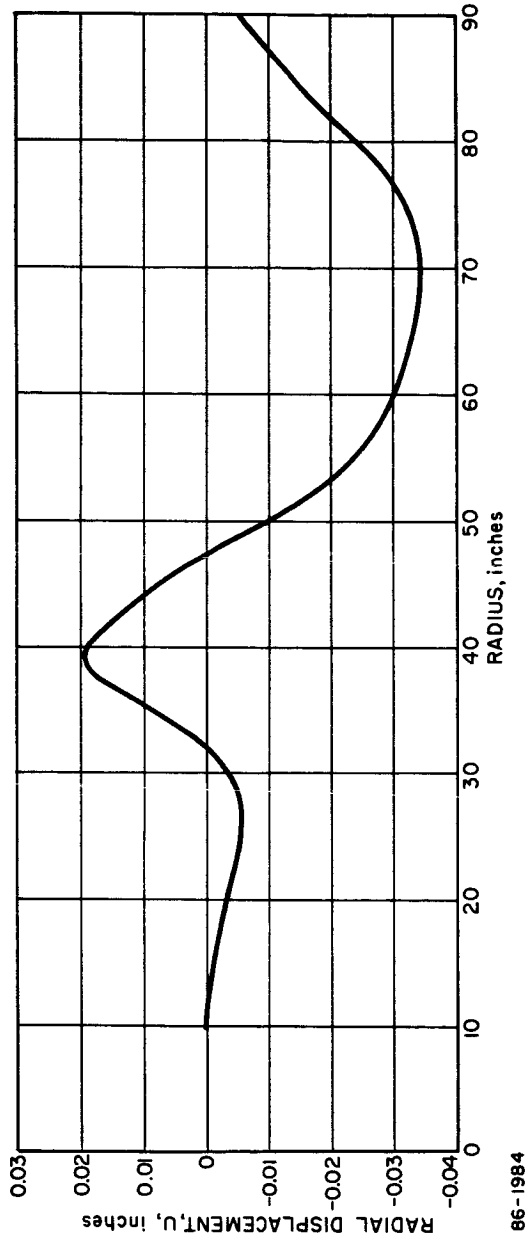

Figure 274 BLUNT CONE RADIAL DISPLACEMENT VERSUS RADIUS

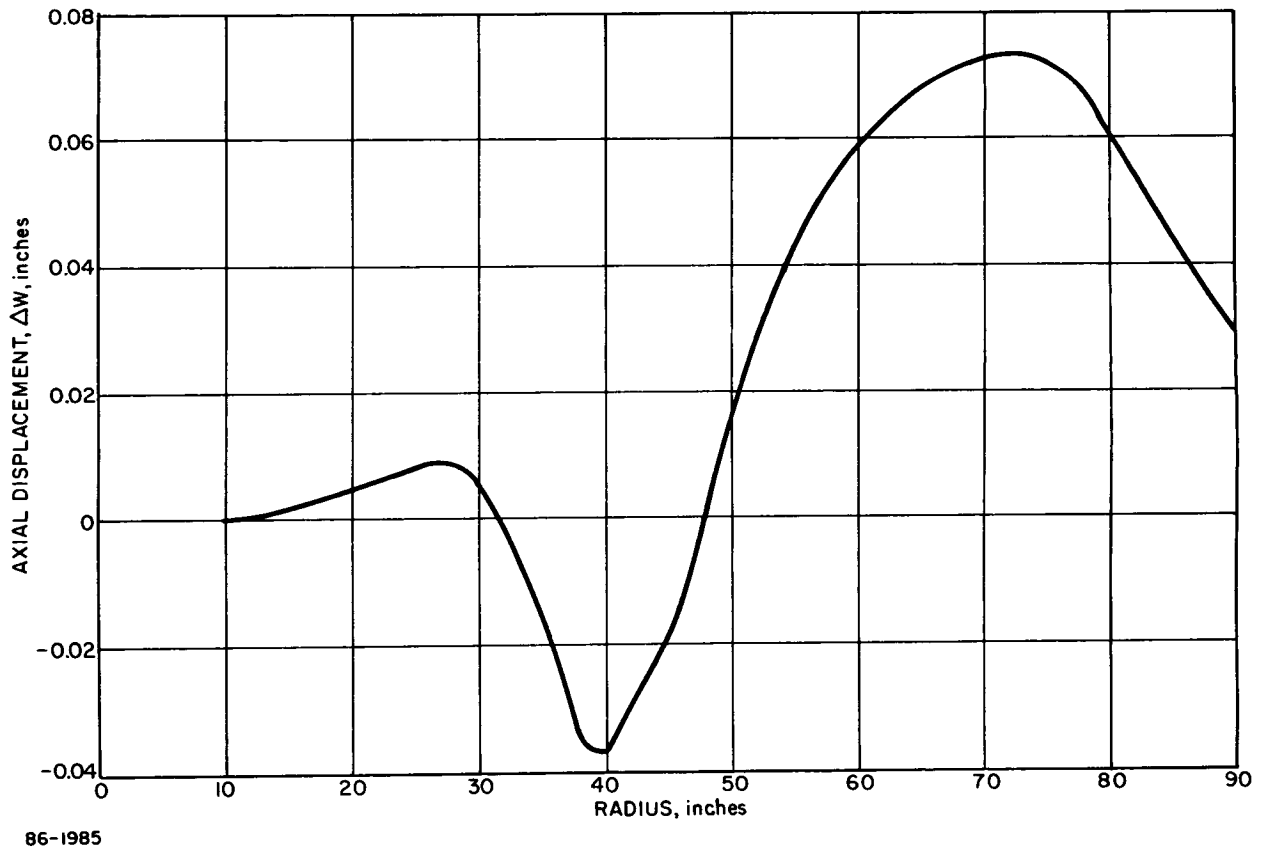

Figure 275 BLUNT CONE AXIAL DISPLACEMENT VERSUS RADIUS

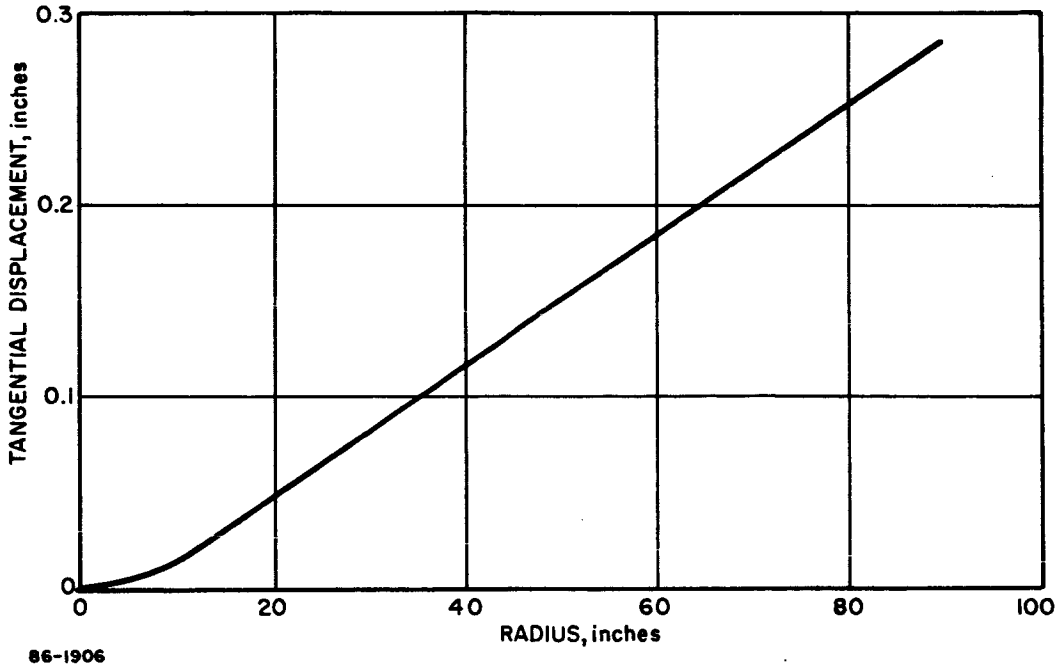

Figure 276 BLUNT CONE UNSYMMETRICAL LOADS TANGENTIAL DISPLACEMENT AT $\phi = 90^{\circ}$

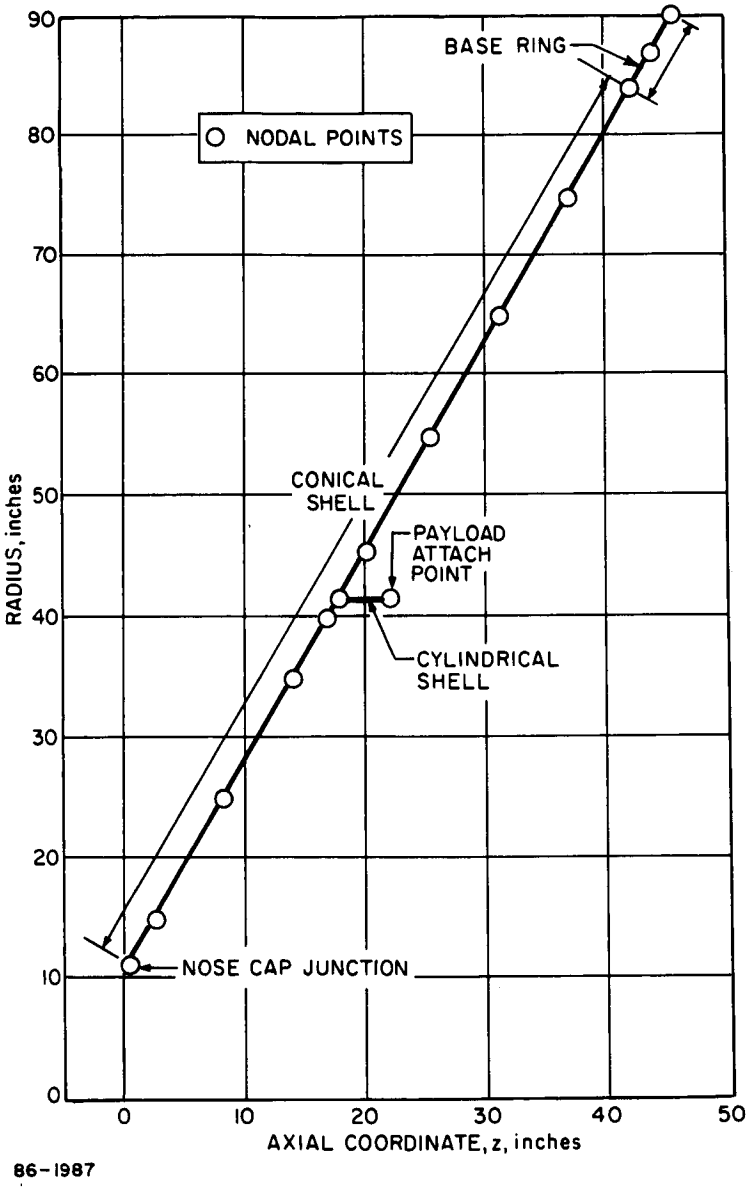

Figure 277 BLUNT CONE ANALYTICAL MODEL FOR VIBRATION ANALYSIS

The base ring structure has been idealized in this model as an equivalent homogeneous shell having the same bending and extensional properties as the ring. Also, the actual conical shell structure (made up of honeycomb sandwich, doublers, etc.) has been replaced by an equivalent homogeneous material, as explained in paragraph 7.1.1.2. The heat shield was found to contribute negligibly to the stiffness characteristics of the shell, and was ignored from this standpoint. The mass of the heat shield, however, is appreciable and was included in the inertia calculations.

The spherical nose cap is attached to the conical shell at four discrete locations around the circumference. Comparisons were made to check the effect of boundary conditions on the natural frequencies. Three cases were considered: the cap integrally joined to the conical shell all along the circumference; the conical shell fixed (fully restrained) at the cap junction; the conical shell free (unrestrained) at the cap junction.

The spherical nose cap is much stiffer than the conical shell, and effectively acts to fully restrain the conical shell at the cap junction. The first two cases are therefore essentially equivalent. The results of vibration analyses showed that, for this configuration, the natural frequencies of the system are about the same whether the conical shell is fixed or free at its small end (at the cap junction). This is apparently due to the fact that the outer portion of the conical shell (at larger radii) has the greatest effect on the vibration characteristics. This was true for all harmonics.

As shown in Figure 277, the configuration was represented by 14 nodal circles. Since there are 4 degrees of freedom at each node, the system had 56 degrees of freedom. This model differed from the model used for the unsymmetrical loads analysis because it was found that the same accuracy (in frequency computations) could be achieved with less nodes. A significant saving in computer time results from a smaller system.

b. Results -- A different set of modal data has been computed for each harmonic number n. The expression for a typical radial displacement w is

$$w(\theta) = A \cos n\theta,$$

where

A is the peak magnitude of w

n is the harmonic number

θ is the circumferential position (angle)

$w(\theta)$ is the radial displacement at the circumferential location θ.

The lowest natural frequency in each harmonic is plotted in Figure 278. The minimum frequency of the system occurs at the second harmonic. Also shown is the theoretical frequency variation with harmonic,

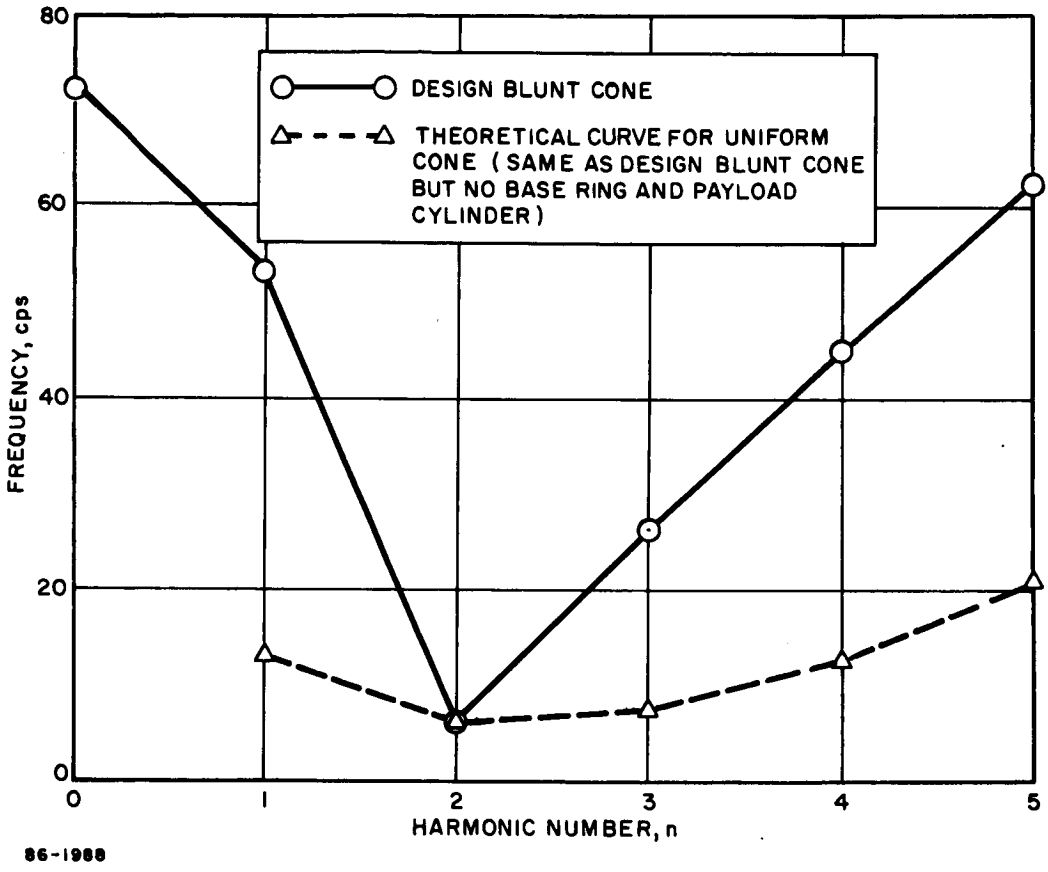

Figure 278 BLUNT CONE FIRST NATURAL FREQUENCY AS A FUNCTION OF HARMONIC NUMBER

computed from Reference 72. The theoretical curve assumes a uniform cone, fixed at the small edge and free at the large edge, with properties identical to the honeycomb sandwich portion of the actual blunt cone configuration. The base ring structure and the payload cylindrical shell have been omitted. Thus the two curves are for the same basic shell, but the actual blunt-cone contains the base ring and the payload cylinder structure.

Results show that, at the second harmonic where the minimum frequency occurs, the stiffening elements do not increase the natural frequency appreciably. However, at other harmonics, the effect is significant. The base ring and payload cylindrical structure cause a large increase in the lowest natural frequency in the other harmonics when compared to the unstiffened cone.

Figures 279 and 280 show the axial (u) and radial (w) modal displacements for n = 0, 1, 2, and 3. These plots correspond to the natural frequencies given in Figure 278.

The n = 0 case corresponds to an axial mode of vibration, since u_θ = constant around the circumference. The n = 1 case is similar to a lateral vibration mode, since each nodal section moves without deforming out of its original circular shape.

For n = 2 and higher, no net translation or rotation of a cross section takes place. Each nodal circle oscillates about its undeformed position with no net motion of the section as a whole.

Results of this study show the shell minimum natural frequency to be 6.3 cps, occurring at the second harmonic. For the first harmonic, the lowest frequency is 53.5 cps. On entering the Mars atmosphere, the spacecraft is subjected to an oscillating aerodynamic force of less than 2 cps. The maximum loading condition occurs at an angle of attack of 10.2 degrees. The pressure distribution at this angle was expressed in terms of its Fourier components. It was found that the zero and first harmonics were sufficient to describe the actual distribution of pressure around the circumference of the spacecraft. The second harmonic contribution was negligible.

Thus the only oscillating component of pressure occurs in the zeroth and first harmonics, with a forcing frequency of about 1.7 cps. Since the minimum shell natural frequency in the first harmonic is 53.5 cps and 72.8 cps in the zeroth, no appreciable dynamic load magnification over the static shell load is expected.

A complete dynamic analysis would include both the shell and the internal structure. Stiffness coefficients for the internal trusswork could be calculated utilizing the STRESS digital computer program described in paragraph 7.1.3.2. The truss stiffness matrix would then be combined with the shell stiffness matrices.

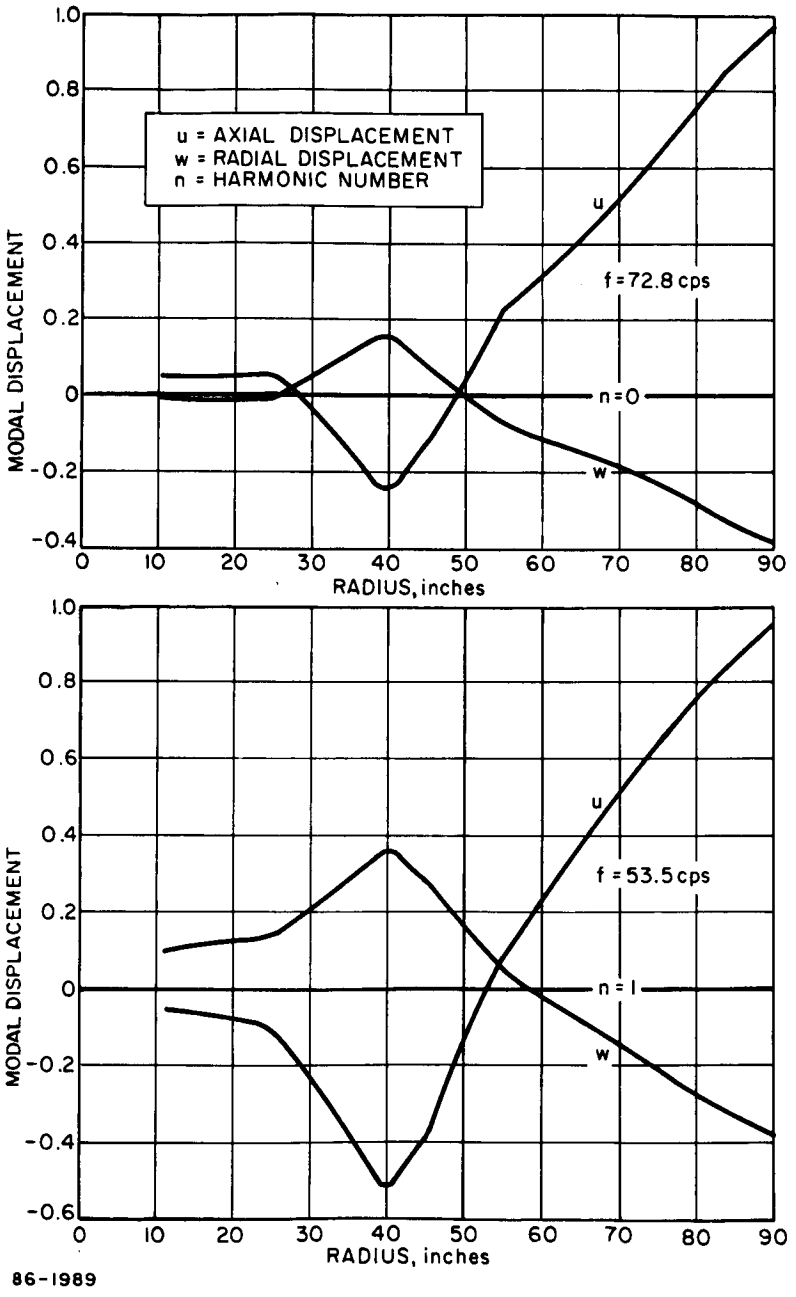

Figure 279 BLUNT CONE MODAL DISPLACEMENTS ZEROTH AND FIRST HARMONICS

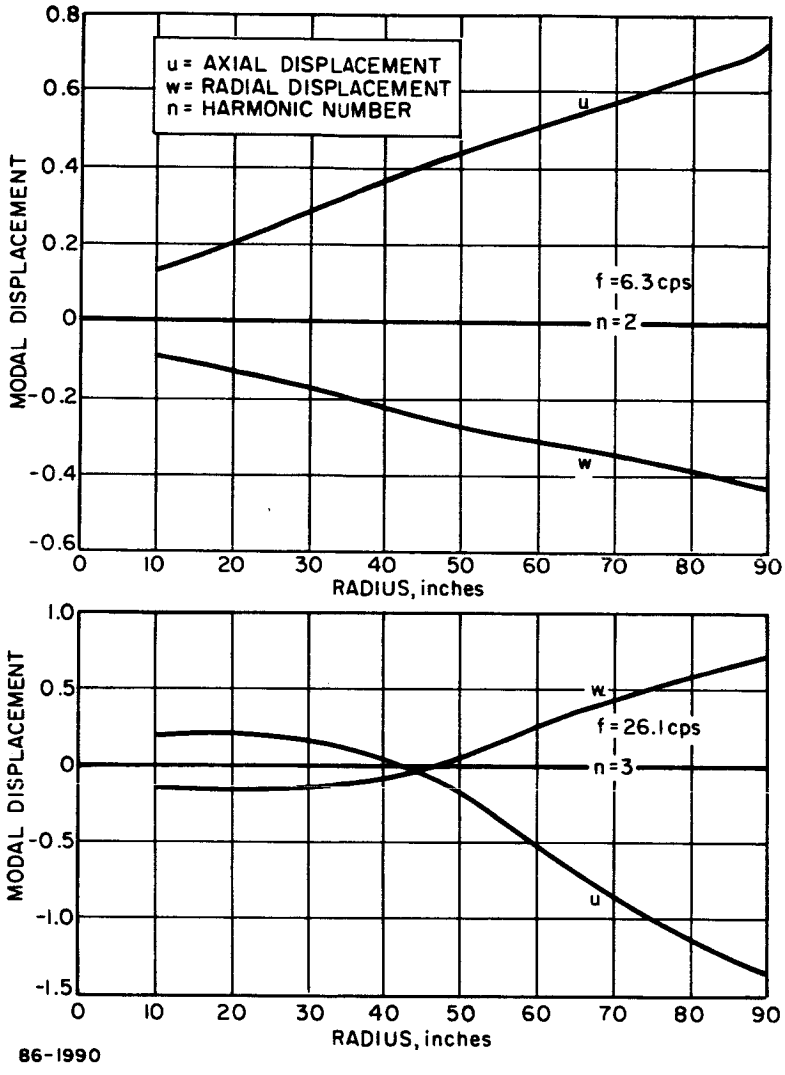

Figure 280 BLUNT CONE MODAL DISPLACEMENTS SECOND AND THIRD HARMONICS

6.3.3.3 Suspended Capsule and Adapter Structure

1. Suspended Capsule Structure -- The suspended capsule structure, Figure 247, was analyzed for the loading conditions summarized in Table XL. The detailed dimensions of the structural members were presented in the design layout, Figure 249.

The analysis of the suspended capsule structure has not been carried to the same depth as the analysis of the entry shell since its design was governed by packaging requirements which were not frozen until late in the conceptual design cycle.

The analysis was conducted in three distinct phases. The first phase was devoted to aiding in selecting suitable load paths and structural member configurations. The configurations in this phase were continually changing in order to satisfy center of gravity location, antenna pattern and aerodynamic requirements, and component packaging requirements.

The second phase began after the structural configuration was frozen. Preliminary analyses were made of the important structural members subjected to the critical loading conditions to verify the initial sizing of these members so that preliminary weight estimates could be computed.

The third phase consisted of development of a detailed analytical model of the suspended capsule structure. The member forces (shear, bending and twisting moments) were then computed for all loading conditions utilizing structural engineering computer programs employing matrix methods (see paragraph 7.1.3.1).

The structural analysis of the suspended capsule structure has progressed to the beginning of the third phase where a preliminary analytical model was developed and results from symmetrical entry loading were obtained.

The preliminary analysis of the second phase indicated that the critical loading condition was associated with the parachute deployment. The normal operating sequence during parachute deployment calls for the entry shell to be deployed after the peak parachute opening shock has passed. For the preliminary analysis, however, the conservative assumption was made that the parachute loads decelerated the suspended capsule alone. All internal forces were also assumed to be carried by the suspended capsule structure.

The maximum parachute loading of 16,000 lbs, times a safety factor of 1.25, was assumed to be acting at an angle of 10 degrees from the centerline of the capsule in order to account for capsule angle of attack and possible nonaxial deployment of the parachute. As can be seen in Figure 247, the parachute loads are introduced into the capsule structure through fittings at joint B. The inertial forces of the internal components, Figure 281, were assumed to be distributed along each radial beam. The internal forces in the members were determined from equilibrium conditions by assuming that the rigidity of the forward ring, element 14, was small compared to the frame longerons, element 6, and all structural joints were pinned. Radial forces were therefore transmitted through the frame longerons and reacted at the aft ring, element 5. The computed internal force distribution is shown in the schematic Figure 282.

The margins of safety determined using this force distribution were given in Table XLIII. All other loading conditions induce smaller internal forces on any of the structural members.

The conclusion drawn from the preliminary analysis is therefore that the preliminary weights as given in Table XLVI are conservative estimates of final design weights.

The preliminary analytical model developed for the third phase of structural analysis of the suspended capsule structure incorporates the members 3, 5, 6, 11, and 14 as shown in Figure 247. This preliminary model does not include an effective width of the afterbody shell acting with the frame longerons or the stiffness of the component boxes and covers. The forward and aft ring were approximated by a series of straight beams. The error associated with this approximation appears to be less than 5 percent.

Initial results were obtained for symmetrical entry loading only. This case was analyzed initially to check the validity of the analytical model. This was subsequently improved to consider the forward mounting ring, element 17, in order to handle parachute loading.

The results for the symmetrical entry case are compared in Figure 283 with the internal forces calculated in the preliminary analysis which used the assumption on the forward ring rigidity. The results of the matrix analysis appear to be valid since symmetrical deformations and equilibrium of forces was observed throughout the structure. It is interesting to note also that the assumption of the rigidity of the forward ring produced results close to those from the matrix analysis. Since the joints were no longer assumed to be pinned, bending and twisting moments were also developed in the

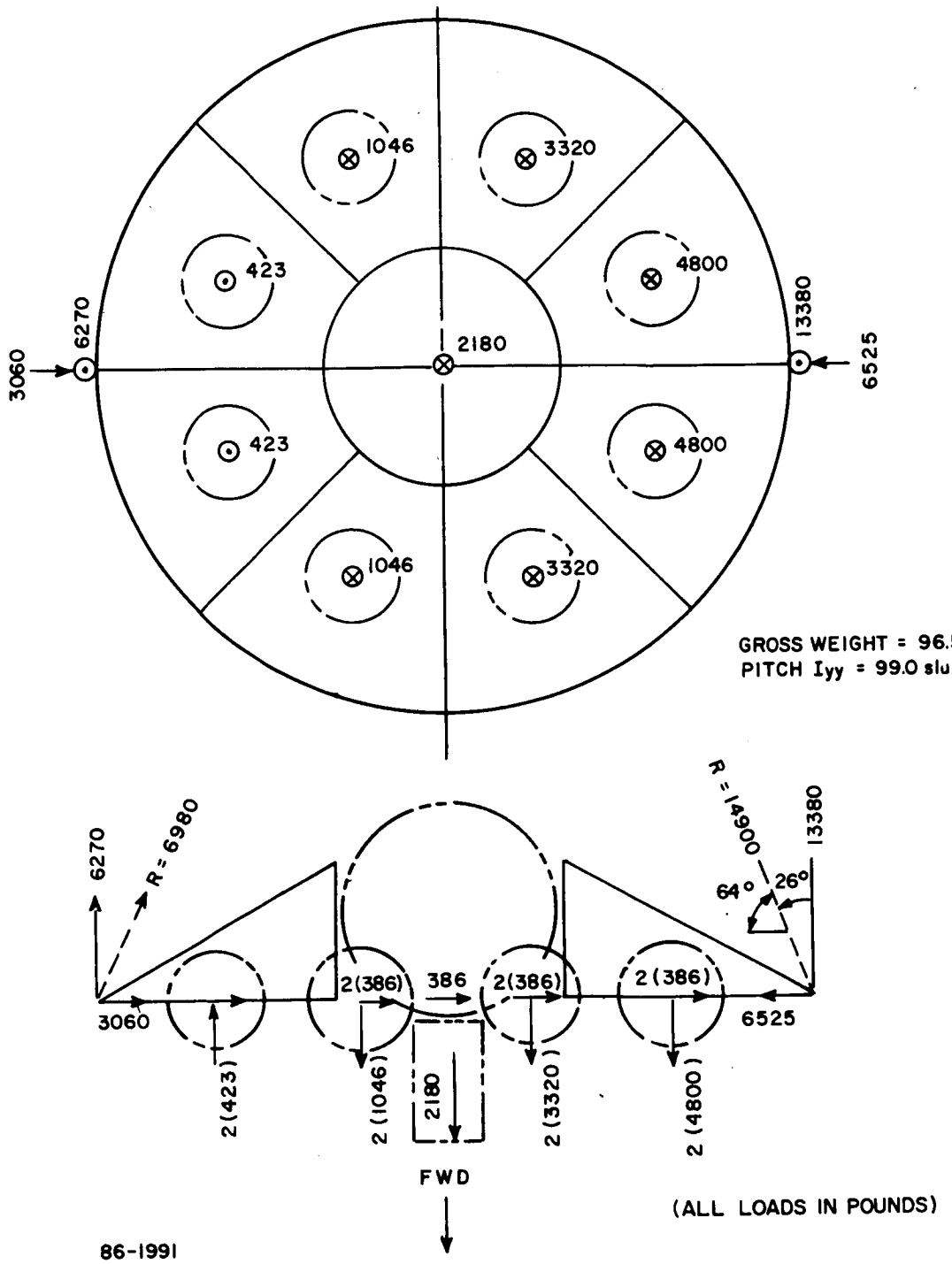

Figure 281 SUSPENDED STRUCTURE--PARACHUTE DEPLOYMENT LOADS--
SHELL OFF--ULTIMATE LOADS

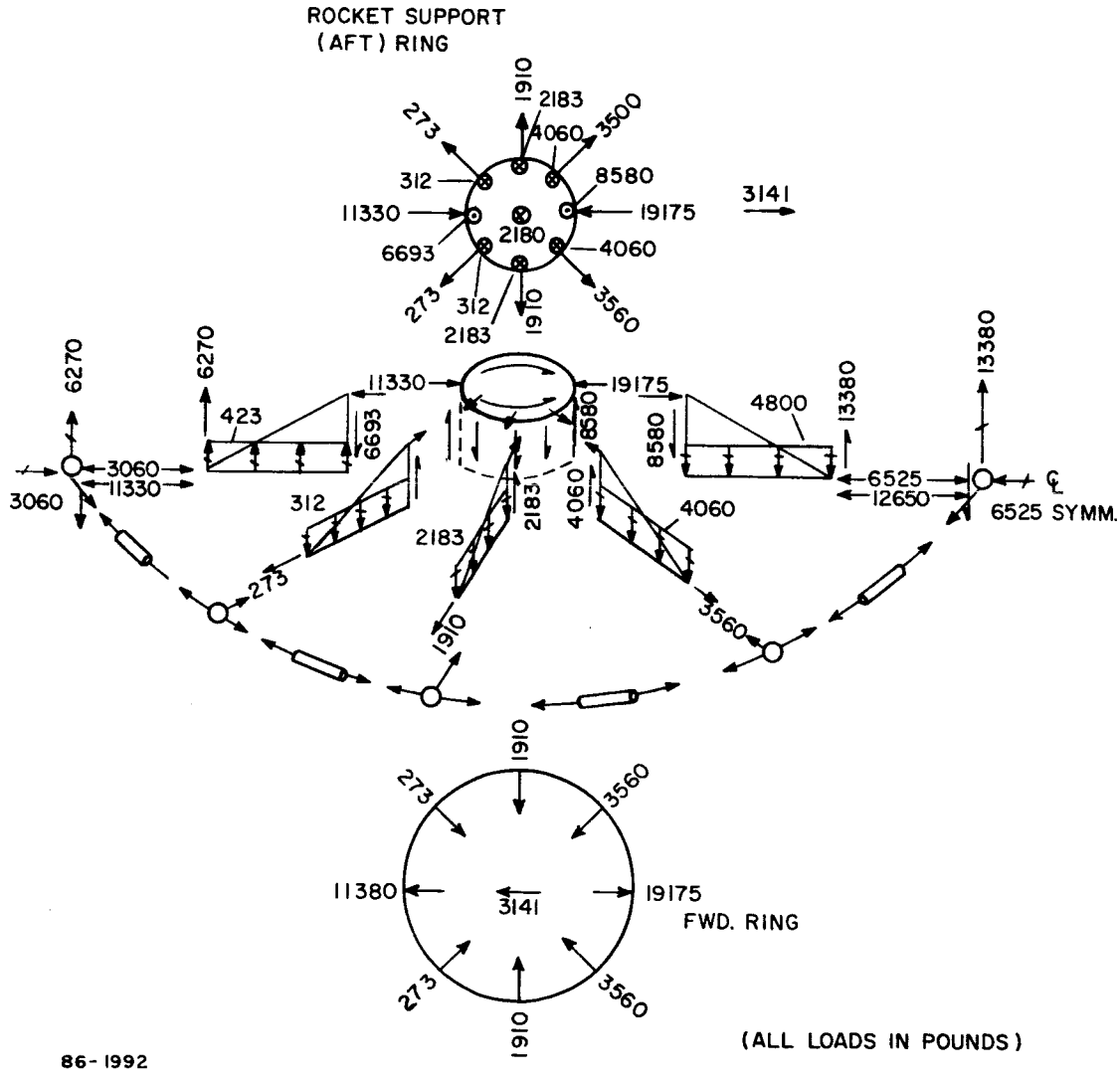

Figure 282 SUSPENDED STRUCTURE--EXPLODED FREE-BODY PARACHUTE DEPLOYMENT LOADS--SHELL OFF -- ULTIMATE LOADS

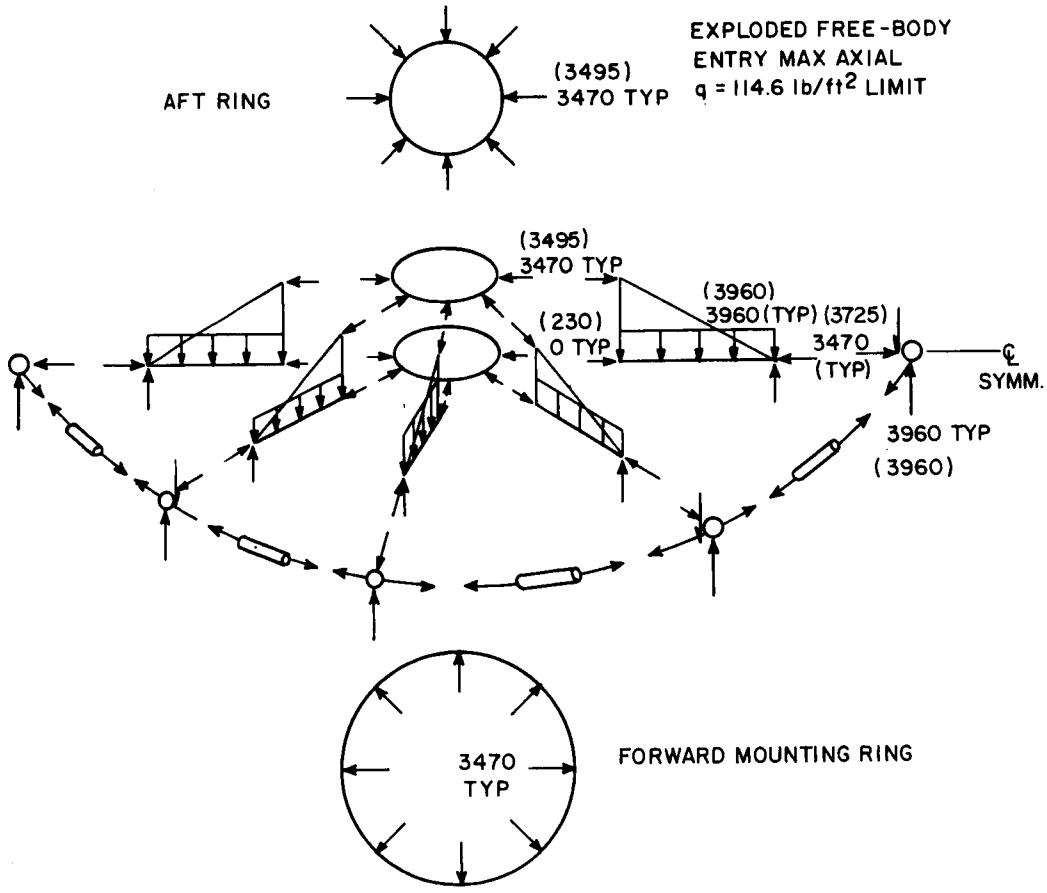

Figure 283 COMPARISON OF PRELIMINARY ANALYSIS RESULTS WITH STRUCTURAL MATRIX ANALYSIS

members as shown in Figures 284 and 285. Note that the forces and moments applied to the members are in the local coordinates of the member, hence have to be transformed into the coordinates of the main structure when equilibrium at a joint is considered. Once the validity of the analytical model is established, the stresses and deflection can be determined for all of the other combinations of loading, both symmetrical and unsymmetrical. The analytical model also can be used for determining stiffness coefficients for use in the dynamic analysis of the suspended capsule structure during launch, entry and parachute deployment.

2. Adapter Structure -- The adapter structure transmits the ground handling, launch and spaceflight maneuver loads to the flight capsule and sterilization canister. The structural configuration consists of a shell reinforced by eight longerons extending from the spacecraft adapter ring through the sterilization canister to the flight capsule mounting ring. The longerons were interrupted at the sterilization canister, which was assumed to act as a bulkhead rigid in a plane normal to the flight capsule axis.

The critical load conditions for the adapter structure occurred during launch and ground handling. The adapter structure loads shown in Figure 286 were obtained by multiplying the loads in Table XL by a safety factor of 1.25. The maximum ground handling loads were specified such that they would not produce a more critical condition than launch loads. The margins of safety for the critical loads condition are given in Table XLIII for the structural configuration given in the design layout of Figure 249.

6.3.3.4 Ablator-Structure Compatibility

The problems of ablator-substructure compatibility has always been a consideration in the design of thermal protection systems for entry vehicles, both for Earth and planetary applications. The problems are associated with differential expansion of the structure and ablator materials and the allowable stresses and strains of the ablator and substructure. The critical conditions which arise for the conceptual design considered here are associated with the allowable stresses in the substructure rather than the strains in the ablator. The Purple Blend Mod 5 material used for the ablator has a large strain to failure even at -100°F; hence a tensile failure is not expected. The substructure stiffness characteristics were determined by the entry aerodynamic surface pressures. These pressures are so small (<2 lb/in^2) that the ablator can impose compressive stresses on the substructure which can approach the critical entry loading stresses that governed the selection of the shell stiffness. After the examination of the various assumptions used in determining the margins

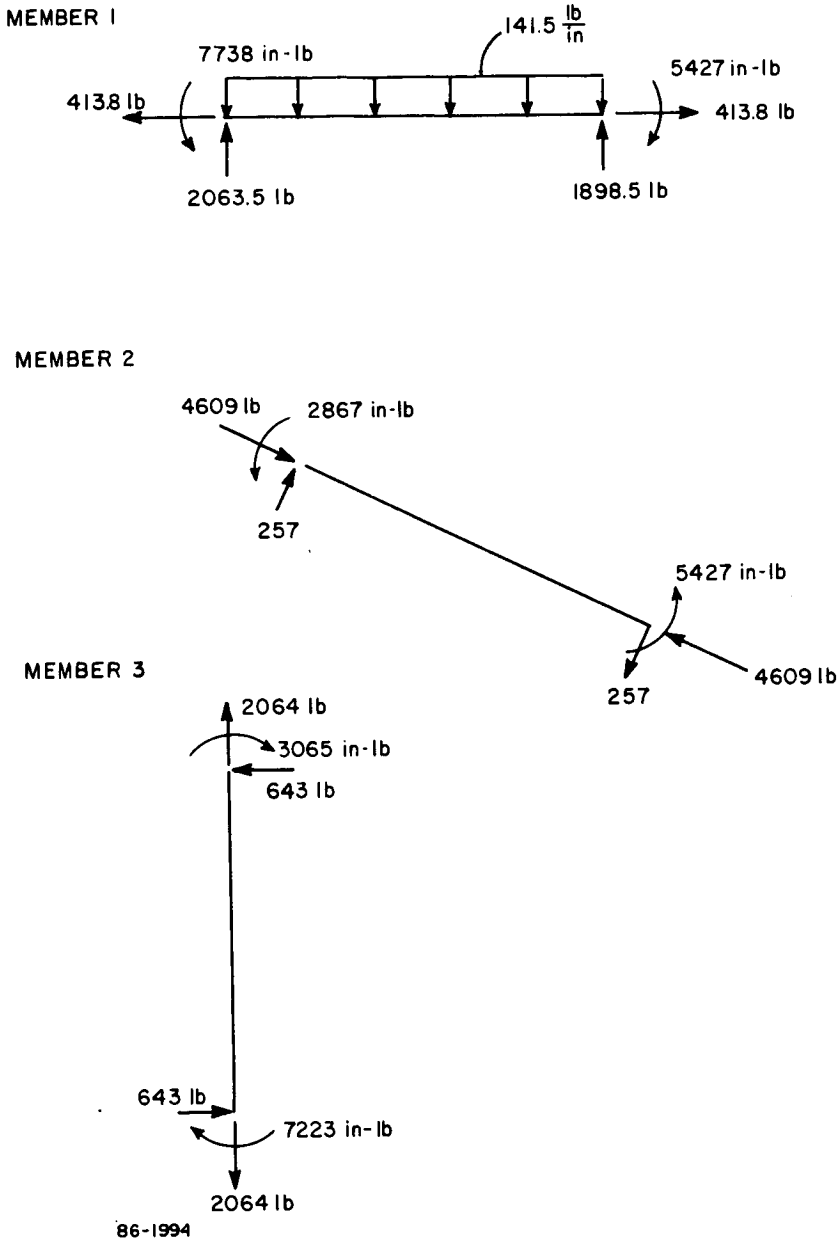

Figure 284 MEMBER FORCES--SYMMETRICAL ENTRY LOADING

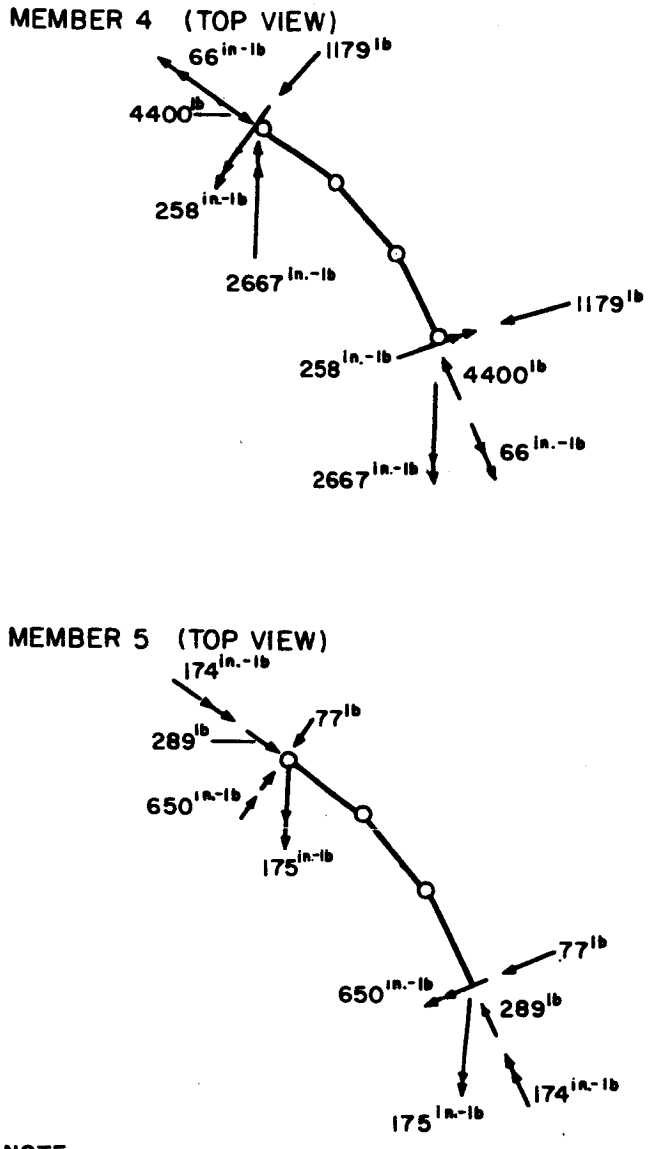

Figure 285 MEMBER FORCES--SYMMETRICAL ENTRY LOADING

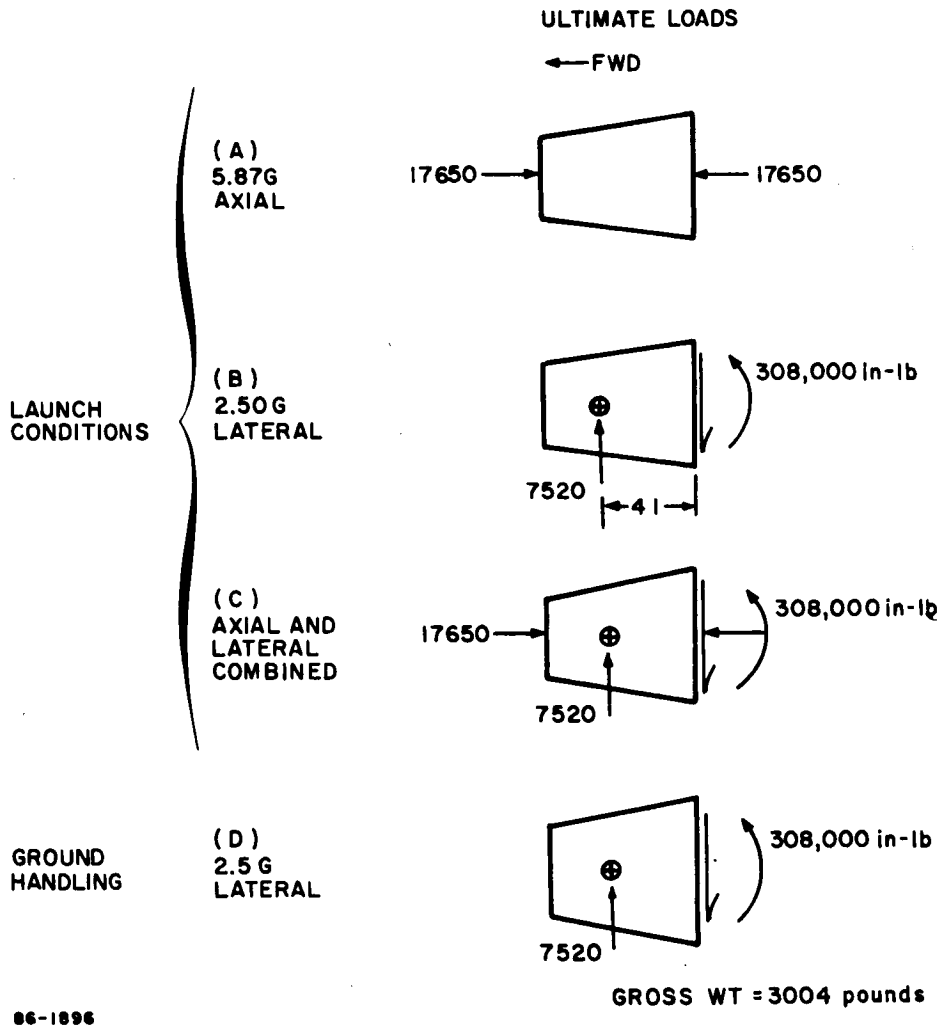

Figure 286 ADAPTER LOAD CONDITIONS

of safety of the structure during spaceflight, it appears that the assumptions are all of a conservative nature, and that the structure is not likely to buckle. The problem is of importance, however, because if a change were made in ablator properties, structural stiffness, or operating temperature range, a critical condition could arise.

1. Mechanical Properties of Reference Materials

a. Purple Blend Mod 5 Ablator -- Preliminary mechanical properties of the Purple Blend Mod 5 ablator are given in Table XLVIII. The elastic modulus is the initial tangent modulus. The direct use of this elastic modulus could lead to erroneous results because the stress-strain curve is nonlinear even at low values of strain. The analysis of the cold soak condition therefore used a secant modulus obtained from the stress-strain curve given in Figure 287 for a temperature of -100°F.

b. 2024-T3 Aluminum Alloy -- The mechanical properties used in the ablator-substructure as well as in the static and dynamic analysis are given in Table XLIX.

2. Spacecraft Cold Soak -- The spaceflight cold soak condition was assumed to be a uniform -100°F. This is the lowest expected temperature during the mission sequence and in all likelihood is an extreme case. The zero stress temperature of the ablator-substructure composite was assumed to be 300°F. This is the temperature experienced during the dry heat sterilization cycle where possible curing and dimensional changes could occur. There is no test data available which confirms that the zero stress temperature is 300°F or whether there is one unique temperature at which the composite is unstressed. The results given in the following paragraphs are quite sensitive to this assumption. There is also the further consideration that the elastomeric composition of the ablator could relax after a period of storage at room temperature thereby reducing the zero stress temperature to room temperature.

The stresses in the entry shell structures for the reference ablator thickness given in Section 9.0 were calculated on the shell computer program No. 1322 described in paragraph 7.1.1.1. A secant modulus of 28,000 lb/in^2 was used for the ablator material. The secant modulus was determined by iterating the shell solution until the stress had the correct value corresponding to the elastic modulus. The results showed that the strain in the ablator was essentially independent of the elastic modulus of the ablator and is directly proportional to relative thermal strain of the ablator and substructure.

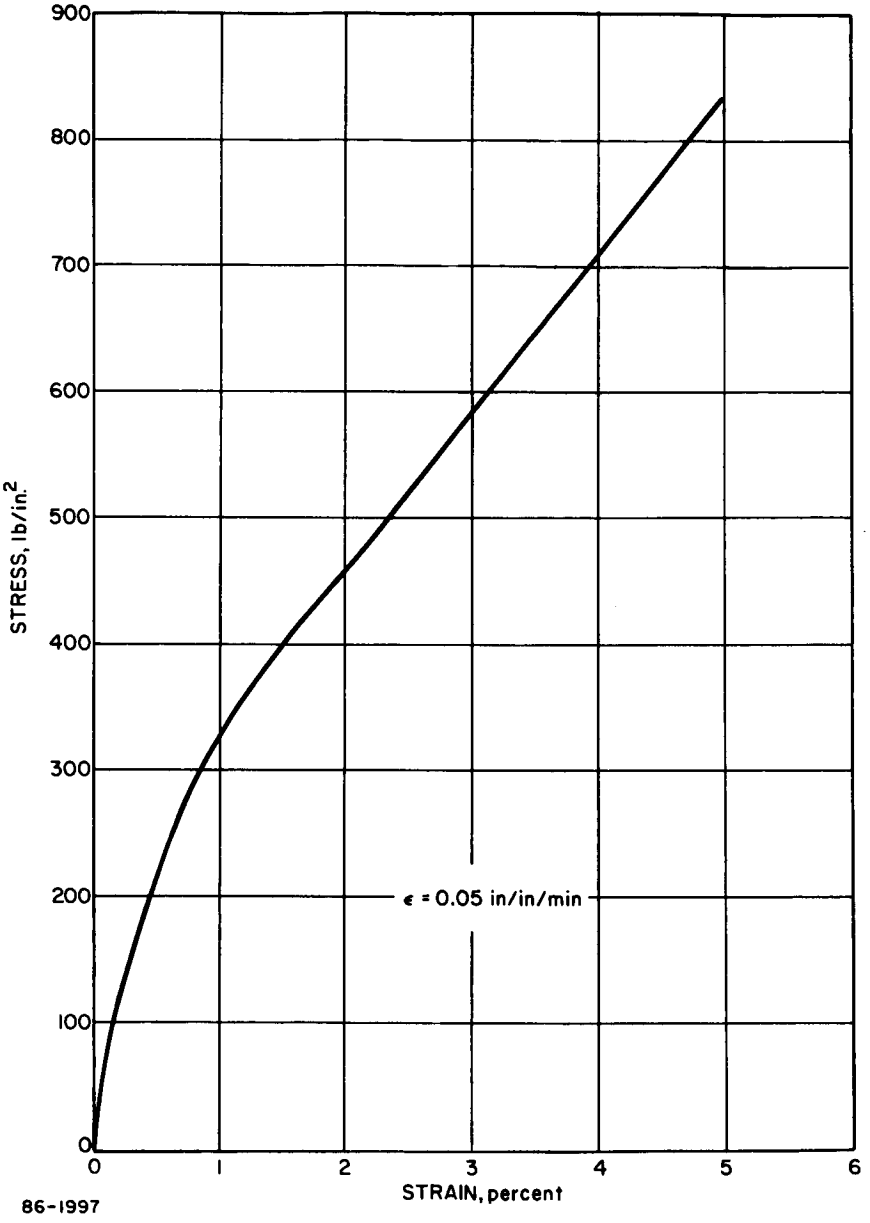

Figure 287 TYPICAL TENSILE STRESS-STRAIN CURVE FOR DRY HEAT STERILIZED LOW DENSITY SILICONE MOD 5

TABLE XLVIII

MECHANICAL PROPERTIES OF PURPLE BLEND MOD 5

(Dry Heat Sterilized)	
Tensile Strength (lb/in.^{2})*	
-100°F	868
75°F	330
300°F	290
Total Strain to Failure (percent)*	
-100°F	5.4
75°F	8.8
300°F	4.8
Elastic Modulus (lb/in.^{2} x 10^{-6})	
-100°F	0.059
- 60°F	0.0478
75°F	0.0099
300°F	0.0087
Coefficient of Thermal Expansion (in./in./°F x 10^{-6})	
-100 to -40°F	54.3
- 40 to 300°F	43.5
Density (lb/in.^{3})	0.024

*Test Strain Rate - 0.05 in./in./min.

TABLE XLIX

MECHANICAL PROPERTIES OF 2024-T3 ALUMINUM ALLOY

Tensile Yield Stress ($lb/in.^2$)	
-100	not available
75°F	48,000 (longitudinal)
	42,000 (transverse)
300°F	42,000 (longitudinal)
	37,000 (transverse)
Compression Yield Stress ($lb/in.^2$)	
-100°F	not available
75°F	40,000 (longitudinal)
	45,000 (transverse)
300°F	36,800 (longitudinal)
	41,400 (transverse)
Compressive Young's Modulus ($lb/in.^2 \times 10^{-6}$)	
-100°F	11.3
75°F	10.7
300°F	10.2
Coefficient of Thermal Expansion ($in./in./°F \times 10^{-6}$)	
68° to 212°F	12.6

This is demonstrated in Figure 288. The straight line is actually a solution of the shell program with the complete shell as described in paragraph 7.1.1.1. The result can be readily verified by simple analytical methods.

The magnitude of the stress distribution in the substructure is essentially directly proportional to the elastic modulus of the ablator. The stress distribution is, however, dependent on the structural shell stiffness and boundary conditions and is seen in Figure 289. The circumferential stress distribution from a radius of 50 to 80 inches is equal to the critical buckling stress determined for the design entry loading. The margin of safety of 0.0 given in Table XLII of paragraph 6.1.3.2 was based on this consideration.

It should also be noted that no buckling could occur unless there were an unbonded area permitting the shell to deform away from the ablator. When the structure and ablator are perfectly bonded the net force on the cross section is zero and no buckling can occur.

A further discussion of this problem is given in paragraph 7.1.2.4.

3. Entry Thermal Stresses -- The temperature distributions prevailing during entry were not available in time for detailed analysis of the reference design. The temperature distribution as given in Section 9.0, combined with the information on mechanical properties of the Purple Blend Mod 5 ablator, indicates that no significant problem will arise, at least in the temperature range where the mechanical properties of the ablator material are available.

The temperature rise of the substructure is approximately 50 degrees at the time of maximum loading on the structural design trajectory. The temperature rise of the ablator is always greater than that of the substructure. The compressive stresses in the substructure developed during cold soak will therefore be relieved from the beginning of the entry heating. By the time of peak loading the temperature rise of the ablator will induce tensile stresses in the substructure. The magnitude of the tensile stresses will be very small since the elastic modulus of the Purple Blend Mod 5 ablator decreases rapidly with increased temperature. The tensile stresses will have a beneficial but very small effect on the substructure since the tensile stresses will reduce the compressive stresses induced by aerodynamic loading.

The temperature rise of the substructure is approximately 200°F at the time of maximum loading in the heating trajectory. For the highest expected initial entry temperature of 100°F, the substructure

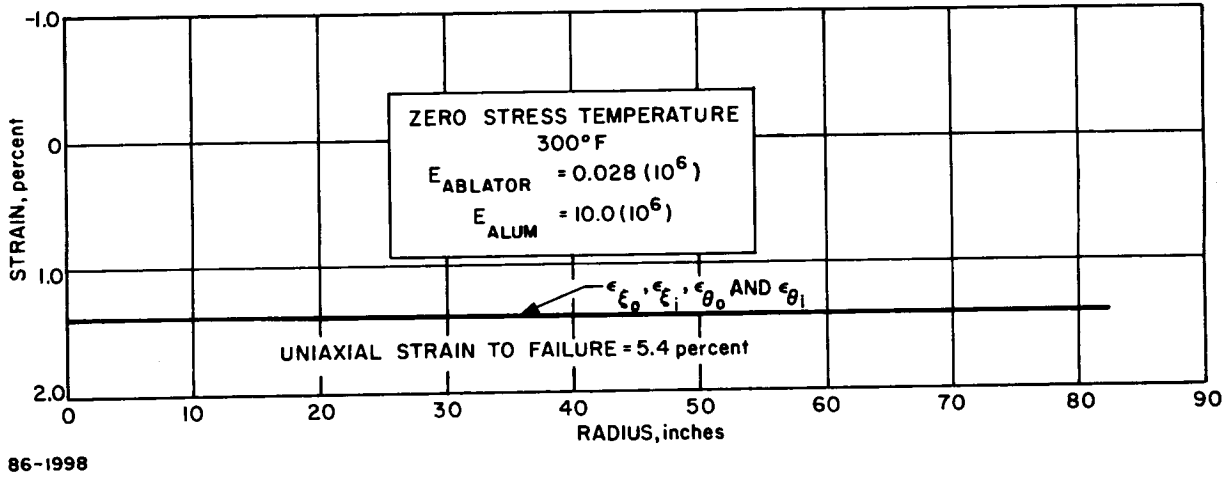

Figure 288 BLUNT CONE STRAIN VERSUS RADIUS SOAK CONDITION, -100°F

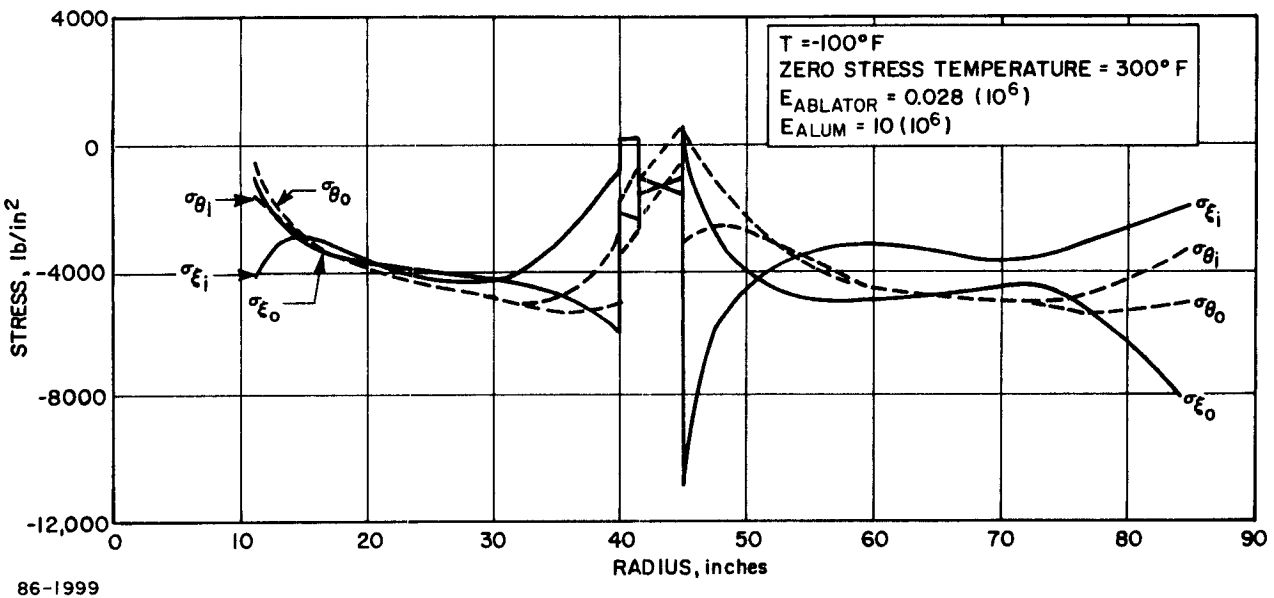

Figure 289 BLUNT CONE FACE SHEET STRESSES -- SPACE FLIGHT COLD SOAK

temperature would therefore be 300°F. This structural temperature is not critical because it is the value assumed during the preliminary and conceptual design analyses, and also because the maximum dynamic pressure for this trajectory is 27 percent of the maximum dynamic pressure on the design trajectory (see Table XXXIX). The temperature rise in the ablator, for this trajectory, will also lead the temperature rise of the structure; hence it will tend to induce tensile stresses in the substructure in a similar manner as on the design trajectory.

6.3.4 Problem Areas

The problem areas that are of importance in the structural analysis and design of the entry shell structure appear at this time to be: (a) the end ring design, (b) a determination of the validity of the methods of stability analysis of the honeycomb sandwich shell, and (c) the possibility of thermal buckling of the substructure during the spaceflight cold soak condition.

Experimental verification of the methods of analysis described in paragraph 7.1.2.1 of the end ring and honeycomb shells are therefore recommended. Cold soak tests of the ablator substructure composite shell plus additional theoretical analysis are also needed in the area of ablator-substructure compatibility.

7.0 STRUCTURAL MECHANICS
THEORETICAL ANALYSIS AND METHODS

7.1 STATIC ANALYSIS

7.1.1 Linear Shell Analysis

7.1.1.1 Symmetrical Loading

1. General Description of Avco Computer Program No. 1322 -- The symmetrical shear forces and bending moments in the entry shell were determined using Avco's generalized shell computer program No. 1322. The numerical analysis is given in Reference 52. The program can handle variable pressure and temperature distributions in multilayer shells with variable thickness and arbitrary geometry. Honeycomb sandwich shells are treated by assigning a zero Young's modulus to the core layer. This implies that the core has infinite shear rigidity since normals to a reference surface remain normal and unextended after deformation of the shell. Body forces due to axial deceleration of the capsule can be accounted for by introducing an equivalent axial surface load intensity. Boundary conditions can either be specified or be the result of an elastic interaction with another shell.

2. Analysis of Sandwich Shells -- For most applications the procedure for the linear analysis of sandwich shells discussed in the previous paragraph is satisfactory. However, shear deformations are sometimes important in a sandwich shell, and it is possible that the effects of normal stress may occasionally be significant. In order to evaluate these effects, a computer program has been developed for the analysis of sandwich shells of revolution.* This program, which is a modification of the earlier Avco computer program No. 1322, carries out a numerical solution of the two following simultaneous second-order differential equations:

$$\left(\frac{rD}{a}\right)\beta'' + \left(\frac{rD}{a}\right)'\beta' - \left[\left(\frac{r'}{r}\right)^2\left(\frac{rD}{a}\right) - \nu\left(\frac{r'D}{a}\right)'\right]\beta + z'\psi$$

$$= r'(rV) - rM_T' + r'Ds_\theta - (rDs_\xi)'$$

*This work was carried out under JPL Contract 951070, "An Integrated Preliminary Design Computer Program for Planetary Atmospheric Entry".

$$\left(\frac{r}{Ca}\right)\psi'' + \left(\frac{r}{Ca}\right)'\psi' - \left[\left(\frac{r'}{r}\right)^2\left(\frac{r}{Ca}\right) + \nu\left(\frac{r'}{Ca}\right) + \frac{z'^2}{G_c h r a}\right]\psi' - z'\beta =$$

$$\left[\nu\left(\frac{r}{Ca}\right)z'V\right]' + \left[\left(\frac{r'}{Ca}\right)z' - \frac{r'z'}{Gha}\right]V - \nu\frac{rr'P_H}{C} - \left(\frac{r^2P_H}{C}\right)' - r\epsilon'_T$$

These differential equations are identical to those solved in computer program No. 1322 except for the additional terms, which account for the core shear and compressibility. The additional terms were based on the analysis of reference 53. Symbols are defined in Table L.

Preliminary results indicate that the effect of normal pressure on deformations is trivial for symmetrical loading but that shear may cause slightly greater effects, possibly on the order of a few percent. The analysis is limited to a shell containing three layers- a core and two identical face sheets. More recent studies tentatively indicate that this restriction can be removed. If this can be done, the analysis can be brought into a form in which it applies directly to a composite shell and heat shield configuration.

The significant stresses in the core are shear stress in the meridional plane and the normal crushing stress. The shear stress is simply,

$$r_\xi = \frac{Q_\xi}{t_c}$$

The crushing stresses at the upper and lower surfaces of the core are

$$\sigma_{nU} = q_U + \frac{N_\xi - \frac{2M_\xi}{t_c}}{2r_\xi} + \frac{N_\theta - \frac{2M_\theta}{t_c}}{2r_\theta}$$

$$\sigma_{nL} = q_L - \frac{N_\xi + \frac{2M_\xi}{t_c}}{2r_\xi} - \frac{N_\theta + \frac{2M_\theta}{t_c}}{2r_\theta}$$

The radii of curvature r_θ and r_ξ are related to r and z by the equations

$$r_\theta = \frac{ar}{z'} \qquad r_\xi = \frac{a^3}{r'z'' - r''z'}$$

TABLE L

NOMENCLATURE FOR SANDWICH SHELLS

Symbols

t_c	thickness of core plus one face sheet
t_f	thickness of face sheet
r	radius measured normal to axis
r_θ, r_ξ	radii of curvature
z	axial coordinate
ξ	meridional coordinate
N	membrane tensile force
M	bending moment
Q	shear in meridional plane and perpendicular to shell wall
ψ	shear in meridional plane and perpendicular to axis of revolution, multiplied by r
V	total force in axial direction divided by $2\pi r$
q_U, q_L	external pressures on upper and lower faces, respectively
p	net normal pressure on shell, radially outward
p_H	component of pressure normal to axis
σ	stress in facing or core
τ	shear stress in core
E	elastic modulus
G	shear modulus
C	$2E_f t_f$
D	$E_f t_c^{\,2} t_f\, 2(1-\nu^2)$, flexural rigidity

TABLE L (Concl'd)

a $(r'^2 + z'^2)^{1/2}$

$()'$ $\frac{d()}{d\xi}$

α_T coefficient of thermal expansion

β rotation of normal to middle surface

T temperature

S_θ $\frac{\sigma_n}{E_c}\left(\frac{1}{r_\theta} + \frac{\nu}{r_\xi}\right)$

S_ξ $\frac{\sigma_n}{E_c}\left(\frac{1}{r_\xi} + \frac{\nu}{r_\theta}\right)$

Subscripts

c core

f facing

L lower

U upper

θ circumferential

ξ meridional

n normal

T thermal

3. Tension Shell Geometry -- The standard operational version of the 1322 shell program accepts geometrical, loading, and material property data at arbitrarily spaced stations along the shell surface; fits curves through the data; and subsequently processes it for use in the numerical integration of the governing differential equations. The procedure was developed in order to simplify the input requirements for complex shell structures and has proved adequate for practically all shell structures except the tension shell configuration. The accuracy of the solution for the tension shell is very dependent on the accuracy of the input geometrical coordinates and their derivatives. The

normal curve-fitting procedures were therefore bypassed in a special modification of the 1322 program, and the geometrical coordinates and derivatives were input directly at each integration point by a subroutine which calculated the quantities from their analytical expressions. The accuracy of the solutions was verified by comparing them with analytical solutions using Newtonian pressure distributions and ideal boundary conditions.

4. Ring Elements -- The 1322 shell program has the capability of handling branched shells; i.e., structures in which three or more shells have a common junction. This capability could be used to include the end-rings of the blunt cone, Apollo and tension shells. For a conceptual design study the additional accuracy, at the expense of increased complexity, was not warranted. The approach used was to simulate the elastic interaction of a ring with the attached shell by specifying the shell element which would have the same extensional and bending rigidity as the actual ring to be joined to the primary shell. The resulting stresses and displacements in the shell would be properly computed while only the correct stress couples and stress resultants would be computed in the ring.

7.1.1.2 Unsymmetrical Loading General Description of the Sabor Computer Program

Sabor (Static Analysis of Bodies of Revolution) is a digital computer program (References 54 and 55) utilizing a matrix displacement approach to solve for static stresses and displacements in a shell of revolution. It can handle either symmetrical or unsymmetrical loadings.* The shell structure may be arbitrary in shape. It is approximated by a series of conical frusta or elements connected to each other at nodal circles. The motion of each element is described by the displacements of the nodes. Four nodal degrees of freedom are considered: axial, radial and tangential translation, and rotation in the meridional plane.

Formulation of the total stiffness matrix (K) of the shell structure is the key step of the SABOR program. The total strain energy of the system is the sum of the strain energies of the individual shell elements. The stiffness matrix may be found for each element by determining the strain energy, which is related to the stresses and strains present in the element. This is accomplished by assuming displacement functions for the nodal coordinates and introducing them into the stress-strain and strain-displacement relationships for the shell element.

The total shell stiffness matrix is then determined by combining the individual element K matrices. A K matrix exists for each harmonic of the Fourier series considered in the analysis and the harmonics are uncoupled from each other.

*In practice SABOR is used primarily for unsymmetrical loading, since program 1322 has greater generality for symmetrical loading.

The external loads acting on the shell are approximated by line loads acting at the nodal circles. The loads are expressed in terms of a Fourier series. Stresses and displacements are determined for each harmonic using the loading and stiffness matrices for that harmonic. Total results are the superposition of the various Fourier components considered. Output is in the form of the four nodal displacements at each node, as well as the stress resultants at each node.

The SABOR program is restricted to a single layer shell. The actual shell is, in general, a honeycomb sandwich structure with an end-ring and a cylindrical shell in the payload attachment region. The actual shell was analyzed by SABOR as an equivalent homogeneous shell having the same flexural rigidity, D, and extensional rigidity, B. The input parameters required by the program are the Young's modulus, E_e, and thickness, t_e, of the equivalent homogeneous shell. These are found by setting the flexural and extensional rigidities of the equivalent homogenous shell, namely,

$$D = \frac{E_e\, t_c^{\,3}}{12\,(1-\nu^2)} \quad \text{and} \quad B = \frac{E_e\, t_c}{1-\nu^2}$$

equal to the corresponding parameters of the sandwich shell. These are

$$D = \frac{E_f\, t_f\, t_c^{\,2}}{2\,(1-\nu^2)} \quad \text{and} \quad B = \frac{2\,E_f\, t_f}{1-\nu^2}$$

where E_f is the Young's modulus of the face sheet, t_f is the face sheet thickness, and t_c is the core depth measured between middle surfaces of face sheets.

It follows from this analogy that a sandwich shell may be replaced by an equivalent homogeneous shell having values of E_e and t_e given by the equations

$$t_e = \sqrt{3}\, t_c\,, \quad E_e = \frac{2}{\sqrt{3}}\, E_f\, \frac{t_f}{t_c}$$

To determine the relative accuracy of the SABOR program, stress couples and stress resultants were calculated for a blunt conical shell under symmetrical loading and compared to calculations made on the identical shell by Avco Computer program No. 1322. The comparison (Figures 290 and 291) shows excellent agreement.

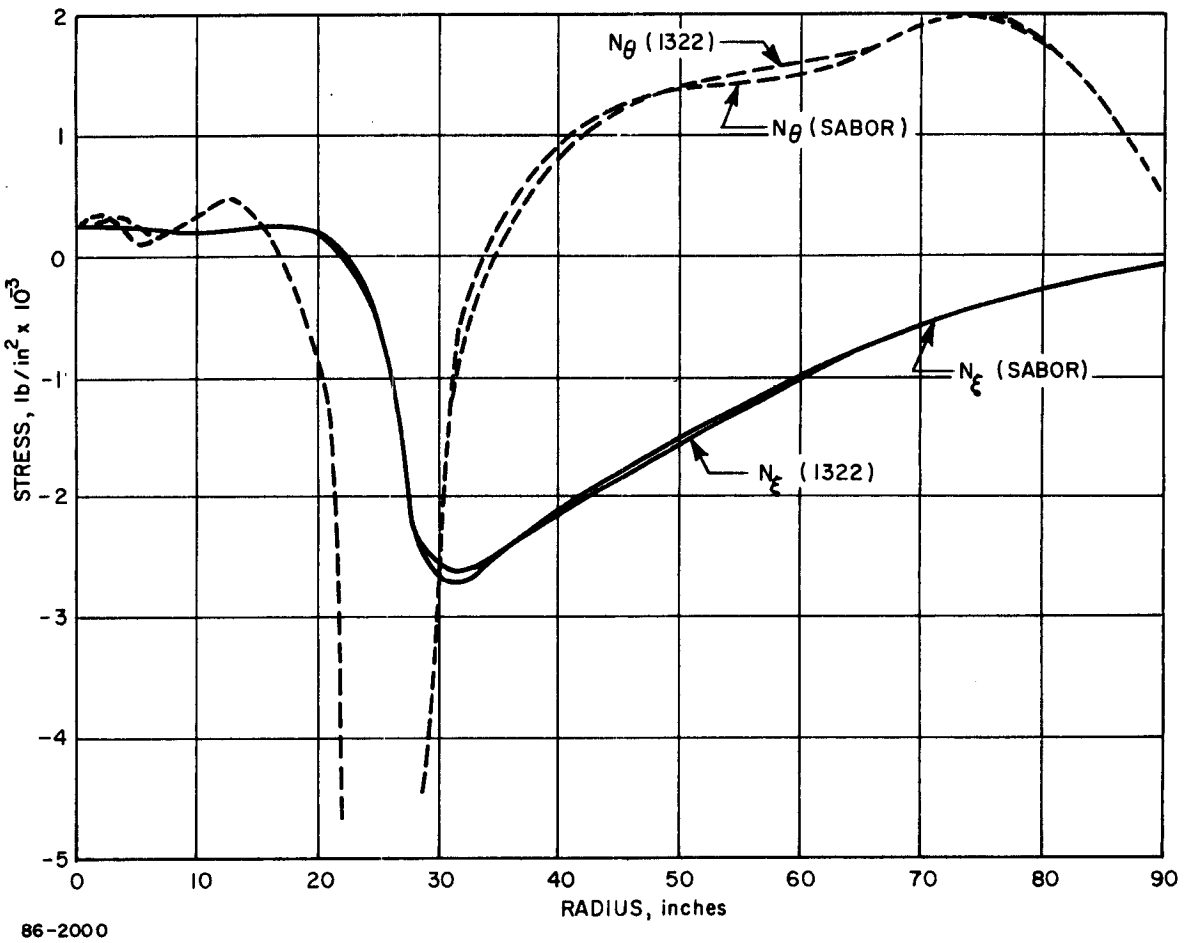

Figure 290 COMPARISON BETWEEN 1322 and SABOR PROGRAMS FOR SYMMETRICAL LOADING BLUNT CONE STRUCTURE

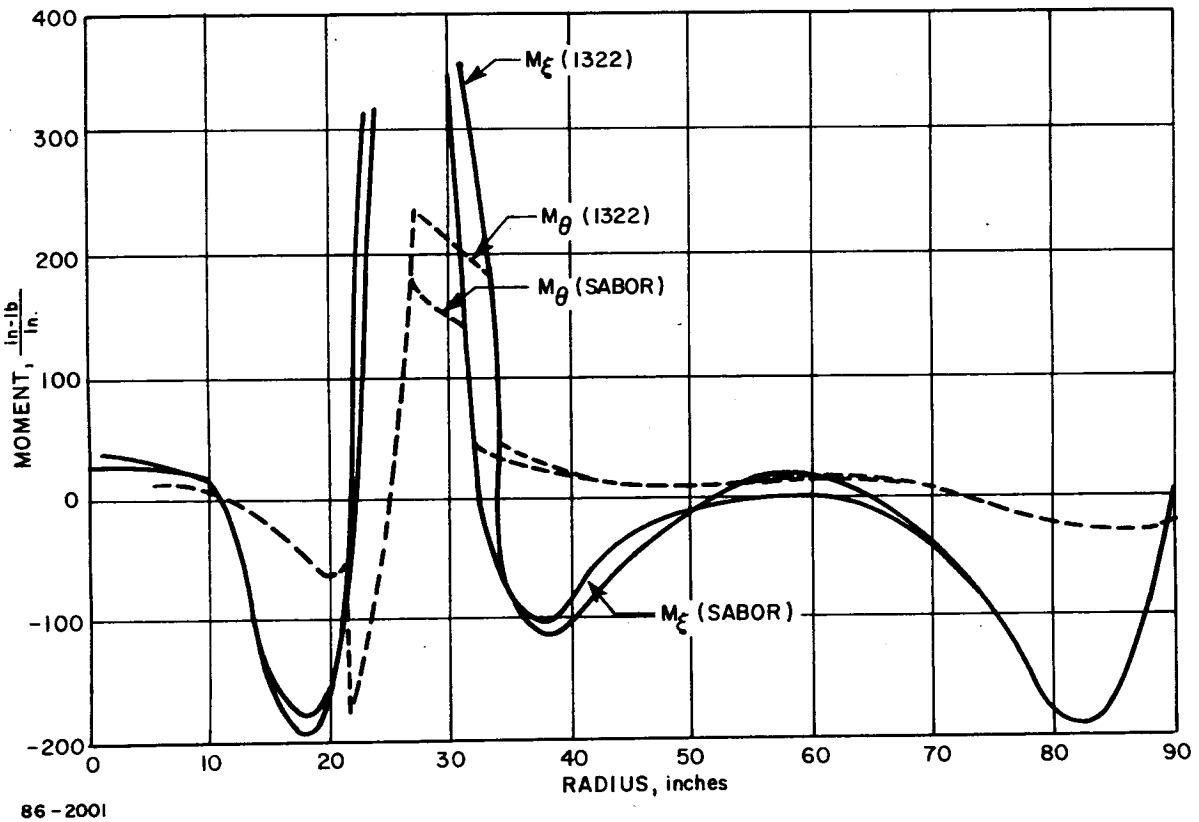

Figure 291 COMPARISON BETWEEN 1322 and SABOR PROGRAMS FOR SYMMETRICAL LOADING BLUNT CONE STRUCTURE

7.1.2 Buckling Analyses

7.1.2.1 Instability of Blunted Conical Shells

1. General Instability -- Several types of instability were considered in the design analyses of the blunted conical shell. The most important was general instability under external surface pressure. The analysis used for this type of buckling was based on experimental results for homogeneous cones given in Reference 56. The recommended design value is $p_{cr} = 0.8\, p_{th}$, where p_{th} is the theoretical critical external pressure for an equivalent cylinder as obtained by Batdorf in Reference 57. This relationship is approximated by

$$p_{th} = \frac{0.855\,(1-\nu^2)^{-\frac{3}{4}}\,E}{(l/R_{av})\left(\frac{R_{av}}{t}\right)^{5/2}}$$

where

l = slant length of cone

R_{av} = average radius of curvature of cone.

To apply this result to a sandwich cone, the concept of equivalent flexural and extensional rigidities mentioned in paragraph 7.1.1.2 is used. Then the following relations apply:

$$t_e = \sqrt{3}\, t_c \quad \text{and} \quad E_e = \frac{2}{\sqrt{3}}\,\frac{t_f}{t_c}\,E_f$$

By substitution of these results into the equation for a homogeneous cone, it is found that

$$p_{cr} = 3.12\,(1-\nu^2)^{-\frac{3}{4}}\left(\frac{t_f}{t_c}\right)\left(\frac{t_c}{R_{av}}\right)^{\frac{5}{2}}\left(\frac{R_{av}}{l}\right)E_f$$

The factor of 0.80 recommended for buckling of homogeneous cones has been included in the foregoing equation for sandwich cones. This equation could possibly be conservative because imperfections might be less significant in sandwich shells than in homogeneous shells.

The relationship for critical buckling pressure is directly applicable to truncated conical shells under hydrostatic pressure, simply supported at both ends. The axial force due to the external surface pressure is reacted at the forward end in the blunt cone, however, with the aft end being force free. The effect of the axial force

condition can be determined by superimposing an axial tensile force whose magnitude is equal and opposite to the force at the aft end of the shell due to the hydrostatic pressure. The interaction of this axial tensile force was estimated by the procedure given in Reference 58. The interaction curve used in the buckling analyses is given in Figure 292 as obtained from Reference 58. The theoretical values for stress ratios based on the hydrostatic buckling pressure, p_o , and axial buckling force, P_o , were used since this would give conservative results for a tensile force. For a compressive axial force, experimental values should be used, however.

A ring is required at the aft end of the conical shell with sufficient stiffness to ensure that the shell will have a collapse pressure no less than the hydrostatic critical pressure. Without a ring at the aft end, the critical buckling pressure could be an order of magnitude less than that corresponding to simple support conditions.

The analysis given here is for a symmetrical pressure distribution. In general, the pressure distribution experienced during entry has an unsymmetrical component. For the majority of the entry environments investigated, the dominant unsymmetrical component corresponds to the first Fourier component, i.e., $\cos\theta$. This component tends to increase the circumferential compressive stress on the windward side of the entry capsule. This component also decreases the meridional tensile force on the leeward side of the entry shell. The margin of safety of the entry shell for the combined symmetrical and unsymmetrical loading component was determined by adding the compressive stresses due to each loading component and comparing the resulting stress to the critical hydrostatic buckling stresses accounting for the interaction with the axial tensile stress. This approach was considered to be valid providing the increased compressive stress, due to the unsymmetrical loading, existed over at least one circumferential wave length of the buckle pattern for symmetrical loading.

2. Buckling of Shell-ring Structure -- Buckling of the shell-ring structure was analyzed by an energy method. The deflection shape was first determined by assuming that the deformations were inextensional, after which the strain energy of the structure and the work done by the applied load during buckling could be calculated. Detailed derivations are given in Appendix B. The resulting formulas are summarized in the following paragraphs.

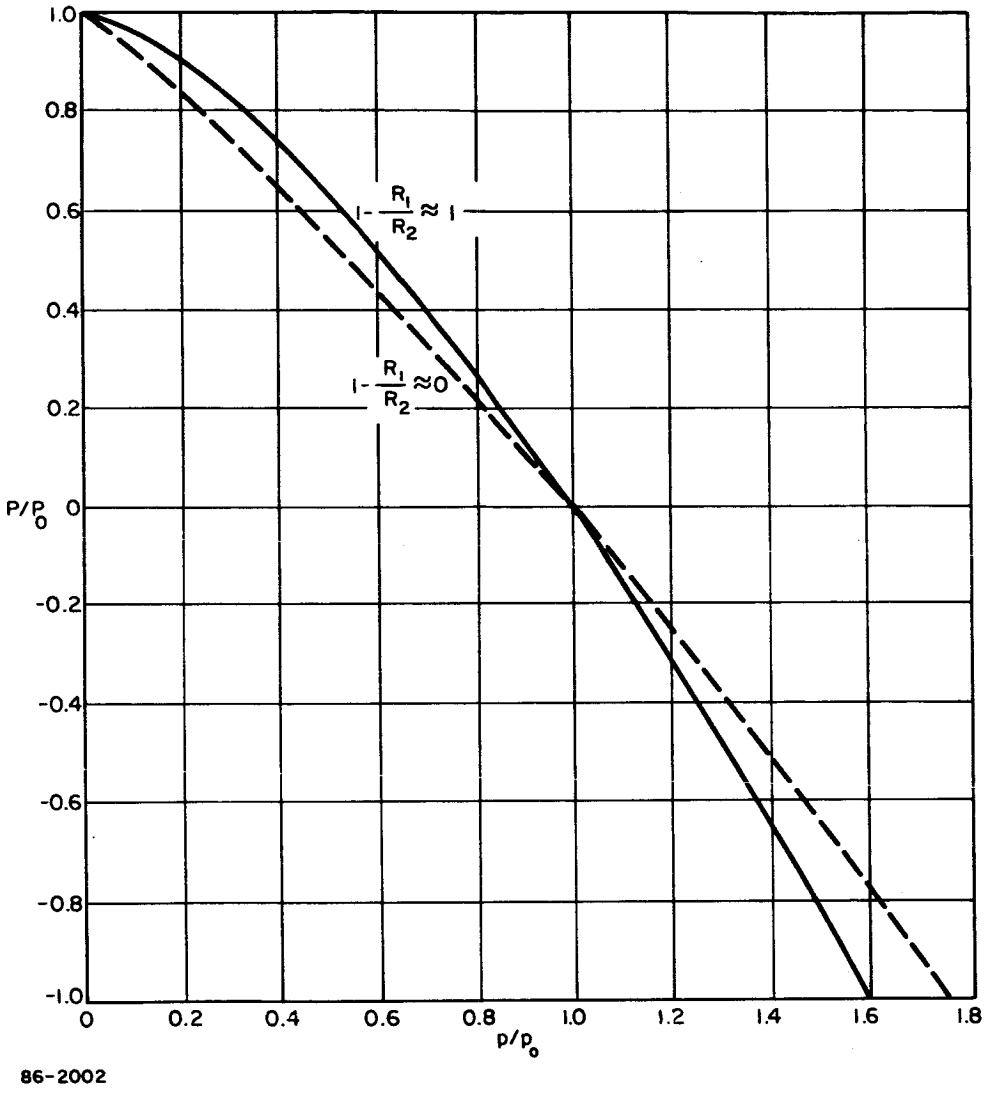

Figure 292 THEORETICAL INTERACTION CURVES FOR CONES UNDER COMBINED AXIAL LOAD AND EXTERNAL UNIFORM HYDROSTATIC PRESSURE

The strain energy of the ring is

$$U = \frac{\pi}{2a^3} \frac{(n^2-1)^2}{n^2 C + B_2} [(n^2 B_1 C + B_1 B_2 - B_{12}^2) \Delta_r^2$$

$$- 2n^2 B_{12} C \Delta_r \Delta_x + n^2 B_2 C \Delta_x^2]$$

where

n = number of lobes around circumference

a = radius

Δ_r, Δ_x = deformations perpendicular and parallel to axis, respectively

B_1, B_2, B_{12} = in plane, out of plane, and coupled rigidities, respectively

C = torsional rigidity

The work done by the uniform pressure is

$$V_{\theta o} = \frac{\pi P_o}{2 \sin \alpha \cos \alpha} \left\{ (n^2 - 1) \frac{(A + Br)^3}{3B} + \frac{\sin^2 \alpha}{n^2} \left[-(n^2 - 1 - \cos^2 \alpha) A^2 r + \cos^2 \alpha \, AB \frac{r^2}{2} + n^2 B \frac{r^3}{3} \right] \right\}_b^a$$

where P_o is the uniform pressure, α is the semi-vertex angle of the cone, and A and B are constants.

The pressure which causes buckling was found by equating the work to the strain energy of the ring. An expression for the strain energy of the shell is also given in Appendix B. This may be added to the strain energy of the ring, but the correction is usually minor.

Relations between Δ_x, Δ_r, A and B are also needed.

These are

$$B = -\frac{A}{b} \left(1 - \frac{\sin^2 \alpha}{n^2}\right)$$

$$\Delta r = A \left(1 - \frac{a}{b} - \frac{a}{b} \frac{\sin^2 \alpha}{n^2}\right) \cos \alpha$$

$$\Delta x = -A \left(1 - \frac{a}{b} - \frac{1}{n^2} + \frac{a}{b} \frac{\sin^2 \alpha}{n^2}\right) \sin \alpha$$

If the load has both symmetrical and unsymmetrical components, the work done by the unsymmetrical component is

$$V_{\theta n} = \frac{\pi P_n}{2 \sin \alpha} \left[A \left(1 - \frac{\sin^2 \alpha}{n^2} \right) \frac{r^2}{2} + B \frac{r^3}{3} \right]_b^a$$

and the solution is found by substituting the foregoing energy expressions into the equation

$$V_{\theta^\circ} + V_{\theta n} = U$$

In this case an abrupt buckling does not occur, but the deformations increase smoothly with load rather than jumping from one equilibrium state to another at a critical buckling load.

The procedure used in the analysis and design of the shell was first to determine the required face sheet and core depth of the honeycomb sandwich wall by considering instability of a shell with simply supported ends, and then determine the critical pressure for buckling of the shell and ring together by using the inextensional buckling theory. The stiffness of the ring was adjusted until both critical pressures were identical. The results are, of course, also applicable to monocoque shells.

3. Instability of Sandwich Construction -- Besides the shell-buckling modes of failure, honeycomb sandwich construction is subject to instability failures associated with the core material. Honeycomb sandwich construction can fail by face-sheet dimpling or wrinkling of the face sheets.

A rough estimate of the stresses necessary to cause face-sheet dimpling can be obtained from the empirical formula of Reference 59:

$$\sigma = \frac{1}{3} E_f \left(\frac{t_e}{S} \right)^{3/2} .$$

where S is the radius of a circle inscribed in the cell. This relationship dictates the maximum size of the honeycomb cell.

From Reference 60, the solution for wrinkling of the facings is

$$\sigma = (1 - \nu^2)^{\frac{2}{3}} (E_f E_c G_c)^{\frac{1}{3}} .$$

where E_c and G_c are the elastic moduli of the core material. This relationship establishes the stiffness requirements for the core. Knowing the stiffness requirements and the maximum cell size, the required foil thickness can be obtained from experimental data. The density is readily obtained from the specification of foil thickness and cell dimensions.

Core shear and crushing failures are discussed in paragraph 7. 1. 1. 1. Because of the lack of experimental verification of these analyses and their application to shells, a density ratio of core to face sheet of 0. 03 as suggested by Reference 61 was utilized in the design analysis.

7.1.2.2 Instability of Spherical Shells

1. General Instability -- The investigation of buckling of a spherical shell is similar to the study of buckling of a conical shell in paragraph 7.1.2.1. Both studies begin with theoretical solutions, but it is necessary in both cases to introduce empirical correction factors in order to get satisfactory results.

For a homogeneous spherical shell, the classical buckling pressure is given in Reference 62 as

$$P_{th} = \frac{2E}{[3(1-\nu^2)]^{\frac{1}{2}}} \left(\frac{t}{R}\right)^2$$

where

t = shell-wall thickness

R = spherical radius of curvature

E = Young's modulus

ν = Poisson's ratio

P_{th} = theoretical buckling pressure

The foregoing theoretical solution does not give satisfactory agreement with test data. Although newer and more sophisticated analytical and numerical solutions are available, none of these are entirely satisfactory either. Because of the importance of imperfections in this type of buckling, test data usually fall well below even the best theoretical solutions. For this reason the present analysis is based upon the experimental results for buckling of a spherical cap which are shown in Figure 293 (References 63, 64, and 65). The geometrical parameter λ used in this figure is defined by the equation

$$\lambda = 2[3(1-\nu^2)]^{\frac{1}{4}} \left(\frac{H}{t}\right)^{\frac{1}{2}}$$

where H is the height of the cap. By conservative curve fitting of the experimental data, it is found that the empirical buckling pressure p can be related to the theoretical buckling pressure q by the equation (Reference 66).

$$\frac{P_{cr}}{P_{th}} = \frac{1.1}{\lambda^{\frac{2}{3}}}$$

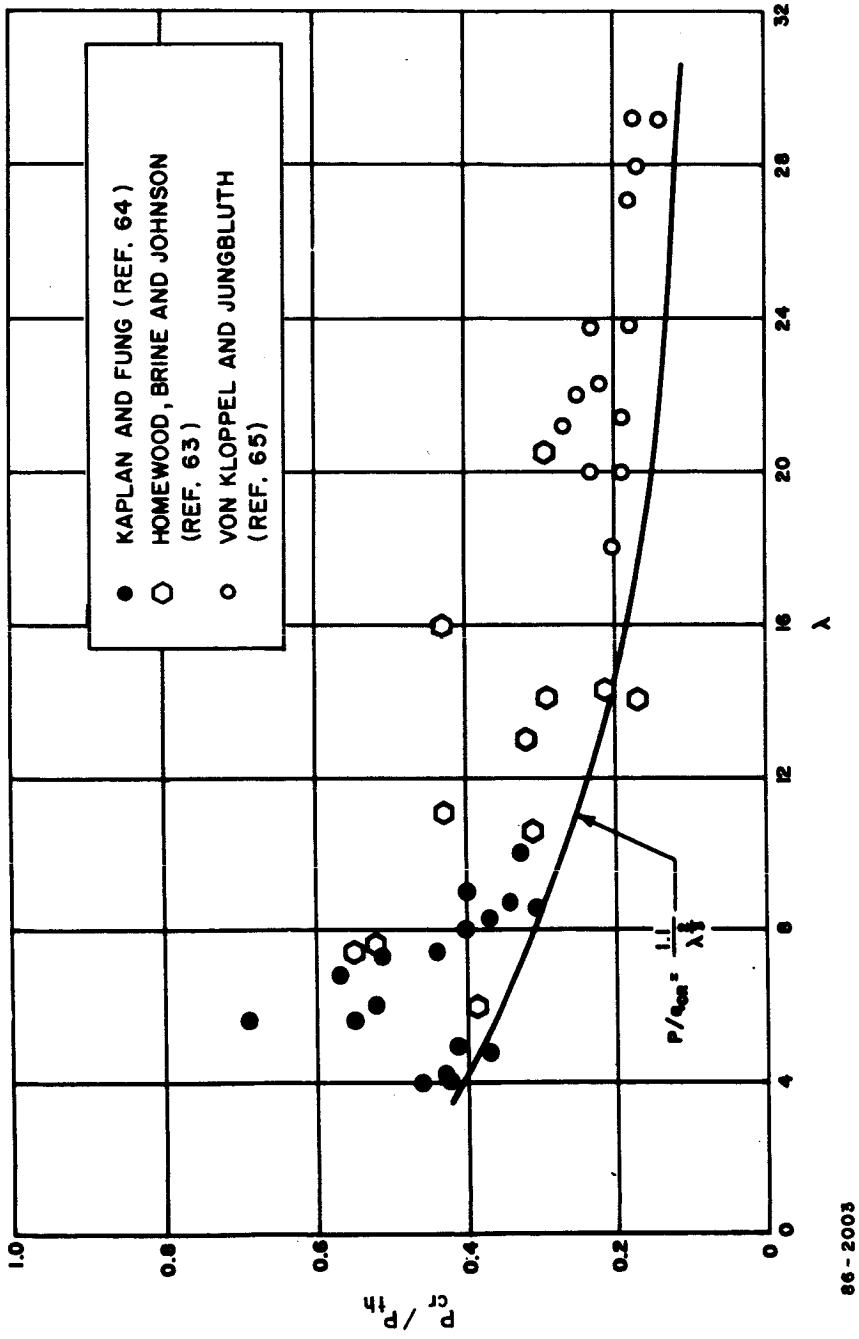

Figure 293 EXPERIMENTAL BUCKLING OF SPHERICAL SHELLS

from which

$$P_{cr} = \frac{0.665\, E t^{\frac{7}{3}}}{(1-\nu^2)^{\frac{2}{3}} R^2 H^{\frac{1}{3}}}$$

By using the analogy explained in paragraph 7.1.1.2, it is found that the equivalent result for a sandwich spherical cap is

$$P_{cr} = \frac{2.78\, E_f t_f t_c^{\frac{4}{3}}}{(1-\nu^2)^{\frac{2}{3}} R^2 H^{\frac{1}{3}}}$$

Where the subscripts f and c refer to the face and core parameters, respectively.

The spherical shell is supported at the forward end with its aft end force-free in a manner similar to the blunted cone. There is undoubtedly an interaction of the resulting tensile force with the buckling under uniform pressure. There was no apparent analysis of this interaction effect available; hence there will be some conservatism in the use of these expressions.

An analysis for determining the stiffness requirement for a ring at the aft end was not completed since the spherical shape was not considered in the conceptual design. The ring requirements were determined using the results for the conical shell. The procedure is undoubtedly conservative because of the inherent greater stiffness of the doubly curved spherical shell.

Core instability failure modes were analyzed in the same manner as described in paragraph 7.1.2.1.

7.1.2.3 Buckling of Circular Rings of Arbitrary Cross Section

The primary use of this ring-buckling analysis was to analyze the stability of the tension shell compression ring. The principal axes of a section of a typical compression ring are not aligned with the axis of revolution. The nonzero product of inertia terms in the moment-curvature relations therefore cause a coupling between the in-plane and out-of-plane buckling. Depending on the cross-sectional stiffness properties, there can be a significant difference between the critical buckling load when the ring is free to deform into its natural buckled form as compared to in-plane or out-of-plane buckling. The critical buckling force, of course, lies between the two extremes. The derivation of the general expression for buckling of a ring is given in Appendix A. The resulting formula is

$$N = \frac{(n^2 - 1)}{2\,(n^2 C + B_2)\,a^2} \left\{ [B_1 (n^2 C + B_2) + (n^2 - 1) B_2 C - B_{12}^2] \right.$$

$$\left. \pm \left\langle [B_1 (n^2 C + B_2) - (n^2 - 1) B_2 C - B_{12}^2] + 4 n^2 (n^2 - 1) B_{12}^2 C^2 \right\rangle^{\frac{1}{2}} \right\}$$

where

N = critical buckling force

n = number of waves around circumference

a = radius of circular ring

B_1, B_2, B_{12} and C = stiffness properties of ring cross section.

The analysis of inextensional buckling of the shell-ring structure in paragraph 7.1.2.1 contains this analysis in principle but in terms of strain energy. The shell-ring analyses also constrains the ring to buckle in a manner compatible with the shell deformations.

It should also be noted that the analysis for ring buckling is valid providing that local instability does not occur first and that the ring is sufficiently compact so that the effective moments of inertia are not significantly reduced by distortions of the cross section which sometimes occur in curved hollow beams. This amount of reduction of the effective moment of inertia lies somewhere between the theoretical results for circular and rectangular cross sections given in References 67 and 68.

7.1.2.4 Thermal Buckling

Since the heat shield has a much higher coefficient of thermal expansion than the shell, thermal buckling of the shell is possible as a result of cooling of the entire structure from an unstressed condition at a higher temperature, or as a result of thermal gradient in which the heat shield is cooler than the shell. This type of buckling can occur only if the bond between the heat shield and shell is absent or faulty.

No completely rigorous analysis has been made but several approximate checks on stability are possible. The simplest procedure is to calculate the compressive forces in the shell resulting from thermal mismatch. The buckling analysis discussed in paragraph 7.1.2.1 is then applied. The result of this calculation is conservative, since it is based on the assumption that the shell can deform freely into alternate inward and outward lobes, whereas the heat shield actually exerts some restraint on motion in the outward direction.

Another mode of buckling is also conceivable. Instability can occur with the formation of a plastic hinge or cusp in the shell. This type of buckling is analyzed in Reference 69. Although this analysis does not apply very accurately to the present problem, it can be used for rough order of magnitude calculation. The results indicate that there is a little tendency for the shell to buckle in this mode.

7.1.3 Suspended Capsule Structure

7.1.3.1 Preliminary Analysis

The suspended capsule structure described in paragraph 6.3.3.3 is statically indeterminate, at least for asymmetrical loadings. In the preliminary analysis assumptions were made as to the internal force distributions in order to obtain results to guide the design layouts. It should be noted that the configuration of the suspended capsule structure, during the preliminary design phase, was governed more by packaging requirements than by structural efficiency. As a consequence, the many changes in configuration did not warrant a detailed analysis since the results would soon become obsolete.

The assumed internal force distributions were used to determine the margins of safety of individual frames and of joints and attachments. The modes of failure considered were yielding, crippling, and buckling of the longerons and beams, and direct shear and bearing stresses in the joints and attachments.

7.1.3.2 Frame Analysis

After the initial sizing of the suspended capsule structure was completed using the procedures described in paragraph 7.1.3.1, the internal payload structure was analyzed as an idealized three-dimensional space frame.

The analysis was performed using the STRESS computer program* (Structural Engineering System Solver). This program uses the stiffness method to analyze two-or-three-dimensional structures with pinned or rigid joints, with prismatic or nonprismatic members, and subjected to concentrated or distributed loads with support motions permissible. The output consists of joint displacement, member distribution, member end forces and reactions. Details and usages of the computer program are given in References 70 and 71.

*Developed by the Department of Civil Engineering at the Massachusetts Institute of Technology.

Although the computer program does not handle curved members directly, satisfactory results may be obtained by approximating curved members as a continuous series of short straight members. The rings in the suspended capsule structural assembly were handled in this manner.

7.2 DYNAMIC ANALYSIS OF SHELLS

7.2.1 General Description of Lumped Parameter Approach

Dynamic loading of the capsule will occur during launch and spacecraft separation, during application of the ΔV force, and during reentry and parachute opening. The dynamic analysis performed in this study was confined to the entry shell in its entry configuration. For complex shell structures, such as those which have evolved in these studies, closed-form analytical solutions of the dynamic problems are not feasible. Instead, a lumped parameter mathematical model of the structure was developed which included all structural discontinuities, such as the end-ring and the payload attachment junction.

Equations of motion were written in a generalized matrix form for this model. The displacements were expressed in terms of modal quantities and generalized coordinates. Mass and stiffness matrices were obtained by utilizing the SABOR computer program for the mathematical model. The mode shapes and frequencies of vibration of the system were then found by numerical methods. The equations of motion then can be solved using this modal information and the forcing function under consideration. Structural loads and displacements thus can be determined as functions of time. This approach is applicable to both symmetric and asymmetric loadings. The forcing function for the asymmetric case is expanded into its Fourier components. Each harmonic is analyzed separately and results are superimposed for total loads and displacements as a function of time.

The SABOR program, as described in paragraph 7.1.1.2, computes the structural stiffness matrix. In addition it computes the structural mass matrix (M). As with the K matrix, the mass matrix for each element is found separately. The displacement function assumed in determining the element stiffness matrix is also used for the element mass matrix. Thus the two matrices are "consistently derived," which results in more accurate solutions. The total mass matrix, M, is formed by combining the individual element mass matrices.

Avco Computer Program 1384 is used to solve the equations of motion. Using the M and K matrices obtained from SABOR, it first computes the modal data (frequencies, mode shapes, modal damping matrix). The program then can solve the generalized equations of motion and compute the transient stresses and displacements of the system.

7.2.2 Comparison with Theoretical Results

Results of vibration analyses using the SABOR and 1384 programs were compared to an existing theoretical solution for conical shells. This theoretical solution is found in Reference 72. The referenced solution deals with both the extensional and the inextensional shell theories as applied to conical shells. These two theories are treated separately and then combined to give final results.

The case used for comparison was a conical shell with uniform thickness, having a semi-vertex angle of 60 degrees. The boundary conditions were fixed at the small end and unsupported at the large end.

The lowest natural frequency of the system in each harmonic is plotted in Figure 294. Very good agreement is demonstrated between the SABOR solution and theoretical results.

7.3 PARAMETRIC ANALYSIS

The initial studies of both the Entry from Approach Trajectory and Entry from Orbit concepts required that estimates be made of the structural weight function over a wide range of entry conditions, diameters, structural materials and construction methods. To accomplish this in time for the results to be useful to the system tradeoff studies, simplified structural analysis methods were used.

7.3.1 Linear Shell Analysis

If a shell design has been optimized for bending stresses at a given diameter, and then a design is required at a new diameter with the pressure distribution and magnitude remaining constant, it can be shown by examination of the differential equations that the stresses will be optimized at the new diameter if shell thicknesses are scaled at the same ratio as the linear geometrical coordinates.

To obtain a new design from a design which has been optimized for bending stresses at a different pressure, the stress resultant, N, and stress couple, M, are assumed to scale directly with the pressure. The new thickness then is selected to satisfy the following equation for an isotropic homogeneous shell wall:

$$\sigma_y = \frac{N}{t} \pm \frac{6M}{t^2} \quad \text{or} \quad t = \frac{1}{2\sigma_y}\left[\,|N| + \sqrt{N^2 + 24\,\sigma_y\,|M|}\,\right]$$

For scaling honeycomb sandwich shells,

$$\sigma_y = \frac{N}{2t_f} \pm \frac{M}{t_f t_c} \qquad (1)$$

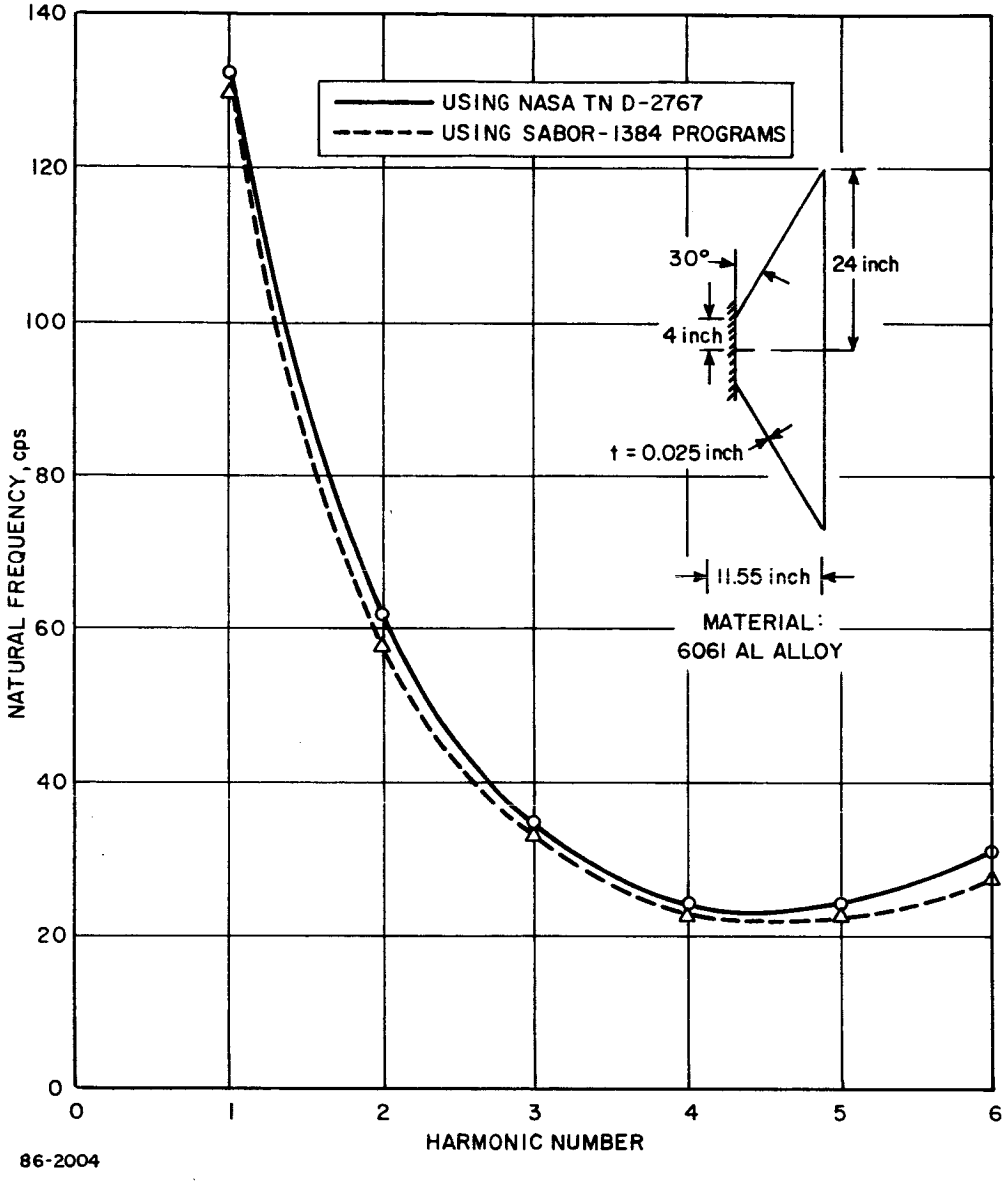

Figure 294 VIBRATION ANALYSIS--COMPARISON OF METHODS FOR FIXED-FREE CONICAL SHELL

represents approximately how stresses are calculated in the shell program using the honeycomb parameters t_f (face sheet) and t_c (core depth measured between mid-planes of face sheets).

For this result only the maximum stress σ is desired, hence the absolute values of N and M, at the point in the shell of interest, are used.

In order to obtain the required t_f and t_c for a given yield stress, σ_y, it is necessary to have another relationship. This can be obtained from the requirement for minimum weight or,

$$W = 2\rho_f t_f + \rho_c t_c \tag{2}$$

solving for t_c in (1) and substituting into (2)

$$W = 2\rho_f t_f + \frac{\rho_c M}{\sigma_y t_f - \frac{N}{2}} \tag{3}$$

To obtain minimum weight

$$\frac{\partial W}{\partial t_f} = 2\rho_f - M\rho_c \sigma_y \left(\sigma_y t_f - \frac{N}{2}\right)^{-2} = 0 \tag{4}$$

or

$$t_{f\,opt} = \frac{1}{\sigma_y}\left[\frac{N}{2} + \left(\frac{M\rho_c \sigma_y}{2\rho_f}\right)^{\frac{1}{2}}\right] \tag{5}$$

and

$$t_{c_{opt}} = \frac{M}{\sigma_y t_{f_{opt}} - \frac{N}{2}} \tag{6}$$

The values of M and N are obtained from the previous design and scaled to the new pressure at various points along the shell. The calculated values of $t_{f_{opt}}$ and $t_{c_{opt}}$ will not be precisely those required for an optimized shell since the N and M distribution is dependent on thickness. The thicknesses, however, are good starting points for the next iteration.

For the preliminary analysis, the stress distribution was considered to be uniaxial when comparing it to the allowable yield stress. Later analyses used the von Mises effective stress for a biaxial stress field for determining the allowable stress or $\sigma_{eff} = \sqrt{\sigma_\xi^2 - \sigma_\theta \sigma_\xi + \sigma_\theta^2}$. If the biaxial yield criterion is used, then the roots of a fourth-order polynomial for a

homogeneous shell wall or a sixth-order polynomial for a sandwich wall have to be obtained in order to determine the required thickness to optimize the shell for bending stresses. A shell synthesis program which uses this procedure is presently under development.

For a quick estimate of the skin thickness requirements for the tension shell, aft of the payload, the maximum meridional stress was determined from the membrane solution given in Reference 73. The thickness was selected so that the allowable stress was not exceeded.

7.3.2 Buckling Analysis

A buckling failure criterion for both the modified Apollo and blunted-cone entry shells was used to obtain the initial structural thicknesses. The weight obtained from these preliminary thicknesses was multiplied by a factor of 1.7 in order to allow for the additional weight required for end-rings, doublers, splices, and attachments. The buckling criterion used for the blunted-cone shell is given in paragraph 7.1.2.1 and the Apollo shell in paragraph 7.1.2.2.

The buckling equations are incorporated in Avco's computer program No. 1886. This program automatically selects the structural thicknesses and computes the resulting weight for a symmetrical Newtonian pressure distribution as a function of structural material and construction. The program can handle monocoque and sandwich construction for spherical shells as well as ring-stiffened configurations for conical shells. The ring-stiffened conical shells are analyzed by an orthotropic conical buckling theory given in Reference 74. The program determines the optimum thicknesses subject to specified constraints of minimum sheet thickness, allowable yield stress, minimum core density and depth. A description of the program is given in Reference 75.

During the course of a parametric study and preliminary design, a simple analytical expression is sometimes useful to quickly determine the effect of varying a structural parameter. The following expressions were derived and represent how shell weight will vary for the important sandwich shell parameters.

For a sandwich shell having the form of a segment of a sphere of radius R and height H, the buckling pressure is, from paragraph 7.1.1.2.

$$P_{cr} = \frac{2.78\, E_f\, t_c^{\frac{4}{3}}\, t_f}{(1-\nu^2)^{\frac{2}{3}} R^2 H^{\frac{1}{3}}} \qquad (1)$$

The weight per unit area is

$$w = 2\rho_f t_f + \rho_c t_c \qquad (2)$$

By solving equation (1) for t_c and substituting the result into Equation (2), it is found that

$$w = 2\rho_f t_f + 0.46 (1 - \nu^2)^{\frac{1}{2}} \left(\frac{p}{E_f}\right)^{\frac{3}{4}} \left(\frac{R^2 H}{t_f^3}\right)^{\frac{1}{4}} \rho_c R \tag{3}$$

Minimization of this result with respect to t_f leads to

$$t_f = 0.363 (1 - \nu^2)^{\frac{2}{7}} \left(\frac{\rho_c}{\rho_f}\right)^{\frac{4}{7}} \left(\frac{p}{E_f}\right)^{\frac{3}{7}} \left(\frac{H}{R}\right)^{\frac{1}{7}} R \tag{4}$$

Substitution of (4) into (3) leads to the equation for optimum weight

$$w = 1.75 (1 - \nu^2)^{\frac{2}{7}} \left(\frac{\rho_f}{E_f}\right)^{\frac{3}{7}} \left(\frac{H}{R}\right)^{\frac{1}{7}} \rho_c^{\frac{4}{7}} p^{\frac{3}{7}} R \tag{5}$$

The value of t_f given by Equation (4) must be checked against the minimum face-sheet thickness permitted by minimum gage requirements and by yield stress. The latter requirement is

$$t_f \geq \frac{pR}{4\sigma_y} \tag{6}$$

If either of these requirements leads to a value of t_f greater than that given by Equation (4), the weight minimization based upon buckling only is not valid, and Equation (3) must be used instead of (5). If t_f is determined by minimum gage thickness, Equation (3) is the final result as it stands. If the yield condition leads to the greatest required value of t_f, the final result is obtained by substituting (6) into (3). This is

$$w = \frac{pR}{2} \left(\frac{\rho_f}{\sigma_y}\right) + 1.20 (1 - \nu^2)^{\frac{1}{2}} \left(\frac{\sigma_y}{E_f}\right)^{\frac{3}{4}} \left(\frac{H}{R}\right)^{\frac{1}{4}} \rho_c R \tag{7}$$

where

R = spherical radius of curvature

t = thickness

p = surface pressure

E = Young's modulus

w = density

c, f, = subscripts referring to core and face sheet parameters

For a conical shell, the starting point is the formula for p derived in paragraph 7.1.2.1. For simplicity it will be assumed that the cone is complete (this is very nearly correct for the 60-degree blunt cone). Then the equation for critical buckling pressure becomes

$$p_{cr} = 8.8\,(1-\nu^2)^{-\frac{3}{4}} E_f \left(\frac{t_f}{R_b}\right)\left(\frac{t_c}{R_b}\cos\alpha\right)^{\frac{3}{2}} \sin\alpha$$

The optimization can now be carried out in the same way as for a spherical shell. For optimum weight based on buckling only:

$$t_f = 0.23\,(1-\nu^2)^{\frac{3}{10}} \left(\frac{p R_b}{E_f \sin\alpha}\right)^{\frac{2}{5}} \left(\frac{\rho_c R_b}{\rho_f \cos\alpha}\right)^{\frac{3}{5}}$$

and

$$w = (1-\nu^2)^{\frac{3}{10}} \left(\frac{\rho_f}{E_f}\cot\alpha\right)^{\frac{2}{5}} \left(\frac{R_b}{\cos\alpha}\right) \rho_c^{\frac{3}{5}}\, p^{\frac{2}{5}} \qquad (8)$$

If the face sheets are selected to satisfy a yield criterion,

$$t_f = \frac{p R_b}{2\sigma_y \cos\alpha}$$

and

$$w = \frac{p R_b}{\cos\alpha}\left(\frac{\rho_f}{\sigma_y}\right) + 0.23\,(1-\nu^2)^{\frac{1}{2}} \left(\frac{2\sigma_y}{E_f}\cot\alpha\right)^{\frac{2}{3}} \frac{\rho_c R_b}{\cos\alpha} \qquad (9)$$

The unit area weight of a gage limited sandwich shell varies as

$$w = 2\rho_f t_f + 0.23\,(1-\nu^2)^{\frac{1}{2}} \left(\frac{p R_b}{E_f t_f \sin\alpha}\right)^{\frac{2}{3}} \frac{\rho_c R_b}{\cos\alpha} \qquad (10)$$

where

α = semi-vertex angle of the conical shell

R_b = base radius.

Whichever condition requires the greatest face thickness governs the design.

Equation (8) demonstrates that for a sandwich shell optimally designed for buckling only, the material efficiency of the face-sheet materials varies as $(\rho_f/E_f)^{2/5}$. If, however, the face sheets have to satisfy a uniaxial yield criterion, the material efficiency varies approximately as ρ_f/σ_y.

The second term of Equation (9) is negligible, since the face sheet would not be at the yield stress unless the pressure was relatively high.

If the sandwich shell face sheets are minimum gage limited, the efficiency varies approximately as $\rho_f t_f$ from Equation (10), or in other words, the material with the lowest density and smallest obtainable gage is the most efficient in this case. The second term in Equation (10) was neglected since minimum gage limited designs normally occur at relatively low pressures.

For a parametric study of buckling of the tension shell compression ring, the cross section of the compression ring was assumed to be a hollow circular tube. The applied load was assumed to be equal to that value of the meridional stress resultant required to suppress the circumferential stress resultant for a Newtonian pressure distribution. The slope of the shell at $R = R_b$ was set equal to 90 degrees. Out-of-plane buckling was selected as the stability criterion, Reference 62.

Forward of the payload reaction circle, the shell is under axial and circumferential compression. The shell thickness was based on a buckling criterion for a cone under hydrostatic pressure, as described in paragraph 7.1.2.1.

8.0 HEAT SHIELD - CONCEPTUAL DESIGN-ENTRY FROM THE APPROACH TRAJECTORY

8.1 INTRODUCTION AND SUMMARY

The initial effort in the heat shield analysis was centered on the parametric study of concepts as outlined in Sections 1.0 and 2.0 to determine the required heat shield weights for the shapes, diameters and critical conditions established by aerodynamic and systems studies. Candidate heat-shield materials were selected as previously proposed and a set of their properties and characteristics was established on the basis of existing data. The uncertainty associated with these data indicated the need for a materials characterization (at least preliminary) program, which was then outlined and executed in conjunction with other "in-house" programs. The interpretation of these data was factored into the next phase of this study and, together with the data obtained from LRC, formed the basis for selection of standard reference property and characteristics data used in the subsequent conceptual design of the heat shield. The properties used were for decontaminated and sterilized materials and the effect of Martian atmosphere and exposure to vacuum, although considered, was not factored in. The response of the heat shield to the radiative heat flux and surface phenomena specific to the Martian atmosphere should be stressed. Considering the uncertainties in the material characteristics, atmosphere definition and the stage of system development, only approximate methods were used in the initial stages of heat shield analysis, while somewhat more exact methods were used for the study of the revised concepts.

8.1.1 Configurations and Concepts

The configurations and mission concepts evaluated during this study have been discussed in sufficient detail in the previous sections of this volume. The use of atmosphere Model 1 and high V_e for the majority of the original concepts, and the use of Model 2 with lower V_e for the revised ones constitute the salient differences between the two sets of concepts.

The use of low M/C_DA and Model 2 for the 1971 mission and high M/C_DA and Model 3 atmosphere for the future mission result in increased weight for the latter. The above differences are a direct consequence of the change in the environmental conditions.

8.1.2 Requirements, Constraints and Design Criteria

The requirements imposed on the heat shield parallel those for the structure through the mission sequence from the factory-to-parachute deployment. During the spaceflight phase the heat shield is aided by the thermal control system and together they assure integrity of the structure and of the payload.

The assurance of the integrity of the structures and of the payload through attenuation of the external thermal environment during entry at minimum weight expenditure is then the objective of the heat shield design.

In achieving this objective the main constraint upon the heat shield is to accommodate the critical environments created during the entry phase (described in Section 2.0) while providing protection for the structure (described in 5.0) to perform its function. It may thus be seen that the design condition for the heat shield stems from the aerodynamic environments and from the structural design criteria which were summarized in the previous sections.

The satisfaction of the design conditions is predicated on the availability, selection and understanding of the behavior of appropriate heat shield materials, i.e., materials displaying a proper combination of thermal, optical and ablative characteristics. As a result complex interactions have to be considered in establishing the heat shield design and material specifications.

On the other hand, the weight of the heat shield is sensitive to the initial conditions (temperatures) existing at the onset of entry. These temperatures depend on the thermal control exercised prior to entry with the attendant spacecraft-flight capsule interface, (discussed elsewhere) and postentry problems. Thus in addition to the environmental, structural and material requirements present in any entry-vehicle design, a set of thermal control constraints on the heat shield (or vice versa) is found.

The requirement for decontamination and sterilization imposes a constraint on the selection of heat shield materials from the beginning of the design process, limiting the choice to only such materials that can satisfy this initial requirement.

The requirements imposed by the definition of mission concepts (multi-mission structure-"B", 1971 mission-"C", and future mission-"D") were relatively straightforward. The heat shield involved in the 1971 and multi-mission structure shells called for use of the critical heating atmosphere (atmosphere 2) associated with the light vehicle ($M/C_DA = 0.15$) since it was deemed relatively simple to increase the required heat shield for the future heavy payload vehicle should the 1971 mission reveal the presence of atmosphere 2. This would not have been the case for the shell structure, which would involve redesign of the entry vehicle, and thus was designed for either the light or heavy payload entering either of the atmospheres for the multi-mission structure. The future mission was, on the other hand, defined for atmosphere 3 and the heavy payload vehicle ($M/C_DA = 0.49$) resulted in the maximum heating environment for which the heat shield was designed. In either case, minimum entry angle and maximum velocity on the V-γ operational map was used for the critical heating design point.

The minimum heat shield structure composite weight is the single most important constraint on the design. A summary of the heat shield critical environmental parameters is given in Table LI for the parametric study and in Table LII for the revised concepts, and in Table LIII for the reference design.

8.1.3 Performance Summary

The criterion for the performance of the heat shield is the minimum weight for a given environmental heat input, or conversely, a maximum capacity for heat input accommodation per pound of heat shielding material for actual entry conditions, and the weight fraction of the total vehicle weight. The performance of various generic shape material combinations for the concepts studied is given in Tables LIX and LX of paragraph 8.3.2.1 and weight fractions are shown in Table LXI of paragraph 8.3.3.

The thermal protection system applied to the blunt cone was an ablative heat shield which appeared to be most efficient for at least the forebody of the probe/lander for the anticipated environmental conditions. These conditions indicated also that low-density and low-conductivity materials with moderately good ablative characteristics were desirable for this application. A number of materials with these characteristics were investigated and are shown in Tables LVI and LVII of paragraph 8.2.2. Of these material candidates only four were selected for further investigation, either on the basis of more acceptable thermal properties (since most of them exhibited similar gross ablative behavior) or minimum degradation in mechanical (as well as thermal) properties when subjected to simulated decontamination and dry-heat sterilization cycles. The preliminary thermal properties and ablative characteristics used in the design studies with these materials are shown in Table LVIII of paragraph 8.2.2.

In the parametric studies preceding the selection of aerodynamic shape and base diameter, the relationships between the heat shield thickness (for the four materials), total aerodynamic heating and allowable structural temperature were established which were then used together with the relationship between aerodynamic heating and base diameter in systems tradeoff studies. The angle of attack effect on heat shield weight was also investigated and was found to be small. Once the reference designs were established for the blunted cone, appropriate local heat shield thickness and weight were calculated and are shown for the reference designs and concepts in Tables LIV and LV for the 1971 and multi-mission structure, and future missions respectively, for the forebody heat shield only. The cork silicone material displayed the minimum requirement for the heat shield weight, and thus was selected for reference purposes. The weight fraction was shown in the same tables. It should be noted however, that studies in progress indicated a possible reversal in weight requirements for the four materials and that manufacturing considerations may favor the Purple Blend Mod 5.

TABLE LI

CRITICAL DESIGN PARAMETERS

D = 197 inches; M/C_DA = 0.4; V_e = 25,000; γ_e = -20 degrees; α = 11 degrees

ATM 1; W = 4500 pounds

		Tension Shell (maximum heat location)	Modified Apollo (stagnation)	Blunt Cone (60°) (stagnation)
Q_c	Btu/ft^2	21,368	1615	6042
Q_r	Btu/ft^2	3,285	2471	609
$\dot{q}_c$	Btu/ft^2-sec	458	31.8	119.8
$\dot{q}_r$	Btu/ft^2-sec	133	100	29.1
$P_{s_{max}}$	lb/ft^2	523	236	227
$r_{max_{sonic}}$	lb/ft^2	5.42	0.94	3.11

TABLE XLI

HEATING SUMMARY

(particle trajectories)

$D = 15$ ft., $\gamma_e = -20°$, $V_e = 23,800$ fps, $Z_e = 800,000$ ft

Concept		Weight (pounds)	Atm.	q_s Maximum (Btu/ft^2/sec)	Q_s (Btu/ft^2)	Q_I (Btu/ft^2)	q Maximum (Btu/ft^2/sec)	Q_r (Btu/ft^2)
Modified Apollo	D	4500	3	49	989	1345	106	963
Modified Apollo	B&C	1450	2	19	753	750[x]	19	304
Blunt cone	D	4500	3	188	4405	2182	7.0	62
Blunt cone	B&C	1390	2	70	2798	803[x]	1.0	19
Blunt tension shell	D	4500	3	291	6824	15090[y]	225	2278
Blunt tension shell	B&C	1435	2	111	4416	4303[z]	38	683

x entire heat pulse laminar

y heat pulse at S/Rn = 14.7 (not sonic point)

z heat pulse at S/Rn = 11.6 (not sonic point)

TABLE LIII

SUMMARY OF HEATING AND HEAT SHIELD DESIGN PARAMETERS (BLUNT CONE)

Flight and Vehicle Parameters \ Design Concept		1971 and Future Multimission Mission	
		Light Vehicle	Heavy Vehicle
M/C_DA	Slugs/ft^2	0.15	0.49
α_e	Degree	11.5	11.5
α Peak Heating	Degree	<1°	<1°
Q_{stag}	Btu/ft^2	2798	4405
$\dot{q}_{max}$ diameter	Btu/ft^2/sec	70	188
Pulse Duration	second	130.	85.
Material Heat Shield		Cork Silicone	
Material Structures		Beryllium 0.020 inch	
$T_{structure}$	°F	300-500	300-500
T at Entry	°F	100-300	100-300
S.F.	--	1.0	1.0
End of Pulse	--	Impact	

TABLE LIV

BLUNT CONE - HEAT SHIELD REQUIREMENTS - LIGHT VEHICLE (ENTRY WEIGHT = 1390 LBS)

M/C_DA = 0.15 slugs/ft^2;
Atmosphere 2;

V_e = 23,800 ft/sec;

γ_e = -20 degrees;

D = 15 ft.

Station (S/R_B)	Q_c (Btu/ft^2)	Q RAD (Btu/ft^2)	Nylon Phenolic		Cork Silicone		Avcoat 5026-99		Purple Blend	
			(inch)	(lb/ft^2)	(inch)	(lb/ft^2)	(inch)	(lb/ft^2)	(inch)	(lb/ft^2)
0.0	2800	19	0.52	1.56	0.45	0.96	0.50	1.00	0.54	1.69
0.2	1875	30	0.48	1.44	0.42	0.90	0.47	0.94	0.51	1.59
0.6	900	76	0.43	1.29	0.38	0.81	0.43	0.86	0.47	1.47
1.0	800	108	0.41	1.23	0.37	0.79	0.42	0.84	0.46	1.44

Weight Fraction = $\frac{\text{Forebody H/S}}{\text{Entry Vehicle}}$ = 17 percent -- cork silicone

TABLE LV

BLUNT CONE - HEAT SHIELD REQUIREMENTS - HEAVY VEHICLE (ENTRY WEIGHT = 4500 LBS)

M/C_DA = 0.49 slugs/ft^2;
Atmosphere 3;

V_e = 23,800 ft/sec;

γ_e = -20 degrees;

D = 15 feet

Station (S/R_B)	Q_c (Btu/ft^2)	Q RAD (Btu/ft^2)	Nylon Phenolic		Cork Silicone		Avcoat 5026-99)		Purple Blend	
			(inch)	(lb/ft^2)	(inch)	(lb/ft^2)	(inch)	(lb/ft^2)	(inch)	(lb/ft^2)
0.0	4400	62	0.56	1.68	0.49	1.04	0.56	1.12	0.63	1.97
0.2	2950	98	0.52	1.56	0.45	0.96	0.50	1.00	0.56	1.75
0.6	1416	250	0.46	1.38	0.41	0.88	0.46	0.92	0.50	1.56
1.0	1900	350	0.48	1.44	0.43	0.92	0.47	0.94	0.51	1.59

Weight Fraction = $\frac{\text{Forebody H/S}}{\text{Entry Vehicle}}$ = 5.7 percent - cork silicone

8.1.4 Conclusions and Problem Areas

On the basis of results obtained during this phase of the program, it is possible to arrive at the following conclusions relating to the heat shield design of the Mars flight capsule.

1) The primary heat shield weights as a fraction of total vehicle weight are the smallest for the modified Apollo followed by the blunt cone and tension shell configurations, in that order.

2) The material which provided, in general, the lightest heat shield is cork silicone, followed by Avcoat 5026-99, low-density nylon phenolic, and Purple Blend, Mod 5. This ranking is likely to change as is also the case with heat shield weights when analysis is undertaken using as a basis the properties resulting from the heat shield material characterization program. *

3) Increased heating resulting from angle of attack, incorporating effects of spin and lunar motion, has only a small effect on overall heat shielding requirements.

4) To assure completeness of the design for the selected configuration, heat shield analyses will have to be performed to determine the effect on performance of the V_e, γ_e, M/C_DA, spin, angle of attack parameters as well as that of material property and characteristic variation, and atmospheric composition.

5) Rearwards entry failure mode should be considered in the design.

8.2 DESIGN CRITERIA

The selection of appropriate safety factors and design criteria is one of overwhelming importance in the course of any design problem. Since the determination of heat shield requirements is a design problem, it is necessary to evaluate pertinent factors related to this general area.

For purposes of discussion, the problem will be subdivided into a discussion of: environmental criteria, materials selection, structural requirements and spaceflight criteria.

*The preliminary characterization program at this stage of analysis was almost complete with respect to determination of the material properties related to the internal energy phenomena associated with cork silicone, Avcoat 5026-99, and Purple Blend Mod 5. The surface (heat shield boundary layer) phenomena were being investigated and preliminary results were available for the entry from orbit study.

8.2.1 Environmental Criteria

With respect to aerodynamic heating environments, conditions yielding the highest integrated heating within the anticipated flight envelope were selected. This implies the highest possible entry velocity and the lowest possible entry angle. During the first phase of this study this corresponded to V_e = 25,000 ft/sec and γ_e = -20 degrees and emphasis on Model 1 atmosphere. During the phase which resulted from redirection from LRC, the preceding was changed to V_e = 23,800 ft/sec and γ_e = -20 degrees with emphasis on atmospheric Models 2 and 3. Tabulations of heating parameters are available in paragraphs 3.1 and 3.4.3.2.

The effects of angle of attack due to lunar motion have been investigated. It was found that the heat shield requirements increased by approximately 2 percent over those for a zero-angle of attack case. The reason for this is that the angle of attack became very small by the time peak heating was achieved. The preceding, of course, also reflects the effects of radiant heating.

In regard to other environmental parameters, such as enthalpy and shear, predictions indicate these to be in the ranges of 12,500 Btu/lb to 100 Btu/lb and 10 lb/ft^2 (tension shell) to 0 lb/ft^2. Such ranges are well within the testing capabilities of arc-jet facilities and the materials characterization effort will fully embrace this range.

The effects of spin as outlined in paragraph 3.2.2.2.3.1 when reflected on heat shield thickness, result in only a small effect with respect to increases (if not decreases) in these thicknesses. In the cases where actual increases in heating were predicted these were found to be small.

8.2.2 Materials Criteria

The general heat flux levels for the various flight capsules investigated indicate that the use of a low-density and low-conductivity material would appear to provide the most efficient (lowest weight) design. In order to determine if certain materials possessed higher efficiency values than others, it was necessary to investigate the results of arc tests conducted at typical entry conditions (cold-wall heat flux, q_c = 100 Btu/ft^2-sec; enthalpy H_m = 8500 Btu/lb). These data are shown in Table LVI using the insulative heat of ablation (q_I^*)*, as defined in References 76 and 77 as the figure of merit. As can be seen from Table LVI the materials listed exhibit roughly the same level of performance at the particular test conditions. It should be noted that the results of the arc tests as indicated in Table LVI do not

*q_I^* is defined as the amount of cold-wall heat a pound of material can absorb without exceeding a specified back face temperature, 600°R in this case. Care should be taken when interpreting test data to obtain this heat of ablation since even for a given material it is a function of original sample thickness and backup composite. In addition, any thermocouple error can result in a false conclusions about the relative performance of the various materials.

necessarily mean that the materials will perform similarly when subjected to the transient entry environment, and indeed it could be possible that under transient conditions the lowest performer from this table could produce, (as shown for certain entry conditions in Reference 76) the lowest weight design. Therefore, one should view this performance data with caution since it provides only approximate comparative data.

TABLE LVI

COMPARISON OF CANDIDATE MATERIALS

Material	Insulative Heat of Ablation (Btu/lb)
Purple blend Mod 5	15, 000
Cork silicone	12, 000
Avcoat 5026-99	11, 000
DC2048	10, 000
Avcoat 5026-39M	11, 000
Avcoat 3008	11, 000
Armstrong 2755 Cork	11, 000

Since the materials to be investigated appeared to perform similarly and possess low density and conductivity, and in addition, a stable char, it was determined that the material to be studied be those described in Tables LVII and LVIII (Reference 7).

In addition to the low-density and thermal conductivity requirement, it is also desirable that these materials provide acceptable ablation characteristics. The cork silicone, Avcoat 5026-00 and low-density nylon phenolic materials exhibit carbonaceous char layers which will combine with the oxygen available in the Mars atmosphere in a combustion process (arc tests indicate that 5026-99 is more susceptible to loss of material by combustion). The purple blend produces a silica-carbon char and its ablation performance appears to be controlled strongly by the environmental conditions or combustion. This latter effect is evident from the results of Reference 77 and also Avco arc tests which indicate expansion of the material at heat flux levels of 100 Btu/ft^2-sec and loss of material at 200 Btu/ft^2-sec. From the above statements it can be seen that to understand properly the ablation behavior of these materials requires a significant amount of arc testing at various heat-flux levels and gas compositions in addition to several shear levels.

TABLE LVII

COMPOSITION OF CANDIDATE HEAT SHIELD MATERIALS

Cork silicone 893-73	72 percent Ground cork 23 percent Silicone binder 5 percent Glass fibers
Purple blend (Mod 5)	66 percent Silicone 16 percent Phenolic microballoon 10 percent Glass 7 percent Quartz fibers 1 percent Cab-O-Sil
Avcoat 5026-99	38 percent Epoxy resin 44 percent Phenolic microballoons 9 percent Refrasil fibers 9 percent Glass fibers
Low density nylon phenolic	50 percent Nylon 25 percent Phenolic 25 percent Phenolic microballoons

TABLE LVIII

PRELIMINARY MATERIAL DESIGN PROPERTIES

Material / Property	Purple Blend Mod 5	Cork Silicone	5026-99	Low Density Nylon Phenolic
K Btu/ft-hr-°F	0.067	0.045	0.045	0.058
ρ lb/ft^3	37.5	25.6	24.0	36.0
C_p Btu/lb-°R	0.387	0.52	0.44	0.40
ϵ	0.60	0.59	0.59	0.80
η_L	0.51	1.26	0.81	0.995
η_T	0.17	0.42	0.27	0.332
H_v Btu/lb	-330	-2390	-1850	-2075
T_A °F	3000	3000	3000	3500

It should be noted that since a requirement exists for decontamination and sterilization survival, materials which failed to pass preliminary criteria related to these conditions have been excluded. In future tests the effect of long-time exposure of materials to space vacuum will have to be factored into the material selection procedure.

8.2.3 Thermo-Structural Criteria

In the course of preliminary thermo-structural design it is a general practice to specify a simple criterion for design such as a maximum allowable structure temperature. When the design progresses beyond this stage and the configuration of the thermo-structural composite is better defined (and vehicle parameters such as M/C_DA also achieve a more advanced definition) it is the usual practice to perform detailed thermo-structural calculations to ascertain integrity and compatibility of the heat shield and structural materials. This threshold was not achieved in the course of this phase of the design primarily due to lack of complete thermophysical characterization of the heat shield material. It should be noted, however, that the preliminary analysis indicated no severe compatibility problems with the materials used as candidate heat shield materials. Their selection was indeed influenced by their favorable mechanical properties.

Another problem which had to be circumvented was the effect of the structure on the required heat shield. Due to lack of timely definition of the structure (normal for this phase of the design effort) it was tacitly assumed that the structure was 0.020-inch minimum gage of beryllium for purposes of the thermodynamic calculations. This then assumes a minimum of structure heat capacity, and as such is conservative (overestimates the weight requirement).

The selected maximum allowable level of 300° F on the structure temperature is per se a reasonable preliminary design value. The resulting 300 to 500° F bondline temperature allowable (if not controlling the design) may be somewhat conservative. However, the selection reflected the uncertainty in the knowledge of the initial entry temperature achievable by the thermal control system. The initial estimates ranged from 100-300° F. Since effectively a 200° F temperature rise was allowed in the heat shield calculations, while using 100° F as the initial condition, the whole approach to the problem did not appear conservative. As later became apparent, this 100° F assumption was about 50° F lower than the average of maximum and minimum predicted spaceflight temperature, and made the situation somewhat nonconservative if one assumes the most extreme free-flight mode.

The third uncertainty arose from the fact that the thermal calculations were generally carried out to beyond Mach 1. A more realistic time would have been the time when Mach 1 is achieved because this is the time of parachute

deployment. This approach tends to make the predictions conservative because extension of the analysis beyond Mach 1 results in continuously rising structure temperatures. Considering, however, that: (a) no thermodynamic safety factor was used in the heat shield calculations, and (b) that a normal rather than the rearward failure mode entry case was evaluated, the above treatment was perhaps justified. Hence, with respect to thermostructural criteria the present designs have two conservative factors relating to: a) the soak time, and b) the assumption of minimum structure capacity, offsetting three nonconservative factors relating to: a) the extreme temperature condition at the onset of reentry, b) the lack of any imposed thermodynamic safety factors; and c) failure mode considerations.

8.2.4 Spaceflight and Landed Payload Temperature Considerations

Due to the lack of specific flight capsule temperature information early in the program, it was assumed that its temperature was uniform at 100° F at the onset of entry. As improved spaceflight information became available, this assumption appeared to be realistic since it is within a few degrees of the average of extreme values anticipated. For a discussion of the specific results see paragraph 6.6.3.2. The question arises as to whether the maximum temperature should not be used. However, in light of the discussion in paragraph 8.2.3, it becomes obvious that such an approach leads to a compounding of safety factors and as such may not be acceptable.

With reference to postentry lander payload temperatures, it was not possible to arrive at this stage of the design at a meaningful estimate of what the temperature rises in the lander payload might be as a result of the entry phase of flight. However, the temperature rise in the crushable material as a result of entry can be reasonably expected to be on the order of approximately 100° F.

8.3 RESULTS AND DISCUSSION

Presented in this section are numerical data, pertinent to the design of a heat shield for a Mars flight capsule, which have been generated in the course of this part of the study. This includes general parametric information which is useful not only from the standpoint of understanding the actual design sequence but also in providing working figures. It is then followed by a section discussing heat shield design analysis. It encompasses such items as detailed heat shield requirements, structural temperature tradeoff, and the characteristics of temperature profiles in a heat shield during the entry phase of flight. The remaining topics deal with comparisons of heat shields for the generic shapes, comparison of materials, and development problem areas. The theoretical analysis, design methods used, and materials characterization efforts are described in Section 10.0 of this book.

8.3.1 General Parametric Data

Two basic schemes have been used for the designs presented in paragraph 8.3.2. During the first part of this study, program 1266 (or 1800) was used. The heat shield design routine of this program is described in References 79 and 80. It should be noted however, that no results presented here were generated by this method since, after redirection was received from LRC regarding entry velocity and atmospheres, the general approach was modified. As a result, all previous results (generated by 1266) became obsolete due to the change in design condition and hence are not reported.

The actual method used in arriving at heat shield thickness requirements is outlined in detail below. Basically, it hinges upon the use of design curves which are generated for typical environments, and as such produce fairly accurate results without the necessity of performing many detailed repeat computations.

The first step in generating thermodynamic design curves relates to the selection of a characteristic heating rate versus time curve. Since in the case of the Mars flight capsule the heating environments differ widely with respect to the existence of turbulent flow, it was necessary to select three characteristic pulses. The first of these was representative of body stations where the flow was all laminar, such as stagnation regions. The second was representative of conditions where the turbulent flow heating was 79 percent of the total heating. The third was characteristic of conditions where 100 percent of the turbulent flow heating prevails (or more realistically where the heating associated with laminar flow is small). An extrapolation scheme for intermediate conditions is discussed later in this section. Once characteristic heating pulses are selected, the values of the integrated heating may be varied by application of suitable multipliers to the heating rate ordinate. This basically provides environments which can be varied over the entire spectrum of integrated heating values. At this stage several values of heating rate multipliers are selected to correspond to desired levels of integrated heating for use in the succeeding steps.

For each of the selected values of integrated heating, one arbitrarily, but with some foresight, selects a number of heat shield thicknesses which are analyzed in detail for their behavior under the heating environments. This was accomplished by means of computer program 1600.1 (also discussed in Section 10.0 and Reference 81). The result is that for each value of integrated heating one arrives at several backface temperatures each of which are associated with one specific heat shield thickness. It then becomes possible to make plots with the ordinate as the backface temperature, the abcissa as the heat shield thickness, and parametric with respect to integrated heating. (For an example refer to Figure 300. By cross plotting for selected values of backface temperature, one arrives at plots of integrated heating versus heat shield thickness required to produce the desired

backface temperature. Thus, given a value of integrated heating, the heat shield thickness required can be readily predicted.

The matter of interpolation for prediction of heat shield requirements must be considered for cases where the turbulent flow heating differs from the proportions (laminar-to-turbulent) for which integrated heating versus thickness functions have been generated. The heating versus thickness plots are used to establish the heat shield thickness requirement at the same level of integrated heating for the various percentages of turbulent heating given on those curves. The next step is to make a cross plot of thickness required versus percentage of turbulent heating and reading the required thickness for the given percentage of turbulent heating.

Figures 295 through 298 are plots of integrated heating versus required heat shield thickness for Avcoat 5026-99, Purple Blend Mod 5, cork silicone, and low-density nylon phenolic respectively. The material properties used to generate these data are discussed in Section 10.0. The initial temperature used in generating these data was 100°F. A minimum structural thickness of 0.020 inch of beryllium was also utilized. The data in the figures reflects no safety factor per se but are believed to be conservative for the reasons outlined in paragraph 8.2.

8.3.2 Thermal Analysis

This section examines in detail the heat shield requirements and generic behavior for various design conditions and capsule configurations. The results are completely based upon the technical approach and analysis outlined in Section 10.0 (Program 1600.1) and design criteria discussed above. The information discussed in 8.3.1 was used in generating some of the results. All of the aerodynamic heating used in these analyses is presented and discussed in Section 2.0.

8.3.2.1 Heat Shield Requirements

This discussion will confine itself primarily to the results obtained during the second part of this study (revised concepts) utilizing atmospheric Models 2 and 3, entry velocity of 23,800 ft/sec and entry angle of -20 degrees. The emphasis is placed on the revised concepts because the first part of the study utilized an entry velocity of 25,000 ft/sec and placed heavy emphasis on the Model 1 atmosphere for purposes of heating load predictions. Neither of these conditions, both of which increase heating, were considered realistic at this stage of design.

Figure 299 is a plot of local heat shield weight required for the modified Apollo configuration. The heat shield thickness variations are constant across the forward face of the configuration. As can be seen from the

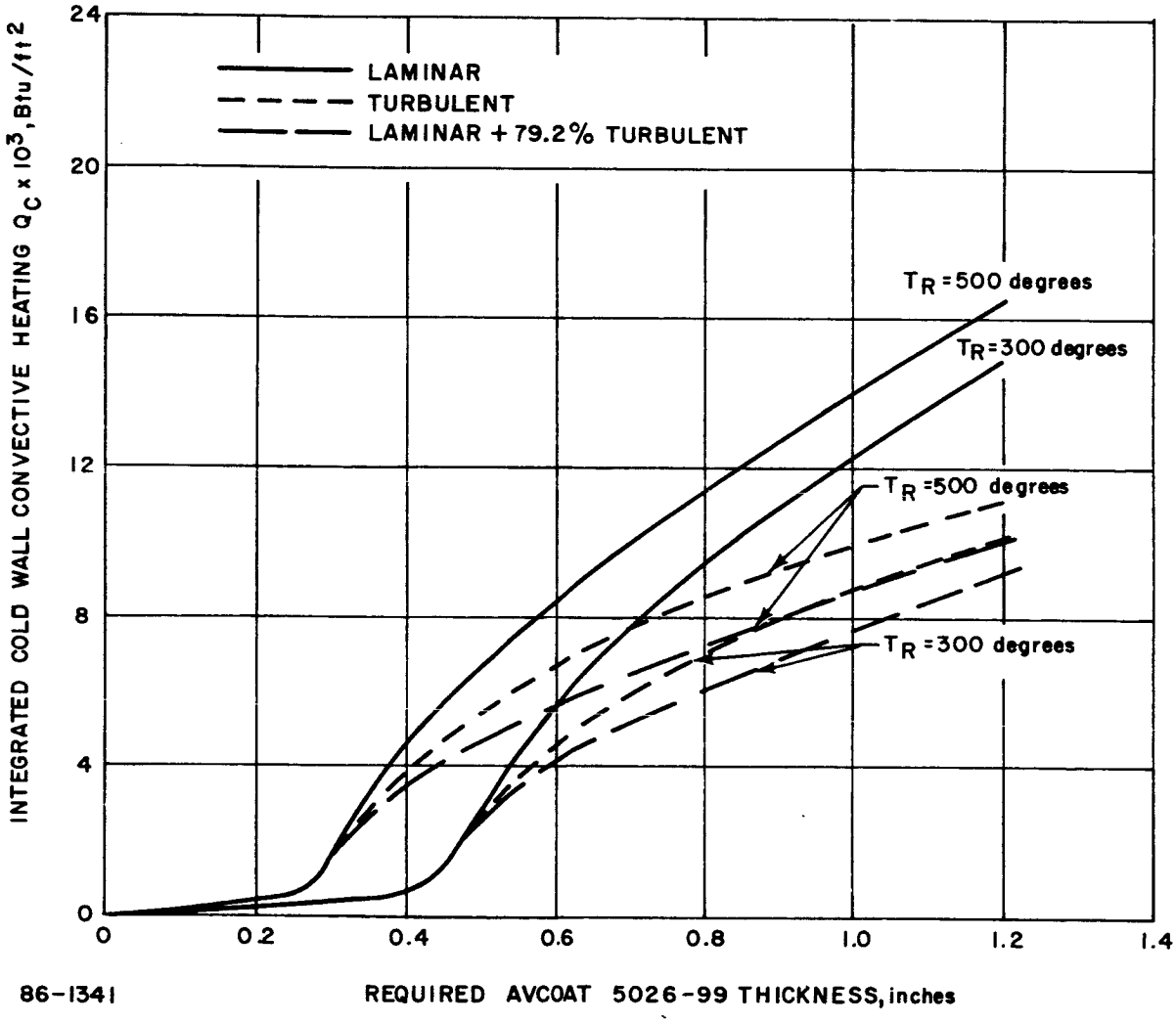

Figure 295 REQUIRED AVCOAT 5026-99 THICKNESS

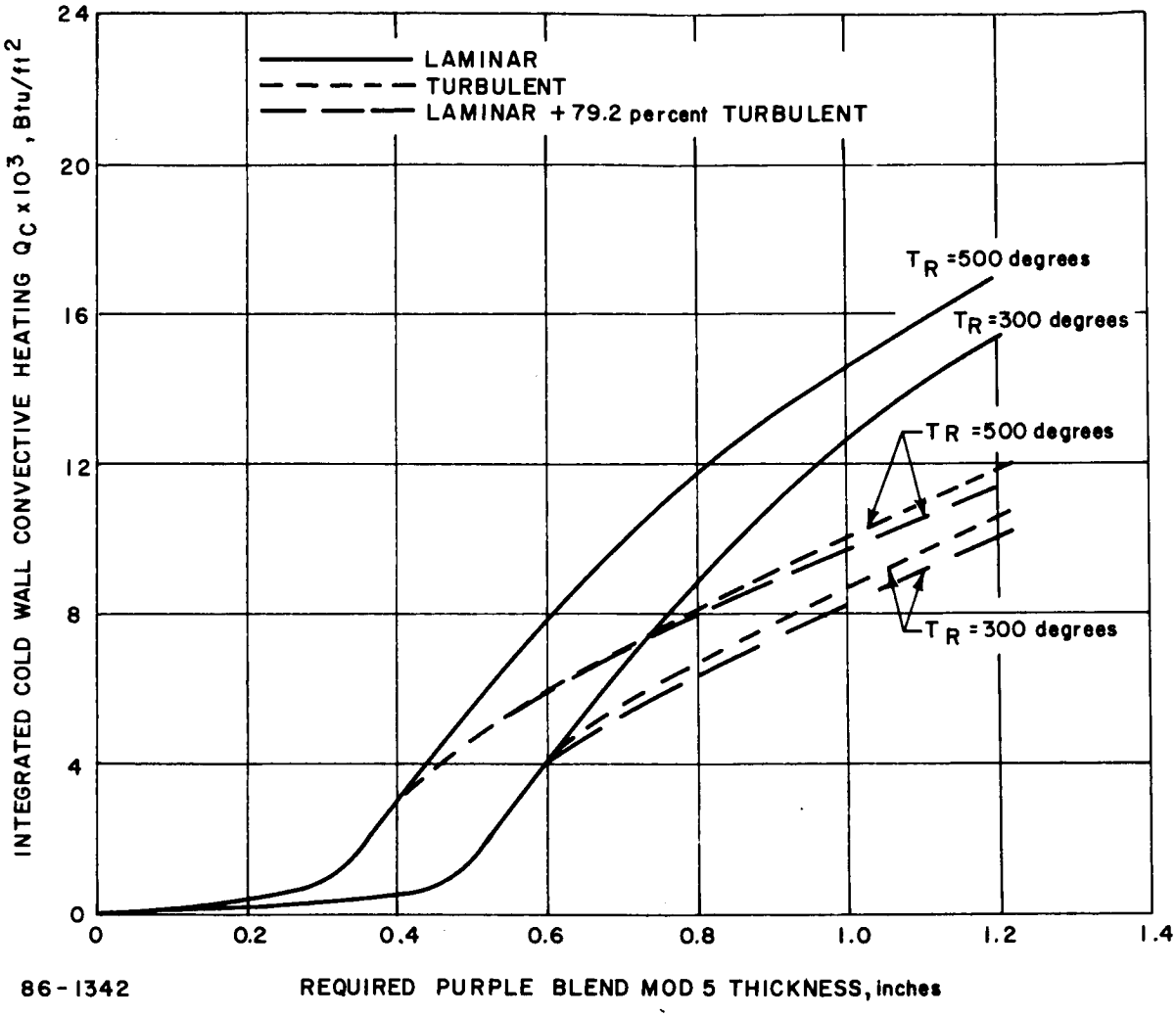

Figure 296 PURPLE BLEND-MOD 5 THICKNESS REQUIREMENTS

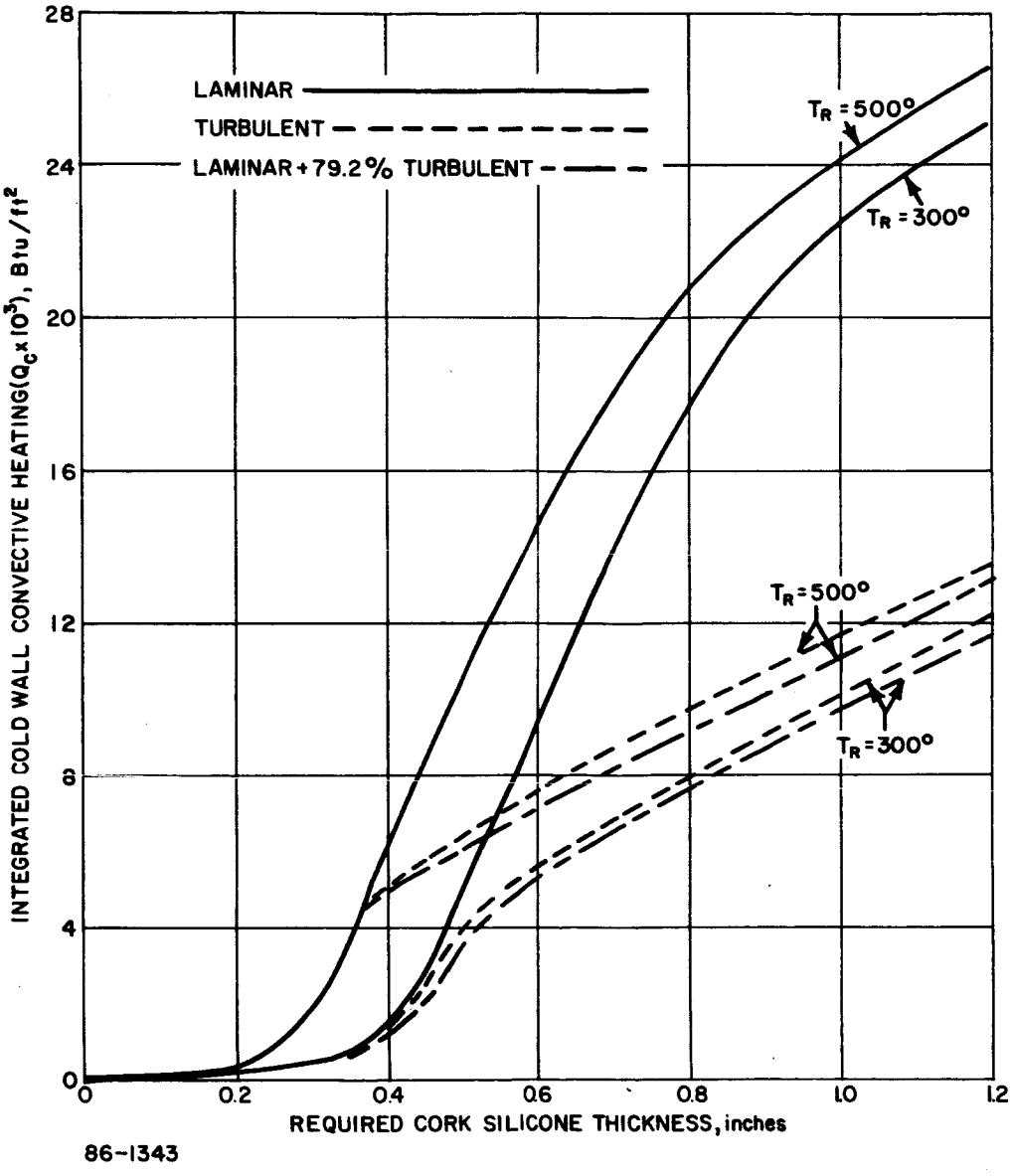

Figure 297 CORK SILICONE THICKNESS REQUIREMENT

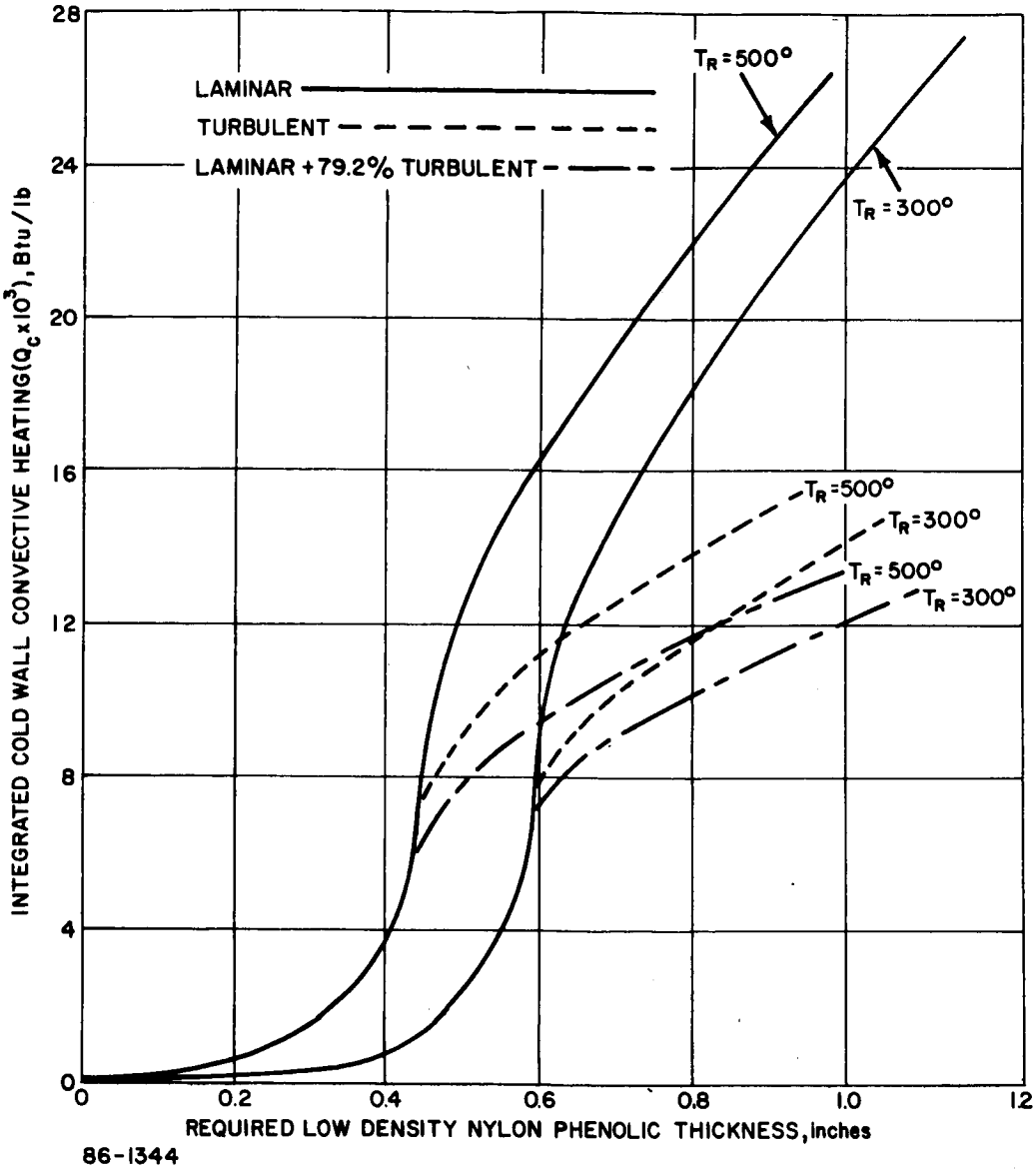

Figure 298 LOW DENSITY NYLON PHENOLIC THICKNESS REQUIREMENTS

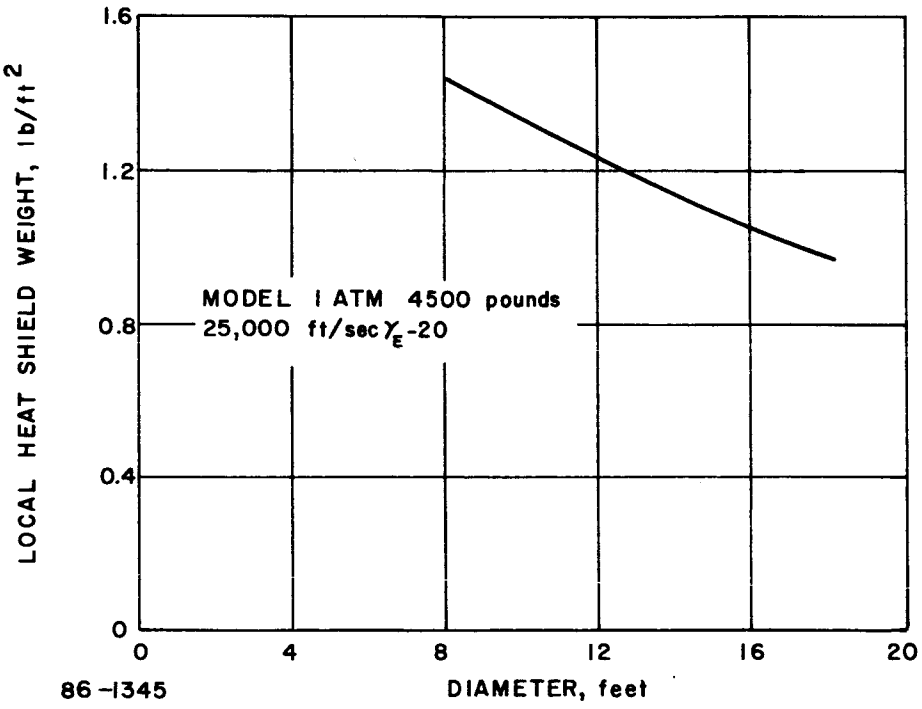

Figure 299 LOCAL HEAT SHIELD WEIGHT--MODIFIED APOLLO CONFIGURATION-CORK SILICONE

figure, the heat shield increases in thickness as the diameter decreases. This trend is to be expected because the heating environment follows the same pattern. It should be noted that these results are for atmospheric Model 1 and the high velocity which was used in the first part of the parametric study. Furthermore, parallel to the decrease in diameter, an increase in M/C_DA is effected since a constant total capsule weight of 4500 pounds is maintained which contributes to the local heat shield weight increases.

Table LIX shows the heat shield requirements for four heat shield materials in terms of both thickness and local heat shield weights for a vehicle with $M/C_DA = 0.15$ slugs/ft^2 and penetrating a Model 2 atmosphere. The three shapes considered are the tension shell, blunted cone, and modified Apollo, all of which were analyzed for the reference diameter of 180 inches. Table LX is similar to the preceding table except that a heavier vehicle is considered (4500 pounds) and the atmospheric Model 3 is used. Both tables also summarize the aerodynamic heating environments by providing the values of integrated convective and radiative heating at each of the body stations considered.

Examination of these results discloses that cork silicone provides the lightest weight heat shield and Purple Blend Mod 5 the heaviest. However, in light of the lack of detailed characterization of the heat shield candidate materials it is well to emphasize that this ranking of the material is only as valid as the material properties used in the analysis. Furthermore, it would not be surprising to see the relative ranking of the candidates change and also the overall heat shield weights shift (probably downward) as a result of studies using materials properties which are derived from the preliminary characterization effort.

The afterbody of both the blunt cone and modified Apollo are predicted to require thermal protection. The amounts of heat shield required varies from 0.080 inch to 0.20 inch of cork silicone. The problem is associated basically with insulation as distinguished from ablation. It is believed that different materials such as foams and insulators (Min K) may provide the optimum afterbody heat shield from a weight point of view. Preliminary calculations indicate large order weight savings over cork silicone for such materials. This area should be further investigated.

8.3.2.2 Structural Temperature Tradeoffs

Figure 300 shows a typical structural temperature variation with thickness for various levels of integrated heating. This is one of the curves which was used to generate the Q versus L curves presented in Section 8.3.1. These curves indicate that in the area of interest ($\approx 300°$ F) an approximate weight saving of 10 percent (high flux) to 20 percent (low flux) can be realized for every 100° F increase in structural temperature.

TABLE LIX

HEAT-SHIELD REQUIREMENTS -- LIGHT PAYLOAD VEHICLE
$M/C_DA = 0.15$ SLUGS/FT^2 ATMOSPHERE 2
$V_e = 23{,}800$ FT/SEC $\gamma_e = -20$ DEGREES

A. Tension Shell

Station (S/RN)	Qc (Btu/ft^2)	Q RAD (Btu/ft^2)	Nylon Phenolic		Cork Silicone		Avcoat 5026-99		Purple Blend	
			(inches)	(lb/ft^2)	(inches)	(lb/ft^2)	(inches)	(lb/ft^2)	(inches)	(lb/ft^2)
0.0	4316	305	0.55	1.60	0.49	1.04	0.55	1.10	0.62	1.94
2.0	1296	305	0.44	1.32	0.40	0.85	0.45	0.90	0.49	1.53
8.0	1992	370	0.48	1.44	0.43	0.92	0.47	0.94	0.52	1.63
14.7	4181	955	0.55	1.60	0.50	1.07	0.57	1.14	0.60	1.88

B. Blunted Cone

Station (S/R_B)	Qc (Btu/ft^2)	Q RAD (Btu/ft^2)	Nylon Phenolic		Cork Silicone		Avcoat 5026-99		Purple Blend	
			(inches)	(lb/ft^2)	(inches)	(lb/ft^2)	(inches)	(lb/ft^2)	(inches)	(lb/ft^2)
0.0	2800	19	0.52	1.56	0.45	0.96	0.50	1.00	0.54	1.69
0.2	1875	30	0.48	1.44	0.42	0.90	0.47	0.94	0.51	1.59
0.6	900	76	0.43	1.29	0.38	0.81	0.43	0.86	0.47	1.47
1.0	800	108	0.41	1.23	0.37	0.79	0.42	0.84	0.46	1.44

C. Modified Apollo

Station (S/R_B)	Qc (Btu/ft^2)	Q RAD (Btu/ft^2)	Nylon Phenolic		Cork Silicone		Avcoat 5026-99		Purple Blend	
			(inches)	(lb/ft^2)	(inches)	(lb/ft^2)	(inches	lb/ft^2)	(inches)	(lb/ft^2)
Blunt Face	753	304	0.42	1.26	0.38	0.81	0.43	0.86	0.47	1.47

TABLE LX

HEAT-SHIELD REQUIREMENTS -- HEAVY PAYLOAD VEHICLE
ENTRY WEIGHT = 4500 lb. ATMOSPHERE 3
V_e = 23,800 ft/sec γ_e = -20 DEGREES
M/C_DA = 0.49 slug/ft^2

A. Tension Shell

Station (S/R_N)	Qc (Btu/ft^2)	Q RAD (Btu/ft^2)	Nylon Phenolic		Cork Silicone		Avcoat 5026-99		Purple Blend	
			(inches)	(lb/ft^2)	(inches)	(lb/ft^2)	(inches)	(lb/ft^2)	(inches)	(lb/ft^2)
0.0	6924	108	0.59	1.77	0.54	1.15	0.66	1.32	0.71	2.22
2.0	3708	108	0.53	1.59	0.48	1.02	0.56	1.12	0.58	1.81
8.0	4928	130	0.56	1.68	0.55	1.18	0.63	1.26	0.65	2.03
14.7	14578	270	1.03	3.09	1.45	3.09	2.08	4.16	1.70	5.31

B. Blunted Cone

Station (S/R_B)	Qc (Btu/ft^2)	Q RAD (Btu/ft^2)	Nylon Phenolic		Cork Silicone		Avcoat 5026-99		Purple Blend	
			(inches)	(lb/ft^2)	(inches)	(lb/ft^2)	(inches)	(lb/ft^2)	(inches)	(lb/ft^2)
0.0	4400	62	0.56	1.68	0.49	1.04	0.56	1.12	0.63	1.97
0.2	2950	98	0.52	1.56	0.45	0.96	0.50	1.00	0.56	1.75
0.6	1416	250	0.46	1.38	0.41	0.88	0.46	0.92	0.50	1.56
1.0	1900	350	0.48	1.44	0.43	0.92	0.47	0.94	0.51	1.59

C. Modified Apollo

Station (S/R_B)	Qc (Btu/ft^2)	Q RAD (Btu/ft^2)	Nylon Phenolic		Cork Silicone		Avcoat 5026-99		Purple Blend	
			(inches)	(lb/ft^2)	(inches)	(lb/ft^2)	(inches)	(lb/ft^2)	(inches)	(lb/ft^2)
R/R_B 1.0	1157	963	0.46	1.38	0.42	0.90	0.47	0.94	0.51	1.59
R/R_B 1.0	1338	385	0.46	1.38	0.42	0.90	0.47	0.94	0.51	1.59

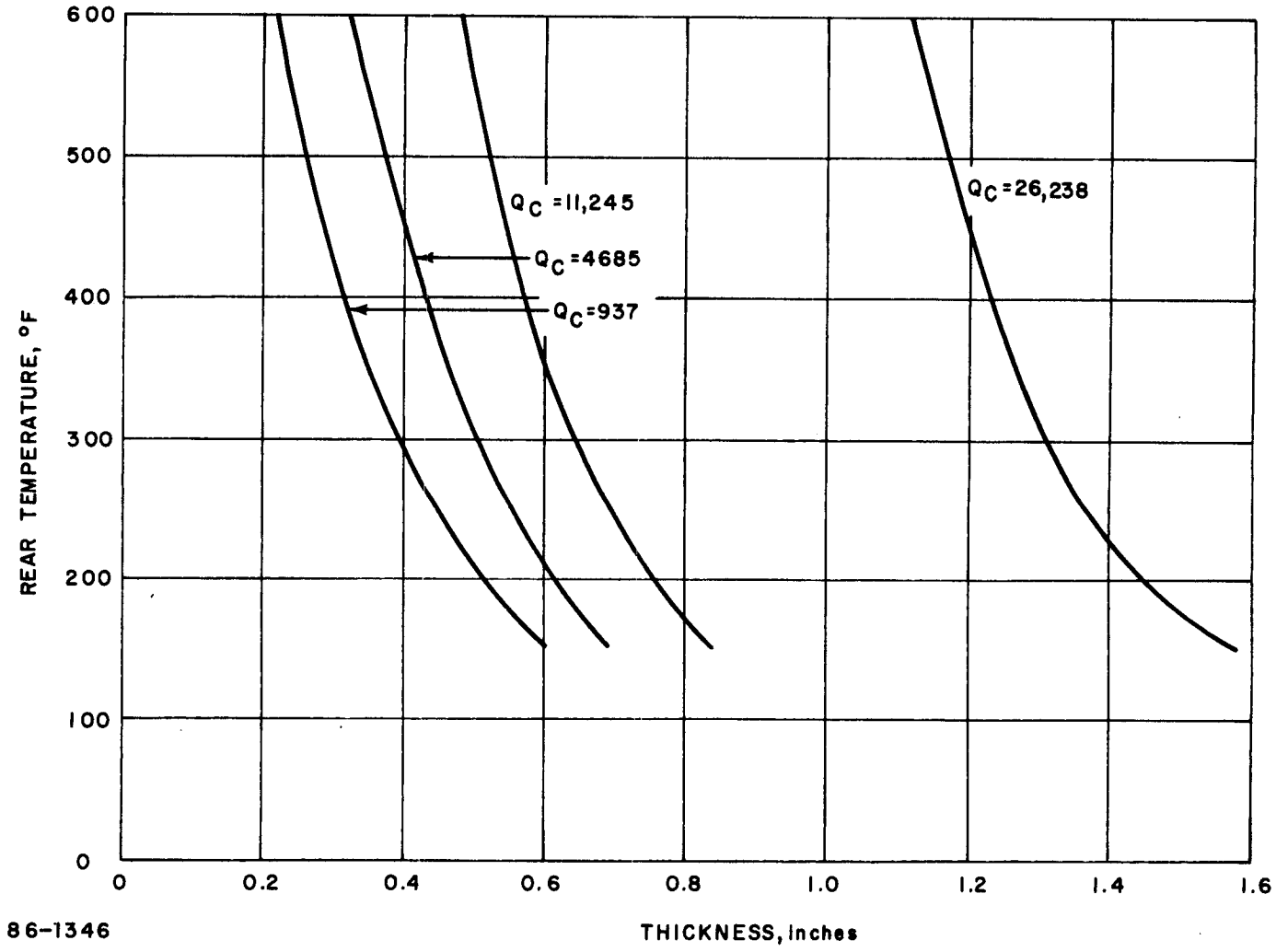

Figure 300 THICKNESS REQUIREMENTS OF CORK SILICONE--LAMINAR HEATING

Therefore it is evident that proper definition of allowable backface temperature and of the initial temperature at the onset of entry must be made to provide a minimum weight design. Although Figure 300 is plotted for cork silicone, it is fairly representative of the other candidate materials. The mean weight variation of the heat shield forebody as a function of the backface temperature is shown in Figure 301.

These figures also assume a structural thickness of 0.02 inch of beryllium. If the structure heat capacity were doubled (0.040 inch of beryllium), the net effect on vehicle heat shield weight would be on the order of a 10-percent reduction. However, this relationship is not linear and the percentage reduction in weight becomes progressively smaller as the structure thickness is increased. It should also be noted that in the case of honeycomb structural members, the concept of a structural capacity can be misleading. Hence, further studies are required in this area once the heat shield material has been fully characterized and the structure finalized.

8.3.2.3 Temperature Distributions

In light of the present state of materials characterization it is somewhat academic to discuss in great detail the predicted temperature gradients in the thermostructural composite during the entry phase. However, it should be mentioned that the proposed method of analysis as discussed in Section 10.0 with the material properties fully characterized, is the only means available for realistically making such predictions. Temperature gradients are, of course, a necessary input in predictions of thermal stresses and strain levels in the thermostructural composite during the entry phase.

A typical set of temperature gradients is shown in Figure 302. These are illustrated for purposes of demonstrating the generic characteristics of such a plot. In this case it should be noted that 0.055 inch of surface recession has been predicted. It should also be noted that the backface temperature begins to rise a long time after peak heating and peak dynamic pressure.

8.3.3 Comparison of Heat Shields for Generic Shapes

Table LXI compares heat shield weight as a percentage of total capsule weight for the cork silicone material. It is observed that, certainly in the case of the $M/C_DA = 0.15$ slug/ft^2 and even in the case of the heavier vehicle, the heat shield is an important subsystem in the sense that it does make a significant contribution to the vehicle weight. The second factor of significance is that as the vehicle weight increases, and hence M/C_DA and heating increase also, the overall fraction of heat shield weight decreases.

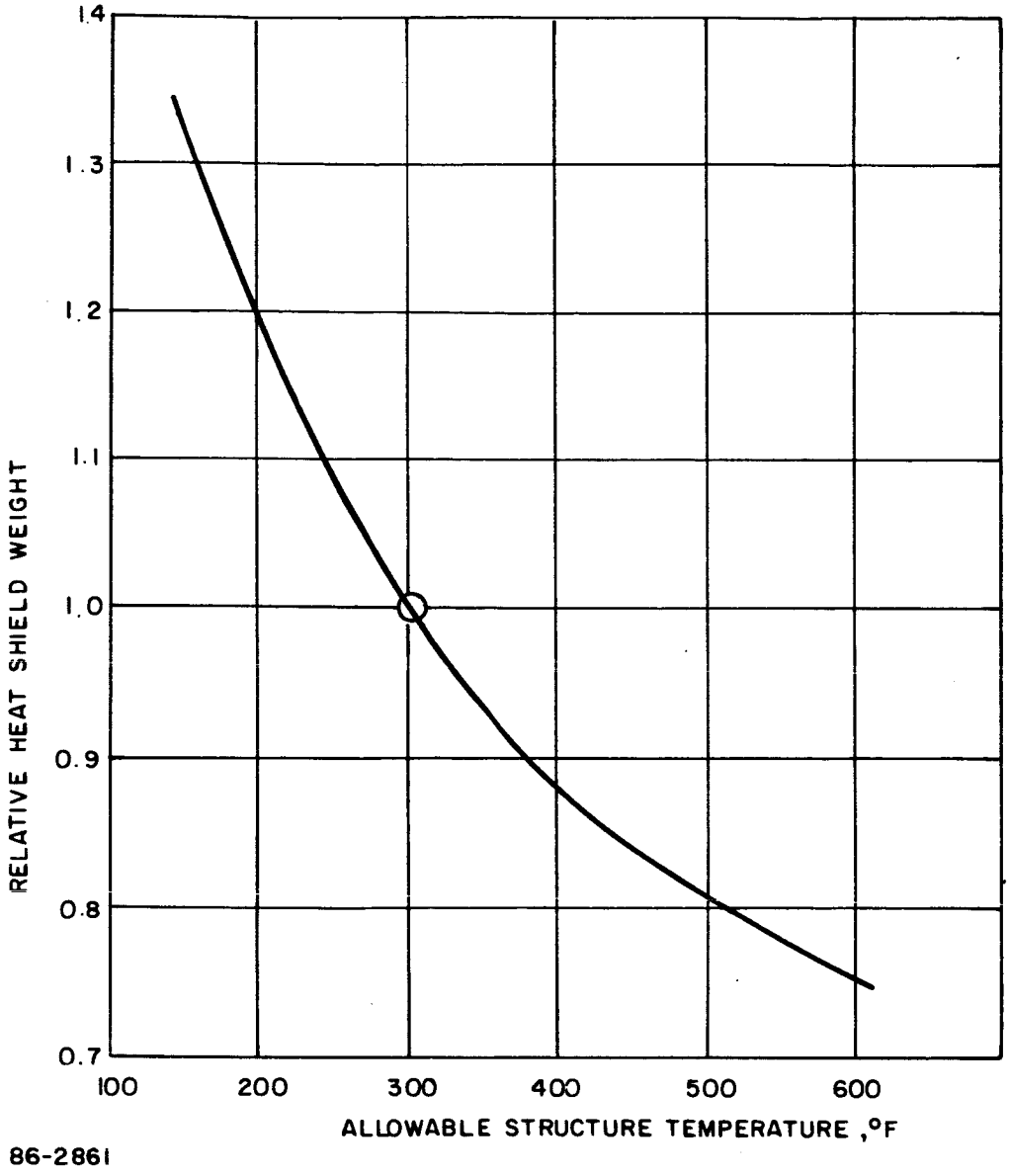

Figure 301 EFFECT OF ALLOWABLE STRUCTURE TEMPERATURE ON HEAT SHIELD WEIGHT (EFAT)

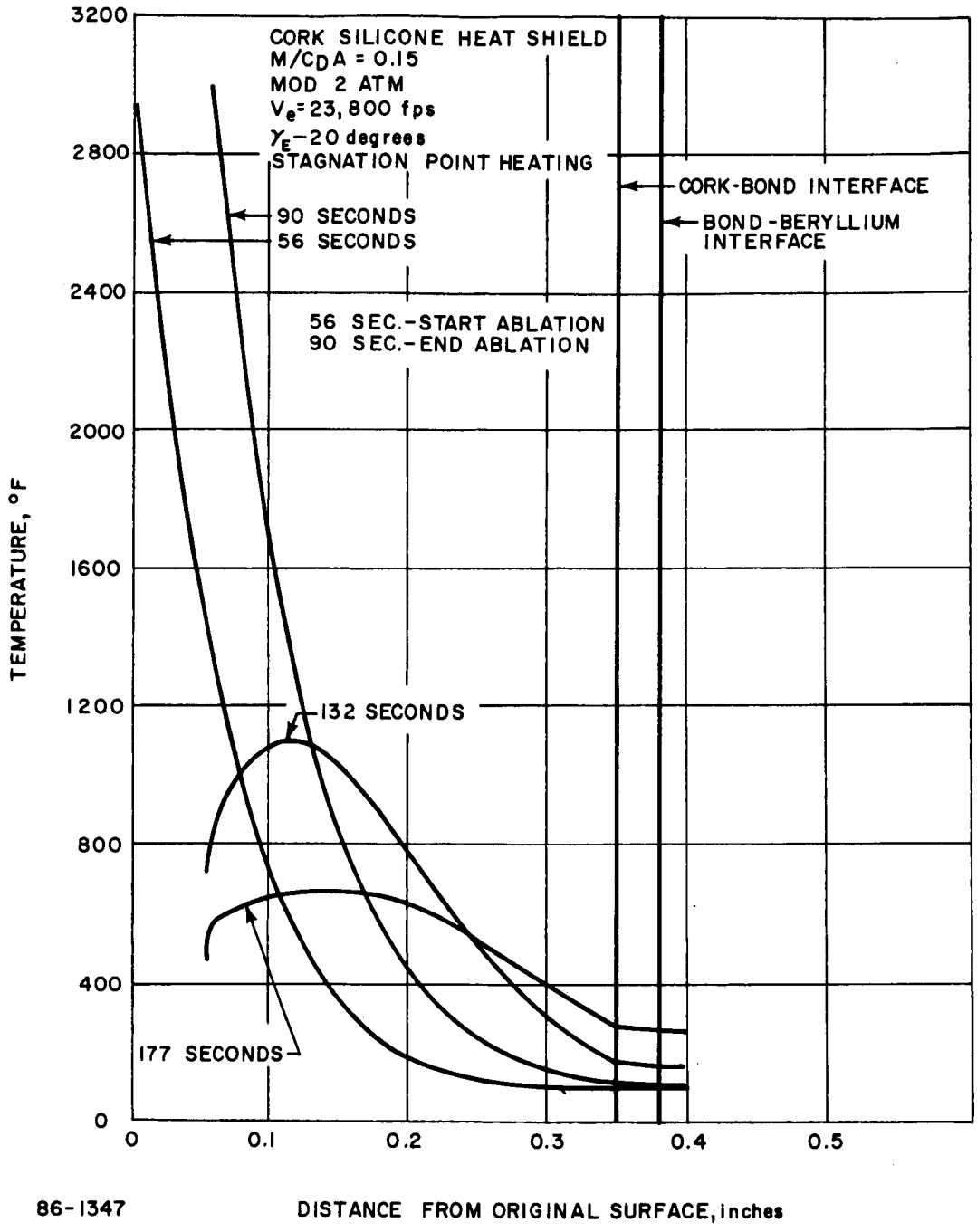

Figure 302 TEMPERATURE GRADIENTS IN THE TENSION SHELL

This is of course due to the increase in the allowable weight. The third significant point is that the heat shield weights for the tension shell are large compared to the other shapes primarily because the body stations with the largest areas are also the ones associated with the highest heating. This disparity would tend to decrease if rearwards entry or large angle of attack was a likely failure mode to consider. The remaining trends regarding these fractions are completely explicable in terms of the values of aerodynamic heating and were described in detail with respect to trends in Section 2.0.

TABLE LXI

HEAT SHIELD* WEIGHT FRACTION
(Cork Silicone)

V_e = 23,800 ft/sec γ_e = 20 degrees Diameter - 180 inches

Shape \ Design Condition	M/C_DA = 0.15 slug/ft^2 Atm 2 (percent)	W = 4500 pounds Atm 3 (percent)
Blunt Cone	17.0	5.7
Modified Apollo	14.2	4.7
Tension Shell	24.6	16.3

*Only primary (front face) heat shield included.

8.3.4 Problem Areas

The problem areas may be broadly placed into two classifications. The first embraces problems which are generally encountered in the design of a conventional entry vehicle. The second classification includes problems which are peculiar to the specific application and as such may be considered unconventional.

The problem areas in the first area (conventional) may be divided into three subclassifications:

1. The basic problem of characterizing the material

a. Preliminary characterization of material thermophysical behavior is based upon limited data on material which is manufactured in a laboratory rather than for production. This is the first opportunity in the development process to describe the material properties required for prediction of heat shield behavior during entry;

b. Characterization process is based upon a much larger number of tests in which samples are produced by a pilot plant. During this phase, a more definitive set of material properties is obtained. Actual heat shield material production samples are then compared with those derived from pilot plant samples taken as the standard.

2. Material process variables effects

Problems encountered in heat shield material processing changes in the scaling-up process from a laboratory batch-to a pilot plant batch-to an actual production run must be investigated in this phase. Small processing changes can induce major disturbances in material behavior in spite of the fact that the chemical composition may not have been varied. Such processing changes are, of course, inherent in the scaling-up procedure.

3. Heat Shield and Other Hardware Fabrication and Assembly Effect on Performance

Thermodynamic problems associated with actual hardware must be investigated in this phase. For instance, the heat shield may be constructed in pieces due to manufacturing or other design constraints. This brings up the problem of heat shield joint discontinuities and the required associated testing in order to establish reasonable confidence that such a design will not fail during exposure to entry environments. Another problem which falls under this broad classification is the behavior of the heat shield material and thermostructural composite under the various environments. The concern here being that related specifically to nonentry environments since, as a result of proper characterization, entry effects should be predictable. Cold-soak environments may for instance yield heat shield material cracks which affect the substructure deleteriously.

The problem areas of the second classification (unconventional) which relate specifically to this mission may be subdivided into four items:

1. Problems related to the Martian atmosphere chemical composition must be resolved. These specifically relate to material behavior. One of the problems lies in the fact that the chemical reactions between the

heat shield material and boundary-layer gases are a function of gas composition. The other problem is related to the fact that the ablating shield releases gases into the boundary layer. This in turn changes the chemical composition of the boundary layer and alters its properties and the heating. The fact that gas is being introduced into the boundary layer also gives rise to what is generically called blowing. The efficiency of this method of heat blockage is a function of the ratio of the molecular weights of both the injected species and the boundary layer gases. For a detailed discussion of such effects see References 81, 82, and 83.

2. The problem of the coupled radiant and convective heating must be further investigated both experimentally and theoretically for the entry from approach trajectory.

3. The problem of possible degradation of the specific heat shield material must be studied from the standpoint of vacuum exposure.

4. The problem of heat shield performance degradation during decontamination and sterilization must be investigated. It parallels the previous one in all respects as well as the cold-soak effects but, by definition, it is not conventional. Although present evidence indicates that the candidate materials selected for this study are sterilizable, it would appear reasonable to undertake action to establish this with a large degree of certainty.

Summarizing the problem areas one can cite the following:

1. Routine problems:
   a. Heat shield material characterization
   b. Heat shield material scale-up
   c. Hardware developmental problems
2. Special problems:
   a. Atmosphere composition
      1) effect of blowing on heating
      2) effect on blowing efficiency
   b. Radiative and convective heating effects
   c. Heat shield degradation due to long vacuum exposure
   d. Heat shield degradation due to exposure to the decontamination and dry heat sterilization cycles.

9.0 HEAT SHIELD - CONCEPTUAL DESIGN - ENTRY FROM ORBIT

9.1 INTRODUCTION AND SUMMARY

The thermal protection system (TPS) consists of the composite of an external layer of heat shielding material bonded to the load-carrying structure. Due to the nature of the aerodynamic entry heating pulse, basically only the three elements (heat shield, bond, and substructure) participate in the heat absorption-rejection cycle affecting the protection of the payload from the extremes of the entry environment.

The objective of the heat shield design is the assurance of the integrity of the structures and of the payload through attenuation of the external thermal environment during entry. In this phase of the program practical ablative heat shields were to be considered; minimum weight was not the overriding consideration.

9.1.1 Configuration Description

An ablative thermal protection system consisting of Purple Blend, Mod 5 ablator, backed up by a ply of fiberglass with stiffened loops protuding into the ablator (for improved mechanical integrity of the decomposed material) was selected for the reference design. This composite was then bonded to the load carrying structure. The details of the overall entry shell design were shown in Section 6.0 (Figure 246). Figures 303 and 345 show the heat shield and stiffened loops configuration. A similar concept, but without fiberglass and loops, was utilized on the secondary and after body heat shield. In local areas of possible aggravation higher density refrasil phenolic inserts were recommended. The thermal protection thickness requirement for the primary heat shield (forebody) and for other areas requiring thermal protection (except the rocket nozzle) is summarized in Tables LXVI and LXVII, paragraph 9.3.4.1.

9.1.2 Requirements, Constraints, and Design Criteria

The requirements imposed on the heat shield parallel those for the structure through the mission sequence from the factory to parachute deployment. During the spaceflight phase, the heat shield is aided by the thermal control system and together they assure integrity of the structure and of the payload.

In achieving the design objectives the main constraint upon the heat shield is to accommodate the critical environments created at the boundaries during the entry phase while providing protection for the structure to perform its function. It may thus be seen that the design condition for the heat shield stems from the aerodynamic environment and from the structural design criteria.

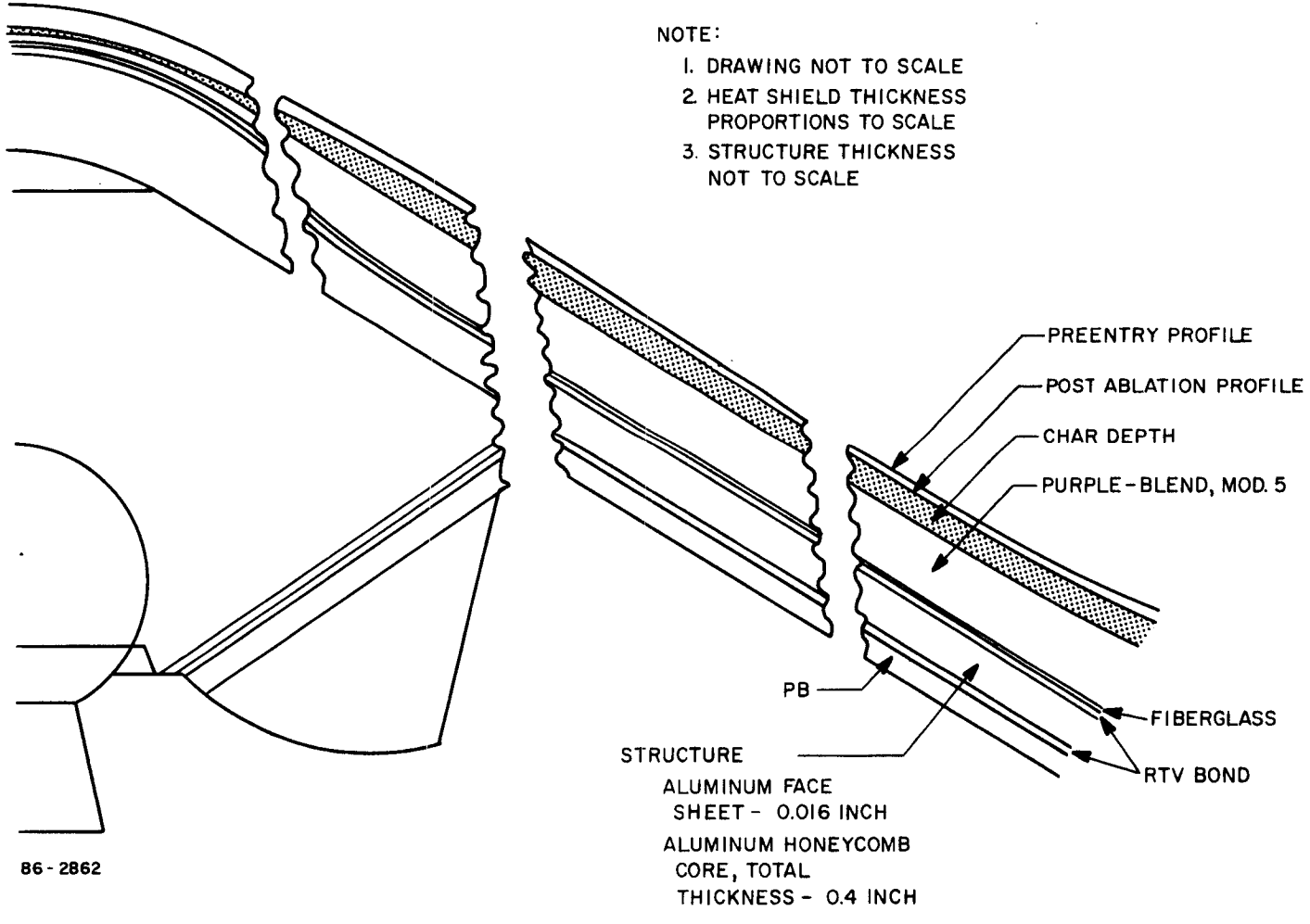

Figure 303 HEAT SHIELD CONFIGURATION

The satisfaction of the design conditions is predicated on the availability, selection and understanding of the behavior of appropriate heat shield materials, i.e., materials displaying a proper combination of thermal, optical and ablative characteristics. As a result, complex interactions have to be considered in establishing the heat shield design and material specifications.

On the other hand, the weight of the heat shield is sensitive to the initial conditions (temperatures) existing at the onset of entry. These temperatures depend on the thermal control exercised prior to entry with the attendant spacecraft-flight capsule interface, (discussed elsewhere) and postentry problems. Thus in addition to the environmental, structural and material requirements present in any entry vehicle design, a set of thermal control constraints on the heat shield (or vice versa) is found.

Finally the requirement for decontamination and sterilization imposes a constraint on the selection of heat shield materials from the beginning of the design process, limiting the choice to only such materials that can satisfy this initial requirement.

A summary of design conditions and criteria used for the reference design is given in Table LXII, while the general system constraints were summarized in Table II.

As may be seen, the general requirements and constraints for entry from orbit do differ from the entry from approach trajectory. Specific thermal design conditions and criteria have also been changed as a consequence of the change in mission objectives and refinement of the design.

The additional system requirements imposed by the definition of the normal and failure modes of entry are discussed under the system tradeoffs (paragraph 9.3 of this book). Suffice it here to say that they involved consideration of critical atmosphere (VM-7), entry angle (minimum) and velocity (maximum), M/C_DA selection, planet rotation effects as affected by landing-site selection and spin, tumble and angle of attack effects.

9.1.3 Heat Shield Concept and Performance Summary

The performance of the heat shield (weight requirements, temperature and density distributions and history, mass loss variations, etc.) was calculated for various entry concepts and design conditions. These were subsequently used in the thermostructural analysis. The reference design conditions and criteria and shown in Table LXII. The reference design configuration was shown in Figure 303 with the basic performance data indicated, while the heat shield thickness and local weight is shown in Table LXVI of paragraph 9.3.4.1. The required total heat shield weight and weight fraction for the various entry modes were also calculated and the resulting weight fraction (primary) for the reference design was determined as 12 percent. The

TABLE LXII

COMPARISON OF THE HEAT SHIELD DESIGNS FOR ENTRY FROM APPROACH TRAJECTORY AND ENTRY FROM ORBIT

Design Concept / Flight Envelope and Vehicle Parameters	HEAT SHIELD			
	Entry from Approach Trajectory		Entry from Orbit	
	Heavy Vehicle (Future Mission)	Light Vehicle ('71 Mission and Multi-Mission Reference Design and Mission	Reference Design	Spin (40 rpm)
D-vehicle diameter, feet	15	15	15	15
W-vehicle weight, pounds	4500	1390	2040	1885
V_e-entry velocity, ft/sec	23,800		15,200	12,900
γ_e-entry angle, degrees	-20		-14	-12.8
M/C_DA - ballistic coefficient, slug/ft^2	0.49	0.15	0.22	0.20
Atmosphere model	3	2	VM-7	
α_e - entry angle of attack, degrees	11		90	86
α peak heating - angle of attack, degrees	1	1	11	59
P_{stag}-pressure-lb/ft^2	835	152	31	93
-Shear, lb/ft^2	0.88	0.33	0.13	0.20
Q_{stag}-integ. heating, Btu/ft^2	4405	2798	2227	2052
$\dot{q}_{stag\ max}$-heating rate, Btu/ft^2/sec	188	70	18.6	23.6
$Q_{max\ diam}$-integrated heating, Btu/ft^2	1890	803	1705	6240
$\dot{q}_{max\ diam}$-heating rate, Btu/ft^2/sec	93	20	24	79
Pulse duration, seconds	85	130	240	220
$T_{bondline}$-temperature, °F	300-500		500	
T at entry - temperature, °F	100-300		100	60
Thermal safety factor	1.0		1.2	
End of pulse	Impact		Parachute Deployment	
Structural material	Beryllium (0.020")		Aluminum	
Structural concept			Al H/C Sandwich	
Heat shield material	Cork Silicone		Purple Blend, Mod. 5	
Approx. weight fraction (forebody only) %	7	20	14	15
Approx. total weight fraction %*			19	28

*(Includes 20-percent contingency)

calculated weight for the primary heat shield not including contingency, but accounting for manufacturability, mounting pad and bond was 253.5 pounds while the secondary heat shield weighed 55.4 pounds, and the afterbody 35 pounds.

It should be noted that the design criteria utilized in the design were nominal. Thus depending on the actual initial entry temperatures and allowable bond-line temperature, the weight requirements or heat shield response will deviate from nominal. For example, the initial temperature at entry calculated from the assumed spacecraft-flight capsule interface was found to vary from -60°F to +15°F, depending on body location and power supply prior to entry (Section 12.0). It had been assumed that the nominal was 100°F. This would either permit lower heat shield weight, or would increase the present safety margin. However, until the interface is defined, a flexible design has to be maintained. The tradeoffs considerations involving selection and characteristics of the material, the effect of the V-γ-D and entry mode variations are discussed in paragraph 9.3 of this book. The three entry modes resulting in three heat shield configurations were discussed in Section 3.0, and involved consideration of either a backup for the ACS system or a failure mode to be contended with in case of ACS malfunction. Thus a heat shield was designed for the case of 40 rpm spin, spin-despin case, and for the reference design tumble-failure mode entry. Nominal entry (particle trajectories) was also considered. Two of the three configurations are shown in Table LXII, where they are also compared with the results of entry from approach trajectory studies. All three configurations are compared in Table LXV of paragraph 9.3.3.

9.1.4 Comparison with the Entry from Approach Trajectory Studies

The entry from approach trajectory and the entry from orbit studies during this program present a rather diverse approach to Mars exploration. To satisfy the two different mission objectives and ensuing payloads a different design philosophy was evolved. While the entry from approach trajectory design was critically weight limited, the weight was not the major consideration in entry from orbit studies. This by itself significantly affected the choice of structural and heat shield materials and concepts. While environments and aerodynamic performance were relatively easy to compare, they did differ and made direct comparison of thermal performance difficult. The entry from approach trajectory design was more general and conceptual in nature, while the entry from orbit design was more specific. Thus, for example, in the first case, four aerodynamic shapes or modifications were evaluated and four heat shield materials were analyzed over a broad range of diameters, while in the second only one shape and two materials were investigated. On the other hand, for the entry from orbit studies, detailed V_e - γ_e - α_e - M/C_DA-D tradeoffs were conducted. Detailed comparison of environments and aerodynamic performance was given in paragraph 3.1.

It was noted that heating resulting from use of Model 2 and VM-7 atmospheres should be similar. However, selection of the $V_e - \gamma_e$ operational map for the reference design for entry from orbit resulted in a significant reduction of entry velocities and shallow (near skip) entry angles. As a result: (a) the radiative heating became negligible; (b) the integrated stagnation heating did not change significantly because of the long duration of the heat pulse (low γ_e); (c) vorticity interaction and entropy variation increased the heating, and (d), consideration of high angles of attack for the entry from orbit design resulted in an order of magnitude heating increase at the maximum diameter point which is the most sensitive to weight changes. Thus, the heat shield design requirements could not be relaxed, especially since the heat shield design for the entry from approach trajectory did not account for the rearwards (tumble) failure mode which was taken into account in the entry from orbit case.

The basic comparison of the thermal protection aspects of the two reference designs is shown in Table LXII. The aerodynamic environment and some design conditions and criteria are also shown as a background for the comparison. It may be noted that, in spite of the seeming relaxation of entry conditions for the entry from orbit case relative to entry from approach trajectory, no major heat shield weight savings were realized. The primary heat shield weight fraction decreased although counteracted to some extent by the a priori heating environment analysis described above. This was due to a combination of several factors; (a) the higher allowable entry from orbit weight due to increased M/C_DA more than compensated for the attendant additional heat shield weight; (b) higher heat capacity of the structure was accounted for and a large temperature increase at the bond line was allowed for the entry from orbit design, (c) the response of the heat shield was calculated at parachute deployment rather than using the conservative calculations until impact for the entry from approach trajectory case and (d) more rigorous evaluation methods of the ablator performance together with a change in the material possibly tended to decrease the weight estimates. On the other hand, the use of a safety factor of 1.2 together with the rearwards entry or tumble failure mode for the entry from orbit design as opposed to no safety factor and no failure mode the entry from approach trajectory would tend to increase the weight of the entry from orbit reference design.

9.1.5 Conclusions and Problem Areas

The thermal protection study showed that Purple Blend, Mod 5, was a typically desirable material for the heat shield, and that for this application it was more efficient than cork silicone. The studies revealed the necessity of use of rigorous ablation-conduction analyses for proper comparison of material performance. Possible weight savings are anticipated for lower entry temperatures but such a conclusion must be held in abeyance until: (a) more detailed material characterization studies are conducted; (b) the

assumption of the effect of Mars atmospheric composition on surface reactions is verified; and (c) its effect on safety margins is determined.

As a result of this study it was concluded that the updating of the atmospheric data and change to entry from orbit, although resulting in lower entry velocities, did not significantly reduce the severity of the heating environment. The angle of attack and spin effects combined with shallow entry angles produced the relatively high heat shield weights and resort to ACS with limited failure mode consideration was desirable to minimize the weight penalty.

The problem areas anticipated in the heat shield design for entry from orbit are not at variance with the previous phase of the study. While the change in entry conditions practically eliminated the consideration of radiative heating, the lower enthalpies encountered may create problems in ground-test entry simulation.

The rearward entry mode indicates significant weight penalties and points again to the need for further heating analysis and experimental data, and perhaps selection of a more efficient material for the afterbody of the vehicle.

The more advanced methods of thermodynamic analysis used in this phase of the study appear to be satisfactory, but require experimental verification. Thus an extensive heat shield material characterization program will be required: 1) to assure confidence in the design thermal performance in Martian atmosphere; 2) to determine mechanical characteristics for low-temperature soak; as well as 3) to determine the effect of decontamination, sterilization and vacuum exposure on thermal and mechanical characteristics. These are of importance as the heat shield weight fraction is of the order of 15 percent.

The application of the heat shield to the structure and its effect on the thermal control coating will require investigation. In the first case, unbonded areas may create problems during cold soak in addition to the usual problems during entry. In the second case, degradation of optical performance may be expected due to outgassing and must be established for thermal control consideration.

9.2 DESIGN CRITERIA

The basic approach to the selection of design criteria for the determination of the thermal protection requirements did not differ from that adopted in the entry from approach trajectory phase of the program; however, as discussed in paragraph 9.1.4 the specific values were different. This approach included the consideration of environmental criteria, material properties and characteristics, structural requirements and evaluation of the initial entry conditions

resulting from the control of spaceflight temperature. These considerations were reflected in Table LXII which summarized the various design criteria and conditions employed.

The heat shield design criteria employed in the present study have been selected in an attempt to make the usual compromise between a light weight design and a degree of conservatism consistent with the state of the knowledge regarding material performance, entry environment, and other pertinent factors.

9.2.1 Environmental Criteria

Aerodynamic heating environments used for design depended on the entry concept evaluated. For the reference design, the usual maximum entry velocity and minimum entry angle resulted in maximum integrated heating; however for the spin backup system the angles of attack associated with lower entry velocities forced the heat shield design point toward the lower velocity, angle of attack and entry angle combination which resulted in a maximum total integrated heating.

In all concepts evaluated the angle of attack together with failure mode considerations had a major effect on the heat shield design. Thus it was necessary to investigate for each location on the heat shield the effect of at least two of the three angles of attack (α_e = 0, 90 and 180 degrees) on the heat shield weight. The latter two were used for the forebody (90 degrees) and secondary and afterbody (180 degrees) heat shields. The environmental criteria were shown in paragraph 3.0 and Table LXII.

9.2.2 Materials Criteria

The initial screening of materials to be used for the heat shield was conducted during the entry from approach trajectory study phase. Although the heat flux levels and enthalpy levels are considerably lower for entry from orbit, the rationale behind the selection has not changed. Furthermore, the time element involved did not permit reevaluation of materials to any great extent. A second look at Purple Blend, Mod 5, cork silicone and Teflon was taken. The latter was eliminated immediately; the Purple Blend Mod 5 was selected for reference and cork silicone for backup (see paragraph 9.3.1) based on experimental data available at the time the choice had to be made. The mechanism of ablation was established for Purple Blend, Mod 5 as that of combustion, after joint examination of data with NASA LRC.

The requirement for survival of decontamination, sterilization, and long time exposure to vacuum and low temperature in space was one of the criteria in the selection.

The thermal properties and ablative characteristics of Purple Blend, Mod 5 used in the design are shown in Table LXIII, results of a detailed material characterization study are discussed in Section 10.0 of this book.

9.2.3 Thermo-Structural and Spaceflight Temperature Criteria

The basic objective of the thermal protection system-attenuation of the thermal environment ot the level tolerable by the structure so that it may satisfy its requirements - implies immediately that the structural temperature limit constitutes the major heat shield design criterion. This, however, is an oversimplification of the problem, as structure heat shield compatibility, and bond material temperature tolerance enter into the picture. In the final analysis, any of the above three criteria may be the controlling factor. Preliminary evaluation of the problem indicated that the bondline temperature may be the controlling factor in this case. Accordingly a maximum allowable bondline temperature of 500°F was used in the present study.

Upon further thermostructural analysis (Section 6.0) it was found to be the controlling factor, as the resulting structure temperatures were within the required limits, and no compatibility problems arose.

The use of the actual structural configuration eliminated the need for selection of structural heat capacity as a specific design criterion assumption. The calculations were terminated at the time of chute deployment, as the structure and heat shield are deployed.

Several methods are available for introducing a controlled conservatism into thermal protection system design. None of the readily available techniques is totally adequate for all systems and for all applications. The method employed in the present design is the use of a simple safety factor on the nominal heat shield thickness requirements. Thus, the final design thicknesses are obtained as 1.2 times the nominal requirements.

The initial temperature of the heat shield was taken as 100°F which was based on the preliminary results of the thermal control study. It should be noted that this design criterion was nominal. Thus, depending on the actual initial entry temperatures (or, for that matter, the allowable bondline temperature), the weight requirements or heat shield response will deviate from nominal. For example, the initial temperature at entry calculated for the assumed spacecraft-flight capsule interface was found to vary from -60°F to +15°F, depending on body location and power supply prior to entry (Section 12.0). Nominal was taken as 100°F. This would either permit lower heat shield weight, or would increase the present safety margin. However, until the interface is defined, a flexible design has to be maintained.

The degree of conservatism inherent in the criteria used and a comparison with the entry from approach trajectory were discussed in paragraph 9.1.4.

TABLE LXIII

THERMAL PROPERTIES AND ABLATIVE CHARACTERISTICS
OF PURPLE BLEND MOD 5

		Virgin	Fully charred
ρ	- lb/ft^3	41.8	16.7
C_p	- Btu/lb-°F	0.34	0.34
K	- Btu/ft-hr-°F	0.075	0.049 (760°R) 0.080 (1100°R) 0.180 (2250°R) 0.240 (4060°R)

REACTION CONSTANTS

ΔH	Btu/lb	1000
A	*	3.9×10^5
B	*	2.0×10^4
η	*	1.0

*Units compatible with $\dot{\rho}$ (lb/ft^3-sec) $= A (\rho - \rho_c)^n \exp(-B/T)$

GASEOUS EFFUSION

C_{p_g}	0.40	Btu/lb-°F

CONDUCTIVITY EXPLICIT FUNCTION RHØK

Density, lb/ft^3	RHØK
16.7	1.0
29.8	0.66
36.2	0.44
40.2	0.21
41.8	0.0

SURFACE ABLATION CHARACTERISTICS

ETA	0.3937
	0.62
Density, lb/ft^3	A3
16.7	6.73×10^8
41.8	1.0×10^6
3.987×10^4	B3
1.0×10^4	HC
Density, lb/ft^3	TW
16.7	2.02
41.8	5.0
1.066×10^4	HV

9.3 RESULTS AND DISCUSSION

The criteria described in the preceeding section were used in the conceptual design of the termal protection system of the probe. The results of a concurrent, limited material characterization program were interpreted and factored into the basic analytical ablation model (Section 10.0). They were consequently utilized in the evaluation of performance and weight requirements of the heat shield. The heat shield material was selected together with NASA LRC for the reference design on the basis of an incomplete characterization program to obtain typical thermal protection requirements.

The conceptual design described in this section was a three-phase process:

1) Parametric correlation of heat shield thickness and aerodynamic environmental parameters was established and used for a parametric study of various factors influencing the heat shield weight.

2) Various system design concepts were analyzed and conceptual heat shield designs evolved.

3) Reference design was established and its performance under various entry conditions was evaluated.

9.3.1 Selection of Material for Design

Materials used in the study of the probe/lander entry from approach trajectory were reviewed prior to this phase of the program. The examination of the experimental data acquired concurrently with this program indicated that the ranking of the materials previously examined may well be reversed, and especially that purple Blend, Mod 5 may perform more efficiently than it was assumed previously in the absence of sufficient data. Even though no formal evaluation was conducted on other materials due to limitations of the time and scope of the contract, it was jointly agreed with NASA LRC that Purple Blend, Mod 5 was to be used for reference purposes in heat shield weight calculations because:

1) The material characterization experiments conducted at Avco indicated significant reduction in weight estimates arrived at during the previous phase of the study. The analysis of the data indicated that Purple Blend, Mod 5 may be lighter than other materials previously considered.

2) The availability of more complete material characteristics for Purple Blend Mod 5 permitted more realistic calculations of weight requirements. Its mechanical properties were found to be quite satisfactory.

3) Manufacturing and development problems associated with Purple Blend Mod 5 appeared to present fewer difficulties than other materials.

More detailed discussion of the materials characterization effort and the interpretation of the experimental data with respect to the internal and external ablation mechanism of Purple Blend, Mod 5 and cork silicone is given in Section 10.0. The behavior of the other ablators considered during the study is also described in Section 10.0. Consideration was also given to the use of Teflon because of communication problems, but the preliminary weight calculation immediately indicated unacceptable weight penalties. Use of "hot structures" was excluded from the scope of the contract by NASA, LRC.

The studies of Section 10.0 and the comparison of typical Purple Blend, Mod 5 and cork silicone heat shield weights shown in paragraph 9.3.4 did bear out the selection of Purple Blend, Mod 5 as a reference material.

The properties and ablative characteristics of the Purple Blend Mod 5 used in the design were shown previously in Table LXIII. A rigorous ablation analysis employing a combustion mechanism was used in the design calculations; however, it must be noted that it was assumed that the Martian atmosphere would sustain the same type of surface reaction as Earth, and that only a small, even if complete, body of experimental data was available for the analysis.

9.3.2 Parametric Studies

The first task undertaken in the probe entry from orbit thermal protection study was a parametric examination of heat shield requirements over a range of the significant parameters. The flight envelope and vehicle parameters considered in the study were the ballistic coefficient, vehicle diameter, entry angle, entry velocity and angle of attack at peak heating. The effect of the allowable bondline temperature rise was also investigated.

9.3.2.1 Basic Parametric Relationships

The thermal loading employed in the parametric study was based on the parametric heating analysis discussed in Section 3.3. An examination of the stagnation point heating data obtained in this portion of the parametric analysis showed that the integrated heating, Q, can be correlated by means of Figure 304 to within ± 5 percent. It has been further found that the integrated stagnation point heating can be represented by Equation (1) to within ± 5 percent over the range $-11° \leq \gamma_e \leq -20$ degrees.

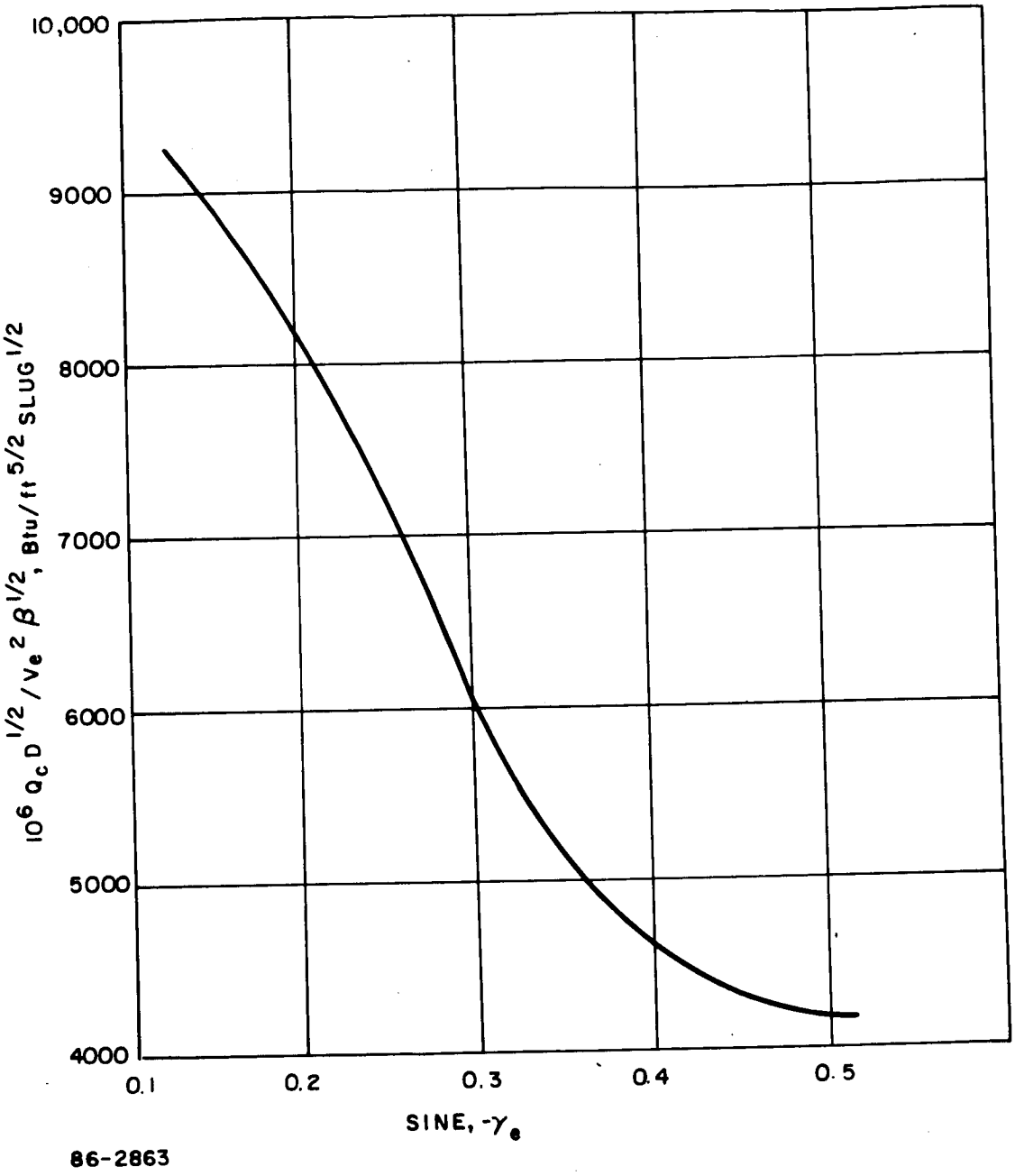

Figure 304 CORRELATION FOR HEATING VM-7

$$Q_s = \frac{V_e^2 \, (M/C_D A)^{\frac{1}{2}}}{10^8 \, D^{\frac{1}{2}} \sin^{\frac{1}{2}} (-\gamma_e)} \left| 4590 + 77.5 \, \gamma_e \right| \qquad (1)$$

Heat shield requirements were obtained by detailed analysis for several of the trajectories in the parametric heating analysis. These were chosen to represent the extremes in heat pulse shape and duration. Using the nominal heat shield requirements for these selected trajectories it was found that a definite correlation existed between the required thickness, the integrated heating and the pulse duration as measured by the sine of the entry angle. This correlation is indicated in Figure 305 which shows the results for Purple Blend, Mod 5 on a beryllium substructure. A similar correlation for an aluminum honeycomb substructure yields Equation (2) for the design heat shield requirement.

$$L \text{ (in)} = 0.0109 \left| Q/\sin (-\gamma_e) \right|^{1/3} \qquad (2)$$

The distribution of heating around the body was taken from the work reported in Section 3.0. The distribution employed for zero-angle of attack is shown in Figure 306. Based on several detailed heating calculations which included the vehicle dynamics, the distribution (for heat shield design purposes) around the body was taken to be independent of angle of attack at peak heating up to values of (S/R_n) equal to 3.5. This was done because zero angle heating up to this point would exceed that obtained for angle of attack (Figure 192). At the maximum diameter the heating is resonably well represented by Equation (3) where $\bar{\alpha}$ is the angle of attack in degrees at peak heating.

$$\left(\frac{Q_B}{Q_{stag}} \right) = 0.290 \left| 1 + 0.0445 \, \bar{\alpha} \right|^3 . \qquad (3)$$

In addition to the effect of angle of attack on heating distribution, there is an effect on the stagnation point heating due to the trajectory perturbation. Accounting for this effect in terms of a modified drag coefficient the final expression employed for stagnation point heating was taken as Equation (4).

$$Q_{stag} = \frac{V_e^2}{10^8} \left\{ \frac{(M/C_D A)}{D \sin (-\gamma_e)} \right\}^{\frac{1}{2}} (4590 + 77.5 \, \gamma_e)(1 + 3 \times 10^{-4} \, \bar{\alpha}^2) \qquad (4)$$

Given a set of the parameters $M/C_D A$, V_e, γ_e, D and $\bar{\alpha}$; heating and heat shield thicknesses were obtained using Equations (2), (3) and (4)

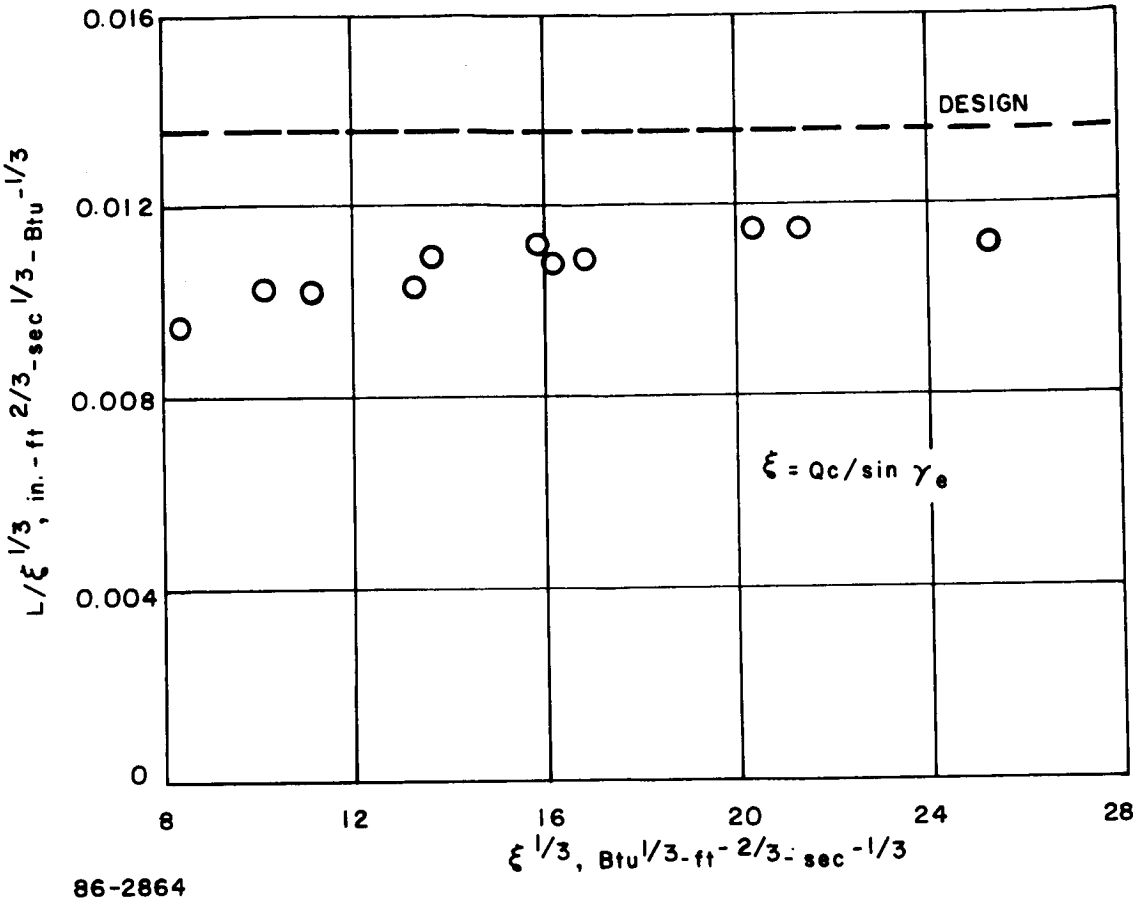

Figure 305 PURPLE BLEND THICKNESS REQUIREMENTS FOR 500°F BOND AND BERYLLIUM STRUCTURE

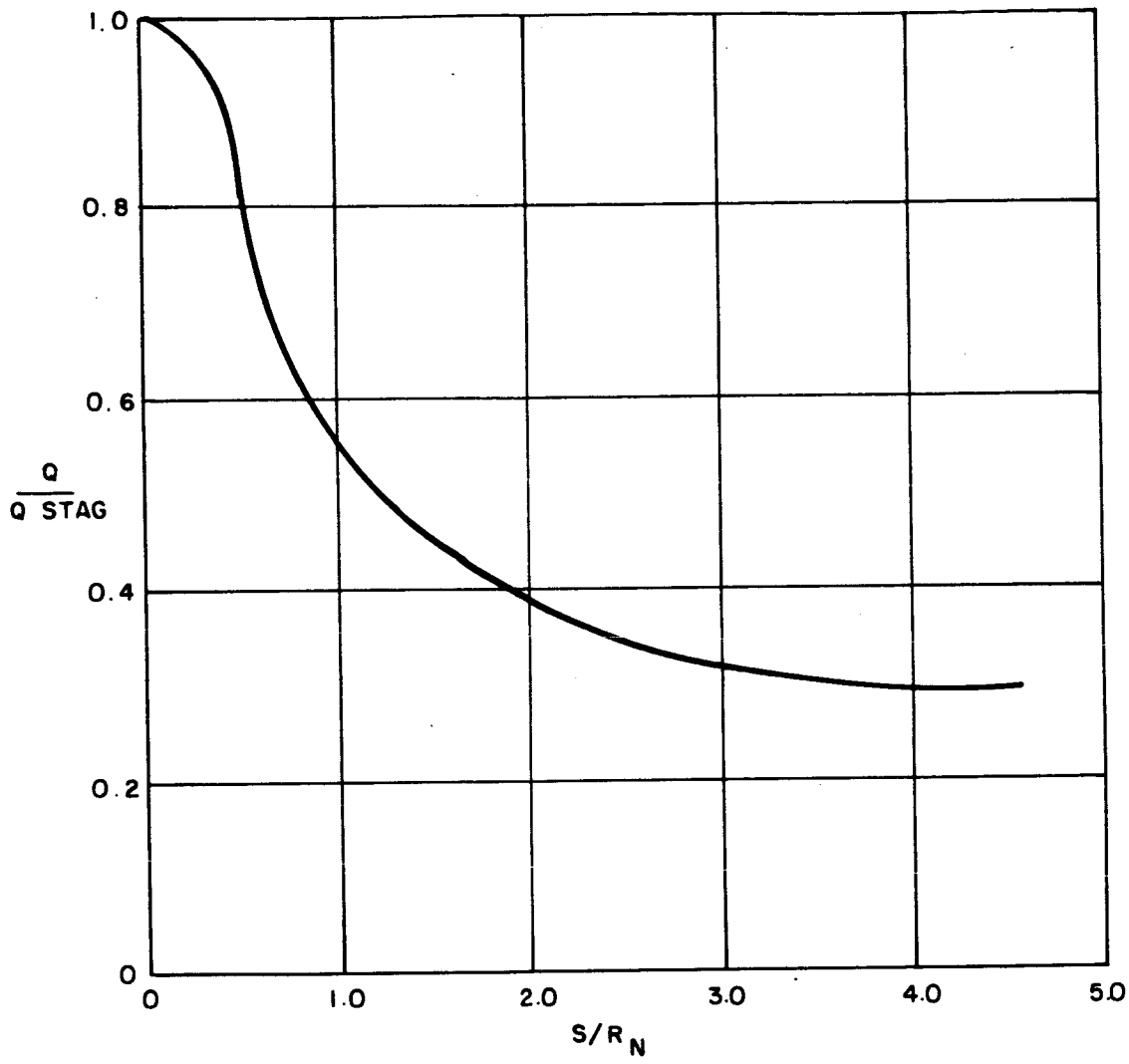

Figure 306 HEATING DISTRIBUTION FOR ZERO ANGLE OF ATTACK

together with Figure 306. The primary heat shield weight including bond was then obtained by numerical integration. The output of the calculation was the required heat shield thickness at each of seven body stations, the total primary heat shield weight and the fraction of total vehicle weight required for primary heat shield. The full parametric study involved all 14400 combinations of the parameters shown in Table LXIV.

9.3.2.2 Generalized Heat Shield Weight Tradeoff

The design objectives and requirements discussed previously establish the general design guidelines to be followed in the tradeoff studies. Basically they should result in a lightweight heat shield design compatible with the structure and thermal control requirements. The over-riding consideration, however, always is the attainment of the mission objectives. The mission objectives and constraints pretty much define the entry environment that the thermal protection system will experience. Nevertheless, in the process of subsystems integration and reconciliation of often diverse subsystem requirements major tradeoffs are possible which will materially affect the weight fraction of an individual subsystem such as the heat shield. These tradeoffs are reflected in the changes of the basic aerodynamic environment vehicle and design parameters and they require a number of parametric studies. This is especially true in the stage of the design when the structural design is not yet firmed up, and the reference entry mode and system are not selected.

The parametric studies discussed in this subsection were based on typical, rather than reference, design values to establish the general trends. Thus, a typical structural heat capacity and particle trajectory heating is used to establish the effects of V_e, γ_e, M/C_DA and vehicle diameter on weight.

Furthermore, the effect of the angle of attack, structural heat capacity and bondline temperature allowable is determined in the general sense.

Using the basic parametric relationships described in 9.3.2.1 correlating the heat shield thickness and the integrated aerodynamic heating with the other pertinent parameters, heat shield weight requirements were established for various modes of entry.

The variation of the heat shield weight requirement for a 15-foot diameter vehicle and 0.20 ballistic coefficient is shown in Figure 307. The heat shield consists of Purple Blend, Mod 5 applied on a typical structure. Since the calculations are based on particle trajectories no angle of attack effect is shown for various combinations of entry velocity and angle. The carpet plot shows a strong influence of entry

TABLE LXIV

RANGE OF FLIGHT ENVELOPE AND VEHICLE PARAMETERS STUDY

Vehicle Diameter	(ft)	10.0	12.5	15.0	17.5						
Vehicle Ballistic Coefficient	(slug/ft^2)	0.14	0.18	0.20	0.22	0.26					
Entry Velocity	V_e ft/sec	11,000	11,500	12,000	12,500	13,000	13,500	14,000	15,000	16,000	
Entry Angle	γ_e degrees	11.0	11.5	12.0	13.0	13.5	14.0	15.0	16.0		
Angle-of-Attack Peak Heat	$\bar{\alpha}$ degrees	0.0	5.0	10.0	15.0	20.0	25.0	30.0	40.0	50.0	60.0

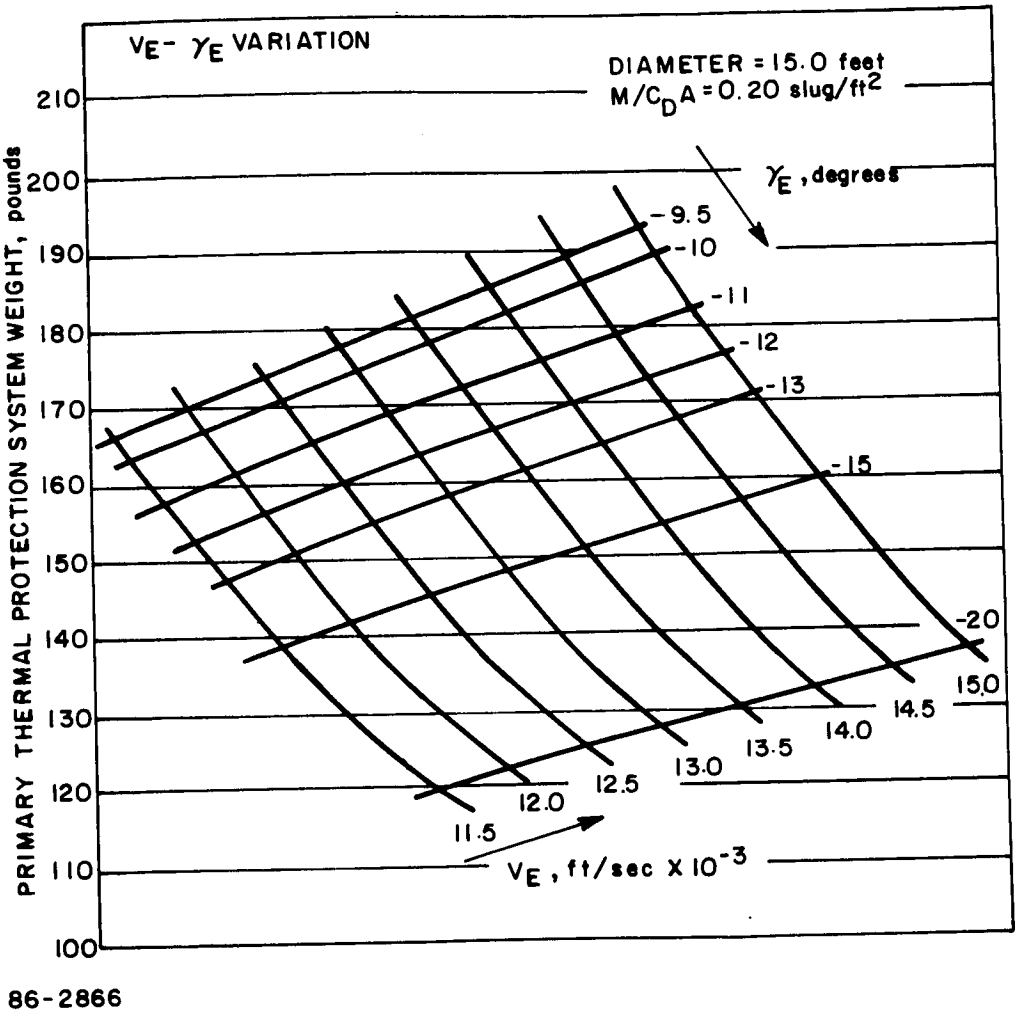

Figure 307 THERMAL PROTECTION SYSTEM WEIGHT

angle on the weight primarily due to the extended heat-soak time. The effect of entry velocity is also significant. It should be noted here that the entry velocities and angles are not independent from each other, but come in combinations based on de-orbit conditions from a given orbit. Consideration must be given to the associated dispersions in entry conditions from a given set of orbit and de-orbit conditions. Furthermore, each of the entry conditions must take into account the associated angle of attack.

General dependence of the heat shield weight on the variation of the ballistic coefficient and the diameter evaluated for a typical structure is shown in Figure 308. The weight is relatively insensitive to M/C_DA, reflecting a small increase in total heating as a function of the coefficient. The larger effect of the diameter is due to the increase in the total area exposed of heating moderated by the decrease in local heating. As in the previous figure, the conditions are for zero-angle of attack with a Purple Blend Mod 5 heat shield. Similar charts were constructed for other entry modes and structures and are further in the text in the discussion of various concepts considered for the application.

The detailed calculations required for the parametric studies were used to obtain the effect of the variation in the bondline temperature on the heat shield weight. This effect is shown in Figure 309 and allows also for an approximation of the effect of the initial entry temperature when converted to temperature rise ($T_{bondline} - T_{initial}$). The effect of change in the allowable temperature increase was found to be significant. Approximately 25 percent in weight may be saved per 100°F allowable temperature rise.

No detailed calculations of the effect of structural heat capacity were made; however, inspection of Figure 305 and Equation (2), and comparison of Figure 307 with Figure 310 indicates that the change from 0.020 inch beryllium to the actual structure used for the reference design resulted in average weight saving of the order

Since the angle of attack is directly related to a set of entry conditions, the study of this effect was deferred until dynamic trajectory data for selected concepts and a reference structural design were available. These are described in the following section.

9.3.3 Design Concept Analysis and Tradeoff

As discussed elsewhere in this book, three design concepts and/or failure modes (all of them based on an attitude control system), were considered.

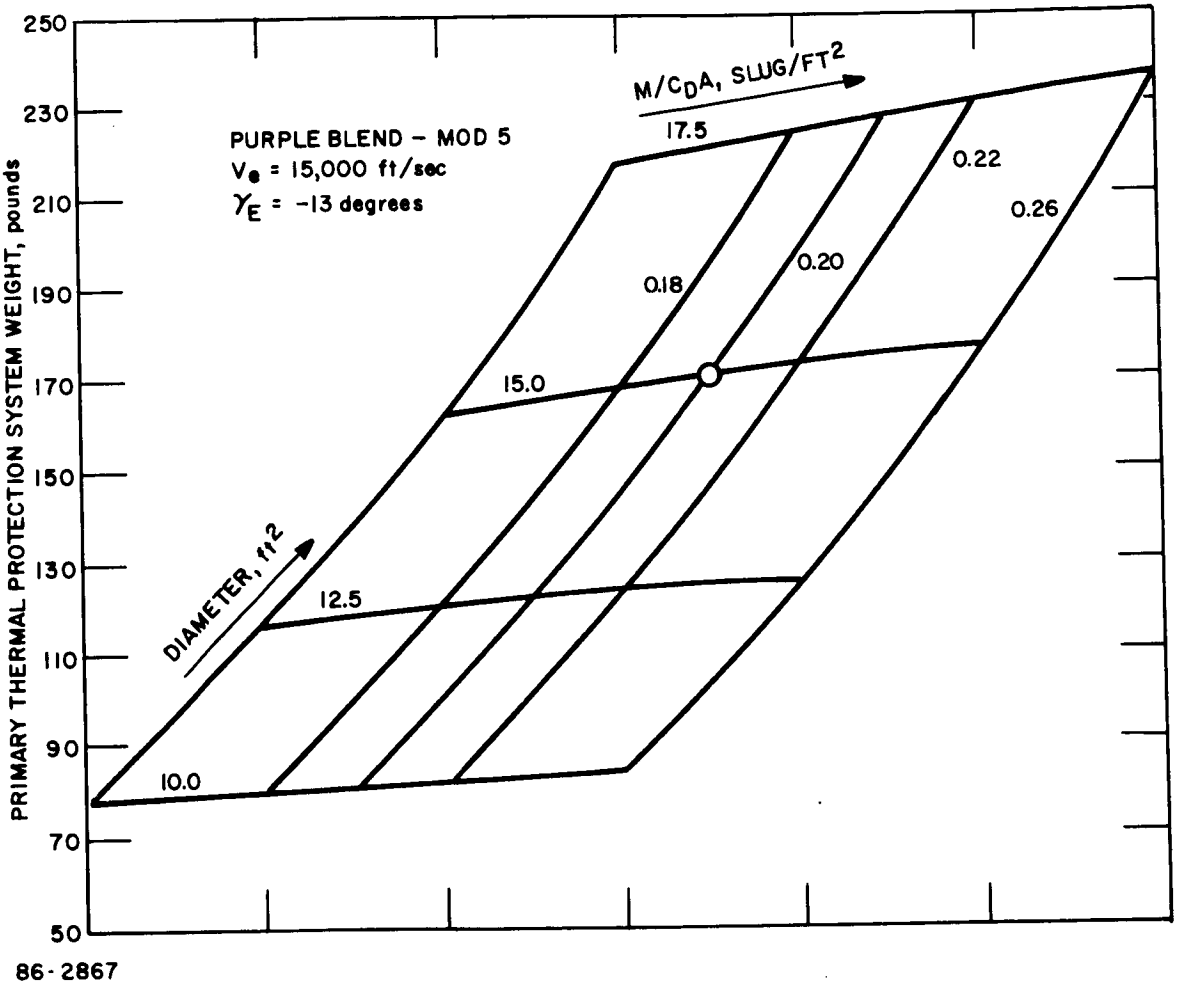

Figure 308 PRIMARY THERMAL PROTECTION SYSTEM WEIGHT--VARIATION WITH DIAMETER AND M/C_DA

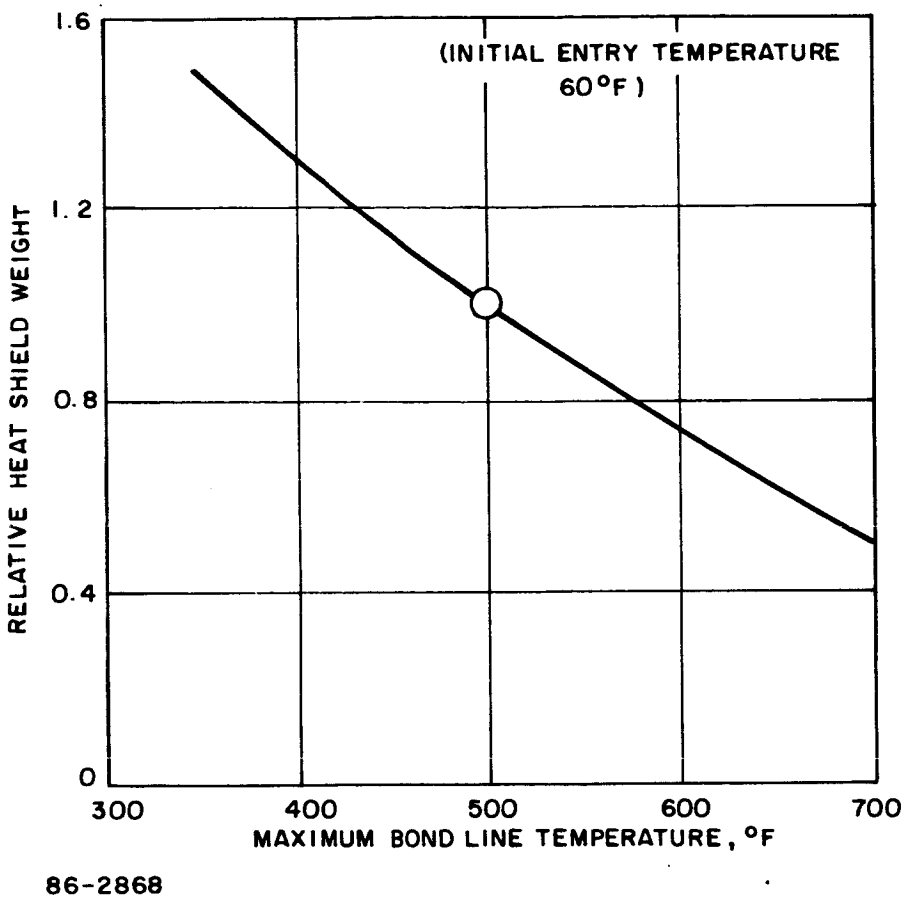

Figure 309 EFFECT OF BONDLINE CRITERIA ON HEAT SHIELD WEIGHT-- PURPLE BLEND MOD 5

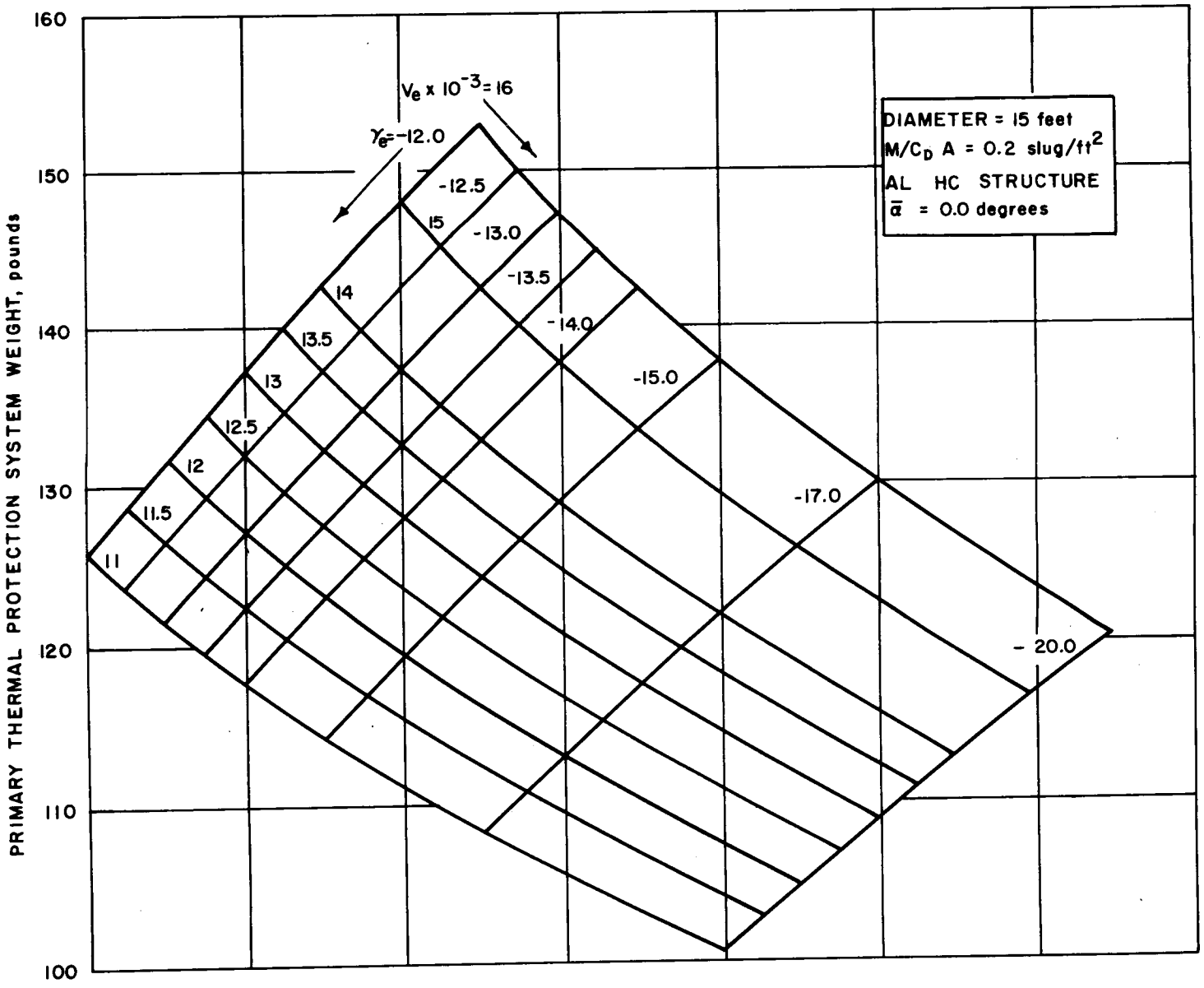

86-2869

Figure 310 VELOCITY AND ENTRY ANGLE EFFECTS

These included a 40-rpm spin backup system, spin-despin failure mode, and a rearwards entry or a tumbling failure mode of entry. Detailed aerodynamic and structural parametric studies utilizing preliminary thermodynamic analysis data provided respectively the reference environments and structural design for the second phase of thermal parametric analysis.

Although it is impractical to present the complete results of the study in this report some of the pertinent results are discussed below. Figure 310 shows the effect of entry angle and velocity on primary thermal protection system weight for the reference structural design and zero-angle of attack.

As in Figure 307 the heat shield consists of Purple Blend Mod 5, but it is calculated here for application on the reference design structure. The carpet plot of this figure assumes zero-angle of attack at peak heating, and the heat shield is calculated for various combinations of entry velocity and angle. The carpet plot shows again a strong influence of entry angle on heat shield weight, primarily due to the relationship of heat-soak time with respect to entry angle. The increase of weight with entry velocity is also significant. Thus, this figure basically shows the effect of the change in the structural configuration from that used in the generalized parametric study to the reference configuration.

The basic trends shown are applicable to the three design concepts under consideration, but do not account for the effect of the angle of attack. In this phase of the system evaluation the diameter and the ballistic coefficient were not fixed, and it was apparent that high angles of attack may be expected. A weight tradeoff between the diameter and M/C_DA for a 30 degree angle of attack and a typical entry condition was made to facilitate selection of the reference design. This tradeoff was made in terms of the weight fraction ($W_{heat\ shield}/W_{total}$) which is more meaningful than absolute weight in the overall system selection. The weight fraction are shown in Figure 311. It may be seen that both the increase in diameter and in the ballistic coefficient are beneficial. The weight fraction decreases in both cases and more strongly with the increase in M/C_DA. This is not surprising as the weight fraction is inversely proportional to the square root of the diameter and of the ballistic coefficient. Thus even though the absolute weight of the heat shield increases (Figure 308) the higher allowable weights more than compensate for it. Since the angle of attack heating indicated that it may be (for a given operational map) the single most critical parameter in its effect on the heat shield weight, a typical set of conditions was selected to determine the relationship of the angle of attack, entry velocity and weight. This relationship is shown in Figure 312. Again it must be noted that actual trajectory calculations will determine the appropriate combination of the parameters (V_e, γ_e, and $\bar{\alpha}$) to be used in the design. It is however quite apparent that since lower entry velocities are asociated with high angles of attack; the effect of angle of attack is

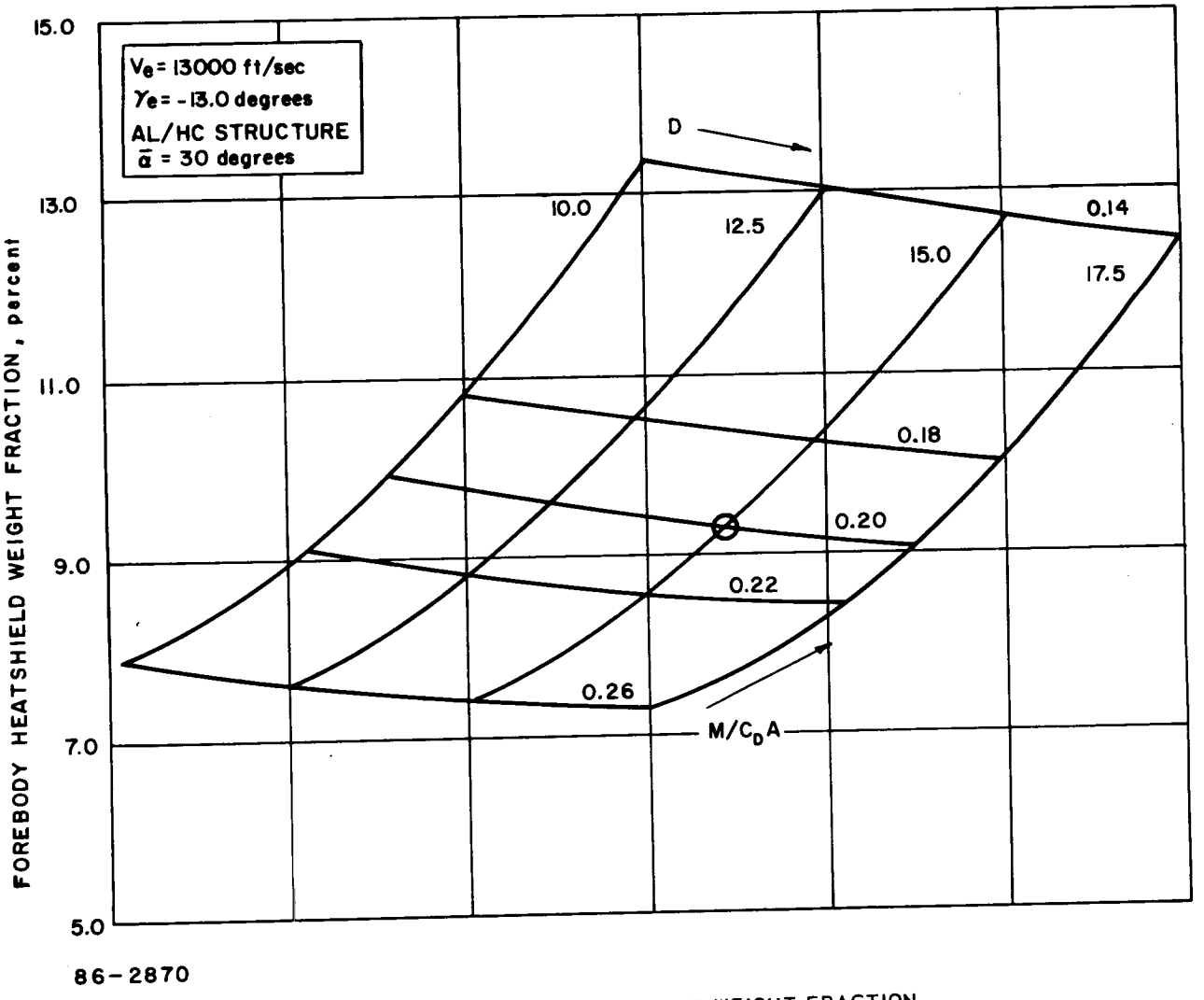

Figure 311 FOREBODY HEAT SHIELD WEIGHT FRACTION

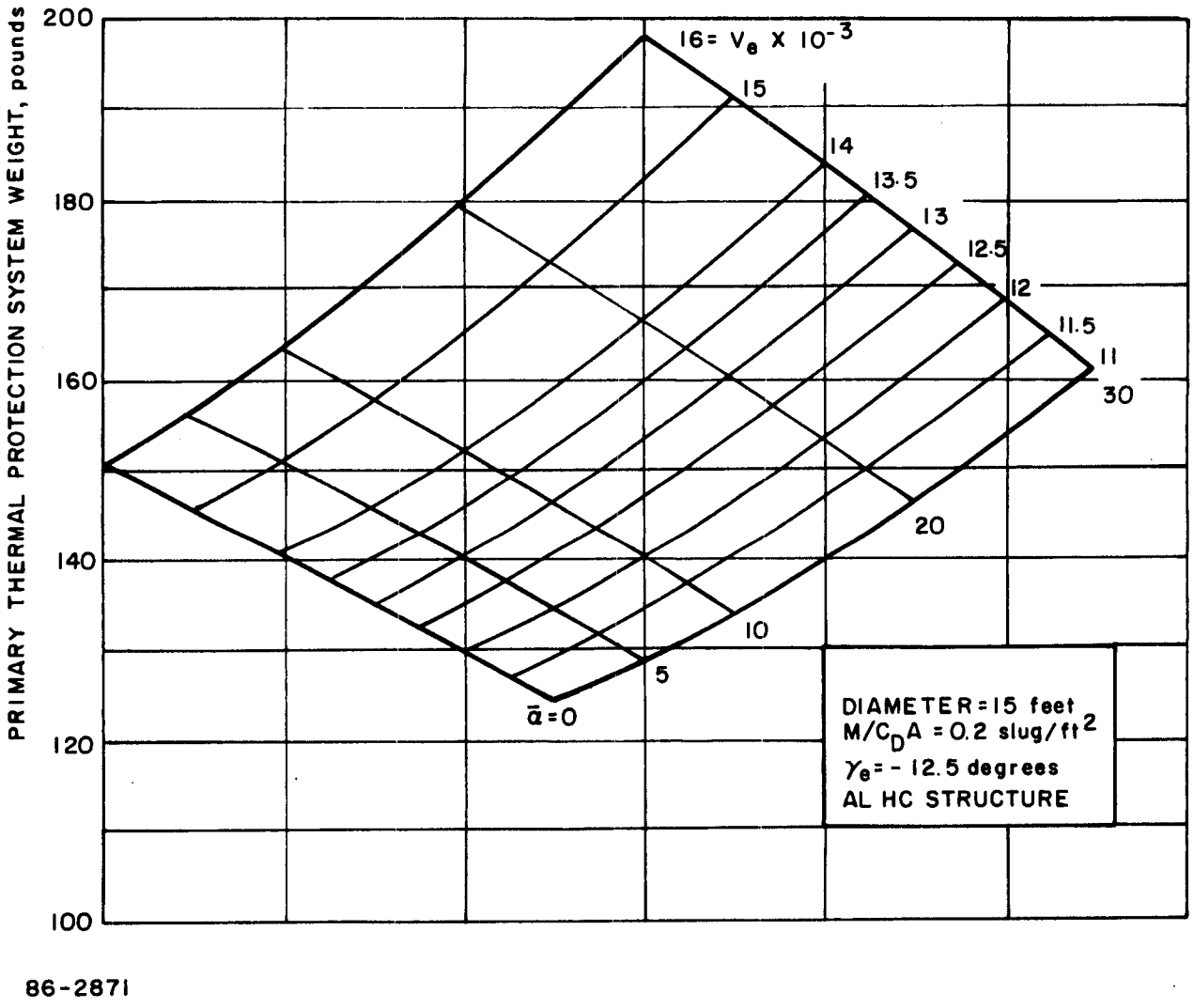

Figure 312 VELOCITY AND PEAK HEATING ANGLE OF ATTACK EFFECTS

quite significant and amounts to approximately 30 percent weight increase over the range of interest.

The above results were of particular interest in the evaluation of the 40-rpm spin backup system and the spin-despin failure mode. These were compared with a nominal case of no malfunction of the ACS system in Figure 313. Figure 313 shows the effects of spin and despin systems on heat shield requirements as compared to the requirement for zero angle of attack. Figure 313 was obtained by combining the parametric study results with the angle of attack results from detailed trajectory calculations for the various allowable entry conditions. It clearly shows the advantage of a reliable attitude control system. The final design concept (tumble) and secondary heat shield weights used to generate Figure 313 were obtained using the same correlation for thickness as for the primary heat shield together with the ratio of afterbody to maximum diameter heating discussed in Section 3.0.

The above results clearly indicated that the spin system unduly penalized the heat shield weight, and the tumble failure mode was adopted for the reference design. The weight of the heat shield for this case is shown in Figure 313 for the primary, secondary, and afterbody protection while Figure 314 shows the primary heat shield weight only. The actual FC V-γ map is superimposed upon the carpet plot of Figure 314. The entry heat shield design point occurs at an entry velocity of 15,200 ft/sec and an entry angle of -14 degrees. To account for the failure mode of tumbling entry and increase in the M/C_DA to 0.22 relative to the conditions of this plot, a heat shield weight penalty of 114 pounds must be taken. The failure mode weight was incorporated in the reference design. The weights shown in this chart are for the primary heat shield (on the shell forward face) and includes bond and a mounting pad between the structure and the bond. The weights shown do not include the weight of the secondary heat shield (on the back side of the shell) and bond which totals 55 pounds, or of the afterbody protection system (approximately 35 pounds).

The three design concepts are compared in Table LXV. The comparison of the weight fractions indicates that while the forebody heat shields are of about the same order, the total protection cost is, however extremely high for the spin system (23 percent not including contingency). Spin-despin and tumble modes are comparable in weights, and the selection of the latter for reference was based on the overall system considerations.

9.3.4 Reference Heat Shield Design and Performance Evaluation

The results of the parametric studies and material evaluation on one hand, and the systems considerations on the other hand, led to the selection of the reference blunt cone entry shell design utilizing an attitude control system for entry stabilization. The investigation of the effect of various

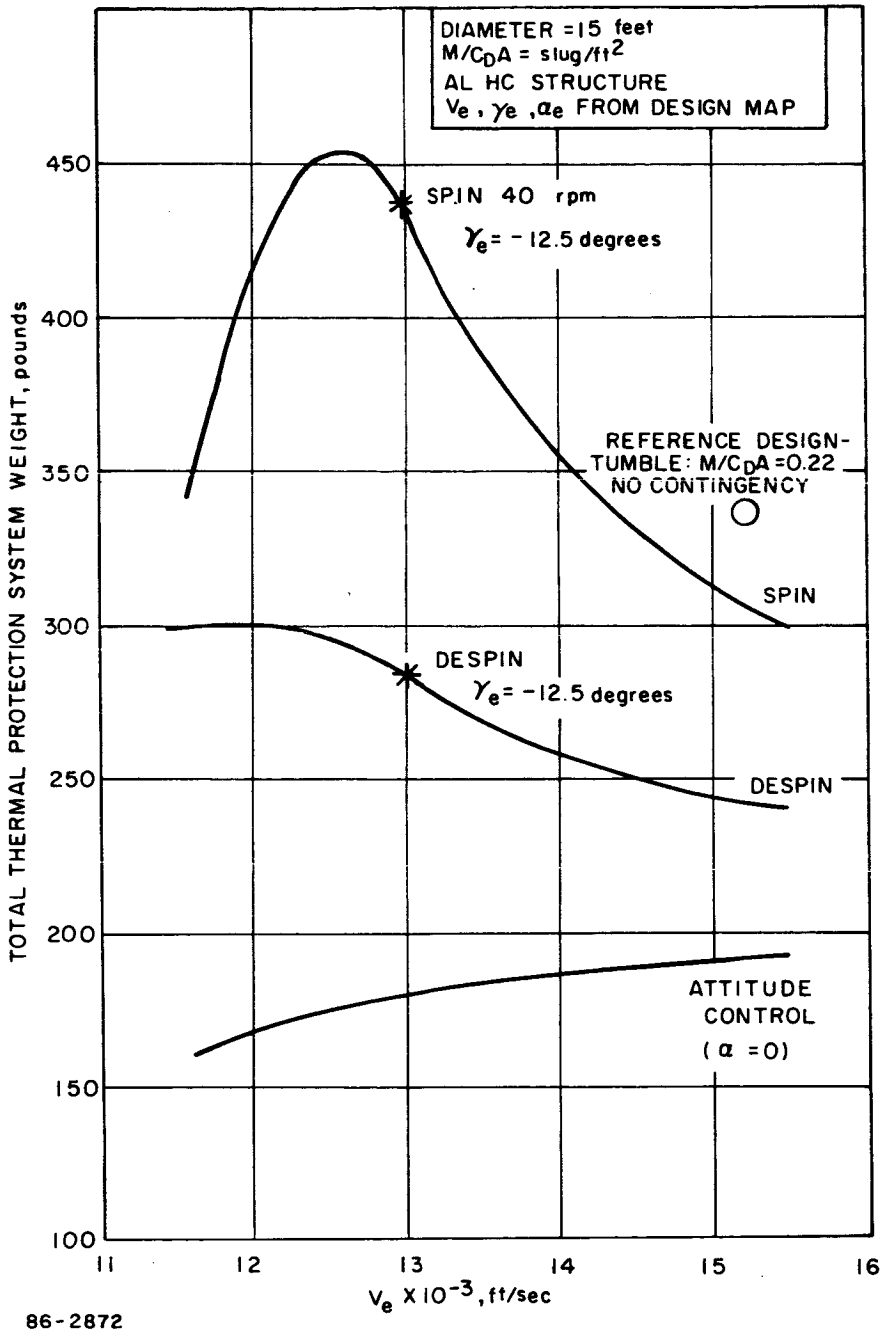

Figure 313 TOTAL THERMAL PROTECTION SYSTEM WEIGHTS

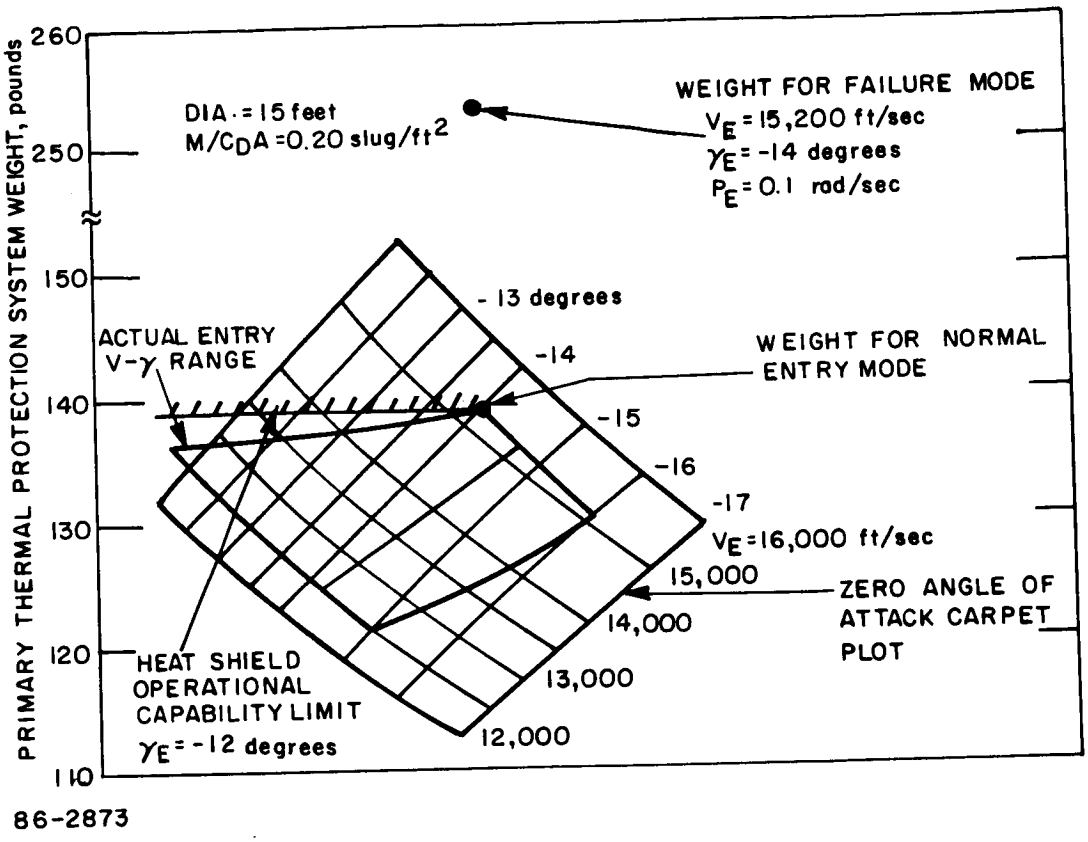

Figure 314 ENTRY SHELL HEAT WEIGHT

TABLE LXV

SUMMARY OF HEATING AND HEAT SHIELD PERFORMANCE DATA (BLUNT CONE)

Design Concept / Flight Parameters	40 rpm Spin	Despin	Present Design
Diameter, feet	15.0	15.0	15.0
Weight, pounds	1855	1855	2040
Entry velocity, ft/sec	12,900	12,900	15,200
Entry angle, degrees	-12.8	-12.8	-14
Atmospheric model	VM-7	VM-7	VM-7
m/C_dA, slug/ft^2	0.20	0.20	0.22
Entry angle of attack, degrees	86	86	90
Total integrated heating, Btu/ft^2	2052	1790	2270
Peak heating rate, Btu/ft^2/sec	23.6	18.8	18.6
Duration of heat pulse, seconds	320	310	240
Angle of attack-peak heating, degrees	59	30	11
Material heat shield	Purple Blend Mod 5		
Material structures	Aluminum Honeycomb		
Limiting bondline temperature, °F	500.0	500.0	500.0
Entry temperature, °F	60	60	100
Saftey factor	1.2	1.2	1.2
End of heating pulse	Parachute Deployment		
Approximate weight fraction (forebody only) percent	12.7	9.3	12
Total weight fraction, percent	23	15	16

backup systems and failure modes considered indicated that rearwards or tumbling entry failure mode should be used for the reference heat shield design. The resulting critical design parameters and environments were listed in Table LXV "Reference Design," and were used together with the general system constraints (Table II) and design criteria (paragraph 9.2) to provide an efficient, although not necessarily minimum weight thermal protection system. Purple Blend, Mod 5 was the ablating heat shield selected for the reference design. The methods and theory used in the design and performance evaluation are described in Section 10.0 of this book, together with the material characteristics. In addition to the evaluation of the heat shield performance for the critical heating design point, other entry conditions described in the heating summaries (Table XX and XXIII) were investigated as reflecting the critical loads design point and the choice of the landing site. The heating and loads design points are evaluated below in detail, while the conditions associated with the landing site were found to be less severe than the reference design conditions, and thus performance for these conditions is not detailed in this report.

9.3.4.1 Thermal Protection System Description

The primary Purple Blend, Mod 5 heat shield requirements presented in Table LXVI are based on the material properties listed in paragraph 9.2 and on the environment which imposes the most severe aerodynamic heating, i.e., an initial angle of attack of 90 degrees (tumble failure mode); VM-7 atmosphere; an entry velocity of 15,200 ft/sec; and an entry angle of -14 degrees. The afterbody heat shield thicknesses listed in Table LXVII were determined on the basis of a 90 degree initial angle of attack. The integrated heating in this case was 115 Btu/ft^2 as compared to 95 Btu/ft^2 for an initial angle of attack of 180 degrees. The secondary heat shield thicknesses, also listed in Table LXVII, were based on an initial angle of attack of 180 degrees. Here, the integrated heating is 117 Btu/ft^2 while the 90-degree initial angle of attack results in a value of 90 Btu/ft^2. The antenna heat shield requirement is listed in Table LXVII. The antenna analysis accounted for entry heating (175 Btu/ft^2) based on an initial angle of attack of 90 degrees and the effects of rocket plume heating (5.9 Btu/ft^2-sec), which was imposed 27 minutes prior to entry for a period of 33.3 seconds.

The antenna may be redesigned using a somewhat different combination of structural material. Instead of using a composite slab of Teflon over a composite of 0.015-inch bond, 0.020-inch fibergalss 0.015-inch bond and another layer of 0.020-inch fiberglass, an alternate design of the antenna may be a Teflon layer placed over a composite of 0.015-inch bond and 0.125-inch refrasil Teflon sandwich containing the printed circuit antenna.

TABLE LXVI

PURPLE BLEND, MOD 5 - FOREBODY HEAT SHIELD REQUIREMENTS

(Reference Design - Failure Mode Tumble)

Body Station S/R_N	Local Weight Ablator lbs/ft^2	Thickness (inches)			
		Ablator	Fiberglass Mounting Pad	RTV Bond	Substructure
0.0	0.348	0.100	0.019	0.020	0.600 AL
1.5	0.985	0.283	↓	↓	0.452 HC*
2.5	0.932	0.268	↓	↓	↓
3.5	0.877	0.252	↓	↓	↓
4.0	0.832	0.239	↓	↓	↓
4.5	1.107	0.318	↓	↓	↓
and 4.56	1.107	0.318	↓	↓	0.050" AL

*Honeycomb -- includes aluminum face sheets and HT 424 bond

TABLE LXVII

THERMAL PROTECTION REQUIREMENTS
ENTRY SHELL AND AFTERBODY HEAT SHIELD THICKNESS

(Reference Design - Failure Mode Tumble)

Location	Material	Thickness		
		Ablator	RTV Bond	Aluminum Structure
Forebody	Purple Blend, Mod 5	see Table LXVI		
Secondary	Purple Blend, Mod 5	0.054	0.020	0.020
Afterbody	Purple Blend, Mod 5	0.072	0.020	0.020
Afterbody (inner shoulder)	Purple Blend, Mod 5	0.384	0.020	0.020
Antenna	Teflon	0.217	-	-
TVC area	Refrasil phenolic inserts	0.660	-	-

The nominal thickness of Teflon required as a function of the antenna bond temperature is presented in Figure 315. If it were desired to limit the antenna bondline temperature to 300°F this would require a nominal thickness of 0.305 inch. A design thickness of 0.366 inch would be used applying the safety factor of 1.2.

Due to the possible aggravation because of protuberances in the area of the TVC nozzles, refrasil phenolic inserts 0.66 inch thick are required. This thickness is calculated with the TVC aggravation factors presented in Section 3.0. Heating from the TVC nozzle plume has been neglected, as it amounts to only 3 to 4 Btu/ft^2. The requirements are listed in Table LXVII. The afterbody inner shoulder, on the other hand, experiences rather high ΔV rocket plume heating which requires that this area be built up with heat shield material. The requirement for this location is listed in Table LXVII as 0.384 inch of Purple Blend.

9.3.4.2 Heat Shield Performance

1. Heat Shield Design Point (Normal and Failure Mode Entry) -- Heat shield design thickness was determined by calculating a nominal thickness for the maximum bondline temperature to reach 500°F and then a safety factor of 1.2 was applied to the nominal thickness. The calculations were based on nominal heating for the failure mode and a 100°F initial entry temperature. The resulting maximum temperatures of the bondline and the structure for the nominal (no safety factor) and design thicknesses are presented in Table LXVIII. It may be noted that the design thickness temperatures are lower than nominal since the heating in both cases is the same. The design bondline and structural temperature histories are illustrated in Figure 316 through 320 for the failure mode of α equal 90 degrees and for a normal entry (zero angle of attack) - they are presented in Figures 321 through 323. The surface recession history is shown in the same figures. The thickness ablated and the final char depth are tabulated in Table LXIX. A distribution of the mass loss was shown previously in Figure 303.

Temperature distributions for the initial angle of attack of 90 degree for S/RN = 0.0, 2.5, 4.5, afterbody and the antenna are presented in Figures 324 through 328 for the times when maximum loading, maximum bond temperatures and maximum heating rate are reached. The same information, but for the normal entry mode (zero angle of attack) and the locations S/RN = 0.0, 2.5 and the afterbody, is shown in Figures 329 through 331.

Density profiles are illustrated in Figures 332 through 334 for the case of initial angle of attack of 90 degrees for S/RN = 0.0, 2.5 and 4.5. Char penetration on the afterbody and secondary heat shield section of

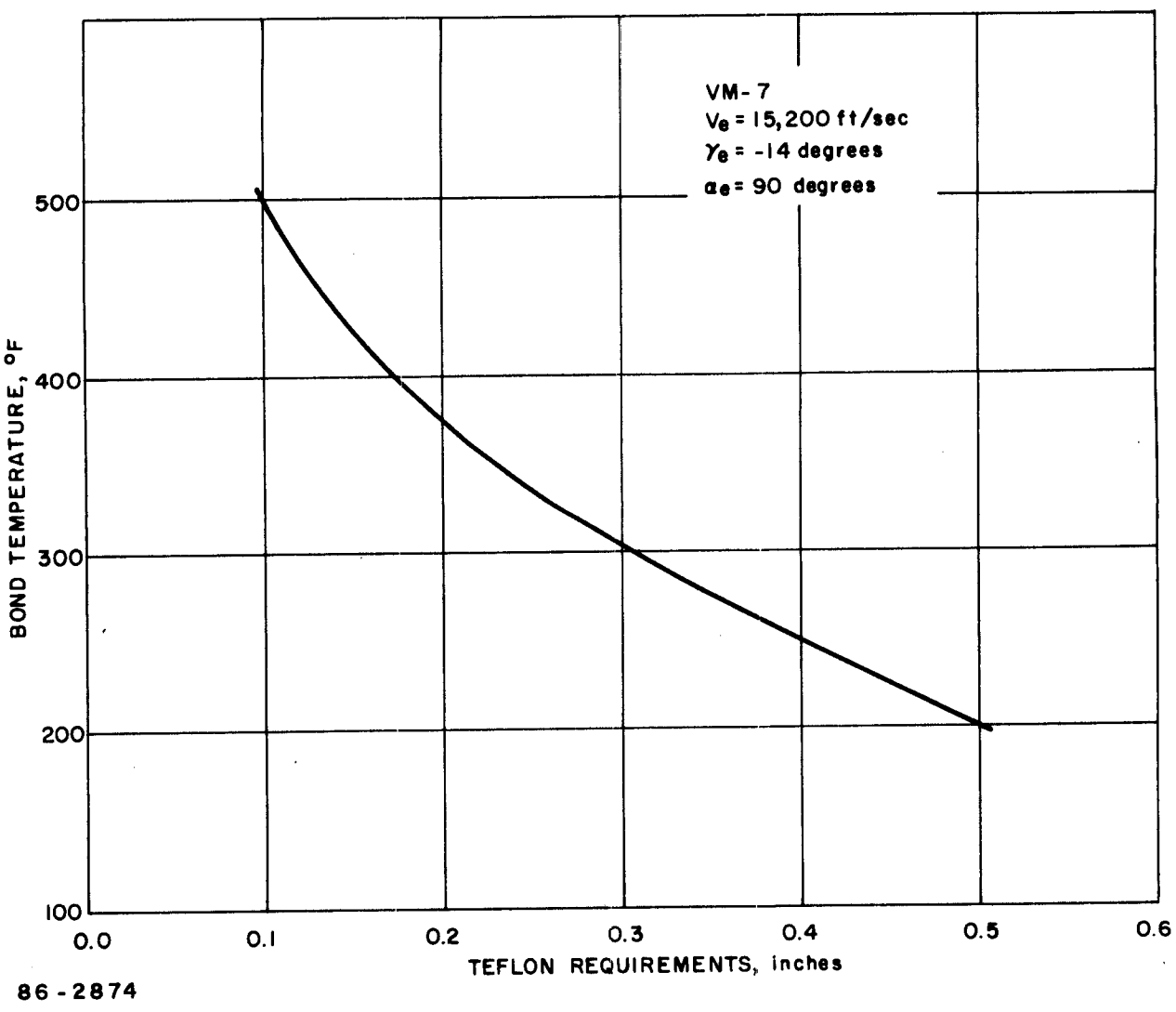

Figure 315 NOMINAL THERMAL RESPONSE OF A NEW ANTENNA DESIGN

TABLE LXVIII

BONDLINE AND STRUCTURAL TEMPERATURE RESPONSE FOR VARIOUS ENTRY MODES

(heat shield design point trajectories V_e = 15,200 ft/sec, γ_e = -14 degrees, VM-7 Atm.)

Body Station S/R_N	Entry Angle of Attack α_e - degrees	Temperature (°F)			
		Heat Shield Nominal Thickness L_{nom}		Heat Shield Reference Design Thickness (L_{nom} x 1.2)	
		Bondline	Structure	Bondline	Structure
Failure Mode					
0	90	500	423	442	363
1.5	90		499	438	438
2.5	90		499	442	442
3.5	90		500	447	447
4.0	90		500	449	449
4.5	90		500	442	441
Afterbody	90		499	479	479
Secondary	180		499	460	459
Antenna window	90	500	496	445	445
Normal Mode					
0.0	0	-	-	378	337
2.5	0	-	-	409	409
Afterbody	0	-	-	423	422

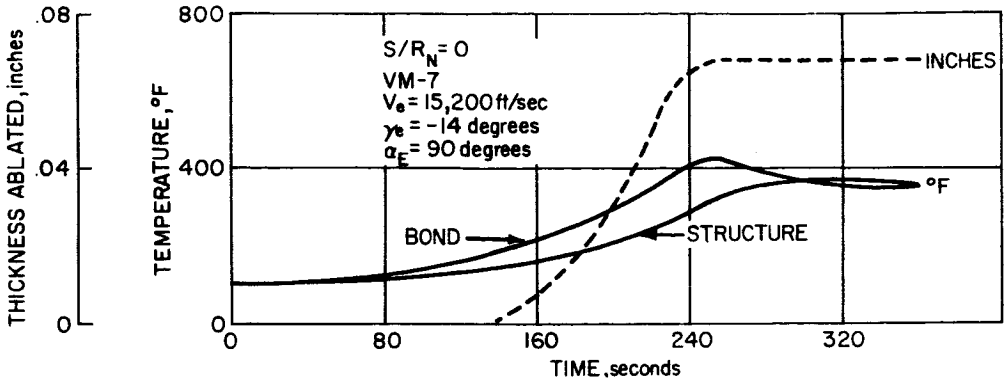

Figure 316 TEMPERATURE AND ABLATION HISTORIES--$S/R_N = 0$

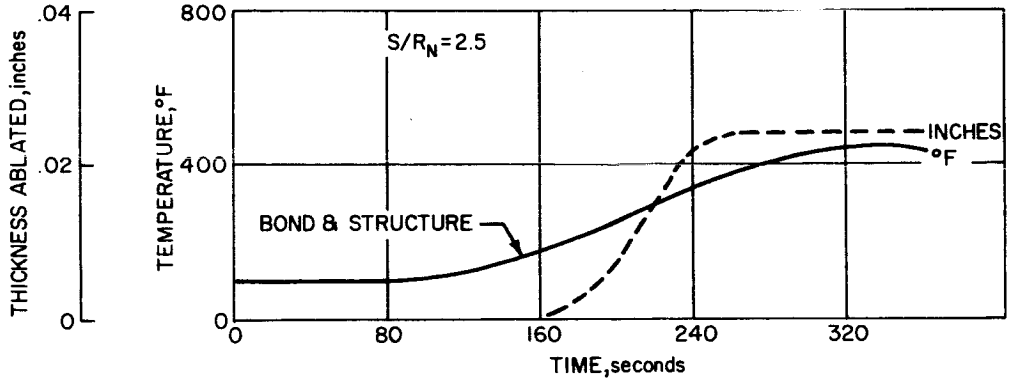

Figure 317 TEMPERATURE AND ABLATION HISTORIES--$S/R_N = 2.5$

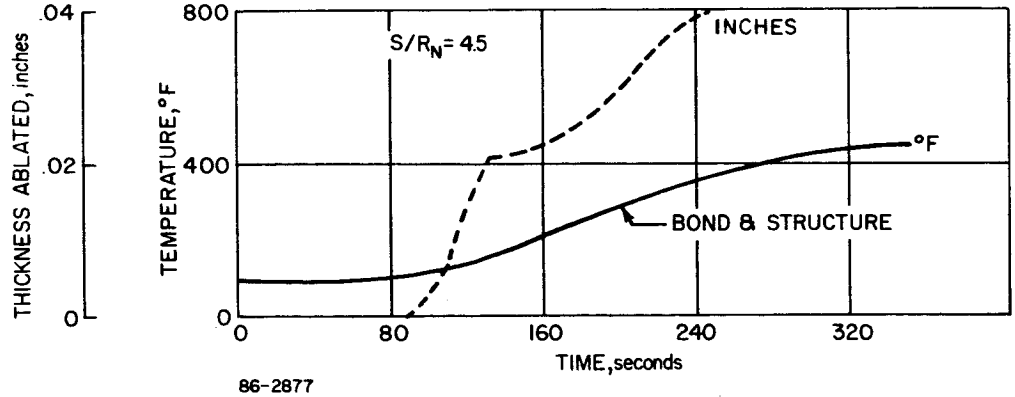

86-2877

Figure 318 TEMPERATURE AND ABLATION HISTORIES--$S/R_N = 4.5$

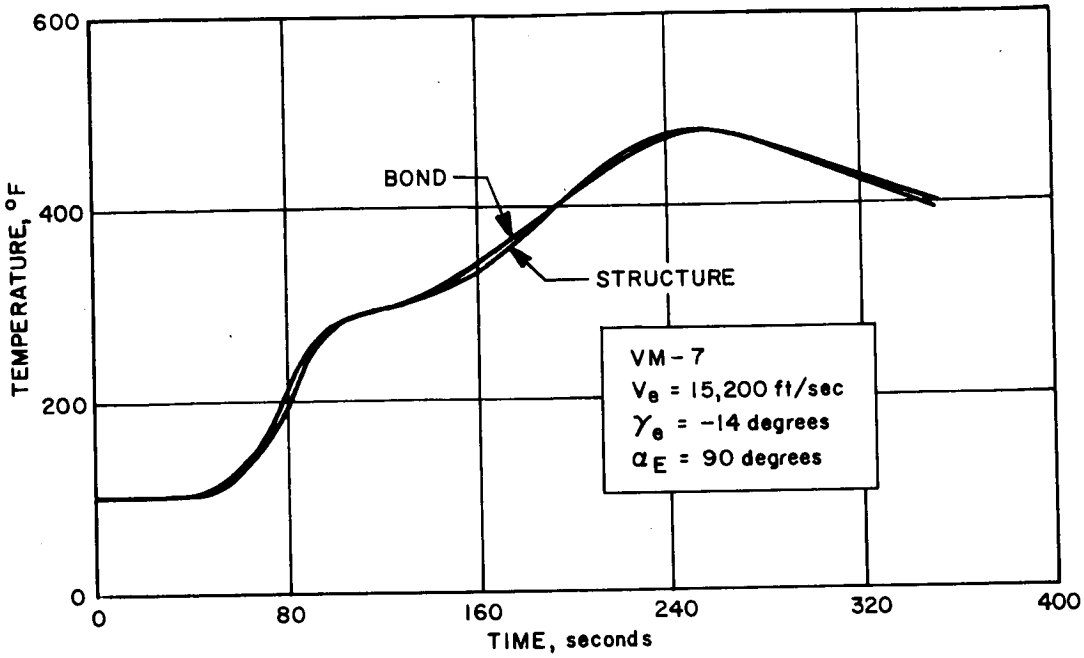

Figure 319 TEMPERATURE HISTORIES FOR THE AFTERBODY BOND AND STRUCTURE

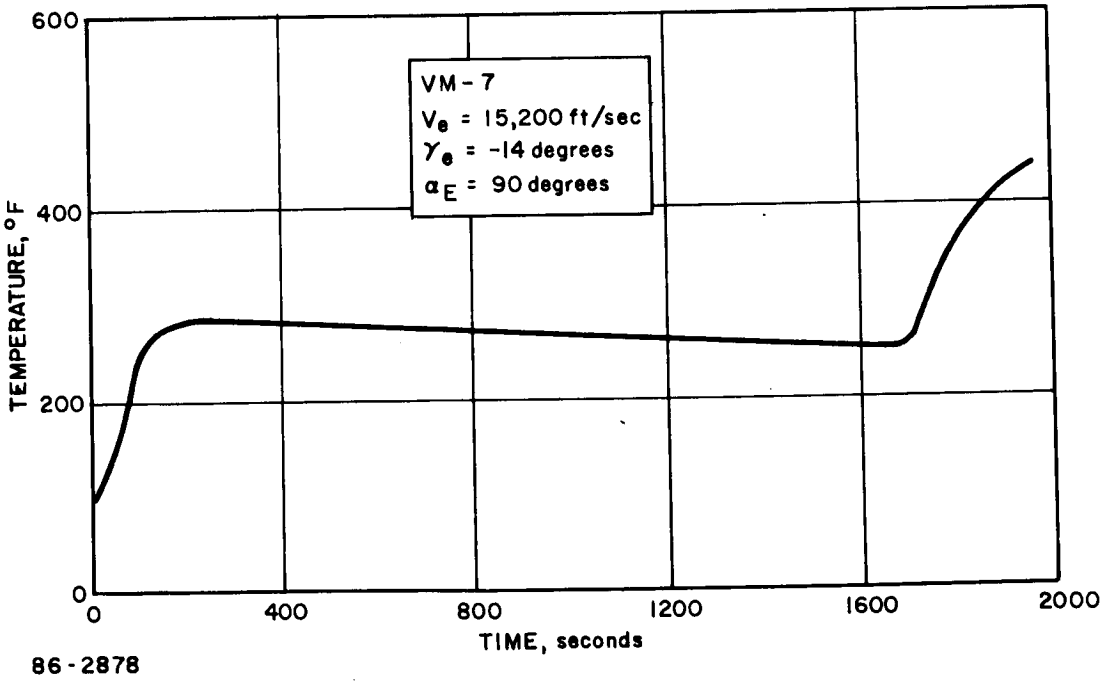

Figure 320 TEMPERATURE HISTORY FOR THE ANTENNA BOND AND STRUCTURE INCLUDING EFFECT OF ROCKET PLUME HEATING

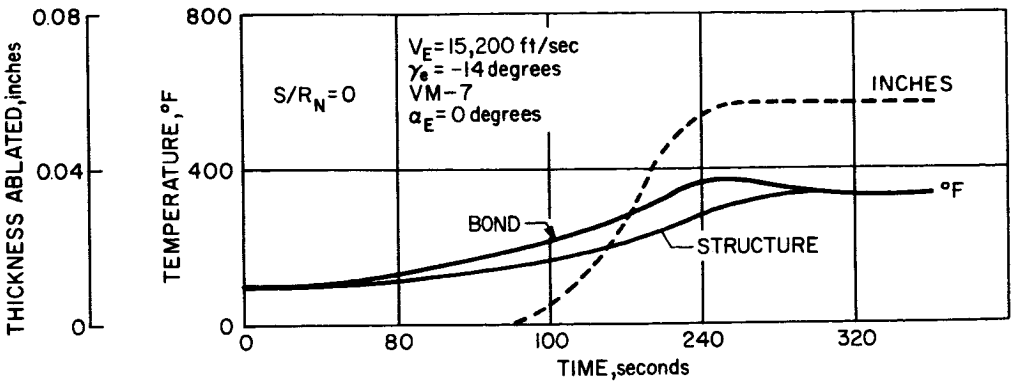

Figure 321 TEMPERATURE AND ABLATION HISTORIES--$S/R_N = 0$

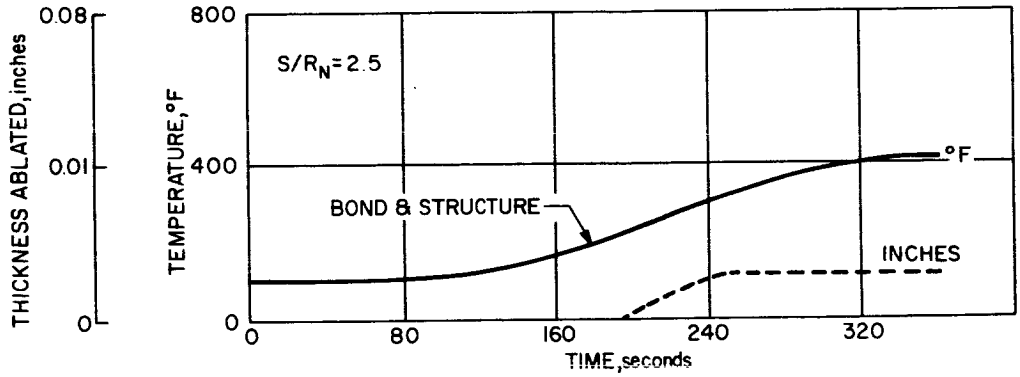

Figure 322 TEMPERATURE AND ABLATION HISTORIES--$S/R_N = 2.5$

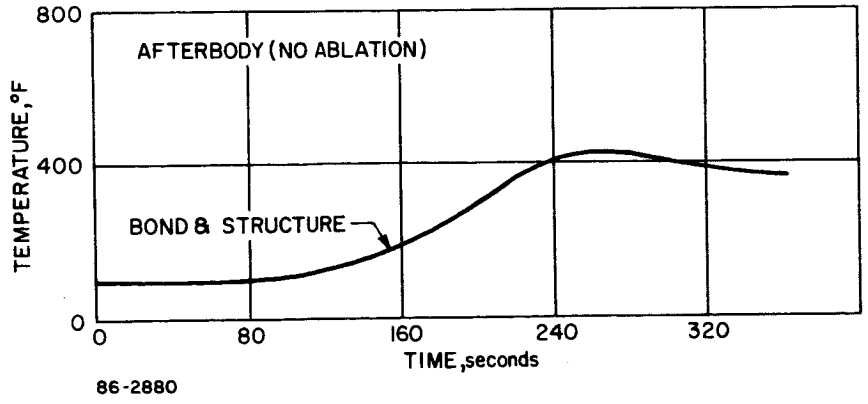

Figure 323 TEMPERATURE AND ABLATION HISTORIES--AFTERBODY (NO ABLATION)

TABLE LXIX

HEAT SHIELD MASS LOSS AND CHARRING RESPONSE FOR FAILURE AND NORMAL ENTRY MODES

(V_e = 15,200 ft/sec, γ_e = -14 degrees, VM-7 Atm.)

Body Station S/R_N	Angle of Attack α_e (degrees)	Amount Ablated (inches)	Final Char Depth (inches)
Failure Mode			
0.0	90	0.068	0.017
1.5		0.036	0.070
2.5		0.024	0.070
3.5		0.013	0.067
4.0		0.008	0.068
4.5		0.040	0.086
Afterbody		0.000	0.001
Secondary	180	0.000	0.001
Antenna Window	90	0.001	-----
Normal Mode			
0.0	0	0.057	0.021
2.5	0	0.000	0.059
Afterbody	0	0.000	0.0005

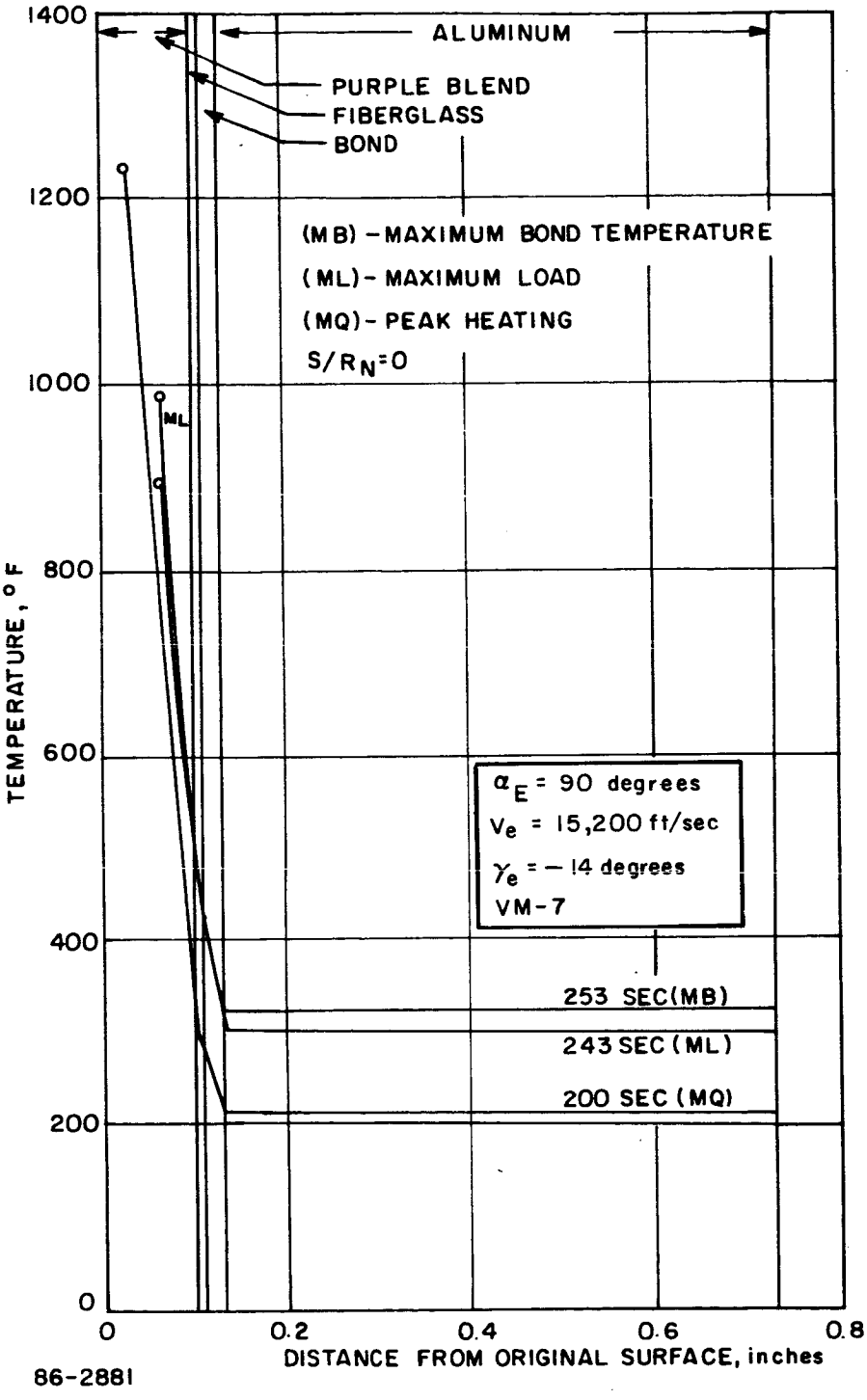

Figure 324 TEMPERATURE DISTRIBUTION--$S/R_N = 0$

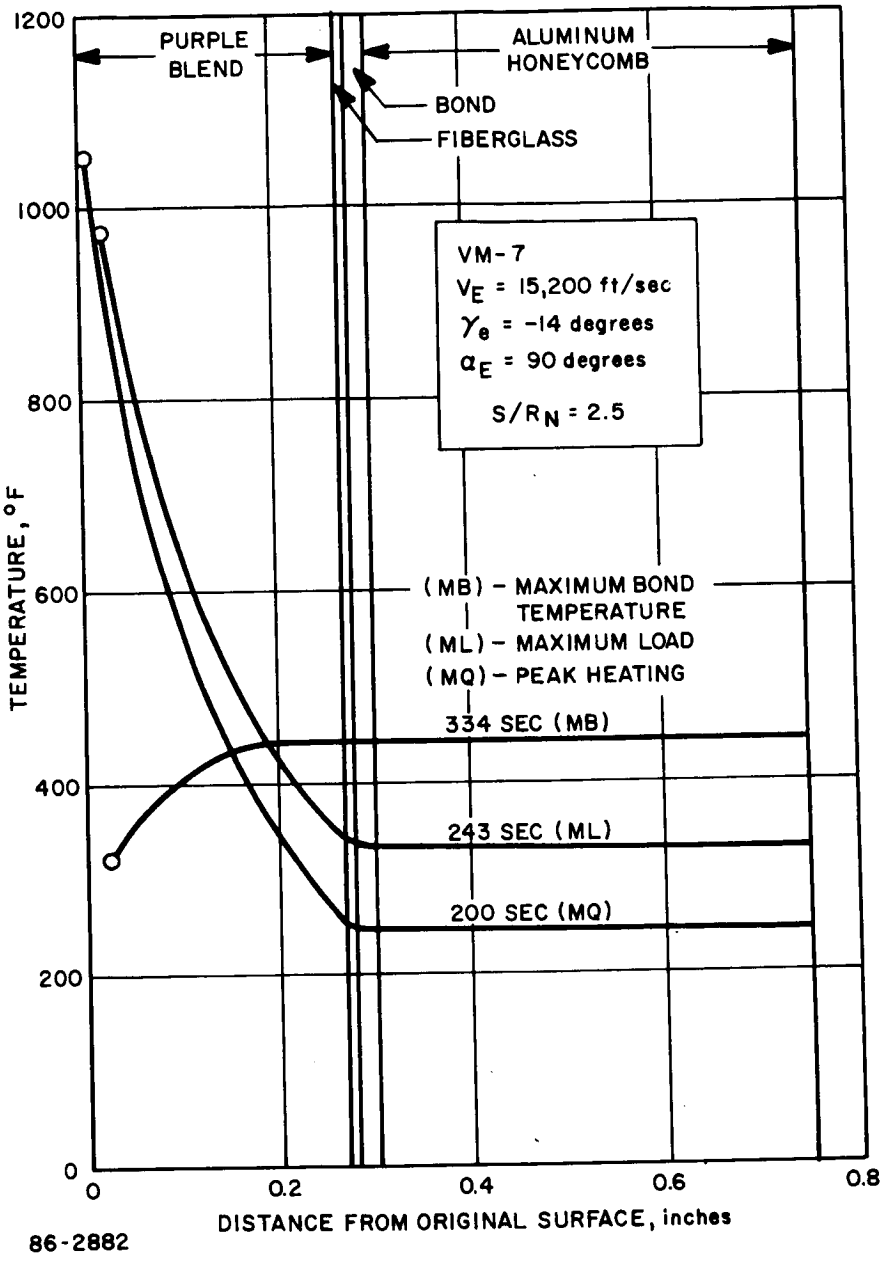

Figure 325 TEMPERATURE DISTRIBUTION--$S/R_N = 2.5$

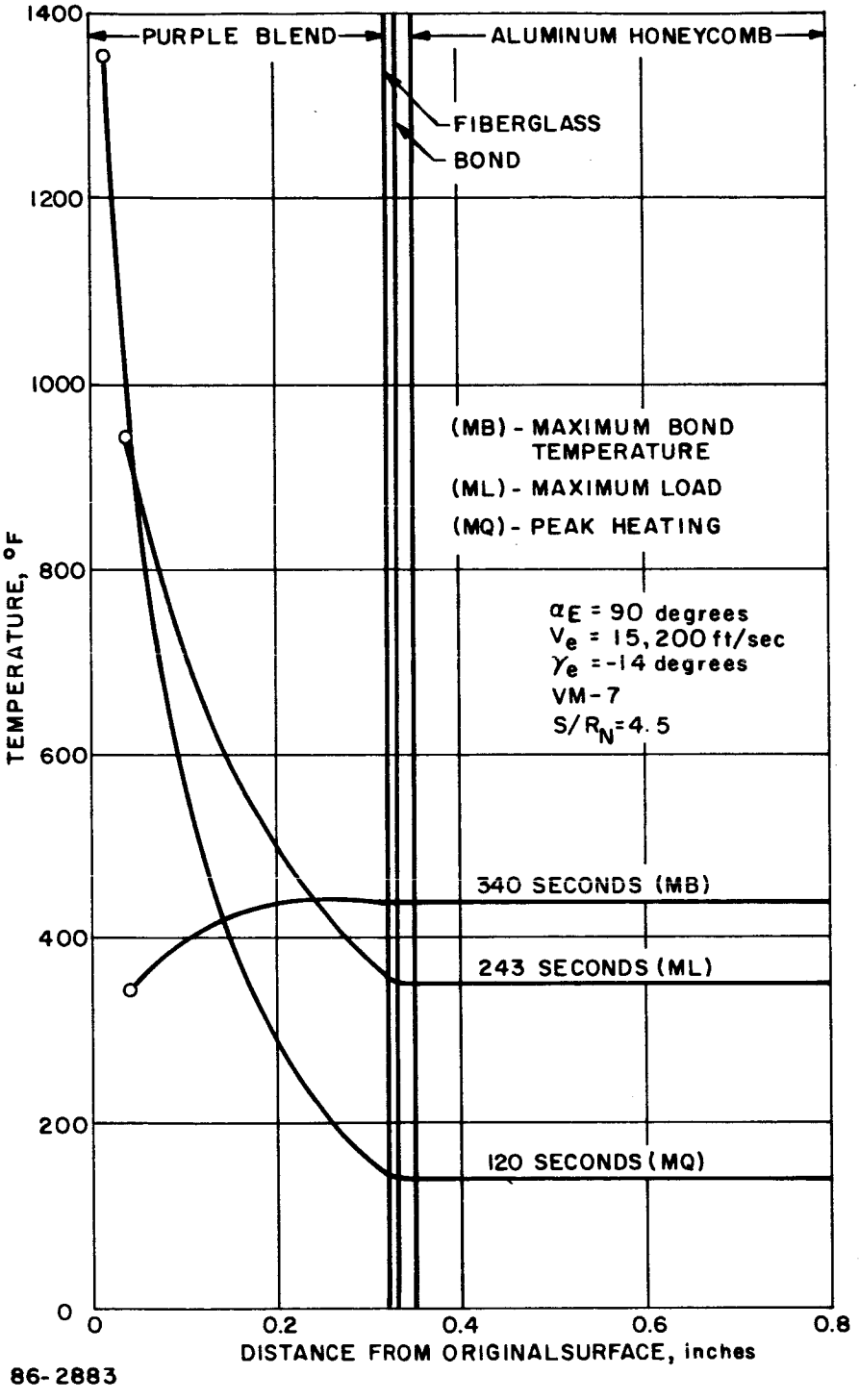

Figure 326 TEMPERATURE DISTRIBUTION--$S/R_N = 4.5$

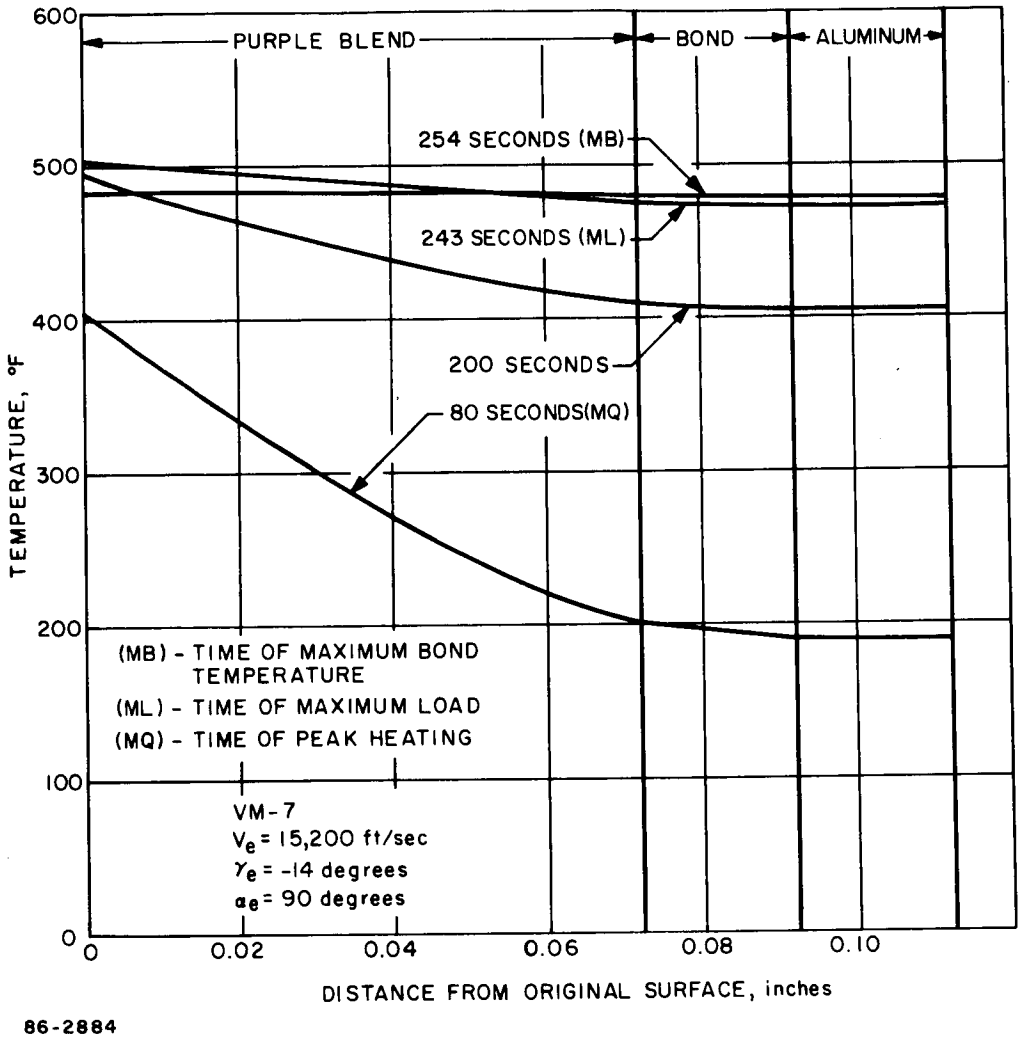

Figure 327 TEMPERATURE DISTRIBUTION--AFTERBODY

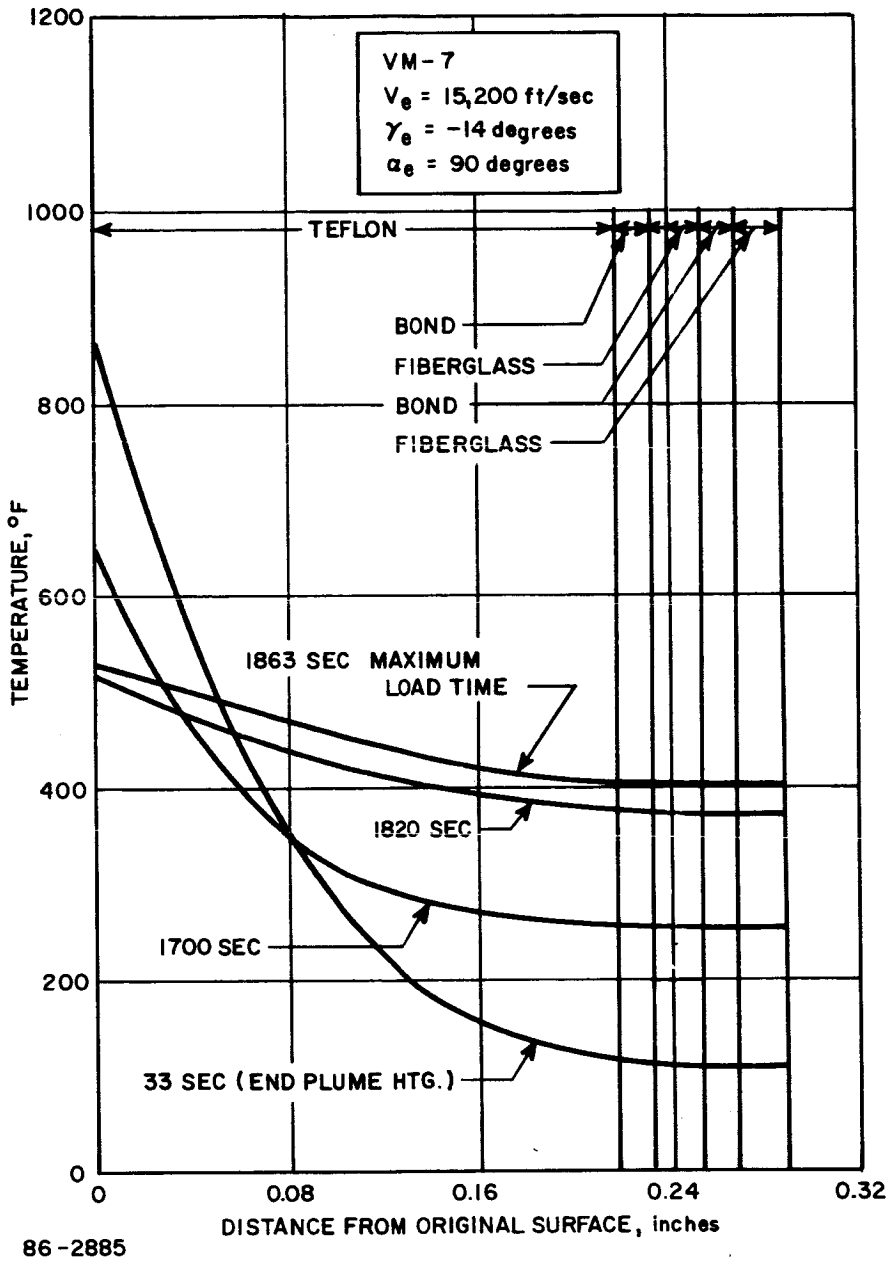

Figure 328 TEMPERATURE DISTRIBUTION--ANTENNA

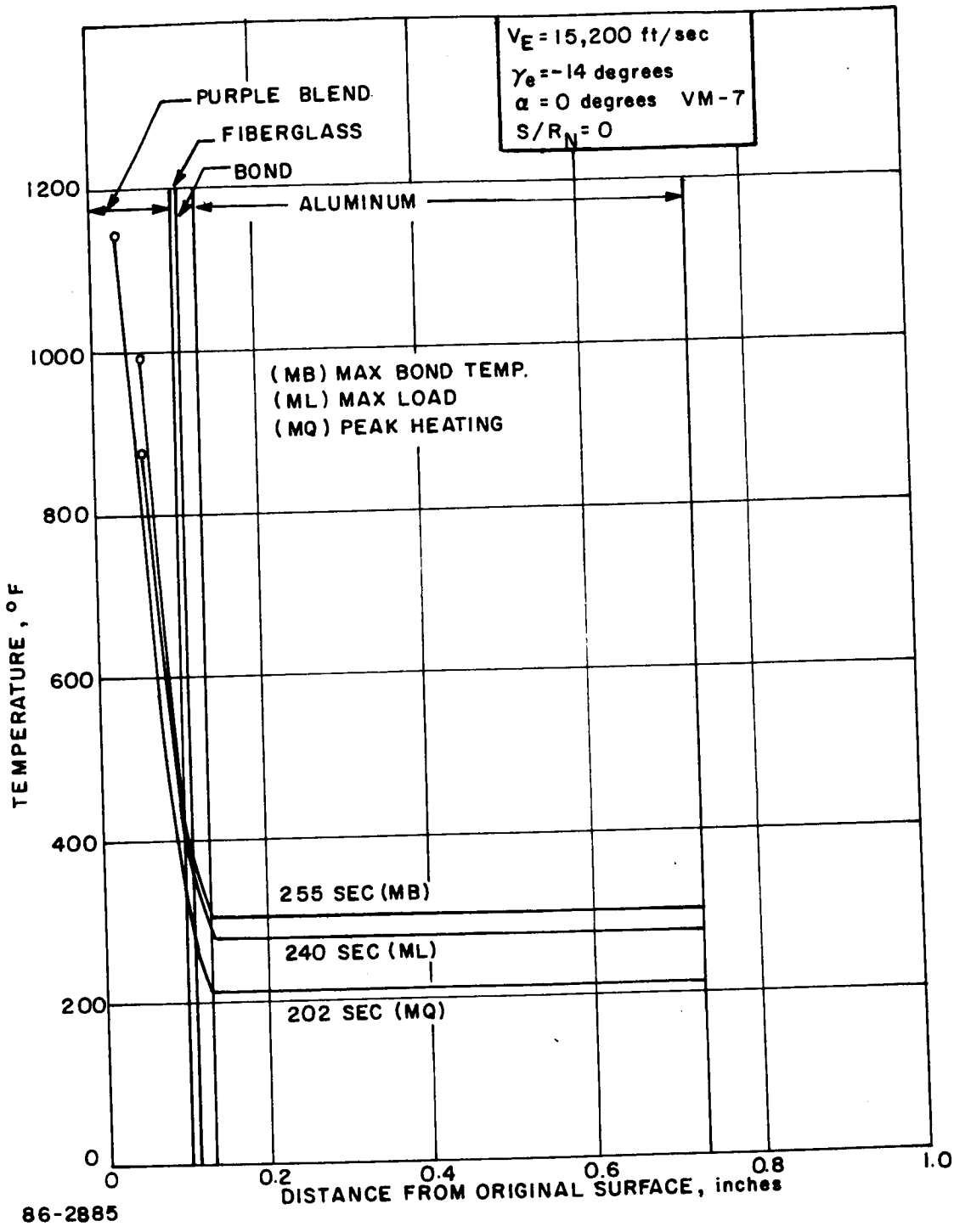

Figure 329 TEMPERATURE DISTRIBUTION S/R_N = 0 DEGREES

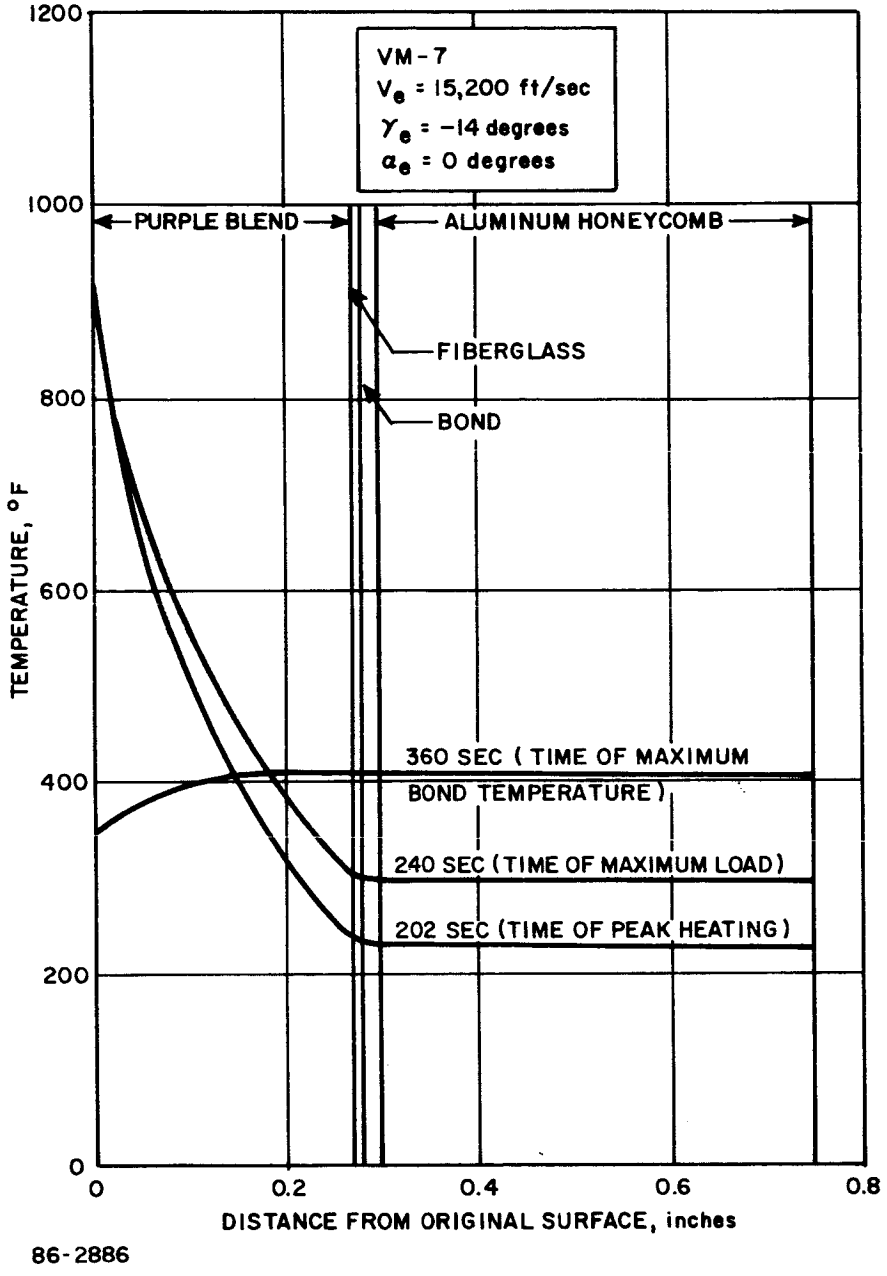

Figure 330 TEMPERATURE DISTRIBUTION AT $S/R_N = 2.5$

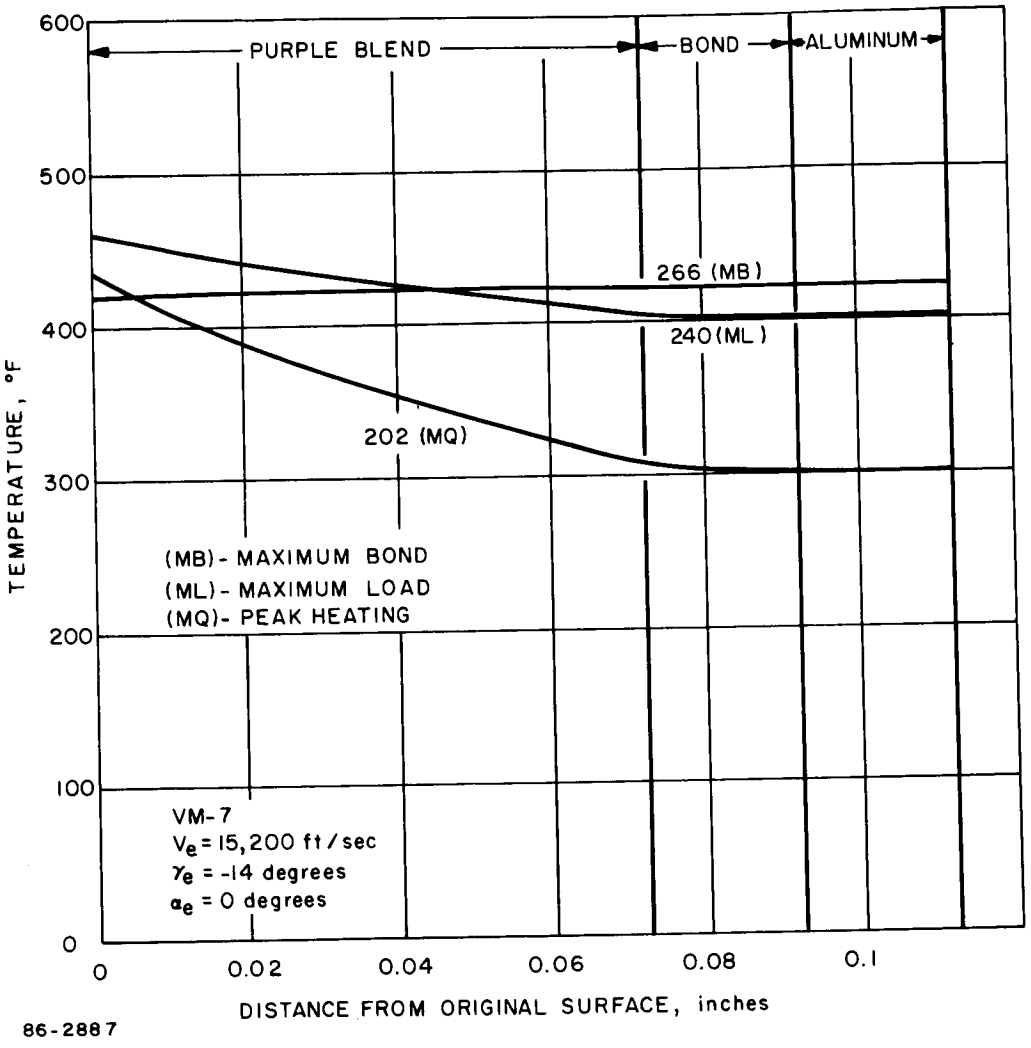

Figure 331 TEMPERATURE DISTRIBUTION--AFTERBODY α = 0 DEGREES

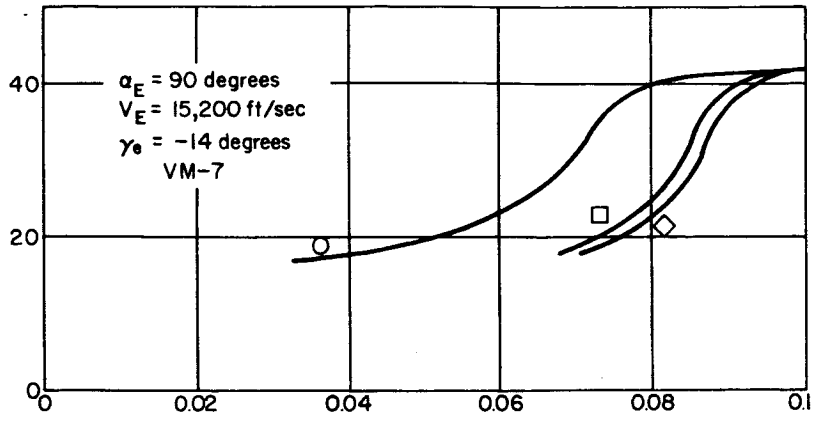

Figure 332 DENSITY PROFILE THROUGH THE HEAT SHIELD--$\alpha = 90^\circ$, $S/R_N = 0$

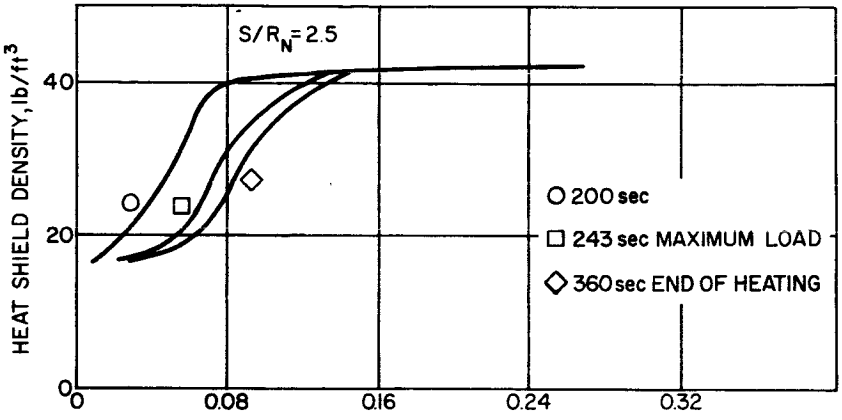

Figure 333 DENSITY PROFILE THROUGH THE HEAT SHIELD--$\alpha = 90^\circ$, $S/R_N = 2.5$

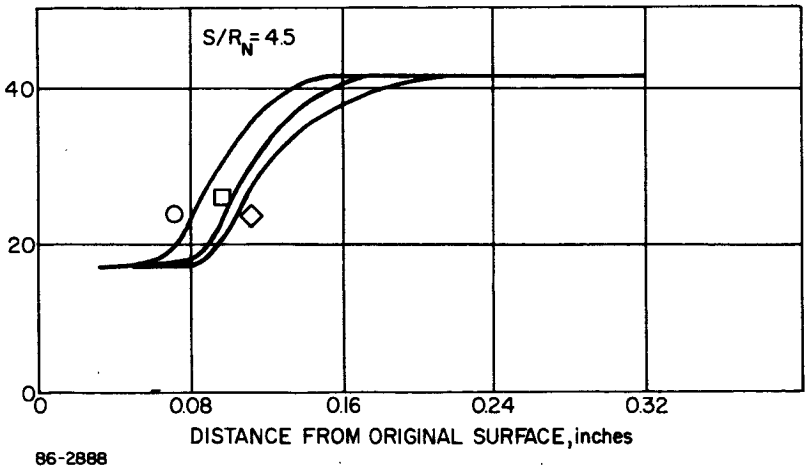

Figure 334 DENSITY PROFILE THROUGH THE HEAT SHIELD--$\alpha = 90^\circ$, $S/R_N = 4.5$

the vehicle is negligible and is not shown on the graph. The surface density is approximately 41 lb/ft^3 after entry compared with a virgin density of 41.8 lb/ft^3. Density profiles for the zero-angle of attack case for S/RN = 0.0 and 2.5 are shown in Figures 335 and 336. These distributions are presented for a time close to peak heating, maximum load and end of heating.

It should be noted that the thermal response of the vehicle is less for the 0-degree angle of attack case than for the 90-degree angle of attack condition. This lower response is due to the lower heating encountered in the 0-degree angle of attack case as is evident from the heating data given in Section 3.0.

2. Structural Design Point -- A comparison of the maximum heating trajectory (VM-7, V_e = 15,200 ft/sec and γ_e = -14 degrees) and maximum loading trajectory (VM-8, V_e = 15,200 ft/sec and γ_e = -16 degrees) is made in Table LXX. Bondline and structure temperature histories as well as the ablation history for the VM-8 atmosphere are shown in Figure 337 and 338 for S/RN = 0.0 and 2.5. Temperature distributions for the same locations are shown in Figures 339 and 340 for the time of maximum heating rate, maximum loading and maximum bondline temperature. Density profiles for S/RN = 0 and 2.5 are illustrated in Figures 341 and 342 for the time of maximum load, end of heating, and close to peak heating.

By comparing the figures for the VM-7 and VM-8 condition as well as using Table LXX it becomes apparent that, due to lower heating, the thermal response of the vehicle is considerably lower for VM-8. Particularly, it should be noted from Figures 315and 340 that the structural temperature at peak load for VM-7 is 360°F while for VM-8 it is only 150°F. The VM-8 or peak loading temperature response was used in the thermo-structural analysis and was found to be well within the original assumptions.

The above analyses have been made considering heating to one side of the heat shield only. This is somewhat nonconservative in the region of the entry shell between the afterbody and outer structural ring. A limited analysis was made for this area of the entry shell for the design thickness and conditions considering heating from both sides of the composite slab. Figure 343 compares the bond temperatures for the two types of analysis. The bond temperature for the two-sided heating calculation area slightly higher than for the front heating only case, but not significantly so.

9.3.4.3 Protuberance Effect

Since the TVC nozzles protrude beyond the outer edge of the entry shell, severe local heating of the heat shield occurs in the vicinity of

TABLE LXX

COMPARISON OF THE TEMPERATURE AND MASS LOSS RESPONSE FOR THE HEAT SHIELD (VM-7, γ_e = -4 DEGREES) AND STRUCTURAL (VM-8, γ_e = -16 DEGREES) DESIGN POINT TRAJECTORIES (α_e = 90 DEGREES)

Body Station (S/R_N)	Max Bondline Temperature (°F)		Max Structure Temperature (°F)		Amount Ablated (inches)		Final Char Depth (inches)	
	Max Heat	Max Load	Max Heat	Max Load	Max Heat	Max Load	Max Heat	Max Load
0.0	442	312	363	201	0.068	0.056	0.017	0.019
2.5	442	229	499	220	0.024	0.021	0.070	0.033

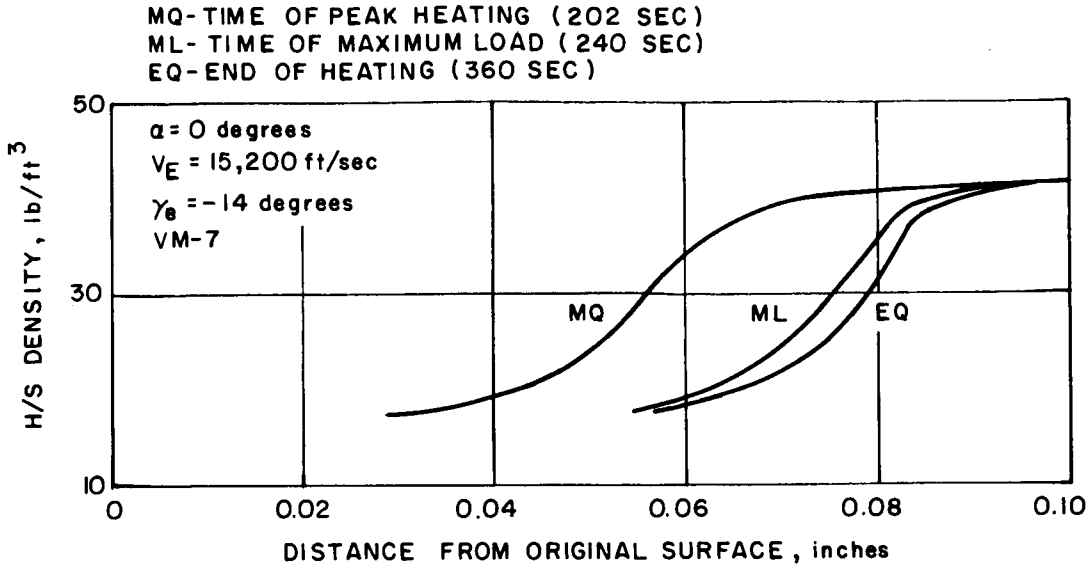

Figure 335 DENSITY PROFILE THROUGH THE HEAT SHIELD AT $S/R_N = 0$

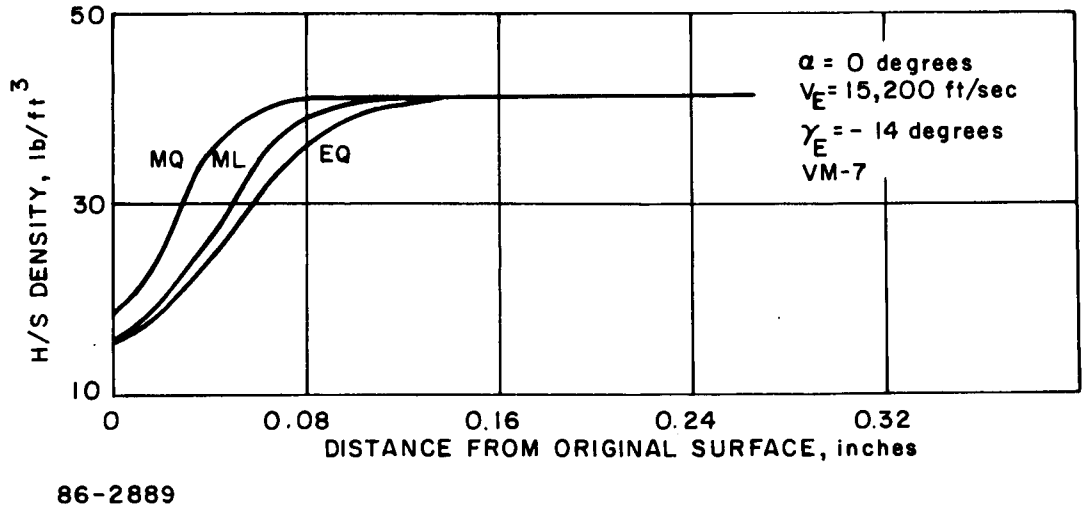

Figure 336 DENSITY PROFILE THROUGH THE HEAT SHIELD AT $S/R_N = 2.5$

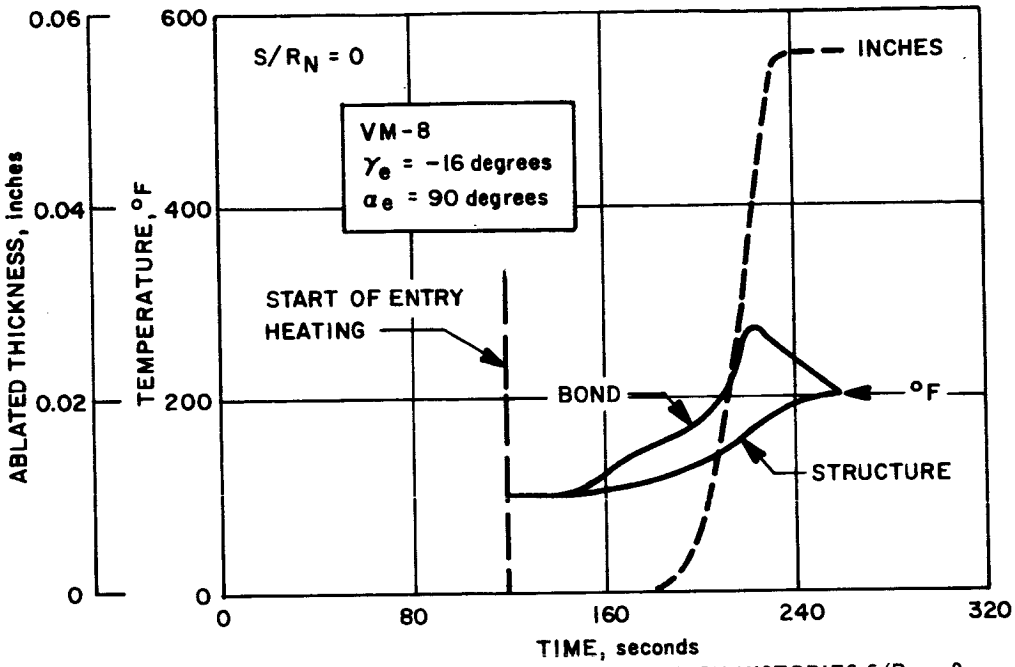

Figure 337 TEMPERATURE AND ABLATION HISTORIES $S/R_N = 0$

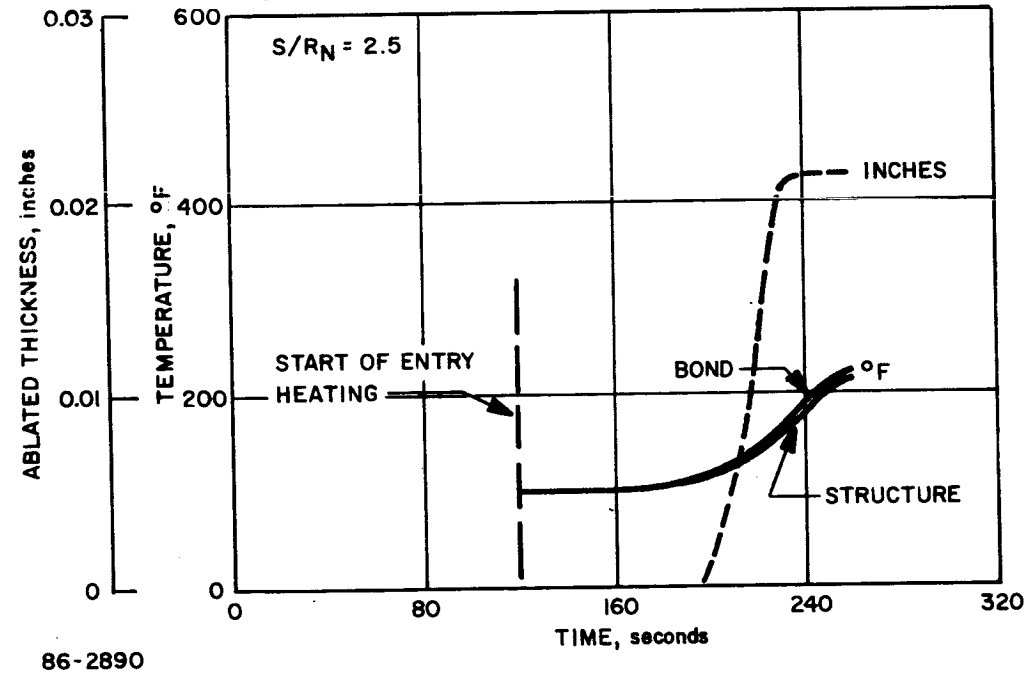

Figure 338 TEMPERATURE AND ABLATION HISTORIES $S/R_N = 2.5$

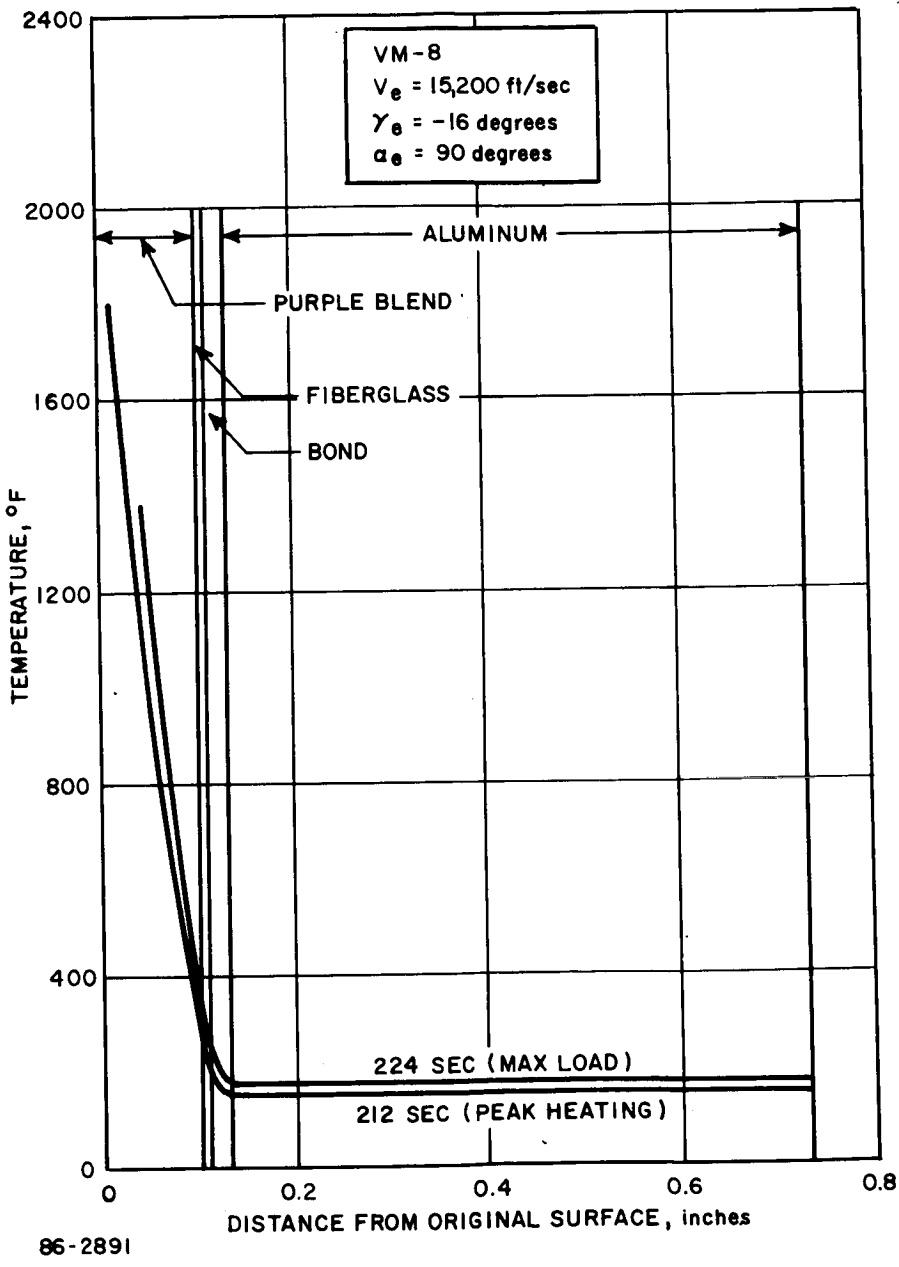

Figure 339 TEMPERATURE DISTRIBUTION AT $S/R_N = 0$

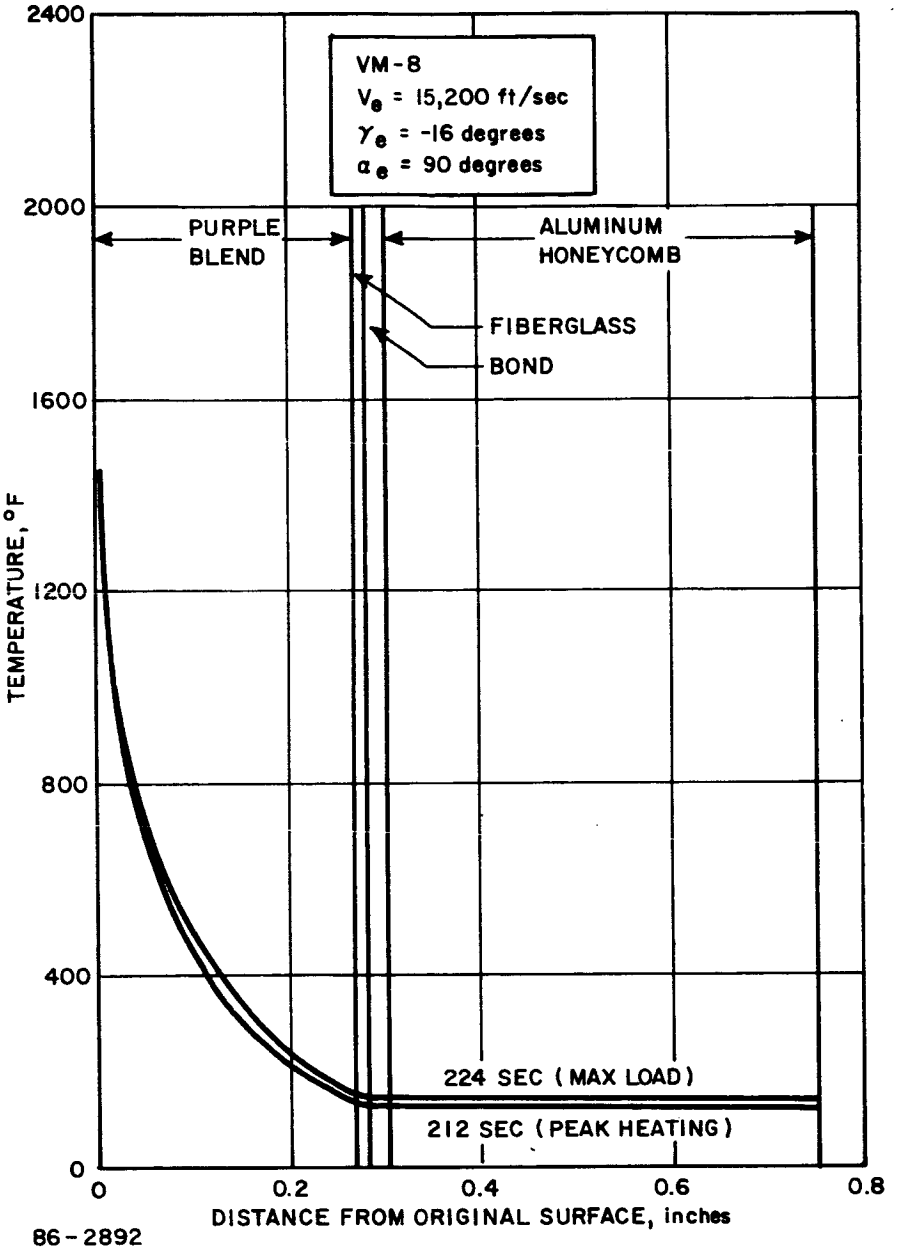

Figure 340 TEMPERATURE DISTRIBUTION AT $S/R_N = 2.5$

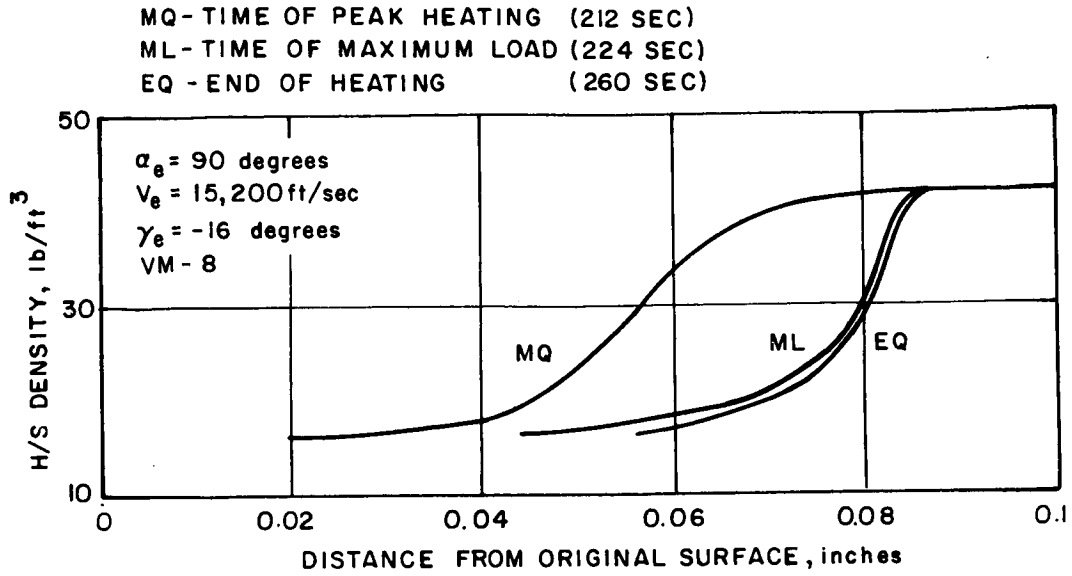

Figure 341 DENSITY PROFILE THROUGH THE HEAT SHIELD AT $S/R_N = 0$

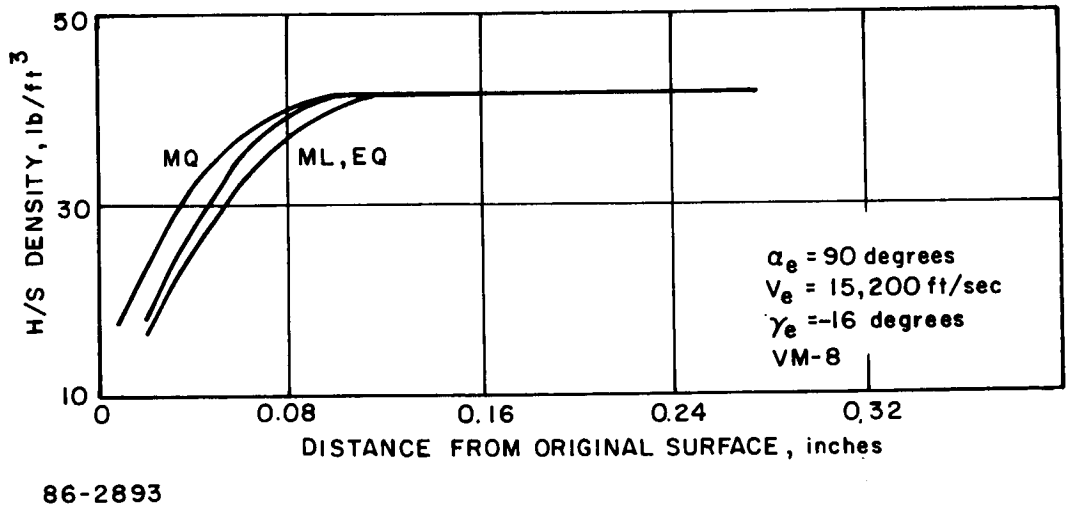

86-2893

Figure 342 DENSITY PROFILE THROUGH THE HEAT SHIELD AT $S/R_N = 2.5$

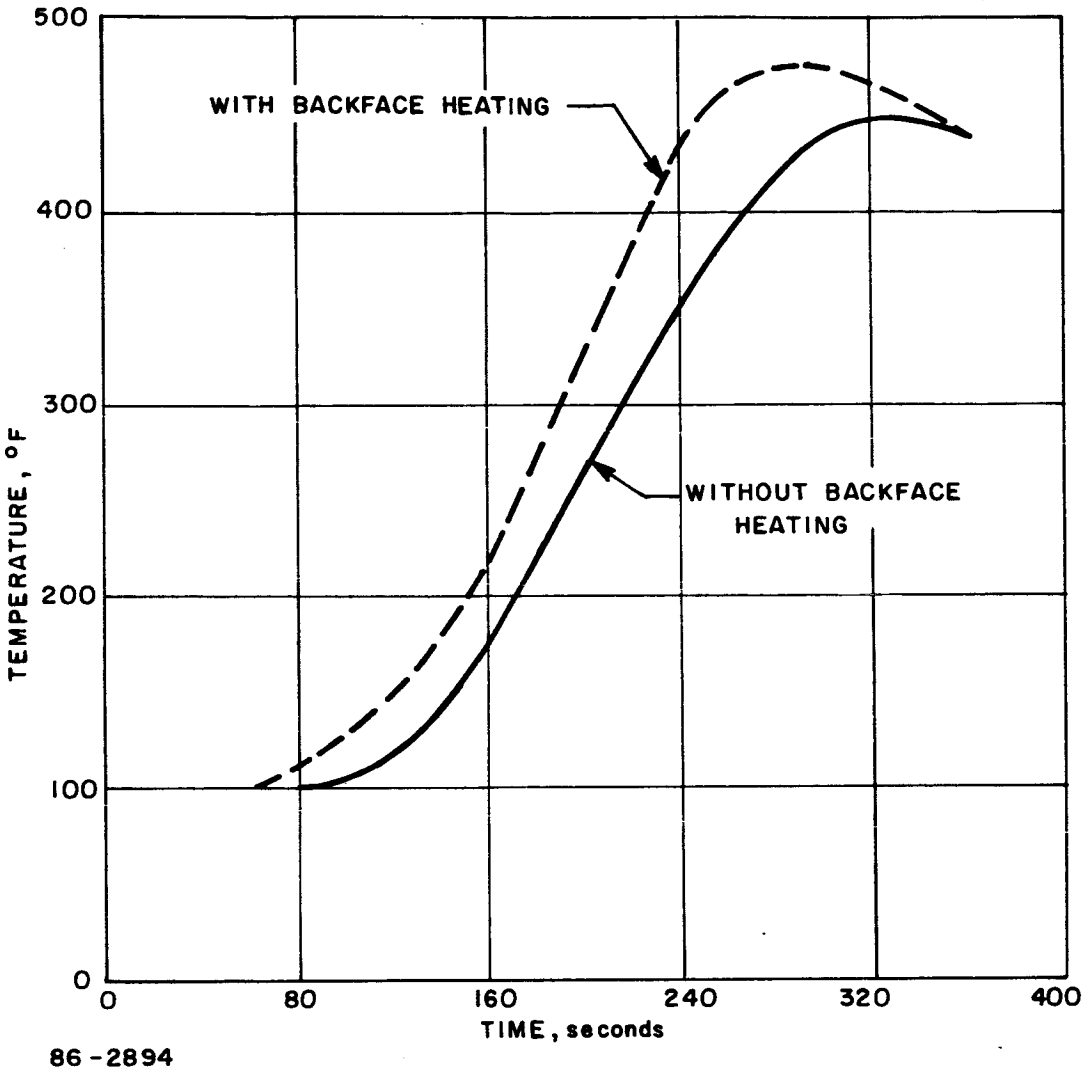

Figure 343 TEMPERATURE HISTORY OF FIRST BONDLINE WITH AND WITHOUT THE EFFECT OF BACKFACE HEATING

the protuberance. The vehicle angle of attack is approximately 90 degrees until a flight time of 90 seconds, then 45 degrees until 150 seconds and finally zero degrees until end of heating. This angle of attack history results in heating 10 times that of the stagnation point during the first 90 seconds, and 5.5 and 1.05 times the stagnation point heating thereafter. Rocket plume heating from the TVC nozzles was not considered in this analysis, as it amounted only to 3-4 Btu/ft^2. Table LXXI indicates the thickness of refrasil phenolic inserts required, and the maximum bondline temperatures resulting from use of these thicknesses. No calculations were made for this area with Purple Blend, Mod 5 as the heat shield material. The thickness of Purple Blend, Mod 5 required here would be excessive (0.90 inch) due to its lower density. Insulation will be required between the valve unit and supporting structural ring as the TVC units will reach elevated temperatures. The exact amount of insulation required was not calculated. A refined two-dimensional analysis will have to be performed to determine accurately the insulation required. Such analysis should assume that the vehicle is not spinning and that a nozzle is exposed to the maximum heating (windward) for the vehicle angle of attack history. It is possible that the overhanging part of the valve may melt off. For the system function this would present no problem, since the nozzle function is completed prior to the entry. However, if one or two burn off while the others remain in place, a slight unbalance of the vehicle may result.

9.3.4.4 Rocket Plume Effect

Rocket plume heating aerodynamic analysis of the ΔV rocket is presented in Section 3.0 and tabulated in Table LXXII. From this table it may be seen that the only significant heating takes place on the antenna dome and the afterbody inner shoulder.

The antenna dome uses Teflon as the heat shield which exhibits a very low emissivity. As a result, a large part of the energy received from the rocket plume is stored in the antenna with the ensuing high bond and structural temperatures at entry. This is illustrated in Figure 319 which shows the very slow decay of the bond and structure temperature due to the rather small amount of heat being radiated from the antenna. As noted in Table LXVII, the antenna heat shield requirement is 0.217 inch of Teflon. If the rocket plume heating were not present, the heat shield requirement would be only 0.117 inch of Teflon.

The afterbody inner shoulder sees the most severe heating from the rocket plume which in this case is more severe than the entry aerodynamic heating. Hence, for this area the rocket plume heating becomes the controlling factor in the design of the heat shield. This is illustrated in the temperature history in Figure 344 which shows the bond and structure temperature reaching the maximum at about the

TABLE LXXI

REFRASIL PHENOLIC INSERT CHARACTERISTIC RESPONSE

	Nominal Thickness (L_{NOM})	Design Thickness (L_{NOM} x 1.2)
Thickness (inches)	0.55	0.66
Maximum Bondline (°F) Temperature	500	390
Amount Ablated (inches)	0.0	0.0

TABLE LXXII

ROCKET PLUME HEATING RATES

Location	Heating Rate (Btu/ft^2-sec)	Total Heating (Btu/ft^2-sec)
Rocket body	1.0	33.3
Afterbody inner shoulder	8.8	293.
Afterbody outer face	0.0	0.0
Antenna dome	5.9	196.5
Antenna cylinder	0.0	0.0
Secondary heat shield	0.0	0.0
After ring	0.0	0.0
TVC hot-gas hardware	0.8	26.6
Aerodynamic flap	0.3	10.0

Stagnation Enthalpy
1354 Btu/lb

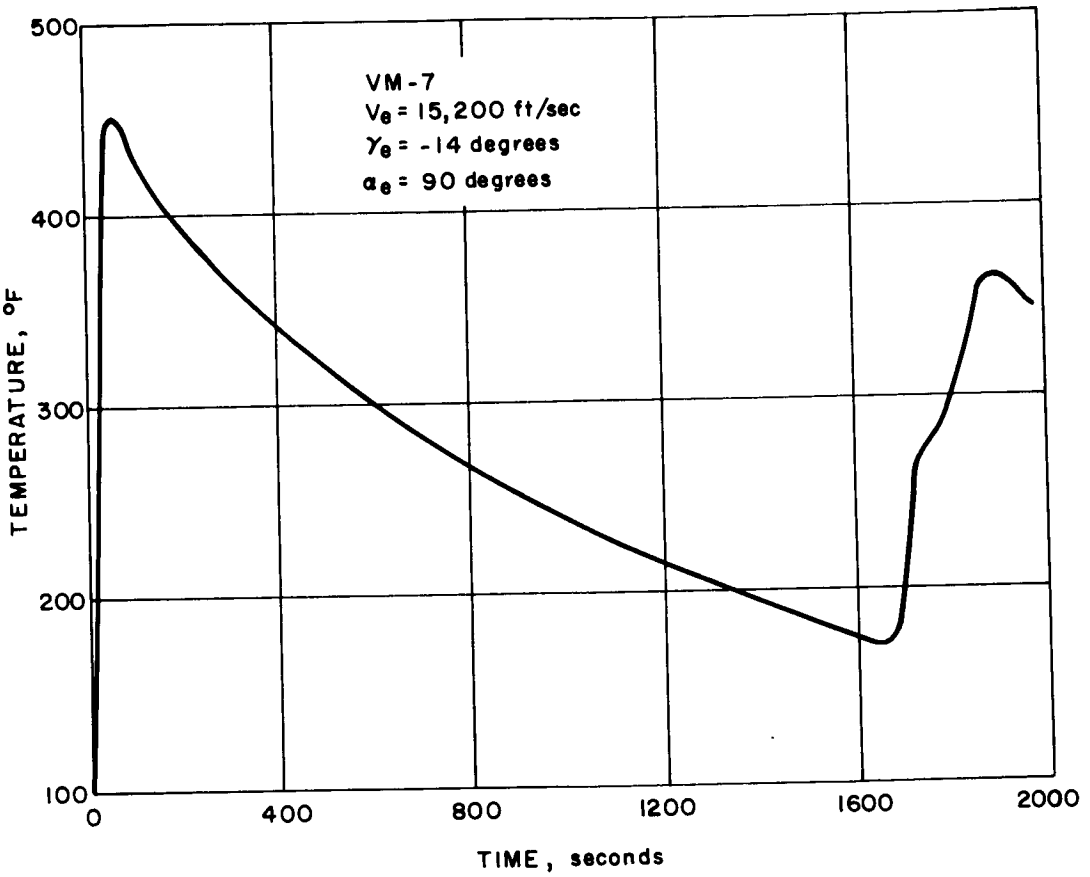

86-2895

Figure 344 TEMPERATURE HISTORY OF THE AFTERBODY INNER SHOULDER -- BOND AND STRUCTURE

time of the ΔV rocket shutoff. The material used as thermal protection of the inner shoulder is Purple Blend, Mod 5 which has a moderate emissivity and results in the decay of bond and structure temperature after the ΔV rocket shutoff and time of entry. The afterbody inner shoulder heat shield requirement including rocket plume effects is 0.384 inch; without the rocket plume effect 0.122 inch of Purple Blend would be required.

10.0 THERMODYNAMICS AND MATERIALS THEORETICAL ANALYSIS, MATERIALS PERFORMANCE, AND FABRICATION*

Several approaches to the design of ablative heat shields are possible. They range from purely experimental evaluation to highly theoretical analysis of all possible environmental and material composition factors. The pitfalls inherent in both extremes are well known and need not be repeated here.

The approach selected for the conceptual design of the probe/lander and probe heat shield represented a compromise between the two extremes. In the entry from approach trajectory studies, somewhat simplified analytical models of the ablation mechanism were used. The parametric nature of the study did not warrant a highly sophisticated approach nor was there available a sufficient body of experimental materials data as required by the more rigorous methods. In the entry from orbit study, more sophisticated theoretical ablation models were used as the results of the material characterization study became available.

Even though more rigorous methods were used, the analysis was not carried to the extremes in the complexity of the ablation model. The approach to the analysis consisted of use of a flexible and sophisticated (but practical) ablation model (Program 1600), independent experimental determination of material properties and ablation characteristics, and subsequent verification of the postulated ablation mechanics by computer simulation of arc tests run under conditions approaching the Mars entry. The effect of the Martian atmosphere, however, was simulated neither experimentally nor on the computer. It was assumed that the surface reactions in the Martian atmosphere would be similar to those in air. The latter assumption will have to be verified.

The experimental program (in conjunction with other Avco Programs) consisted of the determination of various materials thermal properties, ablation characteristics and mechanical properties. Prior to the selection of the materials for the test program, resistance to decontamination, sterilization and low temperature extremes was verified. Vacuum exposure effects will have to be determined at a later date.

The results of the materials testing program were then used in the thermal characterization of the material performance and in the determination of the internal decomposition and surface reaction mechanisms. The results were examined jointly with NASA - LRC and the Purple Blend, Mod 5 surface combustion was adopted for evaluation purposes. Cork silicone displayed similar surface behavior.

*Nomenclature unique to this section is found at the end of Section 10.0.

Finally, the feasibility of fabrication and application of the materials was investigated, and possible methods were suggested. This part of the study is necessary at an early stage of development, as the practicability of a thermal protection design depends heavily on the process variables.

The basic facets of the thermodynamic analysis are described in the following sections: a) Thermal Analytical Model; b) material characterization efforts and c) material fabrication studies. The basic relationships used in the thermal control analysis are also described.

10.1 THERMAL ANALYTICAL MODEL

The analytical model used to describe the thermal behavior of the primary heat shield subjected to planetary entry conditions is necessarily a complex one, since it must involve the solution of a set of nonlinear second-order differential equations with nonlinear boundary conditions. It is a model however, which is readily synthesized by Program 1600, an Avco-developed computer program which is continually up-dated and revised to accommodate formulations for the latest concepts in thermal protection systems. Program 1600 presently provides for a great deal of flexibility of application and is designed to allow for material property variation with time, temperature and space.

The equations presented on the following pages are basically those developed by Munson and Spindler (Reference 81) and embrace the following mechanisms:

1) Transient heat conduction with variable material properties,

2) Internal depolymerization of the resin system with gaseous effusion,

3) Surface combustion reactions, and

4) Surface recession, blowing, radiation, etc.

Consider the cross section through a typical heat shield composite shown schematically in Figure 345. The material affording the thermal protection (P) is backed up by two secondary materials acting as bonding agent (S_1) and structural material (S_2), respectively. The differential equations describing the coupled energy and mass transfer in the primary heat shield are given by the following:

For $S < X < L_1$

$$(\rho C_p)_p \frac{\partial T}{\partial t} = \frac{\partial}{\partial x}\left(k_p \frac{\partial T}{\partial x}\right) + C_g W_g \frac{\partial T}{\partial x} + \dot{\rho} \Delta H_c \qquad (1)$$

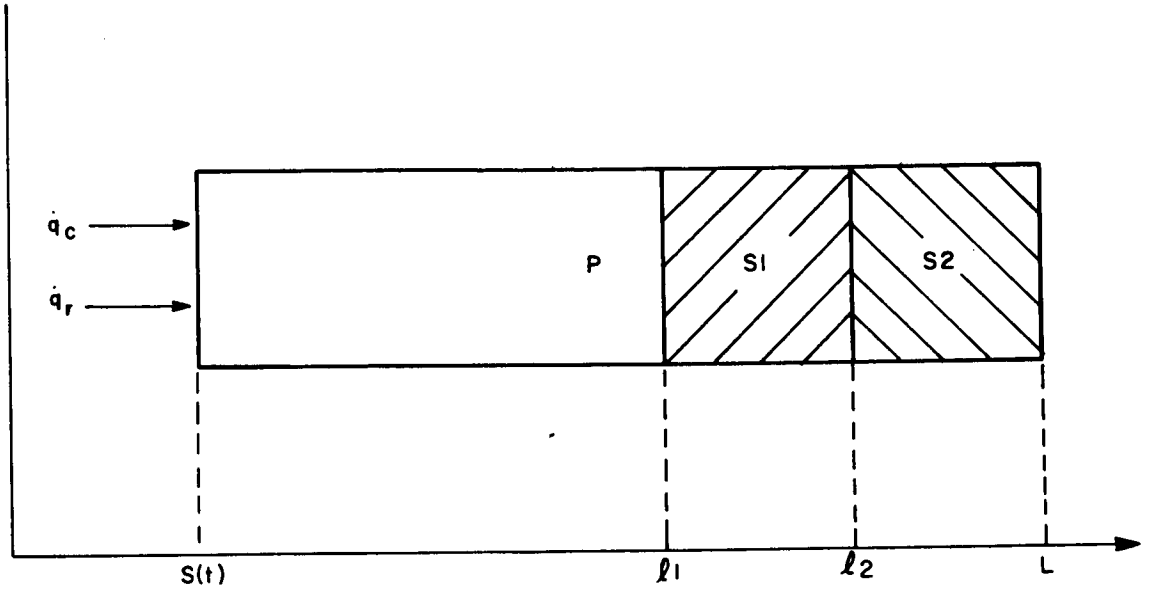

65-4004

Figure 345 GEOMETRY AND COORDINATE SYSTEM FOR TYPICAL HEAT SHIELD-- BOND AND STRUCTURE

where

$$\frac{\partial W_g}{\partial x} = \dot{\rho} \tag{2}$$

and

$$\dot{\rho} = -A\,(\rho - \rho_c)^n \exp(-B/T) \tag{3}$$

$$k = k_v(T) + [k_c(T) - k_v(T)]\,\Gamma_1(\rho) \tag{4}$$

$$Cp = Cp_v(T) + [Cp_c(T) - Cp_v(T)]\,\Gamma_2(\rho) \tag{5}$$

Equation (1) is the energy equation applicable to the charring material and provides for the transpiration of decomposition products through the char, as well as for the energy of decomposition. Equation (2) is a statement of continuity, and Equation (3) is the Arrhenius expression which governs the thermal degradation of the polymeric component of the heat shield. Equations (4) and (5) are explicit functions relating thermal conductivity, k, and specific heat, Cp, to temperature and density.

The two equations below are the energy equations employed for the bond and structural materials, respectively.

For $L_1 < X < L_2$

$$(\rho\, Cp)_{S_1} \frac{\partial T}{\partial t} = \frac{\partial}{\partial x}\left(k_{S_1} \frac{\partial T}{\partial x}\right) \tag{6}$$

and for $L_2 < X < L_3$

$$(\rho\, Cp)_{S_2} \frac{\partial T}{\partial t} = \frac{\partial}{\partial x}\left(k_{S_2} \frac{\partial T}{\partial x}\right) \tag{7}$$

The boundary conditions at the material interfaces and rear surface are:

at $x = L_1$

$$\left(k_{S_1} \frac{\partial T_{S_1}}{\partial x}\right) = \left(k_p \frac{\partial T_p}{\partial x}\right) \tag{8}$$

where

$$W_g(L_1) = 0 \tag{9}$$

at $x = L_2$

$$\left(k_{S_2} \frac{\partial T_{S_2}}{\partial x} \right) = \left(k_{S_1} \frac{\partial T_{S_1}}{\partial x} \right) \tag{10}$$

and at $x = L_3$

$$\left(k_{S_2} \frac{\partial T_{S_2}}{\partial x} \right) = 0 \tag{11}$$

Here Equation (8) is a statement of the equality of the conduction flux across the heat shield-bond interface. Equation (9) is a boundary condition for the continuity equation and indicates the non-porous and non-decomposable nature of the bond. Equation (10) is a statement of the equality of the conduction flux across the bond-structure interface, and Equation (11) is the rear boundary condition, where an adiabatic plane is assumed.

The boundary conditions at the heated surface are defined by the following energy balance.

At $x = s$

$$\frac{\dot{q}_c}{H_s} (H_R - H_w + H') \phi_1 \phi_2 + \dot{q}_R - \epsilon\sigma T_s^4 = \left(- k_p \frac{\partial T}{\partial x} \right) + \rho_s \dot{S} [f_1 hv_1 + f_2 hv_2] \tag{12}$$

where the general expression for surface recession is given by Equation (13).

$$\dot{S} = T_x \left\{ \dot{s}_D \left[1 - \left(\frac{\dot{s}}{\dot{s}_R} \right)^{1/E_7} \right] \right\}^{N_3} + \dot{s}_s - M_Q \left\{ \dot{s}_D \left[1 - \left(\frac{\dot{s}}{\dot{s}_R} \right)^{1/E_7} \right] \right\}^{X_Q} \tag{13}$$

and

$$\dot{s}_R = \left[\frac{A_3}{\rho_s} \right] \left[(P_e)(We) \left(\frac{U_0}{\dot{U}_1} \right) \right]^{E_8} \exp(-B_3/T_s) \tag{14}$$

$$\dot{s}_D = \left(\frac{U_3}{U_2} \right) \frac{(TW)(We)}{(\rho_s)(RT_o)} \left(\frac{\dot{q}_c}{H_3} \right) \phi_1 \tag{15}$$

$$\dot{s}_s = \beta_5 (T_s)^{\beta_6} \exp(-\beta_7/T_s) \tag{16}$$

Equations (14) through (16) describe the behavior of the surface recession as dictated by three distinct types of surface reaction. At low temperatures, the chemical reaction rate which dominates the oxidation process may be described by the Arrhenius expression of Equation (14) involving both temperature and pressure. As the surface temperature increases, the ablation mechanism becomes diffusion controlled and may then be described by Equation (15). At very high temperatures, the sublimation rate of carbon becomes significant, such that only a fraction of the surface material combines with oxygen. The equation governing the sublimation process is written as Equation (16).

The combustion enthalpy H', is given by:

$$H' = \frac{(We)(H_c)}{RT_o} \left(\frac{U_4}{U_5}\right)\left(\frac{U_3}{U_2}\right)\left\{\left(1 - \frac{\dot{s}}{\dot{s}_R}\right)^{1/E_7}\right\} \tag{17}$$

In Equation (12), the quantity ϕ_1 represents the effect of mass injection on the heat transfer coefficient and is given by Equation (18).

$$\phi_1 = \frac{h\,(\text{with mass transfer})}{h\,(\text{no mass transfer})} = \exp\left[-F\,(1 + \alpha F)\right] \tag{18}$$

where

$$F = (\eta_s\, \rho_s\, \dot{s} + Wg\, \eta g)\, \frac{H_s}{\dot{q}_c} \tag{19}$$

The quantity ϕ_2 is a correction for the effects of wall temperature on the convective heat transfer coefficient such that:

$$\phi_2 = \left(\frac{H^*}{H_s^*}\right)^{E_2} \tag{20}$$

where

$$H^* = (1/1-r)\,(0.50-0.22r)\,(H_r/H_s - r)\,H_s + 0.22rH_s + 0.50\,H_w \tag{21}$$

and

$$H_s^* = (1/1-r)\,(0.50-0.22r)\,(H_r/H_s - r)\,H_s + 0.22r\,H_s + 0.50\,H_{wr} \tag{22}$$

The quantity H_{wr} represents the wall enthalpy associated with the conditions for which the original cold-wall heating was evaluated. The quantity r is the recovery factor and E_2 assumes values of 0.185 and 0.502 for laminar and turbulent flow, respectively.

The wall enthalpy H_w, is evaluated for an equilibrium mixture of 0, 0_2, and N_2 at temperature T_s and pressure P_e.

In the studies of the probe/lander, entry from approach trajectory simplified ablation mechanisms were assumed (e. g. constant ablation temperature) and therefore not all of the 1600 program capability was utilized. The method used in that phase of the study was referred to in Reference 80 as Program 1600. 1. Early results were obtained by use of methods described in Reference 80, but they were not reported due to redirection of the program.

10.2 MATERIALS CHARACTERIZATION

The characterization of materials for use as a primary entry thermal protection system involves several types of effort. The initial work consists of a screening of likely candidate materials for the purpose of restricting detailed consideration to a tractable number of "most likely" candidates. This screening process involves limited thermal and mechanical property testing, certain types of ablation testing and, in the present case, an evaluation of the possible effects of vacuum exposure and sterilization procedures on the performance of the material. A second step in the process involves a more detailed selection of properties for the more likely candidates. This selection must be accomplished within the framework of the analytical tools available for evaluating the thermal protection system response during entry. A third phase of the characterization process is associated with an examination of fabrication techniques as dictated by large-scale parts as opposed to the laboratory samples prepared during the initial screening phases. In this section, the work performed in these three phases of the characterization process is discussed.

10.2.1 Material Formulation Studies, Mechanical Properties, and Sterilization Effects on Charring Ablators*

Prior to the start of the contract, various material tests were performed to select a few candidate materials. On the basis of these tests, together with fabrication considerations, three charring ablators were selected for further study. The ablators were Armstrong 2755 cork phenolic, modified NASA Purple Blend (a silicone), and Avcoat 5026-99 (a low-density modification of the Apollo material). Subsequently, a number of different experimental cork and Purple Blend formulations have been prepared with the goal of optimizing the Purple Blend formulation in terms of filler and silicone binder type and concentration and to improve the char-layer stability, the mechanical properties, and the dry-heat sterilization effects of cork.

The approach taken to select the most promising materials involved critical screening of candidate materials followed by a more detailed evaluation of selected candidates to support analytical and design efforts. The screening phase included processing characteristics, mechanical properties, thermal conductivity, specific heat, and ablative tests in that order. The number of candidates was narrowed down during this sequence of tests.

The program involved a systematic formulation study of "Purple Blend" and cork-type materials in conjunction with a processing, mechanical, thermal, and ablative screening program. The primary objectives were:

*The majority of the data reported within this section of the report is the result of an independent research program conducted by the Avco Corporation.

1. Optimize the "Purple Blend" formulation in terms of filler and silicone binder types and concentration

2. Improve the char-layer stability and dry heat sterilization behavior of cork

3. Tabulate existing property data of Avcoat 5026-99 and perform required tests for material characterization.

10.2.1.1 Cork Formulations

Room-temperature tensile tests on 10 experimental cork formulations containing various ratios of 1/4-inch chopped glass strand with silicone binders and Armstrong 2755 cork are summarized in Table LXXIII. The results indicate silicone can be substituted for phenolics as binders for cork and produce composites with equivalent or superior mechanical properties. The improved thermal stability of the silicone binders was demonstrated by subjecting the experimental compounds and Armstrong 2755 cork (phenolic binder) to a postcure that had a maximum temperature of 350°F. The Armstrong cork lost plasticizer and moisture (14.4 percent by weight) and became brittle, while the silicone cork lost only moisture contained in the cork (4 to 5 percent) and remained flexible.

The major problem problem with fiber-reinforced cork was obtaining the proper orientation and distribution of glass strands to stabilize the char layer. This problem appears to have been overcome by process changes and the substitution of glass fibers for glass strands. Cork-silicone formulation 893-23, containing 72-percent ground cork, 25-percent silicone binder, and 3-percent glass fibers was evaluated in the OVERS arc facility, and a substantial improvement in char stability was observed. The preliminary mechanical and thermal properties of this formulation are summarized in Table LXXIV.

10.2.1.2 Purple Blend Formulations

During the preliminary screening of "Purple Blend," the following formulation variations were evaluated:

1. Increased concentrations of quartz fibers, phenolic microballoons, and glass microballoons

2. Silica microballoons substituted for glass microballoons

3. Glass fibers replacing quartz fibers

TABLE LXXIII

ROOM TEMPERATURE MECHANICAL PROPERTIES OF EXPERIMENTAL CORK-SILICONE FORMULATIONS

Formulation No.	Silicone Percent Binder	Percent Filler (1/4-Inch Glass Strand)	Specific Gravity	Tensile Strength psi at 75°F	Total Strain to Failure at 75°F	Elastic Modulus psi x 10^{-6} at 75°
851-81	16	20	.51	209	3.9	.023
851-82	17	15	.54	205	4.0	.019
851-83	16	25	.53	272	2.0	.027
851-88	19	5	.58	279	6.0	.021
851-90	25	20	.61	299	1.0	.048
851-91	25	20	.58	287	2.8	.027
851-93	25	None	.50	243	12.0	.008
851-95	25	None	.55	331	12.0	.007
851-96	25	None	.54	263	10.0	.008
851-97	25	None	.60	142	4.9	.006
Armstrong 2755 Cork			.49	337	12.0	.013
Dry Heat Sterilized Armstrong 2755 Cork*			.42	304	2.8	.019

*Exposed to 3 cycles per JPL-XS-30275-TST-A

NOTE: Armstrong 2755 Cork lost 14.7% weight when dry heat sterilized and 14.4% weight when exposed to postcure conditions utilized to process experimental cork formulation.

TABLE LXXIV

PRELIMINARY PROPERTIES OF GLASS-REINFORCED
CORK SILICONE 893-23

Specific Gravity	.48
Hardness, Shore A	75

Tensile Strength (psi)*	Parallel to Glass Fibers	Perpendicular to Glass Fibers
-100°F	540	170
75°F	170	85
300°F	96	40
Total Strain to Failure (%)*		
-100°F	3	3
75°F	9	16
300°F	4	5
Elastic Modulus (psi x 10^{-6})*		
-100°F	.03	.009
75°F	.007	.0020
300°F	.006	.0012
Coefficient of Thermal Expansion (in/in/°F x 10^{-6})		
-100 to 0°F		60.5
-100 to 20°F	23.2	
0 to 130°F		93.2
20 to 130°F	12.4	
130 to 200°F		33.3
130 to 270°F	1.7	
200 to 300°F		86.5
220 to 300°F	11.0	

Thermal Conductivity (Btu/hr.-ft °F) Parallel to Glass Fibers

179°F	.053
210°F	.054
318°F	.050
395°F	.050

Specific Heat (Btu/lb. °F)

RT to 437°F	.471

*Test strain rate--0.05 in/in/min

TABLE LXXIV (Concl'd)

PRELIMINARY PROPERTIES OF GLASS REINFORCED
CORK SILICONE 893-23

Thermogravimetric Analysis (Helium Atmosphere)

Temperature (°C)	Wt. Loss (%)	Wt. Loss (%)	Wt. Loss (%)
100	1.5	1.5	1.5
200	2.5	2.2	2.0
300	14.0	12.2	10.1
400	37.0	30.6	27.1
500	61.8	60.5	57.5
600	70.5	69.0	67.5
700	72.5	72.4	72.0
800	74.0	73.9	73.0
Heating Rate (°C/Min)	5.0	9.5	21.0

TABLE LXXV

PROPERTIES OF LOW DENSITY SILICONE FORMULATIONS

(Tensile Strain Rate - 0.05 in/in/min)

Formulation No.	NASA Formulation (Purple Blend)	Mod 5	Mod 7	Mod 8
Composition	75% Sylgard 182 15% Eccospheres SI 10% Phenolic M.B.	66% Sylgard 182 16% Phenolic M.B. 10% Eccospheres R 7% 1/4" Quartz Fibers 1% CAB-O-SIL	Mod 5 Fillers with RTV-655	Mod 5 Fillers with RTV-615
Specific Gravity	.60	.68	.68	.68
Tensile Strength (psi)				
-200°F	———	1705	1480	2055
-100°F	275	544	432	1047
75°F	72	167	170	279
300°F	109	131	132	235
Total Strain to Failure (%)				
-200°F	———	3.4	4.2	3.2
-100°F	6.5	8.6	7.0	3.7
75°F	10	5.0	5.8	6.1
300°F	15	4.5	3.1	5.4
Elastic Modulus (psi x 10^{-6})				
-200°F	———	.14	.092	.16
-100°F	.023	.032	.018	.084
75°F	.0021	.0055	.0068	.010
300°F	.0034	.0040	.0064	.0071
Thermal Strain (in/in/°F)	82.5/-100 to 20°F 53.5/-20 to 260°F 32.5/260 to 400°F	47.5/-100 to 0°F 55.0/0 to 240°F 50.0/240 to 300°F	50.0/-100 to 20°F 58.2/20 to 220°F 54.4/220 to 300°F	82.5/-100 to -20°F 60.0/-20°F to 120°F 69.3/120°F to 200°F 62.5/200 to 300°F

TABLE LXXV (Cont'd)

PROPERTIES OF LOW DENSITY SILICONE FORMULATIONS

(Tensile Strain Rate - 0.05 in/in/min)

Formulation	Mod 10	Mod 11	Mod 12	Mod 13
Composition	Mod 5 with 50% Increase in Quartz Fibers	Mod 5 with 25% increase in Phenolic M.B.	Mod 5 with 50% Increase in Eccospheres R	Mod 5 with Eccospheres SI Replacing Eccospheres R
Specific Gravity	.71	.69	.70	.68
Tensile Strength (psi)				
-200oF	----	----	----	----
-100°F	519	545	944	813
75°F	242	266	306	335
300°F	174	195	239	221
Total Strain to Failure (%)				
-200°F	----	----	----	----
-100°F	11.1	8.9	4.9	5.3
75°F	12.3	6.2	7.8	7.1
300°F	6.4	4.2	5.1	4.6
Elastic Modulus (psi x 10^{-6})				
-200°F	----	----	----	----
-100°F	.029	.028	.083	.073
75°F	.0035	.0091	.011	.013
300°F	.0026	.0056	.0056	.0051
Thermal Strain (in/in/°F)	49.5/-100 to 20°F 43.5/20 to 120°F 47.5/120 to 240°F 41.7/240 to 300°F	47.2/-100 to 100°F 52.0/100 to 300°F	60.0/-100 to -20°F 52.5/-20 to 120°F 57.5/120 to 300°F	

TABLE LXXV (Concl'd)

PROPERTIES OF LOW DENSITY SILICONE FORMULATIONS
(Tensile Strain Rate - 0.05 in/in/min)

Formulation No.	Mod 14	Mod 20
Composition	Mod 5 with 1/4" Glass Fibers Replacing Quartz Fibers	Mod 5 with 16/40 Mesh Cork Replacing Phenolic M. B.
Specific Gravity	.73	.68
Tensile Strength (psi)		
-200°F	___	___
-100°F	955	569
75°F	227	219
300°F	229	136
Total Strain to Failure (%)		
-200°F	___	___
-100°F	3.8	9.0
75°F	3.8	26.3
300°F	1.9	15.0
Elastic Modulus (psi x 10^{-6})		
-200°F	___	___
-100°F	.080	.036
75°F	.010	.0032
300°F	.014	.0032
Thermal Strain (in/in/°F)	52.8/-100 to 120°F 49.7/120 to 300°F _____ _____	85.0/-100 to -40°F 73.0/-40 to 80°F 77.0/80 to 220°F 61.2/220 to 300°F

4. Granulated cork substituted for phenolic microballoons

5. RTV-615 and RTV-655 substituted for Sylgard 182; the phenyl group ratio of these resins are 0, 12, and 2.5, respectively based on infrared analysis.

Ten candidate formulations, as described in Table LXXV were processed and tensile properties obtained at -100, 75, and 300°F. Additional tensile tests were performed at 200°F on Mod 5 and the formulations containing RTV-615 and RTV-655 to substantiate the report that increased phenyl group substitution on the silicone polymer would result in a more flexible material at low temperature.

Four additional candidates--Mods 7, 10, 13, and 20--were selected for ablative testing in the Model 500 plasma arc. The test results indicate there is no significant difference in the thermochemical heat of ablation of these four candidates and Mod 5. A weak char zone in the char layer was observed in all Purple Blend modifications tested. This problem was overcome by molding the materials onto a fiberglass sheet containing fiberglass loops as illustrated in Figure 346.

This process was conceived and is currently being used in the abrasive grinding wheel industry (patented by Bay State Adhesives, Division of Avco Corporation, U. S. Patent 2682735). It consists of a loop-pile construction on a backing material to anchor and reinforce a molded plastic. Arc samples were constructed by molding Purple Blend Mod 5 over a thin fiberglass backing material containing fiberglass loops rigidized with phenolic resin. The char layer progressed completely back to the fiberglass base and remained anchored by the fiberglass loops.

Purple Blend Mod 5 has been subjected to three cycles of dry-heat sterilization prior to thermal, mechanical and vacuum-weight loss tests. The results of the thermal and mechanical tests are summarized in Table LXXVI.

Vacuum-weight loss tests were performed on samples that were dry heat sterilized and stored in a desiccator to prevent absorption of gases or moisture. The tests were performed at 72 $\pm$ 3°F and a pressure of 5×10^{-6} torr in a laboratory chamber. The test results show that Mod 5 had a slight weight loss (0.078 percent) and a negligible dimensional change. Additional tests should be performed to determine the effects of vacuum and vacuum-temperature exposure on the mechanical, thermal and ablation properties of the material.

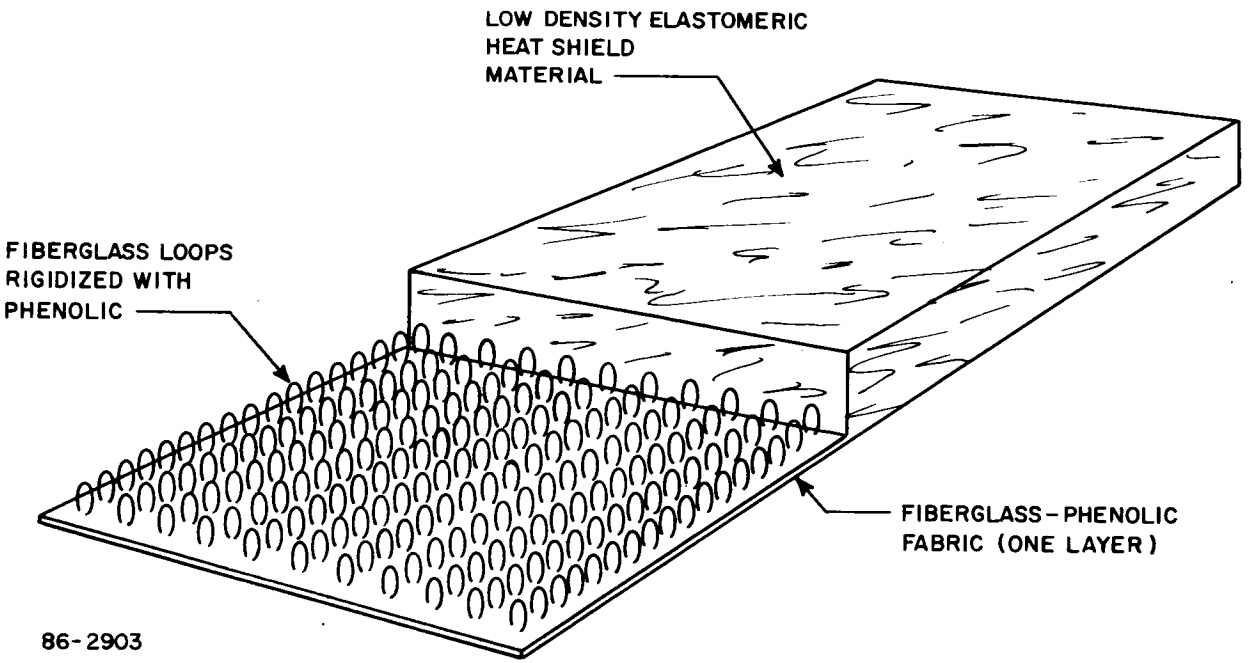

Figure 346 LOOP REINFORCEMENT CONCEPT

TABLE LXXVI

PROPERTIES OF PURPLE BLEND MOD 5
(Dry Heat Sterilized)

Specific Gravity	.67
Hardness, Shore A	86
Tensile Strength (psi)*	
-100°F	868
75°F	330
300°F	290
Total Strain to Failure (%)*	
-100°F	5.4
75°F	8.8
300°F	4.8
Elastic Modulus (psi x 10^{-6})*	
-100°F	.059
75°F	.0099
300°F	.0087
Coefficient of Thermal Expansion (in/in/°F x 10^{-6})	
-100 to 40°F	54.3
40 to 300°F	43.5
Thermal Conductivity (Btu/hr-ft. °F)	
-178°F	.045
86°F	.065
145°F	.075
295°F	.072
Specific Heat (Btu/lb. °F)	
113 to 475°F	.341

*Test Strain Rate - 0.05 in./in./min.

TABLE LXXVI (Concl'd)

PROPERTIES OF PURPLE BLEND MOD 5
(Dry Heat Sterilized)

Thermogravimetric Analysis (Argon Atmosphere)

Temperature (°C)	Wt. Loss (%)	Wt. Loss (%)	Wt. Loss (%)
100	0.0	0.0	0.0
200	0.0	0.5	0.5
300	1.5	3.1	3.2
400	11.5	10.0	7.9
500	54.5	53.4	49.5
600	59.0	58.6	58.3
700	60.5	59.7	59.4
800	61.2	59.9	59.8
Heating Rate (°C/Min)	5.5	9.8	21.0

10.2.1.3 Avcoat 5026-99

The available information on Avcoat 5026-99 was collected and tabulated in Table LXXVII.

10.2.2 Ablative Testing

Arc tests were conducted on several cork and modified Purple Blend formulations, as well as 5026-99 to compare the ablation performance of these materials. These tests were conducted in an air mixture in two different arc facilities -- the OVERS and Model 500.

The nominal heating conditions in the bulk of the OVERS tests were a heat flux of 100 Btu/ft^2-sec and a stagnation enthalpy of 880 Btu/lb chosen as being representative of the proposed mission. Two additional tests at heating rates of 30 and 200 Btu/ft^2-sec were run on the Purple Blend Mod 5. The aerodynamic shear levels in these tests were estimated as less than 1.0 lb/ft^2. The specimen thickness in the OVERS for material comparison purposes was 0.125 inch, which is representative of projected heat shield thicknesses for the Mars entry application. Other specimen thicknesses were employed in each of the above classes of materials to investigate the effect of this parameter. All of these specimens were instrumented at the backface with a thermocouple in a stainless steel disk. The tests were terminated when the backface thermocouple registered 600°F. Results of these tests are given in Table LXXVIII.

The Model 500 tests were run to examine material performance under higher shear levels. The test conditions were a heating rate of 1400 Btu/ft^2-sec and a stagnation enthalpy of 8300 Btu/lb. An aerodynamic shear level of approximately 10 lb/ft^2 was achieved. Model 500 test results are given in Tables LXXIX and LXXX.

The results of the Purple Blend tests in both arcs indicate that most of the formulations exhibited equivalent performance. Purple Blend Mod 13, a material containing silica microballoons in place of glass microballoons, did give a somewhat higher heat of ablation in the OVERS tests than other materials of equivalent thickness. However, since the Purple Blend Mod 5 has been more thoroughly characterized in this and other tests, it will remain as the prime Pruple Blend candidate.

Ablative results for experimental cork materials as compared to Armstrong 2755 cork show varying degrees of performance. Initially, OVERS tests on three experimental cork materials with silicone binders, 893-3, 893-4, 893-5 indicated slightly inferior performance to Armstrong 2755 cork. However, all of these materials, including those containing glass fibers, spalled during test. Under the higher shear conditions of the Model 500

TABLE LXXVII

PROPERTIES OF AVCOAT 5026-99

Specific Gravity	.39
Hardness Shore D	27
Tensile Strength* (psi)	
-35°F	1400
75°F	640
350°F	263
Total Strain to Failure* (%)	
-35°F	1.63
75°F	2.92
350°F	.86
Elastic Modulus* (psi x 10^6)	
-35°F	.13
75°F	.04
350°F	.036
Cofficient of Thermal Expansion (in/in/°F x 10^{-6})	
-100 to 50°F	17.1
Thermal Conductivity (Btu/hr. ft. °F)	
A. Virgin Stock	
245°F	.043
340°F	.046
438°F	.046
B. Stock Charred at 1000°F	
300°F	.030
720°F	.032
985°F	.043
Specific Heat (Btu/lb. °F)	
75 to 485°F	.455

*Test Strain Rate of .05 in/in/min.

TABLE LXXVII (Concl'd)

PROPERTIES OF AVCOAT 5026-99

Thermogravimetric Analysis (Helium Atmosphere)

Temperature (°C)	Weight Loss (%)	Weight Loss (%)	Weight Loss (%)
100	1.8	1.6	1.7
200	2.5	2.5	2.4
300	5.0	5.0	4.4
400	15.5	14.0	8.0
500	42.2	41.3	31.5
600	49.0	47.2	46.6
700	51.2	49.2	50.6
800	53.0	50.2	52.2
ISO at 800 for 3/4 hr.	-	52.5	-
Heating Rate °C/min.	5.0	9.6	21.0

TABLE LXXVIII

OVERS ABLATIVE DATA

Material	Impact Pressure (mm Hg)	Enthalpy, (Btu/lb)	Cold Wall Heat Flux (Btu/ft^2-sec)	Test Time (sec)	Length Loss (inches)	Weight Loss (gm)	Total Emittance ($watts/cm^2$)	Emissivity	Surface Temperature (°K)	Insulative Heat of Ablation (Btu/lb)	Specimen Length (inches)
Armstrong 2755 Cork	8.6	8,600	97	49	0.089	5.7	86	---	2,260	13,900	0.25
	9.2	8,900	97	88	0.135	11.5	100	0.79	2,180	15,000	0.125
Avcoat 5026-99	9.0	8,900	97	63	0.130	6.4	92	0.80	2,120	12,000	0.25
	9.3	8,900	98	44	0.101	5.3	110	0.72	2,280	11,200	0.125
Purple Blend Mod 5*	10.6	9,000	103	165	0.166	8.1	86	0.78	2,100	17,400	0.25
	10.6	8,700	96	75	0.080	4.8	74	0.80	2,010	14,500	0.125
	1.8	8,900	31	192	0.125	9.0	20	0.67	1,520	12,000	0.125
	18.6	9,300	204	33	0.102	5.7	112	0.75	2,230	7,600	0.125
Purple Blend Mod 7*	9.2	8,900	96	68	0.127	3.7	66	0.65	2,050	13,300	0.125
Purple Blend Mod 10*	10.3	8,900	88	58	0.072	3.8	73	0.70	2,070	11,700	0.125
Purple Blend Mod 13*	10.3	8,900	96	94	0.123	4.0	74	0.69	2,080	18,200	0.125
Purple Blend Mod 21*	10.2	9,000	94	57	0.089	3.8	72	0.64	2,110	13,900	0.125
Silicone-Cork Mod 20*	10.3	8,900	96	59	0.110	4.8	56	0.39	2,250	12,400	0.125
Experimental Cork 893-3 65% Cork 15% Glass Fibers 20% Silicone	10.8	8,800	100	44	0.092	5.3	92	0.82	2,120	10,400	0.125
Experimental Cork 893-4 70% Cork 7.5% Glass Fibers 22.5% Silicone	10.3	8,900	100	48	0.103	7.4	103	0.80	2,180	12,500	0.125
Experimental Cork 893-5 75% Cork 25% Silicone	10.2	8,900	100	46	0.116	8.4	105	0.82	2,180	11,800	0.125

*Compositions given in table 6.3

TABLE LXXIX

MODEL 500 ARC ABLATIVE DATA FOR PURPLE BLEND TYPE MATERIALS

Material	Enthalpy, (Btu/lb)	Cold Wall Heat Flux, (Btu/ft^2-sec)	Ablation Rate, (inches/sec.)	Material Density (lb/ft^3)	Thermochemical Heat of Ablation (Btu/lb)	Cold Wall Heat of Ablation (Btu/lb)	Radiant Heat Flux (Btu/ft^2-sec)	Surface Temp., (°R)	Total Emittance ($watts/cm^2$)
Purple Blend Mod 5	7,720	1,420	0.0361	44.3	6,560	10,800	206	5,030	0.68
Purple Blend Mod 7	8,250	1,400	0.0322	43.0	7,110	12,100	237	5,160	0.70
Purple Blend Mod 10	8,250	1,400	0.0339	44.1	6,870	11,200	214	5,030	0.70
Purple Blend Mod 13	8,250	1,400	0.0326	44.2	7,050	11,600	218	5,080	0.68
Silicone Cork Mod 20	8,250	1,400	0.0338	43.3	7,120	11,500	199	5,050	0.64

Note: Purple Blend compositions given in table 6.3.

TABLE LXXX

MODEL 500 ARC ABLATIVE DATA
FOR EXPERIMENTAL CORK MATERIALS

Test Conditions: Heat Flux - 1400 Btu/ft^2-sec
Enthalpy - 8300 Btu/lb.

Material	Density (lb/ft^3)	Rate (in/sec)	Mass Loss Rate (lb/ft^2-sec)
Armstrong Cork 2755	25.6	0.0296	0.0632
Experimental Cork 893-3 65% Cork 15% Glass Fibers 20% Silicone	32.2	0.0504	0.139
Experimental Cork 893-4 70% Cork 7.5% Glass Fibers 22.5% Silicone	33.6	0.0562	0.157
Experimental Cork 893-5 75% Cork 25% Silicone	32.5	0.0694	0.188
Experimental Cork 893-22 72% Cork 3% Glass Fibers 25% Phenolic	30.5	0.0250	0.0638
Experimental Cork 893-23 72% Cork 3% Glass Fibers 25% Silicone	28.7	0.0378	0.0905
Experimental Cork 893-24 72% Cork 3% Glass Fibers 25% Epoxy	34.3	0.0223	0.0637

arc, these experimental cork materials performed very poorly (Table LXXX). Poor fiber orientation and distribution appeared to be a major problem especially under higher shear. To correct this shear sensitivity, experimental cork material 893-23 was prepared with fibers oriented normal to the ablative surface. This fiber modification corrected the spallation problem, but the silicone system still exhibited a lower heat of ablation than the Armstrong 2755 material at these high heat fluxes. Two other fiber-reinforced cork materials, 893-22 and 893-24, were tested to compare phenolic, epoxy, and silicone binders. These data, as shown in Table LXXX indicate that phenolic showed the best ablative behavior followed by epoxy and silicone in that order. The 893-23 silicone-bound cork material has been tested in the OVERS arc with no evidence of excessive spallation.

10.2.3 Thermal Characterization

Thermophysical characterization of a heat-shield-material consists of the definition of its thermodynamic properties permitting complete description of the material's behavior under the influence of entry environments. This clearly implies the need for characterization of the heat shield material. The resultant material properties are then utilized with a method of analysis such as program 1600 in order to predict heat shield behavior during the entry phase of flight. Such a procedure necessarily hinges on the following:

a) The necessary computational tools, such as AVCO programs 1600 and 1850 must be available.

b) Ground-test data pertinent to the specific materials must be available. These data generally consist of thermal conductivity, specific heat and thermal gravimetric analysis which yield properties explicitly as well as appropriate arc jet data which yield properties implicitly and explicitly.

Generally the analytical portion of the characterization of a material is divided into two steps. First, determination of properties pertinent to the description of the material behavior beneath the surface which is exposed to the gas stream. This portion includes heat-transfer parameters associated with conduction through the material in various states of deploymerization and at various temperature levels, the determination of the rate constants and energy associated with the degradation process itself and the effects of the transpiring gaseous products. Second, properties pertinent to the description of the interactions of the material with the boundary layer gases must be determined. This includes all surface effects, such as the blowing of both gases generated by surface sublimation and/or reactions and the gaseous products of the internal degradation

process which have effused. It also includes the properties associated with the prediction of what types of surface reactions occur in different environments as well as the respective energies associated with them. It can also include such effects as mechanical material removal when it is concluded from arc-jet data that such phenomena do occur.

10.2.3.1 Internal Properties

In the interest of brevity and clarity not all of the raw data and analysis are reported here. Emphasis is placed upon description of the properties and comparison of the results of theoretically calculated temperatures using these properties with measured temperatures in arc jet experiments. This is really the crucial test, and the quality of the properties basically hinges on this proof.

The basic theory employed in generating the internal properties is given in Reference 81. The equations which are employed are as follows:

Problem Solved for Internal Characterization

Heat conduction

$$\rho C \frac{\partial T}{\partial t} = \frac{\partial}{\partial x}\left(k \frac{\partial T}{\partial x} \right) + C_g \dot{m} \frac{\partial T}{\partial x} + \dot{\rho} \Delta H$$

$$\dot{\rho} = A(\rho - \rho_c)^n \exp(-B/T)$$

Front surface boundary

$$T(0,t) = f(t)$$

Back surface boundary

$$\frac{\partial T}{\partial x} = 0.$$

Explicit functions used in defining conductivity for states between fully charred and virgin

$$K = K_v + (K_c - K_v) RH\phi K$$

$$C = C_v + (C_c - C_v) RH\phi C$$

Symbols

Symbol	Units	Definition
ρ	lb/ft^3	Material density
C	Btu/lb-^oF	Specific heat of material
k	Btu/hr-ft-^oR	Material thermal conductivity
T	^oR	Temperature
C_g	Btu/lb-^oR	Specific heat of gaseous decomposition products
$\dot{m}$	lb/ft^2-sec	Mass rate of flow
$\dot{\rho}$	lb/ft^3-sec	Rate of change of density with time
ΔH	Btu/lb	Heat of decomposition
ρ_c	lb/ft^3	Char density
A		Reaction rate coefficient
n		Order of reaction
B	^oR	Activation temperature
t	seconds	Time
f(t)		Impressed temperature history (driver)
RHϕK RHϕC		Explicit functions for states between virgin and fully charred

The preceding equations are programmed in Avco Computer Program 1850 which is identical to program 1600 except that the particular option used is specialized to handle a time temperature history impressed at the front boundary. The history used as this input function is generally either thermocouples No. 1 or 2 as shown in Figure 347 depending on thermocouple exposure and response. Obviously the temperatures calculated in this manner are then representative of thermocouples at greater depth. Hence, if thermocouple No. 1 is

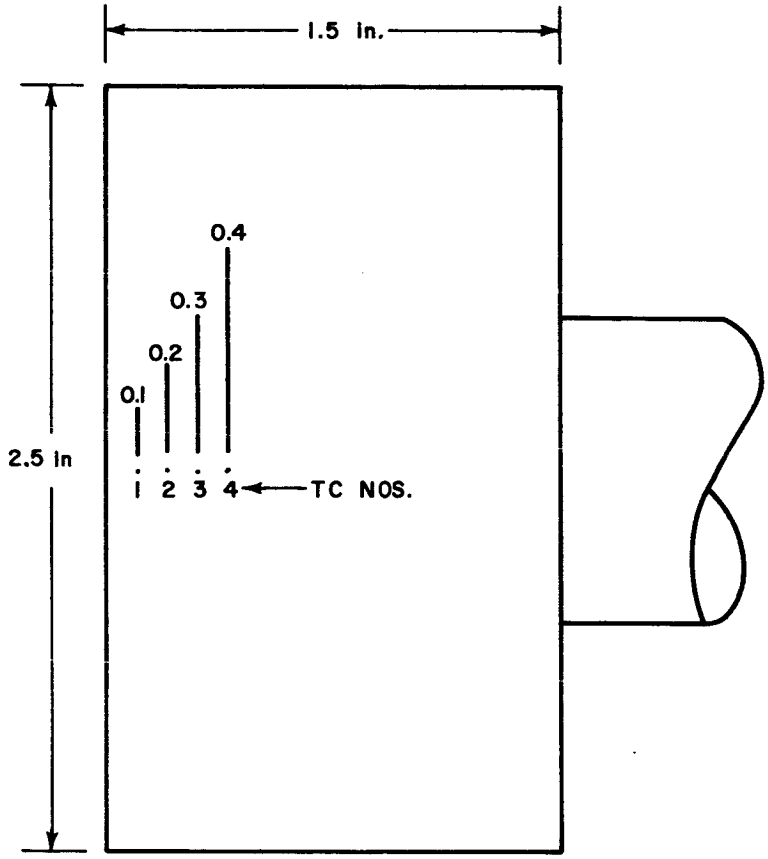

Figure 347 SCHEMATIC OF OVERS TEST SAMPLE

used as the driver, one can calculate meaningful responses for comparison with thermocouples 2, 3, and 4. Accordingly, when thermocouple No. 2 is used to drive the problem, one is able to make predictions for thermocouples 3 and 4. The functions RHϕK and RHϕC are used to define the transition from virgin to charred states. In the theory of Reference 81, assumption of a linear relationship between states is made. In the results presented here, it was found, as is the case with most materials, to deviate from this somewhat in the case of RHϕK.

Bearing in mind all of the preceding discussion, one is in a better position to understand the significance of the results. However, before proceeding with a discussion, it is well to establish a few common points in order to minimize repetition. First, a minimum of two test runs have been always superimposed. These runs generally were made at the same heating rate and stagnation enthalpy. The only environmental change occurred when runs were made with gases other than air, which were also shown as a matter of interest. Unfortunately, test runs which have been superimposed generally do not have the same arc shutoff times. Hence, the driver time temperature history was always taken as the selected thermocouple for the run with the longest run time. Second, in some cases the thermocouples opened thus making the readings invalid. Hence, no data were plotted. Third, the time-temperature history used in the forward boundary (driver) in the theoretical computation is always indicated by the symbol X, the predicted temperatures at each succeeding depth of 0.1 inch are designated by circles, triangles and squares in that order. Fourth, since for all materials two test environmental conditions were employed because this provides greater assurance of the uniqueness of the results, the discussion will generally refer to low-test condition and high-test condition as separate groups. Furthermore, the heating rates and enthalpies, both of which are held constant during a test are typical of values anticipated for the Mars flight capsule.

1. Purple Blend (Mod 5) -- The comparison of experimental and analytical results for Purple Blend Mod 5 is given in Figure 348. The properties used in the analytical prediction are given in Table LXXXI. In all of the experiments there was no length loss associated with purple blend. As a matter of fact, post test measurements showed a slight dimensional increase in center line length of about 0.05 inch. Figure 349 shows a comparison of results for a low heating rate. The data are given by the solid and dashed lines. The analytical predicted response is given by symbols. The two tests superimposed appear to be in good agreement. The arc was shut off at 234 and 372 seconds for tests represented by the solid and dashed lines respectively. The time temperature history used as the driver is that shown by the

TABLE LXXXI

PRELIMINARY (INTERNAL) PROPERTIES

Purple Blend - Mod 5

		Virgin	Fully Charred
ρ	Lb/Ft^3	41.8	16.7
C_p	Btu/Lb-°F	0.34	0.34
k	Btu/Ft-Hr°F	0.075	0.049 (760°R)
			0.080 (1100°R)
			0.180 (2250°R)
			0.240 (4060°R)

Reaction Constants

ΔH	Btu/lb	1000
A	*	3.9×10^5
B	*	2.0×10^4
n	*	1.0

*Units compatible with $\dot{\rho}$ $(lb/ft^3\text{-sec} = A(\rho - \rho_c)^n \exp(-B/T)$

Gaseous Effusion

C_{pg}	0.40	Btu/Lb-°F

Conductivity Explicit Function RHØK:

Density - Lb/Ft^3	RHØK
16.7	1.0
29.8	0.66
36.2	0.44
40.2	0.21
41.8	0.0

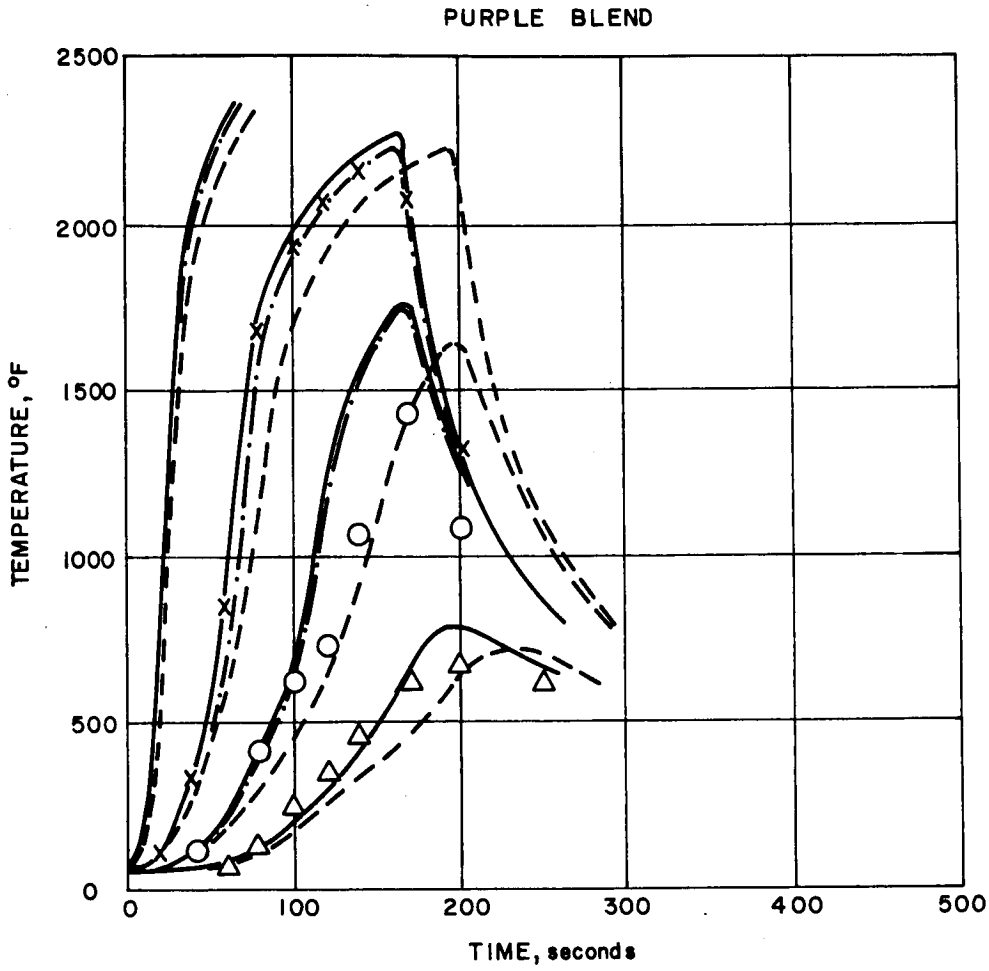

TEST RESULTS: { SOLID LINE ($\dot{q}$ = 98 Btu/ft^2 sec, H = 8400 Btu/lb)
DASH LINE ($\dot{q}$ = 98 Btu/ft^2 sec, H = 8900 Btu/lb)
DASH DOT ($\dot{q}$ = 100 Btu/ft^2 sec, H = 8400 Btu/lb)

COMPUTED DATA: SYMBOLS

[DASH LINE: 40 percent CO_2 60 percent N_2]

86-1351

Figure 348 TEMPERATURE RESPONSE--PURPLE BLEND

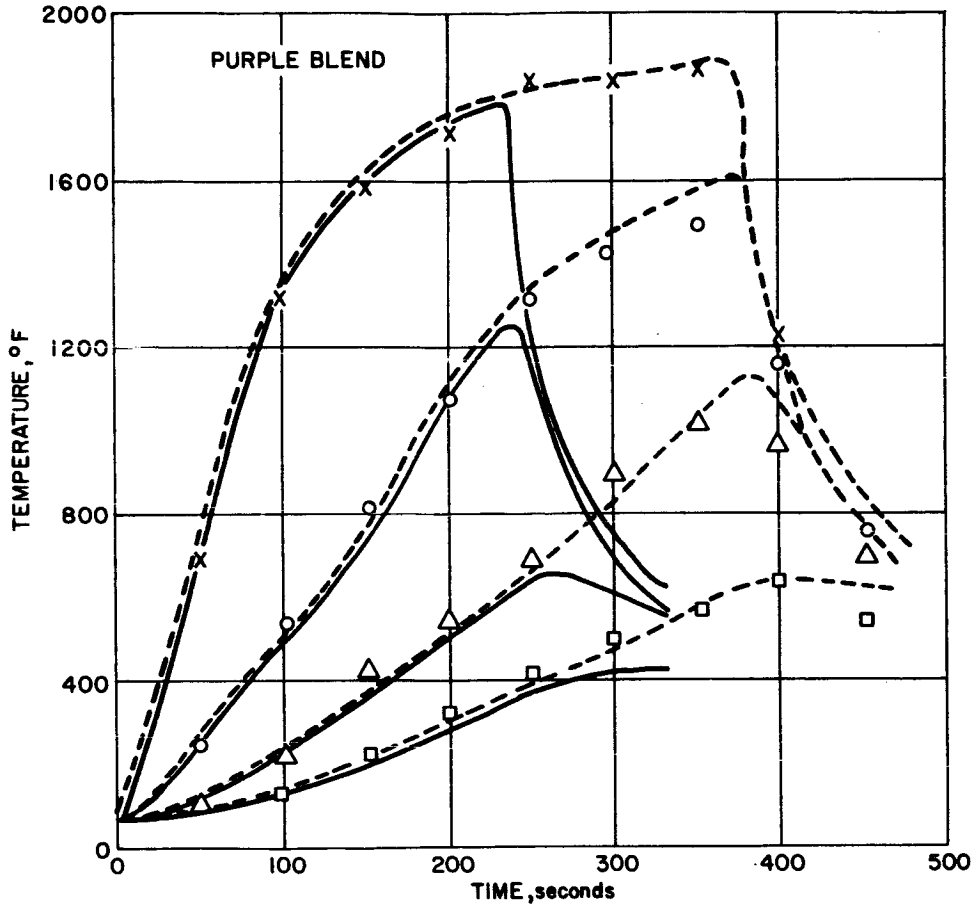

TEST RESULTS { SOLID LINE ($\dot{q}$ = 31 Btu/ft^2-sec, H=8500 Btu/lb)
DASH LINE ($\dot{q}$ = 30 Btu/ft^2-sec, H = 8500 Btu/lb)

COMPUTED DATA: SYMBOLS

86-1349

Figure 349 TEMPERATURE RESPONSE--PURPLE BLEND

symbol X which obviously agrees with thermocouple No. 1. The other symbols (computed points) show the same experimental data corresponding to a high heating rate condition. Three sets of runs have been superimposed. The agreement between the experimental data does not appear as good as was the case previously. The probable reason for this is that small tolerance errors in thermocouple locations would tend to manifest themselves more strongly in this case since higher heating rates induce steeper temperature gradients. Along this same line it is interesting to note that in the case of the sample which was exposed to a gas of 40-percent CO_2 and 60-percent N_2 composition the first and second thermocouples are in essential agreement with samples tested in air. This is a little surprising; however, it should be noted that the third and fourth thermocouples show a more pronounced deviation. The fourth thermocouple for one of the tests in air was lost. The results of the test in CO_2 and N_2 do appear to be anomalous. Hence, further testing would be desirable. The only physical effect of a change in composition should be a change in the net heat transfer rate within the material, and this should affect all of the thermocouples. In Figures 348 and 349 the driving function was thermocouples 2 and 1 respectively. Again, the analytical results exhibit good agreement with experiment. The arc shutoff times were 161, 162, and 193 for the data represented by the dash dot, solid, and dash lines respectively. Again the sample length increase as determined post test was on the order of 0.05 inch.

One can conclude that the material properties given in Table LXXXI produce temperatures which faithfully reproduce arc-jet data for Purple Blend, Mod 5.

2. Cork Silicone -- Figures 350, 351, and 352 present comparisons between experiment and theory for Cork Silicone 893-73. The properties used for the theoretical predictions are given in Table LXXXII. The test data for two tests superimposed in Figure 350 appear to be consistent and exhibit no great anomalies except for thermocouple No. 1 which in one case recorded an unusual jump that was also reflected in thermocouple No. 2. This appears to be a result of instrumentation difficulties. Arc shutoff times of 569 and 615 seconds correspond to the tests represented by solid lines and dashed lines respectively. The thermocouple history used as the driver was No. 1 for the test data indicated by the dashed line. The predicted temperature histories corresponding to the other thermocouple locations show faithful agreement with the test data. The axial length loss determined post test was 0.05 inch. Figures 351 and 352 illustrate identical test data. The agreement between two test runs in air is not as good as was the case at the low heating rate. The probable cause is again due to greater sensitivity of thermocouple-location error because of steeper

TABLE LXXXII

PRELIMINARY (INTERNAL) PROPERTIES

Cork Silicone 893073

		Virgin	Fully Charred
ρ	Lb/Ft^3	30.0	8.1
C_p	Btu/Lb - ^oF	0.47	0.47
k	Btu/Ft-Hr-^oF	0.52	0.04 (750^oR) 0.05 (1150^oR) 0.14 (1750^oR) 0.16 (2250^oR) 0.18 (4060^oR)

Reaction Constants

ΔH	Btu/Lb	1000
A	+	2.9×10^5
B	+	2.0×10^4
n	+	1.0

+units compatible with $\dot{\rho}$ $(lb/Ft^3\text{-sec}) = A(\rho - \rho_c)^n \exp(-B/T)$

Gaseous Effusion

C_{p_g}	0.40	Btu/Lb-^oF

Conductivity Explicit Function RHØK:

Density - Lb/Ft^3	RHØK
8.1	1.0
17.5	0.8
23.5	0.6
26.8	0.4
29.0	0.2
30.0	0.0

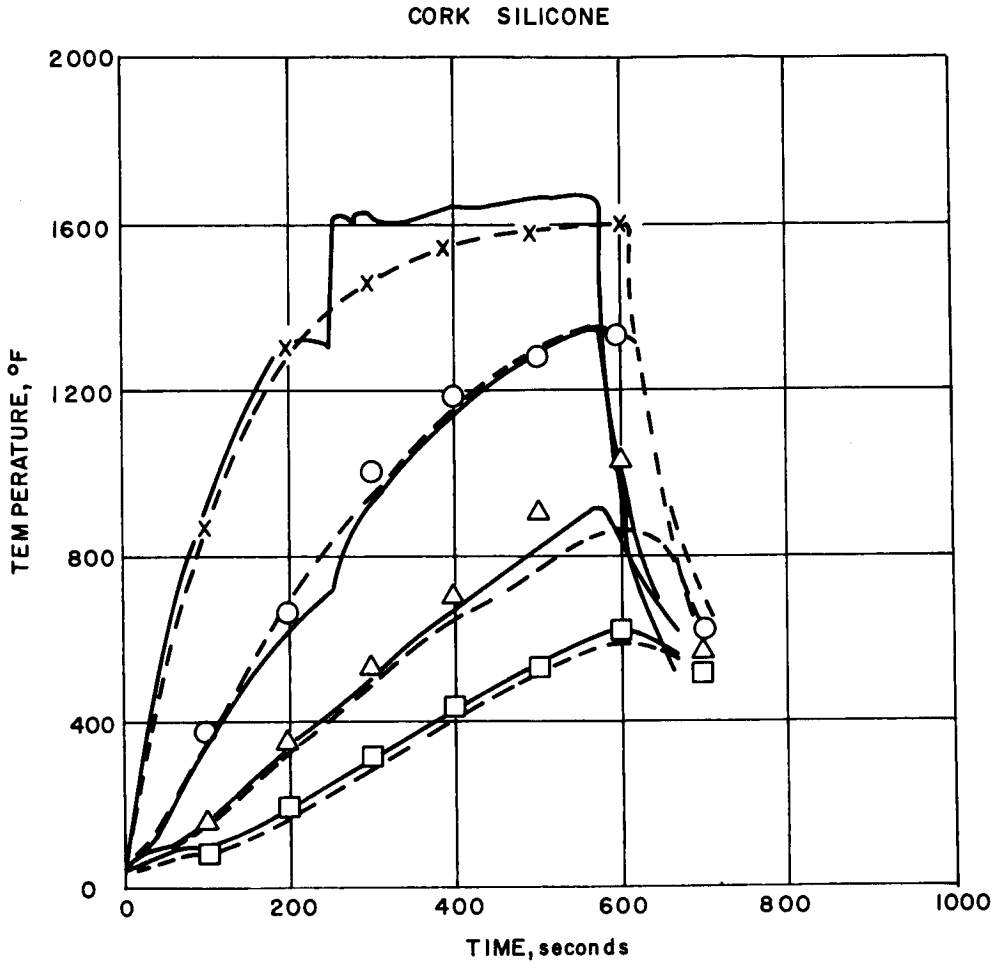

Figure 350 TEMPERATURE RESPONSE--CORK SILICONE

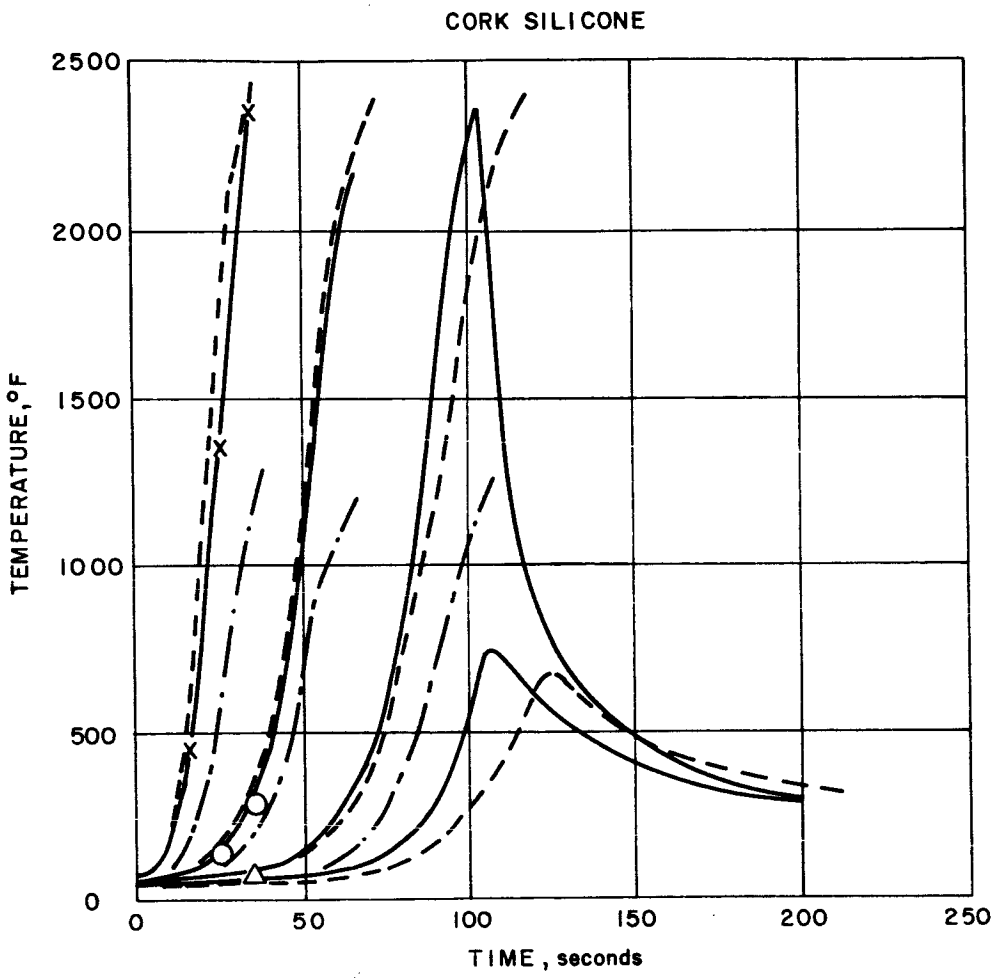

Figure 351 TEMPERATURE RESPONSE--CORK SILICONE

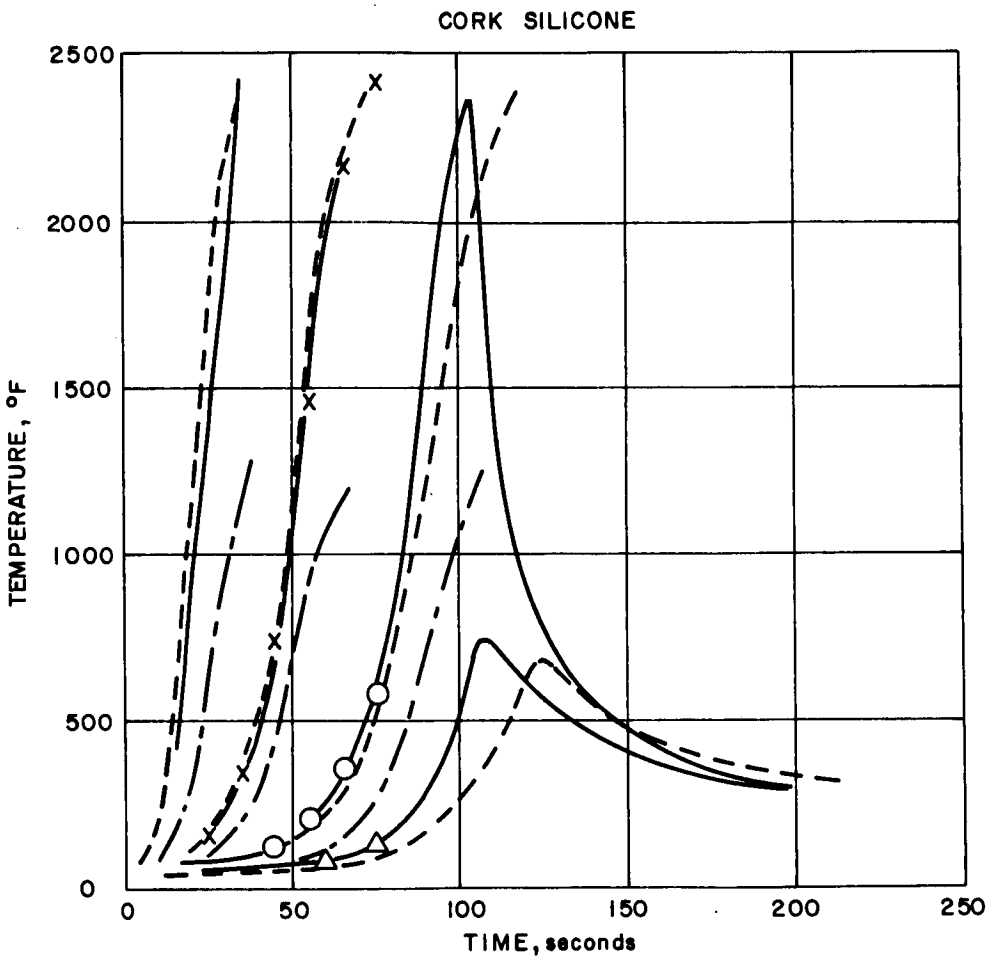

Figure 352 TEMPERATURE RESPONSE--CORK SILICONE

temperature profiles induced by the higher heating rate. Note that in this case the test run in 40-percent CO_2 and 60-percent N_2 exhibits a very definite lagging trend. This is probably due to a reduction in net heating rate propagating through the material as a result of different surface chemistry and blowing efficiency (References 81 and 82). The axial-length loss determined post test was 0.28 inch. In the case of the test run in CO_2 and N_2 gas mixture, thermocouple No. 4 was non-operative. Predicted and measured data show good agreement as given in Figure 351, where as indicated, thermocouple No. 1 was used as the driver. It can be inferred that if thermocouple No. 1 for the CO_2 and N_2 test had been used as a driver the results would exhibit good agreement with theory, as anticipated. Figure 352 illustrates a comparison of test data and theory using thermocouple No. 2 as the driver, as is indicated by the symbol X. One can conclude that temperatures agree well with measured data. Hence, one may conclude that the material properties given in Table LXXXII can be used with a reasonable degree of confidence for cork silicone 893-73.

3. Avcoat 5026-99 -- Figures 353, 354 and 355 illustrate comparisons between test data and analytical predictions for Avcoat 5026-99. The material properties used in the analytical predictions are given in Table LXXXIII. The test data given in Figures 353 and 354 indicate the loss of thermocouple No. 3 in one test and thermocouple No. 4 in the other. The test time for both tests show an arc termination time of 161 seconds. The recorded amount of surface recession for these tests was 0.16 inch. This implies that the first thermocouple became exposed to the air stream during the test. In fact, something unusual happened to thermocouple No. 1 in one of the tests in the vicinity of 90 seconds. This should correspond closely to the proper exposure time and is probably the explanation of its anomalous behavior. The puzzling fact is that the recorded temperatures did not increase markedly. In light of this problem, thermocouple No. 1 was used as a driver only up to 90 seconds. The results so obtained are presented in Figure 353. Theory and experiment seem to correlate quite well. Figure 354 shows a comparison of analysis and test using thermocouple No. 2 as the driver in order to circumvent the problems enumerated with thermocouple No. 1 and to provide comparison at times greater than 90 seconds. Again it should be noted that theory and experiment agree well. Figure 355 shows experimental data for three tests at a higher heating rate. The dash-dot line represents data for a sample in a pure nitrogen stream. Unfortunately this was intended to have been 40-percent CO_2 and 60-percent N2 run, but improper operating procedure led to a pure nitrogen run. Hence, the resultant high enthalpy came about due to a smaller flow rate of gas for the same power setting in the arc. It is interesting to note that at the higher stagnation enthalpy

TABLE LXXXIII

PRELIMINARY (INTERNAL) PROPERTIES

Avcoat 5026-99

		Virgin	Fully Charred
ρ	lb/ft^3	24.3	11.5
C_p	Btu/lb-°F	0.45	0.45
k	Btu/ft-HR-°F	0.046	0.030 (760°R)
			0.042 (1180°R)
			0.085 (1560°R)
			0.165 (1860°R)
			0.230 (2260°R)
			0.280 (4060°R)

Reaction Constants

ΔH	Btu/lb	1000
A	+	3.9×10^5
B	+	2.0×10^4
n	+	1.0

+ units compatible with $\dot{\rho}$ $(lb/ft^3\text{-sec.}) = A\ (\rho - \rho_c)^n \exp(-B/T)$

Gaseous Effusion

C_{pg}	0.40	Btu/lb-°F

Conductivity Explicit Function RHØK

Density - lb/ft^3	RHØK
11.5	1.0
18.3	0.69
21.5	0.49
23.5	0.27
24.3	0.0

5026-99

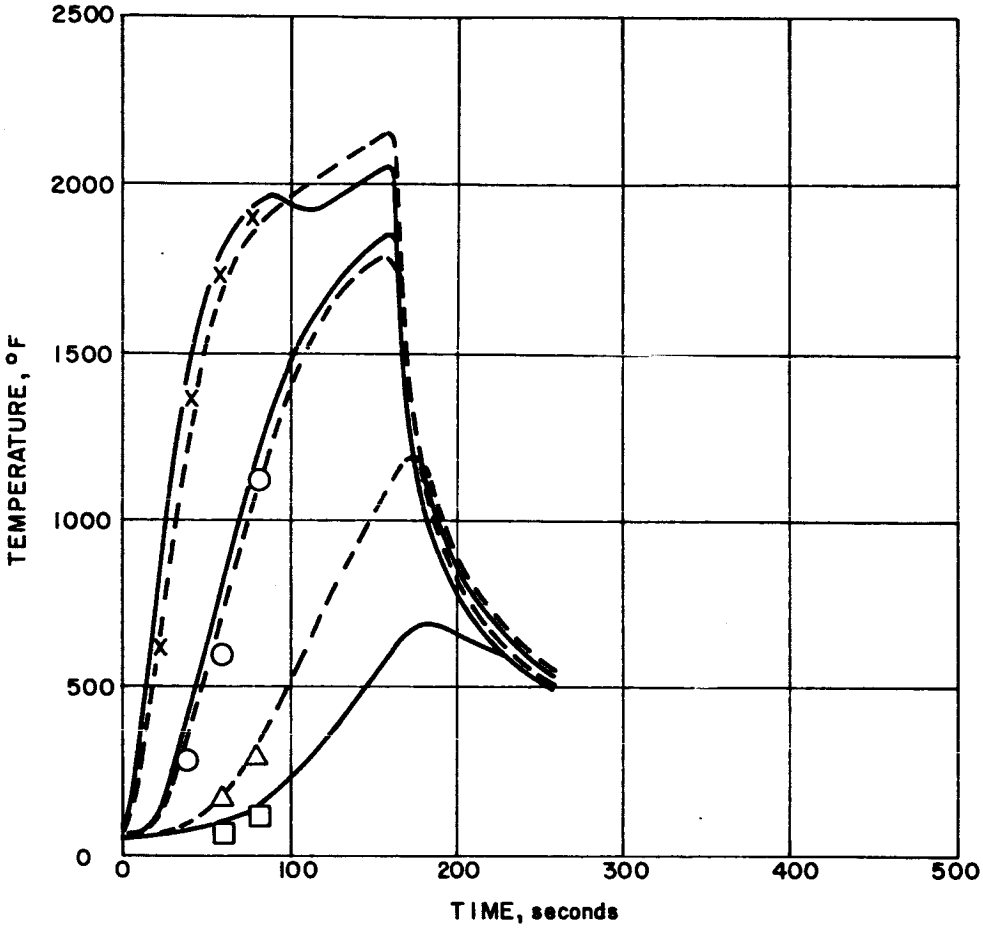

TEST RESULTS: { SOLID LINE ($\dot{q}$ = 28 Btu/ft^2-sec, H=8300 Btu/lb)
DASH LINE ($\dot{q}$ = 30 Btu/ft^2-sec, H=8300 Btu/lb)

COMPUTED DATA: SYMBOLS

86-1355

Figure 353 TEMPERATURE RESPONSE--5026-99

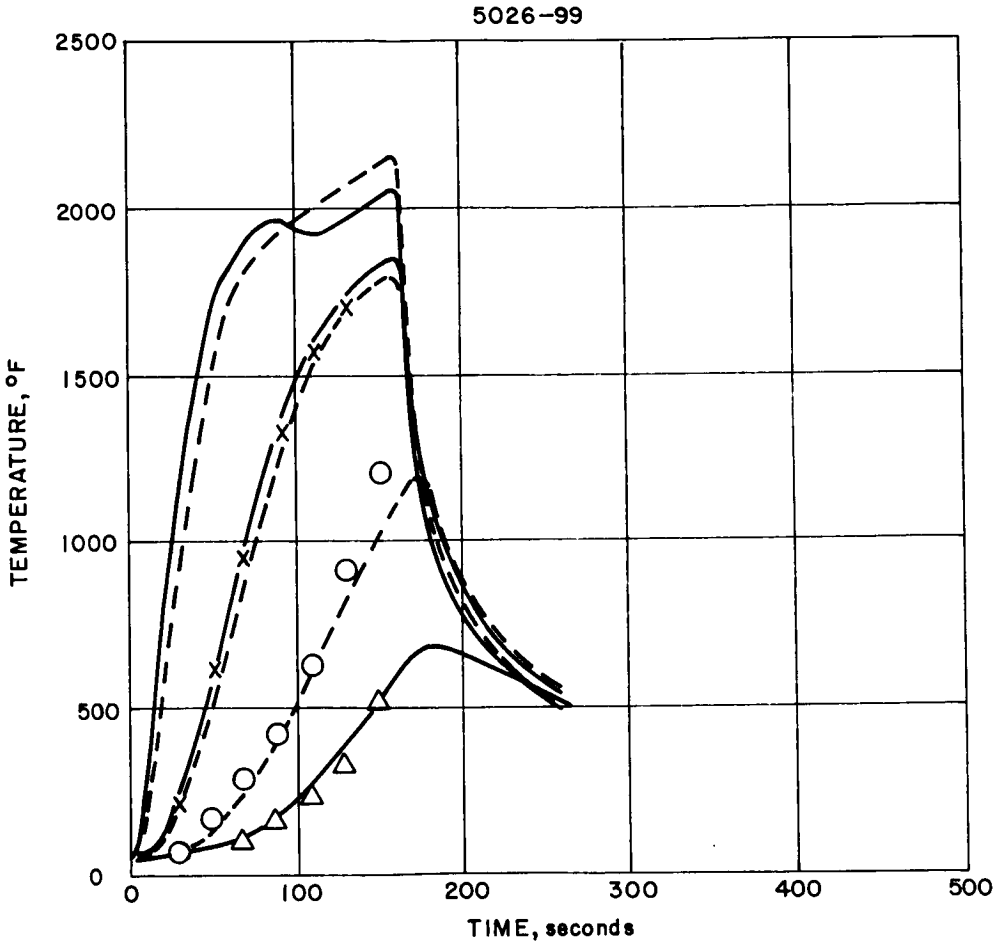

Figure 354 TEMPERATURE RESPONSE--5026-99

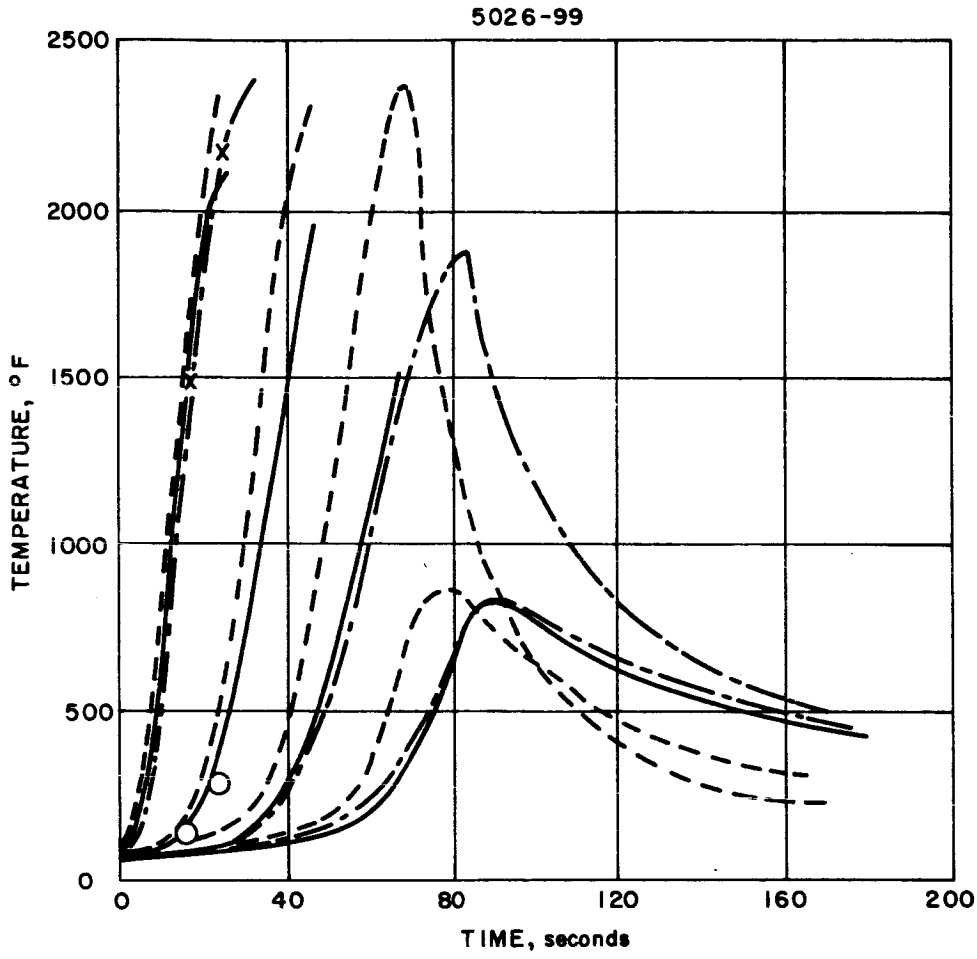

Figure 355 TEMPERATURE RESPONSE--5026-99

the net heat transfer rate to the material should increase as well as the fact that greater energy per unit weight should be consumed by the ablation process. However, unless these factors have completely offset each other, the data appear questionable. The arc run times associated with the solid lines and the dashed line were 80 and 68 seconds, respectively. This compares favorably with a run time of 79 seconds for the run in nitrogen. The amounts of post-test axial recession were 0.18 and 0.20 inch for the solid line and dashed line runs, respectively. The recession associated with the nitrogen run was slightly less or 0.15 inch. Note also that the nitrogen temperature data agree quite well with the run in air represented by the solid line. It appears that more test data are required in order to explain these anomalies. Thermocouple No. 1 was used as a driver and good agreement resulted. From the preceding, one may conclude that the material properties given in Table LXXXIII reproduce test data with a reasonable degree of accuracy for Avcoat 5026-99.

10.2.3.2 Surface Properties

Consistent with the decision to concentrate the effort on Purple Blend Mod 5 as the primary heat shield material, the ablation data were examined to establish values of the parameters which govern the surface ablation process. The mathematical and physical model chosen to represent the processes associated with the surface is basically a combustion controlled model. The primary data source for obtaining ablation properties at Avco is the Model 500 arc-heater test facility. It is believed that the test conditions in this facility are well established and that these conditions are such that steady-state ablation is approached quite closely during the course of a test.

The analysis of ablation test data for the purpose of obtaining values for the several ablation characteristics which describe the performance of the system is a significant problem associated with the thermal design of an entry-vehicle ablative heat shield. The use of sophisticated analytical models for the ablation process in the design activity requires a similar degree of sophistication in the interpretation of the ground-test data for which the design properties are derived. Many of the ground-test data are obtained under conditions which approximate the quasi-steady state insofar as the mass transfer process is concerned.

In the bulk of stagnation-point ablation tests the observational quantities which are reported are a calorimetrically determined heat flux, q_{cal}, a stagnation pressure, P, and a stagnation enthalpy H_o, describing the environmental conditions of the test. The material related quantities which are normally reported are a surface recession rate, $\dot{s}$, and either a surface temperature or the total surface radiation loss, q_r.

In some cases total length loss and test duration are reported in place of surface recession rate and in some cases an external radiant energy flux, F_s, is imposed. Although the environmental parameters of heat flux, enthalpy, and pressure are not strictly independent, they will be treated as such in the present analysis since they are, generally speaking, determined independently.

The steady-state ablative behavior of a char forming material can be described by an energy balance in the form of Equation (1).

$$\frac{q_c}{H_o}(H_o + \gamma Q_2 - H_s)\phi - q_r - \dot{m}\bar{C}_p(T_s - T_{ref}) = \dot{m}Q_1 \qquad (1)$$

In Equation (1) q_c is a "cold-wall" heat flux, ϕ is the ratio of heat transfer with mass addition to that without, $\bar{C}_p$ is an average specific heat of the char and gaseous products at the surface temperature T_s and T_{ref} is a reference surface temperature or "standard ablation temperature" to which the energy terms Q_1 and Q_2 are being corrected. In particular, since no material ablates at a fixed temperature, the term in $\bar{C}_p$ removes this variation from Q_1 thus making Q_1 a "true constant". The quantity Q_1 contains the latent heats of charring and vaporization of the material together with the sensible or $C_p \Delta T$ heats for the system. Q_1 will be a constant if the heat of vaporization is independent of temperature over the range of surface temperatures in the test series and if the "reaction zone" temperature for the char forming reaction is nearly constant in the series.

Equation (1) can be rewritten in the form of Equation (2) which is a linear form suitable for statistical treatment.

$$Y = Q_1 - Q_2 X \ , \qquad (2)$$

where:

$$Y \equiv \frac{q_c}{\dot{m}H_o}(H_o - H_s)\phi - \frac{q_r}{m} - \bar{C}_p(T_s - T_{ref}) \ ,$$

$$X \equiv \frac{\gamma q_c}{\dot{m}H_o}\phi \ .$$

The quantity ϕ, which is the effect of mass addition on heat transfer, has been written in numerous ways in the literature. The form most frequently employed at Avco is given by Equation (3) and is a result of a survey of existing analytical and experimental work on this subject.

$$\phi = \exp\{-f(1+\alpha f)\} \tag{3}$$

where:

$$f = \frac{\eta \dot{m} H_o}{q_c}$$

The parameter η is to be determined from the test data and depends on the material, on the free-stream gas and on the flow conditions, i.e., axisymmetric stagnation point, laminar flat plate, etc. The quantity α in Equation (3) has been found to be independent of flow conditions and material and to have a "best value" near 0.618.

To be precise, the combination $(\eta \dot{m})$ appearing in the definition of f should be separated into a portion due to the surface removal and a portion due to the gaseous products of the charring reaction. It is impossible, however, to separate these two components on the basis of steady-state ablation experiments hence, the use of a lumped term with the necessary separation to be accomplished by other means.

For each experimental point values are obtained for the quantities Y and X as defined by Equations (2) and (3). The procedure for finding best values of Q_1, Q_2, and η is based on finding least-squares values of Q_1 and Q_2 for a sequence of values of η, then finding the best values of the three constants such that Equation (4) is satisfied.

$$\frac{\partial}{\partial \eta} \sum_{i=1}^{N} (Y_i - \hat{Y}_i)^2 = 0 \quad . \tag{4}$$

In Equation (4) the summation is over all experimental points, Y_i is the "observed" value of Y, and $\hat{Y}_i$ is the value computed on the basis of the least-squares values of Q_1 and Q_2. Although the data analysis outlined above is quite general, it should be noted that the quantities Q_1 and Q_2 cannot be separated on the basis of experiments which involve a single mode of heat transfer (convective) and which are carried out in a gas of fixed chemical composition (air). Since the available experimental data were obtained in air, it is necessary to assign a value to Q_2.

The data available on the ablation of Purple Blend Mod 5 are shown in Table LXXXIV. The preceding analysis has been applied to these data for an assumed value of Q_2 of 10,000 Btu/lb. Figure 356 shows

TABLE LXXXIV

MODEL 500 TEST DATA FOR PURPLE BLEND MOD 5

Sample No.	H_o (Btu/lb)	$\dot{q}_c$ (Btu/ft^2-sec)	$\dot{s}$ (in/sec)	q_r (Btu/ft^2-sec)
1	9890	1300	0.0292	232
2	7720	1420	0.0361	206
3	3890	920	0.0304	156
4	9780	1400	0.0300	232
5	6560	1440	0.0407	186
6	4040	900	0.0335	144

Average Density 41.8 lb/ft^3

Average Emissivity 0.62

Environmental Gas Normal Air

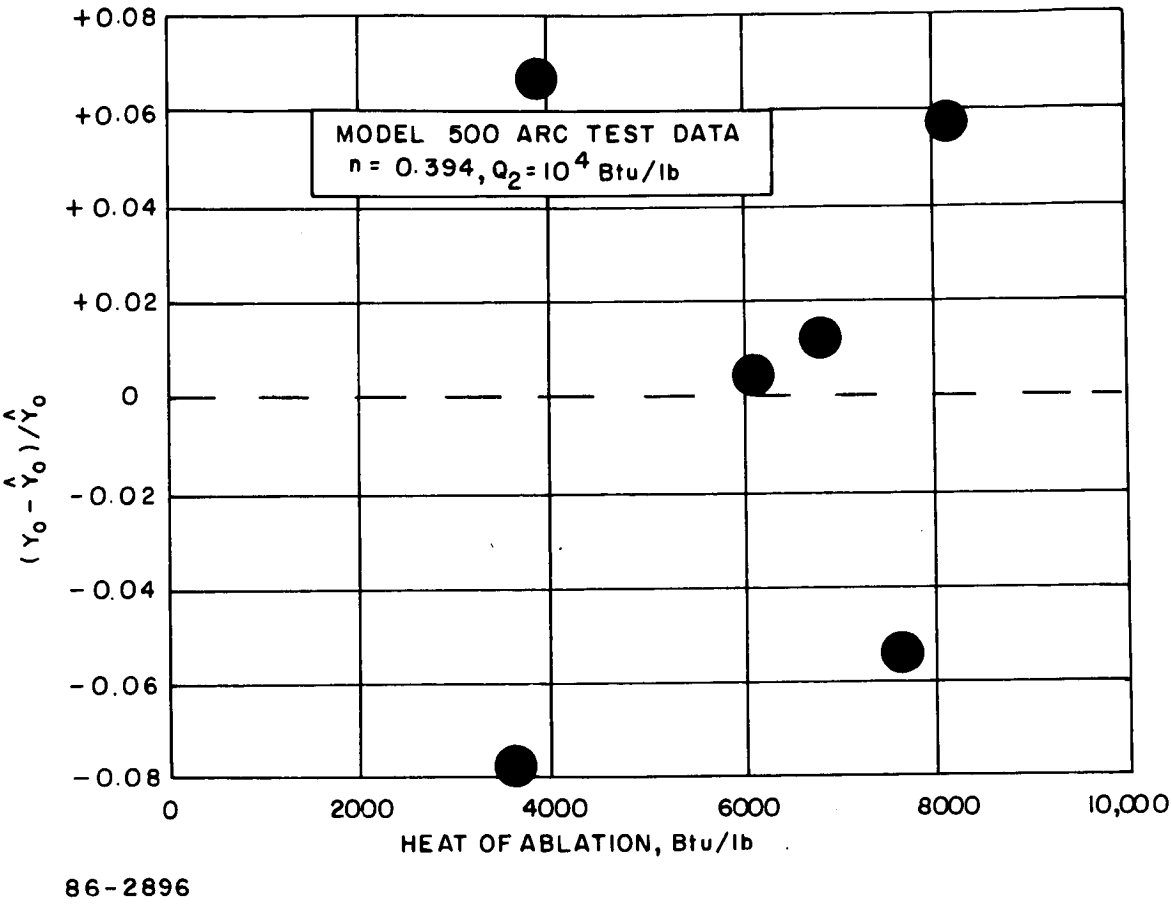

Figure 356 PURPLE BLEND MOD 5

a comparison between measured and predicted values of the quantity Y plotted against the experimental heat of ablation. As can be seen from the figure, the maximum error in Y is less than ± 10 percent. Table LXXXV shows the surface ablation characteristics either assumed or derived from the test data for Purple Blend Mod 5. The assumed combustion mechanism as implied by the properties given in Table LXXXV has been compared with a more conventional vaporization mechanism to indicate an effect of the assumed mechanism on the design of the heat shield. Figure 357 shows the heat shield-bond interface temperature history computed by the two methods. As can be seen from the figure, there is no significant difference in the predicted bondline temperature, hence, the combustion mechanism was employed in all design calculations under the assumption that it is a more realistic representation of the actual material behavior.

A preliminary analysis of the ablation data on Cork Silicone (893-27) indicates performance which is about 10 percent poorer than Purple Blend on a surface recession basis with a surface temperature nearly 20 percent higher than Purple Blend for the same environmental conditions. Since the application involves primarily the insulative performance of the material, subsequent effort was concentrated on the Purple Blend. Further study should be made of the choice of materials in the event of a "real life" design study since the present choice has been somewhat arbitrary from a thermal standpoint.

10.3 MATERIAL FABRICATION STUDIES

10.3.1 Purple Blend Formulations

One of the major advantages of the silicone elastomers is their applicability to a variety of processing techniques. Mixing of components is accomplished by use of a Hobart dough mixer as shown in Figure 358. Ingredients are sequentially added to the pot and blended until a uniform mix is obtained. Several application methods have been studied at Avco with four showing the most promise for low-density heat shields. The following is a brief description of these techniques as applicable to the materials being proposed.

10.3.1.1 Compression Molding

Compression molding is the most convenient technique for preparing experimental formulations for evaluation. It may also be the best approach for prefabrication of leading edge panels and caps for probes. Using this technique, the material is loaded uniformly into a metal mold and pressed at a relatively low pressure (~100 lb/in^2). The moldability of the compound can be adjusted by the addition of colloidal silica (Cabosil) during mixing.

TABLE LXXXV

SURFACE ABLATION CHARACTERISTICS
PURPLE BLEND MOD 5

Emissivity (ϵ)	0.62	
Blowing parameter (η)	0.394	
Combustion enthalpy (H_c)	10,000 Btu/lb (O_2)	
Heat of vaporization (h_v)	10,660 Btu/lb	
	Virgin	Charred
Reaction Rate Constants		
A_3 (in/sec-atm$^{1/2}$)	0	6.73×10^8
N	1/2	1/2
B_3 (°R)	3.99×10^4	3.99×10^4
Weight fraction carbon	0	0.5

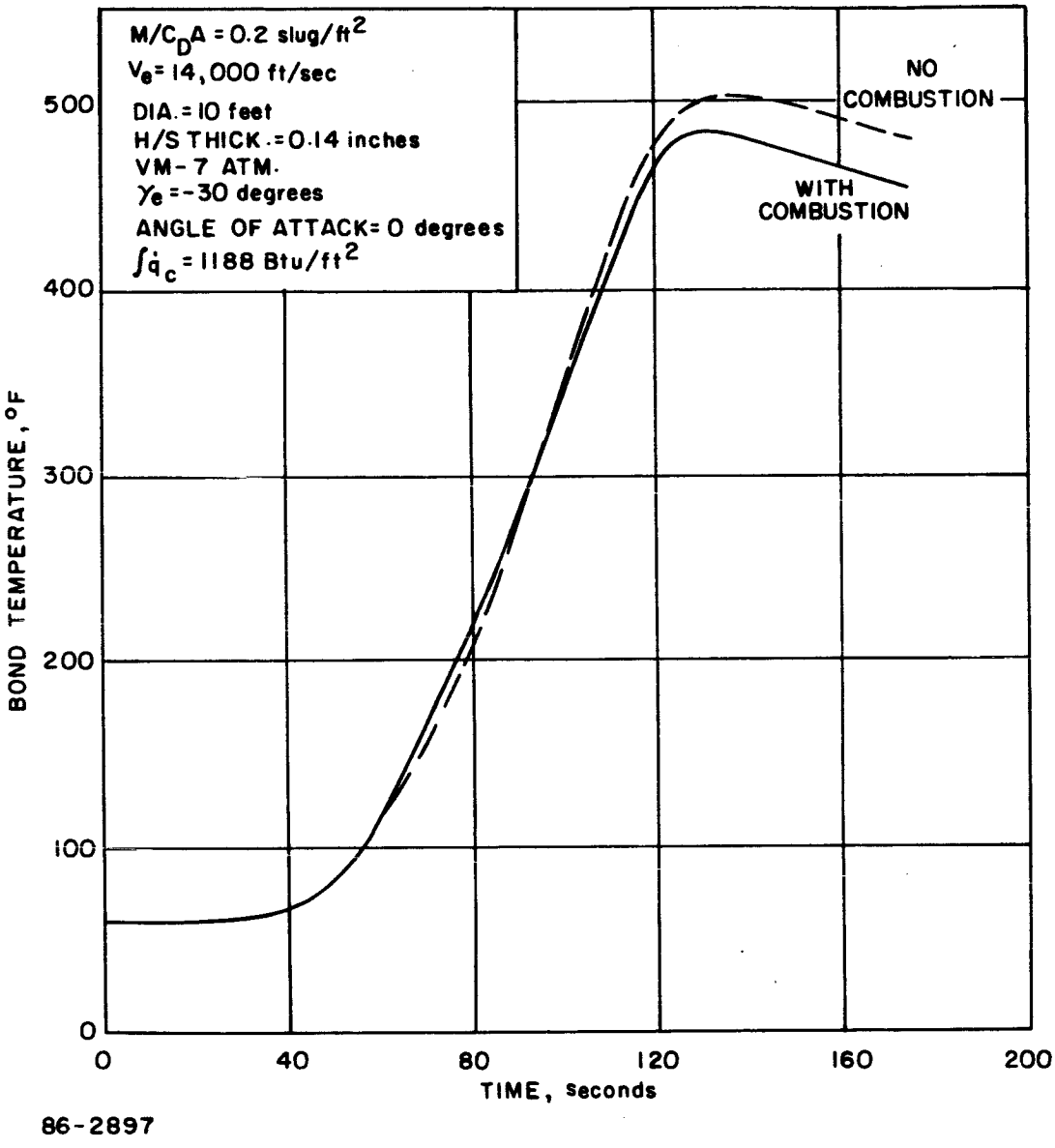

Figure 357 BOND TEMPERATURE HISTORY PURPLE BLEND--MOD 5-60-DEGREE BLUNT CONE

Figure 358 LOW DENSITY SILICONE FORMULATION AFTER MIXING IN HOBART

10.3.1.2 Direct Application of Preforms

The molded material described above can be removed from the mold prior to cure. In this case, it is described as an uncured preform. This preform can be applied to and cured directly on a substructure. By the use of bag molding techniques, it has been demonstrated that several uncured preforms can be applied to a structure and be cured into a continuous homogeneous heat shield.

10.3.1.3 Injection Into Honeycomb Cells

Avco has developed a pressure injection or "gunning" technique that is currently the production method for filling honeycomb with ablator on the Apollo program. The rheological characteristics of the low-density silicone materials can be adjusted to take advantage of this technique. Honeycomb panels have been successfully filled with Mod 5 low-density silicone ablator using this technique. Figure 359 shows fabrication of such a panel. Figure 360 is a sample of the filled honeycomb material using this technique.

10.3.1.4 Spraying

The most versatile and most promising application technique for the elastomeric materials is spraying. Both airless and air-atomized equipment has been used for this purpose. An Avco modified air atomized spray system, shown in operation in Figure 361, has shown the most promising results. Formulations with 0-4-percent silica fibers have been sprayed and flowed to a smooth surface and full density with application of moderate heat. At 7-percent fiber loading, it is necessary to dilute the mix with solvent to obtain a workable viscosity with air-atomized equipment. The gas sprayed material can be cured to a specific gravity of 0.35 or bag molded after spraying to a specific gravity of 0.60.

Purple Blend Mod 5 was applied to a probe mockup structure in conjunction with NASA Contract 8-20502, "Development of a Typical Mars Landing Capsule Sterilization Container." The material was reduced to 70-percent solids by the addition of solvents and applied with a modified air-atomizing spray system, vacuum bagged, and cured. Figures 362 through 365 show the fabrication of the probe mockup heatshield.

The preliminary mechanical properties of compression molded and sprayed and vacuum bagged Purple Blend Mod 5 are summarized in Table LXXXVI.

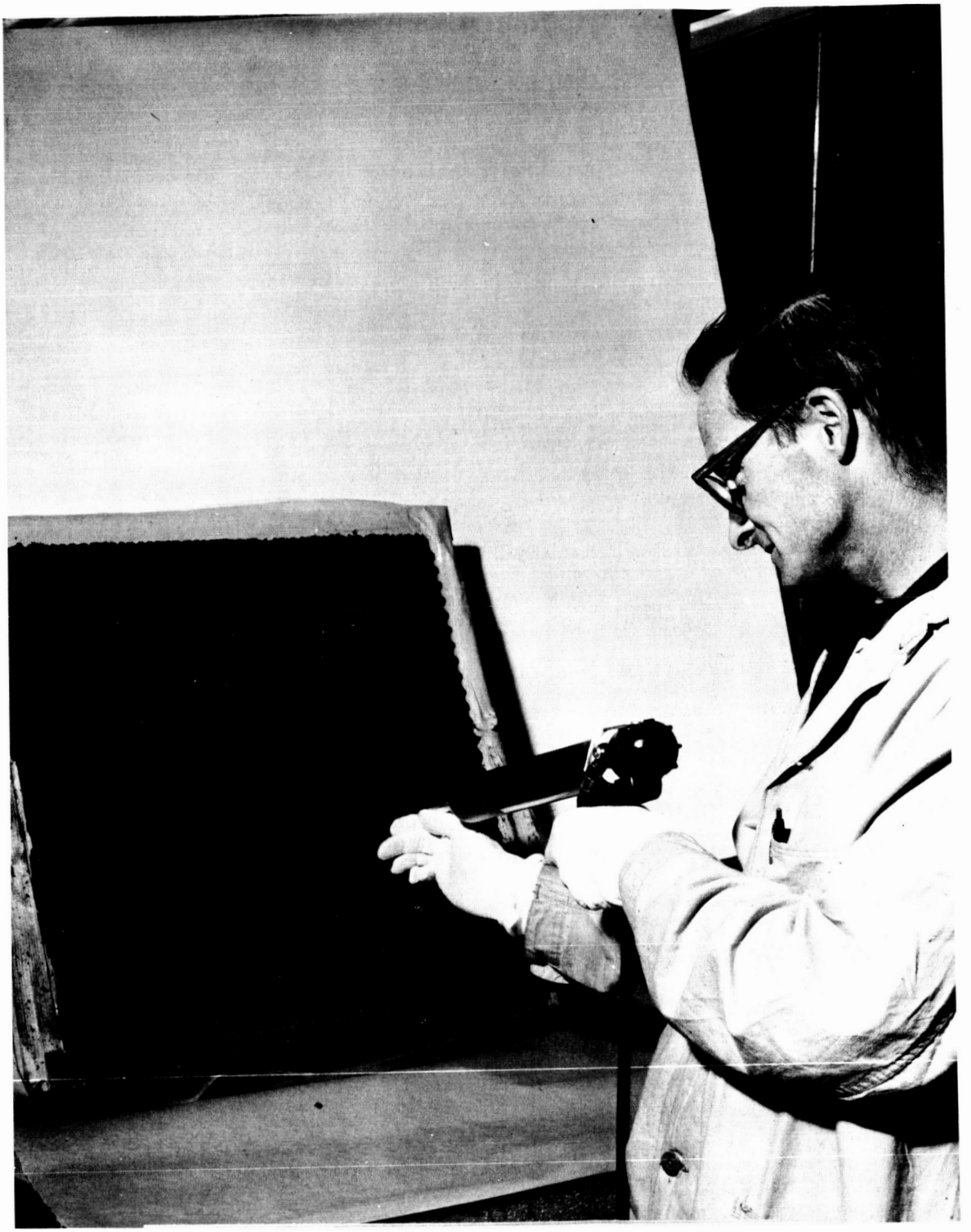

Figure 359 "GUNNING" OF LOW DENSITY SILICONE IN TO FIBERGLASS HONEYCOMB

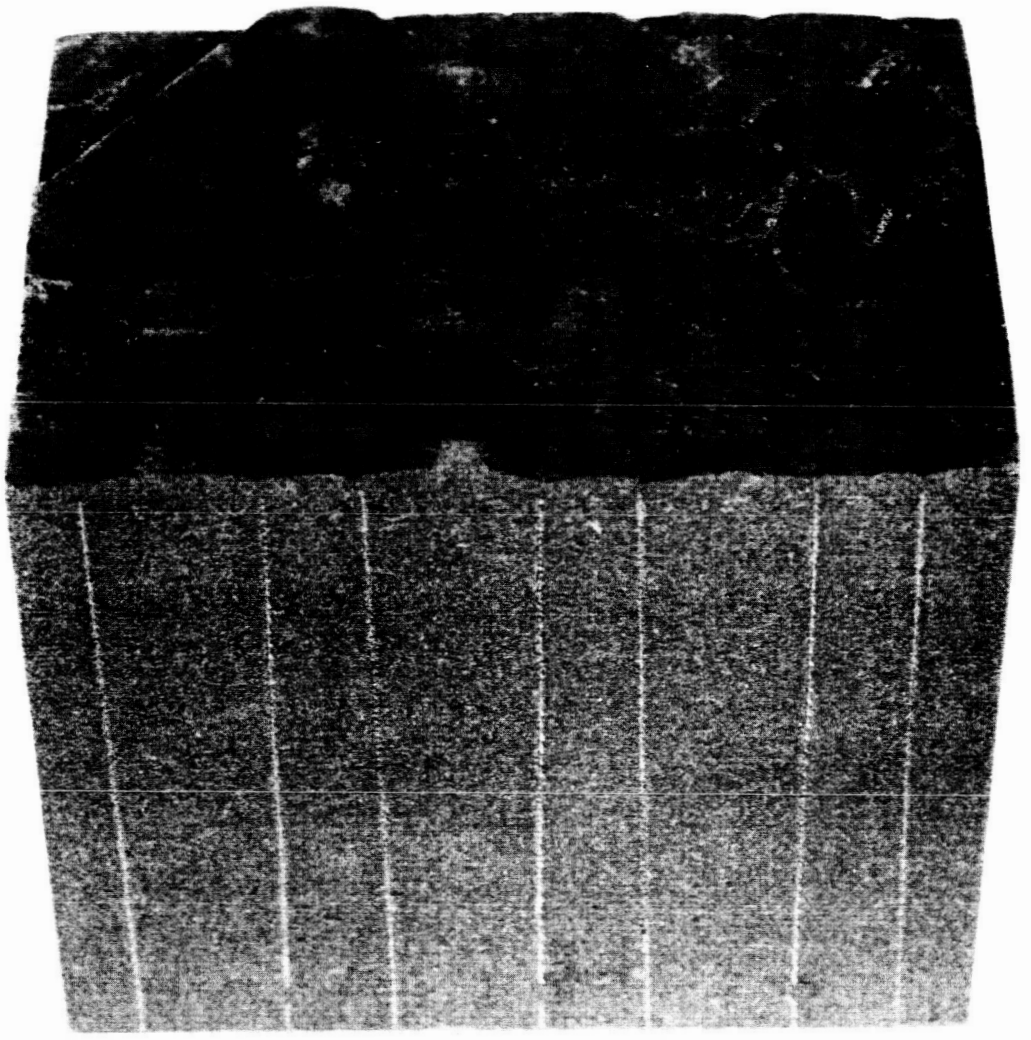

Figure 360 CORSS-SECTION OF HONEYCOMB REINFORCED LOW-DENSITY SILICONE FABRICATED USING "GUNNING" PROCESS

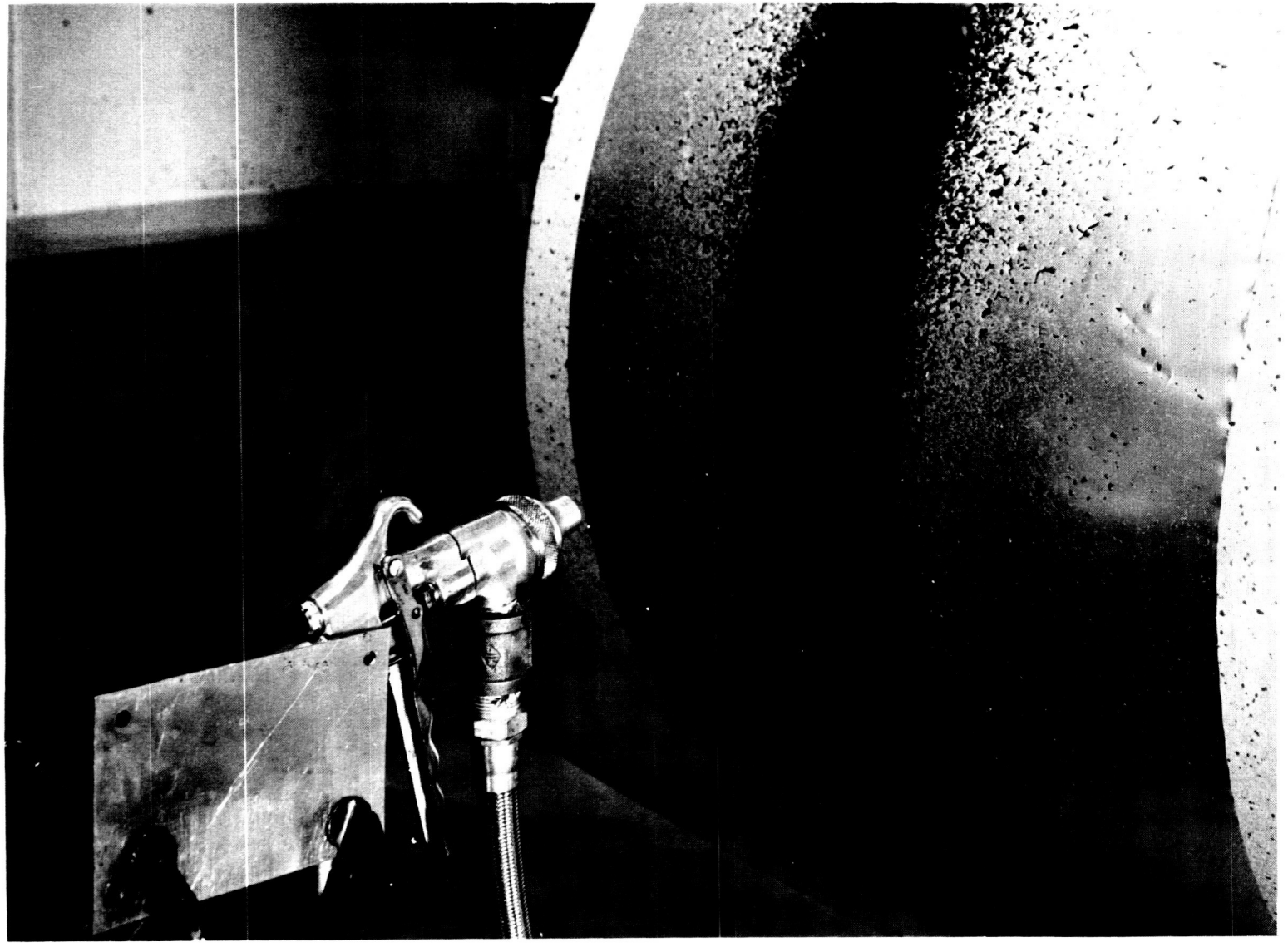

Figure 361 SPRAYING OF LOW DENSITY SILICONE ABLATOR

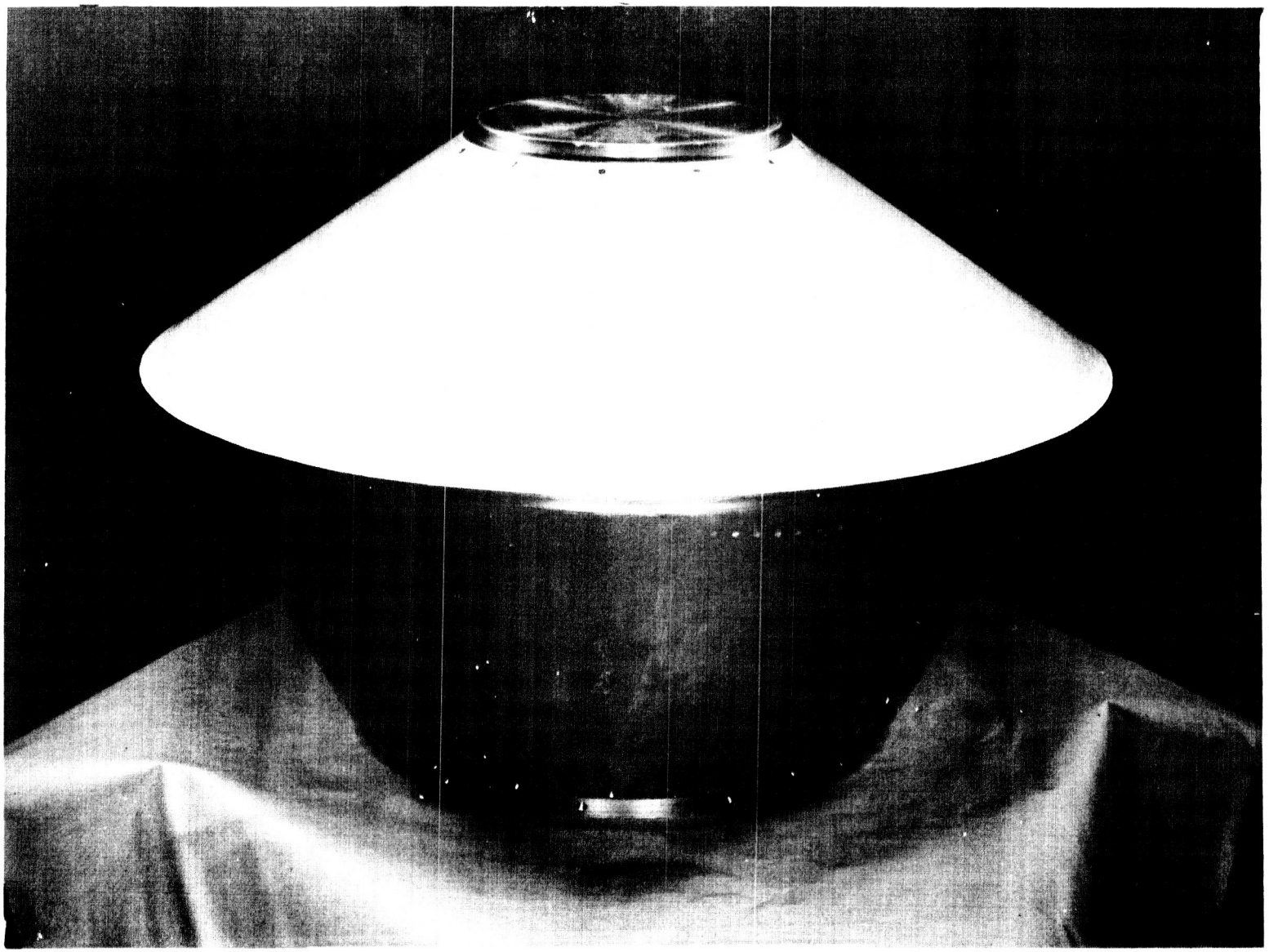

Figure 362 MARS PROBE MODEL STRUCTURE

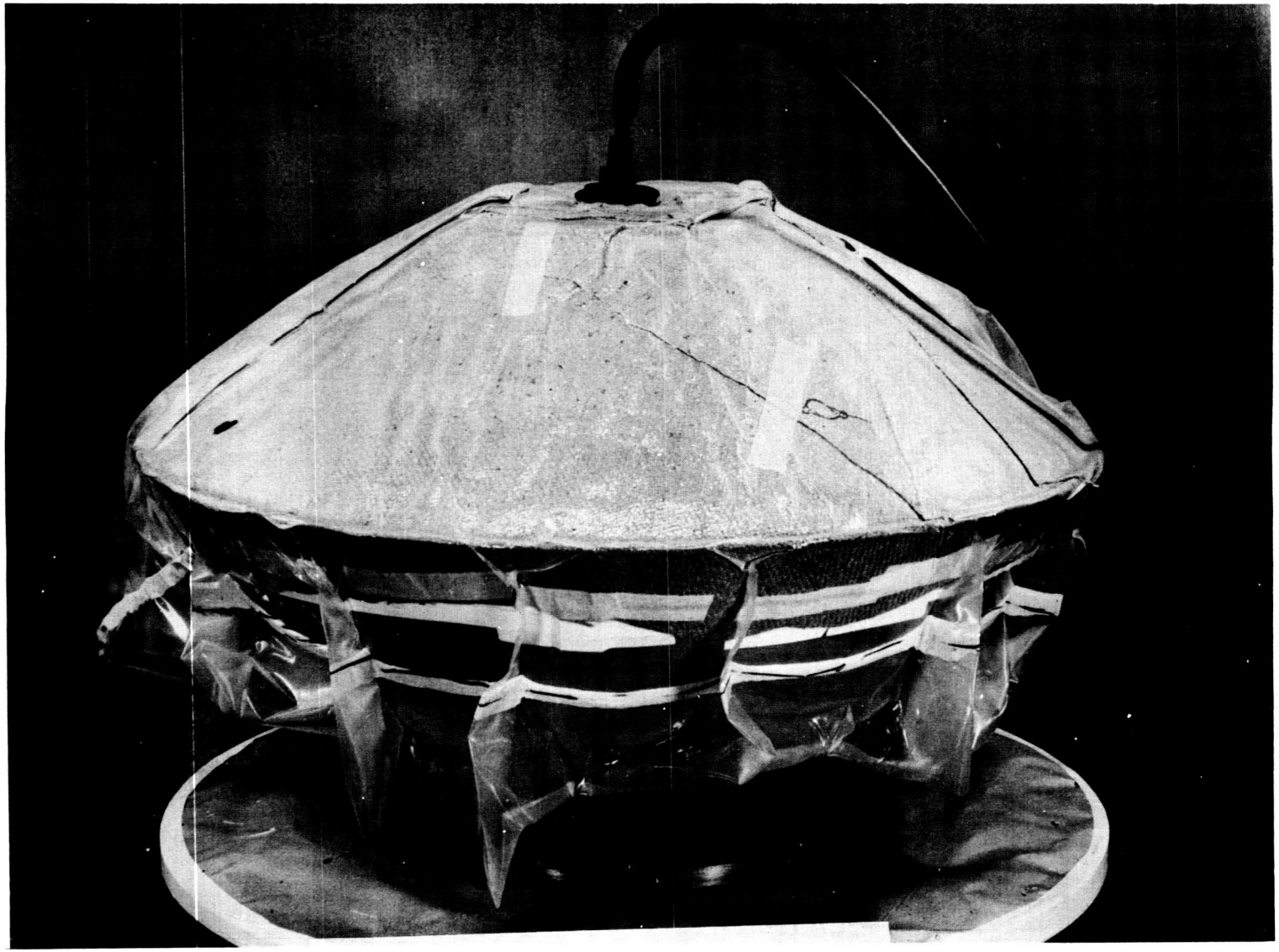

Figure 363 VACUUM-BAG CURING OF LOW DENSITY SILICONE HEAT SHIELD

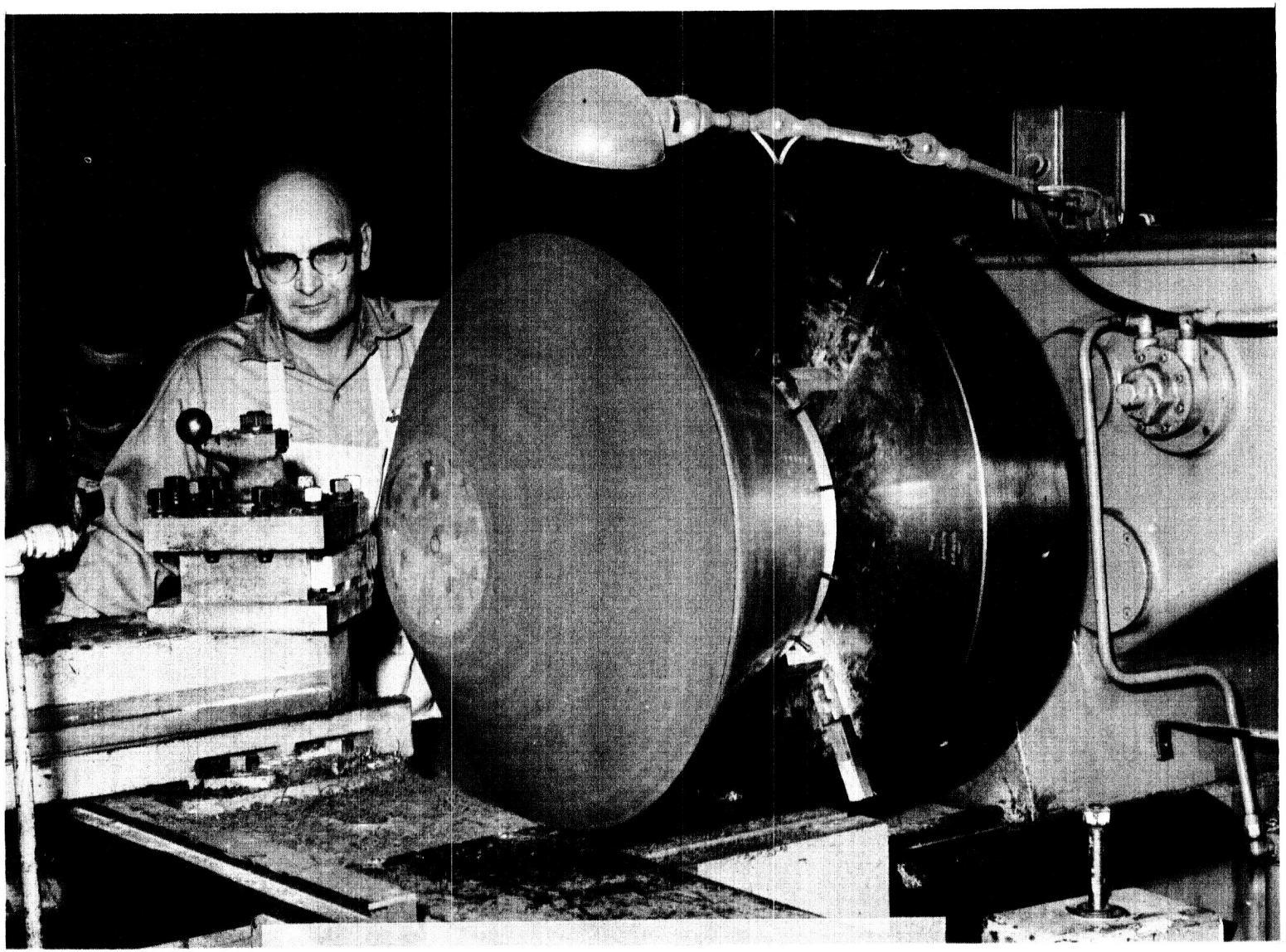

Figure 364 MACHINING OF MARS PROBE MODEL SILICONE HEAT SHIELD

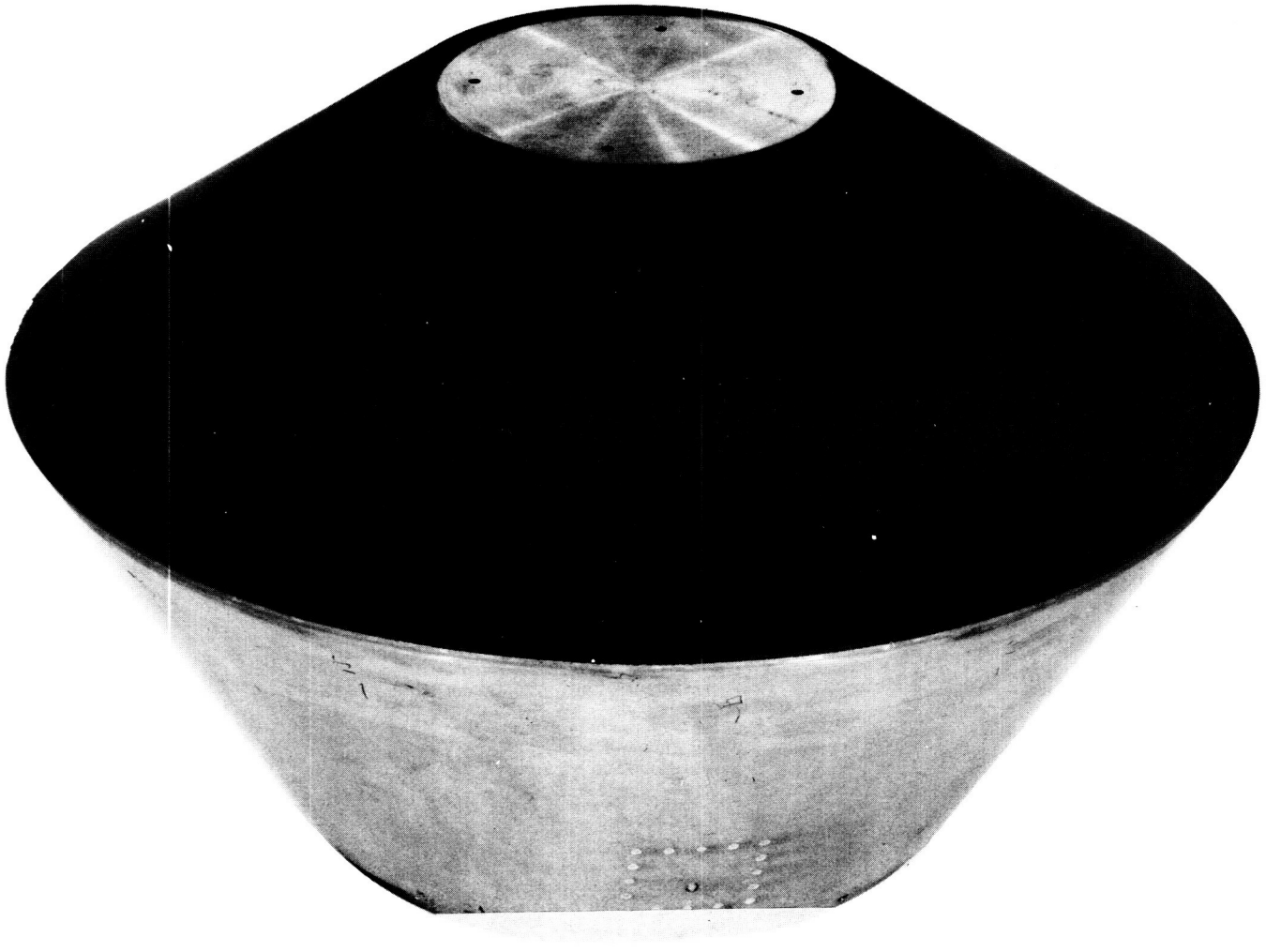

Figure 365 MARS PROBE MODEL WITH LOW-DENSITY SILICONE HEAT SHIELD

TABLE LXXXVI

PRELIMINARY PROPERTIES OF PURPLE BLEND MOD 5

Fabrication Technique	Compression Molded to Stops	Compression Molded to Stops	Sprayed and Vacuum Bagged
Cure	4 hrs at 200°F	4 hrs at 200°F	4 hrs at 200°F and 29 in. Hg
Postcure	4 hrs each at 225, 275 and 350°F	4 hrs each at 225, 275 and 350°F	4 hrs each at 225, 275 and 350°F
Environmental exposure	non	3 cycles of dry heat sterilization per JPL XS-30275-TST-A	none
Specific gravity	0.68	0.67	0.58
Tensile Strength (psi)*			
-100°F	544	868	489
75°F	167	330	146
300°F	131	290	128
Total Strain to Failure (percent)*			
-100°F	8.6	5.4	7.8
75°F	5.0	8.8	5.3
300°F	4.5	4.8	4.9
Elastic Modulus (psi x 10^{-6})*			
-100°F	.032	.059	.043
75°F	.0055	.0099	.0064
300°F	.0040	.0087	.0043
Coefficient of Thermal Expansion (in/in/°F x 10^{-6})			
-100 to 0°F	47.5		
0 to 240°F	55.0		
240 to 300°F	50.0		
-100 to -40°F		54.3	
-40 to 300°F		43.5	
-100 to -40°F			62.5
-40 to 300°F			36.3

*Tensile Test Strain Rate - 0.05 in/in/min.

10.3.2 Avcoat 5026-99

Formulation and mixing of ingredients for Avcoat 5026-99 is similar to procedures described for the elastomeric materials. The compound is mixed to a dough consistency in a Hobart mixer of the type shown in Figure 358. The materials can then be compression molded with moderate pressure and heat or removed from the mold prior to cure as a compacted preform. The preforms can be applied to a structure and bag-molded in place.

Pressure injection or "gunning" into honeycomb, as shown in Figure 359, is another technique applicable to this type of material.

10.3.3 Cork Formulation

Components of the cork formulations a re mixed in a Hobart mixer and compression molded into billets. The preform techniques utilized with the epoxy and silicone systems are not applicable to cork because of the large bulk factor associated with its compaction. The material can be molded to shape or sheets can be sliced from molded billets for application using a "wallpapering technique."

The selection of a final fabrication process will depend on the particular formulation selected, the configuration, substructure materials and heat shield thickness. In any event, extensive process studies will be eventually required to establish a reliable application technique. These studies would include equipment, material, and process variables leading to evaluation and proof testing of hardware configurations.

10.4 THERMAL CONTROL ANALYSIS

The complexity of thermal control problems lies primarily in the involved configuration layouts and the ensuing large number of locations where temperature must be calculated. The calculations of the multidimensional heat flow patterns and difficulty in predicting the resistance to heat flow encountered between various joints and surfaces are some of the difficulties encountered in the analysis. The theoretical analysis of the heat flow problems on the other hand is relatively simple as it basically amounts to the reduction of the heat transfer problem to an electrical analog. Conductive, convective and radiative heat transfer between the various structural parts and components of significance and the environment are considered where applicable. With the aid of a digital or analog computer, a temperature history is calculated by performing a heat balance simultaneously for all volume elements. The analytical procedure was presented in References 84 and 85. A transient heat conduction program, Avco No. 1896, was used besides an analog computer to produce transient and steady-state temperature histories for a variety of conditions.

In order to study the temperature time history of any component or complete system the general heat balance must be set up:

$$m_1 c_1 dT_1/dt = \sum Q_{in} - \sum Q_{out} \qquad (1)$$

The solution to the above will give the temperature T_1 of mass m_1 with specific heat c_i as a function of time with the inputs and outputs expressed by ΣQ_{in} and ΣQ_{out}. The energy exchange between the mass m_1 and adjacent components can be of radiative as well as of conductive nature. Therefore, including all such effects the more general expression is

$$m_i c_i dT_i/dt = \sum Q_{ei} - \sum \frac{A_{ci,j} K_{i,j}}{l_{ij}} (T_i - T_j) - \sum A_{ri} F_{ij} \sigma (T_i^4 - T_j^4) \qquad (2)$$

The first term on the right hand side states the energy input to component "i" due to electric and external energy (equipment turned on and off). The second term is a measure of conductive couplings effect between "i" and all other components which are conductively connected with "i". The lengths and cross sections of the conductive paths are expressed by $l_{i,j}$ and $A_{ci,j}$ respectively while $K_{i,j}$ is the specific conductivity of the material.

The third term contains the radiative coupling effect with surroundings or space. $E_{i,j}$ includes the geometric view factor as well as the surface characteristics: ϵ values.

For any component exposed to sun light the Q_e term must also include this absorbed energy expressed by

$$Q_{sun} = A_p \alpha \cdot S$$

Where A_p is the projected area perpendicular to the sun vector with solar constant S. α is the absorbtivity of the surface for solar radiation.

Due to the random nature of the inputs ΣQ_e a closed solution is not possible but the multitude of simultaneous differential equations for all nodes can be solved by either digital or analog computation techniques.

For a body exposed to space condition, the average temperature level is determined from

$$T = \sqrt[4]{\frac{A_P}{A_T} \cdot \frac{\alpha}{\epsilon} \cdot \frac{S}{\sigma}}$$

The main parameters are: the ratio of projected to total radiation area A_P/A_T, α/ϵ ratio and solar constant S with σ = the Stephan-Boltzman constant. A_P/A_T is 0.25 for a sphere, $\frac{1}{\pi}$ for an infinite long cylinder and 0.5 for a plate perpendicular to the sun. α/ϵ may range from 0.15 for white coatings to 10 for highly polished metallic surfaces.

Figure 366 shows for example - T vs S for $\alpha/\epsilon = 0.2$ $A_P/A_T = 0.213$, a cylinder with $l = D$.

While the above only gives the average temperature based on a simple overall heat balance, the more complete picture can only be obtained by including the effects of the other parameters: material, physical and optical properties, geometric location (local gradients, local cold spots, minimizing heat gain or loss by insulation).

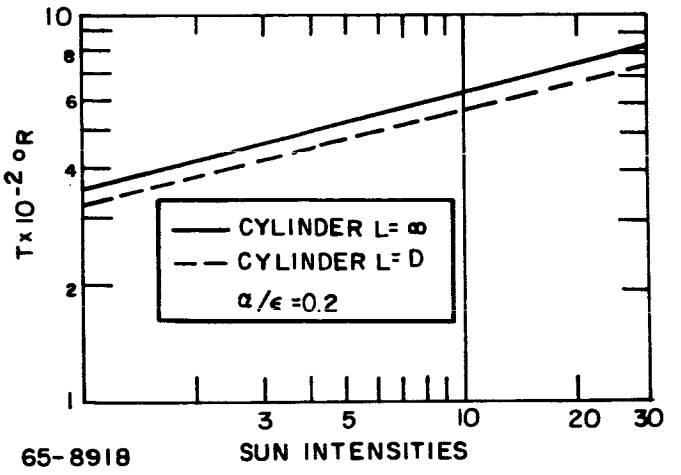

Figure 366 SKIN TEMPERATURES VERSUS SUN INTENSITY

NOMENCLATURE

Symbol	Description
A, A_3	Reaction rate coefficients
B, B_3	Activation temperatures
C_g	Specific heat of gaseous decomposition products
C_p	Specific heat of solid material
E_2	Exponent associated with heating factor
E_7, E_8	Reaction orders
f_1	Weight fraction of carbon
f_2	Weight fraction of resin
H_c	Heat of combustion per pound of oxygen
ΔH_c	Heat of decomposition
H_R	Recovery enthalpy
H_s	Stagnation enthalpy
H_w	Wall enthalpy
H_{wr}	Reference enthalpy
H'	Combustion enthalpy
hv_1	Heat of vaporization of carbon
hv_2	Heat of vaporization of resin
k	Conductivity
L_1, L_2, L_3	Coordinates of material composite
M_Q	Multiplication factor
N_3	Reaction and diffusion exponent
n	Decomposition reaction order
P	Primary heat shield material
P_e	Local static pressure
$\dot{q}_c$	Local cold-wall convective heat transfer rate
$\dot{q}_R$	Local radiative heat transfer rate
RT_o	Gas constant
r	Recovery factor

NOMENCLATURE (Concl'd)

Symbol	Description
S_1, S_2	Secondary materials
$\dot{s}$	Surface recession rate
$\dot{s}_D$	Surface recession rate for diffusion controlled ablation
$\dot{s}_R$	Surface recession rate for reaction rate controlled ablation
$\dot{s}_s$	Surface recession rate for sublimation controlled ablation
T	Temperature
TW	Reciprocal of free carbon weight fraction
Tx	Multiplication factor
t	Time
U_0, U_1	Molecular weights of atmosphere and oxygen, respectively
U_2, U_4	Atomic weight of oxygen
U_3, U_5	Atomic weight of carbon
We	Mass concentration of oxygen in the boundary layer
W	Mass flow rate of gaseous decomposition products
X_Q	Exponent for diffusion reaction
a	Variable heating reduction constant
$\beta_5, \beta_6, \beta_7$	Material constants
Γ	Multiplier
ϵ	Emissivity
η_g, η_s	Transpiration coefficients
ρ	Material density
σ	Stefan-Boltzmann constant

Subscripts (unless otherwise defined)

c	Char material
v	Virgin material
s	Surface

11.0 THERMAL CONTROL ANALYSIS PROBE/LANDER, ENTRY FROM THE APPROACH TRAJECTORY

11.1 INTRODUCTION AND SUMMARY

11.1.1 General Requirements and Objectives

The function of the thermal control system is to maintain electronic components, batteries, structural members, and the heat shield within the operating temperature limits dictated by the operative and nonoperative conditions in the various phases of flight. The system must be compatible with the spacecraft and the power available within the general weight allocations. The system should be designed to minimize these requirements. It must be compatible with other systems and allow for departures from nominal performance conditions during all the phases of the mission. To provide for reliable operation it should minimize the requirement for active systems and assure that its passive elements do not degrade the performance of other materials and they themselves are not degraded by the presence of the other.

The specific requirements imposed on the thermal control system included provision to minimize the disturbance to the flight spacecraft, after entry-vehicle separation, to maintain temperature control during the post-separation and post-impact phases without external power and to be compatible with the communications requirements in regard to the applicability of metallic coatings, in particular for the landed capsule.

The objective was to define thermal control requirements and a system for an entire 1971 mission profile of selected flight capsule configurations and to study the interaction of various parameters of significance. Neither selection of the design nor a performance analysis of a reference conceptual design were initiated due to the reorientation of the program.

In order to achieve the objectives it is necessary to consider: thermal coatings, power requirements, insulation requirements, and the effect of various perturbations on the overall systems thermal balance. Furthermore, temperature histories for significant structural members and internal components as well as boundary and initial conditions for the entry thermal protection system must be established. Proper design and performance evaluation of the system requires accurate thermal interface definition between the flight spacecraft and the flight capsule. It is then necessary to determine the relationships between the various allowable temperatures, power available for heating, and the optical property requirements for thermal control coatings. Detailed requirements and design criteria are discussed below.

11.1.2 Design Criteria and Limitations

The specific criteria used in the design, assumptions made concerning the planetary vehicle (PV) geometry (flight spacecraft/flight capsule interface) and various limitations imposed on the system are summarized below.

11.1.2.1 Thermal Interface

As noted previously, performance evaluation of the flight spacecraft/flight capsule system requires accurate thermal interface definition to assess the power required during cruise. Because of the absence of spacecraft definition and accurate thermal interface information, a reference was established assuming that the base of the sterilization canister is isothermal at -20°F near Mars and at + 60°F near Earth. This assumption was based on a consideration of high radiative interchange between the spacecraft and the adjacent (assumed in close proximity) sterilization canister base or direct sun impingement. It was felt that this was a reasonable case since no data on the spacecraft diameter and solar panel arrangement was available, and direct sun impingement at the sterilization canister base was within the range of possibilities. The effects of various other spacecraft/capsule thermal interface assumptions on flight capsule temperatures are discussed in paragraph 12.3.1.1.

11.1.2.2 Power

In the absence of specific information, it was assumed that a reasonable amount of power (less than 200 watts) is available from the spacecraft (until flight capsule separation) for thermal control of critical components. No (or very limited) power is assumed to be available from separation to post-impact.

11.1.2.3 Temperature

Temperature limitations for structural members and components are shown in Table LXXXVII. The batteries are the most critical components and require particular thermal control attention during all phases of the mission. Initially, an attempt was made to maintain the battery temperature at a minimum of + 60°F (non-operative or operative) during all mission phases. This requirement was later relaxed after new data on battery (Ni-Cd) allowable lower temperature limits had been obtained.

TABLE LXXXVII

TEMPERATURE LIMITATIONS FOR STRUCTURAL MEMBERS AND COMPONENTS

Critical Component or Subsystem	Typical Temperature Specification	Critical Phase of Operation	Thermal Design Approach
Batteries	-65 to +160° F nonoperative 40 to +160° F operative (+60 to +160° F nonoperative and operative assumed for this study)	a) Cruise near Mars (low temperature b) Post-separation, dependency on entry vehicle orientation relative to the sun c) Post-impact (diurnal cycle)	1. Insulation + heaters using spacecraft power 2. Low-ϵ coatings on ext. surface of heat shield and afterbody. Insulation and warm-up prior to separation.
Propulsion	-60 to 300° F nonoperative 0 to 140° F operative	Just prior to separation and post-separation.	ΔV rocket: electrical heater and insulation.
Instrumentation	-35 to 300° F nonoperative 0 to 140° F operative	Post-impact	Insulation + heat sink
Electronics	-35 to 300° F nonoperative 0 to 140° F operative	Post-impact	Insulation + heat sink
Parachute System	-35 to 300° F	Entry	Insulation for entry heating
Explosive Systems	-160 to 300° F	Space flight, cruise mode	Overall system design
Heat Shield and Structure	To be determined (low entry temperatures desired)	Entry Entry	Ablation shield insulation (if required)
Impact Attenuator	-160 to 300° F nonoperative	Impact	Overall systems design, low ϵ on heat shield.
Sterilization Canister	-160 to 300° F	Space flight, cruise mode and mid-course maneuver	High α/ϵ
Flight spacecraft/flight capsule interface	+60° F -20° F	Cruise near Earth Cruise near Mars	If lower temperatures obtained due to S/C - F/C interface heaters to be installed in the H/S

11.1.2.4 Coatings

Communications systems requirements for coating materials are as follows:

Heat Shield	No restriction (Metal or non-metal)
Structure	No restriction (Metal or non-metal)
Afterbody	No restriction (Metal or non-metal)
Landed Capsule Shell	
(Impact Attenuator)	Non-metal
Payload outer shell	
Spherical concept	Non-metal
Oblate Spheroid concept Metal	(except antenna plots)

11.1.3 Design and Performance Summary

The scope of the thermal control system study in this phase of the program was largely limited to the investigation of critical conditions which may arise during the mission and to the establishment of the limiting thermal control system requirements for the conceptual flight capsule design to be evolved.

The effect of the entry vehicle shape (including afterbody) and its size (shadowing effects) was also investigated to determine whether such selection would be seriously affected by thermal control considerations. The actual design, selection of coatings, power supply definition, and performance analysis were deferred to the second phase of the study. Due to the reorientation of the program, such studies were not initiated for the entry from approach trajectory, but were conducted instead for the entry from orbit (Section 12.0).

However, the examination of performance characteristics anticipated for the blunted cone 1971 mission, based on the limitations given in Table LXXXVII and the parametric results shown in Figures 367 and 368 led to a tentative recommendation for the thermal control system which is shown in Figure 369. This system consists of low- ϵ (0.05) coatings on the primary and secondary heat shield faces and moderately low ϵ (α/ϵ = 1 to 3) coatings on the afterbody to maintain the critical components (batteries) within allowable temperature limits during the postseparation phase.

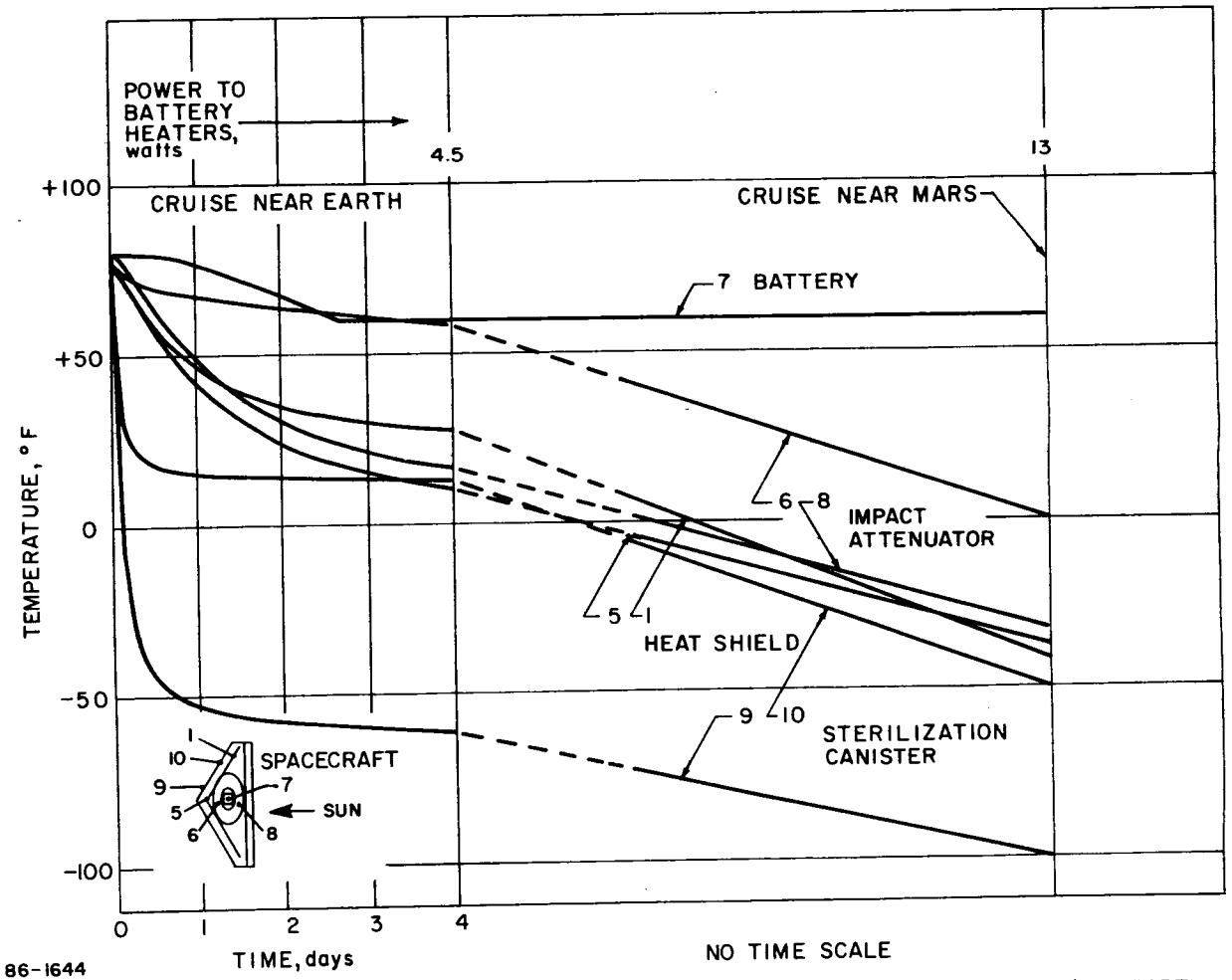

TEMPERATURES AND POWER REQUIREMENT BASED ON ISOTHERMAL S/C-F/C INTERFACE TEMPERATURES (+60 EARTH, -20 MARS)

Figure 367 BLUNTED CONE 180-INCH DIAMETER ENTRY SHELL WITH OBLATE SPHEROID CAPSULE, CRUISE NEAR-EARTH AND NEAR-MARS TEMPERATURE HISTORY

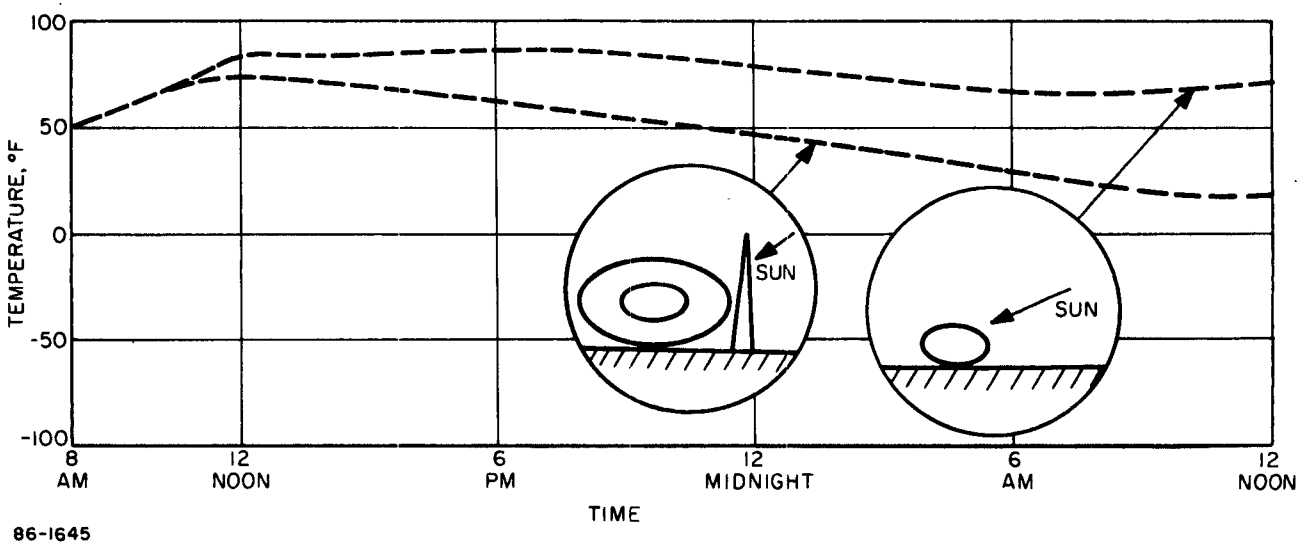

Figure 368 POST-IMPACT BATTERY TEMPERATURE HISTORY

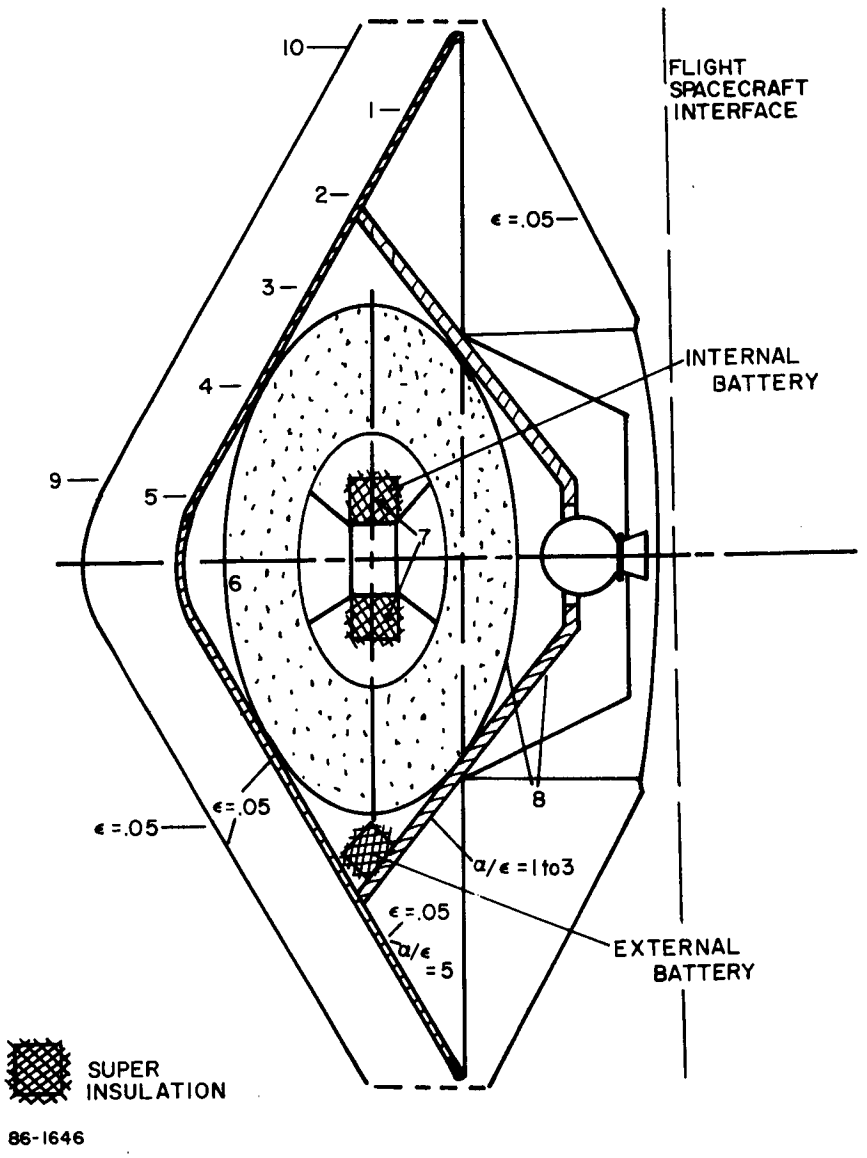

Figure 369 BLUNTED CONE 180-INCH DIAMETER ENTRY SHELL WITH OBLATE SPHEROID CAPSULE, EFFECT OF AFTERBODY ON POSTSEPARATION TEMPERATURES

Since the external battery would tend to cool down to low temperatures, some heat will have to be supplied to it during cruise, it will have to be warmed up further prior to separation and superinsulation will be required to maintain its operative temperatures (40°F to 160°F) during post separation. The internal battery may not require heat during cruise; however, it also will have to be insulated and warmed up prior to separation to maintain a sufficiently high operative temperature for post-impact use. The above design will accommodate anticipated postseparation sun orientation angles (53 to 90 degrees) and will not cause overheating for a zero-sun orientation angle. The oblate spheroid payload capsule, with its metallic surface, will operate within prescribed limits. It may be thus seen that the postseparation phase presents the most difficult thermal control problem.

11.1.4 Conclusions and Problem Areas

The broad nature of the entry from approach trajectory system studies precluded an early definition of a reference or nominal flight capsule design. The large number of variables and unknowns in the mechanical design at this stage made it impossible to specify a reference thermal control system. It was possible, however, to recommend a basic approach and it was possible to draw a set of generalized conclusions. The conclusions, of course, depend on the assumptions that were made during the study.

1. Cruise -- Payload temperatures will be maintained within specifications by use of coatings and a limited supply of power to critical components. Depending on the shape selected, 5 to 7 watts are required near Earth and 13 to 14 watts near Mars. The capsule should be maintained in the shade of the spacecraft and should be equal or smaller than the spacecraft and solar panel projected area to prevent overheating in the vicinity of the Earth. For the same reason the ejection of the sterilization canister lid is not advisable during the early phase of the cruise.

2. Midcourse Maneuver -- Large temperature gradients will develop in the sterilization canister and elevated temperatures (above 400°F) will be reached. While the thermal balance of the capsule may not be affected appreciably, excessive (over 300°F) hot spots may develop in the heat shield. Lower α/ϵ ratios (reduced α) may be desirable. Early removal of the sterilization canister lid would aggravate the situation.

3. Postseparation -- This is the critical phase for the thermal control system as practically no power is available. Consideration of two extreme sun orientation angles (90 degrees and 0 degree) revealed that the former results in low temperature problems while the

latter results in high temperature problems. The solution for the blunted cone appears to be the use of coatings suitable for 0 degree sun orientation angle (moderately low α/ϵ) however components (battery) insulation and warmup of the battery prior to separation to highest possible levels is recommended since 53- to 90-degree angles are very likely to occur. Provision of internal capsule power would cause an undue weight penalty in a weight critical system.

4. Entry -- No thermal effect other than heating of the outer impact attenuator shell and a small internal payload temperature increase ($0.5^{o}F$ is a typical value) due to internal power dissipation can be expected during entry. Entry heating effects were discussed in Section 8.0.

5. Parachute Descent -- The temperature of the outer layer of the impact attenuator drops significantly. The internal payload temperature increases only slightly (typical value, $4^{o}F$) from internal heat dissipation.

6. Post Impact -- Thermal control of the oblate spheroid capsule with a high α/ϵ metallic coating (except in the area of the antenna slots) appears to be feasible if the capsule is well insulated internally and the temperature is raised before separation and maintained through impact. Thermal control of the spherical capsule appears to be difficult because a non-metallic (dielectric), and therefore high-emitting, surface coating is required to satisfy communication antenna requirements.

A metallic afterbody is highly desirable since it allows thermal control of the landed capsule over a wide range of temperatures during mission phases prior to impact, while the coating properties of the landed capsule outer shell (impact attenuator) remain constant at a value best suited for the post-impact phase.

A comparison of the various generic entry-shell shapes yielded the following conclusions:

a. Cruise -- No definite preference for either the Apollo or blunted cone configuration is apparent, although the latter requires slightly less power. The tension shell would require more power than either of the others.

b. Postseparation -- The blunted cone appears inferior to the other two shapes because it has a small projected-to-total area ratio for large sun orientation angles. The tension shell appears superior as the area ratio is most favorable and might result in a similar coating requirement for sun orientation angles from 0 to 90 degrees.

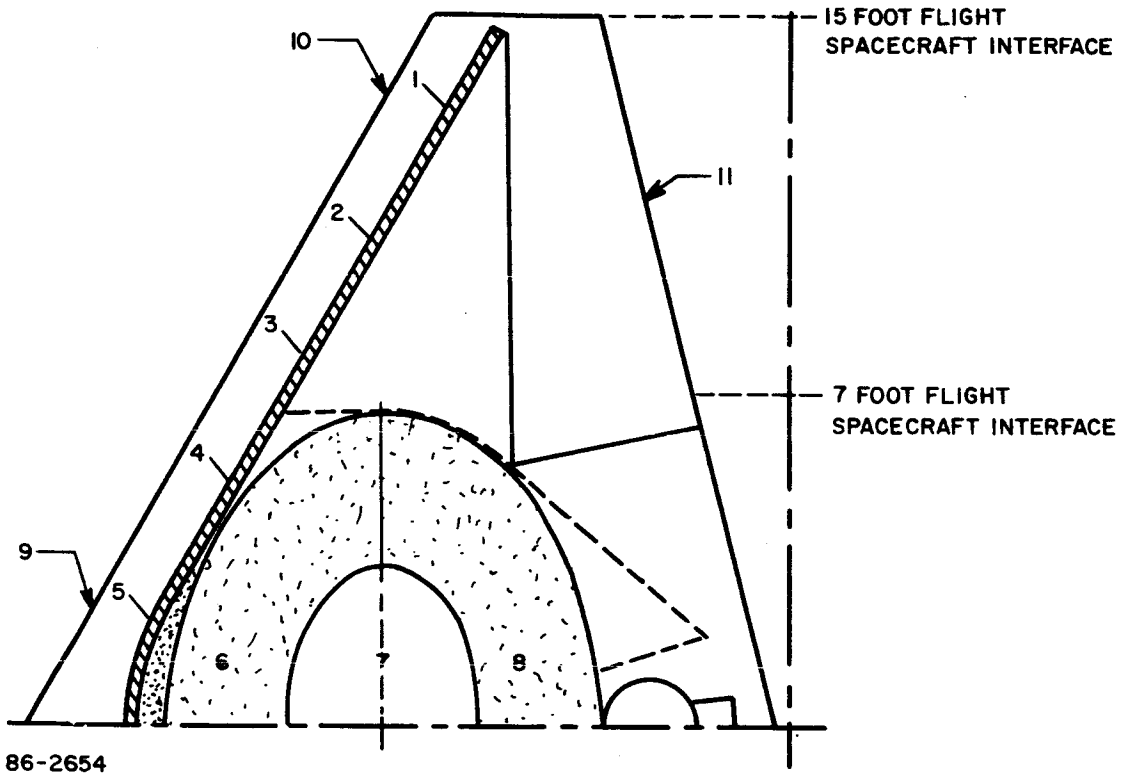

Figure 370 REFERENCE CONCEPT BLUNTED CONE/OBLATE SPHEROID CONFIGURATION

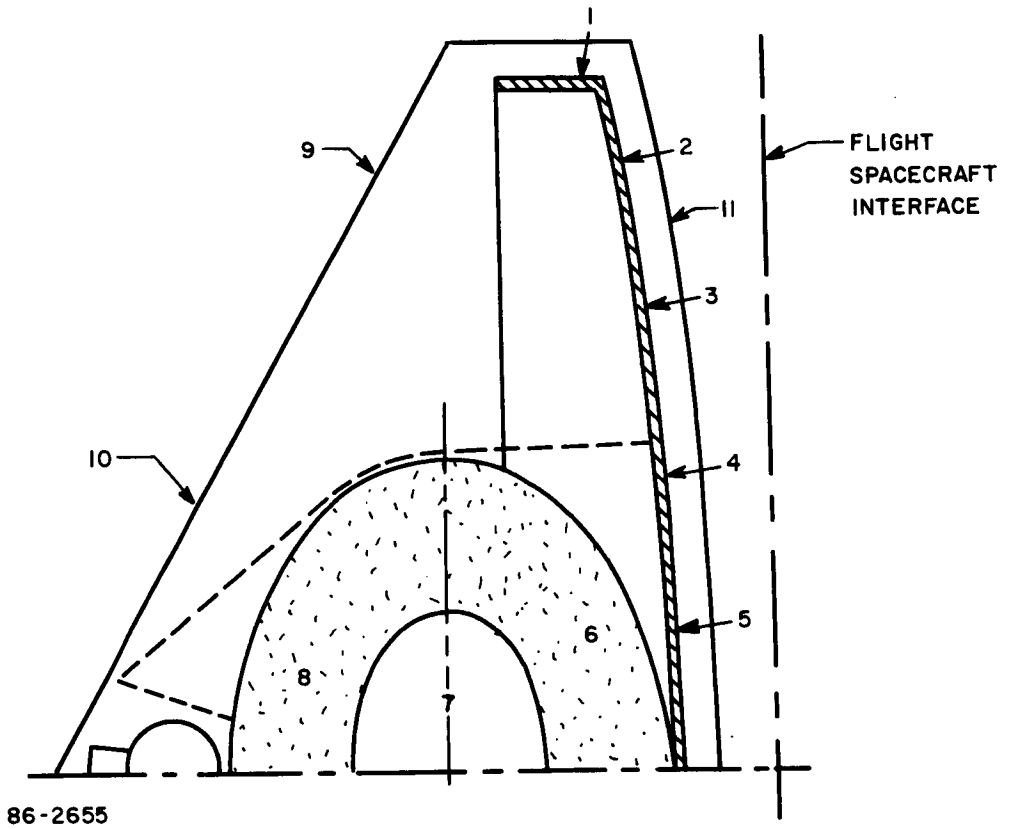

Figure 371 REFERENCE CONCEPT APOLLO SHAPE/OBLATE SPHEROID CONFIGURATION

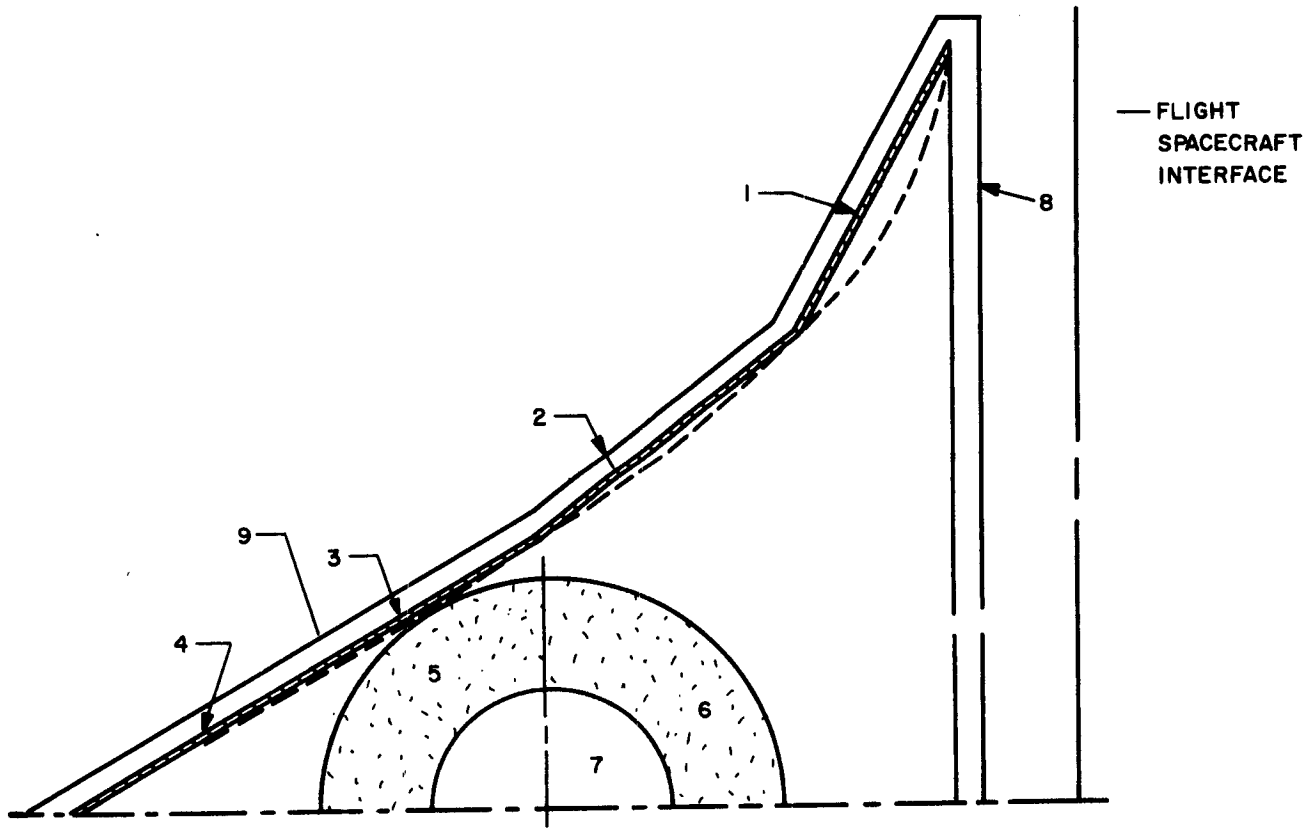

86-2656

Figure 372 REFERENCE CONCEPT TENSION SHELL/SPHERICAL CAPSULE CONFIGURATION

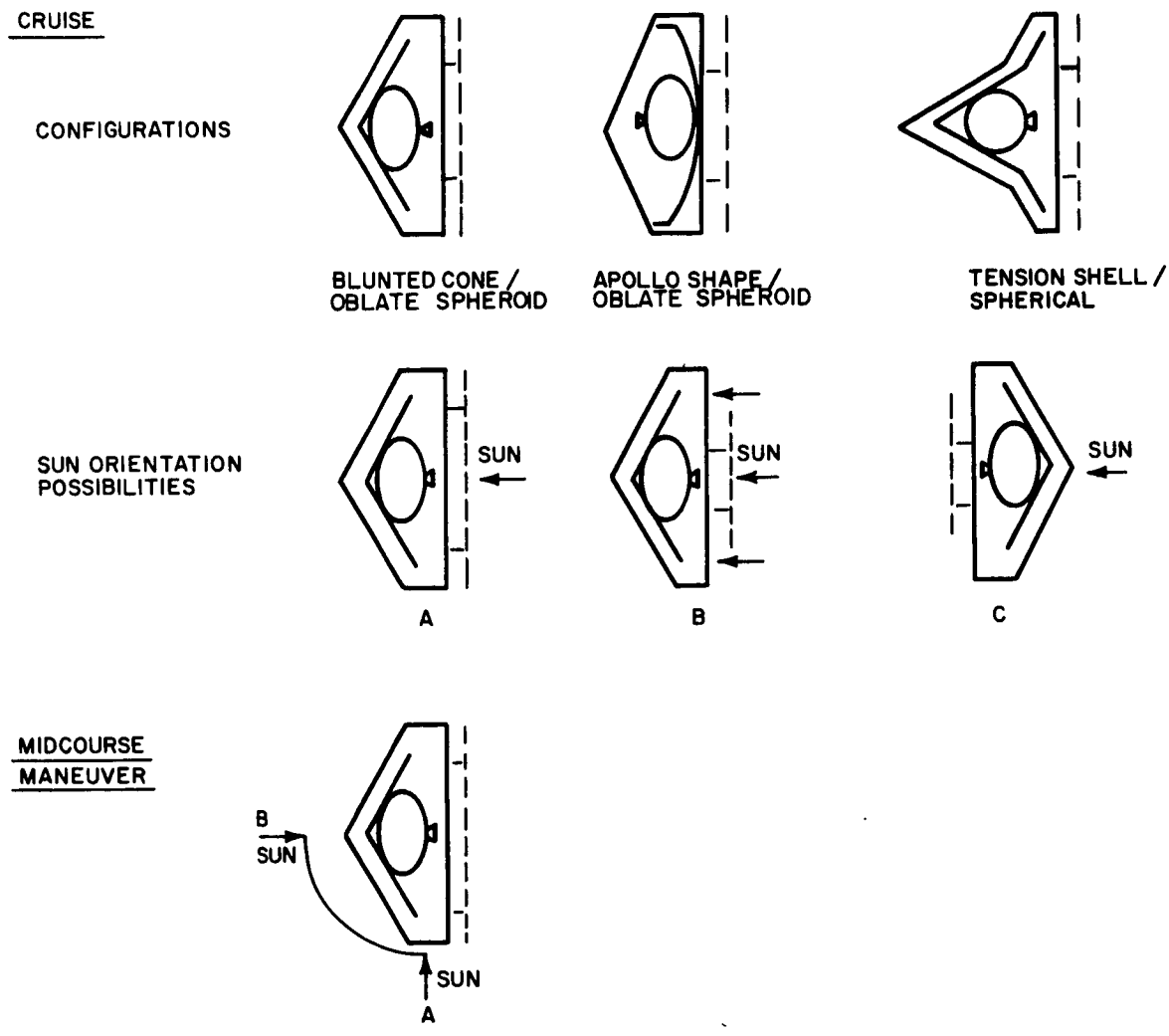

Figure 373 TYPICAL ENTRY SHELL ORIENTATION POSSIBILITIES RELATIVE TO THE SUN, CRUISE, AND MIDCOURSE MANEUVER

The effect of the afterbody and internal payload configuration was noted above.

The study revealed several problem areas anticipated for the flight capsule design and development. Among those are the urgency for exact definition of the thermal interface between the flight spacecraft and flight capsule; the need for mission definition required for the postseparation phase (sun orientation angles) and the difficulty in thermal control during the post-impact phase due to the absence of power in the landed capsule. Flight hardware development testing is required to ascertain stability of thermal control coatings and to define the various internal thermal resistances.

11.2 RESULTS AND DISCUSSION

An investigation was conducted of critical conditions which may arise during the mission sequence for the probe/lander flight capsule. The bulk of the study was conducted prior to the definition of the conceptual design and was therefore largely based on preliminary data; many assumptions had to be made with respect to the flight capsule and component packaging configurations. The results are presented in the order of the occurrence of mission phases. The geometry used in the heat flow and temperature determinations is shown in Figures 370, 371, and 372 for the blunted cone, Apollo shape and tension shell respectively. Design criteria and constraints have been previously shown in Table LXXXVII.

11.2.1 Cruise from Earth to Mars

The thermal balance of the flight capsule during the cruise phase is maintained by conductive and radiative heat exchange between the spacecraft and the sterilization canister base, in addition to sun impingement at the sterilization canister (base or lid), internal power provided for thermal control of critical components, and radiation to space from the sterilization canister.

The flight spacecraft/flight capsule thermal interface is difficult to define and is influenced by a variety of conductive and radiative heat-transfer-governing parameters. The assumptions which were actually made were discussed in paragraph 11.1.2. Long-duration sun impingement on the sterilization canister during cruise is possible in two cases (Figure 373). In one case, the flight capsule is permanently oriented away from the sun and totally or partially shaded by the spacecraft. In the other case, the capsule is permanently oriented toward the sun. From thermal control considerations, it appears that the first case is more favorable than the second case, especially for large flight capsule diameters. High solar heat fluxes near Earth tend to overheat critical payload components and may cause undesirably high thermal gradients in structural members.

Shown in Table LXXXVIII are temperatures which can be expected on a 180-inch diameter flight capsule (blunted cone/oblate spheroid, Figure 370 during cruise near Earth when the capsule is either totally or partially shaded by the spacecraft. The materials assumed are shown in Table LXXXIX. Maximum steady-state heat shield temperatures are 365 degrees for the partially shaded case and 25°F for the other case - a very significant difference. The corresponding battery temperatures are 175°F and 26°F. The battery maximum temperature limit is exceeded by 5°F in the first case, while some internal power is required in the second case to maintain the battery temperature. These results indicate that the overall entry vehicle temperature increases substantially with an increase of the area of the sterilization canister which is exposed to the sun. The high solar heat flux near Earth may cause overheating of critical components which would then require additional means for thermal control (e.g. radiation shielding on the sun-exposed area of the sterilization canister).

The effect of the sterilization canister on the flight capsule thermal balance during cruise is also of concern. Shown in Table XC are results for the tension shell 197-inch diameter entry vehicle with spherical capsule (Figure 372). It can be seen that high thermal gradients develop across the heat shield and impact attenuator during cruise near Earth without the sterilization canister lid and that the entry vehicle overall temperature level is reduced significantly. Lowest heat shield temperatures are -128°F versus -62°F near Mars for the cases of canister lid off and on respectively. Thus, early sterilization canister lid ejection is not advisable. The sterilization canister acts favorably as a radiation shield, raises the entry vehicle cruise temperature level, and reduces the temperature gradient across the entry vehicle during a midcourse maneuver.

A typical temperature history for the cruise phase is shown in Figure 367. All temperatures decrease rapidly from the launch temperature and assume essentially steady-state values within 4 days. The temperature of structural members is constantly decreasing as the flight spacecraft approaches Mars, while the battery is maintained at 60°F by power provided from the spacecraft. Additional internal power during cruise is required for all three entry vehicle configurations. Typical values of power required are 4.5 watts near Earth and 13 watts near Mars for the blunted cone/oblate spheroid (Table XCI), and 7 watts near Earth and 14 watts near Mars for the Apollo shape/oblate spheroid configuration (Figure 371 and Table XCII. The somewhat higher requirements in the latter case result from the fact that the landed payload is oriented towards outer space during cruise. It is concluded that the battery can be maintained within specified limits during the cruise phase by passive means (surface coatings) and internal power for these two shapes. As may be seen from Table XC, the tension shell would require more power as the battery tends to reach lower temperatures than in the other shapes without a power supply.

TABLE LXXXVIII

CRUISE NEAR EARTH AND NEAR MARS, EFFECT OF SPACECRAFT DIAMETER ON STEADY STATE TEMPERATURES
(Blunted cone 180-inch diameter entry shell with oblate spheroid capsule)

Structure or Component				Spacecraft 15 ft Dia(1)		Spacecraft 7 ft Dia(2)	
	Node Designated	α/ϵ	ϵ	Near Earth	Near Mars	Near Earth	Near Mars
Heat shield	1	5.0	0.05	+25	-44	+365	+198
	2	5.0	0.05	+19	-48	+372	+196
	3	5.0	0.05	+14	-50	+340	+175
	4	5.0	0.05	+ 5	-54	+248	+130
	5	5.0	0.05	+ 2	-54	+221	+116
Impact attenuator	6			+ 9	-52	+242	+125
Battery	7	-	-	+26	-41	+175	+ 76
Impact attenuator	8	-	-	+51	-28	+ 88	+ 13
Sterilization canister	9	5.0	0.05	-63	-100	+ 94	+ 18
	10	5.0	0.05	+13	-50	+271	+144
Comments on battery temperature				Too cold	Too cold	Too warm	Within limits

(1) Lander completely shaded by spacecraft

(2) Lander partially shaded by spacecraft, capsule facing spacecraft

Note: No internal power to battery

TABLE LXXXIX

MATERIAL REFERENCE FOR THERMAL CONTROL ANALYSIS

	Blunted Cone		Apollo Shape		Tension Shell	
	Material	Thickness	Material	Thickness	Material	Thickness
Heat Shield	Si-Cork	0.5	Si-Cork	0.5	Purple blend	0.125
Internal face sheet	Beryllium	0.02	Beryllium	0.02	Fiberglass	0.125
External face sheet	Beryllium	0.02	Beryllium	0.02	----	----
Honeycomb structure	St. Steel	1.0	St. Steel	1.0	----	----
Steriliz. canister	Aluminum	0.07	Aluminum	0.07	Aluminum	0.07
Impact attenuator (1)	(2)	15.0	(2)	15.0	(2)	15.0

(1) Spherical and oblate Spheroid concept.

(2) Fiberglass Honeycomb/Polyurethane foam.

All dimensions in inches

TABLE XC

CRUISE NEAR EARTH AND NEAR MARS STEADY-STATE TEMPERATURES
(Tension shell 197-inch diameter entry shell with spherical capsule)

Structure or Component				Without Sterilization Canister				With Sterilization Canister	
				Near Earth		Near Mars		Near Earth	Near Mars
	Node Designated	a/ϵ	ϵ	No Int. Heat	Int. Heat	No Int. Heat	Int. Heat	Int. Heat	Int. Heat
Heat shield	1	5.0	0.05	+ 49	+49	-28	-28	+51	-29
Heat shield	2	5.0	0.05	+ 46	+46	-31	-30	+50	-29
Heat shield	3	5.0	0.05	-139	-109	-161	-112	-47	-55
Heat shield	4	5.0	0.05	-154	-126	-175	-128	-54	-62
Impact attenuator	5	-	-	-129	-98	-152	-101	-42	-50
	6	-	-	+51	+55	-26	-22	+53	-26
Battery	7	-	-	-37	+56	-84	+52	+51	+55
Sterilization canister Base	8	-	-	+60	+60	-20	-20	+60	-20
Sterilization canister lid	9	5.0	0.05	-	-	-	-	-148	-156

TABLE XCI

CRUISE NEAR EARTH AND NEAR MARS STEADY-STATE TEMPERATURES
(Blunted cone 180-inch diameter entry shell with oblate spheroid capsule)

Structure or Component				No Internal Power		Internal Power(1)	
	Node Designated	a/ϵ	ϵ	Near Earth	Near Mars	Near Earth	Near Mars
Heat shield	1	5.0	0.05	+25	-44	+26	-41
Heat shield	2	5.0	0.05	+19	-48	+20	-42
Heat shield	3	5.0	0.05	+14	-50	+16	-43
Heat shield	4	5.0	0.05	+ 5	-54	+ 9	-39
Heat shield	5	5.0	0.05	+ 2	-54	+ 7	-38
Impact attenuator	6	-	-	+ 9	-52	+13	-33
Battery	7	-	-	+26	-41	+58	+53
Impact attenuator	8	-	-	+51	-28	+58	0
Sterilization canister	9	5.0	0.05	-63	-100	-63	-100
Sterilization canister	10	5.0	0.05	+13	-50	+13	-50
Sterilization canister base	11	-	-	+60	-20	+60	-20

(1) Internal power to battery: 4.5 watts near Earth, 13 watts near Mars, required to maintain the temperature within specified limits.

TABLE XCII

CRUISE NEAR EARTH AND NEAR MARS STEADY-STATE TEMPERATURE
(Apollo shape 180-inch diameter entry shell with oblate spheroid capsule)

Structure or Component				No Internal Power		Internal Power (1)	
	Node Designated	α/ϵ	ϵ	Near Earth	Near Mars	Near Earth	Near Mars
Heat shield	1	5.0	0.05	+28	-39	+29	-34
	2	5.0	0.05	+31	-37	+33	-31
	3	5.0	0.05	+32	-38	+34	-29
	4	5.0	0.05	+34	-36	+40	-22
	5	5.0	0.05	+35	-35	+41	-20
Impact attenuator	6	-	-	+33	-36	+41	-18
Battery	7	-	-	+ 7	-52	+60	+60
Impact attenuator	8	1.6	-	-27	-73	-14	-44
Sterilization canister lid	9	5.0	0.05	+ 6	-54	+ 7	-51
	10	5.0	0.05	-38	-82	-35	-75
Sterilization canister base	11	-	-	+60	-20	+60	-20

(1) Internal power to battery: 7 watts near Earth, 14.2 watts near Mars, required to maintain the temperature within specified limits.

Note: Lander completely shaded by spacecraft, heat shield facing spacecraft.

The effect of a midcourse maneuver on the capsule thermal balance is of interest especially for the case near Earth with high solar heat flux impinging on the canister lid. A typical case is shown in Figure 374. Two extreme fixed flight capsule orientation cases relative to the sun are considered. These are shown as cases "A" and "B" in Figure 374. It can be seen that the entry vehicle overall thermal balance is not affected appreciably by the rapid transient temperature rise of the thin-wall sterilization canister. Landed payload temperatures remain within tolerable limits. The canister lid can reach temperatures as high as 500°F and high gradients across the lid are developed in case A, since one-half of the canister is steadily exposed to the sun, while the other half is exposed to space. Thus the sterilization canister acts favorably as a radiation shield and reduces the temperature gradient across the entry vehicle during a midcourse maneuver. Local heating of the entry shell, however, may occur if the planetary vehicle remains in a fixed attitude for an extended time period and if the canister lid thermal coating displays a high α/ϵ value ($\alpha/\epsilon \cong 5.0$). If, for the final design, a hot spot on the shield were observed, the coating would have to be changed to a lower α/ϵ value while retaining a low emittance.

11.2.2 Postseparation

The entry shell thermal environment during the postseparation phase follows a relatively simple cycle. Solar heat is absorbed by areas exposed to the sun (projected areas), heat is radiated from areas exposed to space (total areas) and none, or very limited, internal power is available. Initial temperatures of the entry-shell structure and components are those attained at the end of cruise near Mars, while the temperature of the battery is maintained around 60°F (if not warmed up prior to separation). One major problem in analyzing the postseparation phase of a particular entry-vehicle configuration is the wide range of possible orientations relative to the sun as shown in Figure 375.

The range of possible ZAP-angles is from 30 to 140 degrees (ZAP angle is defined as the angle between the Mars-sun vector and the lander approach asymptote). Considering a range of thrust application angles from 15 to 90 degrees, the total span of δ- angles is 170 degrees, where δ- angle is defined as the angle between the Mars-sun vector and the negative entry-vehicle longitudinal axis. It is not possible to thermally control a vehicle over such a wide span of δ -angles with one coating system since the ratio of projected area to total area is a function of δ variation and the thermal balance is governed by this ratio. In order to determine basic thermal control requirements, two extreme cases were analyzed for a spinning entry vehicle. In case A the sun was impinging on the entry shell at an angle of 90 degrees relative to the main axis; in case B the sun was parallel to the main axis, impinging on the entry shell at the payload capsule. A coating system selection was attempted so that

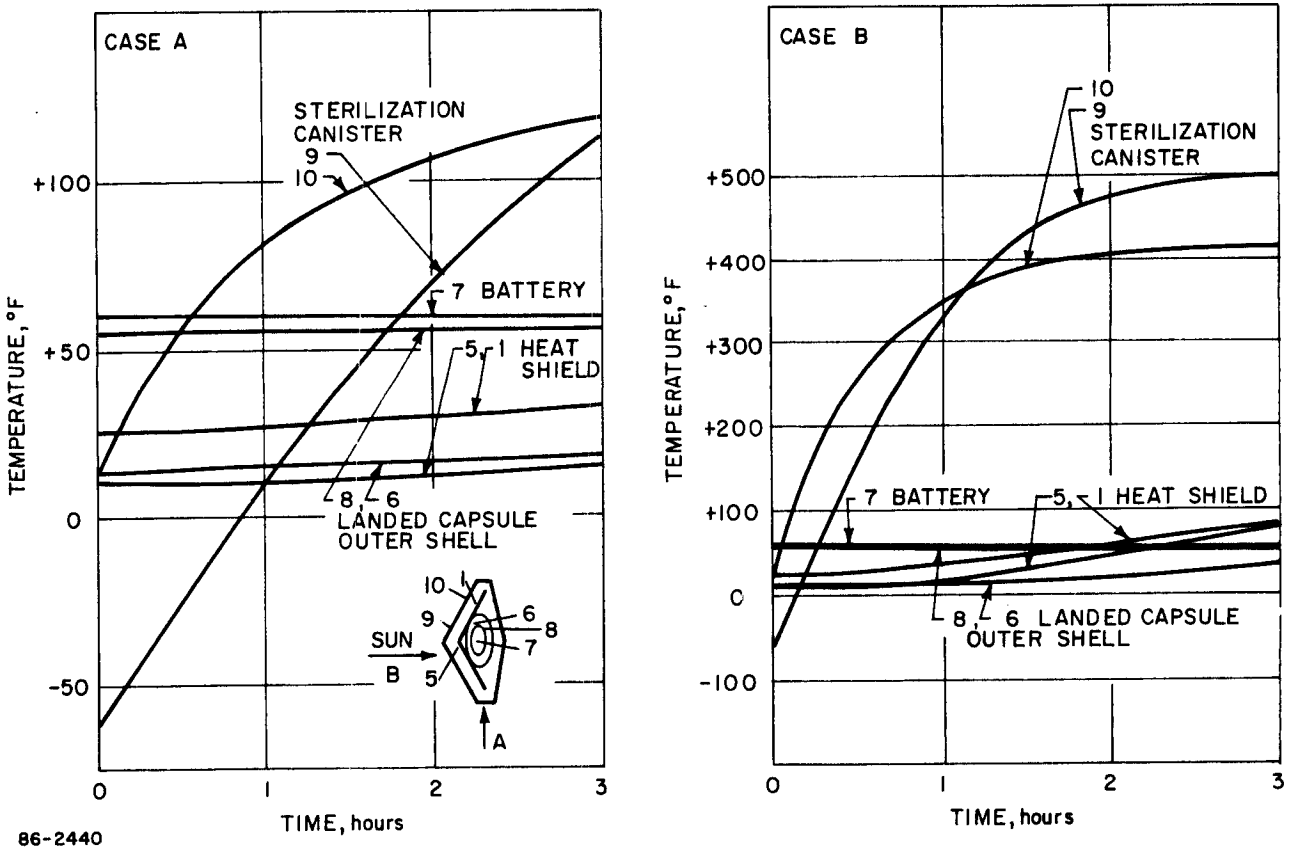

Figure 374 BLUNTED CONE 180-INCH DIAMETER ENTRY SHELL WITH OBLATE SPHEROID CAPSULE, MIDCOURSE MANEUVER NEAR-EARTH TEMPERATURE HISTORY

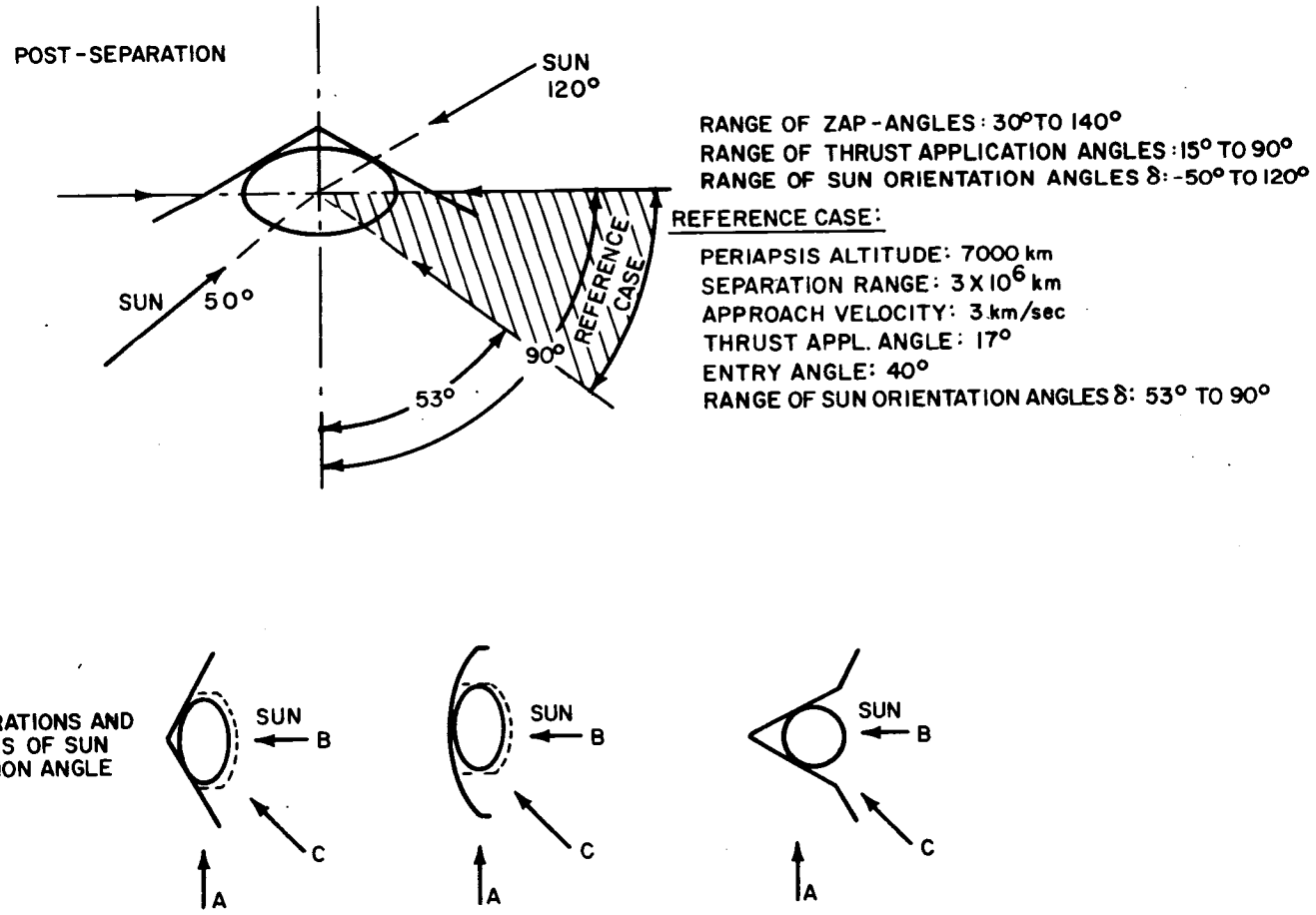

Figure 375 TYPICAL ENTRY SHELL ORIENTATION POSSIBILITIES RELATIVE TO THE SUN, POSTSEPARATION

the heat shield temperature would not exceed maximum allowable limits before entry and the battery temperature would remain within specifications without additional heat for at least one of the two cases under consideration. A typical case is shown in Table XCIII and Figure 376. All temperatures are essentially increasing in case B and decreasing in case A. Steady-state temperatures are reached in about 24 hours. The battery temperature could be maintained within specifications in case B; in Case A, however, additional internal power would be required, which is a very undesirable situation because of the heavy weight penalty.

The maximum heat shield temperature is around 230°F for case B. To reduce heat shield temperatures, desirable for the purpose of heat shield weight reduction, a reduction of the α/ϵ ratio of the heat shield coating system and an increase of the α/ϵ ratio of the afterbody coating system would be required in order to maintain the temperature balance for a particular orientation relative to the sun.

This problem area was also investigated for other entry shell configurations (Tables XCIV and XCV. Although case A tended to produce low temperatures without addition of power for all shapes, the tension shell presented the least problem and thus would have required the least power expenditure. Furthermore, it appeared feasible to select coatings for the tension shell and Apollo for case A which would have raised the battery temperature to acceptable levels. Only addition of power or warmup before separation (and superinsulation) alleviated the problem for the blunt cone. However, coatings which would be acceptable for case A would result in an overheat condition when applied in case B. Thus for any of the shapes, one has to define the likely sun orientation angles or use the approach suggested above for the blunt cone.

With additional internal heat (20-watts blunted cone/oblate spheroid configuration, 13.2-watts Apollo shape/oblate spheroid configuration), cases A and B could be satisfied with one coating system. A semi-active (shutter) thermal control system may solve both cases A and B for the Apollo shape and tension shell configuration. The ratio of projected area to total area for the blunted cone is so unfavorable that a shutter system could not control this configuration. In any case such an approach results in large weight penalties. At this stage of the design evolution the blunt cone was tentatively selected (from other system considerations) for further evaluation. Therefore a reference case (design and mission specification) was selected for coating system recommendation over a range of δ-angles (53 to 90 degrees, Figure 375) for the blunted cone/oblate spheroid configuration with a metallic afterbody. Preliminary investigations indicated that the reference configuration can be controlled thermally over the anticipated range of δ - angles by the means suggested previously (warmup and superinsulation). This approach possibly may apply to the 0-90 degree

TABLE XCIII

POST-SEPARATION STEADY-STATE TEMPERATURES, EFFECT OF INTERNAL POWER

(Blunted cone 180-inch diameter entry shell oblate spheroid capsule)

Structure or Component				Afterbody, nonmetallic coating (1)		
				Case A		Case B
	Node designated	α/ϵ	ϵ	No Heat	Heat (2)	No Heat
Heat shield	1	5.0	0.05	+8	+8	+229
	2	5.0	0.05	+8	+10	+224
	3	5.0	0.05	+13	+17	+211
	4	5.0	0.05	+25	+35	+105
	5	5.0	0.05	+27	+38	+76
Impact attenuator	6	-	-	+15	+32	+103
Battery	7	-	-	-78	+60	+60
Comments on battery temperature				Too low	Within limits	Within limits

(1) $\alpha/\epsilon = 1.0, \quad \epsilon = 0.8$

(2) 20 watts required

Case A: Sun impinging normal to the entry shell main axis

Case B: Sun impinging parallel to the entry shell main axis (on the afterbody)

Note: Internal power to battery thermostatically cut off at + 60°F.

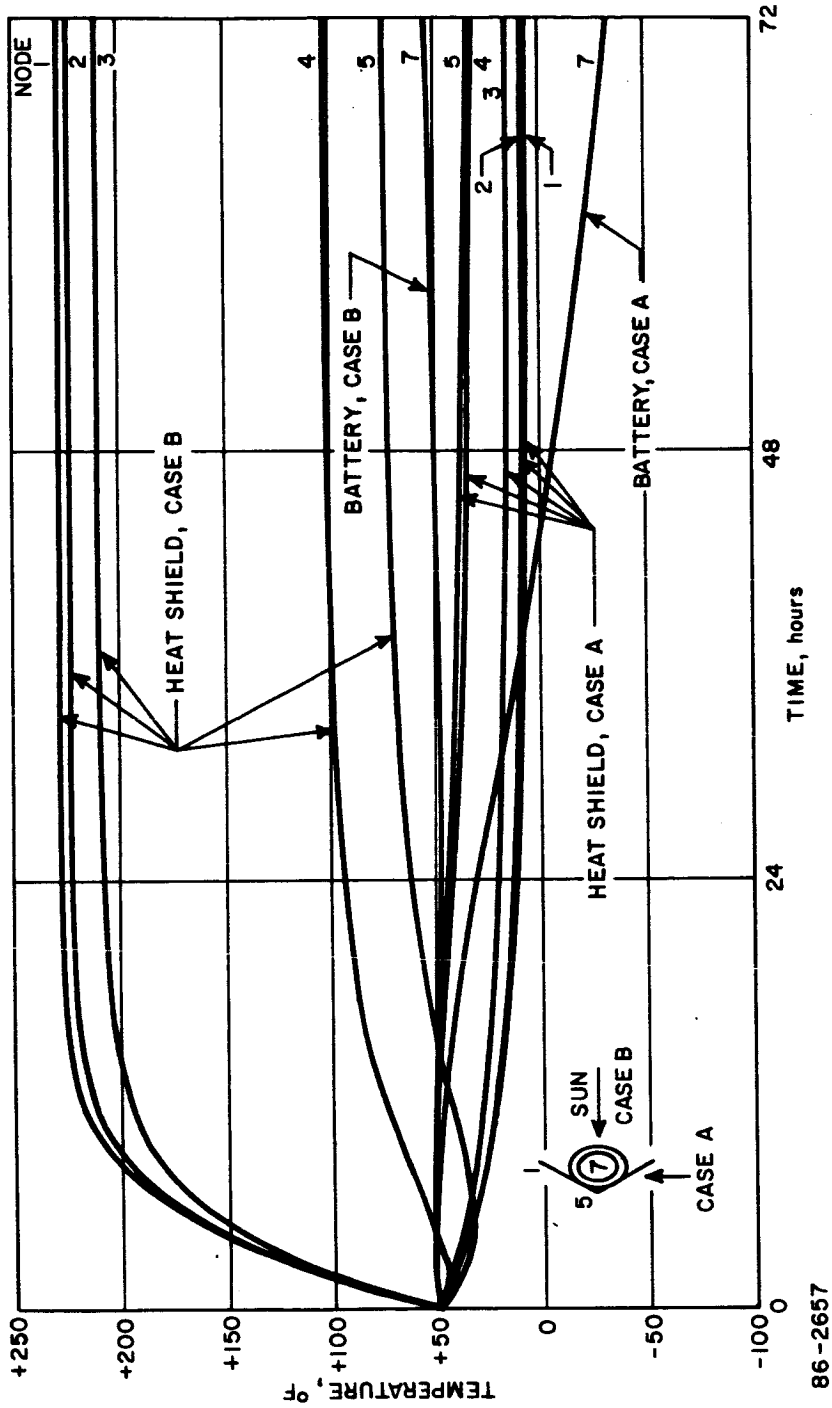

Figure 376 BLUNTED CONE 180-INCH DIAMETER ENTRY SHELL WITH OBLATE SPHEROID CAPSULE, POSTSEPARATION TEMPERATURE HISTORY

TABLE XCIV

POST-SEPARATION STEADY-STATE TEMPERATURES, EFFECT OF INTERNAL POWER
(Apollo shape 180-inch diameter entry shell with oblate spheroid capsule)

Structure or Component	Node designated	α/ϵ	ϵ	Afterbody, Non-metallic Coating(1)		
				Case A		Case B
				No Heat	Heat (2)	No Heat
Heat shield	1	5.0	0.05	+38	+40	+ 73
	2	5.0	0.05	-30	-26	+214
	3	5.0	0.05	-41	-33	+220
	4	5.0	0.05	- 2	+19	+110
	5	5.0	0.05	- 2	+17	+ 83
Impact attenuator	6	-	-	+23	+43	+117
Battery	7	-	-	-39	+60	+ 58
Comments on battery temperature				Too low	Within limits	Within limits

(1) $\alpha/\epsilon = 1.0, \epsilon = 0.8$
(2) 13.2 watts required.
Case A: Sun impinging normal to the entry shell main axis
Case B: Sun impinging parallel to the entry shell main axis (on the afterbody)

TABLE XCV

POST-SEPARATION TEMPERATURES AFTER 4 DAYS AND 20 DAYS
(Tension shell 197-inch diameter entry shell with oblate spheroid capsule)

Structure or Component	Node Designated	Case A				Case B			
		a/ϵ	ϵ	4 days	20 days	a/ϵ	ϵ	4 days	20 days
Heat shield	1	5		-14	-14		0.05	+99	+99
	2	5		+83	+83		0.05	+93	+93
	3	5		+151	+149		0.05	-29	-26
	4	5		+156	+154		0.05	-238	-250
Impact attenuator	5	-	-	+149	+148	-	-	+21	+34
	6 (1)		0.5	-123	-124	0.2		+183	+186
Battery	7	-	-	+25	+12	-	-	+84	+109
Comments on battery temperature				Too Low				Within Limits	

(1) Afterbody
Case A: Sun impinging normal to the entry shell main axis
Case B: Sun impinging parallel to the entry shell main axis (on the capsule)
Note: Temperatures reflect the result of a different coating system in Case A and Case B.

range also. It was concluded that the postseparation phase presents the most difficult control problem in the absence of a heat source in the capsule itself for cases of unfavorable δ - angles.

Because of the weight penalties associated with inclusion of afterbodies into the design, it is necessary to ascertain their desirability and importance from a thermal control point of view. A metallic or metal-coated afterbody acts as an internal radiation shield during cruise and reduces the heat transfer between the sterilization canister and entry vehicle to some extent. The effect is small and it can be compensated for by additional power from the spacecraft. The situation, however, is quite different during the postseparation phase. The entry vehicle temperature depends now on areas exposed to sun or outer space and surface coating properties only. An afterbody is therefore desirable, since it allows postseparation temperature control of the landed capsule over a wide range while the coating properties of the landed capsule outer shell remain constant at a value best suited for the parachute and post-impact phase. This effect is shown in Table XCVI and Figure 377. The temperature of the battery is controlled within a range of 82°F in case A and 148°F in case B by purely passive means by varying α/ϵ from 1.0 to 5.0 for the cases with afterbody. This result also points out the need for close control of tolerances in actual coatings, since deviations in coating optical properties can have a pronounced effect on the system's thermal balance.

11.2.3 Entry

The interactions, effects, and implications of the temperatures at the onset of entry upon heat shield performance were discussed in Section 8.0 of this book. The temperatures in the post-entry phase related to the landed payload have been demonstrated to impose negligible burden when the skin of the impact attenuator was permitted an average temperature rise of 125°F during the entry phase. The temperature of the impact attenuator layer adjacent to the skin increased by 3°F only; the internal payload temperature increased by 0.5°F as a result of 65-watts internal heat dissipation. These results were for a maximum entry time of 187 seconds. The lack of proper characterization of the thermophysical properties for the heat shield (discussed in Section 8.0) precluded detailed predictions of the temperature rise in the skin of the impact attenuator. However, it appears to be quite feasible to allow an average temperature rise at this location in the order of 125°F. Hence, it is anticipated that no critical problem will arise in this area.

11.2.4 Parachute Descent

A heat balance on the landed payload during parachute descent has to account for the following environmental conditions. The capsule loses

TABLE XCVI

POST-SEPARATION STEADY-STATE TEMPERATURES, EFFECT OF AFTERBODY
(Blunted cone 180-inch diameter entry vehicle with oblate spheroid capsule)

Structure or Component	Node Designated	No Afterbody				Afterbody Metallic Coating				Afterbody, Non-Metallic Coating			
		α/ϵ	ϵ	Case A	Case B	α/ϵ	ϵ	Case A	Case B	α/ϵ	ϵ	Case A	Case B
Heat shield	1	5.0	0.05	+7	+229	5.0	0.05	+8	+229	5.0	0.05	+8	+229
	2	5.0	0.05	+8	+224	5.0	0.05	+9	+224	5.0	0.05	+8	+224
	3	5.0	0.05	+14	+212	5.0	0.05	+16	+213	5.0	0.05	+13	+211
	4	5.0	0.05	+28	+109	5.0	0.05	+33	+116	5.0	0.05	+25	+105
	5	5.0	0.05	+30	+81	5.0	0.05	+36	+89	5.0	0.05	+27	+76
Impact attenuator	6	-	-	+20	+112	-	-	+30	+126	-	-	+15	+103
Battery	7	-	-	-48	+120	-	-	+4	+208	-	-	-78	+60
Impact attenuator	8 (1)	1.0	0.8	-139	+131	5.0	0.05	-31	+320	1.0	0.8	-202	+7
Comments on battery temperature				Too Low	Too high			Too Low	Too high			Too Low	Too high
Battery, temperature difference (Case A versus Case B)				168°				204°F				138°F	

(1) Afterbody
Case A: Sun impinging normal to the entry shell main axis
Case B: Sun impinging parallel to the entry shell main axis (on the landed capsule/afterbody

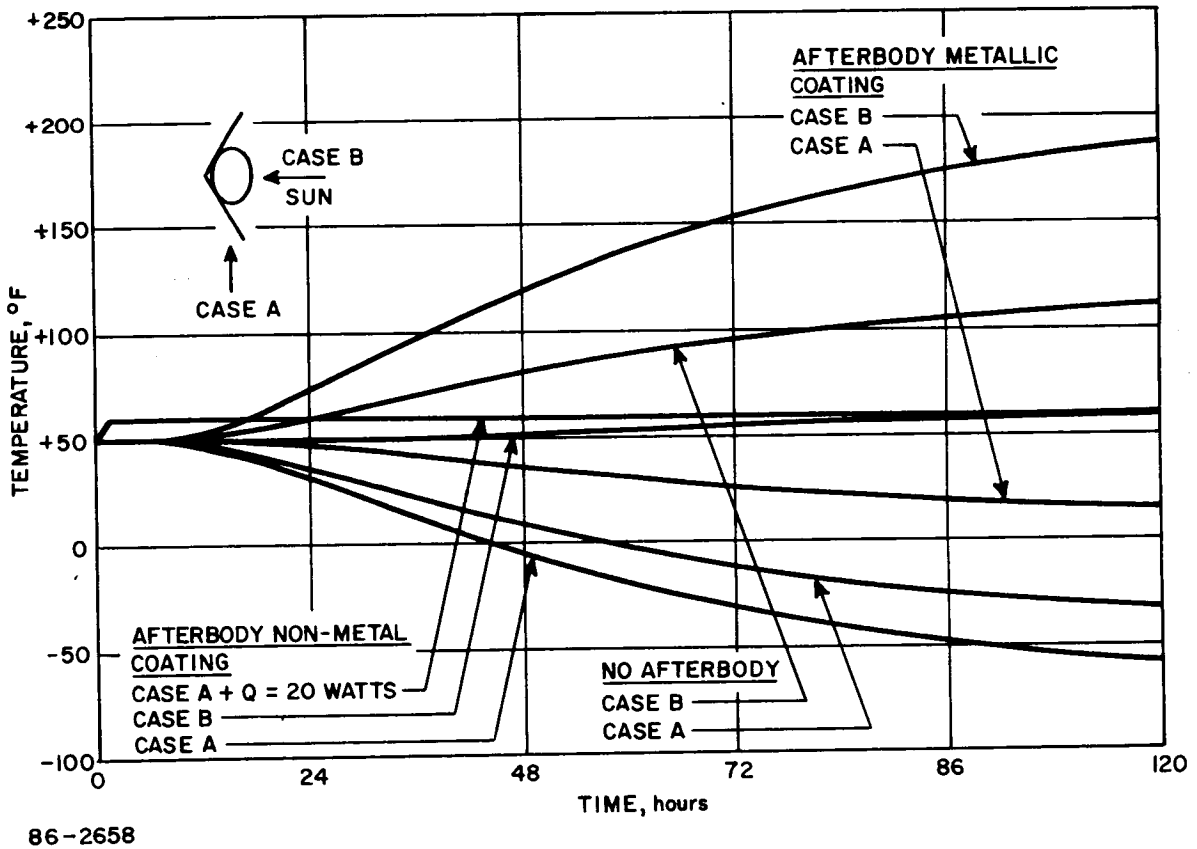

Figure 377 BLUNTED CONE 180-INCH DIAMETER ENTRY SHELL WITH OBLATE SPHEROID CAPSULE, EFFECT OF AFTERBODY ON POSTSEPARATION TEMPERATURES

heat by forced convection cooling and internal heat is dissipated from the internal payload system. Initially, the landed payload is at the postseparation, steady-state temperature, with the exception of the outer layers of the impact attenuator which increased in temperature during entry. The payload temperature did not change appreciably during entry as discussed before. A temperature history for the most unfavorable case, a full open parachute descent in Model 2 atmosphere over a descent time of 850 seconds, is shown in Figure 378. The temperature of the outer impact attenuator layer decreases by around 90°F. The internal payload temperature, however, is not effected by the external environment and increases slightly due to internal power dissipation. Thus, it appears feasible to control initial internal payload temperatures after impact by heat addition before flight spacecraft separation.

11.2.5 Post Impact

A post-impact thermal balance of the landed capsule has to take into account a variety of possible environmental conditions. For this particular study, two diurnal temperature profiles were considered: a lower profile from -22°F to -202°F and an upper profile from -110°F to + 71°F (References 86 and 87). The upper profile is within the range suggested in Reference 88. Each profile was approximated by a sine curve from dawn to dusk and a constant nightime temperature. The selected landing site was Solis Lacus, the time of landing 8:00 a.m., local sun time. Internal power is dissipated at a rate of 124 watts for 3.5 hours after impact, 4 watts for the following 23 hours followed by one hour of 124 watts.

A variety of possible landed capsule environmental conditions after impact are shown in Figure 379. The essential difference between the two analyzed configurations, spherical and oblate spheroid, (Figure 380) is that a metallic coating can be tolerated over the oblate spheroid shape while a nonmetallic coating is mandatory for the spherical shape to satisfy the communications antenna requirements. The spherical capsule is therefore losing its energy at a high rate through thermal radiation from its highly emitting surface. Internal superinsulation may improve this undesirable situation and temperature control by additional internal power may then be feasible. The oblate spheroid configuration, in contrast, can be well controlled thermally by application of a low emitting metallic surface coating. A dielectric coating, however, is required in the area of the antenna slot. A temperature history is shown in Table XCVII and Figure 381 for various conditions. Partial or non-ejection of the impact attenuator is desirable for the sphere. It is neither desirable nor detrimental for the oblate spheroid configuration. In any case, it appears that raising of the internal payload temperature to the highest possible level before separation from the spacecraft, together with a well-designed

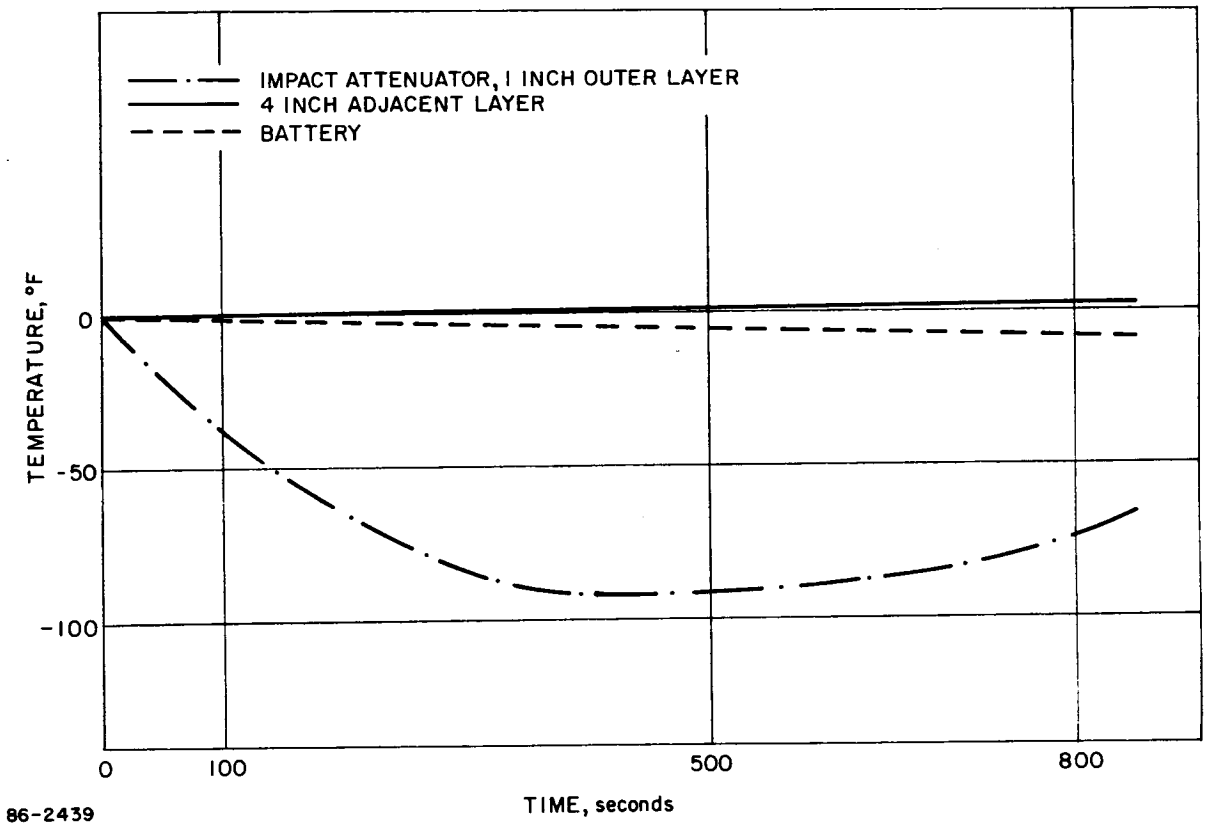

Figure 378 TEMPERATURE HISTORY OF LANDED PAYLOAD DURING PARACHUTE DESCENT

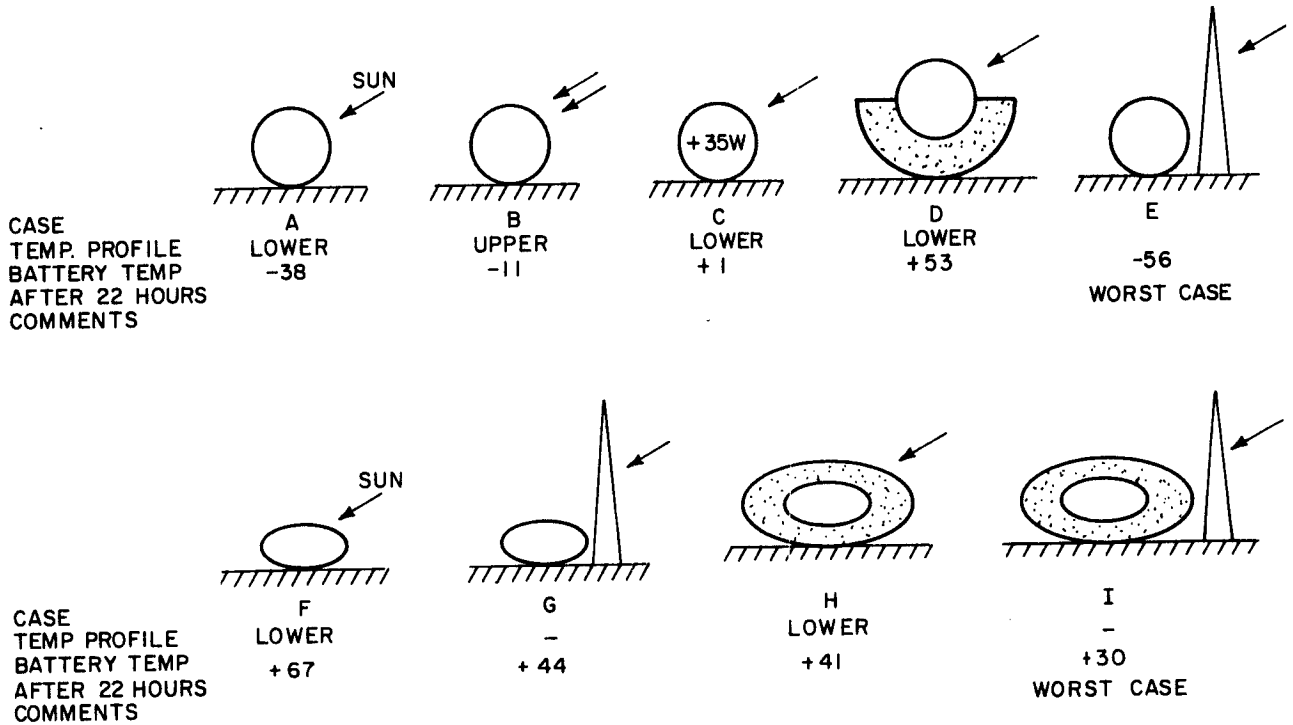

Figure 379 POST-IMPACT CASES CONSIDERED IN ANALYSIS

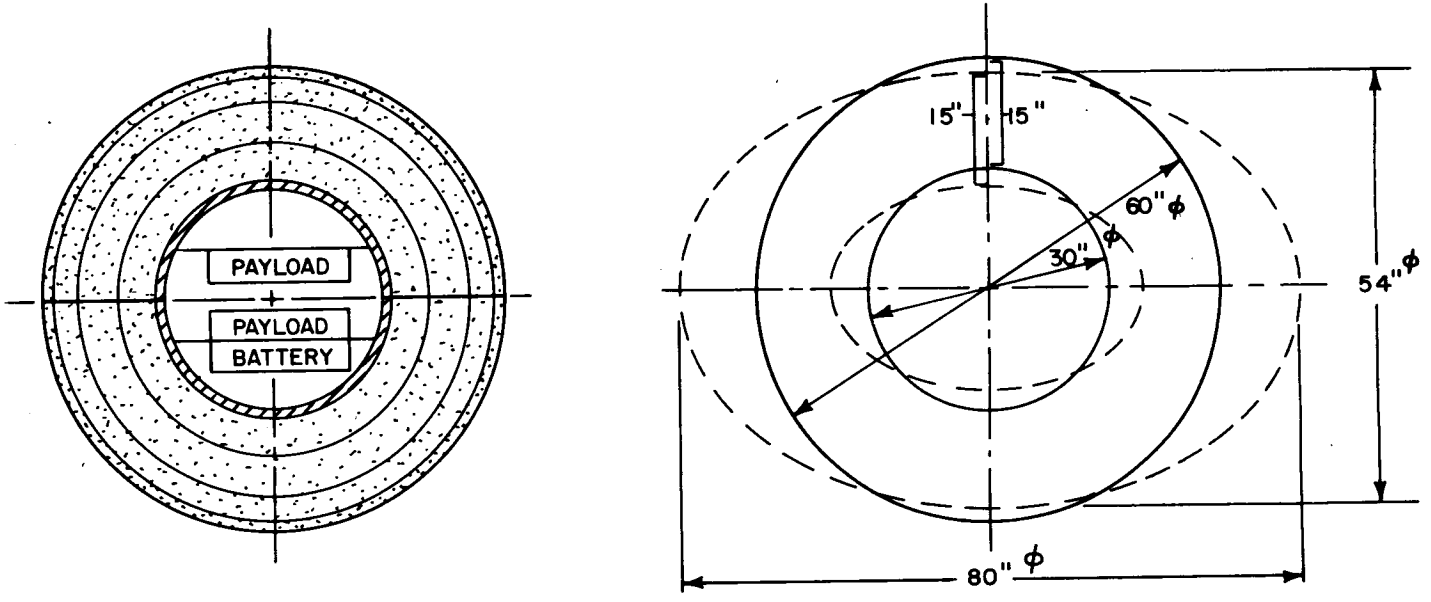

SPHERICAL CONCEPT

COMPARISON SPHERICAL / OBLATE SPHEROID

86-2437

Figure 380 REFERENCE CONCEPT SPHERICAL AND OBLATE SPHEROID CAPSULE

TABLE XCVII

POST-IMPACT BATTERY TEMPERATURE HISTORIES

Case	A	B	C	D	E
Configuration	Sphere	Sphere	Sphere	Sphere	Sphere
Temp. Profile	Lower	Upper	Lower	Lower	No Sun
Impact Attenuator	Off	Off	Off	Lower on	Off
Internal Heat	No	No	35W (Battery)	No	No
Comments					Worst Case
8 A. M.	+50	+50	+50	+50	+50
12 noon	+43	+54	+43	+58	+40
6 P. M.	+30	+56	+30	+71	+17
12 Midnight	- 3	+23	+21	+70	-23
6 A. M.	-38	-11	+ 1	+53	-56
12 noon	-58	-29	-34	+43	-82
6 P. M.	-62	-32	-46	+45	-99

TABLE XCVII (Concl'd)

Case	F	G	H	I
Configuration	Oblate Sph.	Oblate Sph.	Oblate Sph.	Oblate Sph.
Temp. Profile	Lower	No Sun	Lower	No Sun
Impact Attenuator	Off	Off	On	On
Internal Heat	No	No	No	No
Comments				Worst Case
8 A. M.	+50	+50	+50	+50
12 Noon	+83	+76	+78	+75
6 P. M.	+87	+65	+68	+63
12 Midnight	+79	+54	+57	+48
6 A. M.	+67	+44	+51	+30
12 Noon	+72	+42	+32	+19
6 P. M.	+80	+40	+27	+ 9

Note: +50 °F assumed before impact for all Nodes.
Convection effects not considered.

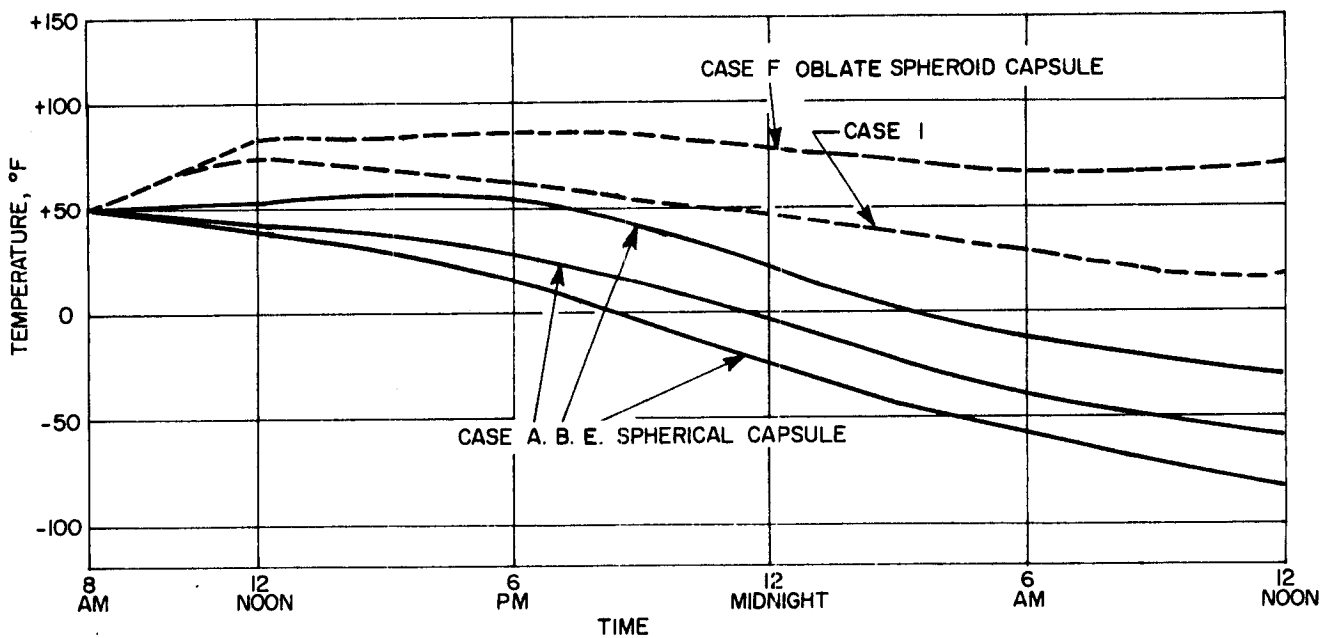

Figure 381 POST-IMPACT PAYLOAD TEMPERATURE HISTORY

and insulated capsule and some additional internal power, thermostatically controlled, makes temperature control possible for one diurnal cycle without the necessity of more complicated thermal control devices. More detailed studies, however, are required before final conclusions can be drawn, since this study did not include the effect of forced convection associated with surface winds.

11.2.6 Comparison of Thermal Control Requirements for Various Concepts and Shapes

During cruise, slightly lower power requirements have been established for the blunted cone than for the Apollo shape. The tension shell battery temperatures were the lowest when no power was supplied, thus it would appear that it would cause the highest power demand. No preference should be given to any configuration if it were assumed that the relatively slight amount of excess power required is available. The power requirement may, of course, be much higher if more unfavorable flight spacecraft/flight capsule interface assumptions are made.

Comparing the postseparation mission phase, it was concluded that the blunted cone concept is inferior to the other two because of its small ratio of projected area to total area when exposed to the sun under an unfavorable orientation angle. This problem can be overcome, however, by sufficient insulation and payload preheating before capsule separation from the spacecraft. The most favorable area ratio is displayed by the tension shell. This, together with the fact that the extremes of sun orientation angles result in less dissimilar coating requirements, indicates the preference for the tension shell. Comparing the two payload configurations, it was concluded that the oblate spheroid capsule is far superior to the spherical capsule because of its low emittance which makes it less prone to environmental variations.

11.2.7 Problem Areas

The preceeding study indicated several areas where information is needed and where problems may be anticipated.

1. Flight Spacecraft/Flight Capsule Thermal Interface -- Exact definition of the flight spacecraft/flight capsule thermal interface is mandatory for the establishment of accurate temperature histories and power requirements during cruise.

2. Midcourse Maneuver -- Sterilization canister lid coating must be carefully selected to avoid heat shield local hot spots.

3. Postseparation Sun Exposure -- Entry vehicle orientation relative to the sun during the critical postseparation phase is a function of the selected mission and must be clearly defined for systems optimization.

4. Postseparation and Post-Impact Survival Insurance

a. Payload survival after impact requires highly efficient insulation as well as sufficient power available from the spacecraft to raise the payload temperature to the maximum allowable level before separation.

b. Survival after impact depends to a large extent on environmental parameters (atmosphere, terrain model, etc.) and more accurate information is necessary to increase the payload post-impact operation reliability.

In addition, the stability of the selected coatings will have to be ensured to survive all the environmental conditions in flight as well as the decontamination and dry-heat sterilization cycles.

12.0 THERMAL CONTROL ANALYSIS - PROBE, ENTRY FROM ORBIT

12.1 INTRODUCTION AND SUMMARY

12.1.1 System Description

The recommended thermal control system is shown in Figure 382 together with the flight spacecraft/flight capsule (FS/FC) interface configuration and characteristics used in the design and performance studies. The system consists of low emittance coatings (ϵ = 0.05 external, ϵ = 0.10 internal) on the sterilization canister lid surfaces as well as (ϵ = 0.05) on the primary heat shield and on both faces of the sterilization canister base facing the afterbody and spacecraft. The surfaces of the secondary heat shield and the afterbody are uncoated since the solar absorptance (α) and infrared emittance (ϵ) if the heat shield material surface (or of a selected sealer/paint) are acceptable from thermal control considerations thus simplifying the development and manufacturing effort. Heating elements required to maintain the heat shield temperature above a specified minimum are imbedded in the heat shield substructure. Payload modules requiring thermal control are isolated from the structure and those requiring heat either to maintain minimum allowable temperatures during cruise and Mars orbit or to be warmed up to their minimum operative temperatures prior to separation contain heating elements. The actual power supplied to the components will be regulated by thermostatic controls.

12.1.2 Requirements, Constraints, and Assumptions

The objective of this study was first to define the general thermal control requirements of the entry vehicle and sterilization canister and then to design and evaluate the specific thermal control system for the application. This included selection of coatings, determination of power requirements during the various mission sequences and conduct of a performance analysis for a selected reference case (design and typical mission). It was not attempted to design for internal thermal control of components; these were treated as "black boxes" of known mass and internal heat dissipation. The decontamination and sterilization phase is of concern, but only in the sense of the thermal control system surviving it rather than from a functional standpoint. It is recommended, however, that heaters integrated for thermal control purposes also be used during the sterilization cycle.

The theoretical analysis background for this study has been presented in Section 10.0.

General requirements on the thermal control system have been outlined in paragraph 11.1.1 and are applicable to the entry-from-orbit entry vehicle version as well. Specific thermal control requirements imposed on the

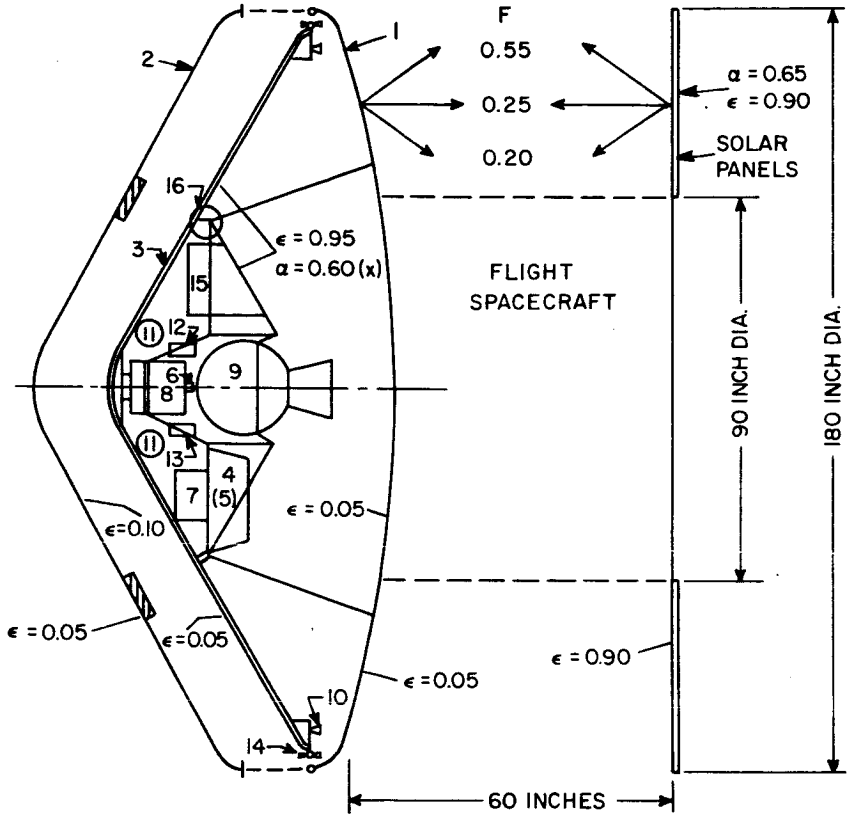

1 CANISTER BASE
2 CANISTER LID
3 ENTRY SHELL
4 TELECOMMUNICATIONS AND POWER MODULE (2)
5 INSTRUMENTATION MODULE
6 ACCELEROMETERS (3)
7 PENETROMETERS (4)
8 TELEVISION
9 ΔV PROPULSION
10 ACS REACTION NOZZLES (12)
11 ACS COLD GAS TANK (2)
12 ACS ELECTRONICS
13 ACS SENTRY GYRO
14 TVC REACTION SUBSYSTEM (4)
15 PARACHUTE
16 ENTRY SHELL SEPARATION MECHANISM
(x) PURPLE BLEND, UNCOATED

86-2660

Figure 382 REFERENCE DESIGN AND RECOMMENDED THERMAL CONTROL SYSTEM

system are to ensure that the disturbance to the spacecraft after entry vehicle separation is minimized and that thermal control is maintained until spacecraft separation with a reasonable amount of power from the spacecraft and without external power during postseparation. Specific reference design conditions and requirements are outlined in detail in Table XCVIII. Assumptions made in regard to the flight spacecraft/ flight capsule interface (see also paragraph 11.1.2) are of a critical nature for proper design and performance evaluation. Both interfaces are mutually affected and the relationship between the various capsule temperatures, power and coating requirements are completely governed by interface parameters as shown in paragraph 12.3.1.1. Because of the absence of specific information, certain assumptions had to be made either in regard to the interface geometry and configuration or its thermodynamic state. Several alternatives were studied, and the first approach (geometry and configuration) based on data published in the literature (Reference 89) was taken and shown to be conservative, resulting in low temperatures for critical components and the heat shield. Consequently, a relatively high power requirement was established.

12.1.3 Performance Summary

The performance of the selected thermal control system for the reference capsule design and typical reference mission sequence is summarized in Table XCIX and Figure 383.

The performance studies for the system were made in several steps. First, the power requirement was established for heating the components only, and the resulting heat shield temperatures were established. Secondly, the power was supplied to the heat shield alone, and component temperatures were calculated. It was thus determined that the feasible and efficient system design definitely required power supply to the capsule, otherwise the component and the heat shield temperatures fell below acceptable levels. Furthermore, it was established that heat had to be supplied to the heat shield in larger proportion than to the components. Supplying the latter would "burn" them out before the heat shield reached minimum allowable temperatures, while heating of the heat shield to acceptable levels (200 watts and -27°F heat shield temperature during Mars orbit) would also raise the temperature of most components to levels not requiring separate heating. Other components could be warmed up with a minimum of power expenditure, while heaters, however, will be required for most components for a warmup prior to separation.

During cruise from Earth to Mars, flight capsule thermal control is achieved by passive means (thermal control coatings) and a reasonable amount of power from the spacecraft to the entry shell and to some critical components through heating elements. The entry-shell temperature can be maintained between -50°F and -20°F with 90 watts near Earth and 140 watts

TABLE XCVIII

REFERENCE DESIGN CONDITIONS AND REQUIREMENTS

Phase	Environment	Condition or Requirement
1. Prelaunch Decontamination/ sterilization	ETO decontamination and temperature cycle (294°F)	Conductive, convective and radiative heat interchange. Internal power to reduce temperature gradients and shorten heat-up times.
2. Cruise* Near Earth	Space; FC in shade of FS	Radiative heat interchange between FS solar panel backface and canister base. Power from FS available if required to heat critical components.
Midcourse maneuver	Space; FC in sun (Earth intensity)	Total maneuver time assumed 3 hours. No fixed FC orientation relative to the sun.
Near Mars	Space: FC in shade of FS	Decreased radiative FS solar panel backface/canister base interchange. Power from FS available if required to heat critical components.
3. Mars Orbit* Orbit injection maneuver	Space; FC in sun (Mars intensity)	Maneuver time: 1 to 4 hours. No fixed FC orientation relative to the sun.
Orbit	Space; FC in shade of FS, planetary thermal effects	Time in orbit: 3 to 10 days Orbital data: hp = 700, 1000, 1500 km ha = 4000, 10, 000, 20, 000 km Orbit inclination: 40 to 60 degrees Selected orbits: h_p h_A (A) 700 x 20, 000 (B) 1000 x 10, 000 (nominal case) (C) 1500 x 4000
Presseparation		Power available from FS to heat H/S and critical components. Time: 242 minutes before separation all equipment "on".
4. Postseparation	Space; Entry vehicle in sun. orientation depends on orbital parameters	Maximum time in orbit after separation: 0.5 hours.
De-orbit		Maximum time de-orbit to entry: 0.5 hours.
De-orbit to entry		Non spinning (evtt. tumbling) vehicle Sun orientation: Orbit Sun orientation angle (1). (A) 14 degrees (B) 24 degrees (C) 61 degrees All equipment "on" through impact; power from FC battery.
5. Entry	Entry heating	Time from entry to chute deployment: Min: 301 seconds (VM8, V_e = 14, 150 ft/sec, γ_e = -15.8 degrees) Max: 415 seconds (VM3, V_e = 15, 200 ft/sec, γ_e = -14.6 degrees) Max heating: (VM7, V_e = 15, 200 ft/sec, γ_e = 14.6 degrees, t_e = 348 sec)
6. Parachute descent (1) SUN SUN ORIENTATION ANGLE	Mars atmospheric environment	Parachute descent time Atm: VM3 time: 249 Chute Deployment Velocity (fps): 660 Altitude: 27, 500 feet VM4 324 540 27, 500 feet VM7 171 915 27, 500 feet VM8 163 816 at M = 1.2 (All data for γ_e = 50 degree; A/W = 5 ft²/lb)

*FS-FC interface data not available for assumed configuration and conditions: See Figure 382.

TABLE XCIX

TEMPERATURE SUMMARY FOR REFERENCE DESIG

Subsystem or Component	Ground (Sterilization) (Temp. °F)	Cruise				Planeta		
		Near Earth		Near Mars		Orbit		Prese Wa
		Temp. (°F)	Power (watts)	Temp. (°F)	Power (°F)	Temp. (°F)	Power (watts)	Temp (°F)
Primary Heat Shield	+294		90(2)		140		200	
Stagnation Point		-43		-26		-27	-	-69
Maximum Diameter		-45		-39		-27	-	-70
Sterilization Canister	+294							
Base		-57	-	-70	-	-85	-	-86
Lid		-80	-	-80	-	N.A.	N.A.	N.A.
Telecommunications and Power Module(2)	+294							
Battery		-55	-	-55	-	-52	-	+40
Electronics		-55	-	-55	-	-52	-	0
Engineering Experiment	+294							
Instrumentation Module		-35	7	-35	7	-35	7	0
Television		+ 5	3	+5	3	+5	3	+20
Others								
Afterbody	+294	-55	-	-55	-	-52		-52
ΔV Rocket	+294	-55	-	-55	-	-52	-	-52
Total Power Required, watts			100		140		210	

(1) Typical case (nominal orbit).

(2) Additional 50 watts during cruise near Earth would raise the heat shield temperature level by app

(3) Additional 50 watts during preseparation warmup would raise the heat shield temperature level by

(4) Additional 100 watts during preseparation warmup would raise the heat shield temperature level b

y Orbit paration rmup Power (watts)	Component Checkout Temp. (°F)	Component Checkout Power (watts)	Postseparation (1) Temperature (°F)	Entry Temperature Rise (°F)	Parachute Descent Temperature (°F)
50(2, 4)		200			N.A.
-	-57		-60	+320	N.A.
-	-58		+53 to -12	+320	N.A.
-	-86	-	N.A.	N.A.	N.A.
N.A.	N.A.	N.A.	N.A.	N.A.	N.A.
60		-	Temperatures approach maximum allowable operating temperatures from internal power generation before impact.		
60		-			
30					
5					
30					
	-49		-12 to +17	+360	
-	-49		-20	N.A.	N.A.
230		200			

oximately 25 °F.

pproximately 14 °F.

approximately 28 °F.

706-2

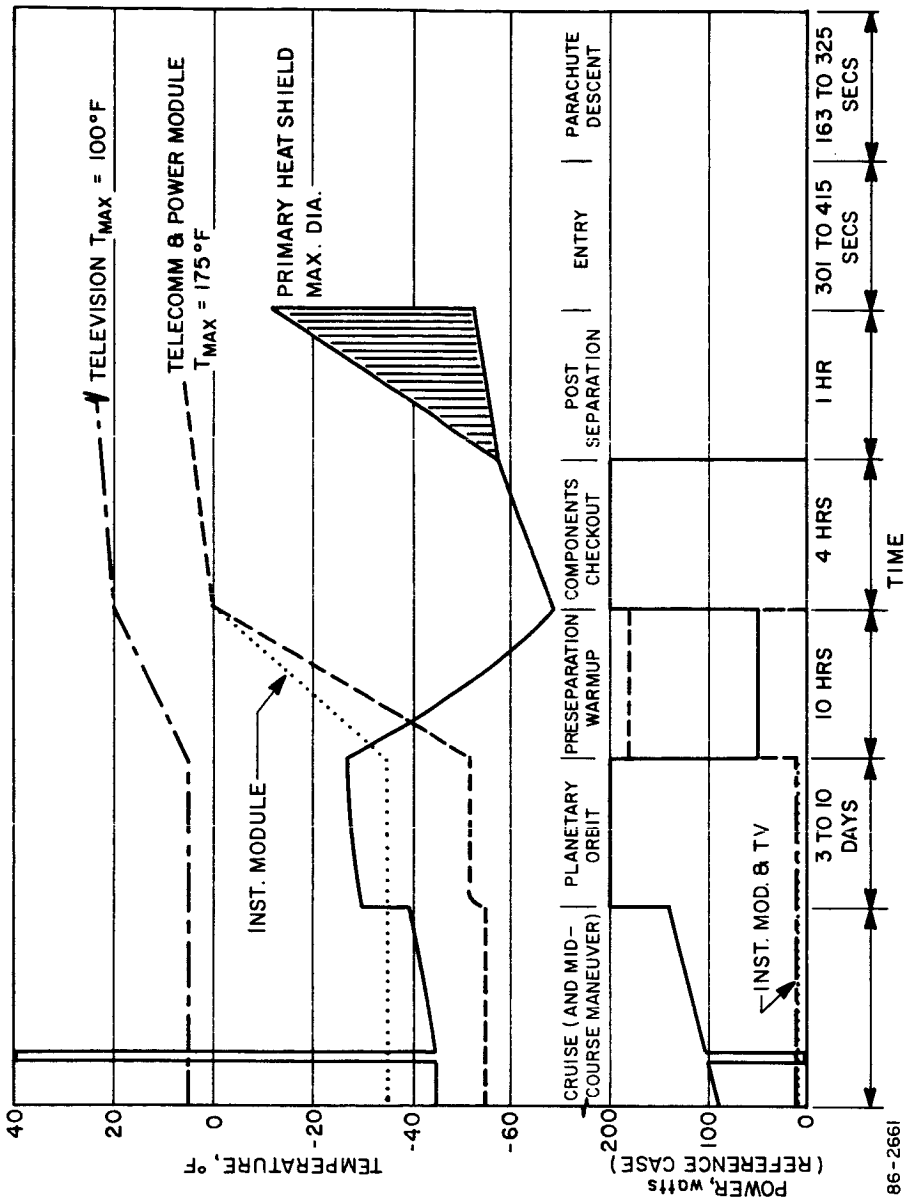

Figure 383 TEMPERATURE AND POWER CONSUMPTION HISTORY FOR REFERENCE DESIGN AND REFERENCE FLIGHT (TYPICAL COMPONENTS)

near Mars before sterilization canister lid ejection. This anticipated power supply will maintain the temperature of most components above their minimum nonoperative temperature. Critical components requiring additional heat (10 watts) during cruise are the instrumentation module and television.

A 3-hour midcourse maneuver near Earth causes high temperatures (above 400°F) in the sterilization container structure, while the thermal balance of the entry vehicle is not affected appreciably. The heat shield average temperature can rise as high as 75°F. In local areas, however, the heat shield temperature can approach the maximum allowable temperature of + 300°F.

In this case, potential degradation of the heat shield will have to be accounted for in the thermal protection design and material selection.

After sterilization canister lid separation prior to Mars orbit injection, the entry-shell temperature would drop to about -160°F without power supply or to -93°F with 100 watts additional power. To raise the entry shell and capsule overall temperature level, 200 watts are supplied to the entry shell through heaters imbedded in the heat shield substructure utilizing power from the flight spacecraft. The added power raises the heat shield temperature to -27°F during the planetary orbit phase while most of the components reach -52°F. An additional 10 watts to the instrumentation module and TV maintains their temperature at -35 and + 5°F respectively. This is the desired nonoperative temperature level for the components.

Component warmup for checkout operation prior to entry-vehicle separation requires 180 watts for a period of 10 hours (reference case). Components are warmed up from their planetary orbit steady-state temperature levels (above minimum nonoperative temperatures) to their minimum operative temperatures. Full power supply to the entry shell is interrupted during this 10-hour period and reduced from 200 watts to 50 watts; the balance of 150 watts plus an additional 30 watts are utilized for component heating. The primary heat shield temperature drops from -27°F to -70°F during this period and remains well above the lower acceptable limit, tentatively established at -100°F for the Purple Blend. Results of a tradeoff study between power, heatup time and temperatures are presented in paragraph 13.3.2.2. and indicate that at the expense of an additional 30 to 130 watts, the preentry temperature may be brought up to the orbit equilibrium. The peak power demand depends on the selected orbit in the sense that all temperatures must be raised before separation to such a level that desired conditions are achieved before entry.

The postseparation phase does not entail any performance difficulties because of its short duration (1 hour) and the anticipated variation of sun orientation angles (nominal case 24 degree, extreme cases 14 degrees and 61 degrees relative to the entry vehicle main axis). These conditions

resulted in relatively low initial entry temperatures (from 100°F to + 20°F for all cases considered) in various parts of the vehicle, which should be conducive to large weight savings (or increased safety margins) in the heat shield requirement, while not imposing any (or very small) penalties in the structure weight (potential increase in honeycomb core depth). Temperatures of power dissipating payload components increase during the post-separation phase but remain well within acceptable limits to ensure maximum efficiency in the performance from entry through impact.

The effect of entry heating on entry vehicle structural members has been discussed in detail in Section 9.0. An anticipated maximum temperature rise between 320°F and 360°F (entry-shell backface and afterbody structure) over the short entry period does not create any particular thermal control problems and can be handled, if required, by radiation shielding and application of insulation in areas of concern.

All critical components are designed in such a manner that they approach their maximum operating temperature during operation from checkout before separation to impact. If properly designed, integrated and insulated, individual thermal control of components during the parachute descent phase is of no particular concern. An exception is the television whose thermal control problems are discussed in Volume V, Books 4, paragraph 7.1.8.2

Concurrently with the analysis of thermal control system performance for the reference design, a parametric study was conducted to correlate the power requirement with that of the coating emittance. This was done to establish the allowable excursion in the emittance values due to space exposure, or to allow leeway in coating specifications, without detriment to either the component or heat shield temperatures. The parametric study indicated satisfactory performance for power levels from 100 to 250 watts and emittances ranging from 0.05 to 0.10. These performance characteristics are quite favorable as they indicate relatively small sensitivity of emittance-power relationship within quite feasible limits.

12.1.4 Comparison with Entry from Approach Trajectory Studies

Passive thermal control, supported by heat supply to critical components on demand, is utilized for the entry-from-approach-trajectory and entry-from-orbit design.

12.1.4.1. Cruise

Power from the flight spacecraft is required in both designs to maintain critical components above a minimum level. In the entry-from-approach-trajectory case, heat was supplied only to the payload (maintained at + 60°F) and the capsule overall temperature level was

maintained within tolerable limits at the same time, assuming an isothermal flight spacecraft/flight capsule interface. The entry-from-orbit cruise temperature is maintained basically through spacecraft power supplied to heaters embedded in the entry-shell structure, while additional heat is supplied only to two critical components. Entry-shell heaters are required to maintain the critical heat shield temperature within specifications after sterilization canister lid separation before planetary orbit injection. The much higher power demand in the entry-from-orbit case results from two facts; first, the necessity to operate for a prolonged time (3 to 10 days) in a planetary orbit with the sterilization canister lid off; secondly, from a more realistic spacecraft/capsule interface assumption. Also, the internal packaging configuration for the two cases is quite different. In the entry-from-approach-trajectory case, the entry vehicle is separated soon after sterilization canister lid separation. Relatively low emittance primary heat shield coatings are required in both cases.

12.1.4.2. Postseparation

The long duration (up to 20 days) of the postseparation period and the possibility of unfavorable sun orientations in the entry-from-approach trajectory make this phase most critical and controls the system requirements. The primary heat shield and afterbody coating system has to be selected to satisfy in particular the postseparation thermal control demand, requiring a low to moderate emittance. Special warmup and superinsulation of the batteries is required to assure their operation during the period when power from the spacecraft is not available. The entry-from-orbit case, in contrast, does not require particular thermal control attention due to the short-duration (1 hour) of the postseparation phase.

12.1.4.3. Entry and Parachute Descent

The impact attenuator material of low conductivity which encapsulates the critical payload simplifies the thermal control effort during the entry and parachute descent phase of the entry-from-approach-trajectory design. On the other hand, since post-impact operation is not required, entry-from-orbit thermal control should not be of particular concern if critical components are properly designed, integrated and insulated.

12.1.4.4. Post Impact

The numerous problems involved in entry-from-approach-trajectory post-impact thermal control are eliminated for the entry-from-orbit mode.

12.1.5 Conclusions and Problem Areas

Results of this study indicate that capsule thermal control can be maintained from launch to impact by passive means augmented by a reasonable amount of power (less than 300-watts peak demand) from the spacecraft supplied to the heat shield substructure and components during cruise and orbit. Reliable performance, however, depends on a variety of precautions like low-ϵ coatings and superinsulation in areas exposed to unfavorable environmental conditions.

The study of the reference design performance for a typical mission sequence revealed that: a) the critical consideration governing the selection of the thermal control system and thus the power drain imposed on the spacecraft was the flight capsule/spacecraft thermal interface configuration; b) the near Mars orbit phase was the critical phase of the operation (although space cruise was quite similar) because of the separation of the sterilization canister prior to orbit injection and c) the coatings emittance performance, although important, is not critical within the 0.05-to 0.10-range for 100 to 300 watts power availability.

The following is a summary of areas where information is needed and where problems are anticipated:

1. Flight spacecraft/flight capsule thermal interface data
2. Entry shell heating element integration and coatings
3. Thermal contact resistance data

12.2 DESIGN CRITERIA AND LIMITATIONS

12.2.1 Power

In the absence of specific data, it was assumed that a reasonable amount of power (between 100 watts and 300 watts) is available from the flight spacecraft from launch to flight capsule separation. From separation to impact, no power is available and thermal control must be maintained by purely passive means. The problem is simplified, however, to some extent since all critical components are operating during this relatively short phase and generate sufficient heat to maintain their thermal balance.

It is assumed that power during cruise is obtained from solar energy conversion panels integral with the spacecraft. The maximum power output from solar cells is a strong function of the temperature (Figure 384) and a reasonable range of temperatures has been assumed for this study (paragraph 12.3.1.1) together with a practical spacecraft-flight capsule interface configuration (Figure 382).

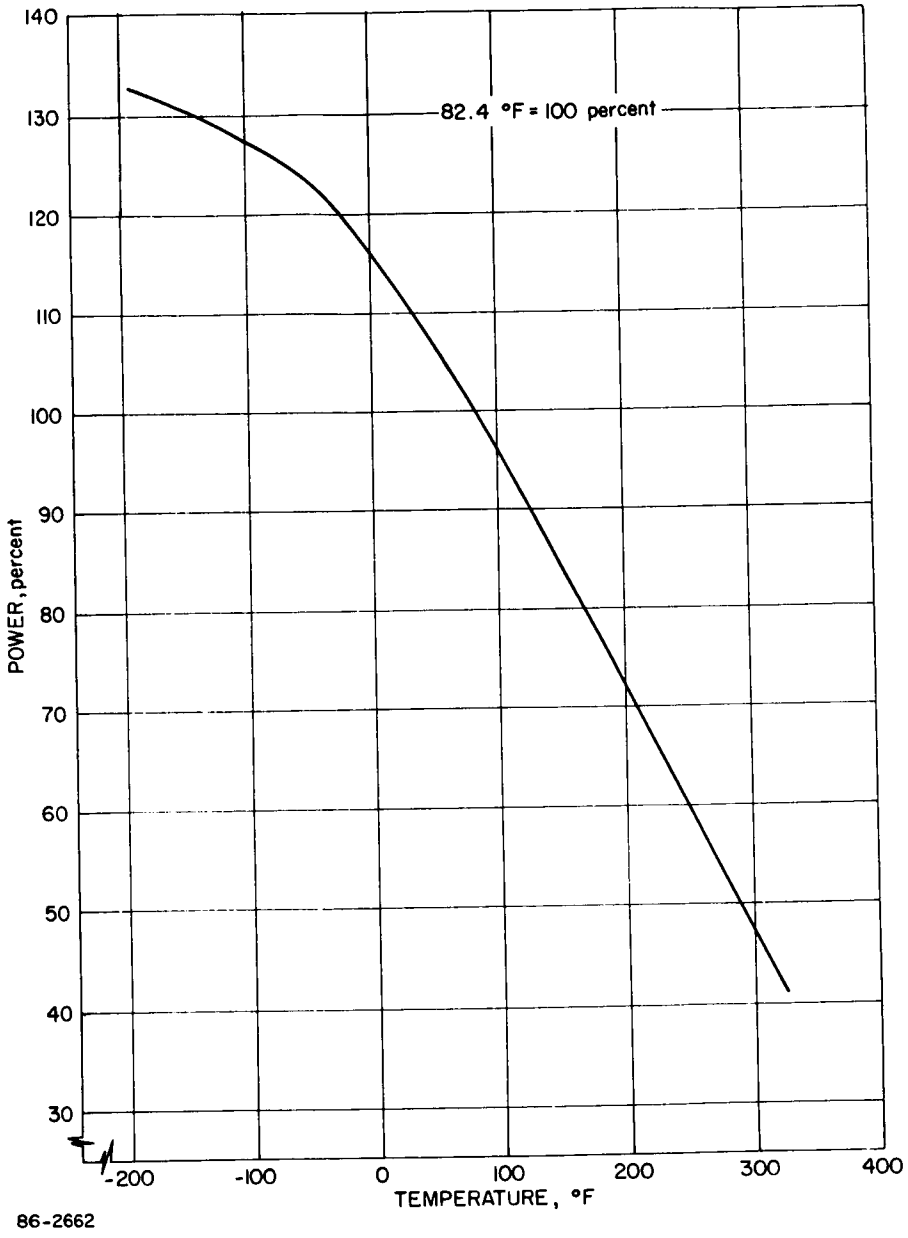

Figure 384 MAXIMUM POWER OUTPUT FROM TYPICAL SILICON SOLAR CELL VERSUS TEMPERATURE

12.2.2 Temperature

Temperature limitations for structural members and components are outlined in detail in Table C. Critical components requiring power during any phase of the mission are indicated. The most critical component is the television camera; a constant power supply is required during cruise. Less critical, but requiring more attention than the remaining components, is the instrumentation module. Lower temperature limits of the ΔV- rocket have not been verified experimentally and are based on the best information obtainable to date.

12.3 RESULTS AND DISCUSSION

The nature of the thermal control problems precludes detailed design or parametric studies prior to a fairly well advanced definition of the flight hardware and components. On the other hand the mechanical design cannot proceed without an understanding of the thermal control problems which may be generated by lack of their consideration.

In the early stages of the system evolution, it is feasible to determine some of the critical and controlling design factors by inspection of the projected mechanical design and selection of a typical mission sequence. It is then possible to conduct a limited parametric study of those factors and their influences, and select an approach to the design. In the studies of the entry-from-approach trajectory, the thermal control studies had to be terminated at this stage since more detailed definition of the hardware was accomplished simultaneously. A more detailed parametric analysis would entail tradeoffs between power supply, optical characteristics of the coatings, and effect of mission envelope on the selection of the system together with the limits of its operating capability. The final criteria consist of power supply and the resulting temperature distribution. Accordingly, this section is divided in chapters describing; a) the general and limited parametric study, and b) reference design evaluation for a nominal mission sequence after the design freeze. The latter chapter includes also a parametric evaluation of the performance for various options in orbit selection and operating temperatures of the components and the heat shield.

12.3.1 Parametric Studies

The parametric studies described below were conducted prior to the design freeze and as such are somewhat general in nature. Three factors (spacecraft/capsule interface, coating emittance, and power supply) which were deemed critical in the design were evaluated and an approach to the thermal control design was selected.

12.3.1.1 Spacecraft-flight Capsule Interface Effects

The impact of assumptions regarding the spacecraft/capsule thermal interface on the capsule temperatures and power requirements was

anticipated to be serious. However, these assumptions had to be made in lieu of a specified interface configuration. It was realized that a correlation of these basic assumptions with actual conditions would eventually influence the selection of the system and therefore a rather detailed study of their effect on a typical system response was made.

Physically, the influence of the interface is reflected in the heat flow patterns to and from the base of the sterilization canister and in the base temperatures. Due to the many uncertainties involved (e.g.: size of the spacecraft and solar panel radiating area; distance between spacecraft and sterilization canister base; radiative characteristics of the solar panel backface area and of the spacecraft; actual solar panel and spacecraft temperatures; actual conduction between the spacecraft and capsule), a simplified reference case was developed. This case was based on data found in Reference 89 and it was compared with a variety of other possible approaches. The various cases of practical and theoretical interest were then compared and the "reference case" rated within the range of possible approaches.

The "reference case" is based on the following assumptions (Figure 382): a) The spacecraft (7.5-foot diameter) is completely surrounded by solar panels; b) the outer diameter of the solar panels is equal to the outer diameter of the capsule (15 feet) such that the sterilization canister base is completely shaded during cruise; and c) the spacecraft/sterilization canister base distance is 5.0 feet.

Using this geometry as a basis, the radiative interchange distribution is expected to be as follows: a) 25 percent interchange between solar panel backface and sterilization canister base; b) 20 percent interchange with the spacecraft (assumed in an adiabatic thermodynamic state); and c) 55 percent radiated to space from the solar panel backface and sterilization canister base as well.

Since the spacecraft was assumed to be adiabatic, no transfer of energy by conduction was considered between the spacecraft and capsule, while the 20 percent radiative interchange with the spacecraft was assumed to be reradiated and retained in the system. The solar panel optical properties were assumed to be $\alpha = 0.65$, and $\epsilon = 0.90$. The α -value selected is somewhat lower than that commonly used in today's hardware; it was assumed, however, only after an examination of solar panel average temperatures calculated for the system. An α -increase from 0.63 to 0.88 resulted in a solar panel temperature increase from 20°F to 75°F. The effect on the heat shield is small (3°F at a power level of 200 watts) but more pronounced on the component-(12°F) and canister base (32°F) temperature level (Figure 385). Final selection of the solar panels was beyond the scope of this study. The α -value selected resulted in solar panel temperatures

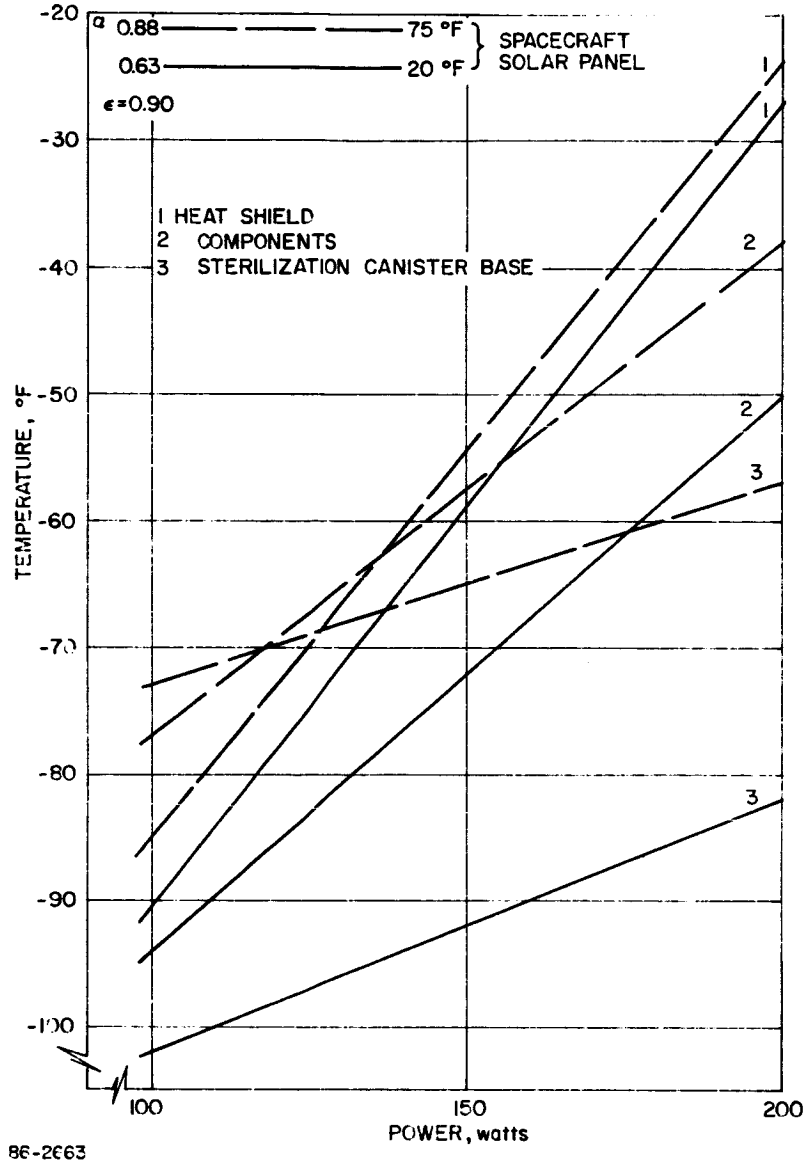

Figure 385 EFFECT OF SOLAR PANEL BACKFACE TEMPERATURE ON FLIGHT CAPSULE TEMPERATURE LEVEL

of around + 20°F near Mars and + 120°F near Earth. Results of a tradeoff study indicating the effect of various assumptions concerning the thermodynamic state of the interface boundary (adiabatic, insulated, isothermal, etc.) on the flight capsule average temperature are summarized in Figure 386 for various internal power levels. They are discussed below for the cases investigated.

1. Reference Case -- The chosen approach is shown to be conservative for realistic conditions and power levels required (200 watts). Flight capsule average temperatures were found to range from -97°F (100 watts) to - 52°F (200 watts). The heat shield temperatures for these cases are -92°F and -27°F, while sterilization canister base temperatures are -106°F and -85°F, respectively, as shown in Figure 387 for $\epsilon = 0.05$. It can also be seen that component temperatures follow a similar trend.

2. Sterilization Canister Base 100 percent Radiating to Space, No Radiative Interchange with the Spacecraft -- This is a highly idealized case; however, it established the lowest theoretical temperature limit the capsule could reach. The capsule average temperature level is maintained at -145°F with 100 watts and -85 with 200 watts internal power.

3. Sterilization Canister Base 55 Percent Radiating to Space, No Radiative Interchange With The Spacecraft -- This case considers a spacecraft-capsule interface such that a maximum of energy (from radiation interchange considerations) is radiated to space while the remaining 45 percent are contained in the capsule system. The case is applicable to an interface where the spacecraft and solar panel backface are completely insulated. From practical (spacecraft design) considerations, however, it appears that this case is not desirable since it would tend to overheat the spacecraft and, in particular, the solar panels. Average capsule temperatures approach the reference case at a power level of 200 watts.

4. Sterilization Canister Base Perfectly Insulated -- This boundary condition (if attainable) would appear to be very attractive for flight capsule thermal control design. When compared with the reference case, it indicates that higher flight capsule average temperatures can be achieved with less power, and in particular, when 200 watts are supplied to the entry shell. It should be noted, however, that this case (as shown) represents an idealized situation and it is questionable whether it can be approached in reality considering the large areas involved, the severe environments, etc. Thus, it would not be representative of critical conditions that might be expected during the mission and its use would be contrary to the specified design guidelines.

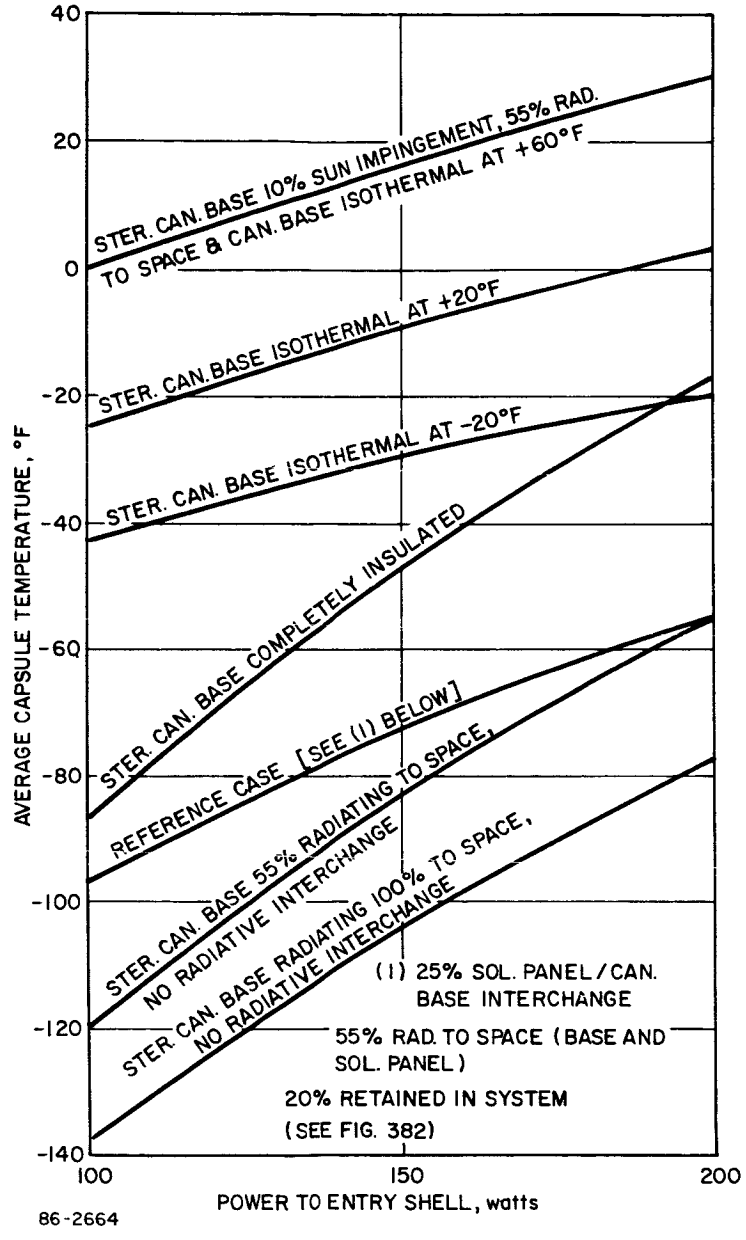

Figure 386 COMPARISON OF THE EFFECT OF INTERFACE ASSUMPTIONS ON FLIGHT CAPSULE AVERAGE TEMPERATURE NEAR MARS

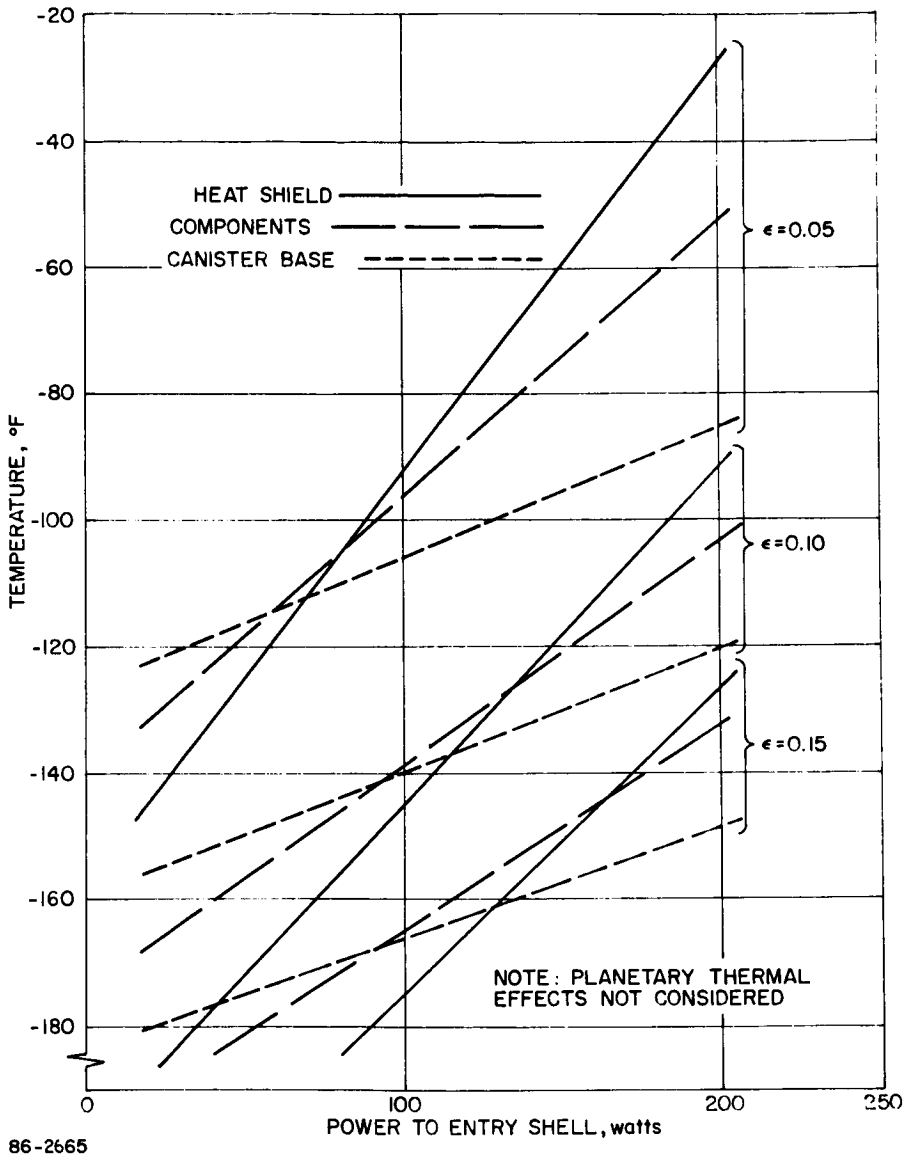

Figure 387 HEAT SHIELD TEMPERATURE VERSUS POWER TO ENTRY SHELL, CRUISE NEAR MARS, AND ORBIT -- STERILIZATION CANISTER LID OFF

5. Isothermal Sterilization Canister Base -- The assumption of an isothermal sterilization canister base (also equivalent to direct sun impingement) was the approach selected during the entry-from-approach-trajectory study (see paragraph 11.1.1.2). The isothermal approach is realistic for either high radiative interchange between the spacecraft and the adjacent (assumed in close proximity) sterilization canister base, sterilization canister base insulation and internal base heating, or direct sun impingement at the sterilization canister base. In particular, the latter possibility appeared (and still appears) to be a relatively easy and practical method of substantially reducing the level of electrical energy required for flight capsule heating. In turn, the need for extremely large solar panels may therewith be eliminated and smaller solar panels can then be arranged in such a way as to allow a certain percentage of direct sun impingement on the sterilization canister base. For example, 10-percent sun impingement at the sterilization canister base will raise the average temperature level by 87°F if compared with the reference case (100 W). A substantial amount of power, however, will still be required to maintain the temperature gradient across the capsule within tolerable limits, especially at the more remote (from the base) sections. The effect of sterilization canister base temperature variation on heat shield temperature is shown in Figure 388. The heat shield temperature is below the tolerable lower limit (-100°F) for all assumed sterilization canister base temperatures from +100°F to -90°F when no additional heat is supplied to the entry shell. A supply of 100 watts to the heat shield will maintain its temperature above -100°F over the range of sterilization canister base temperatures assumed; less than 100 watts will be required if 10-percent direct sun impingement at the sterilization canister base is allowed.

The mutual dependence of the surfaces involved in flight spacecraft/flight capsule radiative energy interchange is shown in Figure 389. The rates of solar panel backface radiation to the sterilization canister base and sterilization canister increases with decreasing sterilization canister base temperature as does the rate of sterilization canister base radiation to space. At a given sterilization canister base temperature (-100°F), the net heat exchange is zero, while energy exchange takes place above or below this temperature in one or the other direction. Concluding this paragraph it may be said that all attempts to define the spacecraft/capsule thermal incterface relationship cannot amount to more than somewhat academic studies of basic relationships until the actual interface is exactly defined.

12.3.1.2 Tradeoff Between Coating Optical Properties and Power Supply Requirements

The most critical flight capsule structural component as far as the temperature control is concerned is the heat shield material/bond/substrate composite of the entry shell. The geometrical complexity

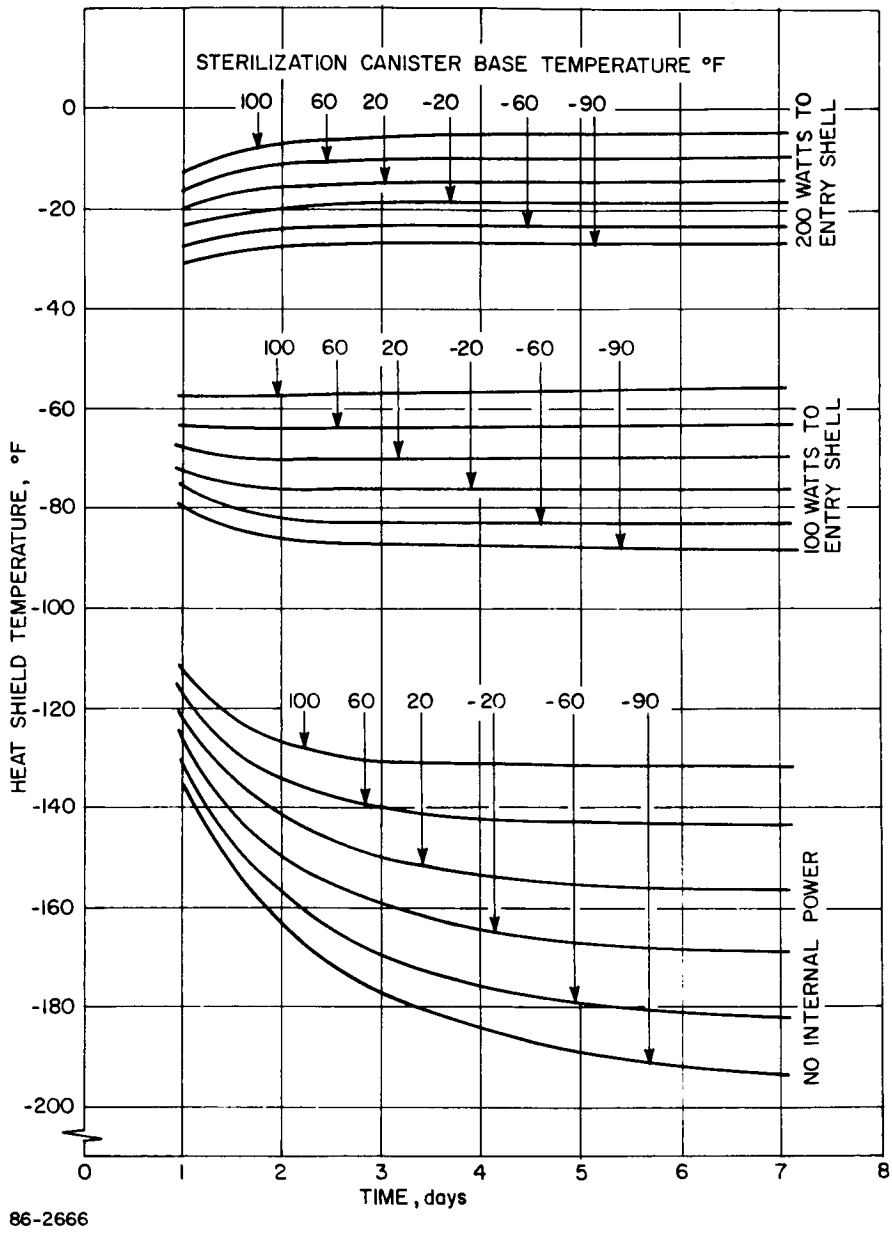

Figure 388 EFFECT OF CANISTER BASE TEMPERATURE VARIATION ON HEAT SHIELD TEMPERATURE

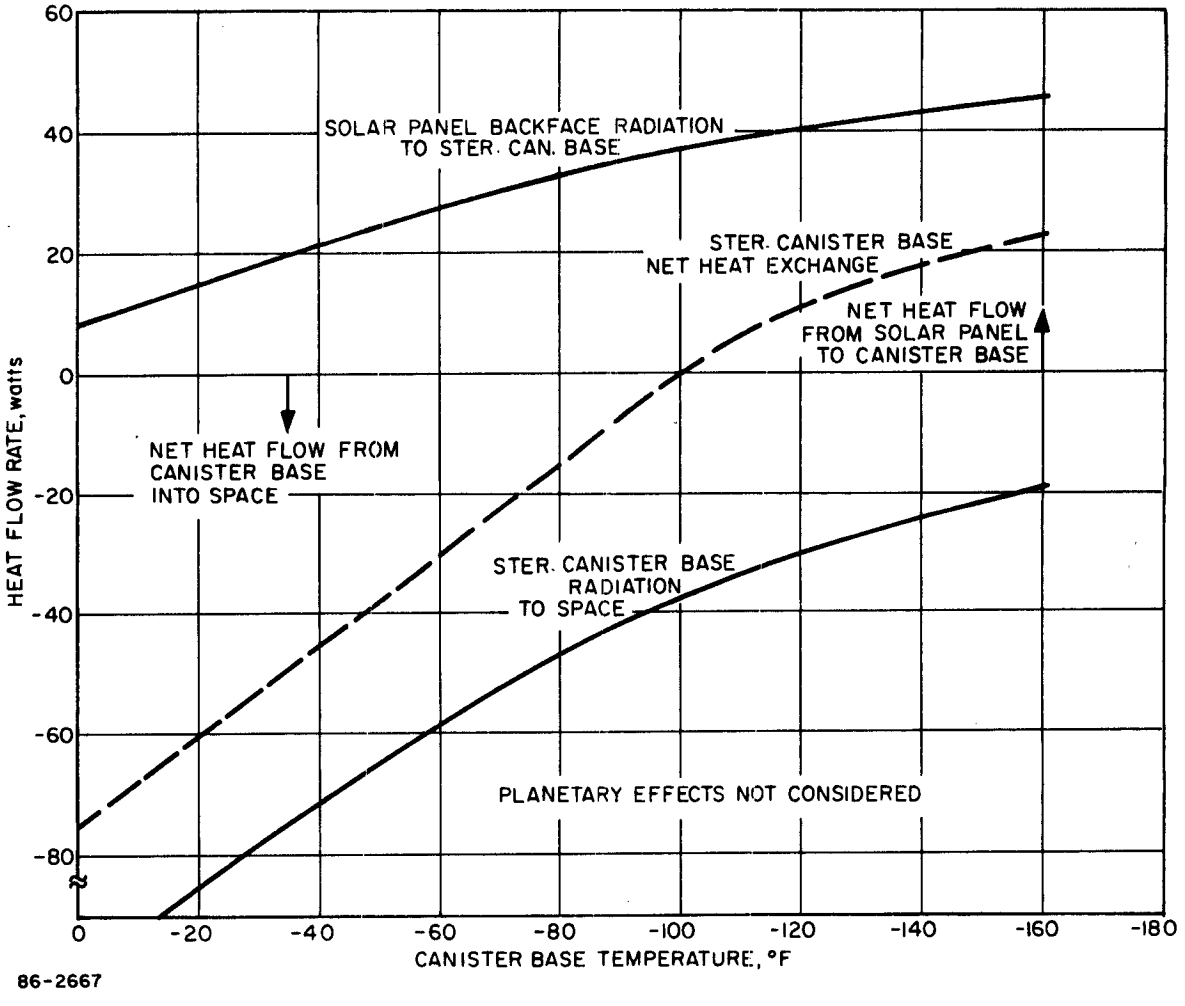

Figure 389 CANISTER BASE RADIATIVE HEAT EXCHANGE RATE AS A FUNCTION OF CANISTER BASE TEMPERATURE -- CRUISE NEAR MARS AND ORBIT

of the reacting interfaces, the attachment of various component modules and the large size of the entry shell make this subsystem the most difficult to control within the capsule. The entry shell is directly exposed to the most severe environment for an extended period of time during the Mars cruise and planetary orbit phases. It will approach a low-temperature equilibrium thermodynamic state after sterilization canister lid ejection if no additional heat is supplied from an external source. The basic means to maintain the temperature of a body during space exposure is to reduce its surface emittance to achieve a maximum energy preservation within the system. A low-ϵ (metallic) coating is thus highly desirable for application to the surface of the primary heat shield. Low emittance is characteristic of highly reflective coatings of a metallic nature. The lower ϵ - limit is dictated by many considerations of diverse nature (e. g. coating application, handling, degradation during environmental exposure, etc.). Actual achievement of the low emittance limit is essentially the result of an extensive development program. Phenomena affecting coating performance (outgassing, optical stability, etc.) have been discussed in Volume III of this report. One of the important factors affecting the performance, the coating optical stability after exposure to the various severe simulated mission environments, may not be known before completion of the development effort. It was therefore desirable to select a coating with reasonable optical properties for this study and to determine the effects of a change in optical properties (increase of ϵ) on the thermal balance. For the reference design case, the heat shield coating emittance was specified to be 0. 05. An examination of Figure 387 shows that the heat shield material allowable lower limit (-100°F) is not exceeded for power levels between 100 and 200 watts with an ϵ-value of 0. 05. The figure also shows that an increase from ϵ = . 05 to ϵ =. 10 may also be acceptable for the heat shield within the 200-watt limit, but may not be acceptable for the components. An increase of the above order would not be expected but a 10 to 20-percent deviation can eventually be approached by a variety of unfavorable coating degrading influences. The impact of an assumed ϵ -value variation on heat shield, component and sterilization canister base temperature levels is also indicated in the same figure.

Utilization of a coating with a higher ϵ -value than 0. 05 will require more power to the entry shell. For example, 104 watts are required to maintain the heat shield temperature at 90°F with ϵ = 0. 05; a coating with an ϵ -value of 0. 10 will require 202 watts, a power increase of 94 percent. Components and sterilization canister base temperatures follow a similar trend, aggravating the situation since an emittance deviation not only requires more power to the entry shell but also more power to the components to maintain their minimum non-operative temperature level.

High power requirements make utilization of a coating with an ϵ-value above 0.10 questionable. Satisfactory performance is indicated for power levels from 100 to 250 watts and emittances ranging from 0.05 to 0.10. These performance characteristics are quite favorable as they indicate a relatively small sensitivity of the emittance-power relationship within quite feasible limits.

Further tradeoff between the coating-emittance-power-requirement and temperature response of various elements may be required when peak power demand during the warmup period is considered. This is particularly important when the spectrum of orbits under consideration is examined and the component and heat shield temperatures are calculated for the post separation phase. These studies are discussed in paragraph 12.3.2. If higher demand on power is exerted, or power failure during cruise is considered, lower emittance coatings may be necessary. The importance of emittance for this latter case (power failure during cruise or orbit) is illustrated in Figure 390. Whether such a failure mode should be considered would depend on the overall planatery vehicle system criteria.

12.3.1.3 Selection of Thermal Control Approach

A thermal control approach during cruise and planetary orbit which utilizes heaters integrated into the entry shell and critical components, has been selected after completion of several parametric and performance studies.

After a reference spacecraft/capsule configuration was selected for the purpose of the study (paragraph 12.3.1.1), power requirements were estimated. First, a "no power" case was investigated. Some typical coatings used in the interface study (based on the entry-from-approach-trajectory phase results) were employed in this investigation to determine the severity of the situation. The results of this evaluation indicated a 100-200 watt power demand for a preliminary design configuration, for lower power heatshield temperatures fell below -150°F and the component environment reached approximately -100°F. In the next phase the distribution of power between the components and heat shield was determined in three steps: a) all power to the components; b) all power to the heat shield; and c) various proportions of power to the component and the heat shield. The last step was repeated for the reference design configuration during performance evaluation studies.

Power requirements were thus established when heat was supplied only to the components in such manner that they were maintained at various levels within allowable limits (e.g.: at their lower nonoperative limit, operative limit and at +80°F). The resulting heat shield temperatures

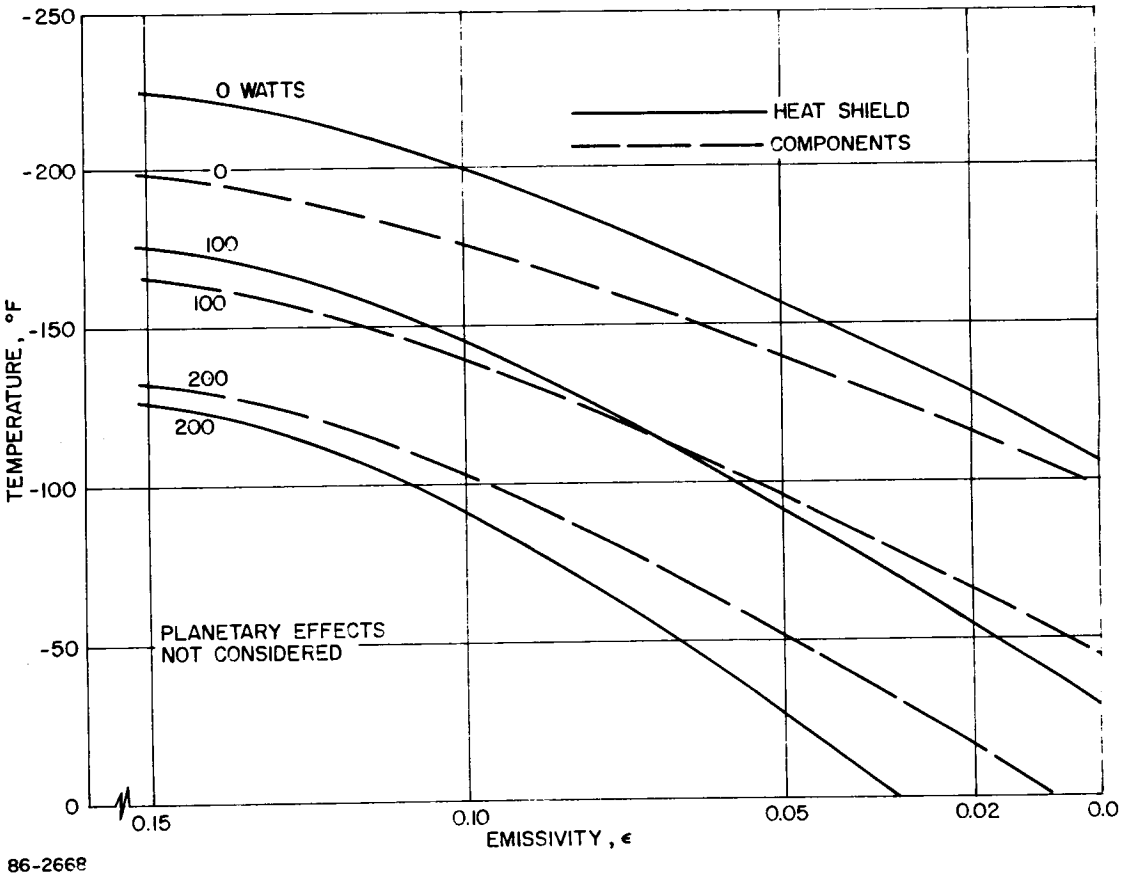

Figure 390 HEAT SHIELD AND COMPONENTS TEMPERATURE VERSUS HEAT SHIELD EMISSIVITY CRUISE NEAR MARS AND ORBIT -- CANISTER LID OFF

were established, and it was determined that it is not feasible to maintain heat shield temperatures through power supply to the components. The supply of 200 watts directly to the components would overheat them before the heat shield would reach minimum allowable temperatures. Secondly, power was supplied to the heat shield alone and component temperatures were checked. It was found that 200 watts supplied directly to the heat shield would maintain the heat shield at -27°F and would raise the temperature of most components to levels not requiring separate heating, (above -65°F) while others could be warmed up with a minimum of power expenditure. It was thus determined that the feasible and efficient system design definitely required power supply to the heat shield or entry shell. Furthermore, it was established that heat had to be supplied to the heat shield in larger proportions than to the components. Next the emittance - power tradeoff discussed in paragraph 12.3.1.2 was conducted.

Once the maximum power requirement was established, a tradeoff study was conducted to determine whether the power level selected would be sufficient to raise component temperatures to minimum operating levels before separation, by reducing the power to the entry shell and supplying it to the components instead of during the warmup and checkout phases. Results of this investigation are reported in paragraph 2.3.2.2.

The thermal control approach to satisfy postseparation requirements was to determine the transient entry vehicle temperature rise for three orbits, one nominal and two extreme cases (Table XCVIII). The primary heat shield was coated (low ϵ) as required during orbital space exposure, the secondary heat shield and afterbody were left uncoated. The examination of temperature distributions was used to establish the peak power demand during the previous mission phase (warmup and checkout) as that demand would be affected by the limits imposed for the pre-entry temperatures.

12.3.2 Reference Flight Capsule Design Evaluation

The main objective of the thermal control system is to maintain electronic components, batteries, structural members, and the heat shield within their operating temperature limits as prescribed by their operative and nonoperative conditions in the various phases of flight. It must be compatible with the flight spacecraft and the power available on board within the general weight allocations. It must be compatible with other systems and allow for departures from the nominal performance condition (allow for failure modes) during all phases of the mission. To provide for reliable operation, it should minimize the requirement for active systems, and assure that its passive elements do not degrade the performance of other materials and they themselves are not degraded by the presence of the others. The system selected for this application is described below and its performance under various conditions is assessed.

12.3.2.1 Thermal Control Systems Description

The thermal control system which was evolved to satisfy the above considerations reflected the approach outlined in paragraph 12.3.1.3. The additional consideration in the design of the system was to minimize the development program time and cost. Thus an attempt was made to stay within the state of the art in thermal coating selection. Whenever possible, the use of coating was altogether avoided and the primary material optical properties utilized.

1. Sterilization Canister -- The sterilization canister consisting of the canister base and canister lid, is a thin shell (0.03 inch) aluminum structure. From the thermal control standpoint, the presence of the sterilization canister is favorable since it acts as a radiation shield during cruise while the capsule is exposed to the space environment. This advantage, however, is partly diminished when the sterilization canister lid is in direct contact with the entry vehicle. This is the case, for example, when conductive pads are located between the entry shell and the sterilization canister lid for support purposes. The capsule is exposed to the lowest temperature thermal environmental level near Mars as the sterilization canister lid is separated before injection into Mars orbit. The advantage of the sterilization canister lid is therefore not utilized during the most critical environment (from temperature/power requirement considerations). During a midcourse maneuver where the capsule is directly exposed to the sun at near Earth intensity, the sterilization canister lid prevents direct sun impingement at the heat shield and reduces thermal gradients within the capsule. The sterilization canister base is primarily involved in energy exchange between the spacecraft/capsule during cruise and planetary orbit. It receives radiative energy from the solar panel backface and radiates to space as well. The sterilization canister base and lid are coated externally with a low emitting coating ($\epsilon = 0.05$) to preserve energy within the capsule system. A low α is very desirable to reduce midcourse maneuver thermal gradients. The optical properties of the internal surfaces are not critical; however, minimization of spacecraft energy balance disturbances after entry vehicle separation led to the selection of an $\epsilon = 0.05$ coating for the interior of the sterilization base while the lid interior specification was selected as $\epsilon = 0.10$. Thus, no special coating is required for the internal lid surface. The desired ϵ-value is not critical and can be obtained by polishing of the base metal. The sensitivity of the thermal balance to the surface optical properties was briefly investigated. It was shown that an ϵ-increase from 0.05 to 0.10 (externally and internally) will result in a heat shield temperature drop of 19°F (Figure 391). An emissivity increase from 0.05 to 0.10 at the interior surface will cause only a minor temperature

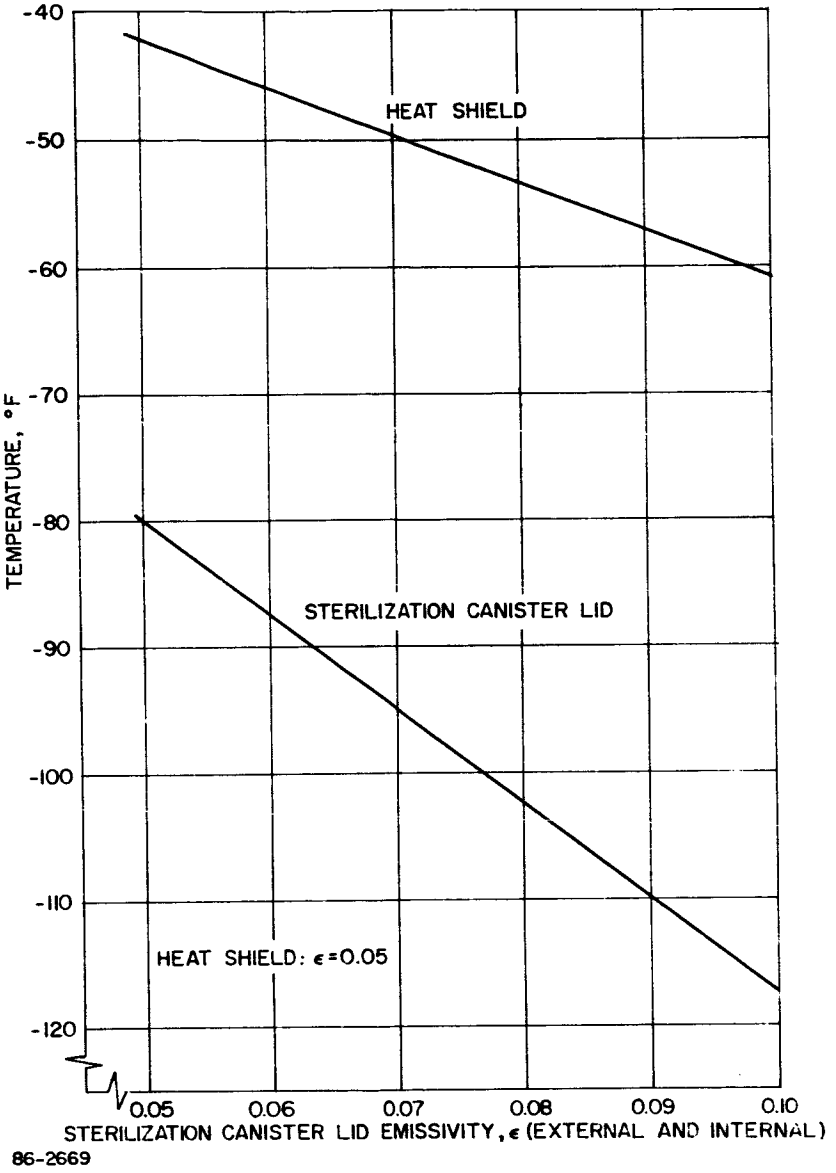

Figure 391 EFFECT OF STERILIZATION CANISTER LID ϵ - VARIATION ON HEAT SHIELD TEMPERATURE

drop but simplify manufacturing appreciably. Coating optical properties are achieved, for example, by bonding of a metallized and Si-oxide coated Polyimide (Kepton) film (α/ϵ = 3.0 to 5.0, with ϵ = 0.04 or higher) to the internal base surface during manufacturing and to external surfaces preferably after dry-heat sterilization. The coating mentioned above is one of many possibilities. The final coating selection would form a part of the development program and is discussed elsewhere in this report (Volume III).

2. Thermal Protection System -- A low -ϵ coating was specified for the primary heat shield surface to preserve energy during cruise and planetary orbit after sterilization canister lid separation. Results of post separation temperature studies (paragraph 12.3.2.2) indicate that no thermal control coating is required at the secondary heat shield and afterbody and that the thermal control requirements are satisfied by utilization of the optical properties (α = 0.60, ϵ = 0.95) of the virgin heat shield material (Purple Blend Mod 5). The low -ϵ value (ϵ = 0.05 to 0.10) required for coating of the primary heat shield can be obtained, for example, by spray-or vapor deposition of metals (gold, silver, aluminum) or the application of prefabricated metallic or metallized plastic foils. A variety of influencing factors (outgassing, optical properties stability, mechanical stability, etc.) have to be considered before a final coating can be specified. The final selection of the coating type and application method is part of the thermal control coating development program and was discussed in detail in Volume III of this report. Heating elements are imbedded in the heat shield substructure to maintain the capsule temperature level within allowable limits during cruise and orbit. Heating element integration into the heat shield material/bond/substructure system, again, is part of the development program.

3. Components -- All components of interest, with the exception of the TVC subsystem and the ACS reaction control nozzles, are located within and fastened to the suspended capsule structure. Critical components are those which require additional heat for active thermal control to remain above a specified minimum nonoperating temperature during cruise and Mars orbit or those which require warmup to their minimum operating temperatures before the preseparation checkout procedure. From thereon, the heat generating components do not require heat addition; they are designed, arranged and mounted in such a manner that their heat-sink capability is fully utilized and their temperature does not exceed maximum allowable limits before impact. An analysis has shown the feasibility of this design philosophy by considering gross properties. The final design specification, however, will require exact knowledge of materials involved, interior design and configuration of the conductive and radiative paths, contact

resistances, etc. The need for testing in connection with a thermal control model has been pointed out in the appropriate section of the development program. (Volume III).

Components which do no require any particular attention from the standpoint of thermal control are the TVC subsystem, the ACS reaction control nozzles, and the ACS cold-gas tank. The temperatures of all three are allowed to drop as low as -100°F in their nonoperative or operative state and are well controlled within the capsule thermal environment and during their operation from capsule separation to planetary entry. Critical payload components (electronics, batteries, engineering experiment instrumentation) are contained in modules (see also Table C), and equipped with thermostatically controlled heaters for on-off power supply as required to maintain minimum temperatures. The modules are well insulated from the structure to minimize heat loss during the preseparation warmup phase. The batteries, located in the telecommunications and power module, are thermally insulated from the high heat-generating radio and data handling system.

Components requiring constant heat supply during cruise and planetary orbit (instrumentation module and TV) to remain above their minimum nonoperating temperature require particular attention as far as insulation is concerned. Lightweight superinsulation is recommended for use in the critical areas. Final requirements will have to be determined during the development effort (thermal control model testing).

4. ΔV - Rocket Subsystem -- The thermal environment of the ΔV-rocket may present thermal control problems. The minimum allowable operative and nonoperative temperature is specified at -40°F; lower temperatures (-52°F) during cruise and Mars orbit are reached in the reference case. In the absence of actual low temperature test data for the ΔV rocket and a clear definition of the actual flight spacecraft/flight capsule thermal interface, no attempt has been made for thermal control of this particular subsystem, although its thermal control performance appears now to be a marginal problem. If necessary the overall power supply to the entry shell would have to be raised.

5. Parachute Subsytem -- Temperature control between -100°F and +150°F from cruise to entry does not appear to be critical. Thermal insulation (superinsulation blankets) is recommended for shielding from entry heating if required.

TABLE C

TEMPERATURE LIMITATIONS FOR STRUCTURAL MEMBERS AND COMPONENTS

Subsystem or Component	Location	Typical Temperature Specification (°F)		Critical Phase of Operation or Environment	Thermal Design Approach
		Nonoperative	Operative		
1. Flight Capsule	-				
Entry shell structure	-	-100	(a)	Mars cruise and orbit	Heaters installed in the H/S (1) using FS power
Entry shell heat shield material		-100 to + 300	-100 (b)		
Sterilization canister		-150 to +300(c)		Cruise, midcourse maneuver	High α/ϵ
2. Power and power control Battery	Telecommunication & Power Module	-65 to + 160	+40 to +160	Mars cruise and orbit (low temperatures) Preseparation to entry (high temperatures	Insulation and (2) heaters using FS power. Insulation and heat sink.
3. Telecommunications	Same as battery	-65 to +275	0 to +175	Same as battery	Same as battery (2)
4. Data handling	Same as battery	-65 to + 275	0 to +175	Same as battery	Same as battery (2)
5. Engineering experiment	Instrumentation module	-40 to +140	0 to +100	Same as battery	Same as battery (1)(2)
Accelerometers	Suspended capsule	-65 to +275	0 to +175	Same as battery	Same as battery (2)
Penetrometers	Same as accelero-meters	-65 to +275	0 to +175	Same as battery	Same as battery (2)
Television	Suspended capsule	0 to +140	+20 to +100	Parachute descent to impact	Insulation and (1)(2) heaters using FS power
6. Retrorocket subsystem	Suspended capsule structure	-40 to + 70 (d)		Mars cruise and orbit	Insulation and (1) heaters using FS power (if required)
7. Attitude control subsystem					
Reaction control	Entry shell	-100 to +275		Preseparation to entry	None
Tank-cold gas	Suspended capsule structure	-100 to +275		Preseparation to entry	None
Platform	Suspended capsule structure	-65 to +275	0 to +175	Preseparation to entry	Insulation and (2) heaters and FS power during cruise (if required) and preseparation
Sentry gyro	Suspended capsule structure	-65 to +275	0 to +175	Preseparation to entry	(2)
8. Thrust vector control subsystem	Entry shell	-100 to +300		Preseparation	None required
9. Parachute subsystem	Suspended capsule structure	-100 to +150		Entry, parachute descent	Insulation for entry heating
10. Separation systems	Various	-160 to +300		Mars cruise to entry	None required

(a) As required by thermal structural compatibility with the heat shield
(b) Tentative for Purple Blend Mod 5
(c) Limitations defined by structural design requirement
(d) Lower limit not verified

(1) Power required during FS cruise and orbit
(2) Preseparation power required for heating to minimum operating temperature

6. Separation Systems -- The various separation subsystems within the overall system will require attention during the development phase. No particular problem, however, is foreseen in regard to thermal control.

12.3.2.2 Thermal Control System Performance

The performance of a thermal control system may be described in terms of the temperature distribution and history resulting from its operation, and in terms of its power consumption and distribution. The temperature distributions, power distribution, and consumption history for the system described previously, and operating during a nominal mission sequence is described below. The effect of some variation from the nominal sequence at the end of the Mars orbit and during the postseparation phase are also discussed. A temperature and power requirements summary for the heat shield and critical components during the mission from the beginning of the cruise to entry are shown in Table CI and Figure 392.

1. Cruise from Earth to Mars and Planetary Orbit -- The thermal balance of the flight capsule during cruise is maintained and governed by the radiative energy exchange between the spacecraft solar panel backface and the sterilization canister base, direct sun impingement on the sterilization canister lid during the midcourse maneuver, internal power provided for thermal control in critical areas (entry shell, components), and radiation to space from the sterilization canister base and lid. Conductive heat transfer between the spacecraft/capsule will be finite in the actual hardware, but it was deemed negligible for the purpose of this study.

It was assumed (paragraph 12.2) that a reasonable amount of power (between 100 and 300 watts) will be available during cruise from spacecraft solar cell energy conversion for capsule temperature control. This power was then used in the critical areas as required to maintain minimum nonoperative temperatures in all locations within the flight capsule.

Shown in Figures 393 and 394 are cruise near Earth and near Mars and planetary orbit steady-state temperatures (See also Table CI and Figure 392). Heat shield and component temperatures can be maintained at various low or high levels during cruise depending on the amount of total power available (Figures 395 and 396). The case shown in the summary and in Figure 393 considers the minimum power requirement (90 watts near Earth, 140 watts near Mars) during cruise required to control the majority of critical components (lower temperature limit - 65°F) without additional power supplied directly to them. Power is supplied essentially through the entry-shell heaters,

Subsystem or Component	Location	Coating Properties	
		α	ϵ
1. Flight Capsule Structure	Flight capsule		
Primary H/S - stag. point		0.25	0.05
- max. dia.		0.60	0.95
Secondary H/S-max. dia.		0.60	0.95
Afterbody		0.60	0.95
Canister base		0.25	0.05
Canister lid		0.25	0.05
2. Power and Power Control-Battery (2)	Telecommunication and power module	-	-
3. Telecommunications (2)	Same as battery	-	-
4. Data Handling (2)	Same as battery	-	-
5. Engineering experiment - Instr. module Accelerometers Penetrometers (4) Television	Instrumentation module suspended capsule structure	-	-
6. Retrorocket Subsystem	Susp. capsule structure	0.90	0.90
7. Attitude Control Subsystem		-	-
Reaction control	Entry shell		
Tank-cold gas	Suspended caps. structure		
Platform	Suspended caps. structure		
Sentry gyro	Suspended caps. structure		
8. Thrust Vector Control	Entry shell	-	-
9. Parachute System	Susp. caps. structure	-	-
Power required for thermal control	Entry shell		
	Components		
	Total		

Notes: (x) See secondary heat shield, maximum diameter.

Numbers in parentheses refer to 100 watts to the entry shell during preseparatio

TABLE CI

TEMPERATURE AND POWER REQUIREMENTS SUMMARY

Ground	Cruise				Planetary Orbit				
	Near Earth		Near Mars		Orbit (3 to 10 days)		End of Preseparation Warmup	End of Preseparation (10 hrs)	
Sterilization Temperature	Temp.	Power	Temp.	Power	Temp.	Power	Temp.	Power	End of Co
(°F)	(°F)	(watts)	(°F)	(watts)	(°F)	(watts)	(°F)	(watts)	Checkout
294	-43	90	-26	140	-27	200	-69(-55)	50(100)	-57(-43)
	-45	-	-39	-	-27	-	-70(-56)		-58(-44)
	-45	-	-39	-	-27	-	-70(-56)		-58(-44)
	-55		-55		-52	-	-52		-49
	-57		-70		-85	-	-86		-86
	-80		-80		NA	NA	NA	NA	NA
	-55	-	-55		-52	-	+ 40	60	
	-55	-	-55		-52	-	0	55	
	-55	-	-55		-52	-	0		Tempera
	-35	7	-35	7	-35	7	0	30	
	-55	-	-55		-52		0	2	
	-55	-	-55		-52	-	0	16	
	+5	3	+5	3	+5	3	+20	5	
	-55	-	-55	-	-52	-	-52	-	-49
	-45	-	-39	-	-28	-	-70	-	-58
	-55	-	-55	-	-27	-	-69	-	-58
	-55	-	-55	-	-52	-	0	7	Tempera
	-55	-	-55	-	-52	-	0	5	
294	-45	-	-39	-	-28	-	-70	-	-58
	-55	-	-55	-	-52	-	-50	-	-48
		90		140		200		50 100	
		10		10		10		180 180	
		100		150		210		230 (280)	

warmup.

732-2

	Postseparation			Entry	Parachute Descent
	End of Post Separation (1 hr.)				
	Nominal Orbit	Extreme A	Extreme B		
mponent	1000 x 10,000 km	700 x 20,000 km	1500 x 4000 km	304 to 415 sec.	163 to 324 sec.
(4 hrs)	Temp. (°F)	Temp. (°F)	Temp. (°F)	Temp. rise (°F)	
200	-60	-60	-62 to -53	320	
	(-45)	(-45)	(-48 to -39)		
	-53 to -12	-41 to -11	-103 to -42	320	
	(-39 to + 2)	(-27 to + 3)	(-88 to -28)		
	-50 to -9	-38 to -9	-105 to -39		
	(-36 to +5)	(-24 to + 6)	(-91 to -25)		
	-12 to + 17	+ 3 to + 20	-74 to + 2	360	
	(same)	(same)	(same)		
	NA	NA	NA	NA	NA
NA	NA	NA	NA	NA	NA
ures approach maximum allowable operating limits from internal power dissipation					
	-20	-18	-31		
	(x)	(x)	(x)		
	-58				
ures approach maximum allowable operating limits from internal power dissipation					
	(x)	(x)	(x)		
200					
200					

732-13

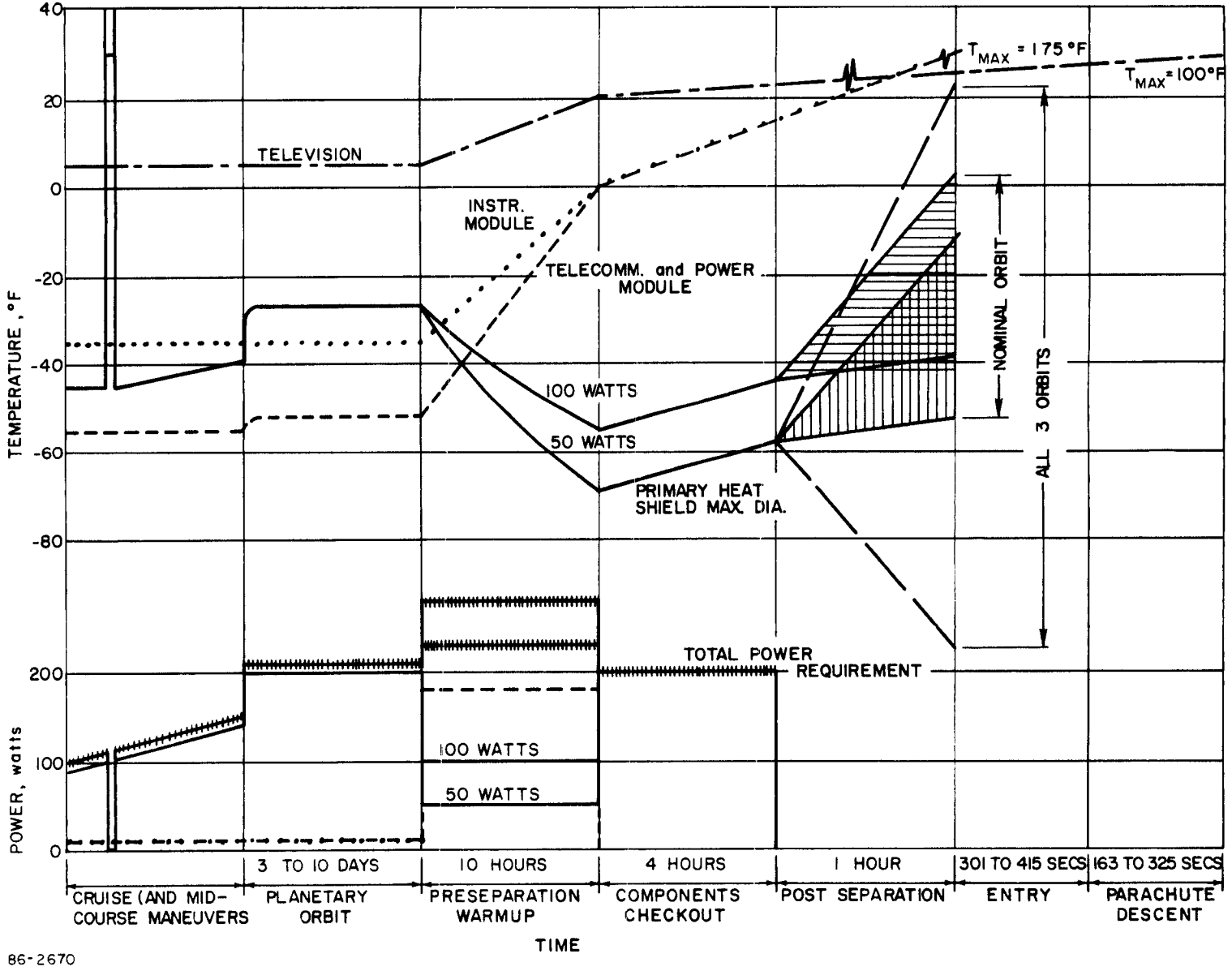

Figure 392 TEMPERATURE AND POWER REQUIREMENTS HISTORY

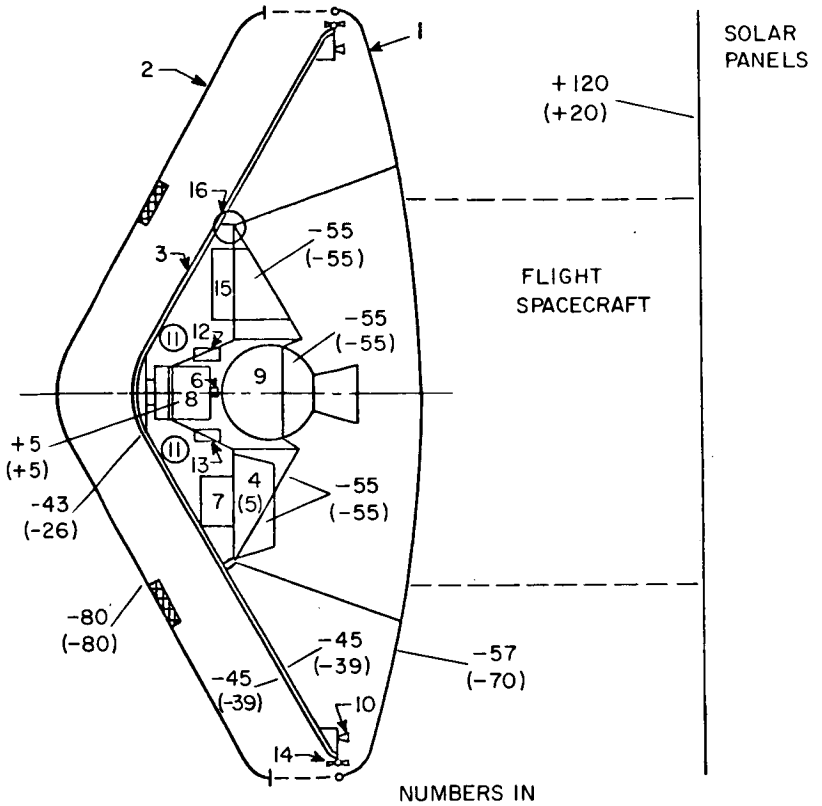

1 CANISTER BASE
2 CANISTER LID
3 ENTRY SHELL
4 TELECOMMUNICATIONS AND POWER MODULE (2)
5 INSTRUMENTATION MODULE
6 ACCELEROMETERS (3)
7 PENETROMETERS (4)
8 TELEVISION
9 ΔV PROPULSION
10 ACS REACTION NOZZLES (12)
11 ACS COLD GAS TANK (2)
12 ACS ELECTRONICS
13 ACS SENTRY GYRO
14 TVC REACTION SUBSYSTEM (4)
15 PARACHUTE
16 ENTRY SHELL SEPARATION MECHANISM

86-2671

Figure 393 TEMPERATURE DISTRIBUTION--CRUISE NEAR EARTH AND NEAR MARS, STERILIZATION CANISTER LID ON

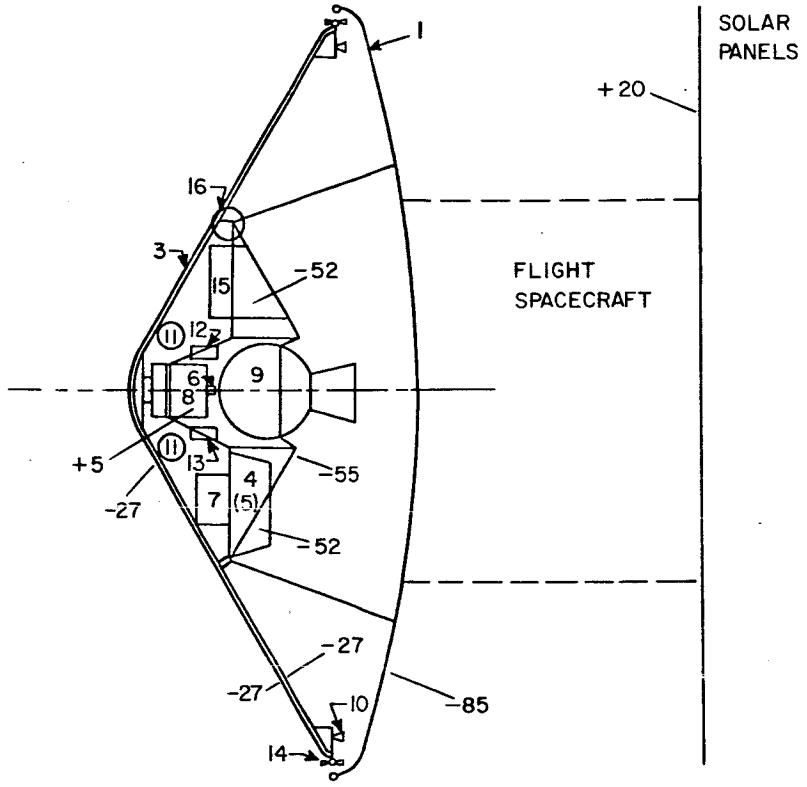

1 CANISTER BASE
3 ENTRY SHELL
4 TELECOMMUNICATIONS AND POWER MODULE (2)
5 INSTRUMENTATION MODULE
6 ACCELEROMETERS (3)
7 PENETROMETERS (4)
8 TELEVISION
9 ΔV PROPULSION
10 ACS REACTION NOZZLES (12)
11 ACS COLD GAS TANK (2)
12 ACS ELECTRONICS
13 ACS SENTRY GYRO
14 TVC REACTION SUBSYSTEM (4)
15 PARACHUTE
16 ENTRY SHELL SEPARATION MECHANISM

86-2672

Figure 394 TEMPERATURE DISTRIBUTION--CRUISE NEAR MARS AND ORBIT, STERILIZATION CANISTER LID OFF

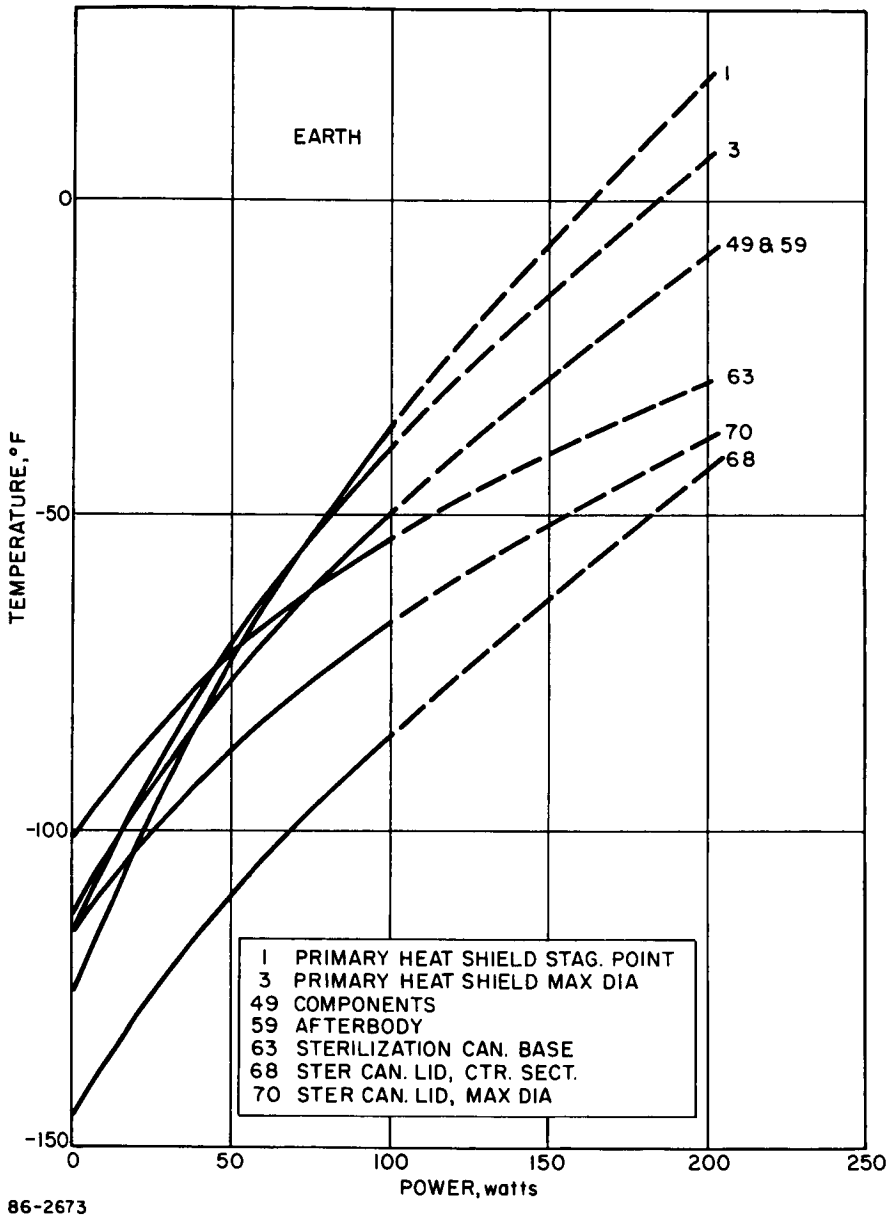

Figure 395 TEMPERATURE VERSUS POWER TO THE ENTRY SHELL, CRUISE NEAR EARTH

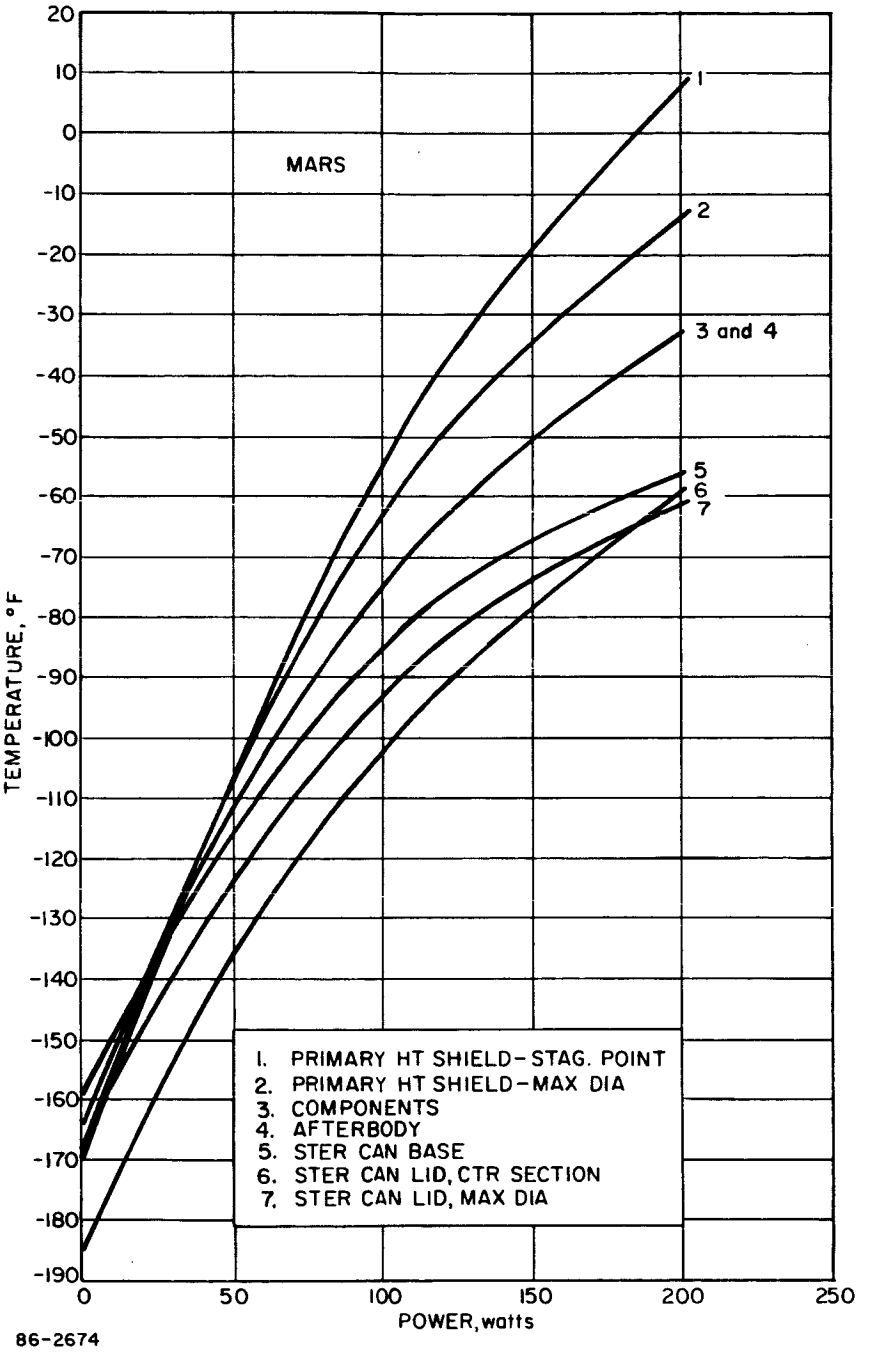

Figure 396 TEMPERATURE VERSUS POWER TO THE ENTRY SHELL, CRUISE NEAR MARS--STERILIZATION CANISTER LID ON

except the 1.0 watts to maintain the instrumentation module at -35°F and the TV at +5°F. The resulting heat shield temperatures are well controlled; the lower temperatures do not fall below -26°F. The power level to the entry shell is increased from 90 to 140 watts in the vicinity of Mars to maintain the temperature of the components and the heat shield material at essentially the same level during both portions of the cruise. The entry-shell heater power is then stepped up after lid separation to 200 watts. This is done because during the 3- to 10-day planetary orbit period (without the canister lid), 200-watts entry-shell power plus 10 watts for the instrumentation module and television are required to maintain the entry shell at a temperature level within acceptable limits during the following preseparation warmup sequence.

A temperature history for the heat shield, sterilization canister base and components after sterilization canister lid separation (Figure 397) shows that the time to establish equilibrium conditions is a function of the power to the entry shell. The temperature change rate versus time is shown in Figure 398. With 200 watts power to the entry shell, temperature equilibrium is established in less than 3 days.

It should be noted here that cruise and planetary orbit temperatures as well as power requirements are largely affected by spacecraft/capsule interface assumptions and data presented are applicable to the selected reference case only. The general trend, however, should be similar even for a design based on different spacecraft/capsule interface assumptions.

The effect of a midcourse maneuver near Earth on heat shield temperatures has been investigated previously (paragraph 11.3.1) for the entry from approach trajectory case. Results are generally applicable to the enetry from orbit study as well since the energy exchange between the spacecraft/capsule interface is negligible compared to the high solar energy influx resulting from direct sun impingement. It should be noted here that the temperatures shown are average temperatures and that local heating will occur if the planetary vehicle is in a fixed attitude for an extended time period. This effect is shown in Figure 399.

If the sterilization canister coating displays a high α/ϵ value ($\alpha/\epsilon = 5.0$), sterilization canister temperatures may well be over 400°F and the heat shield temperature may be excessive (over 300°F). A lower α/ϵ ratio (reduced α while retaining a low ϵ) may be desirable.

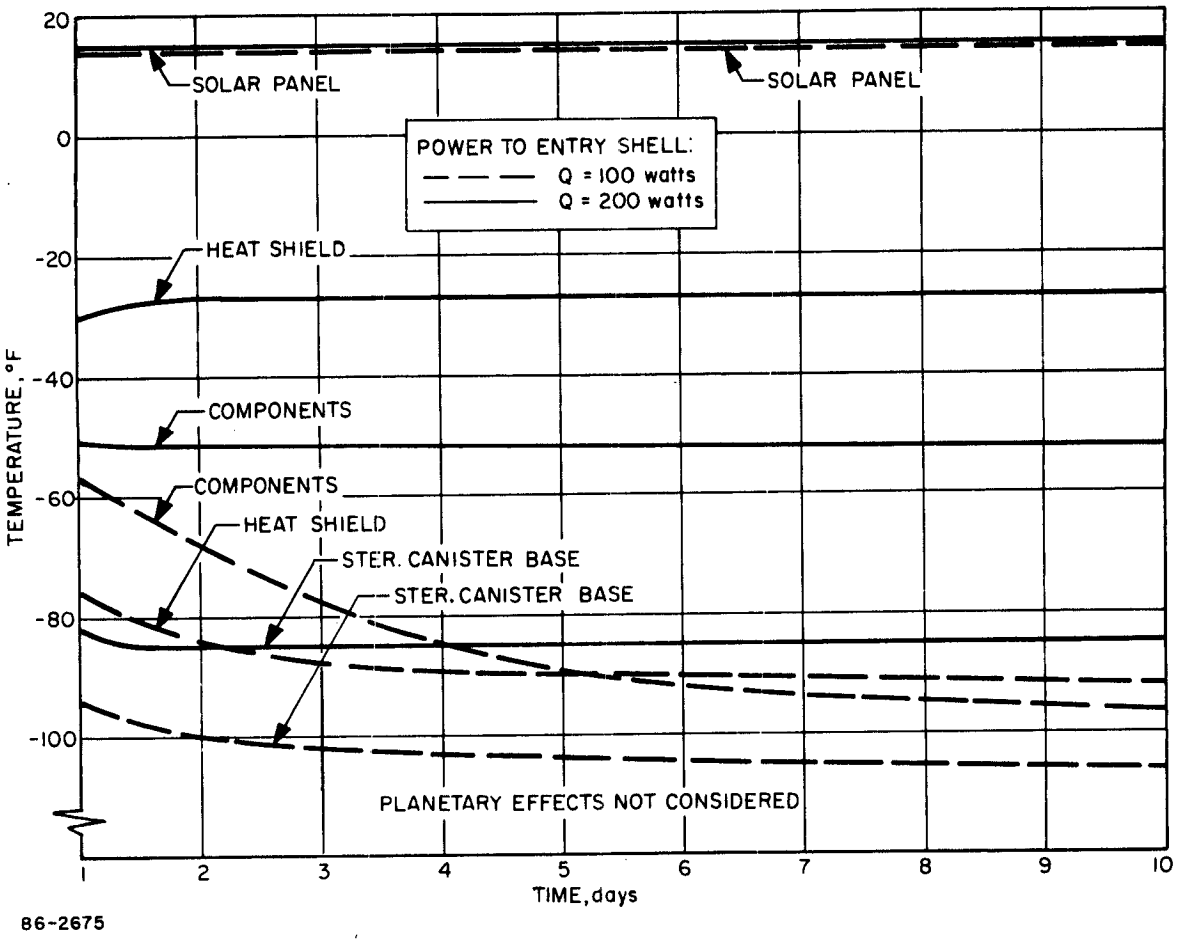

Figure 397 TEMPERATURE VERSUS TIME -- CRUISE NEAR MARS AND ORBIT

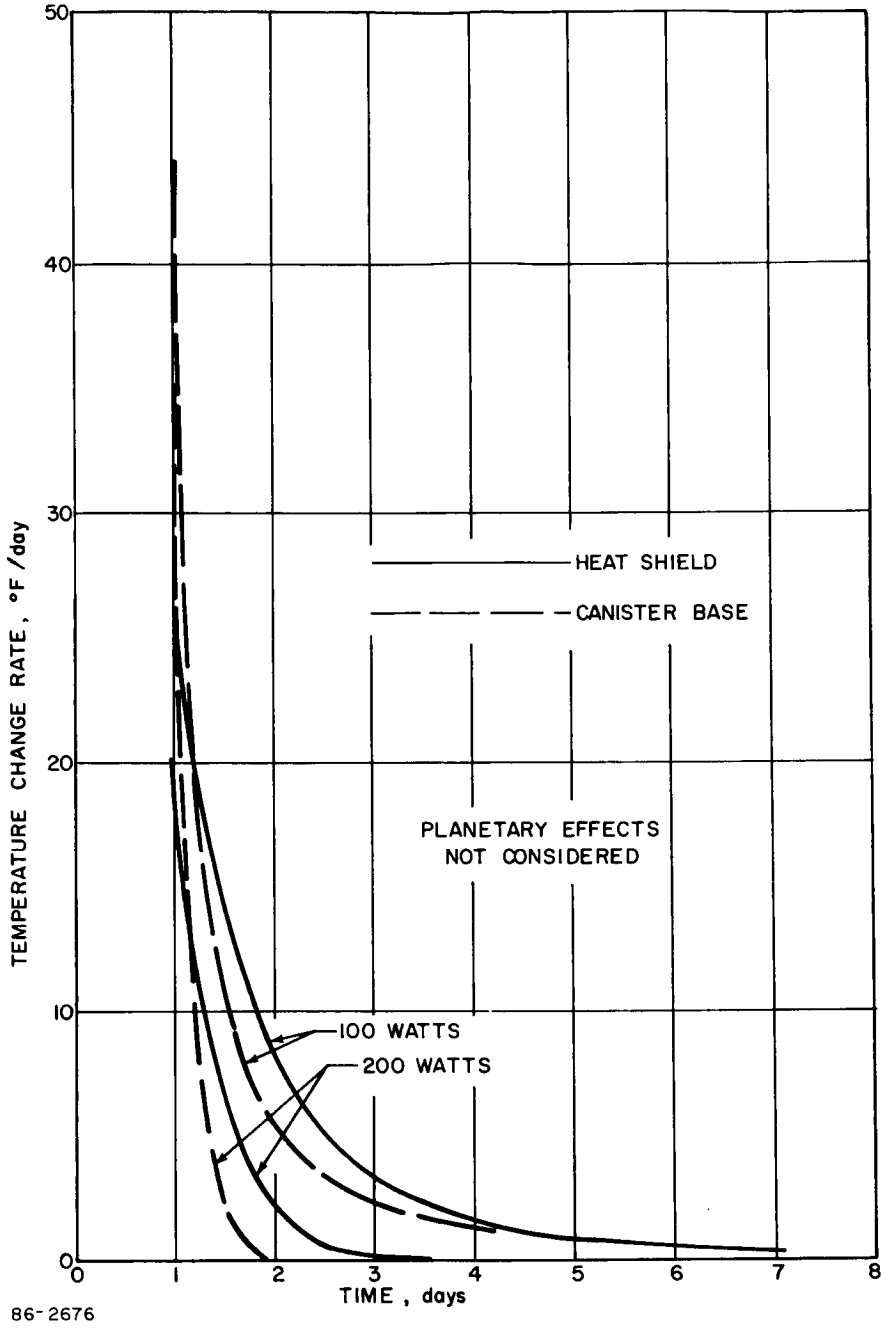

Figure 398 TEMPERATURE CHANGE PER DAY VERSUS TIME TO APPROACH EQUILIBRIUM -- CRUISE NEAR MARS

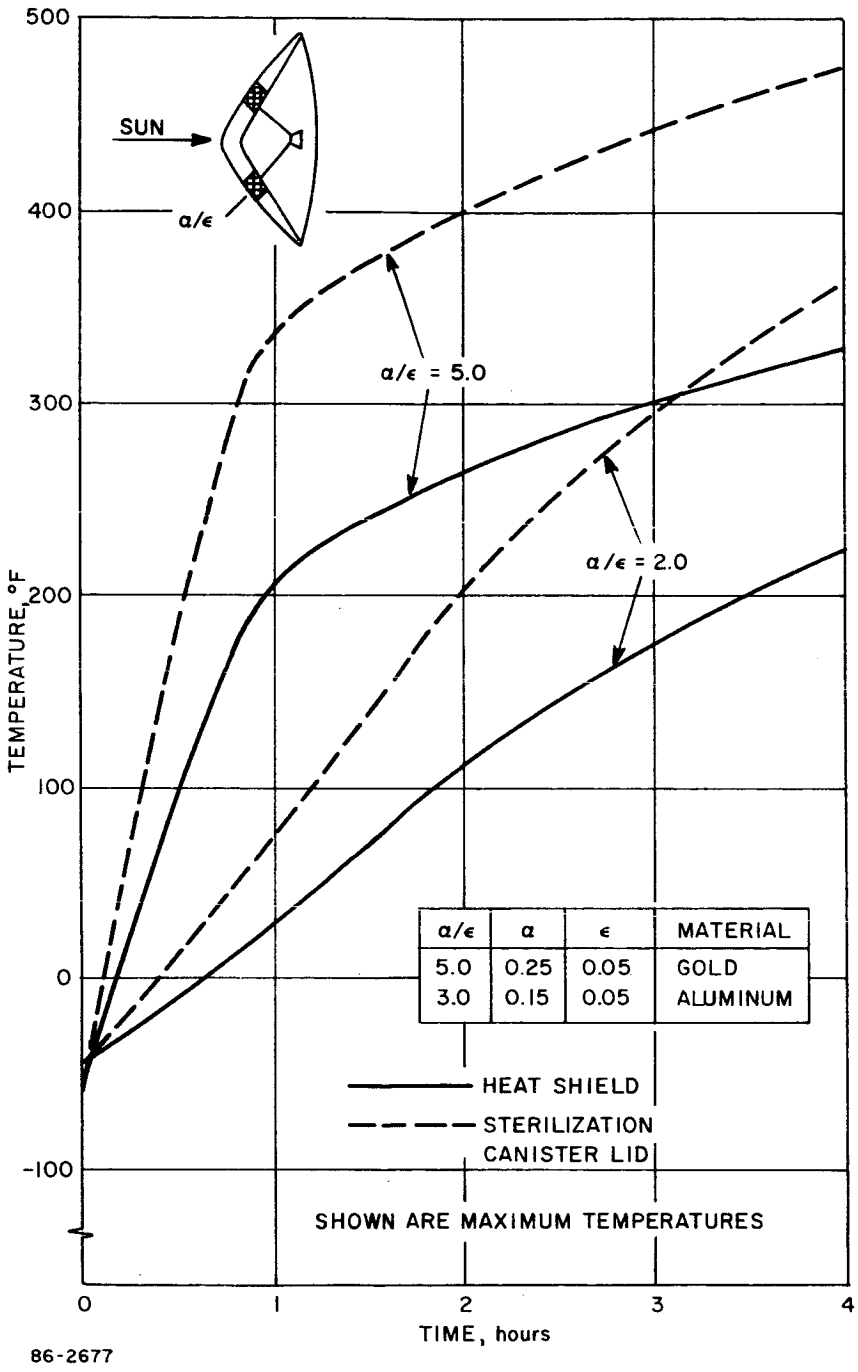

Figure 399 EFFECT OF A MIDCOURSE MANEUVER NEAR EARTH ON HEAT SHIELD TEMPERATURE

Planetary thermal effects (thermal radiation and albedo) are of a cyclic nature and will influence the temperature distribution across the heat shield to some extent. No critical problems, however, are foreseen since the coating α/ϵ ratio is high and temperature is primarily controlled by the addition of internal power. The chosen reference design concept considers the worst case (from power requirement considerations) by neglecting planetary thermal effects.

2. Preseparation Warmup and Components Checkout Period -- All critical components have to be warmed up to their minimum acceptable operative temperature level (See Table C) prior to the 4-hour components checkout period while the planetary vehicle is still in orbit. The components warmup period is critical insofar as available power from the spacecraft is limited. Specification of thermal control requirements for this phase of the mission is therefore essentially a tradeoff between the amount of power allocated to the entry shell and components, and the desired entry shell lower temperature level before flight capsule separation and preseparation warmup time. The power required to the components is determined by their physical properties (mass, specific heat), desired temperature rise rate and their heat loss to the environment by thermal conduction and radiation. This demand was calculated to amount to 180 watts for a warmup period of 10 hours. Assuming that the total power available is of the order of 230 watts, 50 watts would then remain available for entry-shell heating. The effect of entry shell power input variation and cutoff on the heat shield and components temperature level is shown in Figure 400. A total entry-shell power cutoff over a period of 10 hours causes an entry-shell temperature drop of 57°F, while a reduction from 200 watts to 50 watts will result in a 43°F temperature drop. The 180/50-watt (component-to-heat shield input ratio) case was selected for reference and is shown in Figure 392 and Table CI. A 180/100-watt power distribution case assuming that a total of 280 watts is available from the spacecraft for a period of 10 hours is shown in the same figure for comparison purposes.

After the preseparation warmup period, all components are turned "on" for 4 hours and dissipate sufficient energy to maintain their operating temperature without additional heat. Full power (200 watts) is then switched back and supplied to the entry shell over the 4-hour components checkout period and brings the heat shield temperatures up again to a higher level (-58°F) before entry vehicle separation.

Peak power demand during this period ranges from 230 watts (20 watts above the orbital phase) to 280 watts depending on the desired temperature of the heat shield at entry (Figure 400). This in turn depends

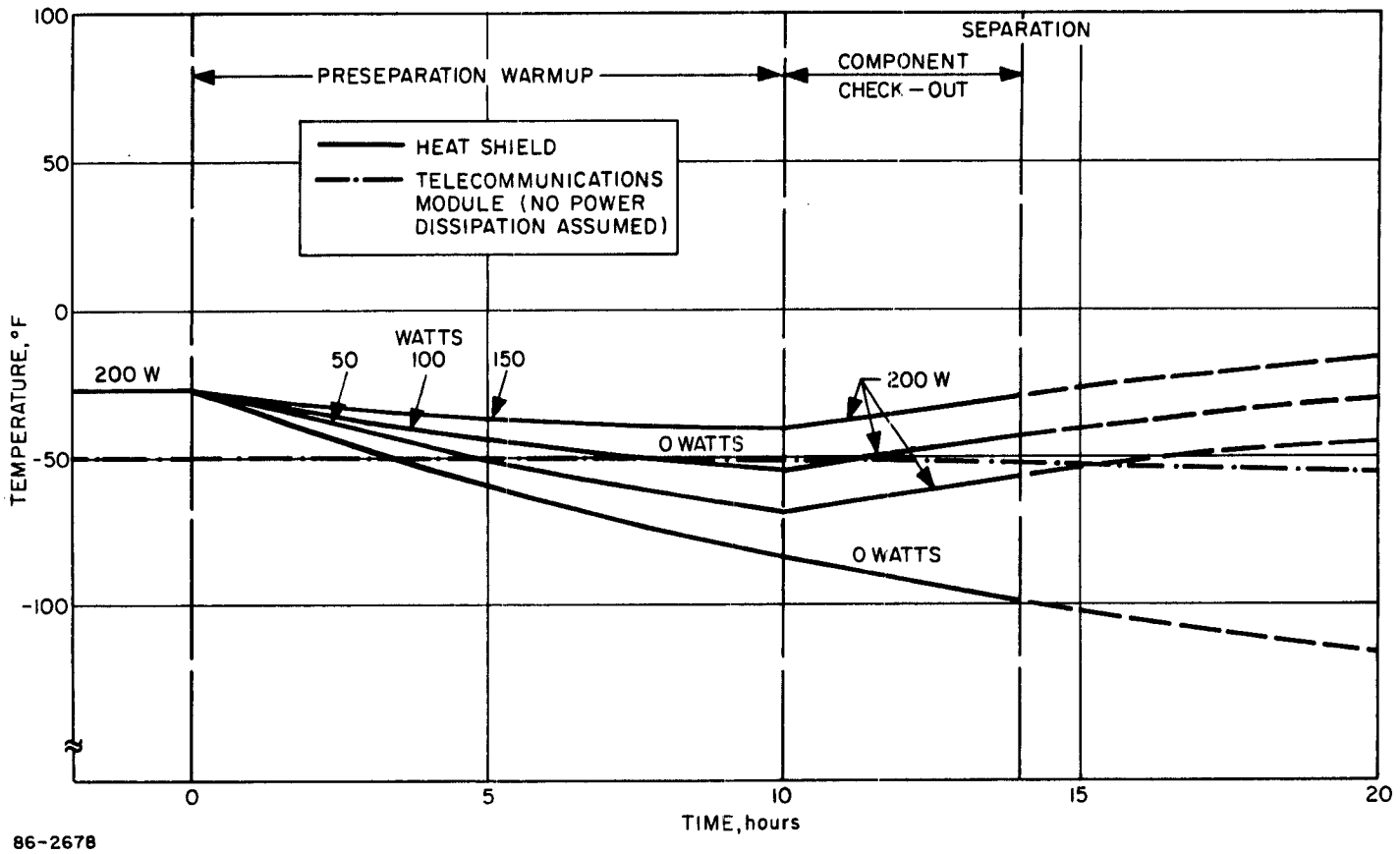

Figure 400 EFFECT OF ENTRY SHELL POWER VARIATION ON HEAT SHIELD AND COMPONENT TEMPERATURES, MARS ORBIT -- STERILIZATION CANISTER LID OFF

on the postseparation temperature history as affected by the orbit selected for the planetary vehicle from system considerations. The peak power demand is discussed in more detail below.

It is concluded that thermal control over this particular period of concern can be handled by proper components design and distribution of the available power within the capsule.

3. Postseparation -- During the mission phase from flight capsule separation to entry, the entry vehicle is in free flight for a maximum duration of 1 hour. The thermal balance is maintained by solar energy absorbed by areas exposed to the sun (projected areas), energy radiated from areas exposed to space (total areas), and the internal energy dissipated. The temperature of exposed entry vehicle sections is essentially a function of the ratio of projected area to total area, coating properties, and exposure time. If coating properties and time are fixed, the ratio of projected area to total area remains variable and is a function of the entry vehicle orientation relative to the sun.

Considering three orbits, one nominal and two extreme cases, the range of possible orientations is between 14 and 61 degrees with the nominal case at 24 degree (see also Table XLVIII). The effect of orientation on the entry vehicle temperature level has been investigated. Typical temperature distributions for the three orbits considered are shown in Figures 401 through 405. It is assumed that the nonspinning entry vehicle stays in the de-orbit attitude from de-orbit to entry. Only a small temperature gradient (in the order of 1°F to 5°F) develops across the entry-shell thickness for all cases considered. Larger thermal gradients develop in the radial direction. Their magnitude is determined by the coating properties and projected area exposed. It is shown that smaller sun orientation angles are more favorable than larger angles and thermal gradients in the entry shell are significantly decreasing with decreasing sun orientation angle. All temperatures remain within tolerable limits during the relatively short postseparation phase, and no performance difficulties are anticipated. However, consideration of the two extreme orbit cases (700 x 20,000 km and 1500 x 4000 km) indicates for the same power supply prior to separation a difference in the initial entry temperatures. Relatively low initial entry temperatures in any of these cases (from -105°F to +20°F) in various exposed sections should be conducive to large weight savings (or increased safety margins) in the heat shield requirement, while not imposing any (or very small) penalties in the structure weight (potential increase in honeycomb-core depth). Temperatures of power dissipating payload components increase (due to their operating condition) during the postseparation

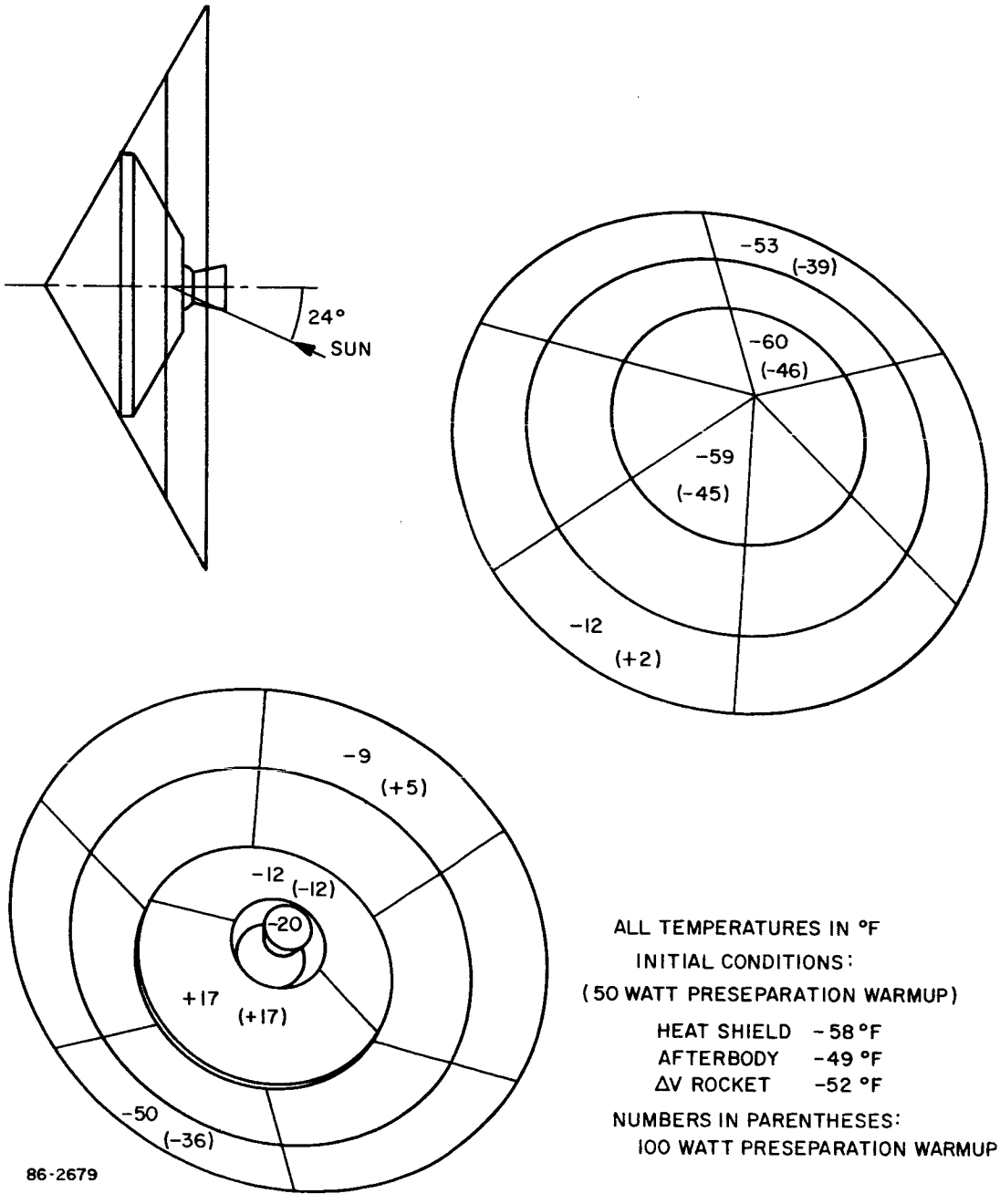

Figure 401 POSTSEPARATION TEMPERATURE DISTRIBUTION 1000 x 10,000 km ORBIT--NOMINAL CASE

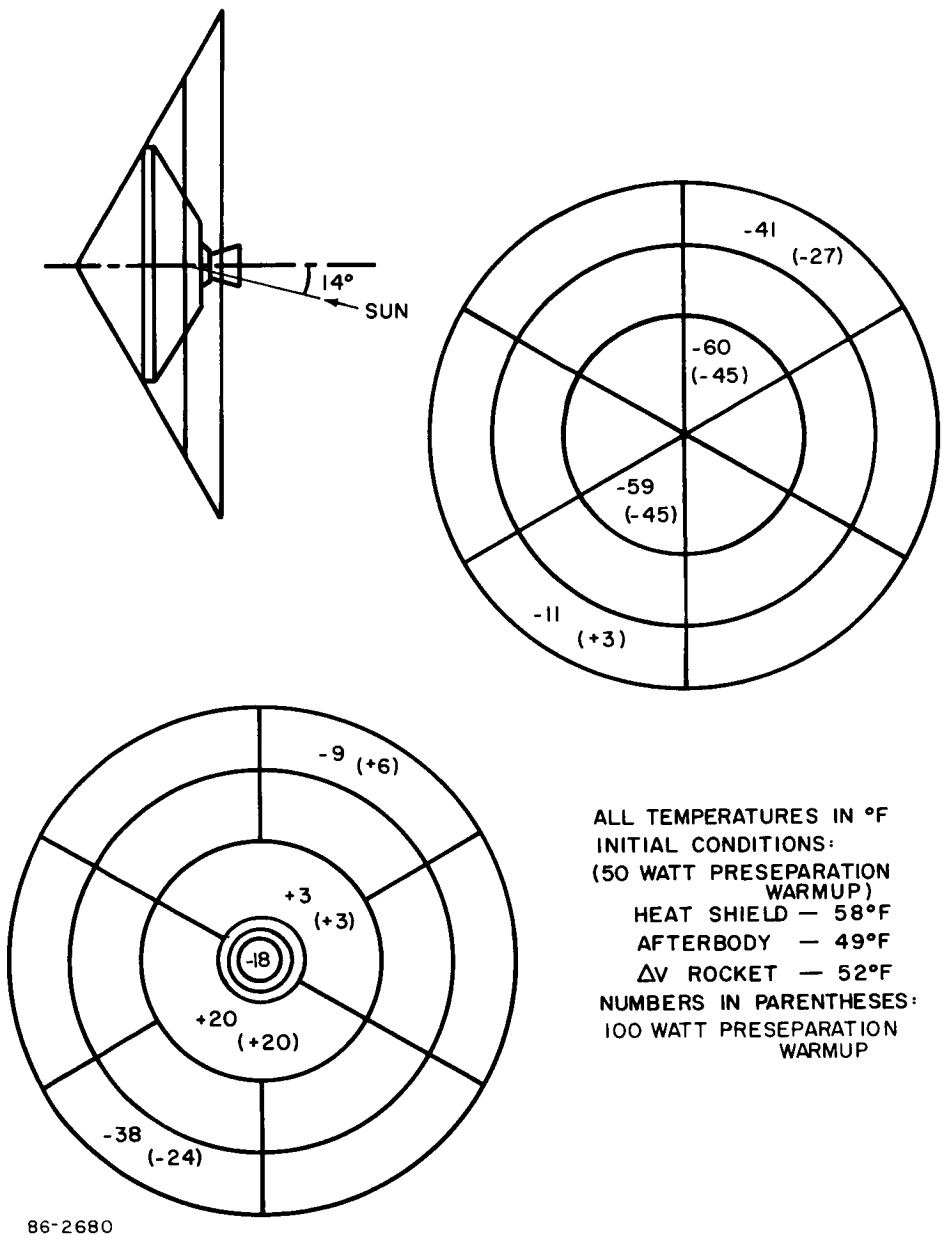

Figure 402 POSTSEPARATION TEMPERATURE DISTRIBUTION 700 x 20,000 km ORBIT

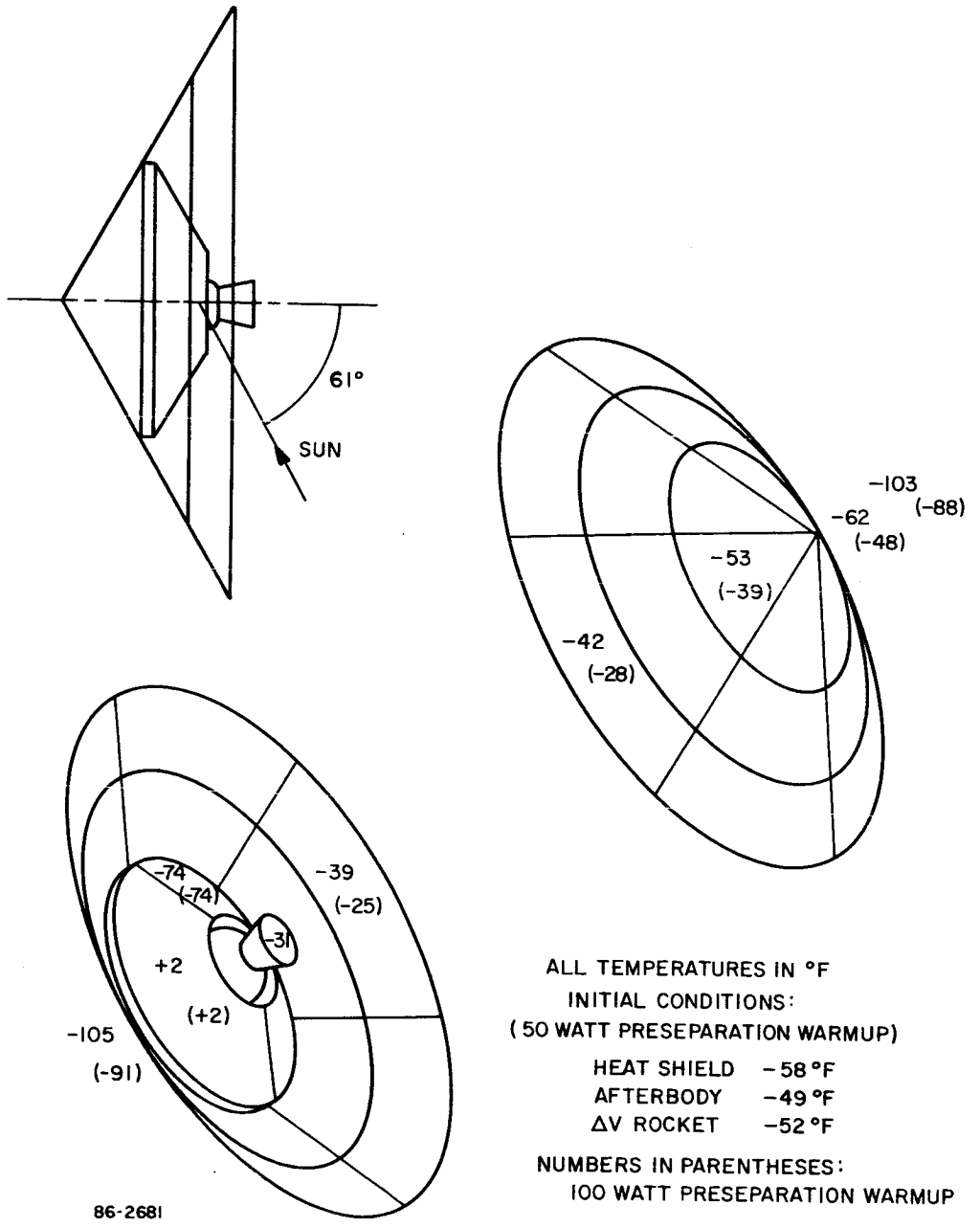

Figure 403 POSTSEPARATION TEMPERATURE DISTRIBUTION 1500 x 4000 km ORBIT

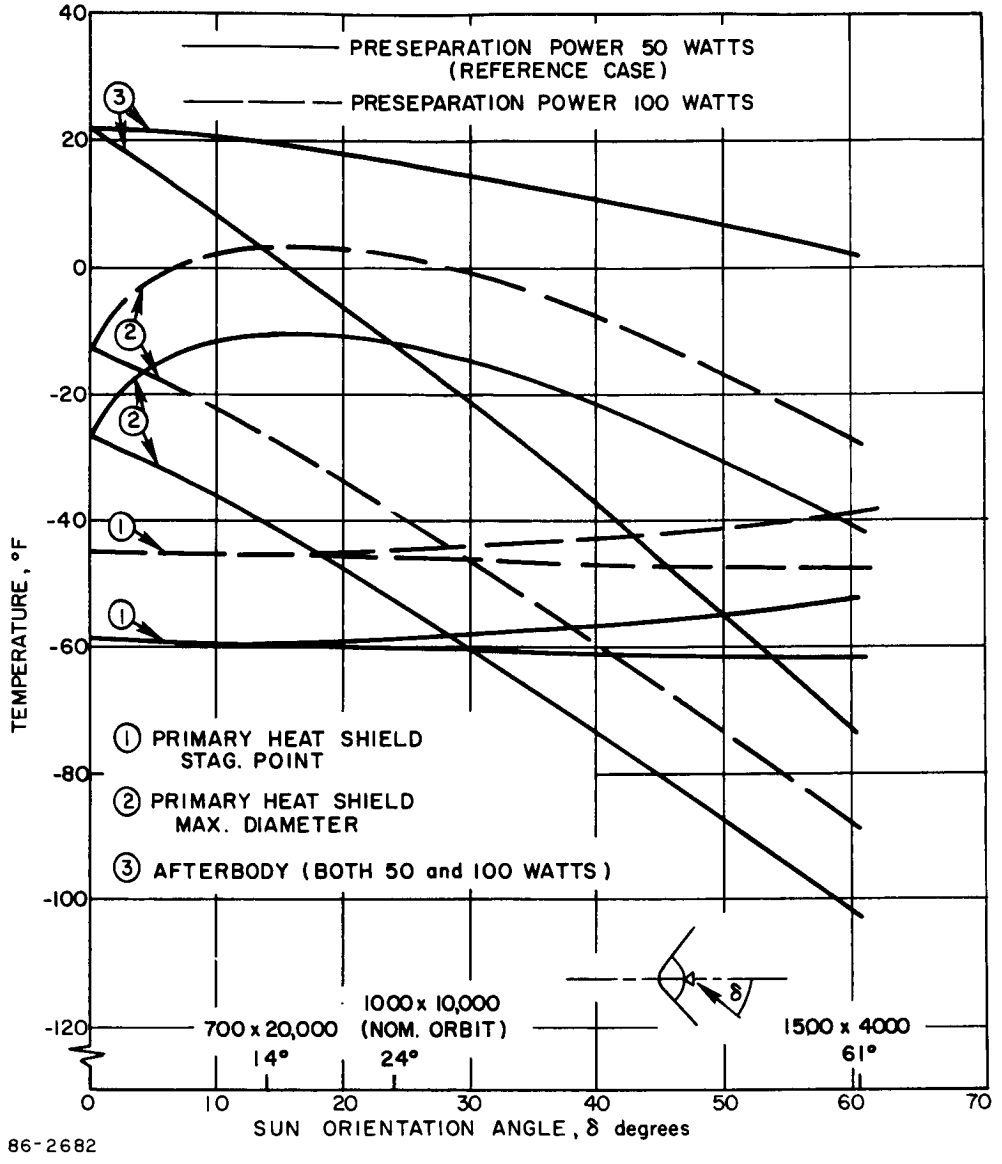

Figure 404 END OF POSTSEPARATION TEMPERATURES FOR VARIOUS ORBITS AND PRESEPARATION POWER LEVELS

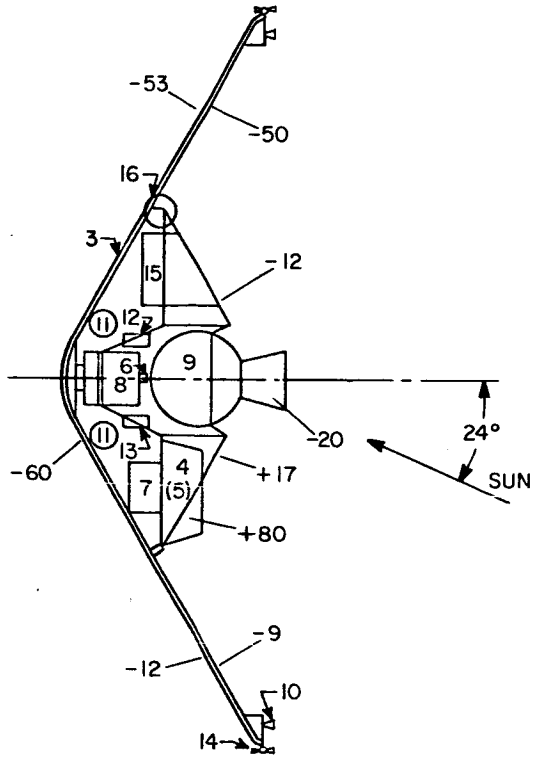

(ALL TEMPERATURES IN °F)

4 TELECOMMUNICATIONS AND POWER MODULE (2)
5 INSTRUMENTATION MODULE
6 ACCELEROMETERS (3)
7 PENETROMETERS (4)
8 TELEVISION
9 ΔV PROPULSION
10 ACS REACTION NOZZLES (12)
11 ACS COLD GAS TANK (2)
12 ACS ELECTRONICS
13 ACS SENTRY GYRO
14 TVC REACTION SUBSYSTEM (4)
15 PARACHUTE
16 ENTRY SHELL SEPARATION MECHANISM

86-2683

Figure 405 TEMPERATURE DISTRIBUTION AT THE END OF POSTSEPARATION--NOMINAL ORBIT

phase but remain well within acceptable limits to ensure maximum performance from entry to impact. Considering a tumbling entry vehicle as a failure mode case, even less of a problem is anticipated than with a vehicle in fixed sun orientation. The vehicle will assume an average temperature level which is well within the temperature boundaries investigated.

Returning to the observed (Figure 392 and Table CI), differences in the heat shield temperatures obtained prior to entry when a nominal power supply distribution was utilized (no excess peak demand over the orbit requirement), it may be noted that the heat shield temperatures drop slightly below the accepted -100°F lower limit. (See Sections 6.0 and 10.0 for discussion of low-temperature tolerance of Purple Blend Mod 5 and structural performance.) This limit may vary with the final ablator selection and ultimately will depend on the results of a test program and, since it may either be lowered or increased, it is well to consider the implications of a higher heat shield temperature requirement. In the same Figure 392 and Table CI as well as Figure 397, the temperature response for the nominal (zero excess power) case are compared with cases where additional 50 to 100 watts are supplied during warmup period. For the extreme orbit (1500 x 4000Km), it may be seen that the minimum heat shield temperatures rise by 14°F and 28°F respectively for 50 watts and 100 watts additional heat supply.

It may be thus concluded that if approximately 200 watts are available from the spacecraft, thermal control may be achieved for the reference design over the range of orbital conditions selected for the system. An additional 50-100 watts would easily permit deviations in the lower temperature limit imposed on the heat shield material, based on the preliminary test data.

4. Entry to Impact -- The effect of entry heating on entry vehicle structural members has been discussed in Section 9.0 of this book. An examination of anticipated entry shell and afterbody backface temperatures revealed that a maximum temperature rise of 320°F and 360°F respectively is expected. Energy influx during entry takes place during a relatively short time period (between 301 and 415 seconds) and is reversed by convective cooling during the even shorter (between 163 and 324 seconds) parachute descent phase. All components are well insulated from the structure. The need for specification of additional insulation is subject to the development test program results (thermal control model). All components are operating and dissipate heat while they are approaching their maximum operative temperature limit. Provided that critical components are properly designed, integrated and insulated, thermal control during entry and parachute descent does not appear to present critical problems. An exception,

however, is the television subsystem. Thermal control problems associated with the television module are discussed in Volume V, Book 4, Section 7.1.8.2 of this report.

12.3.3 Problem Areas

The preceeding analysis of the thermal control system requirements and its performance indicated supplemental information will be needed and where problems may be anticipated:

1. Flight Spacecraft/Flight Capsule Thermal Interface Data

The study has shown the impact of thermal interface assumptions on cruise and orbit temperatures and power requirements. The availability of actual interface data is mandatory for capsule optimization and integration into a particular planetary vehicle.

2. Flight Capsule Coatings and Entry Shell Coatings and Heating Element Integration

The selection and application of coatings and the integration of heating elements into the complex entry shell structure (bond) ablative material/coating system is an area of concern. The coating selection and application procedures must be compatible with the decontamination and sterilization process. The stability of the coatings under the above and flight environmental conditions will have to be established.

3. Thermal Contact Resistance Data

Data obtained under simulated conditions are required for design optimization.

4. ΔV Rocket

Additional experimental data on performance after exposure to low (-100 to -40°F) temperatures must be obtained.

REFERENCES

1. Levin, G. M., D. E. Evans, V. Stevens (Ed.) NASA Engineering Models of the Mars Atmosphere for Entry Vehicle Design, NASA TN D-2525 (November 1964).

2. Nichols, J. O. and Nierengarten, Aerodynamic Characteristics of Blunt Bodies, IR 32-677, JPL (1964).

3. Keyes, J. W., Longitudinal Aerodynamic Characteristics of Blunted Cones at Mach Numbers of 3.5, 4.2 and 6.0, NASA TN D-2201.

4. Lees and Lester, Laminar Heat Transfer over Blunt-nosed Bodies at Hypersonic Flight Speeds, Jet Propulsion (April 1956).

5. Comparative Studies of Conceptual Design and Qualification Procedures for a Mars Probe/Lander, Part I Report, Volume IV-Technical Analyses, Book 1, Avco RAD-TR-65-29, (8 October 1965).

6. Nichols, J. O. and E. A. Nierengarten, Static Aerodynamic Characteristics of Blunted Cones and Round Shouldered Cylinders Suitable for Planetary Entry Vehicles at a Mach Number Range of 1.65 to 9.00, N64-29212 (1964).

7. Nichols, J. O. and E. A. Nierengarten, Aerodynamic Characteristics of Blunt Bodies, JPL, TR No. 32-677, 1964.

8. Keyes, J. W., Longitudinal Aerodynamic Characteristics of Blunted Cones at Mach Numbers of 3, 5, 4, 2, and 6. NASA TN-D-2201 (February 1964).

9. Keyes, J. W., "Longitudinal Aerodynamic Characteristics of Blunted Cones at Mach Numbers 3.5, 4.2 and 6.0," NASA TND-2201, February 1964.

10. Shaw, D., D. Fuller, C. Babb, "Effects of Nose Bluntness, Fineness Ratio, Cone Angle, and Model Base on the Static Aerodynamic Characteristics of Blunt Bodies at Mach Numbers of 1.57, 1.8 and 2.16 and at Angles of Attack up to 180°," NASA TND-1781 (May 1963).

11. McCarthy, J. F., Jr., T. Kubata, A Study of Wakes behind A Circular Cylinder at M = 5.7, AIAA Jour. (April 1964).

12. Fenske, J. F., Preliminary Results of Static Force and Pressure Tests for Shape 801-D at Supersonic Speeds, JPL Test 225, Aero Memo 101, (December 1956).

13. Avco RAD Memorandum K400-OLZ-4, From O. Zappa to H. Hurwicz, Langley TD Meeting (Aerodynamics Side Meeting) (June 1965).

14. Feldman, S., Hypersonic Conical Shock for Dissociated Air in Thermodynamic Equilibrium, Jet Propulsion (December 1957).

15. Shapiro, A., The Dynamics of Thermodynamics of Compressible Fluid Flow, Ronald Press Co., New York (1953).

16. Liepmann and Roshko, Elements of Gasdynamics, John Wiley and Sons, New York (1957).

17. Courant and Friedricks, Supersonic Flow and Shock Waves, Interscience Publishers, Inc., New York (1948).

18. Howarth, L., Modern Developments in Fluid Dynamics - High Speed Flow, Clarendon Press, Oxford (1953).

19. Kaattari, G. E., Predicted Gas Properties in the Shock Layer Ahead of Capsule-Type Vehicles at Angles of Attack, NASA TND-1423 (October 1962).

20. Kaattari, G. E., Predicted Shock Envelopes About Two Types of Vehicles at Large Angles of Attack - NASA TND-860 (1961).

21. Spencer, D. F., An Evaluation of the Communication Problem for a Blunt Mars Entry Capsule and a Potential Method for the Elimination of Blackout, Tech. Report No. 32-594, JPL (April 1964).

22. Moe, M. M., and B. A. Troesch, The Computation of Jet Flows with Shocks," Report TR-59-0000-00661, Space Technology Laboratories, Inc., May 12, 1959.

23. Kemp, N. H., P. H. Rose, and R. H. Detra, Laminar Heat Transfer around Blunt Bodies in Dissociated Air, JAS, 26 (July 1959).

24. Rose, P., R. F. Prostein, and M. C. Adams, Turbulent Heat Transfer Through a Highly Cooled Partially Dissociated Turbulent Boundary Layer, JAS, 25 (December 1958).

25. RAD, Mars-Venus Capsule Parameter Study, Vol. 1, Avco RAD-TR-64-1 (March 1964).

26. Horton, T. E. and T. L. Babineaux, An Experimental Assessment of the Effect of Large Amounts of Argon in Planetary Atmospheres on Stagnation Point Heating, to be published at the AIAA Winter Meeting (January 1966).

27. Zappa, O. L., Reissue of Simplified Sharp Cone Calculations, Avco RAD, TR-S210-63-289 (6 November 1963).

28. Ferri, A., V. Zakkay, and L. Ting, Blunt Body Heat Transfer at Hypersonic Speed and Low Reynolds Number, J. Aerospace Sciences (December 1961).

29. Cheng, H. K., The Blunt Body Problem in Hypersonic Flow at Low Reynolds Numbers, IAS Paper No. 63-92 (January 1963).

30. Truitt, R. W., Hypersonic Turbulent Boundary Layer Interference Heat Transfer in Vicinity of Protuberances, J.AIAA, pp. 1754-55, (September 1965).

31. Surber, T. E., Heat Transfer in the Vicinity of Surface Protuberances, J. Spacecraft and Rockets, Vol. 2, No. 6, pp. 978-80 (November-December 1965).

32. Nestler, D. E., I. Musser, Correlations for Convective Heat Transfer, Pressure Distribution and Shock Detachment Distance for Blunt Axisymmetric Forebodies, G. E. - MSVD, Technical Memorandum No. 149 (January 1960).

33. Charwat, A. F., C. F. Dewey, Jr., J. N. Roos, and J. A. Hitz, An Investigation of Separated Flows - Part 11: Flow in the Cavity and Heat Transfer, J. Aerospace Sciences, Vol. 28, No. 7, pp. 513-527 (July 1961).

34. Nicoll, K. M., A Study of Laminar Hypersonic Cavity Flows, AIAA Paper 64-47 (January 1964).

35. Morgan, B. M., Aerodynamic Heating Aggravation Due to Protuberances in Turbulent High Velocity Flow, Avco/RAD Suo-TR 64-30 (4 March 1964).

36. Burbank, P. B., R. A. Newlander, and J. K. Collins, Heat Transfer and Pres-measurements on Attacked Protuberances in a Supersonic Turbulent Boundary Layer at Mach Number of 2.65, 3.51, and 4.44, NASA Tech. Note TN-D-1372 (December 1962).

37. Sandborn, U. A., and K. Heron, Measurements of Heat Transfer on a Flat Plate, Avco/RAD TM-63-40 (June 1963).

38. Morris, S. D. and O. L. Durkin, Pressure and Heat Transfer Tests on a Blunt 12.5 degree Cone with Protrusions at Mode 10, AEDC, Technical Documentary Department No. AEDC-TOR-63-81 (May 1963).

39. Cardia, W. H., "Local Heat Transfer Coefficient in a Nozzle with High Speed Laminar Flow, AIAA Journal, vol. 3, No. 12, pp. 2183-88 (December 1965).

40. Bach, L. H., P. F. Massier, H. C. Gier, Convective Heat Transfer in a Convergent-Divergent Nozzle, Tech. Report No. 32-415, JPL (November 15, 1963).

41. Van Tassell, W., and P. Levine, Simplified Heating Relations, Memorandum No. T510-TR-59-202, Avco/RAD (October 1959).

42. Grabow, R. M., The Evaluation of Turbulent Boundary Layer Thicknesses for Use in Blunt Body Aerodynamic Heating Analyses, Memorandum No. TR-S210-63-210, Avco/RAD (September 1963).

43. Katzen, E. D. and G. E. Kaattari, Flow Around Blunt Bodies Including Effects of High Angles of Attack, Nonequilibrium and Vapor Injection, AIAA Publication CP-9 (October 1964).

44. Guy, L. D., Tension Shell Structures for Low Density Entry Vehicles, Presented at AIAA Second Annual Meeting (July 1965).

45. Thomas, G. M. and W. A. Menard, Experimental Measurements of Nonequilibrium and Equilibrium Radiation from Planetary Atmosphere, AIAA Publication CO-9 (October 1946).

46. Mars-Venus Capsule Study, Vol. 1 Avco/RAD TR-64-1.

47. Page, W. A. and J. O. Arnold, Shock-Layer Radiation of Blunt Bodies at Reentry Velocities, NASA TR R-193 (1964).

48. Technical Memorandum RAD-TM-62-70, Avco/RAD (September 1962).

49. JPL Entry Vehicle Design - Computer Program Users Manual, RAD TR-65-23, Avco/RAD (20 September 1965).

50. Robb, A. F. and P. C. DiCarlo, Aerodynamic and Heating Characteristics of the Ames Spherical Probe, and Simulation of Martian Trajectories on Earth, Avco/RAD Memo (19 January 1965).

51. Levine, P. and O. L. Zappa, Approximate Heating and Loading Relationships for Ballistic Missile Reentry. Avco/RAD TR (27 November 1961).

52. Radkowski, P. P., "Stress Analysis of Thin Orthotropic Multilayer Shells of Revolution," AIAA paper No. 2889-63, presented at the AIAA Launch and Space Vehicle Shell Structures Conference, Palm Springs, California (April 1963).

53. Reissner, E., "Small Bending and Stretching of Sandwich Type Shells," NACA Report No. 975 (1950) (also published as NACA TN 1832, 1949).

54. Percy, J. H., et. al., "Application of Matrix-Displacement Method to Linear Elastic Analysis of Shells of Revolution," AIAA Journal, vol, 3, pp. 2138-2145 (1965).

55. Percy, J. H., et. al., "Sabor III: A Fortran Program for Linear Elastic Analysis of Shells of Revolution by the Matrix Displacement Method," MIT Aeroelastic and Structures Laboratory TR 121-6, (NASA STAR Document N65-36654).

56. Weingarten, V. I., and P. Seide, "Elastic Stability of Thin-Walled Cylindrical and Conical Shells Under Combined External Pressure and Axial Compression," AIAA Journal, vol. 3, pp. 913-920 (1965).

57. Batdorf, S. B., "A Simplified Method of Elastic Stability Analysis for Thin Cylindrical Shells," NACA Report No. 874 (1947).

58. Seide, P., "Calculations for the Stability of Thin Conical Frustums Subjected to External Uniform Hydrostatic Pressure and Axial Load," Journal of the Aerospace Sciences, vol. 29, pp. 951-955 (1962).

59. Norris, C. B., and W. J. Komers, "Short-Column Compressive Strength of Sandwich Construction as Affected by the Size of the Cells of Honeycomb Core Materials," U. S. Forests Products Laboratory Report No. 1817 (1956).

60. Yusuff, S., "Theory of Wrinkling in Sandwich Construction," Journal of the Royal Aeronautical Society, vol. 59, pp. 30-36 (1955).

61. NASA Space Vehicle Design Criteria, "Buckling of Thin-Walled Circular Cylinders," NASA SP-8007, vol. III, Part C, Chapter 2.

62. Timoshenko, S., and J. M. Gere, "Theory of Elastic Stability," McGraw-Hill Book Company, second edition, sections 7.10 and 11.13 (1961).

63. Homewood, R. H., A. C. Brine, and A. E. Johnson, "Instability of Monocoque Shells," Society for Experimental Stress Analysis, Paper No. 457, presented at Washington, D. C. (May 1959).

64. Kaplan, A., and Y. C. Fung, "A Nonlinear Theory of Bending and Buckling of Thin Elastic Shallow Spherical Shells," NACA TN-3212 (1954).

65. Kloppel, K., and O. Jungbluth, "Beitrag zum Durchslag Problem dunn wandiget Kugelschalen," Der Stahlbau, vol. 22, pp. 121-130, 288, Springer, Berlin (1935).

66. Mars-Venus Capsule Parameter Study, Avco/RAD TR-64-1, vol. 1, prepared for JPL, pp. 173-184 (March 1964).

67. Den Hartog, J. P., "Advanced Strength of Materials," McGraw-Hill Book Company, Section 34 (1951).

68. Timoshenko, S., "Strength of Materials, vol. 1, third edition, van Nostrand, Sections 50 and 84 (1955).

69. Langhaar, H., and A. Boresi, "Buckling of a Long Fiber-Wound Cylindrical Shell Due to Stresses Caused by Windings," Journal of Applied Mechanics, Vol. 32, pp. 81-86 (1965).

70. Fenves, S. J., R. D. Logcher, and S. P. Mauch, "Stress: A Reference Manual - A Problem Oriented Computer Language for Structural Engineering," MIT Press (1964).

71. Fenves, S. J., R. D. Logcher, S. P. Mauch, and K. F. Reinschmidt, "Stress: A User's Manual, A Problem Oriented Computer Language for Structural Engineering," MIT Press (1964).

72. Platus, D. H., Conical Shell Vibrations," NASA TN D-2767 (1965).

73. Anderson, M. S., et. al., "A Tension Shell Structure for Application to Entry Vehicles, NASA TN D-2675 (March 1965).

74. Serpico, J. C., "Elastic Stability of Orthotropic Conical and Cylindrical Shells Subjected to Axisymmetric Loading Conditions," AIAA Journal, Vol. 1, pp. 128-137 (1963).

75. JPL Entry Vehicle Design Computer Program Users Manual Avco/RAD-TR-65-23 (1965).

76. Thermal Protection Systems: Application Research of Materials Properties and Structural Concepts, Technical Documentary Report No. ASD-TDR-62-656, Avco RAD (July 1962).

77. Analysis of the Effects of Environmental Conditions on the Charring Ablators. NASA, Langley Research Center.

78. W117-K4000-6, Letter from J. A. Gautraud to W. C. Hayes, (15 July 1965).

79. Brown, J. D. and F. A. Shukis, An approximate Method for Design of Thermal Protection Systems, presented at the IAS 30th Annual Meeting, Aerospace Forum II (January 1962).

80. JPL Entry Vehicle Design Computer Program Users Manual RAD TR-65-23. Avco/RAD (September 1965).

81. Munson, T. R. and Spindler, R. J., Transient Thermal Behavior of Decomposing Materials, Part I: General Theory and Application to Convective Heating, presented at the 30th IAS Annual Meeting, New York, Paper No. 62-30 (January 1962).

82. Liu, Chia-Seng, Mass Transfer Cooling in Laminar Boundary Layers with Hydrogen Injected into Nitrogen and Carbon Dioxide Streams, M. S. Thesis, Department of Mech. Eng., University of Delaware, (NASA Research Grant (NSG 356) (June 1965).

83. Simon, H. A., C. S. Liu, J. P. Hartnett, and C. L. Chang, Binary Couette Flow with Hydrogen injected into Carbon Dioxide and Nitrogen Streams, Technical Report No. 32, Dept. of Mech. Eng., University of Delaware, Newark Delaware (June 1964).

84. Conceptual Design Studies of an Advanced Mariner Spacecraft, Avco/RAD Report No. RAD-TR-64-36, Volume III, Lander Design (October 1964).

85. Gifford, F., The Surface-Temperature Climate of Mars, Astrophysical Journal 123, pp. 154-161 (1956).

86. Gifford, F., The Surface Temperature Climate of Mars, Astrophysical Journal, 123, pp. 154-161 (1956).

87. Sutton, W. M. and J. Strong, Radiometric Observations of Mars, Astrophysical Journal, 131, pp. 459-469 (1960).

88. Spencer, D. F., Mars Engineering Atmosphere and Surface Models, JPL document (semifinal draft) (July 1965).

89. The New Study Models of the Voyager Spacecraft produced for JPL by GE, Boeing, and Thompson Ramo Wooldridge on p. 83 of: Engineering Problems in Capsule Sterilization, by V. J. Magistrale Jet Propulsion Laboratory, Astronautics and Aeronautics (February 1966).

APPENDIXES

A. BUCKLING OF A CIRCULAR RING OF ARBITRARY SECTION

B. INEXTENSIAL BUCKLING OF A CONICAL SHELL-RING STRUCTURE

APPENDIX A

BUCKLING OF A CIRCULAR RING OF ARBITRARY SECTION

An analysis is presented for three-dimensional buckling of a circular ring of arbitrary section. A formula is derived which includes the known solutions for pure in-plane and pure out-of-plane buckling as special cases.

1.0 BASIC RELATIONS

The following expressions for the curvatures are found from geometry (Reference 62.)*

$$\kappa_1 = \frac{1}{a^2}\left(\frac{d^2\Delta_r}{d\theta^2} + \Delta_r\right), \tag{1a}$$

$$\kappa_2 = \frac{1}{a^2}\left(\frac{d^2\Delta_x}{d\theta^2} - a\phi\right), \tag{1b}$$

$$\psi = \frac{1}{a}\frac{d}{d\theta}\left(\phi + \frac{w}{a}\right) \tag{1c}$$

The moments are related to the curvatures by the equations (Reference 68).

$$M_1 = B_1\kappa_1 - B_{12}\kappa_2, \tag{2a}$$

$$M_2 = B_2\kappa_2 - B_{12}\kappa_1, \tag{2b}$$

$$T = C\psi \tag{2c}$$

If the principal axes of the section are not aligned with the axis of revolution, it can be seen that the nonzero product of inertia term B_{12} causes a coupling between in-plane bending and out-of-plane bending.

Combination of the two foregoing sets of equations leads to the following moment-displacement relations

$$M_1 = \frac{B_1}{a^2}\left(\frac{d^2\Delta_r}{d\theta^2} + \Delta_r\right) - \frac{B_{12}}{a^2}\left(\frac{d^2\Delta_x}{d\theta^2} - a\phi\right) \tag{3a}$$

* Symbols for this Appendix are defined in Table A-1 .

$$M_2 = \frac{B_2}{a^2}\left(\frac{d^2\Delta_x}{d\theta^2} - a\phi\right) - \frac{B_{12}}{a^2}\left(\frac{d^2\Delta_r}{d\theta^2} + \Delta_r\right) \tag{3b}$$

$$T = \frac{C}{a}\left(\frac{d\phi}{d\theta} + \frac{1}{a}\frac{d\Delta_x}{d\theta}\right) \tag{3c}$$

By considering equilibrium of a differential element, it is found that*

$$\frac{dM_1}{d\theta} = -N\frac{d\Delta_r}{d\theta} \tag{4a}$$

$$\frac{dM_2}{d\theta} - T = -N\frac{d\Delta_x}{d\theta} \tag{4b}$$

$$\frac{dT}{d\theta} + M_2 = 0 \tag{4c}$$

2.0 DERIVATION OF BUCKLING EQUATION

Substitution of the moment displacement equations into the equilibrium equation leads to the following set of three-simultaneous equations in Δr , Δx and ϕ:

$$\frac{d}{d\theta}\left\{\left[B_1\left(\frac{d^2}{d\theta^2} + 1\right) + N_a^2\right]\Delta_r - B_{12}\frac{d^2\Delta_x}{d\theta^2} + B_{12}a\phi\right\} = 0 \tag{5a}$$

$$\frac{d}{d\theta}\left\{B_{12}\left(\frac{d^2}{d\theta^2} + 1\right)\Delta_r - \left(B_2\frac{d^2}{d\theta^2} - C + N_a^2\right)\Delta_x + (B_2 + C)a\phi\right\} = 0 \tag{5b}$$

$$-B_{12}\left(\frac{d^2}{d\theta^2} + 1\right)\Delta_r + (B_2 + C)\frac{d^2\Delta_x}{d\theta^2} + \left(C\frac{d^2}{d\theta^2} - B_2\right)a\phi = 0 \tag{5c}$$

By eliminating Δ_x and ϕ from this system of equations, a single equation in Δ_r is found

$$\left(\frac{d^2}{d\theta^2} + 1 + \frac{Na^2}{B_1}\right)\left[B_2\left(\frac{d^2}{d\theta^2} + 1\right)^2 + \frac{Na^2}{C}\left(C\frac{d^2}{d\theta^2} - B_2\right)\right] + Na^2\frac{B_{12}^2}{B_1 C}\left(\frac{d^2}{d\theta^2} + 1\right) - \frac{B_{12}^2}{B_1}\left(\frac{d^2}{d\theta^2} + 1\right)^2\left\{\frac{d\Delta_r}{d\theta} = 0\right. \tag{6}$$

This equation is satisfied by assuming a sinusoidal deflection shape. With the substitution

$$\Delta_r = \bar{\Delta}_r \cos n\theta$$

* Timoshenko, S., "Kippsicherheit des Gekrümmten Stabes mit Kreisförmiger Mittellinie," Collected Papers, McGraw-Hill Book Company, New York, pp. 371-376 (1953).

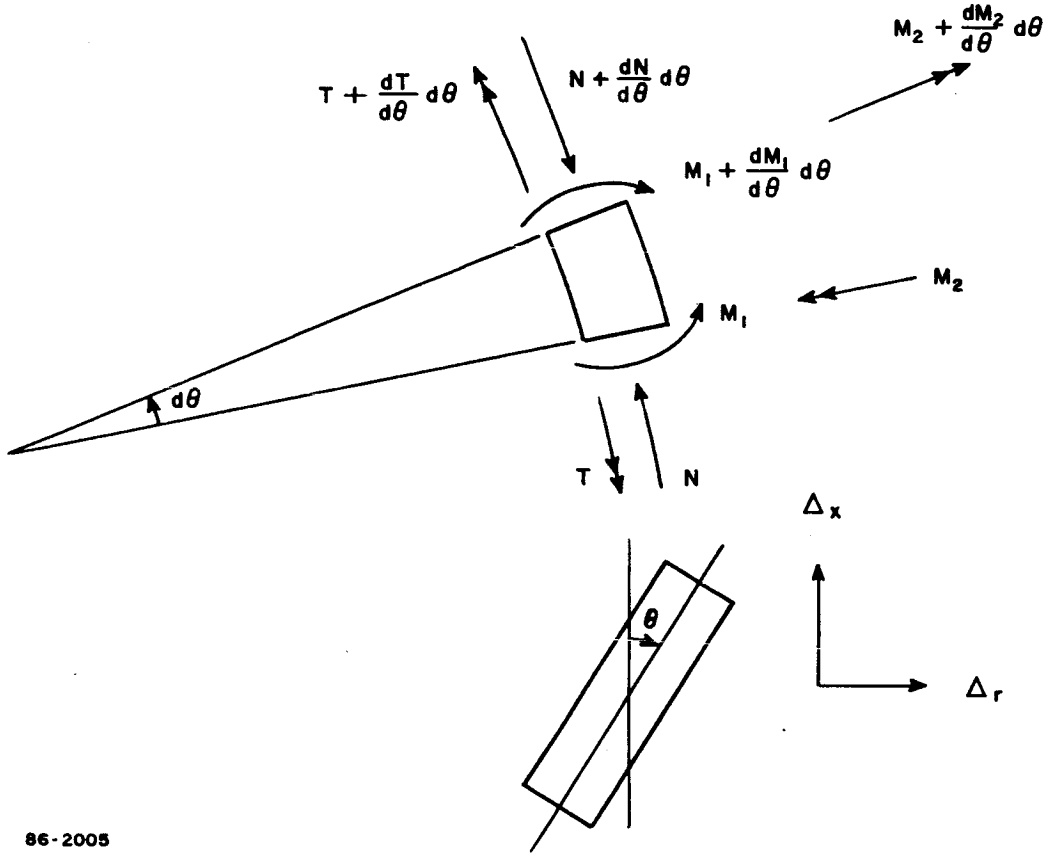

Figure A-1 EQUILIBRIUM OF A DIFFERENTIAL ELEMENT OF A CIRCULAR RING

and some algebraic rearrangement of terms, the following quadratic equation is obtained for the buckling load:

$$(n^2 C + B_2)N^2 - \frac{n^2-1}{a^2}[B_1(n^2 C + B_2) + (n^2-1) B_2 C - B_{12}^2] N + \frac{(n^2-1)^3}{a^4} C(B_1 B_2 - B_{12}^2) = 0$$

Solving this equation for N, it is found that

$$N = \frac{n^2 - 1}{2(n^2 C + B_2) a^2} \left\langle [B_1(n^2 C + B_2) + (n^2 - 1) B_2 C - B_{12}^2] \right.$$

$$\left. \pm \left\{[B_1(n^2 C + B_2) + (n^2 - 1) B_2 C - B_{12}^2]^2 - 4(n^2 - 1) C (B_1 B_2 - B_{12}^2)(n^2 C + B_2)\right\}^{1/2} \right\rangle$$

or

$$N = \frac{n^2 - 1}{2(n^2 C + B_2) a^2} \left\langle [B_1(n^2 C + B_2) + (n^2 - 1) B_2 C - B_{12}^2] \right.$$

$$\left. \pm \left\{[B_1(n^2 C + B_2) - (n^2 - 1) B_2 C - B_{12}^2]^2 + 4n^2 (n^2 - 1) B_{12}^2 C^2\right\}^{1/2} \right\rangle \qquad (7)$$

3.0 SPECIAL CASES

This result can be checked for the special case in which a principal axis of inertia is parallel to the axis of revolution. In this case $B_{12} = 0$, and the general solution (7) becomes

$$N = \frac{n^2 - 1}{2(n^2 C + B_2) a^2} \left\langle [B_1(n^2 C + B_2) + (n^2 - 1) B_2 C] \pm [B_1(n^2 C + B_2) - (n^2 - 1) B_2 C] \right\rangle$$

from which

$$N = (n^2 - 1) \frac{B_1}{a^2}$$

or

$$N = (n^2 - 1)^2 \frac{B_2 C}{(n^2 C + B_2) a^2}$$

These are the known solutions for pure in-plane buckling and pure out-of-plane buckling, respectively (Reference 62).

The general solution can also be checked in the limiting case in which the radius of curvature a is infinite, i.e., the ring becomes a straight column. Let L be the have wavelength of buckling. Then $n = \pi a/L$. Also, $L/a = 0$. The final result in this case is

$$N = \frac{\pi^2}{L^2} \left\langle \left(\frac{B_1 + B_2}{2}\right) \pm \left[\left(\frac{B_1 - B_2}{2}\right)^2 + B_{12}^2\right]^{1/2} \right\rangle$$

The two values of the expressions in angle brackets are equal to the principal moments of inertia multiplied by E. Hence the resulting values of N are the Euler buckling loads in the two principal planes of the column.

4.0 RESULTS

Returning to the general solution (7), it is easily found that the minimum buckling load occurs when $n = 2$. Then the final result becomes

$$N = \frac{3}{2(4C + B_2)a^2} \left\langle [(4B_1 + 3B_2)C + (B_1 B_2 - B_{12}^2)] \right.$$

$$\left. + \left\{[(4B_1 - 3B_2)C + (B_1 B_2 - B_{12}^2)]^2 + 48 B_{12}^2 C^2\right\}^{1/2} \right\rangle$$

TABLE A-1

NOMENCLATURE FOR BUCKLING OF A CIRCULAR RING OF ARBITRARY SECTION

M_1	in-plane moment	C	torsional rigidity
M_2	out-of-plane moment	κ_1	in-plane change of curvature due to bending
T	torsional moment	κ_2	out-of-plane curvature
N	compressive force	ψ	twist
Δ_r	radial displacement	θ	polar angle
Δ_x	displacement normal to plane	n	number of lobes around circumference
ϕ	angle of twist	E	modulus of elasticity
B_1	in-plane flexural rigidity, EI_1	G	shear modulus
B_2	out-of-plane flexural rigidity, EI_2	I	moment of inertia
B_{12}	coupled flexural rigidity, EI_{12}	a	radius

APPENDIX B

INEXTENSIONAL BUCKLING OF A CONICAL SHELL-RING STRUCTURE

1.0 LOGEOMETRICAL RELATIONS AND STRAIN ENERGY

For a conical shell with one end simply supported and the other end free, the deformations are essentially inextensional. The strain-displacement relations are*

$$\epsilon_l = \frac{\partial u}{\partial l} \tag{1a}$$

$$\epsilon_\theta = \frac{1}{r}\frac{\partial v}{\partial \theta} + \frac{u}{r}\sin\alpha + \frac{w}{r}\cos\alpha \tag{1b}$$

$$\epsilon_{l\theta} = r\frac{\partial}{\partial l}\left(\frac{v}{r}\right) + \frac{1}{r}\frac{\partial u}{\partial \theta} \tag{1c}$$

and the curvatures are

$$\kappa_l = \frac{\partial^2 w}{\partial l^2} \tag{2a}$$

$$\kappa_\theta = \frac{1}{r^2}\frac{\partial^2 w}{\partial \theta^2} + \frac{1}{l}\frac{\partial w}{\partial l} - \frac{1}{r^2}\frac{\partial^2 v}{\partial \theta^2}\cos\alpha \tag{2b}$$

$$\kappa_{l\theta} = \frac{1}{\sin\alpha}\frac{\partial}{\partial l}\left[\frac{1}{l}\left(\frac{\partial w}{\partial \theta} - v\cos\alpha\right)\right] \tag{2c}$$

The assumption of inextensional deformations leads to expressions for the displacements. First, since $\epsilon_l = 0$, u is given by the equation

$$u = \frac{A}{n^2}\sin\alpha\cos\alpha\cos n\theta \tag{3a}$$

The constant has been chosen as $(A/n^2)\sin\alpha\cos\alpha$ because this simplifies the subsequent analysis. v is found by setting $\epsilon_{l\theta} = 0$. The result is

$$v = -\frac{1}{n}(A + Br)\cos\alpha\sin n\theta \tag{3b}$$

* Symbols for this Appendix are defined in Table B-1.

Where B is a second constant of integration. Finally, by setting $\epsilon_\theta = 0$, w is found:

$$w = \left[A \left(1 - \frac{\sin^2 \alpha}{n^2} \right) + Br \right] \cos n\theta \tag{3c}$$

Equivalent results may be found in the literature*

The curvatures are now found by substituting Equations (3) into Equation (2) The results are

$$\kappa_l = 0 \tag{4a}$$

$$\kappa_\theta = - \frac{n^2 - 1}{r^2} (A + Br) \cos n\theta \tag{4b}$$

$$\kappa_{l\theta} = \frac{n^2 - 1}{n r^2} A \sin \alpha \sin n\theta \tag{4c}$$

The strain energy of the deformed shell is

$$U = \frac{Da}{2} \iint [(\kappa_l + \kappa_\theta)^2 - 2(1 + \nu)(\kappa_l \kappa_\theta - \kappa_{l\theta}^2)] \, dl \, d\theta \tag{5}$$

Substitution of Equations (4) into (5) leads to the result:

$$U = (n^2 - 1) \frac{\pi D}{2 \sin \alpha} \int_0^{2\pi} \int_b^a \frac{1}{r^3} \left[(A + Br)^2 + \frac{2}{n^2} (1 - 2) \sin^2 \alpha \, A^2 \right] dr$$

$$= (n^2 - 1) \frac{\pi D}{2 \sin \alpha} \left[\left(\frac{1}{b^2} - \frac{1}{a^2} \right) \left(\frac{1}{2} + \frac{1 - \nu}{n^2} \sin^2 \alpha \right) A^2 + 2 \left(\frac{1}{b} - \frac{1}{a} \right) AB + ln \frac{a}{b} B^2 \right] \tag{6}$$

2.0 WORK DONE BY THE PRESSURE DURING BUCKLING

To find the work done on an element during buckling, the forces are summed and multiplied by the corresponding displacements. The force in the normal direction which develops on a differential element during buckling is

$$\frac{N_\theta}{r^2} \left(\frac{\partial^2 w}{\partial \theta^2} - \frac{\partial v}{\partial \theta} \cos \alpha \right) r \, d\theta \, dl$$

*Love, A. E. H., "A Treatise on the Mathematical Theory of Elasticity," section 351, Dover Publications, New York (1944).

As a result of relative rotation of the sides of an element which are initially aligned with the axial generatrices, the force N_θ also develops a component in the axial direction which has the value

$$\frac{N_\theta}{r^2} \frac{\partial^2 u}{\partial \theta^2} \; r \, d\theta \, dl$$

It is assumed that the stresses in the shell during buckling remain the same as the prebuckling stresses, which are essentially membrane stresses. Then N_θ is

$$N_\theta = \frac{pr}{\cos \alpha}$$

The total work done by N_θ, integrated over the area of a cone, is

$$V = \frac{-1}{2 \cos \alpha} \int_{b/\sin \alpha}^{a/\sin \alpha} \int_0^{2\pi} p \left[\frac{\partial}{\partial \theta} \left(\frac{\partial w}{\partial \theta} - v \right) w + \frac{\partial^2 u}{\partial \theta^2} u \right] d\theta \, dl$$

Integrating by parts with respect to θ, it is found that

$$V = \frac{1}{2 \cos \alpha} \int_{b/\sin \alpha}^{a/\sin \alpha} \left\{ -p \left[w \left(\frac{\partial w}{\partial \theta} - v \right) + u \frac{\partial u}{\partial \theta} \right]_0^{2\pi} \right.$$

$$\left. - \frac{1}{\sin \alpha} \int_0^{2\pi} \left[\left(\frac{\partial w}{\partial \theta} \right)^2 + w \frac{\partial v}{\partial \theta} + \left(\frac{\partial u}{\partial \theta} \right)^2 \right] r \, d\theta \right\} dl$$

The expression in brackets vanishes and the result becomes

$$V = \frac{1}{2 \sin \alpha \cos \alpha} \int_a^b \int_0^{2\pi} p \left[\left(\frac{\partial w}{\partial \theta} \right)^2 + u \frac{\partial v}{\partial \theta} + \left(\frac{\partial u}{\partial \theta} \right)^2 \right] r \, d\theta \, dr \qquad (7)$$

Substitution of Equations (3) into (7) leads to

$$V = \frac{\pi p}{2 \sin \alpha \cos \alpha} \left\{ (n^2 - 1) \frac{(A + Br)^3}{3B} + \frac{\sin^2 \alpha}{n^2} \left[- (n^2 - 1 - \cos^2 \alpha) A^2 r \right. \right.$$

$$\left. \left. + \cos^2 \alpha \; AB \frac{r^2}{2} + n^2 B^2 \frac{r^3}{3} \right] \right\}_b^a \qquad (8)$$

3.0 BOUNDARY CONDITIONS

Equations (6) and (8) furnish the inextensional solution for buckling of a cone under external pressure. A relation between A and B is also needed. This is obtained from the support conditions in each particular application. In the present case, the inner end is simply supported and the outer end is free. Then $w = 0$ where $r = b$, and it is found from Equation (3c) that

$$B = -\frac{A}{B}\left(1 - \frac{\sin^2 \alpha}{n^2}\right) \tag{9}$$

The problem is now solved by using Equation (9) to eliminate B from (6) and (8), after which U is set equal to V_θ. Since the shell is usually attached to a ring at the end $r = a$, it is also desirable to have relations between the constant A and the deflections perpendicular and parallel to the axis at $r = a$. The desired results are found by observing that

$$\Delta_r = w_a \cos \alpha + u_a \sin \alpha$$

$$\Delta_x = -w_a \sin \alpha + u_a \cos \alpha$$

Therefore, from (3a), (3c), and (9)

$$\Delta_r = A\left(1 - \frac{a}{b} + \frac{a}{b}\,\frac{\sin^2 \alpha}{n^2}\right) \tag{10}$$

and

$$\Delta_x = -A\left(1 - \frac{a}{b} - \frac{1}{n^2} + \frac{a}{b}\,\frac{\sin^2 \alpha}{n^2}\right) \tag{11}$$

4.0 EFFECTS OF STIFFENING RING

The analysis up to this point gives a complete solution for buckling of an unstiffened conical shell with a free end. When a ring is present at the end, the strain energy of the structure is increased. The strain energy of the deformed ring can be found by starting with the expression*

$$U = \frac{a}{2}\int (M_1 \kappa_1 + M_2 \kappa_2 + T\psi)\, d\theta$$

and applying the results of Appendix A. By using the moment curvature relations (2) of Appendix A, the expression for U can be rewritten

* The nomenclature used here for the ring is the same as in Appendix A, Table A-1.

$$U = \frac{a}{2}\int (B_1 \kappa_1^2 + B_2 \kappa_2^2 - 2B_{12} \kappa_1 \kappa_2 + C\psi^2)\, d\theta$$

Using equations (1) of Appendix A and making the substitutions

$$\Delta_r = \bar{\Delta}_r \cos n\theta, \qquad \Delta_x = \bar{\Delta}_x \cos n\theta, \qquad \phi = \bar{\phi} \sin n\theta$$

the following expression for U is found:

$$U = \frac{\pi}{2a^3}\, [(n^2 - 1)^2 B_1 \bar{\Delta}_r^2 - 2(n^2 - 1) B_{12} \bar{\Delta}_r (n^2 \bar{\Delta}_x + a\bar{\phi})$$

$$+ B_2 (n^2 \bar{\Delta}_x + a\bar{\phi})^2 + n^2 C (\bar{\Delta}_x + a\bar{\phi})^2]$$

For a ring which deforms freely during buckling, the proper relations between Δ_r, Δ_x, and ϕ would be those which make the buckling load a minimum. These relations would be given by Equations (5) of Appendix A. In the present case, the deformation of the ring must be compatible with the deformation of the shell. Hence Δ_r and Δ_x are given by Equations (10) and (11). It could also be postulated that the angle of rotation ϕ of the ring follows the assumed inextensional mode of the shell, but this would not be entirely realistic, since the rotational stiffness of a shell is not very great in comparison with that of a ring. The more conservative procedure which will be followed here is to assume that the ring finds its own preferred value of ϕ without restraint from the shell. ϕ is then found in terms of Δ_r and Δ_x by using Equation (5c) of Appendix A. By substituting the result into Equation (6), the final expression for U_{ring} is obtained:

$$U_{ring} = \frac{\pi}{2a^3}\, \frac{(n^2 - 1)^2}{n^2 C + B_2}\, [(n^2 B_1 C + B_1 B_2 - B_{12}^2)\, \bar{\Delta}_r^2$$

$$- 2n^2 B_{12} C\, \bar{\Delta}_r \bar{\Delta}_x + n^2 B_2 C\, \bar{\Delta}_x^2]$$

5.0 EFFECT OF UNSYMMETRICAL LOAD

In some cases the pressure may have an unsymmetrical as well as a symmetrical component. It will be assumed that the pressure distribution has the form

$$p = p_o + p_n \cos n\theta$$

If the pressure distribution is more complicated, it can be expressed as the sum of a series of sinusoidal terms. The work done by the unsymmetrical component is simply

$$V_{\theta n} = \frac{a}{2}\iint p_n \cos n\theta \; w \, d\theta \, dl$$

Substitution of the value of w from Equation (3c) leads to

$$V_{\theta n} = \frac{\pi p_n a L}{2}\left(A + \frac{BL}{2}\right)$$

This term may be added to the work done during buckling under symmetrical load, which is given by Equation (8).

TABLE B-1

NOMENCLATURE FOR BUCKLING ANALYSIS OF CONICAL SHELL

ϵ	extensional strain
κ	curvature
α	semi-vertex angle of cone
r	radius measured normal to axis
l	meridional coordinate measured from vertex
x	axial coordinate
u, v, w	displacements in meridional, circumferential, and normal directions, respectively
n	number of lobes around circumference
U	strain energy
V	potential energy of load
D	flexural rigidity
ν	Poisson's ratio
N	membrane force
p	external pressure
a	radius at free end
b	radius at supported end